Lecture Notes in Networks and Systems 1008

Mykola Nechyporuk
Volodymir Pavlikov
Dmytro Krytskyi *Editors*

Integrated Computer Technologies in Mechanical Engineering - 2023

Synergetic Engineering, Volume 1

Springer

Lecture Notes in Networks and Systems 1008

The series "Lecture Notes in Networks and Systems" publishes the latest developments in Networks and Systems—quickly, informally and with high quality. Original research reported in proceedings and post-proceedings represents the core of LNNS.

Volumes published in LNNS embrace all aspects and subfields of, as well as new challenges in, Networks and Systems.

The series contains proceedings and edited volumes in systems and networks, spanning the areas of Cyber-Physical Systems, Autonomous Systems, Sensor Networks, Control Systems, Energy Systems, Automotive Systems, Biological Systems, Vehicular Networking and Connected Vehicles, Aerospace Systems, Automation, Manufacturing, Smart Grids, Nonlinear Systems, Power Systems, Robotics, Social Systems, Economic Systems and other. Of particular value to both the contributors and the readership are the short publication timeframe and the world-wide distribution and exposure which enable both a wide and rapid dissemination of research output.

The series covers the theory, applications, and perspectives on the state of the art and future developments relevant to systems and networks, decision making, control, complex processes and related areas, as embedded in the fields of interdisciplinary and applied sciences, engineering, computer science, physics, economics, social, and life sciences, as well as the paradigms and methodologies behind them.

Indexed by SCOPUS, INSPEC, WTI Frankfurt eG, zbMATH, SCImago.

All books published in the series are submitted for consideration in Web of Science.

For proposals from Asia please contact Aninda Bose (aninda.bose@springer.com).

Mykola Nechyporuk · Volodymir Pavlikov ·
Dmytro Krytskyi
Editors

Integrated Computer Technologies in Mechanical Engineering - 2023

Synergetic Engineering, Volume 1

Springer

Editors
Mykola Nechyporuk
National Aerospace University – Kharkov
Aviation Institute
Kharkov, Ukraine

Volodymir Pavlikov
National Aerospace University – Kharki
Aviation Institute
Kharkov, Ukraine

Dmytro Krytskyi
National Aerospace University – Kharkov
Aviation Institute
Kharkov, Ukraine

ISSN 2367-3370 ISSN 2367-3389 (electronic)
Lecture Notes in Networks and Systems
ISBN 978-3-031-61414-9 ISBN 978-3-031-61415-6 (eBook)
https://doi.org/10.1007/978-3-031-61415-6

This Springer imprint is published by the registered company Springer Nature Switzerland AG
The registered company address is: Gewerbestrasse 11, 6330 Cham, Switzerland

Preface

The International Scientific and Technical Conference “Integrated Computer Technologies in Mechanical Engineering”—Synergetic Engineering (ICTM) was established by the National Aerospace University “Kharkiv Aviation Institute.”

The Conference ICTM’2023 was held in Kharkiv, Ukraine, during December 2023. During this conference, technical exchanges between the research communities were carried out in the forms of keynote speeches, panel discussions, as well as special sessions. In addition, participants were treated to a series of receptions, which forged collaborations among fellow researchers. ICTM’2023 received 202 papers submissions from different countries.

All of these offer us plenty of valuable information and would be of great benefit to the experience exchange among scientists in modeling and simulation. The organizers of ICTM’2023 made great efforts to ensure the success of this conference. We hereby would like to thank all the members of ICTM’2023 Advisory Committee for their guidance and advice, the members of program committee and organizing committee, and the referees for their effort in reviewing and soliciting the papers, and all authors for their contribution to the formation of a common intellectual environment for solving relevant scientific problems. Also, we are grateful to Springer-Janusz Kacprzyk and Thomas Ditzinger as the editor responsible for the series “Lecture Notes in Networks and Systems” for their great support in publishing these selected papers.

ICTM-2023 Committees

Steering Committee

Honorary Chair

Oleksii Lytvynov	Doctor of Law, Professor (National Aerospace University “Kharkiv Aviation Institute,” Kharkiv, Ukraine

Executive Chair

Mykola Nechyporuk	Doctor of Technical Sciences, Professor (National Aerospace University “Kharkiv Aviation Institute,” Kharkiv, Ukraine)

Program Committee Chair

Volodymyr Pavlikov	Doctor of Technical Sciences, Professor (National Aerospace University “Kharkiv Aviation Institute,” Kharkiv, Ukraine)

Program Committee (In Alphabetical Order)

An Bo	Doctor of Philosophy, Associate Professor (Nanyang Technological University, Nanyang, Singapore)
Yevgeniy Bodyanskiy	Doctor of Technical Sciences, Professor (Kharkiv National University of Radio Electronics, Kharkiv, Ukraine)
Valeriy Danylov	Doctor of Technical Sciences, Professor (National Technical University of Ukraine “Igor Sikorsky Kyiv Polytechnic Institute,” Kyiv, Ukraine)
Anatolii Dolmatov	Doctor of Technical Sciences, Professor (National Aerospace University “Kharkiv Aviation Institute,” Kharkiv, Ukraine)
Mariia Dorosh	Doctor of Technical Sciences, Associate Professor (Chernihiv National University of Technology, Chernihiv, Ukraine)

Olha Pohudina	Doctor of Philosophy, Associate Professor (National Aerospace University "Kharkiv Aviation Institute," Kharkiv, Ukraine)
Illia Polosukhin	NEAR.ai, San Francisco, CA, USA
Mykola Ponomarenko	Doctor of Technical Sciences, Senior Research Associate (Tampere University, Tampere, Finland)
Volodymyr Ponomaryov	Doctor of Technical Sciences, Professor (Instituto Politécnico Nacional, Mexico City, Mexico)
Viktor Popov	Doctor of Philosophy (Joint Stock Company FED, Kharkiv, Ukraine)
Karol Przystalski	Doctor of Philosophy (Jagiellonian University, Kraków, Poland)
Anatoliy Sanin	Doctor of Technical Sciences, Professor (Oles Honchar Dnipro National University, Dnipro, Ukraine)
Nataliya Shakhovska	Doctor of Technical Sciences, Professor (Lviv Polytechnic National University, Lviv, Ukraine)
Olga Shypul	Doctor of Philosophy, Associate Professor (National Aerospace University "Kharkiv Aviation Institute," Kharkiv, Ukraine)
Oleksandr Sokolov	Doctor of Technical Sciences, Professor (Nicolaus Copernicus University, Toruń, Poland)
Yuriy Stoyan	Corresponding Member of the National Academy of Science of Ukraine, Doctor of Technical Sciences, Professor (A. Pidgorny Institute of Mechanical Engineering Problems of the National Academy of Sciences of Ukraine, Kharkiv, Ukraine)
Tibor Szalay	Doctor of Philosophy, Associate Professor (Budapest University of Technology and Economics, Budapest, Hungary)
Ihor Turkin	Doctor of Technical Sciences, Professor (National Aerospace University "Kharkiv Aviation Institute," Kharkiv, Ukraine)
Mykhaylo Ugryumov	Doctor of Technical Sciences, Professor (V. N. Karazin Kharkiv National University, Kharkiv, Ukraine)
Valerii Volosyuk	Doctor of Technical Sciences, Professor (National Aerospace University "Kharkiv Aviation Institute," Kharkiv, Ukraine)
Benoit Vozel	Doctor of Philosophy, Associate Professor (University of Rennes 1, Rennes, France)

Charles K. Whitehead	Doctor of Sciences, Professor (Cornell University, Ithaca, NY, USA)
Sergey Yakovlev	Doctor of Physics and Mathematics, Professor (National Aerospace University "Kharkiv Aviation Institute," Kharkiv, Ukraine)
Michael Yudelson	Doctor of Philosophy (Carnegie Mellon University, Pittsburgh, PA, USA)
Volodymyr Zaslavskyi	Doctor of Technical Sciences, Professor (Taras Shevchenko National University of Kyiv, Kyiv, Ukraine)
Andrew Zavgorodniy	Doctor of Philosophy (LinkedIn, Milpitas, CA, USA)

Organizing Team

(National Aerospace University "Kharkiv Aviation Institute," Kharkiv, Ukraine)

Publication Chair

Dmitriy Kritskiy

Members (in Alphabetical Order)

Andrii Bykov
Vasylysa Kalashnikova
Oleksandr Karatanov
Olha Krytska
Olga Shypul

Contents

Information Modeling

Information Technology in the Creation of Rocket Space Systems

Aerospace Engineering

Statistical Analysis of Airplane Pressure Altitude Datasets

Ivan Ostroumov(✉)

National Aviation University, Liubomyra Huzara Avenue, 1, Kyiv 03058, Ukraine
ostroumov@ukr.net

Abstract. Pressure altitude is primary data for airplane vertical positioning. Modern air transportation system uses flight leveling system based on pressure altitude readings. This altitude is calculated by a hypsometric equation based on International Standard Atmosphere model from measured static pressure data at altitude of airplane location. Pressure altitude on board heavy airplanes is measured by an Air Data System and shared with other airspace users and ground facilities of Air Traffic Control with a specific data link. Different errors affect reading of pressure altitude. In the paper, we provide a statistical analysis of pressure altitude data to create an error model. We consider usage of Probability Density Functions (PDF) to analyze error distribution. A Triple Univariate Generalized Error Distribution (TUGED), Double Exponential PDF (DEPDF), normal PDF (NPDF), and kernel PDF (KPDF) are used in statistical data analysis. In the numerical demonstration, we use pressure altitude data fixed by Flight Data Recording System to analyze PDF and estimate probabilities (risks) of cleared flight level loss.

Keywords: Air Navigation · Pressure Altitude · Statistical Analysis · Air Data System · Data Processing · Safety · Aviation

1 Introduction

Operation of modern air traffic system is grounded on some criteria of efficiency from one side and insuring minimal levels of flight safety from another one. Air transportation uses a network of flight routes to perform traffic control safely [1]. Airspace users enter this network at the final point of Standard Instrument Departure (SID) procedure. This network includes waypoints and linear edges between two nearest nodes [2]. Airplanes are moving in the network by a sequence of waypoints. The sequence of waypoints to be used is specified in the flight plan. Flight plans have to be submitted to the aviation authority before any take-off. Civil aviation authority proceed with all submitted flight plans taking into account forecasted weather distribution to manage traffic flows based on criteria of safety.

To manage applied traffic on the edge between each pair of waypoints a vertical separation is used [3, 4]. Values of vertical separation specify flight level (FL). Air traffic controller specify for each airspace user a particular FL to ensure minimum separation levels that make air traffic flow safely. Flight levels are grounded on pressure altitude

M. Nechyporuk et al. (Eds.): ICTM 2023, LNNS 1008, pp. 3–14, 2024.
https://doi.org/10.1007/978-3-031-61415-6_1

counted from Mean Sea Level (MSL). A pressure altimeter is used on-board an airplane to measure altitude and for maintaining a cleared flight level.

Primary surveillance radars are used as the main surveillance sensor on the side of the air navigation service provider [5, 6]. However, there are no sensors that can measure pressure altitude remotely outside the airplane. Readings of pressure altimeter are transmitted automatically downside by digital data link in Automatic Dependent Surveillance-Broadcut (ADS-B) or by information message of secondary surveillance radar [7, 8]. Received pressure altitude values are used for air traffic control (ATC). ATC uses raw altitude data without any data processing or improvements in visualization.

On-board pressure altimeter sensor is working under influence of vary of factors which can reduce performance significantly. In addition, each sensor provides measurements with errors.

Pressure altimeter uses a hypsometric equation to calculate altitude by measuring value of static pressure at the point of airplane location. Static pressure depends on parameters of atmosphere that could fluctuate with weather changes [9, 10]. Atmosphere fluctuation covers significant airspace volumes [11]. However, the same weather influence within particular airspace readings of static pressure in different airplanes provides a small influence on relative altitude between airspace users, which supports safe air traffic.

Pressure altimeter is widely used in Unmanned Aerial Vehicles (UAV) to control altitude [12, 13]. In low-range UAV pressure altitude data is used in reference to pressure altitude at ground level to obtain reference altitude to the ground.

Wide range of sensor operational limits, simple structure, and low cost make a pressure altimeter present in the equipment list of any fly vehicle [14, 15]. Also, pressure altimeter could be referred to the primary altitude measuring system on-board. A set of altitude data gives a vertical profile of airplane flight and could be used in a variety of applications. Vertical profile is useful for automatic flight phase identification algorithms of automatic flight control systems [16, 17]. Pressure altitude is calculated from measured static pressures in a computation unit based on a set of sensors, that makes action on the reliability analysis of a total system [18, 19].

In the paper, we provide a statistical analysis of pressure altitude data and develop software for accumulated data proceeding of airplane altitude data based on multiple flight realizations of unique flight connection. Software could be useful to estimate a parameter of probability density function that could be used to create a model of sensor errors. Also, software provides an estimation of a confidence band for altitude based on a predefined value of evidence.

2 On-Board Equipment

There are different configurations of pressure altimeter installation. Some of them could be fully mechanical based on aneroid box (small gas camera with constant pressure) and mechanical circles to rotate arrows that point to particular values of MSL altitude in a circular scale. A mechanical instrument for pressure altitude measurements is mostly used in general aviation. Also, there are some mechanical instruments which include some electrical sensors to transform mechanical forces acting on an aneroid box to electrical signals. A resistance electrical scheme is used to transform mechanical variation to the range of voltage in two wires. Unfortunately, precision of aneroid box into pressure variation could not give the best pressure readings.

Most heavy airplanes use an Air Data System (ADS) for measuring all parameters which correspond to the airflow. A common ADS interconnection scheme is shown in Fig. 1. ADS uses specific static pressure ports to grab part of air and move it by hermetic tube system to the sensor unit. Due to airplane maneuvering, airflow could apply to the body of airplane at different angles. In particular scenarios, some part of dynamic pressure could be caught by air static ports. In order to reduce influence of dynamic pressure in static readings two sets of static pressure ports are used at the beginning of fuselage on the left and right sides at the point where airflow has minimal disturbances. Up and bottom locations have been never used due to appearance of a dynamic component in climbing and descending phases of flight. Pressure readings are performed by a digital sensor which measures and provides output data in binary form. ARINC 429 could be used for digital data transferring from sensor to the central processing unit.

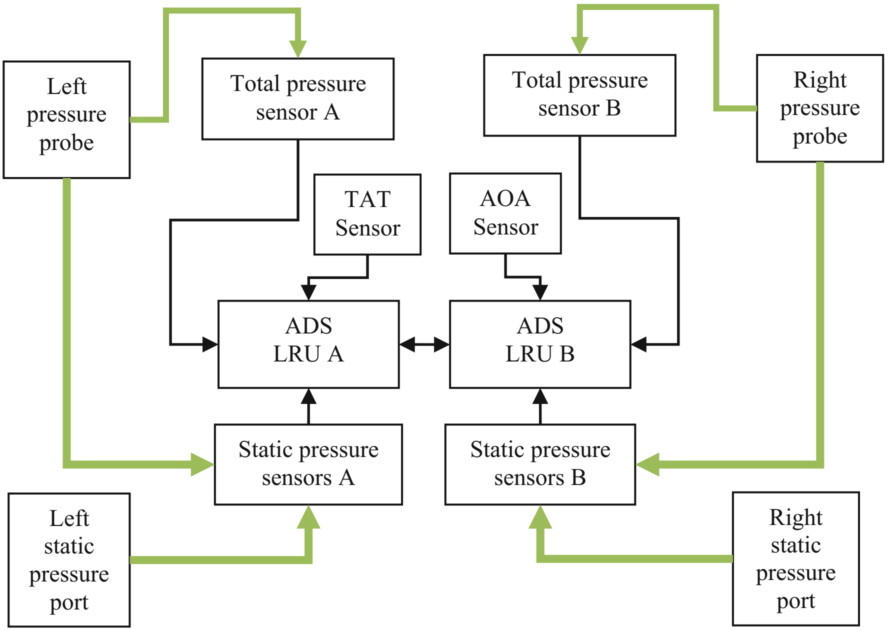

Fig. 1. Air Data System sensor connections scheme.

Also, ADS provides calculation of airspeed based on dynamic pressure measurements. Pitot probes are used to catch airflow out of the compressed airflow near the airplane body. Thus, pitot probes are moved out fuselage at some distance. A cached portion of air is applied to total and static pressure sensors. In addition, ADS uses specific probes to measure total air temperature (TAT) and Angle of Attack (AOA). Result of measurements in digital form comes to the processing equipment of ADS. Two identical ADS processors are placed in the avionics bay as typical line-replaced units (LRU). Two sides of ADS increase reliability of parameters provided [20].

Pressure altitude is calculated based on static pressure and international standard atmosphere (ISA) values [21, 22]:

In case if $\tau_i \neq 0$.

$$h = \left[\left(\frac{p}{p_i} \right)^{\frac{-\tau_i R}{g}} - 1 \right] \frac{T_i}{\tau_i} + h_i, \tag{1}$$

In case if $\tau_i = 0$

$$h = \frac{RT_i}{-g} ln\left(\frac{p}{p_i} \right) + h_i, \tag{2}$$

where p is a static pressure [Pa]; τ is standard vertical temperature gradient [K/km]; R = 8314.3 is universal gas constant [J/(Kkmol)]; g = 9.8 is a standard acceleration due to gravity [m/s^2]; T is a reference temperature; i is number of atmospheric layer.

Values of parameters p_i, τ_i, T_i, and h_i in (1) and (2) depending on the altitude layer. These parameters for three basic atmospheric layers are presented in Table 1.

Table 1. Parameters of atmospheric layers.

Atmospheric layer, i	Standard pressure, p_i, [Pa]	Altitude, h_i, [m]	Reference temperature, T_i, [K]	Vertical temperature gradient, τ_i, [K/km]
1	101325	0	288.15	–6.5
2	22632	11 000	216.65	0
3	5474	20 000		1.0

Pressure altitude measurements were performed in a noisy environment. There are two main error components: instrument and position errors [23, 24]. Instrument error includes noise related to sensor and ADS processing equipment operation. Position error is a result of catching some influence of total pressure in static probes. In this case, p is not the actual static pressure required in (1) and (2). Position error depends on the place of pitot tube and static pressure ports. To minimize influence of position error multiple places of catching air are used. As an example, two static ports and two/three pitot probes on different sides of airplane body are used to minimize influence of position error.

3 Statistical Analysis

During the en-route phase of flight, airplanes have to maintain a cleared FL. FLs are set up by ISA pressure altitude. Taking into account a reduced vertical separation minimum FL below 410FL are placed each 300 m and 600 m increment is used for FL above 410FL [25]. Each airspace user has to maintain the central altitude of each cleared FL.

Unexpected weather action, noise, and performance of automatic flight control system result in pressure altitude fluctuation. Statistical analysis of raw pressure altitude data for en-route phase of flight helps to study the error model more precisely and makes it possible to estimate the risk of cleared flight level loss which is a valuable safety component [26]. Identification of horizontal flight could be done with a simple vertical speed threshold or by a probability-based method of flight phase identification [27]. The dataset of one flight usually is short for statistical analysis. We could recommend using a database of historical flights of one particular airframe to get length enough of the dataset.

Different sources of data could be used in statistical analysis. Data obtained by ADS-B ground network usually is not periodic and includes multiple gaps. Data from Flight Data Recording (FDR) System is much more useful. FDR dataset is synchronized and may be archived with different frequencies. Also, FDR usually provides data from both ADS LRUs separately, which gives two pressure altitude reading for each time.

Fluctuation of pressure altitude could be studied with probability density functions (PDF). Statistical analysis of data gives PDF distribution which could be used as an error model for particular equipment configuration. We consider a few PDFs: Triple Univariate Generalized Error Distribution (TUGED), Double Exponential PDF (DEPDF), normal PDF (NPDF), and kernel PDF (KPDF).

NPDF is described by only two parameters mean (μ) and standard deviation error (σ):

$$\mu = \frac{1}{n}\sum\nolimits_{i=1}^{n} h_i, \tag{3}$$

$$\sigma = \sqrt{\frac{1}{n-1}\sum\nolimits_{i=1}^{n}(h_i - \mu)^2}, \tag{4}$$

where n is the dataset length.

DEPDF consists of two components: the first one describes the main lobe and the second one controls tails:

$$DEPDF = \frac{\alpha}{2a_1 b_1 \Gamma(b_1)} exp\left(-\left|\frac{h-m}{a_1}\right|^{b_1^{-1}}\right) + \frac{1-\alpha}{2a_2 b_2 \Gamma(b_2)} exp\left(-\left|\frac{h-m}{a_2}\right|^{b_2^{-1}}\right), \tag{5}$$

where α is distribution coefficient; $a_{1,2}$ is scale coefficient; $b_{1,2}$ *is* shape coefficient; Γ is gamma-Euler function; m is mean value.

A TUGED model uses three components represented by separate generalized error distributions [28]. Three components of TUGED take into account sensor measuring error, error of maintaining airplane at cleared FL, and influence of rare factors:

$$TUGED = \alpha f(a_1, b_1, h) + \beta f(a_2, b_2, h) + (1 - \alpha - \beta) f(a_3, b_3, h), \tag{6}$$

$$f(a, b, h) = \frac{1}{2ab(b)} exp\left(-\left|\frac{h-b}{a}\right|^{b^{-1}}\right), \tag{7}$$

where α and β are weight coefficients; a is scale coefficient; b is shape coefficient.

In DEPDF and TUGED calculated by (5) and (6) specific constraints could be used to make adequate parameter fitting: $0.5 \le b \le 1$; $1 \le a$; $0 \le \alpha \le 1$; $0 \le \alpha + \beta \le 1$.

During the fitting process with DEPDF and TUGED a tail component could be tuned precisely to obtain adequate data with a small learning sample.

Also, a common KPDF [29, 30] may be used for fitting pressure altitude dataset:

$$\text{KPDF} = \frac{1}{nl}\sum\nolimits_{i=1}^{n} f\left(\frac{h - D_i}{l}\right) \tag{8}$$

where n is dataset length; l is bandwidth; $f(x)$ is kernel; D_i is i-th element of input pressure altitude dataset.

Different kernel functions could be used as a core function. We use the Gaussian kernel function in the following form:

$$f(x) = \exp\left(\frac{-x^2}{2\int^{e} xp\left(-\frac{x^2}{2}\right)dx}\right). \tag{9}$$

Different PDF gives a range of results that could be applied to different types of analysis.

4 Software

Specific software has been developed to provide statistical analysis of pressure altitude data based on datasets provided by FDR system. Airlines use specific software for analyzing the whole sequence of recorded parameters. This software includes decoding and visualization tools for representation of data by each available parameter. Also, common FDR processing software supports extraction of any parameter sequence in a separate file. Therefore it makes sense to use a folder of extracted pressure altitude data in separate files for each flight as input for statistical pressure altitude analysis.

Statistical analysis involves usage of big data, due to all flights datasets could be processed together to make PDF fitting process possible. A structure scheme of developed software in C++ is presented in Fig. 2.

At the beginning of software run an input folder with datasets is analyzed to detect a set of files to be imported. A path for input folder is specified in the menu settings. Reading of files is based on a template of data representation. Imported data are saved in local variables. Pressure altitude is analyzed only for en-route flight phase automatical detected. Identified time of horizontal flight is used to cut pressure altitude data. Based on input data we analyze an altitude of cleared FL. Cleared FL is used to calculate deviation of current pressure altitude. Values of these deviations are stored together for different FLs and will be used in statistical data analysis.

A histogram of airplane deviations from cleared FL could be created based on frequency. Archive of airplane deviations from cleared FL is used to calculate the mean (3) and standard deviation error (4). Coefficients of DEPDF and TUGED are estimated

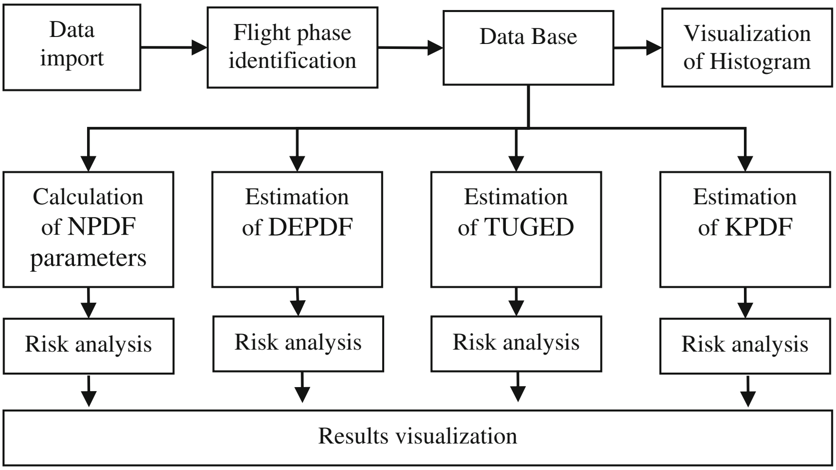

Fig. 2. Structure scheme of software for statistical analysis.

based on Maximum Likelihood Method with constraints. The fitting of KPDF is based on frequency distribution.

Coefficients of PDFs are used to estimate probabilities of airplane being out of cleared FL. These probabilities are calculated as area below a particular model of PDF within cleared FL perils (300 m or 600 m). Estimated risk values for DEPDF and TUGED are going to be bigger than NPDF and KPDF due to intended PDF tail tuning.

Visualization toolbox represents a histogram of deviations from cleared FL by plotting different PDF models.

5 Numerical Demonstration

In a numerical demonstration, we use flight data recorded by the FDR system. We use 23 realizations of one flight connection performed with the unique regional airplane An-140 during September-October 2007. The full data set includes about 0.27×10^6 data points. For all flights, FL 130 was cleared level. After detecting en-route phase of flight total size of data was about 0.16×10^6 points. FDR provides pressure and reference to aerodrome altitudes from both ADSs. It gives two pressure altitude measurements at each second of flight.

Pressure altitudes fluctuation at en-route phase of flight for one flight from both ADSs are presented in Fig. 3. A histogram of pressure altitude fluctuation at en-route phase for one flight is presented in Fig. 4 with a bin width of 5 m.

Results of statistical data processing for total dataset which include 0.16×10^6 data points for en-route are represented in Fig. 5. Fitting gives the following results:

NPDF: $\mu = -0.18$ m; $\sigma = 9.29$ m;

DEPDF: $\alpha = 0.3$; $m_1 = 0.59$ m; $m_2 = 0.01$ m; $a_1 = 2.6$; $a_2 = 14.4$;$b_1 = 0.5$; $b_2 = 0.5$;

TUGED: $\alpha = 0.45$; $\beta = 0.45$; $m_1 = 0$ m; $m_2 = 0$ m; $m_3 = 0$ m; $a_1 = 30$; $a_2 = 10$;$a_3 = 2$; $b_1 = 0.5$; $b_2 = 0.5$;$b_3 = 1$.

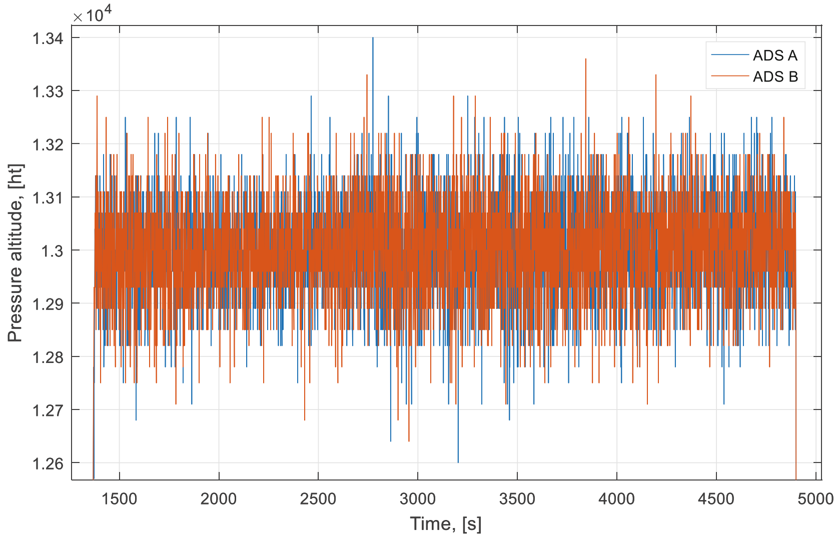

Fig. 3. Pressure altitude fluctuation at an en-route phase of flight.

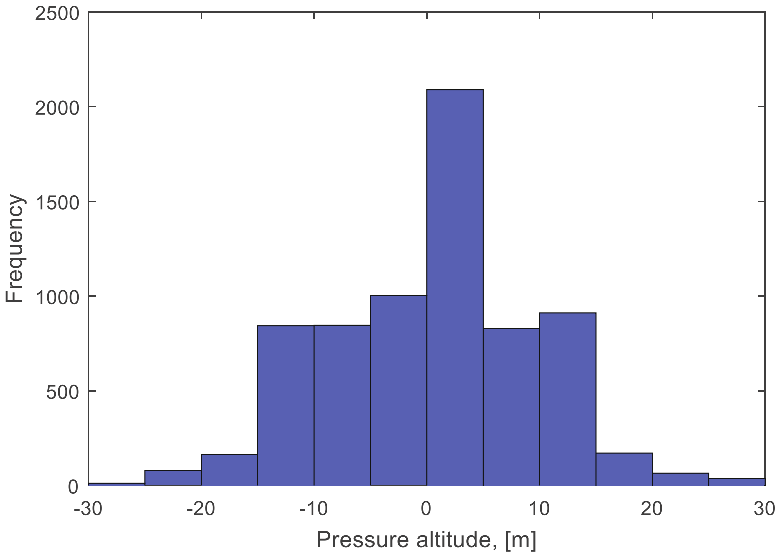

Fig. 4. Histogram of pressure altitude fluctuation at an en-route phase of flight.

ADS for this class of airplanes gives data with a scale of two meters. That makes a histogram with 1 m bin width space distributed. Statistical analysis with KPDF with 1 m bin width is tension to scale of represented data. Fitted KPDF are fluctuate periodically within the study range of pressure altitude.

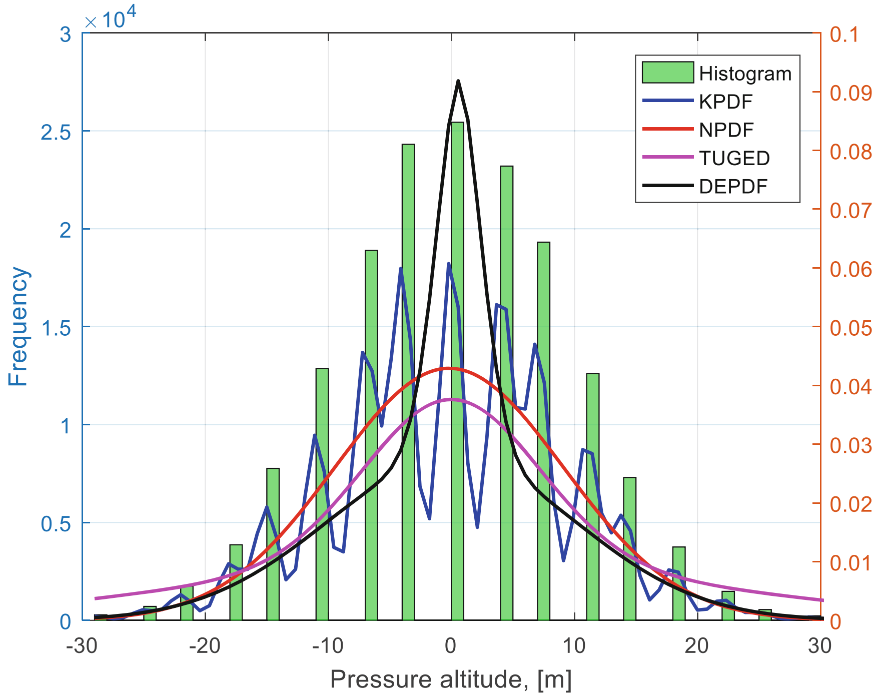

Fig. 5. Results of statistical analysis.

Results of fitting with DEPDF have an identified main core and tails. TUGED provides results with especially increased tails which may help for cases of small learning samples, because rare events may not be appeared during the finite sample length.

Based on estimated PDFs (NPDF, DEPDF, TUGED, and KPDF) we could estimate the risk of flight level loss. We could use ±100 m for perils to estimate the probability of airplane being out of cleared FL. These probability values could be estimated as an area under PDFs in the range from $-\infty$ to left perils plus an area in the range from right peril to $+\infty$.

Results of probability (risk) estimation for the case of cleared FL loss is following:

- TUGED: $P(-100 < h > 100) = 1.2 \times 10^{-6}$;
- DEPDF: $P(-100 < h > 100) = 1.1 \times 10^{-7}$;
- NPDF: $P(-100 < h > 100) = 3.4 \times 10^{-27}$.

Obtained results admit possibility to use TUGED and DEPDF analysis for risk estimation related to factors acting into pressure altitude.

6 Conclusions

Pressure altitude is an important parameter of air traffic safety. Altitude readings from standard pressure isobaric level is a simple approach to organizing safe air traffic flow with insuring minimum vertical separation. Vertical separation minimum is developed based on errors of pressure altitude sensor to ensure safe maintenance of cleared flight levels. Pressure altimeter is affected by different errors action that results in fluctuation of pressure sensor readings. Statistical analysis of pressure altitude during an en-route phase of flight makes it possible to identify confidence bands for particular equipment used on-board of airplane.

Results of statistical analysis indicate about perspective to use DEPDF and TUGED to analyze errors action on static pressure sensors in readings of pressure altitude. ADS-B data could not be considered as input for statistical analysis due to the low length of the dataset. Data fixed in the flight data recorder system includes readings of both ADSs that gives two datasets with a high frequency of updating for pressure altitude statistical analysis.

Results of pressure altitude statistical analysis give probabilities of airplane being out of cleared flight level. Numerical demonstration gives a risk of flight level loss at levels of 1.2×10^{-6} for TUGED and 1.1×10^{-7} for DEPDF. Obtained results could be useful in safety analysis based on equipment type and for error clusterization.

References

1. Mihetec, T., Odic, D., Steiner, S.: Evaluation of night route network on flight efficiency in Europe. Int. J. Traffic Transp. Eng. **1**(3), 132–141 (2011)
2. Ivashchuk, O., Kuzmenko, N.S., Sushchenko, O., Averyanova, Y., Yanovsky, F., Shcherbyna, O.: A configuration analysis of Ukrainian flight routes network. In: 16th International Conference on the Experience of Designing and Application of CAD Systems, pp. 6–10. IEEE, Lviv, Ukraine (2021)
3. Dias, F.H., Hijazi, H., Rey, D.: Disjunctive linear separation conditions and mixed-integer formulations for aircraft conflict resolution. Eur. J. Oper. Res. **296**(2), 520–538 (2022). https://doi.org/10.1016/j.ejor.2021.03.059
4. Ostroumov, I.V., Kuzmenko, N.S.: Statistical analysis and flight route extraction from automatic dependent surveillance-broadcast data. In: Integrated Communications Navigation and Surveillance Conference (ICNS), pp. 1–9. IEEE, Dulles, VA, USA (2022). https://doi.org/10.1109/ICNS54818.2022.9771515
5. Volosyuk, V., Zhyla, S., Pavlikov, V., Ruzhentsev, N., Tserne, E., Popov, A.: Optimal method for polarization selection of stationary objects against the background of the earth's surface. Int. J. Electron. Telecommun. **68**(1), 83–89 (2022)
6. Zhyla, S., Volosyuk, V., Pavlikov, V., Ruzhentsev, N., Tserne, E., Popov, A.: Practical imaging algorithms in ultra-wideband radar systems using active aperture synthesis and stochastic probing signals. Radioelectronic Comput. Syst. **105**(1), 55–73 (2023)
7. Technical Provisions for Mode S Services and Extended Squitter, Doc 9871, First Edition, Monreal, Canada, ICAO (2008)
8. Kuzmenko, N.S., Ostroumov, I.V.: Performance analysis of positioning system by navigational aids in three dimensional space. In: 1st International Conference System Analysis & Intelligent Computing IEEE, pp. 101–104. IEEE, Kyiv, Ukraine (2018)
9. Averyanova, Y., Larin, V., Kuzmenko, N., Zaliskyi, M., Solomentsev, O.: Turbulence detection and classification algorithm using data from AWR. In: 2nd Ukrainian Microwave Week (UkrMW), pp. 518–522. IEEE, Kharkiv, Ukraine (2022)
10. Ruzhentsev, N., Zhyla, S., Pavlikov, V., Volosyuk, V., Tserne, E., Popov, A.: Radio-heat contrasts of UAVs and their weather variability at 12 GHz, 20 GHz, 34 GHz, and 94 GHz frequencies. ECTI Trans. Electr. Eng. Electron. Commun. **20**(2), 163–173 (2022)

11. Popov, A., Tserne, E., Zhyla, S., Volosyuk, V., Pavlikov, V., Ruzhentsev, N.: Invariant polarization signatures for recognition of hydrometeors by airborne weather radars. In: Computational Science and Its Applications ICCSA 2023. Lecture Notes in Computer Science, vol. 13956, pp. 201–217. Springer, Cham (2023)
12. Sushchenko, O., Averyanova, Y., Kuzmenko, N., Zaliskyi, M., Solomentsev, O.: Algorithms for design of robust stabilization systems. In: Computational Science and Its Applications ICCSA 2022. Lecture Notes in Computer Science, vol. 13375, pp. 198–213. Springer, Cham (2022)
13. Larin, V., Solomentsev, O., Zaliskyi, M., Shcherban, A., Averyanova, Y.: Prediction of the final discharge of the UAV battery based on fuzzy logic estimation of information and influencing parameters. In: 3rd KhPI Week on Advanced Technology (KhPI Week), pp.44–49. IEEE, Kharkiv, Ukraine (2022)
14. Liu, X.X., Zhao, X.B., Pang, C.L.: Research on SINS/GNSS/CNS/pressure altimeter federated filtering adaptive fault tolerance method. In: China Satellite Navigation Conference, pp. 444–454, Springer Nature Singapore (2022). https://doi.org/10.1007/978-981-19-2580-1_38
15. Sushchenko, O., Bezkorovainyi, Y., Solomentsev, O., Kuzmenko, N., Averyanova, Y.: Airborne sensor for measuring components of terrestrial magnetic field. In: 41st International Conference on Electronics and Nanotechnology (ELNANO), pp. 687–691. IEEE, Kyiv, Ukraine (2022)
16. Kuzmenko, N., Ostroumov, I., Bezkorovainyi, Y., Averyanova, Y.: Airplane flight phase identification using maximum posterior probability method. In: 3rd International Conference on System Analysis & Intelligent Computing (SAIC), pp. 1–5, IEEE, Kyiv, Ukraine, (2022). https://doi.org/10.1109/SAIC57818.2022.9922913
17. Havrylenko, O., Dergachov, K., Pavlikov, V., Zhyla, S., Shmatko, O., Ruzhentsev, N.: Decision support system based on the electre method. In: Data Science and Security. Lecture Notes in Networks and Systems, vol. 462, pp. 295–304. Springer, Singapore (2022)
18. Zaliskyi, M., Solomentsev, O., Larin, V., Averyanova, Y., Kuzmenko, N.: Model building for diagnostic variables during aviation equipment maintenance. In: 17th International Conference on Computer Sciences and Information Technologies (CSIT), pp. 160–164. IEEE, Lviv, Ukraine (2022)
19. Solomentsev, O., Zaliskyi, M., Sushchenko, O., Bezkorovainyi, Y., Averyanova, Y.: Data processing through the lifecycle of aviation radio equipment. In: 17th International Conference on Computer Sciences and Information Technologies (CSIT), pp. 146–151 IEEE, Lviv, Ukraine (2022)
20. Solomentsev, O., Zaliskyi, M., Averyanova, Sushchenko, O.: Method of optimal threshold calculation in case of radio equipment maintenance. In: Data Science and Security. Lecture Notes in Networks and Systems, vol. 462, pp. 69–79. Springer, Singapore (2022)
21. ICAO Standard Atmosphere. Doc 7488. ICAO (1993)
22. Grigorie, T.L., Dinca, L., Corcau, J.I., Grigorie, O.: Aircrafts' altitude measurement using pressure information: barometric altitude and density altitude. Wseas Trans. Circ. Syst. **9**(7), 503–512 (2010)
23. Rodi, A.R., Leon, D.C.: Correction of static pressure on a research aircraft in accelerated flight using differential pressure measurements. Atmos. Measur. Tech. **5**(11), 2569–2579 (2012). https://doi.org/10.5194/amt-5-2569-2012
24. Reasor, D.A., Bhamidipati, K.K., Woolf, R.K.: Numerical predictions of static-pressure-error corrections for a modified T-38C aircraft. J. Aircr. **52**(4), 1326–1335 (2015). https://doi.org/10.2514/1.C032925
25. Air traffic management, Procedures for Air Navigation Services, Doc. 4444, ICAO (2016)
26. A Unified Framework for Collision Risk Modelling in Support of the Manual on Airspace Planning Methodology for the Determination of Separation Minima. Doc. 9689. ICAO (2009)

27. Kuzmenko, N.S., Kharchenko, V.P., Ostroumov, I.V.: Identification of unmanned aerial vehicle flight situation. In: 5th International Conference Actual problems of unmanned aerial vehicles development: APUAVD-2017, pp. 116–120, IEEE, Kyiv, Ukraine (2017). https://doi.org/10.1109/APUAVD.2017.8308789
28. Ostroumov, I.V., Marais, K., Kuzmenko, N.S., Fala, N.: Triple probability density distribution model in the task of aviation risk assessment. Aviation **24**(2), 57–65 (2020). https://doi.org/10.3846/aviation.2020.12544
29. JooSeuk, K., Scott, C.: Robust kernel density estimation. Mach. Learn. Res. **13**(1), 2529–2565 (2012)
30. Zhixiao, X., Yan, J.: Kernel density estimation of traffic accidents in a network space. Comput. Environ. Urban Syst. **32**(5), 396–406 (2008)

Forced Nonlinear Bending Vibrations of Beams with Two Breathing Cracks

K. Avramov[1,2,3](✉), S. Malyshev[4], V. Miroshnikov[1], and I. Hariachevska[5]

[1] National Aerospace University N.Ye. Zhukovsky "KhAI", Kharkiv, Ukraine
[2] Anatolii Pidhornyi Institute of Mechanical Engineering Problems of the National Academy of Sciences of Ukraine, Kharkiv, Ukraine
avramov@nas.gov.ua
[3] Kharkiv National University of Radio Electronics, Kharkiv, Ukraine
[4] National Technical University "Kharkiv Polytechnic Institute", Kharkiv, Ukraine
[5] V. N. Karazin, Kharkiv National University, Kharkiv, Ukraine

Abstract. The nonlinear bending vibrations of the cracked beams are studied. The beam structure has two breathing cracks, which are described by two contact parameters. The nonlinear beam vibrations are described by finite degrees of freedom nonlinear dynamical system, which are derived by using the Galerkin technique. The numeric continuation method is implemented to study the nonlinear forced vibrations of beams. The bifurcation behavior of forced vibrations is analyzed numerically. The period- doubling bifurcations and the Naimark-Sacker bifurcations of the cracked beam are analyzed.

Keywords: nonlinear bending vibrations · cracked beam · bifurcation behavior

1 Introduction

The dynamic features of the structures with cracks are used frequently to perform the nondestructive testing. The sensitive of the cracked structure oscillations to the parameters of defects is applied in this testing. The cracks parameters can be obtained from the oscillations of cracked structure [1, 2], which are nonlinear. Several efforts were carried out to analyze this problem. The partial differential equation of the cracked beam oscillations are derived in [3]. The partial differential equations of cracked beam motions are transformed into the system of the ordinary differential equations by the Galerkin technique [4]. The partial differential equations of the beam with cracks motions are derived from a variation method in [5, 6]. The parametric vibrations of the beam with crack are analyzed in [7]. The nonlinear normal modes of beams with crack are considered by Chati with co-authors [8]. The nonlinear oscillations of cracked beam are considered by Caddemi with co-authors [9]. The nonlinear oscillations of the cracked beam satisfy the system of the partial differential equations with delta function [10]. The rotor with crack is considered in the paper [11]. The geometrical nonlinear vibrations of beam with open crack are considered by Bikri and co-authors [12]. The oscillations of the cantilever beam with two cracks are analyzed in [13]. Chaotic motions are observed as a result of periodic-doubling bifurcations.

M. Nechyporuk et al. (Eds.): ICTM 2023, LNNS 1008, pp. 15–24, 2024.
https://doi.org/10.1007/978-3-031-61415-6_2

The bending vibrations of the beam with two cracks are considered with simply supported boundary conditions. The beam oscillations with the breathing crack are described by the partial differential equation with contact parameters. The finite degrees of freedom nonlinear system is obtained by expansion of the beams motions using the structure eigenmodes and the Galerkin technique. The continuation numerical algorithm is used to study the bifurcations of nonlinear periodic oscillations. The periodic-doubling bifurcations and Naimark- Sacker bifurcations are detected numerically to analyze sub-harmonic vibrations and almost periodic motions.

2 Equations of the Structure Oscillations

The nonlinear oscillations of the flexural beam with rectangular cross section and breathing cracks are considered. The breathing crack has nonlinear properties, i.e. it opens and closes. The Euler beam theory is used to obtain the mathematic model of the structure. The beam material satisfies the Hooke's law. The structure vibrations are described by the partial differential equation [14]:

$$E_0 I_0 \left\{ \left[1 - \sum_{i=1}^{2} b_i \, \gamma_i \delta(x - x_{0i}) \right] u''_{XX} \right\}''_{XX} + m\ddot{u} = p(x, t) \, , \tag{1}$$

where $\delta(x - x_{0i})$ is delta function; $x_{0,1}$; $x_{0,2}$ are cracks locations coordinates; γ_i is parameter of the damage intensity; $\mathbf{B} = (b_1, b_2)$ are parameters of the contacts, which describe the breathing of the crack; u is flexural displacements; $p(x, t)$ is external distributional force; m is distributed mass; $E_0 I_0$ is bending stiffness of the undamaged beam.

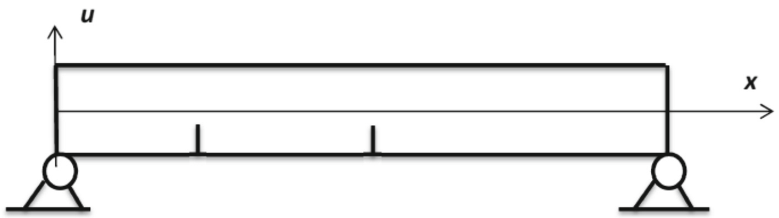

Fig. 1. Cracked beam with simply-supported boundary conditions

The left defect and the right one (Fig. 1) are indicated by C and D. If the parameter $b_i = 1$, then open crack is observed. The close crack is observed, if $b_i = 0$. The parameter u''_{xx} is used to indicate the breathing of crack. Then the crack opening and closing satisfy the following relations:

$$\begin{cases} u''\big|_{x=x_{0,i}} > 0 \, ; \;\; b_i = 1 \, ; \\ u''\big|_{x=x_{0,i}} < 0 \, ; \;\; b_i = 0 \, . \end{cases} \tag{2}$$

Four types of the cracked beam motions are considered with respect to the parameters b_i.

$b_1 = 0;\ b_2 = 1$; the defects C and D are closed and opened, respectively;
$b_1 = b_2 = 0$; both defects C and D are closed;
$b_1 = 1;\ b_2 = 0$; the defects C and D are opened and closed, respectively;
$b_1 = b_2 = 1$; the defects C and D are opened.

The cracked beam oscillations are described by finite degree of freedom piecewise-linear dynamical system. Phases of the beam motions are described by the set of contact parameters (b_1, b_2). These phases eigenmodes are indicated by $W^{(i)}_{b_1,b_2}(\xi)$; $i = 1, 2, \ldots$.. The beam with two closed cracks has the eigenmode $W^{(i)}_{0,0}(\xi) = \sin(i\pi\xi)$, where $\xi = \frac{x}{L}$; L is length of the beam.

The Galerkin technique is used to transform the partial differential Eq. (1) into the finites degree of freedom piecewise-linear dynamical system. Then the following expansion is used:

$$u(\xi, t) = \sum_{i=1}^{N_C} q_i(t)\Psi_i(\xi)\ , \tag{3}$$

$$\Psi_i(\xi) = (1 - b_1)b_2 W^{(i)}_{0,1}(\xi) + (1 - b_1)(1 - b_2)W^{(i)}_{0,0}(\xi) + b_1(1 - b_2)W^{(i)}_{1,0}(\xi)+$$
$$b_1 b_2 W^{(i)}_{1,1}(\xi)\ .$$

The finite degrees of freedom piecewise-linear dynamical system is derived as:

$$\sum_{i=1}^{N_C} \left[M_{ji}(q)\,\ddot{q}_i + R_{ji}(q)q_i\right] = \tilde{p}_j(t)\ ; j = 1, \ldots, N_C \tag{4}$$

where

$$\tilde{p}_j(t) = \int_0^1 p(\xi, t)\,\Psi_j(\xi)d\xi\ ; M_{ji}(q) = m\int_0^1 \Psi_i(\xi)\Psi_j(\xi)d\xi$$

$$R_{ji}(q) = \frac{E_0 I_0}{L^4}\int_0^1 \left\{\left[1 - \sum_{\nu=1}^{2} b_\nu\gamma_\nu\delta(\xi - \xi_{0\nu})\right]\Psi_i{''}(\xi)\right\}''\Psi_j(\xi)d\xi\ ;$$

$q = \left(q_1, \ldots, q_{N_C}\right)$ are generalized coordinates; $\xi_{0\nu} = \frac{x_{0\nu}}{L}$. The elements of the matrix $R_{ji}(q)$ are obtained as:

$$R_{ji}(q) = \tilde{\omega}_i^2 m\int_0^1 \Psi_i(\xi)\,\Psi_j(\xi)d\xi\ , \tag{5}$$

where $\tilde{\omega}_i$ are the beam oscillations eigenfrequencies. The integrals $\int_0^1 \Psi_i(\xi)\,\Psi_j(\xi)d\xi$ are calculated as:

$$\int_0^1 \Psi_i(\xi)\,\Psi_j(\xi)d\xi \;=\begin{cases} \int_0^1 W_{0,1}^{(i)}W_{0,1}^{(j)}d\xi\,;\;\; G(\xi_{01},q)>0\,;\; G(\xi_{02},q)<0\,; \\ \int_0^1 W_{0,0}^{(i)}W_{0,0}^{(j)}d\xi\,;\;\; G(\xi_{01},q)>0\,;\; G(\xi_{02},q)>0\,; \\ \int_0^1 W_{1,0}^{(i)}W_{1,0}^{(j)}d\xi\,;\;\; G(\xi_{01},q)<0\,;\; G(\xi_{02},q)>0\,; \\ \int_0^1 W_{1,1}^{(i)}W_{1,1}^{(j)}d\xi\,;\;\; G(\xi_{01},q)<0\,;\; G(\xi_{02},q)<0\,; \end{cases} \tag{6}$$

$$i=1,...,N_C;\; j=1,...,N_C,$$

where $G(\xi,q) = \sum_{i=1}^{N_C} i^2\sin(i\pi\xi)\,q_i(t)$. The values $\int_0^1 \Psi_i(\xi)\,\Psi_j(\xi)d\xi$ depend on the cracks motions, which are defined by constrains $G(\xi_{01},q)$ and $G(\xi_{02},q)$. The eigenmodes meet the orthogonality conditions:

$$\int_0^1 W_{b_1b_2}^{(i)}W_{b_1b_2}^{(j)}d\xi = \pi_i^{(b_1,b_2)}\,\delta_{ij}\,;\, b_1=0,\;1\,;\;\; b_2=0,\;1\; i=1,...,N_C;\; j=1,...,N_C, \tag{7}$$

where δ_{ij} is Kronecker delta; $\pi_i^{(0,0)}=0.5$.

The material damping is accounted in subsequent analysis. Then the system (4) has the following form:

$$\begin{cases} \ddot{q}_j+\delta_j\dot{q}_j+\omega_{0,1}^{(j)2}q_j = F_j^{(0,1)}(t)\,;\;\; G(\xi_{01},q)>0\;;\;\; G(\xi_{02},q)<0\;; \\ \ddot{q}_j+\delta_j\dot{q}_j+\omega_{0,0}^{(j)2}q_j = F_j^{(0,0)}(t)\,;\;\; G(\xi_{01},q)>0\;;\;\; G(\xi_{02},q)>0\;; \\ \ddot{q}_j+\delta_j\dot{q}_j+\omega_{1,0}^{(j)2}q_j = F_j^{(1,0)}(t)\,;\;\; G(\xi_{01},q)<0\;;\;\; G(\xi_{02},q)>0\;; \\ \ddot{q}_j+\delta_j\dot{q}_j+\omega_{1,1}^{(j)2}q_j = F_j^{(1,1)}(t)\,;\;\; G(\xi_{01},q)<0\;;\;\; G(\xi_{02},q)<0\;, \end{cases} \tag{8}$$

$$j=1,...,N_C,$$

where

$$F_j^{(0,1)}(t)=\frac{1}{m\pi_j^{(0,1)}}\tilde{p}_j(t);\; F_j^{(0,0)}(t)=\frac{2}{m}\tilde{p}_j(t);\; F_j^{(1,0)}(t)=\frac{1}{m\pi_j^{(1,0)}}\tilde{p}_j(t);$$
$$F_j^{(1,1)}(t)=\frac{1}{m\pi_j^{(1,1)}}\tilde{p}_j(t)\;;$$

$\omega_{b_1b_2}^{(j)}$ are eigenfrequencies of beam motions phases; $\omega_{0,0}^{(j)}=j^2\pi^2\sqrt{\frac{E_0I_0}{mL^4}};\; j=1,2,...$

The piesewise-linear dynamical system (8) consists of linear subsystems. The dynamical system (8) is nonlinear owing to linear constraints $G(\xi_{01}, q)$, $G(\xi_{02}, q)$. In the subsection analysis the structure vibrations under the action of the concentrated force $p(\xi, t)$ are considered.

$$p(\xi, t) = \delta(\xi - \xi_F)\hat{p}(t) \ ,$$

where $\xi_F = 0.75$. Then the dynamical system (8) can be rewritten as:

$$\ddot{q}_j + \delta_j \dot{q}_j + \omega_{0,0}^{(j)2} q_j + R_j(q) = Z_j(q)\hat{p}(t) \ , j = 1, ..., N_C, \tag{9}$$

where

$$R_j(q) = \Lambda_{0,1}^{(j)} q_j \ H\big[G(\xi_{01}, q)\big] H\big[-G(\xi_{02}, q)\big] + \Lambda_{1,0}^{(j)} q_j H\big[-G(\xi_{01}, q)\big] H\big[G(\xi_{02}, q)\big] + \Lambda_{1,1}^{(j)} q_j H\big[-G(\xi_{01}, q)\big] H\big[-G(\xi_{02}, q)\big] \ ;$$

$$\Lambda_{0,1}^{(j)} = \omega_{0,1}^{(j)2} - \omega_{0,0}^{(j)2} \ ; \ \ \Lambda_{1,0}^{(j)} = \omega_{1,0}^{(j)2} - \omega_{0,0}^{(j)2} \ ; \ \ \Lambda_{1,1}^{(j)} = \omega_{1,1}^{(j)2} - \omega_{0,0}^{(j)2} \ ;$$

$$Z_j(q) = H_j^{(0,0)} + \left[H_j^{(0,1)} - H_j^{(0,0)}\right] H\big[G(\xi_{01}, q)\big] H\big[-G(\xi_{02}, q)\big] + \left[H_j^{(1,0)} - H_j^{(0,0)}\right] H\big[-G(\xi_{01}, q)\big] H\big[G(\xi_{02}, q)\big] + \left[H_j^{(1,1)} - H_j^{(0,0)}\right] H\big[-G(\xi_{01}, q)\big] H\big[-G(\xi_{02}, q)\big] \ ;$$

$$H_j^{(0,0)} = \frac{2}{m} \sin(j\pi\xi_F); \ H_j^{(b_1,b_2)} = \frac{W_{b_1,b_2}^{(j)}(\xi_F)}{m \int_0^1 W_{b_1,b_2}^{(j)2} d\xi} \ ; b_1 = 0, \ 1 \ ; \ \ b_2 = 0, \ 1 \ ;$$

$H[x]$ is Heaviside function.

The dimensionless parameters are applied as:

$$\vartheta_j = \frac{q_j}{2d} \ ; \ j = 1, ..., N_C; \ \tau = \omega_{0,0}^{(1)} t, \tag{10}$$

where $2d$ is of the beam height. The dynamical system (9) has the following dimensionless form:

$$\vartheta_j'' + \overline{\omega}_{0,0}^{(j)2} \vartheta_j + \hat{\delta}_j \vartheta_j' + r_j(\vartheta) = z_j(\vartheta)\tilde{p}(\tau) \ , j = 1, ..., N_C, \tag{11}$$

where

$$\tilde{p}(\tau) = A_F \cos(\Omega\tau) \ ; \ \vartheta_j' = \frac{d\vartheta_j}{d\tau}; \ \ \vartheta = \left(\vartheta_1, ..., \vartheta_{N_C}\right); \ \hat{\delta}_j = \frac{\delta_j}{m\omega_{0,0}^{(1)}}; \ \ \overline{\omega}_{0,0}^{(j)} = \frac{\omega_{0,0}^{(j)}}{\omega_{0,0}^{(1)}}$$

$$z_j(\vartheta) = h_j^{(0,0)} + \left[h_j^{(0,1)} - h_j^{(0,0)}\right] H[G(\xi_{01}, \vartheta)] H[-G(\xi_{02}, \vartheta)] + \left[h_j^{(1,0)} - h_j^{(0,0)}\right] H[-G(\xi_{01}, \vartheta)] H[G(\xi_{02}, \vartheta)] + \left[h_j^{(1,1)} - h_j^{(0,0)}\right] H[-G(\xi_{01}, \vartheta)] H[-G(\xi_{02}, \vartheta)] \ ;$$

$$H_j^{(b_1,b_2)} = \frac{1}{m} h_j^{(b_1,b_2)}\,;\; b_1 = 0, 1;\; b_2 = 0, 1\,;$$

$$r_j(\vartheta) = \lambda_{0,1}^{(j)} \vartheta_j\, H[G(\xi_{01}, \vartheta)]H[-G(\xi_{02}, \vartheta)] + \lambda_{1,0}^{(j)} \vartheta_j H[-G(\xi_{01}, \vartheta)]H[G(\xi_{02}, \vartheta)] + \lambda_{1,1}^{(j)} \vartheta_j H[-G(\xi_{01}, \vartheta)]H[-G(\xi_{02}, \vartheta)]\,;$$

$$\lambda_{0,1}^{(j)} = \frac{\Lambda_{0,1}^{(j)}}{\omega_{0,0}^{(1)2}};\; \lambda_{1,0}^{(j)} = \frac{\Lambda_{1,0}^{(j)}}{\omega_{0,0}^{(1)2}};\; \lambda_{1,1}^{(j)} = \frac{\Lambda_{1,1}^{(j)}}{\omega_{0,0}^{(1)2}}\,; j = 1, ..., N_C.$$

The functions $z_j(\vartheta)$, $r_j(\vartheta)$ can be rewritten as:

$$r_j(\vartheta) = \vartheta_j \Big\{ \lambda_{0,1}^{(j)}\; H[-G(\xi_{02}, \vartheta)] + \lambda_{1,0}^{(j)} H[-G(\xi_{01}, \vartheta)] + \left(\lambda_{1,1}^{(j)} - \lambda_{1,0}^{(j)} - \lambda_{0,1}^{(j)}\right) H[-G(\xi_{01}, \vartheta)]H[-G(\xi_{02}, \vartheta)] \Big\}\,;$$

$$z_j(\vartheta) = h_j^{(0,0)} + \left[h_j^{(0,1)} - h_j^{(0,0)}\right] H[-G(\xi_{02}, \vartheta)] + \left[h_j^{(1,0)} - h_j^{(0,0)}\right] H[-G(\xi_{01}, \vartheta)] + \left[h_j^{(0,0)} + h_j^{(1,1)} - h_j^{(0,1)} - h_j^{(1,0)}\right] H[-G(\xi_{01}, \vartheta)]H[-G(\xi_{02}, \vartheta)]\,.$$

3 Numerical Analysis of Nonlinear Oscillations

The nonlinear oscillations of cracked beam with simply supported boundary conditions are studied numerically. The system parameters are the following:

$2d = 1 \cdot 10^{-2}\ m\,;\ b = 1 \cdot 10^{-2}\ m\,;\ E = 2.1 \cdot 10^{11}\ Pa\,;\ \rho = 7800\ {}^{kg}\!/\!_{m^3}\,;\ L = 0.2\ m$;

$$A_F = 0.01\,;\ \hat{\delta}_1 = \hat{\delta}_2 = 0.005;\ \xi_{01} = 0.25;\ \xi_{02} = 0.5 \tag{12}$$

The periodic oscillations of the dynamical system (11) are analyzed numerically by the continuation technique [15–19]. The bifurcation behavior and stability analysis are performed by multipliers calculations [31]. The second order sub-harmonic oscillations are expanded into the Fourier series as:

$$\vartheta_j(\tau) = \sum_{i=0,1,\ldots} C_{i/2}^{(j)} \cos\left[\frac{i\Omega\tau}{2} + \Theta_{i/2}^{(j)}\right] \tag{13}$$

The harmonics amplitudes $C_{i/2}^{(j)}$ are used to present the results of the frequency response analysis.

The periodic orbits of forced vibrations are studied with the lengths of the cracks $\overline{a}_1 = \overline{a}_2 = 0.4 \cdot 10^{-2}\ m$. The second order sub-harmonic oscillations are analyzed. These motions are observed due to the periodic- doubling bifurcations of the harmonic motions. Such bifurcation behavior is shown on Figs. 2 and 3, where the second and the third harmonics of the Fourier series are presented versus the forced frequency. The

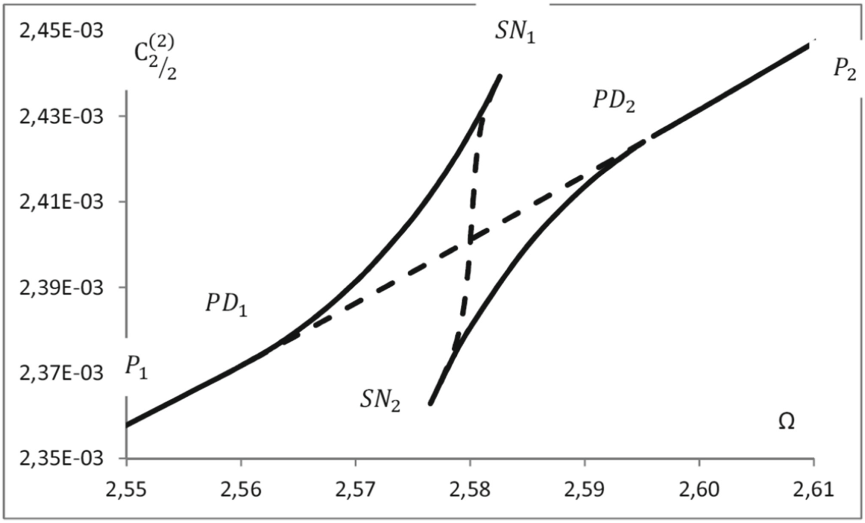

Fig. 2. Frequency response of Fourier series amplitude $C_2^{(2)}/2$

bifurcation scenario of periodic orbits is treated for general form of dynamical system in [20]. The stable motions and unstable motions are shown by solid lines and dotted lines, respectively. As follows from the Figs. 2 and 3, the second order sub-harmonic oscillations undergo the saddle-node bifurcations SN_1, SN_2.

The structure bifurcation scenario is considered with the system parameters (12) and $\xi_{01} = 0.25$; $\xi_{02} = 0.5$; $A_F = 0.01$; $\hat{\delta}_1 = \hat{\delta}_2 = 0.005$; $\overline{a}_1 = \overline{a}_2 = 0.2 \cdot 10^{-2}\ m$. The periodic doubling bifurcations are observed in points PD_5, PD_6 (Fig. 4). The harmonic vibrations, which belongs to the main resonance, are shown by the curve (P_7P_8). The period- doubling bifurcation points PD_5 and PD_6 belong to harmonic motions. The unstable harmonic motions are observed in the range $\Omega \in [1.964; 1.988]$. In the bifurcation points PD_5 and PD_6, the second order sub-harmonic vibrations is arisen. The Fourier series amplitudes $C^{(1)}_{1/2}$ of ϑ_1 are shown versus the forcing frequency Ω. The saddle-node bifurcations points SN_3, SN_4 and Naimark- Sacker points NS_1 and NS_2 belong to the branch of second order sub-harmonic oscillations (Fig. 4).

The bifurcation points NS_1 and NS_2 results in the almost periodic oscillations, which occur in the range $\Omega \in [1.974; 1.976]$. Stroboscopic phase plane of almost periodic oscillations are shown on Fig. 5 at $\Omega = 1.975$. The generalized coordinate ϑ_1 and the generalized velocity ϑ_1' are presented on the stroboscopic plane (Fig. 5) at time instants $\tilde{\tau}_j = j2\pi;\ j = 1, 2, \ldots.$

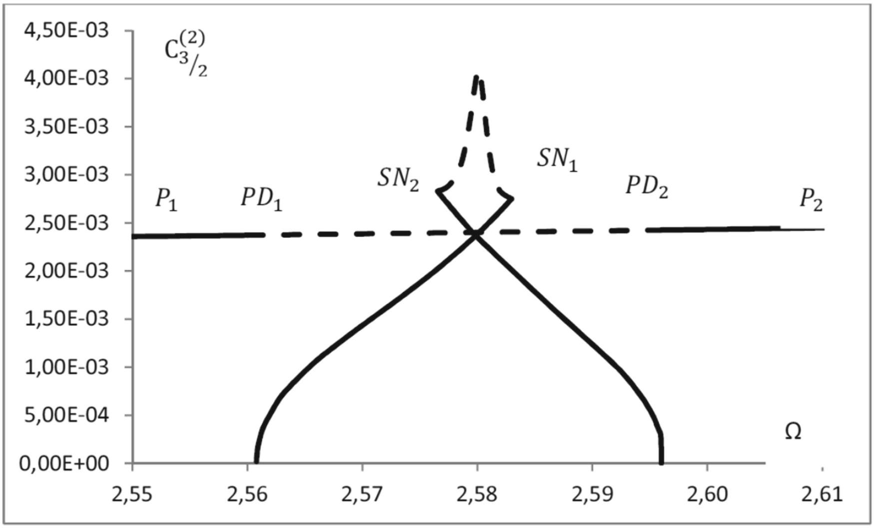

Fig. 3. Frequency response of Fourier series amplitude $C_3^{(2)}/2$

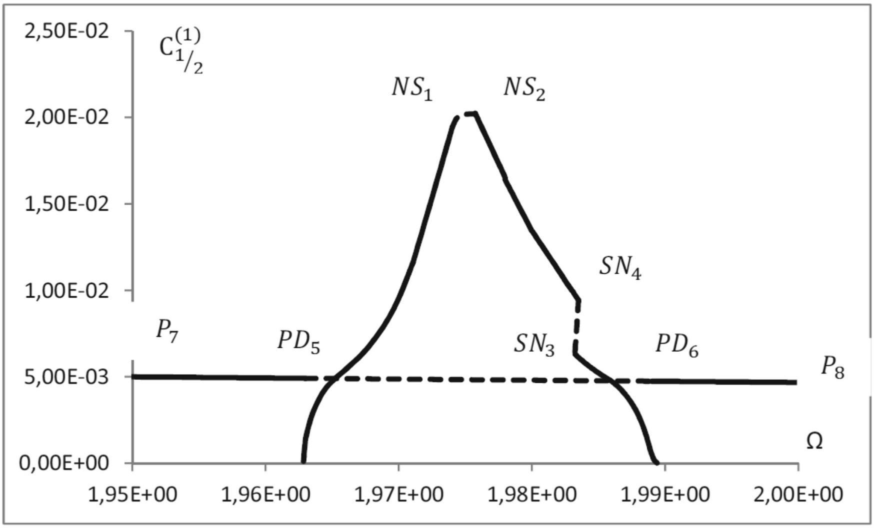

Fig. 4. Frequency response of the amplitude $C_2^{(2)}/2$ of the sub-harmonic motions

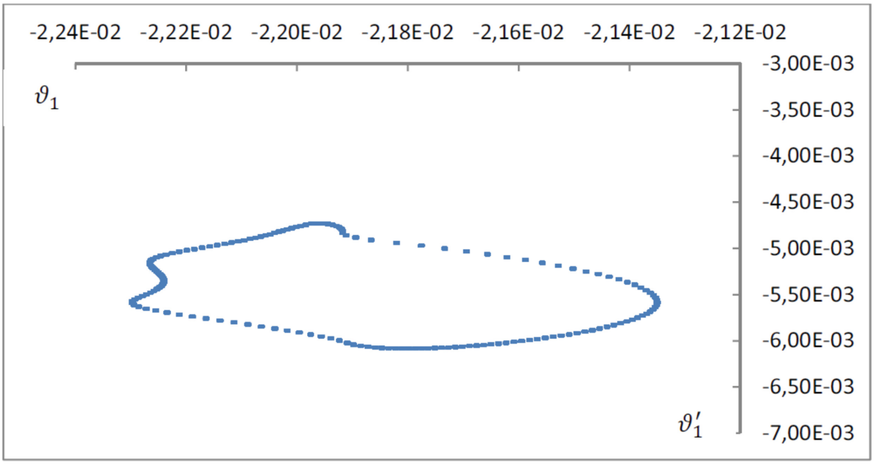

Fig. 5. Stroboscopic phase plane of almost periodic oscillations at $C_2^{(2)}/2$

4 Conclusions

The new mathematical model of beam nonlinear oscillations with two breathing cranks is suggested in the form of piecewise-linear finite degrees of freedom dynamical system. The structure motions are separated on four linear subsystems, which are determined by opening and closing of the cracks. The opening and closing of the crack are described by constraints, which have the forms of inequalities. The derived mathematical model can be generalized to arbitrary number of defects in beam.

In general, the obtained dynamical system is strongly nonlinear, if the value of crack length is commensurable with beam height. The dynamical system is weakly nonlinear for small value of crack length.

As follows from the numerical analysis, the continuation technique is very useful tools for analysis of nonlinear oscillations of beam with two cracks. The application of the continuation method for analysis of stability and bifurcations is very successful too.

References

1. Dimarogonas, A.D.: Vibration of cracked structures: a state of the art review. Eng. Fract. Mech. **55**, 831–857 (1996)
2. Bovsunovsky, A., Surace, C.: Non-linearities in the vibrations of elastic structures with a closing crack: a state of the art review. Mech. Syst. Signal Process. **62–63**, 129–148 (2015)
3. Christides, S., Barr, A.D.S.: One- dimensional theory of cracked bernoullieuler beams. Int. J. Mech. Sci. **26**, 639–648 (1984)
4. Shen, M.H.H., Pierre, C.: Free vibrations of beams with a single – edge crack. J. Sound Vib. **170**, 237–259 (1994)
5. Shen, M.H.H., Chu, Y.C.: Vibrations of beams with a fatigue crack. Comput. Struct. **45**, 79–93 (1992)
6. Chondros, T.G., Dimarogonas, A.D., Yao, J.: A continuous cracked beam vibration theory. J. Sound Vibr. **215**, 17–34 (1998)

7. Ng, T.Y., Lam, K.Y., Li, H.: Dynamic stability of rotating blades with transverse cracks. Shock. Vib. **10**, 187–194 (2003)
8. Chati, M., Rand, R., Mukherjee, S.: Modal analysis of a cracked beam. J. Sound Vibr. **207**, 249–270 (1997)
9. Caddemi, S., Cali, I., Marletta, M.: The non-linear dynamic response of the Euler-Bernoulli beam with an arbitrary number of switching cracks. Int. J. Non-Linear Mech. **45**, 714–726 (2010)
10. Tsyfansky, S.L., Beresnevich, V.I.: Detection of fatigue cracks in flexible geometrically non-linear bars by vibration monitoring. J. Sound Vib. **213**, 159–168 (1998)
11. Ballo, I.: Non-linear effects of vibration of a continuous transverse cracked slender shaft. J. Sound Vib. **217**, 321–333 (1998)
12. Bikri, K.E., Benamar, R., Bennouna, M.M.: Geometrically non-linear free vibrations of clamped–clamped beams with an edge crack. Comput. Struct. **84**, 485–502 (2006)
13. Avramov, K., Malyshev, S.: Bifurcations and chaotic forced vibrations of cantilever beams with breathing cracks. Eng. Fract. Mech. **214**, 289–303 (2019)
14. Caddemi, S., Calio, I.: Exact closed-form solution for the vibration modes of the Euler-Bernoulli beam with multiple open cracks. J. Sound Vibr. **327**, 473–489 (2009)
15. Seydel, R.: Tutorial on continuation. Int. J. Bifurcat. Chaos **1**, 3–11 (1991)
16. Seydel, R.: Nonlinear computation. Int. J. Bifurcat. Chaos **7**, 2105–2126 (1997)
17. Avramov, K.V.: Nonlinear beam oscillations excited by lateral force at combination resonance. J. Sound Vib. **257**, 337–359 (2002)
18. Avramov, K.V.: Bifurcations of parametric oscillations of beams with three equilibrium. Acta Mech. **164**, 115–138 (2003)
19. Avramov, K.V., Mikhlin, Y.: Forced oscillations of a system containing a snap- through truss, close to its equilibrium position. Nonlinear Dyn. **35**, 361–379 (2004)
20. Guckenheimer, J., Holmes, P.: Nonlinear Oscillations, Dynamical Systems and Bifurcations of Vector Fields. Springer-Verlag, New York, Heidelberg, Berlin (1983)

Algorithm for Selecting the Optimal Technology for Rapid Manufacturing and/or Repair of Parts

Valeriy Sikulskyi[1], Kateryna Maiorova[1], Olga Shypul[1](✉), Viacheslav Nikichanov[1], Oleg Tryfonov[1], Iryna Voronko[1], and Oleksandra Kapinus[2]

[1] National Aerospace University "Kharkiv Aviation Institute", 17 Chkalova Street, Kharkiv 61070, Ukraine
o.shipul@khai.edu

[2] The Ukrainian-American Joint Venture "KODA", Bahaliia Street, Kharkiv 22, Ukraine

Abstract. The subject of the study is the technology of rapid production and/or repair of parts for which there is no design documentation, in order to return them to working state as soon as possible. Such technologies are built on the basis of reverse engineering operations, with the further use of additive and extractive technologies. The work is aimed at finding the optimal technology for rapid production and/or repair of parts. To achieve the goal, schemes of technological operations have been developed according to various methods of production of parts from specified metals and the mass of the workpiece. The labor intensity of work for each technological operation of part production and the total labor intensity of work in the manufacture of a single part and a batch of parts are calculated and compared. An experimental study of the production of the part using reverse engineering technologies, additive and extractive technologies was carried out, and different methods of its production were compared according to the parameter of labor intensity. An algorithm for selecting the optimal technology for rapid manufacturing and/or repair of parts is proposed, provided that labor intensity and manufacturing time are minimized, taking into account the accuracy and volume of manufacturing.

Keywords: reverse engineering · 3D printing · additive manufacturing technology · Digital Mock-Up · labor intensity

1 Introduction

The serviceability of the existing fleet of aircraft of the Armed Forces of Ukraine (AFU) is currently ensured by the extension of the established resource indicators and the implementation of refurbishments. But there are important peculiarities. Aircraft operation of domestic design and production for instance type AN-24, AN-26 and AN-30 is carried out under the developer's supervision – Ukrainian state enterprises. The situation is more complicated with foreign aircrafts, which are not subject to field supervision. In accordance with the current regulatory framework of Ukraine on maintaining the airworthiness of aviation equipment technical support for such foreign aircraft is carried out

M. Nechyporuk et al. (Eds.): ICTM 2023, LNNS 1008, pp. 25–39, 2024.
https://doi.org/10.1007/978-3-031-61415-6_3

through the formation of directions and principles of the general strategy for managing the technical condition of these aircraft and the introduction on its basis of appropriate technologies for maintaining their airworthiness [1].

Aggressive war against Ukraine has clearly shown the need to create specific technology capable of implementing the idea of rapid production and/or repair for the earliest possible return to combat state of objects of military equipment including foreign ones. The solution of this issue is impossible without the use of modern machines with numerical control (CNC), coordinate measuring machines (CMM), 3D scanners, etc. Such technologies allow to digitize and reproduce real objects and are known as reverse engineering. Such technologies of reverse engineering use existing object for production as a primary source of information, involves scanning of parts, transformation of the obtained scanned surfaces into portraits, development of Digital Mock-Up (DMU) [2]. The DMU built in CAD system can be used as a primary source of production in CAM system to produce technological means and parts using CNC machining or 3D printing. In the specified conditions, the choice of production technology that ensures rapid production and/or repair of objects must be justified by the effectiveness of the used production time with the provision of specified accuracy.

2 Literature Review and State-of-the-Art

Fierce competition among manufacturers of the machine-building industry for the rapid production or repair of parts with the assurance of the required quality requires the use of state-of-the-art reverse engineering technologies, additive and extractive technologies based on high-speed cutting (HSC) or CNC machines [3, 4], as well as information automated production support [5]. The paper [6] presents positive results from the introduction of reverse engineering technologies into the already existing established production. It is noted that reducing the production time is possible already at the stages of technical preparation of production. It is proved that the lowest indicators of labor intensity on the example of the manufacture of a helicopter stabilizer were when using reverse engineering in order to create the Digital Mock-Up (DMU). Positive results from the use of reverse engineering based on various methods and applications are presented in a number of works [7–9], which confirms the prospects of such technologies.

Additive technologies are worthy of competition with traditional technologies (stamping and milling based on HSC/CNC). Thus, the paper [10] presents the efficiency of PLA–plastic tooling made by 3D printing by fused deposition modeling (FDM), in comparison with the same steel tooling made by milling. In [11] the advantages of selective laser sintering (SLS) are shown and three-dimensional binder printing (3DP) compared to casting. The results of the work [12] prove the advantages of additive manufacturing technology by laser sintering of technological equipment, in particular dies of complex shapes, due to the elimination of correction processes after production and surface treatment. Separately, it should be noted that in the above works [10–12] there are no studies of the labor intensity of the use of additive technologies.

It should be noted that the basis for all these technologies is the DMU of the part, which reflects the physical essence of the object in the CAD system as the primary source of information [2]. Therefore, the production of parts begins with the creation of the part‘s DMU. The next step should be to decide which technology to use to manufacture the part: traditional methods of CNC based stamping, casting or milling or 3D printing and finishing operations, if necessary, etc. Analyzing the works [3–12], it can be concluded that the authors avoid quantitative evaluation in the creation of the DMU and the production of the part according to it. According to many authors, the rapid production of a part is achieved through the use of modern means of receiving, transmitting and processing information. Literary sources lack complete data on the time and labor intensity of reverse engineering works, additive and extractive technologies. At the same time, the creation of an optimal rapid repair technology, which combines technological systems of reverse engineering, production using additive and extractive technologies, requires economic calculations, both at the design stages and for its further improvement.

3 The Goal and Tasks of the Study

The goal of this study is to develop an algorithm for selecting the optimal technology for rapid manufacturing and/or repair of parts under the condition of minimizing labor intensity and production time, taking into account accuracy and volume of production.

To achieve this goal, the following tasks have been formulated:

- to develop the schemes of technological operations according to various scenarios for the production of parts from specified metals and the mass of the workpiece;
- to determine the labor intensity of work for each technological operation of manufacturing a part and calculate the total labor intensity of the work of manufacturing a single part and a batch of parts;
- to experimental research the production of a part using reverse engineering methods, additive and extractive technologies and compare different methods of its production according to the parameter of labor intensity.

4 Calculation of the Labor Intensity of the Selected Production Technology

The objects of this study are parts of military equipment and aircraft that are subject to rapid production and/or restorative repair, provided that there is no design documentation for them and that require the creation of a primary source of production by means of reverse engineering. At the same time, the primary source of information is the example of a restoring part. In most cases, this applies to single and small-scale production. The choice of an effective technology for rapid production and/or restorative repair of such objects is based on minimizing production time, in particular the labor intensity of the work, provided that the specified quality indicators of the production object are ensured.

The analysis of the labor intensity of the parts manufacturing according to the researched technologies was carried out in stages. Thus, the first stage of the technology of restorative repair by means of reverse engineering, which is the same for all the technologies considered in the study, in accordance with the conditions of the task, includes operations to restore the geometry of the part (Fig. 1). In particular, the first stage includes the following technological operations: 1 – using special CMM or scanners reproduction from an existing part (Part) the part's portrait (Pp), 2 – creation of a process model (MPp), and 3 – development of the part's DMU.

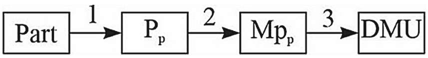

Fig. 1. A scheme of technological operations for part's DMU development by reverse engineering.

The steps of 1-2-3 operations are the same for any part considered technologies. The following 4-5-6-…-n operations for studied manufacturing methods varying.

The study considers only the quantitative indicators of the labor intensity of the technological operations using various technologies. The authors understand that labor intensity indicators alone do not provide a complete economic state of the process. At the same time, the conclusions of this study allow us to compare the effectiveness of the investigated technologies, provided that the labor intensity of manufacturing is a decisive factor. The constant indicators and analysis of the execution time of the stages of reverse engineering technology given in Table 1 are based on the data of the works [6, 13] and correspond to the scheme of technological operations for the creation of part's DMU (Fig. 1).

Table 1. The constant indicators [3].

Technological operation/stage	1	2	3
Labor intensity $\begin{bmatrix} t_{\max} \\ t_{\min} \end{bmatrix}$, man-hours	$\begin{bmatrix} +3 \\ +2 \end{bmatrix}$	$\begin{bmatrix} +8 \\ +6 \end{bmatrix}$	$\begin{bmatrix} +12 \\ +9 \end{bmatrix}$

Analyzing the data in Table 1, we can say that the total labor intensity of reverse engineering operations to restore the geometry of the part (Fig. 1) is [+23, 0; +17,0].

Individual indicators were determined by the method of expert evaluation, a survey of specialists of enterprises, reference literature. To add up the values, it was decided to use the maximum-minimum method (max-min) with the direct transfer of the value, taking into account that the labor intensity parameter satisfies us as a result, i.e. the maximum and minimum [6].

Labor intensity indicators were determined for both conventional CNC machining and high-speed cutting HSC.

Figure 2 shows the scheme of technological operations 4–5 for the manufacture of a part by milling from a plate using CNC.

Fig. 2. A scheme of technological operations for the part manufacture from a plate-blank.

When milling a workpiece into a part for each appropriate stage, the following time must be considered:

- stage 4 – creation of the process model for CNC – [+15; +6], man-hours;
- stage 5 – the part processing from the workpiece by HSC – [+1,17; +0,02], man-hour and by casting [+11,73; +0,21], man-hour;

Table 2 shows the time required to process the workpiece (stage 5, Fig. 2), for the mass of the part (1 kg) made of aluminum alloys or high-strength steel.

Table 2. Time spent on manufacturing 1 kg of part using HSC and CNC

Stages	Preparation of the workpiece	HSC processing of Al alloy	CNC machining of Al alloy	HSC processing of Steel	CNC machining of Steel
Time, min	$\begin{bmatrix} +20 \\ +2 \end{bmatrix}$	$\begin{bmatrix} +70,37 \\ +3,70 \end{bmatrix}$	$\begin{bmatrix} +704 \\ +37 \end{bmatrix}$	$\begin{bmatrix} +23,75 \\ +1,25 \end{bmatrix}$	$\begin{bmatrix} +237,5 \\ +12,5 \end{bmatrix}$

It was assumed HSC processing productivity to be 100 [cm^3/(min·kW)], and 10 [cm^3/(min·kW)] for CNC machining. It was also considered that when processing the parts approximately 5…10% of the blank mass made by casting is removed, and 10…20% of the blank mass made by stamping.

Figure 3 shows a scheme of technological operations 4-…-8 for the part manufacture by CNC machining from a casted into a molded-blank.

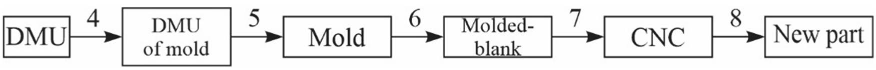

Fig. 3. A scheme of technological operations for the part manufacture from a casted blank.

When using casting technology in the manufacture of a part blank, the following time must be taken into account for each appropriate stage:

- stage 4 – creation of a DMU of the technological mean (here is a mold) and a model of its processing – [+11, 73; +0, 62], man-hours;
- stage 5 – mold making, drying – [+6; +3], man-hours;
- stage 6 – casting, cooling, cleaning of the workpiece – [+4; +3], man-hours;
- stages 7–8, which are identical to stage 5 (Fig. 2) – processing the workpiece after casting (removing 5… 10% of the material) – by HSC processing [+0, 12; +0, 01], man-hours, and by CNC machining [+1, 17; +0, 02], man-hours.

Figure 4 shows the scheme of technological operations 4-…-8 for the manufacture of a part by stamping with subsequent processing using CNC.

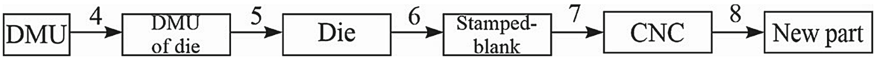

Fig. 4. A scheme of technological op−erations for the manufacture of a part by stamping.

When performing the technology of stamping a workpiece in the manufacture of a part, the following time must be taken into account for each appropriate stage:

- Stage 4 – creation of a DMU of the technological mean (here is a die) and a model of its processing – [+8; +4], man-hours;
- stage 5 – production of a CNC stamp or other method – [+24; +16], man-hours;
- Stage 6 – stamping of the workpiece, heating, cutting, heat treatment, tumbling – [+1, 0; +0, 5], man-hours for 1 part;
- Stages 7–8, which are identical to stage 5 (Fig. 2) – processing the workpiece after stamping (removal of 10… 20% of the material) – by HSC processing [+0, 24; +0, 02], man-hours, and by CNC machining [+2, 34; +0, 04], man-hours.

Figure 5 shows the scheme of technological operations 4-…-7 of manufacturing a part by 3D printing or laser sintering, followed by finishing operations [14, 15] to ensure the accuracy of the part's surfaces.

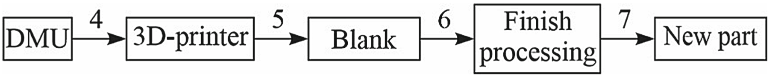

Fig. 5. A scheme of technological operations for the manufacture of a part by 3D printing/laser sintering.

When performing laser sintering technology or 3D printing of a workpiece/part for each relevant stage, the following time must be taken into account:

- stages 4–5 – creation of a process model for 3D printing/laser sintering – [+4; +3], man-hours;
- stages 6–7 – machining, heat treatment, finishing operations – [+2; +1, 5], man-hours.

Table 3 shows calculations of the labor intensity of manufacturing one part by HSC processing and CNC machining, according to the schemes of additive and extractive technologies (Fig. 2, 3, 4 and 5), starting from stages 4-…-n, and including data on the labor intensity of reverse engineering (Table 1).

Table 3. Labor intensity of manufacturing one part using the max-min method.

Selected manufacturing technology of the part	Labor intensity of stages 4-…-n $\begin{bmatrix} t_{\max} \\ t_{\min} \end{bmatrix}$, man-hour		The total labor intensity of the work of stages 1-…-n $\begin{bmatrix} t_{\max} \\ t_{\min} \end{bmatrix}$, man-hour	
	by HSC processing	by CNC machining	by HSC processing	by CNC machining
Casting	$\begin{bmatrix} +21,85 \\ +6,63 \end{bmatrix}$	$\begin{bmatrix} +22,9 \\ +6,64 \end{bmatrix}$	$\begin{bmatrix} +44,85 \\ +23,64 \end{bmatrix}$	$\begin{bmatrix} +45,9 \\ +23,64 \end{bmatrix}$
Milling from a plate	$\begin{bmatrix} +16,17 \\ +6,02 \end{bmatrix}$	$\begin{bmatrix} +26,73 \\ +6,21 \end{bmatrix}$	$\begin{bmatrix} +39,17 \\ +23,02 \end{bmatrix}$	$\begin{bmatrix} +49,73 \\ +23,21 \end{bmatrix}$
Stamping	$\begin{bmatrix} +33,24 \\ +20,52 \end{bmatrix}$	$\begin{bmatrix} +35,34 \\ +20,54 \end{bmatrix}$	$\begin{bmatrix} +56,24 \\ +37,52 \end{bmatrix}$	$\begin{bmatrix} +58,94 \\ +37,54 \end{bmatrix}$
3D printing or laser sintering	$\begin{bmatrix} +6,0 \\ +4,5 \end{bmatrix}$		$\begin{bmatrix} +29,0 \\ +21,5 \end{bmatrix}$	

Using the schemes (Figs. 2, 3, 4, 5 and 6), the calculation of labor intensity for a batch of parts of 100 pcs was obtained. The results of labor intensity, taking into account the technical preparation of the production of the manufacture of one and a batch of parts of 100 pcs, are presented in Table 4.

The results of the total labor intensity, taking into account all stages of production, including reverse engineering, the manufacture of one and a batch of 100 parts, are presented in Table 5.

Based on the results of the calculations, a diagram of the labor intensity of manufacturing a batch of parts up to 100 pieces was constructed (Fig. 6).

The analysis of the diagram (Fig. 6) shows that given the least labor intensity the most efficient technology is reverse engineering and high-speed machining of the stamped workpiece or CNC milling of the plate-blank. In all other cases (casting and 3D printing) labor intensity is slightly reduced with HSC processing and its use can be considered inexpedient. It is worth noting that the worst labor intensity in small-scale production is casting due to the large number of operations that are long in time. 3D-printing is significantly inferior to the processes of dimensional processing with the removal of allowance in small-scale production, mainly due to the low productivity of printing material.

However, if the main thing is the rapid production of one part, then according to the diagram (Fig. 6), almost all the technologies under consideration have relatively the same labor intensity, provided that the enterprise already has a die, mold for casting, HSC and/or CNC equipment, or a 3D printer. If we are talking about the need to create technological means, then the use of 3D printing for the manufacture up to 10 parts, becomes more expedient.

Table 4. Labor intensity of work in the manufacture of one and 100 pcs of parts.

Selected manufacturing technology of the part	Labor intensity $\begin{bmatrix} t_{max} \\ t_{min} \end{bmatrix}$, man-hour				
	Technical preparation of production	Production of one part		Production of 100 pcs of parts	
		by HSC processing	by CNC machining	by HSC processing	by CNC machining
Casting	$\begin{bmatrix} +34,73 \\ +17,62 \end{bmatrix}$	$\begin{bmatrix} +10,12 \\ +6,01 \end{bmatrix}$	$\begin{bmatrix} +11,17 \\ +6,02 \end{bmatrix}$	$\begin{bmatrix} +1012 \\ +601 \end{bmatrix}$	$\begin{bmatrix} +1117 \\ +602 \end{bmatrix}$
Milling from a plate	$\begin{bmatrix} +38,0 \\ +21,0 \end{bmatrix}$	$\begin{bmatrix} +1,17 \\ +0,02 \end{bmatrix}$	$\begin{bmatrix} +11,73 \\ +0,21 \end{bmatrix}$	$\begin{bmatrix} +117 \\ +2 \end{bmatrix}$	$\begin{bmatrix} +1173 \\ +21 \end{bmatrix}$
Stamping	$\begin{bmatrix} +55,0 \\ +37,0 \end{bmatrix}$	$\begin{bmatrix} +1,24 \\ +0,52 \end{bmatrix}$	$\begin{bmatrix} +3,34 \\ +0,54 \end{bmatrix}$	$\begin{bmatrix} +124 \\ +52 \end{bmatrix}$	$\begin{bmatrix} +334 \\ +54 \end{bmatrix}$
3D printing or laser sintering	$\begin{bmatrix} +23,0 \\ +17,0 \end{bmatrix}$	$\begin{bmatrix} +6,0 \\ +4,5 \end{bmatrix}$		$\begin{bmatrix} +600 \\ +450 \end{bmatrix}$	

Table 5. The total labor intensity of work in the manufacture of one and a batch of parts is 100 pcs.

Selected manufacturing technology of the part	Total labor intensity per part $\begin{bmatrix} t_{max} \\ t_{min} \end{bmatrix}$, man-hour		Total labor intensity per 100 pcs of parts, $\begin{bmatrix} t_{max} \\ t_{min} \end{bmatrix}$, man-hour	
	by HSC processing	by CNC machining	by HSC processing	by CNC machining
Casting	$\begin{bmatrix} +44,85 \\ +23,63 \end{bmatrix}$	$\begin{bmatrix} +45,9 \\ +23,64 \end{bmatrix}$	$\begin{bmatrix} +1046,73 \\ +618,62 \end{bmatrix}$	$\begin{bmatrix} +1151,73 \\ +619,62 \end{bmatrix}$
Milling from a plate	$\begin{bmatrix} +39,17 \\ +21,02 \end{bmatrix}$	$\begin{bmatrix} +49,73 \\ +21,21 \end{bmatrix}$	$\begin{bmatrix} +155 \\ +23 \end{bmatrix}$	$\begin{bmatrix} +1211 \\ +42 \end{bmatrix}$
Stamping	$\begin{bmatrix} +56,24 \\ +37,52 \end{bmatrix}$	$\begin{bmatrix} +58,34 \\ +37,54 \end{bmatrix}$	$\begin{bmatrix} +179 \\ +89 \end{bmatrix}$	$\begin{bmatrix} +389 \\ +91 \end{bmatrix}$
3D printing or laser sintering	$\begin{bmatrix} +29,0 \\ +21,5 \end{bmatrix}$		$\begin{bmatrix} +623 \\ +467 \end{bmatrix}$	

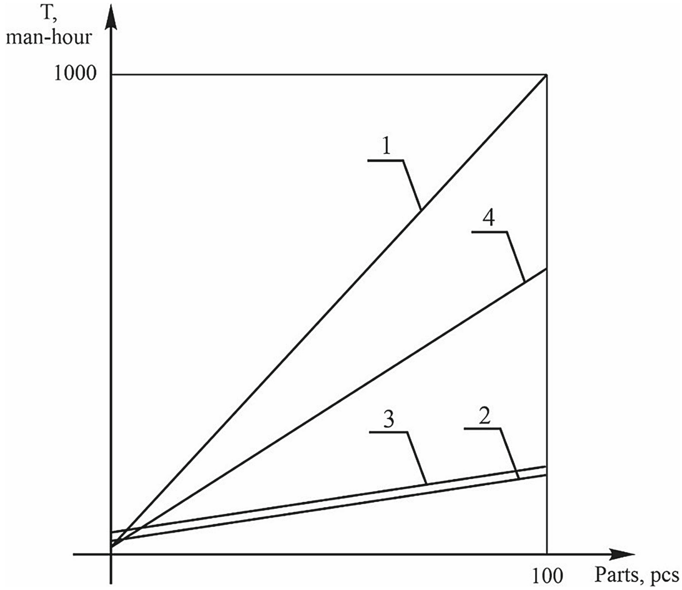

Fig. 6. A diagram of the labor intensity of manufacturing a batch of parts up to 100 pieces: by casting (1), by milling HSC/CNC from a plate (2), by stamping (3), and by 3D printing (4).

5 Experimental Research

The part shown in Fig. 7 was chosen for the experimental research. Given that there is no design documentation for the test part, reverse engineering technology was used to create its geometry. It should be noted that the part had a worn appearance with fuzzy edges and surfaces.

Fig. 7. Experimental detail.

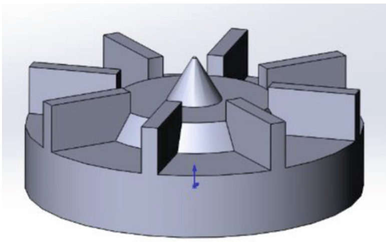

Fig. 8. Analytical standard of the part.

The part was scanned using a 3D scanner ARTEC SPACE SPIDER (USA) and, according to the technological operations of the scheme shown in Fig. 1, its DMU (Fig. 8) was created with the definition of its dimensions (Fig. 9).

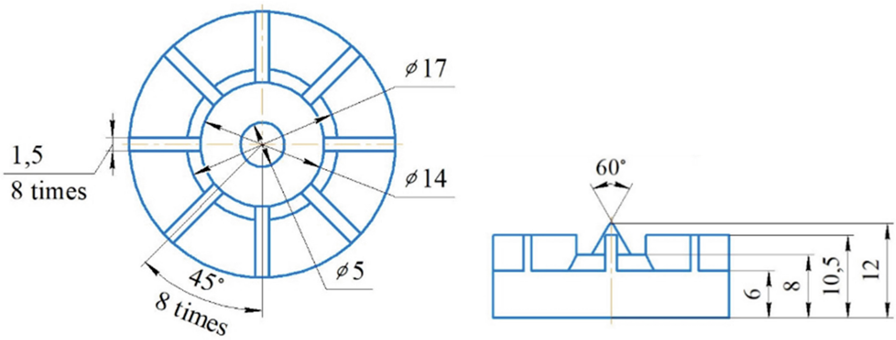

a b

Fig. 9. Geometric dimensions of the test part in top view (a) and side view (b).

5.1 Manufacturing a Part by 3D Printing

The next steps were the preparation for the manufacture of the part using additive technology in accordance with the technological operations of stages 4-…-7 (Fig. 5). Fig. Figure 10 shows a part made using 3D printing. To understand the need for finishing operations, the part was additionally scanned and its portrait was obtained in order to compare the obtained geometry of the part by 3D printing with its analytical geometry DMU (Fig. 11).

Fig. 10. The part is made by 3D printing.

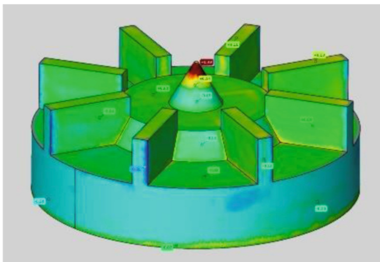

Fig. 11. Control of the geometry of a 3D printing part.

Analysis of the control of the 3D printed part with its DMU showed a deviation in the accuracy of the additive technology from −0.03 to + 0.49 mm. The maximum deviation is observed in the upper cone of the part (highlighted in red in Fig. 11), which is not critical when the tolerance for deviation of the part is ± 0.5 mm. In this case, in the calculations of the labor intensity of work on the manufacture of the part, it is not necessary to take into account the stages of finishing operations 6–7 (Fig. 5). If the requirements for the accuracy of manufacturing a part are more stringent, that is, less than ±0.5 mm, then the stages of finishing operations should be taken into account in the calculations of labor intensity, which will increase its performance.

5.2 Production of a Part by Stamping

Stamping of the blank of the test part (Fig. 7) took place in the die, which is shown in Fig. 12.

a b c d

Fig. 12. Preparation for stamping a workpiece (a) in a die (b) with a die (c) and a punch (d).

The stamped workpiece (Fig. 13) was also scanned to obtain a portrait to control its dimensions and compare it with the analytical geometry (DMU) (Fig. 14).

Fig. 13. The part is made by stamping.

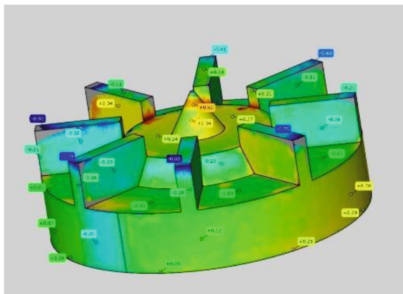

Fig. 14. Inspection of the stamped part.

The control of the geometry of stamped part with its DMU showed a deviation in the accuracy from −0.94 to + 0.58 mm (Fig. 14). The maximum deviation is observed in the upper cone of the part similar to the part made by 3D printing. Such a result can be satisfactory provided that the part tolerance is ±1.0 mm. In this case, in the calculations of the labor intensity of work on the manufacture of a part by stamping, it is not necessary to take into account the stages 7–8 of processing the workpiece in the final part using HSC or CNC (Fig. 4), which will reduce its performance. At the same time, the resulting deviations are critical when the part size is allowed to be ±0.5 mm or less. Therefore, it will be advisable to use the following stages 7–8 of processing the stamped HSC or CNC workpiece (Fig. 4), which will increase the labor intensity.

5.3 Comparative Analysis of the Labor Intensity of the Work of Manufacturing a Part by 3D Printing and Stamping

Calculations have established that the total labor intensity of reverse engineering operations of creating a part DMU is from 23 to 17 man-hours (Table 1). For the test part (Fig. 7) the total labor intensity of the works was experimentally obtained as 18 man-hours. The obtained experimental values confirm the calculated data for the reverse engineering and are accepted for the subsequent stages of part's production.

Preparation of the part for 3D printing was carried out in accordance with the technological operations of the scheme shown in Fig. 5. The time for preparation for printing and direct printing of the test part (stages 4–5, Fig. 5) was [+2; +1, 5] man-hour, which is 2 times less than the pre-set [+4; +3] man-hour. This may be due to the fact that the part has a simple shape, small size and low weight up to 100 g (Fig. 9). If it is necessary to perform finishing operations (stages 6–7, Fig. 5), the labor intensity of the work of stages 4–7 is [+4; +3] man-hour, and the total labor intensity of work, including the stages of reverse engineering, is [+27; +17] man-hour. With a satisfactorily obtained quality of the printed part as such, where finishing operations of stages 6–7 are not required (Fig. 5), the total labor intensity is the lowest [+25; +18, 5] man-hour.

The results of experimental studies of the manufacturing time and labor-intensive work of the test part by stamping according to the scheme (Fig. 4) and taking into account reverse engineering operations (Fig. 1) almost completely coincide (the deviation at the stages does not exceed ±1%). Labor intensity indicators are significantly affected by the need to perform finishing operations for processing surfaces, edges, etc. It should be noted that the time required for stamping a blank in a die compared to printing is drastically different, in particular, it takes 1–1.5 h to print a test part, and only 30 s for its stamping in a die. Calculations on the total labor intensity of work, taking into account the stages of reverse engineering for [+45; +38] the manufacture of a prototype part, was man-hour, which is 1.8 times more than in the manufacture of the same part by 3D printing. With satisfactory quality of the stamped part, when steps 7 – 8 can be neglected (Fig. 4) the total labor intensity is slightly reduced and amounts to [+44; +37, 5] man-hour.

6 Algorithm for Selecting the Optimal Technology for Rapid Manufacturing and/or Repair of Parts

In accordance with the specified conditions of rapid production and/or repair of parts, the selection of the optimal technology according to the parameter of minimization of production time can be carried out on the basis of the analysis of such input data as the volume of production, the accuracy of the dimensions of the part, the terms of production, the availability of technological equipment and equipment, etc. The algorithm for such a selection for the studied part was developed and presented in Fig. 15.

A feature of the proposed technologies for rapid production and/or repair of parts is that they are based on the common stage of obtaining the primary source of information by means of reverse engineering, and the subsequent use of extractive and additive technologies, as well as traditional stamping and casting technologies.

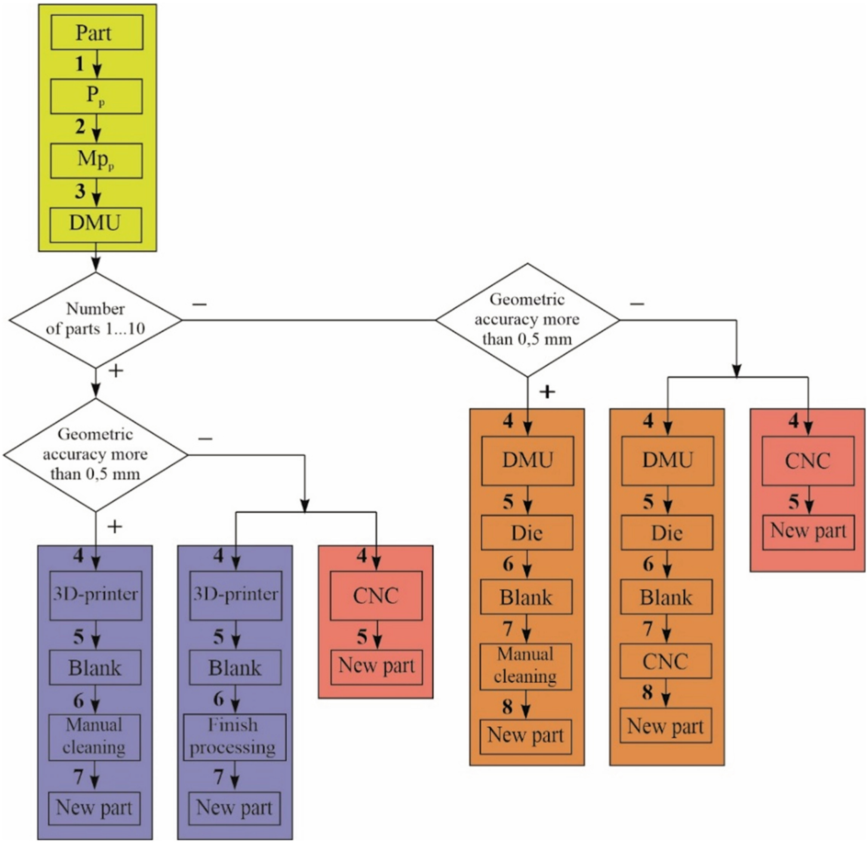

Fig. 15. Algorithm for Selecting the Optimal Technology for Rapid Manufacturing and/or Repair of Parts.

According to the proposed algorithm for selecting the optimal technology for rapid manufacturing and/or repair, for example, parts in the amount of more than 10 pieces in the conditions of small-scale production (up to 100 pieces) and dimensional accuracy of more than ±0.5 mm, the justified use of stamping technology. With the same number of parts, but a geometric accuracy of less than ±0.5 mm, it will be appropriate to use CNC machining or HSC processing from a stamped-blank or milling from a plate-blank with CNC machining or HSC processing.

If the number of parts is less than 10 pieces and the geometric accuracy is more than ±0.5 mm, it is recommended to use a 3D printer followed by manual finishing. With the same number of parts, but the geometric accuracy is less than ±0.5 mm, it is advisable to use CNC machining or HSC processing when milling from a plate-blank or stamped-blank.

Stages 4-…-n in the presented algorithm may vary depending on input conditions (complexity of the part, presence of internal cavities, roughness indicators, etc.) and output data (park of existing equipment, technological means, etc.). Stages 1–3 remain the same for any chosen method of manufacturing the part until the stage of creating its analytical geometry (DMU). It should be noted that the labor intensity and time required to create a DMU will be almost the same for parts that differ in design, provided that the appropriate CMM or scanner is used.

7 Conclusions

It has been proven that the technology of rapid production and/or repair of parts can be built on the basis of reverse engineering operations, additive and extractive technologies, which reduces production time indicators. At the same time, the volume of parts production and quality requirements have a significant impact.

Calculated labor intensity of technological operations of reverse engineering, which has constant indicators according to the maximum-minimum method. The given data of the labor intensity of technological operations for different technology scenario can be used to estimate the production time according to the researched technologies.

An algorithm for selecting the optimal technology for rapid manufacturing and/or repair of parts is proposed, provided that labor intensity and manufacturing time are minimized, taking into account the accuracy and volume of manufacturing.

References

1. Kharchenko, O.V., Pashchenko, S.V.: Conceptual principles of further development of aviation of the armed forces of Ukraine. Collection of Scientific Papers of the State Research Institute of Aviation. Vyp. **16**(23), 6–11
2. Maiorova, K., Vorobiov, I., Boiko, M., Suponina, V., Komisarov, O.: Implementation of reengineering technology to ensure the predefined geometric accuracy of a light aircraft keel. Eastern-Eur. J. Enterprise Technol. **6**(1)(114), 6–12 (2021). https://doi.org/10.15587/1729-4061.2021.246414
3. Maiorova, K., Sikulskyi, V., Vorobiov, I., Kapinus, O., Knyr, A.: Study of a geometry accuracy of the bracket-type parts using reverse engineering and additive manufacturing technologies. In: Nechyporuk M., Pavlikov V., Kritskiy D. (eds.). Integrated Computer Technologies in Mechanical Engineering. ICTM 2022 (2022)
4. Plankovskyy, S., Kapinus, O., Maiorova, K., Myronova, S.: Improving the Method of Virtual Localization of Near-Net-Shaped Workpieces for CNC Machining. Lecture Notes in Networks and Systems, vol. 667 LNNS, pp. 119–128 (2023). https://doi.org/10.1007/978-3-031-30251-0_10
5. Shevel, V., Kritskiy, D., Popov, O.: Toward building a functional image of the design object in CAD. Computation **10**(8), 134 (2022). https://doi.org/10.3390/computation10080134
6. Sikulskiy, V., Maiorova, K., Vorobiov, I., Boiko, M., Komisarov, O.: Implementation of reengineering technology to reduce the terms of the technical preparation of manufacturing of aviation technology assemblies. Eastern-Eur. J. Enterprise Technol. **3**(1(117)), 25–32 (2022)
7. Landman, D.: Reverse engineering source code: Empirical studies of limitations and opportunities. [Thesis, externally prepared, Universiteit van Amsterdam] (2017)
8. Ivanov, V., Dimitrov, L., Ivanova, S., Volkova, M.: Reverse engineering in the remanufacturing: metrology, project management, redesign. In: Karabegović, I. (ed.) NT 2021. LNNS, vol. 233, pp. 169–176. Springer, Cham (2021). https://doi.org/10.1007/978-3-030-75275-0_20

9. Durupt, A., Bricogne, M., Remy, S., Troussier, N., Rowson, H., Belkadi, F.: An extended framework for knowledge modelling and reuse in reverse engineering projects. Proc. Inst. Mech. Eng. Part B-J. Eng. Manuf. **233**(5), 1377−1389 (2019).https://doi.org/10.1177/0954405418789973
10. Tondini, F., Arinbjarnar, U., Basso, A., Nielsen, C.V.: 3D printing to facilitate flexible sheet metal forming production. Procedia CIRP **103**, 91–96 (2021). https://doi.org/10.1016/j.procir.2021.10.014
11. Shi, Y.S., et al.: Additive manufacturing and foundry innovation. China Foundry **18**(4), 286–295 (2021). https://doi.org/10.1007/s41230-021-1008-8
12. Oter, Z.C., et al.: Benefits of laser beam based additive manufacturing in die production. Optik **176**, 175–184 (2019). https://doi.org/10.1016/j.ijleo.2018.09.079
13. Voronko V., Tkachenko I., Dyachenko Y., Voronko I., Zawistovskiy D.: Methodology for calculating the productivity of electrochemical machining in stationary electrolyte. In: Nechyporuk M., Pavlikov V., Kritskiy D. (eds.) Integrated Computer Technologies in Mechanical Engineering - 2021. ICTM 2021. Lecture Notes in Networks and Systems, vol. 367, pp. 47–56. Springer, Cham (2022). https://doi.org/10.1007/978-3-030-94259-5_5
14. Plankovskyy, S., Popov, V., Shypul, O., et al.: Advanced thermal energy method for finishing precision parts. In: Gupta, K., Pramanik, A. (eds.) Advanced Machining and Finishing, pp. 527–575. Elsevier, Amsterdam (2021). https://doi.org/10.1016/B978-0-12-817452-4.00014-2
15. Plankovskyy, S., Shypul, O., Tsegelnyk, Y., Pankratov, A., Romanova, T.: Amplification of heat transfer by shock waves for thermal energy method. In: Nechyporuk, M., Pavlikov, V., Kritskiy, D. (eds.) ICTM 2020. LNNS, vol. 188, pp. 577–587. Springer, Cham (2021). https://doi.org/10.1007/978-3-030-66717-7_49

The Eco-Ergonomics Issues of the Digital Workplace

Galyna Mygal[1](✉), Olga Protasenko[2], and Natalia Kobrina[3]

[1] Lviv Polytechnic National University, 12 Stepan Bandera Street, Lviv 79013, Ukraine
halyna.v.myhal@lpnu.ua

[2] Simon Kuznets Kharkov National University of Economics, 9a Science Avenue, Kharkiv 61166, Ukraine
olha.protasenko@hneu.net

[3] The National Aerospace University "Kharkiv Aviation Institute", 17 Chkalov Street, Kharkiv 61070, Ukraine
n.ko-brina@khai.edu

Abstract. Digitalization provides an opportunity to perform operations faster and more efficiently, and ecologization decreases the ecological footprint. It provides a sustainable development of society. However, on the other hand, employees often feel tense because of information overload, multitasking, and an unregulated regime. The increase in the use of digital devices raises the load on the energy supply system and creates the problem of outdated equipment disposal. The analysis of the issue showed to increase employees' performance and safety and ensure the further implementation of society's sustainable development concept, it is necessary to develop and implement eco-ergonomics digital workplaces. However, there is a lack of research on the digital workplace and its influence on human performance and well-being. Therefore, the work aims to investigate the impact of the eco-ergonomics of the digital workplace on employee's performance and well-being during the working process.

Keywords: eco-ergonomics · digital workplace · digitalization · ecologization · safety

1 Introduction

Currently, the necessary components of society development are the processes of digitalization and ecologization. Digitalization provides an opportunity to perform many operations of various complexity more quickly and efficiently, and ecologization allows for a decrease in the human ecological footprint. Undoubtedly, this gives society many positive results but also causes problems. The biggest of them is the difficulty of transforming workplaces by the requirements of digitalization and ecologization. Why is this so? To date, worker activity is mainly related to the search, use, exchange, creation and organization of information in the digital environment. At the same time, the employee's stay at a particular workplace is not necessary, and the working tasks don't have a strict

M. Nechyporuk et al. (Eds.): ICTM 2023, LNNS 1008, pp. 40–51, 2024.
https://doi.org/10.1007/978-3-031-61415-6_4

schedule. In this situation, the illusion arises that the employee has comfortable working conditions not tied to the workplace and timetable, and the negative impact on the environment is negligible due to digitalization. However, this is not the case. In such conditions of activity, the employee is often in a tense state caused by information overload, multitasking and an unregulated regime, and the increase in the use of digital devices increases the load on the energy supply system and creates the problem of equipment disposal.

Ergonomics can help overcome this problem since the physical and mental health of the employee and the eco-safety of work processes can be ensured if the materials, equipment and software are designed in harmony with the employee's psychological, physiological and eco-social needs and characteristics [1]. That is why, over the last decade, the eco-ergonomic organization of human activity at the digital workplace has become a central issue of ergonomics [2–6].

2 Literature Review

Digital Workplace. The idea of human safety at the workplace is multi-component. The workplace elements are different in origin and impact on a person but closely related parts. Most commonly, researchers consider them in the context of traditional workplace organization when there is an office space where employees work. And in this case, the operations and their sequence to ensure the employee's safety are known. However, current realities are new types of activities that require a review of the approach to ensuring employee safety at the workplace. A prime example in this case is freelancing, which does not have requirements for the location of the employee's workplace, the duration of working hours, working conditions, etc. One more example is the lockdowns due to the COVID-19 pandemic, which led to the mass transfer of workers to remote mode, during which no one controls workplace safety, which caused problems with mental and physical health for workers due to the inability to separate work time from personal one, isolation from society, etc. All this determined the necessity to create a digital workplace. A digital workplace is a virtual analogue of a physical workplace that combines technologies used to work in a digital environment [7–9]. Creating a digital workplace makes it possible to increase creativity in work by decreasing the level of template operations, introducing new forms of work task distribution, applying flexible work schedules, etc. Thus, the digital workplace improves employee productivity through a more user-friendly work environment.

However, despite the rapid spread of digital workplaces, workers and employers do not always get the desired result. Such a situation is often due to insufficiently thought-out organization of the workplace, which can lead to a slowdown in the speed of operations, incorrect actions and other negative consequences [10–12]. As a result, the employee's productivity decreases. That is why digital workplaces need research, and an effective tool for this is new directions of ergonomics, such as digital ergonomics, information ergonomics, computer ergonomics, etc. [1].

Ergonomic Features of Human Activity in a Digital Working Environment. Digitalization and the growth of automation allowed significant technological progress. However, it also substantially changed the requirements for cognitive abilities and psychophysiological capabilities of a person. Today, the difficulties of digital thinking, clip thinking and even “digital autism” are actively discussed despite the high level of digital competence, even in children. Thus, digitalization has created an ergonomic contradiction, which consists of the fact that the growth of automation leads to the complications of the human-machine interaction problem. At the same time, digital systems have unique ergonomic questions associated with the characteristics of the human operator and the technical features of digital workplaces.

The ergonomic challenges of digital workspaces and increased automation are:

1. An increase in mental load but also a deterioration in skills due to automation.
2. Increased requirements for cognitive abilities.
3. Increasing the role of cognitive distortions in decision-making.
4. Decrease/distortion of sensory signals (limited field of vision, decrease in auditory, proprioceptive and olfactory sensations).
5. Deterioration of health indicators and, as a result, quality of life.
6. Distortion of the psychological and emotional perception of the workplace, especially when working remotely at home.
7. Misunderstanding by employers or performers themselves of human physiology and its capabilities and limitations in processing information associated with fatigue, distraction, and switching of attention.
8. The need to focus on the subject despite easy access to information resources.
9. The problem of trust or distrust in automation.

In addition, today, still unresolved aspects of the ergonomic support of human performance under digitalization are: the creation of a highly functional human-machine interface; training, professional selection and ensuring the reliability of operators; forecasting the risks of operators’ activities.

Workplace Eco-Friendliness. An essential component in designing a digital workplace is eco-friendliness. After all, as mentioned above, digitalization does not mean reducing the negative impact of humans on the environment. In addition, digital device exploitation can also hurt a worker’s health. For example, the use of equipment with low-quality materials can provoke the occurrence of allergic reactions, headaches, etc. An eco-digital workplace should contribute to energy-effective use of resources, reducing the ecological footprint and creating eco-safe working conditions [13–19].

Ensuring workplace eco-friendliness is a difficult task to solve, and it requires the application of various knowledge fields. The literature analysis on workplace eco-sustainability studies showed many works in this direction [20–22]. At the same time, the disadvantage of most research is the emphasis on permanent workplaces in office premises, while in today’s realities, the analysis of mobile workplaces has priority. Thus, there is a lack of research on the eco-sustainability and ergonomics of digital workplaces. The solution may be the application of the principles of eco-ergonomic evaluation of workplaces [20, 23–25]. At the same time, the ecological component will be responsible for compliance with environmental norms and standards at the workplace, and the ergonomic element will be responsible for creating and maintaining appropriate safety requirements for human working conditions. It will ensure the control and maintenance of eco-friendliness, comfort and safety of the digital workplace.

Thus, to ensure the society's sustainable development, it is necessary to control and support the eco-friendliness, safety and comfort of digital workplaces. **The aim** is to investigate the impact of the eco-ergonomics of the digital workplace on employee's performance and well-being during the working process.

3 Materials and Results

During research general and special research tools were used:

1. Subject-object, logical, deductive and inductive methods.
2. Statistical observations, correlation and comparative analyses.

The methodological and theoretical basis of the research is the works of leading experts in various fields of knowledge. The interdisciplinary nature of the work is due to the need to use the results of such scientific areas as ergonomics, ecology, sociology, and economics. The empirical basis of the study was the research results on digital workplaces, into the ecology and ergonomics of workplaces by domestic and foreign scientists, reports of international organizations on the safety of workers at workplaces, materials of periodicals, conferences and seminars on this issue.

As it's known, ergonomics is a science that creates practical solutions to ensure the most safe and comfortable working conditions for people through the various scientific areas (psychology, physiology, engineering, etc.). This approach makes ergonomics flexible because it instantly responds to the emergence of new requests in society regarding safety and finds the most effective solutions to answer them.

In light of the importance of implementing the processes of digitalization and ecologization, one of the main directions of modern ergonomics has become ensuring the eco-ergonomics of the digital workplace. That is why, in recent years, ergonomics has added new elements to the workplace assessment – eco-friendliness and the level of digitalization [12]. It led to the transition from standard ergonomic assessment of workplaces to eco-ergonomic one [20], the principles of which can be applied to create an eco-ergonomic digital workplace (Fig. 1).

Let's consider in more detail what eco-ergonomic assessment is and how it combines ecological and ergonomic aspects to ensure human comfort in the workplace. Eco-ergonomic assessment is a relatively new concept in ergonomics. Its task is to find an optimal combination of working conditions and technological support at the workplace. This combination must meet modern psychophysiological, social, engineering and ecological requirements. The following indicators are used in the eco-ergonomic assessment of the workplace:

1. Eco-friendliness of workplace materials (chipboard, fibreboard, MDF, wood, plastic, etc.).
2. Methods of creating and maintaining working conditions in the premises (existence of ventilation, air conditioning and heating systems, lighting quality, etc.).
3. The workplace interior (materials from which subsidiary furniture is made, floor covering, wall covering, ceiling, etc.).

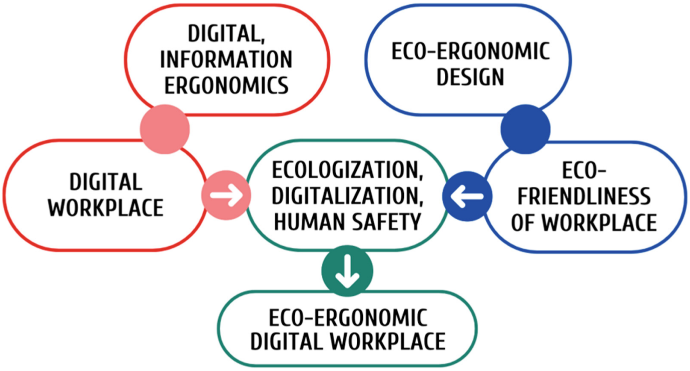

Fig. 1. The creation of an eco-ergonomic digital workplace.

4. Features of the exterior (existence of parking zones and their location, etc.).
5. Ecological needs (requests) of the employee.

The first indicator assesses the quality of the materials of the work elements since it is not only the convenience of the organization of the workplace that is important but also the impact on the human health of the materials from which they are made. The significance of the indicator is that new materials are used to create workplace elements. They have become widespread due to their low price, the possibility of application in various fields, the ability to withstand significant loads and other characteristics. At the same time, their eco-safety and impact on the worker's health during operation have been studied superficially, which means the possibility of distant negative consequences for employees because of permanent contact with them. The example of using a material such as a chipboard confirms this. Several decades ago, the chipboard was widely used for furniture manufacture because of its low price, speed and ease of obtaining. However, it was found that chipboard includes glue containing formaldehyde, which can provoke the development of carcinogenic diseases in humans. That is why evaluating the eco-safety of workplace materials is mandatory when designing the eco-ergonomic digital workplaces.

The second indicator – methods of creating and maintaining working conditions indoors – is used to support ecological working conditions. Now, many different systems are keeping the necessary working conditions in the workplace. However, they differ significantly in eco-friendliness concerning the environment and the worker. To explain this statement, consider the following example. Today, humans use air conditioning to support the necessary micro-climatic conditions indoors. Air conditioning has several advantages. For instance, it quickly creates and maintains the micro-climatic conditions in the premise that meet the requirements, are energy efficient, etc. However, they also have a drawback – bacteria accumulating on the filters of air conditioners can provoke the development of chronic diseases of the respiratory tract in workers. Thus, on the one hand, air conditioners usage is essential for creating comfortable working conditions at workplaces (especially in office premises), but, on the other hand, they are ecologically dangerous for humans. This situation occurs when applying most systems for creating and maintaining working conditions. That is why it is necessary to evaluate their environmental impact on the state of health of employees.

The workplace interior is the third indicator used in the workplace eco-ergonomic assessment. The indicator significance is the assessment of the materials used to decorate the premise. The production of modern finishing materials uses chemical and synthetic components, the quality and eco-safety of which are not evaluated. Moreover, some materials do not have certificates of compliance with sanitary requirements. Thus, the interiors of many premises have a hidden danger, which consists of the influence of chemicals contained in finishing materials on human health. In this case, an example of using such a finishing material is linoleum. This material has several varieties, but linoleums made of synthetic components have become the most widespread. They are the most often used. Of course, they have a lot of advantages, including a low price compared to other coatings, the absence of special requirements for the floor for its use, a long service life, wear resistance, etc. However, there are significant drawbacks and, above all, the chemical composition, which includes toxic resins, xylene, toluene and other components, which are hazardous to human health. Constant exposure to such material leads to the threat of developing carcinogenic diseases, allergic reactions and other negative consequences. Therefore, the eco-ergonomic assessment must include estimating decorative materials quality (coverings on the walls, floor, ceiling, subsidiary furniture, etc.).

The next indicator – the features of the premise exterior – is also essential in the eco-ergonomic assessment of the workplace since it determines the influence of external factors (for example, the content of harmful substances in the air, the proximity of the location of dangerous objects, the frequency of garbage removal and the possibility of its sorting, etc.) on human health. The importance of this indicator is in considering factors that are rarely taken into account by researchers since they are not directly related to the company's activity and, therefore, insignificant to it. At the same time, the influence of such factors on a worker can have a significant negative impact on health. An example is the location of parking zones. Most often, they are located near the company's buildings. In the winter, drivers who use the parking area spend a certain amount of time warming up the car engine, which pollutes the air with fuel combustion products. Thus, these hazardous substances enter the premises near the parking area during ventilation, and workers, accordingly, breathe this air.

The last indicator is the ecological needs (requests) of employees. Its necessity is connected with the application of sustainable development strategies of society. The realisation of the worker's ecological needs contributes to the creation of safe working conditions due to the use of eco-materials to ensure the working process. It, in turn, increases the psychological comfort of workers due to the feeling of maximum safety and decreases morbidity due to the minimal use of materials that can damage worker's health [20].

The above can be summarised and presented in the eco-ergonomics assessment of the digital workplace (Table. 1).

The eco-ergonomics assessment of the digital workplace includes sixteen digital workplace characteristics. Each characteristic has an estimated range from 1 to 5 points. One point corresponds to an unsatisfactory level of eco-ergonomics of the workplace,

Table 1. The eco-ergonomics assessment of the digital workplace (sample).

№	Digital workplace characteristics	Eco-ergonomics, points
	Eco-friendliness of enterprise infrastructure:	
1	special parking areas	5
2	chaotic parking of cars	1
	Building eco-friendliness:	
3	concrete construction	5
4	brick construction	4
5	breeze block building	3
	⋮	⋮
	Overall score:	

and five points – to a satisfactory level. At the end of the assessment, it is necessary to determine the general level of eco-ergonomics of the workplace. The eco-ergonomics of the workplace include unsatisfactory, average and satisfactory levels.

4 Discussion

The approbation of the eco-ergonomics assessment of the digital workplace was carried out at Simon Kuznets Kharkiv National University during 2021–2022. Students in the first year of study were chosen as testees. The total number of testees was 157. During the research, students were online learning, actively moved and worked from different locations. Thus, students worked using the digital workplaces. During the study, the following indicators were estimated:

1. The eco-ergonomics of the digital workplace.
2. Students' performance.
3. Students' well-being.

The eco-ergonomics of the digital workplace was assessed using the above-described assessment and the "Subjective assessment of the eco-ergonomics of the digital workplace" test. For the convenience of conducting the research, the test was placed on the free Internet service Online Test Pad.

The "Subjective assessment of the eco-ergonomics of the digital workplace" test included questions concerning the subjective perception of the features of the eco-ergonomics organization of the digital workplace and how it affects the testee's performance. The subjective assessment of the eco-ergonomics of the digital workplace was measured in points in the range from 1 to 100.

The student's performance was estimated using the "Student's performance" test. For the convenience of conducting research, the test was placed on the free Internet service Online Test Pad.

The student's well-being was estimated using the "Subjective well-being" test. The subjective well-being assessment was measured in points in the range from 1 to 100. The test was placed on the free Internet service Online Test Pad.

Testees passed the eco-ergonomics assessment of the digital workplace, the "Subjective assessment of the eco-ergonomics of the digital workplace" test, the "Student's performance" test, and the "Subjective well-being" test through an Internet link. Students could do it using any digital device with an Internet connection. The results were generalized in the analytical database of the Online Test Pad. Based on this, files were created for further data processing. We visualized the results using graphs.

In the first stage, students were divided into three groups according to their performance indicators:

1. The first group includes 51 students with a high level of performance (average grade point in the range of 90…100 points).
2. The second group involves 53 students with an average level of performance (medium grade point in the range of 74…89 points).
3. The third group includes 53 students with a satisfactory level of performance (average grade point in the range of 60…73 points).

Then, based on the results of the students' testing, a correlation was performed to establish the relationships between students' performance and the eco-ergonomics of the digital workplace.

The analysis of changes in students' performance and the results of assessing the eco-ergonomics of the digital workplace showed that the eco-ergonomics of the workplace affects the students' performance. It is revealed in the following pattern: the higher the level of the eco-ergonomics of the digital workplace, the higher the students' performance and the smaller range of values in which it varies (Fig. 2).

In the second stage, students were divided into three groups based on their well-being:

1. The first group includes 52 students with well-being level 90…100 points.
2. The second group involves 53 students with well-being level 70…89 points.
3. The third group includes 52 students with well-being level 60…69 points.

Comparative and correlation analyses of changes in the eco-ergonomics of the digital workplace and students' well-being in groups showed that the eco-ergonomics of the digital workplace positively correlated with students' well-being (Fig. 3).

Based on the presented results, the following conclusions were obtained:

1. The eco-ergonomics of the digital workplace affects the students' performance. It was revealed in the following pattern: the higher the eco-ergonomics of the digital workplace, the higher the students' performance. Thus, teaching students the basics of eco-ergonomics organization of the digital workplace will increase their productivity.
2. The relationship between the student's well-being and the eco-ergonomics of the digital workplace was revealed. It was found the following pattern: the higher the level of the eco-ergonomics of the digital workplace, the higher the level of students' well-being. Thus, the eco-ergonomics of the digital workplace affects students' well-being.

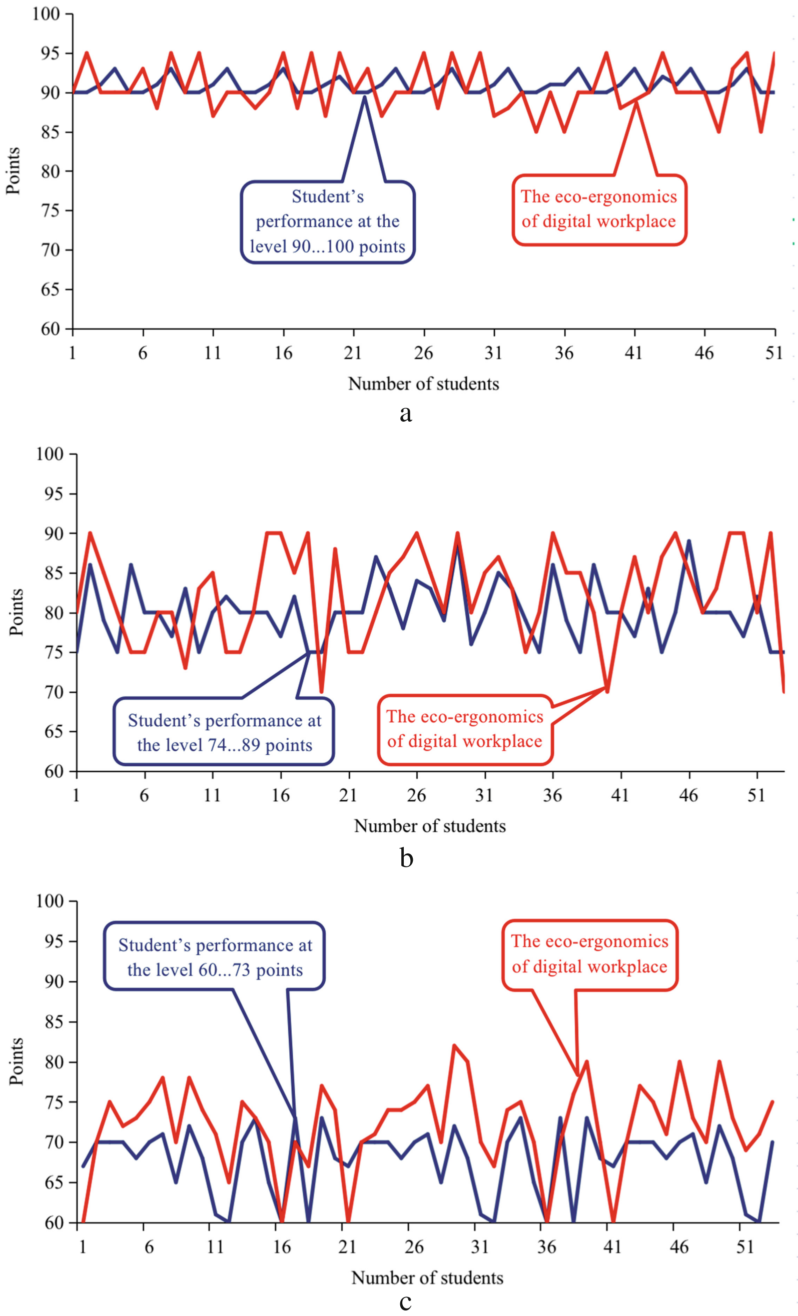

Fig. 2. Comparative analysis of changes in students' performance and the eco-ergonomics of the digital workplace in groups: (a) high level of students' performance; (b) average level of students' performance; (c) low level of students' performance.

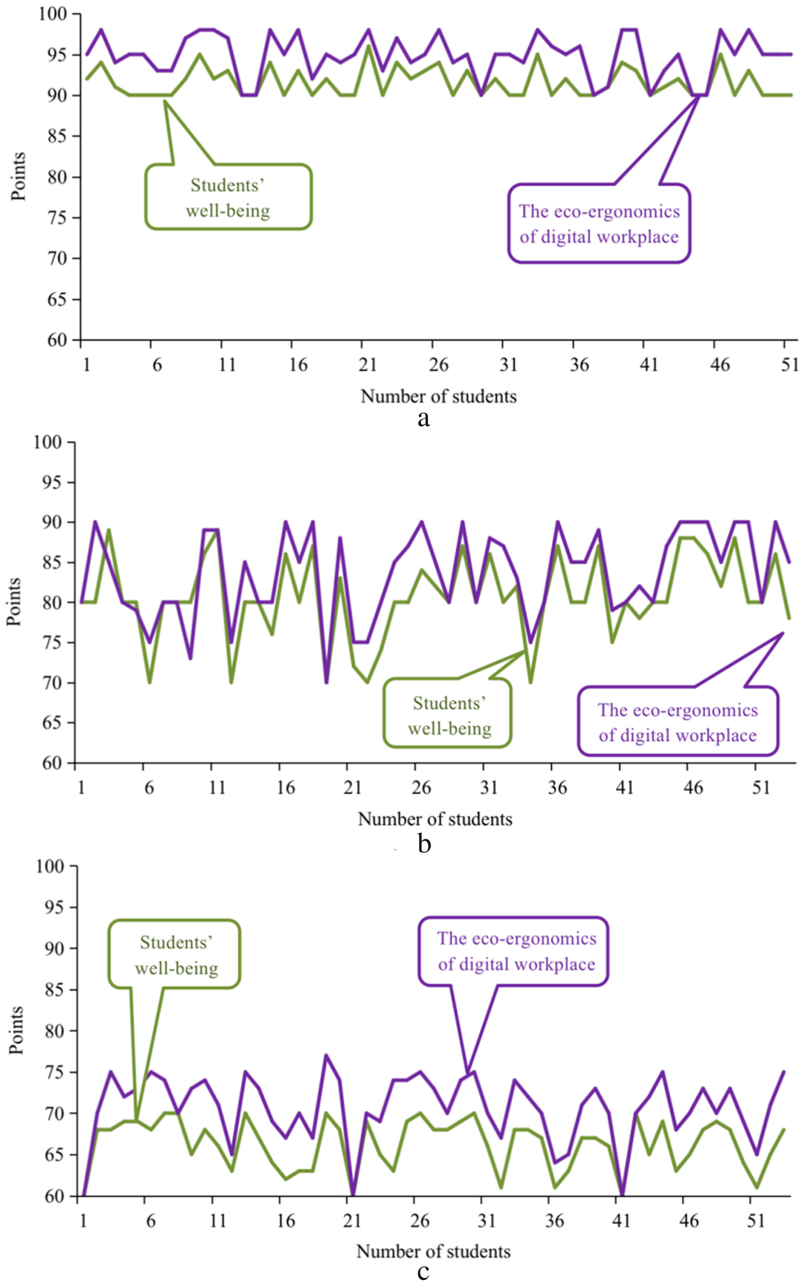

Fig. 3. Comparative analysis of changes in students' well-being and the eco-ergonomics of the digital workplace in groups: (a) well-being level 90…100 points; (b) well-being level 70…89 points; (c) well-being level 60…69 points.

Therefore, the goal of the research has gained practical confirmation. The employee's performance and well-being depend on the level of the eco-ergonomics of the digital workplace.

5 Conclusions

Thus, the digitalization and ecologization of human activity are currently essential for society's sustainable development. The result of the eco-digitalization of human activity should be an eco-ergonomic digital workplace, which will increase worker's performance and safety during work. The necessity of such a workplace has been proven based on a study of the impact of the eco-ergonomics of the digital workplace on student's performance and well-being during online learning. An effective tool in the eco-ergonomics digital workplace development and implementation is ergonomics, for which this problem has become crucial over the last decade.

References

1. Protasenko, O.F., Mygal, G.V.: Ergonomics 4.0: digitalization problems and overcoming them. Municipal Econ. Cities **177**(3), 182–188 (2023)
2. Caterino, M., Rinaldi, M., Fera, M.: Digital ergonomics: an evaluation framework for the ergonomic risk assessment of heterogeneous workers. Int. J. Comput. Integr. Manuf. **36**(2), 1–21 (2023)
3. Franssila, H., Okkonena, J., Savolainena, R.: Developing measures for information ergonomics in knowledge work. Ergonomics **59**(3), 435–448 (2016)
4. Mygal, G.V., Protasenko, O.F.: New concepts of modern ergonomics. Open Inf. Comput. Integr. Technol. **79**, 162–171 (2018)
5. Protasenko, O.F., Mygal, G.V.: Human factors: the problem of man-machine interaction under the digitalization conditions. Sci. J. Polonia Univ. **48**(5), 198–210 (2021)
6. Parasuraman, R., Mehta, R.: Neuroergonomics: a review of applications to physical and cognitive work. Front. Hum. Neurosci. **7**, 889 (2013)
7. Mygal, G., Protasenko, O., Kobrina, N., Mykhailova E.: Ergonomic thinking in the design of human-machine systems. Bull. National Tech. Univ. KhPI **1**(15), 42–52 (2023)
8. Work 4.0 Homepage. https://en.wikipedia.org/wiki/Work_4.0. Accessed 20 Aug 2023
9. Kolot, A.M., Herasymenko, O.O.: The concept of "Work 4.0": theoretical and applied principles of formation and development. Econ. Forecast. **1**, 7–31 (2020)
10. Bordi, L., Okkonen, J., Mäkiniemi, J.-P., Heikkilä-Tammi, K.: Communication in the digital work environment: implications for wellbeing at work. Nord. J. Work. Life Stud. **8**, 29–48 (2018)
11. Baptista, J., Stein, M.-K., Klein, S., Watson-Manheim, M.B., Lee, J.: Digital work and organisational transformation: emergent digital/human work configurations in modern organisations. J. Strat. Inf. Syst. **29**, 1–10 (2020)
12. Oeij, P.R.A., Dhondt, S., Rus, D., Van Hootegem, G.: The digital transformation requires workplace innovation: an introduction. Int. J. Technol. Transf. Commer. **16**(3), 199–207 (2019)
13. Balaban, O., Puppim de Oliveira, J.A.: Sustainable buildings for healthier cities: assessing the co-benefits of green buildings in Japan. J. Cleaner Product. **163**, 68–78 (2017)
14. Alwisy, A., BuHamdan, S., Gül, M.: Evidence-based ranking of green building design factors according to leading energy modelling tools. Sustain. Cities Soc. **47**, 101491 (2019)

15. Franco, M.A.J.Q., Pawar, P., Wu, X.: Green building policies in cities: a comparative assessment and analysis. Energy Buildings **231**, 110561 (2021)
16. Liu, T., et al.: Sustainability considerations of green buildings: a detailed overview on current advancements and future considerations. Sustainability **14**(21), 14393 (2022)
17. Online environmental consultant of the enterprise Homepage. http://ecologiya.com.ua/. Accessed 23 July 2023
18. Work Environment: What it is, Types and Elements to Create it Homepage. https://www.questionpro.com/blog/work-environment/. Accessed 02 July 2023
19. Raziq, A., Maulabakhsh, R.: Impact of working environment on job satisfaction. Procedia Econ. Finance **23**, 717–725 (2015)
20. Protasenko, O.F., Mygal, G.V.: Eco-ergonomic designing of working environment. Open Inf. Comput. Integr. Technol. **89**, 104–122 (2020)
21. Thatcher, A.: State of Science: ergonomics and global issues. Ergonomics **61**(2), 197–213 (2018)
22. Morales, K.L.: Synergies between ergoecology and green ergonomics: a contribution towards a sustainability agenda for HFE. Hum. Fact. Organizational Design Manag. **1**, 771–776 (2014)
23. What is the workplace environment and why is it important? Homepage. https://ifeelonline.com/en/occupational-health/workplace-environment/. Accessed 21 July 2023
24. Wilson, J.R.: Fundamentals of systems ergonomics. Work **41**, 3861–3868 (2012)
25. Hedge, A.: Green buildings need good ergonomics. Ergonomics **56**(3), 492–506 (2013)

Analysis of Particle Parameters of Multi-channel Mixed Cross-Section Right-Angle Cold Spray Nozzle Structure

Tan Kun(✉)

National Aerospace University "Kharkiv Aviation Institute", 17 Chkalova Street, Kharkiv 61070, Ukraine
tankun09@126.com

Abstract. Cold spray technology is a solid-state deposition technology. The particles are accelerated in the Laval nozzle and plastically deform after deposition with the substrate to form a coating. The nozzle is an important part of cold spray technology, which will directly affect the coating performance and has been paid attention to and studied in engineering applications. This article combines circular cross-sections and rectangular cross-sections to form a hybrid cross-section right-angle cold spray nozzle; based on the single-channel nozzle, multi-channel nozzles are gradually studied. The results show that the three-channel nozzle has better heating characteristics than the single-channel nozzle; it has better acceleration characteristics and particle utilization efficiency than the double-channel nozzle, and the velocity flow field in the expansion section is more uniformly distributed along the axial direction; The three-channel nozzle can make particles flow out from the velocity center area at the exit of the expansion section, and the particle size has the greatest contribution to velocity; the three-channel nozzle can achieve the deposition of a variety of particle materials on the substrate, and can also achieve the velocity conditions required for the compaction of coatings by Al_2O_3 particles; the three-channel mixed cross-section right-angle cold spray nozzle is suitable for spray deposition in compact space; the multi-channel nozzle provides a reference for the research on cold spray nozzles opinion.

Keywords: Cold spraying · multi-channel nozzle · velocity · temperature · Al Alloy

1 Introduction

Cold spray technology is a new type of supersonic solid-state deposition technology that accelerates particles to supersonic speeds through accelerating media (hydrogen, nitrogen, helium, air), and produces plasticity through the impact between particles/substrate and particles/particles deformation, ultimately achieving deposition of particles on the substrate and forming an effective coating [1, 2]. Compared with thermal spraying technology, cold spraying technology has the characteristics of less oxidation, small residual stress and mainly compressive stress, simple operation and low cost [3, 4]; it is often suitable for oxidation-sensitive and heat-sensitive products. Materials such as Al, Al6061,

M. Nechyporuk et al. (Eds.): ICTM 2023, LNNS 1008, pp. 52–65, 2024.
https://doi.org/10.1007/978-3-031-61415-6_5

Cu, Ti, Zn, etc. Cold spray technology is capable of depositing metals, alloys, polymers and mixtures [5, 9]. Cold spray technology is mainly used to repair and protect the surface of parts, and is also widely used in the field of additive manufacturing technology [10–12].

Cold spray nozzle is an important part of cold spray technology and has been widely concerned and studied in engineering applications. The early cold spray nozzle structure used the Laval nozzle, whose cross-section was circular. Laval nozzles usually come in two forms: conical and bell-shaped. The difference between these two nozzles lies in the design of the expansion section. Currently, most cold spray nozzle structures are conical nozzles [13]. The cross-sectional shapes of Laval nozzles include circular, rectangular and oval, as shown in Fig. 1; cold spray nozzles with circular cross-sections are more common; cold spray nozzles with rectangular cross-sections can be used to spray thinner rotating body specimens and workpieces; cold spray nozzles with oval cross-sections are the rarest and extremely difficult to machine.

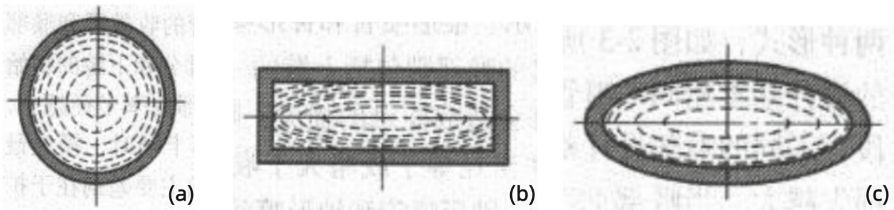

Fig. 1. Three different nozzle cross-sections. a: circular cross-section; b: rectangular cross-section; c: elliptical cross-section

Single-channel axially symmetric cold spray nozzles are more common, but there are relatively few research works on multi-channel cold spray nozzles. Hu [14] and Dolmatov [15] studied multi-channel cold spray nozzles with rectangular cross sections. The cold spray nozzle mainly completes the part of accelerating particles, of which the speed and temperature of the particles before they reach the substrate are the most important. The factors that affect the speed and temperature of the particles include technical parameters and structural parameters respectively. Technical parameters include: temperature and pressure of gas, temperature and size of spray powder. Structural parameters: particle inlet position and spraying angle, parameters of the throat and expansion section [16, 17]. Arndt [18] can control the contact time between the particles and the acceleration medium by adjusting the position of the particle inlet, ensuring that the particles have a higher temperature before reaching the substrate. The temperature of particles is a key parameter that affects the speed. In order to obtain the target coating, the existing cold spray nozzle has certain limitations. Therefore, this article proposes a new multi-channel hybrid cross-section right-angle cold spray nozzle. The technical characteristics of the technology are that it combines nozzles with circular and rectangular cross-sections, Its advantages are: the length of the expansion section is short, the operation is simple, and it is suitable for spray deposition in tight space areas.

This article studies the particle acceleration and heating characteristics of single-channel, dual-channel and three-channel hybrid cross-section right-angle cold spray nozzles. The multi-channel hybrid cross-section right-angle cold spray nozzle is a hand-held cold spray device that solves the problem that some parts cannot be sprayed with long straight cold spray nozzles. Hu [14] verified the authenticity of this problem. The throat of the multi-channel hybrid cross-section right-angle cold spray nozzle is designed with a multi-channel right angle, so that the internal airflow and particles can turn at the throat. The particles passing through the throat can achieve a 90° turn under the action of the carrier gas coupling force, and the particles continue to flow. Acceleration continues in the expansion section of the nozzle; a new multi-channel hybrid cross-section right-angle cold spray nozzle is studied. By analyzing the particle injection position and combining the spray parameters (nitrogen pressure, temperature and powder particle size), the acceleration after powder injection is and the influence of heating characteristics, ultimately achieving the spraying of a variety of materials.

2 Simulation Method and Material Model and Hybrid Cross-Section Right-Angle Cold Spray Nozzle Model

2.1 Simulation Methods and Material Models

Solidworks simulation software was used to simulate and analyze the particle flow in single-channel and multi-channel hybrid cross-section right-angle cold spray nozzles. Comparing the residual diagram, the $\kappa - \varepsilon$ turbulence model has a better convergence speed; comparing the mass flow error, the $\kappa - \varepsilon$ turbulence model has the smallest mass flow error, so the turbulence model is used [17]; without considering wall slip and heat transfer, the $\kappa - \varepsilon$ turbulence intensity is 2% [17]; the carrier gas is nitrogen, the pressure inlet is 3 Mpa−5 Mpa, the pressure outlet is ambient atmospheric pressure, the initial temperature of nitrogen is 400 K-1200 K, the inlet of the convergence section is the pressure inlet, and the outlet of the expansion section is the pressure exit.

The purpose of developing the multi-channel mixed cross-section right-angle cold spray nozzle is to meet the spraying needs of a variety of particles; spraying particles Al, Al6061, Cu, Ni, Zn, Mg and Al_2O_3; the materials are all spherical particles, and the particle size range is 10−40 um.

2.2 Hybrid Cross-Section Right-Angle Cold Spray Nozzle

This article focuses on single-channel, dual-channel and three-channel hybrid cross-section right-angle cold spray nozzles; for the research method of multi-channel right-angle cold spray nozzles refer to Hu [14], who also use computational fluid dynamics based on single-channel Hybrid cross-section right-angle cold spray nozzle further study on multi-channel hybrid cross-section right-angle cold spray nozzle. Figure 2 shows a single-channel right-angle cold spray nozzle. The internal channel of the single-channel right-angle cold spray nozzle is composed of four parts: a cylindrical section, a contraction section, a throat and an expansion section; the cross-sections of the cylindrical section and the expansion section are circles. The cross-section of the constriction section and throat is rectangular; the hybrid cross-section right-angle cold spray nozzle is a combination of rectangular cross-section and circular cross-section nozzle. The diameter of the cylindrical section is 11.5 mm, the curvature of the lower part of the contraction section is 97 mm, the thickness of the contraction section and the throat is 3.5 mm, the turning radius of the throat is 6 mm, and the exit diameter of the expansion section is 6.06 mm.

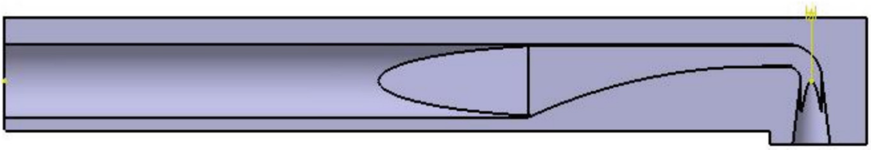

Fig. 2. Single-channel mixed cross-section right-angle cold spray nozzle

3 Analysis of Single-Channel and Multi-channel Mixed Cross-Section Right-Angle Cold Spray Nozzles

For the convenience of description in this article, the single-channel hybrid cross-section right-angle cold spray nozzle is referred to as the single-channel nozzle; the double-channel mixed cross-section right-angle cold spray nozzle is referred to as the two-channel nozzle; the three-channel mixed cross-section right-angle cold spray nozzle is referred to as the three-channel nozzle.

4 The Single-Channel Nozzle

The analysis shows that it is more reasonable for the particle inlet of the single-channel hybrid cross-section right-angle cold spray nozzle to be located outside the turning part of the throat; as shown in Fig. 3(a), it is a spherical Al_2O_3 with an inlet pressure of 3 Mpa, an initial temperature of 700 K, and a particle size of 40 um. Flow conditions inside the nozzle. It can be seen from the figure that the Al_2O_3 particles do not collide with the inner wall of the nozzle, which is related to the position and angle of injection of Al_2O_3 particles; the velocity V1 of particle Al_2O_3 injection and the air flow velocity V2 are acute angles, so the speed of particle Al_2O_3 in the expansion section of the nozzle is the resultant speed is V3, as shown in Fig. 3(b). The position of the Al_2O_3 particle inlet is located outside the turning part of the throat and very close to the expansion section of the nozzle. The particles are accelerated by nitrogen, and the high-temperature nitrogen can heat the particles. The temperature of the particles has a greater impact on the deposition process and coating performance [16], by studying the location of the particle inlet, thereby increasing the heating time of the nitrogen gas to the particles. Therefore, the single-channel hybrid cross-section right-angle cold spray nozzle cannot fully heat the particles, and the position of the Al_2O_3 particle inlet is not conducive to later actual operations.

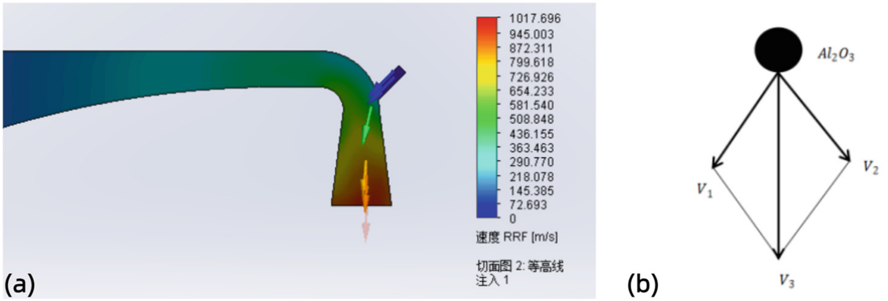

Fig. 3. The flow of in the nozzle (a) and the velocity analysis of Al_2O_3 particles in the nozzle (b)

5 The Multi-channel Nozzle

Figure 4 shows a double-channel hybrid cross-section right-angle cold spray nozzle. Block A at the throat of the nozzle divides the nozzle throat into channel A and channel B; combined with the design experience of a single-channel hybrid cross-section right-angle cold spray nozzle, locating the spray powder inlet of the double-channel mixed cross-section right-angle cold spray nozzle inside the connection between the throat and the contraction section can increase the heating time of the nitrogen gas to the particles; expand the multi-channel mixed cross-section right-angle cold spray nozzle the expansion length is set to 25 mm to ensure that the particles have sufficient deposition speed before depositing the substrate.

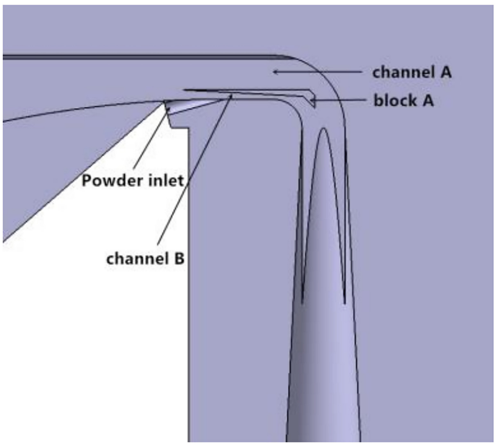

Fig. 4. The double-channel mixing cross-section right-angle cold spray nozzle

As shown in Fig. 5, the inlet pressure is 5 Mpa, the initial temperature is 600 K, and the flow conditions of Al_2O_3, Al and Cu particles of different particle sizes inside the double-channel mixing cross-section right-angle cold spray nozzle. It can be seen from Fig. 5 that all three types of particles collide with the inner wall of the expansion section of the nozzle. The particles will decelerate during the deposition, which is detrimental to spraying. When the particles enter channel B from the injection port, the particles collide with the inner wall of channel B of the nozzle. Collision occurs because the direction of particle injection is at an angle to the direction of air flow; collision of spray particles in channel B is unavoidable, but particle collisions on the inner wall of the expansion section of the nozzle should be minimized. The main acceleration stage of particles is in the expansion section of the nozzle., otherwise it will affect particle acceleration.

It can be seen from Fig. 5 that under the same working conditions, as the particle size increases, the earlier the particle hits the inner wall of the nozzle expansion section; because the larger the particle size, the larger the particle surface area, the greater the resistance encountered during the particle acceleration process. Large, indicating that particle size is also an important factor affecting particle acceleration. In the expansion section of the nozzle, the high-speed airflow area is biased to the right side of the expansion section, showing an asymmetric distribution along the axial direction of the expansion section.

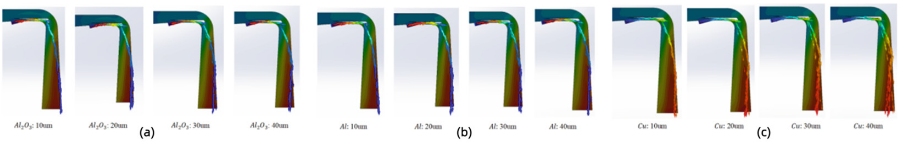

Fig. 5. The flow of Al_2O_3, Al, and Cu particles of different sizes in the double-channel nozzle

Figure 6 shows the speed analysis of particles just entering the expansion section of the double-channel nozzle. The nitrogen flow speed is V_2, and the initial speed of particles entering the expansion section is V_1. Therefore, the actual speed of particles in the nozzle is V_3, but the speed direction of V_3 it is not along the axial direction of the nozzle expansion section, so the particles will hit the inner wall of the expansion section during acceleration. From a theoretical analysis, the target velocity of particles in the expansion section of the nozzle is V_3^*, so it is necessary to ensure that the carrier gas velocity is V_2^*, so that the particles will not collide with the inside of the nozzle during the acceleration process in the expansion section.

In order to ensure that the particles will not collide with the inner wall of the nozzle expansion section during acceleration, block B is added on the basis of the double-channel mixing type cross-section right-angle cold spray nozzle. The block B at the nozzle throat divides the nozzle throat into channel B and channel C, as shown in Fig. 7, are the specific parameters of the optimized three-channel hybrid cross-section right-angle cold spray nozzle and throat channel. After the particles are accelerated in channel A, they merge with the nitrogen coming in from channel B, thereby changing the velocity direction of the powder, ensuring that the particles will not collide with the inner wall of the nozzle expansion section, and completing the acceleration of the particles in the nozzle.

Al_2O_3 particles with particle sizes of 10 um, 20 um, and 30 um were simulated and analyzed in a three-channel mixed cross-section right-angle cold spray nozzle. The temperature range is 800 k−1000 K, the pressure range is 3–5 MPa, and the spraying

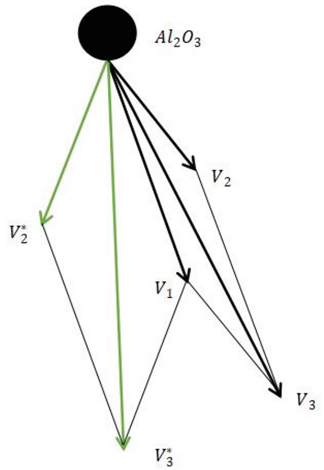

Fig. 6. Velocity analysis of sprayed particles just entering the expansion section

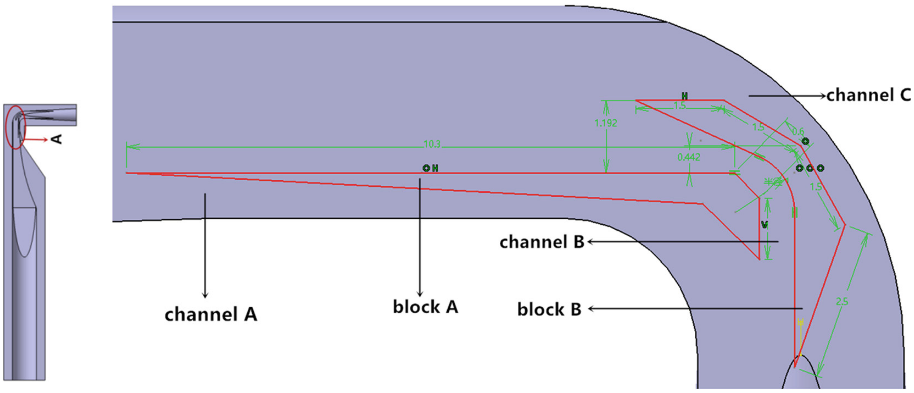

Fig. 7. The specific parameters of the three-channel hybrid cross-section right-angle cold spray nozzle and throat channel

distance is 20 mm. It is obtained that the velocity of Al_2O_3 particles before reaching the substrate/coating, as shown in Table 1.

It can be seen from Table 1 that nitrogen pressure, temperature and particle size of Al_2O_3 particles will all affect the speed of particle Al_2O_3 in the nozzle; Alhulaifi [19] scholars also reached the same conclusion. The contribution rate of influencing factors to the objective function can be studied using RSM, and the contribution rate of each influencing factor can be obtained. From Table 1, it can be seen that the impact of Al_2O_3 particle size on speed is greater than the pressure and temperature of nitrogen, so it is recommended to choose particle size. Al_2O_3 particles with diameters of 10 um and 20 um.

Table 1. The velocity before the particles reaches the coating under different working conditions.

N_2 Pressure/Mpa	N_2 Temperature/K	Powder size/um	Velocity/m/s
3	800	10	551.691
		20	454.704
		30	402.650
	900	10	584.719
		20	477.986
		30	420.891
	1000	10	607.147
		20	493.696
		30	433.343
4	800	10	576.308
		20	479.043
		30	430.683
	900	10	603.584
		20	498.367
		30	446.833
	1000	10	624.004
		20	507.352
		30	455.895
5	800	10	597.075
		20	502.665
		30	450.424
	900	10	625.237
		20	522.341
		30	466.143
	1000	10	652.233
		20	590.753
		30	483.301

Figure 8 shows the flow conditions of 10 um and 20 um Al_2O_3 particles inside the expansion section of the nozzle under different working conditions. It can be seen from Fig. 8 that the three-channel hybrid cross-section right-angle cold spray nozzle can ensure that all Al_2O_3 particles can be smoothly ejected from the exit of the nozzle, the Al_2O_3 particles will not collide during the acceleration process inside the expansion section of the nozzle; the vast majority of Al_2O_3 particles flow out from the velocity center area at the exit of the expansion section, ensuring that the Al_2O_3 particles are in the the best acceleration state; the velocity flow field in the expansion section of the three-channel hybrid cross-section right-angle cold spray nozzle is symmetrically distributed along the axial direction; adding channel B can improve the recovery coefficient (K) of Al_2O_3 particles in the three-channel hybrid cross-section right-angle cold spray nozzle, the nitrogen flow of channel B can slightly adjust the outflow direction of the particles coming from channel A, thereby improving the utilization rate of Al_2O_3 particles in the spraying process and better economy.

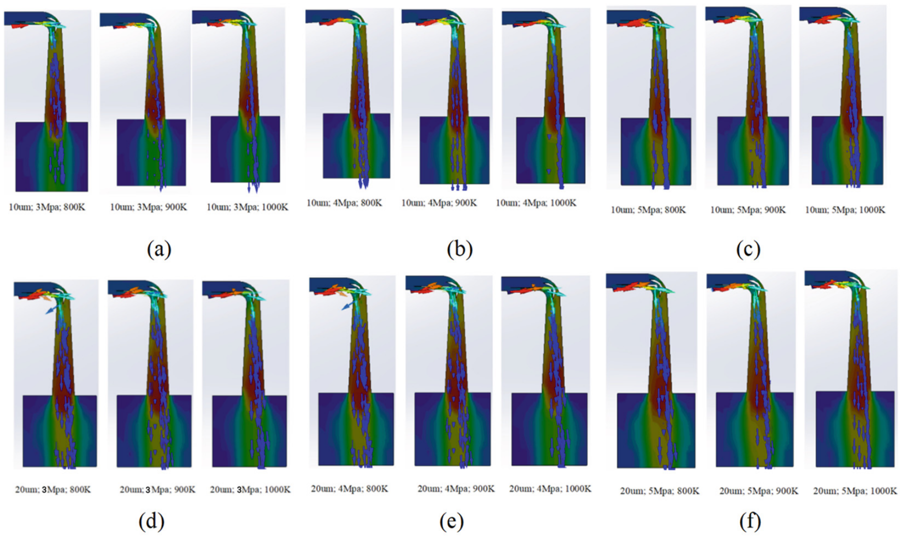

Fig. 8. Al_2O_3 particles flow in the nozzle throat and expansion section under different working conditions

6 Velocity and Temperature Analysis of Particles in the Three-Channel Nozzle

The critical velocity of particles is the main indicator that determines whether the spray material can be deposited on the substrate; the critical velocity is related to the material properties and temperature; the critical velocity calculation formulas (1) and (2) can be used to calculate the particle speed. The critical velocity of materials Al, Al6061, Cu, Ni, Zn and Mg at different temperatures; the critical velocity of some materials are referred to [14, 20]; as shown in Table 2.

$$V_{Critical} = \sqrt{C_p(0.7 \cdot T_m - T_i)} \tag{1}$$

$$V_{Critical} = \sqrt{\frac{F_1 \cdot 4 \cdot \sigma_{TS} \cdot \left(1 - \frac{T_i - T_r}{T_m - T_r}\right)}{\rho} + F_2 \cdot C_p(T_m - T_i)} \tag{2}$$

Where: C_p: the specific heat; T_m: the melting point; T_i: s impact temperature. $F_1 = 3.8, F_2 = 0.3$, ρ: the particle density, σ_{TS}: the tensile strength. T_r: the reference temperature (293 K).

The critical velocity of Zn particles is very low. When the temperature is 400 K, the critical velocity is 299 m/s; when the temperature is 500 K, the critical velocity is 274 m/s; therefore, the deposition of Zn particles on the substrate is easy to achieve, which is caused by the Zn particles. The physical properties of Zn determine that when the temperature is greater than 500 K, Zn particles will become soft, which is beneficial to deposition.

Al particles are easy to obtain, low density, high ductility and good corrosion resistance, making them the most common raw material in cold spraying; Al particle is a very easy material to deposit when the temperature is 400 K-600 K, the deposition speed of Al particles ranges from 517−570 m/s, and the melting point of Al particle is 900 K, so the temperature of nitrogen does not need to be too high to achieve deposition on the substrate; research shows that some relatively minor problems appear on the surface of pure Al coatings. Shallow craters with smooth edges [21] indicate that the surface roughness of the pure Al coating is large, the porosity is high, the hardness is low, and the wear resistance is poor, which seriously restricts the application of cold spray Al coatings [22].

The critical velocity of Mg particles is higher than that of Zn particles and Al particles when the temperature is 400 K−600 K, the critical velocity of Mg particles is 629−573 m/s.

The deposition of Ni particles is more difficult. When the temperature is 1100 K, the critical velocity is 564 m/s; when the temperature is 1200 K, the critical velocity is 552 m/s; Ni is a high-temperature resistant material and has high hardness, so the deposition of Ni particles is relatively difficult; Ni particles requires higher carrier gas (nitrogen, helium) temperature.

The influence of ceramic Al_2O_3 on the relative coating performance [23–25], Analyzed the acceleration characteristics of Al_2O_3 in the three-channel nozzle has important guidance and reference significance; Through calculation and analysis, it can be known that the melting point of Al_2O_3 is very high, so the critical velocity of Al_2O_3 is very large, so it is difficult to deposit Al_2O_3 particles; Continue to spray Al_2O_3 particles on the pure Al coating with higher roughness and higher porosity, so as to reduce the porosity and roughness of the pure Al coating surface [20]; Therefore, Al_2O_3 particles can be used as a spray material for tamped and strengthened coating, and the velocity before the collision with the coating is guaranteed to be greater than 590 m/s.

As shown in Table 2, the nitrogen pressure is 5 Mpa, the particle size is 10 um, and the spraying distance is 20 um. The speed and temperature parameters of the particles before they hit the substrate after being accelerated through the three-channel hybrid cross-section right-angle cold spray nozzle. It can be seen from the parameters in Table 2 that the critical velocity is related to the physical properties of the particles, and is also related to the temperature of the nitrogen. The higher the temperature, the smaller the critical velocity; the criterion for determining whether the particles can be deposited is: the speed when the particles reach the substrate greater than the critical velocity of the particles; increasing the temperature of nitrogen can increase the velocity of the particles before they reach the substrate, indicating that increasing the temperature is beneficial to the deposition of particles on the substrate.

It can be seen from Table 2 that the five types of particles are accelerated and heated in the three-channel hybrid cross-section right-angle cold spray nozzle; nitrogen at the same temperature, the heating effect of the sprayed particle is similar; comparing the temperature of the particles before they reach the substrate/coating, it shows the particles have been heated during the acceleration process in the nozzle, which will be beneficial to the deposition process of the particles.

Combining the physical properties of Al_2O_3 particles, it can be seen that Al_2O_3 particles are a very good material for consolidating coatings; through numerical simulation, the nitrogen temperature is 400 K−1200 K, and the speed of Al_2O_3 particles before reaching the substrate/coating is 437−701 m/s, which can suitable for the compaction of Cu, Mg, Al, Al6061, and Zn coatings. The simulation results show that the three-channel hybrid cross-section right-angle cold spray nozzle can deposit a variety of materials on the substrate.

Table 2. Velocity and temperature parameters of different particles before they deposit the substrate after being accelerated by three-channel nozzle.

Temperature/K		400	500	600	700	800	900	1000	1100	1200
Powders										
Al_2O_3	V_{max}/m/s	437	489	532	566	597	625	652	677	701
	T_{impact}/K	366	437	507	579	651	724	797	873	944
Ni	V_{max}/m/s	–	–	–	–	–	–	546	569	582
	$V_{critical}$/m/s	–	–	–	–	–	–	574	564	552
	T_{impact}/K	–	–	–	–	–	–	796	874	950
Cu	V_{max}/m/s	–	–	456	481	504	–	–	–	–
	$V_{critical}$/m/s	–	–	480	467	452	–	–	–	–
	T_{impact}/K	–	–	510	582	655	–	–	–	–
Mg	V_{max}/m/s	487	547	602	644	–	–	–	–	–
	$V_{critical}$/m/s	630	600	570	540	–	–	–	–	–
	T_{impact}/K	368	441	513	586	–	–	–	–	–
Al	V_{max}/m/s	462	518	568	–	–	–	–	–	–
	$V_{critical}$/m/s	570	544	517	–	–	–	–	–	–
	T_{impact}/K	367	439	510	–	–	–	–	–	–
Al6061	V_{max}/m/s	–	585	625	647	671	–	–	–	–
	$V_{critical}$/m/s	–	573	557	541	532	–	–	–	–
	T_{impact}/K	–	410	526	639	756	–	–	–	–

(*continued*)

Table 2. (*continued*)

Temperature/K Powders		400	500	600	700	800	900	1000	1100	1200
Zn	V_{max}/m/s	398	443	–	–	–	–	–	–	–
	$V_{critical}$/m/s	299	274	–	–	–	–	–	–	–
	T_{impact}/K	368	441	–	–	–	–	–	–	–

Note: V_{max}: Maximum velocity before the powder deposited on the substrate; $V_{critical}$: Critical velocity of powder deposition; T_{impact}: Maximum temperature before the powder deposited on the substrate;

7 Conclusions

This article discusses, analyzes and demonstrates the structures of single-channel and multi-channel hybrid cross-section right-angle cold spray nozzles. The research results show that the three-channel hybrid cross-section right-angle cold spray nozzle is feasible; the influence of spray parameters (nitrogen pressure, temperature and powder particle size) on the acceleration and heating characteristics after particle injection is analyzed.

The three-channel nozzle has better heating characteristics than the single-channel nozzle; it has better acceleration characteristics and particle utilization efficiency than the double-channel nozzle, and the velocity flow field in the expansion section is more uniformly distributed along the axial direction.

Particle size has the greatest contribution to particle velocity; The position where particles collide with the inner wall of the expansion section is related to the particle size. The larger the particle size, the earlier the particle will hit the inner wall of the nozzle expansion section. The particle size is proportional to the resistance it receives.

The three-channel nozzle can correct the velocity direction of the particles that are partially resisted by flowing inside the nozzle, thereby ensuring that the particles will not collide with the inner wall of the expansion section during the acceleration process of the expansion section, and the particles that are subject to resistance will all exit from the exit of the expansion section. The velocity center area flows out, thereby improving the utilization of the resistance received during the spraying process.

The three-channel hybrid cross-section right-angle cold spray nozzle can realize the deposition of a variety of granular materials (Al, Al6061, Cu, Mg, Zn) on the substrate; it can also meet the speed conditions required for the compaction of the coating by the particles Al_2O_3. At the same time, the three-channel hybrid cross-section right-angle cold spray nozzle is suitable for spraying in tight spaces. It has the characteristics of small expansion section length and simple operation.

This article focuses on the acceleration and heating characteristics of commonly used particles in a three-channel hybrid cross-section right-angle cold spray nozzle; later analysis of the velocity characteristics of particles turning in the throat and the impact of the chamfering of the edges of Block A and Block B on the throat on the nitrogen flow field and the influence of the acceleration characteristics of sprayed powder, a multi-factor coupling effect was established to improve the three-channel hybrid cross-section right-angle cold spray nozzle.

Acknowledgement. The author would like to thank the China Scholarship Council for its support (NO. 201908360307).

References

1. Zhang, J.H., Sun, R.: Research progress of laser cladding on titanium alloy surface. Mater. Rev. **28**(6), 89–93 (2014). https://doi.org/10.16490/j.cnki.issn.1001-3660.2020.08.011
2. Pan, X.Y., Liang, W.P., Miu, Q., Ren, B.L., Liu, W.: Tribological behavior of plasma chromized layer on TC21 alloy at different temperatures. J. Nanjing Univ. Aeronaut. Astronaut. **48**(1), 35–41 (2016)
3. Xiong, T.Y., Wu, J., Jin, H.Z.: Introduction to a new technology-cold gas dynamic spray. Corros. Sci. Protect. Technol. **13**(5), 267–269 (2001)
4. Schmidt, T., Assadi, H., Grtner, F.: From particle acceleration to impact and bonding in cold spraying. J. Therm. Spray Technol. **18**(5), 794–808 (2009).https://doi.org/10.1007/s11666-009-9357-7
5. Tan, K., Markovych, S., Wenjie, H.U.: Review of application and research based on cold spray coating materials. Aerosp. Tech. Technol. **1**(1), 47–59 (2021). https://doi.org/10.32620/aktt.2021.1.05
6. Shorinov, O.: Finite element analysis of thermal stress in Cu2O coating synthesized on Cu substrate. Arch. Mater. Sci. Eng. **115**(2), 58–65 (2022). https://doi.org/10.5604/01.3001.0016.0753
7. Shorinov, O.V., Polyviany, S.A.: Simulation of gas flow with nanocomposite carbon-containing powders in supersonic nozzle. Metallofiz. Noveishie Tekhnol. **44**(5), 601–611 (2022). https://doi.org/10.15407/mfint.44.05.0601
8. Volkov, A., Shorinov, O., Polyviany, S.: Deposition of titanium-containing coatings by low-pressure cold spraying. In: Nechyporuk, M., Pavlikov, V., Kritskiy, D. (eds.) Integrated Computer Technologies in Mechanical Engineering - ICTM 2021, Lecture Notes in Networks and Systems, vol. 367, pp. 565–574. Springer, Cham (2022). https://doi.org/10.1007/978-3-030-94259-5_48
9. Yin, S., Cavaliere, P., Aldwell, B.: Cold spray additive manufacturing and repair: fundamentals and applications. Addit. Manuf. **21**, 628–650 (2018). https://doi.org/10.1016/j.addma.2018.04.017
10. Tan, K., Markovych, S., Wenjie, H.U.: Review of manufacturing and repair of aircraft and engine parts based on cold spraying technology and addictive manufacturing technology. Aerosp. Tech. Technol. **1**(3), 53–70 (2020). https://doi.org/10.32620/aktt.2020.3.06
11. Raoelison, R.N., Verdy, C., Liao, H.: Cold gas dynamic spray additive manufacturing today: deposit possibilities, technological solutions and viable applications. Mater. Des. **133**, 266–287 (2017). https://doi.org/10.1016/j.matdes.2017.07.067
12. Sova, A., Grigoriev, S., Okunkova, A., et al.: Potential of cold gas dynamic spray as additive manufacturing technology. Int. J. Adv. Manuf. Technol. **69**, 2269–2278 (2013). https://doi.org/10.1007/s00170-013-5166-8
13. Li, Q.: Structure design and optimization of cold spray gun. Shenyang University of Technology. http://cdmd.cnki.com.cn/article/cdmd-10142-2008203950

14. Hu, W., Tan, K., Markovych, S., Cao, T.: Research on structure and technological parameters of multi-channel cold spraying nozzle. Eastern-Eur. J. Enterp. Technol. **5**(1 (113)), 6–14 (2021). https://doi.org/10.15587/1729-4061.2021.242707
15. Dolmatov, A.I., Polyviany, S.A.: Interaction of solid particles from a gas stream with the surface of a flat nozzle. Metallophys. Adv. Technol. **43**(3), 319–328 (2021). https://doi.org/10.15407/mfint.43.03.0319
16. Tan, K., Markovych, S., Hu, W.: On the characteristics of cold spray technology and its application in aerospace industries. Earth Environ. Sci. **719**(3), 032023 (2021). https://doi.org/10.1088/1755-1315/719/3/032023
17. Kun, T., Jie, H.W., Markovych, S., Wang, Y.: Dimet Laval nozzle expansion section analysis and optimization. J. Eng. Sci. **8**(2), 6 (2021). https://doi.org/10.21272/jes.2021.8(2).f2
18. Arndt, A., Pyritz, U., Schiewe, H., Ullrich, R.: Method and device for the cold-gas spraying of particles having different solidities and/or ductilities. US Patent 8197895, B2 (2012). https://patentscope.wipo.int/search/en/detail.jsf?docId=WO2008084025
19. Alhulaifi, A.S., Buck, G.A.: A simplified approach for the determination of critical velocity for cold spray processes. J. Therm. Spray Technol. **23**(8), 1259–1269 (2014). https://doi.org/10.1007/s11666-014-0128-8
20. Canales, H., Markovych, S., Dolmatov, A.: Calculation of the critical velocity of low pressure cold sprayed materials. Issues Des. Product. Aircraft Struct. **3**, 86–91 (2014). http://nbuv.gov.ua/UJRN/Pptvk_2014_3_11
21. Li, L., Luo, H., Du, H., Ren, Y., Xiang, Q., Xiong, T.: Influence of alumina content on apparent morphology and microstructure of cold sprayed Al- composite coatings. Surf. Technol. **12**(5), 1–11 (2021)
22. Chen, J.X., Wang, Q., Luo, S.S.: Microstructure and properties of cold sprayed Al- coating on AZ31 magnesium alloy. Chin. J. Nonferrous Metals **28**(9), 1720–1729 (2018)
23. Gong, J.G., Jia, Z.M., Gao, L.: Performance study of cold spraying Al/SiO2 coating on AZ31 magnesium alloy. Light Metals **5**, 43–47 (2018)
24. Wang, H.T., Yao, H.L., Yi, Z.H.: Microstructure and properties of cold-sprayed SiC/Al nanocomposite coatings. China Surf. Eng. **31**(6), 98–108 (2018)
25. Tao, Y.S., Xiong, T.Y., Sun, C.: Effect of α- on the properties of cold sprayed Al/α- composite coatings on AZ91D magnesium alloy. Appl. Surf. Sci. **256**(1), 261–266 (2009). https://doi.org/10.1016/j.apsusc.2009.08.012

Analysis of the Urban Air Mobility for the Unmanned Aerial Vehicle

Maksym Yena(✉), Andriy Bykov, and Oleksandr Karatanov

National Aerospace University "Kharkiv Aviation Institute", 17 Chkalova Street, Kharkiv 61070, Ukraine
yenamaxim98@gmail.com

Abstract. The research topic Unmanned Aerial Vehicle (UAV) Traffic Management Models, Methods and Information Technology concerns the development and testing of technologies to help control and manage UAV traffic to ensure safe, efficient and controlled flights. This is important to ensure the safety of the skies, as well as the efficient use of airways and to prevent collisions and conflicts. The study includes the study of traffic management models and algorithms, as well as the evaluation of their effectiveness and applicability in real conditions. The study briefly describes the main aviation groups that can be involved in providing flight traffic management, the main problems in the USA and possible problems in Ukraine, and also considers the main ways of solving problems and implementing a centralized, competitive system of monitoring and regulation of small aviation elements. The main mathematical features and limitations are analyzed. The goal of this research is to contribute to the improvement of UAV traffic management by proposing innovative solutions and strategies. By enhancing the quality of traffic control, the safety of airspace operations can be ensured, collisions and conflicts can be prevented, and the efficient utilization of airways can be achieved. The findings of this study have the potential to benefit both the aviation industry and regulatory bodies involved in UAV traffic management.

Keywords: Traffic Management · Unmanned Aerial Vehicles · Automated Control · Flight Path Optimization · Monitoring and Detection Systems · Air Traffic Safety · Intelligent Flight Control · Aviation · Unmanned Aviation Devices · Navigation · Route Planning · Efficiency · Security · Control · UTM

1 Introduction

Research Object: UTM (Unmanned Traffic Management) system.

Research Subject: Quantitative and qualitative criteria used in UTM for UAV traffic management.

Research Goal: Understanding and analyzing the quantitative and qualitative criteria applied in the UTM system to ensure safety, efficiency, and controllability of UAV traffic. The research aims to investigate the characteristics of these criteria, their interrelationships, and their impact on the operation of the UTM system. The findings of this research can be valuable for enhancing the functionality and development of UTM systems.

M. Nechyporuk et al. (Eds.): ICTM 2023, LNNS 1008, pp. 66–74, 2024.
https://doi.org/10.1007/978-3-031-61415-6_6

Aircraft Traffic Management (UTM) technology refers to the systems, methods and technologies used to manage the flow of unmanned aerial vehicles (UAVs) in airspace. This includes monitoring the UAV flight path, ensuring safe separation between UAVs and avoiding conflicts with other aircraft. UTM technology also involves the exchange of information between drones, ground control stations and air traffic control systems to ensure safe and efficient operations in the airspace.

The purpose of UTM technology is to facilitate the integration of aircraft into the airspace while ensuring the safety of other aircraft and people on the ground. UTM technology can also cover other critical functions such as flight planning and authorization, real-time monitoring and tracking of UAVs, and incident reporting and resolution.

In addition, UTM technology can be integrated with other systems such as air traffic control, weather monitoring and flight information systems to provide a comprehensive solution for safe and efficient UAV traffic management.

UTM regulation is essential to ensure safe and secure integration of UAVs into the airspace system, protect privacy and security, and standardize procedures and technologies (Fig. 1).

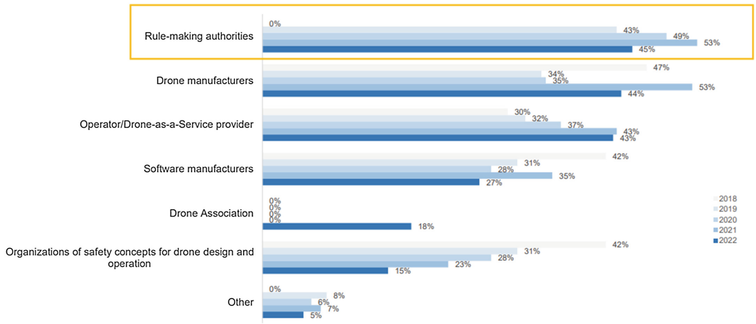

Fig. 1. The tendency to increase the number of regulatory bodies for the registration of UAVs [1]

It is important for UAV operators to be aware of and comply with the regulations and standards that apply to their operations to ensure the safe and legal operation of their UAVs (Fig. 2).

2 The Human Factor in the UAV

U-space (or Universal systems) and UTM (or Unmanned Traffic Management) are terms that do not have widely accepted or standardized definitions in the context of information technology or aviation systems. Since these terms do not have widely known and fixed meanings, I can provide general information about possible interpretations of these terms that can be used in different contexts [3]. A Universal system (U-system) is a term that can refer to a system that has a general or universal character and typically means that this system can be applied in different fields or has a wide range of applications. Unmanned Traffic Management (UTM) is a term that is commonly used in the context of unmanned

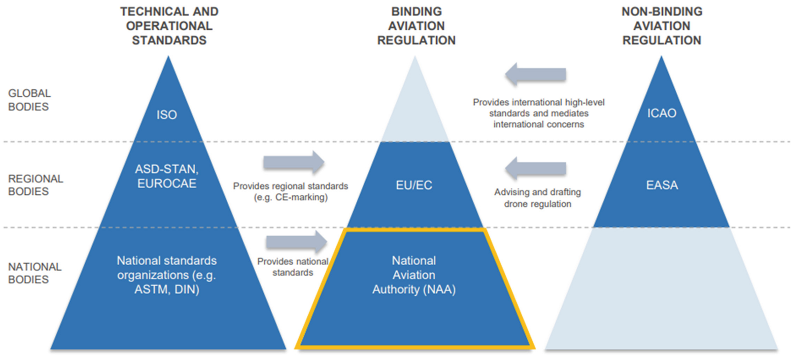

Fig. 2. Basic rules and areas of impact registration on UTM [2].

aviation (UAVs) and refers to a system designed to manage and regulate UAV traffic in airspace [4]. UTM is used to ensure the safety and efficiency of unmanned flights, including UAV registration, route planning, obstacle detection, flight coordination, and interaction with manned air traffic. It is important to note that these terms may have other specific definitions or be used in different contexts, so the specific meaning of these terms should be clarified according to the context in which they are used [5].

In the UTM system, various hardware and software components are used to ensure the functionality and efficiency of UAV traffic management. Some of these components include: Onboard UAV Components: These include autopilots, sensors, antennas, transmitters, and other devices that enable the UAV to carry out missions and transmit information. Ground-based Components: This equipment, located on the ground, interacts with the UAV. It may include receivers, transmitters, radio stations, servers, antennas, and other devices that allow for control and monitoring of the UAV [6].

Communication Infrastructure: This is the data transmission and communication system that provides connectivity between the UAV and the UTM system. It may include satellite links, communication networks, internet networks, radio channels, and other means of data transmission. Servers and Computing Resources: UTM utilizes servers and computing resources for data processing and analysis, route planning, conflict detection, decision-making, and providing information to operators and other stakeholders [7].

Geofencing Systems: These are software and hardware tools used to define and control UAV access to specific airspace zones. They may include radar systems, obstacle detection systems, identification and authentication systems, and other means to ensure safety and collision avoidance [8].

Data Processing and Storage Systems: UTM processes large volumes of data such as planned routes, flight information, sensor data, and other information.

Data storage systems, databases, analytical tools, and other data processing and analysis tools are used for this purpose. Considering the rapid advancements in technology and the continuous improvement of UTM systems, the hardware and software components may vary and evolve based on the needs and requirements of unmanned aviation and air traffic management [9].

The human factor is a complex and unpredictable element of U-space as it relates to the integration of unmanned aerial systems (UAS) into airspace.

The human factor includes the behavior, decision-making, and interaction of various stakeholders involved in the operation of UAVs, including UAV pilots, UAV operators, air traffic controllers, and other airspace users [10].

Here are some ways the human factor affects U-space:

1. pilot error;
2. communication failure;
3. non-compliance with regulatory acts;
4. lack of awareness;
5. cyber security risks.

To eliminate the human factor in U-space, it is important to prioritize safety culture and training for all stakeholders involved in the operation of UAS [11]. This includes UAV pilots, UAV operators, air traffic controllers and other airspace users. Effective communication and collaboration between stakeholders can also help reduce human risk.

In addition, UAV regulations and standards should be constantly reviewed and updated taking into account the development of UAS technology and operations, as well as human factors, some studies are given in Tables 1 and 2 [12].

Table 1. Human factor of reaction to ATS

Human factor	
5 min 57 s	The average response time to a PBX order
1 min 52 s	Median ATS order response time
37%	of pilots respond to an ATS command within 1 min

Table 2. Response time from UAS pilots

Category	Vt	Range of speeds for initial approach	Range of final of speeds	Maximum speeds for circling
C (typical aerospace jet)	121–140 kt	160–240 kt	115–160	180
The distance traveled in 1min 52s	3.76–4.36 nm	4.98–7.47 nm	3.58–4.98	5.6 nm
The distance traveled in 5 min 57 s	12–13.88 nm	15.87–23.8 nm	11.4–15.87	17.85 nm

The integration of the Droneradar application with the PansaUTM system (accredited for operational use) provides most of the U1-U3 services. Among them, in particular, it should be noted:

1. Information about the possibility of a flight at a given place and time [13];
2. two-way non-verbal communication between civil and military air traffic services and the UAS pilot;
3. dynamic reconfiguration of airspace;
4. the ability to submit an operational flight plan where required (for example, in CTR, at a selected time). The Droneradar application informs when and where to submit an operational flight plan;
5. the possibility of automatic flight acceptance at the strategic and tactical levels;
6. air traffic services have the opportunity to make decisions regarding the capacity of selected airspace elements (segments) [14];
7. the possibility of strategic integration with various stakeholders such as LAU (local administrative units) – the flight plan will be adopted after its approval by all stakeholders;

The development and implementation of UTM technology is critical to the development of the drone industry and safe integration into the airspace. It is an important area of research and development for governments, organizations and companies around the world [15].

The technology of managing the traffic of unmanned aerial vehicles in Ukraine is necessary to improve the safety and efficiency of flights of small aviation elements. It will help manage traffic, adjust altitude and flight course, eliminate crossing routes and collisions, improve take-off and landing processes and manage other factors that affect the safety and efficiency of flights. It can improve the effectiveness of UAVs in various applications such as delivery, monitoring and data collection, survey and damage assessment, as well as defense and security [16].

3 Mathematical Methods and Models that Can Be Applied to UAV

The architecture between the lower-level control and the higher-level control of UAVs may vary depending on the specific implementation of the system. However, the overall architecture can include the following levels: Low-Level Control: This level is responsible for direct control of the UAV, ensuring its stability and flight safety [17]. It handles basic operations such as stabilization, autopiloting, navigation, and executing commands from higher-levels. Mid-Level Control: This level performs tasks related to route planning, coordination, and conflict resolution among UAVs. It determines optimal routes to achieve flight objectives, avoid obstacles, and interact with other UAVs and aerial objects. High-Level Control: This level is responsible for higher-level strategy and decision-making. It involves mission planning, resource allocation, traffic management, and coordination with the UTM system [18]. The high-level control may include functions such as automatic airspace zoning and decision-making regarding flight safety and reliability. These levels interact with each other, transmitting information and commands from the higher level to the lower level for UAV control. Each level has its functionality and responsibility, contributing to efficient and safe UAV management [19] (Fig. 3).

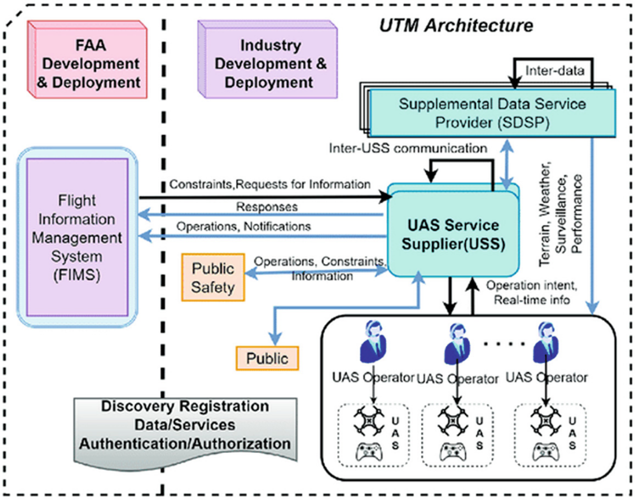

Fig. 3. US-based UTM architecture

Mathematical methods are used in UAV traffic management technologies to analyze, plan and optimize routes, assess risks and spatial resources, predict weather and other external conditions, as well as to solve control and management tasks. This may include the use of optimization algorithms, statistical methods, mathematical modeling and other tools [20].

The purpose of these methods is to ensure maximum efficiency, security and efficiency in traffic management.

Some examples of mathematical methods used in traffic management are the method of optimal route planning, the A* algorithm, Bellman-Ford and Johnson-Lee, Dijkstra.

The optimal route planning method is used to plan the route considering many constraints such as geographical, energy and time constraints. This method uses mathematical programming to find the optimal route that minimizes energy expenditure or flight time.

The algorithm for calculating the optimal route can depend on many factors, such as weather conditions, flight altitude restrictions, geographical restrictions, obstacles, etc. However, some of the basic mathematical methods that can be used in solving this task include:

Optimization methods: For example, the use of optimization algorithms, such as the modified Dijkstra algorithm (most often, this algorithm is the basis for building an optimization route and selecting the best alternatives from the existing ones) or the A* algorithm for calculating the optimal route by minimizing time or distance:

$$\begin{gathered} Y_{s,t} - Y^{min} \geq 0,\ D^{max} - D_{s,t} \geq 0,\ J^{max} - J_{s,t} \geq 0,\ X_{s,t} - X^{min} \geq 0, \\ X_e - \ln(1 - Z_e) \end{gathered} \tag{1}$$

In Dijkstra's initial algorithm, the label of the j-th node, which can be reached from node s through the vessel node i, has the form [Rs,j, i], where the value of the cost Rs,j, corresponding to the given path, is additive and is calculated by the formula:

$$R_{s,j} = R_{s,i} + R_{i,j.} \tag{2}$$

The $R_{s,j}$ rib cost, $R_{i,j}$ – the value is taken with the label and node.

These formulas give an extended representation of the Dijkstra's algorithm and also provide a basis for representing future UAV trajectories in the form of a graph with edges.

Unmanned aerial vehicle (UAV) traffic management techniques may include the use of flight models, route planning, condition monitoring, and positioning using GPS.

In unmanned aerial vehicle (UAV) mathematical models, various formulas and equations can be used to simulate and analyze various aspects of UAV flight, such as air traffic control, routing, collision avoidance, and communication network design. Here are some examples of equations that can be used in these models [21]:

- linear and non-linear programming models to optimize flight routes, fuel consumption and safety constraints;
- differential equations for modeling the dynamic behavior of UAVs in air space;
- stochastic models for assessing collision probability and safety risks;
- graph theory models for analysis of communication networks between UAVs and ground control stations;
- control theory models for designing control algorithms for UAV guidance and navigation.

These mathematical models can aid in data-driven decision-making and improve the safety and efficiency of UAV traffic control systems.

4 Conclusions

In this work, the main features and characteristics of UAV traffic control systems were considered. The main restrictions and existing laws are considered, as well as legal details related to the peculiarities of the operation of the UAV.

Also analyzed are the key limitations of potential pilots (the so-called human factor), namely the reaction speed of drone operators.

The key features of the drone industry, the reasons for its development, as well as areas for future growth and possible legal justifications for this are analyzed.

The regulatory bases that have changed over the past 5–10 years along with the laws that regulate this or that action is given.

The key algorithms are considered, which can be presented as a basis for potential development and used as a basis for future traffic control systems.

References

1. Alotaibi, E.T.S., Al-Rawi, H.: A complete multi-robot path-planning algorithm. Auton. Agents Multi-Agent Syst. **32**(5) (2018). https://doi.org/10.1007/s10458-018-9391-2
2. Barer, M., Sharon, G., Stern, R., Felner, A.: Suboptimal variants of the conflict-based search algorithm for the multi-agent pathfinding problem. In: Seventh Annual Symposium on Combinatorial Search (2014)
3. Bauranov, A., Rakas, J.: Designing airspace for urban air mobility: a review of concepts and approaches. Prog. Aerosp. Sci. 125, 100726 (2021). https://doi.org/10.1016/j.paerosci.2021.100726
4. Bertram, J., Wei, P., Zambreno, J.: Scalable fastMDP for pre-departure airspace reservation and strategic de-conflict. In: AIAA Scitech 2021 Forum (2021)
5. Bhattacharya, S., Kumar, V., Likachev, M.: Distributed optimization with pairwise constraints and its application to multi-robot path planning. In: Robotics: Science and Systems VI, vol. 177. Robotics: Science and Systems Foundation (2010).https://doi.org/10.15607/RSS.2010.VI.023http://www.roboticsproceedings.org/rss06/p23.pdf
6. Bin Mohammed Salleh, M.F., et al.: Preliminary concept of adaptive urban airspace management for unmanned aircraft operations. In: AIAA Information Systems-AIAA Infotech at Aerospace, January 8–12, 2018. Kissimmee, Florida, USA (2018). https://doi.org/10.2514/6.2018-2260
7. Bnaya, Z., Felner, A.: Conflict-oriented windowed hierarchical cooperative A*. In: 2014 IEEE International Conference on Robotics and Automation (ICRA). IEEE (2014)
8. Cekmez, U., Ozsiginan, M., Sahingoz, O.K.: A UAV path planning with parallel ACO algorithm on CUDA platform. In: 2014 International Conference on Unmanned Aircraft Systems (ICUAS). IEEE (2014)
9. Chamseddine, A., Zhang, Y., Rabbath, C.A., Join, C., Theilliol, D.: Flatness-based trajectory planning/replanning for a quadrotor unmanned aerial vehicle. IEEE Trans. Aerosp. Electron. Syst. **48**(4), 2832–2847 (2012). https://doi.org/10.1109/TAES.2012.6324664
10. Chung, S.-H.: Applications of smart technologies in logistics and transport: a review. Transp. Res. E **153**, 102455. https://doi.org/10.1016/j.tre.2021. City Population, 2020. China: Zhejiang (2021). https://www.citypopulation.de/en/china/zhejiang/admin/
11. Cohen, L., Uras, T., Kumar, T.S., Koenig, S.: Optimal and bounded-suboptimal multi-agent motion planning. In: Twelfth Annual Symposium on Combinatorial Search (2019)
12. Cohen, L., Uras, T., Kumar, T.S., Xu, H., Ayanian, N., Koenig, S.: Improved solvers for bounded-suboptimal multi-agent path finding. In: IJCAI (2016)
13. Felner, A., et al.: Search-based optimal solvers for the multi-agent pathfinding problem: summary and challenges. In: Proceedings of the 10th Annual Symposium on Combinatorial Search, SoCS 2017 (2017)
14. Gilboa, A., Meisels, A., Felner, A.: Distributed navigation in an unknown physical environment. In: Proceedings of the Fifth International Joint Conference on Autonomous Agents and Multiagent Systems. ACM Press, New York, USA (2006). https://doi.org/10.1145/1160633.1160735
15. Surynek, P.: A novel approach to path planning for multiple robots in bi-connected graphs. In: 2009 IEEE International Conference on Robotics and Automation, May 12–17, 2009. IEEE, Kobe, Japan (2009). https://doi.org/10.1109/ROBOT.2009.5152326
16. Ushijima, H.: UTM project in Japan. In: Proceedings of the Global UTM Conference, Montreal, QC, Canada, 26 (2017)
17. Van Den Berg, J.P., Overmars, M.H.: Prioritized motion planning for multiple robots. In: 2005 IEEE/RSJ International Conference on Intelligent Robots and Systems, August 2–6, 2005. IEEE, Edmonton, Alta., Canada (2005). https://doi.org/10.1109/IROS.2005.1545306

18. Yu, J., LaValle, S.M.: Multi-agent path planning and network flow. In: Frazzoli, E., Lozano-Perez, T., Roy, N., Rus, D. (Eds.), Algorithmic Foundations of Robotics X. Springer Berlin Heidelberg, Berlin, Heidelberg (2013). https://doi.org/10.1007/978-3-642-36279-8_10
19. Yu, J., LaValle, S.M.: Structure and intractability of optimal multi-robot path planning on graphs. In: Proceedings of the 27th AAAI Conference on Artificial Intelligence, pp. 14–18 (2013)
20. Yu, J., LaValle, S.M.: Optimal multirobot path planning on graphs: Complete algorithms and effective heuristics. IEEE Trans. Robot. **32** (5) (2016). https://doi.org/10.1109/TRO.2016.2593448
21. Shrestha, R., Oh, I., Kim, S.: A survey on operation concept, advancements, and challenging issues of urban air traffic management. Front. Future Transp **2**, 626935 (2021). https://doi.org/10.3389/ffutr.2021.626935

Mathematical Modeling of the Thermal State of the Brush-Holders Device in a Three-Dimensional Setting

Oleksii Tretiak, Anton Kovryga, Pavlo Makarov, Nataliia Penkovska, and Stanislav Kravchenko(✉)

National Aerospace University "Kharkiv Aviation Institute", Kharkiv 61070, Ukraine
ksatfer@gmail.com

Abstract. This article examined design options for high-speed Turbogenerators of medium and high power. Particular attention was paid to the operating features of the generator cooling system. The probabilities of occurrence of emergency situations at electric generators of power plants caused by failures of various types are given, based on the results of statistical data processing. The detailed analysis of the design of the brush-holders device of Turbogenerators was carried out. The factors influencing the design of brush-holders are indicated. The main causes of damage are considered and the ways of development and improvement of the existing design structure are determined. The analysis of the calculation methods of the ventilation and heat removal systems was carried out. The temperatures values were obtained as the result of modeling the brush-holder thermal state in the SolidWorks Flow Simulation environment. The principles of three-dimensional calculation of the thermal state of the brush-holders device of Turbogenerators in a three-dimensional formulation by the CFD method using the results of analytical calculations are considered.

Keywords: Turbogenerator · Brush-Holders Device · Three-Dimensional Calculation · Thermal State · Ventilation

1 Introduction

Modern global worldwide trends in the design of electric machines require revision and improvement of existing design and calculation methods. The use of three-dimensional approaches to calculating the stress-strain state of design structures provides wide opportunities for improving structures, increasing their reliability and reducing mass.

Thermal and Nuclear Power Plants, which are equipped with high-speed Turbogenerators, mainly of medium and large power, currently occupy a significant part of electricity production all over the world. Usually, Turbogenerators are made in a two-pole version, which corresponds to a rotation speed of 3000 rpm for a current frequency in the network of 50 Hz, or 3600 rpm for a current frequency in the network of 60 Hz. Four-pole Turbogenerators are also sometimes found. Such a high rotation speed imposes its limitations on the design and operation of Turbogenerators. High rotation speed and, as

M. Nechyporuk et al. (Eds.): ICTM 2023, LNNS 1008, pp. 75–90, 2024.
https://doi.org/10.1007/978-3-031-61415-6_7

a result, high mechanical stresses determine the design of the rotor in the form of a long cylinder made of high-alloy steel with increased mechanical and magnetic properties. Large mechanical stresses arising from centrifugal force in the teeth and body of the rotor, and especially in the retaining rings, limit the diameter of the rotor, which for a rotation speed of 3000 rpm cannot exceed 1200–1250 mm.

The cooling system of active and constructive parts of the machine also has a great influence on the design. Low power Turbogenerators are characterized by air cooling, which ensures simplicity of design and maintenance. Turbogenerators of higher power are usually made with hydrogen and liquid cooling, and the design and principle of operation of the cooling system of these machines of different manufacturers can differ significantly from each other.

Turbo generators of medium and high power always have a closed cooling system, in which the cooling conductor (air, gas, distillate or oil) of the machine, while the cooling conductor itself is heated. The need for a closed system is dictated by strict requirements for the condition of cooling media: cleanliness, electrical and chemical properties, moisture content, etc. Heat-exchange devices are installed in a closed cooling system. In these devices, which are fed with technical water, losses from the cooling media of the Turbogenerator are diverted to the technical water. At the same time, the cooling conductor lowers its temperature to rated temperature, and the technical water heats up.

Usually, heat exchangers are designed in such a way that at rated temperature of cold technical water entering them, which is equal to 33 °C, rated temperature of the cold cooling conductor in the Turbogenerator is 40 °C, but for the location of the Turbogenerator in a tropical climate, these temperatures can be higher.

In Fig. 1 the general view and main components of a Turbogenerator with a water-hydrogen cooling system rated 250 MW is shown.

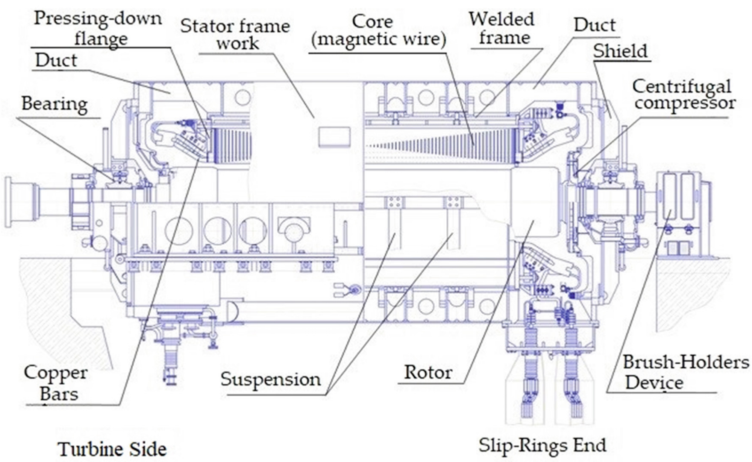

Fig. 1. Design of Turbogenerator rated 250 MW

Let's consider the design of serial Turbogenerators in more detailed way.

The middle part of the stator consists of three coaxially arranged orthotropic layers, which includes:

1) the welded frame is a thin cylindrical shell with frames and stringers namely tightening prisms, made of steel. At both ends of the prisms there are pre-stressed threaded tails that are under significant dynamic and thermo-mechanical loads. The number of such tails is more than fifty;
2) the core is manufactured of magnetically conductive compressed ring segments made of sheets of electro-technical orthotropic steel, interspersed with the same segments made of fiberglass, in the axial direction the core is fixed with the help of pressing-down flanges, the thickness of the core can be compared to its diameter;
3) the slot part of the bar winding is made of copper conductors interspersed with copper tubes for coolant (dis-tilled water), with insulation based on a mineral-polymer basis.

The rotor, as mentioned above, is a steel cylinder with grooves in which the excitation winding is located. The rotor winding (excitation winding) consists of trough-shaped conductors forming axial channels through which the cooling gas passes. Retaining rings of the rotor are designed to absorb centrifugal forces from the face end parts of the excitation winding. At the working end of the rotor shaft there is a coupling, which is designed to connect the rotor to the turbine shaft.

At the face end parts of the stator there are ducts in which gas coolers are located. Shields are attached to the ducts, which are a support for sliding bearings.

For the complete serviceability operation of the Turbogenerator, it shall be equipped with support systems, namely with excitation system, a water system, a hydrogen system, an oil system and a thermal control system.

The excitation system is for feeding of the rotor winding with direct current and control this current according to the required law depending on the operating mode of the Turbogenerator. Modern Turbogenerators are usually equipped with thyristor excitation systems. The excitation current of the Turbogenerator is automatically adjusted when the load changes (both active and reactive) in accordance with the set control characteristics.

In the case of a sharp decrease in generator voltage or oscillation of generators, which usually occur during emergency situations in the electrical network, a rapid increase in excitation current (forcing) compared to the rated one is required to keep the generator in parallel operation with the rest of the system. The excitation forcing mode is a difficult mode for the generator, since the excitation current during forcing can exceed twice the nominal values. The duration of forcing should usually be limited to 10–30 s.

Water, hydrogen and oil systems are designed to provide the Turbogenerator with distilled water (which serves to directly cool the stator winding), hydrogen (which fills the internal volume of the machine to remove losses in other parts of the generator) and oil (which provides lubrication and cooling of the bearings) respectively. All specified types of cooling media require cleaning during operation to ensure their regulatory parameters.

The thermal control system is designed to control the temperatures of the active parts of the generator and its cooling media in order to check the compliance of these temperatures with the requirements of regulatory norm documentation and to prevent emergency situations caused by high temperatures.

For Turbogenerators of large and medium power, one of the most difficult components to design is the brush-holders device (BHD). Ensuring the operability of all elements of the brush-holders device (BHD) requires a wide range of knowledge from the design engineer in various scientific fields, because the design includes both highly loaded contact electrical connections (slip rings in combination with the rotor current supply) on the rotor rotating at high speed, as well as structural elements of the brush-holders device (brushes, brush-holders, ventilation system), which shall ensure uninterrupted operation and convenient and quick adjustment and regulation.

From the diagram of typical emergency situations (see Fig. 2), which was built based on the results of statistical processing of data on the occurrence of emergency situations at electrical generators of power plants caused by failures of various types, it can be seen that 14% of all failures are caused by brush-holders devices [1, 2]. Such a sufficiently high rate of failures indicates that increasing the reliability of this unit is an urgent task today, because the phenomena occurring in working of the brush-holder device are quite complex and require further study.

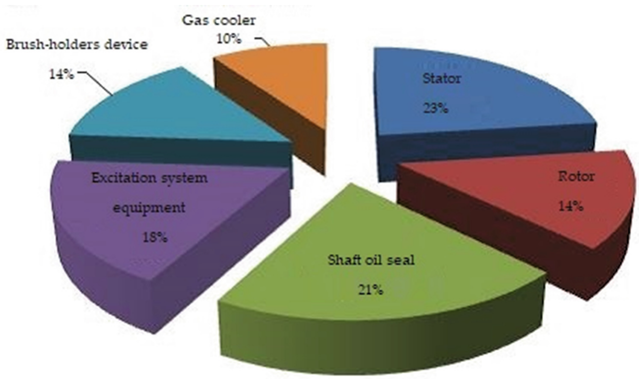

Fig. 2. Data Diagram on the Occurrence of Typical Emergency Situations of Electric Generators

According to statistical data, the main reasons for failures of the brush-holders device are:

- circular fire;
- heating of slip rings above the maximum permissible value;
- uneven wearing out of brushes;
- local beating of slip rings;
- vibration and chipping of brushes;
- reduction of insulation resistance below the maximum allowable value.

An important feature of the brush-holders device design is that when performing the thermal calculation, it is necessary to solve the thermal problem with three types of heat release: electrical losses in the classical setting, losses due to the friction of the brushes against the slip ring and additional losses caused by the action of parasitic currents. In papers [3–5], the main methods of calculation and design of the brush-holders device of electric machines of similar types are described, but they do not allow establishing a real picture of the thermal state of the brush-holder device in a three-dimensional form. In this regard, in order to meet the requirements of reliability and operation, it is expedient to review the existing methods in order to implement the solution in software complexes using CFD methods.

2 Design and Purpose of the Brush-Holders Device

The brush-holders device is the unit which provides direct current supply from the stationary current-carrying parts of the excitation circuit to the rotating excitation winding of the generator rotor by means of a sliding contact.

The brush rocker (the fixed part of the brush-holders device) is a ring busbars on which brush-holders with sliding contact brushes are installed. The number of brushes installed on each pole of the brush-holders device is determined by the maximum excitation current of the rotor winding and the permissible current of the brushes.

The slip rings (rotating part of the brush-holders device) are installed on the rotor of the Turbogenerator, they are electrically isolated from the rotor shaft and from each other. The slip rings are connected to the rotor winding of the Turbogenerator by means of a current drain, which usually passes through the central hole of the rotor. Slip rings are made of special hard wear-resistant steel and are hot-fitted onto a steel sleeve insulated with micanite or fiberglass, which in turn, is fitted onto the shaft. In some designs, slip rings are fitted to the insulated end of the shaft without a steel intermediate sleeve.

The thermal mode of the slip rings is very stressed, mainly due to high frictional losses of the brushes against the slip rings. Therefore, slip rings are equipped with special channels, and if necessary, with individual fans. On the outer surface of the slip rings, a helical cut of a rectangular profile is made to improve the working conditions of the brushes: without such a cut, due to the high rotational speed, due to viscosity, air shall be sucked under the brushes, which will detach the brushes from the slip ring. In addition, the cutting slightly increases the cooled surface of the ring.

In accordance with the requirements of regulatory norm and technical documentation, the working time before failure of the Turbogenerator shall be 27,000 h, and the service life, subject to compliance with the terms and scope of scheduled inspections and repairs, shall be 40 years. At the same time, its maneuverability indicators are:

- 10^4 stop-start cycles during the entire service life, but no more than 330 during one year;
- $2 \cdot 10^4$ unloading and loading cycles for the entire service life within the full adjustment range.
- The same requirements apply to the brush-holders device, as a component part of the Turbogenerator.
- General technical requirements to the brush-holders device are as follows:
- uniform arrangement of brushes along the surface of the slip ring and ensuring the same pressing force of all brushes during the entire period of operation;
- ensuring the conduction of the rated excitation current at the rated excitation voltage (including in the case of excitation forcing of a given value and duration) with a minimum voltage drop during the switching process, without overheating and electrical breakdown;

– ensuring of mechanical strength of rotating elements of the brush-holders device at maximum rotational speed of the rotor;
– installation of resistance temperature detectors of the brush-holders device elements;
– diagram of ventilation system of the brush-holders device shall be opened with the intake of cooling air from the machine room and the release of heated air back into the machine room.

Modern trends in the design of the brush-holders device also provide for the following technical solutions:

– the presence of a corrosion-resistant coating of the traverse busbars;
– the presence of a place to install an insulated brush on each polarity for the possibility of monitoring the condition of the insulation;
– equipping with quick-removable brush-holders;
– connection of the excitation busbar to the crossbar busbars in two points to reduce the unevenness of the current between the brushes;
– installation of brushes on the slip ring with an offset (in “staggered” order).

In Fig. 3 the general view of Turbogenerator rated 200 MW with a brush-holders device is shown.

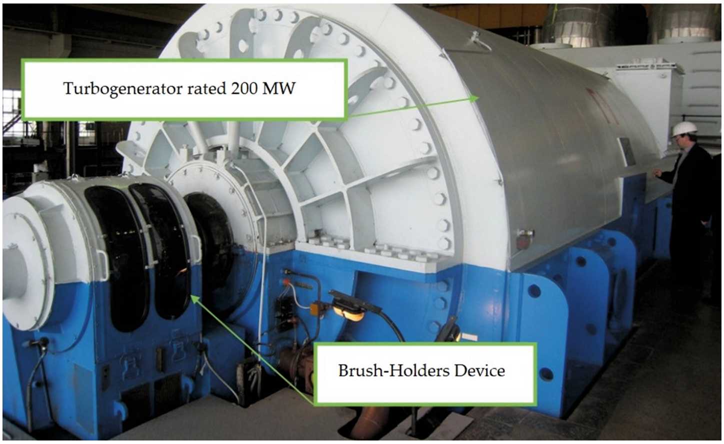

Fig. 3. General View of Turbogenerator with the Brush-Holders Device

3 Factors Affecting the Calculation of the Brush-Holders Device

On Turbogenerators of high and medium power, unipolar electric brushes of the EG4 brand or monopolar electric brushes of the 611OM brand were traditionally used on the positive pole and EG2AF on the negative pole.

However, in recent years, modern electric brushes LFC 554 produced by the Mersen company have become widespread, both for new brush-holders device and for replacing brushes on existing equipment. These brushes are made from natural, artificial graphite and coal tar. To obtain a good consistency, this mixture is baked in an oven at 1000 °C, the resulting material has a light structure, low density and low electrical resistance.

Physical characteristics of the brush material: density – 1.25 g/cm^3, specific resistance – 2,000 μΩ cm, bending strength – 10 MPa. Recommended operating conditions: current density is from 6 to 13 A/cm^2; peripheral speed is up to 100 m/s; pressing force is from 110 to 180 gf/cm^2; temperature is 40…80 °C.

During the operation of the same brush, the electrical and thermal characteristics may change depending on the technical condition of the brushes. Thus, the thermal calculation shall take into account these factors to ensure reliable operation with a sufficiently long service life of the brushes.

Let's consider the given Diagram for calculating of the spot of contact of the brushes in the brush-holders device (see Fig. 4). This important characteristic depends on the grade of graphite brush, electrical contact and film [6]. The film is a complex mixture of metal oxides, carbon and water, which forms on the annular sliding surface. The properties of the film and the quality of the contact are affected by the following factors:

- temperature, pressure and humidity of the environment;
- the presence of polluting impurities;
- sliding speed;
- pressure on the brushes;
- the amount of current transmitted by the brush-holders device.

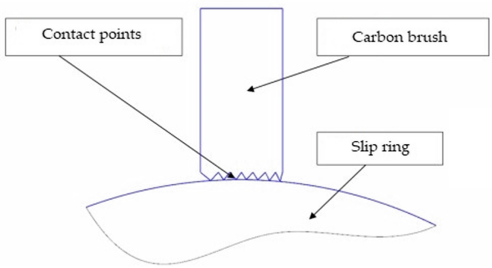

Fig. 4. Calculation Diagram of the Contact Spot

Table 1 shows typical values of contact voltage drop reduction obtained under specific operating conditions of Mersen brushes. The data are listed for each of the brush types and grouped into five categories: from "extremely low" to "high" one.

In order to provide the carbon brush work without overheating, it is necessary that its friction coefficient μ be low and constant over time. However, this coefficient does not have a normative value and is the result of many factors that depend on the quality of the carbon brush, the rotor rotation speed, the operating conditions of the slip rings and the environmental conditions. In this way, it is impossible to set the exact value of μ for the calculation of the brush-holders device, and it is only possible to provide an approximate range of values. However, this is sufficient for most practical numerical calculations or projects.

Table 1. Pressure drop value in the contact and friction coefficient

Designation	Value	Pressure drop, V	Friction Coefficient, μ
E	Significant	>3	$\mu > 0.20$
M	Average	2.3…3	$0.12 < \mu < 0.20$
B	Low	1.4…2.3	$\mu < 0.12$
TB	Very Low	0.5…1.4	–
EB	Extremely Low	<0.5	–

The problem of analytically solving the problem of calculating the non-stationary temperature field in the microcontact zone was considered in paper [7]. When creating a simulation model of electrical-frictional interaction, the task of non-stationary heat transfer of each contact element of the transition surface of the spot was solved. In Fig. 5 the Diagram of determining of the microcontact spot is shown.

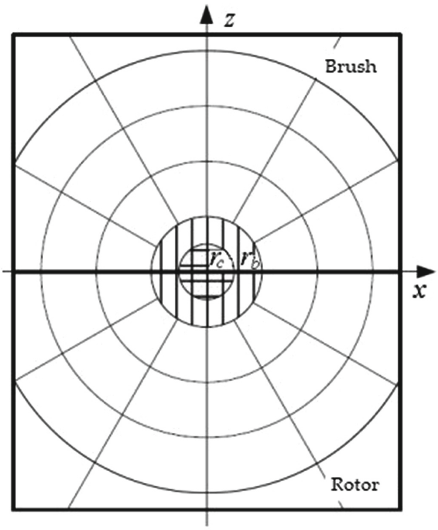

Fig. 5. Model of MicroContact Spot

Using the COMSOL Multiphysics environment, the authors developed a non-stationary three-dimensional model of an electrical microcontact (see Fig. 6) and presented the results of a numerical experiment that showed the fundamental possibility of building a multifactor model. However, at present, this task can be solved only for an individual case and cannot be extended to the entire brush-holders device.

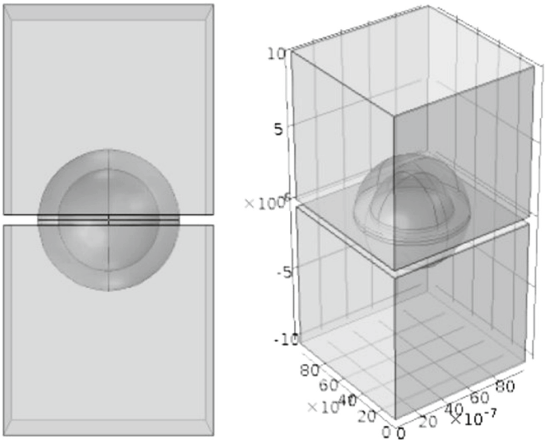

Fig. 6. Three-Dimensional Model of MicroContact in COMSOL

4 Example of Calculating the Thermal State of the Brush-Holders Device

Consider the formulation of the problem of the cooling system.

During operation of the generator, the temperature of parts and assemblies increases due to the influence of currents and friction. However, for all elements, including the shield, there is a limit temperature, exceeding which is unacceptable due to the possible failure of the entire electric generator. A system of forced ventilation of the air defense system is used to ensure a proper stable temperature mode of operation of the brush-holders device. The complex shape of the bodies flowing around the flow, the speed modes of the gas flow, the presence of rotating units requires consideration of the flow as a non-laminar conductor. At the same time, relatively small values of the pressure in the working chamber (usually easy access to the brush-holders device shall be provided directly from the machine room of the power plant, i. e. the pressure is 1 atm.) and the ventilation speed make it possible to consider the cooler as an incompressible gas.

The laws of conservation of energy for a gas flow in a Cartesian coordinate system that rotates with an angular speed Ω around the axis passing through the origin of the coordinate system can be written in the following form:

$$\begin{gathered}
\frac{\partial p}{\partial t} + \frac{\partial}{\partial x_i}(pu_i) = 0, \\
\frac{\partial pu_i}{\partial t} + \frac{\partial}{\partial x_i}(pu_i u_i) + \frac{\partial p}{\partial x_i} = \frac{\partial p}{\partial x_j}(\tau_{tj} + \tau_{tj}^R) + S_i, \\
\frac{\partial pH}{\partial t} + \frac{\partial pu_i H}{\partial x_i} = \frac{\partial}{\partial x_j}\left[u_i\left(\tau_{ij} + \tau_{tj}^R\right) + q_i\right] + \frac{\partial p}{\partial t} - \tau_{tj}^R \frac{\partial u_i}{\partial x_i} + p\varepsilon + S_i u_i \\
H = h + \frac{u^2}{2},
\end{gathered} \tag{1}$$

where u – is flow rate; h – is flux density vector; p – the pressure; H – the potential energy; ρ – the liquid density; ν – the kinematic viscosity; f – the external force acting on the liquid.

The equations are supplemented by expressions of the state of the gas, which determine the nature of the gas, and empirical dependences of the density, viscosity, speed, and thermal conductivity of the gas depending on the temperature.

The Navier-Stokes equation has the form:

$$\frac{d\vec{u}}{dt} = -(\vec{u} \cdot \nabla)\vec{u} - \frac{1}{\rho}\nabla\vec{p} + v\Delta\vec{u} + \vec{f} \tag{2}$$

The Navier-Stokes equation is supplemented by the continuity equation:

$$\frac{\partial \rho}{\partial t} + \mathrm{div}(\rho\vec{u}) = 0 \tag{3}$$

Thus, a system of four equations is obtained for a laminar fluid: three Navier-Stokes equations in projections on the axis and continuity equations for four unknowns: three components of the speed vector and hydro-dynamic pressure.

To describe the turbulent regime, the Reynolds decomposition is used, according to which the arbitrary value x can be written as the sum of its average value $\overline{x}_1$ and deviation x_i':

$$x_i = \overline{x}_i + x_i' \tag{4}$$

As a result, we get the averaged as per Reynolds Navier-Stokes equations, which are also called the Reynolds equations, as well as the averaged continuity equation.

The continuity equation for an incompressible fluid has the form:

$$\frac{\partial u_i}{\partial x_i} = 0 \tag{5}$$

Then for the average speed $\overline{u}_1$:

$$\frac{\partial \overline{u_i}}{\partial x_i} = 0 \tag{6}$$

If we subtract the last two equations, we get the continuity equation for deflection:

$$\frac{\partial u_i'}{\partial x_i} = 0 \tag{7}$$

In this way, you can write the equation in components:

$$\rho\frac{\partial u_i}{\partial t} + \frac{\partial}{\partial x_j}\left(\rho u_i u_j\right) = \rho g_i + \frac{\partial \sigma_{ij}}{\partial x_j}, \tag{8}$$

where σ_{ij} – is stress in the liquid, determined by the formula:

$$\sigma_{ij} = -p\delta_{ij} + \mu\left(\frac{\partial u_i}{\partial x_j} + \frac{\partial u_j}{\partial x_i}\right), \tag{9}$$

where δ_{ij} – is Kronker's delta function defined as:

$$\begin{cases} \delta_{ij} = 1, \ i = j \\ \delta_{ij} = 0, \ i \neq j \end{cases} \tag{10}$$

Using the Reynolds decomposition, the general equation can be written in the following form:

$$\rho\left(\frac{\partial \overline{u_i}}{\partial t} + \overline{u_j}\frac{\partial \overline{u_i}}{\partial x_j}\right) = p\overline{g_i} + \frac{\partial}{\partial x_j}\left(\overline{\sigma_{ij}} - \rho\overline{u_i' u_j'}\right) \tag{11}$$

This equation is known as the Reynolds equation. This equation is quite similar to the Navier-Stokes equation and differs only in the additional component on the right-hand side $\rho\overline{u_i' u_j'}$. This component is called the Reynolds stress and is a symmetric second-order tensor consisting of six independent components. Thus, for a turbulent fluid there are still the same four equations and already ten unknowns: three velocity components, hydrodynamic pressure and six Reynolds stresses.

To close the system of equations, it is necessary to determine the relationship between the Reynolds stresses and the parameters of the averaged flow. This relationship is determined using various turbulence models. One of these models is the standard turbulence model k–ε, where the concept of turbulent viscosity is introduced:

$$-\rho\overline{u_i' u_j'} = \mu_t\left(\frac{\partial u_i}{\partial x_j} + \frac{\partial u_j}{\partial x_i}\right) \tag{12}$$

Next, we proceed directly to obtaining the standard k-ε model from two equations, which is currently considered as a standard model for describing turbulence and solving engineering problems. In this model, two important concepts are introduced namely generation P and dissipation ε. The physical meaning of the generation of turbulence P consists in the generation of new vortices and pulsations, which form turbulence. Dissipation ε, on the other hand, is the dissipation of large eddies into smaller ones, leading to flow averaging and turbulence reduction. Two transport equations allow considering turbulence in space and time. This model is semi-empirical and is based on a phenomenological approach and experimental results.

After multiplying the Reynolds equation by u_j and performing simple algebraic transformations, we obtain:

$$\begin{aligned} \partial_t\overline{u_i' u_j'} + \bar{u}_k\partial_k\overline{u_i' u_j'} &= -\tfrac{1}{\rho}\left(\overline{u_j'\partial_i p} + \overline{u_i'\partial_j p}\right) - 2v\overline{\partial_k u_i' \partial_k u_j'} \\ &-\partial_k\overline{u_k' u_i' u_j'} - \overline{u_j' u_k'}\partial_k u_i - \overline{u_i' u_k'}\partial_k u_j + v\nabla^2\overline{u_i' u_j'} \end{aligned} \tag{13}$$

Let's define the kinetic energy of turbulence as $k = 0,5\overline{u_i' u_j'}$ and substitute it in the last equation, taking $i = j$:

$$\partial_t k + \bar{u}_k\partial_k k = -\frac{1}{\rho}\partial_i\overline{u_i' p} - v\overline{\partial_k u_i' \partial_k u_i'} - \frac{1}{2}\partial_k\overline{u_k' u_i' u_i'} - \overline{u_i' u_k'}\partial_k u_i + p\nabla v \tag{14}$$

The second addend on the right side of the resulting equation is responsible for energy dissipation:

$$\varepsilon = v\overline{\partial_k u_i' \partial_k u_i'} \tag{15}$$

While the fourth addend of the right-hand side of the resulting equation is the generation P:

$$P = -\overline{u_i' u_k'}\partial_k u_i \tag{16}$$

Next, it is assumed that:

$$-\partial_j\left(\frac{1}{2}\overline{u'_j u'_i u'_i} - \frac{1}{\rho}\overline{u'_j p}\right) \approx \partial_j\left(v_T \partial_j k\right) \tag{17}$$

Thus, it is possible to write the following equation of kinetic energy k:

$$\partial_t k + \bar{u}_j \partial_j k = P - \varepsilon + \partial_j\left(\left(v + \frac{v_T}{\sigma_k}\right)\partial_j k\right), \tag{18}$$

Where σ_k – is the parameter, which provides necessary dimensionality for addend with ν_T. Usually accepted $\sigma_k = 1$.

Similarly, the equation for dissipation ε is written:

$$\partial_t \varepsilon + \bar{u}_j \partial_j \varepsilon = \frac{C'_{1\varepsilon} P - C'_{2\varepsilon}\varepsilon}{T} + \partial_j\left(\left(v + \frac{v_T}{\sigma_\varepsilon}\right)\partial_j \varepsilon\right), \tag{19}$$

where $T = k/\varepsilon$ provides the necessary dimensionality, and constants $C'_{1\varepsilon}$, $C'_{2\varepsilon}$, σ_ε are input, as the form of the last equation is only assumed but not derived analytically.

Solving the problem of determining the thermal state of the brush-holders device was carried out in several stages:

1. Determination of heat release.
2. Determination of pressure characteristics of the fan.
3. Development of a three-dimensional model.
4. Calculation of the thermal state.

The specific resistance of copper adopted in the calculations is $1.75{\cdot}10^{-8}$ Ω·m at a temperature of 15 °C, and the specific resistance of steel is $1.3{\cdot}10^{-7}$ Ω·m at a temperature of 15 °C.

The calculated total losses, which are removed by air, are 10050 W. Calculation of losses was carried out by an analytical method according to the methodology [8, 9].

The calculation of the pressure characteristic of the fan was carried out by the analytical method [10].

Calculation parameters of the centrifugal fan:

– fan static pressure 1800 Pa;
– air rated loss 2,26 m^3/sec.;
– air speed at the fan inlet 23 m/sec.;
– air speed at the fan outlet 65 m/sec.

Calculation of air movement and thermal state of the brush-holder device was performed in a three-dimensional setting using the Solid Works Flow Simulation software application package, which allows numerical simulation of internal and external flows with liquids or gases. In order to model the flow, the solution of the Navier-Stokes equations for the movement of a viscous liquid in a three-dimensional setting, mediated by Reynolds and supplemented by the k-ε-model of turbulence, is used. Sufficient accuracy of this module allows it to be used to solve most engineering tasks. The main methods and description of the mathematical apparatus used in SolidWorks Flow Simulation are presented in [11–13].

Modeling of air flow movement in the body of the brush-holders device was carried out with standard settings of the detailing of the calculation grid with additional thickening in narrow channels. Such parameters make it possible to determine with sufficient accuracy the features of the flow caused by the complexity of the flow part.

The following values by volume were chosen as criteria for the convergence of the solution: minimum, average and maximum static pressure, average mass flow rate; on the specified surfaces namely the average heat flow. The calculation was performed until the convergence criterion was reached and at least three blowing out of the calculation area were carried out.

In Figs. 7, 8 and 9 shows the Diagrams of pressures, cooling air speeds, and temperatures for the rated operating mode of a 200 MW Turbogenerator. The flow inside the brush-holders device (BHD) is turbulent. There are no air blocking zones.

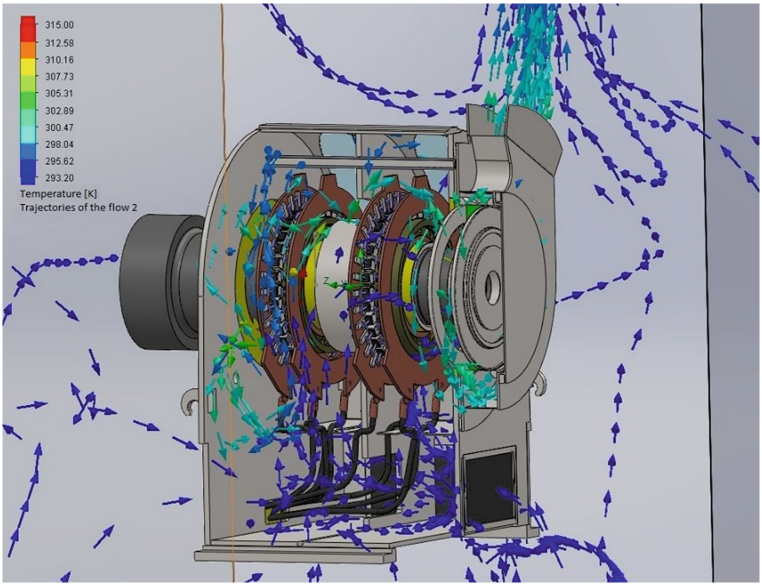

Fig. 7. Diagram of Air Temperatures in Steady State Operation Mode

In the design of the brush-holders device insulating materials of the heat resistance class F are used, for which the maximum permissible temperature is 155 °C. At the same time, the permissible temperatures are usually taken a class lower compared to the insulation used, i.e. in this case according to heat resistance class B (120 °C).

The temperature values, obtained as a result of the simulation of the thermal state of the brush-holders device in the Solid Works Flow Simulation environment, satisfy the requirements for the designed new electric machines. The calculation error does not exceed the measurement error, which allows to evaluate the serviceability of the brush-holders device at the design stages, and the obtained values do not exceed the maximum permissible temperatures according to IEC 60034-1 [14] for slip rings.

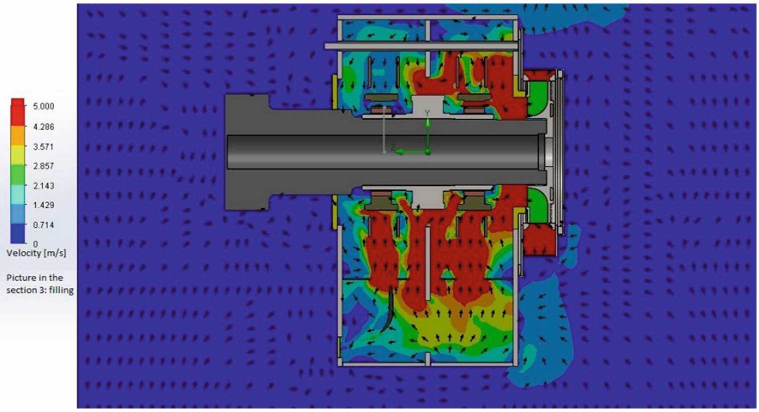

Fig. 8. Diagram of Air Speeds in Steady State Operation Mode

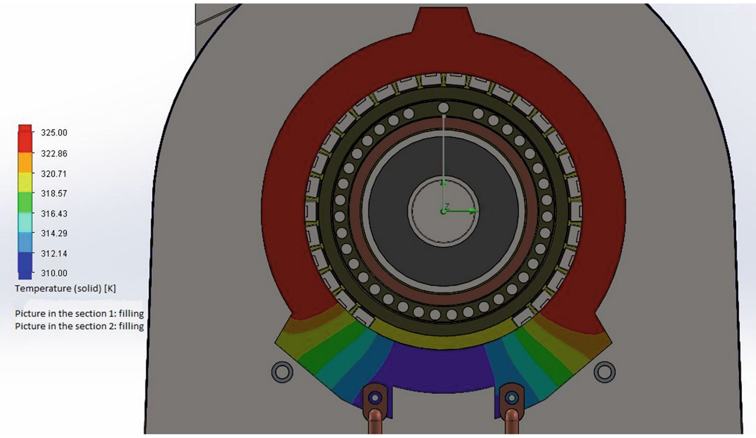

Fig. 9. Temperature Diagram in Steady State Operation Mode

The temperature distribution values obtained from the results of the analysis of the thermal state can be used for further calculations of the mechanical stress state of the elements of the brush-contact device in a three-dimensional setting to determine thermal stresses [15–18].

In particular, thermal stresses shall be taken into account when calculating the stressed-strain state of slip rings, which during operation are under the influence of centrifugal forces due to the rotation of the rotor. A characteristic feature of this unit is also the possibility of a gradual reduction during operation of the outer diameter of the slip rings under the action of frictional forces and in the case of restoring the quality of the surface of the slip ring by boring during the repair of the Turbogenerator. Such a decrease in diameter accordingly mixes the cross-section of the ring and leads to an increase in stresses, which shall also be taken into account during calculations.

For stationary parts of the brush-holders device, the issues of ensuring strength are not so important, because usually such structures shall first of all provide sufficient rigidity to prevent increased vibration, due to which significant reserves of strength of the elements are provided. However, thermal deformations in some elements can affect the frequency of natural oscillations of the structure, which shall be taken into account during the corresponding calculations.

5 Discussion

The problem of determining the thermal state of the brush-holders device in a three-dimensional setting, taking into account heat release caused by electrical and mechanical influences is solved in the paper. A combination of the analytical method of calculation with the solution in a three-dimensional formulation by the CFD method using the Solid Works Flow Simulation software complex is proposed.

References

1. Tretiak, O., et al.: Stress-strained state of the thrust bearing disc of hydrogenerator-motor. Computation **11**(3), 60 (2023). https://doi.org/10.3390/computation11030060
2. Tretyak, O.V.: The strength of turbo-generators and high-power hydro-generators. Institute of Mechanical Engineering Problems named after A.M. Pidgorny of National Academy of Sciences of Ukraine, p. 396, Kharkiv (2020)
3. Stone, G.C., Gupta, B.K., Lyles, J.F., Sedding, H.G.: Experience with accelerated aging tests on stator bars and coils. In: IEEE International Symposium on Electrical Insulation, Toronto, pp. 356–360 (1990)
4. Qiao, G., Liu, G., Shi, Z., Wang, Y., Ma, S., Lim, T.C.: A review of electromechanical actuators for more/all electric aircraft systems. Proc. Inst. Mech. Eng. Part C J. Mech. Eng. Sci. **232**(22), 4128–4151 (2018). https://doi.org/10.1177/0954406217749869
5. Say, M.G.: Alternating Current Machines, 4th edn., p. 543, Pitman Publishing, Lanham (1976)
6. Putignano, C., Afferrante, L., Carbone, G., Demelio, G.: A new efficient numerical method for contact mechanics of rough surfaces. **49**(2), 338–343 (2012)
7. Ilyin, A.V., Plokhov, I.V., Kozyreva, O.I., Andrusich, A.V.: Three-dimensional modeling of nonstationary temperature field in the microcontact. Bull. Pskov Univ. Ser. Econ. Tech. Sci. **2**(5), 208–214 (2014)
8. Gerling, D.: DC-machines. In: Gerling, D. (ed.) Electrical Machines. Mathematical Engineering, vol. 4, pp. 37–88. Springer, Heidelberg (2015). https://doi.org/10.1007/978-3-642-17584-8_2
9. Tretiak, O., Kritskiy, D., Kobzar, I., Arefieva, M., Nazarenko, V.: The methods of three-dimensional modeling of the hydrogenerator thrust bearing. Computation **10**, 152 (2022). https://doi.org/10.3390/computation10090152
10. Warnes, L.A.A.: DC machines. In: Electronic and Electrical Engineering. Macmillan New Electronics Series. Palgrave, London (1994). https://doi.org/10.1007/978-1-349-13012-2_13
11. International Standard, DSTU EN IEC 60034-33:2022 Electric rotating machines. Part 33. Synchronous hydrogenerators, including motor generators. Special requirements (2022). http://online.budstandart.com/ua/catalog/doc-page.html?id_doc=102789. Accessed 14 Aug 2023
12. Akin, J.: Finite Element Analysis Concepts via SolidWorks, p. 303. World Scientific, New Jersey;·London;·Singapore;·Beijing;·Shanghai;·Hong Kong;·Taipei;·Chennai (2009)

13. Jichao, H., et al.: Numerical analysis of end part temperature in the turbogenerator end region with magnetic shield structure under the different operation conditions. Int. J. Therm. Sci. **132**, 267–274 (2018)
14. IEC 60034-1:2022. Rotating Electrical Machines - Part 1: Rating and Performance, 14th edn. International Standard (2022)
15. Kvitka, A.L., Voroshko, P.P., Bobrovitskaya, S.D.: Stress-Strain State of Bodies of Revolution, p. 209. Naukova Dumka, Kyiv (1977)
16. Valavi, M., Nysveen, A., Nilsen, R., Le, B.J., Devillers, E.: Analysis of magnetic forces and vibration in a converter-fed synchronous hydrogenator. In: 2017 IEEE Energy Conversion Congress and Exposition (ECCE), Cincinnati, OH, USA, pp. 1838–1844 (2017). https://doi.org/10.1109/ECCE.2017.8096018
17. Waqar, S., Guo, K., Sun, J.: FEM analysis of thermal and residual stress profile in selective laser melting of 316L stainless steel. J. Manuf. Process. **66**, 81–100 (2021)
18. Sheikh, U.A., Jameel, A.: Elasto-plastic large deformation analysis of bi-material components by FEM. Mater. Today: Proc. **26**(Part 2), 1795–1802 (2020)

Process-Induced Stresses and Deformations of Hobe Block During Shrinkage and Cooling

Sergiy Melnikov[1], Igor Taranenko[1], Tetyana Nabokina[1], and Andrii Kondratiev[2(✉)]

[1] National Aerospace University "Kharkiv Aviation Institute", 17 Chkalova Street, Kharkiv 61070, Ukraine

[2] O.M. Beketov National University of Urban Economy in Kharkiv, 17 Marshal Bazhanov Street, Kharkiv 61002, Ukraine

andrii.kondratiev@kname.edu.ua

Abstract. Aluminum honeycomb cores are usually formed after assembling of a block of roll foil, its gluing and stretching into the hexagonal cell. In the process of the block formation, shrinkage stresses and deformations arise on the faces of honeycomb cells because of adhesive shrinkage and effect of the temperature field. Such stresses and deformations lead to a significant decrease in the mechanical characteristics of the honeycomb core and sandwich structures based on it. For the hobe block, we performed finite-element modeling of its stress-strain behavior, arising because of adhesive shrinkage and significant difference in the coefficients of linear thermal expansion of adhesive and foil, and identified the main reason for the occurrence of the technological camber of honeycomb core faces having a large impact on their stability during loading. The method of analysis of this type of honeycomb cell defect has been developed. Our findings allow making the quantitative assessment of the technological camber of honeycomb faces and giving the reasonable recommendations to standardize its tolerance band. The recommendations provide the fixed level of shrinkage deformations and the corresponding coefficient of linear thermal expansion at different moulding temperatures. It is shown that by choosing adhesives with less shrinkage and lower coefficient of linear thermal expansion of material of the adhesive being cured at relatively low temperatures, tolerance band for the relative technological camber can be regulated within 0…1.4. Results of the work allow solving a number of new problems in the technology of assembling honeycomb structures for the various classes of equipment.

Keywords: Camber of honeycomb faces · Adhesive · Foil · Thermal expansion

1 Introduction

The priority in the improvements of modern aerospace, automotive, railway and shipbuilding engineering is given to the reduction of structures' weight [1–3]. Wide opportunities for the significant reduction of weight of various objects are created by using the sandwich structures with honeycomb cores [4, 5]. These honeycomb structures consist

M. Nechyporuk et al. (Eds.): ICTM 2023, LNNS 1008, pp. 91–101, 2024.
https://doi.org/10.1007/978-3-031-61415-6_8

of thin composite face sheets and aluminium honeycomb core comprising a set of even thinner walls [6]. However, quality of the honeycomb core, its functional properties and their stability are determined by its manufacturing technology [7, 8]. The honeycomb core manufacturing has become an independent industry, serving the consumers in various fields of technology, including up to 70% of honeycombs of various materials used in aerospace engineering [9]. In addition, the highest demands are made on the honeycomb cores for aircraft structures [10, 11]. The pronounced technological heredity of honeycombs, resulted from technological imperfections or defects, leads to integral changes in the predicted properties of the honeycomb core itself and deviations in the bearing capacity of a sandwich structure based on it [12].

In this regard, there is an urgent problem of the development of scientifically grounded methods for standardizing the production tolerances for the main parameters of the process of manufacturing of honeycomb cores for the structures of various classes of equipment. The purpose of this study is to develop a method for analyzing the defects in the honeycomb cell shape associated with the parameters of the hobe block forming mode, which have the largest impact on the nominal mechanical characteristics of the honeycomb core.

2 Literature Review

A number of papers cover the systematic study of typical technological defects of honeycomb cores. The paper [13] provides the parametric study of the impact of various structural defects on the mechanical characteristics of honeycombs. To reduce the impact of defects, the paper proposes the computer vision methodology to monitor the deformation of each cell of the honeycomb core. Simultaneous joint curing of the face sheets and honeycomb core to eliminate the defects arising in the process of honeycomb structures' assembly by gluing is proposed in [14]. The paper [15] contains the results of studies of the possibilities to consider the technological imperfections of honeycombs in the design of honeycomb structures. A technique for optimization of tolerances for the manufacturing of honeycomb core of a sandwich panel ensuring the specified bearing capacity of the structure has been proposed. However, this approach to standardization of tolerances for the parameters of the honeycomb cell shape is not focused on the technological capabilities of performance of the relevant operations in the honeycomb core manufacturing process. Instead, it is aimed at securing the regulated deviation of the bearing capacity of a specific honeycomb structure. The impact of various structural defects of the honeycomb core on strength of the structure is studied in [16] with the use of finite-element modeling, but the proposed technique can be extended to other types of honeycomb structures with certain adjustments only. Approximation methods for assessment of the impact of various structural defects of honeycombs on the honeycomb structure strength are developed and proposed in [17, 18]. Reliability of the results is confirmed by finite-element modeling. Most of the works reviewed contain the results of studies of the possibilities to consider various technological imperfections of honeycomb core manufacturing in the design of sandwich structures with honeycomb core. However, approaches to standardization of tolerances for honeycomb defects implemented in these papers are focused on securing the regulated deviation of the bearing capacity of a specific honeycomb structure, instead of technological capabilities of performance of the relevant operations in the honeycomb core manufacturing process. Therefore, the results obtained in these papers do not solve the problem of standardizing tolerances in the honeycomb core manufacturing in its technological setting.

Among many types of honeycomb cores, differing in their cell configuration and manufacturing technology, the most common are hexagonal cells [19]. These honeycombs are usually formed after assembling of a hobe block, its gluing and stretching into the hexagonal cell [20]. The honeycomb cell shape is obtained as a result of applying an adhesive strip with the required pitch on the roll foil using a pattern cylinder, and further combining of the roll material into a block with adhesive strips shifted by half a pitch in staggered arrangement. During moulding of this hobe block, the adhesive may shrink. Furthermore, moulding occurs at the temperature increasing up to 185 °C [21]. As a result of shrinkage and effect of the temperature field, shrinkage stresses and deformations, associated with the significant difference in the coefficients of linear thermal expansion of the foil material and adhesive, arise in the foil. At the secondary stage of manifestation of this stress-strain behavior (after partial stress relaxation), the released hobe block features the technological cambers of cell faces, which lead to a significant decrease in the mechanical characteristics of the honeycomb core. However, the mechanism of occurrence of the initial technological camber of the honeycomb core faces and their quantitative determination still remain unexplored and unspecified. On the one hand, the difficulty of this problem solving is apparently connected with low values of the cambers themselves being of the same order (or less) with the foil thickness, and lack of reliable means and methods of measurement for their experimental determination [22, 23]. On the other hand, it can be explained by the uncertainty and multifactorial nature of the very mechanism of their occurrence [24, 25]. Therefore, until now the approach proposed in [26] is implemented as the best-case scenario, based on setting of the values of technological cambers and subsequent determination of the honeycomb core physico-mechanical characteristics at these values. The resulting discrepancy between theoretical and experimental values is related to the qualitative assessment of honeycomb manufacturing technology [27].

3 Research Methodology

Behavior of the hobe block during its formation was modeled by considering a section of width l with four strips of foil of thickness δ_c, discretely glued with the adhesive layer of thickness η with the pitch a_c (Fig. 1).

Dimensions of the element adopted for calculations are as follows: $l = 9a_c = 45$ mm; $b = 20$ mm; $\delta_c = 0.03$ mm; $\eta = 0.01$ mm. Elastic characteristics of the foil material: $E_c = 69$ GPa; $G_c = 26.54$ GPa; $\mu_c = 0.3$. Elastic characteristics of the adhesive: $E_\eta = 3$ GPa; $G_\eta = 1.15$ GPa; $\mu_\eta = 0.3$.

We used for calculations one of the software complexes of finite element analysis with capabilities that allowed us to solve a wide range of problems [28]. The hobe block element in the finite element analysis was modeled with 8–node 3D finite element type Solid (three translational degrees of freedom were considered for each node). The total number of finite elements is 12400 elements. The model was fixed along the linear

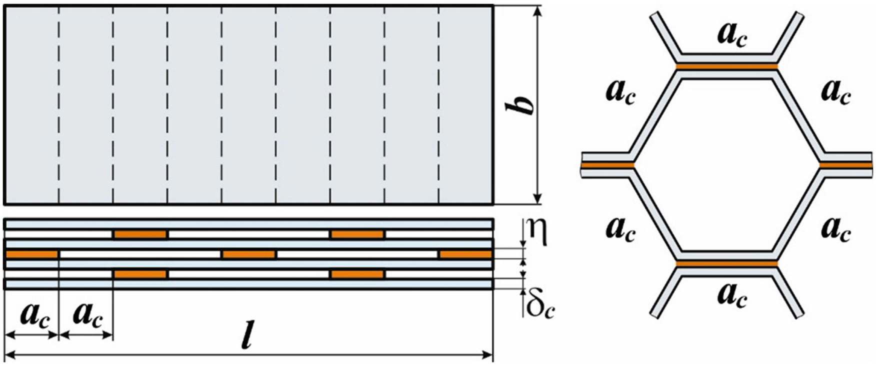

Fig. 1. Hobe block element model

displacements u_y on the lower surface of central section of the foil and along the linear displacements u_x and u_z in the central node of the lower surface. Study of the convergence of the numerical solution showed that with such a number of finite elements in the models the normal and shear stresses varied insignificantly (by a maximum of 5%). Analysis of the quality of generated finite element models did not reveal any critical errors. The generated finite-element model with the conditions of fixing is shown in Fig. 2.

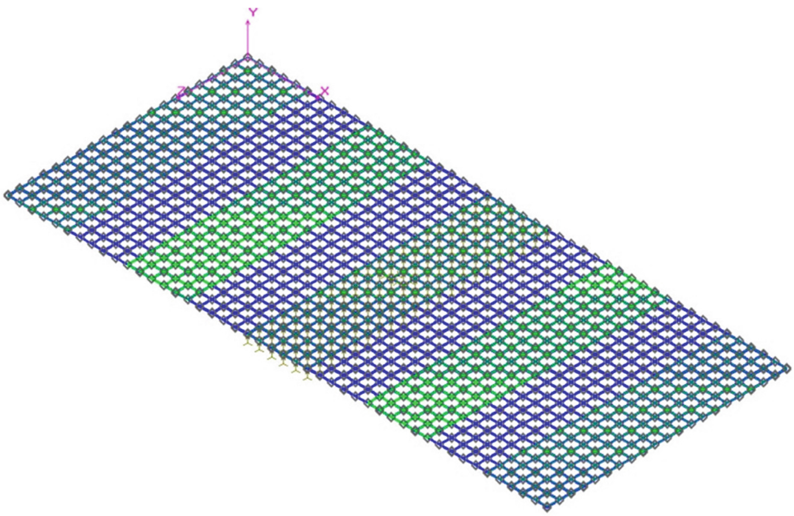

Fig. 2. Finite-element model of hobe block element

The adhesive layer shrinkage was modeled by setting the corresponding coefficients of linear thermal expansion and temperature difference ΔT for the foil and adhesive material in the model.

For different adhesives, the value of the relative linear shrinkage deformation varies within a wide range. For example, it is equal to (5…7)% for polyimide binders and (0.3…1)% for epoxy binders [29, 30].

To set the shrinkage deformation itself $\varepsilon_{sh} = 5\%$ without taking into account the temperature effect, the following values were adopted:

– conditional coefficient of linear thermal expansion of the foil material $\alpha_c = 1 \cdot 10^{-15}$ 1/°C (actually corresponding to its zero value);
– coefficient of linear thermal expansion of the adhesive material $\alpha_\eta = 5 \cdot 10^{-4}$ 1/°C (actually corresponding to free spreading of the adhesive);
– temperature difference $\Delta T = -100$ °C.

It corresponds to shrinkage deformation $\varepsilon_{sh} = 0.05$.

Cooling of the hobe block was modeled by defining the temperature difference $\Delta T = -160$ °C and using this temperature field in the further calculations of stress-strain behavior. In our studies, we adopted:

– coefficient of linear thermal expansion of the foil material $\alpha_c = 23.8 \cdot 10^{-6}$ 1/°C;
– coefficient of linear thermal expansion of the adhesive material $\alpha_\eta = 5 \cdot 10^{-5}$ 1/°C.

4 Results and Discussion

The patterns of deformation of the hobe block element models during shrinkage and cooling are shown in Fig. 3.

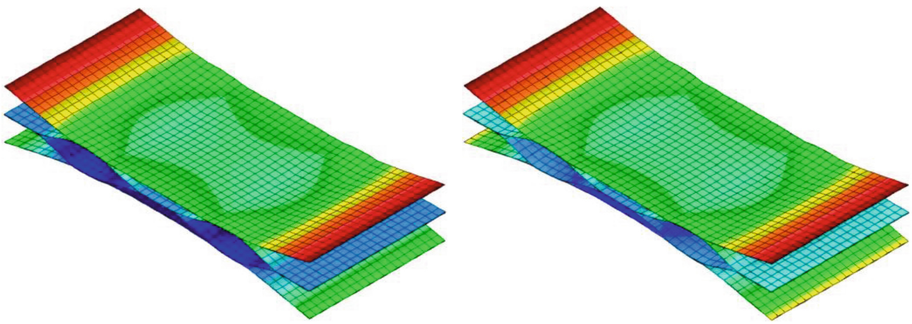

a b

Fig. 3. Deformed state of the hobe block element model: a – during shrinkage; b – during cooling.

The maximum vertical displacement is 0.039 mm during shrinkage, and 0.0027 mm during cooling. Maximum reduced Mises stresses during shrinkage are 213.86 MPa in the adhesive layer and 93.88 MPa in foil. Maximum reduced stresses during cooling are 17.93 MPa in the adhesive layer and 7.75 MPa in foil.

The graphs of distribution of linear displacements u_y during shrinkage in the center and single face in the direction of the X axis are shown in Fig. 4, a, in the direction of the Z axis in Fig. 4, b, and double face in Fig. 5.

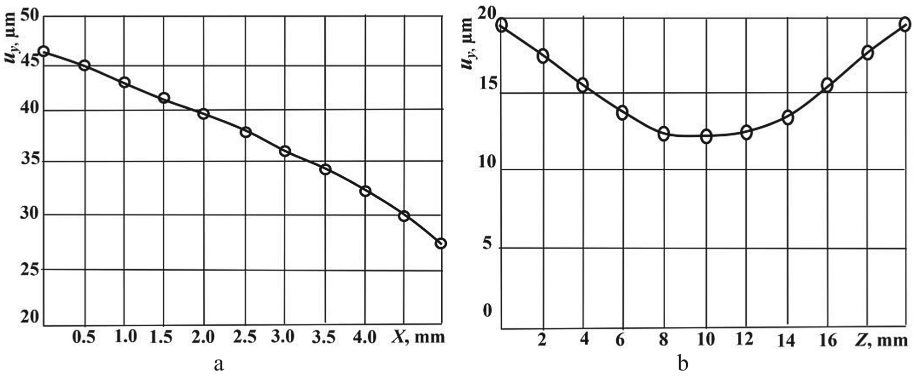

Fig. 4. Graph of linear displacements u_y during shrinkage: a – in the center of the single face (along the X axis); b – in the center of the single face (along the Z axis)

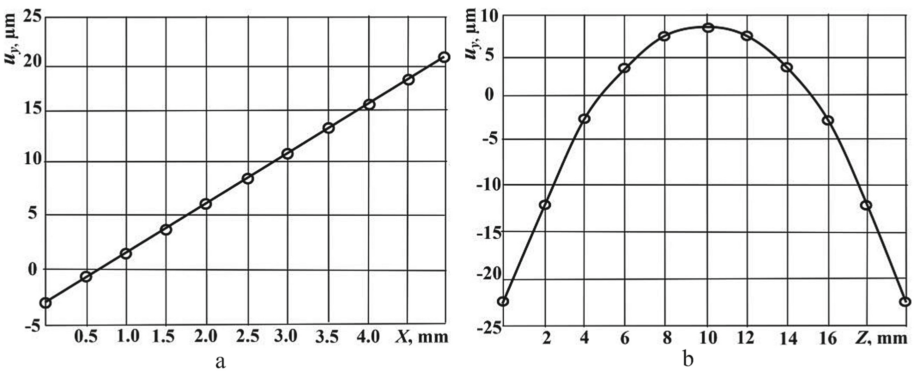

Fig. 5. Graph of linear displacements u_y during shrinkage: a – in the center of the double face (along the X axis); b – in the center of the double face (along the Z axis)

The graphs of distribution of linear displacements u_y during cooling in the center and single face in the direction of the X axis are shown in Fig. 6, a, in the direction of the Z axis in Fig. 6, b, and double face in Fig. 7.

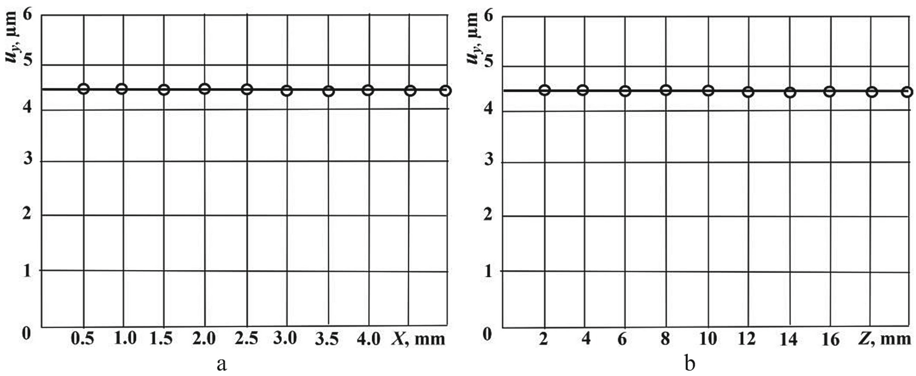

Fig. 6. Graph of linear displacements u_y during cooling: a – in the center of the single face (along the X axis); b – in the center of the single face (along the Z axis)

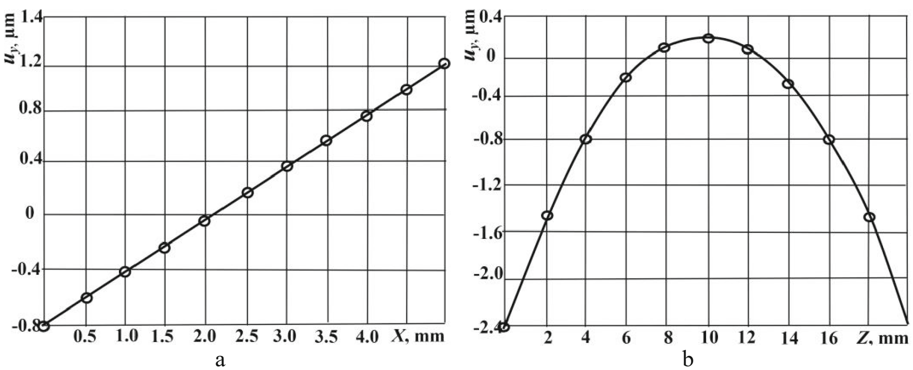

Fig. 7. Graph of linear displacements u_y during cooling: a – in the center of the double face (along the X axis); b – in the center of the double face (along the Z axis)

In the studies considered above the extreme values of shrinkage $\varepsilon = 0.05$ and temperature of hobe block moulding $\Delta T = 160$ °C were adopted. Since the shrinkage deformation and deformation associated with the difference in the coefficient of linear thermal expansion of foil and adhesive are independent, then, when assuming the absence of relaxation of process-induced stresses, maximum possible technological camber of the honeycomb core cell face (depth of a bulge or depression) theoretically reaches the value

$$f_{\Sigma} = u^{sh}_{y\,\max} + u_{y\,\max} = 0.039 + 0.0027 = 0.0417 \text{ mm}.$$

Therefore, the maximum possible relative camber at foil thickness $\delta_c = 0.03$ mm can be

$$\bar{f}_{\sum} = \frac{f}{\delta_c} = \frac{0.0417}{0.03} = 1.39.$$

Values of tolerances for technological camber of the honeycomb core cell faces for the corresponding tolerance bands on ε_{sh}, ΔT and α_η are given in Table 1.

Table 1. Recommended tolerance bands for technological camber of honeycomb core faces for adhesives with different values of ε_{sh}, ΔT and α_η for aluminum foil (AMg-2N).

ε_{sh}	ΔT, °C	$\alpha_\eta \cdot 10^6$, 1/°C	$\bar{f}_{tech}$
0.005	160	60	0.261
		40	0.178
	120	60	0.229
		40	0.166
	100	60	0.212
		40	0.160
0.02	160	60	0.651
		40	0.568
	120	60	0.619
		40	0.556
	100	60	0.602
		40	0.550
0.03	160	60	0.911
		40	0.828
	120	60	0.879
		40	0.816
	100	60	0.862
		40	0.810
0.05	160	60	1.431
		40	1.348
	120	60	1.399
		40	1.336
	100	60	1.382
		40	1.330

By choosing adhesives with less shrinkage and lower coefficient of linear thermal expansion of the adhesive material α_η, being cured at relatively low values of ΔT, it is apparent that tolerance band for the relative technological camber can be regulated within $0 \leq \bar{f}_{tech} \leq 1.4$, as recommended in [26].

5 Conclusions

Based on the mathematical models of defects associated with the parameters of hobe block forming mode (adhesive shrinkage and differences in the coefficients of linear thermal expansion of the adhesive and foil), we identified the main reason for the occurrence of the technological camber and validated the relevant tolerance bands. The method of analysis of the above honeycomb core defects has been developed. Our findings allow making their quantitative assessment and giving the reasonable recommendations to standardize the tolerance band for the technological camber of honeycomb core faces for adhesives, which provide the fixed level of shrinkage deformations and the corresponding coefficient of linear thermal expansion at different temperatures of the hobe block moulding.

References

1. Panchenko, S., Gerlici, J., Vatulia, G., Lovska, A., Pavliuchenkov, M., Kravchenko, K.: The analysis of the loading and the strength of the FLAT RACK removable module with viscoelastic bonds in the fittings. Appl. Sci. **13**, 79 (2023). https://doi.org/10.3390/app13010079
2. Fomin, O., Logvinenko, O., Burlutsky, O., Rybin, A.: Scientific substantiation of thermal leveling for deformations in the car structure. Int. J. Eng. Technol. **7**(4.3), 125–129 (2018). https://doi.org/10.14419/ijet.v7i4.3.19721
3. Misura, S., Smetankina, N., Misiura, I.: Optimal design of the cyclically symmetrical structure under static load. In: Nechyporuk, M., Pavlikov, V., Kritskiy, D. (eds.) ICTM 2020. LNNS, vol. 188, pp. 256–266. Springer, Cham (2021). https://doi.org/10.1007/978-3-030-66717-7_21
4. Maiorova, K., Vorobiov, I., Boiko, M., Suponina, V., Komisarov, O.: Implementation of reengineering technology to ensure the predefined geometric accuracy of a light aircraft keel. East.-Eur. J. Enterp. Technol. **6**(1(114), 6–12 (2021). https://doi.org/10.15587/1729-4061.2021.246414
5. Golovanevskiy, V., Kondratiev, A.: Elastic properties of steel-cord rubber conveyor belt. Exp. Tech. **45**(2), 217–226 (2021). https://doi.org/10.1007/s40799-021-00439-3
6. Wang, Z.G.: Recent advances in novel metallic honeycomb structure. Compos. Part B Eng. **166**, 731–741 (2019). https://doi.org/10.1016/j.compositesb.2019.02.011
7. Birman, V., Kardomateas, G.A.: Review of current trends in research and applications of sandwich structures. Compos. Part B Eng. **142**, 221–240 (2018). https://doi.org/10.1016/j.compositesb.2018.01.027
8. Qi, C., Jiang, F., Yang, S.: Advanced honeycomb designs for improving mechanical properties: a review. Compos. Part B Eng. **227**, 109393 (2021). https://doi.org/10.1016/j.compositesb.2021.109393
9. Tiwary, A., Kumar, R., Chohan, J.S.: A review on characteristics of composite and advanced materials used for aerospace applications. Mater. Today: Proc. **51**(1), 865–870 (2022). https://doi.org/10.1016/j.matpr.2021.06.276
10. Vargas-Rojas, E., Nocetti-Cotelo, C.A.: Alternative proposal, based on systems-engineering methods, aimed at substituting with carbon-epoxy laminates the load-bearing aluminum sandwiches employed in the structure of a small satellite. Adv. Space Res. **66**, 193–218 (2020). https://doi.org/10.1016/j.asr.2020.04.004
11. Kondratiev, A.V., Kovalenko, V.O.: Optimization of design parameters of the main composite fairing of the launch vehicle under simultaneous force and thermal loading. Space Sci. Technol. **25**(4(119)), 3–21 (2019). https://doi.org/10.15407/knit2019.04.003

12. Castanie, B., Bouvet, C., Ginot, M.: Review of composite sandwich structure in aeronautic applications. Compos. Part C: Open Access **1**, 100004 (2020). https://doi.org/10.1016/j.jcomc.2020.100004
13. Wang, Z.G., Li, Z.D., Zhou, W., Hui, D.: On the influence of structural defects for honeycomb structure. Compos. Part B Eng. **142**, 183–192 (2018). https://doi.org/10.1016/j.compositesb.2018.01.015
14. Zebrine, D., Wadhwani, E., Nutt, S.: Surface porosity development in tool-side facesheets of honeycomb core sandwich structures during co-cure. Adv. Manuf.-Polym. Compos. Sci. **8**, 43–55 (2022). https://doi.org/10.1080/20550340.2022.2056313
15. Gaydachuk, V., Koloskova, G.: Mathematical modeling of strength of honeycomb panel for packing containers and packaging with regard to deviations in the filler parameters. East.-Eur. J. Enterp. Technol. **6**(1(84)), 37–43 (2016). https://doi.org/10.15587/1729-4061.2016.85853
16. Xu, P., Xiao, X.L., Yao, S.G., Kong, L.X.: Study on effect of offset defect on mechanical property of honeycomb structures. Structures **34**, 275–285 (2021). https://doi.org/10.1016/j.istruc.2021.07.073
17. Chen, D.H., Masuda, K.: Effects of honeycomb geometry on stress concentration due to defects. Compos. Struct. **188**, 55–63 (2018). https://doi.org/10.1016/j.compstruct.2017.12.047
18. Chen, D.H., Masuda, K.: Estimation of stress concentration due to defects in a honeycomb core. Eng. Fract. Mech. **172**, 61–72 (2017). https://doi.org/10.1016/j.engfracmech.2017.01.009
19. Siivola, J.T., Minakuchi, S., Mizutani, T., Kitamoto, K., Takeda, N.: Monitoring of dimple formation in honeycomb sandwich structures using distributed fiber optic sensors. J. Sandwich Struct. Mater. **23**, 3645–3668 (2021). https://doi.org/10.1177/1099636220935821
20. Baran, I., Cinar, K., Ersoy, N., Akkerman, R., Hattel, J.H.: A review on the mechanical modeling of composite manufacturing processes. Arch. Comput. Methods Eng. **24**(2), 365–395 (2017). https://doi.org/10.1007/s11831-016-9167-2
21. Li, Y., Xiao, Y., Yu, L., Ji, K., Li, D.S.: A review on the tooling technologies for composites manufacturing of aerospace structures: materials, structures and processes. Compos. Part A Appl. Sci. Manuf. **154**, 106762 (2022). https://doi.org/10.1016/j.compositesa.2021.106762
22. Peng, F.H., et al.: Adaptive modal identification of honeycomb thin-walled composite structures with pit defects under thermal modal testing using variational mode decomposition technique based on digital image correlation. Thin-Walled Struct. **188**, 110827 (2023). https://doi.org/10.1016/j.tws.2023.110827
23. Mills, J.A., et al.: Identifying defects in aerospace composite sandwich panels using high-definition distributed optical fibre sensors. Sensors. **20**, 6746 (2020). https://doi.org/10.3390/s20236746
24. Hu, C.Q., et al.: LSTM-RNN-based defect classification in honeycomb structures using infrared thermography. Infrared Phys. Technol. **102**, 103032 (2019). https://doi.org/10.1016/j.infrared.2019.103032
25. Tkachenko, D., Tsegelnyk, Y., Myntiuk, S., Myntiuk, V.: Spectral methods application in problems of the thin-walled structures deformation. J. Appl. Comp. Mechan. **8**(2), 641–654 (2022). https://doi.org/10.22055/jacm.2021.38346.3207
26. Kondratiev, A., Nabokina, T.: Effect of technological camber in the facets of a cellular filler on its physical and mechanical characteristics. East.-Eur. J. Enterp. Technol. **5**(7(101)), 6–18 (2019). https://doi.org/10.15587/1729-4061.2019.179258
27. Li, W., Atsushi, D., Oh, Y.H., Jirathearanat, S., Wu, Z.A., Chua, B.W.: Influences of skin thickness, core topology, depth and direction on flexural deformation and ductile failure of Al honeycomb-based sandwich structures. Compos. Part B Eng. **239**, 109957 (2022). https://doi.org/10.1016/j.compositesb.2022.109957

28. Caliri, M.F., Ferreira, A.J.M., Tita, V.: A review on plate and shell theories for laminated and sandwich structures highlighting the finite element method. Compos. Struct. **156**, 63–77 (2016). https://doi.org/10.1016/j.compstruct.2016.02.036
29. Slyvynskyi, V.I., Alyamovskyi, A.I., Kondratjev, A.V., Kharchenko, M.E.: Carbon honeycomb plastic as light-weight and durable structural material. In: Proceedings of the 63rd International Astronautical Congress 2012, IAC 2012, Naples, Italy, vol. 8, pp. 6519–6529 (2012)
30. Kurennov, S.S., Barakhov, K.P., Dvoretskaya, D.V., Poliakov, O.G.: Stress distribution in the eccentrically loaded lapped adhesive joint. An analytical model. In: Nechyporuk, M., Pavlikov, V., Kritskiy, D. (eds.) ICTM 2021. LNNS, vol. 367, pp. 3–13. Springer, Cham (2022). https://doi.org/10.1007/978-3-030-94259-5_1

Temperature and Velocity Changes of ZrO_2 Particles in the Process of HVOF Spraying by Twin-Combustion-Chamber Burner

Kostiantyn Danko[1], Oleksandr Shorinov[2](✉), Yurii Neveshkin[2], and Sergii Polyvianyi[3]

[1] Zaporizhzhia Machine-Building Design Bureau "Progress State Enterprise" Named After Academician O. H. Ivchenko, 2 Ivanova Steet, Zaporizhzhya 69068, Ukraine

[2] National Aerospace University "Kharkiv Aviation Institute", 17 Chkalova Street, Kharkiv 61070, Ukraine

o.shorinov@khai.edu

[3] Joint Stock Company "Motor Sich", 15 Motorobudivnykiv Avenue, Zaporizhzhia 69068, Ukraine

Abstract. This study aims to calculate the velocity and temperature of zirconium oxide (ZrO_2) particles in the channel of a twin-combustion-chamber burner for high-velocity oxygen fuel (HVOF) spraying, specifically from the cutoff of the burner mixing chamber to the substrate. The calculations incorporated methylacetylene-allene fraction gas and oxygen as fuel components. The temperature and particle velocity were determined for ZrO_2 particles with diameters of 20, 40, and 60 μm. Gas flow and particle parameters were calculated utilizing an established mathematical model. The model facilitates the determination of flow and particle parameters within the gas burner pathway and from the outlet section to the substrate. The experiment was conducted in two phases. During the first phase, the temperature and velocity of the gas stream from the burner inlet to the substrate were established. The second phase involved calculating the temperature and velocity of the particles based on the collected data. The results indicate that the thermal relaxation conditions for the sprayed material are significantly enhanced due to the burner's original design, resulting in an expansion of the possibilities for controlling the spraying process. The scientific novelty is obtaining the velocity and temperature relationships of ZrO_2 particles measuring 20, 40, and 60 μm during HVOF spraying in the twin-combustion-chamber burner channel and the segment-leading from the outlet to the substrate. The practical importance of these findings is their ability to inform the development of technological processes and recommendations for applying HVOF-sprayed wear-resistant coatings.

Keywords: Coating · High-Velocity Gas-Thermal Spraying · Zirconium Oxide · Gas Stream

M. Nechyporuk et al. (Eds.): ICTM 2023, LNNS 1008, pp. 102–111, 2024.
https://doi.org/10.1007/978-3-031-61415-6_9

1 Introduction

The development of engineering and technology leads to the growing need for functional coatings that can solve the problem of extending the life cycle of critically loaded parts by improving the physical and mechanical properties of the surface layer. This increases parts' corrosion and erosion resistance, resistance to abrasive wear, heat resistance, and oxidation resistance. The possibilities for restoring the working surfaces of worn parts are expanding [1]. In the aerospace industry, applying thermal barriers and other functional coatings on parts made of relatively inexpensive structural materials has found application [2]. For these coatings, it is important to select the base and intermediate materials and determine the stress-strain state of the coating-substrate system to prevent defects and fractures [3–5].

One of the ways to improve the quality and reduce the cost of coatings is to develop new and improve existing equipment for their application. For thermal spraying processes, the burner is the most critical component in ensuring quality and cost-effectiveness [6]. Similar to a supersonic nozzle for cold spraying [7–9], the burner is used to heat and accelerate the particles of the material being sprayed. There is a wide variety of burner designs for high-velocity oxygen fuel spraying [10]. For each design, mathematical models have been developed that enable production-purpose accurate predictions of coating parameters by controlling process parameters, including temperature, velocity of sprayed particles, and fuel component ratios.

The study aims to determine the temperature and velocity parameters of sprayed ZrO_2 powder particles from the twin-combustion-chamber burner channel's inlet to the substrate. Achieving this requires calculating the parameters of the combustion products in the burner channel and beyond. Subsequently, the velocity and temperature of the material particles to be sprayed must be measured.

2 Literature Review

The development of models for the processes in particular equipment samples continues to be a pressing matter despite many studies on oxygen fuel spraying modelling. The significance of this issue stems from the intricate interplay between factors such as the specific installation's geometry and layout, the chemical and thermodynamic characteristics of the combustible mixture, the chemical and thermodynamic properties of the material to be sprayed, the intended purpose of the installation, and the corresponding operational conditions [11, 12].

During the analysis of existing publications on this topic, certain correspondences between the developed model and known studies were revealed in terms of:

- modelling the combustion of a combustible mixture of methylacetylene-allene fraction gas with oxygen [13]; however, this work considers a burner device of a different type and fails to analyze the composition of methylacetylene-allene fraction gas;
- modelling of a burner device with external and internal combustion chambers [14–16]; however, these studies have differences from the burner considered in this work and calculations were performed for a different combustible mixture;

– modelling of gas and thermodynamic processes in other devices [17]; however, the study considers general theoretical aspects that need to be combined to obtain the required model;
– modelling of high-velocity spraying devices [18, 19]; however, these works consider other types of burners (usually single-combustion-chamber) and combustible mixtures;
– thermochemical reference data of the components of the combustible mixture and the materials to be sprayed [20–22].

Thus, a crucial scientific objective is to model the kinematic and energy parameters of material particles sprayed via high-velocity oxygen fuel spraying by employing a twin-combustible-chamber burner.

3 Methodology

3.1 Model of Gas Flow at the Ejector Outlet

A schematic representation of the burner for high-velocity oxygen fuel spraying used in the study is shown in Fig. 1.

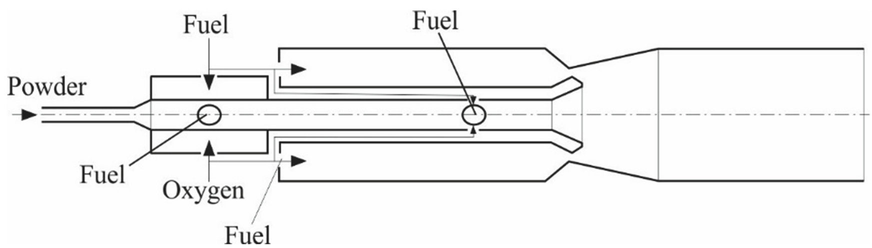

Fig. 1. Schematic representation of the burner for high-velocity oxygen fuel spraying used in the study.

In order to understand the trajectory of particles sprayed from the burner inlet to the substrate, it is important to first examine the gas flow from the nozzle exit to the substrate. A fundamental model, outlined in [18, 23, 24] and visually depicted in Fig. 2, was utilized to establish a foundational understanding.

In this figure, L_G is the length of the gas-dynamic section from the nozzle exit to the transition to subsonic flow (according to [23], for Mach numbers from 1 to 3, $L_G = 1 + 6L_W$); L_W is the length of the periodic structure (wave); l is the position of the reflection point of the incident shock; L_S is the distance from the nozzle exit to the substrate; D is the nozzle inner diameter. The flow model contains the following sections: a) gas-dynamic supersonic section of the L_G stream, where the velocity $\upsilon_{g.ss}$ and the temperature $T_{g.ss}$ of the gas are assumed constant; b) section of subsonic stream flow to the substrate, its length $L_{SS} = L_S - L_G$. Subsequent calculations are performed according to the method [23]. L_G is a function of the Mach number for the gas flow at the nozzle cutoff M_0 and burner diameter D:

$$L_G = D\left(4,2 + 1,1M_0^2\right). \tag{1}$$

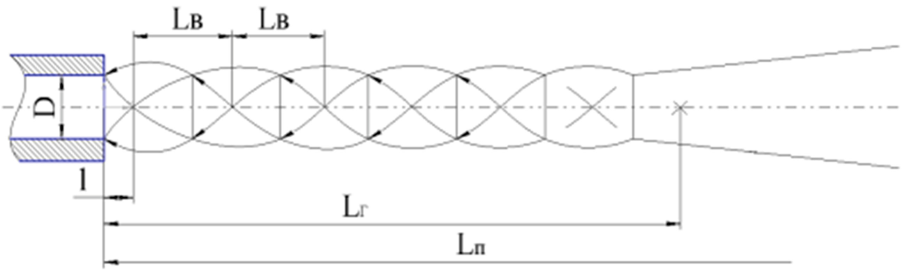

Fig. 2. Illustration of the gas flow model at the nozzle exit.

For output diameter $D = 38$ mm and the Mach number

$$M_0 = \frac{w}{a} = \frac{w}{\sqrt{kRT}}, \tag{2}$$

we obtain $M_0 = 1.206$, $L_G = 0.220$ m. The velocity and temperature of the gas flow in the gas-dynamic section of the stream can be assumed constant [23]. Beyond this section, the temperature and gas velocity values change significantly due to the increase in the intensity of interaction with the surrounding air. The changes in the velocity and temperature of the gas flow beyond the nozzle exit can be described with sufficiently high accuracy by empirical relations (3) and (4) [23]:

$$\frac{\upsilon}{\upsilon_0} = 1 - \exp\left(\frac{\alpha}{1 - x/L_{nc}}\right), \tag{3}$$

$$\frac{T - T_R}{T_0 - T_R} = 1 = \exp\left(\frac{\beta}{1 - x/L_{nc}}\right), \tag{4}$$

where x is the distance along the stream axis from the ejector mixing chamber cutoff; α and β are experimental coefficients (in these calculations, $\alpha = 0.85$, $\beta = 1.25$ [24]).

3.2 Model of Particle Acceleration and Heating by Gas Flow

The model is detailed in [18, 23, 24]. The technique consists of the sequential determination of particle velocity and temperature. The acceleration of a particle of the sprayed material moving in a two-phase flow is described by the following Eqs. (5)–(7) [23]:

$$m_p \frac{dV_p}{dt} = \frac{1}{2} C_x \rho_g A_p \left(V_g - V_p\right)\left|V_g - V_p\right|, \tag{5}$$

where m_p and υ_p are the particle mass and velocity, respectively; C_x is the drag coefficient of the particle; υ_g and ρ_g are the gas velocity and density, respectively; A_p is the area of projection of the particle on the plane perpendicular to the direction of the flow velocity vector.

After simple substitution

$$\frac{dV}{dt} = \frac{dV}{dx} \cdot V$$

and

$$m_p = \frac{\pi d_p^3 \rho_p}{6}$$

we obtain (6):

$$\frac{d}{dx} \cdot V_p = \frac{3C_x \rho_g \left(V_g - V_p\right) \left|V_g - V_p\right|}{4\rho_p d_p V_p}, \tag{6}$$

whereas

$$C_x = \begin{cases} 24/\mathrm{Re}, \ \ if \ \ \mathrm{Re} < 0.5; \\ 24/\mathrm{Re} + (1 + 0.15\mathrm{Re}^{0.687}), \ \ if \ \ 0.5 \le \mathrm{Re} < 1000, \\ 0.44, \ \ if \ \ \mathrm{Re} > 1000. \end{cases} \tag{7}$$

In the following calculations, the assumption is made that the Reynolds number is determined in the interval $0.5 \le \mathrm{Re} < 1000$ and is calculated by formula (8):

$$\mathrm{Re} = \frac{d_p \rho_g \left|V_g - V_p\right|}{\eta_g}. \tag{8}$$

The properties of ZrO_2 particles are shown in Table 1.

Table 1. Properties of ZrO_2 particle.

Powder characteristics	Value
Density ρ_p, kg/m3	5700
Molecular weight	123.22
Melting temperature T_m, K	2950
Boiling point T_b, K	4573
Particle diameter d_p, um	20; 40; 60
Specific heat capacity C_p, J/(mol*K)	$\mathrm{C_p = f(T)}$

4 Results and Discussion

4.1 Results of Calculation of Gas Velocity and Temperature

The results of calculations of gas parameters are presented in the form of graphs in Fig. 3.

The solid line indicates the change in gas flow velocity beyond the mixing chamber; the dashed line indicates the temperature change. The graph shows a gas flow velocity drop and temperature drop beyond the gas-dynamic section.

Thus, when summarizing the results obtained, we obtain graphs of changes in the gas flow velocity and temperature from the burner inlet to the substrate, presented in Fig. 4.

The dashed line on the graph depicts the temperature of the gas flow, while the solid line represents the change in velocity. The sudden parameter shifts are associated with the second fuel inlet and outlet leading to the mixing chamber.

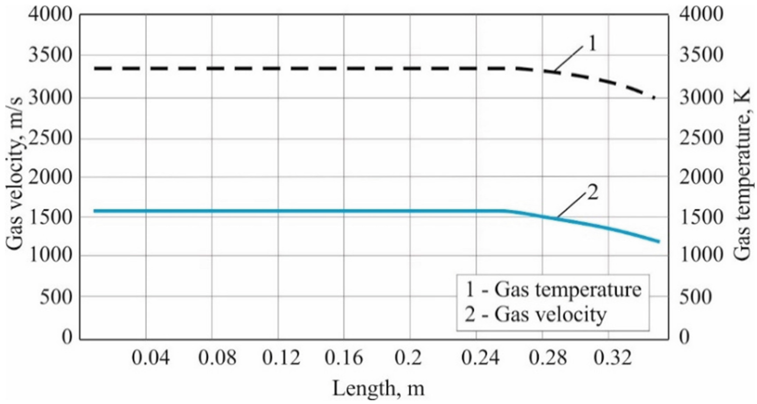

Fig. 3. Changes in gas flow velocity and temperature from the ejector mixing chamber cutoff to the substrate.

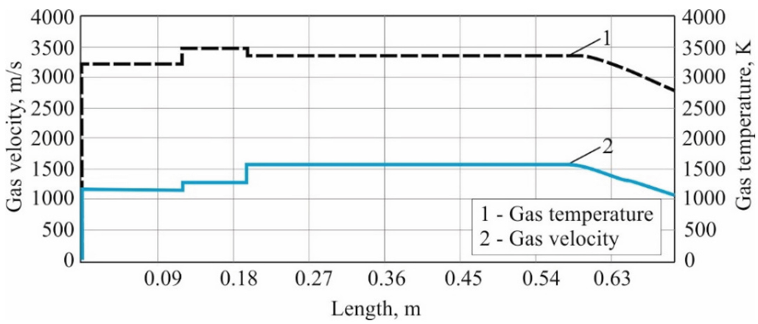

Fig. 4. Changes in gas flow velocity and temperature from the nozzle inlet to the substrate.

4.2 Results of Calculation of Particle Velocity and Temperature

The differential equation solution was performed in Mathcad for ZrO_2 particles with diameters of 20, 40, and 60 μm. The solution is presented as a graph in Fig. 5. Solid line *1* shows the change in the velocity of combustion products, and dashed lines *2–4* show the velocity of ZrO_2 particles. Due to particle inertia, the velocity change graph has no sudden shifts observed in the graph of the combustion product velocity. This results in a gradual increase in velocity from the burner inlet to the substrate.

Based on the analysis of the graphs of changes in the velocity of zirconium oxide particles shown in Fig. 5, a decrease in the particle velocity from 1114 m/s to 886 m/s is noted with an increase in particle diameter from 20 μm to 60 μm. At a distance of 400 mm from the burner exit, the velocity of ZrO_2 particles of 20, 40, and 60 μm is 1114, 955, and 886 m/s, respectively. As can be seen from the graphs, the inertia of particles of 40 μm and 60 μm fractions is sufficient to maintain the tendency of increasing velocity at this distance from the exit of the burner mixing chamber. Meanwhile, particles with a diameter of 20 μm begin to slow down. The velocity of 20 μm ZrO_2 particles at a distance of 400 mm from the burner outlet exceeds the velocity of combustion products

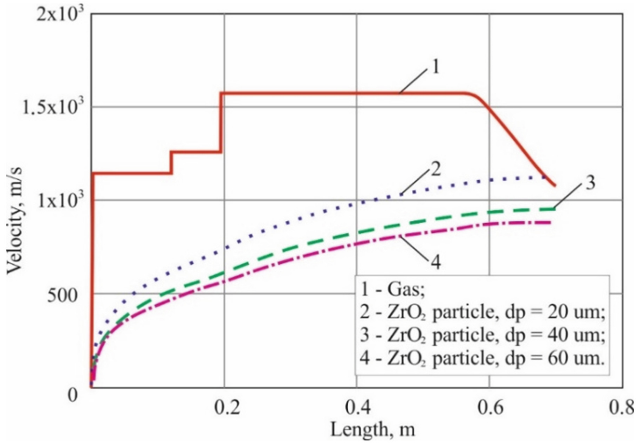

Fig. 5. Graph of the velocity change of ZrO_2 particles with diameters of 20, 40, and 60 μm from the burner inlet to the substrate.

by 45 m/s. This indicates that the flow of combustion products slows down the particles when their velocities are equalized (371 mm from the burner exit).

Calculation of particle heating temperature by gas flow is performed according to Eq. (9):

$$m_p \frac{d}{d\tau} H_{p.imp} = \alpha \left(T_g - T_p \right) \pi d_p^2 \tag{9}$$

And its components (10)–(13):

$$m_p = \frac{\pi d_p^3 \rho_p}{6} \tag{10}$$

$$dH_{p.imp} = C_p dT_p, \tag{11}$$

$$\alpha = \frac{\lambda_g}{d_p} \left(2 + 0,6 \mathrm{Re}^{1/2} \mathrm{P}_r^{1/3} \right), \tag{12}$$

$$\mathrm{P}_r = \frac{C_{pg} \eta_g}{\lambda_g}. \tag{13}$$

After substitutions we obtain Eq. (14):

$$\frac{d}{dx} T_p = \frac{6\alpha \left(T_g - T_p \right)}{V_p C_p \rho_p d_p} \tag{14}$$

According to [23], the specific heat capacity of the particle material is also a function of temperature (15):

$$c_{pZrO2} = 16.64 + 1.8 \times 10^{-3} T - 3.36 \cdot 10^5 T^{-2} (\mathrm{kal}/(\mathrm{mol} \cdot \mathrm{grad})) \tag{15}$$

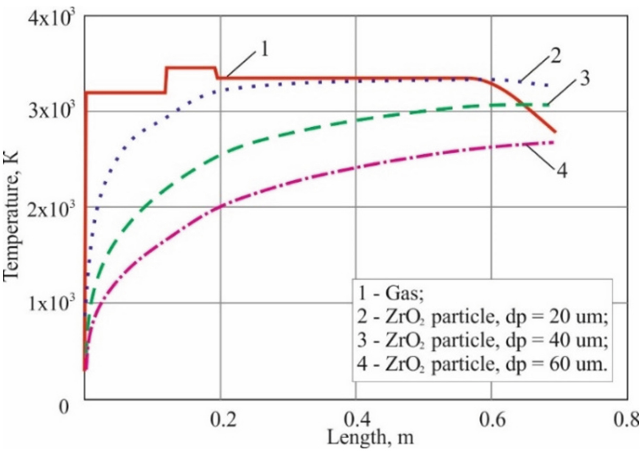

Fig. 6. Graph of gas flow temperature changes and ZrO_2 particles of 20, 40 and 60 µm from the burner exit to the substrate.

The solution of the differential equation was performed in the Mathcad package and is presented as a graph in Fig. 6.

As can be seen from the graphs in Fig. 6, as the diameter of the ZrO_2 particles increases, the temperature at the moment of contact with the substrate decreases from 3260 K to 2680 K. Meanwhile, the temperature of ZrO_2 particles of 60 µm continuously increases in this area to a value of 2680 K, while the temperature for particles of 20 µm and 40 µm increases only in a certain area. For example, at a distance of 178 mm from the burner exit, the temperature of 20 µm particles is equalized with the temperature of the combustion products (3340 K) and does not change over the next 92 mm. Upon reaching a distance of 270 mm from the burner outlet, the temperature of 20 µm ZrO_2 particles begins to decrease and reaches 3260 K at the moment of contact with the substrate. The temperature of 40 µm ZrO_2 particles, having reached a maximum value of 3080 K at a distance of 338 mm from the burner exit, begins to decrease, reaching a value of 3040 K at a distance of 400 mm. Due to thermal inertia, the temperature decrease rate for ZrO_2 particles is significantly lower than the temperature decrease rate for combustion products.

5 Conclusions

The calculation of the progress of changes in velocity and temperature of the sprayed material particles during high-velocity oxygen fuel spraying using a twin-combustion-chamber burner of the original design has been performed. Zirconium oxide (ZrO_2) with particle diameters of 20, 40, and 60 µm was chosen as the spraying material. The previously proposed model used for calculations allows determining the velocity and temperature of the spraying material particles at any moment from the burner inlet to the substrate, and is a useful tool for researchers and technologists involved in improving functional gas-thermal coatings. Further work will be carried out to develop practical recommendations to improve the performance characteristics of aircraft parts and other critical parts by applying gas-thermal coatings, including the burner described in the study.

References

1. Volkov, A., Shorinov, O., Polyviany, S.: Deposition of titanium-containing coatings by low-pressure cold spraying. In: Nechyporuk, M., Pavlikov, V., Kritskiy, D. (eds.) ICTM 2021. LNNS, vol. 367, pp. 565–574. Springer, Cham (2022). https://doi.org/10.1007/978-3-030-94259-5_48
2. Mehta, A., et al.: Processing and advancements in the development of thermal barrier coatings: a review. Coatings **12**(9), 1318 (2022). https://doi.org/10.3390/coatings12091318
3. Shorinov, O.: Finite element analysis of thermal stress in Cu_2O coating synthesized on Cu substrate. Arch. Mater. Sci. Eng. **115**(2), 58–65 (2022). https://doi.org/10.5604/01.3001.0016.0753
4. Baranov, O., et al.: Recent innovations in the technology and applications of low-dimensional CuO nanostructures for sensing, energy and catalysis. Nanoscale Horiz. **8**, 568–602 (2023). https://doi.org/10.1039/D2NH00546H
5. Breus, A., Abashin, S., Serdiuk, O.: Control of stress conditions in growth of copper oxide nanostructures. In: Nechyporuk, M., Pavlikov, V., Kritskiy, D. (eds.) ICTM 2022, LNNS, vol. 657, pp. 111–122. Springer, Cham (2023). https://doi.org/10.1007/978-3-031-36201-9_10
6. Kuzmin, V., et al.: Supersonic DC plasma torch for deposition of high-density wear-resistant coatings. Mater. Today: Proc. **19**(5), 2152–2156 (2019). https://doi.org/10.1016/j.matpr.2019.07.230
7. Shorinov, O.V., Polyviany, S.A.: Simulation of gas flow with nanocomposite carbon- containing powders in supersonic nozzle. Metallofizika i Noveishie Tekhnologii **44**(5), 601–611 (2022). https://doi.org/10.15407/mfint.44.05.0601
8. Hu, W., Tan, K., Markovych, S., Cao, T.: Research on structure and technological parameters of multichannel cold spraying nozzle. East.-Eur. J. Enterp. **5**(1–113), 6–14 (2021)
9. Dolmatov, A.I., Bilchuk, O.V.: Modelling of gas flow with solid particles in a short nozzle. Metallofizika i Noveishie Tekhnologii **40**(9), 1257–1271 (2018). https://doi.org/10.15407/mfint.40.09.1257
10. Abhishek, K., Anupama, B., Singh, H., Gupta, N., Saleh Mashkour, M., Kansal, L.: Super alloy coatings for enhanced corrosion and oxidation resistance in extreme environments. E3S Web Conf. **430**, 01135 (2023). https://doi.org/10.1051/e3sconf/202343001135
11. Prateek, S., Rajnish, G., Saxena, K.K., Srivastav, V.K., Vasudev, H., Kumar, N.: Data-driven materials science: application of ML for predicting band gap. Adv. Mater. Process. Technol. **2023**, 1–10 (2023). https://doi.org/10.1080/2374068X.2023.2171666
12. Sharma, R.K., Das, R.K., Kumar, S.R.: Effect of HVOF spraying parameters on fracture, erosion and thermal properties of Fe alloy-based coating materials. Proc. Inst. Mech. Eng. Part L J. Mater. Des. Appl. **235**(7), 1703–1711 (2021). https://doi.org/10.1177/1464420721999682
13. Yevdokymenko, Y., Kysil, V.M., Frolov, G.A.: Methodical bases for creating installations for high velocity flame spraying. Naukovì notatki **66**, 98–107 (2019)
14. Yevdokimenko, Y., Kysil, V.M., Frolov, G.A.: The energy efficiency of burners for high-velocity gas-flame spraying. Aerosp. Tech. Technol. **7**, 12–17 (2011)
15. Ribu, D.C., et al.: Experimental investigation of erosion corrosion performance and slurry erosion mechanism of HVOF sprayed WC-10Co coatings using design of experiment approach. J. Market. Res. **18**, 293–314 (2022). https://doi.org/10.1016/j.jmrt.2022.01.134

16. Yevdokymenko, Y., Kysil, V., Frolov, G., Buchakov, S.: Two-stage configuration burner device for high velocity air liquid-fuel spraying. Visnyk dvyhunobuduvannya **2**, 143–148 (2015)
17. Liu, S.: Optimization and Improvement of a novel HVOF process fueled with ethanol. Doctoral thesys (2022) https://www.theses.fr/2022UBFCA003.pdf. Accessed 28 Nov 2023
18. Mingheng, L., Christofides, P.D.: Modeling and control of high-velocity oxygen-fuel (HVOF) Thermal Spray: a tutorial review. J. Therm. Spray Technol. **18**(5), 849–857 (2009). https://doi.org/10.1007/s11666-009-9309-2
19. Dolmatov, A.I., Sergeev, S.V., Kurin, M.O., Voronko, V.V., Loza, T.V.: Kinematics of the solid particle accelerated by a flow of gas in a supersonic nozzle and work hardening of the processed surface. Metallofizika i Noveishie Tekhnologii **37**(7), 871–885 (2015). https://doi.org/10.15407/mfint.37.07.0871
20. Rumble, J.: CRC Handbook of Chemistry and Physics. 103rd edn. CRC Press, Boca Raton (2022)
21. Jess, A., Wasserscheid, P.: Chemical Technology: from Principles to Products, 2nd edn. Wiley-VCH Verlag, GmbH, Weinheim (2020)
22. Pierson, H. O.: Handbook Of Refractory Carbides & Nitrides: Properties, Characteristics, Processing and Applications. William Andrew Inc., New York (2022)
23. Danko, K.: Simulation of gas flow inside double-chamber burner passage for supersonic gas-flame spraying. Visnyk dvyhunobuduvannya **1**, 130–138 (2017)
24. Kuzmin, V., Gulyaev, I., Sergachev, D., Vashchenko, S., Lysakov, A., Palagushkin, B.: Supersonic air-plasma spraying of carbide ceramic coatings. Mater. Today: Proc. **38**(4), 1974–1979 (2021). https://doi.org/10.1016/j.matpr.2020.09.150

Robust Parametrical Optimization of Discrete System for Stabilization of Apparatus of Land Moving Vehicles

Olha Sushchenko(✉) and Yurii Bezkorovainyi

National Aviation University, Lubomyra Huzara Ave., 1, Kyiv 03058, Ukraine
sushoa@ukr.net

Abstract. This paper deals with creating the approach to the discrete system assigned used for stabilization observation equipment of land moving vehicles. The state-space mathematical description has been created. The system's state and control in the vector form are shown. The analysis of discrete transformations has been carried out. The advantages of Tustin method are demonstrated. The possibilities of MATLAB for the implementation of discrete transformations are studied. Features of synthesis of the discrete stabilization system are described. Features of calculating the quality index based on norms of the transfer function of the stabilization system are given. The comparative analysis of different discretization methods is represented. The algorithm of the robust parametrical optimization is proposed. Simulation results including transient process and Bode diagram are given. The results in the form of transient processes prove the efficiency of the proposed approach. The obtained results can be useful for moving objects using observation apparatus of the wide class.

Keywords: Robust Parametrical Optimization · Stabilization System · Ground-Moving Vehicle · Discretization · Mathematical Model · Simulation

1 Introduction

Recently, the urgency of creating new promising systems for stabilizing land-based moving objects has been increasing. The creation of these systems is based on the use of techniques of synthesis and analysis, which would allow the successful development of new samples of systems of the studied class, one of the features of which is the purpose for operation in off-road conditions and resistance to the effects of disturbances. In view of this, the synthesis of such systems should be carried out with simultaneous consideration of their quality and robustness. For this, there is a need to create a description of the system of stabilization of a moving ground object in the space of states, which allows the use of computing tools for the automated design of optimal systems.

Considerable attention is paid to the creation of new perspective systems of motion and movement of ground objects for various purposes. The general principles of creating models of drives of stabilization systems are considered in many works, for example [1,

M. Nechyporuk et al. (Eds.): ICTM 2023, LNNS 1008, pp. 112–122, 2024.
https://doi.org/10.1007/978-3-031-61415-6_10

2]. A detailed model of a nonlinear system with all nonlinearities taken into account is presented in [3]. However, for the proposed method of synthesis, it is necessary to have a model in the space of states. The problem of creating a discrete robust aircraft control system is presented in [4, 5]. The method of parametric synthesis of a continuous robust system of stabilization of a ground-moving object is presented in [6].

In the paper, we propose an approach to robust parametrical optimization of the discrete stabilization system assigned for ground-moving vehicles with observation equipment. The ways of discretization of the studied system are proposed. The abilities of MATLAB to accomplish the earlier mentioned problem are analyzed. The steps of the optimizing procedure are listed. The results of synthesis are represented as transient processes and logarithmic amplitude-frequency characteristics of the synthesized system are given.

The paper is structured in the following form. In Sect. 2 we represent the state-space description of the stabilization system, in Sect. 3 ways of discretization of the created model are considered, Sect. 4 analyses features of synthesis of the discrete model, Sect. 5 represents a procedure of the robust parametrical optimization, results of optimization are represented in Sect. 6.

2 Mathematical Description of Discrete Stabilization System

The widespread application of computational aids is a present-day tendency in the creation of stabilizers of the studied type. At the same time, the transformation of the synthesized continuous regulator to the discrete form is not acceptable, since the dynamics of the continuous system and the converted discrete system are significantly different [7–9]. This is due to the contradiction between the requirements for choosing the quantization interval of the system. On the one hand, the accuracy requirements require a small quantization interval, on the other hand, due to the difficulty of hardware implementation, the conditions of the Kotelnikov theorem are fulfilled with a minimum margin [10, 11]. Therefore, the parametric synthesis of a continuous system with a discrete regulator requires a separate study. The main principles of building the optimal synthesis technique remain the same as for the parametric synthesis of a continuous regulator. But at the same time, there are some significant features.

The model of the studied system in the state space has the form:

$$\begin{cases} \dot{x} = Ax + Bu; \\ y = Cx + Du, \end{cases} \tag{1}$$

where x are state variables in the vector form; u are controls in the vector form; A, B, C, D are matrices, which describe controls and properties of the system; y are observations in the vector form.

For the studied state-space description (1), state variables and controls vectors, and appropriate matrices look like

$$x = \begin{bmatrix} x_1 \\ x_2 \\ x_3 \\ x_4 \\ x_5 \end{bmatrix} = \begin{bmatrix} \varphi_{wm} \\ \dot{\varphi}_{wm} \\ \varphi_m \\ \dot{\varphi}_m \\ U \end{bmatrix}; u = \begin{bmatrix} 0 & 0 \\ -\frac{M_{im}}{J_{wm}} & 0 \\ 0 & 0 \\ 0 & \frac{U_{pwm}}{T_a} \\ 0 & 0 \end{bmatrix};$$
$$A = \begin{bmatrix} 0 & 0 & 0 & 0 & 0 \\ -\frac{c_r}{J_{wr}} & -\frac{f}{J_{wr}} & \frac{c_r}{n_r J_{wr}} & 0 & 0 \\ 0 & 0 & 0 & 1 & 0 \\ -\frac{c_r}{n_r J_m} & 0 & -\frac{c_r}{n_r^2 J_m} & -\frac{f_m}{J_m} & \frac{c_m}{R_w J_m} \\ 0 & 0 & 0 & -\frac{c_e}{T_a} & -\frac{1}{T_a} \end{bmatrix}; B = \begin{bmatrix} 0 & 0 \\ -\frac{M_{im}}{J_{wm}} & 0 \\ 0 & 0 \\ 0 & 0 \\ 0 & \frac{U_{pwm}}{T_a} \end{bmatrix} \tag{2}$$
$$C = \begin{bmatrix} 0\,1\,0\,0\,0 \\ 0\,0\,0\,0\,1 \end{bmatrix}; D = \begin{bmatrix} 0\,0 \\ 0\,0 \end{bmatrix}.$$

where J_{wr} is the inertial moment of working module; φ_{wm} is the turn of working module; f_m is the coefficient of linearization of moment of friction in bearings of the working module; M_{im} is the imbalance moment; c_r is the rigidity of the reduction gear; n_r is the ratio of the reduction gear; J_m is the inertial moment of the motor; φ_m is the turn of the motor; c_m is the coefficient of stseady load at the motor axle; R_w is resistance of windings of the motor's armature; U is the signal of the motor's armature; U_{pwm} is the signal of pulse-width-modulator; c_e is the coefficient of electromotive force; T_a is the time constant of motor armature.

3 Discretization of Model

The use of computational procedures for the optimal synthesis of discrete regulators requires the representation of the description of the control object in a discrete form with the same discreteness period as the discreteness of the regulator [12–14]. At the same time, various algorithms can be used, for example. Construction of a discrete representation of a continuous system using a zero-order extrapolator. A more accurate transformation from a continuous form to a discrete form is provided by Tustin's bilinear approximation. This transformation implements an approximate relationship to represent the exponent.

$$\text{z} = e^{sT_s} \cong \frac{1 + \text{s}T_s/2}{1 - \text{s}T_s/2}, \tag{3}$$

that is applied for calculating relations of values s and z for discrete and continuous representations for transfer functions. The transfer function of the continuous system is transformed into discrete $H_d(z) \cong H(s)$ by permutation.

$$s \cong \frac{2}{T_s}\frac{z-1}{z+1}. \tag{4}$$

It should be noted that in control theory and digital signal processing there are diverse ways of presenting of transfer functions of discrete systems [15, 18]. In the theory of control, a variable z is used, and polynomials in the numerator and denominator are located in the direction of decrease of powers of polynomials. The value z^{-1} is applied in digital signal processing. Such an approach is chosen due to the simpler engineering realization of the second method of the discrete transfer function task. The creation of an algorithm for the optimal parametrization of a discrete system should be performed based on the industrial realization of regulators, where it is generally accepted to represent the transfer functions of a digital regulator as a function of a variable z^{-1}. In general, the regulator can include both continuous and digital links. It is considered expedient to use z-transformation of the first type to represent the control object and continuous links, and z-transformation of the second type for the links of the digital part of the regulator. It should be noted that in some cases, the creation of a digital regulator of a given structure can be based on known continuous links that ensure certain properties of the system. Bringing the transfer coefficient of a continuous link to the transfer function in the format of a digital filter could be done using two functions of the MATLAB system: *c2d* (conversion of continuous *tf*-models into discrete ones) and *filt* (conversion of a *tf*-model in the format of a digital filter) [15, 17].

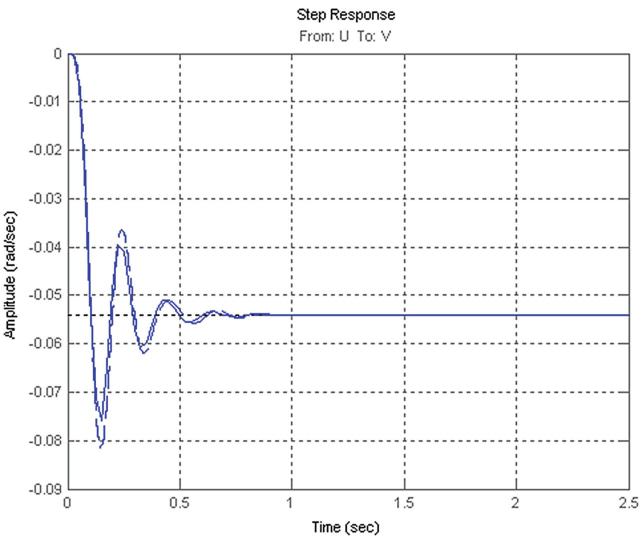

Fig. 1. Transient process on the angle speed of continuous (solid) and discrete (dotted) stabilizer in tracking mode.

The choice of discretization and extrapolation method significantly affects the accuracy of transforming a continuous description into a discrete one. The data using the zero-order extrapolator are presented in Figs. 1, and 2. The results of applying Tustin's fractional-rational approximation without correction are presented in Figs. 3, and 4.

Therefore, for the researched, it is considered appropriate to apply the Tustin method.

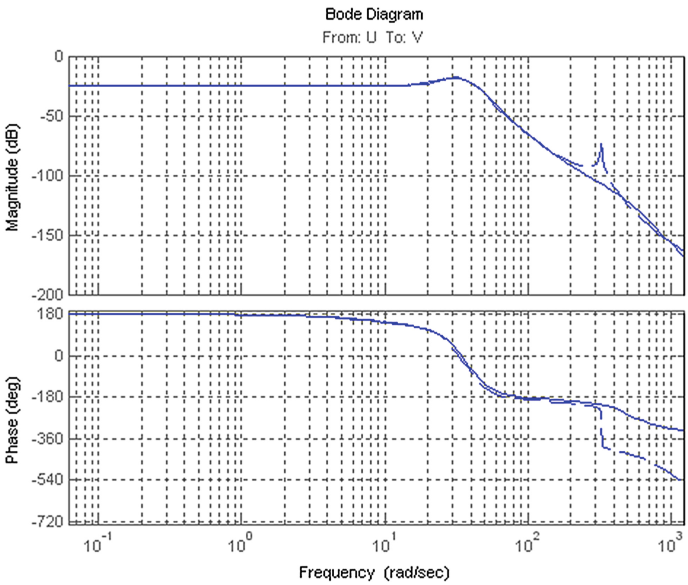

Fig. 2. Logarithmic amplitude-frequency characteristics of continuous (solid) and discrete (dotted) stabilization system in tracking mode.

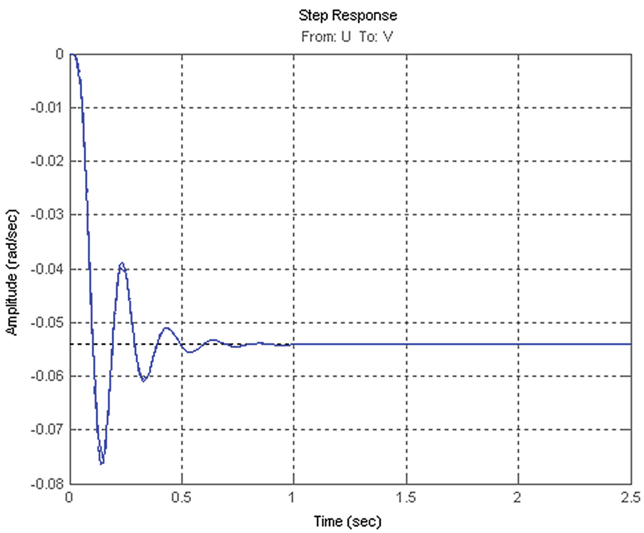

Fig. 3. Transients on the angle speed of continuous (solid) and discrete (dotted) stabilizer in stabilization mode.

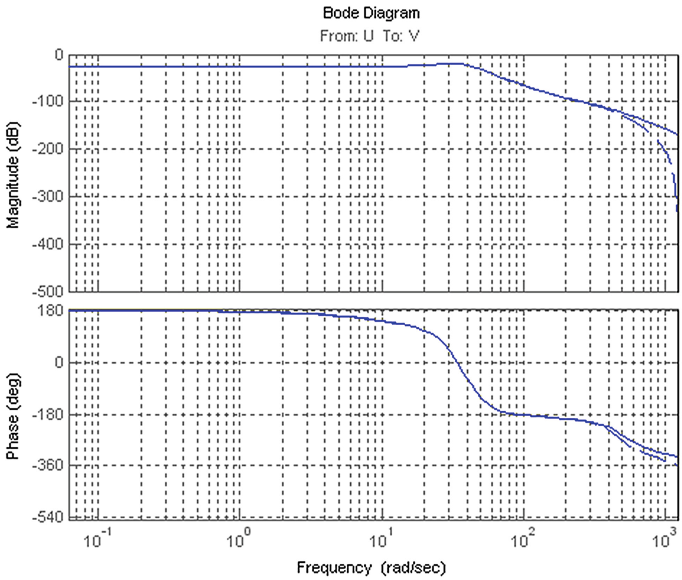

Fig. 4. Logarithmic amplitude-frequency characteristics of the angle speed of continuous (solid) and discrete (dotted) stabilizer in stabilization mode.

4 Features of Synthesis of Discrete Stabilization System

Specific problems related to astaticism for a discrete system are solved by finding a minimal realization, similar to the case with a continuous system [20]. As for balanced implementation, it is possible for continuous systems [21–23]. In the case of a discrete system, it is desirable to scale the model matrices in the state space using a similarity transformation with a diagonal matrix T and a scalar coefficient α such that the matrix [16, 19].

$$\begin{bmatrix} TAT^{-1} & TB/\alpha \\ \alpha CT^{-1} & 0 \end{bmatrix} \tag{5}$$

has small condition numbers of eigenvalues of the matrix.

To perform the operation (5), it is possible to use the *ssbal* function, with which, based on the four matrices of the state-space model A, B, C, D, it is possible to obtain a scaled model TAT^{-1}, TB/α, αCT^{-1} and a transformation matrix T such that $\bar{x} = Tx$, where $\bar{x}$ is the new state vector of the model [17, 19].

Differences in the organization of the procedure for the parametric synthesis of a discrete system also apply to the composition of the penalty function. As in the previous case, the stability condition is the finding of all poles of the transfer function of the loop system in the left semi plane of the complex variable. But taking into account the z-transformation, the region of stability is a circle of unit radius, in which the poles of the transfer function of the loop system should be located.

The procedure of parametric optimal synthesis of a discrete system has its features for calculating the components of a complex quality indicator, namely H_2 and H_∞ norms.

For a discrete system, the H_∞ norm is calculated by the relation [16, 19, 24].

$$H(z) = \max_{\theta \in [0,x]} \sigma_{max}(H\left(e^{j\theta}\right)), \tag{6}$$

and for determination (6) by computational means, it is necessary to use the built-in function norm. As for the H_2-norm, in the case of a discrete system, it should be considered as the square root of the quality indicator, which in turn is defined as the trace of the Gramian. For a continuous state-space, the Gram function for evaluating the controllability and observability of the system is determined by the expressions [19, 25]

$$W_c = \int_0^\infty e^{A\tau} BB^T e^{A^T\tau} d\tau; \; W_o = \int_0^\infty e^{A^T\tau} C^T C e^{A\tau} d\tau. \tag{7}$$

For discrete systems, Gram functions of controllability and observability are defined by expressions [19]

$$W_c = \sum\nolimits_0^\infty A^k BB^T \left(A^T\right)^{k,}; \sum\nolimits_0^\infty \left(A^T\right)^k C^T C A^k. \tag{8}$$

Controllability Gramians are calculated by solving the continuous Lyapunov equation and its discrete analog [19]

$$AW_c + W_c A^T + \mathrm{B}B^T = 0; AW_c A^T - W_c + \mathrm{B}B^T = 0. \tag{9}$$

Similarly, to determine the observability Gramians, it is necessary to solve the equation [19]

$$A^T W_o + W_o \mathrm{A}\; C^T \mathrm{C} = 0; A^T W_o \mathrm{A} - W_o + C^T \mathrm{C} = 0. \tag{10}$$

Controllability Gramians are used to determine the weighting coefficients of quality indicators.

The H_2-norms are determined by solving the Lyapunov matrix equations, which for continuous and discrete systems, respectively, have the form [19]

$$\mathrm{AX} + \mathrm{X}A^T + \mathrm{Q} = 0; A^T \mathrm{XA} - \mathrm{X} + \mathrm{Q} = 0. \tag{11}$$

Where A, Q are square matrices of the same dimension.

Expressions (7)–(11) are used for determining the combined quality index of the discrete stabilization system.

5 Robust Parametrical Optimization of Discrete Stabilization System

So, the parametric optimization procedure of a continuous navigation and stabilization system with a discrete regulator includes the following steps.

1. Compilation of a continuous mathematical model of the combined system “control object-motor” as a single device connected by an elastic connection based on the consideration of the stiffness of the reducer.

2. Selection of the structure of the discrete regulator of the stabilization and guidance system.
3. Justification of the method of discretization and bringing the continuous combined model “control object-motor” and the meter to a discrete form.
4. Compilation of a mathematical description of the stabilization and guidance system in accordance with previously given structural schemes.
5. Compilation of a complete mathematical model of the studied system with all nonlinearities peculiar to industrial systems (signal limitation, hysteresis, insensitivity zone), and on the basis of the Simulink package, the control object, engine, and gyroscopic meter can be represented as continuous models, and the regulator, pulse-width modulator and voltage amplifier – in the form of discrete models, respectively.
6. Obtaining transfer functions of an open and closed system.
7. Implementation of the minimal implementation of the model.
8. Model scaling based on the similarity transformation algorithm.
9. Assignment of initial values and execution of the Nelder-Mead optimization algorithm, with cyclic execution of the following steps:
   - calculation of norms for the designed system, taking into account the peculiarities of their calculation for discrete systems;
   - determination of poles, analysis of their arrangement relative to the unit circle and calculation of the corresponding penalty function;
   - determination of the complex quality indicator with the penalty function.
10. Performing an analysis of the designed system by the following steps
   - determination of H_2, H_∞ norms and construction of logarithmic magnitude-frequency characteristics of the system with calculation of stability reserves;
   - analysis of indicators of the transition process using the system model, taking into account all its inherent nonlinearities;
   - verification of the angular stiffness of the system by moment using a complete nonlinear model of the system.
11. Conclusion on completion of the parametric optimization procedure or its continuation with renewed starting conditions or renewed weight coefficients of the combined quality indicator.

6 Modelling Results

The data of the parametric synthesis of a continuous system with a discrete controller in the guidance regime are presented in Figs. 5, and 6.

A comparative analysis of synthesis results with different approaches to discretization using (3), (4) is given in table (Table 1).

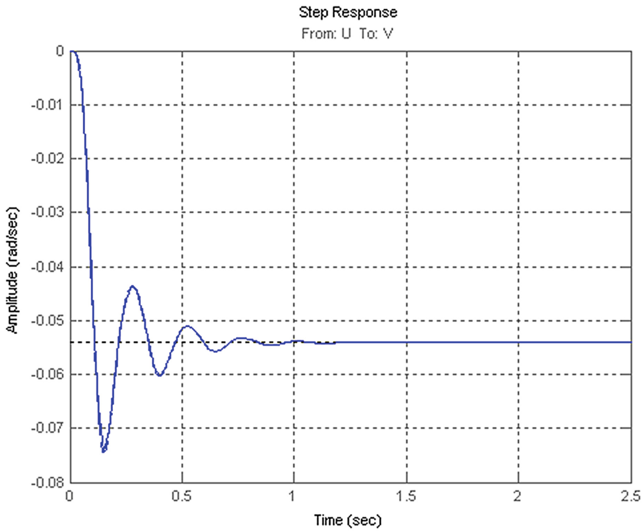

Fig. 5. The transient process on angle speed for the synthesized system.

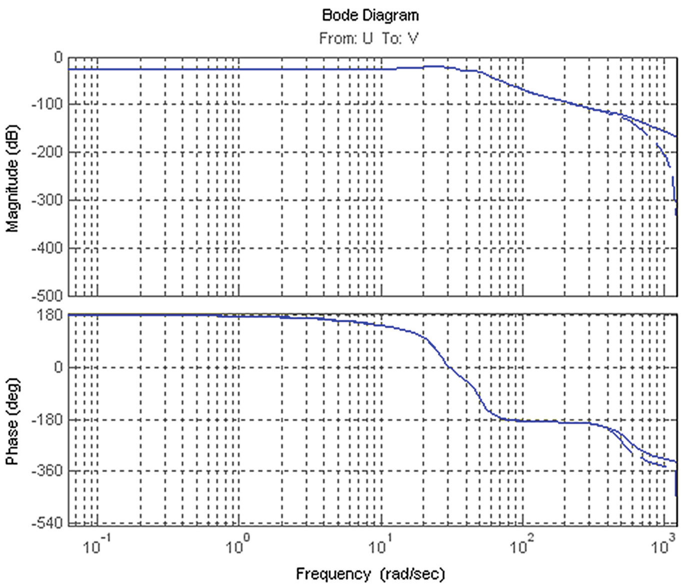

Fig. 6. Logarithmic amplitude-frequency characteristics of synthesized system.

Table 1. Comparison of discretization methods

Mode type	H_2	H_∞	ΔA, dB	$\Delta\varphi$, deg
Continuous model	0.318	0.126	59.5	91.1
Model discretized by method of extrapolation of zero order	0.461	0.1403	49.5	91.2
Model discretized by Tustin approximation	0.3653	0.1248	49.5	91.2

7 Conclusions

A model was created in the state space of the stabilization system of a moving terrestrial object and its discretization was performed.

Features of robust parametrical optimization for discrete stabilizing system are considered.

A comparative analysis of the ways to discretize stabilization system has been done.

An algorithm of the method of synthesis of a discrete robust system of stabilization of a moving ground object is presented.

In future work, the optimization procedure will be improved using a genetic algorithm.

References

1. Hilkert, J.M.: Inertially stabilized platform technology. IEEE Control. Syst. Mag. **1**, 26–46 (2013)
2. Masten, M.K.: Inertially stabilized platforms for optical imaging systems. IEEE Control. Syst. Mag. **1**, 47–64 (2008)
3. Sushchenko, O.A., Tunik, A.A.: Robust stabilization of UAV observation equipment. In: 2nd International Conference on Actual Problems of Unmanned Air Vehicles Development (APUAVD), pp. 176–180. IEEE, Kyiv (2013). https://doi.org/10.1109/APUAVD.2013.6705318
4. Fu, J., Ma, R.: Stabilization and Hinf Control of Switched Dynamic Systems. Springer, Berlin (2020)
5. Kuznetsov, B.I., Nikitina, T.B., Bovdui, I.V.: Structural-parametric synthesis of rolling mills multi-motor electric drives. Electr. Eng. Electromech. **5**, 25–30 (2020)
6. Sushchenko, O.A.: Robust control of angular motion of platform with payload based on $H\infty$-synthesis. J. Autom. Inf. Sci. **48**(12), 13–26 (2016)
7. Scogestad, S., Postlathwaite, I.: Multivariable Feedback Control. Analysis and Design. John Wiley & Sons, London (2005)
8. Zerrik, El.H., Castillo O.: Stabilization of Infinite Dimensional Systems. Springer, Cham (2021). https://doi.org/10.1007/978-3-030-68600-0
9. Sushchenko, O.A., Bezkorovainyi Y.M., Golitsyn, V.O.: Fault-tolerant inertial measuring instrument with neural network. In: 40th International Conference on Electronics and Nanotechnology (ELNANO), pp. 797–801. IEEE, Kyiv (2020). https://doi.org/10.1109/ELNANO50318.2020.9088779

10. Bezkorovainyi, Y.N., Sushchenko, O.A.: Improvement of UAV positioning by information of inertial sensors. In: 5th International Conference on Methods and Systems of Navigation and Motion Control (MSNMC), pp. 151–155. IEEE. Kyiv (2018) https://doi.org/10.1109/MSNMC.2018.8576307
11. Kuznetsov, B.I., Nikitina, T.B., Bovdui, I.V.: Multiobjective synthesis of two degree of freedom nonlinear robust control by discrete continuous plant. Tech. Electrodynamics **5**, 10–14 (2020)
12. Sanfelice, R.G.: Hybrid Feedback Control. Princeton University Press, Princeton (2021)
13. Sushchenko, O.A., Shyrokyi, O.V.: H2/H∞ optimization of system for stabilization and control by line-of-sight orientation of devices operated at UAV. In: 3rd International Conference Actual Problems of Unmanned Aerial Vehicles Developments (APUAVD), pp. 235–238. IEEE, Kyiv (2015). https://doi.org/10.1109/APUAVD.2015.7346608
14. Wang, L.: PID Control System Design and Automatic Tuning Using MATLAB/Simulink. Wiley, Hoboken (2020)
15. Le, A.T.: Adaptive Robust Control Systems. Intech Open, Vienna (2018)
16. Kwakernak, H., Silvan, R.: Linear Optimal Control Systems. Wiley, New York (1972)
17. Asadi, F.: State-Space Control Systems: The MATLAB/Simulink Approach. Morgan & Claypool, Sun Rafael (2021)
18. Tunik, A.A., Abramovich, O.A.: Parametrical robust optimization of the discrete flight control systems. Proc. Natl. Aviat. Univ. **17**(2) 31–37 (22023)
19. Doyle, J., Glover, K., Khargonekas, P.: State-space solution to standard H2 and H∞control problems. IEEE Trans. Autom. Control **34**, 831–847 (1989)
20. Lia, Y., Huang, N.Z., Jiang, T.: Selective Maintenance Modelling and Optimization. Springer, Cham (2023). https://doi.org/10.1007/978-3-031-17323-3
21. Niu, S.S., Xiao, D.: Process Control. Springer, Berlin (2022). https://doi.org/10.1007/978-3-319-61143-3
22. Osadchyi S., Zozulia, V.: Synthesis of optimal multivariable robust systems of stochastic stabilization of moving objects. In: 5th International Conference Actual Problems of Unmanned Aerial Vehicles Developments (APUAVD), pp. 106–111. IEEE, Kyiv (2019). https://doi.org/10.1109/APUAVD47061.2019.8943861
23. Wright, S.J., Recht, B.: Optimization for Data Analysis. Cambridge University Press, Cambridge (2022)
24. Zoppoli, R., Sanguineti, M., Gnecco, G., Parisini, T.: Neural Approximations for Optimal Control and Decision. Springer, Cham (2020). https://doi.org/10.1007/978-3-030-29693-3
25. Osadchy, S.I., Zozulya, V.A., Bereziuk, I.A., Melnichenko, M.M.: Stabilization of the angular position of hexapod platform on board of a ship in the conditions of motions. Autom. Control. Comput. Sci. **56**(3), 221–229 (2022)

Modeling Hole Edge and Burr Formation During Drilling Using LS-DYNA

Valeriy Sikulskyi[1], Kateryna Maiorova[1](✉), Vadim Garin[1], Vitalii Myntiuk[1], and Stanislav Sikulskyi[2]

[1] National Aerospace University "KhAI", Chkalova Street, 17, Kharkiv, Ukraine
kate.majorova@ukr.net
[2] Corning Incorporated, 184 Science Center Dr, Painted Post, NY, USA

Abstract. Drilling is one of the most utilized technological processes in machining and manufacturing. Due to its scale, optimizing drilling parameters for increased productivity and quality has an overwhelming impact on manufacturing labor intensity and final product cost and performance. The quality of hole edges and its roughness, including the presence of burrs, are important parameters determining the part quality and might require post-processing for high-performance applications. Thus, optimizing the drilling process for forming holes with minimum roughness and burrs is a critical task and requires a comprehensive understanding of the process. This work investigated the major drilling parameters for hole forming with drill bits of various degrees of wear. Numerical modeling, particularly explicit finite element approach, was validated with the experiment and exploited due to the limitations of experimental tools to observe a full spectrum of internal material behavior during the dynamic process. The results have shown that hole edge burrs and drilling force progressively increased with the larger drill bit wear, while residual strains mostly varied their concentrations and affected larger material volume around the holes.

Keywords: Drilling modeling · hole edge burrs · drill bit wear · residual strain · drilling force · LS-DYNA

1 Introduction

Machining plays the key role in part fabrication with its labor intensity fraction varying in the range of 30–60% for multi-product manufacturing. For instance, the global number of aviation engine and aircrafts parts produced by means of cutting and abrasive machining is estimated at approximately fifty thousand and up to several hundred thousand, respectively [1].

For complex parts, labor intensity of hole forming can reach up to 70–80% of the overall labor intensity for part mechanical processing. Meanwhile, required quality and precision of the holes are dictated by environment and operating conditions of the part. Furthermore, high precision parts are essential for proper functioning of modern and high-speed systems due to the corresponding dynamic loads and vibrations that limit

M. Nechyporuk et al. (Eds.): ICTM 2023, LNNS 1008, pp. 123–136, 2024.
https://doi.org/10.1007/978-3-031-61415-6_11

life and reliability of parts and assemblies. Thus, ensuring the quality of the entrance and exit hole edges, the accuracy of dimensions, shapes, surface morphology parameters and the cleanliness of the hole cylindrical surface are extremely important for structure reliability, durability, and workability.

In general, optimum drilling parameters depend on various factors, including properties of the processed material, drill bit type, drilling regime, hole geometry and size, which makes achieving the given quality more complex for a hole than for a shaft [2]. Thus, when cost and labor intensity is of priority, one of popular engineering solutions during hole-basis selection is increasing its IT Grade by 1, i.e., loosening tolerance of the hole rather than the shaft. Consequently, H8/g7 fit is a widely accepted choice based on hole forming cost and technological simplicity for reaching required shaft tolerance. Nevertheless, most drilling parameters are typically determined empirically. To ensure validity of this empirical study, a set of experiments is typically conducted prior to that, which itself is a costly and time-consuming process. Alternatively, this set of experiments can be effectively accomplished through numerical modeling. Furthermore, numerical modeling of drilling allows to observe additional parameters of the process, such as the strain and stress in the processed material during the drilling as well as their residual values. While tool such as digital image correlation (DIC) enables experimental observation of strain field on external surfaces in the vicinity of the hole, numerical modeling provides the data for entire material domain affected by the drilling and is particularly useful to understand final edge shape after hole forming [3]. Thus, selection of drilling parameters for improved quality of hole edges is a critical task in time and cost perspective, for which numerical modeling can not only provide a solution for an applied problem but also to extend the scientific knowledge of the problem.

2 The State-of-The-Art and the Study Purpose

Common methods of machining can deliver the roughness required across most industries on the surfaces that are processed directly. However, roughness of the surface edges, including hole edges, typically have roughness of three to four times higher than for directly processed surfaces [4, 5]. It is worth noting that this relation exists not only for metallic parts, but also for nonmetallic and composites ones [6]. There are currently more than a hundred methods of edge post-processing with an order of magnitude more tooling types. Nevertheless, the process of correct implementation of these methods is not yet resolved to the desired level of completion [5]. In recent years, one could notice the tendency to focus on several most utilized and promising edge post-processing methods which require knowledge of actual edge geometry and its material properties after the primary machining [7]. Hence, the effectiveness of these edge post-processing methods relies on understanding the dependence of edge geometry and its material properties on machining regimes and conditions, e.g., type and geometry of grill bit, processed material properties, part thickness, hole diameter, drilling rpm and feed.

Based on [8], one of the most complicated cases of edge forming is for parts with various types of surfaces. Figure 1 shows schematics of hole forming through drilling normal and at an angle to the surfaces of different types: flat, cylindrical internal and external, and spherical. Hole edges on the entrance and exit faces of the workpiece typically have the highest roughness (Fig. 1, a–c). However, when a workpiece has a premade orifice in the path of the drill bit, this orifice will also have high roughness on its internal edges. Moreover, if the diameter of this orifice is smaller than of the drill bit (Fig. 1, d), the roughness on the internal edges of the orifice becomes even higher due to the chips that are stuck in the orifice, dragged by the drill bit, and further damage the orifice edges.

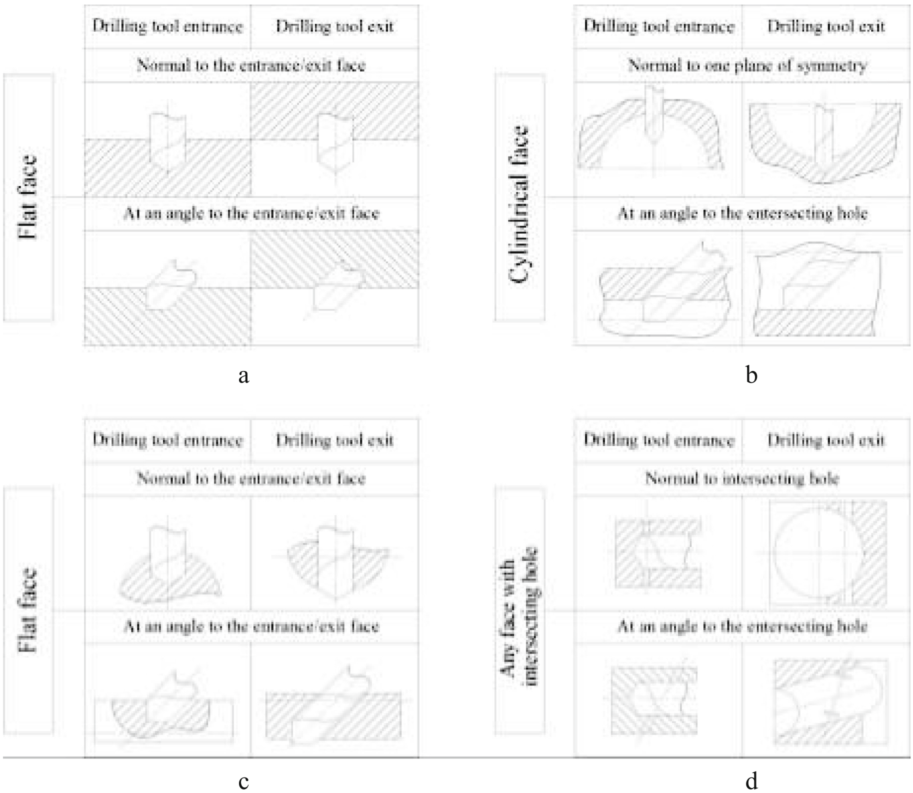

Fig. 1. Schematics of hole forming by drilling in complex parts normal and at an angle to (a) flat, (b) spherical, (c) cylindrical faces, and (d) with intersecting hole smaller than the drill bit.

Considering the variety of parameters, new solutions for hole forming are still in search and require further analysis. While empirical tests are often still more practical for that kind of study, they are costly and demand logistical preparation. To meet today's demand in timing and high-quality solutions, numerical approaches are adopted, particularly in the areas where the model can generate useful results without comprehensive validation if critical and accurate inputs are provided. Thus, the goal of this work is to develop a robust numerical model for hole forming through drilling that would adequately predict parameters of hole edges at entrance and exit faces of a metal part and establish relations between the hole edges' parameters and drill bit wear. Establishing these relations allows quantifying the importance of drill bit wear and optimizing drilling regime, drill bit type, its sharpening, etc.

3 Literature Review

Machining regime and tool type play significant roles in delivering metallic parts with high-quality hole edges [9, 10]. It is known that reduction in roughness of hole edges on entrance and exit faces leads to improved geometric tolerance and increased lifespan of the part by 70–90% [11]. For instance, [12] presents practical solutions to partially prevent formation of hole edge defects by improving the drill bit shape and other cutting tools. However, such solutions also lead to increased costs and are rarely practical for cost-sensitive mass production. The paper [13] shows the prospect of using spiral drills to achieve high accuracy of the hole shape, diameter and required surface roughness according to field experiments. In practice, such comprehensive studies are more reliable than numerical modeling, but they are expensive and require special equipment. Study [14] proposes and studies numerically a complex technology for detecting surface defects (burrs) of the forming of parts, which are divided into three types and which are permissible for the admission of parts into production, however, it does not guarantee the high quality of all part elements (surfaces, surface joints, shape accuracy edge, absence of traces of preliminary processing, etc.). The condition of the cutting edges of the drill is important for obtaining a high-quality hole, but literature lacks the criteria for assessing the wear of drills and standards for their change or sharpening. As a result, in practice, the drill bit is replaced when the hole quality is already compromised and insufficient. Study in [15] is aimed at the use of high-temperature processes that effectively improve the quality of surfaces, edges and minimize burrs and residues of cutting products, independently of the type of drill and drilling regime. However, controlling these high-temperature processes is complicated as drill bit type and drilling regime (cooling and lubrication, temperature of the cutting zone, wear of the tool, etc.) largely affect temperature and material properties in the vicinity of formed defects. Therefore, despite the positive results in works [14, 15], the approaches solely relying on global temperature control are limited. According to the authors in [16], the main parameters of interest are the tool rotational and feed speeds, and the hole depth, the optimal values of which can be determined by analyzing the effect of these parameters on the roughness of processed faces and wear of the drill secondary faces using the Taguchi method. The Taguchi method consists of orthogonal arrays of ANOVA (analysis of variance) and the signal-to-noise (S/N) ratio. The research results are in tabular and graphical form and must be compared and confirmed by field experiments. However, despite the positive practical benefit of work in [16], the labor intensity and skill demand of such work is high. In many instances, drilling process experiments were adequately replaced with numerical modeling using commercial finite element (FE) software, including ANSYS [17–19], Abaqus/CAE [20, 21], Simufact Forming [22, 23], and LS-DYNA [24, 25]. Note that LS-DYNA is currently the leader among the software for numerical simulation of dynamic and static phenomena in the field of engineering and materials science. LS-DYNA has quite powerful capabilities for modeling complex dynamic processes physics that is present during drilling [26]. The main problem is developing a robust model that, given high-quality input data, can provide useful and reliable results without comprehensive validation process.

Thus, taking into account the worldwide knowledge and research on hole drilling and forming their faces and edges, it is reasonable to conduct preliminary field experiments to clarify problem formulation and input parameters for achieving the adequate numerical model.

4 Experimental Procedures

In this work, experiments were conducted to determine the effects of worn drill bit on formation of burrs on the hole edges. Holes were drilled in 5 mm thick samples of aluminum cast alloy AM 4.5kd (analog to the US alloy ANSI 201.0) at constant speed of drill bit edge of 15 m/min and feed of 0.05 mm/rev with diameter drill bits of three cases of wear. All drill bits are 8 mm in diameter and have point angle of 118°. The experiment output is the size and shape of the hole burrs due to the wear of each drill bit.

Below are the results of the three experiments, which will be further used to assist in developing the numerical model. The three cases of drill bit wear are the following: case A – sharp drill bit (Fig. 2, a1), case B – drill bit with the worn vertices of the cutting edges as a typical starting point of the wear (Fig. 2, b1), and case C – drill bit with a rounding of the cutting edge along its whole length as for a heavily worn drill bit (Fig. 2, c1). Figure 2, a2–c2, shows corresponding burrs formed during the hole drilling with the three cases of drill bit wear. As expected, sharp drill bit resulted in the smallest burr on the hole edge, while still being considerably larger than the surface roughness of the entrance face (Fig. 2, c2). Case B drill bit leads to a much worse results than the sharp drill bit with the hole edge having both larger well-attached burrs and residual material often called hanging chads (Fig. 2, b2). These hanging chads are formed from the material layer near the exit of the drill bit which breaks due to reaching stress limit and plastically bends during the drill bit exiting the workpiece. As case C shows (Fig. 2, c2), the most worn drill bit requires larger axial force during the drilling and even more material residue is left in the form of hanging chads. Interestingly, case C also results in well-attached burrs of larger height suggesting larger plastic deformation in the workpiece material before the drill bit exits it. When quantified, the formed burrs can be sized as 0–0.15 mm for case A, 0.4–0.5 mm for case B, and 0.9–1.7 mm for case C.

Besides the study of effects of drill bit wear of hole edge quality, effects of cylindrical exit face and drill angle were briefly examined. To minimize experimental variability, only sharp drill bit was used with the diameter of the bit smaller than the curvature of the radius of the cylindrical exit face. The results of this examination are shown in Fig. 3. An asymmetry in burr formation was observed when flat workpiece was drilled at 75° to the face (Fig. 3, a). For both concave and convex cylindrical faces, burr asymmetry was observed even when drilling was performed normal to the face surface (Fig. 3, b–c).

Overall, the above results show that even sharp drill bits result in significant burrs on the exit hole edge, which are further worsened with the drill bit wear. Moreover, cylindrical exit face adds nonregularity in burrs shape, sizing, and potentially material properties, which would require special technological operations for their processing.

Fig. 2. Drill bits used in the experiments with different cases of wear: (a1) sharp, (b1) worn vertices of the cutting edge, (c1) worn cutting edge along its whole length; and (a2–c2) corresponding formed hole edges on the exit face of the workpiece with well-attached burrs and hanging chads.

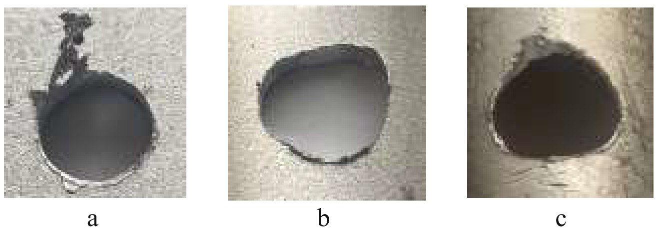

Fig. 3. Images of hole edge burrs on the workpiece exit (a) flat face when drilling performed at 75° to the face; (b) concave cylindrical face when drilling performed normal to the face; and (c) convex cylindrical face when drilling performed normal to the face.

5 Numerical Modeling of Drilling

Considering the dynamic nature of the drilling process large deformation, and high contact nonlinear of the problem, LS-DYNA commercial FE software was selected for the numerical modeling of the problem [26]. This section describes the developed numerical modeling and the obtained results.

5.1 Explicit Formulation of the Model

Mathematically, explicit simulation in LS-DYNA is performed by solving finite element semi-discrete equation of motion as follows:

$$M_a^n = P^n - F^n + H^n, \tag{1}$$

where M_a^n – inertia force vector (structural mass matrix multiplied by the acceleration vector); P^n – applied load vector; F^n – internal load vector; H^n – 'hourglass' force vector due to reduced integration solid element used in the model. The damping forces are not present in Eq. 1 as no damping was added to the model.

The above equation is solved at time t^n. Transition to time t^{n+1} is performed through the numerical central difference integration as follows:

$$a^n = M\left[\text{unknown template}\right] \tag{2}$$

$$v^{n+1/2} = v^{n-1/2} + a^n \Delta t^n \tag{3}$$

$$u^{n+1} = u^n + v^{n+1/2} \Delta t^{n+1/2}, \tag{4}$$

where $\Delta t^{n+1/2} = \frac{\Delta t^n + \Delta t^{n+1}}{2}$ is a half timestep; v and u – vectors of nodal velocities and translations, correspondingly. Geometry is updated by adding the translations of each timestep to the initial nodal positions.

5.2 Drill Bit Geometry

LS-DYNA modeling was performed in ANSYS Workbench (WB) environment due to its capability to facilitate geometry changes, automatic remeshing, and enhanced post-processing tools. Initial geometry can be seen in Fig. 4 and consists of 3D bodies representing a workpiece, drill bit solid body, and a set of surfaces defining the external faces of the drill bit. Simulations are performed in accordance with the experiment

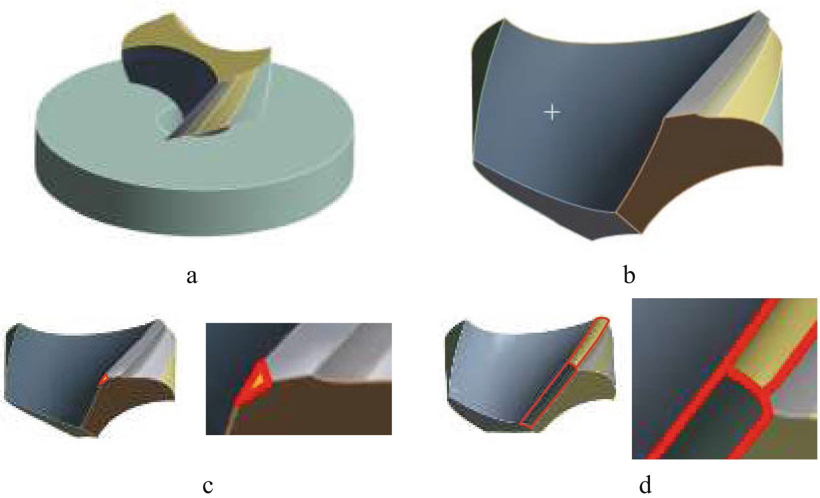

Fig. 4. Geometry of the (a) workpiece and drill bit, and close up view of the drill bit (b) without defects (case A), (c) with worn vertices of the cutting edge (case B), and (d) with worn cutting edge along its whole length (case C).

conducted in this study on the effects of drill bit wear on hole edge formation (Fig. 2). To reduce simulation time, workpiece thickness was reduced by four times. Drill bit sizing was proportionally decreased while maintaining the physics of the process by adjusting drill bit rpm to maintain the velocity of the cutting edge vertices.

The diameter of the workpiece model is selected to be twice the size of the drill bit to minimize the effect of boundary conditions on the drilling zone according to the Saint-Venant's principle.

5.3 Materials of the Drill Bit and Workpiece

Drill bit stiffness is not critical for the present analysis and thus is modeled as a rigid body using *MAT-RIGID card available in LS-DYNA with the assigned material as for a typical steel (density of 7.85 g/cm^3, Young's modulus of 200 GPa, and Poisson's ratio of 0.3). Aluminum workpiece is modeled as an isotropic plasticity material model *MAT_POWER_LAW_PLASTICITY which uses a power law hardening rule and yield stress obeying the below equation [27]:

$$\sigma_y = k\varepsilon^n = k\left(\varepsilon_{yp} + \overline{\varepsilon}^p\right)^n, \tag{5}$$

where k – strength coefficient, n – hardening exponent, ε^{-p} – effective plastic strain (logarithmic), and ε_{yp} – elastic strain to yield, which is determined by solving for the intersection of the linearly elastic loading equation with the strain hardening equation. Strength coefficient, k, of 545 MPa and hardening exponent, n, of 0.0545 were selected from ANSYS Granta database as for ANSI 201.0-T7 aluminum cast alloy, which is an analog to the AM 4.5 kd alloy used in the experiment of this work [26]. Plastic failure strain for element deletion, EPSN, was used to perform material erosion during drilling.

Figure 5 shows true stress-strain curves of the utilized power law plasticity model. Bilinear model with the same yield and ultimate stresses and strains was added to the graph to emphasize nonlinearity of the utilized power law material model. Suitability of the bilinear model can also be evaluated for future modeling of hole edge and burr forming during drilling to improve simulation computational time. Additionally, *MAT_JOHNSON_COOK plastic model of aluminum alloy 7039 was added for comparison as a frequently used model for machining numerical modeling [28].

5.4 Boundary Conditions and Loads

As Fig. 6 demonstrates, the workpiece is constraint by fixing translations of the nodes on its cylindrical surface. The drill bit is supplied 1836 rpm rotational speed and 6.14 mm/s vertical feed, which are defined in the rigid body coordinate system and similar to the parameters used in the experiment. To maintain drill bit vertical, it is also constraint for horizontal translations and rotations about other two horizontal axis as shown in Fig. 6.

The contact is defined by *CONTACT_ERODING_SINGLE_SURFACE card that considers contact between any surfaces including newly formed surfaces after the erosion (deletion) of the elements due to drilling [29].

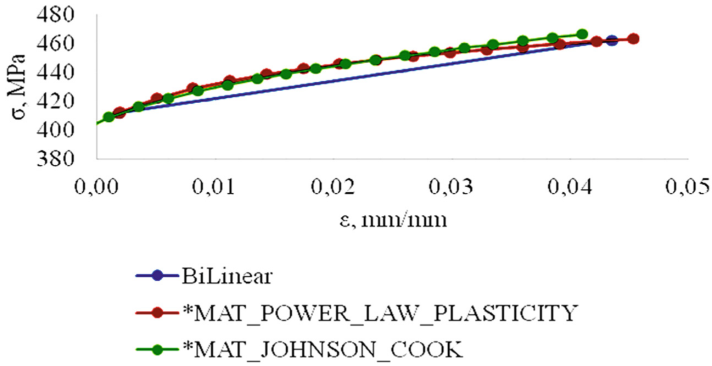

Fig. 5. True stress-strain curves of ANSI 201.0-T7 aluminum cast alloy used for the workpiece in the study and modeled with *MAT_POWER_LAW_PLASTICITY and Bilinear plastic material models, and Al 7039 modeled with *MAT_JOHNSON_COOK plastic material model for comparison.

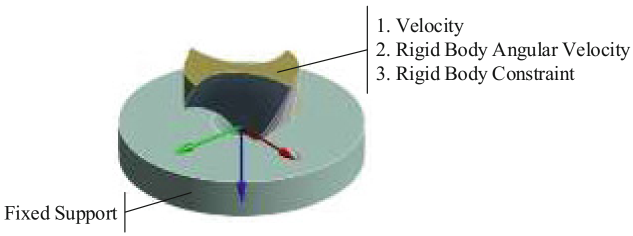

Fig. 6. Boundary conditions and rigid body motion applied to the bodies of the model.

5.5 Discussion of Numerical Modeling Results

The drilling process near the entrance face and in the center of the workpiece is not drastically different between the three cases of drill bit wear in terms of the plastic strain field (Fig. 7, a). Nevertheless, a clear difference between the drill bit wear cases was observed for the exit face of the workpiece. While the sharp drill bit (case A) cuts the material until it exits the workpiece and only leaves well-attached burrs (Fig. 7, b), worn drill bits considerably deform material near the exit face and results in an unbroken material layer that separates locally along its circumference from the main workpiece body, forming hanging chad (Fig. 7, c). By comparing Fig. 2 and Fig. 7, a qualitative similarity between the experimental and modeled hole edge topology for different cases of drill bit wear can be observed. Quantitative comparison was performed based on the average burr size and differed from experimentally obtained values by no more than 10%.

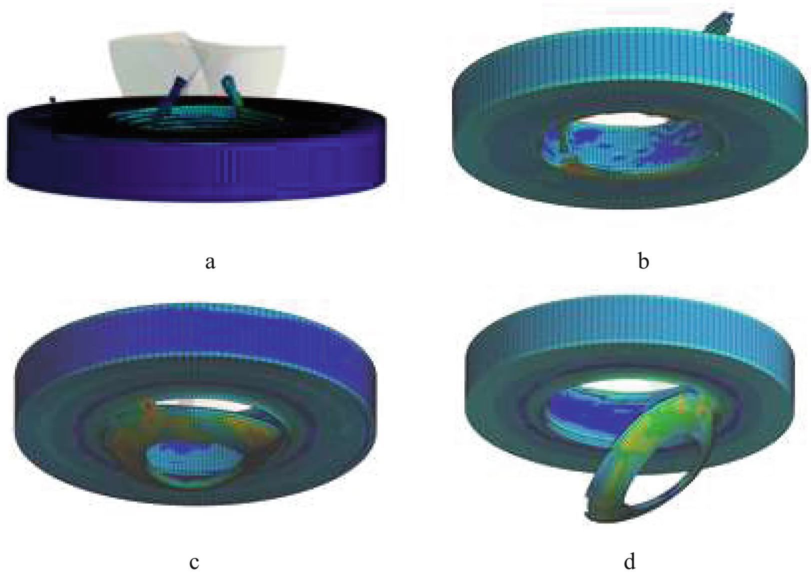

Fig. 7. Modeling results for workpiece with contours of equivalent stress (a) during the initial stage of drilling, and after drilling with (b) sharp drill bit, (c) drill bit with worn vertices of the cutting edge, and (d) drill bit with worn cutting edge along its whole length.

Figure 8, a, demonstrates variation of total reaction force with time for the three considered cases. As expected, the force is the lowest for the sharp drill bit (case A), while for the worn drill bits of cases B and C, the forces are approximately two and three times larger than with the sharp drill bit, respectively. As was mentioned earlier, numerical modeling allows unveiling parameters and material states observing which experimentally, especially during the dynamic process, is complicated or practically impossible. As such, when stress state is analyzed in the workpiece, average von Mises stresses are similar in the two cases of worn drill bits with a small difference in the peak stress values (Fig. 8, b). However, both cases of worn drill bits have significantly higher stresses compared to the sharp drill bit case. Similar trends were observed for the average residual stresses in the workpiece.

However, residual strains particularly in the vicinity of the formed hole are different for the three considered cases of drill bit wear as shown in Fig. 9. Residual strains in this domain are of great interest as they dictate material properties and hole reliability for its application.

In case B, residual strains are lower than in the other two cases while the average residual strains within the whole workpiece are the same across the three cases. The major difference in the residual strain map of the hole formed with the sharp drill bit is the depth of the layer with high residual strains.

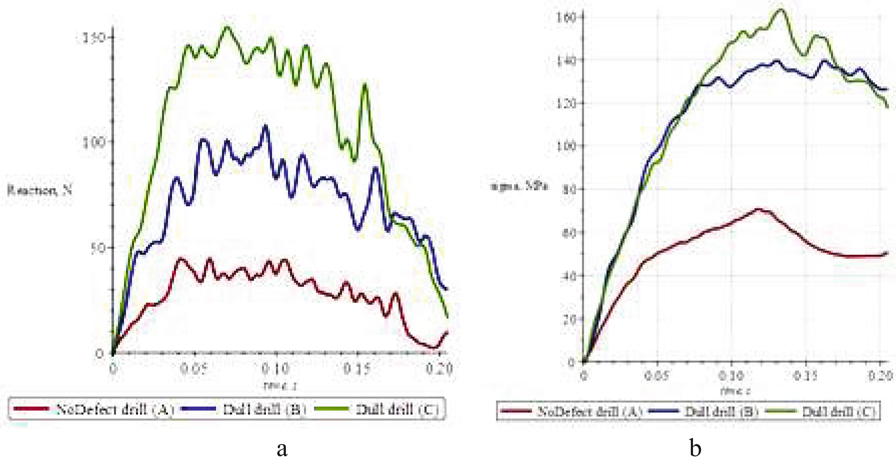

Fig. 8. Variation of (a) total reaction force and (b) average von Mises stresses in the workpiece during the drilling process.

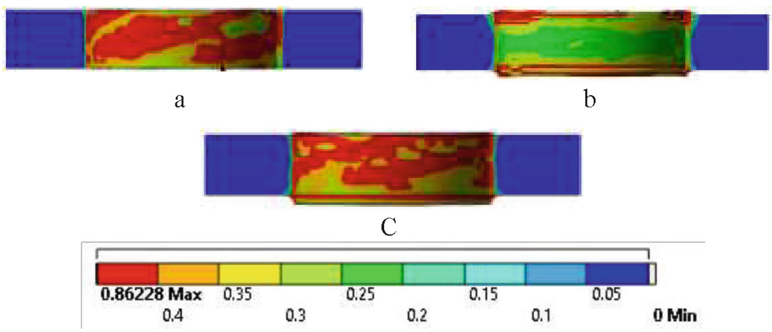

Fig. 9. Distribution of residual strains within the holes formed by drill bit with (a) sharp cutting edge (case A), (b) worn vertices of cutting edge (case B), and (c) worn cutting edge along its whole length (case C).

6 Conclusions

Based on the performed experimental and numerical studies, the following conclusions were drawn:

1. Numerical model of the drilling process was developed and validated for the purpose of obtaining realistic hole edge shape and burrs on the exit face of the workpiece when drill bits of various wear degrees are used. Being validated, the model was used to investigate mechanical parameters in the workpiece observing which experimentally is complicated. Furthermore, the model now can be used to investigating hole edge and burr forming for different scenarios which fundamentally do not violate assumptions of the model, such as drilling at an angle to flat and curved faces of the workpiece,

optimizing drilling parameters for these scenarios, and selecting appropriate drill bit sharpening.

2. Numerical simulation demonstrated that the main physical difference in forming holes with worn drill bits is the increased force required to maintain proper drilling process with given tool rotation and feed. Particularly, two- and three-times larger forces were obtained in the modeling for the drill with worn vertices of the cutting edge and the worn cutting edge along its whole length, respectively. Furthermore, drill bits with different degree of wear results in drastically different hole edge topology and burrs on the exit face of the workpiece. While the sharp drill bit (case A) cuts the material until it completely exits the workpiece and only leaves well-attached burrs (Fig. 7, b), worn drill bits considerably deform material near the exit face and results in an unbroken material layer that separates locally along its circumference from the main workpiece body, forming large burrs and hanging chad (Fig. 2, b2–c2 and Fig. 7, c–d).
3. Numerical modeling showed that residual stresses and strains in the vicinity of the hole and hole edges formed with worn drill bits are about twice as large as and affect significantly thicker layer of workpiece material than for the case of a sharp drill bit Interestingly, no considerable difference in the residual values were observed between the two studied cases of drill bit wear. However, the drill bit with worn vertices of the cutting edge resulted in largest residual strains concentrated near hole edges on both entrance and exit faces. Meanwhile, the drill bit with worn cutting edge along its whole length resulted in relatively evenly distributed residual strains across the cylindrical surface of the formed hole.

Acknowledgements. The authors would like to express their gratitude to CADFEM UA LLC, an official partner of ANSYS, Inc.in Ukraine, for providing software support.

References

1. Gupta, K., Gupta, M.K.: Developments in nonconventional machining for sustainable production: a state-of-the-art review. Proc. Inst. Mech. Eng. C: J. Mech. Eng. Sci. **233**(12), 4213–4232 (2019). https://doi.org/10.1177/0954406218811982
2. Nee, A.Y.C.: Handbook of Manufacturing Engineering and Technology. Springer, London (2015). https://doi.org/10.1007/978-1-4471-4670-4
3. Arabul, E., Lunt, A.J.G.: A novel low-cost DIC-based residual stress measurement device. Appl. Sci. **12**, 7233 (2022). https://doi.org/10.3390/app12147233
4. ASME B46.1-2019. Surface Texture (Surface Roughness, Waviness, and Lay) (2019)
5. Gillespie, L.K.: Deburring and Edge Finishing Handbook. Society of Manufacturing Engineers, Dearborn (1999)
6. Maiorova, K., Vorobiov, Iu., Andreev, O., Lupkin, B., Sikulskiy, V.: Forming the geometric accuracy and roughness of holes when drilling aircraft structures made from polymeric composite materials. East.-Eur. J. Enterp. Technol. **2**(116), 71–80 (2022)
7. Sikulskiy, V., Maiorova, K., Vorobiov, Y, Fomichev, P., Myronova, S.: Convergence technology of vehicle parts surface finishing. Transp. Probl. **18**(1), 117–127 (2023). https://doi.org/10.20858/tp.2023.18.1.10

8. Sikulskyi, V., Maiorova, K., Bychkov, I., Myronova, S., Sikulskyi, S.: Shape of part edges with the various surface finish of the adjacent surfaces. In: Nechyporuk, M., Pavlikov, V., Kritskiy, D. (eds.) ICTM 2022. LNNS, vol. 657, pp. 134–145. Springer, Cham (2023)
9. Damiana, B., Daniela, K., Piotra, M.: Deburring and smoothing the edges using vibro-abrasive machining. Procedia Eng. **192**, 28–33 (2017). TRANSCOM 2017: International scientific conference on sustainable, modern and transport. https://doi.org/10.1016/j.proeng.2017.06.005
10. Niknam, S.A., Davoodi, B., Davim, J.P., Songmene, V.: Mechanical deburring and edge-finishing processes for aluminum parts – a review. Int. J. Adv. Manuf. Technol. **95**(1), 1101–1125 (2018). https://doi.org/10.1007/s00170-017-1288-8
11. Kumar, M., Bajpai, V.: Experimental investigation of top burr formation in high-speed micro-milling of Ti6Al4V alloy. Proc. Inst. Mech. Eng. Part B: J. Eng. Manuf. **234**(4), 730–738 (2019). https://doi.org/10.1177/0954405419883049
12. Jin, S.Y., Pramanik, A., Basak, A.K., Prakash, C., Shankar, S., Debnath, S.: Burr formation and its treatments – a review. Int. J. Adv. Manuf. Technol. **107**(5–6), 2189–2210 (2020)
13. Hassan, M.H., Abdullah, J., Franz, G., Mahmoodian, R.: Effect of twist drill geometry and drilling parameters on hole quality in single-shot drilling of CFRP/Al7075-T6 composite stack. J. Compos. Sci. **5**(189), 1–14 (2021). https://doi.org/10.3390/jcs5070189
14. Abele, E., Schützer, K., Güth, S., Meinhard, A.: Deburring of cross-drilled holes with ball-end cutters – modeling the tool path. Prod. Eng. Res. Devel. **12**, 25–33 (2018). https://doi.org/10.1007/s11740-017-0781-0
15. Plankovskyy, S., Popov, V., Shypul, O., et al.: Advanced thermal energy method for finishing precision parts. In: Gupta, K., Pramanik, A. (eds.) Advanced Machining and Finishing. Elsevier, Amsterdam, pp. 527–575 (2021). https://doi.org/10.1016/B978-0-12-817452-4.00014-2
16. Yakubu, S.O., Bello, Y.: Optimization of machining parameters of low carbon steel for turning operation using Taguchi analysis. Niger. J. Trop. Eng. **16**(1), 682–696 (2022). NJTE 2022 – 011
17. Wang, T., Liu, X., Liu, Z., et al.: ANSYS is used on drilling inner blind hole on deep hole. Wireless Pers. Commun. **103**, 1077–1088 (2018). https://doi.org/10.1007/s11277-018-5497-8
18. Liu, X., Feng, Y.: FEA of BTA deep hole drilling based on ANSYS. IOP Conf. Ser.: Mater. Sci. Eng. **611**, 012021 (2019). IOP Publishing Ltd. https://doi.org/10.1088/1757-899X/611/1/012021
19. Zhang, Z., et al.: Dynamic characteristic analysis of micro-hole gun drill based on ANSYS. J. Phys.: Conf. Ser. **1750**, 012043 (2021). IOP Publishing Ltd. https://doi.org/10.1088/1742-6596/1750/1/012043
20. Vorobiov, I., Nechyporuk, N., Maiorova, K.: Experimental and numerical investigations on impulse self-pierce riveting of lightweight aircraft aluminium and mixed structures. In: Proceedings of 22nd International Scientific Conference Transport Means 2018, pp. 121–128 (2018)
21. Le, S., Wongsa-Ngam, J.: Stress analysis in upper fillet and rail-end bolt hole at rail joint. IOP Conf. Ser.: Mater. Sci. Eng. **1137**, 012050 (2021). https://doi.org/10.1088/1757-899X/1137/1/012050
22. Voronko, I., Voronko, V., Dyachenko, Y., Shapar, S.: Process simulation of hole mandrelling in steel aircraft parts. Hung. J. Ind. Chem. **51**(1), 1–7 (2023). https://doi.org/10.33927/hjic-2023-01
23. Voronko, V., Dyachenko, Y., Voronko, I., Zastela, O., Myronova, S.: Technology of holes strengthening by pneumo-impulse hole mandrelling. In: Nechyporuk, M., Pavlikov, V., Kritskiy, D. (eds.) ICTM 2022. LNNS, vol. 657, pp. 3–15. Springer, Cham (2023). https://doi.org/10.1007/978-3-031-36201-9_1

24. Zhang, K., Zhang, S., Zheng, R., Zhang, K.: Numerical simulation study of fragment damage based on ANSYS/LS-DYNA. J. Phys.: Conf. Ser. **2449**, 012022 (2022). International Conference on Applied Mathematics and Digital Simulation (AMDS 2022). https://doi.org/10.1088/1742-6596/2449/1/012022
25. Kim, M.-S., Yoo, W.-K., Kim, W., Hwang, S., Kim, C.-Y., Lee, S.S.: Numerical study investigating the blasting efficiency of the long and large-diameter uncharged hole-boring method with deck charge technique. Appl. Sci. **13**(4), 2099 (2023). https://doi.org/10.3390/app13042099
26. LS-DYNA. Theory Manual, Compiled By John O. Hallquist, Livermore Software Technology Corporation, 7374 Las Positas Road Livermore, California 94551 (2006). ISBN 0-9778540-0-0
27. Hallquist, J.O.: LS-DYNA. Keyword User's Manual. Volume II. Material Models, 09/27/21 (r: 14196). Livermore Software Technology (LST), an ANSYS Company (2021)
28. Johnson, G.R., Cook, W.H.: A Constitutive Model and Data for Metals Subjected to Large Strains, High Strain Rates, and High Temperatures. In: Proceedings 7th International Symposium on Ballistics, The Hague, pp. 541–547 (1983)
29. LS-DYNA. Keyword User's Manual. Volume I, Version 971. Livermore Software Technology (LST), an ANSYS Company. ISBN 0-9778540-2-7. https://www.academia.edu/40555890/LS_DYNA_KEYWORD_USERS_MANUAL_VOLUME_I

Aerodynamic Interaction of Minivan Vehicles During an Overtaking Maneuver

Sergey Filipkovskij[1](✉) and Andrii Avershyn[2]

[1] National Aerospace University "Kharkov Aviation Institute", Kharkov 61070, Ukraine
s.filipkovskij@khai.edu

[2] Kharkov National Automobile and Highway University, Kharkov 61002, Ukraine

Abstract. The minivan has the largest usable volume compared to other passenger car body layouts with the same dimensions. Therefore, it is most advisable to use it in commercial transportation. At the same time, they have the largest lateral surface area, so they experience the greatest wind loads. In the modern era, vehicles are focused on automation to make driving a comfortable experience for the driver. The most important task is control during various maneuvers. Aerodynamic forces significantly affect vehicle control during maneuvers. They must be taken into account when self-driving. The overtaking maneuver of one vehicle by another is a complex, non-stationary process in which complex transient aerodynamic forces arise. The close proximity of two vehicles is characterized by the mutual influence of the aerodynamic structures generated by the vehicles. Improving methods for mathematical modeling of the aerodynamic characteristics of minivan-type vehicles is an actual task and determines the direction of research. The problem of numerical modeling of air flow around vehicles is formulated. A numerical experiment technique has been developed for modeling external flows around vehicles in a non-stationary setting. A study of the flow around vehicles during overtaking made it possible to calculate aerodynamic forces. The dependences of aerodynamic forces on the relative position of vehicles have been established. The lateral aerodynamic forces acting on cars during overtaking are of the same order as the aerodynamic drag forces. These forces must be taken into account in automatic vehicle control systems.

Keywords: Minivan Vehicle · Overtaking Maneuver · Aerodynamic Force · Numerical Modeling

1 Introduction

A minivan has the largest usable volume compared to other passenger car body layouts with the same dimensions. Therefore, it is most advisable to use it in commercial transportation. At the same time, they have the largest lateral surface area, so they experience the greatest wind loads.

In the modern era, vehicles are focused on automation to make driving a comfortable experience for the driver. In the automotive industry, various aspects of vehicle automation are considered [1]. Self-driving technology in general is becoming more widespread

M. Nechyporuk et al. (Eds.): ICTM 2023, LNNS 1008, pp. 137–150, 2024.
https://doi.org/10.1007/978-3-031-61415-6_12

and has the potential to revolutionize the global transportation system [2]. The article [3] reviews and studies the key technologies of self-driving cars, namely: car navigation system, path planning, environmental perception and vehicle control. The most important task is control during various maneuvers. Aerodynamic forces significantly affect vehicle control during maneuvers. They must be taken into account when self-driving.

The overtaking maneuver of one vehicle by another is a complex, non-stationary process in which complex transient aerodynamic forces arise. The close proximity of two vehicles is characterized by the mutual influence of the aerodynamic structures generated by the vehicles. As a result, the forces and moments acting on the vehicle change as the distance between them changes. This may affect their stability and create a safety hazard. In addition, aerodynamic performance is affected by both vehicle position changes and the rate of change. The study of such processes is difficult both in wind tunnels and during road tests. Currently, it is most advisable to conduct such studies using CFD methods. A more detailed study of this issue will help drivers avoid accidents when maneuvering and effectively operate unmanned vehicles in the future.

Overtaking is characterized by a sharp change in aerodynamic coefficients (lateral force and roll moment) as the vehicles are close to each other. Most often, these deviations can be compared to sudden changes in road conditions and wind speeds, which can cause the driver to lose control. Aerodynamic phenomena associated with maneuvers may be similar to those experienced by a vehicle when overcoming an obstacle, and may be associated with the vehicle generating side gusts. Research and improvement of the aerodynamic characteristics of cars began to be addressed at the dawn of the automobile era. Initially, it was a blind copying of forms from related industries such as shipbuilding and airship construction. Since the 1990s, there has been a rapid growth in research in the field of racing car aerodynamics using numerical methods.

The overtaking maneuver between two identical vehicle models was studied using experimental and numerical means in [4]. In this paper, the maneuver was considered a quasi-stationary process, one of the models (the overtaken vehicle) was fixed, and the other (the overtaking vehicle) was installed at different axial distances from the overtaken vehicle. In [5], using aerodynamic tests, a study was carried out of the change in aerodynamic characteristics for a commercial van and an articulated truck when overtaking on a bridge platform in a headwind. Article [6] is devoted to the study of the aerodynamic characteristics of an overtaken bus in a headwind, special attention is paid to the analysis of the kinetic energy of turbulence around the bus in comparison with conditions without a headwind and at a yaw angle of 30°. [7] reviewed the current status and direction of development of the Shear Stress Transport (SST) turbulence model, presenting extensions for improved wall processing and zonal formulation of Detached Eddy Simulation (DES). In [8], modifications were made to two developed hybrid Computational Fluid Dynamics (CFD) strategies, namely Delayed Detached Eddy Simulation (DDES) and DDES with improved wall modeling capabilities (IDDES).

In [9], a two-way analysis of unsteady aerodynamics was carried out in order to obtain a complete understanding of the mutual influence when performing a bus overtaking maneuver using the SST model, DES and overset mesh technology, taking into account the influence of lateral distance and cross wind. [10] discusses the use of the DDES turbulence model based on a model with one Spalart-Allmaras (S-A) equation. The study

[11] attempted to identify the main source of discrepancy and determine how to reduce the problem of separation and Model Stress Depletion (MSD) on finer meshes. [12] investigates a class of high order Runge-Kutta time discretization with Total Variation Diminishing (TVD) suitable for solving with stable spatial discretization. The study [13] was carried out to identify the patterns of changes in aerodynamic force, moment, yaw angle and lateral displacement of an overtaken sedan and an overtaking sedan. In this article, the motion of the car is not specified, but is modeled taking into account wind interaction. The results showed that the body position and lateral space of the two vehicles are critical to the stability of the vehicles during the overtaking maneuver. [14] studies the process of overtaking of a vehicle making a right turn at an intersection by a vehicle moving in a straight line.

Analysis of publications indicates that research into road vehicle aerodynamics is often carried out in full-scale automotive wind tunnels without taking into account real-life traffic conditions, which can significantly change the aerodynamic characteristics of an isolated vehicle. The aerodynamics of minivan-type vehicles have been little studied, despite the broad prospects for their use for commercial purposes including self-driving. Therefore, improving methods for mathematical modeling of the aerodynamic characteristics of minivan-type vehicles is an actual task and determines the direction of research.

2 Calculation Model

The issue of overtaking one vehicle by another was resolved as the movement of one vehicle relative to a stationary other vehicle, blown by a counter flow of air (Fig. 1).

Numerical modeling of stationary and unsteady flows was performed using the Open FOAM software package. The computational domain was built according to the wind tunnel principle. The solid model is immersed in the computational domain with $L \times H \times W = 10l \times 5l \times 5l$ dimensions (Fig. 1 a) where $l = 5$ m is the length of the car. The computational domain was described by a tetrahedral mesh containing about 10 million nodes with condensations near solid surfaces to describe the boundary layer. The vehicle is a minivan with the dimensions shown in the Fig. 1 b.

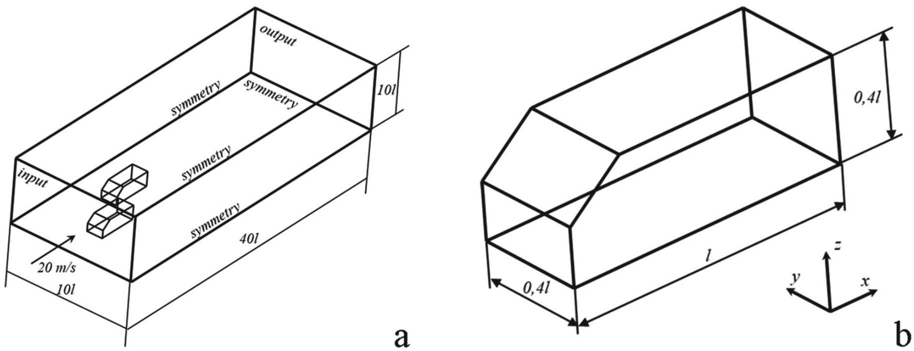

Fig. 1. Scheme of the computational area around cars (a), three-dimensional model (b)

Viscous turbulent flow is described by the system of Navier-Stokes equations in a region with moving boundaries [15]. To integrate the Navier-Stokes equations, the Beam-Warming difference scheme was chosen [15, 16].

To more accurately describe the flow core and circulation zones, models have been developed that take into account to varying degrees the convective transport of large turbulent eddies, diffusion and changes in the energy spectrum of turbulent eddies. Such models are described by partial differential transport equations with several empirical parameters, including turbulent viscosity – ν or turbulence parameters: kinetic energy – k, dissipation rate of turbulence kinetic energy – ε, specific vorticity dissipation rate – ω [17].

Integration of the complete averaged Navier-Stokes equations was carried out by a difference scheme of the 2nd order of accuracy based on the Total Variation Diminishing (TVD) approximation. The system is closed by the Shear Stress Transport (SST) or Spalart/Allmaras (SA) turbulence model equations [11, 18], depending on the nature of the problem in the k-ε formulation. To describe the effects of viscosity in the boundary layer on some structural elements, wall functions ($Y+$) are used [7]. In this case, the minimum value of the boundary layer variable is selected under the condition $Y+ < 5$. Outside the computational domain, an undisturbed flow is assumed.

The atmospheric environment was described by the ideal gas model. In the numerical experiments, the following boundary conditions were specified: the speed of the oncoming air flow is directed along the longitudinal axis of the car, it is equal to 20 m/s and coincides with the speed of the roadway. At a distance, the pressure of the standard atmosphere P_∞ is set.

3 Study of the Aerodynamic Characteristics of Vehicles During Approaching on the Same Traffic Lane

When approaching before overtaking, the overtaking vehicle Car2 moves behind the overtaken Car1 with a relative speed of $v_r = 1$ m/s, as shown in Fig. 2.

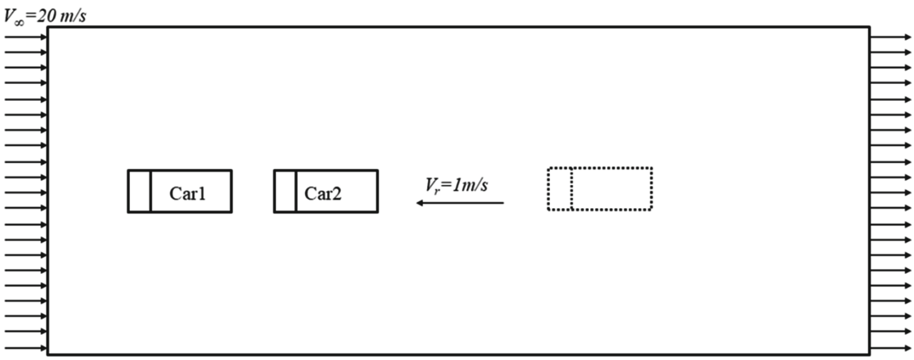

Fig. 2. Diagram of approaching

The results of calculating the unsteady air velocity field around vehicles are presented in Fig. 3. Figure 4 shows the change in the field of excess air pressure around vehicles. In these figures, the distance is reduced from 10 m to 1 m.

Car2 enters the rarefied air zone behind Car1 when it catches up with it. This can be clearly seen in Fig. 4. There is a high pressure zone in Car1's front side, but there is no such zone in Car2's front side. At a distance of 2 m, Car2 is entirely in the zone of lowest pressure.

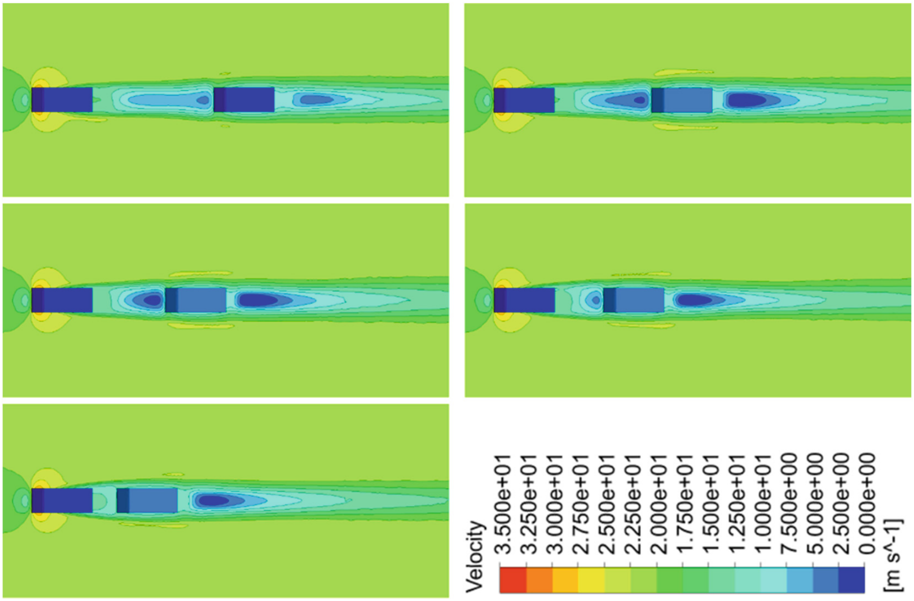

Fig. 3. Change in the field of absolute values of air velocities upon approach.

4 Study of the Aerodynamic Characteristics of Vehicles During Shifting to a Parallel Traffic Lane

When Car2 enters a parallel lane, it moves along the road at the same speed as Car1 and across the road at a relative speed of $v_r = 1$ m/s, shifting as shown in Fig. 5.

The results of numerical modeling of the air velocity field and the excess pressure field around vehicles are presented in Figs. 6 and 7. Here Car2 is shifted to the right by 4 m.

Car2 gradually moves out of the air rarefaction zone behind Car1, but the compression and rarefaction zones around the cars continue to influence each other. This can be seen from the fact that the pressure increase zone in front side of the Car1 is larger than in front side of the Car2.

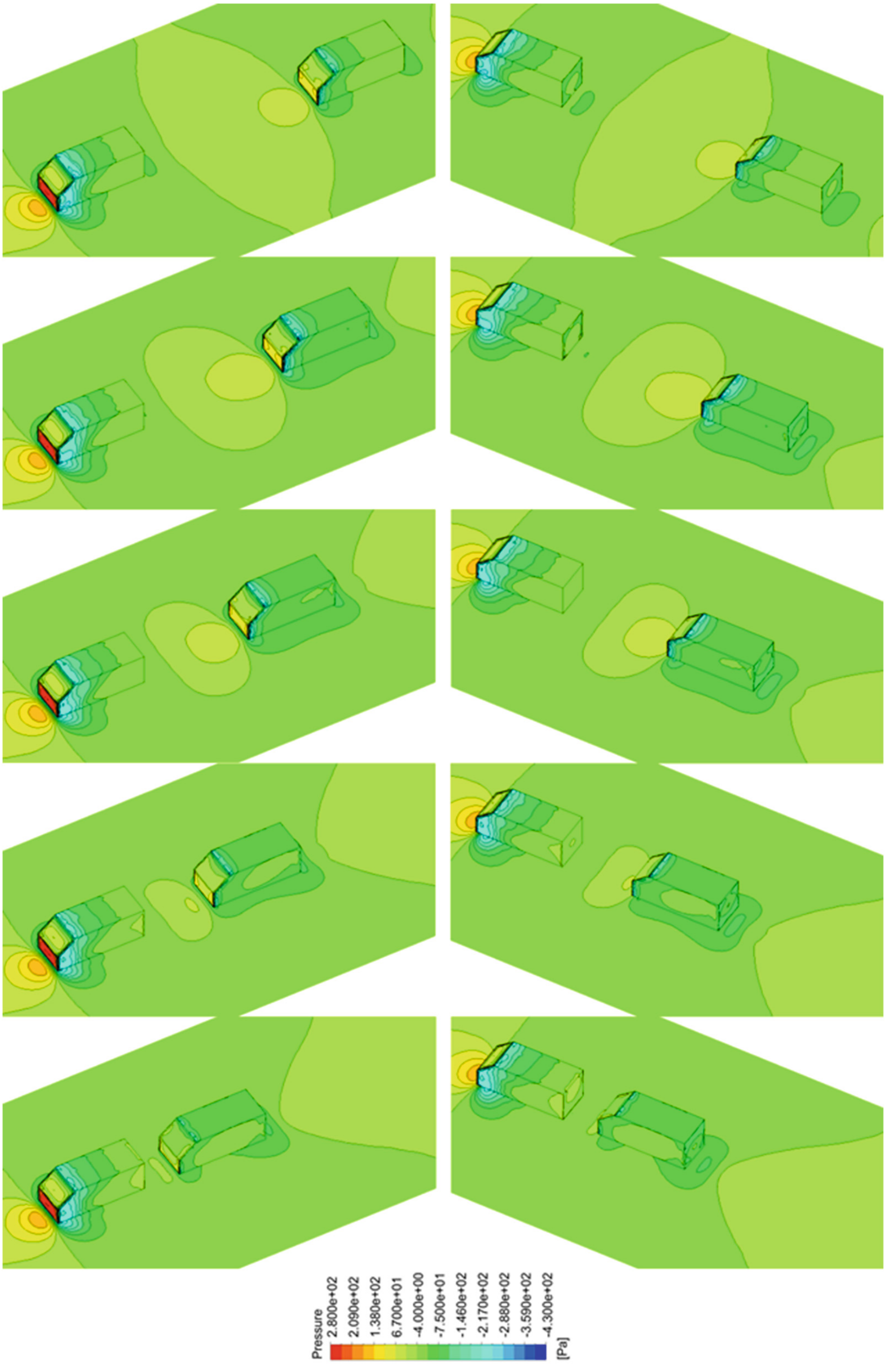

Fig. 4. Change in the field of excess air pressure upon approach

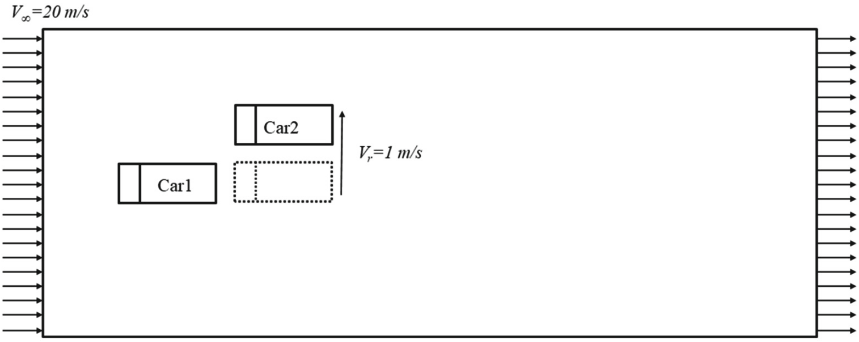

Fig. 5. Shifting to a parallel traffic lane scheme

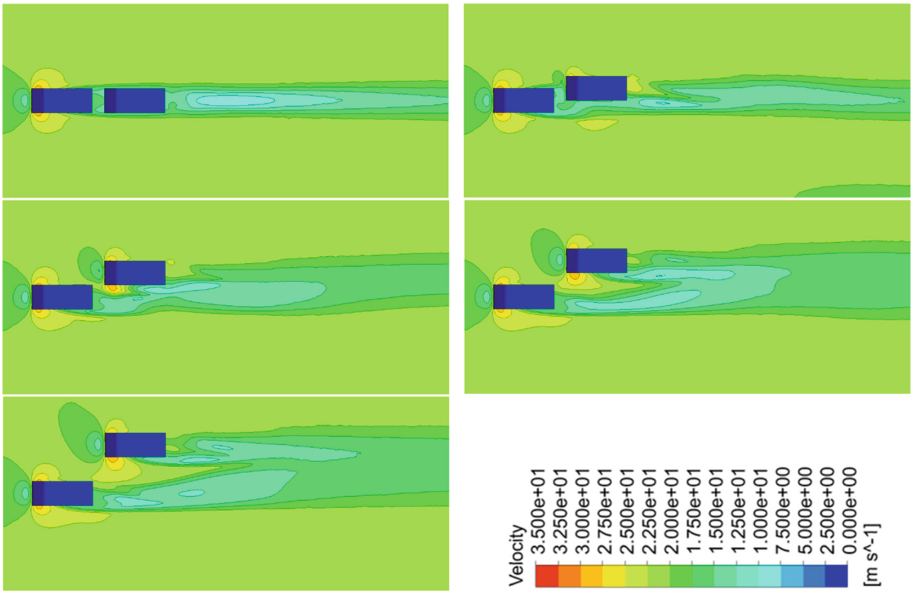

Fig. 6. Change in the field of absolute values of air speeds during shifting traffic lanes.

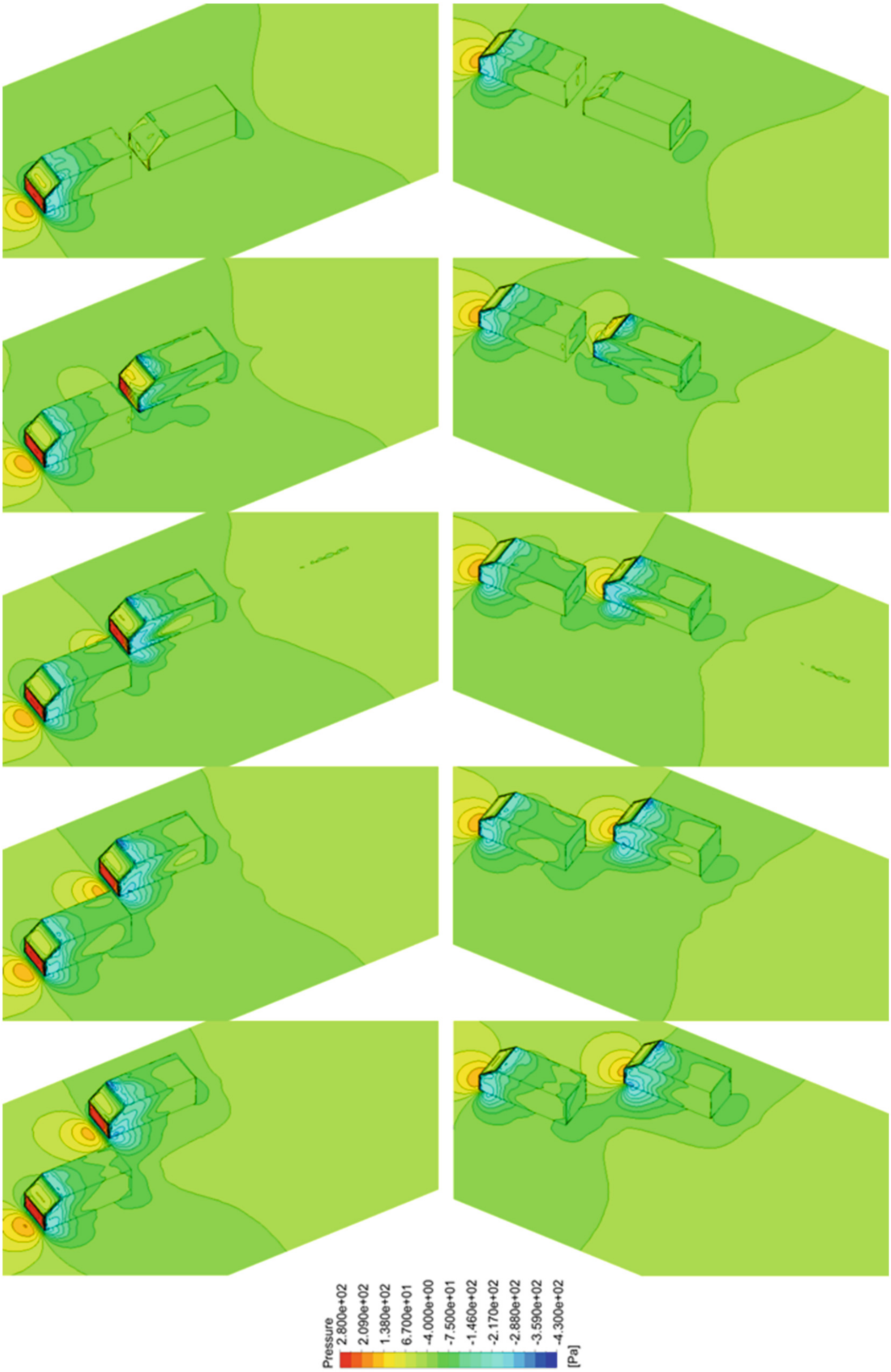

Fig. 7. Change in air pressure field during shifting traffic lanes

5 Study of the Aerodynamic Characteristics of Vehicles During Overtaking

When overtaking, the overtaking vehicle Car2 moves parallel to the overtaken Car1 with a relative speed of $v_r = 2$ m/s, as shown in Fig. 8.

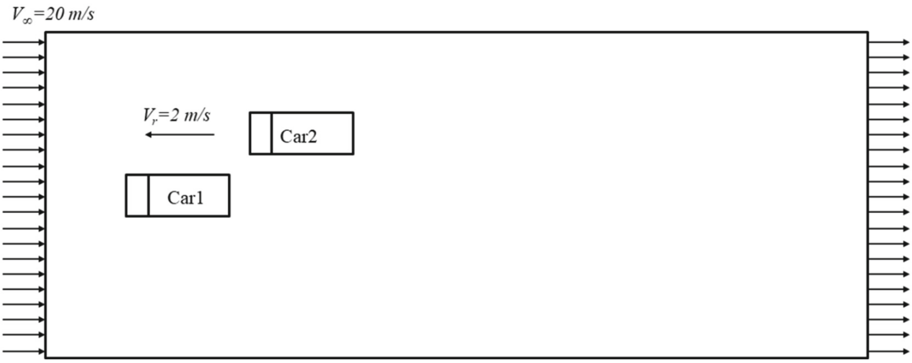

Fig. 8. Overtaking scheme

The results of calculating unsteady velocity and pressure fields are presented in Figs. 9 and 10. In the final position Car2 is 2 m ahead of Car1.

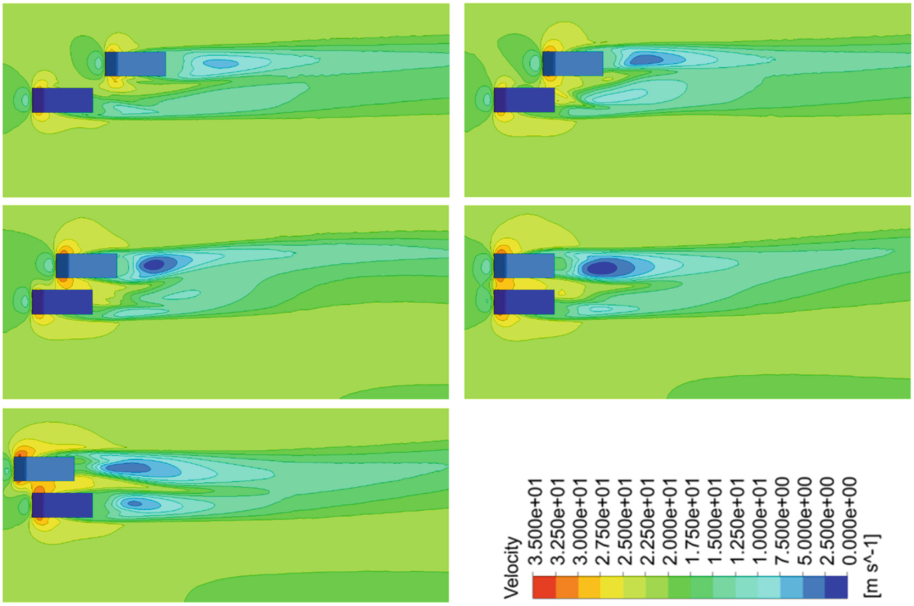

Fig. 9. Change in the air velocity field during parallel movement

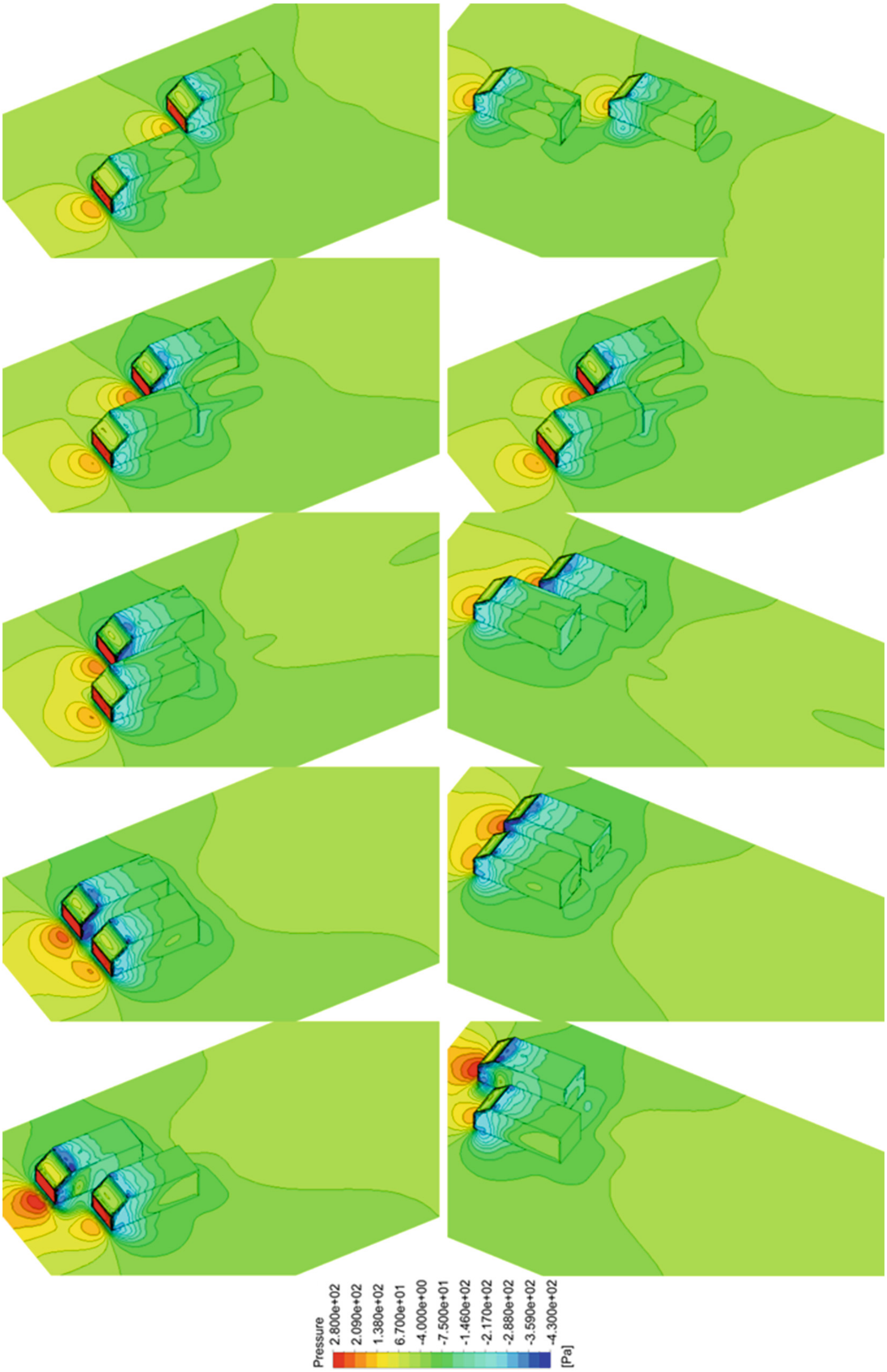

Fig. 10. Change in air pressure field during parallel movement

When driving in parallel, the compression and vacuum zones around the cars continue to influence each other. In this case, the influence of the car moving at a higher speed predominates. As Car2 moves forward, the pressure increase in front of Car2 becomes greater than in front of Car1.

6 Analysis of Numerical Simulation of Overtaking Three Stages

At the first stage, the aerodynamic drag of Car2 is less than the drag of Car1 because Car2 falls into the air rarefaction zone of Car1, as can be seen in Fig. 3. This rarefaction usually becomes noticeable at a distance of (20 – 30) *l* for a car moving at a speed of more than 20 m/s. It pulls Car2 and Car1 towards each other. In this case, the aerodynamic resistance of Car1 decreases compared to the resistance during independent movement due to the fact that the body of Car2 fills the area of low pressure behind Car1. Graph in Fig. 11 shows that the aerodynamic drag coefficient cx of Car2 is less than that of Car1 by approximately 35%.

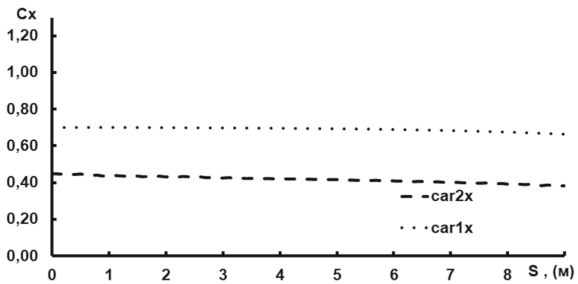

Fig. 11. Aerodynamic drag coefficient of vehicles as the distance decreases

When Car2 enters a parallel lane, the aerodynamic drag of both cars increases as Car2 leaves the area of low pressure Car1. At the same time, while Car2 is behind Car1, the c_x of Car2 remains less than that of Car1 because a noticeable aerodynamic interaction remains, when a distance between the sides of both cars has the order of the width of the car body. This can be seen in the graph in Fig. 12.

Directly when overtaking, two cars move in parallel and their influence on each other gradually equalizes. When the projections of their bodies to the direction of movement coincide, their drag coefficients are equal. This can be seen in the graph in Fig. 13 in position $S = 6$ m. Further, when Car2 comes forward its c_x becomes greater than Car1 c_x.

At the first stage, when the air flow is symmetrical relative to the longitudinal axes of the vehicles, there are no lateral forces. When Car2 moves laterally, the flow around the car becomes asymmetrical. Lateral aerodynamic forces appear, acting on both cars. They strive, on the one hand, to return Car2 to the low pressure zone, and on the other hand, to attract Car1 to Car2. The change in the coefficients of lateral aerodynamic forces c_y is shown in Fig. 14. Lateral aerodynamic forces are approximately four times less than the drag forces at this stage.

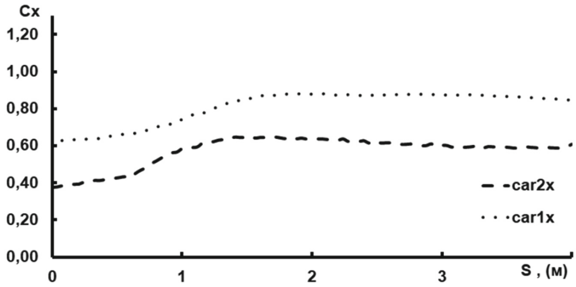

Fig. 12. Aerodynamic drag coefficient of vehicles when Car2 is shifted to a parallel traffic lane

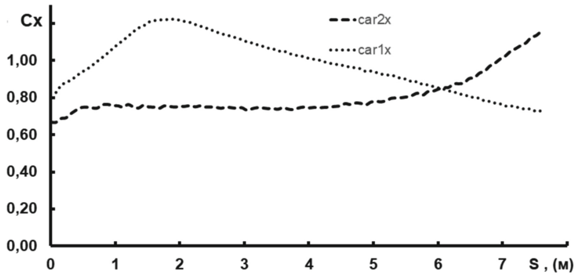

Fig. 13. Aerodynamic drag coefficient of vehicles during overtaking

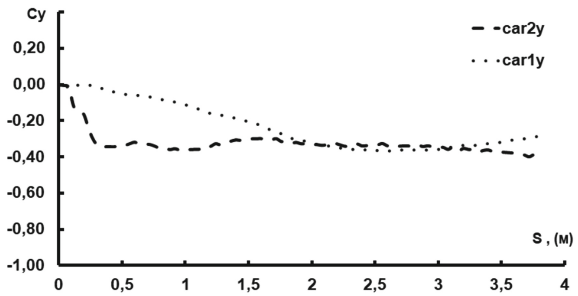

Fig. 14. Coefficient of lateral aerodynamic forces when Car2 is shifted to a parallel traffic lane

Directly during overtaking, while Car1 is 1/3 of a length ahead of Car2, aerodynamic forces push Car1 away from Car2. When Car2 comes forward, it pulls Car1 towards it. The change in the coefficients of lateral aerodynamic forces c_y is shown in Fig. 15.

Similar results were obtained for sedans in article [13], which can be considered as confirmation of the reliability of our results.

Transient analysis gives us insight into the aerodynamic interaction between two vehicles. Thanks to this, it is possible to evaluate the influence of aerodynamic forces acting on vehicles during overtaking. Understanding this influence allows us to design intelligent vehicle driving systems.

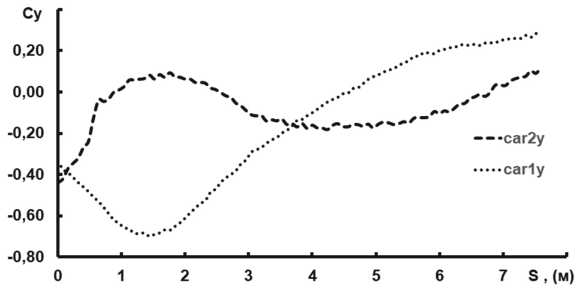

Fig. 15. Coefficient of lateral aerodynamic forces of vehicles during overtaking

7 Conclusions

The problem of numerical modeling of air flow around vehicles is formulated; A numerical experiment technique has been developed for modeling external flows around vehicles in a non-stationary setting.

A study of the flow around vehicles during overtaking made it possible to calculate aerodynamic forces. The dependences of aerodynamic forces on the relative position of vehicles have been established. The lateral aerodynamic forces acting on cars during overtaking are of the same order as the aerodynamic drag forces. These forces must be taken into account in automatic vehicle control systems.

Analysis of aerodynamic forces must be taken into account when designing the body shape and automation of the driving system of advanced unmanned vehicles.

References

1. Memon, Q., Ahmed, M., Ali, S., Memon, A.R., Shah, W.: Self-driving and driver relaxing vehicle. In: 2nd International Conference on Robotics and Artificial Intelligence (ICRAI), pp. 170–174, Rawalpindi, Pakistan (2016). https://doi.org/10.1109/ICRAI.2016.7791248
2. Fathy, M., Ashraf, N., Ismail, O., Fouad, S., Shaheen, L., Hamdy, A.: Design and implementation of self-driving car. Procedia Comput. Sci. **175**, 165–172 (2020). https://doi.org/10.1016/j.procs.2020.07.026
3. Zhao, J., Liang, B., Chen, Q.: The key technology toward the self-driving car. Int. J. Intell. Unmanned Syst. **6**(1), 2–20 (2018). https://doi.org/10.1108/IJIUS-08-2017-0008
4. Sun, H., Karadimitriou, E., Li, X.M., Mathioulakis, D.: Aerodynamic interference between two road vehicle models during overtaking. J. Energy Eng. **145**(2), 1 (2019). https://doi.org/10.1061/(ASCE)EY.1943-7897.0000601
5. Chen, N., Sun, H., Wang, X., Zhang, L.: The aerodynamic characteristics of road vehicles overtaking on bridge deck under crosswinds. Adv. Civil Eng. ID **8847219**, 1–12 (2020). https://doi.org/10.1155/2020/8847219
6. Yudianto, A., Sofyan, H., Fauzi, N.A.: Aerodynamic characteristics of overtaking bus under crosswind CFD investigation. CFD. Lett. **14**(8), 20–32 (2022). https://doi.org/10.37934/cfdl.14.8.2032
7. Menter, F. R., Kuntz, M., Langtry, R.: Ten years of industrial experience with the SST turbulence model. In: Proceedings of the 4th International Symposium on Turbulence, Heat and Mass Transfer, pp. 625–632. Begell House Inc., West Redding (2003)

8. Gritskevich, M.S., Garbaruk, A.V., Schütze, J., et al.: Development of DDES and IDDES formulations for the k-ω shear stress transport model. Flow Turbulence Combust. **88**, 431–449 (2012). https://doi.org/10.1007/s10494-011-9378-4
9. Liu, J., Gu, Z., Huang, T., Li, S., Zheng, L., Sun, K.: Coupled analysis of the unsteady aerodynamics and multi-body dynamics of a small car overtaking a coach. J. Autom. Eng. **233**(14), 3684–3699 (2019). https://doi.org/10.1177/0954407019831559
10. Siggeirsson, E.M., Andersson, N., Wallin, F.: Sensitivity study of the SA-DDES shielding function. In: 2018 AIAA Aerospace Sciences Meeting, pp. 1–12 (2018). https://doi.org/10.2514/6.2018-1355
11. Vatsa, V.N., Lockard, D.P., Spalart, P.R.: Grid sensitivity of SA-based delayed-detached-eddy-simulation model for blunt-body flows. AIAA J. **55**(8), 2842–2847 (2017). https://doi.org/10.2514/1.J055685
12. Gottlieb, S., Shu, C.-W.: Total variation diminishing Runge-Kutta schemes. Math. Comput. **67**(221), 73–85 (1998). https://doi.org/10.1090/S0025-5718-98-00913-2
13. Su, C., Hu, Z., Zhang, Q., Yuan, X., Zhang, C., Wang, Y.: Coupling analysis of transient aerodynamic and dynamic response of cars in overtaking under crosswinds. Eng. App. Comput. Fluid Mech. **14**(1), 1215–1227 (2020). https://doi.org/10.1080/19942060.2020.1803970
14. Tang, H., Tong, D., Zhang, X., Chen, H., Zhou, N.: Study on aerodynamic characteristics between right turning vehicles and straight running vehicles. Innov. Sci. Technol. **2**(2), 25–31 (2023). https://doi.org/10.56397/IST.2023.03.05
15. Johansson, M., Katz, J.: Lateral aerodynamics of a generic sprint car configuration. SAE Trans. **111**, 2331–2338 (2002)
16. Beam, R., Warming, R.: An implicit factored scheme for the compressible Navier-Stokes equations. AIAA J. **33**(2), 393–402 (1978)
17. Huang, T., et al.: Aerodynamic stability of vehicle passing through a bridge tower at high speed under crosswind conditions with different road adhesion coefficients. Alex. Eng. J. **77**, 461–478 (2023). https://doi.org/10.1016/j.aej.2023.07.001
18. Prabhakaran, S., Doss, L.J.T.: Total variation diminishing finite volume schemes for one dimensional advection-diffusion equation and the relationship between flux limiter and mesh parameters. Int. J. Pure Appl. Math. **101**(2), 233–250 (2015). https://doi.org/10.12732/ijpam.v101i2.9

Experimental Research of Electrofinishing Processing of High Precision Parts as a Composition of Convergence Technology

Valeriy Sikulskyi[1], Kateryna Maiorova[1](✉), Serhii Krasovskyi[1], Andrii Rebrin[1], and Viktor Agarkov[2]

[1] National Aerospace University "KhAI", Chkalova Street, 17, Kharkiv, Ukraine
kate.majorova@ukr.net

[2] Deputy CEO of Standardization Issues State Enterprise "Kharkiv Regional Research and Production Center for Standardization, Metrology and Certification", Kharkiv, Ukraine

Abstract. The subject of this study is the convergence technology of finishing processing of high-precision parts. A comparative analysis of known methods of parts finishing processing used in the production of hydraulic, pneumatic aerospace and other transport assembly components according to literature sources has been performed. It has been shown that there are the prospects for further research of methods for creating a integrated convergence technology. Experimental studies have been performed on some samples made of steel 20 with a diameter of 20 mm by the electrosuperfinish scheme. It has been found that in the processing zone a decrease in roughness has occurred from a value of Ra 5.0 to Ra less than 2.0, due to concentration of current density and pulse action on the material with a frequency of 500 Hz – thus, productivity increase is 1.75 compared to the sample under the same conditions in a stationary electrolyte. The experiment has demonstrated either that the proposed method gives opportunity to interrupt the processing, over a wide range of time, which in turn affords regulating the indicators of geometric accuracy both of the part diameter and surface roughness. The analysis of experimental data allows us to conclude about the adequacy of the accepted theory as to the concept of finishing technology for high-precision parts. The scheme of concentration (focusing) of the current flow and the mode for electrosuperfinishing due to the movement of the electrode relative to the part surface has been tested, which resulted in achieving the effect of surfaces polishing and oxidation products removing. It has been shown in this study the further prospects of research in the field of convergence technology of high-precision parts finishing processing, which ensure the geometric accuracy of micro- and nano-precision parts, precision processing of shafts and small-diameter holes, and increasing the processing accuracy up to 0.001 mm.

Keywords: Convergence Technology · Surface Finishing · Superfinishing · Electrochemical Honing · Precision Parts · Accuracy

M. Nechyporuk et al. (Eds.): ICTM 2023, LNNS 1008, pp. 151–162, 2024.
https://doi.org/10.1007/978-3-031-61415-6_13

1 Introduction

There is a wide variety of surface finishing methods for various shapes, sizes and materials of high-precision parts [1]. Such a large number of methods exist because it's the microgeometry of the part surface, formed after the finishing processing, determines its future functional properties and service life [2].

The need to use surface finishing technologies in mechanical engineering is assessed by researchers in different ways, depending on the technological processes they recommend for achieving the parts required parameters. In each specific case, in order to achieve a high level of functional properties of hydraulic aggregates components and friction pairs, it is necessary to create individually the surfaces with required parameters. It should be considered that the choice of finishing technology for cleaning and forming the microrelief is determined by the material, shape, sizes and accuracy of parts, by the subsequent processing, level of surfaces contamination, as well as their purpose, operating conditions, etc. In any case, the main task that should be solved by any of those methods or their combination, chosen by the manufacturer, is to ensure the specified functioning, service life and reliability of assembly components [3].

Therefore, an complex approach to creating the integrated convergence technology for the finishing processing of high-precision parts, which is based on the use of information technologies, and of a combination of nanotechnologies, thermochemical, electrochemical and mechanical processing methods, is a relevant problem.

2 Purpose and Objectives of the Study

The purpose of this work is to provide the specified parameters of quality of high-precision parts surface roughness by convergence technology as finishing processing. This approach should guarantee high reliability and service life of the product as a whole.

To achieve the goal determined, the following tasks have been solved:

- comparative analysis of known methods of parts finish processing used to achieve a required surface roughness parameters.
- experimental studies of electrofinishing processing on the sample of roller processed as an object of, on one hand, convergence technology, combining surface finishing methods of cleaning and surface finishing, on other hand – by processing in a stationary electrolyte.

3 Literature Review and State-of-the-Art of Known Surface Finishing Methods

An attempt to systematize a variety of surface finishing processes has been made in the study [3], which presents the current state of high-performance, effectively controlled in automated production methods for surface finishing of mechanical and physical-technical methods for processing the parts surfaces. It has been shown in the study the capabilities of advanced conventional and abrasive machining, and examples of their highly effective integrated application in production the parts made of difficult-to-cut materials.

However, the authors of this study have identified the **energy** methods as the most promising and progressive ones for the parts surface finishing [4]. At the same time, a number of methods that directly relate to a surface finishing are not sufficiently presented: superfinishing, honing, polishing, and others, which consider the task of providing minimal roughness and high accuracy of parts.

The study [5] shows that tool wear is one of the factors that directly affects the quality, the cost of the part and the expenses for production in general. This study describes the prediction of surface roughness value (Ra) and tool temperature (°C) for turning using artificial neural network (ANN) method and multilinear regression model (MLRM). The results have shown that the ANN method is more effective than the regression model to estimate surface roughness and tool temperature, but requires practical testing and confirmation of the adequacy of the method and model. Testing of surface roughness prediction is presented in the study [6] on the holes of aerospace structural assembly components made of a polymer composite material. However, despite their positive results, they are not sufficient to assess the quality of the metal parts surfaces, which requires additional research.

Ultra-precision machining (UPM) as a type of nanotechnology is already a usual practice of mechanical processing of solid materials. In [7] it is reported that components of optical devices require ultra-precision processing. UPM can provide high precision of complex components and devices with nanometric level of surfaces processing. However, the process requires the deep comprehensive study as the non-linear and complex nature of the UPM process arises a major challenge to predict the parameters of surface formation and its finishing. Recent achievements in Industry 4.0 and machine learning provide effective means to optimize UPM process parameters, particularly by a in-process monitoring and forecasting, thus avoiding the traditional trial-and-error method. The study [7] attempts to provide a comprehensive and critical review of state-of-the-art of the surface monitoring and forecasting in UPM processes.

An analysis and prognosis of further research in this area using artificial intelligence (AI) and digital technologies to solve practical UPM problems in real time is also presented here in. However, as in the studies [4, 5], as in [7] one there is no approbation, which requires the further studies. The study [8] shows theoretical results on the formation the surface roughness of edge of conjuncted surfaces and it has been found that with increasing the surfaces roughness indicators, the edge fillet radius also increases. Data from the study [8] can be used as an addition to the studies [5] and [6] with subsequent testing.

The study [9] has presented the modeling of surface roughness of processed parts depending on cutting parameters (spindle speed, depth of cut, and feed rate) and the processing vibration in the end-milling process. To determine the effect of cutting parameters on surface roughness the analysis of variance has been used. The results show that the combined influence of spindle speed and depth of cut significantly influences the surface roughness. The comparison of the prediction performance of multiple regression models and neural network-based models shows that ANN models provide higher prediction accuracy for all training data with $R = 0.96$ and root mean square error (RMSE) $=$ 3.0% compared to regression models with $R = 0.82$ and RMSE $= 7.57\%$. Independent processing tests have been performed to check the modelling results; the results are that the ANN model, based on cutting parameters with mechanical vibration, has a higher average prediction accuracy (93.14%) than the models with three cutting parameters. Finally, the possibility of using the predictive model as the basis for developing an online surface roughness recognition system has been successfully demonstrated in a contour milling test. This study shows that predictive models based on cutting process parameters with considering the machining stability will provide the accuracy prediction in application to milling processes.

In the study [10], surface roughness has been considered as an important measurable parameter that helps to ensure the quality of the ready product. The authors explain that the use of cutting fluid in the processing zone minimizes heat generation in the tool-workpiece interface, which reduces the surface roughness. In this study, cutting fluid with aluminum oxide nanoparticles of 30 and 40 nm in size is used while turning the AISI 304 steel. The input parameters selected for the study include cutting speed, depth of cut, feed rate, and nanoparticle concentration. Three machine learning-based models, including linear regression (LR), random forest (RF), and support vector machine (SVM), are further used to estimate the surface roughness and compare the experimental values with the predicted values. The coefficient of determination (R2), mean absolute percentage error (MAPE), and mean square error (MSE) have been used to evaluate the accuracy of the predicted values. Random Forest outperformed the other two models at both 30 and 40 nm particle sizes with R-squared of 0.8176 and 0.7231, respectively. Therefore, the research results in [10] present a new approach to predict surface roughness by changing the particle size of cutting fluid, which can save time and waste both of material and energy. However, despite the positive results of the selected models, they require clarification for each specific material with the selection of coolant nanoparticles. An addition becomes the study [11], which explores a method based on the process of magnetorheological finishing (MRF), the mechanism of which is to reduce the roughness Ra on the outer surface of cylindrical parts of high precision made of non-magnetizable materials. The test samples in this study are made of non-magnetizable, soft and lightweight aluminum (Al). The apparatus used for this experiment perform two main motions: the first uses linear alternating motion to improve processing conditions, and the second one uses rotational motion of the sample. The experimental results have allowed us to draw a conclusion about the feasibility of using this method in surface finishing of cylindrical aluminum parts.

The study [12] compares thermochemical, gas detonation and thermo-energy methods, where the advantages of the last one over the others have been presented. It should be noted that to ensure the specified roughness of high-precision parts when using the thermal pulse method, the main thing is to provide the optimal conditions of surface processing. That is, the melting of irregularities and burrs should be performed in way that guarantee the avoiding of negative consequences due to effects of high-temperature and aggressive products of combustion. The authors of the study [12] state that such conditions shall be met by matching the characteristics of the heating source and the part, followed by organizing the process of local removal of combustion products. However, the study has not indicated a method or technique to set the thermal pulse processing modes for high-precision parts. Intuitively, the authors have determined these modes experimentally, which is very labor-intensive and expensive way. The research is complemented by the study [13], in which the authors have presented process automation using a digital twin. However, despite the positive results obtained in this study, they are not sufficient for using in manufacturing and require additional research.

Today, an alternative is the electrochemical method, which is based on the process of anodic electrochemical dissolution of materials in an electrolyte environment under the influence of a high-density current. A number of studies has presented the positive results of electrochemical honing technology using the example of processing the parts of gas turbine engines when: stitching precision holes of small diameter and complex geometric shape [14]; processing of the flow part of thin-walled compressor blades and blisks; microstructuring and surface texturing of parts [15]; shaping of elements of promising seals; processing of parts made of difficult-to-cut materials [16].

Provision of high quality surfaces of parts such as gears based on the electrochemical method is also shown in the study [17]. This study contains a detailed description of the process principle, technological capabilities, equipment details, influence of input parameters, regression models developed, aspects of machined surface integrity. The authors note this method as one of the most potential microfinishing processes where material is removed by anodic dissolution combined with the mechanical action of abrasive grains. The prospects and importance of such superfinishing operations in the technology of manufacturing the high-precision parts have been confirmed by scientists from many countries [18–20]. However, their main disadvantage is that it is practically a craft production, during which it is difficult to ensure high quality surfaces of parts with increased precision and especially the specified roughness.

Considering the worldwide experience in the use of finishing and superfinishing methods for processing the high-precision parts, as well as the results of analysis of literature, in order to achieve the goal of such parts precision rate and increase their service life, there is a need in a further research and in the creation of a unified integrated convergence technology. An attempt to create it is shown in the concept of the authors of the study [21]. An explanation of the proposed concept could be as follows. For workpieces with a surface roughness of about Rz 10…40, the thermal pulse processing alone is not enough to obtain mating surfaces, with low surface roughness, and as a result, the honing and superfinishing become compulsory additional operations. And, vice versa, processing of the smoother surfaces by thermal pulse processing, especially after honing and after superfinishing, worsens the surface roughness, which has been experimentally proven by the authors of the study [5]. Electrochemical processing of all surfaces of parts shall be performed as a final operation, the purpose of which is to increase the smoothness of the parts surfaces, to remove micro and nanoparticles by chemical dissolution, while achieving individual dimensional accuracy with deviations of up to 0.001 mm.

In comparison with the well-known superfinish technology, the electrosuperfinish has the base which has been proposed by the authors of the study [21] as the principle of exposure to a high-density focused current of constant or pulsed action (6), which is located in the superfinish holder (3) and moves relative to the surface of the part (1) (Fig. 1). During processing, rapid dissolution of surfaces protrusions in the rough relief occurs, and in the "cavities" of parts surfaces, dissolution occurs in a slow mode. Therefore, for processing parts such as "shafts" it is advisable to use electro-superfinishing, and for the parts with processing of internal surfaces and holes – electro-honing.

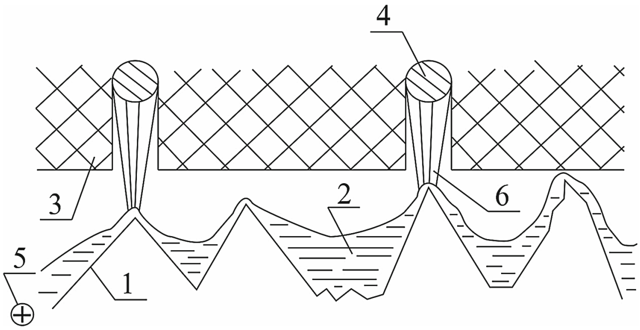

Fig. 1. Scheme of concentration (focusing) of the current flow during electrochemical superfinishing, where are profile of the part roughness (1); top contour of the oxide film (2); superfinishing tool holder (3); cathode (4); anode – processed part (5); focused current flow (6)

The product (1) immersed in the electrolyte is covered with an oxide film (2), which constantly dissolves and forms again throughout the entire process. It shall be emphasized that one of its functional purposes is to create a protective environment between the metal and the electrolyte. Processing of the metal surface occurs directly under the film due to the exchange of electrons and ions between the anode and electrolyte. It should be noted that the thickness of the formed film is always less at the peaks of the surface roughness, therefore it is from those peaks that the process of metal dissolution starts. And vice versa, in the valleys of surface irregularities the film layer is thicker and slower exchange processes of charged particles are observed in them. The speed of surface polishing shall be influenced by changing the temperature, current and stirring the electrolyte.

A distinctive peculiarity of the proposed scheme that for the concentrating (focusing) the current flow during electrosuperfinishing is used the movement of the electrode relative to the surface of the part, which allows the following:

- to increase the current density by reducing the width of the cathode gap;
- to use a direct current source instead of a pulsed one, while achieving a polishing effect;
- to remove oxidation products while maintaining the cleanliness of the surface of parts;
- to intensify a mixing of the solution and to form the oxide film of a stable size.

4 Experimental Study of Electrosuperfinishing Processing on the Example of Processing the Roller

Experimental studies have been performed on an installation for electrochemical processing of small-sized parts in a stationary electrolyte, model EZI-2M (Fig. 2). The samples have been made of cylindrical steel 20 with a diameter of 20 mm and a length of 60 mm. The sample rotation motor has been powered by an EZI-2M installation with the ability to regulate both the DC current and voltage values.

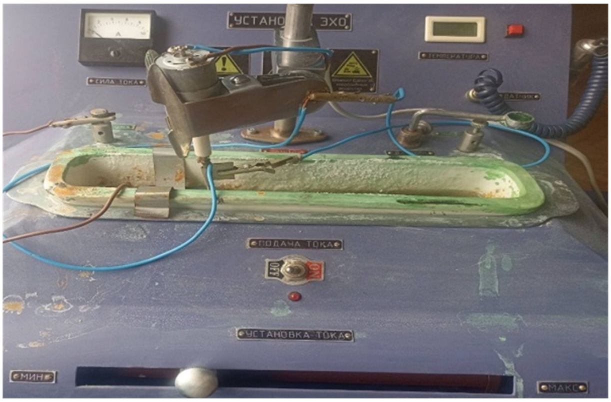

Fig. 2. Installation for electrochemical processing of parts model EZI-2M.

The processing has taken place in a 10% sodium chloride solute at a temperature of 30 °C and at sample rotation speed of 500 1/min. The current value has been set for all samples to 1 A, which corresponded to a current density in the processing zone of 2.2–2.5 A/cm^2. Measurements have been performed periodically, in 10-min increments, in the range from 0 to 60 min. After each processing interval, the roughness of the sample has been measured in 3 sections along its length and in 4 positions along the radius of each section. The sample has been divided into three zones: 1-processing zone without current concentration; zones 2 and 3 have had a concentrated current flow along the generatrix of the cylindrical sample. Surface roughness has been measured with a TMR-120 device.

The studied sample has been installed in a special cassette of the sample processing unit using the electro-finishing method with the possibility of rotation driven by a motor (Fig. 3).

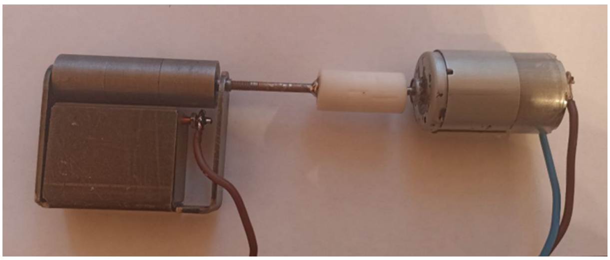

Fig. 3. External view of the sample processing unit using the electrofinishing method.

There are the measurement results in Table 1. The roughness values measured at 4 points of one section are reduced to the average value, which more clearly reflects changes in roughness after processing (Table 2).

Table 1. Results of measurements of sample roughness at different processing time.

Parameters	Surface Roughness, Ra							
	min	0	10	20	30	40	50	60
Zone 1	Point 1	4,58	4,21	4,2	4,18	3,15	3,15	3,15
	Point 2	5,52	4,63	4,6	4,6	4,15	4,15	4,15
	Point 3	4,47	4,13	4,1	4,0	3,54	3,54	3,54
	Point 4	4,83	4,67	4,42	4,3	3,14	3,14	3,14
Zone 2	Point 1	5,20	4,83	3,04	2,83	2,53	2,20	2
	Point 2	5,07	2,21	2,21	1,94	1,94	1,72	1,52
	Point 3	5,23	2,28	2,28	2,19	2,11	2,04	1,79
	Point 4	4,43	2,39	2,37	2,09	2,0	1,96	1,73
Zone 3	Point 1	4,31	3,91	2,71	2,33	2,09	2,0	1,82
	Point 2	4,24	2,28	2,28	2,17	2,04	1,92	1,64
	Point 3	4,52	2,37	2,35	2,22	2,22	1,68	1,44
	Point 4	4,57	4,08	2,5	2,5	2,42	2,38	2,03

Table 2. The average surface roughness values (Ra) in the measured sections of the workpiece.

Time, min	0	10	20	30	40	50	60
Zone 1	4.845	4.41	4.33	4.27	3.50	3.5	3.5
Zone 2	4.9825	2.928	2.48	2.26	2.15	1.98	1.76
Zone 3	4.41	3.16	2.46	2.31	2.19	2.0	1.73

A graphical representation of the change in the samples surface roughness over the processing time has been presented in Fig. 4. Analysis of the graph of the change in the samples surface roughness over the processing time shows that in the zone of conventional electrochemical processing in a stationary electrolyte there is a smooth decrease in roughness from a value of Ra 5.0 to Ra about 3.5 under the conditions defined. These data are confirmed by the studies of other authors [9]. In the processing zone with a concentrated current density and pulsed action on the material with a frequency of 500 Hz, a decrease in roughness has occurred from a value of Ra 5.0 to Ra less than 2.0, which is 1.75 more productive compared to the sample under the same conditions defined in a stationary electrolyte. This confirms the more significant effect of pulsed current on the process of dissolving the micro-protrusions of surface roughness, which is obviously explained by the authors' assumptions about the concentration (focusing) of the current flow during the movement of the electrode over micro-roughness, and it dissolves exactly the peaks of the protrusions more effectively.

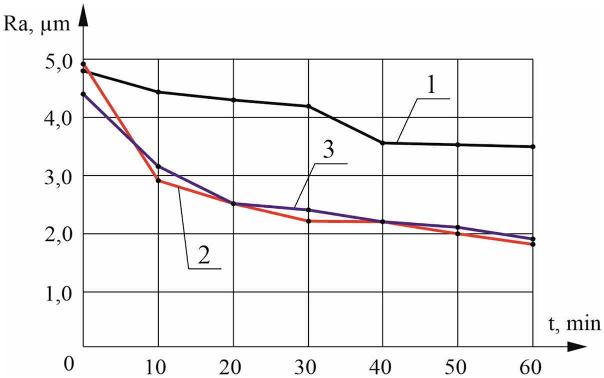

Fig. 4. Graph of changes in the roughness of samples during processing: a zone with conventional electrochemical processing in a stationary electrolyte (1) and a zone of processing with a concentrated current density and pulsed action on the material with a frequency of 500 Hz (2) and (3)

At the same time, in a processing zone with a concentrated current density and pulsed action on the material with a frequency of 500 Hz, such a reduction in roughness occurs more effectively at the initial stage of processing. So, in the first 10 min of processing, the roughness has decreased by 60% of the total decrease in 60 min. This fact once again confirms that large microroughnesses produce concentration (focusing) of the current flow to a greater extent during the movement of the electrode over the microroughnesses.

Simultaneously the measurements of the diameter of the samples have been performed after each stage of processing. The nominal diameter of the sample has been 20 mm, therefore Table 3 shows only changes in diameters in three zones along the length of the sample relative to the initial diameter in the measured section.

Table 3. Results of measurements of changes in sample diameters at different processing time.

Processing time, min	0	10	20	30	40	50	60
Δd, мм Zone 1	0	0,0035	0,0064	0,0048	0,0024	0	0
Δd, мм Zone 2	0	0,024	0,05	0,08	0,084	0,12	0,16
Δd, мм Zone 3	0	0,028	0,055	0,083	0,089	0,16	0,18

The measurements have been performed with a micrometer clamp with a division value of 0.002 mm. A graphical representation of the change in sample diameters over processing time is presented in Fig. 5.

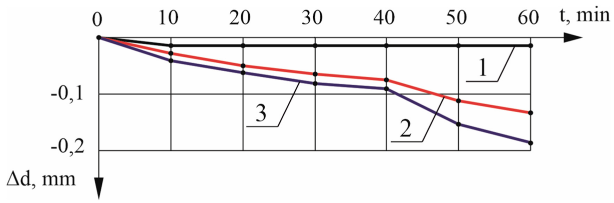

Fig. 5. Graph of changes in sample diameters during processing time of zone (1) with conventional electrochemical processing in a stationary electrolyte and zones (2) and (3) with processing of the material with a concentrated current density and pulsed action with a frequency of 500 Hz

Analysis of the data of both graphs and tables has shown that the results of measuring the diameters of the samples over the processing time have had the same nature as the change in the roughness of the samples during the processing time. The difference in the gradient of the characteristics of changes in sample diameters during processing time compared to the characteristics of changes in the roughness of samples is obviously explained by different measuring tools to determine these two quantities. Although there is correlation between roughness and the solid body boundary, apparently the real experiments are not enough to define it. However, the smooth nature of the graphs of changes in the roughness and diameters of the samples suggests that this processing method give opportunity to interrupt the processing over a wide range of time and, thus, achieve the high accuracy of product diameters (up to 0.001 mm) while simultaneously the surface roughness of the processing part surface improves.

Further improvement of the presented convergence technology for finishing processing of high-precision parts could be continued in research of technologies of coating by nanomaterials to provide the necessary physical and chemical surfaces properties of parts.

5 Conclusion

A comparative analysis of known methods of parts surface finishing, used to achieve the required surface roughness, has shown the promising prospects of convergence technology of high-precision parts producing. It is shown that among the many processes, which by their characteristics could be the components of convergence technology, it's the electrochemical processing have a prominent place, as well as the method and device for electrosuperfinishing proposed by the authors.

Experimental researches of electrofinishing processing in comparison with processing in a stationary electrolyte using the samples of roller surface fininshing have shown the effectiveness of the pulsed current using in the process of dissolving the microprotrusions of surface roughness. It has been found that in the processing zone with a concentrated current density and pulsed action on the material with a frequency of 500 Hz, a decrease in roughness have occurred from a value of Ra 5.0 to Ra less than 2.0, which is 1.75 more productive compared to the sample processed under the same conditions in a stationary electrolyte. Also, the analysis of the experimental results has discovered an active decrease in roughness during the first 10 min of processing, which proves the adequacy of the accepted theory about the concentration (focusing) of the current flow during the movement of the electrode over micro-roughness.

Convergence technology for high-precision parts has been developed in order to achieve precision and increase of the service life of such parts. It has been noted that the proposed processing method allows to interrupt the process over a wide time range, which resulted in achieving the high accuracy (up to 0.001 mm) while simultaneously improving the surface roughness of the processed part. Further research may involve the implementation of experimental study on more complex high-precision parts with the determining of rational conditions to obtain the necessary precision parameters of such parts surfaces.

References

1. Gupta, K., Gupta, M.K.: Developments in nonconventional machining for sustainable production: a state-of-the-art review. Proc. Inst. Mech. Eng. Part C. J. Mech. Eng. Sci. **233**(12), 4213–4232. (2019). https://doi.org/10.1177/0954406218811982
2. Khorasani, A.M., Yazdi, M.R.S., Safizadeh, M.S.: Analysis of machining parameters effects on surface roughness: a review. Int. J. Comput. Mater. Sci. Surf. Eng. **5**(1), 68–84 (2012)
3. Gillespie, L.K.: Deburring and Edge Finishing Handbook, p. 404. Society of Manufacturing Engineers, Dearborn (1999)
4. Unune, D.R., Mali, H.S.: Current status and applications of hybrid micro-machining processes: a review. Proc. Inst. Mech. Eng. Part B. J. Eng. Manuf. **229**(10), 1681–1693 (2015). https://doi.org/10.1177/0954405414546141
5. Bilgiç, H.H., Güvenç, M.A., Çakır, M., Mistikoglu, S.: A study on prediction of surface roughness and cutting tool temperature after turning for S235JR steel. Konya J. Eng. Sci. **7**, 966–974 (2019). https://doi.org/10.36306/konjes.624725
6. Maiorova, K., Vorobiov, I., Andreev, O., Lupkin, B., Sikulskiy, V.: Formation of the quality of holes obtained by drilling in aviation structures made from polymer composite materials. Eastern-Eur. J. Enterp. Technol. **3**(123), 59–67 (2023). https://doi.org/10.15587/1729-4061.2023.279618
7. Manjunath, K., Tewary, S., Khatri, N., Cheng, K.: Monitoring and predicting the surface generation and surface roughness in ultraprecision machining: a critical review. Machines **9**(12), 369 (2021). https://doi.org/10.3390/machines9120369
8. Sikulskyi, V., Maiorova, K., Bychkov, I., Myronova, S., Sikulskyi, S.: Shape of part edges with the various surface finish of the adjacent surfaces. In: Nechyporuk, M., Pavlikov, V., Kritskiy, D. (eds.) Integrated Computer Technologies in Mechanical Engineering - 2022. ICTM 2022. LNNS, vol. 657, pp. 134–145. Springer, Cham (2023). https://doi.org/10.1007/978-3-031-36201-9_12
9. Lin, Y.-C., Kung-Da, W., Shih, W.-C., Hsu, P.-K., Hung, J.-P.: Prediction of surface roughness based on cutting parameters and machining vibration in end milling using regression method and artificial neural network. Appl. Sci. **10**(11), 3941 (2020). https://doi.org/10.3390/app10113941

10. Dubey, V., Sharma, A.K., Pimenov, D.Y.: Prediction of surface roughness using machine learning approach in MQL turning of AISI 304 steel by varying nanoparticle size in the cutting fluid. Lubricants **10**(5), 81 (2022). https://doi.org/10.3390/lubricants10050081
11. Gheisari, R., Ghasemi, A.A., Jafarkarimi, M., Mohtaram, S.: Experimental studies on the ultra-precision finishing of cylindrical surfaces using magnetorheological finishing process. Prod. Manuf. Res. Open Access J. **2**(1), 550–557 (2014). https://doi.org/10.1080/21693277.2014.945265
12. Losev, A., Bychkov, I., Selezneva, A., Shendryk, V., Shendryk, S.: Cleaning of parts with detonating gas mixtures. In: Tonkonogyi, V., Ivanov, V., Trojanowska, J., Oborskyi, G., Pavlenko, I. (eds.) Advanced Manufacturing Processes III, pp. 602–612. Springer. Lecture Notes in Mechanical Engineering, Cham (2022). https://doi.org/10.1007/978-3-030-91327-4_58
13. Shypul, O., Garin, V., Tkachenko, D., Zaklinskyy, S., Tryfonov, O., Plankovskyy, S.: Development of a digital twin of reservoir filling by gas mixture component. In: Shkarlet, S., et al. (eds.) Mathematical Modeling and Simulation of Systems MODS 2022 LNNS, vol. 667, pp. 85–98. Springer, Cham (2023). https://doi.org/10.1007/978-3-031-30251-0_7
14. Ruszaj, A., Gawlik, J., Skoczypiec, S.: Electrochemical machining – special equipment and applications in aircraft industry. Manage. Prod. Eng. Rev. **7**(2), 34–41 (2016). https://doi.org/10.1515/mper-2016-0015
15. Rao, P.S., Jain, P.K., Dwivedi, D.K.: Electro chemical honing (ECH) of external cylindrical surfaces of titanium alloys. Procedia Eng. **100**, 936–945 (2015). https://doi.org/10.1016/j.proeng.2015.01.452
16. Sudhakar Rao, P., Dwivedi, D.K. Jain, P.K.: Study and prediction of surface finish of external cylindrical surfaces of titanium alloys by electro-chemical honing (ECH) Process. Processing and Fabrication of Advanced Materials – XXIII, pp. 557–565. https://doi.org/10.1016/j.proeng.2015.01.452
17. Misra, J.P., Jain, P.K., Dwivedi, D.K.: Electrochemical honing – a novel technique for gear finishing. In: Katalinic, B. (ed.) DAAAM International Scientific Book, pp. 365–383. DAAAM International, Vienna (2011). https://doi.org/10.2507/daaam.scibook.2011.29
18. Voronko, V., Tkachenko, I., Dyachenko, Y., et al.: Methodology for calculating the productivity of electrochemical machining in stationary electrolyte. In: Nechyporuk, M., Pavlikov, V., Kritskiy, D. (eds.) Integrated Computer Technologies in Mechanical Engineering - 2021. ICTM 2021. LNNS, vol. 367, pp. 47–56. Springer, Cham (2022). https://doi.org/10.1007/978-3-030-94259-5_5
19. Zhang, Y., Xu, Z., Xing, J., Zhu, D.: Effect of tube-electrode inner diameter on electrochemical discharge machining of nickel-based superalloy. Chinese J. Aeronaut. **29**(4), 1103–1110 (2016). https://doi.org/10.1016/j.cja.2015.12.016
20. Kar, S., Patowari, P.K.: Electrode wear phenomenon and its compensation in micro electrical discharge milling: a review. Mater. Manuf. Process. **33**(14), 1491–1517 (2018). https://doi.org/10.1080/10426914.2018.1453144
21. Sikulskiy, V., Maiorova, K., Vorobiov, I., Fomichev, P., Myronova, S.: Convergence technology of vehicle parts surface finishing. In: XIV International Scientific Conference on Transport Problems 2022, Katowice – Silesia, 29 June – 1 July 2022, Katowice, vol. 18, is. 1, pp. 117–127 (2023). https://doi.org/10.20858/tp.2023.18.1.10

ML-Approach for Modeling Viscoelastic and Physically Nonlinear Materials Based on Symbolic Regression

Nataliia Fomenko(✉) and Oleksiy Larin

National Technical University, Kharkiv Polytechnic Institute, Kharkiv, Ukraine
nataliia.fomenko@infiz.khpi.edu.ua, oleksiy.larin@khpi.edu.ua

Abstract. This paper explores the application of symbolic regression, a technique rooted in genetic programming, to model the nonlinear hyperelastic and viscoelastic deformation behaviors of materials. The research focuses on two theoretical models (Neo-Hookean and Mooney-Rivlin) for hyperelastic material identification and generalized linear viscoelastic model. The models in their combinations are discovered in the context of soft bio tissue deformation. Synthetic datasets are generated based on these models, and symbolic regression is employed to obtain mathematical expressions representing the material behavior. The study presents the results of an implementation of the symbolic regression procedure based on those datasets in the form of analytical expressions and graph-tree structures. The iterative dependencies of the convergency of the symbolic regression for the analyzed cases are carried out. The results showcase the capability of the symbolic regression approach in capturing the time-dependent and complex nature of viscoelastic deformation. However, the problem of identification of the models that represent periodic time-varying that is set in a parametric way is figured out. It is shown the iterative dependencies of the convergency of the symbolic regression for the analyzed cases.

Keywords: Symbolic Regression · Viscoelasticity · Hyperelastic Materials · Data-driven material modeling

1 Introduction

Many engineering applications required to use rubber-like and plastics materials that demonstrate hyperelasticity with geometrical and physical nonlinearity as well as viscoelasticity behavior. The last is also corresponds with the problems of modeling of soft biomaterials. Mathematical models of such material behavior are used in a wide range of practical applications, where computer simulations help to design, synthesis, analysis and prognosis. These models based on different theoretical statements but always rely on natural experiments.

Despite the fact that there are many different complex nonlinear models when applied to real data, the convergence is often unsatisfactory. It is not obvious which model is the best. Multiparameter complex models should be flexible to describe complex behavior

M. Nechyporuk et al. (Eds.): ICTM 2023, LNNS 1008, pp. 163–172, 2024.
https://doi.org/10.1007/978-3-031-61415-6_14

but they stack with the poor and non-guaranteed convergence of traditional nonlinear regression procedures. Moreover, complex models are difficult to use in further analyses from the computational point of view.

Relatively modern trends in this field are directed at soft computing and machine learning [1] approaches for the identification of the material models and their parameters best fitting. From different data-driven frameworks, a method of symbolic regression was recently proposed for a wide range of material science and mechanics applications and could be a promising tool. Successful cases of symbolic regression usage are found in the generation of analytical equations for wind speed forecasting [2]; in the problem of the collision of two masses, which leads to obtaining asymptotic expansions [3]; physical-based material science problems like an effective many-body multi-scale potential model [4]. An interesting, but slightly exotic application of symbolic regression is found in the solution of the problem of efficient specific subject area knowledge integration [5].

In this paper, we propose to study the usage of the symbolic regression approach for obtaining the models of nonlinear hyperelastic and viscoelastic material deformation.

2 Symbolic Regression

Regression analysis is the main statistical method for building mathematical models of objects or phenomena based on experimental data. So, in simple terms, we're looking for a relationship between the input (independent variables) and the output (dependent variable). The goal is to find a mathematical equation that best fits the data and allows making predictions about the output based on the input. It can be done in many ways. Conventional regression methods define the model structure in advance and then optimize model parameters. Symbolic regression, however, derives simultaneously the structure and parameters of the model based on the data.

2.1 Genetic Programming

Symbolic regression is usually implemented using genetic programming (GP). It is a method for automatically creating computer programs from a problem statement, which is a subtype of evolutionary algorithms that use the principles of natural selection to evolve a population of programs to solve a problem. The main distinguishing feature of GP is that it does not select the best values of model parameters, but searches for a solution by changing the structure of the model. But at the same time, the obtained structure may not give us any idea about the actual operation of the system [6].

In GP, solutions are represented as hierarchical structures, often in the form of tree structures. These trees are composed of functions, that represent operations or actions and terminals that represent variables or constants. The tree structure is evolved over time to generate candidate solutions. A population of candidate programs is randomly generated to start the evolutionary process. Each program in the population corresponds to a tree structure. The fitness of each program is evaluated by measuring how well it performs the desired task. The user defines a fitness function that quantifies the performance of a program with respect to the problem at hand.

First, the user must define some basic building blocks (mathematical operations and variables to be used); then the algorithm tries to build a model using them. Then GP uses a physical symbol system divided into two sets. The first set, called the terminal set, contains the symbols for the independent variables, as well as parameter constants, if necessary. The content of this set is determined only by the nature of the problem to be solved. All the basic operators used to form the function are in a second set called the function set. For example, the second set may contain arithmetic operators (−, +, *, /), and possibly others such as log, sqrt, and sin(), depending on the intended complexity of the regression [6].

2.2 Technical Stack

Today, a number of ready-made programmed solutions for using symbolic regression are presented.

- gplearn is a Python package, that extends the scikit-learn machine learning library to perform GP with symbolic regression [7].
- Deep Symbolic Optimization (DSO) is a deep learning framework for symbolic optimization tasks [8, 9].
- PySR is developed alongside the Julia library SymbolicRegression.jl, which forms the powerful search engine of PySR [10].
- symreg – Python library, that works with a modified NSGA-II algorithm, and applies NumPy functions for vectorized evaluation of input [11].
- QLattice is a supervised machine learning tool for symbolic regression, based on the Python module Feyn, which defines the criteria that the models must meet [12].
- Operon – C++ framework for symbolic regression that uses GP [13].

In this study we opted for Deep Symbolic Optimization. The main features of this package are listed below, and the hyperparameters that were varied to achieve better results on our data are described.

Three main hyperparameters are used to tune the algorithm for its better validation:

1. Functional of quality that is formulated from the sense of metrics that is used.
2. A policy optimizer, which is an algorithm for optimizing the parameters.
3. Token optimization options.

Metric. Regression metric maps true and estimated values to a scalar. Error estimation is carried out using root mean square error normalized by standard deviation.

$$NRMSE = \frac{1}{\sigma_y}\sqrt{\frac{1}{n}\sum\nolimits_{i=1}^{n}(y_i - f(X_i))^2} \tag{1}$$

where n – dataset size, f – possible approximation function, (X, y) – given dataset, σ_y – standard deviation of the target values.

A Policy Optimizer. It is an algorithm for optimizing the parameters of a parametrized policy. Among the proposed ones, the default method – Adam turned out to be the best. The following characteristics for it were set:

$$learning\_rate = 0.01 \tag{2}$$

$$entropy\_weight = 0.01 \quad (3)$$

Token Optimization Options. Degree specifies the degree of the polynomials to be fit.

$$degree = 2 \quad (4)$$

Regressor is the underlying regressor used to learn the polynomial coefficients. We used the least squares method.

3 Application of Symbolic Regression to the Approximation of Nonlinear Hyperelasticity

In the current study we will test to use symbolic regression approach for the identification of the models of hyperelastic materials. For this goal a synthetic data was formed based on 2 theoretical models: Neo-Hookean and Mooney-Rivlin.

According to Neo-Hookean model in incompressible statement, the Cauchy stress, for uniaxial deformation could be generated from the following expression:

$$\sigma_{uniax} = \mu(\lambda^2 - 1/\lambda) \quad (5)$$

where μ is the shear modulus.

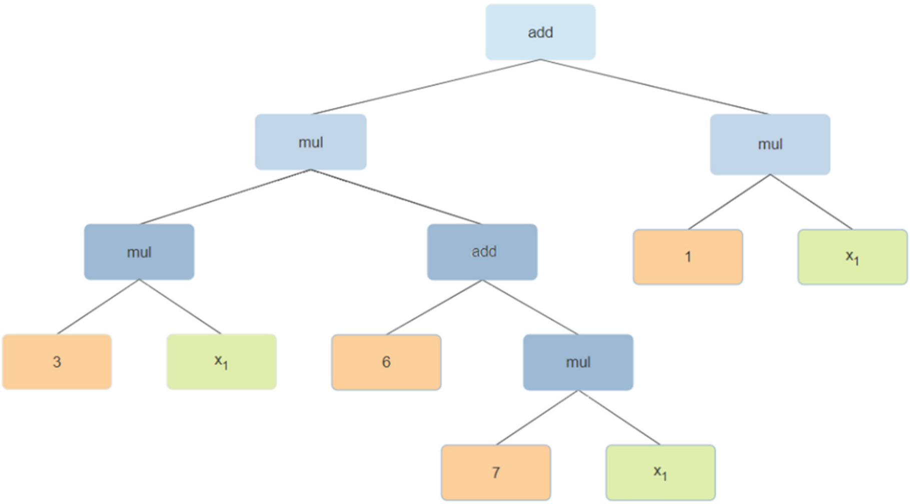

Fig. 1. Tree of the obtained expression for Neo-Hookean material

Based on the formula (5) the learning dataset with 10 values was generated. That data is used for the symbolic regression approach. The method gives us as the model

$$\mathrm{f} = 3.0 \cdot x_1 \cdot (7 \cdot x_1 + 6.0) + 1.0 \cdot x_1 \quad (6)$$

where f – is a model that generated, x_1 – the independent variable that in the current problem corresponds to strains (stretches)

Within the 2000 iterations with the accuracy $R = 0.9862$. On the Fig. 1 it is shown the graph-tree of the model that is generated by symbolic regression. The result of the approximation is plotted in the Fig. 2.

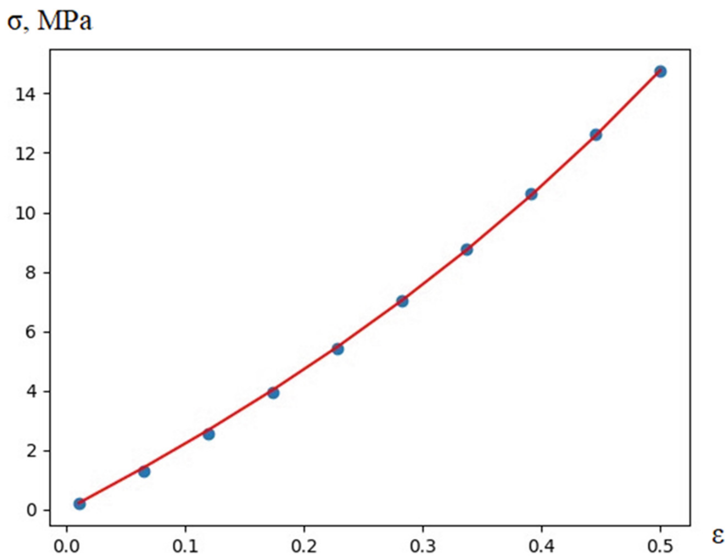

Fig. 2. Approximation for the Neo-Hookean model

Next we generated data based on the Mooney-Rivlin model. The expression for calculating the Cauchy stress for the incompressible version of the MR model under uniaxial deformation is following:

$$\sigma_{uniax} = 2\left(\lambda^2 - \frac{1}{\lambda}\right)\left[C_{10} + \frac{C_{01}}{\lambda}\right] \tag{7}$$

where C_{10} and C_{01} are material parameters.

Based on the formula (7) the learning dataset with 15 values was generated. The method gives us as the model

$$f = 2x_1 - \frac{-x_1 + \frac{3}{x_1}}{x_1} \tag{8}$$

where f – is a model that generated, x_1 – the independent variable that in the current problem corresponds to strains (stretches)

Within the 2000 iterations with the accuracy R = 0.9822. The result of the approximation is plotted in the Fig. 3. Figure 4 shows how the accuracy of expression selection by SR changes depending on the iteration number.

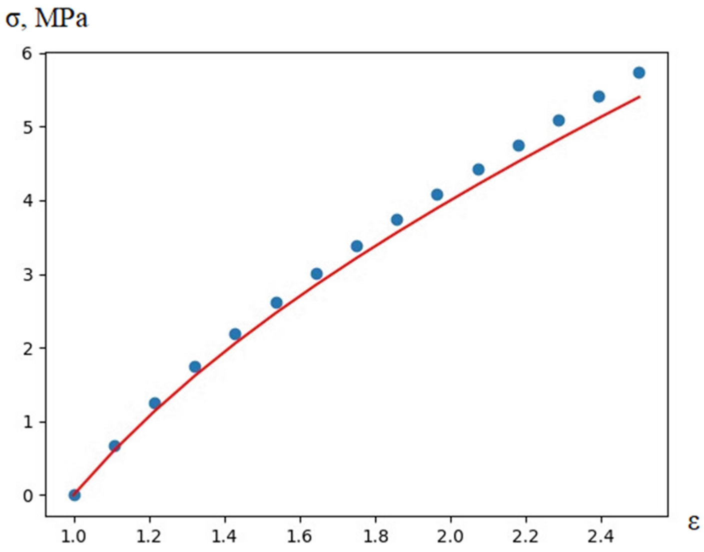

Fig. 3. Approximation for the Mooney-Rivlin model

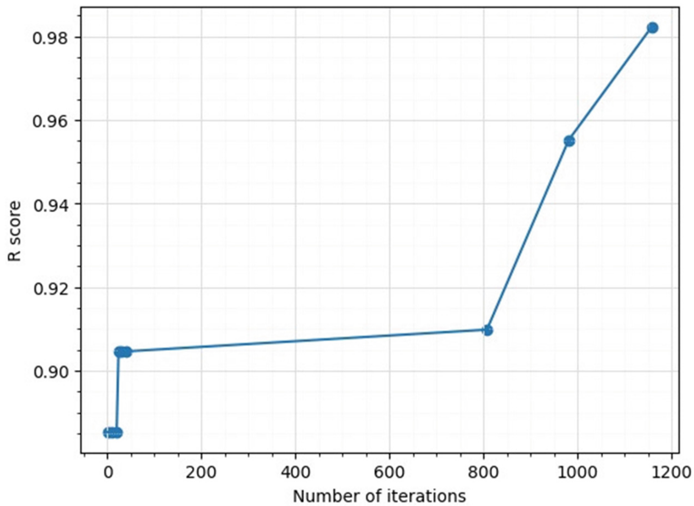

Fig. 4. The change of R from the number of iterations

4 Application of Symbolic Regression to the Approximation of Viscoelastic Behavior

We were interested in whether it was possible to obtain a parameterized form of the ellipse equation using symbolic regression. This is due to the fact that the stress-strain graph for viscoelastic deformation of soft tissues resembles an ellipse. This can be seen in the characteristic hysteresis loops [14]. And deformations and stresses are time-dependent.

In the Fig. 6, the dots represent the data submitted for training, and the line represents the expression obtained using symbolic regression.

Training on two-dimensional data, i.e. simultaneously on time (t) and strains (ε) did not give the desired results, R was at most 0.8, but the approximating function had a large error at either the starting or ending points (Fig. 5). So it was decided that the model will be fitted on the data (t, σ), where σ are stresses.

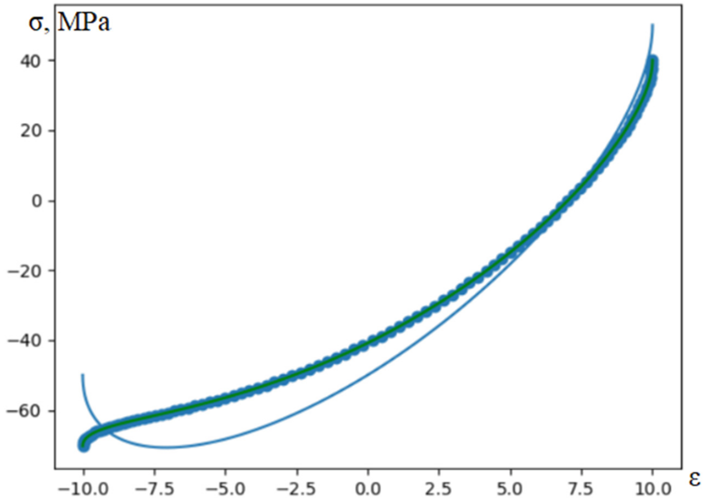

Fig. 5. Approximation function taking into account multidimensionality.

Let's take t at half the period, that is, from 0 to π. The dependence of stresses on time will be taken as follows:

$$\sigma = C_1(C_2 \sin t + C_3 \cos t) \tag{9}$$

where C_1, C_2, C_3 – some material constants.

In view of the above the learning dataset with 100 values was generated. The method gives us as the model (10).

$$\mathrm{f} = (5 \cdot x_1 + 4 \cdot cos(x_1)) \cdot (2 \cdot x_1 + 3 \cdot sin(x_1) + 10 \cdot cos(x_1)) \tag{10}$$

where f – is a model that generated, x_1 – the independent variable that in the current problem corresponds to strains (stretches)

Within the 2000 iterations with the accuracy $R = 0.9231$. On the Fig. 6 it is shown the graph-tree of the model that is generated by symbolic regression. The result of the approximation is plotted in coordinates (ε, σ) in the Fig. 7.

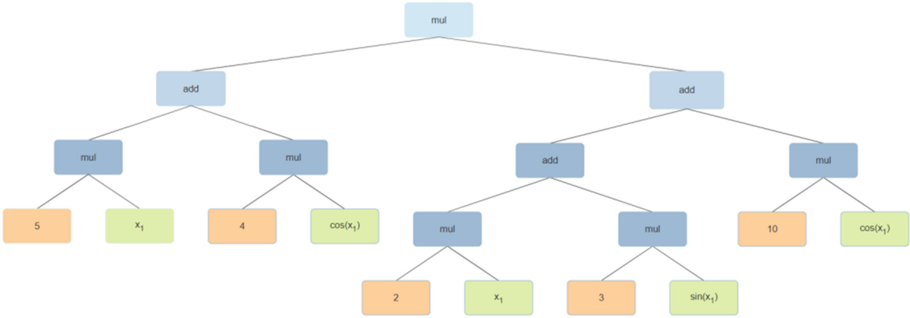

Fig. 6. Tree of the obtained expression for the half of the period

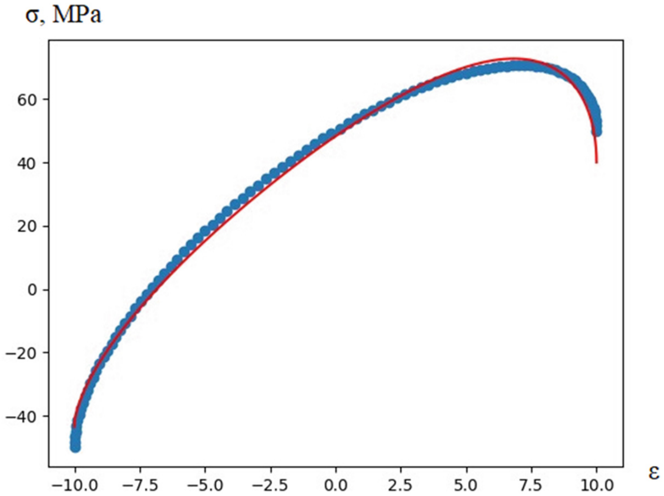

Fig. 7. Approximation for the half period

Consider that t now is from 0 to 2π the learning dataset with 100 values was generated. The method gives us as the model

$$f = (4 \cdot sin(x_1) + 4 \cdot cos(x_1)) \cdot (x_1 + (2 \cdot sin(x_1) + 2 \cdot cos(x_1)) \cdot (3 \cdot sin(x_1) + 3 \cdot cos(x_1)) + sin(x_1) + 1) \quad (11)$$

where f – is a model that generated, x_1– the independent variable that in the current problem corresponds to strains (stretches)

Within the 2000 iterations with the accuracy R = 0.8189. The result of the approximation is plotted in coordinates (ε, σ) in the Fig. 8. Figure 9 shows how the accuracy of expression selection by SR changes depending on the iteration number.

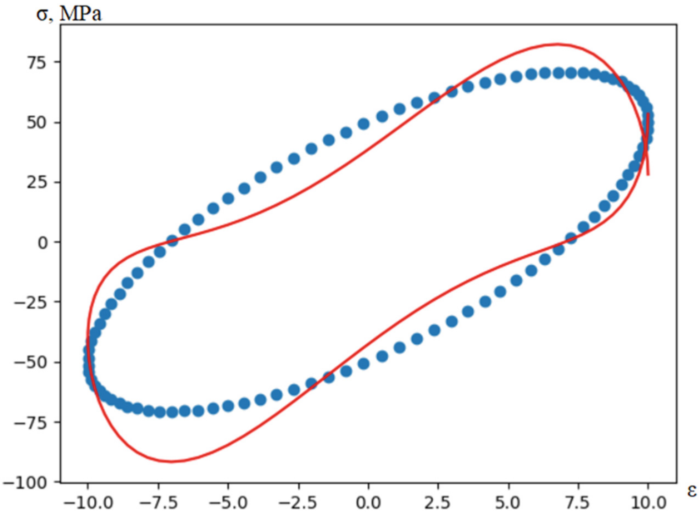

Fig. 8. Approximation for the period

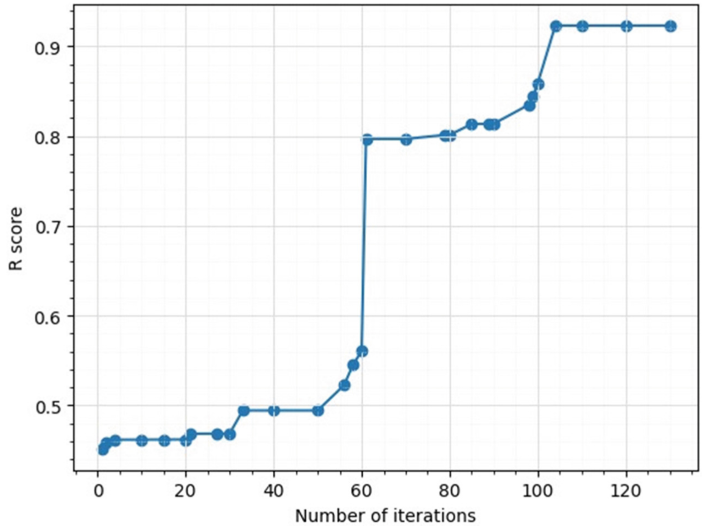

Fig. 9. The change of R from the number of iterations

5 Summary

A study was conducted on the application of the symbolic regression method to the approximation of the behavior of materials. Synthetic data of hyperelastic materials (Neo-Hooke and Mooney-Rivlin models) and a linear viscoelastic model were generated, which in combination can describe deformations of soft biotissues. The results are presented in the form of analytical expressions, as well as a graph tree structure. Graphs of the approximating functions in comparison to the input data were also plotted and iterative dependences of the convergence of the symbolic regression were performed for the analyzed cases. The results demonstrate the ability of the symbolic regression approach to capture the time-dependent and complex nature of viscoelastic deformation. However, there is a problem of identifying models representing periodic changes in time given in a parametric way, which is of interest for further research.

References

1. Viazovychenko, Y., Larin, O.: Stochastic Optimization Algorithms for Data Processing in Experimental Self-heating Process. In: Nechyporuk, M., Pavlikov, V., Kritskiy, D. (eds.) Integrated Computer Technologies in Mechanical Engineering - 2020. ICTM 2020. Lecture Notes in Networks and Systems, vol. 188, pp. 644–653. Springer, Cham (2021). https://doi.org/10.1007/978-3-030-66717-7_55
2. Abdellaoui, I.A., Mehrkanoon, S.: Symbolic regression for scientific discovery: an application to wind speed forecasting. In: 2021 IEEE Symposium Series on Computational Intelligence (SSCI) (2021). https://doi.org/10.1109/ssci50451.2021.9659860
3. Abdusalamov, R., Kaplunov, J., Itskov, M.: Discovering asymptotic expansions for problems in mechanics using symbolic regression. Mech. Res. Commun. **133**, 104197 (2023). https://doi.org/10.1016/j.mechrescom.2023.104197
4. Hernandez, A., Balasubramanian, A., Yuan, F., Mason, S.A.M., Mueller, T.: Fast, accurate, and transferable many-body interatomic potentials by symbolic regression. NPJ Comput. Mater. **5**(1), 112 (2019). https://doi.org/10.1038/s41524-019-0249-1
5. Keren, L.S., Liberzon, A., Lazebnik, T.: A computational framework for physics-informed symbolic regression with straightforward integration of domain knowledge. Sci. Rep. **13**, 1249 (2023). https://doi.org/10.1038/s41598-023-28328-2
6. Merikoski, J.: Data based models. In: Pohjolainen, S. (ed.) Mathematical Modelling, pp. 55–78. Springer, Cham (2016). https://doi.org/10.1007/978-3-319-27836-0_5
7. GPlearn package documentation. https://gplearn.readthedocs.io/en/stable/
8. Petersen, B.K., Mundhenk, T.N., Kim, S.K., Santiago, C.P., Kim, J.T.: Deep symbolic regression (2021)
9. Landajuela, M., et al.: A unified framework for deep symbolic regression. Adv. Neural Inf. Process. Syst. **35**, 1–14 (2022)
10. Cranmer, M.: Interpretable Machine Learning for Science with PySR and Symbolic Regression (2023). https://doi.org/10.48550/ARXIV.2305.01582
11. SymReg documentation. https://pypi.org/project/symreg/
12. Broløs, K.R., et al.: An approach to symbolic regression using Feyn (2021). https://doi.org/10.48550/ARXIV.2104.05417
13. Burlacu, B., Kronberger, G., Kommenda, M.: Operon C++. In: Proceedings of the 2020 Genetic and Evolutionary Computation Conference Companion. ACM, 08 July 2020. https://doi.org/10.1145/3377929.3398099
14. Fomenko, N., Larin, O.: Computational analysis of viscoelastic deformation of human blood vessels with a plaque of statistically predicted size. In: IEEE 3rd KhPI Week on Advanced Technology (KhPIWeek). IEEE, 03 October 2022 (2022). https://doi.org/10.1109/khpiweek57572.2022.9916349

Touches to the Portrait of the Aviation Designer and Military Pilot Kostyantyn Kalinin

Kryvokon Oleksandr[1](✉) and Kryvokon Natalia[2]

[1] Historical Sciences, Kharkiv State Aviation Enterprise, Kharkiv, Ukraine
Kryvokon.og@gmail.com
[2] Psychological Sciences, Department of Psychology and Pedagogy, National Academy of the National Guard of Ukraine, Kharkiv, Ukraine

Abstract. The article is dedicated to the exploration of the lesser-known aspects of the life of the prominent designer and aviator of the 20th century, Kostyantyn Oleksiyovych Kalinin.

The purpose of the study is to develop existing notions about Kalinin's personality and life path through historical-psychological analysis. The relevance of the publication is determined by the need to revive historical memory and form a more objective picture (free of ideological overlays) of the life activities of the famous aircraft designer. This will help professionals in the field understand the reasons that prevented the realization of Kalinin's creative potential and the implementation of his most progressive and forward-looking aviation discoveries and developments.

The subject of the study is biography of K.O. Kalinin, particularly the events between 1916 and 1919, which later led to political repression, his arrest, and execution. As a **result** of the analysis of newly introduced documents and data, it was revealed that from December 1918, K.O. Kalinin was the commander of the 1st Volyn (Zhytomyr) Aviation Division, and from February 1919, he commanded the air squad of the Army of the Ukrainian People's Republic (UPR) and the Ukrainian Galician Army (UGA), and was also an inspector of the UGA. In the summer and autumn of 1919, he served as the head of the aviation warehouse of the Active Army of the UPR. Later, Kalinin voluntarily agreed to cooperate with the Bolsheviks, concealing some facts of his biography. Describing in 1938 the events that occurred from 1918–1919, Kostyantyn Oleksiyovych tried to avoid repression and save his life. He aimed to realize himself as an aviation designer in his homeland. Partially, he succeeded: from 1923 to 1935, Kalinin designed a series of aircraft, including experimental ones. However, the Bolshevik authority neglected the talent, design skills, and achievements of this extraordinary inventor, aviator, and engineer. On October 22, 1938, after interrogations and torture on fabricated charges, Kostyantyn Oleksiyovych Kalinin was executed.

Conclusions: Researching the biographies and achievements of famous domestic aircraft designers allows a better understanding of how the aviation industry developed in our country and what factors influenced this process. A deeper knowledge of the fate, life path, and personal characteristics of K.O. Kalinin will help future aircraft builders form the necessary worldview, value orientations, and personal qualities to overcome contemporary challenges and aspire to develop domestic aircraft construction.

M. Nechyporuk et al. (Eds.): ICTM 2023, LNNS 1008, pp. 173–185, 2024.
https://doi.org/10.1007/978-3-031-61415-6_15

Keywords: K.O. Kalinin · aviation industry · historical memory · history of technology

1 The Problem Statement

It is considered that the history of technology is one of the most objective branches of historical science, as it investigates the peculiarities of the creation, development, and application of technical devices and systems. This can be described and studied based on objective data such as documents, patents, and technical specifications. However, the creators of technical achievements are specific individuals, whose inventions and design developments profoundly impact others' lives, the economy, culture, society, and civilization as a whole. The cultural-historical and political conditions under which scientific and technical progress takes place significantly determine the directions and results of the inventors' and engineers' endeavors. Therefore, by studying the biographies of people who have achieved success in a particular field, we aim not only to become familiar with their innovative thinking and achievements but also to understand the historical and socio-cultural context in which famous designers and inventors were formed and functioned. In doing so, we form historical memory, the main purpose of which is to find answers to the questions: Why do we remember these people and their achievements? What is valuable in their experience? What from the work of these famous individuals should we preserve and use for further technical progress? What facilitated or hindered the disclosure of a person's creative potential and the realization of their innovations?

Therefore, research dedicated to the historical-psychological analysis of the life events and paths of our famous compatriots who have contributed to global technical science and practice, particularly in such a vital field as aircraft construction, is timely.

The purpose of this publication is to develop existing notions about the personality and life path of the outstanding designer and aviator, Kostyantyn Oleksiyovych Kalinin.

2 Presentation of the Main Material

The name of the aviation designer Kostyantyn Oleksiyovych Kalinin (1887–1938) is well known to the general public thanks to many publications about him that have appeared in periodicals and professional publications over the last few decades. Several documentaries and television programs have been made about him. Moreover, in 1986, aviation journalist M.B. Lyakhovetsky published the book "All in the Wing", dedicated to the life and work of K.O. Kalinin. While working on this book, the author used a wide range of documentary materials, including memories of comrades, students, and colleagues of the aircraft designer, and press from the 1920s and 1930s.

The book is fundamentally based on the recollections of Andrii Trifonovich Rudenko, who worked for a long time with K.O. Kalinin, including as the deputy chief designer at the Kharkiv Aviation Plant [1].

The book "All in the Wing" became the first major work about K.O. Kalinin, who entered history as the creator of a whole series of aircraft and as the founder and chief designer of the Kharkiv and Voronizh aviation plants. Unfortunately, the book was prepared under the conditions of Soviet censorship, which led to significant inaccuracies and gaps in Kalinin's biography. Furthermore, some formulations in the book show an attempt to portray the famous aircraft designer as an ideological communist and great supporter of Bolshevik power, which, in our opinion, does not correspond to reality (Fig. 1).

Fig. 1. Konstantin Kalinin among his colleagues. Newsreel footage taken around 1930.

The memories of A.T. Rudenko and the book by M.B. Lyakhovetsky initiated further research into the biography of K.O. Kalinin, particularly by the aviation historian V.S. Savin, who published his own book in 1994 titled "Planet 'Kostyantyn': The History of Aviation and the Country Through the Prism of the Life of Designer Kalinin.". Based on archival-historical sources, the author much more deeply revealed the biography and creative achievements of the designer of the first domestic passenger aircraft K-1, K-3, K-4, K-5, the giant aircraft K-7, and the first tailless combat aircraft K-12. It is worth noting that his book still attracts the attention of both domestic and foreign aviation historians. At the time of researching Kalinin's biography, V.S. Savin had the opportunity to work in Russian archives and obtained invaluable materials from the personal archive of the designer's daughter, Nelli Kostyantynivna. He dedicated his book to her, which now serves as a primary source for other researchers of K.O. Kalinin's biography and his activity as an aviation designer.

In addition to V.S. Savin, the life path of K.O. Kalinin and his contribution to the development of domestic and global aircraft construction were also studied by A.I. Kharuk, M.O. Zgurovsky, V.V. Tatarchuk, and others. However, some pages of the biography of this extraordinary personality remain unexplored or have not found proper coverage in the scientific literature. This particularly applies to his participation in World War I, service in the units of the Air Fleet of the Ukrainian State, and the circumstances that forced him to side with the Bolsheviks. The theme of Kostyantyn Kalinin's formation as a military pilot, who proved himself in combat conditions, is also not sufficiently illuminated. Therefore, we set ourselves the task of filling these gaps in K.O. Kalinin's biography, clarifying certain pages, and supplementing them with new facts of scientific interest.

Let us recall that Kostyantyn Oleksiyovych Kalinin was born in Warsaw on January 24 (February 5) 1887, in the family of titular counselor Aleksey Kirillovich Kalinin. M.B. Lyakhovetsky writes that the father of the future aircraft designer descended from Ukrainian peasants living in the Valuyki area of the Voronizh province and had the surname Kalyna-Malyna, but during his service in the Tsar's army, for convenience, he was recorded as Kalinin [2, p.9]. Aleksey Kalinin rose to the rank of staff captain and, upon retirement, received the title of personal nobleman. His mother, Marianna Frederikovna von Braun, was Polish and came from an impoverished noble family [3, p.8].

Under Soviet rule, Kostyantyn Kalinin had to conceal his noble origin and even his place of birth, though this did not save him from Stalin's repressions. In 1938, among the standard and fabricated accusations that the NKVD put forward against the famous aircraft designer, they recalled his service in the Tsarist and Petliurist armies, which in the Stalinist regime was equated with a state crime.

But let's return to the origins of his life path.

Kostyantyn Kalinin's father died when his youngest son was barely five years old, so the boy's upbringing was mostly done by his mother. She gave him a good home education, which later allowed him to graduate externally from a real school in Warsaw and to enter a teacher's seminary in the town of Andreyevo or Jędrzejów in the Kelect Voivodeship, which Kostyantyn graduated with honors. To help his family, he worked for a while as a turner at the foundry and mechanical plant in Korstein and taught at a private school in the town of Wodzisław. In 1905, Kalinin joined the Polish Socialist Party, participated in the distribution of revolutionary proclamations, for which he was arrested and spent six months in prison [3, p.10].

In 1909, K.O. Kalinin entered the Odessa Infantry School, which he graduated with first-class honors [4]. We can assume that it was during his studies that the young cadet saw the first flights on airplanes carried out by glider pilots of the Odessa Aero Club and became acquainted with the theory of aeronautics. It was from this time that the young man developed a passionate fascination with aviation and a desire to fly, which he was able to realize only in 1916, when he became a student at the Gatchina Military Aviation School. However, he began his military career as a second lieutenant of the 3rd Siberian Rifle Artillery Brigade, then as an assistant to the head of the training team of the artillery division. During World War I, he served in the 5th Separate Heavy Artillery Division of the 20th Infantry Division, which fought on the Western Front [4]. But even during the war, the dream of aviation never left him.

On February 27, 1916, Kalinin wrote a report to the head of the Gatchina Military Aviation School, requesting permission to train at the mentioned school to then continue his service in one of the aviation units of the active army. His report was approved, and from April 1, 1916, he became a student at the aviation school. Due to the acute shortage of aviators at the front, the training at the school, which usually lasted about a year, was shortened to six months. The theoretical course included the basics of aviation, particularly aerodynamics, aviation engines, aeromechanics, and about a dozen other specialized subjects. Some lectures were conducted at the Saint Petersburg Polytechnic Institute, where Kalinin first became acquainted with the wind tunnel and aerolab.

Officers underwent industrial training at the Lebedev factory, which at that time was producing French “Voisin” aircraft with “Salmson” engines [3].

In the military aviation class where Kalinin studied, there were about fifty officer-students from various branches of the military. He was one of the best. M. Zgurovsky writes that K.O. Kalinin was fortunate to study under the famous aviation expert, Colonel Sergii Ulyanin, who educated a whole array of outstanding aviators. At that time, the name of this aeronaut, pilot, and aircraft designer was as legendary in the Russian Empire as the names of Sergii Utochkin, Mykhailo Yefimov, and the designer and pilot Igor Sikorsky. Among Ulyanin’s students were such extraordinary personalities as Petro Nesterov, Evgraf Kruten – a famous air fighter and one of the first developers of fighter aviation tactics, Olexander Kazakov – a celebrated ace of World War I, Yan Nagurskiy – the first polar aviator, and many others [5].

On June 25, 1916, K.O. Kalinin made his first solo flight on a “Farman-7” training biplane, and overall, during three months of training, he performed over 200 flights, of which 69 were solo [6]. After successfully passing his exams, he received the rank of military pilot and was assigned to serve in the 26th Corps Aviation Squadron, which was part of the 9th Russian Army fighting on the Romanian Front. Mostly, Lieutenant Kalinin flew on the “Voisin” aircraft, conducting aerial reconnaissance of German positions, and quickly established himself as a brave and competent pilot. He also participated in air battles and bombings of enemy positions. For destroying a bridge over the Bystrytsia river ‘with two bombs, he was awarded the Order of St. Stanislaus 3rd degree with swords and bow. He had previously been awarded two Orders of Anna of the 4th and 3rd degrees [3, p.33].

The command highly rated K.O. Kalinin’s officer qualities and professional knowledge. Therefore, at the beginning of November 1916, he was appointed head of the technical department of the 26th aviation squadron, responsible for maintaining the entire fleet of aircraft in working order. For some time, Lieutenant Kalinin also performed the duties of the commander of the aviation squadron [4].

A. Kharuk notes that in the summer of 1917, the entire Russian army aviation numbered 84 aviation squadrons: 24 fighter, 44 corps, 4 artillery, and 12 army. They were distributed among five fronts, two of which – the Southwestern and Romanian – were located in Ukraine [7]. In June-July 1917, during the retreat, the aviation of these fronts suffered significant losses, which were never compensated. At that time, the core of the army aviation fleet consisted of French-designed aircraft, mostly assembled at Russian enterprises. These included fighters and reconnaissance aircraft such as “Nieupor”, “SPAD”, “Voisin”, “Caudron”, “Morane” of various modifications, with 214 of them on the Southwestern and Romanian fronts. Russian-designed aircraft were represented by “Anade” reconnaissance planes from the Odessa firm “Anatra”. But overall, the situation of the reconnaissance aviation was very poor. The most common reconnaissance aircraft on the Southwestern and Romanian fronts were various modifications of “Farmans” and “Voisins”, numbering respectively 47 and 20. These were bulky biplanes with pusher propellers and low-powered engines. The characteristic propeller placement on these aircraft blocked the tail sectors of fire for the onboard machine gun, making the aircraft practically defenseless against fighter attacks. This flaw was exacerbated by low speed and insufficient maneuverability [7].

It was on such machines that Kostyantyn Kalinin had to fly. However, in the spring of 1917, Russia purchased fifty of the newest “Farman-40” aircraft in France, which were given to the best Russian pilots. One of them was received by Kalinin, who, along with his subordinate mechanics, set about assembling the airplane [3, p.45]. Unlike many other pilots who disliked manual labor, K.O. Kalinin was not averse to it and eagerly delved into the smallest technical details.

We can conclude that K.O. Kalinin was a promising pilot and officer in the Russian Imperial Army. This is evidenced by the service appraisal materials of the military pilot, Lieutenant of the 5th Separate Heavy Artillery Division, Kostyantyn Kalinin: “He has a balanced, calm, decisive, and noble character. Excellent mental abilities, quickly grasps and assimilates everything new. Able to assess the situation and quickly choose the correct decision. Firm, consistent, and logical in his decisions. Has good theoretical and practical preparation for aviation service, to which he is devoted and loves. Respected by comrades, strict, fair, and approachable with lower ranks, quickly understands people and rarely makes mistakes about them. Will be a strict, fair, and authoritative leader. Loves flying very much and flies excellently - bravely, thoughtfully, cautiously, and beautifully. Extremely persistent during combat missions, cautiously bold, cool-headed, and brave. Capable of combat work in very difficult conditions. Has organizational skills and can inspire people with vitality and a desire to work. Highly desired as a squadron commander” (emphasized in the document) [3].

Interestingly, Kostyantyn Kalinin continued to fly even when he was already working as the chief designer at the Kharkiv Aviation Plant. He participated in the test flights of his aircraft, although it involved significant risk to his life. This was also the case during the first test flight of the giant aircraft K-7 when, contrary to instructions, K.O. Kalinin took the seat of the second pilot. Due to technical sabotage, the aircraft almost crashed and was landed at the airfield with great difficulty. For his brave actions, the chief pilot Snegirev was thanked, but the chief designer Kalinin was reprimanded for the unauthorized flight on the experimental aircraft without the necessary permission [1, p.31]. But let’s return to the fateful events of 1917.

In the summer of 1917, amidst the democratization that swept the Russian troops, K.O. Kalinin was elected commander of the 26th Corps Aviation Squadron, which was still on the Romanian Front. This decision was confirmed by the order of the Field Aviation and Aeronautics Administration at the Headquarters of the Supreme Commander on September 6, 1917. Probably at the same time, he was promoted to the military rank of staff captain. In this position, new leadership and professional qualities of K.O. Kalinin emerged, both as a pilot and as a commander. Notably, he was one of the first to use radio communication to adjust artillery fire from the air, significantly enhancing its effectiveness. However, the overall situation on the Romanian Front was deteriorating, and under the pressure of Austro-German forces, the Russian army was forced to retreat.

At the end of November 1917, the 26th Corps Aviation Squadron, commanded by K.O. Kalinin, was located at one of the field airfields in the city of Suceava in Bukovina. Later, the Military Committee of the aviation squadron decided to immediately evacuate the aircrafts and aviation property to the territory of Russian-controlled Bessarabia, and from there to the city of Mogilev-Podolsky. Soon, the German troops launched an offensive along the entire Eastern Front from the Baltic to the Black Sea and captured

Mogilev-Podolsky. The political situation in Russia also changed. After the Bolshevik coup, the Civil War began, and in Ukraine, all power passed to the Central Rada.

On December 4, 1917, an order from the Government of the Ukrainian People's Republic arrived at the front, subordinating the Southwestern and Romanian Fronts to the Central Rada, resulting in the formation of a single Ukrainian Front. The 26th Corps Aviation Squadron was disbanded. This marked the beginning of events related to the creation of the Armed Forces of the Ukrainian State and its Air Fleet.

As known, on December 13, 1917, the Ukrainian Central Rada officially formed the Air Fleet, and on December 26, an order was issued by the General Secretary of Military Affairs of the Ukrainian People's Republic (UPR), Symon Petliura, appointing military pilot Lieutenant Colonel Viktor Pavlenko as the "head of aviation affairs of the Ukrainian People's Army." During these days, many officers of the Tsarist army, including Staff Captain Kostyantyn Kalinin, faced a difficult question: "What to do next?" Some of his friends joined the aviation of the Polish Army, others went to the Don region to join General Kaledin, and still others switched to serving the Bolsheviks. Kostyantyn Kalinin sided with the Ukrainian People's Republic, and it seems this was a deliberate and conscious decision. As V.S. Savin writes, the Volyn Aviation Division, in which Kalinin served as a pilot, sided with Petliura and, after the removal of supporters of Hetman Skoropadsky, was renamed the 1st Republican. On December 2, 1918, at the request of the soldiers' committee, Kostyantyn Kalinin was appointed commander of the division. He held this position until January 20, 1919. He was granted the rank of captain and his division participated in battles against Skoropadsky's army near Kyiv. At the end of December 1919, Captain Kalinin was appointed inspector of the Kyiv district [3, p.58].

K.O. Kalinin himself describes this period of his activity somewhat differently. In particular, in the testimonies he gave on September 5, 1937, in connection with the so-called party "purges" taking place at the Voronizh Aviation Plant, he notes that he "sympathized with the Central Rada, whose manifesto seemed to him democratic and progressive" [3, p.60]. Obviously, he refers not to a manifesto, but to the Third Universal of the Ukrainian Central Rada, which proclaimed the Ukrainian People's Republic on November 7 (20), 1917. At that time, K.O. Kalinin was already in Kyiv (Svyatoshino) and, as he states, lived near the 3rd aviation park. It is worth noting that during the Ukrainian Revolution, the 3rd (Kyiv) aviation park was the first aviation unit to Ukrainianize and come under the command of the Directorate of the Air Fleet of the UPR. Overall, four aviation parks declared themselves Ukrainianized, two of which were located in Kyiv, and two others in Odessa and Poltava. They included over 120 trained pilots with combat experience [3, p.59].

Therefore, we can conclude that K.O. Kalinin's presence in the 3rd aviation park was not accidental. Further in his testimonies, he states that he joined the group of engineer V.F. Bobrov, which tried to organize air communications, and helped him in developing the project of air lines. V.V. Tatarchuk, who researched the biography of V.F. Bobrov, also pays attention to this fact. He notes that K.O. Kalinin was one of the 12 signatories of the "Report of Ukrainian aviation specialists on the use of aviation in peacetime", submitted to the Ministry of Trade and Industry of the UPR in March 1918 [8]. According to some sources, among the authors of this document were also Colonel Viktor Pavlenko and the Kasianenko brothers, Andriy and Hryhoriy, with whom K.O. Kalinin was already acquainted.

After the takeover by Hetman Skoropadsky, Kalinin moved to Zhytomyr and joined the 1st Volyn (Zhytomyr) Aviation Division, commanded by Colonel V. Hartman at that time. In many sources, it is mentioned that from December 1918, K.O. Kalinin was in the position of commander of this aviation division, and from February 1919, he commanded the air squadron of the UPR and UGA Army, and was also the inspector of UGA. In the summer and autumn of 1919, he also served as the head of the aviation warehouse of the Active Army of the UPR. Although Kalinin himself does not specify his service in the Air Fleet of the Ukrainian State, this can be traced in his testimonies mentioned above. The document is titled (in the original language) «Сведения о моем пребывании на территории белых: Центральной Рады, Директории и Петлюры в 1918 и 1919 гг.» ("Information about my stay in the territory of the Whites: Central Rada, Directorate and Petliura in 1918 and 1919") and is quite valuable and informative. It should be noted that the original of this document is kept in the archival-criminal case of K.O. Kalinin in Russia. His daughter, Nelli Kalinina, managed to obtain a copy of this document and passed it to V.S. Savin, who published it in the book "Planet 'Kostyantyn'". For the purpose of introduction into scientific circulation, we present the full text of this document in the Ukrainian translation with some of our notes and explanations.

"Information about my stay in the territory of the Whites: Central Rada, Directorate, and Petliura in 1918 and 1919."

In Mogilev-Podolskiy, where I arrived with the aviation squadron from the city of Beltsy, fleeing from the Romanian occupants, the Central Rada was in power. After a few days, Mogilev-Podolskiy was occupied by Austrian troops. The squadron's people dispersed, leaving a few pilots and soldiers. I went to Kyiv, occupied by the Germans, and lived near the third aviation park (Svyatoshino), where I joined, as a pilot, the group of engineer V.F. Bobrov[1], who was then starting the organization of air communications. I helped him develop the project of air lines and securing the material part for this. This was during the Central Rada. At that time, I sympathized with the Central Rada, whose manifesto seemed to me then democratic and progressive, but I disagreed with the policy that led to the invasion of Wilhelm's army[2]. My work with Bobrov continued until the appearance of the Hetman, installed by the German command, because work on air routes was covered up. I lived in Kyiv for another month, then moved to Zhytomyr, where the remnants of the aviation squadron from Mogilev-Podolskiy moved.

There, together with pilot Bogomolov (word unclear), we picked up an abandoned car, repaired it, and for 2–3 months engaged in transport, carrying passengers to Kyiv and back.

[1] **Bobrov Viktor Flavianovich -** the first rector of the Kyiv Polytechnic Institute (since December 15, 1921) and the first director of the Kyiv Aircraft Repair Plant "Remvozduh No. 6" (now the State Enterprise "Kyiv Aviation Plant "Aviant").

[2] **Wilhelm's army** - Wilhelm Franz von Habsburg-Lotringen (Vasyl Vyshivany), Ukrainian military figure, politician, diplomat, poet, Austrian archduke (archduke) of the Habsburg dynasty. During the Ukrainian revolution, he was a colonel of the Legion of Ukrainian Riflemen..

During this time, Colonel Hartman[3], who commanded in the old army a division which our former squadron was a part of and whose remnants were then in Zhytomyr and were declared as a division, took over its command. In November, when the insurgent movement against the Hetman intensified, a state of siege was declared in Zhytomyr, and all former officers and soldiers of the old army were mobilized. We, the pilots, former officers, were gathered by Hartman and he announced that we were mobilized, that there is no Ukraine, but a South Russian army, which is subordinate to General Keller[4]. Anyone who disobeys will be executed. Tomorrow morning we are to march on foot against the 'bandits' who are advancing on Berdychiv.

I told him that these are not bandits, but the insurgent Ukrainian people, against whom I will not go. He threatened me with execution if I do not follow his order.

I warned the soldiers about the meeting and Hartman's decision.

In the morning, only a few armed officers went 'to the front' with Hartman, and they were bayoneted by the insurgents.

I stayed with the soldiers of the squadron and those pilots who did not go with Hartman. By evening, the insurgent units under Oskilko's.[5] command entered the city.

The soldiers' committee of the aviation division proposed me to be the commander. We were included in the composition of the arrived insurgent army.

A few days later, the 3 operational aircraft of the division were sent by me to Kyiv for an operation against the Hetman and there bombed the Hetman's forces.

Soon after the capture of Kyiv, Oskilko called me to the staff and ordered to send the aircraft to Mozyr, from where the Bolsheviks were advancing. He sent me to the airfield accompanied by his adjutant. Noticing that he was not knowledgeable in aviation matters, I ordered to put bombs without detonators in the planes, and explained to the pilot Khimich that after returning, to report that fog hindered the flight. That's what was done. The plane quickly returned, the pilot reported the fog. Oskilko called me again, shouted that he would shoot me, arrested me, and sent me for interrogation to his chief of staff, whom I managed to convince that indeed the weather was a hindrance. I saw that the weapons of the Directorate were directed against the people, against the Bolsheviks.

The next day, Oskilko's staff and his units left Zhytomyr. The Red units entered the city, and a Revkom was formed, to which we handed over the motor transport and machine guns.

Soon the Red units left, and after some time, the Haydamaks entered the city.

These last events greatly shook me. I was in a state of complete confusion and depression, lost faith in the revolutionary nature and national character of the Central Rada, Directorate, Ukrainian parties.

---

[3] **Hartman Volodymyr Evgenovich (1885–1918) -** Russian military pilot, colonel. In 1917, he commanded the 9th aviation division on the Romanian front. During the times of the Ukrainian State, he commanded the Zhytomyr Air Division for a short time.

[4] 4 **General Keller -** in 1918, one of the leaders of the White Movement, a monarchist. In the same year, he was killed by the Petlyurites**.**

[5] **Oskilko Voladimyr Panteleymonovych (1892–1926) -** a Ukrainian military and public figure of the times of the Ukrainian People's Republic, corporal general of the army of the Ukrainian People's Republic.

I went to Kyiv at the demand of the aviation staff, which declared me mobilized. In Kyiv, I was in the same state. Newspaper squabbles, nothing definite, disputes about peace with the Bolsheviks, with whom I believed, cannot and does not want to fight the Ukrainian nation. Newspaper reports that a delegation of the Directorate is coming to negotiate peace. I believed this.

The aviation staff appointed me as the inspector of the Kyiv district. I could not avoid this. The district commissar Murashko[6] supervised and watched over me.

The head of aviation Pavlenko[7] ordered to evacuate the material part of the Zhytomyr division and its part that was on the Volyn post to Proskuriv[8].

There was no peace, there was Petliurism. I went to Zhytomyr, instructed to load the property, saw the negative attitude of the people towards this and, without waiting for the loading to be completed, went to Proskuriv in the hope that (word unclear) would not happen and that after the strike near Kyiv, Petliura would give up the fight and peace would come, which I yearned for above all. I could not find in myself the necessary strength and awareness to rise against Petliurism and die honorably in this fight.

I had no threads that connected me with the Bolsheviks and could clarify my consciousness and direct my will.

In Proskuriv, the echelons of the aviation base from Kyiv arrived under the command of Kudry, which were not part of the Kyiv district, and the property of the Zhytomyr division. All this was on wheels waiting for further dispatch and in a state of uncertainty and confusion. Soon, an echelon with Samosenko's Haydamaks arrived in Proskuriv, who committed a Jewish pogrom. The command of the aviation echelons, on their own initiative, provided, though passive, resistance to the pogromists, surrounding a significant part of the city and not allowing the pogromists there. Samosenko threatened to fight the aviation units, but did not dare, and we saved at least part of the city.

In a few days, the staffs and the Directorate on wheels arrived in Proskuriv, an order came to evacuate to Galicia, to the village of Krasne, to the front against the Poles. This did not last long. The retreat began. Near Ternopil, the head of aviation Pavlenko appointed me as the acting inspector of aviation and ordered to take the echelons away from Ternopil. I moved them further from the specified in Volochysk, knowing that the Reds were under Volochysk. I had a secret hope to break out of the Petliurist state. I was in the front carriage of the train-workshop. At night in Volochysk, the arrived echelon was suddenly sent back by the order of the head of the unit guarding the station.

I was removed from the post and left in reserve.

Shortly thereafter, everything moved to Kamianets-Podilskyi. There, I worked on the project of air communications, of course, without success. By autumn, I was appointed

[6] **Murashko Vasyl Opanasovych (1894–1976) -** a military pilot, commander of the Kyiv Aviation Detachment of the Air Fleet of the Ukrainian People's Republic, the last head of the Air Fleet Directorate of the Ukrainian People's Republic (1921–1922).

[7] **Pavlenko Viktor Oleksiyovych (1886–1932) -** a Ukrainian public-political and military figure. From November 1918 to December 1920, commander of the aviation of the Army of the Ukrainian People's Republic, Lieutenant General. Formed four aviation regiments, a squadron of bombers, began to create an aviation school.

[8] **Proskuriv** is now the city of Khmelnytskyi..

as the head of the warehouse of the aviation base. Many at the aviation base were thinking and looking for opportunities to escape from Petliurism.

In December, along with one of the employees of the aviation base, a local resident, I left Kamianets for his village in the area occupied by Denikin's forces. The landlady of the apartment where I lived in Kamianets gave me notes to her relative, a teacher in Dunayivtsi, and to her sister in Nova Ushytsia. I reached Dunayivtsi on foot. The teacher helped hire a cart, and with my wife and child, we went to Nova Ushytsia. In Dunayivtsi and Nova Ushytsia, there were Denikin's forces. In Nova Ushytsia, at the sister's of my landlady, I left all my military documents because if they fell into the hands of Denikin's forces, it would not have been good for me, but without them, I could pass as a 'free' man. I had a passport, previously prepared by me at the aviation staff. In Nova Ushytsia, we reached Zhmerynka and Vinnytsia by carts and got to Kalynivka, where a Soviet armored train was stationed. Explaining to the commissar where I was coming from, I asked to be taken to Kozyatyn, where the armored train was heading. In Kozyatyn, I went to the commandant of the Zhmerynka-Berdychiv direction, handed him my fake passport, told him who I was and where I had been. The commandant, after discussing it with the members of the Revkom, sent me to Kyiv, from where the staff of the XII Army sent me to Moscow at the disposal of the aviation army [3, p.60–63].

It is worth noting that different biographers of K.O. Kalinin have described the circumstances of his switch to the Bolsheviks differently. For instance, B.M. Lyakhovetsky wrote that during the war, Kalinin supposedly fell into Petliura's captivity. To avoid fighting against Soviet Russia, he called himself an intendant and served as the head of a warehouse, and in 1919 supposedly escaped from Petliura's captivity and joined the liberated Soviet territory. The author also claimed that having arrived in Moscow, Kalinin joined the Red Army and fought as a military pilot against internal counter-revolution and foreign interventionists [2, p.19]. These statements have not found documentary confirmation. However, it must be recognized that K.O. Kalinin voluntarily agreed to cooperate with the Bolsheviks, concealing some facts of his biography. And although he was enlisted in the reserve of the Red Army and then sent to study at the Moscow Aviation Technical School (later renamed the Zhukovsky Air Force Engineering Academy), he was already under close surveillance by the Cheka.

In his time, researching the biography of Kostyantyn Kalinin, V.S. Savin found in the Russian State Military Archive a «Список летного состава и военвоздухов, служивших в белой армии и оставленных в Красном Воздушном Флоте» ("List of flight personnel and military air force members who served in the White army and remained in the Red Air Fleet") (RGVIA, f.29, op.4, spr.635, ll.154–199). This list was compiled based on checks by the Cheka on 94 aviation specialists. Among them was Kalinin. Therefore, it is not surprising that in February 1922, the Moscow City Commission for the Cleansing of the Ranks of the VKP(b) expelled him from the party members for one year as a former Socialist-Revolutionary and intellectual who participated in Petliurism and did not show himself in party work" [9]. Later, the Zhukovsky Air Force Engineering Academy was reorganized into an Academy, and 63 "unreliable" students, including Kostyantyn Kalinin, were expelled from this educational institution. He was only a few exams away from obtaining a diploma in aircraft engineering [3,78].

Returning to the testimonies that K.O. Kalinin gave shortly before his arrest, it is worth noting that he wrote them in the midst of mass political repressions carried out in the USSR against the technical intelligentsia. Perhaps that is why some of Kalinin's formulations show a certain bias towards the Directorate of the Ukrainian People's Republic, which he calls "Petliurism," and loyalty to the Bolshevik movement. Obviously, with such 'sincere' testimonies, the famous aircraft designer and, at that time, director of the Voronizh Aviation Plant tried to avoid repression and save his life. But it did not help. The Soviet system could not forgive him for "White Guardism," "Petliurism," or the innate intelligence that distinguished K.O. Kalinin against the faceless and gray mass. He was too bright and extraordinary a personality. This was said by those who personally knew K.O. Kalinin or worked under his leadership, including A.T. Rudenko, who left very valuable memories of him. According to our data, they were written around 1955, when the process of rehabilitating K.O. Kalinin was ongoing. It is no coincidence that the author collected and included in his memoirs feedback from famous people, including writer Ostap Vyshnya, aircraft designers O.Ya. Shcherbakov and Z.Ya. Itskovich, who contributed to the rehabilitation of K.O. Kalinin [1]. Unfortunately, these people could not protect him earlier, in 1937–1938, when the chief designer was literally crucified by ideological communists and demanded expulsion from the party.

As evidenced by the materials of the archival-criminal case of K.O. Kalinin, on September 7, 1937, the party committee of Voronizh Aviation Plant No. 18 raised the issue of expelling him from the VKP (b) members, as a former Socialist-Revolutionary who participated in Petliurism and concealed his past when joining the party. On November 25, 1937, at the general assembly of the party organization of the plant, he was expelled from the party, putting forward additional absurd accusations, and on November 29, this decision was supported by the district party committee. This became a signal for the arrest and imprisonment of K.O. Kalinin, whose name was already on the execution lists.

He was arrested on April 1, 1938, and after numerous interrogations and tortures, was shot on October 22, 1938. In the report fabricated by the employees of the Voronizh Regional NKVD Department and which became the formal reason for the arrest, it was said that the investigation of the case of the spy-sabotage-wrecking organization at plant No. 18 revealed that Kalinin K.O. was an active participant in the organization and conducted subversive work along the line of confusing the drafting economy" [3, p.289].

The official accusation was based on Article 58, parts 6, 7, 8 of the Criminal Code of the RSFSR, which provided for the application of the highest measure of social protection to the convicted person – execution. Meanwhile, his voluntary switch to the Bolsheviks in 1920 as well as his merits as an aviation designer and organizer of the aviation industry, and his sincere confessions were not taken into account. As an honest and sincere person and officer, he believed the demagogic statements of the Bolsheviks. And this was Kalinin's fatal mistake, for which he paid with his life. And not only him, but thousands of other officers, engineers, professors, who believed the Bolsheviks and cooperated with them, were later repressed.

In his book [3], V.S. Savin presents the testimony of K.O. Kalinin's daughter, who said that after the Bolshevik coup, her father was repeatedly offered to leave the country, including by his brother Vladimir, who fled to Poland, and the famous aircraft designer Igor Sikorsky, who emigrated to the USA. But Kostyantyn Oleksiyovych refused. And this was another fatal mistake on his part. Yes, during the Soviet times, despite all circumstances and obstacles, Kostyantyn Kalinin managed to realize himself as an aircraft designer, had popular recognition, and was even awarded the Order of the Red Banner of Labor. But his finest hour lasted a little over a decade, approximately from 1923 to 1935, when he designed a whole series of aircraft, including experimental ones that were ahead of their time. We think, under other circumstances, Kostyantyn Kalinin could have done much more, not only for domestic but also for world aviation. However, the Soviet authorities killed him at the peak of his creative flight, not allowing him to complete the projects he started.

3 Conclusions

Researching the biography and achievements of well-known domestic aircraft designers helps to better understand how the aviation industry developed in our country and what factors influenced this process. A deeper understanding of the fate, life path, and personal characteristics of K.O. Kalinin will assist future aircraft builders in forming appropriate worldview concepts, valuable orientations, and personal qualities to overcome contemporary challenges and aspire to develop domestic aircraft construction.

References

1. Rudenko. A.T.: Memories of K.O. Kalinin Photocopy of typewritten text. Museum of Aviation of the Kharkiv State Aviation Enterprise (undated)
2. Lyakhovetsky, M.B.: Everything in the wing: pages of the life and work of the aircraft designer. In: Kalinin, K.A., Prapor, Kharkiv, 184 p. (1986)
3. Savin, V.S.: Planet “Konstantin”, 312 p. Osnova, Kharkov (1994)
4. Rdiva, F.: op. 1. file 1389, sheet 2 (2008)
5. Zgurovsky, M.: Interrupted flight: Konstantin Kalinin, his life and airplanes. Dzerkalo tyzhnia, September 5–12 (No. 33), p. 11 (2008). (illustration, portrait, photo)
6. Rdvia, F.: op. 1, reference 569, sheet 88, 125, 126,127 (2008)
7. Kharuk, A.I.: Wings of Ukraine: Air Force of Ukraine, 1917–1920, 96 p. Tempora, Kyiv (2008). (fig)
8. Tatarchuk, V.V.: Scientist in the field of aircraft construction V.F. Bobrov (1884–1946): biography milestones (to the 130th anniversary of his birth). History of Science and Biography. Electronic Scientific Publication, No. 3 (2014)
9. RDVA, F.24699, item 1, file 1, sheet 32

Control Systems and Engineering

Efficiency of Protective Textile Smart Systems Using Electronic Tags

Mykola Riabchykov[1](✉), Viktoriia Mytsa[2], Oksana Tkachuk[1], Olena Pakholiuk[1], and Dmytro Melnyk[1]

[1] Lutsk National Technical University, Lutsk 43018, Ukraine
mykola.riabchykov@lntu.edu.ua
[2] Khmelnytskyi National University, Khmelnytskyi 29016, Ukraine

Abstract. The possibilities of creating textile smart systemsfor protective clothing operating at elevated temperatures are investigated. The main performance indicators of textile products in such conditions are determined. Protective clothing for working in an environment of elevated temperatures provides for the possibility of working in temperatures from 40 to 160°. For these purposes, fire-resistant polyester fibres are used. The service life of such materials is limited, and for high temperatures, the total service life can be several hours. An indicator of the integrated accumulation of thermal damage is proposed to monitor the condition of a textile product. The automated monitoring of the state of the protective system is provided by an integrated electronic complex, including a temperature sensor, a contactless NFC transmitter, an NFC tag, and an external NFC reader. Experiments in which electronic tags were heated to high temperatures under mechanical stress were conducted. Microscopic studies demonstrate certain changes in the structure of electronic tags. The main indicator of an electronic tag is not its appearance, but its performance. The ability to record and read information is proposed as such an indicator. The studies demonstrate the practical invariance of the response time up to a temperature of 130–140° and a slight increase with long-term heating to a temperature of 160–170°, which exceeds the maximum values of the functioning of protective textile systems.

Keywords: smart clothing · electronic tags · data storage

1 Formulation of the Problem in General Terms

Digitalisation is penetrating all areas of human activity. At the same time, certain problems arise in the interaction of a complex dynamic system in terms of safety and reliability [1]. Safe working conditions remain a priority in the process of introducing any new technical system [2]. It is necessary to take into account external conditions, conditions of comfortable stay, and the capabilities of modern protective and digital means. One of the problematic areas is technologies related to work in high temperature environments. An example of such conditions is hot welding at the factory «Ukrainian Power Machines» (Fig. 1, photo from https://ukrenergymachines.com/clients/services/welding-production).

M. Nechyporuk et al. (Eds.): ICTM 2023, LNNS 1008, pp. 189–197, 2024.
https://doi.org/10.1007/978-3-031-61415-6_16

Fig. 1. Working at elevated temperatures (https://ukrenergymachines.com/clients/services/welding-production)

Working in temperatures that can exceed 100 °C undoubtedly requires both protective means and means of control. It is necessary to monitor both the working conditions and the condition of the protective equipment itself, as damage to the latter can lead to fatal consequences.

2 Research on the State of the Issue

The main means of protecting workers in conditions of high temperatures is the use of special protective clothing [3].

Article [4] notes the main factors necessary for the functioning and operation of protective clothing. The requirement to ensure proper conditions should be accompanied by ensuring the necessary performance, protective, and hygienic properties of materials, including conditions for recording damage.

The main achievements in the creation of special materials for the manufacture of protective clothing for welders are given in the study [5].

Modern conditions dictate fundamentally new approaches to solving these problems. Achievements in the field of smart clothing, which is capable of solving several pressing problems by modern means, come to the fore [6, 7]. At the same time, several problems of such systems are noted, including the stability of smart characteristics during the operation of these products [8], as well as their implementation in real products [9].

According to the problem, smart clothing must have the ability to store, process, and transmit information during operation under the influence of high temperatures and other objective and subjective factors.

The study [10] describes the methods of registration, storage, and transmission of information from clothing, which is exploited with the help of special electronic tags.

Electronic tags are used in various quantities in the construction of clothing to ensure the rapid transfer of information [11]. There is no data on the durability of such tags. It is noted [12] that the use of electronic tags will significantly improve many of the processes that ensure the functioning of smart clothing, but data on the conditions of its functioning are needed.

Study [13] considers the problems of quick identification of clothing. The parameters that are desirable to remember are noted, while the means of storing information are absent. Article [14] proposes an improved system for recognizing tags on clothing to improve manual labeling methods. The possible directions for the introduction of real electronic tags remain unclear.

Diekel F. et al. [15] substantiate the expediency of using environmental labels, which should contain data on the environmental impact during the life cycle of a textile product. The principles of recording information on such tags are not defined.

Traceability guarantees using clothing labeling methods are considered by Santos-Roldán L. et al. [16]. It is noted that the information on existing labels is incomplete and insufficient. At the same time, modern methods cannot provide the necessary and sufficient amount of such information.

The need for environmental labeling of clothing to inform environmentally conscious consumers is also noted in the study [17]. The authors present methods of environmental labeling in the textile and clothing industry to assess the effectiveness of products based on sustainability, while electronic tags are not studied.

Maguire H. and Fahy F. [18] note the disadvantages of using traditional labels on clothing in the process of sustainable use. This is due to the widespread disregard for the information provided on the labels.

Study [19] confirms the relevance of using smart clothing for various special purposes, while additional research is needed for the real conditions of using existing electronic devices to solve specific problems.

The main challenges are to create conditions for recording the accumulation of temperature and other loads for further assessment of the condition of protective textiles. The purpose of the study is to substantiate the possibility of creating smart textile products capable of continuously recording working conditions based on the use of modern electronic tags.

3 Basic Requirements for Protective Materials and Products Used in High-Temperature Environments

The need for workwear is growing by around 15–20% every year worldwide. Not only is the demand for special purpose clothing growing, but also the quality requirements of customers. Special clothing must fulfill its main function - to protect workers from adverse production and environmental factors. In the case of farce-major situations at work, various types of workwear can save human health and life. Any type of workwear must be completely safe and not become a source of additional danger in an extreme situation.

Protective clothing is clothing that covers or replaces one's own clothing and is designed to protect against one or more types of hazards. That is why new types of workwear are in demand today, which not only have high functional characteristics but also feature personalization and individual style.

An analysis of many types of human professional activity in historical retrospect highlights clothing as an important protective component. The development of textile and clothing production processes, further mechanization, and automation of technological processes for the design and manufacture of modern special-purpose clothing has made it possible to solve a number of problems with regard to its protective properties.

Mandatory certification of special-purpose clothing for compliance with regulatory and technical documentation is provided, as well as mandatory licensing by employers of permanent workplaces for compliance with labor protection requirements.

Textile materials for special clothing vary, as do the protective functions they perform. The first and foremost function of fabrics for special-purpose products should be reliability and ease of use.

Protective clothing for work in high-temperature environments provides for the possibility of working in temperatures ranging from 40 to 160 °C. Flame-retardant polyester fibers are used for these purposes. Examples of such fibers include Proban KS-52, Flame-Stat Lite, Tecasafe HA 9001, Nomex BV-107, and Nomex ADV 240. Meanwhile, the operating time of such materials is limited, and for high temperatures, the total operating time can be determined by several hours [20].

It should be taken into account that reaching a critical temperature in the textile material leads to qualitative changes that negate its further use [21].

4 Development of a System of Registration of Operating Conditions of Special Textile Products

To collect and record data on the condition of protective clothing, it is proposed to use electronic devices incorporated into the design of a textile product. Such devices have a sufficient degree of miniaturization to be compactly placed on the product. The temperature is recorded using a miniature temperature sensor 1 (Fig. 2). Further solutions are based on the use of near-field communication (NFC) sensors. The temperature data is transmitted to a contactless NFC transmitter 2, which creates a magnetic field 3 to record the information on the NFC label 4.

The accumulation of thermal damage occurs in an environment of elevated temperatures when exposed to them for a certain period of time. In the following, we denote the current time of operation of the textile product by the letter τ, the current temperature T.

Obviously, a certain temperature level does not cause significant damage. Higher temperatures lead to an accumulation of damage. This problem is beyond the scope of this study, but it is clear that there is a certain function $f(T)$ that determines the degree of damage as a function of temperature. The integral value of the damage function is written on the electronic tag:

$$F = \int f(T) d\tau \tag{1}$$

The condition for the functioning of a textile product is to limit the accumulated damage to the critical value $F < Fcr$.

Fig. 2. Scheme of registration of accumulated temperature damage: 1 - temperature sensor; 2 - contactless NFC transmitter; 3 - antenna; 4 - NFC tag; 5 - external NFC reader.

The current value of the damage function is recorded by an external NFC reader 5.

This system can be easily incorporated into the design of a textile product without changing its functional forms and design features. The ease of use and fixation ensures high reliability and efficiency. The presence of electronic devices allows such devices to be classified as smart systems that independently accumulate information and are able to signal problems.

5 The Ability of Protective Textile Smart Systems to Function in Real-World Conditions

The real problems of such smart systems may arise in the event of their possible damage when operating at elevated temperatures. In this case, it is desirable to determine the risks of their quality operation [22]. Undoubtedly, the operating conditions of electronic devices should exceed those for textile materials, which allows them to be transformed into smart systems in a wide range of temperatures and other adverse conditions. For these purposes, experiments were conducted in which electronic tags were heated to high temperatures under mechanical stress. At the same time, microscopic studies of the structure of electronic tags were carried out. Figure 3 shows the surface of an electronic tag when heated to certain temperatures.

The structure of electronic tags is undergoing certain changes. In particular, heating to 110 °C leads to a general darkening of the working surface of the tag. Heating to 150 °C leads to the appearance of contrasting areas. With further heating, the contrast and number of such areas increase. Despite certain changes in color and structure, there is no general loss of integrity of the electronic tag.

The main indicator of an electronic tag is not its appearance, but performance indicators. As such an indicator, the possibility of recording and reading information is offered.

Fig. 3. Damage to electronic labels during heating 1–110 °C, 2–150 °C, 3–180 °C.

During conducting experimental research, electronic tags were heated to a certain temperature and kept for a certain time, after which attempts were made to record and read information. Despite certain structural changes shown in Fig. 3, they practically do not affect the main properties of electronic devices up to a certain limit.

Figure 4 shows the average time from the click of the electronic tag depending on the heating temperature.

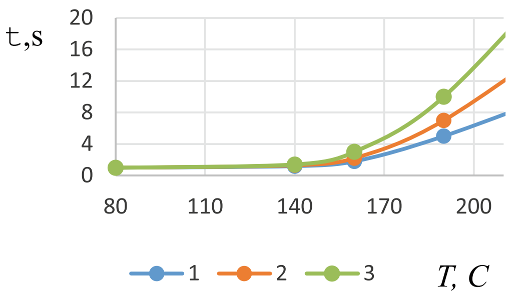

Fig. 4. The average time of reading information from electronic labels depending on the temperature: 1 - hold for 0.5 h; 2 - hold for 1 h; 3 - hold for 1.5 h.

Heating up to 140 °C with an arbitrary exposure time does not affect the ability of electronic devices to transmit and receive information. Starting from the level of 140 °C, certain shorts are recorded. The capabilities of the tags are preserved, but the activation time begins to increase. It should be noted that practically up to the level of 170–180 °C, the tag mainly retains its properties, although an increase in the heating time leads to an increase in the activation time, which can negatively affect the work efficiency.

Short-term operation of electronic tags is also possible at higher temperatures up to 180–200 °C, which in any case exceeds the requirements for protective clothing in the most stressful conditions.

Research was also conducted on the effect of abrasive damage on the ability of electronic tags to store and transmit information. The results demonstrate high stability and preservation of information without a noticeable increase in the operating time with the number of erasing cycles up to 150–270 °C. Therefore, damage to electronic tags without a change in integrity has little effect on the effectiveness of electronic tags to perform their functions.

At the same time, the conditions under which the integrity of the electronic tag is damaged have a negative impact on its further functioning. This fact can affect the technological conditions for fixing electronic tags placed on textile products. Attempting to thread electronic tags using sewing equipment in most cases results in the termination of the functioning of the tags in their main functions.

6 Constructive Schemes Location of Electronic Systems in Textile Products

A separate issue in using electronic means for temperature recording may be their location in the construction of a protective textile product. This arrangement solves the contradictory issue of ease of access, manufacturability, and the choice of the location with the highest temperature. In various cases, such locations may be associated with the specifics of the product type, the presence of structural or protective elements, the zone and type of load, etc. [23, 24].

The use of specific types of protective clothing depends on the nature of the work and the requirements related to the temperature conditions in the respective workshop or industry. To work in high-temperature conditions, a list of types of products defined by the relevant regulatory documents is used, the most common of which are trousers, overalls and jackets.

The attributes and features of the artistic and design characteristics of special-purpose products allow for a number of geometric transformations to optimize the design [25]. A significant number of protective structural elements in these products allows for the

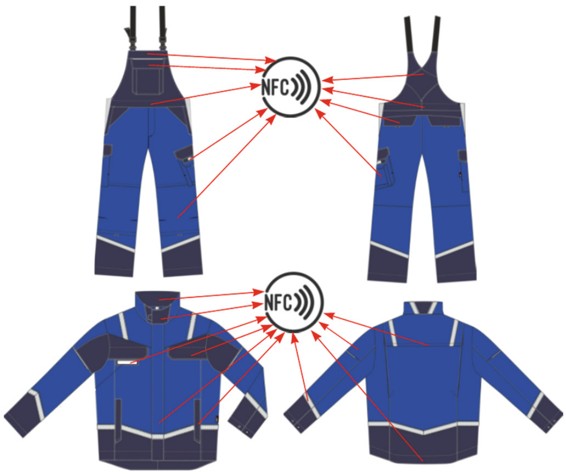

Fig. 5. Possible locations for electronic tags in overalls and jackets

widespread use of electronic tags in different quantities in different areas. Variants of applying electronic labels on different parts of overalls and jackets are presented in Fig. 5.

Since electronic tags do not require contact or direct visibility, their location can vary and be used in some areas for reading and in others for recording information.

7 Conclusions

The feasibility of using electronic labels to create protective textile smart products has been proven. Reasonable requirements for similar systems requiring operation in conditions of 40–160^0 C. Reasonable integral function of accumulation of temperature damage to textile material. The proposed scheme for registering accumulated temperature damage, which includes a temperature sensor, a contactless NFC transmitter, an NFC tag, and an external NFC reader. The possibility of functioning of the proposed system up to temperatures of 170–1800, which exceeds the operational requirements for protective products, has been proven. Design schemes for the location of electronic tags in protective clothing systems are proposed.

References

1. Mygal, G., Mygal, V., Protasenko, O., Klymenko, I.: Cognitive aspects of ensuring the safety, dependability and stability of a dynamic system's functioning in extreme conditions. In: Nechyporuk, M., Pavlikov, V., Kritskiy, D. (eds.) Integrated Computer Technologies in Mechanical Engineering - 2021. ICTM 2021. LNNS, vol. 367, pp. 195–206. Springer, Cham (2022). https://doi.org/10.1007/978-3-030-94259-5_18
2. Ginevičius, R., Trishch, R., Bilan, Y., Lis, M., Pencik, J.: Assessment of the economic efficiency of energy development in the industrial sector of the European Union area countries. Energiesthis **15**(9), 3322 (2022). https://doi.org/10.3390/en15093322
3. Kasimova, A., Muxamedova, Z., Tashbayeva, D., Sattarova, D.: Production of special work clothes to ensure safety of miners' activities and operational, protective and hygienic properties of the fabrics used. AIP Conf. Proc. **2789**, 040018 (2023). https://doi.org/10.1063/5.0145909
4. Komarkova, P., Glombikova, V., Vesela, D.: Comfort properties of special clothes worn by sufferers from atopic dermatitis. Text. Res. J. **93**(9–10), 2063–2077 (2023). https://doi.org/10.1177/00405175221138979
5. Zubkova, N., Naganovskii, Y., Levakova, N.: Fabrics for working clothes protecting from sparks and molten metal spatters. Fibre Chem. **53**, 388–390 (2022). https://doi.org/10.1007/s10692-022-10309-2
6. Eike, R.J., Depping, A., Cliett, A., Michaelson, D., Li, Y.: Initial insights of laundry detergent and additive impact on e-textile surface resistivity. Text. Res. J. **93**(13–14), 3109–3127 (2023). https://doi.org/10.1177/00405175231152876
7. Riabchykov, M., Alexandrov, A., Trishch, R., Nikulina, A., Korolyova, N.: Prospects for the development of smart clothing with the use of textile materials with magnetic properties. Tekstilec. **65**(1), 36–43 (2022). https://doi.org/10.14502/tekstilec.65.2021050
8. Riabchykov, M., Nazarchuk, L., Tkachuk, O., Stytsyuk, V.: Creation of smart compression garment using magnetic nanotextiles. Res. J. Text. Appar. (2023). https://doi.org/10.1108/RJTA-08-2022-0095

9. Riabchykov, M., Mytsa, V., Bondarenko, M., Popova, T., Nechipor, S., Nikulina, A., Bondarenko, S.: Formation of complex 3D surfaces scans for garment CAD. Fibres Text. **30**(3), 13–18 (2023). https://doi.org/10.15240/tul/008/2023-3-002
10. Maia, V.C., Oliveira, K.M., Kolski, C., Travassos, G.H.: Using RFID in the engineering of interactive software systems: a systematic mapping. Proc. ACM Human-Comput. Interact. **7**(EICS), 183, 1–37 (2023). https://doi.org/10.1145/3593235
11. Shaikh, A., Jabari, S., Xiao, R., Buruk, O., Hamari, J., Virkki, J.: Passive RFID-based phone call system integrated into clothing and furniture. In: 7th International Conference on Smart and Sustainable Technologies (SpliTech), pp. 1–5 (2022). https://doi.org/10.23919/SpliTech55088.2022.9854371
12. Jankowski-Mihułowicz, P., Pawłowicz, B., Kołcz, M., Węglarski, M.: Identification Efficiency in RFIDtex Enabled Washing Machine. IEEE Access **11**, 103814–103829 (2023). https://doi.org/10.1109/ACCESS.2023.3317510
13. Jiang, X., Chen, Z., Chi, C., Sha, S., Zhang, J.: Research on intelligent recognition of trouser silhouettes based on label optimization. J. Eng. Fibers Fabr. **18**, 1–9 (2023). https://doi.org/10.1177/15589250231168950
14. Shi, Y., Zhu, M.: Clothing label recognition based on improved Inception algorithm. In: Proceedings 12246, 2nd International Conference on Signal Image Processing and Communication, 1224621 (2022). https://doi.org/10.1117/12.2643474
15. Diekel, F., Mikosch, N., Bach, V., Finkbeiner, M.: Life cycle based comparison of textile ecolabels. Sustainability **13**(4), 17512021 (2021). https://doi.org/10.3390/su13041751
16. Santos-Roldán, L., Palacios-Florencio, B., Berbel-Pineda, J.M.: The textile products labelling analysis and requirements. Fash Text **7**, 11 (2020). https://doi.org/10.1186/s40691-019-0202-4
17. Ziyeh, P., Cinelli, M.: A framework to navigate eco-labels in the textile and clothing industry. Sustainability. **15**(19), 14170 (2023). https://doi.org/10.3390/su151914170
18. Maguire, H., Fahy, F.: Unlocking insights in the everyday: exploring practices to foster sustainable maximum use of clothing. Clean. Responsib. Consum. **8**, 100095 (2023). https://doi.org/10.1016/j.clrc.2022.100095
19. Zhang, C., et al.: Customizing triboelectric nanogenerator on everyday clothes by screen-printing technology for biomechanical energy harvesting and human-interactive applications. Adv. Mater. Technol. **8**(4), 2201138 (2023). https://doi.org/10.1002/admt.202201138
20. Ostapenko, N., et al.: Definition of the main features of material assemblies for thermal protective clothing during external high-temperature effect modelling. Tekstilec **64**(2), 136–148 (2021). https://doi.org/10.14502/Tekstilec2021.64.136-148
21. Riabchykov, M., Vilkov, S., Nechipor, S., Popova, T.: Two-dimensional studies of thermo-mechanical properties of textile materials for 3D formation. Vlakna a Textil **25**(2), 87–92 (2018)
22. Trishch, R., Nechuiviter, O., Hrinchenko, H., Bubela, T., Riabchykov, M., Pandova, I.: Assessment of safety risks using qualimetric methods. MM Sci. J. 6668–6674 (2023). https://doi.org/10.17973/MMSJ.2023_10_2023074
23. Slavinska, A., Matiukh, S., Mytsa, V., Syrotenko, O., Dombrovska, O.: Devising a method for the interactive arrangement of structural elements of men's jacket models. East.-Eur. J. Enterp. Technol. **1**(115), 56–66 (2022). https://doi.org/10.15587/1729-4061.2022.251065
24. Slavinska, A., Syrotenko, O., Mytsa, V., Dombrovska, O.: Simulation model of the morphological field of data for constructing a universal design of trousers. East. Eur. J. Enterp. Technol. **1**(1–103), 52–61 (2020). https://doi.org/10.15587/1729-4061.2020.211997
25. Slavinska, A., Mytsa, V., Syrotenko, O., Dombrovska, O.: Method of optimization of geometric transformations of design surfaces of a man's jacket. IOP Conf. Ser. Mater. Sci. Eng. **1031**(1), 012021 (2021). https://doi.org/10.1088/1757-899X/1031/1/012021

Modeling of Complex Spatial Structures Through the Example of the "Slavyanka UAS 7" Reaper

Andrew Larin[1], Alexander Trubayev[1](✉), Oleksandr Tymchenko[2], Oleksii Vodka[1], and Kseniia Potopalska[1]

[1] National Technical University, Kharkiv Polytechnic Institute, 2, Kyrpychova Street, Kharkiv 61002, Ukraine
trubayev@gmail.com

[2] LLC Ukr.Agro-Service, 12B, Plitochnaya Street, Kharkiv 61000, Ukraine

Abstract. A strategy for modeling of complex mechanical systems based on the calculation and experimental approach has been developed. It suggests that the structural elements should be replaced by simpler ones, but by those that are equivalent to the original elements in terms of the dynamics and strength properties. It makes it possible to reduce the dimensions of the finite element models, as well as to increase their efficiency and reliability.

The reaper's three rotors (stripper beater, stripping drum and an auger) were modelled as integral and uniform cylindrical cases with a given bending rigidity and respective weight. This being done, the rotors' rigidity properties were determined experimentally. This research being held, the experimental values of the structures' natural frequencies were determined by using a vibration measuring complex based on the microelectromechanical sensor ULTRA-V-I.

The calculation and experimental research for the strength of the "Slavyanka UAS 7" stripper reaper, manufactured by Ukr.Agro-Service LLC, have enabled us not only to lighten its structure, but also to issue recommendations on designing a reaper with a working width of nine meters, introduced into the production.

Keywords: Stripper Reaper "Slavyanka UAS 7" · Ukr.Agro-Service LLC · Finite Elements Method · Stress-Strain State · Spectrum of Natural Frequencies

1 Introduction

The finite elements method (FEM) is currently the main method in different areas of the engineering activity for calculating structures, particularly, for strength. Being versatile, this method enables taking into account many specific features of the structure and to reach structural solutions which reduce the consumption of materials. However, to use it for rather complex structures, the design engineer should pay enough attention, sufficient to build an adequate model.

Due to this, the built model and the calculation results need a thorough checkup. If the researcher has an experience of calculating similar structures, the results obtained may

M. Nechyporuk et al. (Eds.): ICTM 2023, LNNS 1008, pp. 198–208, 2024.
https://doi.org/10.1007/978-3-031-61415-6_17

be compared with previous ones, and their similarity can serve as an indirect proof that the model and calculation are correct. In absence of such experience, and if the researcher has no data to compare the result obtained, then, if the structure concerned has already been manufactured, it is possible to make experiments proving that the results obtained are correct. Given the above, calculating the strength of complex structures requires meticulous checking for the correctness of the finite element model built.

Currently, research on complex structures is focused on their modernization and optimization by varying parameters and analyzing external loads [1–3]. The application of FEM to determine the stress state of such structures is a rather voluminous and complex task. Often the creators simplify a complex model, limiting themselves to the consideration of an ordinary beam structure [4–9]. Of course, simplifying the model is not only possible, but also expedient. However, the simplified model needs to be checked for compliance with the real design.

One of the methods of such checkup is comparing the spectrum of the model's natural frequencies and those of the real structure.

This research being held, the experimental values of the structures' natural frequencies were determined by using a vibration measuring complex based on the microelectromechanical sensor ULTRA-V-I.

Apart from the complexity in building the structure's model, there is the second circumstance to be taken into account, which is the dimensionality of the finite element model. High dimensionality considerably increases the duration of calculations and the volume of necessary memory, which is particularly important in making variable calculations. Mechanical engineering structures often have built-in shafts that rotate around fixed axes and are connected to the main part by using bearings. If these elements are rather complex, in order to simplify the model, we propose replacing them with simpler ones that are equivalent in strength and dynamic characteristics.

The strategy for building the mechanical model and for making strength calculations will be demonstrated through the example of the reaper "Slavyanka UAS 7" manufactured by Ukr.Agro-Service LLC (Kharkiv). This mounted stripper reaper is designed for harvesting all spiked and panicle grain crops, seeds of fodder and medicinal herbs by direct combining by threshing standing plants (see Fig. 1) [10, 11].

The operation principle of the header is to thresh standing plants by stripping them with the combs located on the stripper cylinder of the reaper. In this case, the plant stem is captured by the combs and pulled through the gap between their teeth, freeing itself from grains or seeds.

To ensure that the grain does not spill onto the ground during threshing, a beater stripper is used, which directs the flying grains forward into the general flow. Thus, up to 80% of the grain is released from the ear. The resulting mass, under the influence of inertial forces and air flow, moves to a screw conveyor and is fed into the combine thresher by the feeder house for final grinding and separation.

2 Setting a Task

The calculations are made for defining stresses and deformations of the reaper parts while operated and transported in order to study the possibility of simplifying its design, as well as the possibility of manufacturing the reaper with a larger working width and,

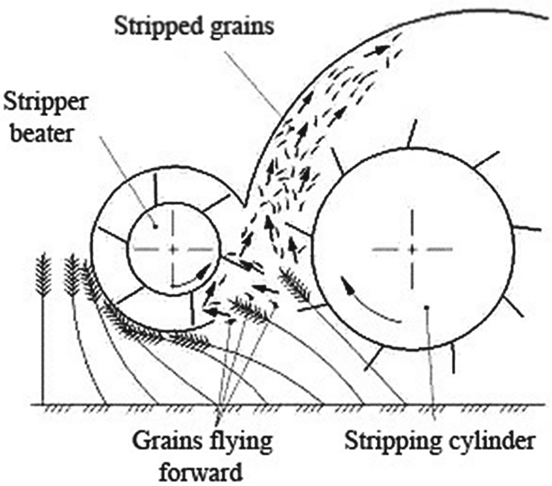

Fig. 1. Operation principle of the reaper

accordingly, with greater productivity. The solution to this problem is based on the condition of equal strength. This means that the stresses in all parts of the structure should, if possible, be at the same level.

To carry out the planned studies, the finite element model of the frame is built at the first stage. To make it verified, it is suggested to define experimentally the spectrum of natural frequencies and to compare it with the design values. Next, a quasi-static calculation is performed, i.e. the stresses and deformations of the reaper parts are determined under the influence of external disturbing forces, gravity and inertia forces, but without taking into account its elastic vibrations. This means that we neglect the inertial forces that arise when the frame oscillates as an elastic body, which is predetermined by a small influence of the external periodic disturbing forces.

3 Description of the Reaper Structure

The reaper is structurally made in the form of a frame welded from channel beams 10 and 12 mm wide and a long plate 6 mm thick. It is covered with welded structure side panels and two casings, which are open shells made of sheet iron 1 mm thick. There are four rotors installed inside the frame: the stripper beater divided into two parts in the middle by an intermediate support, a stripping drum and an auger. The rotors are supported by rolling bearings which are attached to the side panels. The drive for the operating rotors is also attached to the left panel. The main parts of the reaper are shown in Fig. 2

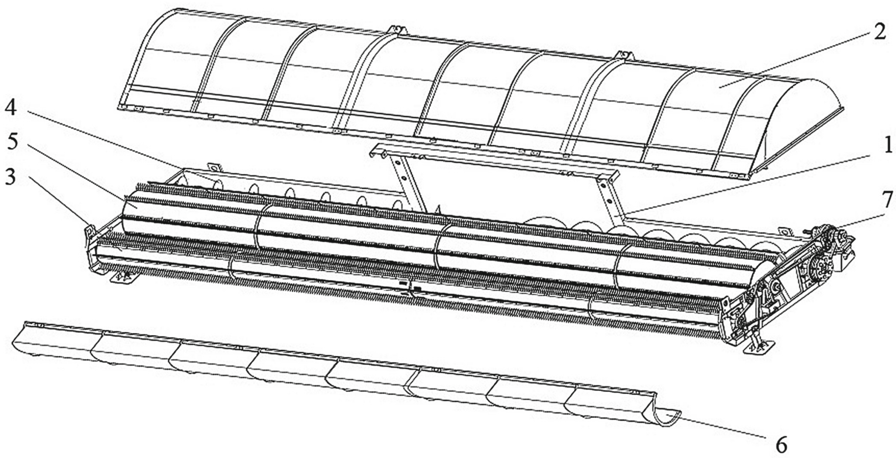

Fig. 2. Reaper body structure. 1 – frame; 2 – upper case; 3 – stripper beaters; 4 – auger; 5 – stripper cylinder; 6 – front casing; 7 – drive of the operating parts

4 Defining the Load

The load is made up by the inertia and gravity forces of the reaper parts. The reaper's frame is fixed to the feeder house of the combine harvester (Fig. 3). The inertia forces may be caused by acceleration acquired by the reaper as the harvester is moving on an uneven soil. To define them, we need to determine the motion law of the harvester's feeder house which coincides with the motion of the harvester's body.

At the same time, it is considered that the attachment points of the reaper to the feeder house and the rotors to their supports do not have flexibility.

The reaper's vertical motion caused by kinematic excitation from the harvester is studied. The maximum acceleration occurs when the harvester hits an obstacle or when its wheels fall into a hole. This being done, the vertical motions of the reaper suspension points are specified as a function of time. It should be noted that in the calculations it is the maximum acceleration value that matters.

Upon hitting an obstacle, the harvester's speed vector changes its direction, which means that a vertical component appears. At the same time, the speed value decreases due to the loss of energy caused by the obstacle and wheel deformation, as well as due to the harvester's lift.

At the beginning of the motion concerned, the acceleration is directed backward and upward, and the inertial force vector is directed forward and downward, respectively. At the final moment of hitting an obstacle, the vertical component of the speed decreases, and the inertia force vector is directed upward, which reduces the load. Approximate calculations show that the harvester's acceleration value when hitting an obstacle should not exceed 20 m/s^2, i.e. 2g.

In the second case, when the harvester wheels fall into a hole, at the beginning of the motion the acceleration is directed downward, and the inertial force reduces the load from the weight. This is followed by an impact from the wheel-ground contact,

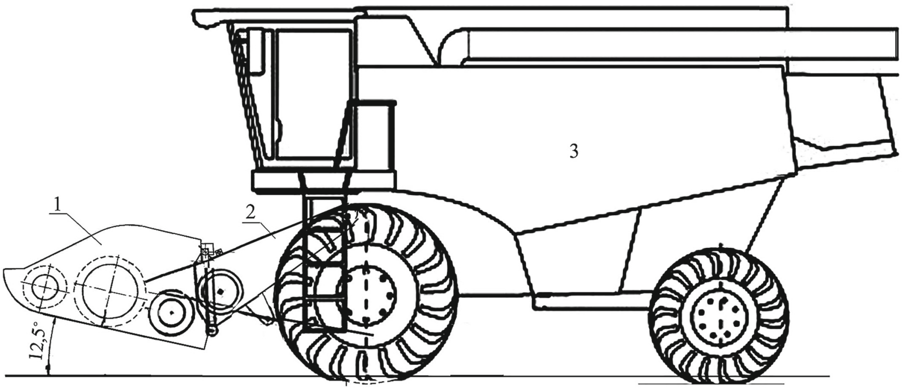

Fig. 3. Diagram of mounting the reaper to the combine harvester. 1 – reaper; 2 – feeder house; 3 – combine harvester

during which the acceleration rapidly changes the direction. Its value in this terrain can be estimated based on the speed at which the wheel falls into the hole, and based on the deformation of the wheel and the soil. Approximate calculations show that here the acceleration value should not exceed 20 m/s2 either. At the same time, it is directed upward, and the inertia force is directed downward. Thus, we can conclude that the maximum overload, even in the most extreme case, cannot exceed 2g. This means that when carrying out calculations, you should simply increase the weight of all reaper parts by three, which can be done by setting the density of the material from which these parts are made as three times higher than the true value.

5 Selecting Parameters for Casings Substituting the Real Rotors

As noted before, the stripper beaters, stripper cylinder and auger are mounted inside the reaper case. These rotors are quite complex systems, each based on a cylindrical casing made of steel 1 mm thick. Above these casings, there are components providing the functions of these rotors to be done. Thus, the stripper is equipped by “fingers” fixed by bolts to the supporting plates placed inside the casing, while the auger has a thin metal spiral. At the same time, the manufacturing technology of these rotors does not ensure the possibility to reliably describe their design parameters. This is due to the fact that various parts are attached to the casings using bolted connections which have gaps, or by welding of which the seams may not be continuous. Such manufacturing deviations do not affect the performance of the rotors, but they cannot be reliably modeled.

In contrast to dynamic calculation, the quasi-static calculation of the frame does not require building such rotor models to include their various structural elements, such as fingers, power elements, etc. It is enough to define them as solid homogeneous cylindrical casings with a given bending rigidity and corresponding weight, and to include them into the complete design model instead of real rotors.

This being done, it is suggested to determine the rotors’ rigidity properties experimentally. Thus, it is enough that the static deflection of the real rotor coincides with the deflection of the substituting one. The experiments carried out under static loading of the rotor give a large scatter of deflection values due to their smallness. Therefore, to determine the bending rigidity of the rotors, their natural frequencies were measured with free bearing. Since the shape of the static deflection of the rod practically coincides with the first vibration shape, it is sufficient to determine only the value of the first natural frequency. When doing this, it is necessary to check whether or not the properties of the casing appear in the rotor at the first natural frequency.

The frequency of these vibrations was determined using the mentioned vibration measuring complex [11]. A series of experiments were carried out using different places for attaching the load and for mounting the vibration sensor on the rotors. The rotor was installed on two supports, after which free vibrations were excited in it. To do this, a load weighing 20 kg was suspended on it using a steel wire. Then the wire was cut and the load broke, which caused free oscillations of the rotor.

Along with this, natural frequencies were determined through calculation using FEM. The results from the comparison of the experimental and calculated values of the first natural frequencies of the rotors are given in Table. 1. It showed that the calculation gives overestimated values. The experimental bending rigidity of the rotors is lower than the calculated values due to the fact that the actual structure is welded, and the welds are not always entirely welded. In the model, the structure is solid and the welds are not taken into account in any way. In addition, the model does not take into account possible gaps in threaded and rivet joints of the rotor parts.

Table 1. Experimental and calculated values of the first natural frequency of the rotors

Rotor name	Frequency value, Hz		Error
	Experiment	Calculation	
Auger	11	16,4	49%
Stripper	17	22,9	35%
Beater	27	35,9	33%

Figure 4 and 5 represent the first three vibration shapes of the stripper and auger. They reveal that in these rotors, the first vibration shape is bending, and the properties of the casings almost do not appear. Therefore, this case does not require striving for absence of casing shapes of vibrations in the substituting rotor.

6 Experimental Checkup of the Reaper Model

To verify the model, the natural frequencies of the entire structure were experimentally determined. To do this, the reaper suspended to the harvester was shaken, thereby exciting free vibrations. It should be noted that with such excitation only the first two natural frequencies appear, and the second shape of vibrations is manifested much less. Comparing the experimentally obtained frequencies with the calculated values gives a fairly good coincidence for the first natural frequency and somewhat worse for the second one

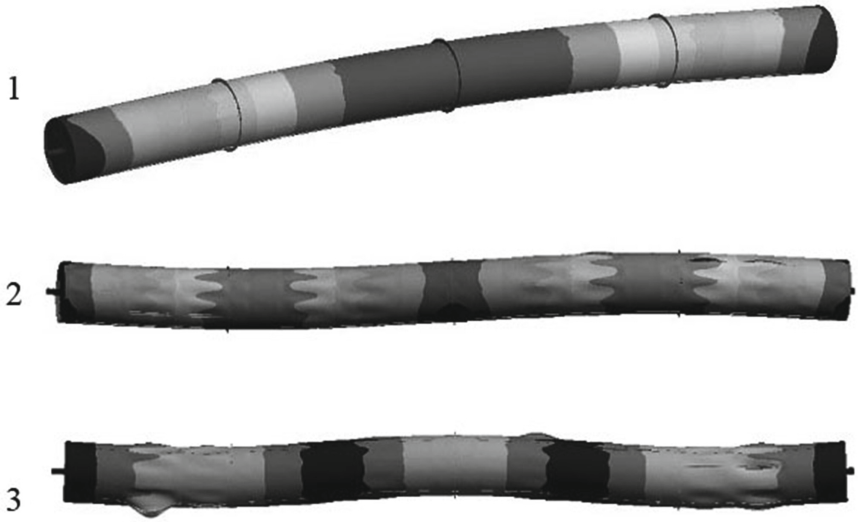

Fig. 4. Stripper vibration shapes

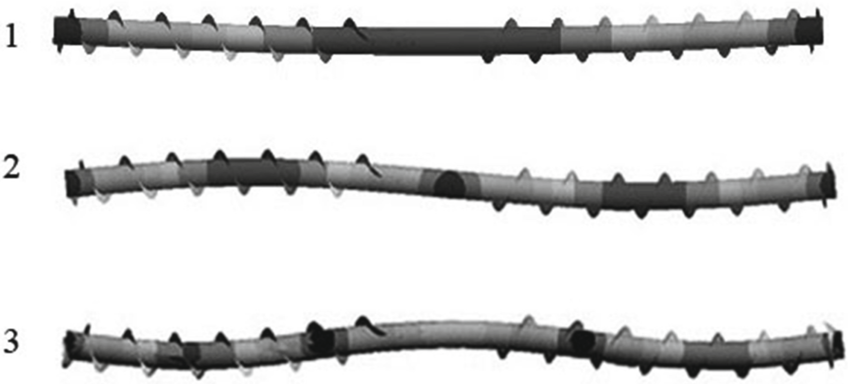

Fig. 5. Auger vibration shapes

(see Table 2). The overestimated calculated values, compared to the experimental ones, are also explained by the greater rigidity of the constructed model than the rigidity of the real structure. As with the rotors, the welded structure of the reaper is not continuous as it appears in the model, which reduces its rigidity, as compared to the rigidity of the model.

The second series of experiments consisted of determining deflections under static loading of the reaper. The experiments were carried out for two cases. First, the motions of the header parts were determined when it was suspended from the feeder house of the harvester. It was found that, when the reaper is raised, the structure rotates around a

Table 2. Values of the reaper's natural frequencies (Hz)

Frequency No	Experimental values	Calculated values	Error
1	1.65	1.93	17%
2	3.35	5.71	70%

horizontal longitudinal axis passing through the so-called threshold at an angle of less than 0.1° (0.0017 rad). The maximum motion in this case is 2.4 mm. The calculated value of the motion of the reaper's right edge (viewed from the harvester side) when suspended from the hoist is approximately 1.7 mm. In this case, the error is 29%.

In the second experiment, the deflection of the reaper standing on supports mounted along its edges was determined. To do this, an additional load weighing 2 kN was placed in the middle of the reaper at the place where the intermediate support of the beaters was attached. The experiment showed that the deflection from this load is approximately 0.5 mm. The maximum calculated deflection value from the additional load was 0.31 mm (error 38%).

As expected, the calculated motion values turned out to be lower than the experimental ones, which is also explained by the lower rigidity of the real welded structure compared to the model.

7 Calculations for the Reaper Under the Maximum Load

Next, using FEM, the motions and stresses in the structure of the reaper suspended from the harvester under the influence of overload in the most unfavorable situation were determined. It occurs when the front wheels fall into a ditch 30 cm deep. In this case, the harvester's acceleration is $2g$, and the load corresponds to triple the gravity of the reaper.

The calculations showed that the equivalent stresses, determined by the Mises criterion, in most parts of the reaper do not exceed 50 MPa with permissible stresses of about 210 MPa.

The only place where overload is observed is the frame with which the reaper is attached to the feeder house. In places where stresses are concentrated, their values even exceed the permissible values. Figure 6. Shows the distribution of stresses in this zone. However, such excess of permissible stresses is not dangerous, since we are talking about an extreme situation, and not about a cyclic load, thus stress concentrators do not pose a danger.

As for the distribution of motions, the calculation showed that the maximum motions are observed in the middle of the stripper and auger, reaching the values of about 5 mm. As for the body of the reaper itself, the maximum sagging, which is 3 mm, is observed on the right side, when viewed from the harvester side. Figure 7 shows the total motions of the reaper elements under the influence of the load specified. Motions in a real structure may be greater due to the reasons stated above.

Based on the research accomplished, work was carried out to reduce the reaper weight through the use of thinner sheet steel and smaller rolled sections. The weight of

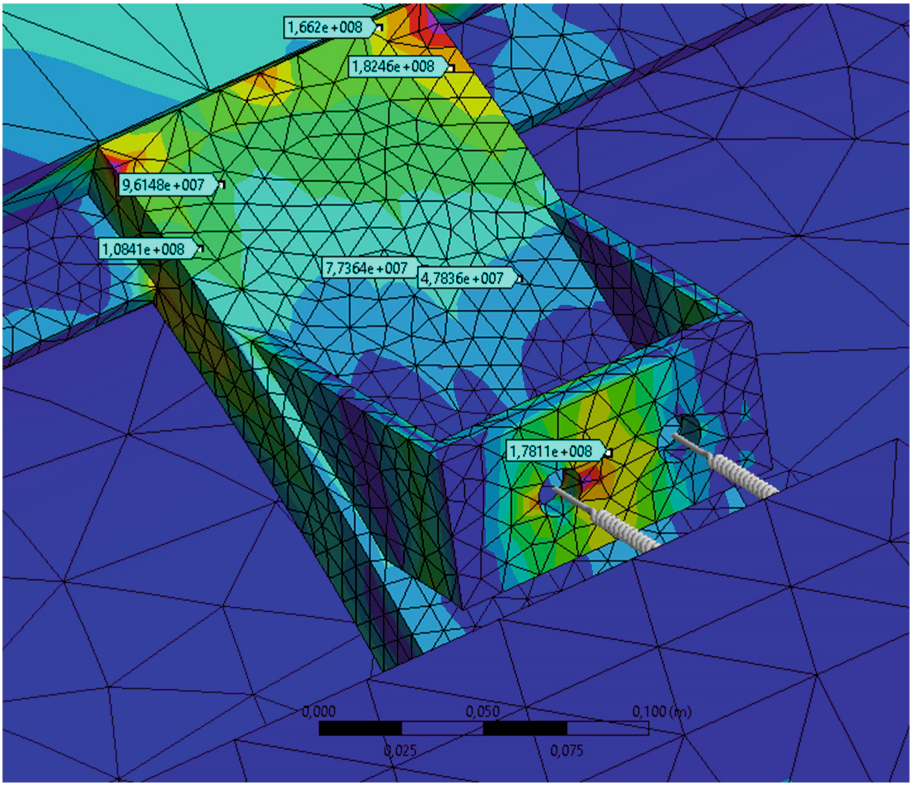

Fig. 6. Equivalent stresses by Mises for the most loaded area

the steel economized was about 60 kg with the total reaper weight being 2700 kg and the weight of the load-bearing structural elements being 1200 kg. At the same time, the model was previously rebuilt by taking into account the lightweight elements, and the calculations were repeated. They showed that such change had little effect on the overall pattern of stress distribution. As for the maximum stresses observed in the concentration zone on the frame with which the reaper is attached to the feeder house, they decreased by 37%. The fact that this is observed when the load is reduced by only 5% can be explained by the specific features of the FEM, which gives an unstable solution in the zone of stress concentration under a complex stress state condition.

The maximum calculated values of motion of the lightweight reaper body are 4–5% lower, which basically corresponds to a 5% reduction in load. At the same time, the deflections of the reaper rotors practically did not change, since the structure lightening should not affect them. When assessing the motions, it should be taken into account that the reaper elements that are not load-bearing have been lightened, and in general its rigidity should remain practically unchanged, while the effective force due to the forces of inertia and gravity is reduced, like the weight, by 5%.

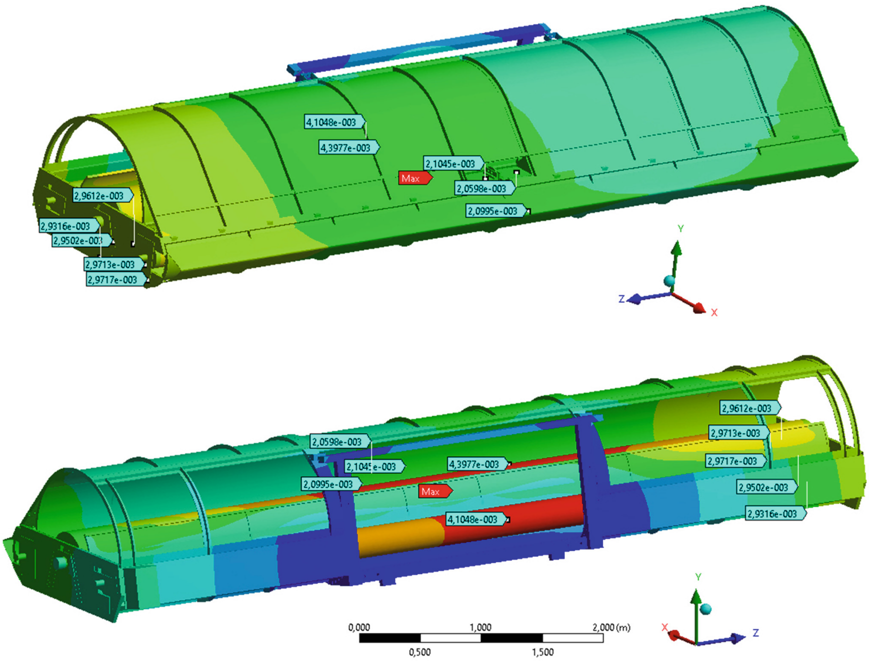

Fig. 7. Motion of the reaper's elements with the maximum load

8 Conclusions

A strategy for modeling complex mechanical systems has been developed, based on a calculation and experimental approach. It involves replacing complex elements with simpler ones, but equivalent to the original ones in terms of dynamic and strength characteristics. This allows to reduce the dimensionality of finite element models, as well as increase their efficiency and reliability.

It should be noted that the rigidity properties of a finite element model of a complex welded or riveted structure do not fully correspond to its real characteristics. This is due to the manufacturing technology of such products, in which the integrity of the structure is not fully respected due to the presence of unwelded areas of welds or gaps in rivet and bolted joints. The model was partially refined by inserting replacement shafts or rotors into it, the characteristics of which were determined experimentally.

As a result, we can conclude that such compound structures cannot be adequately described using a model in which the individual elements are rigidly connected to each other. In this regard, the results obtained when calculating such models are rather qualitative than qualitative. However, they make it possible to distinguish the most loaded areas, as well as make proposals for lightening the structure.

The calculated and experimental strength studies of "Slavyanka UAS 7" reaper performed by Ukr.Agro-Service LLC have made it possible not only to lighten the design, but also to give recommendations for the design of the reaper with a working width of nine meters, which has been introduced into production.

References

1. Ivanyshyn, V.V., Iliyashyk, V.I.: Duhanets′ Analysis of design features and operation of CLAAS LEXION 750, 760 TERRA TRAC combine harvesters for harvesting agricultural crops. Agricult. Technol. Econ. Techn. Sci. (30), 80–88 (2019)
2. Duhanets′, V.I., Hrushets′kyy, S.M., Tokarchuk, O.O., Bonchyk, V.S., Fedirko, P.P.: Analysis of the main malfunctions of grain harvesters and ways to improve their efficiency when harvesting grain, legumes and other crops. Technol. Energy Transp. Agric. Indus. **120**(1), 21–29 (2023). https://doi.org/10.37128/2520-6168-2023-1-3
3. Babiy, O.V., Dzyura, V.O., Holovets′kyy, I.V.: Study of the effect of vertical oscillations of the sprayer boom on the uniformity of spraying. Tsentral′noukrayins′kyy naukovyy visnyk. Tekhnichni nauky. **5**(36), S.216–226 (2022). https://doi.org/10.32515/2664-262X.2022.5(36).1.216-226
4. Zhang, Z., et al.: A rotational energy harvester utilizing an asymmetrically deformed piezoelectric transducer subjected only to unidirectional compressive stress. Energy Rep. **9**, 657–668 (2023). https://doi.org/10.1016/j.egyr.2022.12.027
5. Li, Y., Yan, P.: A compliant mechanism based piezoelectric beam energy harvester with multimode frequency up conversion. Energy Rep. **10**, 932–940 (2023). https://doi.org/10.1016/j.egyr.2023.07.044
6. Fu, H., et al.: Rotational energy harvesting for self-powered sensing. Joule **5**(5), 1074–1118 (2021). https://doi.org/10.1016/j.joule.2021.03.006
7. Lin, T., et al.: Modeling and field testing of an electromagnetic energy harvester for rail tracks with anchorless mounting. Appl. Energy **213**, 219–226 (2018). https://doi.org/10.1016/j.apenergy.2018.01.032
8. Yang, Y., Pian, Y., Liu, Q.: Design of energy harvester using rotating motion rectifier and its application on bicycle. Energy **179**(15), 222–231 (2019). https://doi.org/10.1016/j.energy.2019.05.036
9. Fan, K., et al.: A string-suspended and driven rotor for efficient ultra-low frequency mechanical energy harvesting Energy Convers. Manag. **198**, 111820 (2019). https://doi.org/10.1016/j.enconman.2019.111820
10. Shvartsman, M.Y., Timchenko, A.V., Brovin, A.V.: Stripping harvesting technology. A manual on the basics of engineering and technology (2021)
11. Sisolin, P.V., Koval′, S.M., Ivanenko, I.M.: Machines for harvesting grain crops by combing ears. KOD, Kirovohrad (2010)

Development of an Automated System for Analyzing the Stress-Strain State of the Elevator Structure, Taking into Account Operational Conditions

Aleksander Trubayev(✉), Bohdan Kashchei, Myкola Manilich, and Heorhii Semenenko

National Technical University "Kharkiv Polytechnic Institute", Kyrpychova Street, Kharkiv 61002, Ukraine
trubayev@gmail.com

Abstract. In CAD/CAE SolidWorks, a model of the grain storage building has been developed for the analysis of the stress-strain state, considering operational conditions. A typical precast reinforced concrete silo body, consisting of 60 silos arranged in ten rows, was used as the subject of the study. The following operating conditions were considered: an empty building; a building with full loading of specific silos according to the designer's rules; loading of silos with a specific grain volume according to the rules and with violations of the rules; fully loaded grain storage building. An automated system for determining the stress-strain state via finite element method, depending on the distribution of products in the structure, has been developed. After inputting initial data on grain placement in the silos, the system automatically calculates and displays data on the stresses and displacements of the building. Using the automated system, stress and displacement values of the structure were obtained for different loading scenarios. The stress-strain state was compared with regulatory indicators for various grain placement options. The developed automated system allows for the construction of an artificial intelligence system that will determine a rational sequence of loading and unloading the grain storage building, taking into account the stress-strain state of the structure.

Keywords: Automatic System · Stress-Strain State · Grain Storage Building · Finite Element Method

1 Introduction

The agriculture sector of Ukraine plays a significant role in the economy, contributing to 9.3% of the GDP according to State Statistics [1]. The production volumes of cereals and oilseeds have exceeded the country's needs and are actively exported. However, the growth rate of the harvest has outpaced the construction of grain storage complexes, resulting in a 44% deficit in storage capacity relative to the volume of harvested products as of 2018 [2]. In this context, the rational and safe operation of existing grain storage facilities is crucial for the country's economic development.

M. Nechyporuk et al. (Eds.): ICTM 2023, LNNS 1008, pp. 209–219, 2024.
https://doi.org/10.1007/978-3-031-61415-6_18

Sufficient attention has been given to the issues of operational reliability and current repairs of grain storage structures. For instance, the causes of damages and methods of restoration of such structures have been discussed by authors in [3].

It is noteworthy that the transition from a planned to a market economy has changed the methods and approaches to the loading regime of silo structures. This transition demands a flexible approach from managers and operational services in accommodating diverse batches of grains and oilseeds in these structures while ensuring compliance with strength and reliability criteria. Modern data collection methods enable the monitoring of structural conditions. For example, in [4], a list of possible sensor systems for tracking loads on buildings is provided. While this approach is one way to monitor the current situation, it requires significant additional capital investments. This work proposes a system for analyzing the condition of structures without using additional equipment, which reduces the initial investment cost.

Modern software tools are widely used for building analysis. In [5], analytical calculations of a concrete silo are compared with software calculations, concluding the equivalence of the obtained results. Additionally, the work in [6] presents an experimental dependence of pressure on enclosing structures as a function of the distance from the silo axis. However, according to existing standards [7], the pressure can be considered evenly distributed.

Among the types of grain storage, attention is drawn to prefabricated reinforced concrete silo bodies built in the 1970s–1980s. These structures were constructed using standard designs, and their operational lifespan is 30–50 years, with hundreds of loading-unloading cycles. Over the period of operation, these structures have accumulated fatigue deformations, and the degradation of concrete and reinforcement has occurred [8]. An analysis of the stress-strain state (SSS) of the silo body is provided by the authors in [9], with a conclusion on the adequacy of the obtained results and actual data on damages. Maintaining the authors' approach to the problem, the analysis of the structure's condition during changes in storage volumes can be considered.

In light of the above, the task of assessing the SSS of a grain storage facility, especially when expanding storage volumes, is a relevant issue for the operation of grain storage facilities made of prefabricated reinforced concrete. This assessment should be conducted before making decisions on placing additional grain volumes to prevent exceeding the normative values of SSS parameters. The integration of SSS assessment and decision-making systems developed for elevator complexes [10] will not only optimize the placement of grain batches according to technological requirements but will also allow these tasks to be performed with consideration for the reliability of the operating structures.

2 Problem Formulation

For the research, a silo structure made of precast reinforced concrete was used, which was constructed according to the standard project "3.702-1/79", developed by the Central Research and Design Institute for Grain Processing Equipment in 1981. The structure consists of a grid of vertical columns with capitals, on which conical bottoms rest, and on the latter, in turn, the walls of the silos. Each column, except for the external ones, supports four conical bottoms.

Based on the known project documentation data, models of the column with the capital, the bottoms, and the silo walls are built in CAD/CAE SOLIDWORKS, and the entire silo structure is assembled from these elements.

Loads on the elements are determined from their self-weight and from the full loading of the silo with wheat grain with a density of 7.9 kN/m^3 (according to [7], you can choose either the tabular value of 9 kN/m^3 or the value obtained by measurements; we consider the value of 7.9 kN/m^3 optimal based on practical operating experience). To assess rational computation volumes with an acceptable level of accuracy, the results of the finite element method (FEM) are compared with different mesh sizes.

The automated system for analyzing the stress-strain state (SSS) should allow determining its numerical characteristics when changing the loaded silos. By changing the order of loading grain into the silos, it is possible to find a rational loading scheme for a known amount of additional grain. To implement the stated task, the following stages need to be carried out:

- Develop an automated system based on CAD/CAE SolidWorks for the analysis of the grain storage building, taking into account operational conditions;
- Determine the stress-strain state analysis of the silos based on the FEM, taking into account various loading schemes. The investigation should simulate the mass of wheat in a fully loaded silo (136 512 kg).
- Investigating the Effects of Improper Loading Schemes on the Stress-Strain State of Silo Structures.

3 Calculation of the Physical and Mechanical Properties of Reinforced Concrete

The calculation of the physico-mechanical characteristics of reinforced concrete may be approximately conducted in the following manner. The volume of concrete M300 in the column К − 1 is $V_\mathrm{c} = 1.8\ \mathrm{m}^3$, and the mass of reinforcement is $m_\mathrm{s} = 185{,}8$ kg. Then the volume of reinforcement, taking into account the density of the reinforcement according to Table 1, is determined as follows:

$$V_s = \frac{m_\mathrm{s}}{r_\mathrm{s}} = \frac{185,8\,\mathrm{kg}}{7850\,\mathrm{kg/m^3}} = 0,024\,\mathrm{m}^3 \tag{1}$$

Let's determine the volumetric fraction of reinforcement in column К − 1:

$$\mu_s = \frac{V_\mathrm{s}}{V_s + V_\mathrm{c}} = \frac{0,024\,\mathrm{m}^3}{1,8\,\mathrm{m}^3 + 0,024\,\mathrm{m}^3} = 0,0132 \tag{2}$$

Physical and mechanical characteristics of concrete and reinforcement for column К − 1 were used during the investigation shown in Table 1.

To determine the averaged parameters of reinforced concrete, it is suggested to use the Halpin-Tsai mixture rule, according to which the modulus of elasticity and Poisson's ratio are determined by the following expressions.

$$E_{\mathrm{r.c.}} = E_\mathrm{s}\mu_\mathrm{s} + E_\mathrm{c}(1 - \mu_\mathrm{s}) \tag{3}$$

Table 1. Physical and mechanical characteristics of concrete and reinforcement for column K – 1

Name, designation, Unit of measurement	Concrete M300	Reinforcement A-III
Elastic modulus, E, Pa	0,255 10^{11}	1,96 10^{11}
Poisson's ratio, ν	0,2	0,3
Volumetric mass density, r, kg/m^3	2 410	7 850
Cube compressive concrete strength, $f_{\text{ck.cube}}$, MPa	13,24	
Mean tensile strength, f_{ctm}, MPa	0.98	
Yield strength, R_s, MPa		333,43

$$\begin{gathered} \nu_{\text{r.c}} = \nu_s \mu_s + \nu_c (1 - \mu_c) \\ E_{\text{r.c}} = 0,279\ 10^{11} \text{Pa}, \nu_{\text{r.c}} = 0,2. \end{gathered} \tag{4}$$

Henceforth, we will consider that reinforced concrete possesses such properties throughout the entire structure.

4 Automated Silo Loading System

The automated system is developed using the.NET framework and the C# programming language.

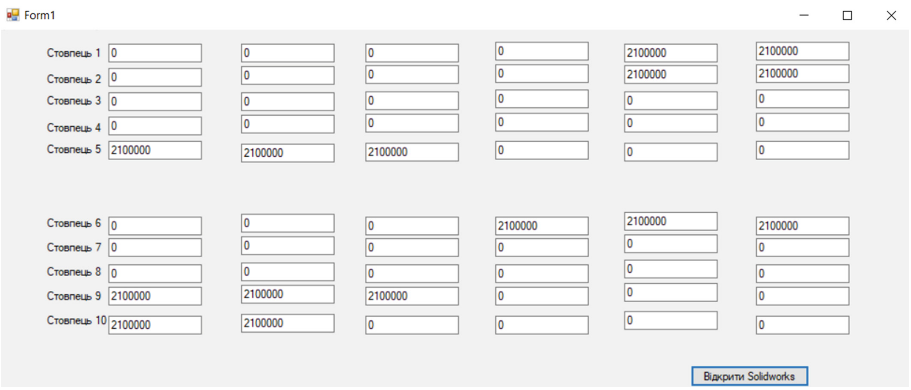

Fig. 1. Screenshot of Program Interface

The created interface (Fig. 1) allows the user to input the grain mass for each silo. Afterward, the user clicks on the "Start Investigation" button, initiating the SolidWorks software. The model of the elevator structure with the specified silo weights is loaded, and the computation process begins. Subsequently, the user can obtain results in the form of displacement and stress distribution throughout the structure. The logic, algorithm, and workflow sequence are illustrated in Fig. 2 and Fig. 3.

The displayed data shows the properly loaded distribution of silos in the grain storage building (Fig. 2).

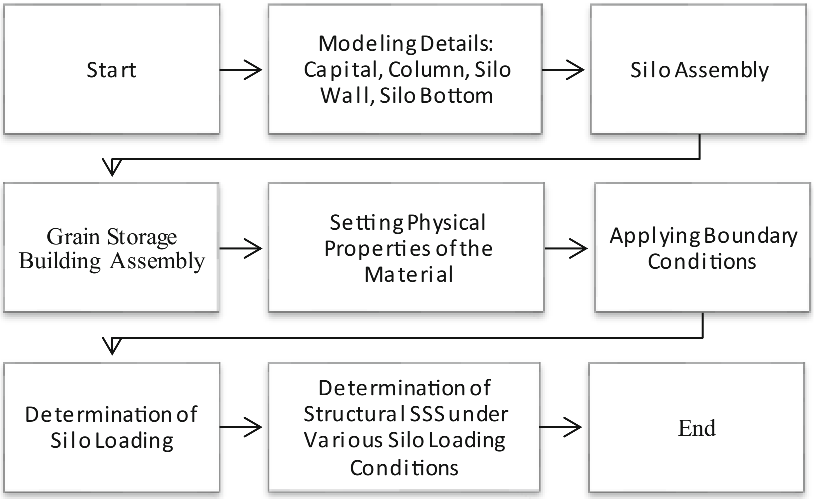

Fig. 2. Algorithm for Determining the SSS of grain storage building

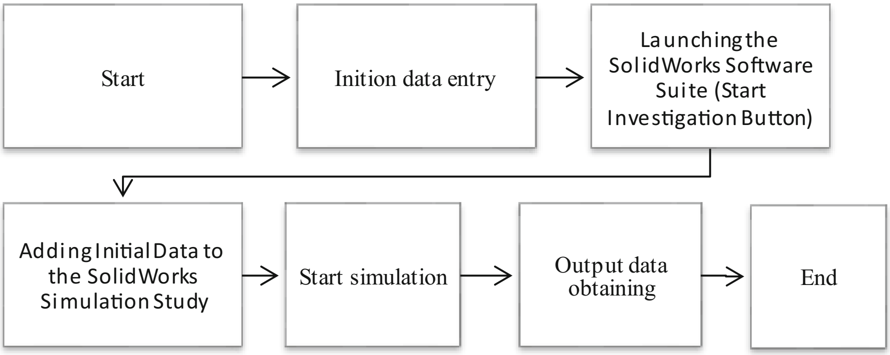

Fig. 3. Algorithm of the Automated System Operation

5 Grain Storage Building Modeling

The elevator model consists of a set of silos (Fig. 4), the bottoms of which (Fig. 7) are supported by columns (Fig. 5) and connected to walls of square cross-section (Fig. 6) through column capitals (Fig. 8).

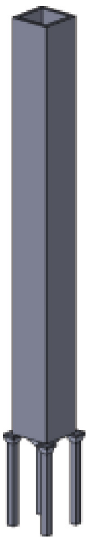

Fig. 4. Individual silo model

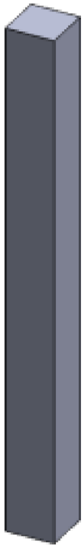

Fig. 5. Column Model

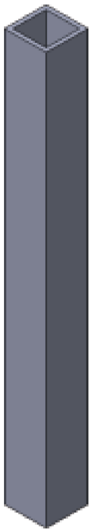

Fig. 6. Model of Silo Walls

The grain storage building is made of precast reinforced concrete and includes 60 silos, as depicted in Fig. 9.

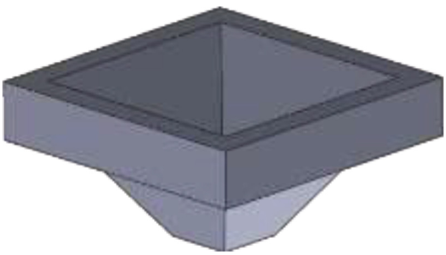

Fig. 7. Silo Bottom Model

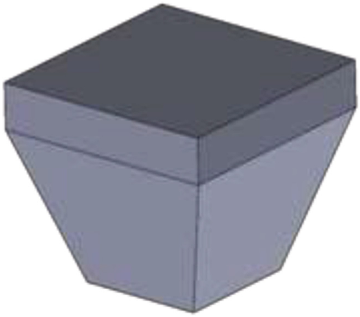

Fig. 8. Column capital model

6 Study of the Stress-Strain State of a Separate Silo

To assess the convergence of the Finite Element Method (FEM) results, a numerical investigation was conducted using meshes of various sizes. Five calculations were performed with different finite element sizes and varying levels of discretization in FEM. The number of elements and the corresponding mesh element size are given in meters:

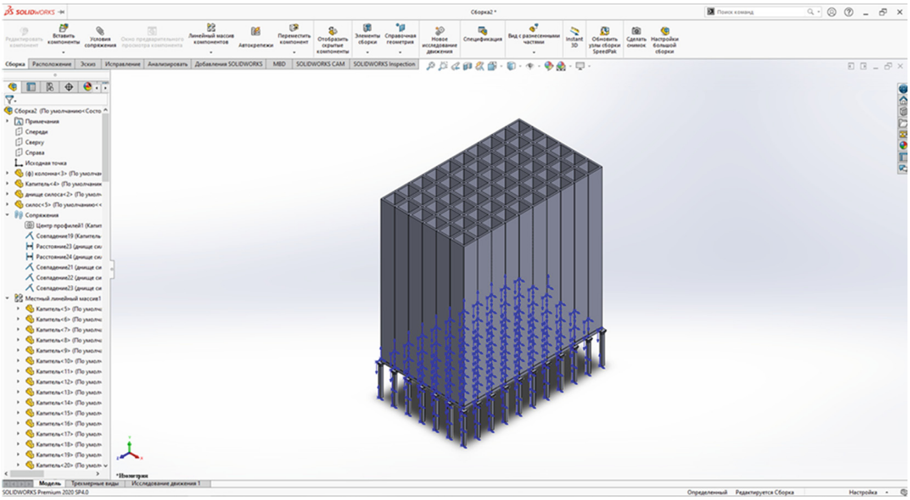

Fig. 9. Grain storage building model

1) mesh 0,600 × 0,03 × 0,03;
2) mesh 0,500 × 0,025 × 0,025;
3) mesh 0,400 × 0,02 × 0,02;
4) mesh 0,300 × 0,015 × 0,015 м;
5) mesh 0,2727 × 0,0136 × 0,0136.

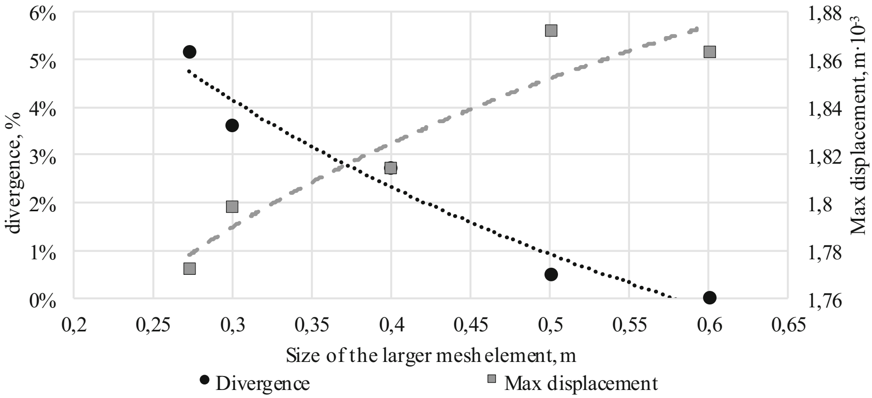

Fig. 10. Combined diagram assessing the convergence of FEM results for an individual silo.

From Fig. 10, it can be concluded that the mesh element size 0,400 × 0,02 × 0,02 (m) is acceptable for conducting calculations.

7 Analysis of Results Under Different Scenarios of Grain Allocation in the Silos Building

Figures 11, 12 and 13 depict various configurations of grain placement in the elevator that were used for comparing results. The red color indicates loaded silos, while the light gray represents empty ones. Stresses and displacements in a properly loaded grain storage building are shown in Figs. 14 and 15.

The principal compressive stresses in the concrete do not exceed the cube compressive concrete strength:

$$\sigma^{c}_{P.C.} = 2,85\,\mathrm{MPa} < f_{ck.cube} = 13,5\,\mathrm{MPa} \tag{5}$$

The stress distribution according to von Mises is provided in Fig. 14. It should be noted that the values of maximum stresses are inflated as they are observed at points on the edge (where the angle is 90°, resulting in distorted results in 3D modeling). In this case, to assess real stresses, it is necessary to consider values in the vicinity of the edge and on the columns. In this case, the maximum value of equivalent von Mises stresses in the reinforcement satisfies the strength criterion:

$$\sigma^{s}_{\mathrm{i.}} = 15,64\ \mathrm{MPa} < R_s = 333\,\mathrm{MPa} \tag{6}$$

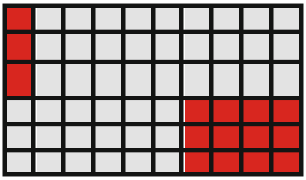

Fig. 11. Incorrect Configuration #1 of Grain Placement

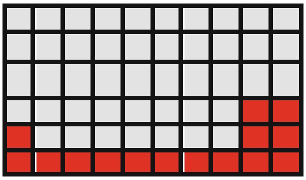

Fig. 12. Incorrect Configuration #2 of Grain Placement

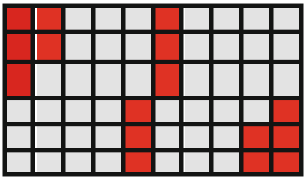

Fig. 13. Correct Configuration of Grain Placement

In Fig. 16 graphically shows comparisons of maximum stresses and displacements for various options for placing grain in silos. For clarity, the data were normalized. The SSS parameters of a fully loaded silo are taken as 100%:

– displacement $3.03 \cdot 10^{-3}$ m;
– stress 28.067 MPa.

Analyzing the results obtained, we can note a significant increase in displacements (45%) of the silo loaded with grain in violation of the rules and recommendations for operation, compared to displacements in a fully loaded silo.

At the same time, the stresses obtained when considering the placement options according to Fig. 11 and Fig. 12 do not exceed the stresses in a fully loaded grain storage building. of the structure.

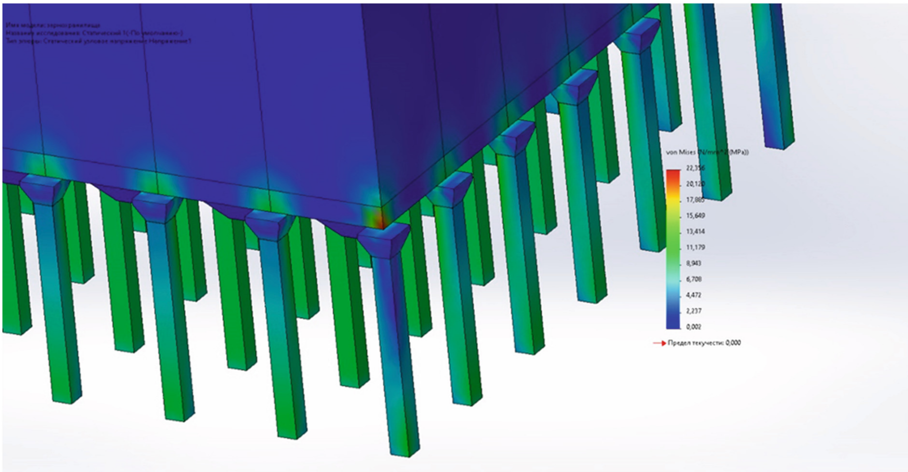

Fig. 14. Stresses in the grain storage building with proper grain placement

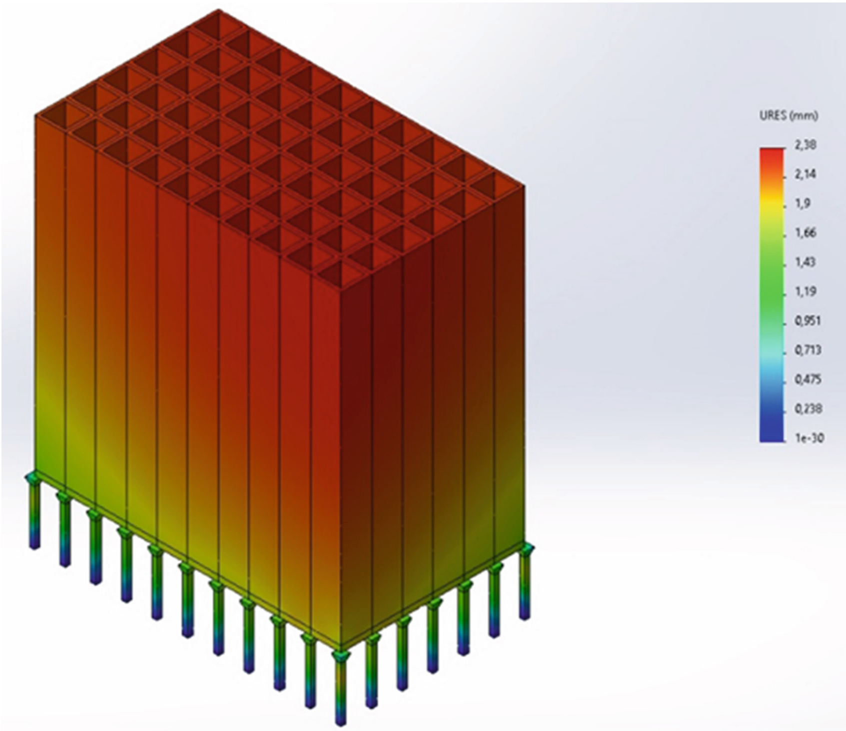

Fig. 15. Displacements in the properly loaded grain storage building

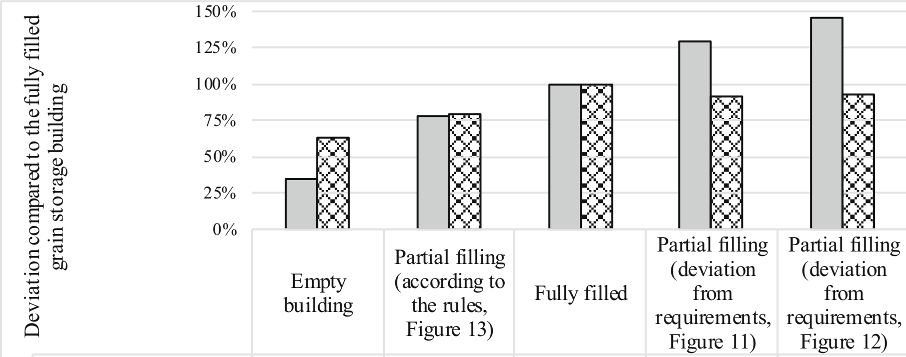

	Empty building	Partial filling (according to the rules, Figure 13)	Fully filled	Partial filling (deviation from requirements, Figure 11)	Partial filling (deviation from requirements, Figure 12)
Max. displacements, 100%:=3,03 mm	34%	79%	100%	129%	146%
Max. stress, за 100%:=28,067 Mpa	63%	80%	100%	92%	93%

Fig. 16. Results under different loading schemes of the grain storage building

8 Conclusions

An automated system has been developed to determine the stress stain state in the grain storage building under various silo loading schemes during its exploitation. The influence of different silo loading schemes on the state of the elevator structure has been investigated. It has been demonstrated that certain erroneous loading schemes, especially for a small grain volume, lead to a 45% increase in displacements compared to those in a fully loaded building. Such loading schemes can result in critical situations related to the inclination of the structure. The developed automated system allows for the construction of an artificial intelligence system capable of determining a rational sequence for loading and unloading the grain storage buildings.

References

1. https://web.archive.org/web/20210912210451/https://data.gov.ua/dataset/a43badfc-90e7-4947-90a4-512705bf2adc/resource/3fbec822-0389-4575-b8e6-664df39e16db/download/4-virobnitstvo-ta-rozpodil-valovogo-vnutrishnogo-produktu-za-vidami-ekonomichnoyi-diialnosti-va.xlsx. Accessed 26 Nov 2023
2. https://www.apk-inform.com/ru/news/1100055#.W3KDdOjFLIU. Accessed 26 Nov 2023
3. Maraveas, C.: Concrete silos: failures, design issues and repair / strengthening methods. Appl. Sci. **10**, 3938 (2020). https://doi.org/10.3390/app10113938,lastaccessed2023/11/26
4. Maraveas, C., Bartzanas, T.: Sensors for structural health monitoring of agricultural structures. Sensors **21**, 314 (2021). https://doi.org/10.3390/s21010314,lastaccessed2023/11/26
5. Warade, A.R., Shende, T.G.: Analysis and design of long concrete silo having different height and diameter under earthquake effect. In: National Conference on ‘Advances in Engineering, Technology and Applied Sciences’ - NCAETAS-2019 © IJSRSET, vol. 5, no. 6 (2019). https://ijsrset.com/paper/5600.pdf. Accessed 26 Nov 2023

6. Fank1, M.Z., do Nascimento, J.W.B., Cardoso, D.L., Meira, A.S., Willrich, F.L.: Vertical pressures and compressive friction force in a large silo. Engenharia Agrícola Jaboticabal **38**(4), 498–503 (2018). https://www.scielo.br/j/eagri/a/mzMg4phFszk47mQKtFNbrJJ/?format=pdf&lang=en. Accessed 26 Nov 2023
7. DSTU-N B EN 1991-4:2012 EUROCODE 1. ACTIONS ON STRUCTURES. PART 4. SILOS AND TANKS (EN 1991-4:2006, identical text)
8. Pshinko, O.M.: Restoration of operational suitability of concrete, reinforced concrete and stone structures: tutorial. In: Pshinko, O.M., Savytskyi, M.V., Zinkevich, A.M. (eds.) Dnipropetrovsk national Railway University transport named after Acad. V. Lazaryan – Dnipro, vol. 220, pp. 8–12 (2018)
9. Larin, O.O., Trubayev, O.I., Udayev, V.V.: Computer analysis of strength of grain elevator columns under various loading options. In: 2018 Interuniversity Collection "SCIENTIFIC NOTES", Lutsk, no. 63, pp. 98–113 (2018)
10. Svityy, I.M.: Modeling the dynamics of grain stocks at a grain receiving enterprise: conceptual, mathematical, and simulation models. Autom. Technol. Bus. Process. **10**(1), 58–63 (2018)

Information Modeling

Understanding the Relationship Between the Russian War in Ukraine and COVID-19 Spread in Canada Using Machine Learning Techniques

Dmytro Chumachenko[1,2](✉) and Plinio Morita[2,3,4]

[1] National Aerospace University "Kharkiv Aviation Institute", Kharkiv 61070, Ukraine
dichumachenko@gmail.com
[2] University of Waterloo, Waterloo N2L 3G1, Canada
[3] Centre for Digital Therapeutics, Techna Institute, University Health Network, Toronto M5G 2C4, Canada
[4] University of Toronto, Toronto M5S 1A1, Canada

Abstract. The COVID-19 pandemic has caused significant health, social, and economic disruptions globally, exposing healthcare systems' vulnerabilities and disparities in healthcare access and outcomes. The global response to the pandemic has included a variety of measures, including public health interventions, social distancing measures, travel restrictions, and vaccine campaigns. Mathematical and computer modeling has played a crucial role in understanding and combatting the pandemic. The Russian war in Ukraine has caused immense difficulties for medical personnel and severely impacted the accessibility and availability of medical care, disrupting the country's COVID-19 vaccination and prevention efforts. The paper aims to assess the impact of the Russian war in Ukraine on the COVID-19 epidemic process in Canada. We used forecasting methods based on statistical machine learning to build a COVID-19 distribution model. Results showed high accuracy in predicting cumulative new cases and deaths in Canada for 30 days. The model was then applied to the first 30 days of the full-scale Russian invasion to Ukraine, and the study concluded that forced migration of Ukrainians to Canada did not have a significant impact on the epidemic's dynamics. The study's experimental results suggest that the developed model can be used in public health practice.

Keywords: Epidemic Model · COVID-19 · Polynomial Regression · Machine Learning · Forecasting · War

1 Introduction

The COVID-19 pandemic is a complex global health crisis caused by the severe acute respiratory syndrome coronavirus 2 (SARS-CoV-2) virus, which has rapidly spread across the globe, resulting in significant morbidity, mortality, and social and economic disruptions [1]. This pandemic has highlighted the vulnerability of healthcare systems worldwide. It has challenged healthcare professionals' and researchers' capacity to implement

M. Nechyporuk et al. (Eds.): ICTM 2023, LNNS 1008, pp. 223–234, 2024.
https://doi.org/10.1007/978-3-031-61415-6_19

effective measures to control the transmission of the virus, develop vaccines, and improve patient management. The pandemic has also exposed disparities in healthcare access and outcomes, particularly among vulnerable populations [2]. It has raised concerns about the long-term impact of the pandemic on global health, the economy, and societal norms [3].

The COVID-19 pandemic has significantly impacted Canada's public health, social, and economic landscapes, resulting in unprecedented challenges and disruptions. Canada was among the first countries to report COVID-19 cases, with initial outbreaks linked to international travel [4]. The pandemic's emergence led to widespread public health measures, including physical distancing, mandatory masks, and business closures. Despite significant efforts to control the transmission of COVID-19, Canada has experienced multiple waves of the pandemic of varying severity across provinces and territories [5]. The pandemic has also highlighted longstanding health and social disparities, disproportionately impacting marginalized populations, including Indigenous communities and racialized groups. Canada's response has been characterized by coordinated federal-provincial-territorial efforts, investments in research, and a vaccine rollout campaign that prioritizes those at the highest risk of severe outcomes [6].

The global response to the COVID-19 pandemic has involved a variety of measures aimed at controlling the spread of the virus, including public health interventions, social distancing measures, travel restrictions, and vaccine campaigns [7]. These measures have been implemented at different stages of the pandemic and have varied in effectiveness depending on the context, socio-economic factors, and compliance with public health guidelines. Public health interventions, such as testing, contact tracing, and isolation, have been critical for identifying cases, breaking transmission chains, and preventing outbreaks. Social distancing measures, including mask mandates, physical distancing, and business closures, have effectively reduced viral transmission rates and flattened the epidemic curve [8]. Travel restrictions have been used to limit the importation of cases and prevent the spread of new variants. Finally, the development and deployment of vaccines have played a crucial role in protecting vulnerable populations and reducing the burden of COVID-19. A comprehensive approach combining multiple strategies and emphasizing community engagement, health equity, and global solidarity is needed to control the COVID-19 pandemic effectively.

Mathematical and computer modeling has been critical in understanding and combatting the COVID-19 pandemic [9]. These models have been used to predict the spread of the virus [10], evaluate the impact of public health interventions [11], assess the social factors impact the epidemic [12], analyze medical data [13], investigate the microorganisms [14], analyze co-infections [15]. Modeling approaches have included epidemiological models, such as the susceptible-infected-recovered (SIR) model, that simulate the spread of the virus within a population; statistical models that analyze the association between risk factors and disease outcomes; and machine learning models that can identify patterns in large datasets [16]. Using modeling has allowed researchers to assess the effectiveness of different interventions, such as social distancing and vaccination campaigns, and to estimate the number of cases, hospitalizations, and deaths under different scenarios.

Since Russia launched a causeless full-scale war in Ukraine on February 24, 2022, the country has suffered an unprecedented large-scale tragedy not seen since World War II and a global humanitarian catastrophe. In the first month of the war, the World Health Organization documented 92 attacks on the Ukrainian healthcare system, including 78 on medical facilities and 11 on medical transport, causing 73 confirmed deaths, and 44 injuries [17]. At the same time, medical personnel and patients alike were also targeted. These attacks were carried out using heavy weapons, which have become part of Russia's wartime strategy, causing immense difficulties for medical personnel while severely impacting the accessibility and availability of medical care in active combat zones and areas temporarily occupied by Russian troops. This has disrupted the continuity of Ukraine's healthcare system, leaving chronically ill patients without access to necessary medications and disrupting the country's COVID-19 vaccination and prevention efforts. Despite recommendations to comply with anti-pandemic measures, the citizens' psychological state due to the war has relegated the issue of the pandemic into the background. The Russian war in Ukraine has stimulated the forced migration of the Ukrainian citizens [18]. During the year since Russia's war's escalation, almost 200,000 Ukrainians have arrived in Canada, and a further close to a million applications have been submitted for the temporary residence under Canada Ukraine Authorization for Emergency Travel [19].

Therefore, the paper aims to assess the impact of the Russian war in Ukraine on the COVID-19 epidemic process in Canada.

2 Current Research Analysis

Infectious disease research frequently employs simulation models to deepen comprehension and forecast disease propagation within communities. Such models, including compartmental models [20], agent-based models [21], and relational models [22], provide insights into infectious disease transmission dynamics. Specifically, compartmental models segment populations into categories like susceptible, infected, and recovered, detailing the shift of individuals between these sections. Agent-centric models mimic singular interactions, highlighting the multifaceted nature of human conduct. Relational models shed light on interpersonal connections, examining how contact structures influence disease spread. Utilizing these modeling techniques, experts can probe the repercussions of varied intervention methodologies and gauge the ramifications of diverse public health protocols on disease distribution.

Shoukat et al.'s research [23] probed the repercussions of self-isolation in diminishing hospital and critical care requisites across Canadian provinces amid the COVID-19 crisis. Through computational modeling, the study outlined hospital and intensive care needs under varying self-isolation scenarios. It inferred that self-isolating individuals with mild symptoms can prolong outbreak peaks and reduce ICU necessities. Nonetheless, with a 40% self-isolation rate, ICU bed demands might surpass the available capacity at outbreak zeniths. This investigation accentuates self-isolation's potential in curtailing hospital and ICU needs and underscores healthcare challenges during the pandemic.

In another study, Tuite et al. [24] assessed the efficacy of several non-pharmaceutical countermeasures in managing the COVID-19 crisis and alleviating healthcare burdens in Ontario. Using a demographically-structured compartmental framework, the study juxtaposed scenarios with variable testing, isolation, and quarantine protocols. Findings indicated that rigorous physical distancing or a synergistic approach combining moderate distancing with enhanced case detection could stabilize the healthcare infrastructure. Dynamic distancing measures could safeguard healthcare capacities, offering inhabitants intermittent psychological and economic solace. This research underscores the potential advantages of specific non-pharmaceutical strategies in navigating the pandemic in Ontario.

Further, Chimmula and his team [25] expounded on crafting a deep learning framework, specifically the Long Short-Term Memory (LSTM) network, for forecasting COVID-19's trajectory and probable conclusion in Canada and globally. Relying on public datasets from John Hopkins University and Canadian health agencies, they contrasted Canadian transmission metrics with Italy and the USA, projecting the epidemic's potential cessation around June 2020. This research is one of the few leveraging LSTM networks for infectious disease predictions.

Jentsch et al. [26] introduced dual social-epidemiological modeling of SARS-CoV-2 transmission, evaluating four prioritization blueprints for vaccine distribution during the pandemic. These approaches encompass oldest-first, youngest-first, uniform, and contact-oriented strategies. Their model postulated that strategies impeding transmission become more potent as community immunity escalates. The optimal vaccination approach hinges on the pandemic's evolution, suggesting that targeting transmission prevention might avert more fatalities than focusing solely on vulnerable demographics.

Wu and collaborators [27] scrutinized how public health initiatives impacted COVID-19's proliferation in Ontario, employing mathematical models to measure the effects of social distancing. Their conclusions revealed that while distancing strategies diminished infection rates daily, per-contact transmission likelihood remained elevated with a sub-optimal case detection rate. Non-essential business closures further pushed the adequate reproduction number below the critical threshold. Their findings advocate for enhanced case identification and individual protective measures as potential alternatives to rigorous distancing.

Machine learning techniques exhibit superior precision in forecasting infectious disease dynamics. However, data detailing forced migration patterns from Ukraine to Canada must be discovered. The present analysis leverages a statistical machine learning approach known as polynomial regression.

3 Materials and Methods

The methodology proposed in this study consists of the following steps:

1. Analysis of COVID-19 morbidity and mortality data in Canada.
2. Building a predictive model of COVID-19 transmission dynamics based on the polynomial regression method.
3. Verification and tuning of the model on cumulative morbidity and mortality data from COVID-19 in Canada from January 25, 2022, to February 23, 2022.
4. Building a retrospective forecast of cumulative morbidity and mortality from COVID-19 in Canada from February 24, 2022, to March 25, 2022.

5. Model performance analysis for two different data samples.

Machine learning regression is a powerful approach to forecasting infectious disease dynamics. Regression models use historical data on disease incidence and demographic and environmental factors to estimate the relationship between these variables and the spread of the disease over time. These models can then be used to make predictions of future disease incidence. The regression approach can be used to predict the number of new cases, the disease's prevalence, and the outbreak's severity. It can also be used to identify risk factors that contribute to the spread of the disease and to develop interventions to mitigate the impact of the disease.

Polynomial regression is a type of regression analysis that models the relationship between a dependent variable and one or more independent variables [28]. When forecasting infectious disease dynamics, the dependent variable would be the number of cases or deaths and the independent variable would be time.

The relationship between the dependent and independent variables is modeled in polynomial regression as the nth-degree polynomial function. This function is represented as:

$$y = \beta_0 + \beta_1 x + \beta_2 x^2 + \ldots + \beta_n x^n + \varepsilon, \tag{1}$$

where y is the dependent variable (the variable being predicted); x is the independent variable (the variable being used to make the prediction); $\beta_0, \beta_1, \beta_2, \ldots, \beta_n$ are the coefficients or parameters of the model; ε is the error term or residual (the difference between the predicted value and the actual value).

The goal of polynomial regression when forecasting is to fit a curve to the historical data that most accurately captures the trend in the data and can be used to predict future values. This is done by minimizing the sum of the squared differences between the actual values and the predicted values for each period in the historical data.

Once the polynomial curve fits the historical data, it can forecast future values by extrapolating the curve beyond the historical period. However, it is essential to note that polynomial regression assumes that the relationship between the dependent and independent variables is a fixed polynomial function, which may not always be accurate for complex and dynamic infectious disease dynamics. Therefore, other machine learning regression approaches, such as time-series analysis or neural networks, may also be used to forecast infectious disease dynamics.

The model accuracy estimate is calculated using mean absolute percentage error:

$$\mathrm{MAPE} = \frac{100\%}{\mathrm{n}} \sum\nolimits_{\mathrm{t}=1}^{\mathrm{n}} \left| \frac{\mathrm{A_t} - \mathrm{F_t}}{\mathrm{A_t}} \right|, \tag{2}$$

where A_t is the actual value; F_t is the forecasted value.

To assess the forecast of the COVID-19 dynamics during the Russian war, the deviations of the forecast data from the registered statistics were calculated:

$$\mathrm{D} = |\mathrm{F_t} - \mathrm{A_t}|. \tag{3}$$

where A_t is the actual value; F_t is the forecasted value.

4 Results

4.1 Model Verification

The dynamical model delineating the progression of the COVID-19 epidemic has been instantiated using the Python programming language. For validation purposes, the model employed cumulative data on morbidity and mortality rates of COVID-19 in Canada, spanning the period from January 25, 2022, to February 23, 2022. This data was sourced from the World Health Organization's COVID-19 Dashboard, as referenced in [29].

Figure 1 presents the results of the retrospective forecast of cumulative new cases of COVID-19 in Canada from January 25, 2022, to February 23, 2022.

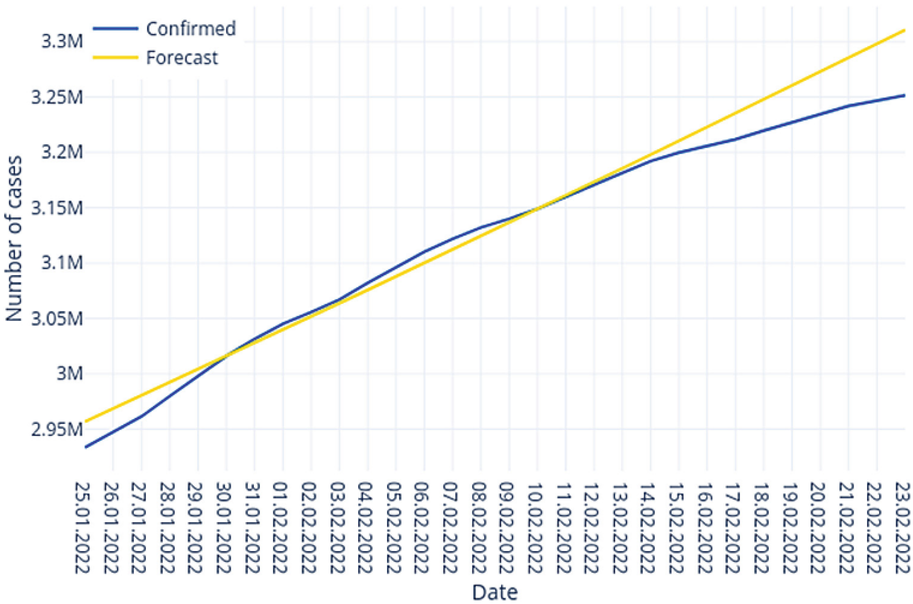

Fig. 1. Forecasting of COVID-19 cumulative new cases in Canada (25.01.22–23.02.2022)

Figure 2 presents the results of the retrospective forecast of cumulative death cases of COVID-19 in Canada from January 25, 2022, to February 23, 2022.

Table 1 shows model accuracy rates for cumulative new cases and deaths of COVID-19 in Canada from January 25, 2022 to February 23, 2022.

As the results of model's performance show, the model has high accuracy, which allows it to be used in public health practice.

4.2 Experimental Results

In order to assess the impact of the Russian war in Ukraine on the dynamics of COVID-19 in Canada, a retrospective forecast of the epidemic process of COVID-19 in Canada was

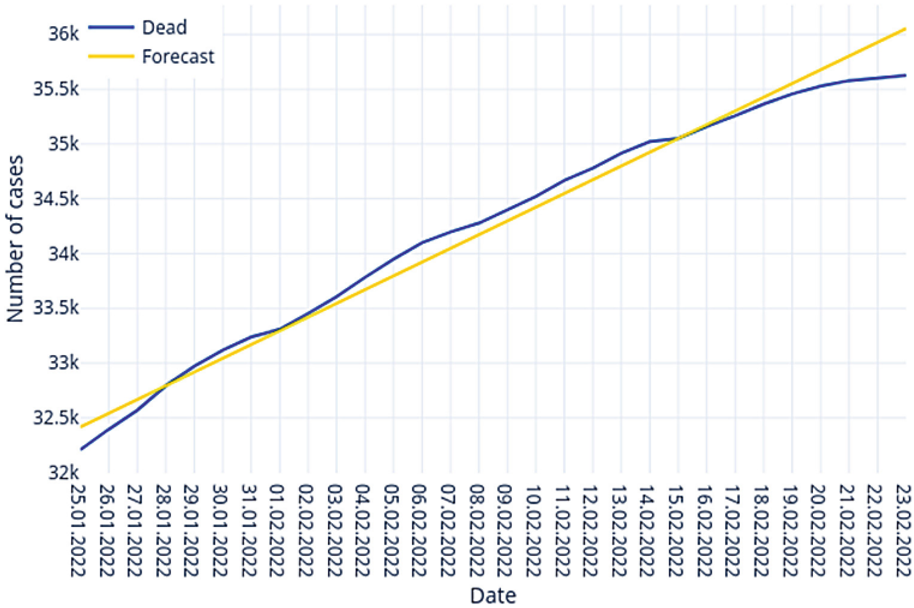

Fig. 2. Forecasting of COVID-19 cumulative death in Canada (25.01.22–23.02.2022)

Table 1. MAPE of retrospective forecast for 25.01.22–23.02.22

Duration of forecast	New cases	Death cases
3 days	0.7211%	0.4658%
7 days	0.4133%	0.2846%
10 days	0.3305%	0.2314%
20 days	0.2526%	0.2956%
30 days	0.4892%	0.3322%

built from February 24, 2022 to March 25, 2022. Cumulative morbidity and mortality data were used.

Figure 3 presents the results of the retrospective forecast of cumulative new cases of COVID-19 in Canada from February 24, 2022, to March 25, 2022.

Figure 4 presents the results of the retrospective forecast of cumulative death cases of COVID-19 in Canada from February 24, 2022, to March 25, 2022.

Table 2 shows model accuracy rates for cumulative new cases and deaths of COVID-19 in Canada from February 24, 2022, to March 25, 2022.

The retrospective projection of cumulative novel cases and fatalities due to COVID-19 in Canada from February 24, 2022, to March 25, 2022, demonstrates notable precision. Concurrently, a comparative assessment of the MAPE model reveals minimal variance when applied to data sets 30 days before and 30 days after the onset of hostilities in the

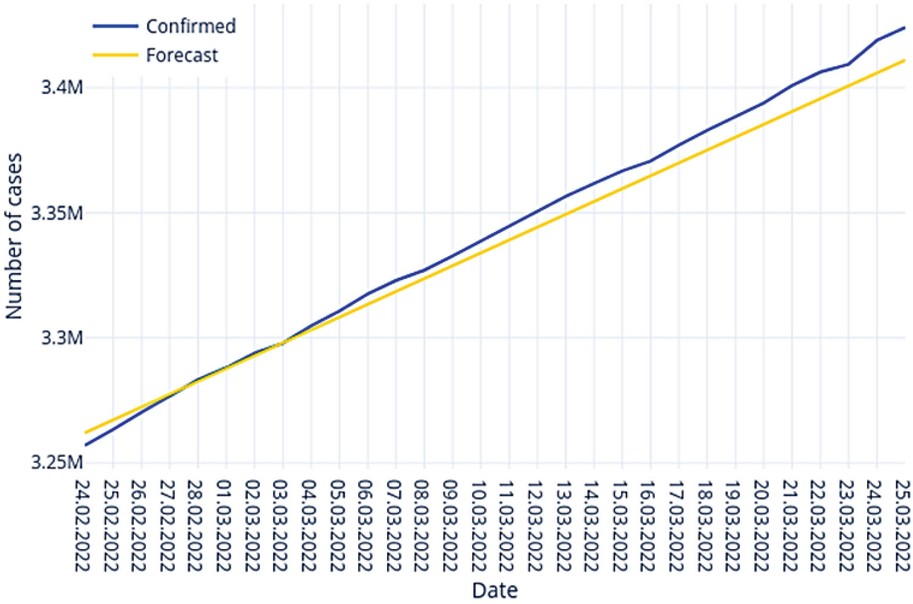

Fig. 3. Forecasting of COVID-19 cumulative new cases in Canada (24.02.22–25.03.2022)

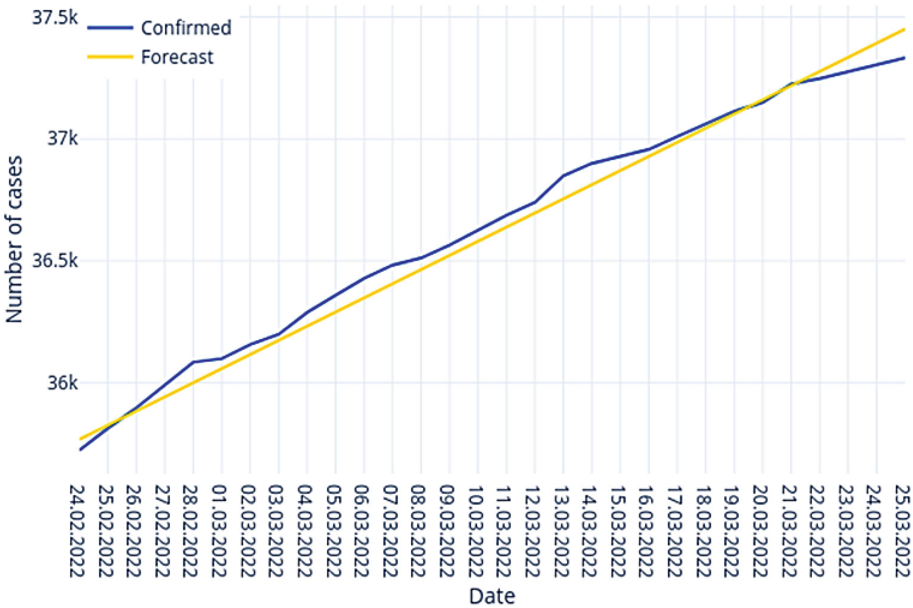

Fig. 4. Forecasting of COVID-19 cumulative death in Canada (24.02.22–25.03.2022)

Table 2. MAPE of retrospective forecast for 24.02.22–25.03.22

Duration of forecast	New cases	Death cases
3 days	0.1099%	0.0662%
7 days	0.0582%	0.1135%
10 days	0.0536%	0.1202%
20 days	0.1068%	0.1442%
30 days	0.1625%	0.1309%

full-scale Russian war against Ukraine. This indicates a consistent trajectory in Canada's epidemic progression. Consequently, it can be inferred that the determinants influencing the COVID-19 dynamics remain unchanged. The influx of Ukrainian migrants to Canada, a consequence of the Russian war in Ukraine, does not appear to be a pivotal factor affecting the epidemic's course.

Figure 5 shows the deviation of daily reported new cases of COVID-19 in Canada from the forecasted values for the period from February 24, 2022, to March 25, 2022.

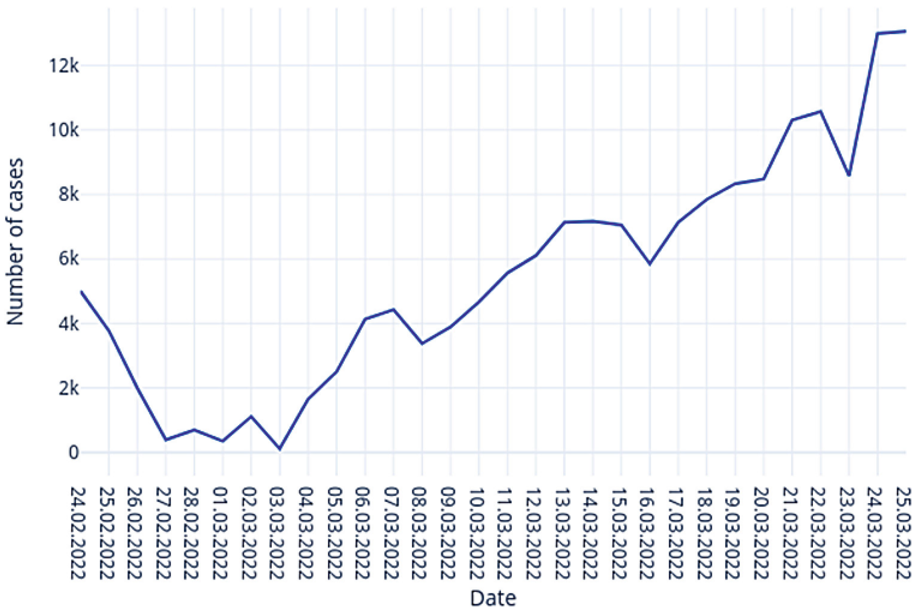

Fig. 5. Deviation of COVID-19 daily new cases from forecasted values (24.02.22–25.03.2022)

Figure 6 shows the deviation of daily reported death of COVID-19 in Canada from the forecasted values for the period from February 24, 2022, to March 25, 2022.

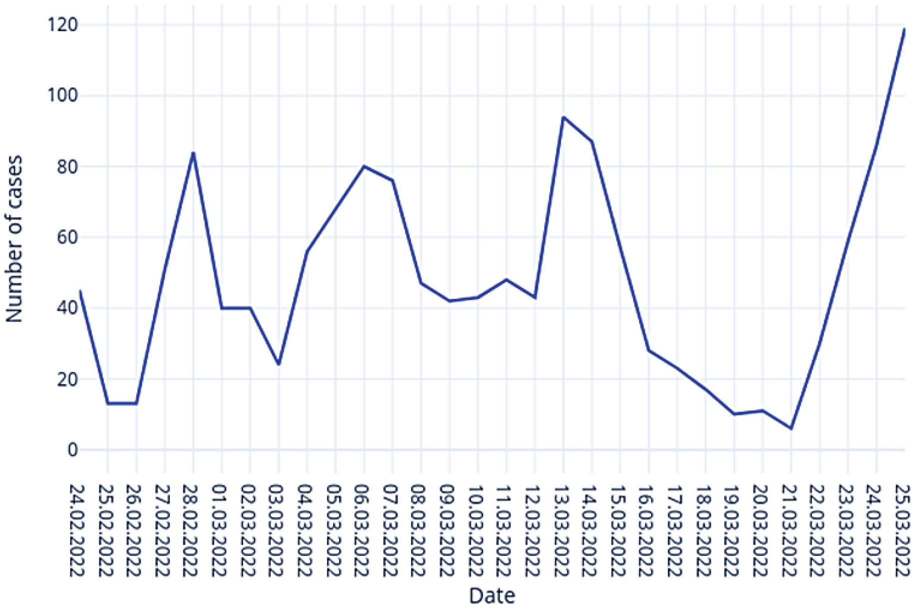

Fig. 6. Deviation of COVID-19 daily death from forecasted values (24.02.22–25.03.2022)

5 Conclusions

This research delineates a systematic approach for evaluating the repercussions of the Russian full-scale invasion of Ukraine on the trajectory of the COVID-19 epidemic progression in Canada. The pertinence of this study is substantiated by the potential influence of the mass migration of the Ukrainian populace, precipitated by Russia's full-scale military invasion of Ukraine, on the dynamics of infectious disease transmission. A prognostic model encapsulating the COVID-19 epidemic trends was formulated to facilitate this assessment, utilizing statistical machine learning techniques.

The model shows high accuracy both for the validated sample from January 25, 2022, to February 23, 2022 (99.52% for new cases, 99.67% for deaths), and for the retrospective forecast from February 24, 2022, to March 25, 2022 (99.84% for new cases, 99.87% for deaths). The absence of a decrease in forecasting accuracy in the period after the start of the escalation of the Russian war in Ukraine suggests that the forced migration of the Ukrainian population to Canada is not an essential factor that affects the dynamics of the COVID-19 epidemic process. This is due to the peculiarities of the support program for Ukrainians, which restrains large migration flows and allows crossing the border only after a lengthy document check and obtaining permission. Another deterrent is the mandatory medical examination, including COVID-19 infection status for all arrivals in the country.

References

1. Cui, C., Li, B., Chen, X.: Group decision-making method of entry policy during a pandemic. Tsinghua Sci. Technol. **29**, 56–65 (2024). https://doi.org/10.26599/tst.2022.9010014
2. McKenna, K., Bouchoucha, S., Redley, B., Hutchinson, A.M.: "Building the plane while flying it" Reflections on pandemic preparedness and response; an organisational case study. BMC Health Serv. Res. **23** (2023). https://doi.org/10.1186/s12913-023-09874-x
3. Raquel, A., Rosa, A., Silva, Reis, D., Eliete, M.: Global research trends related to coronavirus disease 2019 and the aged: a bibliometric analysis. Sao Paulo Med. J. **142** (2024). https://doi.org/10.1590/1516-3180.2022.0662.r1.190523
4. Courdi, C., et al.: How level of understanding and type of used sources relate to adherence to COVID-19 public health measures in Canada. Sci. Rep. **13** (2023). https://doi.org/10.1038/s41598-023-38824-0
5. Cameron-Blake, E., Annan, H., Marro, L., Michaud, D.S., Sawatzky, J., Tatlow, H.: Variation in the stringency of COVID-19 public health measures on self-reported health, stress, and overall wellbeing in Canada. Sci. Rep. 1**3** (2023). https://doi.org/10.1038/s41598-023-39004-w
6. Irwin, P., Taylor, D., Keefe, J.M.: Provincial policies affecting resident quality of life in Canadian residential long-term care. BMC Geriatr. **23** (2023). https://doi.org/10.1186/s12877-023-04074-y
7. Sonkin, R., Alpert, E.A., Katz, D., Jaffe, E.: Maximizing the role of emergency medical services in covid-19 response. Disaster Med. Public Health Prep. **17**, 1–22 (2021). https://doi.org/10.1017/dmp.2021.359
8. Avusuglo, W.S., Bragazzi, N.L., Asgary, A., Orbinski, J., Wu, J., Kong, J.D.: Leveraging an epidemic–economic mathematical model to assess human responses to COVID-19 policies and disease progression. Sci. Rep. **13** (2023). https://doi.org/10.1038/s41598-023-39723-0
9. Zheng, K., Wu, J., Yuan, Y., Liu, L.: From single to multiple: generalized detection of Covid-19 under limited classes samples. Comput. Biol. Med. **164**, 107298 (2023). https://doi.org/10.1016/j.compbiomed.2023.107298
10. Zakariaee, S.S., Naderi, N., Ebrahimi, M., Kazemi-Arpanahi, H.: Comparing machine learning algorithms to predict COVID-19 mortality using a dataset including chest computed tomography severity score data. Sci. Rep. **13**, 11343 (2023). https://doi.org/10.1038/s41598-023-38133-6
11. Chien, F., Nik, H.S., Shirazian, M., Gomez-Aguilar, J.F.: The global stability and optimal control of the COVID-19 epidemic model. Int. J. Biomath. **17** (2023). https://doi.org/10.1142/s179352452350002x
12. Mallick, D., Ray, A., Sudhir Kumar Das, Ghosh, S.: Hesitancy, awareness, and vaccination. Math. Comput. Sci. **2**, 101–113 (2023). https://doi.org/10.1002/9781119896715.ch8
13. Chumachenko, T., Bazilevych, K.: Dimensionality reduction of chronic kidney disease data using principal components analysis. In: CEUR Workshop Proceedings, vol. 3348, pp. 110–115 (2022)
14. Andrianov, A.A., Shuldau, M.A., Furs, K.V., Yushkevich, A.M., Tuzikov, A.V.: AI-driven de novo design and molecular modeling for discovery of small-molecule compounds as potential drug candidates targeting SARS-CoV-2 main protease. Int. J. Mol. Sci. **24**, 8083 (2023). https://doi.org/10.3390/ijms24098083
15. Abioye, A.I., Peter, O.J., Ogunseye, H.A., Oguntolu, F.A., Ayoola, T.A., Oladapo, A.O.: A fractional-order mathematical model for malaria and COVID-19 co-infection dynamics. Healthc. Analyt. **4**, 100210 (2023)
16. Wichmann, B., Wichmann, R.M.: Big data evidence of the impact of COVID-19 hospitalizations on mortality rates of non-COVID-19 critically ill patients. Sci. Rep. **13** (2023). https://doi.org/10.1038/s41598-023-40727-z

17. da Costa, J.P., Silva, A.L., Barcelò, D., Rocha-Santos, T., Duarte, A.: Threats to sustainability in face of post-pandemic scenarios and the war in Ukraine. Sci. Total Environ. **892**, 164509 (2023). https://doi.org/10.1016/j.scitotenv.2023.164509
18. Chumachenko, D., Dudkina, T., Chumachenko, T.: Assessing the impact of the Russian war in Ukraine on COVID-19 transmission in Spain: a machine learning-based study. Radioelectron. Comput. Syst. **1**, 5–22 (2023). https://doi.org/10.32620/reks.2023.1.01
19. Government of Canada: Ukraine immigration measures: Key figures. https://www.canada.ca/en/immigration-refugees-citizenship/services/immigrate-canada/ukraine-measures/key-figures.html
20. Ibrahim, A., Humphries, U.W., Ngiamsunthorn, P.S., Baba, I.A., Qureshi, S., Khan, A.: Modeling the dynamics of COVID-19 with real data from Thailand. Sci. Rep. **13** (2023). https://doi.org/10.1038/s41598-023-39798-9
21. Weng, X., Chen, Q., Sathapathi, T.K., Yin, X., Wang, L.: Impact of school operating scenarios on COVID-19 transmission under vaccination in the U.S.: an agent-based simulation model. Sci. Rep. **13** (2023). https://doi.org/10.1038/s41598-023-37980-7
22. Abbasimehr, H., Noshad, A., Paki, R.: A novel featurization methodology using JaGen algorithm for time series forecasting with deep learning techniques. Expert Syst. Appl. **235**, 121279–121279 (2024). https://doi.org/10.1016/j.eswa.2023.121279
23. Shoukat, A., et al.: Projecting demand for critical care beds during COVID-19 outbreaks in Canada. Can. Med. Assoc. J. **192**, E489–E496 (2020)
24. Tuite, A.R., Fisman, D.N., Greer, A.L.: Mathematical modelling of COVID-19 transmission and mitigation strategies in the population of Ontario, Canada. Can. Med. Assoc. J. **192**, E497–E505 (2020)
25. Chimmula, V.K.R., Zhang, L.: Time series forecasting of COVID-19 transmission in Canada using LSTM networks. Chaos Solit. Fractals **135**, 109864 (2020)
26. Jentsch, P.C., Anand, M., Bauch, C.T.: Prioritising COVID-19 vaccination in changing social and epidemiological landscapes: a mathematical modelling study. Lancet Infect. Dis. **21**, 1097–1106 (2021)
27. Wu, J., et al.: Quantifying the role of social distancing, personal protection and case detection in mitigating COVID-19 outbreak in Ontario, Canada. J. Math. Ind. **10** (2020)
28. Çağlar, O., Özen, F.: A comparison of Covid-19 cases and deaths in Turkey and in other countries. Netw. Model. Anal. Health Inform. Bioinform. **11** (2022). https://doi.org/10.1007/s13721-022-00389-9
29. World Health Organization: WHO COVID-19 dashboard. https://covid19.who.int/

Regression Analysis of Geometric Parameters of "Screw Implant – Maxillary Segment" Biomechanical System

Andriy Kuritsyn[1], Igor Taranenko[2], Vitaly Miroshnikov[2], Vladislav Demenko[2], and Andrii Kondratiev[3](✉)

[1] Kharkiv National Medical University, 4 Nauky Avenue, Kharkiv 61022, Ukraine
[2] National Aerospace University "Kharkiv Aviation Institute", 17 Chkalova Street, Kharkiv 61070, Ukraine
[3] O.M. Beketov National University of Urban Economy in Kharkiv, 17 Marshal Bazhanov Street, Kharkiv 61002, Ukraine
andrii.kondratiev@kname.edu.ua

Abstract. A series of finite element calculations was performed to evaluate the impact of the geometric parameters of the reconstructive structures for "screw implant – maxillary segment" biomechanical system on the stress state of the cancellous tissue. To generate the model, we used high-order 10-node tetrahedral finite elements with the quadratic approximation of displacements that provided high modeling accuracy, in particular, in the areas of the implant thread - bone tissue joint, characterized by a high gradient of components of the stress-strain behavior. The finite element model is represented by 102231 elements. Biomechanical system was rigidly fixed at the frontal sections of the maxillary segment, thus preventing its displacement. The regression analysis of the results of a series of biomechanical system finite element calculations performed by us allowed establishing an analytical relationship between its geometric parameters (implant length and diameter, abutment slope angle) and factor of safety of the cancellous bone. Its linear model with the low coefficient of determination (0.584) and quadratic model providing high enough value of the coefficient (0.875) were used. It is obvious that at the next stages of research, when certain improvements in this direction could be achieved, it will be possible to consider nonlinear phenomena in the regression models in order to obtain the better precision of results. The results of the work will allow us to reveal the main trends in changes of the factor of safety of cancellous tissue relative to the value of traumatic stresses, depending on the implant length and diameter, and abutment slope angle.

Keywords: Resorption · Implant length and diameter · Abutment slope angle

1 Introduction

Today the dental implant surgery is a relatively new, but rapidly developing, area of dentistry [1]. Successful implant surgery should be preceded by the detailed survey of a patient, analysis of the clinical situation and hygienic indicators, as well as the possibility to predict the interaction of implant of a specific configuration with the bone tissues

M. Nechyporuk et al. (Eds.): ICTM 2023, LNNS 1008, pp. 235–246, 2024.
https://doi.org/10.1007/978-3-031-61415-6_20

of the maxillary segment [2]. Therefore, the current research in this field dealing with theoretical modeling of the implant interaction with bone tissues of the maxillary segment under load becomes more relevant [3]. To solve these problems, most researchers choose computer technologies, for example, the finite element method well suited for the analysis of various biological objects which is successively used in dentistry [4]. The main advantage of this method is the possibility to solve the problems for areas of any shape, while the analytical solutions can be obtained for the problems with fairly simple geometry only [5, 6]. This fact, as well as the appearance of a number of high-performance programs effectively implementing the above method make it one of the main tools for studying the systems such as dental ones [7, 8].

2 Literature Review

A large number of research papers deal with the modeling and analysis of interaction of the various implants with the bone tissue. Usually, the authors study the patterns of biomechanics of intraosseous dental implants inserted into the bone tissue, impact of the implant parameters on the stress-strain behavior on the implantation zone, and response of the bone tissue surrounding the implant to the functional loads [9, 10]. Many papers also deal with the evaluation of design of the removable dentures resting on the implants and biological tissues of the oral cavity, distribution of loads and probability of irreversible changes in the bone tissue in the orthopedic treatment [11, 12]. However, most of the papers do not fully consider the features of screw implant biomechanics depending on the geometric parameters of an implant (diameter, length, and angle of abutment crown slope) being of high practical importance [13]. Some papers consider certain aspects of this problem only. For example, the paper [14] analyzes the impact of the implant neck wall thickness and abutment dimensions on the stress-strain behavior of the maxillary segment bone tissues. Modeling results show that increase in the wall thickness of the implant neck from 0.45 to 1.00 mm significantly reduces the load on the implant, abutment, and deformation of the bone tissue. Change in the dimensions of the abutment screw has a significant impact on its stress state; maximum stress reduction is equal to 10% and 29% with the implant diameter increase from 1.4 to 1.6 and 1.8 mm, respectively. The paper [15] studies the effect of the difference in the coverage of the shoulder of abutment collar in the implants on the stress-strain behavior of the bone tissue. The impact of the implant length and pitch of its thread on the stress-strain behavior of the bone tissue is studied in [16]. It is shown that the impact of the implant length is more significant compared to that of the thread pitch. The papers [17–19] deal with the impact of the implant diameter on the stress-strain behavior of the bone tissue. The paper [17] suggests that narrow implants should be used with great care, particularly, in the areas of non-axial loads, while narrow-diameter implants show the adequate behavior in both directions of applied loads. The results of [18] demonstrate the less resistance to fracture in the implants of the smallest diameter; implants with the diameter of 2.5 mm and 3.0 mm are deformed in the area of the implant body, instead of the abutment area. The paper [19] shows that maximum stresses in the bone tissue are observed for implants of less than 3.5 mm in diameter. The purpose of the study [20] is to compare the biomechanical interaction of two wide implants placed in the atrophic posterior part of the upper jaw with unicortical and bicortical attachments, and to substantiate the most favorable attachment from the biomechanical point of view. The tendency to growing stresses and deformations with a decrease in the implant diameter is revealed in [21] for all diameters of the implants under study. The paper [22] studies the impact of the implant diameter and length on the success of implantation. It is shown that placement of implants of short length and narrow diameter corresponds to the maximum intensity of stresses in the bone tissue and is the most dangerous procedure. The paper [23] investigates the simultaneous impact of the implant diameter and the type of its joint with the abutment on the stress-strain behavior of the bone tissue. It is shown that with the increase in the implant diameter the intensity of stresses in the cancellous bone becomes lower. The paper [24] analyzes the impact of length, diameter and angle of slope of the abutments on the stress-strain behavior of the bone tissue. It is demonstrated that implants of different diameters have almost equal distribution of loads on the implant, abutment, and bone. The yield strength is exceeded in the cortical bone when an angled abutment is used. The paper [25] studies the simultaneous impact of the diameter, length, and modulus of elasticity of the dental implant on the values of stress and strain in the surrounding bone. It is shown that these parameters have a significant impact on the stress-strain behavior of the bone. The paper [26] reveals the functional dependence between the main geometric parameters (diameter, length and angle of slope of the abutment crown) of screw implants of different configurations and the stress-strain behavior of the maxillary segment bone tissue. However, this paper shows the linearized functional dependence between the main geometric parameters of the screw implant and stress state of the bone tissue of the maxillary segment, and it results in relatively low coefficients of determination. Thus, it is not possible to obtain an analytical dependence of these parameters.

Given the above, the purpose of this study is to find the functional dependence between the main geometric parameters (diameter, length and angle of slope of the abutment crown) of a screw implant featuring various configurations and stress state of the bone tissue of the maxillary segment, which determines the behavior of “screw implant – maxillary segment” biomechanical system.

3 Research Methodology

The dental implant serving as a support for the dental prosthesis consists of an artificial root made of medical titanium (supporting screw part) and an abutment connecting the support and crown part of the tooth. Supporting part of the implant is screwed directly into the jawbone, and after that a crown is placed on the implant with the use of cement.

In the process of determination of geometric parameters of the maxillary segment and structure of its bone tissue, the data of computer-aided tomography were used.

The maximum occlusal load in the study was taken equal to 300 N; the load was evenly applied over the upper part of the abutment. Based on the initial data, a finite element model describing the biomechanical system under consideration is synthesized (Fig. 1). To generate the model, we used high-order 10-node tetrahedral finite elements with the quadratic approximation of displacements that provided high modeling accuracy, in particular, in the areas of the implant thread - bone tissue joint. The finite element model is represented by 1022310 elements. Non-homogeneous meshing with tetrahedral element size reduction was used to improve the accuracy of calculations. Mapped meshing was applied in the area of bone-implant interface. Minimal mesh size was selected under the results of the convergence test and the convergence criterion was set to be less than 5% changes of the highest stresses in bone between the FE sizes. Biomechanical system was rigidly fixed at the frontal sections of the maxillary segment, thus preventing its displacement.

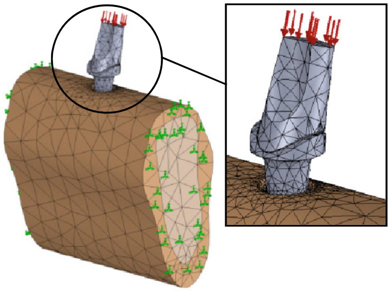

Fig. 1. Finite element model of “screw implant – maxillary segment” biomechanical system

Main assumptions listed below are made in the calculations of the above biochemical system in the finite element software package:

– all materials are considered homogeneous and isotropic ones with the specified mechanical characteristics, while small deformations and displacements are taken into consideration, due to which the Hooke’s law is valid;
– it is accepted that the upper part of the implant neck can come into close contact with the compact tissue (in the absence of bone tissue resorption), and the lower part is considered to be fully osteo-integrated with the surrounding cancellous bone.

For the component parts of the model, the corresponding mechanical characteristics of biological tissues and materials are specified. The adequacy of the values of bone tissue mechanical characteristics taken for calculations to their real indicators for living tissues guaranteed that the results obtained during modeling would correctly reflect the behavior of the considered biomechanical system [27]. Currently, despite the extensive clinical experience, biomechanical properties of bone tissues are not sufficiently studied. For example, the main mechanical characteristics of bone tissues of the lower jawbone described in [28, 29] indicate a large spread. Considering the above, we take for the further study the average statistical values of these characteristics (see Table 1). In addition, the papers [30, 31] indicate that establishing of quantitative indicators of the bone tissue stress state based on fracture stresses cannot provide fully correct and informative data. Therefore, a number of papers introduce an indicator of traumatic stresses in the bone tissue, at which the structural changes thereof occur, resulting in the development of pathologies and, for example, the beginning of bone tissue resorption, etc. [32, 33]. The above papers assume that the value of these stresses for cancellous bone tissue varies in the range of 8 – 15 MPa. In view of the above, we assume for our further study the following values of the main mechanical characteristics and traumatic stresses of the lower jawbone tissues (Table 1).

Table 1. Values of the main mechanical characteristics of the lower jawbone tissues taken for calculations

Type of bone tissue	Modulus of elasticity, GPa	Poisson's ratio	Traumatic stresses, MPa
Compact bone tissue	13.7	0.3	122
Cancellous bone tissue	1.37	0.3	12

Based on the data of implant manufacturers, medical titanium of V grade is used as an implant material, with the mechanical characteristics presented in Table 2 [34].

Table 2. Mechanical characteristics of the implant material

Modulus of elasticity, GPa	Poisson's ratio	Ultimate strength, MPa	Yield strength, MPa
110	0.33	860	450

The study with regard to regulation of the geometric parameters of implants is based on the open data of implant manufacturers; the geometric characteristics are shown in Table 3.

Table 3. Adopted implant configurations

<table>
<tr><th colspan="3">Threaded area (supporting part)</th><th colspan="4">Abutment (upper part)</th></tr>
<tr><th>Titanium implant</th><th>Diameter, mm</th><th>Length, mm</th><th>Aesthetic titanium abutment</th><th>Diameter of orthopedic profile, mm</th><th>Gum height</th><th>Crown slope angle</th></tr>
<tr><td rowspan="6"></td><td>3.4</td><td rowspan="3">10</td><td rowspan="6"></td><td rowspan="6">5</td><td rowspan="6">3.5</td><td rowspan="2">0°</td></tr>
<tr><td>4</td></tr>
<tr><td>4.6</td><td rowspan="2">15°</td></tr>
<tr><td rowspan="3">4</td><td>8</td></tr>
<tr><td>10</td><td rowspan="2">23°</td></tr>
<tr><td>12</td></tr>
</table>

Configuration of the implant with the diameter of the threaded part $d_0 = 4$ mm, height $l_0 = 10$ mm and angle of slope of aesthetic abutment $\varphi_0 = 15°$ was chosen as a reference case for the study.

As a result of modeling in the finite element software package for the considered biomechanical system, the components of stress-strain behavior of all its constituent parts were determined. For the quantitative assessment of the biomechanical system stress state, the distribution patterns for equivalent stresses according to Mises were used. The values of traumatic stresses were taken as the maximum allowable stresses for the bone tissues (Table 1). The use of *FOS* (factor of safety) calculated as a ratio of maximum allowable stresses to current stresses (equivalent according to Mises) can be conveniently used in the analysis of the stress state [35, 36]. It is evident that when $FOS > 1$ the bone tissue of the maxillary segment is provided with the field of stresses acting on all areas of contact with the screw part of the implant that do not exceed the values of traumatic stresses. If $FOS < 1$, this condition is not satisfied, and the occurrence of structural changes in the bone tissue which may develop into its resorption is predicted. Figure 2 shows an example of the obtained *FOS* distribution pattern for the compact and cancellous bone tissue of the maxillary segment for the reference case of the implant. Analysis of the obtained results allowed us to conclude that the most loaded element of the biomechanical system is the cancellous bone, where the minimum *FOS* is significantly less than the factor of safety of the compact bone.

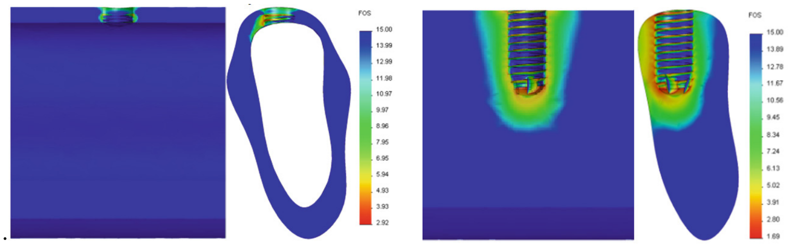

a b

Fig. 2. Patterns of the factor of safety distribution in the bone tissues: a – compact bone tissue; b – cancellous bone tissue

Based on this, in order to qualitatively evaluate the impact of geometric parameters of the implant – diameter (d), length (l), abutment slope angle (φ) on the stress state of "screw implant – maxillary segment" biomechanical system we use the minimum value of *FOS* for the cancellous bone. To perform the analytical calculations of its value at an arbitrary value of these parameters, it is necessary to know the type of function of three variables $FOS = f(d, l, \varphi)$. Taking into account the specificity and complexity of modeling of the considered biomechanical system, the type of this functional dependence can be obtained with the absolute accuracy using the tabular method only, as a result of a series of finite element calculations with the discrete change of implant parameters. Given the above, the required dependency $FOS = f(d, l, \varphi)$ can be found by the method of multiple regression [37]. Each factor of the implant configuration is attributed to the reference value: diameter (d), length (l), abutment slope angle (φ): relative diameter $X_1 = d \big/ d_0$, relative length $X_2 = l \big/ l_0$, and relative slope angle $X_3 = \varphi \big/ \varphi_0$.

Function of the value of the factor of safety (*FOS*) of the cancellous bone of the *i*-th factor can be represented as

$$\overline{FOS}_i = \alpha_0 + \sum_{\mathrm{i}=1}^{n} \alpha_{\mathrm{i}} X_i + \sum_{i=1}^{n} \sum_{j=1}^{n} \alpha_{ij} X_i X_j, \tag{1}$$

where $i = 1 \ldots n$ – sample number in the observations, α_i – regression coefficients showing the average value of change in the quality factor, when the variables of implant configuration (X_1, X_2, X_3) are increased by the unit of measurement; α_0 – free term to be determined.

However, even with the use of simplified regression models their finite element analysis requires a large volume of calculations. Therefore, the results can be limited to the linear regression model:

$$\begin{pmatrix} \overline{FOS}_1 \\ \cdots \\ \overline{FOS}_i \\ \cdots \\ \overline{FOS}_n \end{pmatrix} = \begin{bmatrix} 1 & X_{11} & X_{12} & X_{13} \\ \cdots & \cdots & \cdots & \cdots \\ 1 & X_{i1} & X_{i2} & X_{i3} \\ \cdots & \cdots & \cdots & \cdots \\ 1 & X_{n1} & X_{n2} & X_{n3} \end{bmatrix} \begin{pmatrix} \alpha_0 \\ \alpha_1 \\ \alpha_2 \\ \alpha_3 \end{pmatrix}. \tag{2}$$

To evaluate the column vector (α), the use of the least squares method is the most common, taking as an estimate the column vector ($\tilde{\alpha}$), which minimizes the sum of squares of deviations of $\overline{FOS}$ matrix values being observed from their model values. According to this method, the column vector of estimates of the regression coefficient is determined by the formula:

$$(\tilde{\alpha}) = \left([X]^T [X]\right)^{-1} [X]^T (\overline{FOS}), \tag{3}$$

As a result of step-by-step regression analysis according to the formula (1), the dependence below is obtained

$$FOS = -0.127 + 0.416d + 1.464 \cdot 10^{-3} l + 1.787 \cdot 10^{-3} \varphi. \tag{4}$$

The accuracy of the regression mathematical model (1) can be increased by introducing into it the squares of terms of the effect factors of the same name:

$$\overline{FOS}_i = \alpha_0 + \alpha_1 X_{i1} + \alpha_2 X_{i2} + \alpha_2 X_{i3} + \alpha_4 X_{i1}^2 + \alpha_5 X_{i2}^2 + \alpha_6 X_{i3}^2. \tag{5}$$

Addition of quadratic terms to the model (1) will not require the larger number of finite element calculations, which is especially important as they significantly increase the labor inputs. Implementation of the algorithm of step-by-step regression analysis results in the following regression dependence:

$$FOS = -5.727 - 0.346d + 1.443l + 0.012\varphi + 0.082d^2 - 0.07l^2 - 5.683 \cdot 10^{-4} \varphi^2. \tag{6}$$

4 Results

For comparison, Table 4 presents the results obtained in a series of finite element calculations and with the use of approximation expressions (4) and (6).

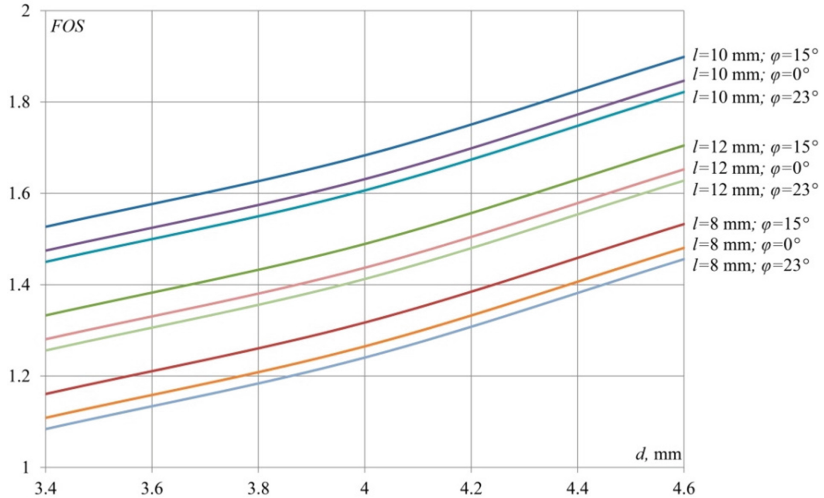

Fig. 3. Dependence of minimum factor of safety (*FOS*) of the cancellous bone on the implant diameter (d) at different lengths (l) and abutment slope angles (φ)

Table 4. Comparison of results obtained in a series of finite element calculations and with the use of approximation expressions for the function $FOS = f(d, l, \varphi)$

Diameter d, mm	Length l, mm	Slope angle φ, deg.	Values of minimum factor of safety (*FOS*) of the cancellous bone				
			Finite element calculation	Linear regression model	Coefficient of determination (R^2)	Quadratic regression model	Coefficient of determination (R^2)
3.4	10	15º	1.46	1.33	0.584	1.544	0.875
4.0			1.69	1.58		1.698	
4.6			2.00	1.83		1.912	
4.0	8	15º	1.33	1.57		1.325	
	10		1.69	1.58		1.698	
	12		1.60	1.58		1.708	
4,0	10	0º	1.56	1.55		1.644	
		15º	1.69	1.58		1.698	
		23º	1.71	159		1.623	

Figure 3, 4 and 5 show the dependences of the minimum *FOS* of the cancellous bone on the geometric parameters of the implant – diameter (d), length (l), and abutment slope angle (φ).

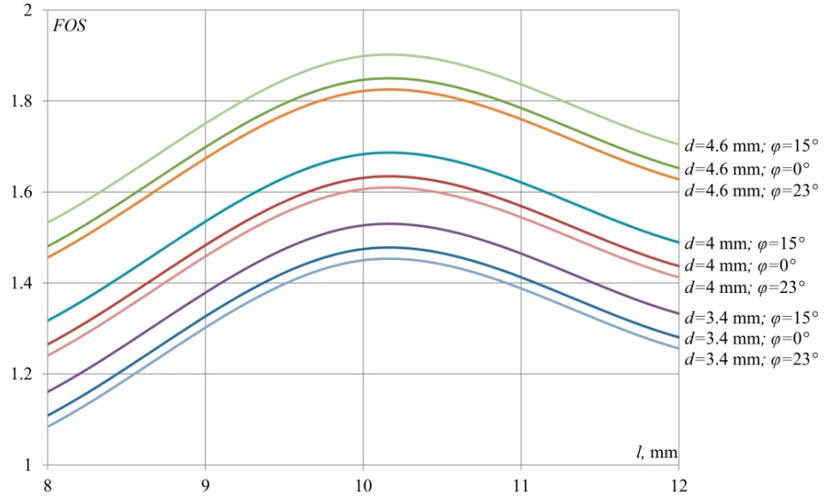

Fig. 4. Dependence of minimum factor of safety (*FOS*) of the cancellous bone on the implant length (l) at different diameters (d) and abutment slope angles (φ)

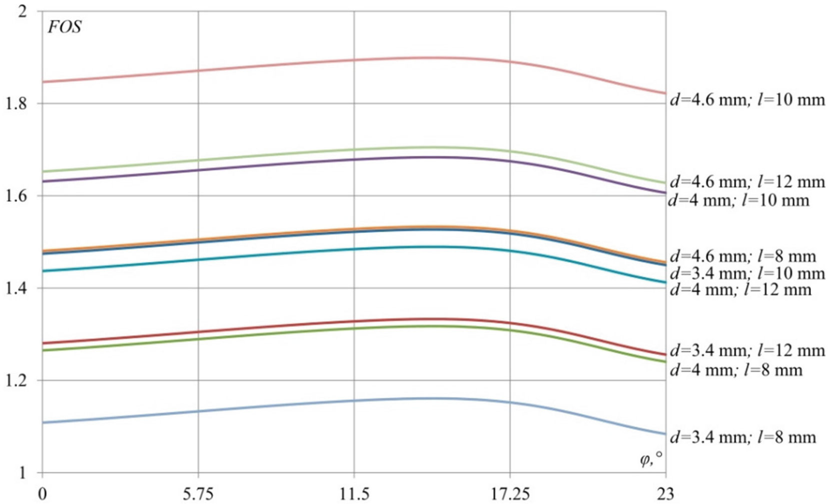

Fig. 5. Dependence of minimum factor of safety (*FOS*) of the cancellous bone on the abutment slope angle (φ) at different diameters (d) and lengths (l)

5 Conclusions

Analysis of the obtained results allows us to draw the conclusions below.

A series of finite element calculations was performed to evaluate the impact of the geometric parameters of the reconstructive structures for "screw implant – maxillary segment" biomechanical system on the stress state of the cancellous tissue. This finite element analysis allowed revealing the main trends in changes of factor of safety *FOS* of the tissue relative to the value of traumatic stresses, depending on the implant length and diameter, and abutment slope angle.

The paper covers the regression analysis of results of a series of finite element calculations of the biomechanical system giving an opportunity to establish an analytical relationship between its geometric parameters and *FOS* of the cancellous bone. Its linear model with the low coefficient of determination ($R^2 = 0.584$) and quadratic model providing high enough value of the coefficient ($R^2 = 0.875$) were used. It is obvious that at the next stages of research, when certain improvements in this direction could be achieved, it will be possible to consider nonlinear phenomena in the regression models in order to obtain the better precision of results.

References

1. Overmann, A.L., et al.: Orthopaedic osseointegration: implantology and future directions. J. Orthopaed. Res. **38**(7), 1445–1454 (2020). https://doi.org/10.1002/jor.24576
2. Verma, A., Singh, S.V., Arya, D., Shivakumar, S., Chand, P.: Mechanical failures of dental implants and supported prostheses: a systematic review. J. Oral Biol. Craniofac. Res. **13**(2), 306–314 (2023). https://doi.org/10.1016/j.jobcr.2023.02.009
3. Kayabasi, O.: Design methodology for dental implant using approximate solution techniques. J. Stomat. Oral Maxillofac. Surg. **121**(6), 684–695 (2020). https://doi.org/10.1016/j.jormas.2020.01.003
4. Li, R.Y., et al.: Biomechanical behavior analysis of four types of short implants with different placement depths using the finite element method. J. Prosthet. Dent. **129**(3), 447 (2023). https://doi.org/10.1016/j.prosdent.2023.01.005
5. Meslier, Q.A., Shefelbine, S.J.: Using finite element modeling in bone mechanoadaptation. Curr. Osteoporos. Rep. (2023). https://doi.org/10.1007/s11914-023-00776-9
6. Kondratiev, A., et al.: Effects of the temperature–time regime of curing of composite patch on repair process efficiency. Polym. **13**(24), 4342 (2021). https://doi.org/10.3390/polym13244342
7. Park, S., Park, J., Kang, I., Lee, H., Noh, G.: Effects of assessing the bone remodeling process in biomechanical finite element stability evaluations of dental implants. Comput. Meth. Progr. Biomed. **221**, 106852 (2022). https://doi.org/10.1016/j.cmpb.2022.106852
8. Alaneme, K.K., Kareem, S.A., Ozah, B.N., Alshahrani, H.A., Ajibuwa, O.A.: Application of finite element analysis for optimizing selection and design of Ti-based biometallic alloys for fractures and tissues rehabilitation: a review. J. Mater. Res. Technol. **19**, 121–139 (2022). https://doi.org/10.1016/j.jmrt.2022.05.001
9. Li, J.M., Jansen, J.A., Walboomers, X.F., van den Beucken, J.: Mechanical aspects of dental implants and osseointegration: a narrative review. J. Mechan. Behav. Biomed. Mater. **103**, 103574 (2020). https://doi.org/10.1016/j.jmbbm.2019.103574
10. de Matos, J.D.M., et al.: Bioengineering tools applied to dentistry: validation methods for in vitro and in silico analysis. Dent. J. **10**(8), 145 (2022). https://doi.org/10.3390/dj10080145

11. Houshmand, B., Ardakani, M.T., Moscowchi, A., Oskoui, I.Z.: Effect of implant design on stress distribution: a finite element study. J. Long-Term Eff. Med. Implants. **32**(4), 39–45 (2022). https://doi.org/10.1615/JLongTermEffMedImplants.2022042799
12. Bachiri, A., Djebbar, N., Boutabout, B., Serier, B.: Effect of different impactor designs on biomechanical behavior in the interface bone-implant: a comparative biomechanics study. Comp. Meth. Progr. Biomed. **197**, 105723 (2020). https://doi.org/10.1016/j.cmpb.2020.105723
13. Zhang, C., Zeng, C., Wang, Z., Zeng, T., Wang, Y.: Optimization of stress distribution of bone-implant interface (BII). Biomater. Adv. **147**, 213342 (2023). https://doi.org/10.1016/j.bioadv.2023.213342
14. Jeng, M.D., Lin, Y.S., Lin, C.L.: Biomechanical evaluation of the effects of implant neck wall thickness and abutment screw size: a 3D nonlinear finite element analysis. Appl. Sci.-Bas. **10**(10), 3471 (2020). https://doi.org/10.3390/app10103471
15. Lee, H.Y., Yang, S.W., Kang, Y.J., Oh, K.C., Kim, J.H.: Influence of shoulder coverage difference of abutment on stress distribution and screw stability in tissue-level internal connection implants: a finite element analysis and in vitro study. J. Prosthet. Dent. **125**(4), 682 (2021). https://doi.org/10.1016/j.prosdent.2020.08.022
16. Pirmoradian, M., Naeeni, H.A., Firouzbakht, M., Toghraie, D., Khabaz, M.K., Darabi, R.: Finite element analysis and experimental evaluation on stress distribution and sensitivity of dental implants to assess optimum length and thread pitch. Comp. Meth. Progr. Biomed. **187**, 105258 (2020). https://doi.org/10.1016/j.cmpb.2019.105258
17. Barbosa, F.T., Zanatta, L.C.S., Rendohl, E.D., Gehrke, S.A.: Comparative analysis of stress distribution in one-piece and two-piece implants with narrow and extra-narrow diameters: a finite element study. PLoS ONE **16**(2), 0245800 (2021). https://doi.org/10.1371/journal.pone.0245800
18. Neto, T.H., Tuzita, A.S., Gehrke, S.A., Moura, R.D., Casati, M.Z., Mesquita, A.M.M.: A comparative analysis of implants presenting different diameters: extra-narrow. Narrow Conventional Mater. **13**(8), 1888 (2020). https://doi.org/10.3390/ma13081888
19. Lee, H., Jo, M., Noh, G.: Biomechanical effects of dental implant diameter, connection type, and bone density on microgap formation and fatigue failure: a finite element analysis. Comp. Meth. Progr. Biomed. **200**, 105863 (2021). https://doi.org/10.1016/j.cmpb.2020.105863
20. Linetskiy, I., Sutcliffe, M., Kondratiev, A., Demenko, V., Linetska, L., Yefremov, O.: A novel method of load bearing ability analysis of short plateau implants placed in compromised bone. In: 2023 IEEE 4th KhPI Week on Advanced Technology (KhPIWeek), pp. 1–6 (2023). https://doi.org/10.1109/KhPIWeek61412.2023.10312831
21. Patil, P.G., Seow, L.L., Uddanwadikar, R., Pau, A., Ukey, P.D.: Different implant diameters and their effect on stress distribution pattern in 2-implant mandibular overdentures: a 3D finite element analysis study. J. Prosthet. Dent. (2022). https://doi.org/10.1016/j.prosdent.2022.04.018
22. Park, J., Park, S., Kang, I., Noh, G.: Biomechanical effects of bone quality and design features in dental implants in long-term bone stability. J. Computat. Des. Eng. **9**(5), 1538–1548 (2022). https://doi.org/10.1093/jcde/qwac069
23. Lee, H., Jo, M., Sailer, I., Noh, G.: Effects of implant diameter, implant-abutment connection type, and bone density on the biomechanical stability of implant components and bone: a finite element analysis study. J. Prosthet. Dent. **128**(4), 716–728 (2022). https://doi.org/10.1016/j.prosdent.2020.08.042
24. de Souza Rendohl, E., Brandt, W.C.: Stress distribution with extra-short implants in an angled frictional system: a finite element analysis study. J. Prosthet. Dent. **124**(6), 728 (2020). https://doi.org/10.1016/j.prosdent.2020.04.022

25. Robau-Porrua, A., Perez-Rodriguez, Y., Soris-Rodriguez, L.M., Perez-Acosta, O., Gonzalez, J.E.: The effect of diameter, length and elastic modulus of a dental implant on stress and strain levels in peri-implant bone: a 3D finite element analysis. Bio-Medical Mater. Eng. **30**(5–6), 541–558 (2020). https://doi.org/10.3233/bme-191073
26. Kuritsyn, A.V., Kutsevlyak, V.I., Kondratyev, A.V.: Determination of functional dependence between the key geometrical parameters of the screw implant of various configuration and the tension of bone fabric of the maxillary segment. Bull. Probl. Biol. Med. **3**(112), 302–309 (2014). https://vpbm.com.ua/en/vpbm-2014-03-3/7114
27. Choi, A.H., Ben-Nissan, B.: Anatomy, Modeling and Biomaterial Fabrication for Dental and Maxillofacial Applications. Bentham Science Publishers, Sharjah (2018). https://doi.org/10.2174/97816810869101180101
28. Matinlinna, J.P.: Handbook of Oral Biomaterial. Pan Stanford Publishing Pte. Ltd., Singapore (2014)
29. Wu, D., Isaksson, P., Ferguson, S.J., Persson, C.: Young's modulus of trabecular bone at the tissue level: a review. Acta Biomater. **78**, 1–12 (2018). https://doi.org/10.1016/j.actbio.2018.08.001
30. Gasik, M., Lambert, F., Bacevic, M.: Biomechanical properties of bone and mucosa for design and application of dental implants. Materials **14**(11), 2845 (2021). https://doi.org/10.3390/ma14112845
31. Lin, C.Y., Kuo, P.Y., Chiu, M.Y., Chen, Z.Z., Wang, H.L.: Soft tissue phenotype modification impacts on peri-implant stability: a comparative cohort study. Clin. Oral Invest. **27**(3), 1089–1100 (2023). https://doi.org/10.1007/s00784-022-04697-2
32. Pegoretti, A., Fambri, L., Zappini, G., Bianchetti, M.: Finite element analysis of a glass fibre reinforced composite endodontic post. Biomaterials **23**(13), 2667–2682 (2002). https://doi.org/10.1016/s0142-9612(01)00407-0
33. Chuiko, A.N., Shinchukovsky, I.A.: Biomechanics in Dentistry: Monograph. Kh.: Fort. Chuiko (2010). 468 p.
34. Welsch, G., Boyer, R., Collings, E.W.: Materials Properties Handbook: Titanium Alloys. ASM International, Matls Park (1993)
35. Kondratiev, A.V., Kovalenko, V.O.: Optimization of design parameters of the main composite fairing of the launch vehicle under simultaneous force and thermal loading. Space Sci. Technol. **25**(4(119)), 3–21 (2019). https://doi.org/10.15407/knit2019.04.003
36. Misura, S., Smetankina, N., Misiura, I.: Optimal design of the cyclically symmetrical structure under static load. In: Nechyporuk, M., Pavlikov, V., Kritskiy, D. (eds.) ICTM 2020. LNNS, vol. 188, pp. 256–266. Springer, Cham (2021). https://doi.org/10.1007/978-3-030-66717-7_21
37. Garson, D.G.: Multiple Regression. Statistical Associates Publishers (2014). 462 p.

Parameters and Characteristics of Parachute Systems for Physical Modelling Precision Airborne Cargo Landing

Olexander V. Betin, Petro G. Kyriienko, Denys O. Betin(✉), and Olena Y. Betina

National Aerospace University «KhAI», Chkalova 17, Kharkiv 61070, Ukraine
{o.betin,p.kirienko,d.betin,o.betina}@khai.edu

Abstract. The main requirements facing the developers of controlled precision airborne cargo landing systems (CPACLS) are to reduce cargo losses and improve landing precision. Modern theoretical knowledge, computational and experimental methods are used to satisfy them. Leading among them is the method of physical modelling of flight modes on free flying dynamically similar models (FDSM). In the problem under consideration, the theoretical foundations of this method are used to substantiate the possibility of conducting flight researches on FDSM of the modes of separation of CPACLS from the carrier aircraft, deployment of the parachute system and performance of steady-state flight in the vertical plane until the moment of cargo landing. At the same time, a literature review was carried out, aimed and analyzing features of device, design and flight tests of parachute systems of CPACLS, as well as similar design and research work on FDSM. The conditions and scales of similarity used in creating FDSM and carrying out flight researches of the parachute system of the CPACLS. The conditions of similarity and technical feasibility of a FDSM in the task of creating model parachute systems and carrying out flight researches of the considered stages of landing of CPACLS are revealed. The ratios for selection of structural materials, and also determination of required and available values of parameters and characteristics of parachute systems of FDSM at modelling of landing of CPACLS are received.

Keywords: Parameters and Characteristics · Parachute Systems · Physical Modelling · Precision Airborne Cargo Landing

1 Introduction

Controlled precision airborne cargo landing systems (CPACLS) refer to new aviation-controlled parachute systems with platforms for delivery various cargoes to hard-to-reach-areas. Minimum configuration of the CPACLS: exhaust and (or) stabilizing parachute (initially it can perform the functions of an exhaust parachute, and then allows to reduce dynamic loads), main gliding parachute, suspension system, cargo platform with cushioning system, on-board computer (or command unit) in the container controlling the slings of the main gliding parachute and cushioning system. To reduce landing time, a round classic landing parachute is often used at the final landing stage [1, 2].

M. Nechyporuk et al. (Eds.): ICTM 2023, LNNS 1008, pp. 247–257, 2024.
https://doi.org/10.1007/978-3-031-61415-6_21

Ejection of CPACLS is carried out through the cargo hatch of the carrier at a distance of up to $L = 50$ km. In this case, the CPACLS are separated from the carrier (Fig. 1, a), the exhaust and stabilizing parachutes are put into operation, and then the main gliding parachute (Fig. 1, b). At the minimum permissible altitude on the signal of altimeter (located on the platform), the round landing parachute is inserted, the cargo is briefly lowered on two parachutes (Fig. 1, c). This ultimately leads to a soft and accurate landing of CPACLS [1, 2].

a b c

Fig. 1. Separation of the CPACLS from the carrier (a), activation of the main gliding parachute (b) and descent of the cargo on two parachutes (c)

CPACLS assembled with payload behave during operation (descent or flight, as well as landing) as aircraft and have an aerodynamic quality k from 4...5 to 10...12 depending on the parachute class, material and design. CPACLS provide accuracy of landing 5...150 m, and also allow to apply the system at different time of day and under various weather conditions (for example, at temperatures from $-50\,°C$ to $+80\,°C$). The flight altitudes CPACLS $H = 0...5000$ m and rarely exceed them at the flight speed of the carrier, and, therefore, and beginning of deployment of the parachute system $V = 250...400$ km/h. As a rule, the mass of airborne cargoes does not exceed $m_c = 1000$ kg. The use of a parachute system, practically self-guided to the beacon, allows, depending on the conditions of application, to reduce cargo losses by up to 20% [1, 2].

During operation of CPACLS there are many factors that influence separation of CPACLS from carrier, deployment of parachute system, performance of steady-flight in vertical plane and achievement of required accuracy of cargo landing. Some of them can be controlled partially (e.g., airspeed, direction and altitude, orientation angles of CPACLS). But due to the special nature of flight, even these can vary during most drops, resulting in inaccurate landing or loss of cargo.

The CPACLS (with the wing on top and the cargo below) is a stable aircraft (the center of mass is located under the point of application of the total aerodynamic force), which seeks to return to its to original position and maintain pitch and zero roll under any disturbance. Despite this, cargo losses are high, necessitating improvements in the design of CPACLS, and this leads to new flight research and testing.

The main requirements facing the developers of CPACLS are: reducing cargo losses and improving landing accuracy. Modern theoretical knowledge, computational and experimental methods are used to satisfy them. The leading among them is the method of physical modelling of flight modes on free flying dynamically similar models (FDSM) – autonomous unmanned experimental reusable aircraft capable of remotely-piloted or autonomic flight according to a given program [3–6].

The results of flight research using FDSM largely determine the fate of new aircraft (or its modification), the direction and pace of its subsequent tests and work on its introduction into mass production. From these positions expediency of careful study and scientifically grounded solution of a complex of problems associated with creation of FDSM does not cause doubts.

At present, the development of a new aircraft is based on much deeper theoretical knowledge. Powerful computers are used in the development process, which enhances the ability to perform time-consuming calculations. There is an increasing amount of testing of aircraft models in wind tunnels and its on-board systems on a variety of stands, mathematical and semi-natural models.

Blowdowns in wind tunnels, tests on rocket carts and other traditional methods of experimental aerodynamics do not provide adequate reproduction of critical flight regimes. Their research in the flight conditions of a full-scale aircraft is associated with unacceptably high costs and risk for the crew of test pilots, and computational methods of study require approbation by experimental data. The methodological gap between aerodynamic tests of models in wind tunnels and flight tests of full-scale aircraft was eliminated by the development of a method of research of flight characteristics on FDSM.

In the practical activities of foreign aviation companies, the method of research of flight characteristics of designed and in-service aircraft on FDSM is widely used. Examples of the high efficiency of using FDSM can be programs carried out in the United States of America related to construction of FDSM and advanced researches of critical flight regimes of McDonnell Douglas F-15, General Dynamics YF-16 and Rockwell's model under the HiMAT program (Fig. 2).

Fig. 2. FDSM developed at NACA

The purpose of this work is to substantiate the possibility of creating parachute systems of FDSM for conducting flight researches on them of the modes of separation of CPACLS from the carrier, deployment of the parachute system and fulfilment of steady flight in a vertical plane until the moment of landing of the cargo. This can be done by obtaining ratios for determining the required and available values of parameters and characteristics of parachute systems of FDSM.

2 Literature Review on the Features of the Device and Flight Tests of Parachute Systems of CPACLS, as Well as Similar Researches on FDSM

The flight modes of CPACLS specified for modelling can be classified as critical flight modes. At the same time, the distinctive feature of CPACLS is the presence in the design not of a rigid wing, but of a load-bearing gliding parachute system. This increases, rather than decreases, the likelihood of CPACLS falling into critical flight regimes and requires additional flight researches on a FDSM [3–6].

There are various approaches to classifying components of CPACLS assembled with payload. For the purposes of this work, it is most convenient to divide them into two groups. The first group – "parachute system" includes: parachute system entry mechanism; exhaust and (or) stabilizing domes with slings; gliding parachute dome with slings; round classic landing parachute with slings; covers, chambers and aprons for laying parachute domes and slings, free ends. The second group – "cargo" includes: suspension system of all components of this group to the parachute system; cargo platform with shock absorption system; on-board computer (or command unit) in the control container of the main gliding parachute slings and shock absorption system; payload [3, 8].

As a rule, exhaust, stabilizing and round classical parachute landing domes are made of capron or nylon fabrics with low, medium and high air permeability. When filled, their domes take a shape of a hemisphere with longitudinal and transverse reinforcements made of capron braid. The perimeter of edge is also reinforced with a capron braid gasket. The slings are attached to it, on which the load is suspended through the free ends. Round parachutes reduce the speed of fall solely by air resistance. During descent, air enters the inner volume of the dome, creating overpressure. A small portion of it seeps through the fabric of the dome. The rest of the air comes out from under the edge, alternately from different sides of the dome [1, 2, 8].

Gliding parachute domes are mainly made of combined weave fabrics. The structure of these fabrics uses hardened reinforced polyester or nylon yarns, which are inserted into the fabric structure crosswise with yarn spacing of 5 to 8 mm. The basic yarn can be of any composition (cotton, silk, polyester, polypropylene) thickness and density. Domes made of such materials are elastic and have variable air permeability depending on the air pressure. The canopy of the gliding parachute in working condition takes the shape of a wing, as the upper and lower surfaces are connected by ribs and spars having an aerodynamic profile. This creates an overpressure of air inside, which comes in through the air intakes located on the front of the wing. A system of thin and strong slings is used to connect the wing and cargo, as well as to control the wing [1, 2].

Since the elements of parachute systems are made of thin elastic materials, in the conditions of its deployment and flight with cargo, the domes and slings work in tension [8].

The most effective solution to the problems of creating CPACLS is the application of a method that uses FDSM as a flight research tool. Such unmanned aerial vehicle is capable remotely-piloted or automatic flight according to a given program – FDSM. This feature determined specific requirements to the strength of FDSM and the necessity to equip them with special systems for the output of FDSM from critical flight situations, braking and soft landing by the simplest and reliable parachute method. Most of the currently created FDSM use round classic landing parachutes as the main parachutes. These parachute systems, as a rule, perform solely the rescue function for which all parachutes were originally conceived [3, 8].

This paper proposes to expand the functions of the parachute system of FDSM and investigate the behavior of the load-bearing gliding parachute system of CPACLS, while reserving rescue function as well.

3 Conditions and Scales of Similarity Used in the Creation of FDSM and Flight Researches of the Gliding Parachute System of CPACLS

The main methodological difficulties and specifics of creating FDSM are related to the need to resolve complex contradictions between similarity conditions and technical feasibility. Reliable transfer of the results of research flights of FDSM to a full-scale aircraft is possible only if the conditions geometric, kinematic and dynamic (aerodynamic and in general) similarity are fulfilled. A FDSM should have the same external shape as a full-scale aircraft, the required by similarity position of the center of mass and mass-inertia parameters, elastic-geometric characteristics and similar laws of the automatic control system. As a result, a FDSM will behave in flight in the same way as a full-sale aircraft under appropriate conditions [3–6, 9, 10].

Considering the conditions of geometric, kinematic and dynamic similarity with respect to the full-scale CPACLS and FDSM, it is possible to distinguish the scales of similarity necessary for modelling [9, 10]:

geometric

$$k_\ell = \frac{\ell_n}{\ell_m} = const_1;\, k_\phi = \frac{\phi_n}{\phi_m} = 1;\, k_s = \frac{S_n}{S_m} = k_\ell^2;\, k_w = \frac{W_n}{W_m} = k_\ell^3, \tag{1}$$

kinematic

$$k_t = \frac{t_n}{t_m} = const_2;\, k_v = \frac{V_n}{V_m} = \frac{k_\ell}{k_t} = const_3;\, k_a = \frac{a_n}{a_m} = \frac{k_\ell}{k_t^2} = const_4, \tag{2}$$

dynamic (overall)

$$\frac{R_n}{R_m} = k_R = const_5, \tag{3}$$

where k_ℓ – scale of linear size; k_ϕ – scale of angles; k_s – scale of areas; k_w – scale of volumes; k_t – scale of times; k_v – scale of linear velocities; k_a – scale of linear accelerations; k_R – scale of forces; ℓ_n, ℓ_m – randomly chosen similar nominal (e.g. characteristic) sizes of compared bodies (full-scale and model); ϕ_n, ϕ_m – angles between respective lines of geometrically similar bodies; S_n, S_m, W_n, W_m – areas and volumes of geometrically similar bodies; t_n, t_m – similar time periods of movement of geometrically similar bodies; V_n, V_m, a_n, a_m – linear velocities and accelerations of the movement of geometrically similar bodies in similar periods of time; R_n, R_m – equally directed forces of the same nature acting on geometrically similar bodies in similar time periods.

In formulas (1)–(3) and further, index "n" defines the relation to the parameters or characteristics of full-scale CPACLS, and index "m" – to the corresponding parameters or characteristics of the FDSM.

The main purpose of the analysis of similarity issues is to obtain the scales of similarity that allow us to find the relationship between the relevant parameters and characteristics of a full-scale CPACLS and a FDSM, as well as the parameters and characteristics of the modelled phenomena. In our case – flight researches of the gliding parachute system of the CPACLS on a FDSM.

For a FDSM as the main parameters are taken characteristic linear size ℓ_m, mass m_m, axial I_{xm}, I_{ym}, I_{zm} and centrifugal I_{xym}, I_{xzm}, I_{yzm} moments of inertia. The scales of similarity of the main parameters of a full-scale CPACLS and a FDSM are as follows [3]

$$k_\ell = \frac{\ell_n}{\ell_m};\, k_M = \frac{m_n}{m_m};\, k_I = \frac{I_{jn}}{I_{jm}} (j = x, y, z, xy, xz, yz), \tag{4}$$

where k_M – mass scale; m_n – mass of a full-scale aircraft; k_I – scale of moments of inertia; I_{jn} – moments of inertia (axial and centrifugal) of a full-scale aircraft with respect to axes similar to the coordinate system of a FDSM.

If scale k_ℓ is taken as the primary scale, then scales k_m and k_I, and other scales, that define the FDSM design, parameters and motion characteristics – derived scales. These scales depend on k_ℓ and implicitly on the flight altitudes H_n of a full-scale CPACLS and H_m of its FDSM. Since the acceleration of gravity g in the range of flight altitudes $H = 0...10000$ m does not change appreciably, at the flight altitudes of the full-scale CPACLS and its FDSM $g_n = g_m$, a, the scale of acceleration of gravity included in full formulas, $k_g = \frac{g_n}{g_m} = 1$ [3, 9, 10].

Therefore, a number of similarity scales for creating FDSM and modelling on them the flight of full-scale CPACLS have the following form [10]:

$$\begin{gathered} k_t = k_V = \sqrt{k_\ell};\, k_a = k_{ol} = 1;\, k_\omega = \frac{1}{\sqrt{k_\ell}};\, k_\alpha = \frac{1}{k_\ell}; \\ k_M = k_R = k_\rho k_\ell^3;\, k_M = k_\rho k_\ell^4;\, k_I = k_\rho k_\ell^5, \end{gathered} \tag{5}$$

where k_ω – scale of angular velocities; k_α – scale of angular accelerations; k_{ol} – scale of operating overloads; k_M – scale moment of forces; $k_\rho = \frac{\rho_n}{\rho_m}$ – scale of air densities; ρ_n, ρ_m – air density at altitudes H_n and H_m.

The scale k_ℓ depends on the accepted similarity criteria (Froude Fr, Reynolds Re and Mach M), that define aerodynamic similarity. Unfortunately, the theoretical basis for determining the necessary combination of similarity criteria goes far beyond the scope of this research, but its application is necessary to substantiate the adequacy of flight researches on FDSM [3]. At the same time, the ratios obtained in [10] should be used when deciding the final choice of the scale k_ℓ.

According to the numerical values of the corresponding parameters of the full-scale CPACLS, the values of scales k_ℓ, k_m, k_I and the transformed ratios (4) in the form of

$$\ell_m = \frac{\ell_n}{k_\ell}; m_m = \frac{m_n}{k_M}; I_{jm} = \frac{I_{jn}}{k_I}(j = x, y, z, xy, xz, yz) \tag{6}$$

values of required basic parameters of FDSM can be obtained.

4 Conditions of Similarity and Technical Feasibility of FDSM in the Task of Creating Model Parachute Systems

The values of the required basic parameters of FDSM should be technically feasible at this level of development of design method and production technology from available structural materials and capabilities of the used operational and scientific-research complex. Minimum technically feasible values of linear and mass-inertial parameters are of greatest interest [3].

In this research, we will focus on the conditions of providing an internal volume sufficient to accommodate onboard equipment and components (and possibly the main and reserve parachute) within the contour of a geometrically similar cargo of a full-scale CPACLS on a FDSM. We introduce the concept of maximum scale linear sizes according to the placement condition

$$k^s_{\ell\ max} = \frac{\ell_n}{\ell^s_{m\ min}}, \tag{7}$$

where $\ell^s_{m\ min}$ – minimum characteristic technically feasible size of FDSM.

One way to calculate it is to use the layout density coefficient of a FDSM ζ_m. In the case under consideration

$$\zeta_m = \frac{W_{eq} + W_{p.s}}{W_{\sum m}}, \tag{8}$$

where W_{eq} – volume of equipment and components of a FDSM; $W_{p.s}$ – volume of parachute system of a FDSM; $W_{\sum \text{м}}$ – internal useable volume of a FDSM.

Volumes occupied by the equipment and parachute system of a FDSM [3]

$$W_{eq} = (1,26\ldots1,30)W_{f.p}; W_{p.s} = \frac{m_{p.s}}{\rho_{p.s}}, \tag{9}$$

where $W_{f.p}$ – volume of finished products of all types of equipment of a FDSM; $m_{p.s}$ – mass of parachute system of a FDSM; $\rho_{p.s}$ – density of the stowed parachute system.

Since the internal useable volumes within the cargo contours of a full-scale CPACLS $W_{\sum n}$ and a FDSM $W_{\sum m}$ are related by the geometric similarity relation

$$\frac{W_{\sum n}}{W_{\sum m}} = k^3_\ell, \tag{10}$$

the, using to above relations, we obtain a formula for determining the scale of linear sizes under the condition of providing the internal volume of a FDSM, sufficient for the placement of onboard equipment and components

$$k_{\ell W} = \sqrt[3]{\frac{W_{\sum n}\zeta_m}{W_{eq} + W_{p.s}}}. \tag{11}$$

Volumetric layout implies, in particular, the procedure of placing equipment and components within the contour of geometrically similar cargo of a full-scale CPACLS on a FDSM. The conditions of their placement (with allowance for the power and auxiliary structure) determine the necessary local scales of linear sizes

$$k_{\ell_i} = \frac{\ell_{ni}}{\ell_{mi}} = \frac{\ell_{ni}}{(1,05\ldots1,15)\ell_i}(i = 1,\ 2,\ 3\ldots), \tag{12}$$

where ℓ_{ni}, ℓ_{mi} – characteristic linear sizes of the compared internal contours of geometrically similar cargoes of a full-scale CPACLS and a FDSM; ℓ_i – the linear size of onboard equipment or component installed on a FDSM.

From them it is necessary to select the scale with the minimum numerical value – $k_{\ell i}$, which is the scale of linear sizes according to the conditions of placing the components within the contour of FDSM.

The scale of linear sizes of the FDSM accepted for further consideration should not exceed $k_{\ell W}$ and $k_{\ell i}$ defined above, i.e. the maximum scale of linear sizes $k^s_{\ell\ max} = \min(k_{\ell W}, k_{\ell i})$, and the minimum technically feasible size of the FDSM

$$\ell^s_{m\ min} = \frac{\ell_n}{k^s_{\ell\ max}}. \tag{13}$$

Although a FDSM must meet the conditions of similarity, it does not have to be structurally similar, but in general, like its parts, to provide the similarity when modelling the specified flight modes of a CPACLS. Therefore, whatever the composition of onboard equipment and components of a FDSM may be, the external shape, total mass, center of mass position, proper and transfer axial and centrifugal moments of inertia for the "cargo" group must comply with similarity relations (6).

Creation of a FDSM is directly related to ensuring the necessary rigidity and sufficient strength of its parachute system design in all possible cases of loading, as well as achieving a similar mass distribution of the parachute system of the CPACLS. The correct choice of structural materials of a FDSM is one of the ways to solve this issue and the following comments are important here [3, 11]:

a) we will assume that the elements of domes and slings of the parachute system of a FDSM, as well as of CPACLS, are made of thin elastic materials and in conditions of deployment and flight with cargo work only in tension;
b) at the same flight modes, the forces R_n и R_m, as well as the operational overloads n^{ol}_n and n^{ol}_m, are related by relations (5), but the calculated forces R^c_m and R^c_n on the units must obey the inequality

$$R^c_m \geq \frac{R^c_n}{k_f k_\rho k^3_\ell}, \tag{14}$$

where $k_f = \frac{f_n}{f_m}$ – scale of safety factors f_n of CPACLS and f_m of FDSM;

c) similarity of deformations can be obtained only if the stiffness axes of dome elements and slings of CPACLS and FDSM are geometrically similarly located in the corresponding sections, and the stiffness characteristics (E_nF_n and E_mF_m) are related by the relation

$$E_mF_m = \frac{E_nF_n}{k_\rho k_\ell^3}. \tag{15}$$

where E_n, E_m – modules of longitudinally elasticity of materials from which domes or slings of CPACLS and FDSM are made; F_n, F_m – cross-sectional areas of the corresponding dome elements or slings of CPACLS and FDSM.

The condition of axial tensile strength for dome elements or slings of CPACLS and FDSM can be represented in the following form [3, 11]:

$$\sigma_{max} = \frac{R^c}{F} \le \sigma_в , \tag{16}$$

where σ_{max} – maximum normal stress from the calculated force R^c over the cross-section area F; $\sigma_в$ – tensile strength of the material used by normal stresses.

In the limit case (($\sigma_{max} = \sigma_в$)) for elements of domes or slings of FDSM and CPACLS (with material tensile strength $\sigma_{в.n}$and $\sigma_{в.m}$) it can be written that

$$R_n^c = F_n\sigma_{в.n}, \quad R_m^c = F_m\sigma_{в.m}. \tag{17}$$

Using relations (14) and (17), as well as (1) with respect to similar areas F_n and F_m, after corresponding transformations we obtain the inequality

$$\sigma_{в.m} \ge \frac{\sigma_{в.n}}{k_f k_\rho k_\ell}, \tag{18}$$

which, to a large extent, affects the choice of dome materials and slings of a FDSM.

For domes (or slings) of parachute systems of CPACLS and FDSM, made each of different but one material under the condition of geometrical similarity (1), the ratio (15) acquires a design form

$$E_m = \frac{E_n}{k_\rho k_\ell} \tag{19}$$

and relates modules of longitudinal elasticity of materials, from which the domes or slings of parachute systems of CPACLS and FDSM are made.

The masses of parachute dome m_p and sling m_s can be determined by the formulas

$$m_p = \rho_p F_p; \, m_s = \rho_s L_s, \tag{20}$$

where ρ_p – surface area of parachute dome material; ρ_s – linear density of sling material; F_p, L_s – surface area of the parachute dome and total length of the parachute slings.

In order to provide dynamic similarity in modelling the motion of the cargo-parachute system, which depends on the similarity of masses and moments of inertia, it is necessary that for the domes and slings of parachutes of CPACLS and FDSM

$$\frac{m_{p.n}}{m_{p.m}} = \frac{\rho_{p.n} F_{p.n}}{\rho_{p.m} F_{p.m}} = k_\rho k_\ell^3; \frac{m_{s.n}}{m_{s.m}} = \frac{\rho_{s.n} L_{s.n}}{\rho_{s.m} L_{s.m}} = k_\rho k_\ell^3. \tag{21}$$

Since the surface areas of the domes and the total lengths of the slings are subject to the conditions of geometric similarity (1), after the necessary transformations, relations (21) will acquire the design form

$$\rho_{p.m} = \frac{\rho_{p.n}}{k_\rho k_\ell}; \rho_{s.m} = \frac{\rho_{s.n}}{k_\rho k_\ell^2}. \tag{22}$$

The way to fill the dome with air when deploying the parachute system [8]

$$S_p^{f.d} = c\sqrt{F_p}, \tag{23}$$

where c – proportionality coefficient depending on the dome construction, type and air permeability of the dome fabric.

The for domes of CPACLS and FDSM (according to geometrical similarity of motions) the condition must be satisfied

$$\frac{S_{p.n}^{f.d}}{S_{p.m}^{f.d}} = \frac{c_n\sqrt{F_{p.n}}}{c_m\sqrt{F_{p.m}}} = k_\ell. \tag{24}$$

where finally we obtain

$$c_m = c_n, \tag{25}$$

i.e. to ensure similarity when modelling the flight of CPACLS on FDSM (among other things), it is necessary for the domes of FDSM to use fabrics with the same proportionality coefficient as for the domes of CPACLS.

5 Conclusions

The purpose of work has been achieved – the possibility of creating parachute systems of FDSM for carrying out on them flight researches of modes of separation of CPACLS from the aircraft-carrier, deployment of the parachute system and performance of steady flight in the vertical plane until the moment of cargo landing, by obtaining ratios for determining the required and available values of parameters and characteristics of parachute system of FDSM. At the same time the literature review and analysis of device features, calculation, design, flight tests and research pf parachute systems of CPACLS and FDSM are performed. The conditions and scales of similarity used in creation of FDSM and carrying out on them flight researches of parachute system of CPACLS are considered. The conditions of similarity and technical feasibility of FDSM in the task of creating model parachute systems have been identified. Ratios for selection of structural materials and determination of values of parameters and characteristics of parachute systems of FDSM at modelling of landing of CPACLS are obtained.

References

1. Knacke, T.W.: Parachute Recovery Systems, Design Manual. NWC TP6575, pp. 5–119. Naval Weapons Center, CA, Santa Barbara (1991)
2. Ploskov, S.Yu.: Modern parachute systems for high-accuracy cargo delivery. Eng. J. Sci. Innov. (3) (2021). https://doi.org/10.18698/2308-6033-2020-3-2066. (in Russian)
3. Betin, A.V., Ryzhenko, A.I., Ryabkov, V.I., Cheranovsky, O.R.: Determination of the Sizes and Mass and Inertial Parameters of Free-Flying Dynamically Similar Aircraft Models. Kh.: Kharkov Aviation Institute (1992). 101 pages (in Russian)
4. Pramod, A., Shankaranarayanan, H., Raj, A.A.B.: A precision airdrop system for cargo loads delivery applications. In: 2021 International Conference on System, Computation, Automation and Networking (ICSCAN), Puducherry, India, pp. 1–5 (2021). https://doi.org/10.1109/ICSCAN53069.2021.9526453
5. Adhikary, A., Maity, T., Samanta, J.: Design and development of a smart parachute control system for military and civilian applications. Turk. J. Comput. Math. Educ. (TURCOMAT) **11**(1), 492–501 (2022)
6. Wachlin, J., Costello, M.: Simulation of the landing dynamics of a guided airdrop system. In: AIAA 2019–3372. AIAA Aviation 2019 Forum, June 2019
7. Chambers, J.R.: Modeling flight: The Role of Dynamically Scaled Free-Flight Models in Support of NASA's Aerospace Programs. NASA SP 2009–575, Washington, USA (2010). 202 p.
8. Lobanov, N.A.: Bases of calculation and designing of parachutes. Mechanical Engineering (1965). 364 pages (in Russian)
9. Betin, O.V., Betin, D.O., Kaluzhynov, I.V., Betina, O.Y.: Criteria and similarity scales in the task of modelling the operation of inflatable air shock absorbers when landing parachute platforms. In: Nechyporuk, M., Pavlikov, V., Kritskiy, D. (eds.) ICTM 2021. AISC, vol. 367, pp. 344–352. Springer, Cham (2021). https://doi.org/10.1007/978-3-030-94259-5_30
10. Betin, O.V., Kyriienko, P.G., Betin, D.O., Betina, O.Y.: Theoretical foundations of physical modeling of the descent and landing process of controlled precision airborne cargo landing systems. In: Nechyporuk, M., Pavlikov, V., Kritskiy, D. (eds.) ICTM 2022. LNNS, vol. 657, pp. 39–50. Springer, Cham (2022). https://doi.org/10.1007/978-3-031-36201-9_4
11. Betin, A.V.: Selection of structural materials for the mode. Problems of design of the flying models for research of critical flight regimes: collected papers of Kharkov aviation institute – Kh., pp. 63–74 (1989). (in Russian)

Crestal Versus Subcrestal Short Plateau Implant Placement

Igor Linetskiy[1], Vladislav Demenko[2], Oleg Yefremov[2], Larysa Linetska[3], and Andrii Kondratiev[4](✉)

[1] General University Hospital in Prague, U Nemocnice 499/2, 128 08 Prague 2, Czech Republic
[2] National Aerospace University "Kharkiv Aviation Institute", 17 Chkalova Street, Kharkiv 61070, Ukraine
[3] National Technical University Kharkiv Polytechnic Institute, 2, Kyrpychova Street, Kharkiv 61002, Ukraine
[4] O.M. Beketov National University of Urban Economy in Kharkiv, 17 Marshal Bazhanov Street, Kharkiv 61002, Ukraine
andrii.kondratiev@kname.edu.ua

Abstract. Plateau implants are widely acknowledged for their high success rates due to their ability to minimize bone stress concentrations. In cases where there is insufficient bone height, crestal implant placement is a viable alternative. Otherwise, subcrestal placement of short implants is recommended as it plays a vital role in preserving crestal bone from overload. In this context, the biomechanical state of the bone is directly influenced by the depth at which the implant is inserted. The objective of this study was to assess the impact of crestal and subcrestal placement of short plateau implants in varying bone quality conditions on peri-implant bone stresses. A 5.0 × 5.0 mm Bicon Integra-CP™ implant was chosen for numerical analysis. Four posterior maxilla models with types III and IV bone, each having a 1.0 mm cortical bone thickness, were utilized. Simulations were conducted at different insertion depths: the implant neck was placed at the crestal level and −1, −2, and −3 mm subcrestal positions. A mean maximal oblique load of 120.92 N was applied to the center of the 7.0 mm abutment. Von Mises equivalent stress distributions in the surrounding bone were examined to identify areas with stress magnitudes exceeding 100 MPa in cortical bone and 5 MPa in cancellous bone.In all scenarios, the highest von Mises equivalent stress values were observed at the implant neck. The results indicated that the 5.0 × 5.0 mm Bicon Integra-CP™ implant, when placed crestally, resulted in safe bone von Mises equivalent stresses and offered promising clinical outcomes. However, in all subcrestal scenarios, the implant placement have led to von Mises equivalent stress values exceeding the acceptable range in cancellous bone due to the absence of contact with cortical bone. Notably, the tested Bicon implant displayed low sensitivity to deteriorating bone quality at the studied subcrestal levels, affirming the positive clinical experience with Bicon plateau implants.

Keywords: Insufficient Bone Height · Insertion Depths · Stress Concentrations

M. Nechyporuk et al. (Eds.): ICTM 2023, LNNS 1008, pp. 258–267, 2024.
https://doi.org/10.1007/978-3-031-61415-6_22

1 Introduction

Dental implants are considered an important option for oral rehabilitation, particularly in the posterior maxillary region [1, 2]. However, it is not possible to place dental implants with an adequate length in some clinical situations, primarily due to the lack of a bone [3]. Posterior maxilla site often presents a challenge for clinicians due to insufficient bone height and quality, making it difficult to achieve sufficient primary stability and implant success [4, 5]. One option to overcome this limitation is using short implants (<8 mm) [6]. Short implant placement has been considered as a less invasive alternative to maxillary sinus augmentation with or without bone grafting, and it is associated with greater simplicity, a shorter surgical duration, and lower morbidity rates and cost [7, 8]. Furthermore, the clinical outcomes of short implants are reportedly similar to those of long implants in the posterior maxillary region [9, 10]. However, the bone-to-implant contact area with short implants may be small, impairing the primary stability and osseointegration process [11] and eventually leading to implant failure [1]. However, the development of implant design such as the plateau root form [12] has increased the success rate to above 90% [13] due to their potential to develop a microbial seal [14] leading to decreased peri-implant bone loss due to microbial invasion and reducing bacterial micro leakage.

2 Literature Review

In cases with poor bone quality, using the widest available implant diameter and placing the implant crestally may be the only way to enhance tolerance to occlusal forces, improve initial stability, and distribute stress favorably in vicinity of the surrounding bone [15, 16]. Unfortunately, crestal placement frequently results in an increase of stress magnitudes at the bone-implant interface, leading to implant failures [17].

In esthetic areas, subcrestal implant placement has become a common approach to preserving mucosa texture and tonality [18, 19]. It was suggested that deeper implant placement can reduce strain levels in peri-implant bone [20].

Different types of implant-abutment connections exhibit various patterns of bone loss. Compared to external connections and internal screwed flat connections, conical internal connections offer increased stability, resistance to micro-movement, reduced bacterial microleakage, and preservation of crestal bone [21].

Implants with morse tapered implant-abutment interfaces have shown a positive impact on bone contact at the implant neck when positioned subcrestally in dogs [22–24]. However, clinical studies using implants with tapered internal implant-abutment interfaces placed at subcrestal levels have yielded conflicting results regarding peri-implant bone loss. It was found that implants placed at the margin level had a significantly higher failure rate compared to those placed approximately 2 mm subcrestally [25].

Conversely, results from a 36-month prospective split-mouth clinical trial [11] and a 3-month prospective randomized controlled clinical trial [26] demonstrated no differences in crestal bone loss for implants placed crestally or subcrestally. Moreover, a prospective 60-month follow-up study showed that peri-implant bone loss was significantly greater for subcrestally placed implants with platform-switched morse taper connections [27].

The objective of this study was to assess the impact of crestal versus subcrestal placement of short plateau implants in various bone quality conditions on peri-implant bone stresses and to evaluate implant perspective under specified functional load.

3 Research Methodology

Four 3D models of the posterior maxilla segment were created to simulate the placement of 5.0×5.0 mm Bicon Integra-CP™ implants in different positions: crestal (C) and three subcrestal positions (S1 (-1 mm), S2 (-2 mm), and S3 (-3 mm)) (Fig. 1). The developed models are successfully implemented in an environment of SolidWorks 2022 software, a leader in the field of CAD systems [28].

The bone segment consisted of 1.0 mm of crestal and sinus cortical bone layers and an 8 mm cancellous bone core, mimicking types III/IV bone with varying cancellous bone elasticity moduli.

The implant was inserted monocortically only in the crestal position, with no cortical bone-implant contact in the S1 and S2 scenarios. In the S3 scenarios, the implant apex contacted with the sinus cortical bone (Fig. 1). The size of the maxilla segment was $40 \times 9 \times 11$ mm (length $\times$ height $\times$ width).

Both the implant and bone were treated as linearly elastic and isotropic materials, with homogeneous material properties [29, 30].

The implant\abutment continuous units were were assumed to be made of a titanium alloy with a modulus of elasticity of 114 GPa and a Poisson's ratio of 0.34 [31]. The Poisson's ratio for bone tissues (cortical and cancellous) was assumed to be 0.3 [32]. The elasticity modulus for cortical bone was 13.7 GPa [32] for both bone quality types, while for Type III bone, the cancellous bone elasticity modulus was 1.37 GPa, and for Type IV, it was 0.69 GPa. The ultimate tension strength of cortical and cancellous bone was 100 and 5 MPa, respectively [31].

In terms of boundary conditions, the disto-mesial surfaces of the bone segment and the upper cortical shell planes in all models were restrained (see Fig. 1). The bone-implant models were analyzed using FE software Solidworks Simulation [33]. 4-node 3D finite elements were generated, with a total count of up to 1,580,000 (Fig. 2).

To ensure identical functional loading in the other scenarios, the abutment length was increased by the subcrestal insertion depth to maintain the same loading application height. Loading of the implant was carried out at the center of the abutment, in 3D, with a mean maximal functional load of 120.9 N [34] applied obliquely. The components of functional loading were 116.3 N in the axial direction, 17.4 N lingually, and 23.8 N disto-mesially. The last two components represented the resultant vector of a 29.5 N horizontal functional load acting in the plane of the critical bone-implant interface.

The assumption of complete osseointegration was applied to simulate the bone-implant interface in all considered scenarios.

Von Mises equivalent stress (MES) was chosen as the indicator of bone failure risk [35, 36]. MES distributions in the critical bone-implant interface of the eight bone-implant FE models were examined to calculate the maximal MES values. Areas with MES exceeding 100 MPa in cortical bone and 5 MPa in cancellous bone were analyzed.

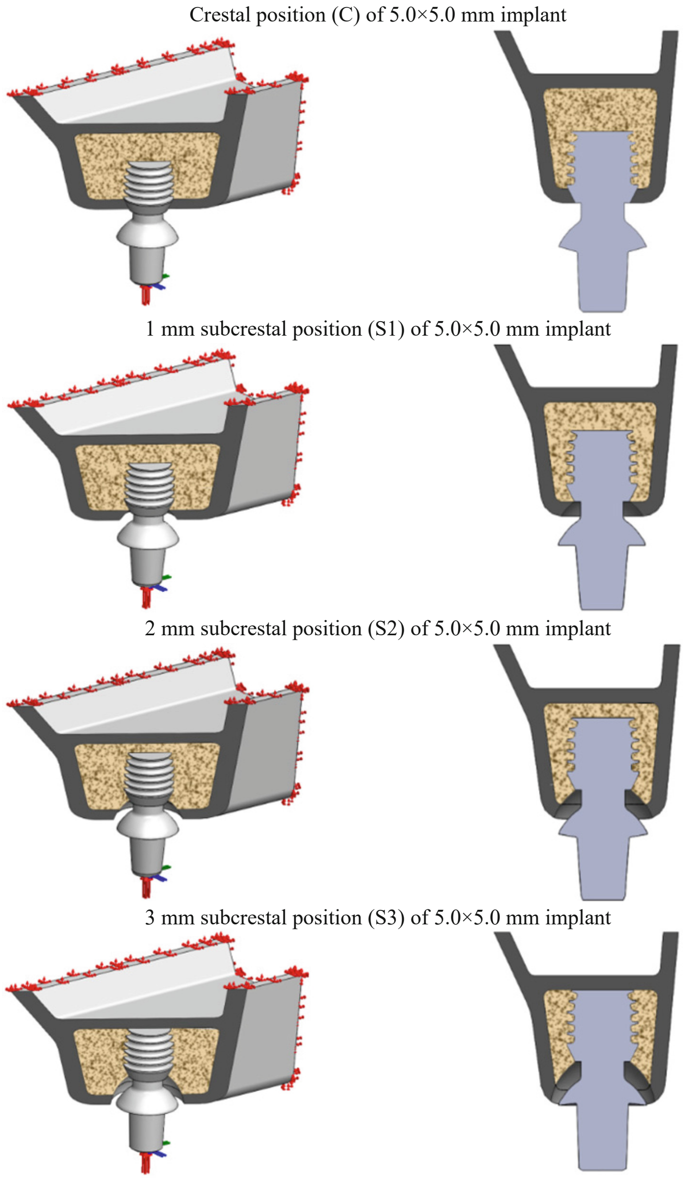

Fig. 1. Maxillary bone segment of 1.0 mm crestal and sinus cortical bone thickness with 5.0 × 5.0 mm implant placed in crestal and subcrestal (1, 2, 3 mm) positions. Oblique loading is applied to the centre of abutment upper surface at 7.0 mm distance from the upper bone margin

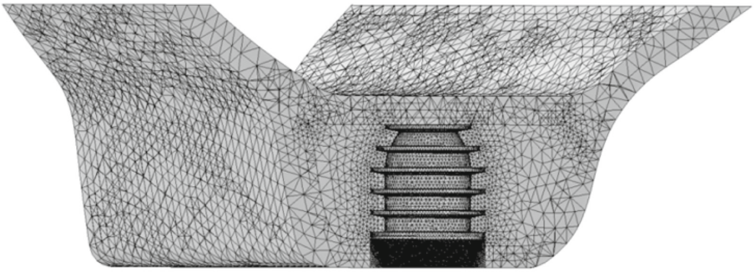

(a)

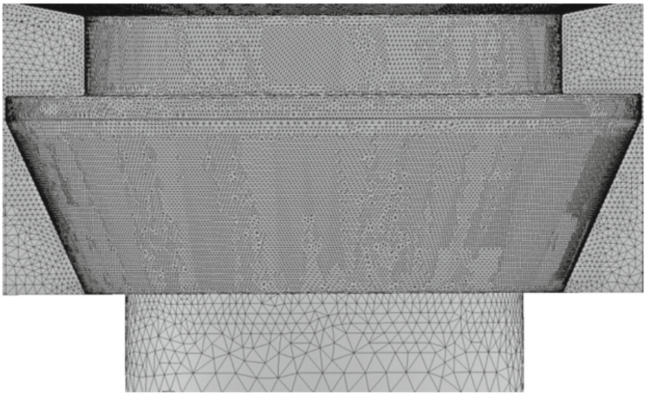

(b)

Fig. 2. FE meshing of maxillary bone segment with 1.0 mm crestal and sinus cortical bone and 4.5 mm diameter/4.0 mm length implant (a), mapped meshing in the neck area of bone-implant contact (b). Minimal value of FE size is 0.025 mm

4 Results

The highest MES values were consistently observed at the implant neck in all scenarios (refer to Fig. 3 and 4).

In the C scenario, the maximal MES values were in the crestal cortical bone and calculated at 21/28 MPa for type III/IV bone. The maximal MES values in cancellous bone were around 5 MPa for both bone types. In the S1, S2, and S3 scenarios, where there was no contact between the implant and cortical bone, the highest MES values were localized in the cancellous bone at the implant neck. In the S1 scenario, they ranged from 18 to 20 MPa, while in the S2 and S3 scenarios, they were between 13 and 14 MPa for both bone quality types.

Another critical area with high MES values was identified at the implant's root. In the C scenario, the maximal MES values were 2 MPa for both bone quality types, while in the S1 scenario, they ranged from 2.5 to 3.5 MPa. For the S2 scenario, they were between 3.5 and 4.0 MPa, and for the S3 scenario, they reached 7 to 10 MPa (for type III/IV bone).

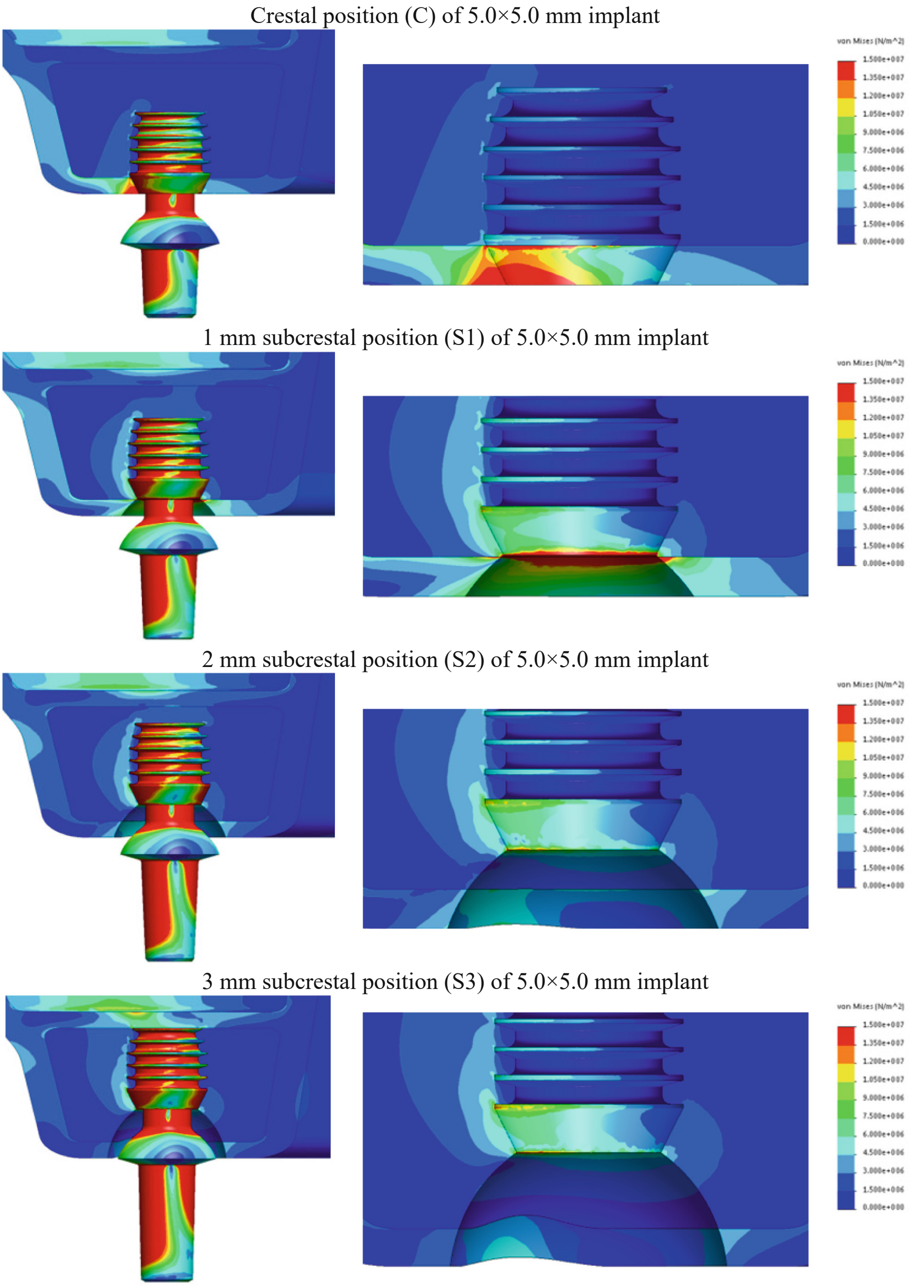

Fig. 3. Ensuring of identical functional loading for crestal and three subcrestal (1, 2, 3 mm) implant insertions by variation of abutment height

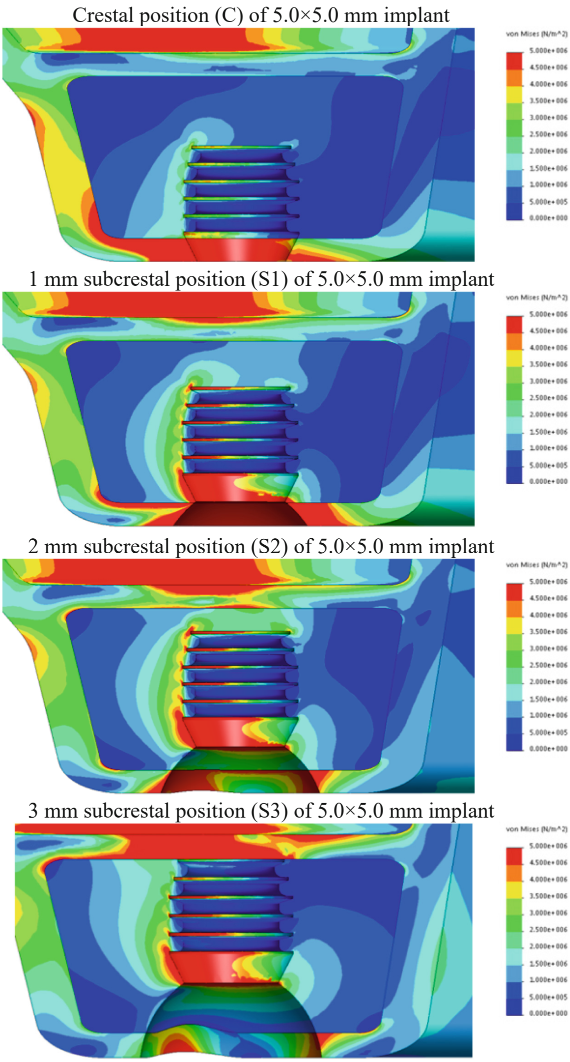

Fig. 4. Typical von Mises stress distribution along the critical bone-implant interface in type III maxillary bone segments for crestal and subcrestal (1, 2, 3 mm) implant placement

5 Conclusion

The investigation revealed that the 5.0 × 5.0 mm Bicon Integra-CP™ implant, when placed crestally, resulted in safe bone MESs and presented promising clinical potential. In contrast, in all subcrestal scenarios, the implant led to MES values surpassing the acceptable range in cancellous bone due to the lack of contact with cortical bone. Nevertheless, the Bicon implant under examination displayed a limited sensitivity to deteriorating bone quality at the investigated subcrestal placement levels. This discovery supports the positive clinical track record of Bicon plateau implants.

References

1. Lemos, C.A.A., Ferro-Alves, M.L., Okamoto, R., Mendonaça, M.R., Pellizzer, E.P.: Short dental implants versus standard dental implants placed in the posterior jaws: a systematic review and meta-analysis. J. Dent. **47**, 8–17 (2016). https://doi.org/10.1016/j.jdent.2016.01.005
2. Cruz, R.S., et al.: Short implants versus longer implants with maxillary sinus lift. A systematic review and meta-analysis. Braz. Oral Res. **32**, e86 (2018). https://doi.org/10.1590/1807-3107bor-2018.vol32.0086
3. Anitua, E., Alkhraisat, M.H., Eguia, A.: On peri-implant bone loss theories: trying to piece together the jigsaw. Cureus **15**, e33237 (2023). https://doi.org/10.7759/cureus.33237
4. Chan, H.L., Suarez, F., Monje, A., Benavides, E., Wang, H.L.: Evaluation of maxillary sinus width on cone-beam computed tomography for sinus augmentation and new sinus classification based on sinus width. Clin. Oral Implants Res. **25**(6), 647–652 (2014). https://doi.org/10.1111/clr.12055
5. Linetskiy, I., Sutcliffe, M., Kondratiev, A., Demenko, V., Linetska, L., Yefremov, O.: A novel method of load bearing ability analysis of short plateau implants placed in compromised bone. In: 2023 IEEE 4th KhPI Week on Advanced Technology (KhPIWeek), pp. 1–6 (2023). https://doi.org/10.1109/KhPIWeek61412.2023.10312831
6. Esfahrood, Z.R., Ahmadi, L., Karami, E., Asghari, S.: Short dental implants in the posterior maxilla: a review of the literature. J. Korean Assoc. Oral Maxillofac. Surg. **43**(2), 70–76 (2017). https://doi.org/10.5125/jkaoms.2017.43.2.70
7. Cannizzaro, G., Felice, P., Leone, M., Viola, P., Esposito, M.: Early loading of implants in the atrophic posterior maxilla: lateral sinus lift with autogenous bone and Bio-Oss versus crestal mini sinus lift and 8-mm hydroxyapatite-coated implants. A randomised controlled clinical trial. Eur. J. Oral Implantol. **2**(1), 25–38 (2009)
8. Felice, P., et al.: Treatment of the atrophic edentulous maxilla: short implants versus bone augmentation for placing longer implants. Five-month post-loading results of a pilot randomised controlled trial. Europ. J. Oral Implantol. **4**(3), 191–202 (2011)
9. Cannizzaro, G., Felice, P., Minciarelli, A.F., Leone, M., Viola, P., Esposito, M.: Early implant loading in the atrophic posterior maxilla: 1-stage lateral versus crestal sinus lift and 8mm hydroxyapatite-coated implants. A 5-year randomised controlled trial. Eur. J. Oral Implantol. **6**(1), 13–25 (2013)
10. Bechara, S., Kubilius, R., Veronesi, G., Pires, J.T., Shibli, J.A., Mangano, F.G.: Short (6-mm) dental implants versus sinus floor elevation and placement of longer (≥10-mm) dental implants: a randomized controlled trial with a 3-year follow-up. Clin. Oral Implants Res. **28**(9), 1097–1107 (2017). https://doi.org/10.1111/clr.12923
11. Al Amri, M.D., Al-Johany, S.S., Al Baker, A.M., Al Rifaiy, M.Q., Abduljabbar, T.S., Al-Kheraif, A.A.: Soft tissue changes and crestal bone loss around platform-switched implants placed at crestal and subcrestal levels: 36-month results from a prospective split-mouth clinical trial. Clin. Oral Implants Res. **28**(11), 1342–1347 (2017). https://doi.org/10.1111/clr.12990
12. Suzuki, M., et al.: Effect of surface modifications on early bone healing around plateau root form implants: an experimental study in rabbits. J. Oral Maxil. Surg. **68**(7), 1631–1638 (2010). https://doi.org/10.1016/j.joms.2009.07.064
13. Maló, P., Nobre, M.D.: Short implants placed one-stage in maxillae and mandibles: a retrospective clinical study with 1 to 9 years of follow-up. Clin. Impl. Dent. Relat. Res. **9**(1), 15–21 (2007). https://doi.org/10.1111/j.1708-8208.2006.00027.x
14. Dibart, S., Warbington, M., Su, M.F., Skobe, Z.: In vitro evaluation of the implant-abutment bacterial seal: the locking taper system. Int. J. Oral Maxillofac. Implants **20**(5), 732–737 (2005)

15. Poovarodom, P., et al.: Effect of implant placement depth on bone remodeling on implant-supported single zirconia abutment crown: a 3D finite element study. J. Prosthodon. Res. **67**(2), 278–287 (2023). https://doi.org/10.2186/jpr.JPR_D_22_00054
16. Huang, B., et al.: Effect of implant placement depth on the peri-implant bone defect configurations in ligature-induced peri-implantitis: an experimental study in dogs. Medic. oral patologia oral y cirugia bucal **23**(1), e30–e37 (2018). https://doi.org/10.4317/medoral.22032
17. Rameh, S., Menhall, A., Younes, R.: Key factors influencing short implant success. Oral Maxillofac. Surg. **24**, 263–275 (2020). https://doi.org/10.1007/s10006-020-00841-y
18. Buser, D., von Arx, T.: Surgical procedures in partially edentulous patients with ITI implants. Clin. Oral Implants Res. **11**, 83–100 (2000). https://doi.org/10.1034/j.1600-0501.2000.011S1083.x
19. Barros, R.R.M., Novaes, A.B., Muglia, V.A., Iezzi, G., Piattelli, A.: Influence of interimplant distances and placement depth on peri-implant bone remodeling of adjacent and immediately loaded Morse cone connection implants: a histomorphometric study in dogs. Clin. Oral Implants Res. **21**(4), 371–378 (2010). https://doi.org/10.1111/j.1600-0501.2009.01860.x
20. Chou, H.Y., Muftu, S., Bozkaya, D.: Combined effects of implant insertion depth and alveolar bone quality on periimplant bone strain induced by a wide-diameter, short implant and a narrow-diameter, long implant. J. Prosthet. Dent. **104**(5), 293–300 (2010). https://doi.org/10.1016/s0022-3913(10)60142-4
21. Ugurel, C.S., Steiner, M., Isik-Ozkol, G., Kutay, O., Kern, M.: Mechanical resistance of screwless morse taper and screw-retained implant-abutment connections. Clin. Oral Implants Res. **26**(2), 137–142 (2015). https://doi.org/10.1111/clr.12303
22. Huang, B.X., Meng, H.X., Zhu, W.D., Witek, L., Tovar, N., Coelho, P.G.: Influence of placement depth on bone remodeling around tapered internal connection implants: a histologic study in dogs. Clin. Oral Implants Res. **26**(8), 942–949 (2015). https://doi.org/10.1111/clr.12384
23. Cochran, D.L., et al.: Soft and hard tissue histologic dimensions around dental implants in the canine restored with smaller-diameter abutments: a paradigm shift in peri-implant biology. Int. J. Oral Maxillof. Implants **28**(2), 494–502 (2013). https://doi.org/10.11607/jomi.3081
24. Calvo-Guirado, J.L., et al.: Narrow- versus mini-implants at crestal and subcrestal bone levels. Experimental study in beagle dogs at three months. Clin. Oral Investig. **19**(6), 1363–1369 (2015). https://doi.org/10.1007/s00784-014-1381-4
25. Lee, E.H., et al.: Effects of installation depth on survival of an hydroxyapatite-coated bicon implant for single-tooth restoration. J. Oral Maxillof. Surg. **68**(6), 1345–1352 (2010). https://doi.org/10.1016/j.joms.2009.12.010
26. Palaska, I., Tsaousoglou, P., Vouros, I., Konstantinidis, A., Menexes, G.: Influence of placement depth and abutment connection pattern on bone remodeling around 1-stage implants: a prospective randomized controlled clinical trial. Clin. Oral Implants Res. **27**(2), E47–E56 (2016). https://doi.org/10.1111/clr.12527
27. Cassetta, M., Driver, A., Brandetti, G., Calasso, S.: Peri-implant bone loss around platform-switched Morse taper connection implants: a prospective 60-month follow-up study. Int. J. Oral Maxillof. Surg. **45**(12), 1577–1585 (2016). https://doi.org/10.1016/j.ijom.2016.09.009
28. Vasilev, R., Skulev, H., Dovramadjiev, T.: Optimization of design opportunities and transfer of information between data 3D graphics program blender and Solidworks CAD system for use in dental industry. In: Abraham, A., Kovalev, S., Tarassov, V., Snasel, V., Vasileva, M., Sukhanov, A. (eds.) IITI 2017. AISC, vol. 680, pp. 42–49. Springer, Cham (2018). https://doi.org/10.1007/978-3-319-68324-9_5
29. Linetska, L., Kipenskyi, A., Demenko, V., Linetskiy, I., Kondratiev, A., Yefremov, O.: Finite element study of biomechanical behavior of short dental implants with bone loss effects – evaluation of bone turnover. In: 2023 IEEE 4th KhPI Week on Advanced Technology (KhPIWeek), pp. 1–6 (2023). https://doi.org/10.1109/KhPIWeek61412.2023.10312964

30. Misura, S., Smetankina, N., Misiura, I.: Optimal design of the cyclically symmetrical structure under static load. In: Nechyporuk, M., Pavlikov, V., Kritskiy, D. (eds.) ICTM 2020. LNNS, vol. 188, pp. 256–266. Springer, Cham (2021). https://doi.org/10.1007/978-3-030-66717-7_21
31. Bozkaya, D., Muftu, S., Muftu, A.: Evaluation of load transfer characteristics of five different implants in compact bone at different load levels by finite elements analysis. J. Prosthetic Dent. **92**(6), 523–530 (2004). https://doi.org/10.1016/j.prosdent.2004.07.024
32. Baggi, L., Cappelloni, I., Di Girolamo, M., Maceri, F., Vairo, G.: The influence of implant diameter and length on stress distribution of osseointegrated implants related to crestal bone geometry: a three-dimensional finite element analysis. J. Prosthet. Dent. **100**(6), 422–431 (2008). https://doi.org/10.1016/s0022-3913(08)60259-0
33. Kondratiev, A., Potapov, O., Tsaritsynskyi, A., Nabokina, T.: Optimal design of composite shelled sandwich structures with a honeycomb filler. In: Ivanov, V., Trojanowska, J., Pavlenko, I., Zajac, J., Peraković, D. (eds.) DSMIE 2021. LNME, pp. 546–555. Springer, Cham (2021). https://doi.org/10.1007/978-3-030-77719-7_54
34. MericskeStern, R., Zarb, G.A.: In vivo measurements of some functional aspects with mandibular fixed prostheses supported by implants. Clin. Oral Implants Res. **7**(2), 153–161 (1996). https://doi.org/10.1034/j.1600-0501.1996.070209.x
35. Kondratiev, A.V., Kovalenko, V.O.: Optimization of design parameters of the main composite fairing of the launch vehicle under simultaneous force and thermal loading. Space Sci. Technol. **25**, (4(119)), 3–21 (2019). https://doi.org/10.15407/knit2019.04.003
36. Falcinelli, C., Valente, F., Vasta, M., Traini, T.: Finite element analysis in implant dentistry: state of the art and future directions. Dent. Mater. **39**, 539–556 (2023). https://doi.org/10.1016/j.dental.2023.04.002

Smoothed Piecewise Linear Lyapunov Function for the First Order Dynamical Systems

Roman Voliansky[1(✉)], Iurii Shramko[2], Nina Volianska[1], Olga Tolochko[1], and Oleksandr Sadovoi[2]

[1] National Technical University of Ukraine "Igor Sikorsky Kyiv Polytechnic Institute", 37, Str. Polytechnichna, Kyiv 03056, Ukraine
volianskyi.roman@lll.kpi.ua

[2] Dniprovsk State Technical University, 2, Dniprobudivska Str., Kamyanske 51918, Ukraine

Abstract. The paper deals with the mathematical backgrounds of design piecewise single-variable Lyapunov functions. These backgrounds are based on the study of the main features of generalized Lyapunov function and using them to analyze the solution of dynamical programming problem. This analysis shows that the optimal control signal, which is supplied to the control plant, depends on the partial derivative of the Lyapunov function. This fact allows us to consider the Lyapunov function as a control signal integral over the perturbed motion variable. If the control signal is produced by the sliding mode controller, our approach defines the Lyapunov function as a non-quadratic absolute value function. Since this function is not differentiable in the origin, it is hard enough to use it while the optimal controller is being designed with optimal theory methods. We avoid this problem by applying a smoothing procedure, which is based on considering a small neighborhood near the fracture point. In this neighborhood, we replace the piecewise linear function with a polynomial one. Factors of the polynomial are defined to have the same function values and its derivatives in the boundary points. In our paper, we show that our approach can be extended to the case of a controller which produces a multilevel signal. Signal of such form causes occurring the piecewise linear Lyapunov function, which can be smoothed by using polynomials. Since such a piecewise function can have a lot of branches, we offer to consider it as two functions, which are defined in their intervals.

Keywords: Lyapunov function · piecewise linear function · sliding mode control · polynomial smoothing

1 Introduction

Modern industrial processes [1, 2], municipal applications [3, 4], transport [5, 6], communications [7, 8], robotic [9–11], scientific research [12, 13], and many other branches of human beings cannot be imagined without using electrical devices and equipment. These devices operate because of various physical laws and these laws cause a quite complex nature of electrical devices. This nature raises an important problem of motion study [14, 15] and design [16, 17] for different electrical devices.

M. Nechyporuk et al. (Eds.): ICTM 2023, LNNS 1008, pp. 268–278, 2024.
https://doi.org/10.1007/978-3-031-61415-6_23

For more than a hundred years the problem of study system dynamics has remained one of the point problems in control theory. A lot of classical and modern control methods have been developed to solve this problem and the Routh-Hurwitz method [18, 19] and method of system frequencies responses [20] are among them. It is necessary to say, that the main drawback of classical methods is the necessity to have a linearized model for the studied plant. Due to the use of nonlinear differential equations to describe the processes in electrical devices, such linear methods can cause errors in the study.

That is why nowadays various modern control methods are used. Quite effective one is a phase plane method [21] and its derivatives like the Poincare map method [22]. These methods require knowing the whole studied system motions and their usage can require a lot of calculations.

Quite a simple method without tons of calculations is a method based on using the apparatus of Lyapunov functions [23, 24]. This method allows to study stability of system motion and design controllers to govern the system along the desired trajectories. The classical approach to defining these functions is based on considering the Lyapunov function as a square polynomial [25]. Such a definition bounds the usage of the Lyapunov method because various modern dynamical system requires to use of more complex apparatus to study [26]. This requirement causes the necessity to design piecewise Lyapunov functions instead of classical polynomial ones [27, 28]. Nevertheless, the known authors do not interrelate these functions with the control algorithm which can be applied in the control system of the considered plant.

We offer to solve this problem by defining the Lyapunov function as the solution to the inverse dynamical programming problem and our paper is organized as follows. At first, we consider the solution of the inverse dynamical programming problem and show the drawbacks defined by it using the Lyapunov function. Then we show method to avoid these drawbacks. Third, we consider the control system with a multi-level output signal and define the Lyapunov function for this system.

2 Definition of Piecewise Lyapunov Function

2.1 Definition of Piecewise Linear Lyapunov Functions

It is a well-known fact that the Lyapunov functions belong to the class of positive definite functions and following expressions define their features

$$V(\mathbf{0}) = 0, \quad \dot{V}(\mathbf{0}) = 0, \tag{1}$$

here we assume that $\mathbf{0}$ is a zero n-th sized vector of system state variables.

The conventional way to satisfy (1) and define the Lyapunov function is the use of 2^{nd} order polynomial. Such an approach has strong physical backgrounds because in this case Lyapunov functions are considered as some generalized kinetic redundant energy which should be dissipated during control system motions. The usage of such Lyapunov functions leads to design linear closed-loop control systems which form exponential motions trajectories. It is clear that it takes quite a lot time to move along these trajectories. Moreover, the above-mentioned polynomial Lyapunov functions do not allow to define nonlinear control laws which can improve system dynamic dramatically. That is why we offer to define Lyapunov functions in another class of mathematical functions.

Let us consider the 1st order differential system which dynamic is given in the operator form as follows

$$s\eta = f(\eta) + bu, \tag{2}$$

here s is a Laplace operator, b is a feedforward channel factor, u is a control effort, and f(η) is system inner nonlinear feedback, η is a system perturbed motion coordinate

$$\eta = x - x^{*}, \tag{3}$$

where x and x^{*} are system real and desired state variables.

We think that (2) moves under nonlinear control law

$$u = -g(\eta) \tag{4}$$

and features of its motion are defined by the simplest integral cost function

$$I_1 = \int_0^{\infty} \left(k\eta^2 + cu^2\right) dt, \tag{5}$$

here k and c are some weight factors.

Let as assume that exist Lyapunov function

$$V = V(\eta), \tag{6}$$

which allows us to take into account (2) and write down following Bellman equation

$$\min\left[\frac{\partial V(\eta)}{\partial \eta} f(\eta) + b\frac{\partial V(\eta)}{\partial \eta} u + k\eta^2 + cu^2\right] = 0. \tag{7}$$

If one differentiates (7) for control signal u, he can write following expression which interrelates system parameters with Lyapunov function and control signal

$$u = -\frac{b}{2c}\frac{\partial V(\eta)}{\partial \eta}. \tag{8}$$

Since we assume that the control signal is already known we can equal (8) and (4) and define partial Lyapunov function derivative for the system coordinate

$$2\frac{c}{b} g(\eta) = \frac{\partial V(\eta)}{\partial \eta}. \tag{9}$$

Thus, one can integrate (9) to define unknown Lyapunov function

$$V = 2\frac{c}{b} \int g(\eta) d\eta. \tag{10}$$

So, analysis of (10) shows that Lyapunov function, which is used to determine system stability features, can be defined by known control signal.

The usage of (10) for sliding mode control systems with control law

$$u = \begin{cases} -1 \; if \; \eta > 0 \\ \;\; 1 \; \; if \; \eta < 0 \end{cases} \tag{11}$$

gives us possibility to define Lyapunov function as weighted absolute value function

$$V = 2\frac{c}{b}|\eta|. \tag{12}$$

In more complex case, when sliding mode controller produces k-th level control signal

$$u = -\begin{cases} u_1 \; if \quad \eta_1 \le \eta < \eta_2 \\ u_2 \; if \quad \eta_2 \le \eta < \eta_3 \\ \vdots \;\; \vdots \qquad\quad \vdots \\ u_k \; if \; \eta_{k-1} \le \eta \le \eta_k, \end{cases} \tag{13}$$

the above-given approach defines Lyapunov function as piecewise linear function

$$V = \begin{cases} 2u_1\frac{c}{b}|\eta| + \eta_0 \; if \quad \eta_1 \le \eta < \eta_2 \\ 2u_2\frac{c}{b}|\eta| + \eta_1 \; if \quad \eta_2 \le \eta < \eta_3 \\ \qquad \vdots \qquad\quad \vdots \qquad\quad \vdots \\ 2u_2\frac{c}{b}|\eta| + \eta_k \; if \; \eta_{k-1} \le \eta \le \eta_k, \end{cases} \tag{14}$$

where η_i are some integration constants.

The detailed analysis of above-define picewise linear Lyapunov functions shows that these functions cannot satisfy at least one of signs of Lyapunov function which are given by (1) due to non-differentiability these functions in the fracture points. Also, it can occur the case when piecewise linear function takes non one zero values. This case can be caused by using discontinuous controller with dead zone.

2.2 Polynomial Smoothing of Piecewise Linear Lyapunov Functions

We offer to avoid the above-mentioned problems by appending some polynomial functions to piecewise linear functions (12) and (14). These functions are defined in a small neighborhood near the fracture points and replace in this neighborhood functions (12) and (14).

Let us show the definition of such function for Lyapunov function (12) (Fig. 1).

To perform above-mentioned modification of the considered Lyapunov function, we select a neighborhood ε, which length is a quite small to make no effects on any system motions. Since function (12) is symmetrical with respect to vertical axis, the points $\pm \eta_p$, which bounds neighborhood ε, are the same distance from the origin. This fact allows to define their coordinates as follows

$$\eta_p = -\eta_p = \frac{\varepsilon}{2}. \tag{15}$$

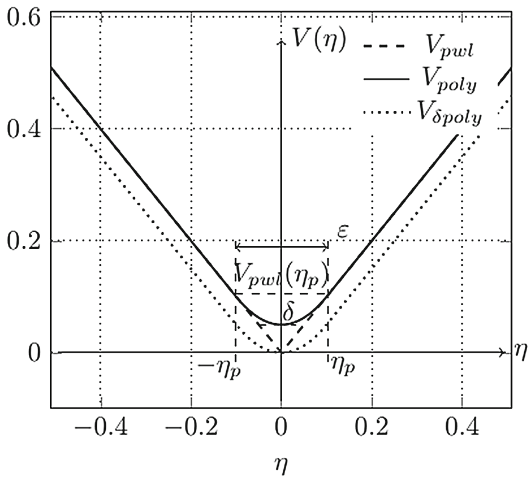

Fig. 1. Single-variable Lyapunov function

In these points piecewise linear function V_{pwl} (12) becomes polynomial V_{poly}

$$V_{poly} = k_2\eta^2 + \delta. \tag{16}$$

To ensure a smooth transition from (12) to (16) it is necessary to demand that (12) and (16) have the same values and the same derivatives in points $\pm\eta_p$.

These demands make it possible to write down following equations

$$2\frac{c}{b}\eta_p = k_2\eta_p^2 + \delta; \quad 2\frac{c}{b} = 2k_2\eta_p, \tag{17}$$

which solution gives us possibility to define unknown polynomial factors

$$\delta = \frac{c\eta_p}{b}; \quad k_2 = \frac{c}{b\eta_p}. \tag{18}$$

Analysis of (18) shows that the less neighborhood ε is, vertical offset δ takes the less value and polynomial term k_2 becomes the greater.

If one takes into account (18), he can combine functions (16) and (12) and write down following piecewise function

$$V_{poly} = \begin{cases} -2\frac{c}{b}\eta & if \quad \eta < -\eta_p \\ \frac{c}{b\eta_p}\eta^2 + \frac{c\eta_p}{b} & if \; -\eta_p \le \eta \le \eta \\ 2\frac{c}{b}\eta & if \quad \eta > \eta_p. \end{cases} \tag{19}$$

Function (19) with terms (18) have nonzero value in the origin for all neighborhoods with nonzero length (solid line in Fig. 1). It is clear that in this case the first condition of (1) is not fulfilled and function (19) cannot be considered as Lyapunov function.

We offer to fix this problem by moving function (19) down along vertical axes by amount δ (dotted line in Fig. 1). In this case (19) can be rewritten in such a way

$$V_{\delta poly} = \begin{cases} -2\frac{c}{b}\eta - \frac{c\eta_p}{b} & if \quad \eta < -\eta_p \\ \frac{c}{b\eta_p}\eta^2 & if \ -\eta_p \le \eta \le \eta \\ 2\frac{c}{b}\eta - \frac{c\eta_p}{b} & if \quad \eta > \eta_p. \end{cases} \tag{20}$$

We call (20) as piecewise Lyapunov function. The main feature of this function is constant offset for big values of perturbed motion coordinate.

This function is designed for the case when controller produce output signals which is symmetrical about zero. At the same time, some applications require to use non-symmetrical control signals and the most known example of such non-symmetry is the producing of unipolar signal

$$u = \begin{cases} -1 & if \ \eta > 0 \\ 0 & otherwise. \end{cases} \tag{21}$$

In this case (20) can be rewritten in such a way

$$V_{\delta poly} = \begin{cases} 0 & if \quad \eta < 0 \\ \frac{c}{b\eta_p}\eta^2 & if \ 0 \le \eta \le \eta_p \\ 2\frac{c}{b}\eta - \frac{c\eta_p}{b} & if \quad \eta > \eta_p. \end{cases} \tag{22}$$

Thus, the proposed approach allows us to extend the Lyapunov function concept and allows to consider Lyapunov functions with non-symmetrical branches which can be caused by the plant nonlinearities or non-symmetrical control.

2.3 Definition of Lyapunov Function for Control System with Multilevel Sliding Mode Controller

In the most general case, the nonlinear controller can produce multilevel output. For example, one can find that it can happen when nonlinear output function has dead zone or when twisting sliding mode control law is implemented.

Let us consider a case when controller produce two-level symmetrical output (Fig. 2)

$$u = -\begin{cases} -2\frac{c}{b}u_1 & if \quad \eta < -\eta_1 \\ -2\frac{c}{b}u_0 & if \ -\eta_1 \le \eta \le 0 \\ 2\frac{c}{b}u_0 & if \quad 0 < \eta \le \eta_1 \\ 2\frac{c}{b}u_1 & if \quad \eta > \eta_1, \end{cases} \tag{23}$$

here u_i are some constant values of controller output.

If one integrates (22) for variable η he can rewrite piecewise linear Lyapunov function (14) in such a way

$$V = \begin{cases} -2\frac{c}{b}u_1\eta + 2\frac{c}{b}(u_0 - u_1)\eta_1 & if \quad \eta < -\eta_1 \\ -2\frac{c}{b}u_0\eta & if \ -\eta_1 \le \eta \le 0 \\ 2\frac{c}{b}u_0\eta & if \quad 0 < \eta \le \eta_1 \\ 2\frac{c}{b}u_1\eta + 2\frac{c}{b}(u_0 - u_1)\eta_1 & if \quad \eta > \eta_1, \end{cases} \tag{24}$$

According to the proposed approach this piecewise linear function can be smoothed by using polynomials. It is clear that since we have four branches in the (22), the three polynomials should be found. The definition one of them for smoothing transition between the second and third branches does not differ from the considered in previous section.

The definition of other smoothing polynomials differs from the considered earlier because of various branches of (22) has different slopes. This fact makes us to consider smoothed polynomial as follows

$$V_{poly} = k_2\eta^2 + k_1\eta_1 + \delta \tag{25}$$

and use it to write equations for both boundary points in neighborhood ε

$$\begin{aligned} &-2\frac{c}{b}u_1\eta_{p1} + 2\frac{c}{b}(u_0 - u_1)\eta_1 = k_2\eta_{p1}^2 + k_1\eta_{p1} + \delta; \quad -2\frac{c}{b}u_1 = 2k_2\eta_{p1} + k_1; \\ &2\frac{c}{b}u_0\eta_{p2} = k_2\eta_{p2}^2 + k_1\eta_{p2} + \delta; \quad 2\frac{c}{b}u_0 = 2k_2\eta_{p2} + k_1. \end{aligned} \tag{26}$$

One can use (26) to define unknown parameters of smoothing polynomial

$$\delta = -\frac{c\eta_{\mathrm{p2}}}{b}\frac{4\eta_{\mathrm{p1}}u_0 - 3\eta_{\mathrm{p2}}u_0 + \eta_{\mathrm{p2}}u_1}{\eta_{\mathrm{p1}} - \eta_{\mathrm{p2}}}; \quad \mathrm{k}_1 = 2\frac{\mathrm{c}}{b}\frac{\eta_{\mathrm{p1}}\mathrm{u}_0 + \eta_{\mathrm{p2}}\mathrm{u}}{\eta_{\mathrm{p1}} - \eta_{\mathrm{p2}}}; \mathrm{k}_2 = -\frac{c}{b}\frac{\mathrm{u}_0 + \mathrm{u}_1}{\eta_{\mathrm{p1}} - \eta_{\mathrm{p2}}}. \tag{27}$$

Parameters of smoothing polynomial between the third and fourth branches can be defined in a similar way.

The usage of polynomial (25) makes it possible to rewrite (22) as follows

$$V_{\delta poly} = \begin{cases} -2\frac{c}{b}u_1\eta + 2\frac{c}{b}(u_0 - u_1)\eta_1 - \delta_{23} & if \quad \eta < -\eta_{p1} \\ k_{212}\eta^2 + k_{112}\eta_1 + \delta_{12} - \delta_{23} & if \quad -\eta_{p1} \le \eta < -\eta_{p2} \\ -2\frac{c}{b}u_0\eta - \delta_{23} & if \quad -\eta_{p2} \le \eta < -\eta_{p3} \\ k_{223}\eta^2 + k_{123}\eta_1 & if \quad -\eta_{p3} \le \eta < -\eta_{p4} \\ 2\frac{c}{b}u_0\eta - \delta_{23} & if \quad -\eta_{p4} \le \eta < -\eta_{p5} \\ k_{234}\eta^2 + k_{134}\eta_1 + \delta_{34} - \delta_{23} & if \quad -\eta_{p6} \le \eta < -\eta_{p7} \\ 2\frac{c}{b}u_1\eta + 2\frac{c}{b}(u_0 - u_1)\eta_1 - \delta_{23} & if \quad \eta > \eta_{p7}, \end{cases} \tag{28}$$

here $\mathrm{k_{ijp}}$ are polynomial terms which are defined according to (27) for various fracture points.

The Lyapunov function (28) is shown in Fig. 2.

All above-designed Lyapunov functions are considered when one of two branches passed through the origin. This fact makes some simplifications in Formulas (27) and (18) but in the most general case, when it is necessary to define smoothed polynomial for two linear functions given as follows

$$V_1 = a_1\eta + y_{01}; \quad V_2 = a_2\eta + y_{02} \tag{29}$$

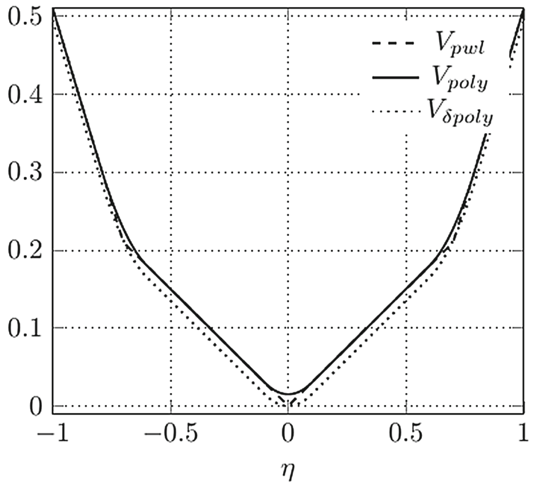

Fig. 2. Piecewise Lyapunov function

one can use the generalized formulas

$$
\begin{aligned}
k_{2ij} &= \frac{a_i^2 - 2a_i a_j + a_j^2}{4\left(a_i\eta_{pi} - a_j\eta_{pi} + y_{0i} - y_{0j}\right)}; \quad k_{1ij} = \frac{a_i^2\eta_{pi} - a_j^2\eta_{pi} + 2a_i y_{0i} - 2a_i y_{0j}}{2\left(a_i\eta_{pi} - a_j\eta_{pi} + y_{0i} - y_{0j}\right)}; \\
\delta_{ij} &= \frac{a_i^2\eta_{pi}^2 - 2a_i a_j\eta_{pi}^2 + a_j^2\eta_{pi}^2 + 4a_i\eta_{pi}y_{0i} - 4a_j\eta_{pi}y_{0i} + 4y_{0i}^2 - 4y_{0i}y_{0j}}{4\left(a_i\eta_{pi} - a_j\eta_{pi} + y_{0j} - y_{0j}\right)}; \\
\eta_{pj} &= -\frac{\mathrm{a}_i\eta_{pi} - \mathrm{a}_j\eta_{pi} + 2\mathrm{y}_{0\mathrm{i}} - 2\mathrm{y}_{0\mathrm{j}}}{a_i - a_j}.
\end{aligned} \tag{30}
$$

Analysis of (28) shows that the designed Lyapunov function in some intervals is defined as linear functions of perturbed motion coordinate and in other intervals it is described by polynomial functions. Thus, to generalize (28) one can define interval of linear functions usage

$$\Omega_{lin} = \left(-\infty, \eta_{p1}\right) \cap \left(\eta_{p2}, \eta_{p3}\right) \cap \left(\eta_{p4}, \eta_{p5}\right) \cap \ldots \cap \left(\eta_{pw}, \infty\right), \tag{31}$$

where w is a number of boundary points in all neighborhoods in which piecewise linear function is smoothed, and intervals where Lyapunov function is polynomial

$$\Omega_{poly} = \left[\eta_{p1}, \eta_{p2}\right] \cap \left[\eta_{p3}, \eta_{p4}\right] \cap \cap \ldots \cap \left[\eta_{p(w-1)}, \eta_{pw}\right] \tag{32}$$

Such intervals allow us to rewrite (28) in a compact form

$$V = \begin{cases} a_i\eta + y_{0i} - \min\left(\delta_{ij}\right) & if \quad \eta \in \Omega_{lin} \\ k_{2i(i+1)}\eta^2 + k_{1i(i+1)}\eta_1 + \delta_{i(i+1)} - \min\left(\delta_{ij}\right) & if \quad \eta \in \Omega_{poly}, \end{cases} \tag{33}$$

here $\min(\delta_{ij})$ means taking the minimal value of factors δ for all intervals.

Function (33) is the most general form of piecewise Lyapunov function. The use of this form gives us possibility to define a wide range of piecewise Lyapunov functions. From one hand, one can construct a piecewise linear function with smoothing which is performed very close to fracture points. From another, it allows to wide an interval Ω_{poly} for whole area where the function is defined and, thus, consider polynomial Lyapunov functions only.

3 Conclusion

The above-given formulas allow us to claim that the solution of inverse dynamical programming problem gives us possibility to define non-square piecewise Lyapunov function for control system with sliding mode controller. Moreover, since output signals amplitude of such controller affects on system dynamic our approach makes it possible to take into account control signal amplitude which interrelate with energy supplied to the considered plant. The use proposed polynomial smoothing for piecewise linear Lyapunov function candidate allows to make this function differentiable for all state variables.

Because of the proposed approach defines piecewise linear functions we see the future development of our approach in studying dynamical system in complex and hypercomplex domains as well as extending it into case of high-order dynamical system.

References

1. Pechenik, M., Burian, S., Pushkar, M., Zemlianukhina, H.: Electromechanical system of turbomechanism when using an alternative source of electric energy. Naukovyi Visnyk Natsionalnoho Hirnychoho Universytetu (2), 61–66 (2022). https://doi.org/10.33271/nvngu/2022-2/061
2. Osadchyy, V., et al.: Adjustable vibration exciter based on unbalanced motors. Sensors **23**(4), 2170 (2023). https://doi.org/10.3390/s23042170
3. Burian, S.O., Kiselychnyk, O.I., Pushkar, M.V., Reshetnik, V.S., Zemlianukhina, H.Y.: Energy-efficient control of pump units based on neural-network parameter observer. Tech. Electrodyn. **2020**(1), 71–77 (2020). https://doi.org/10.15407/techned2020.01.071
4. Kuzmin, V., Petrova, Y., Zaliskyi, M., Lavrynenko, O.: Method for correcting the mathematical model in case of empirical data asymmetry. In: Nechyporuk, M., Pavlikov, V., Kritskiy, D. (eds.) Integrated Computer Technologies in Mechanical Engineering - 2022: Synergetic Engineering, pp. 249–260. Springer, Cham (2023). https://doi.org/10.1007/978-3-031-36201-9_21
5. Sushchenko, O., Salyuk, O.: Approach to automated synthesis of structure for aircraft control system. In: Ostroumov, I., Zaliskyi, M. (eds.) Proceedings of the International Workshop on Advances in Civil Aviation Systems Development, pp. 73–83. Springer, Cham (2023). https://doi.org/10.1007/978-3-031-38082-2_6
6. Sushchenko, O., Bezkorovainyi, Y.: Design of robust aircraft control system. In: Ostroumov, I., Zaliskyi, M. (eds.) Proceedings of the International Workshop on Advances in Civil Aviation Systems Development, pp. 17–29. Springer, Cham (2023). https://doi.org/10.1007/978-3-031-38082-2_2

7. Zuiev, O., Solomentsev, O., Zaliskyi, M., Osipchuk, A.: Efficiency analysis of control algorithms for aviation radio equipment. In: Ostroumov, I., Zaliskyi, M. (eds.) Proceedings of the International Workshop on Advances in Civil Aviation Systems Development, pp. 271–282. Springer, Cham (2023). https://doi.org/10.1007/978-3-031-38082-2_21
8. Voliansky, R., Kluev, O., Sadovoi, O., Sinkevych, O., Volianska, N.: Chaotic time-variant dynamical system. In: Proceedings of the 15th International Conference on Advanced Trends in Radioelectronics, Telecommunications and Computer Engineering (TCSET 2020), art. no. 9088709, pp. 606–609 (2020). https://doi.org/10.1109/TCSET49122.2020.235503
9. Sokhina, Y.: Sliding mode interval controller for the mobile robot. In: Proceedings of the 11th International Scientific and Practical Conference on Electronics and Information Technologies (ELIT 2019) art. no. 8892330, pp. 76–81 (2019). https://doi.org/10.1109/ELIT.2019.8892330
10. Ostroumov, I., Kuzmenko, N., Bezkorovainyi, Y., Averyanova, Y., Larin, V.: Sushchenko relative navigation for vehicle formation movement. In: 2022 IEEE 3rd KhPI Week on Advanced Technology, KhPI Week 2022–Conference Proceedings (2022). https://doi.org/10.1109/KhPIWeek57572.2022.9916414
11. Lou, T.-S., Yue, Z.-P., Jiao, Y.-Z., He, Z.-D.: A hybrid strategy-based GJO algorithm for robot path planning. Exp. Syst. Appl. **238**, 121975 (2024). https://doi.org/10.1016/j.eswa.2023.121975
12. Trotsenko, Y., Brzhezitsky, V., Protsenko, O., Haran, Y.: Experimental laboratory equipped with voltage dividers for power quality monitoring. In: Proceedings of the International Conference on Modern Electrical and Energy Systems (MEES 2019), art. no. 8896471, pp. 270–273 (2019). https://doi.org/10.1109/MEES.2019.8896471
13. Nazarova, O., Osadchyy, V., Shulzhenko, S., Olieinikov, M.: Software and hardware complex for the study of electropneumatic mechatronic systems. In: Proceedings of the 2022 IEEE 4th International Conference on Modern Electrical and Energy System (MEES 2022) (2022). https://doi.org/10.1109/MEES58014.2022.10005698
14. Fiore, M.D., Allmendinger, F., Natale, C.: A general constraint-based programming framework for multi-robot applications. Robot. Comput.-Integrat. Manufact. **86**, 102665 (2024). https://doi.org/10.1016/j.rcim.2023.102665
15. Zhu, C., Yu, T., Chang, Q.: Task-oriented safety field for robot control in human-robot collaborative assembly based on residual learning. Exp. Syst. Appl. **238**, 121946 (2024). https://doi.org/10.1016/j.eswa.2023.121946
16. Du, Z., Li, W., Shi, G.: Multi-USV collaborative obstacle avoidance based on improved velocity obstacle method. ASCE-ASME J. Risk Uncertainty Eng. Syst., Part A: Civ. Eng. **10**(1), 04023049 (2024). https://doi.org/10.1061/AJRUA6.RUENG-1174
17. Mousavi, A., Markazi, A.H.D.: An adaptive fuzzy sliding-mode control method for leader-follower consensus of uncertain non-square nonlinear systems. Int. J. Adapt. Control Signal Process. **36**(12), 3230–3253 (2022). https://doi.org/10.1002/acs.3504
18. Ali, H.M., Ameen, I.G.: Stability and optimal control analysis for studying the transmission dynamics of a fractional-order MSV epidemic model. J. Comput. Appl. Math. **434**, 115352 (2023). https://doi.org/10.1016/j.cam.2023.115352
19. Ndendya, J.Z., Leandry, L., Kipingu, A.M.: A next-generation matrix approach using Routh-Hurwitz criterion and quadratic Lyapunov function for modeling animal rabies with infective immigrants. Healthc. Analyt. **4**, 100260 (2023). https://doi.org/10.1016/j.health.2023.100260
20. Ukhina, H., Afanasyev, I., Sytnikov, V., Streltsov, O., Stupen, P.: The phase response values application of second-order digital frequency-dependent components for calculating transfer function coefficients in robotic systems. CEUR Worksh. Proc. **2711**, 107–120 (2020)
21. Fan, L., Lv, Y., Zhu, Q.: Stability and stabilization analysis of periodic switching stochastic systems based on Lyapunov function with continuous time-varying matrix polynomials. Commun. Nonl. Sci. Numer. Simulat. **128**, 107609 (2024). https://doi.org/10.1016/j.cnsns.2023.107609

22. Alves, A.M., Euzébio, R.D.: Periodic trajectories in planar discontinuous piecewise linear systems with only centers and with a nonregular switching line. Nonlinearity **36**(12), 6747–6776 (2023). https://doi.org/10.1088/1361-6544/ad03a7
23. Pires, B.: Lyapunov function for interacting reinforced stochastic processes via Hopfield's energy function. Statist. Prob. Lett. **205**, 109957 (2024). https://doi.org/10.1016/j.spl.2023.109957
24. Li, L., Zhai, H., Ji, W.: Control of transport constraints for shuttle vehicles based on barrier Lyapunov functions. Results Eng. **20**, 101475 (2023). https://doi.org/10.1016/j.rineng.2023.101475
25. Chu, E.K.-W., Hou, L., Szyld, D.B., Zhou, J.: Numerical solution of singular Sylvester equations. J. Comput. Appl. Math. **436**, 115426 (2024). https://doi.org/10.1016/j.cam.2023.115426
26. Li, Y., Van Kampen, E.-J.: Stability analysis for incremental adaptive dynamic programming with approximation errors. J. Aerosp. Eng. **37**(1), 04023097 (2024). https://doi.org/10.1061/JAEEEZ.ASENG-5097
27. Berger, G.O., Sankaranarayanan, S.: Counterexample-guided computation of polyhedral Lyapunov functions for piecewise linear systems. Automatica **155**, 111165 (2023). https://doi.org/10.1016/j.automatica.2023.111165
28. Ban, J., Seo, M., Kim, S.W., Kim, Y.-J.: $\mathscr{H}2$ reset controller design for linear systems using piecewise quadratic Lyapunov functions. Int. J. Robust Nonl. Control **33**(6), 3731–3748 (2023). https://doi.org/10.1002/rnc.6590

Hybrid Algorithm of Adhesive Joint Shape Optimization

Serhii Kurennov, Kostiantyn Barakhov(✉), Igor Taranenko, Olexandr G. Poliakov, Hanna Barakhova, and Kristina Vernadska

National Aerospace University "Kharkiv Aviation Institute", Kharkiv, Ukraine
k.barakhov@khai.edu

Abstract. The subject of this article is the algorithm for optimization of symmetrical adhesive lapped joint. The goal of the paper is development of the method for optimization problem solving, which allows to unite high rate of calculations with stability of obtained results. This goal can be reached by means of two algorithms of optimization – genetic algorithms implemented on the original stage and swarm of particles algorithm – on the last stage of optimization. The problem of optimization is in finding optimal shape of doublers, i.e. doubler length and function of thickness variation along joint length. To describe stress-strain state of a joint modified Holland-Reissner model is used. To solve direct problem of structural stress state estimation the finite elements method is used. For optimization problem solving combination of multi-population model of genetic algorithm and swarm of particles algorithm are used. Introduction of individuals from other populations to the considered one allows to escape of homogenization of genotypes in separate population and premature breakage of optimization process. To describe doubler shape thickness variation function development of Fourier series are used. Above-mentioned implemented methods allow to create algorithm for topologic optimization which unites advantages of both methods and find solution of considered problem quite quickly. Duration of algorithm realization on Python language requires several minutes only to find optimal parameters.

Keywords: Glued Joint · Optimization · Genetic Algorithm · Particle Swarm Optimization

1 Introduction

Adhesive joints have significant advantages compared to classical mechanical joints, such as light weight, tightness, high aerodynamic efficiency, manufacturability. In addition, gluing does not violate the integrity of the structure of fibrous composite materials and does not reduce their strength, unlike classical mechanical joints [1]. A well-known disadvantage of lap joints is the stress concentration in the adhesive layer at the edges of the gluing area [2]. To reduce stresses in the joint, symmetrical double overlap joints are often used [3], that allows to exclude an eccentricity in the transfer of forces between structural elements. A more general approach to stress reduction in a joint is to use patches of varying thickness. This makes it possible to ensure a more uniform stress state of the joint compared to classical structures [4, 5].

M. Nechyporuk et al. (Eds.): ICTM 2023, LNNS 1008, pp. 279–289, 2024.
https://doi.org/10.1007/978-3-031-61415-6_24

As a rule, the topological optimization problem for overlap joints is posed in a two-dimensional formulation. However, the two-dimensional formulation of the optimization problem, which is based on the use of finite element modeling [4], in a two-dimensional [6, 7] and three-dimensional [8] formulation, is correlated with a significant amount of computations. One of the methods to increase the computational speed for a problem is the use of one-dimensional mathematical models. One-dimensional mathematical models of the joint stress state are used to construct genetic optimization algorithms, for example, in the papers [9, 10] and the same for two types of glue, in the paper [11]. Papers [9, 10] deals with analogous mathematical model for joint stress state. However, genetic algorithm suggested by authors as the method for problem optimization solution at the last stages of analysis is not very effective.

Application of one-dimensional mathematical model also allows to formulate optimization problem in the simpler form. I.e. the problem of non-parametric optimization [12, 13] becomes less labor-intensive. If the shape of doubler id describes by means of definite set of parameters, then optimization problem is reduced to finding optimal values of these parameters.

However, a common disadvantage of genetic algorithms is the decrease in efficiency in the neighborhood of an extremum. For this purpose, various combinations of the genetic algorithm with other optimization methods are proposed. In this paper, in order to increase the efficiency of execution, it is proposed to use the island model of the genetic algorithm at the initial stage, and then improve the resulting solutions using the particle swarm algorithm. Computations have shown the high efficiency of the proposed calculation method.

2 Methodology of Research

Classical method of genetic algorithms possesses good convergence at beginning stages only, but then population become homogenized and further iterations don't lead to perfection of the solution not reaching near optimum values. Therefore, to exclude such premature solution breakage one can suggest different modifications of genetic algorithm, for example, application of several populations. However, this approach, in its turn, leads to increasing duration of calculations and tendency of premature calculation breakage is reduced but it still persists. To elevate the calculation process, authors suggest using combination of genetic algorithm and swarm of particles algorithm. Hybrid algorithms allow to unite advantages of both methods and can be considered as up-to-date direction of optimization methods development [14, 15]. At the original stage genetic algorithm gives definite approximate solution, then it can be improved by means of swarm of particles algorithm.

In the current case one can consider structural mass as optimality criterion. In frames of this approach structure has to keep required load-carrying ability, therefore the space of unknown parameters is restricted by region in which stress in adhesive layer doesn't exceed its allowable margins.

3 Problem Formulation

3.1 Mathematical Model

Equilibrium equations for outer (base) layers have form [9–11]

$$\frac{dN_1}{dx} = -\tau; \;\; \frac{dN_2}{dx} = \tau; \;\; \frac{dQ_1}{dx} = \sigma; \;\; \frac{dM_1}{dx} - s_1(x)\tau - N_1\frac{ds_1}{dx} + Q_1 = 0,$$

where N_1, N_2 are longitudinal forces in base layers; Q_1 are shear force in the patch; M_1 is a bending moment in the patch; τ and σ are tangential and normal stresses in the adhesive layer; s_1 is a distance from the neutral axis of the patch to the adhesive layer, in the case of a symmetrical patch structure $s_1(x) = 0.5\ \delta_1(x)$, where $\delta_1(x)$ is a patch thickness.

The deformation of the base layer is represented by equations:

$$N_1 = B_1(x)\frac{dU_1}{dx}; \;\; N_2 = B_2\frac{dU_2}{dx}; \;\; D_1(x)\frac{d^2w_1}{dx^2} = M_1,$$

where U_1 and U_2 are longitudinal displacements of the base layers; w_1 are transversal displacements of the patch; B_1 and B_2 are stress-strain rigidity values of the layers, if layers are homogenous by the thickness, then $B_1(x) = \delta_1(x)E_1$, $B_2 = \delta_2 E_2$, where E_1 and E_2 is an elastic modulus of the corresponding layer; D_1 is a bending rigidity of the patch, $D_1(x) = \delta_1^3(x)E_1/12$.

We consider the stress values in the adhesive layer proportional to the difference of displacements of the base layers

$$\sigma = Kw_1, \quad \tau = P\left(U_1 - U_2 + s_1(x)\frac{dw_1}{dx}\right),$$

where $K = E_0/\delta_0$, $P = G_0/\delta_0$, where δ_0 is a thickness of the adhesive layer, E_0 and G_0 are elastic modulus and shear modulus of an adhesive.

The system of equations can be reduced to the system of three differential equations relative to the displacements of the layer. Boundary conditions are given below:

$$N_2(0) = F, \;\; N_2(L) = U_1(L) = N_1(0) = Q_1(0) = M_1(0) = 0, \;\; Q_1(L) = \left.\frac{dw_1}{dx}\right|_{x=L} = 0.$$

The goal of considered problem is finding such function $\delta_1(x)$ which ensures minimal structural mass. The value of mass is equal to the doubler cross-section $M = \int_0^L \delta_1(x)dx$ with precision up to constant multiplier and constant term and hasn't to violate required level of structural load-carrying ability.

Generally, joint loses its load-carrying ability due to adhesive layer failure. Therefore, the condition of load-carrying ability level saving is the restriction of stress in adhesive film with definite ultimate values, for example

$$\sigma(x) \le \sigma_0, \;\; \tau(x) \le \tau_0.$$

Moreover, other strength criteria for adhesive layer can be implemented. These criteria depend on adhesive type, technology of adhesive joining and other factors.

3.2 Numerical Solution of the Direct Problem

We will assume, that the function $\delta_1(x)$ and the length L of the gluing is given. Hence, functions $s_1(x)$, $B_1(x)$ and $D_1(x)$ are also known. To solve the obtained system of equations with the corresponding boundary conditions numerically, we used the finite difference method. The gluing area $x \in [0;\ L]$, is divided into a system of nodal points numbered from zero to N. Points with numbers 0 and N are boundary ($x = 0$ and $x = L$ correspondingly). Having written in the difference form the system of differential equations for each of these points, as well as the boundary conditions, we obtain a system of linear equations for the displacements of the base layers at these points. This makes it possible to find stresses in the plate, patch and adhesive layer at the corresponding points.

4 Optimization

4.1 Optimization Genetic Algorithm

As noted above, the solution of the optimization problem in an analytical form seems to be very difficult. However, in contrast to the problem of finding the optimal material distribution along the beam [16], if thickness values $\delta_i^{(1)}$ in neighboring points are significantly different (that can happen due to crossbreeding and mutations), then stress values in the adhesive layer, computed by finite difference method, have unreal jumps, this is the fact, that the mathematical model becomes inadequate. In this paper it is proposed to use a cosine Fourier expansion at the interval $\xi \in [0;\ 1]$ to describe the function $\delta_1(x)$

$$\delta_i^{(1)} = y(\xi_i) = \frac{a_0}{2} + \sum_{k=1}^{M} a_n \cos \pi k \xi_i.$$

If we divide the interval $\xi \in [0;\ 1]$, as well as the interval $x \in [0;\ L]$ into $N + 1$ points ξ_i numerated from 0 to N.

A description of a patch geometrical form as a Fourier series allows us to calculate the mass of the patch rather simply:

$$M = \int_0^L \delta_1(x)dx = \frac{a_0 L}{2}.$$

To implement a genetic algorithm, it is necessary to create a fitness function that would make it possible to rank different sets of parameters L and $a_0,\ a_1, ..., a_M$ (i.e. individual) by quality. We can, for example, write the fitness-function in a following form:

$$\Phi = \frac{a_0 L}{2} + \varphi_1 + \varphi_2,$$

where $\varphi_1,\ \varphi_2$ are penalty functions, which are appointed in the case, if a corresponding solution does not satisfy some restriction.

These functions may have, for example, the following form:

$$\varphi_1 = \begin{cases} Z_1\left(\dfrac{\tau_m}{\tau_0} - 1\right), & \tau_m > \tau_0 \\ 0, & \tau_m \le \tau_0 \end{cases} \qquad \varphi_2 = \begin{cases} Z_2\left(\dfrac{\delta_{\min}}{\delta^{(1)}_{\min}} - 1\right), & \delta^{(1)}_{\min} < \delta_{\min} \\ 0, & \delta^{(1)}_{\min} \ge \delta_{\min} \end{cases}$$

where Z_1, Z_2 are some big numbers, which define the value of the penalty for leaving the solution out of the available area; τ_m are maximum shear stress in the adhesive layer in nodal points ($\tau_m = \max\limits_i\left[0.5\sqrt{\sigma^2 + 4\tau^2}\right]$); $\max\limits_i(\tau_{\max})$ is the maximal value of the maximum shear stress for all points in the area; $\delta^{(1)}_{\min} = \min\limits_i\left(\delta^{(1)}_i\right)$ is a minimal value of the patch thickness.

In this paper, we propose a model with three islands, on the one of which the probability and standard deviation of mutations are higher than on the other two islands. This combination of two relatively stable islands with one island with a higher mutation rate makes it possible to combine the speed of the appropriate solution finding with the stability and preservation of the best solutions in the general population.

The general scheme of the evolutionary algorithm for the one population has the form:

1. Creation of the initial population of vectors $\vec{h}^{(j)}$, where $j = 1, \ldots, n$. Each vector $\vec{h}^{(j)}$ (the individual) contains components $L^{(j)}$ and $a^{(j)}_0,\ a^{(j)}_1, \ldots, a^{(j)}_M$.
2. Calculate the corresponding values $\Phi^{(j)} = \Phi\left(\vec{h}^{(j)}\right)$.
3. *Selection.* We rank the vectors available in the population $\vec{h}^{(j)}$ according to the corresponding values of the fitness function $\Phi^{(j)}$.
4. We select $2k$ elements $\vec{h}^{(j)}$ from the population. It is necessary that the best individuals $\vec{h}^{(j)}$ from the population be included in the sample, which have less values of the fitness-functions.
5. *Parents choice.* We break $2k$ selected individuals into pairs and obtain k pairs of "parents". In the simplest case, we can break it into pairs at random.
6. *Crossover.* We randomly select parameters for each new individual $L^{(j)}$ and $a^{(j)}_0,\ a^{(j)}_1, \ldots, a^{(j)}_M$ from both parent individuals. As a result of such operation, we get a population k of new individuals, "descendants".
7. *Mutations.* In the version of the algorithm implemented by the authors, mutations occur only with a small part of the vector components $\vec{h}^{(j)}$ of individuals, which appear as a result of a "descendant" breeding.
8. After making changes to the genetic code, the descendants return to the main population. After that, individuals are again ranked according to the values of fitness-function $\Phi^{(j)}$ and k the worst individuals are removed from the population.
9. Checking of the stop criterion. If the stop criterion (for example, specified number of reproduction cycles M) is not reached, then we go back to the step 4.

Computations show [10, 11], that in the later iterations of the algorithm, the objective function remains practically unchanged. Therefore, it is proposed to use a combination of the genetic algorithm with the particle swarm algorithm [14, 15]. In this case, the resulting three subpopulations form the initial state of each of the three swarms of particles. And for each of the three swarms, the optimization problem is solved independently. After that, the best solutions are selected, and the values of the desired parameters are averaged over this sample. The scheme of the algorithm is shown in Fig. 1.

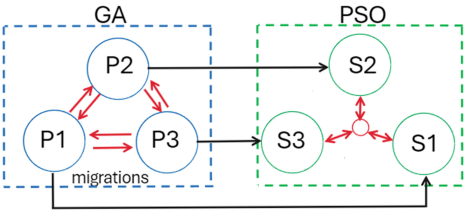

Fig. 1. The thickness of the main plate and the patch

Here P1, P2, P3 are populations 1, 2, and 3 in the genetic algorithm (GA), and S1, S2, S3 are populations of particles in the particle swarm optimization algorithm (PSO). The dark color indicates the population with an increased level of mutagenesis.

The upper and lower limits of the available value area for the desired parameters, which are necessary for the particle swarm algorithm, are calculated as follows:

$$L_{up} = L^* + \frac{L}{\theta},\ L_{lo} = L^* - \frac{L}{\theta},\ a_{k,up}^{(j)} = a_k^{(j)*} + \frac{\left|a_k^{(j)}\right|}{\theta},\ a_{k,lo}^{(j)} = a_k^{(j)*} - \frac{\left|a_k^{(j)}\right|}{\theta}.$$

Here the values denoted by "*", are parameters of the best individual in the subpopulation (swarm). The parameter θ, that defines a width of the interval, is appointed when tuning the algorithm. The authors used the value $\theta = 4$.

So, vectors of the upper and lower restriction of the required parameters have the form:

$$\vec{b}_{lo} = \left(L_{lo},\ a_{0,lo},\ a_{1,lo},\ \ldots, a_{M,lo}\right),\ \vec{b}_{up} = \left(L_{up},\ a_{0,up},\ a_{1,up},\ \ldots, a_{M,up}\right).$$

4.2 Algorithm, Particle Swarm Optimization

In this case, the particle swarm algorithm, which acts with the population (swarm) obtained at the previous stage (genetic algorithm), has the following form:

- the initial coordinates of each particle $\vec{h}^{(j)}$ (individual) will be assigned to the vector of the best-known position of each individual $\vec{p}^{(j)}$;
- the coordinates of the best individual in the swarm (subpopulation) will be assigned to the vector $\vec{g}$;
- to generate velocity vectors for each particle

$$\vec{v}^{(j)} \sim \vec{U}\left(-\left(\vec{b}_{up} - \vec{b}_{lo}\right), \left(\vec{b}_{up} - \vec{b}_{lo}\right)\right),$$

where $\vec{U}\left(\vec{l}, \vec{u}\right)$ is a multidimensional uniform distribution, which has a lower and upper limitations of the solution space $\vec{l}$ and $\vec{u}$.

While the algorithm stop criterion is not met (for example, the execution of a specified number of iterations or stabilization of the target function optimal values), perform the following operations:

– to generate vectors

$$\vec{r}_p = \vec{U}(0, 1) \text{ and } \vec{r}_g = \vec{U}(0, 1),$$

for each particle (individual);

– to renew the velocity of each particle

$$\vec{v}^{(j)} = \omega\vec{v}^{(j)} + \varphi_p\vec{r}_p \odot \left(\vec{p}^{(j)} - \vec{h}^{(j)}\right) + \varphi_g\vec{r}_g \odot \left(\vec{g} - \vec{h}^{(j)}\right),$$

where the operation $\odot$ means component multiplication;

– to renew the particle position by transfer from coordinates $\vec{h}^{(j)}$ into the point with coordinates $\vec{h}^{(j)} = \vec{h}^{(j)} + \vec{v}^{(j)}$;

– if $\Phi\left(\vec{h}^{(j)}\right) < f\left(\vec{p}^{(j)}\right)$ then renew the best known value of the point j, i.e. to assign to $\vec{p}^{(j)}$ the actual coordinates of $\vec{h}^{(j)}$. If $\Phi\left(\vec{p}^{(j)}\right) < f(\vec{g})$ then renew the best known solution for all the swarm, assigning coordinates $\vec{p}^{(j)}$ to the vector $\vec{g}$.

The parameters ω, φ_p, φ_g are selected by the calculator and determine the behavior and effectiveness of the method as a whole. The following values were assigned in this paper: $\omega = 0.6$, $\varphi_p = 1.1$, $\varphi_g = 1.1$.

Therefore, we have three swarms of particles obtained on the previous stage of the algorithm. And we can used use this fact and modify classical genetic algorithm increasing it rate of calculation. One has to note that both genetic and swarm of particles algorithm are, generally, are used as the basis for creation of more complicated method of optimization [18], which implement in their turn clasterization of particles on groups. Let's add possibility of information interchange between these three swarms in this case. And implement above-mentioned algorithm with each swarm for given quantity of iterations. After that we compare the best solution $\vec{g}$, found in each swarm, and find the best from three solutions. After that we transfer the best-found solution to each swarm and repeat optimization cycle with each swarm. Such interchange of information between swarms is repeated definite quantity of times.

5 Results and Discussion

Let us apply the proposed joint optimization algorithm to solve two problems that differ only in the load applied to the joint. The rest of the parameters are the same in both cases: $E_1 = 70$ GPa, $E_2 = 70$ GPa, $\delta_2 = 3$ mm, $\delta_0 = 0.1$ mm, $E_0 = 2.274$ GPa, $G_0 = 0.54$ GPa, $\tau_0 = 15$ MPa, $\delta_{\min} = 0.5$ mm, $\delta_{\max} = 8$ mm. We consider one case of loading the structure: $F = 170$ kN/m. We add a restriction on the value of the derivative of the patch thickness $\left|\delta_1'(x)\right| \leq 0.2$.

As a result of a numerical realization of a given algorithm it was obtained an optimal value of the adhesive area length $L = 31.5$ mm. Graph of change in the patch thickness along the joint length is shown in Fig. 2 (a). The main plate thickness graphs $\delta_2 = 3$ mm

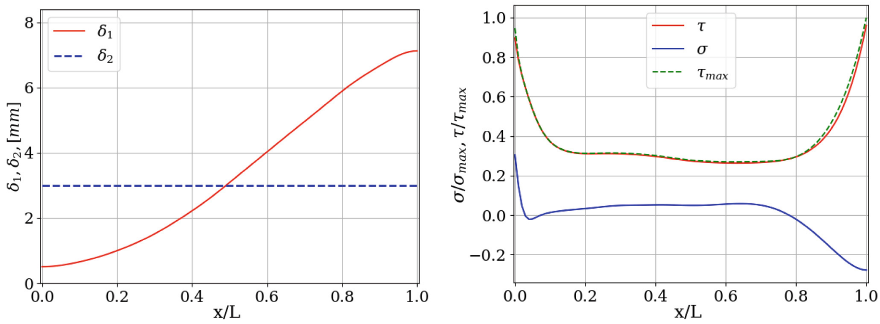

(a) (b)

Fig. 2. The main plate thickness and the patch profile (a); The stress distribution in the adhesive layer (b)

is given for a scale. Stress graphs τ, σ in the adhesive layer and $\tau_{\max}$ diagrams are shown in Fig. 2 (b).

The change in the average truncated value of the objective function in the population (it is 10% of the maximal values are casted out) during the optimization process is shown in Fig. 3 (a). The number of evolutional cycles M is plotted along the horizontal axis. The minimal value of objective function obtained by the genetic algorithm application is equal to $\Phi = 0.0001275$. This value and correspondent parameters of an individual serve as an original point for the operation of swarm of particles algorithm on the next stage of optimization. The diagram of objective function values at the stage of information interchange between swarms is shown on the Fig. 3 (b).

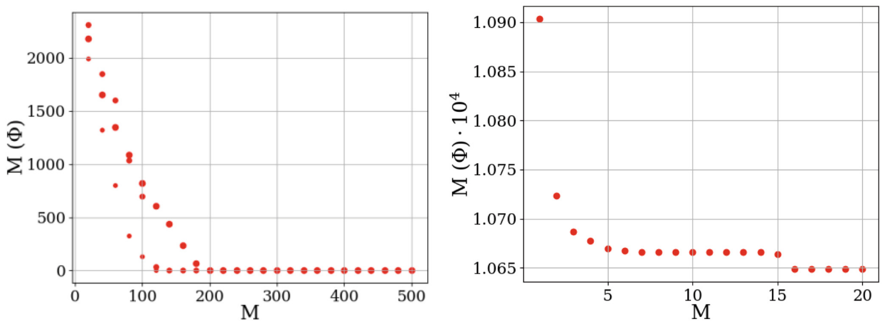

(a) (b)

Fig. 3. Values of objective function at different stages of optimization: (a) – genetic algorithm; (b) – swarm of particles algorithm

Thus, swarm of particles algorithm allows to reduce value of objective function from the $\Phi = 0.0001275$ to $\Phi = 0.0001065$. As we can see, a solution close to the optimal can be found fairly quickly. Increasing the number of iterations of the algorithm up of several thousands does not significantly affect the solution which is found above. However, the application of the particle swarm algorithm to the obtained solutions makes it possible to reduce the value of the objective functions by another 20–25% compared to the results achieved using the genetic algorithm.

6 Conclusions

In order to reduce the computation time, a one-dimensional mathematical model of the stress state of an adhesive joint is used in this paper. To describe the shape of the patch, the expansion of the function in a Fourier series is used. All this together made it possible to create a topological optimization genetic algorithm, which allows us to find a solution to the problem very quickly. The computation time of a Python program is only a few minutes.

Analytical calculations have shown that application of swarm of particles algorithm on the second stage of optimization allows to reduce value of objective functions on 20% approximately comparing with that obtained with the genetic algorithm. It means that suggested approach has advantage comparing with conventional genetic algorithm which was used earlier for the considered problem solution [10, 11].

The results obtained are planned to be developed in several directions, such as structural optimization of composite patches [20]. In addition, it is planned to develop this approach for solving topological optimization problems in a two-dimensional formulation [21, 22], that is a qualitatively more difficult problem. It is also interesting to use more complex optimization algorithms based on the particle swarm algorithm, where it is taken into account not only velocities, but also accelerations of particles [23], and other variants of swarm algorithms as well [24].

References

1. Dveirin, O.Z., Andreev, O.V., Kondrat'ev, A.V., Haidachuk, V.Y.: Stressed state in the vicinity of a hole in mechanical joint of composite parts. Int. Appl. Mechan. **57**(2), 234–247 (2021). https://doi.org/10.1007/s10778-021-01076-4
2. da Silva, L.F.M., das Neves, P.J.C., Adams, R.D., Spelt J.K.: Analytical models of adhesively bonded joints. Part I: Literature survey. Int. J. Adhes. Adhes. **29**(3), 319–330 (2009). https://doi.org/10.1016/j.ijadhadh.2008.0005
3. Amidi, S., Wang, J.: An analytical model for interfacial stresses in double-lap bonded joints. J. Adhes. **95**(11), 1031–1055 (2019). https://doi.org/10.1080/00218464.2018.1464917
4. Ejaz, H., Mubashar, A., Ashcroft, I.A., Uddin, E., Khan, M.: Topology optimisation of adhesive joints using non-parametric methods. Int. J. Adhes. Adhes. **81**, 1 (2018). https://doi.org/10.1016/j.ijadhadh.2017.11.003
5. Arhore, E.G., Yasaee, M., Dayyani, I.: Comparison of GA and topology optimization of adherend for adhesively bonded metal composite joints. Int. J. Solids Struct. **226–227**, 111078 (2021). https://doi.org/10.1016/j.ijsolstr.2021.111078
6. Kaye, R., Heller, M.: Through-thickness shape optimisation of typical double lap-joints including effects of differential thermal contraction during curing. Int. J. Adhes. Adhes. **25**(3), 227–238 (2005). https://doi.org/10.1016/j.ijadhadh.2004.07.006
7. Groth, H.L., Nordlund, P.: Shape optimization of bonded joints. Int. J. Adhes. Adhes. **11**(4), 204–212 (1991). https://doi.org/10.1016/0143-7496(91)90002-y

8. Khadiri, I.E., Zemzami, M., Hmina, N., Lagache, M., Belhouideg, S.: Topology optimization of structures obtained by additive manufacturing: case of 3D beam. In: 2021 7th International Conference on Optimization and Applications (ICOA), 235307775 (2021). https://doi.org/10.1109/icoa51614.2021.9442628
9. Kurennov, S., Barakhov, K., Polyakov, O., Taranenko, I.: Application of genetic algorithm for double-lap adhesive joint design. Archiv. Mech. Eng. **70**(1), 27–42 (2023). https://doi.org/10.24425/ame.2022.144074
10. Kurennov, S., Barakhov, K., Vambol, O.: Topological optimization of a symmetrical adhesive joint. Island model of genetic algorithm. Radioelectron. Comput. Syst. **3**, 67–83 (2022). https://doi.org/10.32620/reks.2022.3.05
11. Kurennov, S., Barakhov, K., Vambol, O.: Topological optimization BI-adhesive double lap adhesive joint. One-dimension model. Int. J. Adhes. Adhes. **126**, 103474 (2023). https://doi.org/10.1016/j.ijadhadh.2023.103474
12. Wei, N., Ye, H., Wang, W., Li, J., Tian, F., Sui, Y.: Topology optimization for hybrid lattice compliant mechanisms with multiple microstructures. Materials **15**(20), 7321 (2022). https://doi.org/10.3390/ma15207321
13. Zhu, B., et al.: Design of compliant mechanisms using continuum topology optimization: a review. Mech. Mach. Theory **143**, 103622 (2020). https://doi.org/10.1016/j.mechmachtheory.2019.103622
14. Robinson, J., Sinton, S., Rahmat-Samii, Y.: Particle swarm, genetic algorithm, and their hybrids: optimization of a profiled corrugated horn antenna. In: IEEE Antennas and Propagation Society International Symposium (IEEE Cat. No.02CH37313), San Antonio, vol. 1, pp. 314–317 (2002). https://doi.org/10.1109/APS.2002.1016311
15. Li, J., Gonsalves, T.: A hybrid approach for metaheuristic algorithms using island model. In: Arai, K. (eds.) Proceedings of the Future Technologies Conference (FTC) 2021, **3**. FTC 2021. LNNS, vol. 360. Springer, Cham (2021). https://doi.org/10.1007/978-3-030-89912-7_24
16. Kurennov, S., Barakhov, K., Taranenko, I., Stepanenko, V.: A genetic algorithm of optimal design of beam at restricted sagging. Radioelectron. Comput. Syst. **1**(101), 83–91 (2022). https://doi.org/10.32620/reks.2022.1.06
17. Zhang, W.-J., Xie, X.-F.: DEPSO: hybrid particle swarm with differential evolution operator. In: Conference Proceedings. 2003 IEEE International Conference on Systems, Man and Cybernetics. Conference Theme – System Security and Assurance (Cat. No. 03CH37483) (SMC 2003), Washington, vol. 4, pp. 3816–3821 (2003). https://doi.org/10.1109/ICSMC.2003.1244483
18. Shami, T.M., El-Saleh, A.A., Alswaitti, M., Al-Tashi, Q., Summakieh, M.A., Mirjalili, S.: Particle swarm optimization: a comprehensive survey. IEEE Access **10**, 10031–10061 (2022). https://doi.org/10.1109/ACCESS.2022.3142859
19. Rana, S., Sarwar, Md., Anwar Shahzad Siddiqui, P.: Particle swarm optimization: an overview, advancements and hybridization. In: Optimization Techniques in Engineering: Advances and Applications, pp. 95–113 (2023). https://doi.org/10.1002/9781119906391.ch6
20. Lee, H., Seon, S., Park, S., Walallawita, R., Lee, K.: Effect of the geometric shapes of repair patches on bonding strength. J. Adhes. **97**(3), 207–224 (2019). https://doi.org/10.1080/00218464.2019.1649660
21. Kupski, J., Teixeira de Freitas, S.: Design of adhesively bonded lap joints with laminated CFRP adherends: review, challenges and new opportunities for aerospace structures. Compos. Struct. **268**, 113923 (2021). https://doi.org/10.1016/j.compstruct.2021.113923
22. Kurennov, S.S., Polyakov, OG., Barakhov, K.P.: Two-dimensional stressed state of an adhesive joint. Nonclassical problem. J. Math. Sci. **254**, 156–163 (2021). https://doi.org/10.1007/s10958-021-05295-5

23. Koshevoy, N., Ilina, I., Tokariev, V., Malkova, A., Muratov, V.: Implementation of the gravity search method for optimization by cost expenses of plans for multifactorial experiments. Radioelectron. Comput. Syst. **1**(105), 23–32 (2023). https://doi.org/10.32620/reks.2023.1.02
24. Bodyanskiy, Y., Shafronenko, A., Pliss, I.: Clusterization of vector and matrix data arrays using the combined evolutionary method of fish schools. Syst. Res. Inf. Technol. **4**, 79–87 (2022). https://doi.org/10.20535/SRIT.2308-8893.2022.4.07

Intelligent Recommendation System for Assessing Hand Hygiene of Healthcare Workers

Valeriia Yevtushenko[1], Maryna Railian[2], and Tetyana Chumachenko[2](✉)

[1] National Aerospace University "Kharkiv Aviation Institute", Kharkiv 61070, Ukraine
[2] Kharkiv National Medical University, Kharkiv 61001, Ukraine
tatalchum@gmail.com

Abstract. Nosocomial infections pose a significant threat to patient safety in healthcare settings globally, with hand hygiene being a crucial preventive measure. This study aims to develop an intelligent recommendation system encapsulated in a mobile application to assess and enhance healthcare workers' hand hygiene practices, thereby reducing nosocomial infections. The system was developed using the MVVM architecture, ensuring a robust, scalable, and maintainable solution. The application was designed in compliance with iOS Human Interface Guidelines to ensure user-friendliness. It includes departmental, workplace, and individual assessment checklists, with a scoring system ranging from 1 to 25 for each item. Technologies such as Firebase for authentication and data storage, Swift Package Manager for dependency management, and various libraries for enhanced functionality were integrated. The application successfully facilitates comprehensive tracking and analysis of hand hygiene practices. The checklist-based approach allows detailed data collection, providing quantifiable insights into compliance levels. Including dark mode and user-friendly interfaces tailored for different user types (new, non-authorized, and authorized users) enhances the user experience. The application's innovative approach combines data analytics with practical utility, making it a valuable tool in nosocomial infection control. The use of modern technologies and adherence to established design principles ensure its relevance and ease of use in healthcare environments. This intelligent recommendation system represents a significant advancement in the application of technology to healthcare challenges, particularly in infection control.

Keywords: hand hygiene · nosocomial infections · recommendation system · Swift · mobile app

1 Introduction

Nosocomial infections, also known as hospital-acquired infections, remain a significant challenge in healthcare settings globally [1]. These infections occur in patients during their stay in hospitals or other healthcare facilities and are not present or incubating at admission [2]. The World Health Organization (WHO) has identified nosocomial

M. Nechyporuk et al. (Eds.): ICTM 2023, LNNS 1008, pp. 290–300, 2024.
https://doi.org/10.1007/978-3-031-61415-6_25

infections as a major issue of public health concern due to their impact on patient morbidity, mortality, and healthcare costs [3]. In Ukraine, as in many parts of the world, the prevalence of nosocomial infections seriously threatens patient safety and healthcare efficiency, highlighting the need for effective control measures [4].

One of the key factors in preventing and controlling nosocomial infections is the hygiene practices of healthcare staff. Hand hygiene, in particular, is the most important measure to prevent the spread of pathogens and reduce infection rates [5]. Despite the simplicity of this preventive measure and the existence of guidelines by health organizations, compliance with hand hygiene practices among healthcare workers still needs to be improved [6]. This gap in practice underlines the need for innovative approaches to promote and monitor adherence to hand hygiene guidelines effectively.

Adopting data-driven methodologies in healthcare represents a paradigm shift, offering a transformative approach to improving patient outcomes and operational efficiency [7]. In recent years, the healthcare industry has witnessed an exponential increase in data generated, ranging from electronic health records to sensor-based monitoring systems [8]. This surge in data availability, coupled with advancements in data analytics, machine learning, and artificial intelligence, has laid the groundwork for the emergence of data-driven medicine [9]. This approach facilitates a more comprehensive understanding of patient care dynamics and allows for optimizing healthcare processes [10].

Within the realm of data-driven healthcare, intelligent recommendation systems have emerged as a pivotal tool [11]. These systems are adept at processing vast and varied datasets, extracting meaningful patterns, and providing bespoke recommendations. In clinical settings, such recommendation systems are increasingly utilized to augment decision-making processes, enhance diagnostic accuracy, and personalize patient care strategies [12]. Their application ranges from predicting patient outcomes and disease progression to optimizing treatment plans and resource allocation.

The potential of these recommendation systems in infection control and prevention is particularly noteworthy. By harnessing the power of data analytics, these systems can identify risk factors for nosocomial infections, monitor compliance with infection control protocols, and suggest targeted interventions [13]. In hand hygiene compliance, an intelligent recommendation system can analyze data from various sources, such as hand hygiene dispensers, surveillance cameras, and staff schedules. By doing so, it can provide real-time feedback to healthcare workers, identify patterns in compliance lapses, and recommend tailored strategies to improve hand hygiene practices.

Integrating such data-driven solutions in healthcare settings holds promise for bridging the gap between hand hygiene guidelines and actual practice among healthcare staff. By providing targeted, evidence-based recommendations, these systems can play a crucial role in enhancing hand hygiene compliance, reducing the incidence of nosocomial infections, and improving overall patient safety [14]. As proposed in this work, the development of an intelligent recommendation system for hand hygiene assessment aligns with the broader goal of leveraging technological innovations to address critical challenges in healthcare.

This work aims to develop an intelligent recommendation system designed explicitly for assessing healthcare staff hand hygiene practices. This system will employ advanced data analytics to evaluate hand hygiene compliance and provide actionable insights to healthcare providers. Furthermore, a mobile application based on this model will be designed to facilitate real-time monitoring and feedback for healthcare staff, thereby enhancing hand hygiene adherence and ultimately contributing to the reduction of nosocomial infections. This paper outlines the proposed system's development process, implementation strategies, and potential impact on healthcare settings in Ukraine and worldwide.

2 Materials and Methods

The following action algorithm was developed to determine the risk of nosocomial infections:

1. The results of the checklist "Availability of antiseptic in mandatory hand hygiene zones" meet the standard (up to 10% non-compliance):
   a. If not, the following actions are recommended – analysis of the discrepancies by the person responsible for infection prevention and control (IPC) in the department, preparation of a memo to the management regarding the purchase of necessary equipment and materials, installation of equipment. A follow-up audit is scheduled for a set term.
   b. If yes, proceed to the next checklist.
2. The results of the checklist "Organization of the hand hygiene system" meet the standard (up to 10% non-compliance):
   a. Depending on the percentage of non-compliance, the following actions are recommended:
      i. 10–30%: Analysis of discrepancies by the department's IPC responsible, developing a plan to address the deficiencies. A follow-up audit is scheduled for a set term.
      ii. 31–60%: Analysis of discrepancies by the IPC responsible, in collaboration with the departmental epidemiologist, development of a plan to address the deficiencies. A follow-up audit is scheduled for a set term.
      iii. Over 60%: An extraordinary meeting of the infection control committee, development of a plan to address deficiencies with designated responsible persons and deadlines. A follow-up audit is scheduled for a set term.
   b. If yes, proceed to the next checklist.
3. The results of the checklist "Equipment of the workplace for hand processing" meet the standard (up to 10% non-compliance):
   a. Depending on the percentage of non-compliance, the following actions are recommended:
      i. 10–30%: Analysis of discrepancies by the department's IPC responsible, preparing a memo to the management regarding the purchase of necessary equipment and materials.
      ii. 31–60%: Analysis of discrepancies by the IPC responsible in collaboration with the departmental epidemiologist, preparation of a memo to the management regarding the purchase of necessary equipment and materials.
      iii. Over 60%: An extraordinary meeting of the infection control committee, developing a plan to address the deficiencies with designated responsible persons and deadlines. A follow-up audit is scheduled for a set term.

   b. If yes, proceed to the next checklist.
4. The results of the checklist "Hand processing technique" meet the standard (up to 10% non-compliance):
   a. Depending on the percentage of non-compliance, the following actions are recommended:
      i. 10–30%: Independent study of regulatory documents regarding hand hygiene rules, followed by a test control of acquired knowledge.
      ii. 31–60%: Study of regulatory documents on hand hygiene rules, practical training in hand processing techniques, followed by a test control of acquired knowledge and evaluation of practical skills by an epidemiologist.
      iii. Over 60%: Referral of the healthcare worker to hand hygiene training with an examination.
   b. If yes, proceed to the next checklist.
5. The results of the checklist "Epidemiological safety during patient care and manipulation (hand processing stage)" meet the standard (up to 10% non-compliance):
   a. Depending on the percentage of non-compliance, the following actions are recommended:
      i. 10–30%: Independent study of regulatory documents regarding hand hygiene rules, followed by a test control of acquired knowledge.
      ii. 31–60%: Study of regulatory documents on hand hygiene rules, practical training in hand processing techniques, followed by a test control of acquired knowledge and evaluation of practical skills by an epidemiologist.
      iii. Over 60%: Referral of the healthcare worker to hand hygiene training with an examination.
   b. If yes, proceed to obtain the overall results.
6. The overall percentage of non-compliance is less than 30%:
   a. If not, the check is successfully passed, and the risk of nosocomial infection is minimal.
   b. If yes, the check is not passed, the following recommendations are obtained:
      i. Conduct a meeting of the Infection Control Committee and develop an Action Plan to improve hand hygiene considering the local context.
      ii. Initiate approval of this Action Plan for improving hand hygiene by the healthcare facility management considering the local context.
      iii. The epidemiologist from the IPC department will coordinate the implementation of the action plan for improving hand hygiene at all stages.
      iv. Training of healthcare facility staff on the basics of patient infectious safety, determination, impact, and prevalence of healthcare-associated infections (HAIs), prevention of HAIs and the role of hand hygiene in it, rules and practices of hand hygiene, patterns of pathogen transmission associated with healthcare provision, with an emphasis on contact (through hands) route of infection.
      v. Preparation of additional educational materials, including data from evaluation reports.
      vi. Preparation of informational materials (stands, posters, leaflets, etc.) on hand hygiene.

vii. Organization of regular meetings to monitor the implementation of measures, discuss the current situation, and adjust the hand hygiene action plan as necessary.

The audit consists of five mandatory checklists: two for the department, one for the workplace, and two for the employee. Each item on the checklist is evaluated on a scale from 1 to 25 points, where one represents a low risk, and 25 indicates an extremely high risk.

A mobile application has been developed based on the proposed action algorithm. The usage scenarios of the developed mobile application anticipate three types of users: "New User", "Non-Authorized User", and "Authorized User", collectively referred to as "User". New and non-authorized users cannot view the app's content; they can authenticate using "Firebase Auth". An authorized user can conduct and view audits and configure data under "Content Management".

Figure 1 presents a class diagram. The "CompletedChecklist" class implements the "DatabaseModel" interface. The "UserChecklist" and "RoomChecklist" classes generalize (inherit from) "CompletedChecklist".

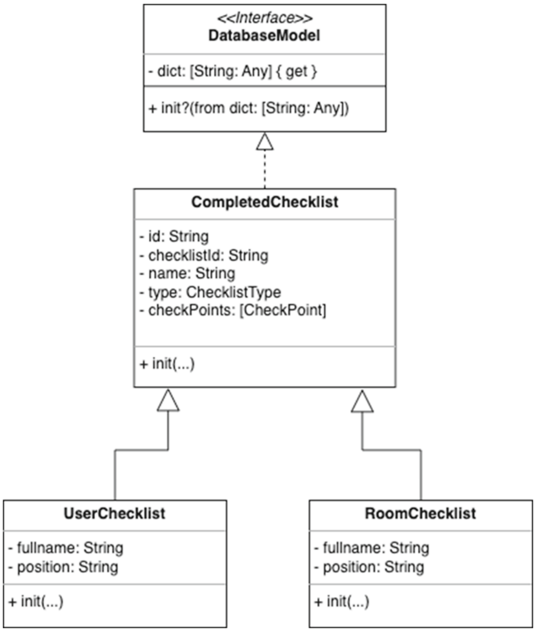

Fig. 1. Class diagram

Figure 2 shows a deployment diagram. The "Mobile Device" is the user's device with an iOS operating environment through which access to the application is obtained. The "Firebase Server" device is an API server (connected to the user's device via the HTTPS protocol). The "Apple Web Service" device is a server from which the application can be downloaded (connected to the user's device via the HTTPS protocol).

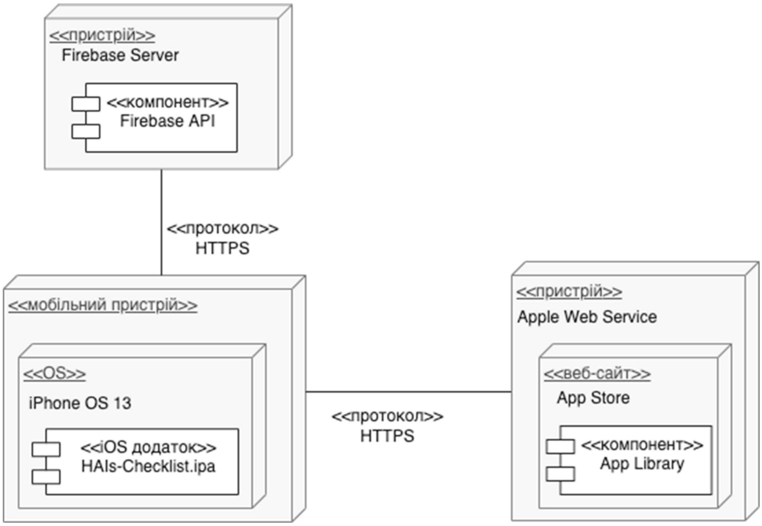

Fig. 2. Deployment diagram

3 Results

The structure of the application classes is built using the principles of the MVVM architecture, so the project's root directory contains three folders named after layers: UI, Services, and Utilities.

The AppDelegate class and the HAIs_ChecklistApp structure are responsible for the overall state of the application, the current scene where the user is located, and the management of these screens. This class is essential to every mobile application written for the iOS operating system.

The Assets directory is created to organize the media resources of the mobile application. It allows storing graphical images and icons with different resolutions for correct display on screens of various sizes and direct use in the project code. It can also house mobile application icons displayed in the iOS system in settings, notifications, and on the screen of installed applications.

The UI directory is created to organize the presentation layer. It is divided into three folders:

- commun, where components reused on different screens are stored. For example, "PasswordSecureField", which is used on the authorization and password update screens;
- auth, where all screens for authorization are located;
- main, where all screens that display and implement the main logic of the application are located.

The Services directory is created to organize the data layer. It is divided into five services:

- DatabaseService – responsible for interaction with Firestore;

- AuthorizationService – responsible for authorization, encapsulates with Firebase auth;
- StorageService – responsible for the secure storage of user data, encapsulates the logic of interaction with KeychainSwift;
- ValidationService – responsible for validating the user's password and email;
- RevisionService – responsible for the current revision, its update, and the result.

Each UI module consists of a view and a viewModel. The view displays UI components and the viewModel for business logic.

During the development process, the dependency manager SPM was used. Swift Package Manager is a tool for managing the distribution of Swift code. It is integrated with the Swift build system to automate the process of downloading, compiling, and linking dependencies. The package manager is included in Swift 3.0 and higher. It helps iOS developers easily add third-party libraries whose code is publicly available.

The libraries used include:

- KeychainSwift is a library that provides a set of helper functions for storing data in Keychain. It was developed to provide a shorter syntax for performing a simple task: reading/writing text values for specified keys;
- Firebase is a platform for developing applications with tools for interacting with Firestore, Cloud storage;
- SwiftLint is a tool for applying Swift style and conventions based on the now-archived GitHub Swift Style Guide. SwiftLint ensures adherence to style guide rules widely accepted by the Swift community.
- SDWebImageSwiftUI is a SwiftUI image-downloading platform based on SDWebImage. It contains all SDWebImage features, such as asynchronous image loading, memory/disk caching, animated image playback, and performance. The framework provides various View structures whose APIs are consistent with SwiftUI instructions.

In the development of the iOS application, it was decided to adhere to the main principles of the Human Interface Guidelines, which include aesthetic integrity, consistency, clear interaction, and user control.

Therefore, standard graphical interface components were used, combined with standard fonts and colors that harmoniously fit into the overall design of the iOS operating system and are used in official Apple applications. It is important to note that the application supports one of the major innovations of iOS 13 – the dark mode theme. This means that the user can switch between light and dark themes, which automatically change the color scheme of the entire operating system interface and all system applications.

Upon launching the application, the user is presented with a loading screen, which remains visible until the application enters the Inactive state.

Once all the main resources required for the application to function have loaded, the user arrives at the "Login" page. If the user has no account, they can navigate to the "Registration" page. The initial interfaces are presented in Fig. 3.

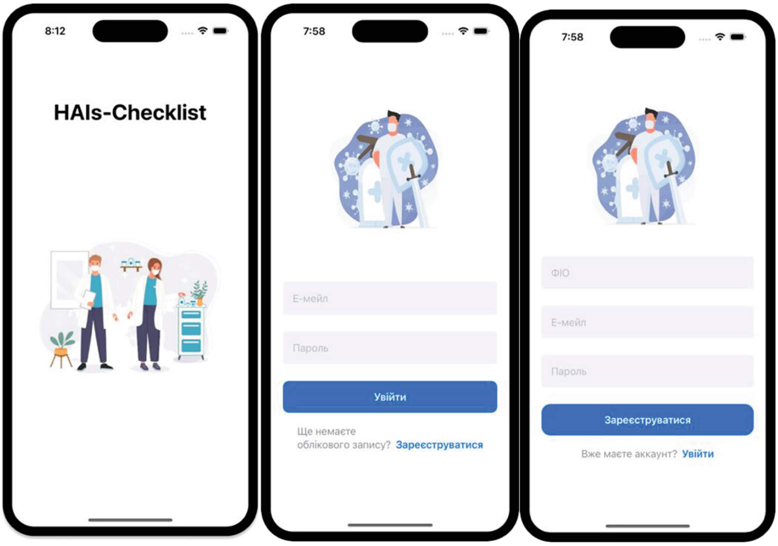

Fig. 3. Initial interfaces.

After successful registration or login, the user lands on a page where they can start the department audit. When the user clicks the "Start Audit" button, a dialog box prompts them to enter the department's name. After specifying the department's name, the user proceeds to a list of checklists. The checklists are divided into three types, the first of which pertains to the entire department. The next type relates to the workplace; the user enters the name of the workplace and responds to the questions. The last type is specific to an individual employee; the user enters the employee's full name and position and then completes the responses to the questions. Each item on the checklist can be rated from 1 to 25. After filling out the five mandatory checklists, a "Finish Audit" button appears. Examples of interfaces with checklists are shown in Fig. 4.

After the user completes the audit, they receive an overall result, which depends on the percentage of successfully passed checks for each item. The user can view detailed information for each checklist by clicking the "Detailed Information" button. Examples of recommendations are presented in Fig. 5.

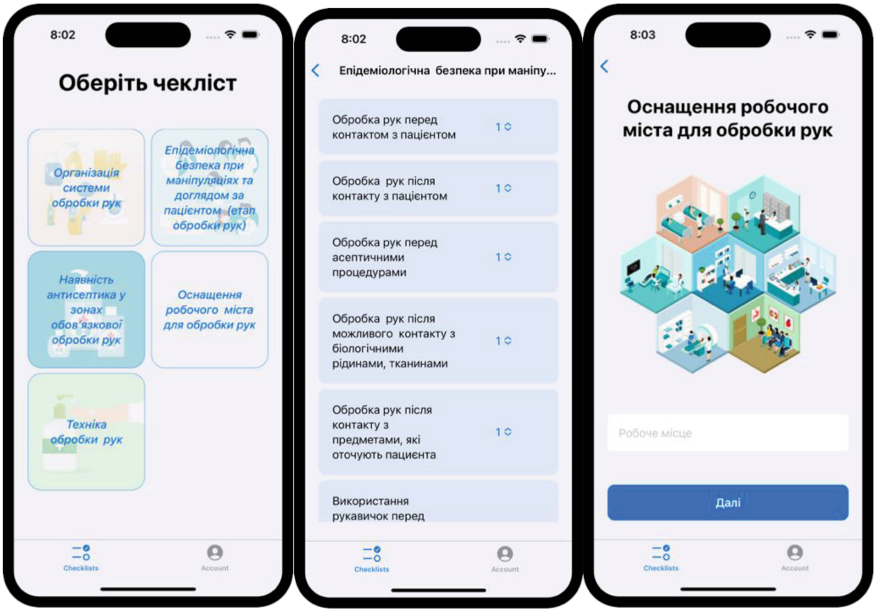

Fig. 4. Checklists interfaces.

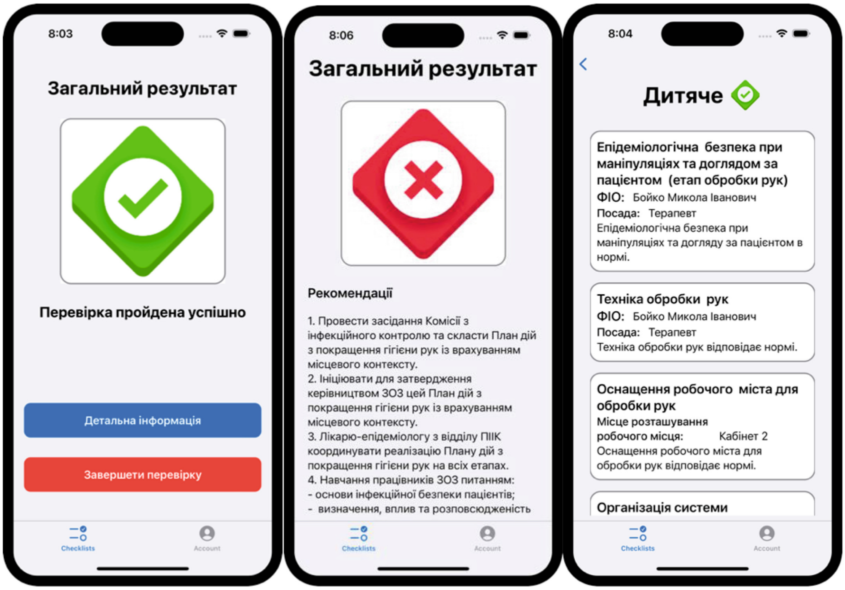

Fig. 5. Recommendations interfaces.

4 Conclusions

This research paper introduces an innovative, intelligent recommendation system for assessing healthcare staff hand hygiene encapsulated in a user-friendly mobile application. The application, rooted in the MVVM architecture, represents both a scientific and practical advancement in healthcare technology. The scientific novelty lies in the application's approach to integrating complex data analytics with a user-centric interface, providing a novel solution to hand hygiene compliance—a critical factor in controlling nosocomial infections.

From a practical standpoint, the system offers a tangible tool for healthcare facilities to enhance their infection control protocols. The checklist-based approach, encompassing departmental, workplace, and individual assessments, comprehensively evaluates hand hygiene practices. This is particularly significant in nosocomial infection control, where precise and actionable data can substantially improve patient safety and overall healthcare quality.

The application's development adheres to iOS Human Interface Guidelines, ensuring a seamless user experience. This adherence, coupled with deploying modern technologies such as Firebase, Swift Package Manager, and various other libraries, underscores the application's practicality and relevance in today's technology landscape.

Future research could focus on expanding the application's capabilities to include predictive analytics, using the accumulated data to forecast potential outbreaks or identify patterns in compliance lapses. Additionally, exploring integration with other healthcare systems, such as EHRs, could provide a more holistic view of the healthcare environment, enhancing the application's effectiveness.

Moreover, the potential for adapting and scaling the system for different healthcare settings and other compliance-based scenarios presents a rich avenue for further exploration. Such adaptations could extend the application's impact beyond hand hygiene, contributing to broader aspects of healthcare management and safety protocols.

This project contributes significantly to improving hand hygiene practices in healthcare settings and sets a new standard for integrating intelligent systems in healthcare. Its success in combining technological innovation with practical application underscores the potential for such systems to impact healthcare outcomes. The project serves as a model for future research and development in the field, offering insights and frameworks that can be adapted and built upon to pursue enhanced patient care and safety.

Acknowledgement. The study was funded by the Ministry of Health of Ukraine in the framework of the research project 0123U100184 on the topic "Analysis of the impact of war and its consequences on the epidemic process of widespread infections on the basis of information technologies".

References

1. Liu, J.-Y., Dickter, J.K.: Nosocomial infections: a history of hospital-acquired infections. Gastrointest. Endosc. Clin. N. Am. **30**, 637–652 (2020). https://doi.org/10.1016/j.giec.2020.06.001

2. Suleyman, G., Alangaden, G.J.: Nosocomial fungal infections. Infect. Dis. Clin. North Am. **35**, 1027–1053 (2021). https://doi.org/10.1016/j.idc.2021.08.002
3. WHO. Global Report on Infection Prevention and Control (2022)
4. Konechnyi, Y., et al.: Epidemiological and microbiological aspects of healthcare-associated infections in Ukraine during the 2009–2019 period. Przeglad Epidemiologiczny **75**, 86–95 (2021). https://doi.org/10.32394/pe.75.09
5. Novák, M., Breznický, J., Kompaníková, J., Malinovská, N., Hudečková, H.: Impact of hand hygiene knowledge on the hand hygiene compliance. Medicinski glasnik: Off. Publ. Med. Assoc. Zenica-Doboj Canton, Bosnia and Herzegovina. **17**, 194–199 (2020). https://doi.org/10.17392/1051-20
6. Akkoc, G., et al.: Reduction of nosocomial infections in the intensive care unit using an electronic hand hygiene compliance monitoring system. J. Infect. Develop. Countr. **15**, 1923–1928 (2021). https://doi.org/10.3855/jidc.14156
7. Mazorchuck, M., Dobriak, V., Chumachenko, D.: Web-application development for tasks of prediction in medical domain. In: 2018 IEEE 13th International Scientific and Technical Conference on Computer Sciences and Information Technologies (CSIT), pp. 5–8 (2018). https://doi.org/10.1109/stc-csit.2018.8526684
8. Johnson, K.B., Stead, W.W.: Making electronic health records both SAFER and SMARTER. JAMA **328**, 523–524 (2022). https://doi.org/10.1001/jama.2022.12243
9. Chumachenko, D.: On intelligent multiagent approach to viral Hepatitis B epidemic processes simulation. In: 2018 IEEE Second International Conference on Data Stream Mining & Processing (DSMP), pp. 415–419 (2018). https://doi.org/10.1109/dsmp.2018.8478602
10. Dotsenko, N., Chumachenko, D., Chumachenko, I.: Modeling of the processes of stakeholder involvement in command management in a multi-project environment. In: 2018 IEEE 13th International Scientific and Technical Conference on Computer Sciences and Information Technologies (CSIT), pp. 29–32 (2018). https://doi.org/10.1109/stc-csit.2018.8526613
11. Brand, S.L., Thompson Coon, J., Fleming, L.E., Carroll, L., Bethel, A., Wyatt, K.: Whole-system approaches to improving the health and wellbeing of healthcare workers: a systematic review. PLoS ONE **12**, e0188418 (2017). https://doi.org/10.1371/journal.pone.0188418
12. Chumachenko, D., Dobriak, V., Mazorchuk, M., Meniailov, I., Bazilevych, K.: On agent-based approach to influenza and acute respiratory virus infection simulation. In: 2018 14th International Conference on Advanced Trends in Radioelecrtronics, Telecommunications and Computer Engineering (TCSET), pp. 192–195 (2018). https://doi.org/10.1109/tcset.2018.8336184
13. Amoon, M., Altameem, T., Hashem, M.: Consistent healthcare safety recommendation system for preventing contagious disease infections in human crowds. Sensors **23**, 9394 (2023). https://doi.org/10.3390/s23239394
14. Wang, C., et al.: A system for computational assessment of hand hygiene techniques. J. Med. Syst. **46**, 36 (2022). https://doi.org/10.1007/s10916-022-01817-z

Information Technology in the Creation of Rocket Space Systems

Preliminary Design Approach for Lattice Composite Keel Beam

Fedir Gagauz(✉) and Serhii Kryvenda

National Aerospace University "Kharkiv Aviation Institute", 17 Chkalova Street, Kharkiv 61070, Ukraine
f.gagauz@khai.edu

Abstract. Application of optimal reinforcement concepts like lattice or wafer and reducing of most cost and time-consuming assembly operations based on integration of attachment fittings into composite structures provide strong opportunities for weight reduction and manufacturing costs of airframe structures. Within this work, the breakthrough manufacturing-oriented solution based on the combination of high-performance lattice design and high-productive automated process is presented. A method for the preliminary design of a composite keel beam is described to determine structural parameters of two families of ribs that meet strength and stability constraints. Finally, a case study on the design of lattice composite keel beam was formulated and solved to demonstrate the capabilities of the proposed design concept and method.

Keywords: Keel Beam · Lattice Structure · Composites · Filament Winding

1 Introduction

The lower central fuselage section of advanced aircrafts generally contains large cut-outs for the main landing gear wheels. To keep the longitudinal structural continuity of the fuselage and to provide necessary bending stiffness of the fuselage under vertical bending loads the keel beam is installed along whole length of lower cut-out.

Keel beam of the fuselage generally is represented by a thin-walled box structure reinforced by stringers and transversal webs, which is connected to the forward and aft pressure bulkheads and often with the center wing box. According to its structural function within airframe the main load case for keel beam design is axial compression that for short- and mid-range passenger aircrafts can reach values of several hundred tones.

Traditional approach for keel beam box manufacturing implies an assembly of 4 panels, stringers and transversal webs into a thin-walled structure using bolted and riveted joints. The main disadvantage of such time-consuming method is expensiveness mostly due to high assembly cost in overall manufacturing price. Though redesign of keel beam with application of composites allows to reduce the weight but does not solve the problem of economic efficiency.

M. Nechyporuk et al. (Eds.): ICTM 2023, LNNS 1008, pp. 303–313, 2024.
https://doi.org/10.1007/978-3-031-61415-6_26

In this paper the novel design approach for composite keel beam is proposed which consists in combination of high-performance lattice-type structure and high-productive winding process to create manufacturing-oriented lattice keel beam with integrated metal fittings that allows to reduce both the weight and manufacturing time as well as costs.

2 Design Approach and Methodology

2.1 Design Concept

Generally, lattice structures represent isogrid- or anisogrid-stiffened cylindrical or conical shells consisting of a system of longitudinal, helical and circumferential ribs (see Fig. 1).

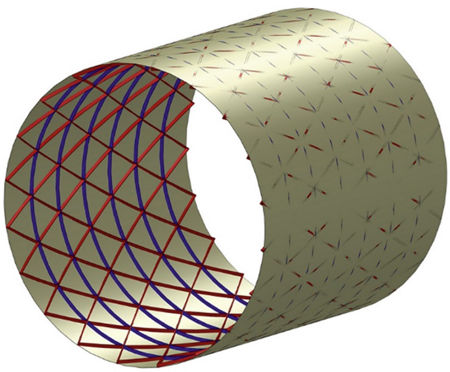

Fig. 1. Typical isogrid structure with circumferential and helical ribs.

Lattice structures can be made either in the form of grid-stiffened frame only (without skin) or can have outside or two-side composite skin. In most cases, lattice structures are produced by filament winding of unidirectional tows or fibers with subsequent autoclave curing.

Since 1980th anisogrid lattice structures are successfully used in space programmes in the form of launchers' sections, interstages, adaptors, etc. [1–4]. In this field, cylindrical and conical lattice structures demonstrate high weight efficiency, technological reliability and low manufacturing costs.

However, efficiency of lattice rocket structures is grounded on their regular cylindrical or conic shape, uniform loading at longwise and roundwise directions by axial forces, and absence of large cutouts. As regards aircraft structures, there were some attempts of geodesic structural scheme implementation in fuselage [5–7].

With account for keel beam loading by axial compressive load, authors believe that lattice design (see Fig. 2) is a strong alternative to reference 4-panels assembly and guarantees high stiffness-to-weight ratio due to 100% use of unidirectional composites stiffness and strength performances along fibers. It should be noted that proposed concept of lattice keel beam allows to explicitly divide it into different regions to define optimal lattice pattern for each region separately, considering inherent loading and respecting condition of ribs continuity. For example, for outer regions (connected to front/aft pressure bulkheads) angle of spiral ribs (relative to longitudinal axis of keel beam) can be selected as small as possible to provide best strength and stiffness to weight ratio while for medium region (for example under center wing box) spiral ribs should be oriented with considering of transverse loads action. Such approach will help to respect both global and local loads and optimize lattice pattern, thus minimize keel beam weight.

2.2 Design Approach

Proposed geometry of lattice keel beam (see Fig. 2) is characterized with three global parameters that define overall keel beam geometry (height H, width B and length of keel beam L) and six local structural parameters:

- cross-sectional sizes, i.e. heights h of helical and circumferential ribs which are generally accepted identical and widths of ribs δ_h, δ_c;
- number of helical and circumferential ribs which correspond to their spacings a_h, a_c;
- the angle of helical ribs φ with respect to the longitudinal axis of keel beam which depends on number of helical (spiral) and circumferential (hoop) ribs.

The fillet radius r along the lateral edges of prismatic shaped keel beam can be set according to technological requirements and determined taking into account minimal possible value for proper laying of composite tape or roving on the tool.

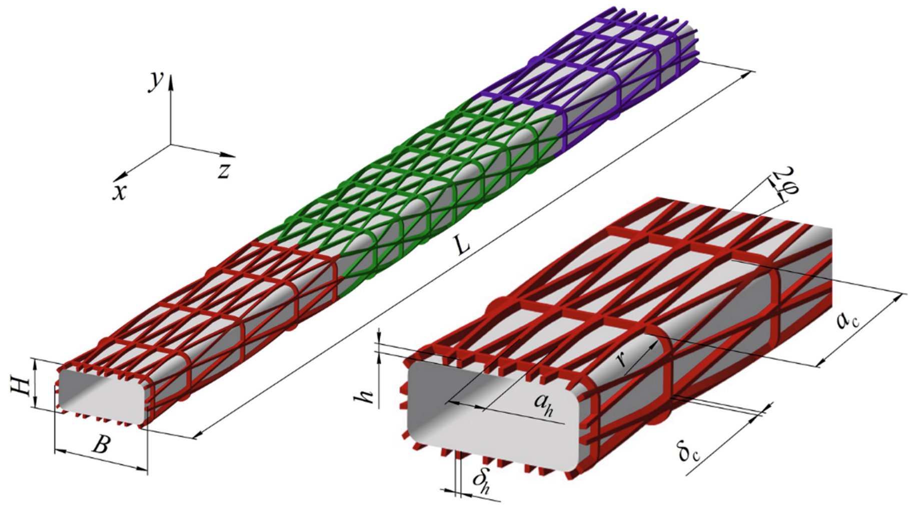

Fig. 2. Lattice conceptual design of keel beam.

Determination of structural parameters for lattice structures was generally based on analytical method [2]. According to design approach described in [8, 9] cylindrical lattice structure is designed for minimum mass considering three design constraints which characterized strength of helical ribs, global stability of the structure and local stability of helical ribs under compressive loading by equivalent force which evaluates with regard to possible bending of lattice structure.

Considering the prismatic overall shape of lattice keel beam and high elongation ratio of structure, the mathematical expressions for optimal design variables presented in [8, 9] for cylindrical lattice structure must be reformulated for use in the preliminary design of lattice keel beam.

Using the common "continuous" approach, the lattice keel beam (discrete system of ribs) can be represented as a smooth prismatic shell or rectangular tube with parameters that keep equivalent axial and bending stiffnesses. In this case two-layered composite shell will consist of one artificial layer obtained by "smearing" of helical ribs and the other layer – by "smearing" of circumferential ribs over the whole surface (Fig. 3).

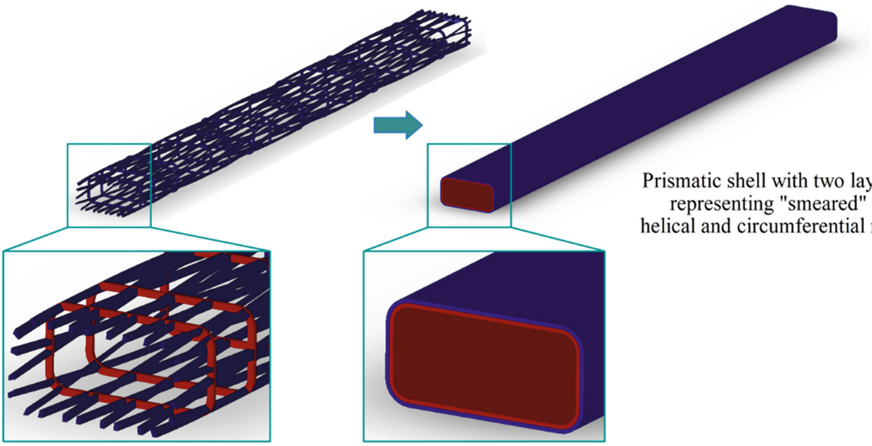

Fig. 3. Simplifying of discrete lattice structure by continuum prismatic shell.

The list of parameters to be optimized for such continuous shell includes dimensionless equivalent widths (thicknesses) of helical and circumferential ribs:

$$\bar{\delta}_h = \frac{\delta_h}{a_h}; \quad \bar{\delta}_c = \frac{\delta_c}{a_c}. \tag{1}$$

Effective membrane stiffnesses of equivalent smooth two-layered composite shell are evaluated according to elasticity modulus of "smeared" ribs:

$$\begin{gathered} A_{11} = E_h h \bar{\delta}_h \cos^4 \varphi; \\ A_{22} = E_h h \bar{\delta}_h \sin^4 \varphi + E_c h \bar{\delta}_c; \\ A_{12} = A_{21} = A_{33} = E_h h \bar{\delta}_h \sin^2 \varphi \cos^2 \varphi, \end{gathered} \tag{2}$$

where E_h, E_c are modulus of elasticity of helical and circumferential ribs respectively.

Four design constraints must be considered and used for minimum mass design of lattice keel beam.

1. Global buckling constraint which can be written using Euler's formula for tube with hollow rectangular cross section:

$$P \le P_{gs} = k_{gs}\frac{\pi^2 A_{11}}{L^2}\left[\frac{H^2}{6}(H + 3B)\right], \tag{3}$$

where H, B, L overall dimensions of lattice keel beam, i.e. height, width and length (see Fig. 2); k_{gs} – coefficient, which depends on the boundary conditions at the ends of keel beam (for conservative design $k_{gs} = 1$).

2. Local buckling constraint in the form of critical distributed forces for rectangular plates [10] which represent the top (bottom) wall of lattice keel beam with "smeared" ribs:

$$P \le P_{lp} = 2(H + B)\frac{\pi^2\sqrt{D_{11}D_{22}}}{B^2}k_{lp}, \tag{4}$$

where k_{lp} – local buckling coefficient depending on the boundary conditions at the edges of plate [10], for conservative design simply supported edges should be accepted:

$$k_{lp} = 2\left(1 + \frac{D_{12} + 2D_{33}}{\sqrt{D_{11}D_{22}}}\right) \tag{5}$$

where bending stiffnesses of plate D_{mn} are defined according to following formula:

$$D_{mn} = A_{mn}\frac{h^2}{12}. \tag{6}$$

3. Local buckling constraint for helical ribs within segment between two circumferential ribs which can be derived from Euler's formula (Fig. 4):

$$P \le P_{lr} = k_{lr}\frac{\pi^2 E_h I_{\min}}{l_h^2}\cdot\frac{4(B + H)}{h}\cos^2\varphi, \tag{7}$$

where l_h – length of helical rib segment, which finally depends on the number of circumferential ribs; I_{min} – moment of inertia in helical rib cross-section; k_{lr} – coefficient of local buckling for helical ribs which depends on the boundary conditions at the ends (for conservative design $k_{lr} = 1$):

$$l_h = \frac{a_h}{2\sin 2\varphi}; \tag{8}$$

$$I_{\min} = \begin{cases} \dfrac{ha_h^3}{12}\bar{\delta}_h^3 & if \quad \dfrac{h}{a_h} > \bar{\delta}_h; \\ \dfrac{h^3 a_h}{12}\bar{\delta}_h & if \quad \dfrac{h}{a_h} < \bar{\delta}_h. \end{cases} \tag{9}$$

4. Strength constraint for helical ribs under compressive loading:

$$P \leq P_{sr} = 4\sigma_h a_h h \overline{\delta}_h (B + H) \cos^2 \varphi, \tag{10}$$

where σ_h – compressive strength of composite material used for helical rib manufacturing.

Design constraints (3), (4), (7) and (10) can be written in terms of safety factors, that allows to transform these conditions in the form of inequalities into equations and found expressions for optimal parameters h, $\overline{\delta}_h$, $\overline{\delta}_c$ and φ with regard to minimum mass. Using of safety factors provides also the possibility to ensure the necessary axial stiffness of lattice keel beam equivalent to the value of total stiffness of stringers and skin removed from fuselage in the zone of cut-out.

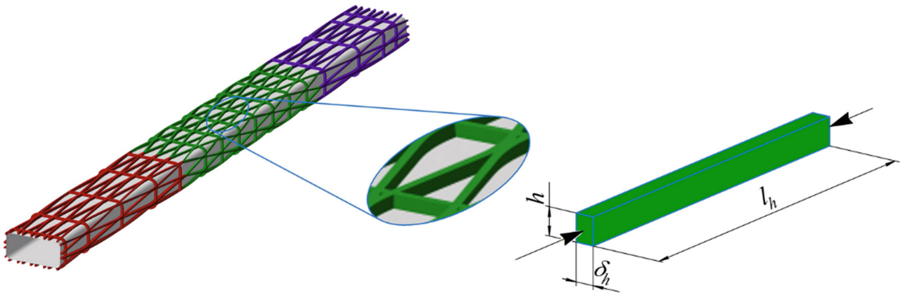

Fig. 4. Representative scheme for formulating the local buckling constraint of helical ribs.

2.3 Conceptual Design of Manufacturing Process

In addition to constraints on design variables which characterize mechanical performance of lattice keel beam, there are also technological requirements depends on specifics of filament winding process or automated tape laying. For example, the lattice pattern is usually selected to ensure continuous winding (or tape laying) process without interruption or moving of the head in the required position. On the other hand, configuration of ribs should allow extracting of whole structure from mandrel.

To maintain the ability to use filament winding of automated tape laying for the manufacture of composite lattice structure, it is necessary to ensure that the fiber placement head returns to the starting point of winding. To solve this kinematic problem, a system of two parallel base planes is considered. The movement of the fiber placement head along the imaginary flat pattern of keel-beam surface obeys the law of reflection. One cycle of head movement should include its double movement – to the opposite section and back.

In order to allow the return of the fiber placement head to the initial point, the surface sweep along the deployment line should be divided into equal steps. If the number of steps n_s is integer, then its length t calculates as

$$t = \frac{S}{n_s}, \tag{11}$$

where S is a perimeter of keel beam cross-section.

During winding the head is moving on i steps and the angle of winding, i.e. the angle of helical ribs

$$\varphi = arctg\frac{i \cdot t}{L}. \tag{12}$$

As was mentioned above, the cycle of fiber placement head ends with its return to the initial base plane. In this case, the head passes the distance equal to $2i$. It should be noted that the number of nodal points on the base plane between the starting and finishing position of head in the amount of ($2i$-1) means the maximum number of additional initial stages, taking into account the number of revolutions of the equipment which is necessary to complete the winding or placement of fiber tow (return of the head to the starting point)

$$\psi \cdot 2i = m \cdot n_s, \tag{13}$$

where ψ is the number of cycles before completing the winding of one tow in helical rib; m – the minimum number of revolutions of mandrel, until completion of the winding of one fiber tow in helical rib.

Thus, kinematic parameters of helical ribs winding (or automated laying of yarn tow on revolved mandrel) are selected according to Eq. (13) to guarantee the end of cycle by returning of the head to the starting point, and this fact will directly determine the angle of helical ribs φ.

With the focus on minimization of assembly operations, proposed lattice design solution makes one more step towards both manufacturing costs and time reduction thanks to metal fittings integration into composite structure (see Fig. 5).

One of the main technological challenges associated with the use of composite lattice structures in aerospace applications is connecting the ends of composite ribs to metal fittings. Using a conventional mechanical joining process usually results in cutting of fibers and originating of stress concentrators. In case of unidirectional composite structure (like ribs in lattice structure) such fiber cuts and stresses concentrators are crucial for structure integrity and safety.

In this case the metal-composite hybrid design solutions [11] can be implemented to ensure technical feasibility of lattice structure by filament winding or automated tape

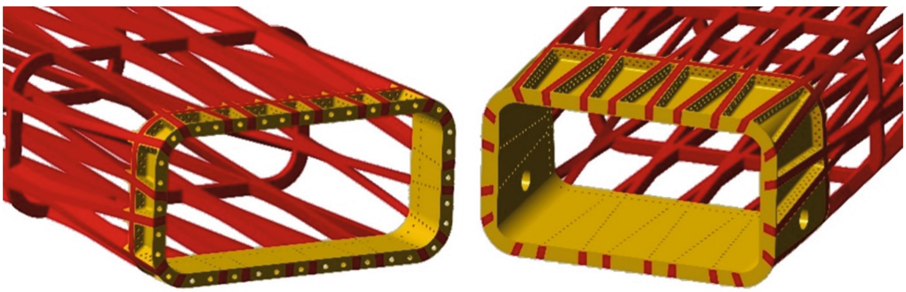

Fig. 5. Conceptual design of the embedded metal fittings for the front and aft pressure bulkheads interfaces.

laying. Joining of composite ribs with metal attachment frame can be realized based on integrated semi-loop joint elements [7] or metal fittings with transversal micropins [11], depending on the selected type of manufacturing method.

Proposed design of lattice keel beam consists in joining of composites with metals, that is based on combination of (i) mechanical gripping or clamping of ribs in slots of metal fittings and (ii) bonding of ribs to the metal fittings during winding. The length of the slots is determined taking into account the strength of the rib-fitting interface using standard methods for designing adhesive joints [12].

Realization of these joints between composite lattice structure and metal fittings preliminary produced and installed at the mandrel does not require any additional assembly operations, thus keel beam with integrated metal fittings can be produced in the frame of one-shot fully-automated process.

3 Case Study

For validation of proposed design concept, the lattice composite keel beam of passenger aircraft was designed. The overall keel beam geometry was described through the length equal to 6 m, width and height of keel beam were set to 500 mm and 305 mm respectively. These parameters approximately correspond to keel beam of A320 aircraft family. Value of axial compressive load on keel beam was accepted equal to 2000 kN. Mechanical properties of unidirectional composite material (carbon fiber reinforced plastic) which is selected for this case study are listed in Table 1.

Table 1. Mechanical properties of unidirectional carbon fiber reinforced plastic.

Parameter	Value
Modulus of elasticity along fiber direction, GPa	147
Compressive strength along fiber direction, MPa	1725

Results of keel beam design with optimal parameters of lattice structure which correspond to minimum mass and satisfy design constraints (3), (4), (7), (10) and (13) are listed in Table 2. Optimization of the rib parameters was carried out within the framework of the general approach to optimizing the mass of structural composite elements [13]. The general view of designed lattice keel beam and dismountable mandrel for manufacturing by winding process are represented in Fig. 6 and Fig. 7.

Table 2. Results of lattice keel beam design.

Parameter	Value
Number of helical ribs with angles $+\varphi$ and $-\varphi$	16
Angle of helical ribs, degrees	12.8

(*continued*)

Table 2. (*continued*)

Parameter	Value
Area of ribs cross-section, mm^2	141.9
Height of ribs, mm	11.9
Length of helical rib segment, mm	409.6
Critical compressive load of one helical rib, kN	60.8
Actual compressive load of helical rib, kN	128.2
Weight of composite ribs, kg	26.7

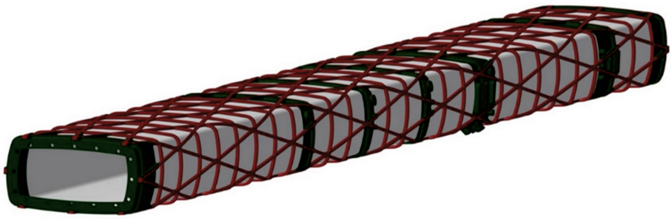

Fig. 6. Composite lattice keel beam with integrated metal fittings.

4 Conclusions

Design concept of composite lattice keel beam with integrated metal fittings was developed. Methodology for preliminary analytical design of composite lattice prismatic structures was presented. The procedure allows to define the configuration of the lattice keel beam under axial compressive load to satisfy strength and stiffness requirements. Technical feasibility and efficiency of presented approach are demonstrated based on numerical case study performed for a specific keel beam with predefined parameters. Manufacturing process was conceptually developed and dismountable tool with preinstalled attachment fittings was designed.

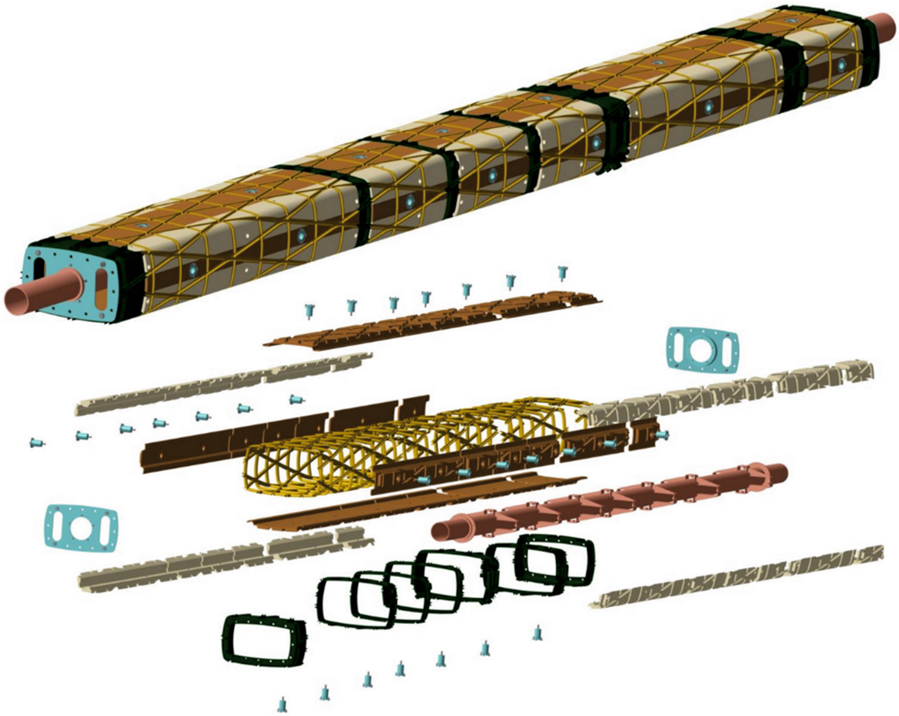

Fig. 7. General view of dismountable mandrel for manufacturing of lattice structure by filament winding process.

References

1. Vasiliev, V.V., Barynin, V.A., Razin, A.F.: Anisogrid composite lattice structures – development and aerospace applications. Compos. Struct. **94**, 1117–1127 (2012)
2. Vasiliev, V.V., Barynin, V.A., Razin, A.F.: Anisogrid lattice structures – survey of development and application. Compos. Struct. **54**, 361–370 (2001)
3. Aoki, T., Yokozeki, T., Terashima, K., Kamita, T.: Mechanical behavior of composite lattice cylinders. In: 55th AIAA/ASME/ASCE/AHS/ASC Structures, Structural Dynamics, and Materials Conference. National Harbor, Maryland (2014)
4. Terashima, K., Kamita, T., Aoki, T., Yokozeki, T., Kimura, G., Uzawa, T.: Experimental study of buckling properties of composite lattice structures for launcher. In: Proceedings of 16th European Conference on Composite Materials (ECCM16), Seville (2014)
5. Murray, I.: Bouncing-Bomb Man: The Science of Sir Barnes Wallis, 1st edn. J.H. Haynes & Co Ltd., Yeovil, Somerset (2009)
6. Liu, D., Lohse-Busch, H., Toropov, V., Hühne, C., Armani, U.: Detailed design of a lattice composite fuselage structure by a mixed optimization method. Eng. Optim. **48**(10), 1707–1720 (2015)
7. Gagauz, F., Kryvenda, S., Shevtsova, M., Smovziuk, L., Taranenko, I.: Manufacturing and testing of composite wafer components with dualpurpose integrated semi-loop joints. In: Proceedings of 16th European Conference on Composite Materials (ECCM16), Seville (2014)

8. Vasiliev, V.V., Razin, A.F.: Anisogrid composite lattice structures for spacecraft and aircraft applications. Compos. Struct. **76**, 182–189 (2006)
9. Totaro, G., Gürdal, Z.: Optimal design of composite lattice shell structures for aerospace applications. Aerosp. Sci. Technol. **13**(4–5), 157–164 (2009)
10. Lekhnitskii, S.G.: Anisotropic Plates. Translation from Russian, 2nd edn. Gordon & Breach, New York (1968)
11. Karpov, Y.S.: Jointing of high-loaded composite structural components. Part 1. Design and engineering solutions and performance assessment. Strength Mater. **38**(3), 234–240 (2006)
12. Kurennov, S.S., Polyakov, O.G., Barakhov, K.P.: Two-dimensional stressed state of an adhesive joint. Nonclassical problem. J. Math. Sci. **254**, 156–163 (2021)
13. Kondratiev, A.V., Kovalenko, V.O.: Optimization of design parameters of the main composite fairing of the launch vehicle under simultaneous force and thermal loading. Space Sci. Technol. **254**(119), 3–21 (2019)

Check for updates

Energy Characteristics of Solar Arrays of the University Microsatellite for Remote Sensing of the Earth

Andrii Pohudin(✉), Sergii Gubin, Yurii Shepetov, Larysa Babakova, and Oleksii Dzvonyskyi

National Aerospace University "Kharkiv Aviation Institute", 17 Chkalova Street, Kharkiv 61070, Ukraine
andrey.pohudin@gmail.com

Abstract. The article evaluates the illumination and temperature of sol-nex batteries of youth microsatellite of remote sensing of the Earth in the radio band. The assessment was carried out using a mathematical model adapted for the design of university spacecraft, describing the orbital parameters of the satellite in the sun vector. The model is implemented in the MathCAD application and tested on known parameters of operating micro-spacecraft. With the help of the model, numerical experiments were conducted to determine the dynamics of the illumination and temperature of the solar panels of the planned university microsatellite with geometric forms CubeSat 3U and orientation to the Earth with the largest axis of inertia.

Keywords: microsatellite · remote sensing · orbit · solar battery · light · temperature · mathematical model

1 Introduction

University microsatellites are one of the most rapidly developing areas of modern experimental space science. It is concentrated in aerospace universities, and the approach to their design is distinctive. They consist in the availability of undergraduate and graduate students to the project with limitations in the development apparatus. This is primarily the possibility of simple and reliable mastery of mathematical and physical modeling of satellite subsystems and development of full-scale aggregates with unclear target task. The design of such devices is based on the CubeSat specification.

The development of CubeSat for ground remote sensing with a passive radio meter requires the use of dimensions of at least 3U. In this size it is rational to organize both the location in the nadir and the adjustment of passive locators on the background radiation with simultaneous imagery in the visible range (Fig. 1). In this arrangement, it is possible to operate the angle polo relative to the velocity vector by means of a reaction wheel (RW). However, the construction of the grid is challenging, as undetectable solar panels are considered in the early stages of development and the energy supply schedule is very

M. Nechyporuk et al. (Eds.): ICTM 2023, LNNS 1008, pp. 314–326, 2024.
https://doi.org/10.1007/978-3-031-61415-6_27

tentative. Moreover, during the development of the microcosm unit power plant it is necessary to repeatedly return to the initial design conditions. Such an approach involves the use of mathematical support to perform operational calculations of the operating modes of small spacecraft power equipment in a limited time. The mathematical support implemented earlier within the student collective allows making necessary calculations [1] with certain adaptation.

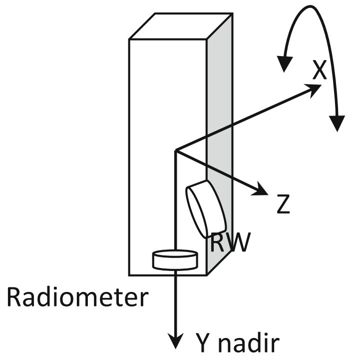

Fig. 1. Arrangement of the ERS microsatellite

Adaptation of the complex of specialized mathematical support for the design of the power system of the university microsatellite is an urgent task in the field of microsatellite engineering. The most important in this complex is the determination of the energy input to the solar batteries of the spacecraft, which determines both the thermal modes of the generator and energy armament.

The presented model implements design calculations of parameters of the solar battery with the possibility of changing the layout.

2 Problem Setting. Orbital Parameters

The input to the solar battery of the spacecraft is direct and reflected solar radiation. Its influence determines energy efficiency and thermal modes. The degree of influence is characterized by the orbital parameters, the type of arrangement of the spacecraft by the placement of solar panels.

It is usually difficult to obtain solutions for a particular mission from an accessible mathematical apparatus developed in leading aerospace universities to determine the level and direction of solar radiation. Since the implementation of the decision is complicated by the lack of accurate initial data on the launch date and planned orbital parameters depending on the launch type. Therefore, the goal is to get a solution for the most generalized task of youth microsatellites and to realize it for a specific application.

Earth remote sensing (ERS) satellites are characterized by Sun-Synchronous Orbit (SAT). Such orbits are implemented in the largest amount of Space-X Falcon-9 missiles, where cluster launch services are provided. A feature of the SSO is that the local travel time of the satellite over the same parts of the Earth's surface is constant. In this case, the angle of illumination of the Earth surface along the satellite track will be the same on all passes. Such orbits are performed with reverse motion and polar inclination i > 900. The angular velocity of the precession of this orbit is roughly equal to the ecliptic velocity of the Sun.

The height of the sun-synchronous orbit must correspond to the orbital period being multiplied by the solar day. For elliptic orbits, it is necessary to form a large semi-axis from the condition of a whole number of turns, as follows [2]:

$$a = \left[\left(\frac{86400}{2\pi N}\right)^2 \cdot \mu\right]^{\frac{1}{3}} \tag{1}$$

where N is the total number of revolutions around the Earth performed by the satellite per day; μ - gravitational parameter of the drawing center (for the Earth = 3,986)10^5 km^3/s^2).

The most applicable orbits are 16, 15 and 14 orbits with altitudes of 300, 600, 900 km. The higher SSOs are less interesting as the increase in altitude decreases the quality of the sounding, the inclination of the orbit increases, and the polar regions leave the coverage area.

Using the properties of the ellipse known from analytical geometry, other orbital parameters are found.

The inclination of the orbit providing the precession of the node line at 360° per year, to compensate for the rotation of the Earth around the Sun, is from the conditions of the accepted apse line [3]:

$$i = \arccos \frac{a^2(1 - e^2)^2(T_c\omega_e - 2\pi)}{3C_{20}\pi R_e^2 N}, \tag{2}$$

where $\omega_e = 0.72921\ 10^{-4}\ s^{-1}$ is the angular speed of rotation of the Earth relative to the stars; $C_{20} = -1098.08 \times 10^{-6}$ is a dimensionless decomposition constant of the Earth's gravitational potential by spherical harmonics of the Legendre polynomial; $R_e = 6378.17$ km - equatorial radius of the Earth; N - the number of turns made PPE per day/

The dependence of the longitude of the ascending node on the number of days per year and the local time of the satellite's ascending orbit is as follows:

$$\Omega = \mathrm{arctg}(\mathrm{tg}\theta \cos\varepsilon) - (12 - t_{an})\pi \big/ 12 \tag{3}$$

where θ - the longitude of the Sun on the ecliptic; ε - inclination of the ecliptic plane to the equator plane ($\varepsilon = 23\ 27'$); t_{an} - is the local travel time of the ascending node of the orbit, expressed in hours.

Based on this expression, you can find the initial longitude of the ascending node at satellite launch.

Due to the inclination of the orbit, the local travel time of the satellite to the ascending node will differ from the local travel time of the necessary point of the Earth's surface:

$$t_{an} = t_l + \frac{\alpha \cdot \sin(i - 90)}{15} \tag{4}$$

Where t_l is the local time of the satellite passing the necessary point of the Earth's surface, expressed in hours; α- the breadth of the necessary point of the Earth's surface, expressed in terms of degrees.

If the point is in the northern hemisphere, it is positive, if in the southern - negative.

As for the coordinate of the point on the equator, over which the satellite should go on the turn on which it passes over the necessary point of the Earth's surface, here, in addition to the inclination of the orbit, it is necessary to consider also the rotation of the Earth:

$$\gamma = \beta + \frac{\alpha}{360} \cdot t_B \cdot \omega_e + \alpha \cdot \sin(i - 90) \tag{5}$$

where β - is the longitude of the required point of the Earth's surface, expressed in degrees; t_B – satellite's orbital period.

3 Problem Solving

The lengths of the shadow are energetically defining. By setting the orbital parameters in the setting of the problem, it is necessary to find a change in the luminosity of the BF panels on the characteristic turns, defined by the minimum value of the average illumination of the panel per t_B (so-called energy-determining turns) or coils with a maximum length of the shadow section. As a rule, the appearance of these turns depends on the angular position of the Sun relative to the orbit plane [3]. In order to find the energy-determining turns, it is necessary to construct a diagram of the evolution of the shadow duration during the year of the orbital flight.

In space energy, the cylindrical model of the Earth's shadow is most commonly used to calculate the orbital luminosity of PPE. It interprets the shadow of the Earth as a cylinder of infinite length opposite to the Sun. The base radius of the cylinder is equal to the average radius of the Earth, its axis is combined with the line Earth - Sun. This model is valid under certain assumptions that are justified in this application: the Earth's sphericity, the parallelism of the sun's rays, the absence of shadows and twilight at the shadow's edge, The earth and the orbital plane of the PPE during the orbital period.

The length of the shadow can be found from the following ratio [4]:

$$\begin{aligned} t_T = \sqrt{a^3/\mu}[(E_{en} - E_{ex}) \\ -e(\sin E_{en} - \sin E_{ex}), \end{aligned} \tag{6}$$

where E_{en} and E_{ex} are eccentric anomalies corresponding to the satellite entering and leaving the shadow.

The eccentric anomalies can be expressed and calculated by knowing the true anomalies of the satellite's entrance and exit from the shadow, from the following expression [4]:

$$\mathrm{tg}\frac{E}{2} = \sqrt{\frac{1-e}{1+e}}\mathrm{tg}\frac{\vartheta}{2} \tag{7}$$

The true anomalies of PPE t at the points of intersection of the orbit with the cylindrical shadow surface, i.e. at the points of entry and exit from the Earth's shadow, are accurate to units of degrees from the following expression [5]:

$$\vartheta_T = 2\text{arctg}\left(\frac{A \pm \sqrt{A^2 + B^2 - Q^2}}{B - Q}\right), \tag{8}$$

where

$$\begin{aligned} A = {} & (\sin\theta \cdot \sin\varepsilon \cdot \sin i - \cos i \cdot \cos\theta \cdot \sin\Omega \\ & + \cos i \cdot \sin\theta \cdot \cos\varepsilon \cdot \cos\Omega) \cos\omega \\ & - \sin\omega(\sin\theta \cdot \cos\varepsilon \cdot \sin\Omega + \cos\theta \cdot \cos\Omega), \end{aligned} \tag{9}$$

$$\begin{aligned} B = {} & (\sin\theta \cdot \sin\varepsilon \cdot \sin i - \cos i \cdot \cos\theta \cdot \sin\Omega \\ & + \cos i \cdot \sin\theta \cdot \cos\varepsilon \cdot \cos\Omega)\sin\omega \\ & + \cos\omega(\sin\theta \cdot \cos\varepsilon \cdot \sin\Omega + \cos\theta \cdot \cos\Omega), \end{aligned} \tag{10}$$

$$Q = \sqrt{1 - (R/R_\pi)^2}. \tag{11}$$

The positive sign in front of the root corresponds to the shadow entry point, the from-negative shadow exit point.

If you give the true anomalies, and then the eccentric anomalies, as a function of the day number in a year, you can then express the duration of the shadow as a function of the day number in a year and draw a graph of the length of the shadow during the year.

The figure (Fig. 8) shows that the duration of the shadow during the year of the orbital flight changes slightly. This is due to the fact that the angle between the normal to the plane of orbit and the vector of direction to the Sun does not change due to the fact that the line of orbital nodes rotates at an angle of 360°per year, and the only possible reason for the change of the duration of the shadow is the rotation of the orbit in its plane (i.e. the secular movement of the perigee) (Fig. 2).

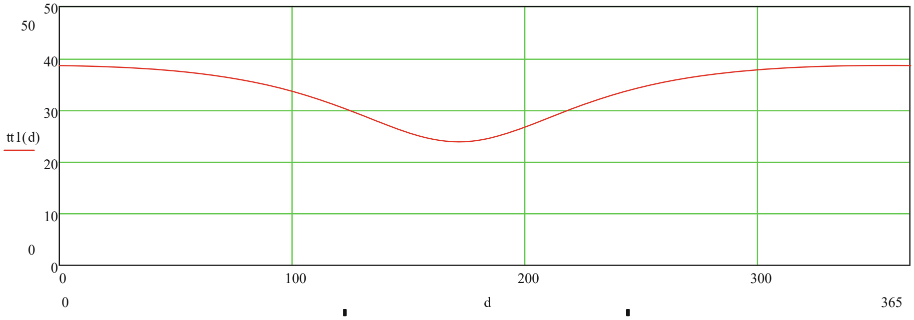

Fig. 2. Seasonal change in shadow length

Circular and quasi-circular orbits are generally used for SSO. This calculation was made for a quasi-circular orbit, so there is a slight change in the length of the shadow section during the year.

Illumination of BF Panels During the Turn. The data on the energy-determining coils are the starting point for the construction of the PV Cells (PV) luminosity diagram. To do this, it is necessary to determine the power of the solar radiation, as well as the power of the energy streams from reflected and own Earth radiation, which fall on a unit of the surface of the PV Cells. The solution will be produced for four panels installed on the chassis of the spacecraft according to the CubeSat specification.

The geocentric inertial CS OXYZ, geocentric orbital CS $OX_1Y_1Z_1$ and associated CS $O_2X_2Y_2Z_2$ are the following coordinate systems (CS) to describe the orbital motion of the PES and to determine its spatial orientation.

The position of BF panels is most convenient to specify in the connected coordinate system, as for small spacecraft they are not orientable, and in this UK coordinates of normals to panels will be unchanged.

The luminosity of the panel PVcan be defined as the product of the solar constant by the luminosity ratio:

$$E = E_0 \cdot K_{OSV} \tag{12}$$

where E0 =1360 Wt/m^2 is the solar constant.

For non-orientable PVs, the luminosity coefficient will change during the turn according to the harmonic law. It can be found as follows:

$$K_{osv} = \Gamma \cdot \cos(\alpha) \tag{13}$$

Where $\Gamma = 1$, if the satellite is in the illuminated area of the orbit; $\Gamma = 0$, if the satellite is in shadow; α - the angle between the external normal to the surface of the BF panel and the vector of direction to the Sun. The value of α depends on the adopted arrangement of the panels and the position of the panels relative to the body of the spacecraft.

The cosine of the angle α, expressed through components **n** and **S** in the geocentric orbital coordinate system, will be equal to:

$$\cos\alpha = nx_1Sx_1 + ny_1Sy_1 + nz_1Sz_1 \tag{14}$$

where the coordinates of the direction vector to the Sun can be found from the following ratios:

$$\begin{cases} Sx_1 = \cos\theta\cos\Omega + \sin\theta\cos\varepsilon\sin\Omega, \\ Sy_1 = \cos\theta\sin\Omega + \sin\theta\cos\varepsilon\cos\Omega, \\ Sz_1 = \sin\theta\sin\varepsilon. \end{cases} \tag{15}$$

As for the coordinates of the normal to the surface of the BF, since the PV cells are non-orientable, we can specify them in a connected coordinate system (nx_2, ny_2, nz_2).

The transition from a linked coordinate system to a geocentric orbital CS shall be effected by a rotation matrix [4]:

$$M(u) = M_i M_\omega M_\vartheta \tag{16}$$

$$M_i = \begin{vmatrix} 1 & 0 & 0 \\ 0 & \cos i & -\sin i \\ 0 & \sin i & \cos i \end{vmatrix} \tag{17}$$

$$M_{\omega} = \begin{vmatrix} \cos\omega & -\sin\omega & 0 \\ \sin\omega & \cos\omega & 0 \\ 0 & 0 & 1 \end{vmatrix} \quad (18)$$

$$M_{\vartheta} = \begin{vmatrix} \cos\vartheta & -\sin\vartheta & 0 \\ \sin\vartheta & \cos\vartheta & 0 \\ 0 & 0 & 1 \end{vmatrix} \quad (19)$$

$$\begin{pmatrix} nx_1 \\ ny_1 \\ nz_1 \end{pmatrix} = M(u) \begin{pmatrix} nx_2 \\ ny_2 \\ nz_2 \end{pmatrix} \quad (20)$$

The rotation matrix here is given as a function from the satellite's latitude argument, respectively, and the coordinates of the normals to the BF panels in the geocentric orbital coordinate system will be expressed as a function of the satellite's latitude argument.

As a result, we get the dependence of PV cell light on the latitude argument of **u** and can construct corresponding diagrams (Fig. 3).

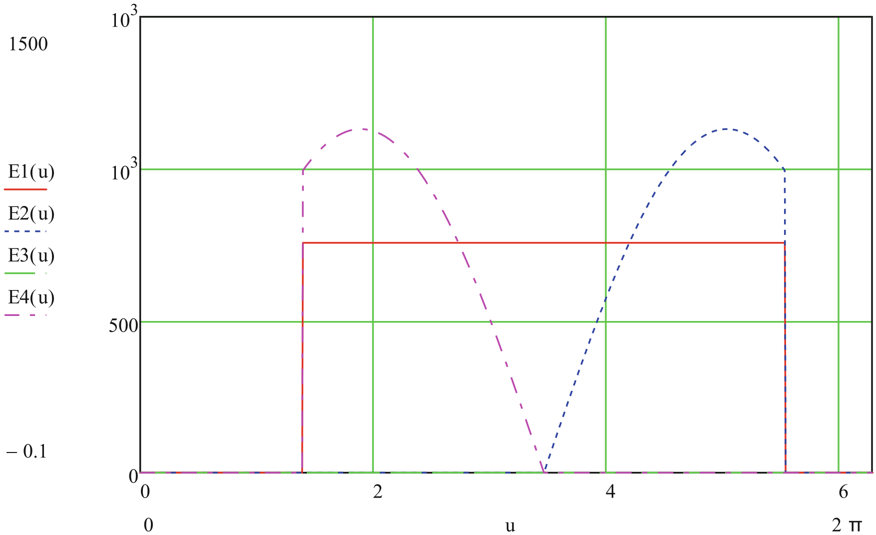

Fig. 3. Variation of the power of solar radiation per unit of PV surface during one turn

The energy flux coming to the surface of the spacecraft from the planet is the sum of two components - its own and reflected solar radiation.

As the mean heat flux through the sphere radius (R + H) is removed in any direction from Earth, it will decrease as $(R/(R + H))^2$, where R is the average radius of the Earth.

The illumination of the BF panels from the Earth's own radiation will be a function of the satellite's latitude argument, and it is possible to construct a diagram of the energy flux change from the Earth's own radiation falling on the BF panel surface unit. The

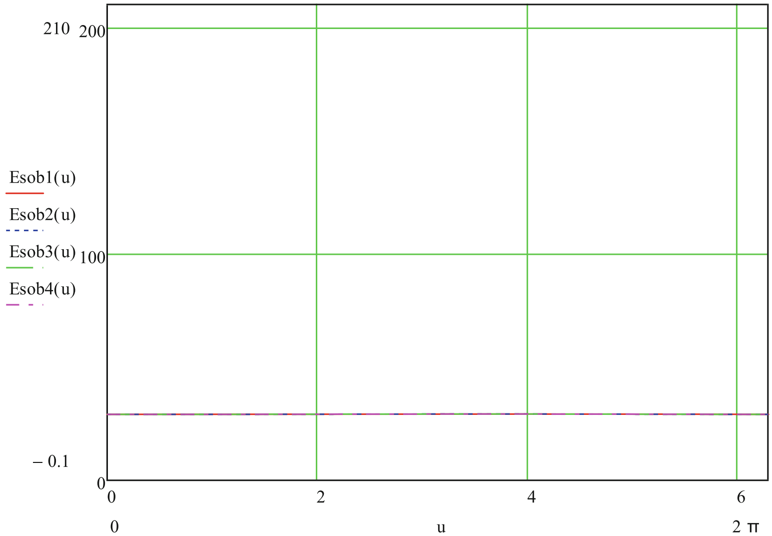

Fig. 4. Change of power of energy streams from the Earth's own radiation falling on a unit of surface of PV, during one turn

results of the calculation are shown in Fig. 4, provided that the spacecraft is uniaxially oriented to Earth.

The reflected radiation consists of fluxes reflected from cloud cover (73%), atmosphere (19%) and underlying surface (8%). Thus, the density of the flux falling on the PV of reflected radiation from the planet depends primarily on the reflectivity, or simply the albedo (α). The value of α depends on a number of factors: the time of the year, the geographic latitude of the location above which the spacecraft is located KA (and most importantly, clouds in the area), the angle of sunlight. In practice, the diffusion law of radiation propagation from the Earth and the uniform value of the average albedo (α_{av}) over its surface are usually adopted. These assumptions are based on the simplicity and satisfactory accuracy of engineering calculations. For Earth $\alpha_{av} = 0.34$ [6].

The density of reflected solar radiation falling on a unit of the PV cell surface can be expressed as a function of the satellite's latitude argument and construct corresponding diagrams for four panels (Fig. 5).

The total illumination of the PV cells is equal to the sum of the illumination from solar radiation, the Earth's own radiation and reflected radiation from the Earth:

$$E_{sum}(u) = E(u) + E_{ref}(u) + E_{own}(u) \tag{21}$$

With the help of this expression it is possible to construct a diagram of change of total illumination of panels PV during one turn.

The results of these calculations can be used to determine the temperature change of BF, to construct characteristics of solar cells and to further use the data at various stages of the design of electric power system (EPS) spacecraft.

Temperature determination of PV values and dependencies of the total luminosity of panels PV during the turn, allow to determine the temperature of panels PV (Fig. 6).

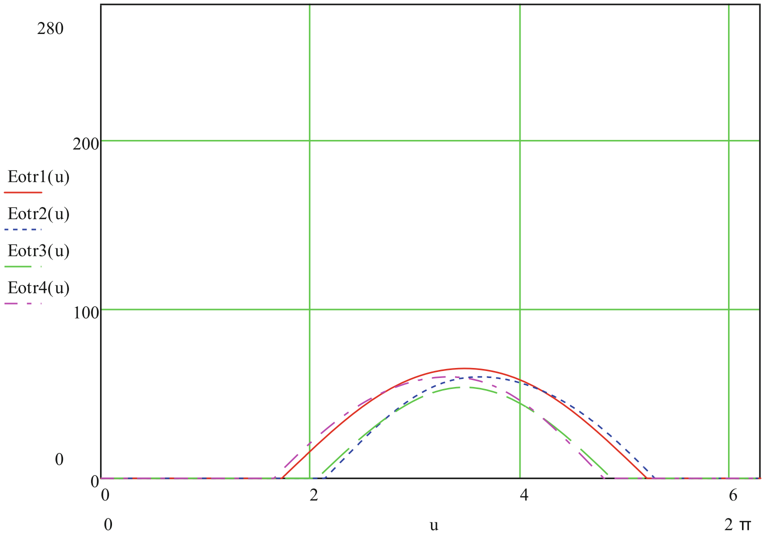

Fig. 5. Change in the power of the energy streams from the reflected salt-nebula radiation from the Earth falling on the unit of the surface of the PV cell

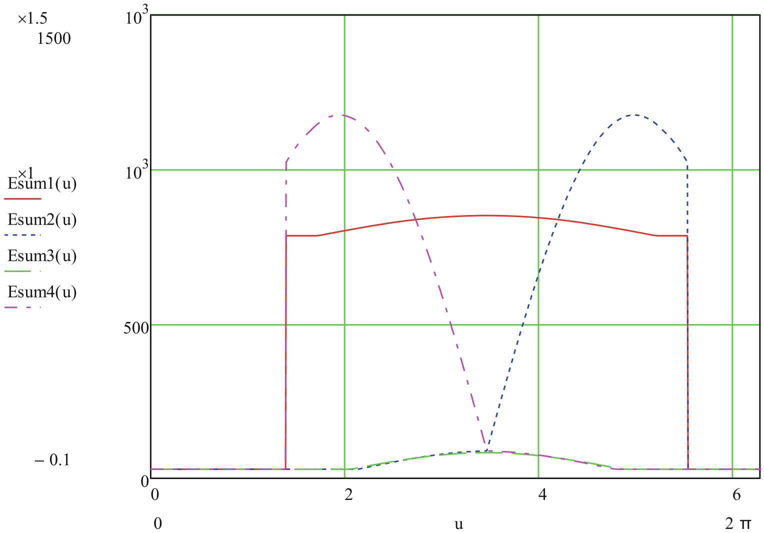

Fig. 6. Change of total luminosity of BF panels, during one turn

To determine the temperature of BF panels for one turn we use the equation of heat balance, which has the form [4]:

$$C_m M_s \frac{dT}{dt} = Q_1 + Q_2 - N_d \tag{22}$$

where Cm is the specific heat capacity of the material of BF panel, J/kg; M_S - specific mass of the panel, kg/m^2; t - time, s; T is the average equilibrium temperature of the panel, K; Q_1 - heat flow from external heat sources, W/m^2; Q_2 - heat flow from internal heat sources, W/m^2; N_d - electrical power panel, W/m^2.

Determine the thermal fluxes from external and internal heat sources, as well as the dependence of specific power on the illumination of the surface of the BF panels and the obtained values will be substituted into the thermal balance equation.

The heat flow from external sources will vary during the turn, as the BF panels are undirected, and depends on:

– direct radiation of the Sun;
– the Earth's own and reflected solar radiation.

Then the heat flow from external heat sources, taking into account all the para-meters, can be described by an expression for which will look like:

$$\begin{aligned} Q_1 &= \alpha_f(E_f + E_{fref} + E_{fown}) \\ &+\alpha_r(E_r + E_{rref} + E_{rown}) \end{aligned} \tag{23}$$

where E_f, E_r - the illumination of the panels BF, and indices "f" and "r" indicate the front and rear surface of the panel; and α_f, α_r- the integral absorption coefficient of the front and rear surface.

The thermal flux from internal sources, taking into account the thermal radiation of the battery itself, can be described:

$$Q_2 = -(\varepsilon_f + \varepsilon_r)\sigma T^4 \tag{24}$$

where σ is Boltzmann's constant; ε_f, ε_r - integral emission coefficients of the front and back side.

Define N_d. To simplify, you can ignore the dependence of the electric power parameters of BF on the temperature. This assumption simplifies the numerical integration procedure of Eq. (22) without significantly reducing the calculation accuracy, as:

– firstly, the N_d from the temperature is a small part (less than 0.5%) of the determining flux Q_1;
– secondly, the fourth degree in the expression for Q_2 significantly reduces the possible error of determination of T due to the temperature dependence of electrical parameters of the battery.

Therefore, the equation for N_d takes the following expression:

$$N_d = (E_f + E_{fown})\eta k_{fil} \tag{25}$$

where E is the illumination of BF panels; η - efficiency of photovoltaic converters;

k_{fil} - coefficient of filling of the working surface of the solar battery panel with solar cells.

Also accept that the reflected radiation is in the spectral range, which coincides with the sensitivity region of the SC.

The results of the calculation can be presented in the form of a diagram of the dependence of specific power on the illumination of the surface of the BF panel during one turn (Fig. 7).

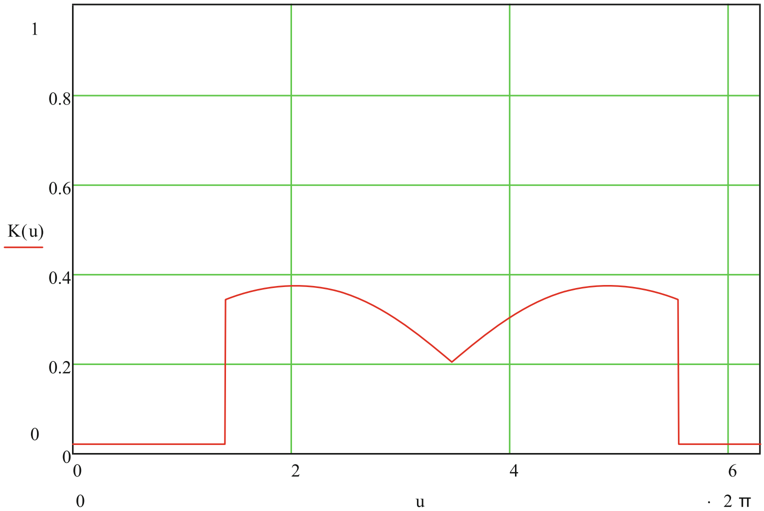

Fig. 7. Change of specific power during one turn

The ratios (23), (24) and (25) are substituted into Eq. (22) and the final form of the thermal balance equation is obtained:

$$\begin{aligned} C_m M_s \frac{dT}{dt} &= \alpha_f (E_f + E_{fref})(1 - \eta k_{fil}) \\ &+ \alpha_f E_{fown} + \alpha_r (E_r + E_{rref} + E_{rown}) \\ &- (\varepsilon_f + \varepsilon_r)\sigma T^4. \end{aligned} \tag{26}$$

Having the above expressions it is possible to substitute all known functions in Eq. (26) and to construct a diagram of temperature change of each panel BF during one turn:

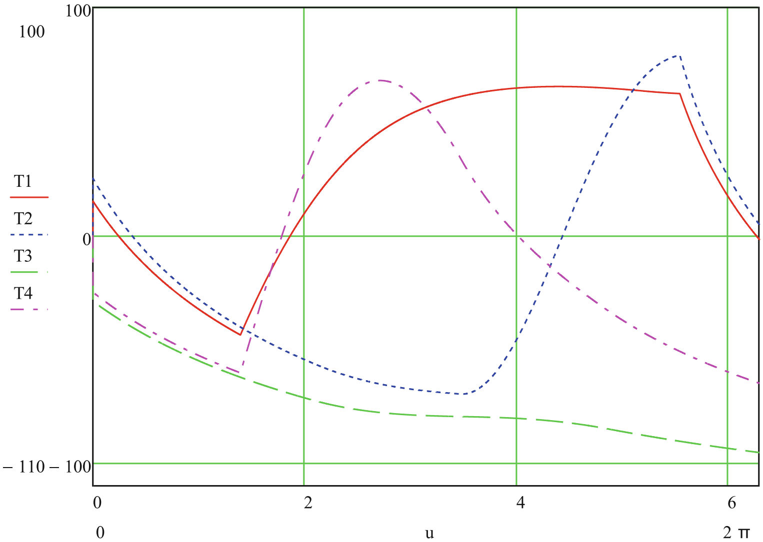

Fig. 8. Temperature change of BF panels during one turn.

4 Conclusion

The constructed mathematical model describing the light and temperature of the photoelectric battery of a small spacecraft was implemented in a simple and accessible MathCAD application. In the tasks of designing the power supply systems of university microsatellites and in the tasks of mastering the simulation of power supply, this implementation of the model is quite acceptable even with reduced precision. A comparison of the calculations made with the results of data on the energy and thermal parameters of ERS spacecraft indicates acceptable tolerances of 5…10%. For university microsatellite projects, this is acceptable given their short-term active existence.

This model for applications in the university design of mice-rosettes represents an intermediate between the model of flight dynamics of the spacecraft, implemented in many different applications [7] and primary generator and spacecraft energy storage models. A significant difference from the previously implemented models [4, 5, 7] is the consideration of the small dimension of the spacecraft and power plant, as well as the limited lifetime of active life. Thus, the mathematical model in the given realization allows to design power systems of small spacecraft.

References

1. Brandt, F., Nickel, S.: The air cargo load planning problem-a consolidated problem definition and literature review on related problems. Eur. J. Oper. Res. **275**(2), 399–410 (2019). https://doi.org/10.1016/j.ejor.2018.07.013
2. Fields, T., Norris, A.: Modeling, development, and testing of medium-scale cruciform parachute systems. In: 26th AIAA Aerodynamic Decelerator Systems Technology Conference, p. 2726. AIAA, Toulouse (2022). https://doi.org/10.2514/6.2022-2726

3. Güven, K., Şamiloğlu, A.T.: direction stabilization and simulation of an aerial delivery system with ram-air parachute, preprint (2022). https://doi.org/10.21203/rs.3.rs-1458039/v1
4. García-Beltrán, C.D., Miranda-Araujo, E.M., Guerrero-Sanchez, M.E., Valencia-Palomo, G., Hernández-González, O., Gómez-Peñate, S.: Passivity-based control laws for an unmanned powered parachute aircraft. Asian J. Control **23**(5), 2087–2096 (2021). https://doi.org/10.1002/asjc.2540
5. Massenio, P.R., Rizzello, G., Naso, D., Lewis, F.L., Davoudi, A.: Data-driven optimal structured control for unknown symmetric systems. In: 2020 IEEE 16th International Conference on Automation Science and Engineering (CASE), pp. 179–184. IEEE, Hong Kong (2020). https://doi.org/10.1109/CASE48305.2020.9216852
6. Jackson, D.: Design, Modeling and Testing of a Cascaded Heading Stabilization Controller for a Cruciform Parachute System. M.S. dissertation, Univ. of Missouri-Kansas City (2021). https://mospace.umsystem.edu/xmlui/handle/10355/84385
7. Alieksieiev, V., Kazan, P., Korolova, O., Dronyuk, I.: Promising modern steerable parachute for unmanned aircraft systems. In: Hu, Z., Zhang, Q., Petoukhov, S., He, M. (eds.) ICAILE 2022, vol. 135, pp. 431–439. Springer, Cham (2022). https://doi.org/10.1007/978-3-031-04809-8_38
8. Zhang, Z., Pei, Z., Tang, Z., Gu, F.: TuSeSy: an intelligent turntable servo system for tracking aircraft and parachutes automatically. Appl. Sci. **12**(10), 5133 (2022). https://doi.org/10.3390/app12105133
9. Salahudden, S., Das, A.T., Sanwale, J., Giri, D.K., Ghosh, A.K.: Sliding mode controller based aircraft automatic landing for alternate profiles. Proc. Inst. Mech. Eng. G J. Aerosp. Eng., 09544100211068903 (2022). https://doi.org/10.1177/09544100211068903
10. Godish, T., Fu, J.S.: Air Quality, p. 464. CRC Press, Boca Raton (2019). https://doi.org/10.1201/9780429105036

Thermal State Determination of the Heat Exchanger in the Three-Dimensional Setting

Pavlo Gakal, Iryna Tretiak, Maria Arefieva, and Viacheslav Nazarenko(✉)

National Aerospace University "Kharkov Aviation Institute", Kharkov 61070, Ukraine
v.v.nazarenko@khai.edu

Abstract. The presented manuscript substantiates the need to calculate the cooling system of modern Turbogenerators using the method of mathematical modeling in the three-dimensional setting. The general formulation of the problem for the calculation of the heat exchanger was carried out, the main initial parameters were determined. The problem of clogging of gas cooling pipes is considered in detail. The influence of this clogging at different percentages of the pipes obstruction on the distribution of cooling gas through them was determined. The operation principle of the cooling system of the 220 MW Turbogenerator is considered. The calculation of the gas coolers in the three-dimensional setting was performed, taking into account the influence of the thermal state of the entire generator structure. The calculation results comparison of the Turbogenerator coolers with the data of experimental studies was also carried out. The combination of the analytical method of calculation with the solution by the mathematical modeling in the three-dimensional formulation by the CFD method.

Keywords: Turbogenerator · Cooling System · Heat Exchanger · Gas Cooler · Three-Dimensional Calculation · Thermal State

1 Introduction

Thermal and Nuclear Power Plants, which are equipped with high-speed Turbogenerators, mainly of medium and large power, currently occupy a significant part of electricity production all over the world. Modern global worldwide trends in the design of electric machines require revision and improvement of existing design and calculation methods. The cooling system of active and constructive parts of the machine also has a great influence on the design. The three-dimensional mathematical modeling method using to calculate the cooling system of modern Turbogenerators provides wide opportunities for improving structures, increasing their reliability and reducing mass.

Stable operation of the generator ventilation system is impossible without strict compliance with the necessary design parameters of the heat exchanger, which ensures cooling of the heated gas to the required temperature, taking into account the real operating conditions. In this regard, within the framework of the proposed unified methodology for the design of generators, based on the three-dimensional modeling, the boundary

M. Nechyporuk et al. (Eds.): ICTM 2023, LNNS 1008, pp. 327–336, 2024.
https://doi.org/10.1007/978-3-031-61415-6_28

conditions were formulated and the calculation of the heat exchanger of the Turbogenerator rated 220 MW, which takes into account the real parameters of the gas, was carried out. That calculation was carried out taking into account the thermal state of the entire system as a whole.

2 General Formulation of the Problem for the Heat Exchanger

Let's determine the main initial parameters for setting the problem. Such parameters are the gas parameters at the heat exchanger inlet (velocity, pressure, temperature); the geometric parameters of the heat exchanger, taking into account the diameters and location of the gas cooling pipes, the temperature of the cooler, the material of the cooling pipes [1–4].

In Fig. 1 shows the real picture of the gas cooler pipes obstruction.

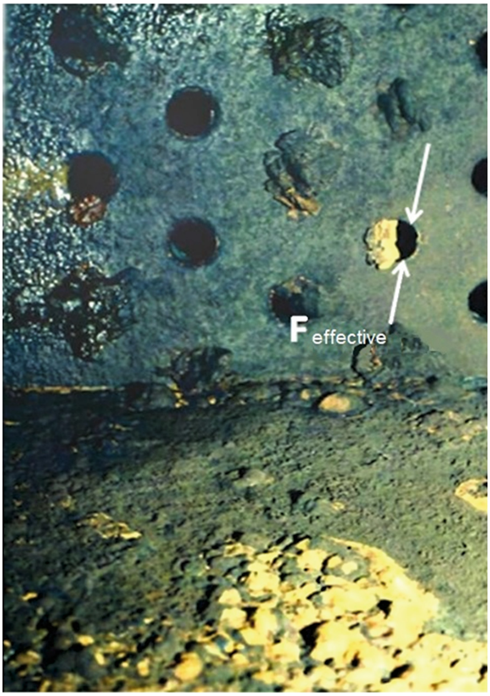

Fig. 1. Obstruction of the Gas Cooling Pipes

When solving the problem, it is necessary to take into account the possibility of heat exchanger operation with partial clogging and obstruction of gas cooling pipes. Pipes of gas coolers of Turbogenerators during their operation are prone to clogging and obstruction, which affects the efficiency of the heat exchanger system. When obstruction is present, the effective diameter of the pipe decreases and the flow parameters of the coolant through them change accordingly. Due to the importance of this problem, regulatory documents for generators introduce restrictions on the presence of pipes obstruction. Based on this, it is necessary to take into account the pipe clogging in the calculation. When the effective area of the working section changes, the water pressure in the pipe changes as if for a sharp jump. At the same time, the values of the full pressure (P) parameter decrease with a decrease in the cross-sectional area F. The presence of clogging in the amount of no more than 11% of the total number (cross-sectional area) of pipes is allowed in accordance with the technical conditions for Turbogenerators rated 200 MW and 300 MW manufactured by JSC "Ukrainian Energy Machines".

3 Ventilation System of the 220 MW Turbogenerator

In Turbogenerators with hydrogen-water and air cooling, two pressure elements are used (Fig. 2) - the axial fan and the centrifugal compressor [5]. The axial fan determines the movement of the cooling gas through the gas cooler and on to the stator core. The stator active steel is cooled using the system of radial channels. For the purpose of more uniform cooling of the stator along its length, eight compartments are organized, in seven of which the gas is directed by the axial fan, and in the eighth, located on the side of the drive, the cooling gas is pumped by the compressor.

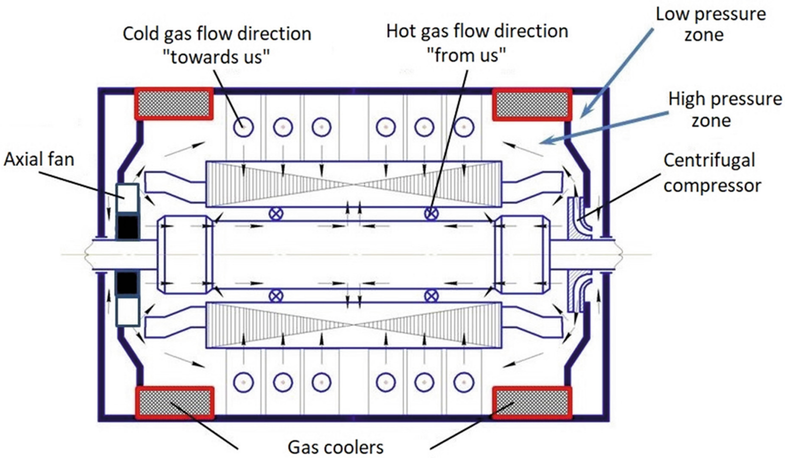

Fig. 2. Ventilation Diagram of the 220 MW Turbogenerator

The rotor winding is cooled by gas, the required flow rate is provided by the compressor, the characteristics of which are shown in Fig. 3. All the gas enters the gap between the stator and the rotor and leaves the gap in the gas coolers from the side of the slip rings.

At the same time, the existing compressor must provide the necessary air flow to maintain the heat balance on all structural elements [6].

Fig. 3. Centrifugal Compressor Characteristics which were Obtained at the Different Clearances in the Labyrinth between the Impeller and the Diffuser

4 Thermal State Determination of the Gas Cooler in the Three-Dimensional Setting

According to the selected diagram of the Turbogenerator ventilation system, presented in Fig. 2, the calculation of gas coolers was performed in the three-dimensional setting, taking into account the influence of the thermal state of the entire structure. Maximum temperatures are accepted in accordance with the technical conditions for 200 MW and 300 MW Turbogenerators manufactured by JSC "Ukrainian Energy Machines".

Long-term operation of the Turbogenerator is ensured with the following parameters of hydrogen and water:

a) hydrogen parameters: excess pressure in the shell – $3.5 \cdot 10^5$ Pa; purity - not less than 97%; temperature at the exit of gas coolers - 50 ºC;
b) parameters of the water entering the gas cooler: consumption – 111.1 l/s; the temperature at the entrance is 42 ºC;
c) parameters of water entering the first circuit of the heat exchanger: consumption - about 56 l/s; the temperature at the entrance is 42 ºC.

In Fig. 4 presents the three-dimensional model, initial and boundary conditions used in the calculation [7–11]. The three-dimensional grid of the gas cooler is shown in Fig. 5.

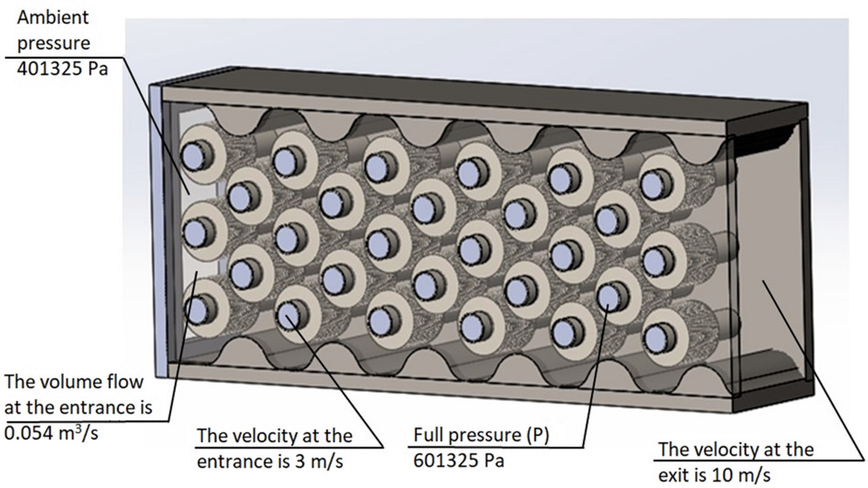

Fig. 4. Three-Dimensional Model of the Heat Exchanger

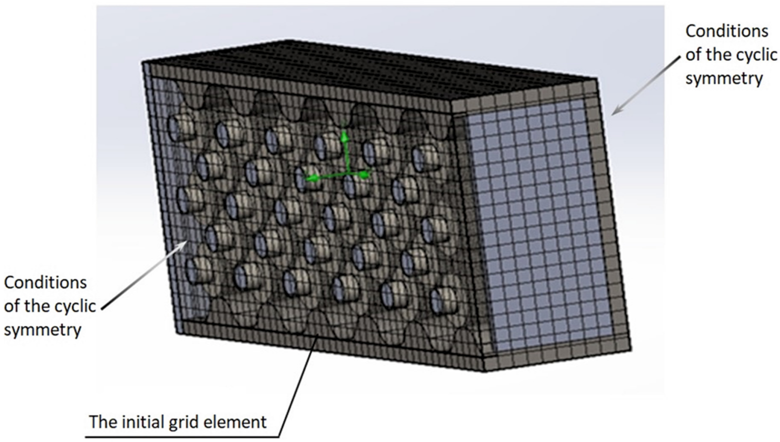

Fig. 5. Three-Dimensional Grid

The following parameters were chosen as conditions for convergence of the solution: the minimum, average, and maximum values of the temperatures of the solid body and the fluid medium; minimum, average and maximum speed, as well as the volume average value of temperature and speed [12–14]. The calculation was carried out until the specified parameters differed by more than 5% in subsequent iterations (when performing at least three purges of the calculation area).

In Fig. 6 shows the results of the three-dimensional calculation of the gas cooler thermal state.

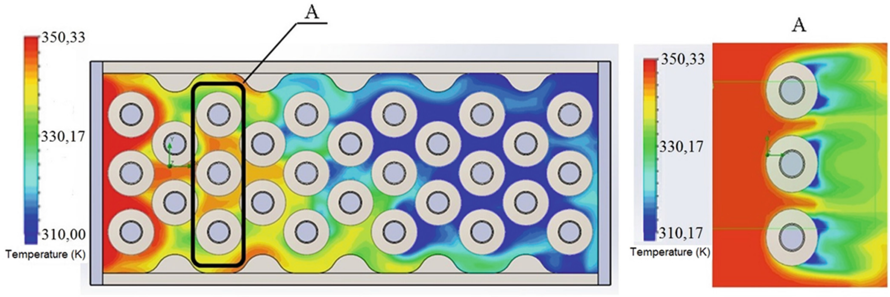

Fig. 6. The Temperature Field in the Heat Exchanger

In Fig. 7 shows the similar temperature field, when the gas cooler pipes are obstructed by 10%, and in Fig. 8 – when the gas cooler pipes are obstructed by 15%.

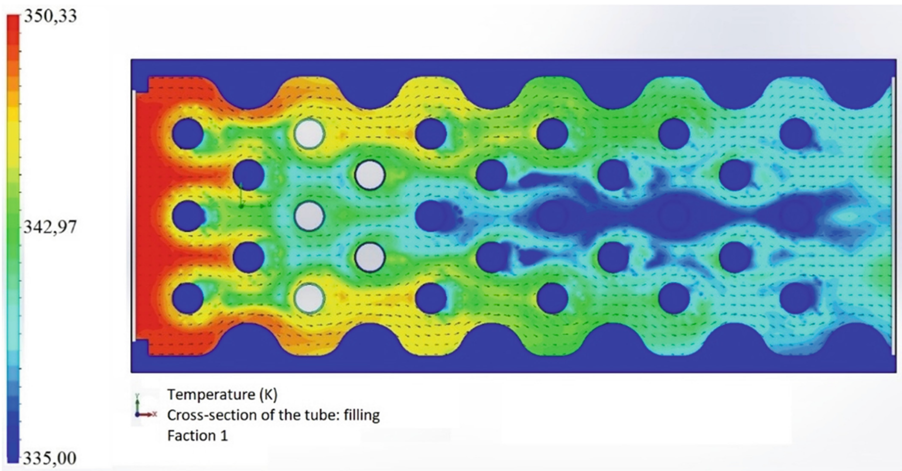

Fig. 7. The Temperature Field in the Heat Exchanger when the Pipes are Obstructed by 10%

5 Comparison of the Calculated and the Experimental Data

When comparing the calculation results of Turbogenerator coolers with the data of experimental studies, in which the refrigerant is cooling, differs in its physical properties from the one used in the experiments, it is necessary to move on the basis of similarity criteria to dimensionless parameters [15, 16].

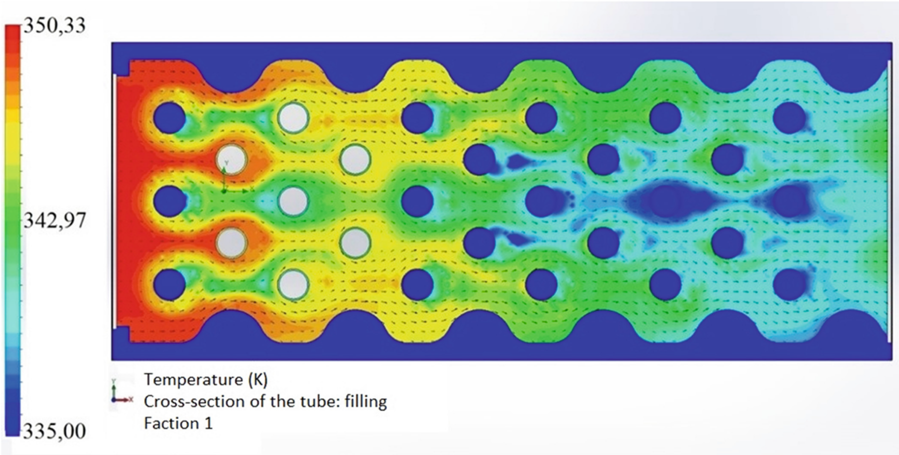

Fig. 8. The Temperature Field in the Heat Exchanger when the Pipes are Obstructed by 15%

Criterion equations for heat transfer intensity and hydraulic resistance have the following dependencies:

$$N_u = f\ (Re;\ Pr), \tag{1}$$

$$E_u = f\ (m;\ Re), \tag{2}$$

where N_u – is the Nusselt number;

Re – is velocity field;

Pr – is temperature field;

E_u – is Euler's criterion;

m – is the number of pipes rows along the depth of the bundle.

When obtaining dimensionless criteria during the processing of experimental data for the physical constants of the cooler, the dependence on the average air temperature is taken into account. The determining geometric size, for example, for pipes with loop-wire fins, the diameter of the loop wire equal to 0.69 mm is taken.

Under the conditions of similarity of Reynolds and Euler, the velocity of the air flow in the intersection was determined in the same way as when processing experimental data, used in the form of graphical dependencies $h_{reduced} = f \cdot (W_{liquid})$ and $\Delta P = f \cdot (W_{liquid})$.

Under the conditions of Nusselt similarity, the convective heat transfer coefficient must be introduced, which does not take into account the thermal resistance of the ribs and reflects only the intensity of the heat transfer process.

The available graphical dependence $E_u = f \cdot (Re)$ (Fig. 9), which was obtained earlier at the stand bench of JSC "Ukrainian Energy Machines", can be represented by the equation in the criterion form for one transverse row of finned pipes, namely:

$$E_u = 6400 \cdot Re^{-2,0} \tag{3}$$

For "m" rows, the equation has the following form:

$$E_u = 6400 \cdot m \cdot Re^{-2,0} \tag{4}$$

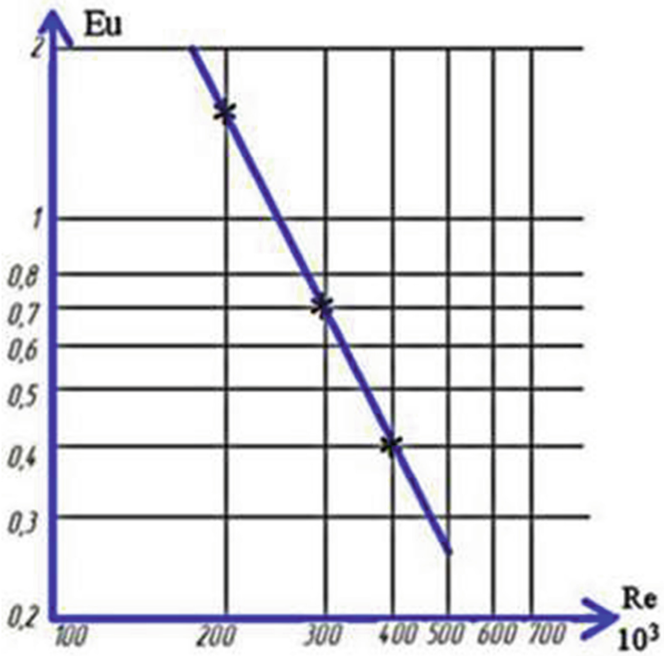

Fig. 9. Dependence of E_u from Re

The control devices with the working range of $0 \div 100°$ with a division value of 0.1 °C were used to measure the temperature. In Fig. 9 experimental values are designated as *. The error is no more than 1%, relative to the calculation.

The obtained equations in the criterion form can be used in heat engineering calculations of heat exchangers only for surfaces having the same geometric characteristics as the investigated surface, with Re numbers ranging from 150 to 500.

During the conducted analysis, it was determined that the error of the proposed method is at the level of the errors of the measuring devices.

6 Discussion

The problem of determining the thermal state of the heat exchanger using as example the 220 MW Turbogenerator in the three-dimensional setting, taking into account heat release caused by the entire generator structure influence was solved. The combination of the analytical method of calculation with the solution by the mathematical modeling in the three-dimensional formulation by the CFD method using the SolidWorks Flow Simulation software complex is proposed.

References

1. Kobzar, K.A., Gakal, P.G., Ovsyannikova, E.A.: Review of methods for analyzing the thermal state of a turbogenerator rotor with direct hydrogen cooling. Newsletter of NTU “KhPI”: collection of scientific works. Ser.: Energy and Heat-Technical Processes and Installation. Kharkiv, NTU “KhPI” **15**(1124), 112–117 (2015). http://library.kpi.kharkov.ua/files/Vestniki/2015_15.pdf
2. Tarnehill, J.C., Anderson, D.A., Pletcher, R.H.: Computation Fluid Dynamics and Heat Transfer, 2nd edn., p. 785. Taylor & Francis, New York (1997)
3. Tretyak, O.V.: The strength of turbogenerators and high-power hydrogenerators. Institute of Mechanical Engineering Problems named after A.M. Pidgorny of National Academy of Sciences of Ukraine, Kharkiv, p. 396 (2020)
4. Stone, G.C., Gupta, B.K., Lyles, J.F., Sedding, H.G.: Experience with accelerated aging tests on stator bars and coils. In: IEEE International Symposium on Electrical Insulation, Toronto, pp. 356–360 (1990)
5. Say, M.G.: Alternating Current Machines, 4th ed., p. 543. Pitman Publishing, London (1976)
6. International Standard: DSTU EN IEC 60034-33:2022 Electric rotating machines. Part 33. Synchronous hydrogenerators, including motor generators. Special requirements (2022). http://online.budstandart.com/ua/catalog/doc-page.html?id_doc=102789. Accessed 14 Aug 2023
7. Tretiak, O., et al.: Stress-strained state of the thrust bearing disc of hydrogenerator-motor. Computation **11**(3), 60 (2023). https://doi.org/10.3390/computation11030060
8. Putignano, C., Afferrante, L., Carbone, G., Demelio, G.: A new efficient numerical method for contact mechanics of rough surfaces. Int. J. Solids Struct. **49**(2), 338–343 (2012)
9. Ilyin, A.V., Plokhov, I.V., Kozyreva, O.I., Andrusich, A.V.: Three-dimensional modeling of nonstationary temperature field in the microcontact. Bull. Pskov Univ. Ser. Econ. Tech. Sci. **2**(5), 208–214 (2014)
10. Gerling, D.: DC-Machines. In: Electrical Machines. Mathematical Engineering, vol. 4. Springer, Heidelberg (2015). https://doi.org/10.1007/978-3-642-17584-8_2
11. Tretiak, O., Kritskiy, D., Kobzar, I., Arefieva, M., Nazarenko, V.: The methods of three-dimensional modeling of the hydrogenerator thrust bearing. Computation **10**, 152 (2022). https://doi.org/10.3390/computation10090152
12. Akin, J.: Finite Element Analysis Concepts via SolidWorks, p. 303. World Scientific. New Jersey (2009)
13. Jichao, H., et al.: Numerical analysis of end part temperature in the turbogenerator end region with magnetic shield structure under the different operation conditions. Int. J. Thermal Sci. **132**, 267–274 (2018)
14. IEC 60034-1:2022: Rotating electrical machines - Part 1: Rating and performance, 14th edn. International standard (2022)

15. Wang, H.: Similarity and Dimensional Analysis. Cambridge University Press (2023). https://doi.org/10.1017/9781108671149.009
16. Tretiak, O., et al.: Modeling of the stress–strain of the suspensions of the stators of high-power turbogenerators. Integrated Computer Technologies in Mechanical Engineering – Synergetic Engineering II. Computation **10**(11), 191 (2022). https://doi.org/10.3390/computation10110191

Damageability Assessment of Impact-Resistant Glass for Transparent Armor Systems

Natalia Smetankina[1](✉), Vadym Khvorostyanyi[2], Denys Ustuhov[3], Volodymyr Bodunov[2], and Iryna Kachinska[2]

[1] Anatolii Pidgornyi Institute of Mechanical Engineering Problems of the National Academy of Sciences of Ukraine, 2/10, Pozharskogo Street, Kharkiv 61046, Ukraine
nsmet@ipmach.kharkov.ua

[2] G.S. Pisarenko Institute for Problems of Strength of the National Academy of Sciences of Ukraine, 2, Sadovo-Botanichna Street, Kyiv 01014, Ukraine

[3] Antonov Company, 1 Akademika Tupolieva Street, Kyiv 03062, Ukraine

Abstract. Currently, much effort is being devoted to developing experimental research methods to determine damage and fracture resistance of brittle materials under local contact load conditions using various indenters and punches. The paper offers an experimental approach for studying the damageability and residual impact resistance of structural elements made of laminated bullet-resistant glass with ballistic damage. The glass is considered as a laminated plate. The approach takes into account the influence of the location of the punch indentation zones relative to the epicenters of ballistic impacts, the network of branched surface and subsurface cracks with glass chips, as well as the influence of the glass edges on the destructive load. Damage to laminated impact-resistant plates was assessed during ballistic tests under conditions close to full-scale ones. The practical significance of the proposed approach lies in the possibility of its use for assessing the damageability and service life of the aircraft laminated impact-resistant glazing with ballistic damage for the period of repair, restoration and modernization of transparent armor systems.

Keywords: Brittle materials · Laminated plate · Local punching

1 Introduction

Multi-element ballistic protection systems for military equipment, structures and fortifications based on armored elements made of metal and ceramic armor, laminated ball-resistant glass are widely used in military operations [1, 2]. Their advantages are the ability to flexibly change the level of protection in accordance with the technical requirements for individual parts of objects, reducing the likelihood of damage to individual elements and simplifying the replacement of damaged elements [3, 4]. The effectiveness of such protection depends on the optimal choice of dimensions of armor elements, taking into account the patterns of their damage, and resistance to repeated shock loads [5, 6]. The fundamental difference between elements of transparent armor is the significantly larger size of the damage and the presence of zones of remote degradation of the mechanical state of laminated glass [7, 8].

M. Nechyporuk et al. (Eds.): ICTM 2023, LNNS 1008, pp. 337–347, 2024.
https://doi.org/10.1007/978-3-031-61415-6_29

Recently, aircraft have been developed that already have protection against small arms fire, and can also be equipped with additional protection. Therefore, the development of new design solutions and the study of physical and mechanical processes during the operation of protective elements is an urgent problem [9, 10].

The purpose of this study is to develop an approach to assess the mechanical condition of laminated bullet-resistant glass with impact damage.

2 Literature Review

Solving the problems of monitoring strength, impact resistance, the scale and nature of damage heterogeneity and reducing the rigidity of modern systems of composite and hybrid ballistic design elements requires the use of developed and improved experimental and computational approaches that take into account production and operational factors to ensure compliance [11, 12].

In the structure of protective glazing, consisting of a laminated impact-resistant plate of silicate float glass and adhesive polymer layers, significant changes in mechanical characteristics occur after ballistic injuries. In impact zones and at certain distances from them, localized damage to glass plates occurs with degradation of their mechanical state, which affects their performance and preservation of their functional properties [13, 14]. That is why research methods that aim to determine the influence of the degree of damage to glass plates during damages on their non-sewing ability are relevant in order to justify the possibility of extending the life of an armor element in real circumstances for a period of time before repairing and restoring transparent armor systems [15, 16].

At the same time, the requirements for the reliability and service life of aircraft glazing must be met under the influence of other static and shock operational loads [17], including during operation of the heating system [18] and bird strikes [19, 20]. To solve these problems, it is necessary to develop methods for research and production monitoring of surface defect parameters, characteristics of the mechanical state of products, and the effectiveness of glass modification modes [21, 22].

In the paper [23], an influence of temperature on the post-cracked response of laminated glass under blast loading was studied. Experiments are carried out at a high strain rate on samples with a polyvinyl butyral (PVB) interlayer between annealed glass. From the cracked tests, it was shown that the adhesion between the glass and PVB layer is increased at lower temperatures.

Experimental tests and numerical simulations of PVB laminated glass under low-velocity impact are presented in [24]. The rate-dependent Taylor-Chen-Kuszmaul model is used to describe the tensile damage characteristic of annealed glass.

A non-linear viscoelastic behavior of laminated glass panels based on the layer-wise plate theory is investigated in [25]. It is shown that polymeric interlayers demonstrate a time-dependent deformation even at room temperature.

A laminated glass at small explosion load was experimentally studied in [26, 27]. It is shown that the empirical formulas are available, with some reference for the anti-explosion design of laminated tempered glass. The influence of interlayer material properties on the impact resistance and the failure mechanism of a laminated glass at the low velocity impact was studied in [28, 29]. Variation of the impact velocity and effect of impact energy levels was analyzed [30].

The paper presents an approach to assessing the mechanical state of ballistic protection structural elements under conditions of the static local punching (indentation) with a steel punch normal to the glass plane at various distances from the edges and damage cells.

3 Research Methodology

Experimental studies were carried out to verify the approach to assessing the mechanical state of laminated glass with impact damage as a result of ballistic tests under static local loading with a punch. The proposed method studies the degree of damage to the first plate in protective glazing structures in the form of laminated impact-resistant plates made of silicate float glass and adhesive polymer layers.

Studies under local static load were carried out on a modernized ZD-4 hydraulic setup for mechanical testing of brittle materials using the GT-12-M8 universal measuring system and the corresponding GlassBend software at the G.S. Pisarenko Institute for Problems of Strength of the National Academy of Sciences of Ukraine. The assessment of the level of stability of the structure of an armored element with multiple damages, the heterogeneity of its damage and the degree of glass fragmentation at different distances from the sources of impacts was carried out when determining the characteristics of the force load on the punch, its movement deep into the material (indentation) and contact pressure. Indentation tests were performed using a rigid conical punch with a flat round top with a diameter of 4 mm and an apex angle of 300 made of hardened steel 45 with hardness HRC $\geq$ 62. The punch is shown in Fig. 1.

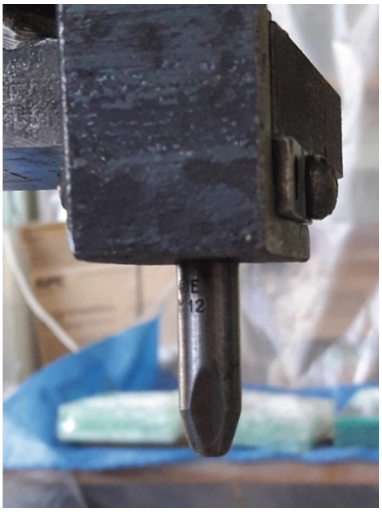

Fig. 1. General view of the punch fixed in the loading crossbar of the ZD-4 universal testing machine.

The object of study is a laminated impact-resistant plate with dimensions 46 mm × 170 mm × 225 mm. The plate consists of six hardened glasses connected by adhesive polymer layers (10–8–8–6–6–3; thicknesses of the layers are presented in millimeters). This plate has been subjected to ballistic tests and has two damages without through penetration from a shot from a firearm with a 7.62 mm caliber ball.

On the test plate, areas were marked for further testing using the indentation punch method. These local areas on the surface of the plate are located at different distances from its edges and damage cells, containing signs of significant destruction in the form of zones of material breakdown at the epicenters of ballistic impacts and crack networks that have significantly disrupted the structure of the glass.

The location coordinates of the damage areas on the surface of the laminated glass armor element sample after impact loading during ballistic tests (sections I and II) and the areas where the punch was indented (areas 1…16) are given in Table 1. The origin of coordinates is the lower left corner of the sample.

Table 1. Coordinates of the affected areas after ballistic tests and punch indentation sections on a laminated protective glass.

Number of area (section)	Coordinates, mm	
	along X-axis	along Y-axis
I	100	110
II	55	140
1	25	25
2	50	50
3	120	50
4	145	60
5	85	25
6	50	25
7	145	25
8	120	25
9	145	105
10	145	200
11	65	200
12	105	200
13	135	165
14	105	175
15	25	200
16	140	135

It was assumed that the minimum distance from the edge or cell of the impact to the point of indentation by the punch was at least 25 mm. The distance between adjacent indentations was also chosen at a level of at least 25 mm. The test using the local static punching method was carried out with forces not exceeding 10,000 N. Before the start of the experimental studies, the distances from the epicenter of each ballistic impact to the punch indentation centers were measured. Additionally, the minimum distances from the indentation areas to the networks of cracks that formed significant surface and subsurface damage to the plate were measured.

Figure 2 shows the punch indentation diagrams of selected areas on the investigated plate presented as dependencies of the load on the punch (P, N) from the displacement (indentation) of the punch (δ, mm).

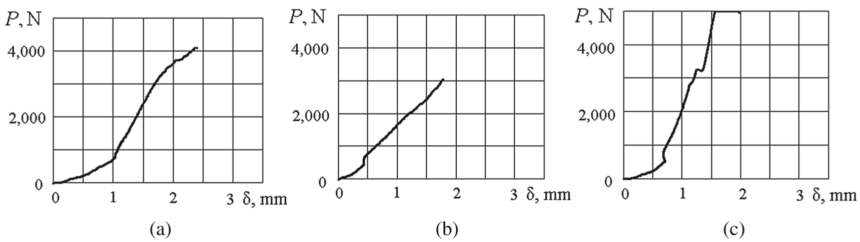

Fig. 2. Test results of a laminated impact-resistant plate under static local load with a punch, presented on indentation diagrams of areas 2 (a), 5 (b) and 7 (c)

Table 2 shows the values of the load, the displacement and the specific pressure under the punch corresponding to the limit state of the material in which the stiffness of the plate decreased sharply due to its local destruction with the formation of cracks, chips and crumbs from small glass particles.

The specific pressure was determined with some assumptions (the pressure on the side faces of the punch was neglected) as the ratio of the applied load P to the area of the base of the punch S. Since a cylindrical punch (round cross-section) with a flat base was used, then the area was calculated as πr^2, where r is the radius of the punch.

Figure 3 shows some areas after indentation. It is seen that in the indentation zone a corresponding type of "crater" was formed with signs of significant cracking and spalling of the material. It was also influenced by a branched network of cracks and chips that appeared after preliminary ballistic damages.

The analysis of the obtained experimental results consisted in finding the dependences of the maximum value of the applied load on the punch on the minimum distances from the centers of the indentation areas to the damage epicenters, the minimum distances of the cracks of the damage areas, and the minimum distances from the centers of the indentation areas to the edge of the plate. It corresponded to the moment of destruction of the first layer. The summary data is shown in Table 3.

A general pattern was observed that in the indentation areas located most remotely from the epicenters of ballistic damages, the destruction of the glass plate occurred at large values of the load applied to the punch, if we consider the entire array of experimental data obtained. And accordingly, the closer the indentation site is to the

Table 2. Experimental data obtained under studying of a laminated impact-resistant plate using the static local punching method.

Number of area	Load on the punch, *P*, N	Displacement (indentation) of the punch, δ, mm	Specific pressure under the punch, *p*, MPa
1	9,562.6	2.168	761
2	4,118.5	2.396	328
3	2,941.8	2.740	234
4	2,333.1	3.216	186
5	3,050.0	1.780	243
6	2,759.2	1.824	220
7	4,970.7	1.968	396
8	4,118.5	2.512	328
9	1,406.7	2.528	112
10	1,413.4	2.304	113
11	3,422.0	5.488	272
12	1,744.8	3.480	139
13	2,116.7	3.912	169
14	2,130.3	3.176	170
15	5,437.2	2.680	433
16	2,238.5	4.068	178

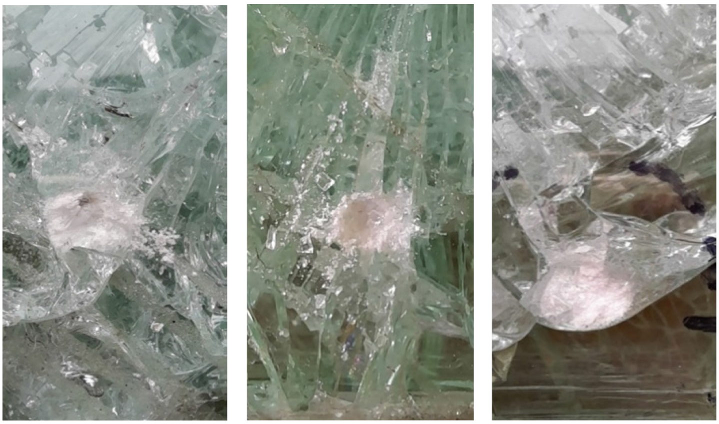

(a) (b) (c)

Fig. 3. The areas 2 (a), 5 (b) and 7 (c) of the laminated impact-resistant plate after testing by static local punching.

affected area, the lower the value of the destructive load was recorded in the tests. For the most distant sites, the load on the punch P ranged from about 3,000 N to 9,500 N (areas 1, 7, 8, 5 and 6), while for the loading sections close to the damage areas, the load on the punch was recorded in the range of about from 3,400 N to 1,400 N (areas 1, 3, 16, 14 and 9). The exception is area 10. It is located at a considerable distance from damage zones. However, the destruction occurred at a small load value ($P = 1,413.4$ N). It should also be noted that the displacement value of the punch for the specified test samples was radically different: for the first section (the remote section) is $\delta = 1.780 \div 2.512$ mm, and for the second section is $\delta = 2.528 \div 5.488$ mm.

The value of the destructive load of the glass plate for the most distant indentation areas is 2 or 3 times higher compared to areas close to the damaged zones. In the diagrams "the load P vs the displacement δ" we can notice the different nature of the dependence curve, which is flatter for areas closer to the affected areas. This indicates a difference in the resistance to penetration of the punch into the material during the experiment for areas in which the structure of the glass is more or less damaged (as a result of preliminary ballistic impacts) due to the appearance of numerous branched networks of cracks, formed chips and its spalling.

Table 3. Experimental results analysis data.

Number of the area	Load on the punch, P, N	Minimum distance from the centers of the indentation areas to the damage epicenters, mm	Minimum distance from the centers of the indentation areas to the nearest cracks of the damage areas, mm	Minimum distance from the centers of the indentation areas to the edge of the plate, mm
1	9,562.6	110	60	25
2	4,118.5	75	25	50
3	2,941.8	60	18	50
4	2,333.1	70	25	25
5	3,050.0	85	40	25
6	2,759.2	96	50	25
7	4,970.7	97	54	25
8	4,118.5	85	42	25
9	1,406.7	50	10	25
10	1,413.4	107	42	25
11	3,422.0	58	40	25
12	1,744.8	75	40	25
13	2,116.7	70	26	35

(*continued*)

Table 3. (*continued*)

Number of the area	Load on the punch, P, N	Minimum distance from the centers of the indentation areas to the damage epicenters, mm	Minimum distance from the centers of the indentation areas to the nearest cracks of the damage areas, mm	Minimum distance from the centers of the indentation areas to the edge of the plate, mm
14	2,130.3	60	30	65
15	5,437.2	65	35	25
16	2238.5	52	15	30

Similar patterns can be traced when analyzing the dependence “the load P vs the minimum distance from the centers of indentation areas to the nearest cracks in the affected areas. For indentation areas located closer to surface and subsurface cracks (areas 9, 16, 3, 4 and 13) compared to more distant areas (areas 1, 7, 6, 8 and 11), the level of destructive load is also less than 2 or 3 times. The presence of cracks and disruption of the continuity of the material sharply reduces its resistance to punch deepening under local contact load. The study of the influence of the plate edge was considered when constructing the corresponding dependence. It should be noted that the proximity of the edge to the indentation area of the punch does not have a significant effect on the destructive load.

4 Conclusion

An experimental approach for studying the damageability and residual impact resistance of a laminated bullet-resistant glass with ballistic damage was developed. Experimental investigations were carried out to assess the mechanical state of structural elements of ballistic protection made of laminated impact-resistant glass under static local punching to determine the influence of the damage degree on load-bearing capacity and the preservation of functional properties.

The influence of the location of the areas of indentation by the punch relative to the epicenters of ballistic damage, the resulting networks of branched surface and subsurface cracks and other changes in the integrity of the glass structure, the proximity of the plate edges on the destructive load was studied. Certain relevant general patterns are shown that indicate differences in resistance to punch penetration into the material.

The results of the experimental studies can be used to justify the possibility of extending the life of armored elements with ballistic damage in real circumstances for a period of time before carrying out repairs and restoration of transparent armor systems for an aircraft glazing [31, 32].

The direction of further research is optimization of the design of protective glazing to reduce the weight of multi-element transparent armor systems [33], as well as various elements of aircraft structures [34, 35].

References

1. Dveirin, O.Z., Andreev, O.V., Kondrat'ev, A.V., Haidachuk, V.Y.: Stressed state in the vicinity of a hole in mechanical joint of composite parts. Int. Appl. Mech. **57**(2), 234–247 (2021). https://doi.org/10.1007/s10778-021-01076-4
2. Kondratyev, A.V., Kovalenko, V.A.: Optimization of design parameters of the main composite fairing of the launch vehicle under simultaneous force and thermal loading. Space Sci. Technol. **25**(4(119)), 3–21 (2019). https://doi.org/10.15407/knit2019.04.003
3. Rodichev, Y., Veer, F., Soroka, O., Shabetya, O.: Structural strength of heat-strengthened glass. Strength Mater. **50**(4), 584–596 (2018). https://doi.org/10.1007/s11223-018-0004-8
4. Veer, F.A., Rodichev, Y.M.: Improving the engineering strength of heat strengthened glass. Heron **61**(2), 121–140 (2017)
5. Bez, A., Bedon, C., Manara, G., Amadio, C., Lori, G.: Calibrated numerical approach for the dynamic analysis of glass curtain walls under spheroconical bag impact. Buildings **11**(4), 154 (2021). https://doi.org/10.3390/buildings11040154
6. Smetankina, N.V., Shupikov, A.N., Sotrikhin, S.Yu., Yareschenko, V.G.: Dynamic response of an elliptic plate to impact loading. Theory and experiment. Int. J. Impact Eng. **34**(2), 264–276 (2007). https://doi.org/10.1016/j.ijimpeng.2005.07.016
7. Khvorostyanyi, V.V., Gogotsi, G.A.: Specific features of glass damage and fracture resistance under the Rockwell indenter scratching of the specimen surface until the edge chipping appearance. Strength Mater. **52**(2), 243–251 (2020). https://doi.org/10.1007/s11223-020-00171-0
8. Galenko, V.Y., Khvorostyanyi, V.V.: Estimation technique for the edge chipping resistance of brittle materials. Strength Mater. **55**(2), 302–308 (2023). https://doi.org/10.1007/s11223-023-00525-4
9. Udi, U.J., Yussof, M.M., Ayagi, K.M., Bedon, C., Kamarudin, M.K.: Environmental degradation of structural glass systems: a review of experimental research and main influencing parameters. Ain Shams Eng. J. **5**, 101970 (2023). https://doi.org/10.1016/j.asej.2022.101970
10. Hana, T., et al.: Experimental and numerical study of viscoelastic properties of polymeric interlayers used for laminated glass: determination of material parameters. Materials **12**(14), 2241 (2019). https://doi.org/10.3390/ma12142241
11. Vedrtnam, A., Pawar, S.J.: Experimental and simulation studies on fracture of laminated glass having polyvinyl butyral and ethyl vinyl acetate interlayers of different critical thicknesses due to impact load. Glass Technol. Eur. J. Glass Sci. Technol. Part A **58**(6), 169–178 (2017). https://doi.org/10.13036/17533546.58.6.005
12. Vedrtnam, A., Pawar, S.J.: Experimental and simulation studies on fracture and adhesion test of laminated glass. Eng. Fract. Mech. **190**, 461–470 (2018). https://doi.org/10.1016/j.engfracmech.2017.12.044
13. Teotia, M., Soni, R.: Applications of finite element modelling in failure analysis of laminated glass composites: a review. Eng. Fail. Anal. **94**, 412–437 (2018). https://doi.org/10.1016/j.engfailanal.2018.08.016
14. Zemanova, A., Zeman, J., Sejnoha, M.: Comparison of viscoelastic finite element models for laminated glass beams. Int. J. Mech. Sci. **131–132**, 380–395 (2017). https://doi.org/10.1016/j.ijmecsci.2017.05.035
15. Smetankina, N.V., Shupikov, A.N., Sotrikhin, S.Yu., Yareschenko, V.G.: A noncanonically shape laminated plate subjected to impact loading: theory and experiment. J. Appl. Mech. Trans. ASME **75**(5), 051004-1–051004-9 (2008). https://doi.org/10.1115/1.2936925
16. Gogotsi, G.A., Galenko, V.Y.: Sensitivity of brittle materials to local stress concentrations on their fracture. Strength Mater. **54**(2), 250–255 (2022). https://doi.org/10.1007/s11223-022-00398-z

17. Denham, C.L., Jansen, R.H.: Initial regulatory and certification approach for the SUSAN electrofan concept. In: AIAA Science and Technology Forum and Exposition (AIAA SciTech Forum), AIAA 2022–2180, San Diego, CA (2022). https://doi.org/10.2514/6.2022-2180
18. Kantor, B.Ya., Smetankina, N.V., Shupikov, A.N.: Analysis of non-stationary temperature fields in laminated strips and plates. Int. J. Solids Struct. **38**(48/49), 8673–8684 (2001). https://doi.org/10.1016/S0020-7683(01)00099-3
19. Shupikov, A.N., Smetankina, N.V.: Non-stationary vibration of multilayer plates of an uncanonical form. The elastic immersion method. Int. J. Solids Struct. **38**(14), 2271–2290 (2001). https://doi.org/10.1016/S0020-7683(00)00166-9
20. Li, K., Jiang, X., Wei, D.: Numerical simulation of bird strike on a s-shaped stealth inlet. In: Zhang, X. (ed.) APISAT 2018. LNEE, vol. 459, pp. 1696–1706. Springer, Singapore (2019). https://doi.org/10.1007/978-981-13-3305-7_136
21. Muniz-Calvente, M., Ramos, A., Fernández, P., Lamela, M.J., Álvarez, A., Fernández-Canteli, A.: Probabilistic failure analysis for real glass components under general loading conditions. Fatigue Fract. Eng. Mater. Struct. **2019**, 1–9 (2019). https://doi.org/10.1111/ffe.13011
22. Ojoc, G.G., Chiper Titire, L., Munteniță, C., Pîrvu, C., Sandu, S., Deleanu, L.: Ballistic response of a glass fiber composite for two levels of threat. Polymers **15**(4), 1039 (2023). https://doi.org/10.3390/polym15041039
23. Samieian, M.A., et al.: Temperature effects on laminated glass at high rate. Int. J. Impact Eng. **111**, 177–186 (2018). https://doi.org/10.1016/j.ijimpeng.2017.09.001
24. Demin, W., Li, D., Zhang, Z.: Simulation study of low-velocity impact on polyvinyl butyral laminated glass based on the combined TCK-JH2 model. Appl. Sci. **9**(15), 3204 (2019). https://doi.org/10.3390/app9153204
25. Naumenko, K., Altenbach, H.: Laminated plates with non-linear visco-elastic interlayer: the governing equations. In: Altenbach, H., Chinchaladze, N., Kienzler, R., Müller, W. (eds.) Analysis of Shells, Plates, and Beams. Advanced Structured Materials, vol. 134, pp. 297–310. Springer, Cham (2020). https://doi.org/10.1007/978-3-030-47491-1_15
26. Li, Z., Wang, Y.: Experiment and simulation of critical parameters for building windows under thermal explosion. Case Stud. Thermal Eng. **26**, 101014 (2021). https://doi.org/10.1016/j.csite.2021.101014
27. Wang, X., Zhong, B., Tang, J., Gao, C., Li, M.: Study on the influence of window glass size on blast-resistant performance. Sustainability **15**, 9325 (2023). https://doi.org/10.3390/su15129325
28. Ranocchiai, G., Zulli, F., Andreozzi, L., Fagone, M.: Test methods for the determination of interlayer properties in laminated glass. J. Mater. Civ. Eng. **29**, 1–8 (2017). https://doi.org/10.1061/(asce)mt.1943-5533.0001802
29. Zhang, Z., et al.: Impact response of laminated glass with varying interlayer materials. Int. J. Impact Eng **139**, 103505 (2020). https://doi.org/10.1016/j.ijimpeng.2020.103505
30. Zemanova, A., Hala, P., Konrad, P., Sovjak, R., Sejnoha, M.: Gradual fracture of layers in laminated glass plates under low-velocity impact. Comput. Struct. **283**, 107053 (2023). https://doi.org/10.1016/j.compstruc.2023.107053
31. Wüest, T., Fildhuth, T., Luible, A.: New Swiss technical specification SIA 2057 for glass structures and its post failure limit state concept. Glass Struct. Eng. **8**(3), 339–351 (2023). https://doi.org/10.1007/s40940-023-00227-y
32. Fildhuth, T., Joos, P., Wüest, T., Haller, M., Stevels, W.: Development and behavior of a thin fitting connection for lamination with structural PVB. Glass Struct. Eng. **7**(3), 415–439 (2022). https://doi.org/10.1007/s40940-022-00198-6
33. Xin, Z., Wang, Y., Fu, Q., Cheng, H., Cheng, X., Zhang, J.: Effect of glass cover layer on the ballistic performance of transparent ceramic armor **47**(20), 29277–29284 (2021). https://doi.org/10.1016/j.ceramint.2021.07.092

34. Misura, S., Smetankina, N., Misiura, I.: Optimal design of the cyclically symmetrical structure under static load. In: Nechyporuk, M., Pavlikov, V., Kritskiy, D. (eds.) ICTM 2020. LNNS, vol. 188, pp. 256–266. Springer, Cham (2021). https://doi.org/10.1007/978-3-030-66717-7_21
35. Kurennov, S., Barakhov, K., Taranenko, I., Stepanenko, V.: A genetic algorithm of optimal design of beam at restricted sagging. Radioelectron. Comput. Syst. **1**(101), 83–91 (2022). https://doi.org/10.32620/reks.2022.1.06

Information Technology in the Design and Manufacture of Engines

Improving the Method of Quality Control of the Fuel Element Shell in Order to Improve the Safety of a Nuclear Reactor

Eduard Khomiak[1](✉), Viktoriia Burdeina[1], Olena Cherniak[2], Nechuiviter Olesia[2], and Tetiana Bubela[3]

[1] Ukraine National Aerospace University "Kharkiv Aviation Institute", Kharkiv, Ukraine
e.khomiak@khai.edu
[2] Ukrainian Engineering Pedagogics Academy, Kharkiv, Ukraine
[3] Lviv Polytechnic National University, Lviv, Ukraine

Abstract. The analysis of existing methods for controlling the quality of nuclear reactor fuel element shell was carried out and it was found that the methods use to detect surface and internal defects is characterized by limited efficiency and requires additional assessment. To evaluate the quality of the surface of the shell material in case of damage and destruction, it is proposed to use a computing device based on the method of fractal theory. It is proposed to use the fractal properties of the structure and the quantitative fractal values. These values make it possible to estimate the degree of the shell material volume change during depressurization of the fuel element. The mathematical model has been developed to describe the process of destruction of the fuel element shell material under the simultaneous impact of high temperature and internal pressure. The criterion for assessing the quality of the fuel element shell integrity has been developed, which considers changes in fuel element shell geometric parameters during damage and destruction of the structure. The obtained practical recommendations can be used to implement the proposed method of quality control of fuel elements shell integrity in modern control system of a nuclear power plant power unit. This method application will make it possible to detect potential depressurization of fuel elements at an earlier stage, which, in comparison with standard methods, can increase the efficiency of the quality control system for the tightness of the shells.

Keywords: quality assessment method · fuel element · control system · structure damage

1 Introduction

The integrity of fuel element shell as main element of nuclear power plant reactor core is one of the most important safety factors.

The analysis of existing control methods showed that they cannot monitor the dynamics of the process of damage and destruction of fuel element shell, and cannot determine

M. Nechyporuk et al. (Eds.): ICTM 2023, LNNS 1008, pp. 351–360, 2024.
https://doi.org/10.1007/978-3-031-61415-6_30

the criteria for shell depressurization. For this reason, it was proposed to develop a quality criterion for the parameters of the structure of fuel element shell based on the use of fractal geometry. This criterion makes it possible to determine the quality of fuel element tightness in real time [1].

The concepts of "risk", "quality" and "safety" are complex, since the quality of fuel element shell is closely related to production and operation. Therefore, nowadays there are regulations and requirements for product quality. Comprehensive fulfillment of such requirements improves the quality of production and operation of fuel elements [2–4].

Thus, to improve the safety, quality, reliability, and economic operation of fuel assemblies of nuclear reactors, an urgent problem is the need to control the process of fuel shell damage accumulation and determine the criterion for fuel assembly depressurization in an automated mode, i.e., quickly, in real time [5–7].

Therefore, the use of automated methods for monitoring the integrity or damage to the fuel element shell to assess the quality of tightness or criterion of depressurization of the fuel element shell is an urgent task and the main factor in the safe and reliable operation of fuel elements [8, 9].

The article aims to enhance the reliability and safety of nuclear reactors in power plants by introducing a quality criterion for fuel element parameters. The proposal suggests criteria for evaluating these parameters utilizing fractal geometry, providing a means to consider changes in geometric factors (external and internal dimensions, shell diameter, and thickness) within the internal structure of the fuel element shell.

2 Materials and Methods

Destructive and non-destructive testing methods are used to inspect the fuel rod shells.

Destructive methods in the process of control destroy the fuel element shell and are used only in production. Therefore, the paper considers non-destructive methods that control the external and internal structure of the fuel element shell during their operation.

Since the causes of fuel element depressurization include: hydrogenation of the fuel shell due to the presence of moisture in the fuel; corrosion of the fuel shell; interaction of the shell with foreign objects in the reactor coolant; interaction of the shell with fuel pellets in the reactor coolant; interaction of the shell with fuel pellets - it is necessary to take these factors into account. These factors should be taken into account in the methods of fuel element shell leakage control, which include:

1. Capillary methods are based on the capillary penetration of indicator liquid droplets into the cavities of surface defects. In the process of control by these methods, a permeable liquid is applied to the cleaned surface of the part a permeable liquid is applied to the cleaned surface of the part, which fills the cavities of surface defects. Then the liquid is removed, and the remaining part of the defect cavities is detected with a developer, which forms an indicator pattern. Capillary flaw detection cannot be used for in-service monitoring of fuel elements. The process of detecting surface defects by the capillary method is shown schematically in dynamics in (Fig. 1).

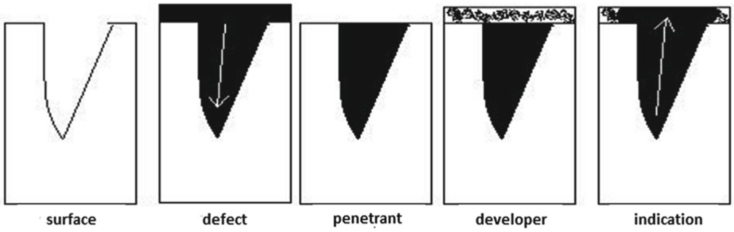

Fig. 1. Diagram of the control sequence by the capillary method

2. The radiographic method of inspection is based on the ability of X-rays to penetrate through the metal and affect the photosensitive X-ray film located on the reverse side of the weld, allowing to control material defects (e.g., micropores, macrocracks).

   When the fuel element shell is penetrated, β-rays and X-rays are absorbed differently by different substances.

   The intensity of X-rays as they pass through a substance change according to the expression 1.

$$I = I_0 \varepsilon^x \tag{1}$$

   where I – is the radiation intensity after passing through the absorber layer; I_0 – is the initial radiation intensity, imp./s; ε – is the nonlinear absorption coefficient by the substance; x – is the thickness of the of the absorber layer.

   It follows from expression (1) that the radiation intensity depends on the thickness of the shell layer of the fuel element, which changes during the operation of the fuel element.

3. Radio wave methods consist in recording changes in the parameters of electromagnetic waves of the radio range in the case of interaction with the material of the fuel element shell surface.

   Usually, waves of the ultra-high frequency (UHF) range with a length of 1…100 mm are used to control fuel elements. Since the radio wave method consists in registering changes in the parameters of electromagnetic waves of the radio range, it is necessary to take into account the appearance of micropores and macrocracks in the surface structure of the fuel element shell in case of their interaction with the material of the fuel element shell.

4. The mass spectrometric method is based on the use of helium as an indicator gas, which is introduced under the fuel shell.

   introduced under the fuel element shell, so it can be used to detect the process of shell depressurization by the percentage of gas in the coolant. Principle of leakage control A fuel element using the gas-filled chamber method is shown in (Fig. 2).

   We can see that the leak detector can determine the relative amount of helium coming out of the fuel element, thus allowing us to detect small holes, cracks in the fuel element shells and welds. As a disadvantage, it should be noted that in the presence of significant through defects in fuel element shell, this control method may not give correct readings, because during vacuuming, all helium can escape from under the fuel element shell.

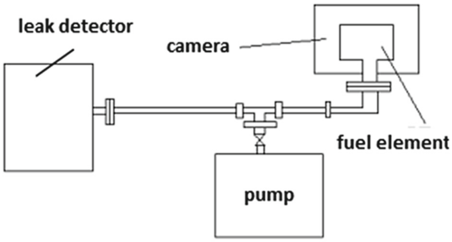

Fig. 2. Structural and functional diagram of the method of gas-filled chamber

5. Method of acoustic-emission control of the shell TVEL. Acoustic emission is a phenomenon of propagation of of elastic vibrations (acoustic waves) generated by by a sudden deformation of a stressed material.

   The vibrations propagate from the radiation source to the sensor(s), where they are converted into electrical signals. AE devices record these signals and display the data on the screen in the form of oscillograms, locations, digital indications, based on which the operator can assess the state and behavior of the structure of the material under tension, detect and locate defects.

   Acoustic emission control: detects developing defects, what is the most dangerous defects. This method is remote, it does not require scanning the surface of the object to find local defects, but only the correct placement of sensors on the surface of the object to locate the source of acoustic emission.
6. Eddy current flaw detection method. The fuel element is removed from the fuel assembly (FA) using a using a special tool, is installed in a case and passes through an eddy current converter. At the same time, the fuel element shell is inspected.

   The analysis of the control results is carried out by comparing the response parameters from artificial defects of the control sample and anomalies detected during eddy current scanning of the fuel element under test. For the initial assessment of the fuel element condition, a scan of the main program window with with the results of the VS scan, shown in (Fig. 3a), which allows us to quickly identify areas of the shell with defects. The characteristics of the detected anomaly are evaluated by the strength (scans of Fig. 3b) and bending characteristics obtained for different moments of gating of the output signal of the eddy current converter (Fig. 3c). These bending characteristics are used also for constructing defect histograms and presenting inspection results in the traditional form (Fig. 3d).

   The parameters of the hodograph (shape, amplitude, angle of inclination) are used to assess the condition of the shell in the abnormal area. The phase and amplitude of the pulse signal hodographs for different shell defects qualitatively correlate with each other similarly to the hodographs of a harmonic signal.

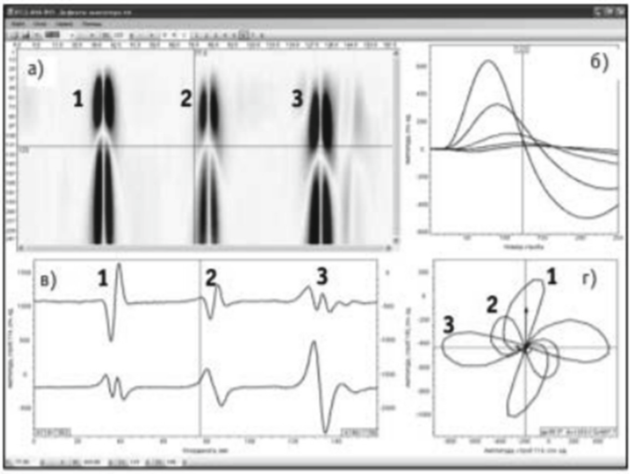

Fig. 3. The main window of the program with the results of the fragment's VS control of the simulator with: 1 - external; 2 - through; 3 - internal defects; a - D-scan; b - A-scans in the vicinity of the through defect; c - VSP bypass signals; d - hodographs

3 Results

The paper proposes that the main physical process of damage accumulation is the creep of the fuel element shell material under the influence of destructive factors for real operating modes of a WWER nuclear reactor.

Therefore, the development of a method for controlling the depressurization (damage) of the fuel element shell consists in determining the parameter of damage to the shell material, which is determined by formula (2):

$$\omega(r) = \frac{A(r)}{A_0} = 1 \tag{2}$$

where $A0$ is the specific scattering characterizing the change in the fuel element shell material;

A(r) is the specific scattering that characterizes the damage intensity over time τ; it depends on the pressure P and temperature T inside the fuel element shell, as well as the fractal increase in the geometric parameters ΔH and is determined by the formula (3):

$$A(r) = F(P, T, \Delta H), \tag{3}$$

It should be noted that local inhomogeneities, micropores, and cracks are formed in the fuel element shell material under the influence of inert gas pressure as a result of a nuclear reaction (temperature rise above 360 °C, exposure to radioactive radiation, etc.). Therefore, the structure of the fuel element shell material is subject to stretching, swelling, and creep, i.e., it assumes an anisotropic, and, therefore, has specific fractal cluster properties.

In addition, on the basis of formulas (2) and (3), a criterion for assessing the tightness or depressurization of the fuel element shell was proposed.

A fuel shell is considered to be sealed if the condition (4):

$$\omega(r) \leq 1, \tag{4}$$

A fuel element is considered to be leaky if the condition according to expression (5):

$$\omega(r) > 1 \tag{5}$$

Thus, the method of controlling the tightness of the fuel element shell was improved by developing a mathematical model that takes into account the fractal properties of the material structure when it is damaged and the conditions for the criterion for assessing the state of the fuel element were determined.

4 Discussion

Ensuring the tightness of fuel element shells is crucial for their safety during operation, storage, and transportation. However, depressurization issues can occur in WWER nuclear reactors. Identifying and unloading assemblies with leaks requires reactor shutdown, causing economic losses. Predicting radioactive contamination and fuel assembly behavior post-depressurization necessitates model development, control methods, and criteria for permissible leaks. Determining causes and implementing measures are essential to reduce depressurization events. Post-reactor research provides comprehensive and reliable information for addressing these challenges.

During WWER nuclear reactor operation, fuel shell corrosion, exposure to fission products, fuel impurities, mechanical impact, and radiation damage can lead to depressurization. Identifying causes, such as technological defects, moisture, burnup/power exceedance, and design imperfections, allows for preventive measures. Established global causes include defects in shell, welds, fuel pellets, and assemblies, as well as issues like contamination, clogging, and damage during maintenance. Causes are categorized as constructive, technological, and operational, involving collaboration among designers, manufacturers, suppliers, and consumers to address depressurization concerns [10–12].

Mechanisms of fuel element depressurization include shell flattening, primary hydrogenation, corrosion (uniform, localized, under deposits), fretting corrosion of casing, shell damage, and fuel interaction with the shell. Occasionally, undetected defects formed during manufacturing contribute. Analysis reveals that in 60% of WWER-1000 nuclear reactor cases, depressurization is due to foreign objects entering the fuel element bundle (operational cause). Two cases involve fretting corrosion between fuel shells, and two (20%) result from technological reasons—internal hydrogenation of the shell [13–15].

Defects in WWER-1000 fuel assembly shells are randomly distributed along the cross-section and are primarily recorded in the area of the beam support lattice or under the lower spacer grids. In fuel assemblies with internal hydrogenation, defects span almost the entire height of the fuel core, making it challenging to separate primary from secondary defects. Post-reactor research revealed that the cause of depressurization in all studied WWER-1000 fuel assemblies was damage to their shells by foreign objects in the coolant flow. The lower end cap of the fuel element experienced the most significant hydrogenation during the formation of secondary defects [16].

Metallographic research [17] revealed that the material structure of the fuel element shell in both leaky and sealed fuel shells is fragmented in cross-section, primarily by radial cracks into several parts. Most of these cracks traverse the entire central zone of the shell material structure. Cross-sections of through defects in leaky fuel shells show more fragmentation compared to the rest of the core. Erosion of pellets, characterized by an enlarged central hole and the absence of a segment, was detected near through defects in leaky fuel shells. Some sections of leaky fuel shells exhibited a reduction in the diameter of the central hole of the pellet. In the peripheral zone of the central structure, the grain size and porosity of leaky fuel shells were almost the same as in sealed fuel shells.

Grain size changes and increased porosity suggest a significant temperature rise (exceeding 1200 °C) in the central zone of the shell material structure in leaky fuel assemblies. This temperature surge results from steam filling the gap between pellets and the shell and reduced thermal conductivity due to an elevated oxygen coefficient ratio. The temperature increase leads to the release of gaseous and volatile fission products beyond the grain boundaries. In certain leaky fuel assemblies, swelling and thermal expansion of the fuel shell occurred due to the mechanical impact of the fuel core on the shell after the gap between them closed [18]. The primary operational factor influencing the temperature of the fuel element shell is the linear power of the fuel shell. Quantitative assessments of inert gases escaping from a leaky fuel element were derived from metallography and gamma-ray spectrometry measurements.

Established processes occurring in the material of WWER fuel shells during operation include radiation hardening and plasticity reduction, radiation and thermal creep, radiation growth, thermomechanical interaction between fuel and shell, and fuel shell deflection associated with thermomechanical interaction in the shell [19–21]. Changes in the fuel element's diameter and length during operation result from dimensional alterations in the shell. Initially, under excessive coolant pressure, the diameter decreases. As burnup increases, this decrease slows to zero, and the shell diameter starts to increase. Simultaneously, with the decrease in shell diameter, the diameter of the fuel pellets increases, indicating fuel swelling and leading to a change in the structure of the fuel element shell material. Considering the analysis of these processes and their consequences, it is proposed to understand the formation of primary and secondary defects in the fuel element shell based on the fractal cluster theory. The process of defect formation in the structure of the fuel element shell material is illustrated in (Fig. 4).

Under the influence of fracture factors on the outer and inner surfaces of the fuel element shell material, primary defects emerge in the form of micropores up to 5 μm in size, considered separate clusters according to the cluster theory. An increase in the number of these micropores results in the formation of macropores up to 500 μm and the creation of cluster aggregations. Subsequently, with elevated temperature, pressure, and increased inert hazardous gas concentration, macropores (cluster aggregations) coalesce, leading to the development of through macrocracks (cluster-cluster structures) and, consequently, the occurrence of a secondary defect in the fuel element shell. The cluster-cluster structure arising from the secondary defect is a porous heterogeneous structure exhibiting specific fractal properties (Fig. 4).

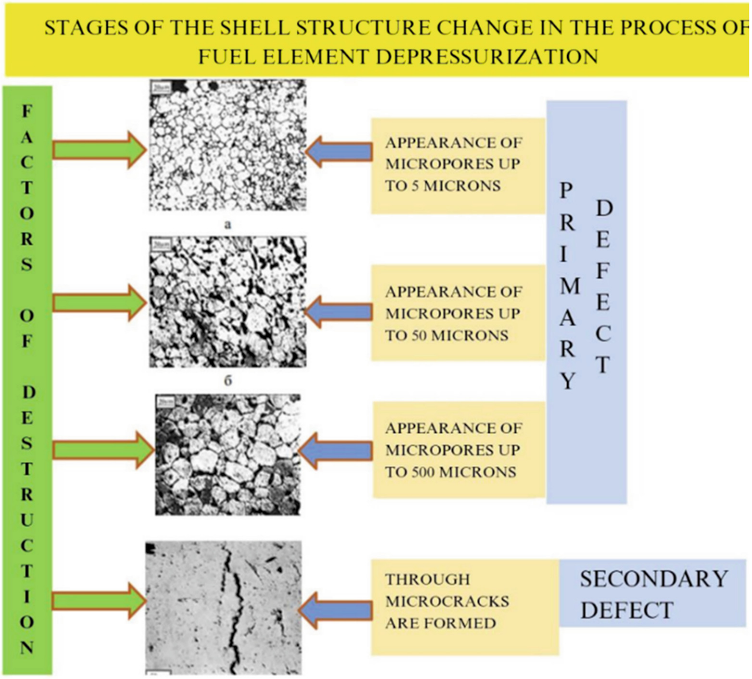

Fig. 4. The process of formation of primary and secondary defects in case of damage to the structure of the fuel element shell material

Hence, it is recommended to investigate the mechanism of damage to the outer and inner surfaces of the material structure during the formation of defects in the fuel element shell to establish depressurization, utilizing the computational framework of the fractal cluster theory. Existing studies lack a method for calculating damage to the fuel shell material leading to its depressurization during fuel element operation [22].

Despite the current understanding of the fuel element shell depressurization process in normal operating conditions of a WWER nuclear reactor, the mechanism remains unknown in approximately 20% of cases [23].

Consequently, operating WWER nuclear reactors lack the technical means, procedures, and algorithms to pinpoint the location of the damaged fuel element in the nuclear reactor core or to localize the defect in the fuel element shell where depressurization occurred [24].

5 Conclusions

A mathematical model has been devised, indicating that the fuel element shell material's damage parameter is notably influenced by the fractal properties of the material structure.

It was found that the depressurization of the fuel element shell depends on the degree of fractal dimension of geometric quantities, such as volume, area, length, inner and outer diameter of the shell.

The ultimate outcome of this study is the identification of defects in the fuel element shell material and the transmission of this information to the automated operator's station, detailing the detected defects and their locations on the fuel element.

This research may be of interest to scientists, engineers, and nuclear power professionals involved in the safety of nuclear power plants, especially in the management and monitoring of the technical condition of nuclear reactors and components, such as fuel elements. The data can also be useful for research teams investigating materials and structures used in nuclear power plants to improve their reliability and safety.

References

1. Budanov, P., Brovko, K., Khomiak, E., Tymoshenko, O.: Improvement of the method of controlling the fuel element shell to improve the safety of a nuclear reactor. Bull. Kharkiv Polytech. Inst. **1**, 26–31 (2020). https://doi.org/10.2998/2224-0349.2020.01.04
2. Trishch, R., Nechuiviter, O., Hrinchenko, H., Bubela, T., Riabchykov, M., Pandova, I.: Assessment of safety risks using qualimetric methods. MM Sci. J., 6668–6674 (2023). https://doi.org/10.17973/MMSJ.2023_10_2023021
3. Kupriyanov, O., Trishch, R., Dichev, D., Bondarenko, T.: Mathematic model of the general approach to tolerance control in quality assessment. In: Tonkonogyi, V., Ivanov, V., Trojanowska, J., Oborskyi, G., Pavlenko, I. (eds.) Advanced Manufacturing Processes III. InterPartner 2021. LNME, pp. 415–423. Springer, Cham (2022). https://doi.org/10.1007/978-3-030-91327-4_41
4. Trishch, R., Cherniak, O., Kupriyanov, O., Luniachek, V., Tsykhanovska, I.: Methodology for multi-criteria assessment of working conditions as an object of qualimetry. Eng. Manag. Prod. Serv. **13**(2), 107–114 (2021). https://doi.org/10.2478/emj-2021-0016
5. Trishch R., Nechuiviter O., Dyadyura K., Vasilevskyi O., Tsykhanovska I., Yakovlev M.: Quasimetric method of assessing risks of low-quality products. MM Sci. J., 4769–4774 (2021). https://doi.org/10.17973/MMSJ.2021_10_2021030
6. Trishch, R., Maletska, O., Cherniak, O., Semionova, J., Jancis, V.: Analysis of the requirements of international and national standards for measurement methods and metrological equipment. Innov. Technol. Sci. Solut. Ind. **1**(11), 156–162 (2020). https://doi.org/10.2478/mspe-2022-0037
7. Panda, A., Anisimov, V., Dyadyura, K., Pandova, I.: The usage of material quality indicators to assess the properties of linear block-copolyurethanes based on oligoeters. MM Sci. J., 5979–5983 (2022). https://doi.org/10.17973/MMSJ.2022_11_2022020
8. Khomiak, E., Budanov, P., Kirisov, K.: Modern approaches and requirements for methods of controlling the hermeticity of the fuel element shell. VPI Bull. **1**(3), 11–16 (2022). https://doi.org/10.31649/1997-9266-2022-162-3-11-16
9. Budanov, P., Khomiak, E., Kyrysov, I., Brovko, K., Kalnoy, S., Karpenko, O.: Building a model of damage to the fractal structure of the shell of the fuel element of a nuclear reactor. Eastern-Eur. J. Enterpr. Technol. **4**(8(118)), 60–70 (2022). https://doi.org/10.15587/1729-4061.2022.263374
10. Yong, S., Linzi, Z.: Robust deep auto-encoding network for real-time anomaly detection at nuclear power plants. Process Saf. Environ. Prot. **163**, 438–452 (2022). https://doi.org/10.1016/j.psep.2022.05.039

11. Bilodid, Ie., Dudka, O., Kovbasenko, Yu.: Analysis of corium criticality in VVER440 during severe accident. In: 29th Symposium of AER on VVER Reactor Physics and Reactor Safety, pp. 22–29. Energoland, Mochovce NPP, Slovakia (2019). http://www.aer-web.com/2019/paper/73
12. Abdul, K., Afzal, A., Mohammed, A.D., Ramis, M.K.: Effect of shell on thermal behavior of nuclear fuel element with non-uniform heat generation. Prog. Nucl. Energy **111**, 1–14 (2019). https://doi.org/10.1016/j.pnucene.2018.10.013
13. Fiorina, C., Clifford, I., Kelm, S., Lorenzi, S.: On the development of multi-physics tools for nuclear reactor analysis based on OpenFOAM: state of the art, lessons learned and perspectives. Nucl. Eng. Des. **387**, 1–15 (2022). https://doi.org/10.1016/j.nucengdes.2021.111604
14. Papin, J.: Behavior of fast reactor fuel during transient and accident conditions. Comprehensive Nucl. Mater. **2**, 339–362 (2019). https://doi.org/10.1016/B978-0-08-102865-0.00039-X
15. Bilodid, I., Dudka, O., Kovbasenko, Y.: Analysis of criticality during a severe accident in VVER-1000 spent fuel pools. Nucl. Radiat. Saf. **3**(91), 11–21 (2021). https://doi.org/10.32918/nrs.2021.3(91).02
16. Saeed, A., Rashid, A.: Development of core monitoring system for a nuclear power plant using artificial neural network technique. Ann. Nucl. Energy **144**, 513–518 (2020). https://doi.org/10.1016/j.anucene.2020.107513
17. Budanov, P., Kyrysov, I., Brovko, K., Rudenko, D., Vasiuchenko, P., Nosyk, A.: Development of a solar element model using the method of fractal geometry theory. Eastern-Eur. J. Enterpr. Technol. **3/8**(111), 75–89 (2021). https://doi.org/10.15587/1729-4061.2021.235882
18. Morkin, M.S.: Features of methods for monitoring the fuel shell tightness in leadcooled fast breeder reactors. Nucl. Energy Technol. **7**(4), 319–325 (2019). https://doi.org/10.3897/nucet.7.78372
19. Jovica, R.: Riznic: pressurized heavy water reactors CANDU. JSME Ser. Thermal Nucl. Power Gener. **7**, 45–68 (2022). https://doi.org/10.1016/B978-0-12-822054-2.00027-1
20. Hrinchenko, H., Trishch, A.: Technical diagnostics and features of measuring NPP power equipment parameters. Am. J. Eng. Res. (AJER) **10**, 269–274 (2021). https://www.ajer.org/papers/Vol-10-issue-5/ZH1005269274.pdf
21. Stary, M., Novotny, F., Horak, M., Stara, M.: Sampling robot for primary circuit pipelines of decommissioned nuclear facilities. Autom. Constr. **119**, 103–303 (2020). https://doi.org/10.1016/j.autcon.2020.103303
22. Tsitsimpelis, I., Taylor, J., Lennox, B., Joyce, J.: A review of ground-based robotic systems for the characterization of nuclear environments. Prog. Nucl. Energy **111**, 109–124 (2019). https://doi.org/10.1016/j.pnucene.2018.10.023
23. Song, B., Park, J., Yun, D.: Depth-adaptive controller for spent nuclear fuel inspections. Nucl. Eng. Technol. **52**(8), 1669–1676 (2020). https://doi.org/10.1016/j.net.2020.01.019
24. Belles, R.J.: Key reactor system components in integral pressurized water reactors (iPWRs). In: Handbook of Small Modular Nuclear Reactors, pp. 95–115 (2021). https://doi.org/10.1016/B978-0-12-823916-2.00005-9

Transient Motions of Solid Propellant Motor Casing at Launch Vehicle Liftoff

Maryna Chernobryvko[2], Konstantin Avramov[1,2,3](✉), Igor Marshuba[2], Viktor Vasechko[2], and Anatolii Kyrpikin[1]

[1] Department of Aircraft Strength, National Aerospace University, N.Ye. Zhukovsky, "KhAI", St. Chkalov 17, Kharkiv 61070, Ukraine
kvavramov@gmail.com

[2] A. Pidhornyi Institute of Mechanical Engineering Problems, National Academy of Science of Ukraine, St. Pozhars′koho 2/10, Kharkiv 61046, Ukraine

[3] Kharkiv National University of Radio Electronics, Kharkiv, Ukraine

Abstract. Use of the composite materials for manufacturing of thin-walled elements of launch vehicle gives several advantages in comparison with traditional materials. The main advantages are high strength of the structure with small mass. Solid propellant motor casing manufactured from carbon-filled plastic is considered. This material is orthotropic. The purpose of this study is development of numerical methods for dynamic deformation of solid propellant motor casing, which is considered as thin-walled structure. The internal impulse excitation acts on the casing of launch vehicle. The compound spherical-cylindrical-spherical shell describes the considered casing under the action of impact pressure. The shear theory is used in simulation. The software for this problem calculation is developed. The verification of the software is carried out by comparison of the obtained results with finite element calculations in the commercial software ANSYS. Dynamic stress state of the motor casing is carried out. The behavior of displacements projections and stress tensor in time are the results of this analysis. Time of growth of impact pressure is equal to 5 ms, Note, that the maximal values of displacements and elements of strain tensor are observed at 10 ms. Thus, the displacements and stresses continue to increase, when the impact pressure stops to increase.

Keywords: Stress State · Orthotropic Material · Equations of Thin-Walled Structure · Compound Shell

1 Introduction

Rockets casings including solid propellant motors casings are manufactured frequently from composite materials. The application of composite materials for launch vehicle thin-walled structures gives several advantages in comparison with traditional materials. The main advantage is increase of the structure strength and decrease of mass. Different criterions are used to calculate the parameters of solid propellant motor casing. For example, the stresses of the thin- walled casings satisfy the strengths criterion.

M. Nechyporuk et al. (Eds.): ICTM 2023, LNNS 1008, pp. 361–372, 2024.
https://doi.org/10.1007/978-3-031-61415-6_31

The purpose of this study is analysis of transient behavior of solid propellant motor composite casing under the action of a pulse pressure, which describes the operation of the engine. The motor casing consists of two truncated hemisphere and the cylindrical shell. Two edges of the bottoms are clamped. Shear, rotary inertia and Hooke's law for the orthotropic material are taken into account. The semi analytical technique is developed to analyze the thin-walled structure stress state. The dynamic of the structure is described by system of linear ordinary differential equations.

2 Literature Review

Important tasks for the designer of solid propellant rocket motors are the determination of the limiting conditions, when the motors may be operated without failure [1]. Operational forces of motor casing result in stress and strain values, which is higher than material capability. This leads to failure of the motor [2]. An elastic cylinder is used to model a solid-propellant rocket motor. Dynamic finite element model is suggested by Wu, Li and Lu [3] to analyze the rocket motor dynamic response. As follows from this paper, the structure dynamic behavior is important to study the structure integrity. Several motor configurations under the action of different loads are studied numerically to preserve the structural integrity [4]. Qu and Zhan [5] suggest the finite element model to compute the Mises stresses amplitudes. Composite casing of solid propellant has material mechanical properties, which depends on strain rate [6]. Su with co-authors [7] measure response of composite propellant coupled with gas flow. Fracture of shell structures under the action of impulse loads are discussed in [8, 9].

Many efforts were carried out to study the composite thin-walled structure dynamics. Shear deformation is accounted to describe the composite shell vibrations in [10]. Reddy shear theory is suggested to analyze multilayers thin-walled structures [11].

3 Research Methodology

3.1 The Problem Formulation and the Main Equations

The compound structure has three parts: right truncated hemispherical shell, cylindrical shell and left truncated spherical shell. This compound structure is shown on Fig. 1. The hemispherical shells have the radius R. The bottom heights are H_1 and H_2 (Fig. 1). The compound structure is clamped at two ends. The middle cylindrical shell length and radius are denoted L and R. The most part of the compound structure has constant thickness h. Thickness is changed from h to 2 h in the region, where two structures are jointed.

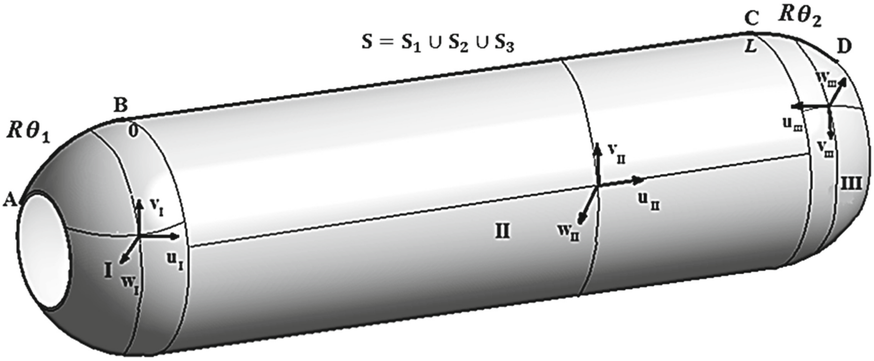

Fig. 1 Thin-walled structure of solid propellant motor

The internal pulse pressure acts on the shell (Fig. 1), which describes the motor operation. The pressure $P_z(t)$ behavior in time is divided on three parts. The linear pressure growth in time occur on the first interval $t < t^*$. On the second interval $t^* \leqslant t < t^{**}$, the pressure has constant value $P_{\max}$. The pressure is decreased on the third interval $t \geqslant t^*$.

As the radial displacements have small values in comparison with shell thickness, the strains-displacements relations are linear. The material of the structure (Fig. 1) is elastic, therefore the Hooke's law is satisfied. The shear is accounted in the structure model.

The middle surface displacements are the unknowns of the considered problem. The points of the cylindrical part middle surface are defined by longitudinal and circumference coordinates (x,ϕ). Perpendicular to the middle surface is denoted by z axis. The projections of the middle surface displacements of the cylindrical shell are the following: $\tilde{u}_x(x, \phi, t)$, $\tilde{u}_\phi(x, \phi, t)$, $\tilde{u}_z(x, \phi, t)$. The coordinate curves take the following values: $0 \leqslant x \leqslant L$, $0 \leqslant \phi < 2\pi$, $-h(x)/2 \leqslant z \leqslant h(x)/2$.

The structure bottoms are analyzed in the spherical coordinates (θ, ϕ). The bottoms middle surfaces displacements projections are $\tilde{u}_\theta(\theta, \phi, t)$, $\tilde{u}_\phi(\theta, \phi, t)$, $\tilde{u}_z(\theta, \phi, t)$.

As the compound structure has orthotropic material, the cylindrical shell mechanical properties are the following: the shear moduli $G_{x\phi}$, G_{xz}, $G_{\phi\ z}$;the Young's moduli E_{xx}, $E_{\phi\phi}$; the Poisson ratios $\mu_{x\phi}$, $\mu_{\phi x}$. The orthotropic bottoms are described by the following mechanical properties: $E_{\theta\theta}$, $E_{\phi\phi}$; $G_{\theta\phi}$,$G_{\theta z}$, $G_{\phi z}$; $\mu_{\theta\phi}$, $\mu_{\phi\theta}$.

The arbitrary point (x, ϕ, z) of cylindrical shell has displacements $u_x(x, \phi, z, t), u_\phi(x, \phi, z, t), u_z(x, \phi, z, t)$ and the rotation angles of the normal to the middle surface $\tilde{\beta}_x(x, \phi, t),\ \tilde{\beta}_\phi(x, \phi, t)$ [12]:

$$\begin{aligned}
&u_x(x, \phi, z, t) = \tilde{u}_x(x, \phi, t) + z\,\tilde{\beta}_x(x, \phi, t),\\
&u_\phi(x, \phi, z, t) = \tilde{u}_\phi(x, \phi, t) + z\,\tilde{\beta}_\phi(x, \phi, t),\\
&u_z(x, \phi, z, t) = \tilde{u}_z(x, \phi, t).
\end{aligned} \tag{1}$$

The strain tensor elements have the following form:

$$\varepsilon_{xx} = \tilde{\varepsilon}_{xx} + z\tilde{k}_{xx},\ \varepsilon_{\phi\,\phi} = \tilde{\varepsilon}_{\phi\,\phi} + z\tilde{k}_{\phi\,\phi},\ \varepsilon_{x\phi} = \tilde{\varepsilon}_{x\phi} + z\tilde{k}_{x\phi}, \tag{2}$$

$$\varepsilon_{xz} = \frac{\partial \tilde{u}_z}{\partial x} + \tilde{\beta}_x,\ \varepsilon_{\phi\,z} = \frac{1}{R}\frac{\partial \tilde{u}_z}{\partial \phi} - \frac{\tilde{u}_\phi}{R} + \tilde{\beta}_\phi \tag{3}$$

where $\tilde{k}_{xx}, \tilde{k}_{\phi\phi}, \tilde{k}_{x\phi}$ are curvature and torsion of the middle surface; $\tilde{\varepsilon}_{xx}, \tilde{\varepsilon}_{\phi\phi}, \tilde{\varepsilon}_{x\phi}$ are strains; $\varepsilon_{xx}, \varepsilon_{\phi\phi}, \varepsilon_{x\phi}$ are arbitrary point strains. The strains and curvature components have the form:

$$\tilde{\varepsilon}_{xx} = \frac{\partial \tilde{u}_x}{\partial x},\ \tilde{\varepsilon}_{\phi\phi} = \frac{1}{R}\frac{\partial \tilde{u}_\phi}{\partial \phi} + \frac{\tilde{u}_z}{R},\ \tilde{\varepsilon}_{x\phi} = \frac{\partial \tilde{u}_\phi}{\partial x} + \frac{1}{R}\frac{\partial \tilde{u}_x}{\partial \phi}, \tag{4}$$

$$\tilde{k}_{xx} = \frac{\partial \tilde{\beta}_x}{\partial x},\ \tilde{k}_{\phi\phi} = \frac{1}{R}\frac{\partial \tilde{\beta}_\phi}{\partial \phi},\ \tilde{k}_{x\phi} = \frac{\partial \tilde{\beta}_\phi}{\partial x} + \frac{1}{R}\frac{\partial \tilde{\beta}_x}{\partial \phi}\ . \tag{5}$$

The partial differential equations (PDEs) system of the structure motions are derived as:

$$\begin{aligned}
&\frac{E_{xx}}{1-\mu_{x\phi}\mu_{\phi\,x}}\left[\frac{\partial^2 \tilde{u}_x}{\partial x^2} + \frac{\mu_{x\phi}}{R}\left(\frac{\partial^2 \tilde{u}_\phi}{\partial x \partial \phi} + \frac{\partial \tilde{u}_z}{\partial x}\right)\right] + \frac{G_{x\phi}}{R}\left[\frac{\partial^2 \tilde{u}_\phi}{\partial x \partial \phi} + \frac{1}{R}\frac{\partial^2 \tilde{u}_x}{\partial \phi^2}\right] = \rho\frac{\partial^2 \tilde{u}_x}{\partial t^2}\\
&G_{x\phi}\left[\frac{\partial^2 \tilde{u}_\phi}{\partial x^2} + \frac{1}{R}\frac{\partial^2 \tilde{u}_x}{\partial x \partial \phi}\right] + \frac{1}{R^2}\frac{E_{\phi\phi}}{1-\mu_{x\phi}\mu_{\phi x}}\left[\frac{\partial^2 \tilde{u}_\phi}{\partial \phi^2} + \frac{\partial \tilde{u}_z}{\partial \phi} + \mu_{\phi x}\frac{\partial^2 \tilde{u}_x}{\partial x \partial \phi}\right] +\\
&\frac{\kappa\, G_{\phi z}}{R^2}\left[\frac{\partial \tilde{u}_z}{\partial \phi} - \tilde{u}_\phi + R\tilde{\beta}_\phi\right] = \rho\frac{\partial^2 \tilde{u}_\phi}{\partial t^2}\ ;\\
&\kappa G_{xz}\left[\frac{\partial^2 \tilde{u}_z}{\partial x^2} + \frac{\partial \tilde{\beta}_x}{\partial x}\right] + \frac{\kappa\, G_{\phi z}}{R^2}\left[\frac{\partial^2 \tilde{u}_z}{\partial \phi^2} - \frac{\partial \tilde{u}_\phi}{\partial \phi} + R\frac{\partial \tilde{\beta}_\phi}{\partial \phi}\right] -\\
&\frac{E_{\phi\phi}}{\left(1-\mu_{x\phi}\mu_{\phi\,x}\right)R^2}\left[\frac{\partial \tilde{u}_\phi}{\partial \phi} + \tilde{u}_z + R\mu_{\phi\,x}\frac{\partial \tilde{u}_x}{\partial x}\right] + P_z = \rho\frac{\partial^2 \tilde{u}_z}{\partial t^2}\ ;\\
&G_{x\phi}\left[\frac{\partial^2 \tilde{\beta}_\phi}{\partial x^2} + \frac{1}{R}\frac{\partial^2 \tilde{\beta}_x}{\partial x \partial \phi}\right] + \frac{E_{\phi\phi}}{R^2\left(1-\mu_{x\phi}\mu_{\phi x}\right)}\left[\frac{\partial^2 \tilde{\beta}_\phi}{\partial \phi^2} + R\mu_{\phi\,x}\frac{\partial^2 \tilde{\beta}_x}{\partial x \partial \phi}\right] -\\
&-\frac{12\kappa\, G_{\phi\,z}}{Rh^2}\left[\frac{\partial \tilde{u}_z}{\partial \phi} - \tilde{u}_\phi + R\tilde{\beta}_\phi\right] = \rho\frac{\partial^2 \tilde{\beta}_\phi}{\partial t^2}.
\end{aligned} \tag{6}$$

The truncated hemispherical shells are analyzed. The inequalities $\theta_1 \le \theta \le \pi/2$, $-2\pi < \phi \leqslant 0$, $-h(\theta)/2 \leqslant z \leqslant h(\theta)/2$; and $\theta_2 \leqslant \theta \leqslant \pi/2$, $0 \leqslant \phi < 2\pi$, $-h(\theta)/2 \leqslant z \leqslant h(\theta)/2$ are true for the left and right hemispherical shells, respectively. The projections of the bottoms displacements $u_\theta(\theta, \phi, z, t)$, $u_\phi(\theta, \phi, z, t)$, $u_z(\theta, \phi, z, t)$, the rotation angles of the normal to the middle surface $\tilde{\beta}_\theta(\theta, \phi, t)$, $\tilde{\beta}_\phi(\theta, \phi, t)$ and middle surface displacements $\tilde{u}_\theta(\theta, \phi, t)$, $\tilde{u}_\phi(\theta, \phi, t)$, $\tilde{u}_z(\theta, \phi, t)$ satisfies the equations [12]:

$$\begin{aligned} u_\theta(\theta, \phi, z, t) &= \tilde{u}_\theta(\theta, \phi, t) + z\tilde{\beta}_\theta(\theta, \phi, t)\ ; \\ u_\phi(\theta, \phi, z, t) &= \tilde{u}_\phi(\theta, \phi, t) + z\tilde{\beta}_\phi(\theta, \phi, t)\ ; \\ u_z(\theta, \phi, z, t) &= \tilde{u}_z(\theta, \phi, t). \end{aligned} \tag{7}$$

The displacements and the strains of the truncated hemispherical shells are the following:

$$\begin{gathered} \tilde{\varepsilon}_{\theta\theta} = \frac{1}{R}\frac{\partial \tilde{u}_\theta}{\partial \theta} + \frac{\tilde{u}_z}{R} + \frac{z}{R}\frac{\partial \tilde{\beta}_\theta}{\partial \theta}\ ; \\ \tilde{\varepsilon}_{\phi\phi} = \frac{1}{R\sin\theta}\frac{\partial \tilde{u}_\phi}{\partial \phi} + \frac{\tilde{u}_\theta}{R\tan\theta} + \frac{\tilde{u}_z}{R} + z\left(\frac{1}{R\sin\theta}\frac{\partial \tilde{\beta}_\phi}{\partial \phi} + \frac{\tilde{\beta}_\theta}{R\tan\theta}\right)\ ; \\ \tilde{\varepsilon}_{\theta\phi} = \frac{1}{R}\frac{\partial \tilde{u}_\phi}{\partial \theta} - \frac{\tilde{u}_\phi}{R\tan\theta} + \frac{1}{R\sin\theta}\frac{\partial \tilde{u}_\theta}{\partial \phi} + z\left(\frac{1}{R}\frac{\partial \tilde{\beta}_\phi}{\partial \theta} - \frac{\tilde{\beta}_\phi}{R\tan\theta} + \frac{1}{R\sin\theta}\frac{\partial \tilde{\beta}_\theta}{\partial \phi}\right); \\ \tilde{\varepsilon}_{\theta z} = \frac{1}{R}\frac{\partial \tilde{u}_z}{\partial \theta} - \frac{\tilde{u}_\theta}{R} + \tilde{\beta}_\theta, \\ \tilde{\varepsilon}_{\phi z} = \frac{1}{R\cdot\sin\theta}\frac{\partial \tilde{u}_z}{\partial \phi} - \frac{\tilde{u}_\phi}{R} + \tilde{\beta}_\phi. \end{gathered} \tag{8}$$

The PDEs of the hemispherical shells motions are the following:

$$
\begin{gathered}
\frac{E_{\theta\theta}}{1-\mu_{\theta\varphi}\mu_{\varphi\theta}}\left\{\frac{1}{R^2\rho}\left[\frac{\partial^2\tilde{u}_\theta}{\partial\theta^2}+\frac{\partial\tilde{u}_z}{\partial\theta}+\mu_{\theta\varphi}\left(\frac{1}{\sin\theta}\frac{\partial^2\tilde{u}_\varphi}{\partial\theta\partial\varphi}+\frac{1}{\tan\theta}\frac{\partial\tilde{u}_\theta}{\partial\theta}+\frac{\partial\tilde{u}_z}{\partial\theta}\right)\right]+\right.\\
\left.+\frac{1}{R^2\rho\tan\theta}\left[\frac{\partial\tilde{u}_\theta}{\partial\theta}+\tilde{u}_z+\mu_{\theta\varphi}\left(\frac{1}{\sin\theta}\frac{\partial\tilde{u}_\varphi}{\partial\varphi}+\frac{\tilde{u}_\theta}{\tan\theta}+\tilde{u}_z\right)\right]\right\}+\\
+\frac{G_{\theta\varphi}}{R^2\rho\sin\theta}\left[\frac{\partial^2\tilde{u}_\varphi}{\partial\theta\partial\varphi}-\frac{1}{\tan\theta}\frac{\partial\tilde{u}_\varphi}{\partial\varphi}+\frac{1}{\sin\theta}\frac{\partial^2\tilde{u}_\theta}{\partial\varphi^2}\right]+\frac{\kappa G_{\theta z}}{R^2\rho\tan\theta}\left[\frac{\partial\tilde{u}_z}{\partial\theta}-\tilde{u}_\theta+R\tilde{\beta}_\theta\right]+\\
+\frac{E_{\varphi\varphi}}{1-\mu_{\theta\varphi}\mu_{\varphi\theta}}\frac{\cos\theta}{R^2\rho\sin\theta}\left[\frac{1}{\sin\theta}\frac{\partial\tilde{u}_\varphi}{\partial\varphi}+\frac{\tilde{u}_\theta}{\tan\theta}+\tilde{u}_z+\mu_{\varphi\theta}\left(\frac{\partial\tilde{u}_\theta}{\partial\theta}+\tilde{u}_z\right)\right]=\frac{\partial^2\tilde{u}_\theta}{\partial t^2},\\
\frac{G_{\theta\varphi}}{\rho R^2}\left[\frac{\partial^2\tilde{u}_\varphi}{\partial\theta^2}+\frac{1}{\sin\theta}\frac{\partial^2\tilde{u}_\theta}{\partial\theta\partial\varphi}+\frac{1}{\sin\theta\tan\theta}\frac{\partial\tilde{u}_\theta}{\partial\varphi}-\frac{\tilde{u}_\varphi}{\tan^2\theta}\right]+\\
+\frac{E_{\varphi\varphi}}{\rho R^2\left(1-\mu_{\theta\varphi}\mu_{\varphi\theta}\right)}\left[\frac{1}{\sin^2\theta}\frac{\partial^2\tilde{u}_\varphi}{\partial\varphi^2}+\frac{1}{\tan\theta\sin\theta}\frac{\partial\tilde{u}_\theta}{\partial\varphi}_{\theta}+\frac{\mu_{\varphi\theta}}{\sin\theta}\frac{\partial^2\tilde{u}_\theta}{\partial\theta^2}+\frac{1+\mu_{\varphi\theta}}{\sin\theta}\frac{\partial\tilde{u}_z}{\partial\varphi}\right]+\\
+\frac{G_{\theta\varphi}}{\rho R^2}\left[\frac{1}{\tan\theta}\frac{\partial\tilde{u}_\varphi}{\partial\theta}-\frac{\tilde{u}_\varphi}{\tan^2\theta}+\frac{1}{\sin\theta\tan\theta}\frac{\partial\tilde{u}_\theta}{\partial\varphi}\right]+\\
+\frac{\kappa G_{\varphi z}}{\rho R^2}\left[\frac{1}{\sin\theta}\frac{\partial\tilde{u}_z}{\partial\varphi}-\tilde{u}_\varphi+\tilde{\beta}_\varphi\right]=\frac{\partial^2\tilde{u}_\varphi}{\partial t^2},\\
\frac{\kappa G_{\theta z}}{R^2\rho\sin\theta}\left[\frac{\partial^2\tilde{u}_z}{\partial\theta^2}-\frac{\partial\tilde{u}_\theta}{\partial\theta}+R\frac{\partial\tilde{\beta}_\theta}{\partial\theta}+\frac{1}{\tan\theta}\left(\frac{\partial\tilde{u}_z}{\partial\theta}-\tilde{u}_\theta+R\tilde{\beta}_\theta\right)\right]+\\
\frac{\kappa G_{\varphi z}}{R^2\rho\sin\theta}\left[\frac{1}{\sin\theta}\frac{\partial^2\tilde{u}_z}{\partial\varphi^2}-\frac{\partial\tilde{u}_\varphi}{\partial\varphi}+R\frac{\partial\tilde{\beta}_\varphi}{\partial\varphi}\right]-\\
-\frac{E_{\theta\theta}}{R^2\rho\sin\theta\left(1-\mu_{\theta\varphi}\mu_{\varphi\theta}\right)}\left[\frac{\partial\tilde{u}_\theta}{\partial\theta}+\tilde{u}_z+\mu_{\theta\varphi}\left(\frac{1}{\sin\theta}\frac{\partial\tilde{u}_\varphi}{\partial\varphi}+\frac{\tilde{u}_\theta}{\tan\theta}+\tilde{u}_z\right)\right]-\\
-\frac{E_{\varphi\varphi}}{R^2\rho\sin\theta\left(1-\mu_{\theta\varphi}\mu_{\varphi\theta}\right)}\left[\frac{1}{\sin\theta}\frac{\partial\tilde{u}_\varphi}{\partial\varphi}+\frac{\tilde{u}_\theta}{\tan\theta}+\tilde{u}_z+\mu_{\varphi\theta}\left(\frac{\partial\tilde{u}_\theta}{\partial\theta}+\tilde{u}_z\right)\right]+\frac{P_z}{\rho h}=\frac{\partial^2\tilde{u}_z}{\partial t^2};
\end{gathered}
\tag{9}
$$

$$+\frac{E_{\theta\theta}}{R^2\rho(1-\mu_{\theta\varphi}\mu_{\varphi\theta})\tan\theta}\left[\frac{\partial\tilde{\beta}_\theta}{\partial\theta}+\mu_{\theta\varphi}\left(\frac{1}{\sin\theta}\frac{\partial\tilde{\beta}_\varphi}{\partial\varphi}+\frac{1}{\tan\theta}\tilde{\beta}_\theta\right)\right]+$$

$$+\frac{G_{\theta\varphi}}{R^2\rho\sin\theta}\left[\frac{\partial^2\tilde{\beta}_\varphi}{\partial\theta\partial\varphi}-\frac{1}{\tan\theta}\frac{\partial\tilde{\beta}_\varphi}{\partial\varphi}+\frac{1}{\sin\theta}\frac{\partial^2\tilde{\beta}_\theta}{\partial\varphi^2}\right]-$$

$$-\frac{E_{\varphi\varphi}}{R^2\rho(1-\mu_{\theta\varphi}\mu_{\varphi\theta})\tan\theta}\left[\frac{1}{\sin\theta}\frac{\partial\tilde{\beta}_\varphi}{\partial\varphi}+\frac{\tilde{\beta}_\theta}{\tan\theta}+\mu_{\varphi\theta}\frac{\partial\tilde{\beta}_\theta}{\partial\theta}\right]=\frac{\partial^2\tilde{\beta}_\theta}{\partial t^2};$$

$$\frac{E_{\theta\theta}}{R^2\rho(1-\mu_{\theta\varphi}\mu_{\varphi\theta})}\left[\frac{\partial^2\tilde{\beta}_\theta}{\partial\theta^2}+\mu_{\theta\varphi}\left(\frac{1}{\sin\theta}\frac{\partial^2\tilde{\beta}_\varphi}{\partial\theta\partial\varphi}+\frac{1}{\tan\theta}\frac{\partial\tilde{\beta}_\theta}{\partial\theta}\right)\right]-$$

$$-\frac{12\kappa G_{\theta z}}{R\rho h^2}\left[\frac{\partial\tilde{u}_z}{\partial\theta}-\tilde{u}_\theta+R\tilde{\beta}_\theta\right]+$$

$$\frac{G_{\theta\varphi}}{\rho R^2}\left[\frac{\partial^2\tilde{\beta}_\varphi}{\partial\theta^2}-\frac{1}{\tan\theta}\frac{\partial\tilde{\beta}_\varphi}{\partial\theta}+\frac{1}{\sin\theta}\frac{\partial^2\tilde{\beta}_\theta}{\partial\theta\partial\varphi}\right]+\frac{2G_{\theta\varphi}}{\rho R^2\tan\theta}\left[\frac{\partial\tilde{\beta}_\varphi}{\partial\theta}-\frac{\tilde{\beta}_\varphi}{\tan\theta}+\frac{1}{\sin\theta}\frac{\partial\tilde{\beta}_\theta}{\partial\varphi}\right]+$$

$$+\frac{1}{\rho R^2\sin\theta}\frac{E_{\varphi\varphi}}{(1-\mu_{\theta\varphi}\mu_{\varphi\theta})}\left[\frac{1}{\sin\theta}\frac{\partial^2\tilde{\beta}_\varphi}{\partial\varphi^2}+\frac{1}{\tan\theta}\frac{\partial\tilde{\beta}_\theta}{\partial\varphi}+\mu_{\varphi\theta}\frac{\partial^2\tilde{\beta}_\theta}{\partial\theta\partial\varphi}\right]-$$

$$-\frac{12\kappa G_{\varphi z}}{\rho R h^2}\left[\frac{1}{\sin\theta}\frac{\partial\tilde{u}_z}{\partial\varphi}-\tilde{u}_\varphi+R\tilde{\beta}_\varphi\right]=\frac{\partial^2\tilde{\beta}_\varphi}{\partial t^2}.$$

The motor composite casing dynamics are described by the linear PDEs (6, 9) and the boundary conditions on two edges.

4 Approach for PDEs Solutions

The PDEs (9, 15) are reduced to the system of the linear ordinary differential equations (ODEs). As the casing is closed, the displacements and the rotation angles are described by the Fourier series [13].

The cylindrical part of the structure is treated. All the partial derivatives with respect to the longitudinal coordinate x are replaced by finite-difference approximations. The Fourier series of the displacements and the rotation angles of the spherical bottoms are substituted into the PDE of motions. As a result, the system of ODEs is derived in the matrix form to describe cylindrical part of the structure [14–16]:

$$\frac{d^2\mathbf{U}_{\mathbf{x},\mathbf{n}}}{dt^2}+\mathbf{C_1}\mathbf{U}_{\mathbf{x},\mathbf{n}}=\mathbf{P}_{\mathbf{x},\mathbf{n}}, \tag{10}$$

where $\mathbf{U}_{\mathbf{x},\mathbf{n}}$ is vector of Fourier series coefficients of displacements and rotation angles; $\mathbf{C_1}$ is constant matrix; $\mathbf{P}_{\mathbf{x},\mathbf{n}}=\left\{\mathbf{P}^{(\mathbf{0})}_{\mathbf{x},\mathbf{n}},\ldots,\mathbf{P}^{(\mathbf{J})}_{\mathbf{x},\mathbf{n}}\right\}$ are Fourier series coefficients of the impact loads.

The system of PDEs is transformed to the system of ODEs to describe the bottom motions. The coefficients of the Fourier series of the displacements $\tilde{\mathbf{U}}_{\mathbf{x,n}}$ are satisfied the system of PDEs:

$$\frac{\partial^2 \tilde{\mathbf{U}}_{\mathbf{s,n}}}{\partial t^2} + \mathbf{A_1} \frac{\partial^2 \tilde{\mathbf{U}}_{\mathbf{s,n}}}{\partial \theta^2} + \mathbf{A_2} \frac{\partial \tilde{\mathbf{U}}_{\mathbf{s,n}}}{\partial \theta} + \mathbf{A_3} \tilde{\mathbf{U}}_{\mathbf{s,n}} = \frac{1}{\rho h} \mathbf{P_n}(\theta, t) \tag{11}$$

where $\tilde{\boldsymbol{U}}_{\boldsymbol{s,n}} = \left\{ \tilde{U}_{\theta,n}(\theta, t), \tilde{U}_{\phi,n}(\theta, t), \tilde{U}_{z,n}(\theta, t), \tilde{B}_{\theta,n}(\theta, t), \tilde{B}_{\phi,n}(\theta, t) \right\}$; $\mathbf{A}_1, \mathbf{A}_2, \mathbf{A}_3$ are constant matrixes. Using the finite differences formulas, the system (11) is transformed into the system of ODEs in matrix form:

$$\frac{d^2 \mathbf{U}_{\mathbf{s,n}}}{dt^2} + \mathbf{C_2} \mathbf{U}_{\mathbf{s,n}} = \mathbf{P}_{\mathbf{s,n}}, \tag{12}$$

where $\mathbf{C}_2$ is square matrix; $\mathbf{P}_{\mathbf{s,n}} = \left\{ \tilde{\mathbf{P}}^{(\mathbf{0})}_{\mathbf{s,n}}, \ldots, \tilde{\mathbf{P}}^{(\mathbf{m})}_{\mathbf{s,n}} \right\}$ is Fourier coefficients of impact loads.

The curve of cylindrical shell and hemispherical shell junction is described by the solutions matching. The Fourier series coefficients for the left bottom last sampling point are equal to the solution of the first sampling point of the cylindrical shell:

$$\hat{\mathbf{U}}^{(\mathbf{M_1})}_{\mathbf{s,n}} = \mathbf{U}^{(\mathbf{0})}_{\mathbf{x,n}},$$

where M_1 is the number of the sampling points of the left bottom in longitudinal direction. The matching conditions for displacements and the rotation angles of the normal to the middle surface have the matrix form:

$$\mathbf{A_4} \left\{ \frac{1}{h_s} \left(\hat{\mathbf{U}}^{(\mathbf{M_1})}_{\mathbf{s,n}} - \hat{\mathbf{U}}^{(\mathbf{M_1-1})}_{\mathbf{s,n}} \right) + \hat{\mathbf{U}}^{(\mathbf{M_1})}_{\mathbf{s,n}} \right\} = \mathbf{A_5} \left\{ \frac{1}{l} \left(\mathbf{U}^{(\mathbf{1})}_{\mathbf{x,n}} - \mathbf{U}^{(\mathbf{0})}_{\mathbf{x,n}} \right) + \mathbf{U}^{(\mathbf{0})}_{\mathbf{x,n}} \right\}, \tag{13}$$

where $\mathbf{A_4}, \mathbf{A_5}$ are constant matrixes. The coefficients of the right bottom Fourier series in the last sampling point are equal to the coefficients of the cylindrical shell Fourier series in the last sampling points:

$$\overline{\mathbf{U}}^{(\mathbf{M_2})}_{\mathbf{s,n}} = \mathbf{U}^{(\mathbf{J})}_{\mathbf{x,n}},$$

where M_2 is the number of the sampling points in longitudinal direction for right bottom coefficients of Fourier series. The matching conditions for displacements and the rotation angles of the normal to the middle surface are presented by the following equation in matrix form:

$$\mathbf{A_6} \left\{ \frac{1}{h_s} \left(\overline{\mathbf{U}}^{(\mathbf{M_2})}_{\mathbf{s,n}} - \overline{\mathbf{U}}^{(\mathbf{M_2-1})}_{\mathbf{s,n}} \right) + \overline{\mathbf{U}}^{(\mathbf{M_2})}_{\mathbf{s,n}} \right\} = \mathbf{A_7} \left\{ \frac{1}{l} \left(\mathbf{U}^{(\mathbf{J})}_{\mathbf{x,n}} - \mathbf{U}^{(\mathbf{J-1})}_{\mathbf{x,n}} \right) + \mathbf{U}^{(\mathbf{J})}_{\mathbf{x,n}} \right\} \tag{14}$$

where $\mathbf{A_6}, \mathbf{A_7}$ are constant matrixes.

The Newmark method [13] is used to solve numerically the systems of ODEs (10, 12).

5 Results of Numerical Analysis

The goal of the numerical study is calculation of the allowable impact pressure, which does not result in loss of motor operation. The geometrical parameters of the structure are the following: $L = 2.95$ m, $h = 0.06$ m, $R = 0.4$ m, $H_1 = 0.3$ m, $H_2 = 0.25$ m. The impact pressure parameters take the following values: $t^* = 5$ ms; $t^{**} = 30$ ms; $P_{\max} = 12$ MPa. The composite material properties take the values: $G_{x\phi} = G_{\theta\phi} = G_{xz} = G_{\phi z} = G_{\phi\theta} = 3.9$ MPa; $E_{xx} = E_{\theta\theta} = 130$ MPa; $E_{\phi\phi} = 125$ MPa; $\mu_{x\phi} = \mu_{\phi x} = \mu_{\theta\phi} = \mu_{\phi\theta} = 0.32$; $\rho = 1400$ kg/m^3.

The stress state of the thin-walled structure is calculated using the approach from the Sect. 3. Two types of spatial discretization are performed for structure dynamics calculations with certain values of step and calculations with a step, which are reduced twice. The convergence of the solutions is observed, if two solutions are close. Moreover, the obtained numerical results are compared with the data of the finite element calculations.

The displacements U of the points, which belong to the generating line of the middle surface, are presented on Fig. 2. The points of the generating line are defined by arc length coordinate s (Figs. 1, 2). Maximal displacements occur at the middle part of the cylindrical shell and smaller values of displacements are observed at bottoms. The casing reaches maximal displacements at time 10 ms. Note, that maximal displacements are 5 mm.

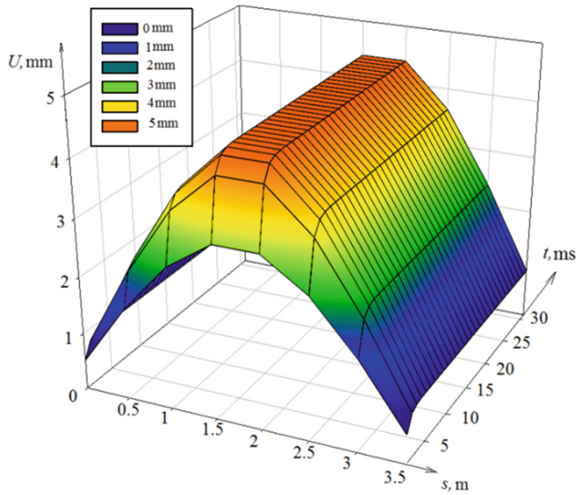

Fig. 2 The displacements of the points, which belong to one generating line of the middle surface

The displacements of the cylindrical part of the structure are presented on Fig. 3. The arc length coordinate s is shown on this figure. The displacements are presented on the range $t \in [0;\ 0.1]$ s.

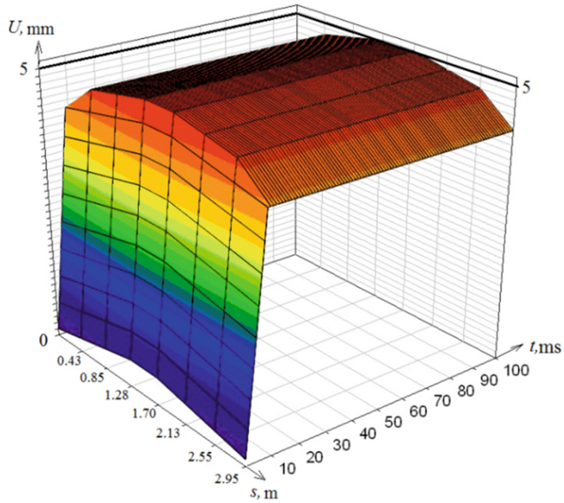

Fig. 3 The displacements of the cylindrical shell generating line

In order to verify the obtained results, the commercial finite element software ANSYS is applied. The results obtained by ANSYS are close to the data, which are obtained by our own software.

The dynamic behavior of the stress σ_{xx} on time is analyzed numerically. Three parameters of impact pressure $P_{\max} = 12$ MPa; $P_{\max} = 13$ MPa; $P_{\max} = 14$ MPa are used for such calculations. The dependence of σ_{xx} on time is shown on Fig. 4. The maximal stress occurs at 10 ms. The thin-walled structure is operable at $P_{\max} = 12$ MPa; $P_{\max} = 13$ MPa.

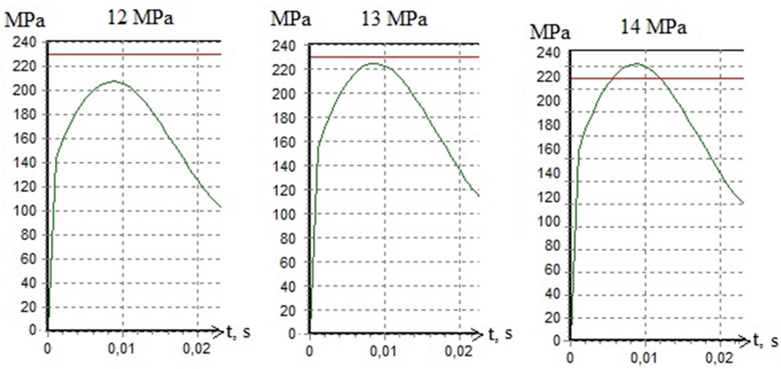

Fig. 4 The behavior of the stresses σ_{xx} in time

6 Conclusion

The transient of the motor composite casing is studied under impact loads with account of shear theory. The dynamics of the thin-walled structure, which consists of the cylindrical shell and two bottoms, is described by the system of PDEs. These PDEs are reduced to the system of ODEs with respect to coefficients of Fourier series of initial solution. The obtained system of ODEs is analyzed numerically.

The displacements and stress state are studied numerically. The results of numerical analysis motor composite casing transient motions are discussed in the present paper. The maximal displacements and stress occur at $t_1 = 10$ ms. The impact loads increase up to $t^* = 5$ ms. The parameters of impact loads are determined to satisfy the operable conditions.

As follows from the numerical study, the obtained results are close to the finite element simulations.

The methodology suggested in this paper is used to design the solid propellant motor composite casing.

References

1. Wubuliaisan, M., Wu, Y., Hou, X.: A unified viscoelastic model of progressive damage and failure for solid propellants. Int. J. Plast. **170**, 103765 (2023). https://doi.org/10.1016/j.ijplas.2023.103765
2. Yldirim, H.C., Ozupek, S.: Structural assessment of a solid propellant rocket motor: effects of aging and damage. Aerosp. Sci. Technol. **15**, 635–641 (2011). https://doi.org/10.1016/j.ast.2011.01.002
3. Wu, Y., Li, Z., Lu, R.: Simulation and visual tester verification of solid propellant slurry vacuum plate casting. Pyrotechnics **45**(6), 871–879 (2020). https://doi.org/10.1155/2021/5026878
4. Marimuthu, R., Rao, B.N.: Development of efficient finite elements for structural integrity analysis of solid rocket motor propellant grains. Int. J. Press. Vessels Pip. **111**, 131–145 (2013). https://doi.org/10.1016/j.ijpvp.2013.06.001
5. Qu, K., Zhan, X.: Finite element analysis of propellant of solid rocket motor during ship motion. Propuls. Power Res. **2**, 50–55 (2013). https://doi.org/10.1016/J.JPPR.2012.12.002
6. Yang, L., Wang, N., Xie, K., Su, X., Li, S.: Influence of strain rate on the compressive yield stress of CMDB propellant at low, intermediate and high strain rates. Polym. Testing **51**, 49–57 (2016). https://doi.org/10.1016/j.polymertesting.2016.02.007
7. Su, W., Wang, N., Li, J., Zhao, Y., Yan, M.: Improved method of measuring pressure coupled response for composite solid propellants. J. Sound Vib. **333**, 2226–2240 (2014). https://doi.org/10.1016/j.jsv.2013.12.003
8. Altenbach, H., et al.: Fast fracture of conic shell under the action of belt explosive charge. In: Altenbach, H. (ed.) Advances in Mechanical and Power Engineering. CAMPE 2021 LNME, pp. 366–376. Springer, Cham (2023). https://doi.org/10.1007/978-3-031-18487-1_37
9. Chernobryvko, M., Avramov, K., Uspensky, B.: Dynamic deformation of functionally graded carbon nanotubes-reinforced composite joined spherical-cylindrical-spherical shell. In: 2022 IEEE 3rd KhPI Week on Advanced Technology, KhPI Week 2022 - Conference Proceedings (2022). https://doi.org/10.1109/KhPIWeek57572.2022.9916392
10. Bert, C.W., Kumar, M.: Vibration of cylindrical shells of bimodulus composite materials. J. Sound Vib. **81**, 107–121 (1982). https://doi.org/10.1016/0022-460X(82)90180-8

11. Reddy, J.N., Liu, C.F: A higher-order shear deformation theory of laminated elastic shells. Int. J. Eng. Sci. **23**, 319–330 (1985). https://doi.org/10.1016/0020-7225(85)90051-5
12. Soedel, W.: Simplified equations and solutions for the variation of orthotropic cylindrical shells. J. Sound Vib. **97**, 226–242 (1983). https://doi.org/10.1016/0022-460X(83)90506-0
13. Avramov, K., Chernobryvko, M.T., A.: Dynamics of solid propellant motor composite casing under impact pressure. Meccanica **53**(13), 3339–3353 (2018). https://doi.org/10.1007/s11012-018-0876-5
14. Avramov, K.: Nonlinear modes of parametric vibrations and their applications to beams dynamics. J. Sound Vib. **322**, 476–489 (2009). https://doi.org/10.1016/j.jsv.2008.07.013
15. Avramov, K., Gendelman, O.: On interaction of vibrating beam with essentially nonlinear absorber. Meccanica **45**, 355–365 (2010). https://doi.org/10.1007/s11012-009-9252-9
16. Avramov, K., Strel'nikova, E.: Chaotic oscillations of plates interacting on both sides with a fluid flow. Int. Appl. Mech. **50**, 303–309 (2014). https://doi.org/10.1007/s10778-014-0633-y

Numerical and Experimental Investigation of the Rotor Blade Joint

Volodymyr Martynenko(✉)

Department of Mathematical Modeling and Intelligent Computing in Engineering, National Technical University "Kharkiv Polytechnic Institute", NTU "KhPI", 2, Kyrpychova Street, Kharkiv 61002, Ukraine
martynenko.volodymyr@gmail.com

Abstract. The paper presents an experimental and numerical study of the tapered socket of the aluminum blade root of the mine main ventilation fan, which is based on the tests of a simplified full-scale model with a discarded airfoil and its subsequent finite element analysis. The calculation model takes into account elastoplastic properties of materials and non-linear contacts with friction. The proposed joint consists of an aluminum tapered blade root, two steel retainers with similar tapered surfaces, and two steel bolts that join the retainers around the root. Pre-tightening the bolts is taken into account in the nonlinear static finite element analysis of the elastoplastic behavior of the structure which allows determining the destructive loads that cause the bolts to break with the subsequent disconnection of the fasteners and the blade to fly out of the seat. The graphs of the von Mises equivalent stresses indicate that the maximum stresses are reached in the working part of the bolts, which fully corresponds to the nature of the destruction of the structure upon reaching the maximum equivalent load on it. The experimental study confirms the correctness of the determination of contact stresses at the tapered socket location. Correspondence of the results of the static analysis with the results of the full-scale experiment makes it possible to draw a conclusion about the correctness of the conducted finite element modelling.

Keywords: Strength · Contact · Bolt joint · Friction · Finite element method

1 Introduction

1.1 Blade Root Design

On the contrary to centrifugal machines, where the fixation usually occurs be means of casting or welding processes [1], there are different technologies for axial rotary machines to fix the blades in the impellers namely: T-root joints [2, 3]; fir-tree root [4]; attaching the blades directly to the disc using welding [5], bolted connection [6] and other technologies; fixation using cylindrical and tapered shelves with pretension [7].

Each of these fixation methods has its advantages and disadvantages and is a compromise between ease of manufacturing, subsequent assembly into a complete structure and maintenance, ability to withstand a certain level of static and dynamic loads, etc.

M. Nechyporuk et al. (Eds.): ICTM 2023, LNNS 1008, pp. 373–383, 2024.
https://doi.org/10.1007/978-3-031-61415-6_32

In axial fans of mine main ventilation, fixation with cylindrical shelves or a tapered connection is usually used. Figure 1 visually compares the von Mises equivalent stresses in the cylindrical and tapered joints of fan blades of approximately the same diameter (3 m) and with approximately the same rotational speed. It follows from the figure that the maximum von Mises equivalent stresses in the blade root for the cylindrical connection are higher than those values for the tapered connection.

At the same time, the tapered joint requires a large pretension, which is achieved by tightening the retainers with bolted connections, that is, in this case, these elements become the most stressed in comparison with the blade root.

That is why these retaining elements require a more detailed study with a check of exceeding the allowable stresses and, accordingly, the fulfillment of the strength criterion when tightening the tapered socket. This work aims to develop and experimentally verify such a numerical algorithm, which is the subject of research, to determine the strength of the tapered connection of the blade of a rotary machine with pretension, which is the object of research.

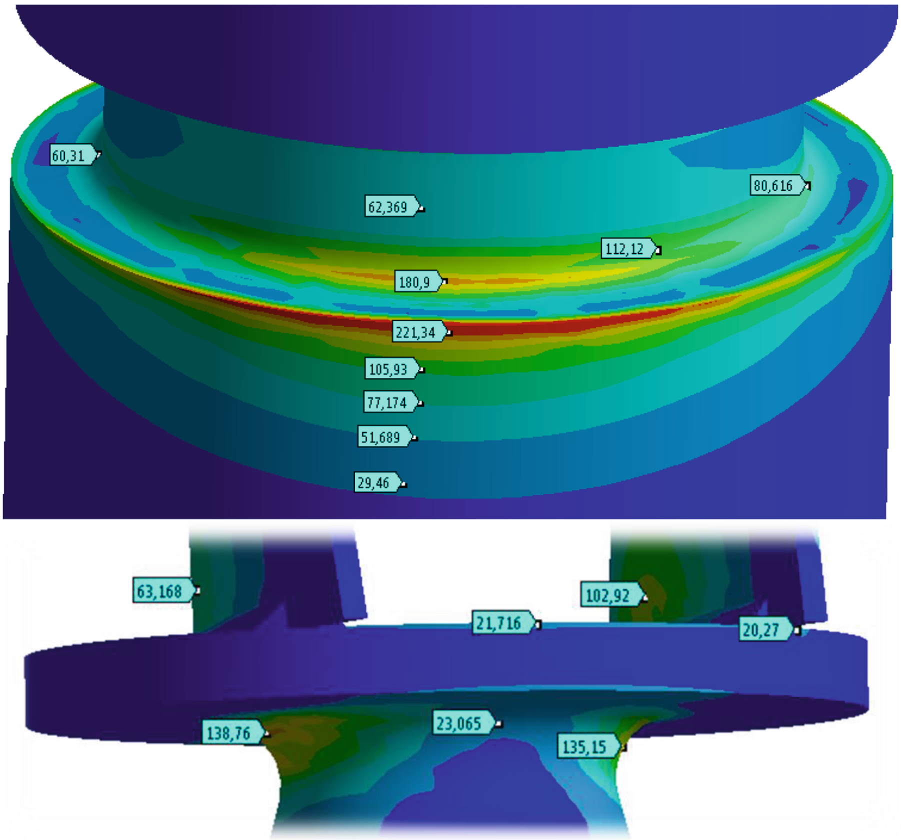

Fig. 1. Contour plot of the von Mises equivalent stresses, MPa in cylindrical (top) and tapered (bottom) connections of axial fans.

1.2 Analysis of Existing Solutions of the Problem

The strength of various types of turbo machine joints is a well-studied topic given the various characteristics of such joints.

For example, the work [2] considers the frictionless contact of the T-root joint of the turbine blade to determine the low cycle fatigue of the root.

The paper [3] develops reduced order model of the fan blade with a frictional contact of the T-root joint to enhance the computational efficiency and accuracy of nonlinear vibrations of large-scale assembly.

The work [4] investigates the low cycle fatigue of a turbine blade fir-tree root for different probabilistic distributions of tolerance ranges and manufacturing processes.

The paper [5] considers the welded joint of the blade of the fan in terms of its structural strength and modal characteristics.

The article [7] develops a calculation model of thick laminates simulating a joint of the composite fan blade subjected to moisture absorption.

The works [8, 9] study the stress-strain state of the fir-tree connection of the steam turbine blade taking into account thermal and plastic deformations which have a significant effect on strength in machines of this type.

The article [10] examines the influence of the geometric parameters of the lock joint between the disk and the vane from the point of view of determining the equivalent stresses in such a joint.

The paper [11] studies the strength of the bolted connection of the composite blades of the wind turbine.

The work [12] investigates the strength of welded joints for their further use in hydraulic vanes.

The paper [13] proposes a new riveted connection between the vanes and the stator disk and conducts an experimental and numerical study of its strength.

The article [14] conducts a design and optimization study of the hybrid connection of the composite blade of the aircraft engine fan stage.

The articles [6, 15] propose a new approach to modelling of a bolted connection of the fan blade of the aircraft engine for the further performance of the structural analyses of the bird strike impact on the blade airfoil.

This work considers the tapered connection of the fan blade with retainers, an example of which is shown in Fig. 2 in the form of geometric and finite element models of an already existing design solution.

The novelty of the work consists in the complexity of the finite-element model which takes into account the pretension of bolts and the nonlinearity of material properties, contacts and deflections, as well as in the experimental investigation of this connection for which the test rig was developed and used.

The goals which were formulated for this research included creation of both the adequate test rig which corresponded to the real operational conditions of the tapered joint of the fan blade under real operation conditions when installed in the impeller, as well as the finite-element model which represented the test rig up to the rupture of bolts with the sufficient accuracy.

This problem formulation should validate the finite-element model for its further use in modelling of the fan blades with this type of joints under real operational conditions

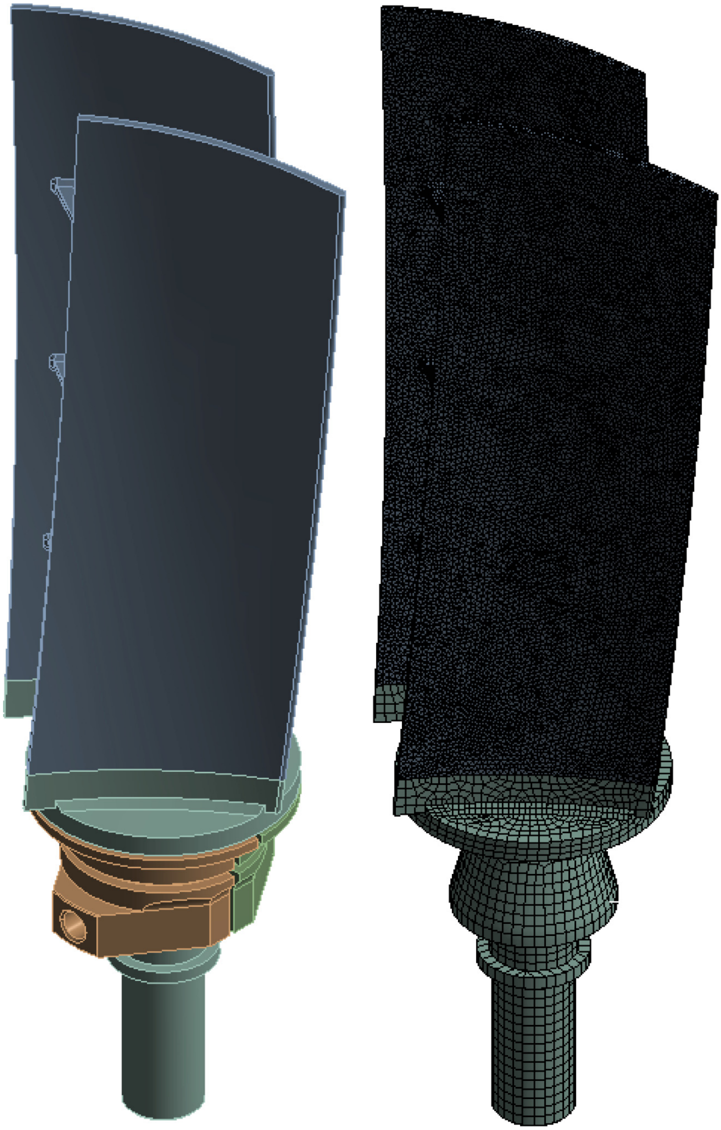

Fig. 2. A fan blade with a tapered joint - the geometric model with retainers (left) and the finite element model without retainers (right).

without the need of the blade rupture tests during the operation of the fan installation which is an expensive (since these are the big fan installations with the diameters more than 3 m) and dangerous (since these fans are rotating with high rotational speeds) task.

2 Problem Formulation

2.1 Experimental Rig and Mathematical Model Comparison

For the experimental research of the tapered joint strength, the stand shown in Fig. 3 which includes an aluminum tapered blade root, steel bolted retainers, and a cylindrical support which acts as a shelf on the fan impeller disc and is in direct contact with the retainers is used.

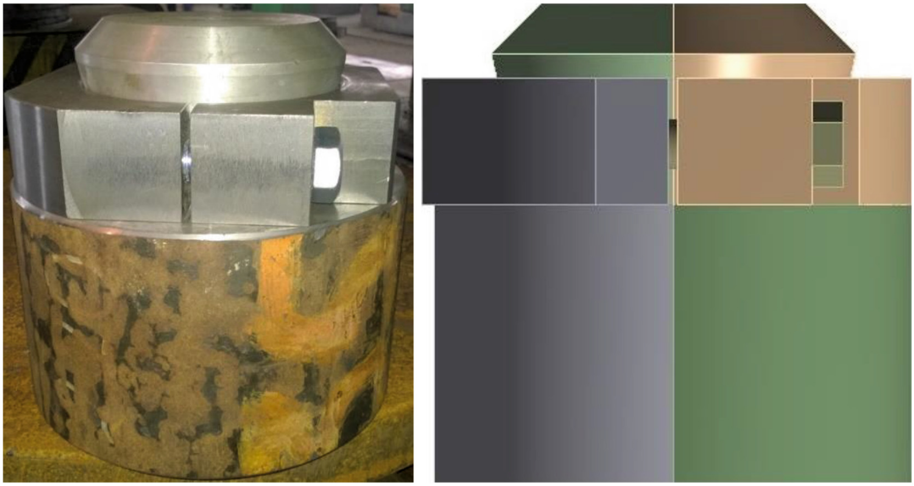

Fig. 3. An experimental rig for studying the strength of a tapered joint in the form of a real structure (left) and a geometric model (right).

The experimental model shown in the figure is upside down compared to the real blade model, i.e. the surface that should be attached to the blade airfoil is at the bottom.

The upper end of the root in the figure (the lower one in the actual design) is loaded by a hydraulic press which forces it to move inside the tapered joint, which is also preloaded by tightening the bolts, and disconnect the retainers additionally loading the bolted joints.

In this way, the effect of the airfoil under centrifugal loads on the tapered socket is simulated in addition to the loads from the pretension of bolted connections.

The loading occurs until the moment of destruction of bolts or the structure as a whole, and a similar process is modeled in the commercial computer-aided engineering software using the finite element analysis taking into account elastic-plastic deformations of materials and without taking into account destructive processes.

The strength assessment in the finite-element code is performed by comparing the von Mises equivalent stresses with the strength limits of the corresponding materials and further determining the load which leads to equivalent stresses equal to the strength limits of the materials. Thus, if the simulation is adequate, the corresponding load level in the real structure should cause failure.

2.2 Calculation Model

Figure 4 shows the finite element and contact models of the experimental rig, which includes a part of the hydraulic press (bottom), a root with retainers and bolts (middle), and a support (top). Nonlinear contacts with appropriate friction coefficients (aluminum-steel, steel-steel) are set between all contacting surfaces (press-root, root-retainers, bolt-retainers, retainers-support). In the figure, red zones correspond to the places where there is a sticking of contact, orange ones correspond to the locations of sliding in the contact and yellow ones correspond to the open contact conditions.

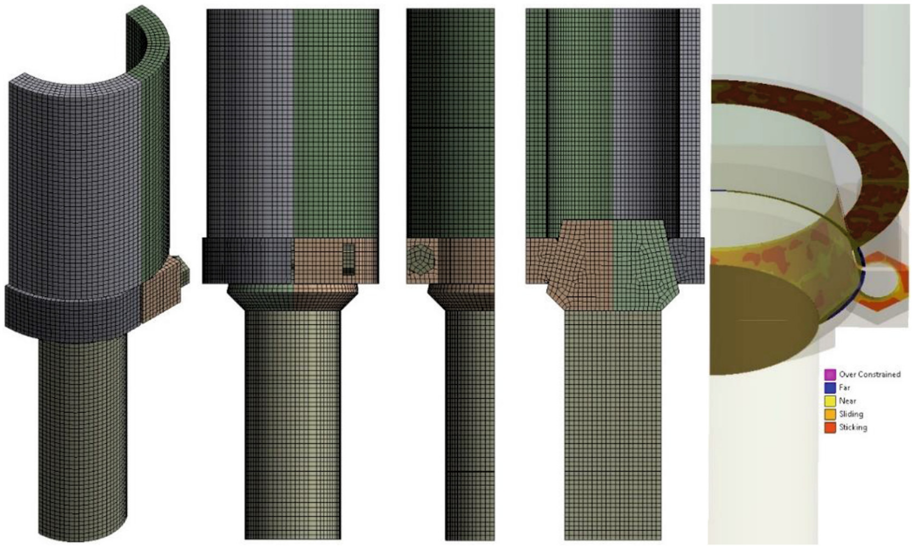

Fig. 4. Calculation model of the experimental rig.

The elastic-plastic material models with a bilinear kinematic hardening to represent the effect of plasticity were used for steel and aluminum as materials of the parts of the test rig.

In addition, the calculations take into account the effect of large deformations on the stress-strain state, i.e. the model includes all three possible types of nonlinearities, namely, nonlinearity of material properties, nonlinearity of contact interactions, and geometric nonlinearity.

In the case of the experimental study and during the simulation, the load was applied gradually from zero to a value which corresponded to the destruction of the sample under study.

The estimation of the finite element discretization error for the numerical model was carried out by comparing the maximum von Mises equivalent stresses as the results of trial static analyzes on the working and twice finer meshes, as well as by comparing similar values on the working mesh with element and nodal derivation of results. In all cases, the working finite element mesh showed an error of less than 2% which is acceptable engineering accuracy.

3 Results and Discussion

The experiment using the test rig shown in Fig. 3 allowed determining the value of load applied to the hydraulic press which was required to destroy the tapered joint. Further this load was specified to cylinder modeling the hydraulic press in the finite element analysis to determine the stress-strain state of the design under this condition and compare it with the strength criterion.

Figure 5 shows the contour plots of von Mises equivalent stresses for a load of 412 kN, which corresponds to the strength limit of the steel from which the bolts are made, namely 845 MPa. According to the von Mises strength criterion, the equivalent stress can be obtained as the RMS of principal stresses σ_1, σ_2, σ_3:

$$\sigma_{eqv} = \{0.5[(\sigma_1 - \sigma_2)^2 + (\sigma_2 - \sigma_3)^2 + (\sigma_3 - \sigma_1)^2]\}^{0.5} \quad (1)$$

The von Mises strength criterion allows determining the part of the design in which the maximal allowable stresses are violated and as a result the rupture occurs as well as the load value at which this violation is obtained. In this case the load represents the pressure of the hydraulic press, however in case or real operation conditions, such a load is a resultant of the centrifugal forces acting on the airfoil and the blade root with a small impact of the aerodynamic loads transmitted to the root through the airfoil.

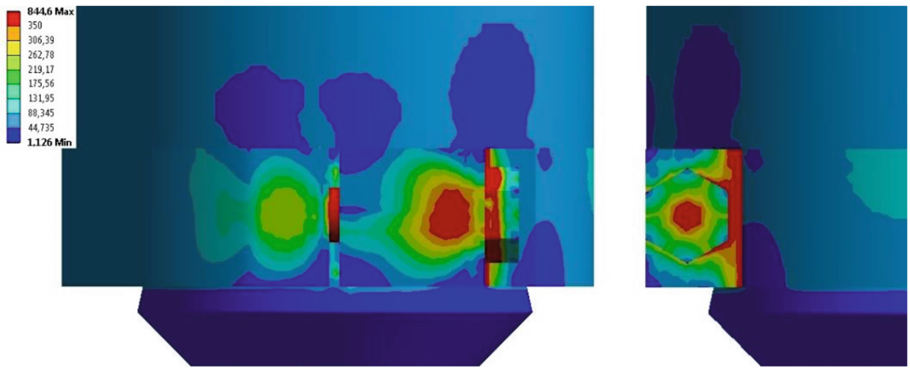

Fig. 5 Contour plots of the von Mises equivalent stresses in the experimental rig, MPa.

It is destruction of bolts that leads to disconnection of the studied tapered joint both as a result of experimental research and in the analysis of the strength criterion for stresses determined using finite element modelling.

Figure 6 shows a bolt that was torn separately during the experimental study and the corresponding picture of the equivalent stresses in it which indicates a thinning of the bolt in the place of maximum equivalent stresses (the shape of the bolt on the contour plot corresponds to the real scale of deformations according to the results of finite element modelling). This thinning is not as significant as in the case of the real bolt because the finite element model is solved using implicit methods which do not allow the modelling of the rupture process.

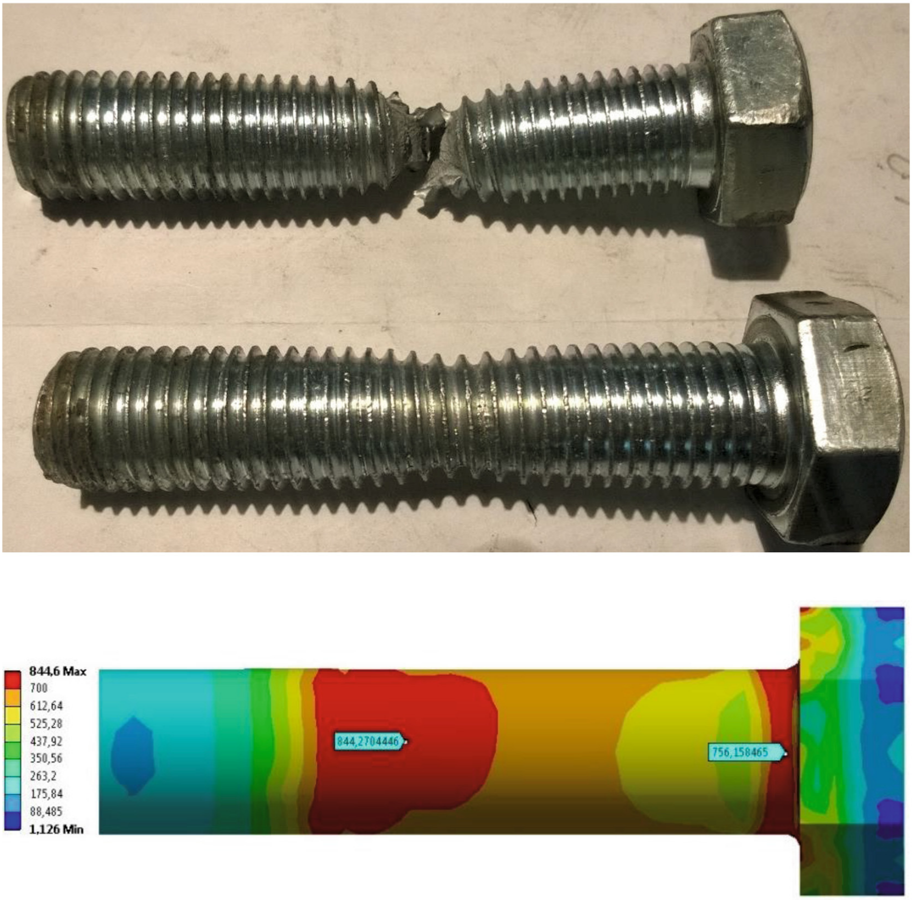

Fig. 6 The bolt torn during the experiment and the von Mises equivalent stresses in it at the moment of rupture, MPa.

In addition, Fig. 7 shows zones of plastic deformations for the aluminum root after the experiment, and for the stress plot, such zones correspond to the red color in which the yield strength of aluminum is exceeded by equivalent stresses. The figure shows that in the real blade root observed after the rupture of bolts, there are the significant zones near the borders of the retainers in which the plastic deformations lead to the obvious change of the root structure similarly to the red zones in the contour plots of the von Mises stresses. At the same time, in the right side of the root shown in the left set of the figure, there are not significant stresses according to the calculation, and the absence of structural changes in this location in the real root confirms this finding of the finite element analysis. Therefore, the pattern of deformation and destruction of elements corresponds to the results of finite element modelling which confirms its adequacy, in particular, the capabilities of the chosen contact models to represent interactions of the structural elements and selected material models and properties to represent the rupture and structural changes of these elements under excessive values of loads.

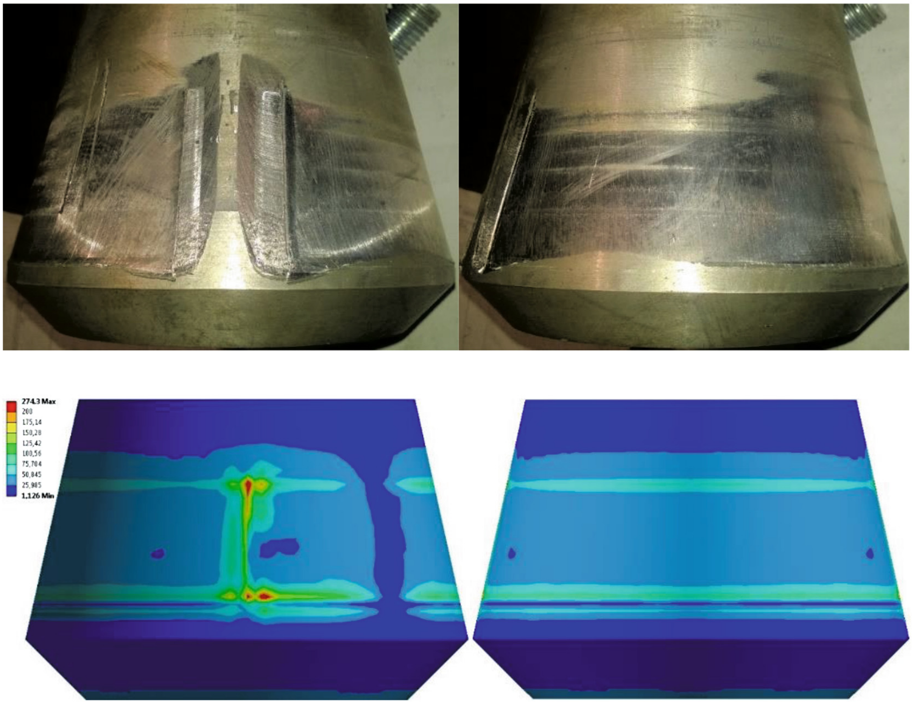

Fig. 7 The actual condition of the root and the von Mises equivalent stresses in it at the moment of bolt rupture, MPa.

4 Conclusions

The proposed approach to the experimental and numerical study of the fan blade tapered joint strength shows a sufficient coincidence of the results.

The fracture load determined by means of the numerical research and the use of the appropriate strength criterion for determining the load which was gradually applied to the experimental sample leads to the destruction of the tapered joint in the experiment as well. At the same time, it should be noted that lower values of the load during experimental research do not lead to destruction, and the difference between the destruction load determined in the experiment and during modelling is within 2% which is an acceptable engineering accuracy.

This fact, as well as the fact that the zones of plastic deformation on the aluminum root and the place of bolt rupture coincide with such points determined as a result of modelling testify to the adequacy of the calculation model, which takes into account all types of nonlinearities and pretension of bolts, and the possibility of using such a formulation of the problem in modelling of the mechanical behavior and failure of a blade with a tapered root in an assembly with an impeller under the action of pretension loads and centrifugal forces during the operation of the fan in real conditions.

References

1. Rozova, L., Martynenko, G.: Information technology in the modeling of dry gas seal for centrifugal compressors. In: CEUR Workshop Proceedings, vol. 2608, pp. 536–546 (2020)
2. Shankar, M., Kumar, K., Ajit Prasad, S.L.: T-root blades in a steam turbine rotor: a case study. Eng. Fail. Anal. **17**(5), 1205–1212 (2010). https://doi.org/10.1016/j.engfailanal.2010.02.006
3. Yuan, J., Schwingshackl, C., Wong, C., Salles, L.: On an improved adaptive reduced order model for the computation of steady state vibrations in large-scale non-conservative system with friction joints. Nonlinear Dyn. **103**, 3283–3300 (2021). https://doi.org/10.1007/s11071-020-05890-2
4. Moneta, G., Jachimowicz, J.: Impact of manufacturing tolerances on stress in a turbine blade fir-tree root. Fatigue Aircraft Struct. **2020**(12), 92–101 (2020). https://doi.org/10.2478/fas-2020-0009
5. Martynenko, V.: Analysis of strength and bearing capacity of the auxiliary mine ventilation fan connected to the rotor of its electrical drive. In: 2020 IEEE KhPI Week on Advanced Technology, pp. 19–23. IEEE, Kharkiv, Ukraine (2020). https://doi.org/10.1109/KhPIWeek51551.2020.9250078
6. Merculov, V., Kostin, M., Martynenko, G., Smetankina, N., Martynenko, V.: Force simulation of bird strike issues of aircraft turbojet engine fan blades. In: Cioboată, D.D. (ed.) International Conference on Reliable Systems Engineering ICoRSE 2021. LNNS, vol. 305, pp. 129–141. Springer, Cham (2022). https://doi.org/10.1007/978-3-030-83368-8_13
7. Canale, G., Kinawy, M., Sathujoda, P., Maligno, A., Citarella, R.G.: Moisture absorption in thick composite plates: modelling and experiments. Multidiscip. Model. Mater. Struct. **16**(3), 439–447 (2020). https://doi.org/10.1108/MMMS-06-2019-0119
8. Palkov, I., Shulzhenko, M.: Thermostressed state of the lock joint of turbine rotor blades of the first stage of K-500–240 steam turbine medium pressure cylinder. J. Mech. Eng. **22**, 36–43 (2019). https://doi.org/10.15407/pmach2019.03.036
9. Palkov, I., Shulzhenko, M.: Stress-strain state of steam turbine lock joint under plastic deformation. J. Mech. Eng. **23**, 28–37 (2020). https://doi.org/10.15407/pmach2020.04.028
10. Grzejszczak, O., Kozakiewicz, A.: An influence of geometrical parameters of the lock of the blade-disc joint on stress in the FEA and DIC methods. Adv. Sci. Technol. Res. J. **15**(1), 209–217 (2021). https://doi.org/10.12913/22998624/131662
11. Qin, Z., Wang, J., Yang, K., Yu, G., Xu, Y., Xu, J.: Design and nonlinear structural responses of multi-bolted joint composite box-beam for sectional wind turbine blades. Compos. Struct. **206**, 801–813 (2018). https://doi.org/10.1016/j.compstruct.2018.08.073
12. Foti, P., Berto, F.: Fatigue assessment of high strength welded joints through the strain energy density method. Fatigue Fract. Eng. Mater. Struct. **43**, 2694–2702 (2020). https://doi.org/10.1111/ffe.13336
13. Benesova, S., Kriz, A., Benes, P.: Analysis of the joint between blade and stator disc in steam turbine. Manuf. Technol. **17**(1), 3–7 (2017). https://doi.org/10.21062/ujep/x.2017/a/1213-2489/MT/17/1/3

14. Jadhav, P., Yella Gruha, L.: Design and optimization of hybrid interface joint in a composite fan blade of aircraft engine. Mater. Sci. Eng. Conf. Ser. **1126**(1), 1–12 (2021). https://doi.org/10.1088/1757-899X/1126/1/012036
15. Merculov, V., Kostin, M., Martynenko, G., Smetankina, N., Martynenko, V.: Peculiarities of the modelling of the bird dynamic impact on fan blades of an aircraft turbojet engine at operating modes. In: Nechyporuk, M., Pavlikov, V., Kritskiy, D. (eds.) Integrated Computer Technologies in Mechanical Engineering - 2021 ICTM 2021. LNNS, vol. 367, pp. 462–473. Springer, Cham (2022). https://doi.org/10.1007/978-3-030-94259-5_39

Numerical Analysis of the Modern Marine Gas Turbine Rotor Stress-Strain State

Natalia Smetankina[1] and Serhii Morhun[2](✉)

[1] Anatolii Pidgornyi Institute of Mechanical Engineering Problems of the National Academy of Sciences of Ukraine, 2/10, Pozharskogo Street, Kharkiv 61046, Ukraine
[2] Admiral Makarov National University of Shipbuilding, 9 Heroiv Ukrainy Avenue, Mykolaiv 54001, Ukraine
serhii.morhun@nuos.edu.ua

Abstract. In this paper the problem of the gas turbine rotor stress-strain state has been studied. The paper outlines a finite elements refined mathematical model of the gas turbine rotor stress-strain state and can be used for the various types of ground or even floating power plants. The developed mathematical model takes into account the curvilinear finite elements of hexagonal type. With the usage of the developed mathematical model the problems of the turbine rotor flow dynamics, heat exchange and stress-strain state have been studied. The turbine rotor displacements and dynamic stresses fields were found for several most dangerous forced vibration modes. The calculated data together with the numerical and experimental investigation of this rotor fluid flow and thermal state will be used for the next stage of studies, concerning the rotor creep, fatigue crack problems.

Keywords: Gas turbine rotor · Finite elements method · Gas flow pressure · Temperature field · Stress-strain state

1 Introduction

For the different types of modern ground or even floating power plants, it is rather necessary to increase the engine's capacity along with the high level of engine's durability and reliability. To achieve these goals, the researchers are forced to solve a number of problems in different areas, such as fluid flow dynamics, heat transfer, mechanics of solid deformable body etc. Furthermore, all of these problems are closely interconnected and the appropriate mathematical models should be designed to take into account all the aspects of the gas turbine rotor working process.

1.1 Flow Dynamics of the Gas Turbine Flow Path

For a long time, in the design of the turbines flow paths at different design stages, fairly simple fluid flow models have been used: one-dimensional, quasi-two-dimensional, two-dimensional (plane and axisymmetric) [1–4]. But nowadays it is necessary to use the computational fluid-dynamic methods in a three-dimensional formulation. The emergence of a three-dimensional viscous model of the working fluid flow through turbine

M. Nechyporuk et al. (Eds.): ICTM 2023, LNNS 1008, pp. 384–396, 2024.
https://doi.org/10.1007/978-3-031-61415-6_33

flow path and the numerical solution to this problem, together with a qualitative increase in the capabilities of computing technology made it possible to proceed in determining the optimal design of turbine flow path [5–8]. The accuracy and versatility of such models also the possibility of their use, both for creating impellers and for the whole rotor, made it possible to abandon the use of simpler one-dimensional and two-dimensional models of fluid flows [3, 5, 8–10].

While conducting such calculations, an important role is played by the model of turbulence [11–16]. So, according to the analysis of the given literature sources, it should be mentioned there is still a large number of unsolved problems regarding the design of ground and floating single shaft gas turbine engines power plants through numerical methods. Thus, one of the investigation tasks is to study the parameters of flow in the blade passages of the three stage single shaft GTE flow path, used for the perspective floating power plants and calculate the fields of flow pressure and temperature that will be the initial data for the rotor forced vibration, stress-strain state and thermal state calculation.

1.2 Gas Turbine Rotor Thermal State Determination

For the investigation of the gas turbine engine rotor stress-strain state we at first need to solve the problem of heat exchange between the gas flow and the turbine rotor.

Various numerical and experimental methods have been developed for the heat transfer study. But the most suitable for the study of heat exchange from the fluid flow to the complex curvilinear solid bodies is the finite elements method (FEM). In the papers [3–10] the planar and space shaped finite elements are given. Thus, in [11] special finite elements of shell type were used. In the paper [12] the prismatic type with eight-nodes finite elements are given and in the paper [13] the tetrahedron –finite elements were also used. But such type of elements can't correctly describe the blade's sharp curvature, caused by the demand of the fluid flow energy exchange laws.

The single crystal turbine blades stress-strain state is studied in papers [14, 15]. But in them all the heat exchange processes are considered linear and the problem of rotor blades cooling has not been considered. Also it should be mentioned that the process of the turbine blade rotor temperature field experimental determination is extremely expensive. The vast majority of publications study only the blades thermal state, rejecting the facts of cooling cavities in blades and disks. But the whole rotor is a unity of solid bodies and that's why the temperature field of the whole rotor is unite too.

Thus, it can be concluded that the determination of single shaft GTE rotor thermal state is the initial data for the rotor stress-strain state calculation.

1.3 Gas Turbine Rotor Stress-Strain State Determination

As it has been mentioned above for the results of the turbine rotor forced vibration and stress-strain state study can't be held without taking the results of the previous problems solution as initial data.

One of the main problems here is adequate determining the characteristics of the rotor forced vibration. For the correct FEM approximation we should consider that turbine blades are solid bodies with curvilinear surfaces. In the paper [4] the studies of steam turbine blades on the base of beam finite elements are given. But the main disadvantage of these models is a usage of the plane finite elements for three dimentional models. These circumstances sharply decrease the reliability of the obtained results. To reject such negative circumstances, in the papers [5—11] the three-dimensional finite element models are used. In the paper [15] the tetrahedron finite elements were used. But such type of elements can't correctly describe constructional inhomogeneity of blade's feather, caused by the presence of cooling channels of sharp curvature inside the blade's feather.

The paper [16] deals with the research of single crystal turbine blades stress-strain state. The full-scale experimental methods of the solid bodies stress-strain state study are given in literature [15–22]. The disadvantages of such methods are in the fact that in them the rotor is not mentioned as the unity of solid bodies and all mechanical processes in it are taken into account as processes for single solid bodies. But due to the complexity of constructing adequate and accurate calculation schemes, there are currently not many publications in which the results of the stress-strain state analysis of turbomachinery elements are given.

Analyzing the huge amount of scientific papers dealing with the problems of fluid flow, heat exchange and mechanics of solid deformable bodies, it can be concluded that there are several unsolved problems concerning the turbomachinery rotors, used in GTE power plants. One of the main problem is the turbine rotor stress-strain state determination. This study would be held taking into account the refined mathematical model on the base of FEM.

2 Research Object and Aim

The *research object* is the turbine rotor stress-strain state. Turbine rotor is considered as a system of blades of the same shape spaced on the surface of impellers. The gas flow passing through the rotor blades rows changes the speed and direction of its movement. So in the rotor impellers, the kinetic energy of the flow is converted into mechanical energy of forced vibration and the heat exchange between the flow and impellers causes the whole rotor thermal extension.

Thus for a correct solution of the turbine rotor stress-strain state problem we are obliged to develop a refined mathematical model that describes complex mechanical, thermal and flow dynamic processes in the turbine rotor.

To achieve this aim, the following tasks must be solved:

- Develop a refined mathematical model describing the flow dynamic, thermal and mechanical processes in rotor on the base of FEM;
- Determine the field of working flow pressure, causing rotor vibration;
- Determine the field of temperature on the rotor surface;
- Determine the rotor forced vibration modes and frequencies spectrum;
- Determine the field of rotor dynamic stresses.

3 Formulation of the Problem

As the stationary coordinate system, the Cartesian right-handed xyz coordinate system with the center at point O is taken (Fig. 1). This coordinate system rotates together with the turbine rotor at a constant angular velocity Ω equal to the angular velocity of rotor.

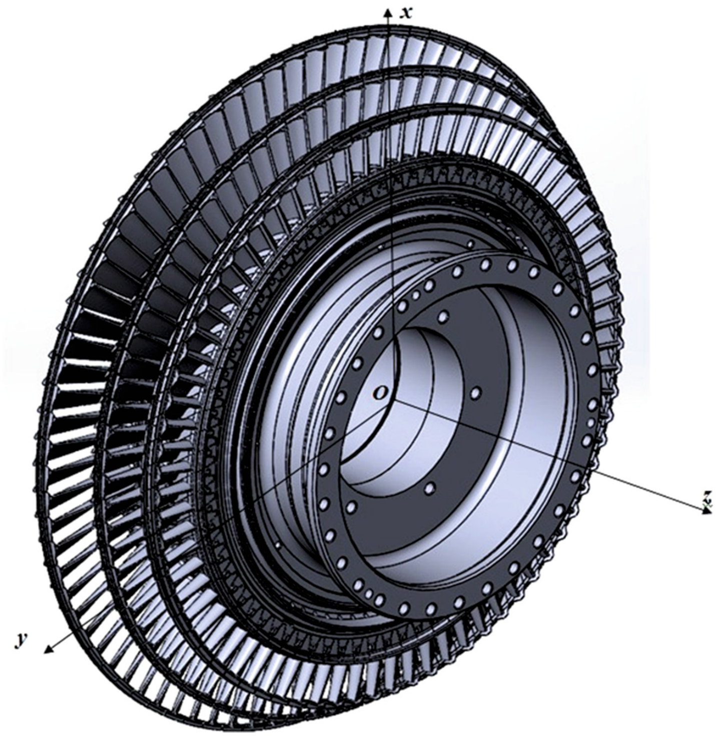

Fig. 1. The 3D model of the gas turbine rotor as a solid body

3.1 The Main Dependences for the Rotor Stress-Strain State Determination

According to the generalized Hooke's law [23–25] the solid body stress-strain state can be described by the next matrix dependence:

$$\{\sigma\} = [D](\{\varepsilon\} - \{\varepsilon_T\}) \quad (1)$$

where $\{\sigma\}$is stress matrix-vector; $\{\epsilon\}$ is elasticity deformation vector; $\{\epsilon_T\}$ is thermal elasticity vector; $[D]$ is elasticity matrix of the turbine rotor material.

The elasticity deformation vector has the following components:

$$\{\varepsilon\} = \begin{Bmatrix} \varepsilon_x \\ \varepsilon_y \\ \varepsilon_z \\ \gamma_{xy} \\ \gamma_{xz} \\ \gamma_{yz} \end{Bmatrix} = \begin{Bmatrix} \frac{\partial U_x}{\partial x} \\ \frac{\partial U_y}{\partial y} \\ \frac{\partial U_z}{\partial z} \\ \frac{\partial U_x}{\partial y} + \frac{\partial U_y}{\partial x} \\ \frac{\partial U_x}{\partial z} + \frac{\partial U_z}{\partial x} \\ \frac{\partial U_y}{\partial z} + \frac{\partial U_z}{\partial y} \end{Bmatrix} \quad (2)$$

where U_x, U_y, U_z are components of the generalized displacement vector

The material elasticity matrix is formed according to paper [17]:

$$[D] = \frac{E(1-\mu)}{(1+\mu)(1-2\mu)} \begin{bmatrix} 1 & \frac{\mu}{1-\mu} & \frac{\mu}{1-\mu} & 0 & 0 & 0 \\ & 1 & \frac{\mu}{1-\mu} & 0 & 0 & 0 \\ & & 1 & 0 & 0 & 0 \\ & & & \frac{1-2\mu}{2(1-\mu)} & 0 & 0 \\ & & & & \frac{1-2\mu}{2(1-\mu)} & 0 \\ & & & & & \frac{1-2\mu}{2(1-\mu)} \end{bmatrix} \quad (3)$$

where E is the rotor material Young's modulus, μ is the Poisson's ratio

The rotor thermal deformation (4) [8, 11, 14, 17]:

$$\{\varepsilon_T\} = \begin{Bmatrix} \varepsilon_{xT} \\ \varepsilon_{yT} \\ \varepsilon_{zT} \\ 0 \\ 0 \\ 0 \end{Bmatrix} = \alpha \begin{Bmatrix} T_x \\ T_y \\ T_z \end{Bmatrix} \quad (4)$$

where α is the material thermal extension coefficient; T_x, T_y, T_z are temperature field projections

To find the field of thermal deformations we need to solve the problem of heat exchange between the flow and the rotor. To find the field of elastic deformations we need to determine the field of the gas flow pressure and the rotor forced vibration amplitudes.

4 Solution to the Problem

4.1 Determination of the Gas Flow Pressure

The state of the gas flow at the flow path is determined by the following parameters: pressure (p); flow temperature (T_f); components of the flow velocity vector: u, v, w. In addition, to describe the properties of a viscous gas being compressed, it is necessary to know its density ρ and viscosity φ, which can be calculated using the above parameters. Thus, the state of any point in a viscous gas flow is given by five variables. So to find the flow pressure, a system of five equations is needed to determine the unknown variables. This system is:

The Navier – Stokes motion equations [2, 3, 12–23]:

$$\begin{aligned}
&\rho\cdot\left(\frac{\partial u}{\partial t}+u\frac{\partial u}{\partial x}+v\frac{\partial u}{\partial y}+w\frac{\partial u}{\partial z}\right)=\rho\cdot x-\frac{\partial p}{\partial x}+2\cdot\frac{\partial}{\partial x}\left(\varphi\frac{\partial u}{\partial x}\right)+\frac{\partial}{\partial y}\left[\varphi\left(\frac{\partial u}{\partial y}+\frac{\partial v}{\partial x}\right)\right]\\
&\quad+\frac{\partial}{\partial z}\left[\varphi\left(\frac{\partial u}{\partial z}+\frac{\partial w}{\partial x}\right)\right]-\frac{2}{3}\cdot\frac{\partial}{\partial x}\left[\varphi\left(\frac{\partial u}{\partial x}+\frac{\partial v}{\partial y}+\frac{\partial w}{\partial z}\right)\right];\\
&\rho\cdot\left(\frac{\partial v}{\partial t}+u\frac{\partial v}{\partial x}+v\frac{\partial v}{\partial y}+w\frac{\partial v}{\partial z}\right)=\rho\cdot y-\frac{\partial p}{\partial y}+\frac{\partial}{\partial x}\left[\varphi\left(\frac{\partial u}{\partial y}+\frac{\partial v}{\partial x}\right)\right]+2\cdot\frac{\partial}{\partial y}\left[\varphi\frac{\partial v}{\partial y}\right]\\
&\quad+\frac{\partial}{\partial z}\left[\varphi\left(\frac{\partial v}{\partial z}+\frac{\partial w}{\partial y}\right)\right]-\frac{2}{3}\cdot\frac{\partial}{\partial y}\left[\varphi\left(\frac{\partial u}{\partial x}+\frac{\partial v}{\partial y}+\frac{\partial w}{\partial z}\right)\right];\\
&\rho\cdot\left(\frac{\partial w}{\partial t}+u\frac{\partial w}{\partial x}+v\frac{\partial w}{\partial y}+w\frac{\partial w}{\partial z}\right)\\
&\quad=\rho\cdot z-\frac{\partial p}{\partial z}+\frac{\partial}{\partial x}\left(\varphi\left[\frac{\partial u}{\partial z}+\frac{\partial w}{\partial x}\right]\right)+\frac{\partial}{\partial y}\left[\varphi\left(\frac{\partial v}{\partial z}+\frac{\partial w}{\partial y}\right)\right]\\
&\quad+2\cdot\frac{\partial}{\partial z}\left(\varphi\frac{\partial w}{\partial z}\right)-\frac{2}{3}\cdot\frac{\partial}{\partial z}\left[\varphi\left(\frac{\partial u}{\partial x}+\frac{\partial v}{\partial y}+\frac{\partial w}{\partial z}\right)\right]
\end{aligned} \tag{5}$$

Energy equation [2, 3, 15, 16]:

$$\begin{aligned}
&\rho\cdot\left(\frac{\partial T_f}{\partial t}+u\frac{\partial T_f}{\partial x}+v\frac{\partial T_f}{\partial y}+w\frac{\partial T_f}{\partial z}\right)=\left[\frac{\partial p}{\partial t}+u\frac{\partial p}{\partial x}+v\frac{\partial p}{\partial y}+w\frac{\partial p}{\partial z}\right]\\
&\quad+\left[\frac{\partial}{\partial x}\left(\theta\frac{\partial T_f}{\partial x}\right)+\frac{\partial}{\partial y}\left(\theta\frac{\partial T_f}{\partial y}\right)+\frac{\partial}{\partial z}\left(\theta\frac{\partial T_f}{\partial z}\right)\right]+\nu\cdot\phi\\
&\phi=2\left[\left(\frac{\partial u}{\partial x}\right)^2+\left(\frac{\partial v}{\partial y}\right)^2+\left(\frac{\partial w}{\partial z}\right)^2\right]+\left(\frac{\partial v}{\partial x}+\frac{\partial u}{\partial y}\right)^2+\left(\frac{\partial w}{\partial y}+\frac{\partial v}{\partial z}\right)^2\\
&\quad+\left(\frac{\partial v}{\partial z}+\frac{\partial w}{\partial x}\right)^2-\frac{2}{3}\left(\frac{\partial u}{\partial x}+\frac{\partial v}{\partial y}+\frac{\partial w}{\partial z}\right)^2.
\end{aligned} \tag{6}$$

Continuity equation [2, 3, 5, 14, 21]:

$$\frac{\partial(\rho u)}{\partial t}+\frac{\partial(\rho u)}{\partial x}+\frac{\partial(\rho u)}{\partial y}+\frac{\partial(\rho u)}{\partial z}=0 \tag{7}$$

The detail solution of the equations system (5, 6 and 7) is given in paper [22]. From this system we can find the flow pressure field.

4.2 Determination of the Rotor Temperature Field

For the Solid Body Temperature Field Determination Next Variation Equation is Used [19, 20, 26, 27]:

$$\delta J_T=0$$

where J_T– thermal functional

For the its minimization, we use the general heat equation:

$$\lambda_x\frac{\partial^2 T}{\partial x^2}+\lambda_y\frac{\partial^2 T}{\partial y^2}+\lambda_z\frac{\partial^2 T}{\partial z^2}=0 \tag{8}$$

where λ_x, λ_y, λ_z are thermal conductivity coefficients, Wt*m/K.

The boundary conditions are next (9):

$$\lambda_x\frac{\partial T}{\partial x}l_x+\lambda_y\frac{\partial T}{\partial y}l_y+\lambda_z\frac{\partial T}{\partial z}l_z+(T-T_0)-q=0 \tag{9}$$

where l_x, l_y, l_z are direction cosines; h is heat transfer coefficient, Wt*m^2/K; T_0 is gas flow temperature, K; q is heat flux density, Wt/m^2.

Thus, on the base of Eqs. (7) and (9) we form the equation of convective heat transfer from turbulent gas flow to the solid body. Thus we can obtain the rotor temperature field:

$$J_T = \frac{1}{2}\int_V \left[\lambda_x\left(\frac{\partial T}{\partial x}\right)^2 + \lambda_y\left(\frac{\partial T}{\partial y}\right)^2 + \lambda_z\left(\frac{\partial T}{\partial z}\right)^2\right]dV + \int_S \left[\frac{1}{2}h(T - T_0)^2 - qT\right]dS \quad (10)$$

where V is turbine rotor volume; S is square of the heat exchanging surfaces.

4.3 Determination of the Turbine Rotor Forced Vibration Amplitudes and Dynamic Stresses Field

We can find the rotor forced vibration amplitudes, using the canonic equation of solid body vibration in matrix form:

$$[M]\left\{\frac{d^2U}{dt}\right\} + [C]\left\{\frac{dU}{dt}\right\} + [K]\{U\} = \{p\} \quad (11)$$

where $[M]$ is the mass matrix; $[C]$ is the damping matrix; $[K]$ is the stiffness matrix; $\{p\}$ is the vector of the flow pressure.

It is assumed that the considered turbine rotor is made without technological deviations, and therefore the rotor is a cyclic symmetrical system consisting of a certain number of homogeneous sections, containing three sectors – each for every impeller (Fig. 2).

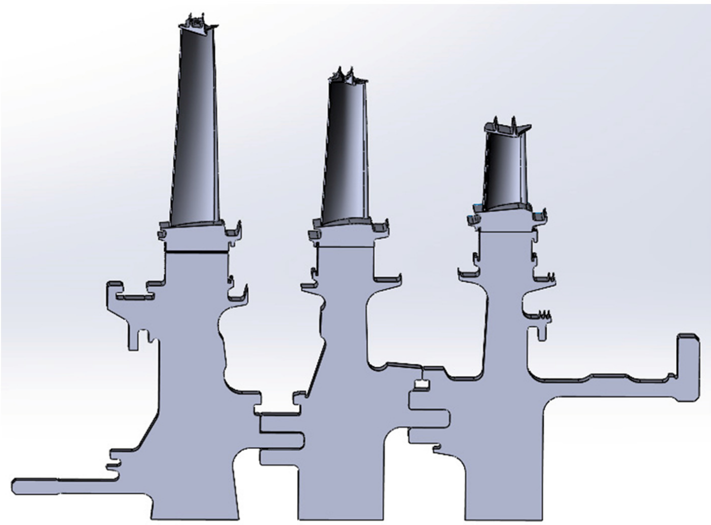

Fig. 2. The turbine rotor section.

The solution of matrix Eq. (11) can be found by spreading out the section generalized displacement in trigonometric row. So:

$$U_J = a_J^1 \cos(k\Omega t) + a_J^2 \sin(k\Omega t)$$
$$(J = 1 \ldots r, k = 1 \ldots g) \tag{12}$$

where a is vibration amplitudes; r is the nodes quantity in the section finite elements model; g is rotor forced vibration harmonic indexes number; υ is the rotor forced vibration frequency.

Here and next the upper indexes 1 and 2would be used later to mark the amplitudes belonging to $\cos(\Omega t)$ (index 1) and $\sin(\Omega t)$ (index 2).

After putting the Eq. (12) in Eq. (10) we receive:

$$M_{IJ}\left(a_J^1 cos(k\Omega t) + a_J^2 sin(k\Omega t)\right)'' + C_{IJ}\left(a_J^1 cos(k\Omega t) + a_J^2 sin(k\Omega t)\right)' +$$
$$+ K_{IJ}\left(a_J^1 cos(k\Omega t) + a_J^2 sin(k\Omega t)\right) = F_I^1 cos(k\Omega t) + F_I^2 sin(k\Omega t)$$
$$(I, J = 1, 2, \ldots, r) \tag{13}$$

Equations (5, 6, 10, 13) don't have analytical solution. Thus we need to use numerical methods. In our case we use the finite elements method FEM.

4.4 FEM Approximation of the Turbine Rotor Model

As the gas turbine rotor geometry is constructional inhomogeneous we need to use the finite elements of special shape functions for its correct approximation. So the developed mathematical model the special curvilinear finite elements of hexagonal type with negative Gaussian curvature have been taken (Fig. 3)

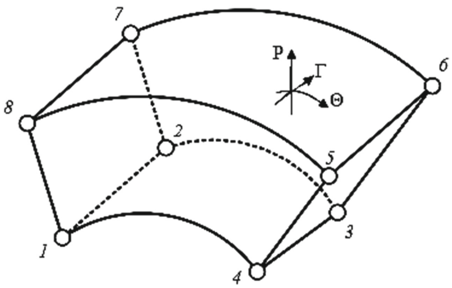

Fig. 3. Hexagonal finite element and its local curvilinear coordinate system PΓΘ

Shape functions description is given by a set of equations for the element curvilinear coordinates:

$$\begin{array}{ll} N_1 = \frac{1}{8}(1-\Theta)(1-\mathrm{P})(1-\Gamma) & N_2 = \frac{1}{8}(1-\Theta)(1-\mathrm{P})(1+\Gamma) \\ N_3 = \frac{1}{8}(1+\Theta)(1-\mathrm{P})(1+\Gamma) & N_4 = \frac{1}{8}(1+\Theta)(1-\mathrm{P})(1-\Gamma) \\ N_5 = \frac{1}{8}(1+\Theta)(1+\mathrm{P})(1-\Gamma) & N_6 = \frac{1}{8}(1+\Theta)(1+\mathrm{P})(1+\Gamma) \\ N_7 = \frac{1}{8}(1-\Theta)(1+\mathrm{P})(1+\Gamma) & N_8 = \frac{1}{8}(1-\Theta)(1+\mathrm{P})(1-\Gamma) \end{array} \tag{14}$$

Connection between the rotor global Cartesian coordinate system and the element local coordinate system is given below:

$$\begin{Bmatrix} x \\ y \\ z \end{Bmatrix} = \sum\nolimits_{i=1}^{8} N_i(\Theta, \mathrm{P}, \Gamma) \begin{Bmatrix} x_i \\ y_i \\ z_i \end{Bmatrix} \tag{15}$$

5 Results and Discussion

The power of the investigated gas turbine is 25 MW. The gas temperature at the entrance to the turbine rotor is 1583 K; total pressure at the stage inlet 0.7578 MPa; rotor speed 9390 rev/min.

As it is obvious from the Eqs. (2, 11) the increase of the turbine rotor dynamic stresses is caused by the growth of the rotor forced vibration frequency. The most dangerous are the low vibration frequencies, because they can cause the resonance state with the rotor rotation frequency. Thus, it is obligatory to obtain the distributions of displacements (mm) and stresses (MPa) for the first four harmonic indexes. The results of such calculations in graphic form are given below (Figs. 4 and 5).

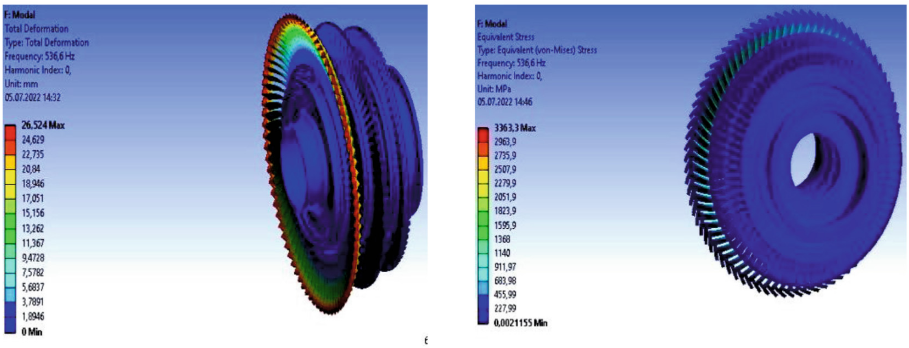

a b

Fig. 4. Turbine rotor displacement (*a*) and dynamic stresses (*b*) fields. Harmonic index $k = 0$, vibration frequency $\Omega = 536.6$ Hz

Analyzing data represented on the Figs. 6–7 it is obvious that the rotor dynamic stresses are first of all caused by the growth of its forced vibration frequency value. The

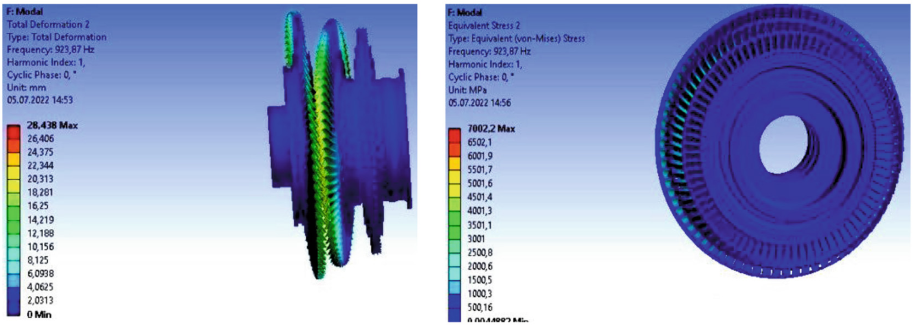

a b

Fig. 5. Turbine rotor displacement (a) and dynamic stresses (b) fields. Harmonic index $k = 1$, vibration frequency $\Omega = 923.87$ Hz

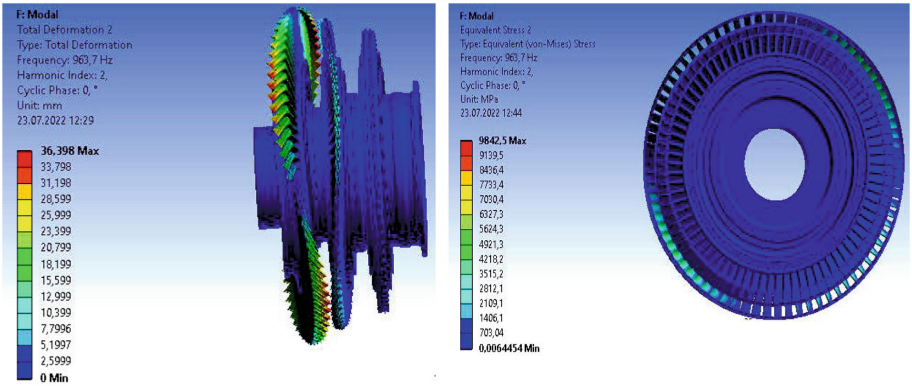

a b

Fig. 6. Turbine rotor displacement (a) and dynamic stresses (b) fields. Harmonic index $k = 2$, vibration frequency $\Omega = 963.7$ Hz

main factors, provoking the biggest displacement of the rotor are the working fluid flow, centrifugal force and thermal extension. For the third impeller blades such displacement is about 50 mm on the top of the blades peripheral section for the vibration frequency of 103.3 Hz. The reasons of this state are the length of the third impellers blades and the absence of the cooling channels in comparison with the blades of first and second impellers. But on the other hand it should be predicted that the third impeller resistance to low cycle fatigue will be more sufficient.

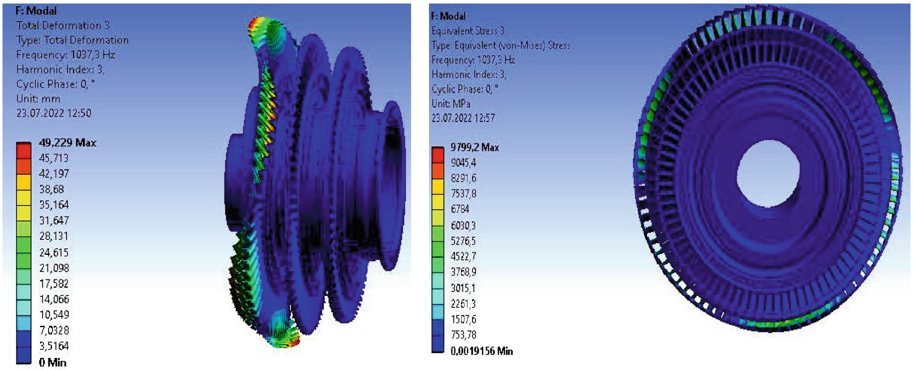

a b

Fig. 7. Turbine rotor displacement (*a*, *b*) and dynamic stresses (*c*) fields. Harmonic index $k = 3$, vibration frequency $\Omega = 1037.3$ Hz

The sharp gap between the highest stresses for harmonic index 0 and harmonic index 3 is nearly 600 MPa. We also observe that this drop of dynamic stresses is caused by the non stationary gas flow influence on the blades feather peripheral and root sections. Due to the rotor geometry the main part of the flow kinetic energy and the hear exchange between the blades and the flow take place in their peripheral part. One more dependence of vast importance is that the maximum dynamic stresses for the vibration mode with the harmonic index $k = 3$ nearly reach the rotor ultimate strength.

6 Conclusion

The study of the modern gas turbine engine rotor stress-strain state has been held. For this problem a refined mathematical model using the curvilinear hexagonal finite elements with eight nodes was developed. Using the developed mathematical model, the problems of the turbine rotor flow dynamics and heat exchange have been studied. The received data has been used as initial for the rotor stress-strain state and forced vibration amplitudes calculation. The level of the rotor dynamic stresses and its forced vibration frequencies for different harmonic indexes are connected directly proportional. The main factors of such dynamic stresses fields are the non-stationary gas flow, causing the irregular pressure field and heat exchange on the rotor surfaces gas flow pressure. The sharp temperature gradient between the peripheral part of the blade, its root part and the disk is also should be taken into account. Such negative factors with the high level of dynamic stresses demand the new studies of the turbine rotor creep and fatigue strength.

References

1. Vassiliev, V., Kostege, V., Schnedler, P., Trishkin, A.: Thermal state analysis of industrial gas turbine blades. In: ASME Turbo Expo: Power for Land Sea and Air Proceedings, pp. 813–824 (2008). https://doi.org/10.1115/GT2005-68951

2. Wang, S., Shouzuo, L., Lei, L., Zhao, Z., Wei, D., Bengt, S.: A high temperature turbine blade heat transfer multilevel design platform. Numer. Heat Transf. Part A App. **79**(2), 122–145 (2021). https://doi.org/10.1080/10407782.2020.1835104
3. Zienkiewicz, O.C.: The Finite Element Method for Solid and Structural Mechanics. Elsevier/Butterworth-Heinemann, Amsterdam, Boston (2014)
4. Mzarbhuiya, H.M.S.M., Pandey, K.M.: Steady state structural analysis of high pressure gas turbine blade using finite element analysis. In: IOP Conference Series: Material Science and Engineering (2017). https://doi.org/10.1088/1757-899X/225/1/012113
5. Ziaei-Asl, A., Tayefe-Ramezanlou, M.: Thermo-mechanical behavior of gas turbine blade equipped with cooling ducts and protective coating with different thickness. Int. J. Mech. Sci. **150**, 656–664 (2019). https://doi.org/10.1016/i.jmecsci.2018.10.070
6. Aniekan, I.E., Oghenefeijro, E.-O.E., Godfrey, A.O.: Thermo-structural analysis of first stage gas turbine rotor blade materials for optimum service performance. Int. J. Eng. Appl. Sci. **10**(2),118–130 (2018). https://doi.org/10.24107/ijeas.447650
7. Kumar, R., Kumar, V.S., Butt, M.M., Sheikh, N.A., Khan, S.A., Afzal, A.: Thermo-mechanical analysis and estimation of turbine blade tip clearance of a small gas turbine engine under transient operating conditions. Appl. Therm. Eng. (2020). https://doi.org/10.1016/applithermaleng.2020.115700
8. Arnab, B., Prabhakar, S., Giacomo, C.: Natural frequency analysis of a functionally graded rotor-bearing system with a slant crack, subjected to thermal gradients. Int. J. Turbo Jet Eng. **40**(3), 243–255 (2023). https://doi.org/10.1515/tjj-2021-0002
9. Eliseev, V., Moskalets, A.: Application of the Lagrange-Ritz-Kantorovich method to the vibration analysis of turbine blades. NTU "KhPI" Bull. Power Heat Eng. Proc. Equip. **8**, 149−152 (2016). https://doi.org/10.20998/2078-774X.2016.08.21
10. Boychenko, N., Ishtyryakov, I.: Characterization of the stress-strain state in a gas turbine engine compressor disk taking into account damage accumulation. Frattura ed Integrita Struturalle **50**, 54–67 (2019). https://doi.org/10.3221/IGF-ESIS.50.07
11. Duriagina, Z.A., Kulyk, V.V., Filimonov, O.S., Trostianchyn, A.M., Sokulska, N.B.: The role of stress-strain state of gas turbine engine metal parts in predicting their safe life. Progr. Phys. Metals. **22**(4), 643−677 (2021). https://doi.org/10.15407/ufm.22.04.643
12. Shakurova, L., Armenise, I., Kustova, E.: Effect of slip boundary conditions on nonequilibrium reacting air flows. J. Theoret. Appl. Mech. **53**(3), 253−269 (2023). https://doi.org/10.55787/jtams.23.53.3.253
13. Skamniottis, C., Courtis, M., Cocks, C.F.A.: Multiscale analysis of thermomechanical stresses in double wall transpiration cooling systems for gas turbine blades. Int. J. Mech. Sci. (2021). https://doi.org/10.1016/j.ijmec.sci.2021.106657
14. Kauss, O., Tsybenko, H., Naumenko, K., Hutter, S., Kruger, M.: Structural analysis of gas turbine blades made of Mo-Si-B under transient thermo-mechanical loads. Compos. Mater. Sci. **165**, 129–136 (2019). https://doi.org/10.1016/j.commatsci.2019.04.23
15. Narasimbachary, S.B., Smith, K., Schinde, R.S., Amann, C., Kadau, K., Iyer, S.: Life assessment of large turbine blades. In: ASME Turbo Expo 2019: Turbomachinery Technical Conference and Exposition Proceeding Paper (2019). https://doi.org/10.1115/GT2019-91630
16. Arkhipov, A.N., Volgina, M.V., Matushkin, A.A., Ravikovich, Y., Kholobtsev, D.P.: Effect of a model and boundary conditions on the results of analyzing the stress-strain state of a low pressure compressor rotor. Struct. Mech. Strength Flight Veh. **61**, 509–516 (2018). https://doi.org/10.3103/S1068799818040025
17. Seok, S., Shahriar, A., Montoya, A.: A finite element approach for simplified 2D nonlinear dynamic contact impact analysis. Arch. Appl. Mech. **93**, 3511–3531 (2023). https://doi.org/10.1007/s00419-023-02451-y

18. Yang, L., Ren, J., Jiang, H., Luan, Y., Ligrani, P.: Experimental and numerical investigation of unsteady impingement cooling within a blade leading edge passage. Int. J. Heat Mass Transf. **71**, 57–68 (2014). https://doi.org/10.1046/ijheatmasstransfer.2013.12.006
19. Furlani, L., Armellini, A., Casarsa, L.: Rotational effects on the flow field inside a leading edge impingement cooling passage. Exp. Thermal Fluid Sci. **76**, 57–66 (2016). https://doi.org/10.1016/j.expthermflusci.2016.03.004
20. Yershov, S. V., Yakovlev, V. A.: The influence of mesh resolution on 3D RANS flow simulations in turbomachinery flow parts. J. Mech. Eng. **24**(1), 13−27 (2021). https://doi.org/10.15407/pmach2021.01.013
21. Morhun, S., Vilkul, S.: Gas dynamic analysis of the modern single shaft gas turbine engine flow path. Int. J. Turbo Jet Eng. (2022). https://doi.org/10.1515/tjeng-2022-019
22. Morhun, S.: Numerical analysis of the gas turbine rotor blades thermal state using a refined mathematical model. In: Shkarlet, S., et al. (eds.) Mathematical Modeling and Simulation of Systems MODS 2021. LNNS, vol. 344, pp. 115–123. Springer, Cham (2022). https://doi.org/10.1007/978-3-030-89902-8_9
23. Kantor, B.Ya., Smetankina, N.V., Shupikov, A.N.: Analysis of non-stationary temperature fields in laminated strips and plates. Int. J. Solids Struct. **38**(48/49), 8673–8684 (2001). https://doi.org/10.1016/S0020-7683(01)00099-3
24. Misura, S., Smetankina, N., Misiura, I.: Optimal design of the cyclically symmetrical structure under static load. In: Nechyporuk, M., Pavlikov, V., Kritskiy, D. (eds.) Integrated Computer Technologies in Mechanical Engineering - 2020 ICTM 2020. LNNS, vol. 188, pp. 256–266. Springer, Cham (2021). https://doi.org/10.1007/978-3-030-66717-7_21
25. Sklepus, S.N.: Numerical-and-analytical method for creep investigation in functionally graded complex-shaped bodies of rotation. Strength Mater. **52**, 235–242 (2020). https://doi.org/10.1007/s11223-020-00170-1
26. Balitskii, A.I., et al.: Improvement of the mechanical characteristics, hydrogen crack resistance and durability of turbine rotor steels welded joints. Energies **15**(16), 6006 (2022). https://doi.org/10.3390/en15166006

A Research on the Influence of Anisotropic Characteristics of Single-Crystal Gas Turbine Blades on Their Durability

Yevhen Nemanezhyn[1,2(✉)], Gennadiy Lvov[2], and Yuriy Torba[1]

[1] State Enterprise "Ivchenko-Progress", Ivanova Street 2, Zaporizhzhia, Ukraine
Yevhen.Nemanezhyn@infiz.khpi.edu.ua
[2] NTU "Kharkiv Polytechnic Institute", Kyrpychova Street 2, Kharkiv 61002, Ukraine

Abstract. One of the key parameters in the gas turbine blade resource design stage is their long-term static strength analysis. Such analysis is crucial for various reasons, including studying anisotropic properties of single-crystal turbine blades composed of nickel heat-resistant alloys with different crystallographic orientations within a wide range of stresses and temperatures. To date, there is no universal methodology for assessing the durability of turbine blades. The existing approaches, documented in numerous literary sources, have both their pros and significant cons. The research, presented in this article, proposes a technique for evaluating the long-term static strength of single-crystal turbine blades. The authors' method involves deriving equations for the distribution of the Larson-Miller parameter using experimental data for various crystallographic orientations of turbine blades. These equations were then used to create a finite-element model demonstrating the parameter's distribution in a cooled high-pressure turbine blade, using the ANSYS Workbench 19.2 software package. With the use of Larson-Miller parameter distribution calculations, the fracture time for each of the three specified crystallographic orientations of turbine blade model was investigated.

Keywords: finite-element analysis · long-term strength · creep · anisotropy · monocrystalline alloy · crystallographic orientation · gas turbine engine

1 Introduction

In the study of the durability of single-crystal gas turbine blades, special attention is paid to the research of the long-term static strength of single-crystal nickel alloys of different crystallographic orientations under changes in a wide range of stresses and temperatures, since these factors are the most influential in the resource design of aircraft gas turbine engines. To date, there are no generally accepted methods for assessing the long-term static strength and calculating the stress-strain state of monocrystalline turbine blades. Isotropic inelastic design models are not suitable for estimating the strength parameters of anisotropic turbine blades, produced from single-crystal alloys. The most acceptable and effective approach to assessing the long-term strength of monocrystalline

M. Nechyporuk et al. (Eds.): ICTM 2023, LNNS 1008, pp. 397–408, 2024.
https://doi.org/10.1007/978-3-031-61415-6_34

gas turbine blades under alternating thermal and cyclic loading is to use micromechanical (physical or crystallographic) models of inelastic deformation of single crystals [1, 2]. Such models take into account the peculiarities of deformation of a single crystal along its sliding systems. The disadvantages of such approaches include: determination of a huge number of unknown parameters of specific materials; inability to use modern finite element analysis software for implementation of such methods, due to the lack of necessary models; development of special software for calculations using these methods. In this case an alternative route lies in usage of a variety of phenomenological models of inelastic materials deformation [3, 4], which also have a number of their own features and disadvantages.

An additional complication in studying the patterns of inelastic deformation of single crystals is the need to take into account the evolution of the initial microstructure γ–γ' of a particular alloy under continuous high-temperature loading. The following factors affect the parameters of such evolution: temperature (stable or variable), time of strain exposure of the material and strain magnitude, features of the crystallographic orientation of specific material samples, structure and chemical composition of a particular nickel alloy [5]. The distribution of the Schmid factor in different octahedral systems of a stereographic triangle can provide a qualitative assessment of the orientation dependence of the strength of single crystals [6].

At the present stage, it is possible to create advanced computational models of inelastic deformation using the finite element method and to perform calculations taking into account the peculiarities of physically nonlinear processes (creep) in single-crystal alloys. Based on the explanations mentioned above, very urgent and topical issue lies in development of a methodology for calculating the long-term strength parameters of turbine blades made of single-crystal nickel alloys.

2 Literature Review

The problem of studying the influence of the properties of single-crystal turbine blades on their long-term strength and creep characteristics is described in a sufficient number of publications. Article [7] mentions the rotor blades of gas turbine engines made of single-crystal nickel alloys. The objective of the authors' study was to model nonlinear deformation during typical operating cycles for further calculation of the blades' safe service life. As a result, they developed a methodology for analyzing anisotropic creep. The authors also proposed models for calculating high-temperature creep and thermomechanical fatigue strength of single crystal samples and turbine blades, taking into account complex non-isothermal loading. The developed model is intended for use in the ABAQUS finite element program, in which inelastic deformation is considered as a combination of instantaneous plastic deformations that depend on the time of thermal and creep deformation.

Scientists in [8] conducted studies using plate samples with holes (which represent full-scale models of cooled single-crystal turbine blades) and without holes. Such an experiment was conducted for samples of two different crystallographic orientations [001] and [111] of a second-generation single-crystal nickel alloy under creep conditions at 980 °C. The test results showed that the cooling holes and crystallographic orientation significantly affect the fracture mechanism and its rate. The authors also used a modified form of the Kachanov-Rabotnov damage law in their study.

Paper [9] discusses the modeling of anisotropic creep and ductility of single-crystal nickel blades. The authors proposed a modified Hill operator to establish empirical correlations for assessing the long-term strength of monocrystalline turbine blades. Study [10], in turn, presents a phenomenological approach based on Hill's work on plasticity. The manifestation of the characteristics of single-crystal materials under mechanical loading is approximated by adopting simplified anisotropy classes that can most accurately reflect the peculiarities of material behavior.

Paper [11] presents the methodological foundations of an approach to solving the problem of finite element modeling of the long-term static strength of cooled single-crystal blades of gas turbine engines. This approach is based on the usage of phenomenological and micromechanical models of material creep. The calculations were carried out taking into account the peculiarities of different crystallographic orientations of the material. The procedure for determining the coefficients of anisotropy of long-term strength based on the calculations for different monocrystalline orientations is presented. The researchers found that the model of micromechanical creep deformation, in comparison with the phenomenological one, allows the most accurate assessment of the long-term strength of turbine blades made of single-crystal alloys.

Publication [12] contains information on the creep, long-term strength, and low-cycle fatigue strength characteristics of the monocrystalline nickel alloy DZ125. These characteristics were analyzed using a modified unified Shabosh viscoplasticity model. This model considers the anisotropic behavior of the material, the effect of cyclic hardening and stress relaxation. When setting the material parameters, the Levenberg-Marquardt optimization procedure was used, which takes into account the properties of a given material in tension, its behavior under cyclic loading, and creep characteristics. The model was built in FORTRAN and integrated into the finite element analysis software UMAT/ABAQUS. The analysis of the results of calculations based on this model has made it possible to establish that such a modified model has practical application for determining the characteristics of low-cycle fatigue strength, creep, and long-term strength of various materials.

This study concentrates on creating a methodology for assessing the long-term strength of single-crystal turbine blades using a finite element 3D-model of a cooled turbine blade made of a monocrystalline nickel heat-resistant alloy.

3 Research Methodology

3.1 Approximation of the Experimental Larson-Miller Curves of the Fourth Generation Single-Crystal Alloy

Experimental data on the long-term strength of single-crystal samples are characterized by incomplete information for a wide range of temperatures and time under load, as well as by a significant scattering of their values. One of the best options for demonstrating and organizing the data of such studies is to use the temperature-time dependences in the form of the Larson-Miller parameter, which is represented by the following expression:

$$P_{LM} = T\left(\log \tau_{fail} + 20\right), \tag{1}$$

where log τ_{fail} – time to sample fracture, h; T – temperature of a material, K.

Figure 1 shows the experimental curve of the Larson-Miller parameter for a fourth-generation single-crystal alloy with crystallographic orientation <001> (A4 alloy) [11]. As an initial step in assessing the long-term strength of a turbine blade, it is necessary to determine the equation of such curve form.

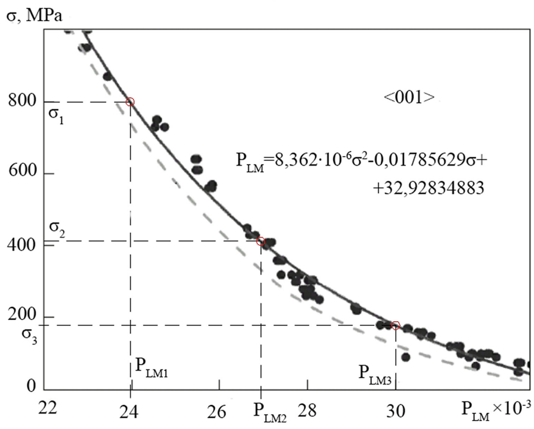

Fig. 1. The Larson-Miller curve and its parabolic equation for the crystallographic orientation <001> of a single-crystal alloy

In order to obtain the equation of the experimental curve, it was approximated by the method of parabolic interpolation. Initially, three arbitrary points were selected on the graph, which were subsequently used for calculations. The coordinates of these points on the graph indicate specific stresses and the corresponding values of the Larson-Miller parameters. In this case, the following coordinates of these points were obtained:

Point 1: $\sigma_1 = 800$ MPa; $P_{LM1} = 23995$.
Point 2: $\sigma_2 = 413$ MPa; $P_{LM2} = 26980$.
Point 3: $\sigma_3 = 179$ MPa; $P_{LM3} = 30000$.

The parabolic equation that describes the Larson-Miller curve in Fig. 1 has the following general form:

$$P_{LM} = C_1\sigma^2 + C_2\sigma + C_3. \tag{2}$$

To perform the approximation, a system of equations with three unknown characteristics was compiled, which has the following form:

$$\begin{cases} P_{LM1} = C_1\sigma_1^2 + C_2\sigma_1 + C_3 \\ P_{LM2} = C_1\sigma_2^2 + C_2\sigma_2 + C_3 \\ P_{LM3} = C_1\sigma_3^2 + C_2\sigma_3 + C_3 \end{cases} \tag{3}$$

Given the coordinates of three points, this system of equations with three C_1, C_2, C_3 unknown constants was solved using Kramer's formulas.

As a result, the parabolic equation of the Larson-Miller parameter for the crystallographic orientation of the single crystal <001> was obtained, which is additionally shown in Fig. 1:

$$P_{LM} = 8,362 \cdot 10^{-6}\sigma^2 - 0,017856\sigma + 32,928349 \tag{4}$$

A similar procedure was carried out for the Larson-Miller parameter curves for additional two crystallographic orientations of the material.

The values of the points selected for the calculation of the equation for the crystallographic orientation <011>:

Point 1: $\sigma_1 = 400$ MPa; $P_{LM1} = 25950$.
Point 2: $\sigma_2 = 259$ MPa; $P_{LM2} = 28150$.
Point 3: $\sigma_3 = 168$ MPa; $P_{LM3} = 30000$.

As a result, the parabolic equation of the Larson-Miller parameter for the crystallographic orientation of the single crystal <011> was obtained after the calculations:

$$P_{LM} = 2,03743 \cdot 10^{-5}\sigma^2 - 0,02902949\sigma + 34,30191038 \tag{5}$$

Figure 2 shows the calculated equation for the single crystal with <011> orientation.

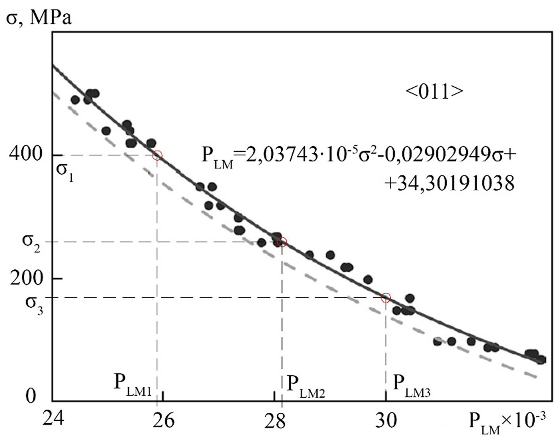

Fig. 2. The Larson-Miller curve and its parabolic equation for the <011> single crystal orientation

The values of the points selected to calculate the value of Larson-Miller parameter equation for the crystallographic orientation <111>:

Point 1: $\sigma_1 = 800$ Pa; $P_{LM1} = 24135$.
Point 2: $\sigma_2 = 457$ Pa; $P_{LM2} = 27094$.
Point 3: $\sigma_3 = 214$ Pa; $P_{LM3} = 30000$.

As a result, after the calculations, the parabolic equation of the Larson-Miller parameter for a single-crystal alloy with <111> crystallographic orientation was also obtained:

$$P_{LM} = 5,68605 \cdot 10^{-6}\sigma^2 - 0,01577419\sigma + 33,11527778. \quad (6)$$

Figure 3 shows the calculated equation of P_{LM} for the crystallographic orientation of a single-crystal alloy <111>.

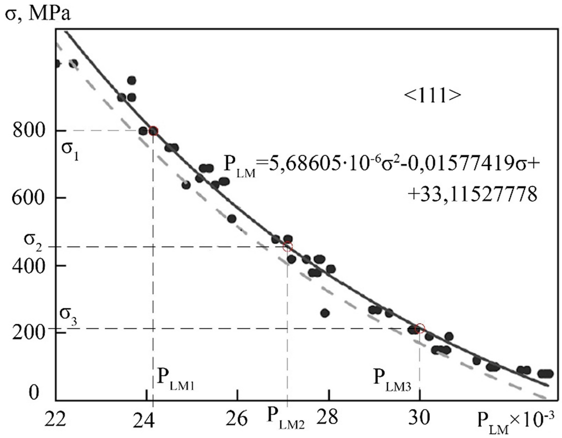

Fig. 3. The Larson-Miller curve and its parabolic equation for the monocrystalline <111> crystallographic orientation

4 Results and Discussion

4.1 Finite Element Modeling of the Distribution of the Larson-Miller Parameter Over the Monocrystalline Gas Turbine Blade

The obtained equations of the Larson-Miller parameter for several crystallographic orientations of the single crystal were used for finite element modeling of its distribution over the turbine blade in ANSYS Workbench 19.2.

The calculation was performed on a 3D-model of a cooled high-pressure turbine blade. The method for obtaining the elastic characteristics of the material and their actual values (Young's modulus, Poisson's ratio, and shear modulus) for different temperatures, as well as the methodology and parameters for a finite-element model construction are described in [13, 14]. As the initial data for the numerical experiment, the creep calculation, where the boundary conditions on the blade surface were the displacement limits on the planes of the blade lock (tail) part in contact with the turbine disk, was used.

The calculations were performed for the load due to centrifugal force at a rotor speed of N = const = 50,000 rpm. The creep time was assumed to be 20,000 s (5,55 h). Acquiring creep constants at a temperature of T = const = 975 °C, according to the Norton-Bailey law, is described in previous publication [15].

The results of the distribution of equivalent stresses at the stage of stationary creep, obtained after the calculation in the "Static Structural" module, are shown in Fig. 4.

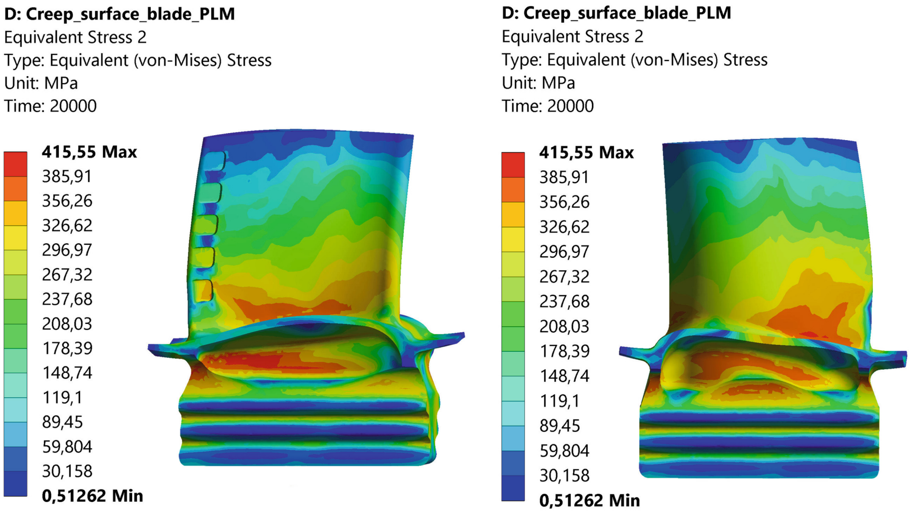

Fig. 4. Euivalent stresses on the blade when calculating creep

To simulate the distribution of the Larson-Miller parameter over the turbine blade, the "User Defined Results" tool, which is a sub-module of ANSYS Workbench, was used. The equations of the Larson-Miller curves obtained by parabolic interpolation for different crystallographic orientations of the single-crystal alloy were entered into the "User Defined Results" sub-module. The equivalent stresses (seqv) obtained from the creep calculation, shown in Fig. 4, were used as the stresses from Eq. (2). Table 1 shows the results of calculating the distribution of the Larson-Miller parameter for different monocrystalline orientations <001>, <011> and <111> of a full-size turbine blade of the cooled design.

Analyzing the obtained calculation results, it can be observed that the lowest value of the Larson-Miller parameter distribution $P_{LM} = 25757$ was shown by blades with <011> crystallographic orientation.

Table 1. The results of calculation of the distribution of the Larson-Miller parameter over the blade

<table>
<tr><th>Crystallographic orientation</th><th>Distribution of P_{LM} over the turbine blade</th></tr>
<tr><td><001></td><td>
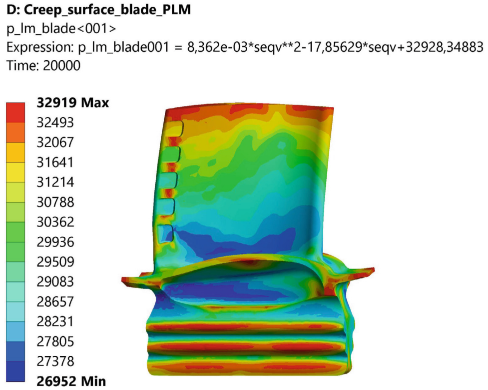

</td></tr>
<tr><td><011></td><td>
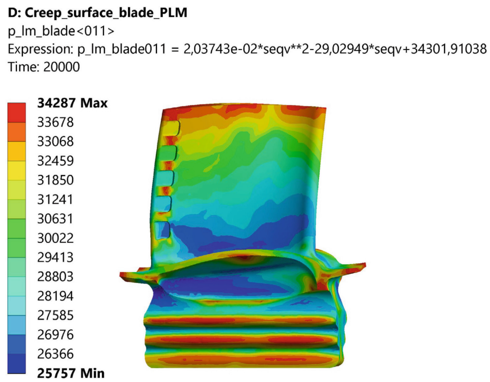

</td></tr>
<tr><td><111></td><td>
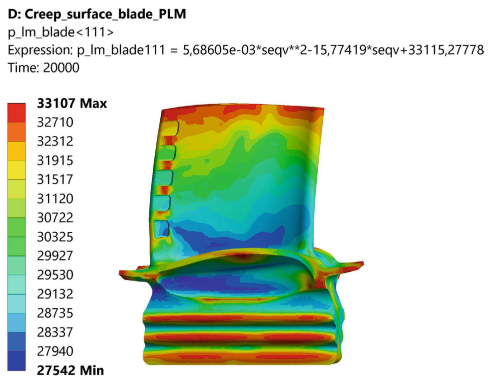

</td></tr>
</table>

When entering the equations of the Larson-Miller parameter distribution for different crystallographic orientations of a single crystal into the User Defined Results sub-module, they were assigned with their own unique identifiers in the “Identifier” column, namely:

- Larson-Miller parameter P_{LM} of single crystal with <001> orientation – identifier p_lm_blade <001>;
- Larson-Miller parameter P_{LM} of single crystal with <011> orientation – identifier p_lm_blade <011>;
- Larson-Miller parameter P_{LM} of single crystal with <111> orientation – identifier p_lm_blade <111>.

The identifiers, mentioned above, were created in order to associate them with corresponding equations of Larson-Miller parameter P_{LM} distribution.

4.2 Comparative Analysis of the Time to Failure of Turbine Blades with Different Crystallographic Orientations

After obtaining the results of calculation of the distribution of the Larson-Miller parameter over the turbine blade, we proceed directly to the calculation of the practical and most indicative parameter in assessing long-term strength, the time-to-failure of the turbine blade. From the general relation (1) of the Larson-Miller parameter, the equation for the time to failure was found:

$$\tau_{fail} = 10^{\left(\frac{P_{LM}}{T} - 20\right)} \tag{7}$$

The resulting equation was entered into the “Expression” column in the “User Defined Results” sub-module, and its previously calculated values of distribution of Larson-Miller parameter over the turbine blade were used via their identifiers. To calculate the time to fracture for each single crystal orientation, the corresponding identifiers of P_{LM} for the crystallographic orientations <001>, <011>, <111> were used. Table 2 shows the results of calculating the time-to-failure for different orientations of the cooled turbine blade of an aircraft gas turbine engine.

The calculation shows that the time-to-fracture of single-crystal turbine blade cast with different crystallographic orientations is equal:

- for <001> orientation: $\tau_{fail} = 39,467$ h;
- for <011> orientation: $\tau_{fail} = 4,3508$ h;
- for <111> orientation: $\tau_{fail} = 117,23$ h.

The lowest value of time-to-failure parameter in this calculation set was shown by the blade composed with <011> orientation and the highest – <111> orientation.

Table 2. Time to failure of a single-crystal turbine blade with orientations <001>, <011>, <111>

<table>
<tr><th>Crystallographic orientation</th><th>Result of calculating the time-to-failure</th></tr>
<tr><td><001></td><td>

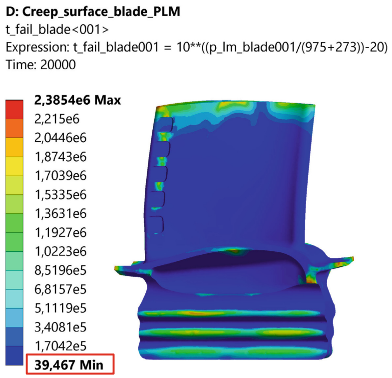

</td></tr>
<tr><td><011></td><td>

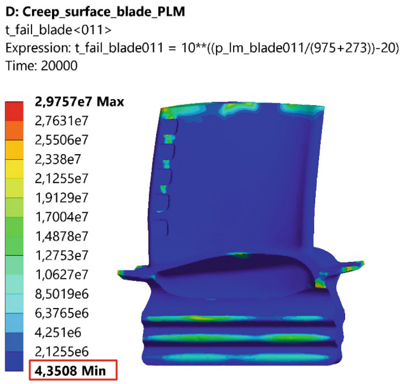

</td></tr>
<tr><td><111></td><td>

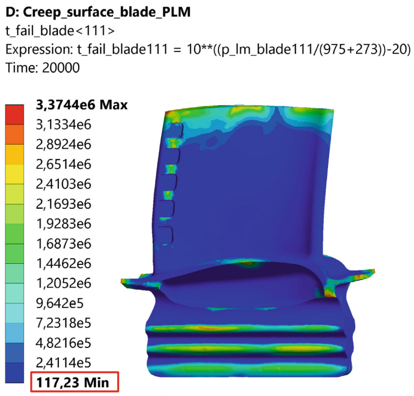

</td></tr>
</table>

5 Conclusions

Based on the information, mentioned in this article, following conclusions can be drawn:

1. The method has been developed for calculating the long-term strength of single-crystal blades of high-temperature turbines operating under conditions of loading by centrifugal forces. The method allows one to take into account the anisotropy of long-term strength characteristics in calculations based on a limited amount of experimental data.
2. The use of finite-element analysis makes it possible to obtain a detailed picture of the stress distribution in cooled blades of complex geometric shapes.
3. Using experimental data on the Larson-Miller parameter, an estimate of the time to failure of blades made of single-crystal alloys with different crystallographic orientations was obtained. This study was carried out taking into account stress redistribution due to creep.
4. Based on the research results, the importance of taking into account the crystallographic orientation of the alloy when calculating the long-term strength of turbine blades is shown. According to the calculation results, the lowest value of time-to-failure parameter, namely 4,3508 h, was shown by the blade composed with <011 > orientation. The highest value of time-to-failure parameter, namely 117,23 h, was demonstrated by the turbine blade manufactured with <111 > crystallographic orientation. Thus, an analysis of the orientation dependence of the time-to-failure allowed us to conclude, that for cooled blades the <111 > orientation is the most preferable.
5. The practical implementation of the developed method requires the systematic accumulation of experimental data on the long-term strength of single-crystal alloys in a wide temperature range.

References

1. Semenov, A.S., Getsov, L.B.: Thermal fatigue fracture criteria of single crystal heat-resistant alloys and methods for identification of their parameters. Strength Mater. **46**, 38–48 (2014). https://doi.org/10.1007/s11223-014-9513-2
2. Busso, E.P., Meissonnier, F.T., O'Dowd, N.P.: Gradient-dependent deformation of two-phase single crystals. J. Mech. Phys. Solids **48**, 2333–2361 (2000). https://doi.org/10.1016/S0022-5096(00)00006-5
3. Besson, J., Cailletaud, G., Chaboche, J.-L., Forest, S.: Non-linear mechanics of materials. Springer, Dordrecht (2010). DOI: https://doi.org/10.1007/978-90-481-3356-7
4. Getsov, L.B., et al.: Computational determination of GTE blades and vanes life. Part 2. Single crystal alloys. Gas. Turb. Technol. **8**, 18–25 (2011)
5. Grishchenko, A.I., Semenov, A.S., Getsov, L.B.: Modeling inelastic deformation of single crystal superalloys with account of γ/γ' phases evolution. Mater. Phys. Mech. **24**, 325–330 (2015)
6. Golubovskii, E.R., Svetlov, I.L.: Time-temperature dependence of anisotropy of creep-rupture strength characteristics of single crystals of nickel-base superalloys. Strength Mater. **34**, 109–119 (2002). https://doi.org/10.1023/A:1015365723962
7. Henderson, M.B., Ward, T.J., Harrison, G.F., Hughes, M.: Creep and thermomechanical fatigue modelling of single crystal superalloy turbine blades. ASME, vol. 4, pp. 1–5, Louisiana, USA (2001). https://doi.org/10.1115/2001-GT-0596

8. Yu, Q.M., Yue, Z.F., Wen, Z.X.: Creep damage evolution in a modeling specimen of nickel-based single crystal superalloys air-cooled blades. Mater. Sci. and Eng. A **477**(1–2), 319–327 (2008). https://doi.org/10.1016/j.msea.2007.05.080
9. Ramaglia, A.D., Villari, P.: Creep and fatigue of single crystal and directionally solidified nickel-base blades via a unified approach based on Hill48 potential function: Part 2 — Low cycle fatigue. ASME 2013, vol. 7A, Proceedings of the ASME Turbo Expo 2013: Turbine Technical Conference and Exposition, USA (2013). https://doi.org/10.1115/GT2013-94676
10. Ramaglia, A.D., Villari, P.: Creep and fatigue of single crystal and directionally solidified nickel-base blades via a unified approach based on Hill48 potential function: Part 1 — Plasticity and creep. ASME 2013, vol. 7A, Proceedings of the ASME Turbo Expo 2013: Turbine Technical Conference and Exposition, USA (2013).https://doi.org/10.1115/GT2013-94675
11. Getsov, L.B., Semenov, A.S., Besschetnov, V.A., et al.: Long-term strength determination for cooled blades made of monocrystalline superalloys. Therm. Eng. **64**, 280–287 (2017). https://doi.org/10.1134/S0040601517040048
12. Haq, A.U., Yang, X.G., Shi, D.Q.: Isothermal fatigue and creep-fatigue interaction behavior of nickel-base directionally solidified superalloy. Strength Mater. **1**, 112–120 (2018). https://doi.org/10.1007/s11223-018-9947-z
13. Nemanezhyn, Ye., Lvov, G., Torba, Yu.: Numerical simulation of the natural frequencies dependence of turbine blade vibrations on single-crystal anisotropy. In: Tonkonogyi, V., Ivanov, V., Trojanowska, J., Oborskyi, G., Pavlenko, I. (eds), InterPartner 2023, Advanced Manufacturing Processes V, LNME, pp. 485–497, Springer, Cham (2023). https://doi.org/10.1007/978-3-031-42778-7_45
14. Nemanezhyn, Ye., Lvov, G., Torba, Yu.: A method for evaluation of the dependence of gas turbine blade vibrations on monocrystalline anisotropy. Aerospace tech. and technol. 4 special issue 2(190), 50–58 (2023). https://doi.org/10.32620/aktt.2023.4sup2.06
15. Nemanezhyn, Ye., Lvov, G., Torba, Yu.: Numerical simulation of the steady creep of single-crystal alloys. In: Nechyporuk, M., Pavlikov, V., Kritskiy, D. (eds), ICTM 2022, LNNS, vol. 657, pp. 421–429, Spinger, Cham (2023). https://doi.org/10.1007/978-3-031-36201-9_36

Utilizing CFD Technology in the Design of the Combustion Chamber for the Hydrogen-Powered Hybrid Energy System

Oleksandr Shmarkov(✉), Serhiy Serbin, and Mykola Bondarenko

Admiral Makarov National University of Shipbuilding, Mykolaiv 54025, Ukraine
shmarkov.oleksandr@gmail.com

Abstract. Addressing issues related to the enhancement of existing thermal engines and combustion processes in their combustion chambers (CC), as well as deepening our understanding of potential challenges in the improvement of gas turbine installations, opens new horizons in modern energy. Hybrid gas-steam power systems utilizing hydrogen gases and pure hydrogen offer a wide range of possibilities and potential technical solutions related to decarbonization. The paper presents the results of using Computational Fluid Dynamics (CFD) technology in the design of the combustion chamber of a hybrid gas-steam power plant with a modular construction that combines two gas turbine engines: a) utilizing the heat of exhaust gases, and b) contact type with steam injection into the combustion chamber. The main characteristics of the gas turbine combustion chamber were determined when implementing steam injection and operating the installation on pure hydrogen. Parameters of the tubular-ring combustion chamber were studied, as well as the influence of separate steam injection into different zones of the chamber to ensure its stable operation without the occurrence of flame blowout zones. Using modern computer design technologies, the impact of the distribution of environmental and energy steam on the ecological performance of a prospective hybrid gas-steam power plant has been investigated.

Keywords: CFD Technology · Hybrid Energy System · Combustion Chamber

1 Introduction

Power engineering is a rapidly developing field closely integrated into industry in many aspects, including the operation of various energy facilities. Guided by modern trends in mechanical engineering and gas turbine engineering, the forefront is occupied by requirements to enhance not only the efficiency indicators of units but also their environmental performance, such as the emission of harmful substances (nitrogen oxides, carbon, and sulfur).

In the past decade, global demand for renewable energy has been rapidly increasing, leading to new challenges for traditional electricity production systems [1, 2]. The

M. Nechyporuk et al. (Eds.): ICTM 2023, LNNS 1008, pp. 409–419, 2024.
https://doi.org/10.1007/978-3-031-61415-6_35

investigation of fuel combustion, particularly fuels devoid of carbon like hydrogen, holds significant importance in tackling the challenge of energy decarbonization. Due to significant differences in the physical properties of hydrogen compared to other types of fuels, such as natural gas, burning hydrogen fuels in the combustion chambers of gas turbine engines is a complex task, especially for low NO_x emissions [3]. The design tasks for new combustion chamber configurations operating on hydrogen and the optimization of their parameters can be addressed using three-dimensional CFD technologies, allowing for a detailed study of the physicochemical characteristics of turbulent chemically reacting flows.

It is worth noting that by using hydrogen as a fuel (either in a mixture or in pure form) as an alternative to natural gas, gas turbines can provide low-carbon or even carbon-free energy solutions. Gas turbines play a key role in ensuring a smooth transition from fossil fuel-based to decarbonized energy systems, as they offer flexible and dispatchable generation to support grids predominantly dominated by intermittent renewable energy [4].

Increasing the efficiency of energy installations can be achieved through the use of hybrid gas-steam power plants [5], which combine the advantages of the gas turbine cycle with the heat recovery from exhaust gases and contact-type gas turbine installations with steam injection into the combustion chamber [6–8]. Previous studies [5] have shown the feasibility of implementing such a hydrogen-operated installation for Floating Production, Storage, and Offloading (FPSO) vessels.

The development of hybrid energy systems leads to the use of gas turbine installations operating on the so-called “Aquarius” cycle [9, 10]. It should be noted that the most commonly used combustion chambers for hydrogen, with pre-prepared fuel-air mixtures, have a significant drawback associated with the potential for flame flashback in the mixture preparation zones [11, 12], as well as the occurrence of acoustic instability [13]. This drawback becomes particularly pronounced when dealing with high hydrogen contents in the mixture and when operating on pure hydrogen.

One way to reduce the risks of flame flashback is the injection of steam into the chemical reaction zone. The combustion of various mixtures of natural gas with hydrogen in dry and steam-diluted modes for rich-quench-lean and premixed combustion chambers has been investigated in [14, 15]. Steam decreases the reactivity of hydrogen, and even relatively small steam content prevents flame flashback from occurring.

The novelty of the proposed method lies in the combination of a) the well-known principle of diffusion combustion of fuel, which ensures a significant reduction in the likelihood of flame flashback when using pure hydrogen, and b) the principle of operating the gas turbine combustion chamber with two-stage steam injection into different parts of the combustion chamber, which reduces nitrogen oxide emissions and meets environmental standards. The first part of this steam (environmental steam) is introduced into the primary zone of the combustion chamber to suppress the formation of nitrogen oxides and lower the temperature in the reaction zone. The second part (power steam) is separately introduced into the dilution zone to increase the mass flow rate of the working fluid.

The purpose of the work is to use CFD technology to design a promising gas turbine combustion chamber operating on hydrogen for a hybrid gas-steam energy system. The study of the working processes of a gas turbine combustion chamber with steam injection and the obtaining of new emission characteristics for fuel-burning devices using modern computational complexes aligns with the general demands of the energy sector aimed at improving the efficiency of power installations and addressing environmental issues.

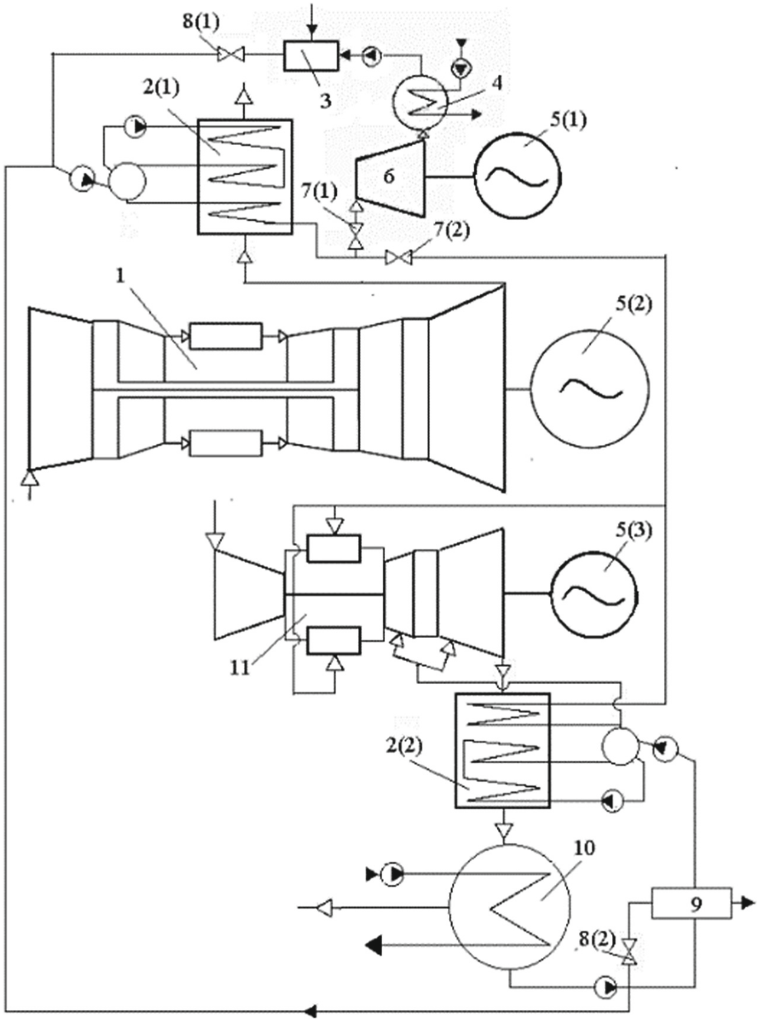

Fig. 1. Thermal scheme of a gas-steam unit with a hybrid cycle: 1 – basic gas turbine engine (GTE); 2(1), 2(2) – heat recovery steam generator (HRSG); 3 – water tank; 4 – condenser; 5(1), 5(2), 5(3) – generators; 6 – steam turbine; 7(1), 7(2) – steam valves; 8(1), 8(2) – water valves; 9 – treatment apparatus; 10 – gas-steam condenser; 11 – contact-type gas turbine engine (CGTE)

2 Selection of Parameters of a Hybrid Energy System

2.1 A Scheme of a Hybrid Gas-Steam Unit

To determine the parameters required for the CFD design of the combustion chamber of a contact-type gas turbine unit, initial calculations were performed for the thermal efficiency of the hybrid gas-steam plant, which is shown in Fig. 1.

A detailed mathematical model for the scheme efficiency calculation was presented in [5]. The prospective gas turbine engine selected as the base engine has a power output of 33 MW, manufactured by State Enterprise "Zorya-Mashproekt", Ukraine, with an efficiency of 38.3% according to ISO parameters [16]. It is noteworthy that the engine was originally designed to operate on natural gas. The feature of the proposed scheme is the combination and summation of the work of 1) a simple thermal scheme gas turbine engine 1, 2) a gas turbine engine 1 with heat recovery in the recovery circuit 2(1), and 3) a contact type gas turbine engine 11 with heat recovery in the recovery circuit 2(2), as well as varying the supply of superheated steam generated in circuits 2(1) and 2(2) into the steam turbine 6. It is assumed that the thermal engines of the hybrid plant operate on hydrogen.

2.2 Selection of Combustion Chamber Initial Parameters

Based on thermodynamic calculations of a hybrid gas-steam power unit operating on hydrogen fuel, one of the potential practical applications for such a system has been chosen, specifically for FPSO vessels used in oil extraction, storage, and shipment. The FPSO vessel selected for potential power plant modernization is the FPSO MV 34 MIAMTE, manufactured in 2009 [17], equipped with three 37 MW gas turbines from Siemens.

Considering the power capacity of the power plant on this vessel, a nominal power mode of 100 MW was chosen for the proposed hybrid gas-steam power unit. The corresponding parameters for the steam-injected combustion chamber are provided in Table 1.

Table 1. Combustion chamber parameters

Parameter	Value
The number of flame tubes	24
Pressure in the combustion chamber, MPa	2.63
Air flow rate through the CGTE compressor G_{cCGTE}, kg/s	55.64
Fuel (hydrogen) consumption, kg/h	3052
Consumption of superheated steam G_{SS} through the CC, kg/s	16.6
Steam temperature, K	743

3 An Approach to Modeling Processes in the Combustion Chamber

A mathematical model of a steam-injection combustion chamber operating on hydrogen has been developed, utilizing the continuity equation, conservation of momentum, conservation of energy, transfer of chemical components in the mixture, and turbulence characteristics [18–20]. The submodel for chemically reacting flows is based on solving equations that describe the convective and diffusive transfer of each component in the reacting mixture [21, 22]. It should be noted that in order to obtain the distribution of concentrations of chemical components across the cross-sections of the combustion chamber, it is necessary to solve the transfer equation

$$\frac{\partial}{\partial t}(\rho Y_i) + \nabla(\rho \vec{v} Y_i) = -\nabla \vec{J}_i + R_i + S_i, \tag{1}$$

where ρ is the density of the mixture; Y_i is the concentration of the j-th component; $\overrightarrow{v}$ is the velocity vector of the working body; $\overrightarrow{J}_i$ is the mass diffusion of the i-th component; R_i is the level of formation of the i-th component as a result of a chemical reaction; S_i is the level of additional formation of the i-th component from the dispersed phase or other sources (for example, when using combustion intensifiers [23. 24]).

During the conduct of three-dimensional calculations, a model for the emissions of nitrogen oxides has been employed. This model consists of a system of mass transfer equations that accounts for convection, diffusion, as well as the formation and decomposition of nitrogen monoxide NO and related compounds. The influence of the component's residence time in the reacting volume on the NO formation mechanism is incorporated into the convective terms, formulated in the Eulerian reference frame. For both "thermal" and "prompt" nitrogen oxides, the transfer equations for NO are solved in vector form based on the conservation of mass equations for individual chemical components in the mixture [25]

$$\frac{\partial}{\partial t}(\rho Y_{\mathrm{NO}}) + \nabla \cdot (\rho \vec{v} Y_{\mathrm{NO}}) = \nabla \cdot (\rho D \nabla Y_{\mathrm{NO}}) + S_{\mathrm{NO}}, \tag{2}$$

where Y_{NO} is the mass concentration of NO; D is the diffusion coefficient; S_{NO} is a source term that is determined depending on the mechanism of formation of nitrogen oxides.

Further details with a comprehensive description of the mathematical model for turbulent chemically reacting flows in a steam-injected gas turbine combustion chamber can be found in [8, 10].

As the subject of investigation, a combustion chamber of a contact-type gas turbine engine produced by "Zorya-Mashproekt" has been chosen. The numerical modeling aims to theoretically study the parameters of the combustion chamber and the influence of the two-stage steam injection on the environmental characteristics of the hybrid installation, as well as to provide practical recommendations for improving the combustion device.

The geometric model of the combustion chamber (Fig. 2) consists of the following main elements: a diffusion swirler, a flame tube, an outlet diffuser, as well as tubes for hydrogen and superheated steam supply. Additionally, the flame tube housing includes eight openings for supplying primary air to the combustion zone and eight openings for supplying secondary air to the mixing (dilution) zone. The diffusion swirler provides the supply of a portion of primary air and environmental steam. Through the collector located in the middle of the flame tube, steam is injected into the dilution zone, creating a high-energy mixture with the working fluid. Moreover, two ducts for flame transfer are provided in the design.

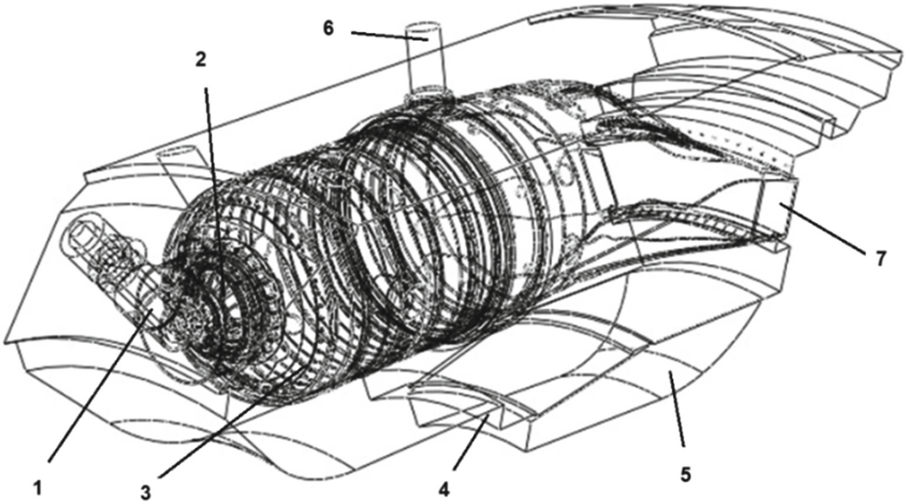

Fig. 2. Three-dimensional geometric model of the combustion chamber: 1 – nozzle for supplying hydrogen and environmental steam; 2 – air swirler; 3 – flame tube; 4 – air inlet after the compressor; 5 – input diffuser; 6 – power steam supply duct; 7 – outlet diffuser of the flame tube

Based on the geometric model, a finite-element model of 1/24 part of the combustion chamber (Fig. 3) was created, which consists of 3.8 million tetrahedra.

Calculations of processes within the combustion chamber of a steam-injected gas turbine engine were carried out using the CFD software suite Ansys Fluent [26].

4 Environmental Characteristics of the Combustion Chamber of a Hybrid Gas-Steam Turbine System

A series of three-dimensional CFD simulations were conducted, varying the amount of steam injected into the primary zone (via nozzle 1 in Fig. 2) and the dilution zone of the combustion chamber through duct 6. The total quantity of superheated steam entering the combustion chamber, denoted as G_{ss}, remained constant.

Figure 4 displays the distribution of mass fractions of water vapor (H_2O) along the longitudinal cross-section of the flame tube under different ratios of $G_{env.s}/G_{cCGTE}$, where $G_{env.s}$ represents the flow rate of environmental steam through the primary zone of the combustion chamber. It's evident that at the maximum supply of environmental steam to the primary zone, vapor concentrations along the length of the flame tube are relatively uniform. Augmenting the steam quantity leads to a decrease in gas temperature and the suppression of nitrogen oxide formation.

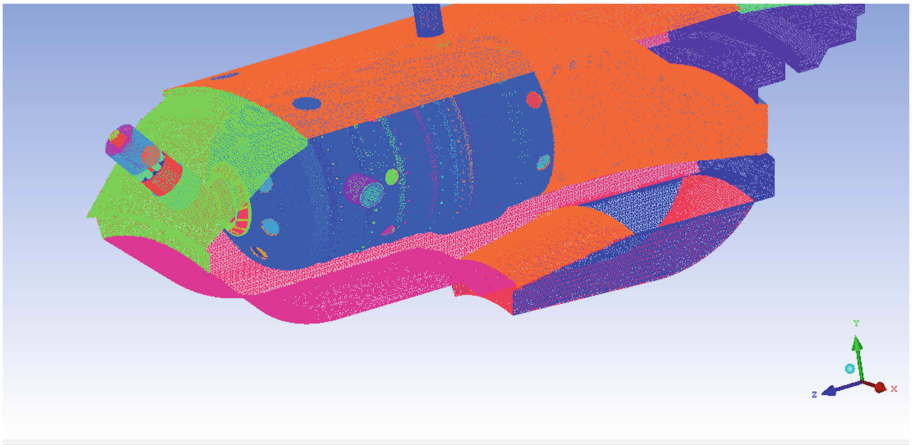

Fig. 3. Finite element model of a combustion chamber with steam injection

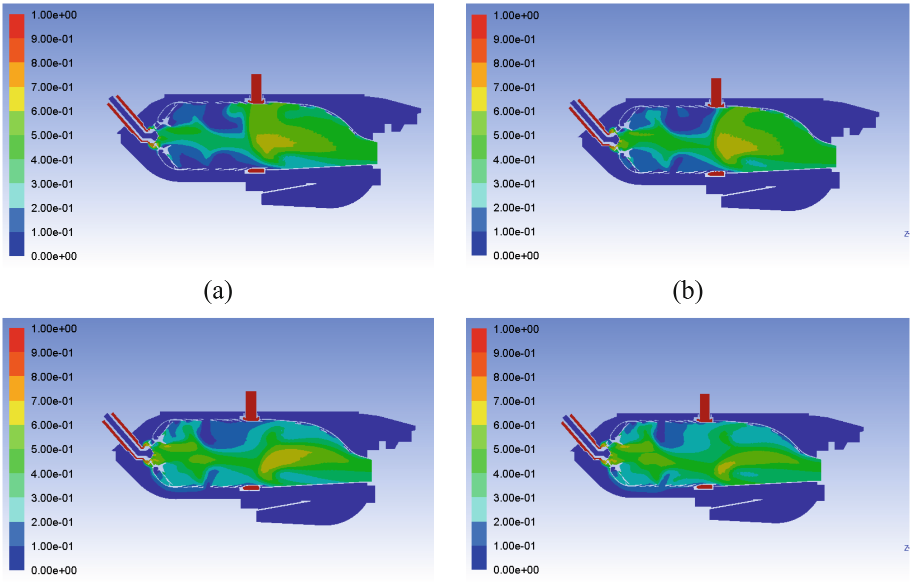

Fig. 4. Mass fractions of water vapor in the cross-section of the flame tube: (a) – $G_{env.s}/G_{cCGTE}$ = 0.03; (b) – 0.06; (c) – 0.12; (d) – 0.15.

This is evidenced by the data presented in Fig. 5, where the mole fraction of nitrogen oxide (NO) in the outlet cross-section of the flame tube is shown for the same ratios of environmental steam and air through the combustion chamber of the contact-type gas turbine engine.

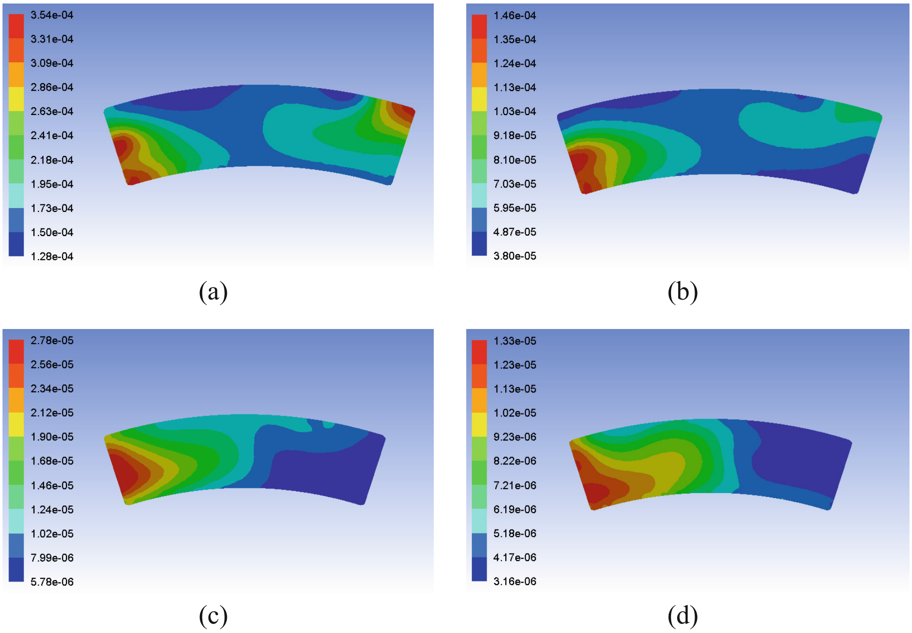

Fig. 5. Mole fractions of nitrogen oxides at the outlet of the flame tube: (a) – $G_{env.s}/G_{cCGTE} = 0.03$; (b) – 0.06; (c) – 0.12; (d) – 0.15.

Figure 6 presents the graphical dependence of emissions of nitrogen oxide NO in the outlet section of the combustion chamber on the ratio $G_{env.s}/G_{cCGTE}$.

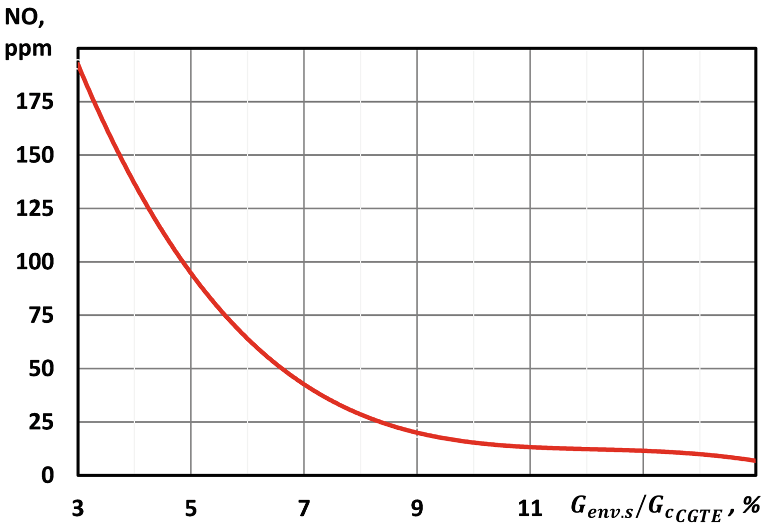

Fig. 6. Emissions of nitrogen oxide NO depending on the ratio $G_{env.s}/G_{cCGTE}$

To comply with European regulations for nitrogen oxide emissions from gas turbine engines [27], which are required to be lower than 25 ppm under nominal conditions, the ratio of $G_{env.s}/G_{cCGTE}$ should be around 0.1. This consideration is crucial when modernizing current-operated contact-type gas turbine engines and designing future ones.

Figure 7 presents distributions of several parameters across the cross-sections of the flame tube for a ratio of $G_{env.s}/G_{cCGTE} = 0.12$.

One can observe the complete combustion of gaseous hydrogen up to the point of introducing primary air into the flame tube. It's also worth noting that the overall non-uniformity coefficient of the temperature field at the exit of the combustion chamber will be higher when steam injection is compared to traditional "dry" chambers.

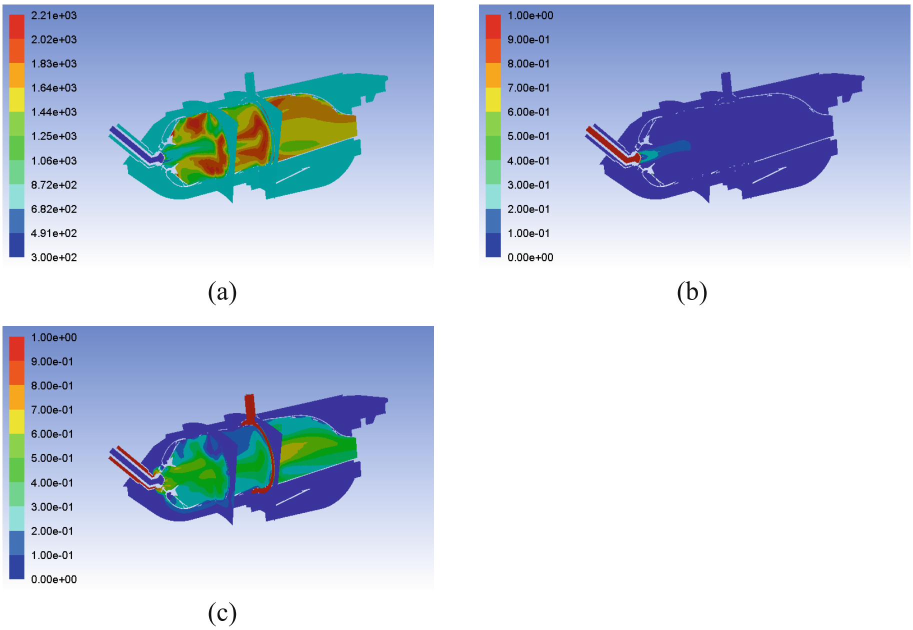

Fig. 7. Contours of temperature, K (a), mass fraction of hydrogen (b) and mass fraction of water vapor (c) in cross-sections of the combustion chamber

This undesirable phenomenon can be mitigated by adjusting the distribution of secondary air around the flame tube's mixer region and modifying the geometry of the mixer itself. It's noteworthy that for all investigated operating modes, there were no instances of flame flashback observed within the volume of the burner device. This reiterates the advantages of the proposed hydrogen combustion method.

5 Conclusion

A hybrid unit scheme operating on hydrogen has been proposed, which includes a simple-cycle gas turbine engine, a gas turbine engine with steam injection into the combustion chamber, and a steam turbine. CFD technology was used to design an advanced combustion chamber powered by hydrogen. A three-dimensional mathematical model for turbulent chemically reacting flows in gas turbine combustion chambers with steam injection has been developed, based on the numerical solution of a system of differential equations that describe the fundamental principles of energy conservation and chemical component transfer in a turbulent chemically reacting system. The estimated emission of nitrogen oxides at the exit of the hybrid gas-steam plant is equal to 12.3 ppm when the ratio of the consumption of environmental steam to the air flow rate through the compressor of the contact-type gas turbine engine is 0.12. This emission level fully complies with international standards for toxic component emissions. For all investigated operating modes of the combustion chamber with two-stage steam injection, no instances of flame flashback were observed within the burner device volume.

References

1. United Nations Organization. Adoption of the Paris agreement: FCCC/CP/2015/L.9. https://documents-dds-ny.un.org/doc/UNDOC/LTD/G15/283/07/PDF/G1528307.pdf?OpenElement. Accessed 17 Nov 2023
2. International Energy Agency: Energy Technology Perspectives 2020. IEA Publications, Paris, France. https://www.iea.org/reports/energy-technology-perspectives-2020. Accessed 17 Nov 2023
3. McAllister, S., Chen, J.Y., Fernandez-Pello, A.C.: Fundamentals of combustion processes. Springer, Mechanical Engineering Series (2011)
4. Gupta, K.K., Rehman, A., Sarviya, R.M.: Bio-fuels for the gas turbine: a review. Renew. Sustain. Energy Rev. **14**(9), 2946–2955 (2010)
5. Serbin, S., Shmarkov, O.: Parameters of the hybrid gas-steam power plant operating on hydrogen fuel. Collection Sci. Works Admiral Makarov National Shipbuilding Univ. **1**(490), 103–110 (2023)
6. Varia, N., Patel, D.. Reddy, B., Srinivas T.: Effects of steam injection on the performance of natural gas combined cycle power generation system. In: CSME International Congress 2018, Toronto, Canada (2018)
7. Cheng, D.Y., Nelson, A.L.C: The chronological development of the Cheng cycle steam injected gas turbine during the past 25 years. In: Proceeding of ASME Turbo Expo 2002, GT-2002–30119, pp. 1–8. Amsterdam (2002)
8. Serbin, S., Mostipanenko, A., Matveev, I.: Investigation of the working processes in a gas turbine combustor with steam injection. In: Proceedings of the ASME/JSME 8th Thermal Engineering Joint Conference, AJTEC2011-44042, T20012, pp.1–6 (2011)
9. Movchan, S.N., Romanov, V.V., Chobenko, V.N., Shevtsov, A.P.: Contact steam-and-gas turbine units of the "AQUARIUS" type: the present status and future prospects. In: ASME Turbo Expo 2009: Power for Land, Sea, and Air, pp. 1–7 (2009)
10. Serbin, S., Burunsuz, K.: Numerical study of the parameters of a gas turbine combustion chamber with steam injection operating on distillate fuel. Int. J. Turbo Jet Eng. Published online by De Gruyter (2020). https://doi.org/10.1515/tjeng-2020-0029

11. Nemir, G., Hamse, H.: Hydrogen-fired gas turbine for power generation with exhaust gas recirculation. Academy of Economics, Society and Technology. http://www.diva-portal.org/smash/get/diva2:1277601/FULLTEXT01.pdf. Accessed 17 Nov 2023
12. Carusotto, S., et al.: Research and development in a diffusive gas Turbine burner for hydrogen compliant applications. Energies **15**(4117), 1–20 (2022)
13. Beital, J., Talibi, M., Sadasivuni, S., Balachandran, R.: Thermoacoustic instability considerations for high hydrogen combustion in lean premixed gas turbine combustors: a review. Hydrogen **2**, 33–57 (2021)
14. Göke, S., et al.: Influence of steam dilution on the combustion of natural gas and hydrogen in premixed and rich-quench-lean combustors. Fuel Process. Technol. **107**, 14–22 (2013)
15. Serbin, S., Washchilenko, N., Dzida, M., Kowalski, J.: Parametric analysis of the efficiency of the combined gas-steam turbine unit of a hybrid cycle for the fpso vessel. Polish Maritime Res. **112**(4), 122–132 (2021)
16. Zorya-Mashproekt: Industrial Application. https://rei.mfa.gov.ua/storage/app/sites/139/zorya-mashproekt-gas-turbine.pdf. Accessed 17 Nov 2023
17. FPSO MIAMTE MV34 - IMO 9416692 (2023). https://www.shipspotting.com/photos/3483441?navList=moreOfThisShip&imo=9416692&lid=3413030
18. Launder, B.E., Spalding, D.B.: Lectures in Mathematical Models of Turbulence. Academic Press, London (1972)
19. Matveev, I.B., Serbin, S.I., Vilkul, V.V., Goncharova, N.A.: Synthesis gas afterburner based on an injector type plasma-assisted combustion system. IEEE Trans. Plasma Sci. **43**(12), 3974–3978 (2015)
20. Serbin, S.I., Matveev, I.B., Mostipanenko, G.B.: Plasma-assisted reforming of natural gas for GTL: Part II - modeling of the methane-oxygen reformer. IEEE Trans. Plasma Sci. **43**(12), 3964–3968 (2015)
21. Matveev, I., Serbin, S., Butcher, T., Tutu, N.K.: Flow structure investigations in a Tornado combustor. In: Collection of Technical Papers - 4th International Energy Conversion Engineering Conference, vol. 2, pp. 1001–1013 (2006)
22. Serbin, S.I., Kozlovskyi, A.V., Burunsuz, K.S.: Investigations of non-stationary processes in low emissive gas turbine combustor with plasma assistance. IEEE Trans. Plasma Sci. **44**(12), 2960–2964 (2016)
23. Magnussen, B.F., Hjertager, B.H.: On mathematical models of turbulent combustion with special emphasis on soot formation and combustion. In: 16th Symp. (Int.) on Combustion. The Combustion Institute, vol. 16(1), p. 719–729 (1977)
24. Gatsenko, N.A., Serbin, S.I.: Arc plasmatrons for burning fuel in industrial installations. Glass Ceram. **51**(11–12), 383–386 (1994)
25. Meloni, R.: Pollutant emission validation of a heavy-duty gas turbine burner by CFD modeling. Machines **1**(3), 81–97 (2013)
26. ANSYS Fluent Theory Guide. ANSYS Inc., 780 p. (2013)
27. Directive 2010/75/EU of the European Parliament and of the Council of 24 November 2010 on industrial emissions (integrated pollution prevention and control). https://eur-lex.europa.eu/legal-content/EN/TXT/?uri=celex:32010L0075. Accessed 17 Nov 2023

Dampers Influence on Sloshing Mitigation in Fuel Tanks of Launch Vehicles and Reservoirs

Kyryl Degtyariov[1](✉), Denis Kriutchenko[1], Ivan Osypov[2], Olena Sierikova[3], and Elena Strelnikova[1,2]

[1] Anatolii Pidhornyi Institute of Mechanical Engineering Problems NAS of Ukraine, 2/10 Pozharskogo Street, Kharkiv 61046, Ukraine
Kdegt89@gmail.com

[2] V.N. Karazin Kharkiv National University, 4 Svobody Square, Kharkiv 61022, Ukraine

[3] National University of Civil Defense of Ukraine, 94 Chernyshevska Street, Kharkiv 61023, Ukraine

Abstract. The main objective of this paper is elaborating effective numerical methods for analyzing influence of different devices installation to mitigate liquid vibrations in partially filled rigid reservoirs. The cylindrical shells with horizontal and vertical baffles are considered as fuel tanks models. The baffles are installed for sloshing mitigation that is especially topical to ensure stability of launch vehicles. The floating cover is also analyzed as sloshing damper. Reduced boundary element method is involved into numerical simulation as well as mode superposition technique. Vibration modes, obtained at solving spectral problems are used onwards as basic functions in series for an unknown potential and a free surface elevation. The effective new method for calculating the one-dimensional singular integrals is used. The novelty of the proposed approach consists in analyzing the different devices efficiency on sloshing mitigation under harmonical loadings. Next stage of the research will be devoted to studying dampers efficiency under impulse and seismic loads.

Keywords: Fluid-Filled Reservoirs · Boundary Element Method · Sloshing Mitigation

1 Introduction

The problems of launch vehicles stability during manoeuvres under variable gravity and filling levels of fuel tanks has been acutely faced by space technology engineers and designers since the middle of the last century. The first missions to Jupiter were unsuccessful due to loss of stability and descent of the launch vehicle from the calculated trajectory. As it has been turned out later, the failures were associated with the coincidence of the frequency of regulating apparatus with the fundamental frequencies of sloshing. It should be noted that sloshing frequencies depend significantly on the liquid filling and gravity levels. Sloshing effects are also crucial in oil reservoirs and other storages for toxic and inflammable liquids under action of suddenly applied intensive loadings. So, a lot of devices are introduced to mitigate sloshing. Among them there are

M. Nechyporuk et al. (Eds.): ICTM 2023, LNNS 1008, pp. 420–430, 2024.
https://doi.org/10.1007/978-3-031-61415-6_36

baffles and floating covers. It should be noted that an adequate check of the damper's effectiveness is only possible after its installation. But very often this is an expensive and not always safe procedure. Therefore, computer modeling the dynamic processes in tanks in the presence of damping devices is relevant in order to choose the most appropriate parameters of partitions and floating covers. Such modelling requires the development of effective methods for numerical analysis of liquid sloshing in reservoirs and fuel tanks. The methods based on boundary elements techniques are proposed and analysed in this paper. The purpose is to estimate the different dampers influence on the process of sloshing mitigation.

2 Literature Review

Since the middle of the last century, the efforts of scientists and engineers have been aimed at creating and testing various damping devices to mitigate sloshing in tanks partially filled with liquids. Since analytic solutions can't be obtained for reservoirs with complicated geometrical shapes, a lot of numerical methods have been proposed for solutions of spectral boundary value problems (SBVP) of liquid sloshing. The solution of the SBVP is essential for obtaining the basic functions in forced vibration analysis [1]. For tanks with horizontal baffles the boundary element method (BEM) was applied in [2], in [3] the iso-geometric BEM was used to study sloshing in reservoirs with porous baffles. The main objective of research devoted to baffles in reservoirs consist in determining the optimal structure parameters [4], in [5] the optimum ring baffle design was proposed to optimize the structural strength of tanks subjected to resonant seismic sloshing. Along with BEM techniques, some advanced numerical methods based on immersion approach and concern with launch vehicle strength and stability should be mentioned [6]. Finite element and finite volume methods also received further development, the impetus for which was the need for correct calculations of the strength and vibrations of new powerful launch vehicles. The finite volumes method has obtained its further development in [7]. Effective variant of coupled finite (FEM) and boundary element methods (BEM) was proposed in [8] for studying the liquid vibrations in tank with baffles. A comprehensive and well-founded review of sloshing research is provided in [9]. To suppress sloshing, various damping devices are used, such as horizontal [10] and vertical [11] baffles, free surface coverings [12], as well as membrane covers [13]. Different elastic baffles were studied in [14]. Innovative materials for strengthening fuel tanks were considered in [15]. Despite significant advances in the study of dampers to reduce sloshing amplitudes, a number of issues remain unexplored. Among them there are floating covers influence, and the mutual action of horizontal and vertical loads. The objective of this paper consists in analyzing the liquid vibrations in the partially filled rigid reservoirs including influence of different devices installed to mitigate sloshing. The paper considers the fluid-filled tanks subjected to coupled vertical and horizontal loadings. The crucial issue here is to analyze the liquid free surface behavior in the tank and to estimate the mitigation of possible level changings. Novelty of the proposed approach consists in analyzing the influence of dampers on sloshing mitigation under coupled vertical and horizontal loading as well as the floating cover installation.

The paper has been organized as follows. At first, the own liquid vibrations are considered in rigid reservoirs without baffles and floating covers. So, the SBVPs [16] are solved. Next, installation of vertical baffles is estimated, and then the multi-domain BEM [17] is applied to spectral problem for cylindrical shell with horizontal baffles. The floating cover installation is discussed further. After receiving the basic functions as a result of the spectral problem solution, the second order system of ordinary differential equations is obtained.

3 Research Methodology

3.1 Problem Formulation

Processes of mitigating liquid vibrations in fuel tanks in presence of different damping devices are considered. Cylindrical shells with and without baffles are chosen as the fuel tanks models. The liquid is supposed to be an inviscid and incompressible one, and its flow induced by the vibrations of the tank walls, is irrotational. So, there exist a potential Φ, satisfying the next boundary value problem:

$$\nabla^2\Phi = 0,\ \left.\frac{\partial\Phi}{\partial\mathbf{n}}\right|_{S_1(t)} = 0, p - p_0 = 0,\ \frac{\partial\Phi}{\partial\mathbf{n}} = \left.\frac{\partial\zeta/\partial t}{\sqrt{1+|\nabla\zeta|^2}}\right|_{S_0(t)} \tag{1}$$

for the Laplace equation in the time-dependant domain $Q(t)$, with boundary surfaces $\partial Q(t) = S_1(t) \cup S_0(t)$, Fig. 1a). Here $S_1(t)$ is the wetted surface of the tank, $S_0(t)$ is the liquid free surface, $\mathbf{n}$ is an outward unit normal vector to the surface, an unknown function $\zeta = \zeta(x, y, t)$ describes the free surface position and level, p is the liquid pressure, and p_0 is the atmospheric pressure.

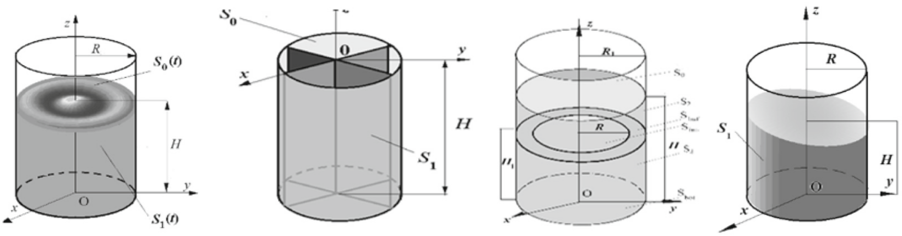

(a) (b) (c) (d)

Fig. 1. Cylindrical shells with different dampers

The Bernoulli equation is used for evaluating the pressure p

$$p - p_0 = -\rho_l\left[\frac{\partial\Phi}{\partial t} + a_x(t)x + (g + a_z(t))\zeta + \frac{1}{2}(\nabla\Phi, \nabla\Phi)\right], \tag{2}$$

where ρ_l is the liquid density, g is the acceleration of gravity, and $a_x(t)$, $a_z(t)$ are driving force accelerations in the horizontal and vertical directions.

To obtain a unique solution of system (1)-(2) the Neumann condition is added [1]. For shells of revolution, the unknown functions ζ and Φ can be expressed in cylindrical coordinate system (r, θ, z) by the next way [18]:

$$\zeta(r, \theta, t) = \sum\nolimits_{k=1}^{\infty} \sum\nolimits_{k=1}^{\infty} d_{kj}(t) \cos(j\theta) \zeta_{kj}(r), \tag{3}$$

$$\Phi(r, \theta, z, t) = \sum\nolimits_{k=1}^{\infty} \sum\nolimits_{j=0}^{\infty} \dot{d}_{kj}(t) \cos(j\theta) \varphi_{kj}(r, z). \tag{4}$$

Here functions $d_{kj}(t)$ are unknown time-dependent coefficients for each wave number j, the basic functions $\zeta_{kj}(r)$ and $\varphi_{kj}(r, z)$ are solutions of the linear SBVP [19] formulated at surfaces $S_0 = S_0(0)$ and $S_1 = S_1(0)$, independent on time. These SBVPs are following:

$$\nabla^2 \varphi_{kj} = 0, \left. \frac{\partial \varphi_{kj}}{\partial \mathbf{n}} = 0 \right]_{S_1}, \frac{\partial \varphi_{kj}}{\partial \mathbf{n}} = \left. \frac{\partial \zeta_{kj}}{\partial t} \right|_{S_0}. \tag{5}$$

The next relations are valid on the free surface

$$\zeta_{kJ}(r) = \left. \frac{\partial \varphi_{kJ}(r, z)}{\partial z} \right|_{S_0} = \frac{\chi_{kj}^2}{g} \varphi_{kj}(r, H). \tag{6}$$

Here $z = H$ is the free surface elevation in the state of rest, Fig. 1a). So, function $\zeta(r, \theta, \mathrm{t})$ is presented by the following series:

$$\zeta(r, \theta, \mathrm{t}) = \frac{1}{g} \sum\nolimits_{k=1}^{n} \sum_{j=1}^{m} \cos(j\theta) \chi_{kj}^{2} \varphi_{kj}(r, H) d_{kj}(t). \tag{7}$$

where χ_{kj}^2 are fundamental frequencies [20]. Supposing spectral problem (5) is solved, the obtained basic functions $\varphi_{kj}(r, z)$ are substituted into linearized dynamical boundary conditions on the free surface. This leads to the following differential relations:

$$\begin{gathered} \sum\nolimits_{k=1}^{M} \sum\nolimits_{j=0}^{m} \ddot{d}_{kj}(t) \cos(j\theta) \varphi(r, H) + a_x(t) r + \\ \sum\nolimits_{k=1}^{M} \sum\nolimits_{j=0}^{m} d_{kj}(t) \cos(j\theta) \chi_{kj}^2 (1 + a_z(t)/g) \varphi_{kj}(r.H) = 0. \end{gathered} \tag{8}$$

As in [1, 21] the only 0$^{\text{th}}$ and 1$^{\text{st}}$ harmonics are accepted for study.

Performing dot product of relations (8) by functions $\varphi_{lm}(r, H) \cos m\theta$, $m = 0{,}1$, due orthogonality of basic functions [1], one can obtain the second order system of ordinary differential equations relative to $d_{0k}(t)$, $d_{1k}(t)$ for $k = 1,\ldots,M$.

$$\ddot{d}_{k0}(t) + \chi_{k0}^2 (1 + a_z(t)/g) d_{k0}(t) = 0, \tag{9}$$

$$\ddot{d}_{k1}(t) + \chi_{k1}^2 \left(1 + \frac{a_z(t)}{g}\right) d_{k1}(t) + a_x(t) F_{k1} = 0, F_k = \frac{(r, \varphi_{k1})}{(\varphi_{k1}, \varphi_{k1})}.$$

Suppose that the tank under consideration was at state rest at the initial time.

3.2 Fuel Tank Without Baffles

The unknown potential $\Phi(r,\theta,z,t)$ is presented using Green's third identity as follows:

$$2\pi\Phi(P_0) = \iint_S \frac{\partial\Phi}{\partial\mathbf{n}} \frac{1}{|P - P_0|} dS - \iint_S \Phi \frac{\partial}{\partial\mathbf{n}} \frac{1}{|P - P_0|} dS. \tag{10}$$

Here $S = S_1 \cup S_0$, both points P and P_0 are at the surface S, and by $|\mathrm{P} - \mathrm{P}_0|$ is the Cartesian distance between points P and P_0 is denoted. With substituting boundary conditions (5) and (6) into equality (10), and dropping indexes *kj*, the following system of singular integral equations is obtained:

$$2\pi\varphi + \iint_{S_1} \varphi \frac{\partial}{\partial\mathbf{n}}\left(\frac{1}{r}\right) dS_1 - \frac{\chi^2}{g} \iint_{S_0} \varphi \frac{1}{r} dS_0 + \iint_{S_0} \varphi \frac{\partial}{\partial z}\left(\frac{1}{r}\right) dS_0 = 0, \tag{11}$$

$$-2\pi\varphi - \iint_{S_1} \varphi \frac{\partial}{\partial\mathbf{n}}\left(\frac{1}{r}\right) dS_1 + \frac{\chi^2}{g} \iint_{S_0} \varphi \frac{1}{r} dS_0 = 0, \; r = |P - P_0|.$$

Such systems are solved numerically for each vibration mode *kj*, For the shell of revolution, system (11) is reduced to the one-dimensional ones

$$2\pi\varphi(z_0) + \int_\Gamma \varphi(z)\Theta(z, z_0) r(z) d\Gamma - \int_0^R q(\rho)\Xi(P, P_0)\rho d\rho = 0, P_0 \in S_1, \tag{12}$$

$$2\pi\varphi(z_0) + \int_\Gamma \varphi(z)\Theta(z, z_0) r(z) d\Gamma - \int_0^R q(\rho)\Xi(P, P_0)\rho d\rho = P_0 \in S_0.$$

Here Γ is the shell of revolution's generatrix, $q(\rho) = \frac{\partial\varphi}{\partial\mathbf{n}}$, and

$$\Theta(z, z_0) = 4/\sqrt{a + b}\left\{\frac{1}{2r}\left[\frac{\rho^2 - \rho_0^2 + (z_0 - z)^2}{a - b} E_l(k) - F_l(k)\right] n_r + \frac{z_0 - z}{a - b} E_l(k) n_z\right\}, \tag{13}$$

$$\Xi(P, P_0) = \frac{4}{\sqrt{a + b}} F_l(k), \; a = \rho^2 + r_0^2 + (z - z_0)^2, \; b = 2\rho\rho_0.$$

In kernels (13) the following generalized elliptical integrals are introduced

$$E_l(k) = (-1)^l\left(1 - 4l^2\right)\int_0^{\pi/2} \cos 2l\theta \sqrt{1 - k^2 \sin^2\theta} d\theta, \tag{14}$$

$$F_l(k) = (-1)^l \int_0^{\pi/2} \frac{\cos 2l\theta d\theta}{\sqrt{1 - k^2 \sin^2\theta}} d\theta, \; k^2 = \frac{2b}{a + b}, \; l = 1.$$

For numerical evaluation of the obtained singular integrals the effective numerical method is used [22]. After solving system (11) the basic functions $\varphi_{kj}(r, z)$ are substituted into Eqs. (9) for simulating the filling level time-history.

3.3 Fuel Tank with Vertical Baffles

The liquid free vibrations in the rigid cylindrical tank of radius R with two vertical baffles are considered, (Fig. 1b). For this tank the wetted surface S_1 is following:

$S_1 = \{z = 0 \cup r = R \cup \theta = 0 \cup \theta = \frac{\pi}{2}\}$.

So, for this quarter shell the following linear boundary value problem is formulated:

$$\nabla^2\Phi = 0, \; \frac{\partial\Phi}{\partial r}\bigg|_{r=R} = 0, \quad \frac{\partial\Phi}{\partial z}\bigg|_{z=0} = 0, \quad \frac{1}{r}\frac{\partial\Phi}{\partial\theta}\bigg|_{\theta=0,\theta=\frac{\pi}{2}} = 0, p - p_0 = 0\frac{\partial\Phi}{\partial\mathbf{n}}$$
$$= \frac{\partial\zeta}{\partial t}\bigg|_{S_0} \tag{15}$$

With integral presentation (10), the resolving system of singular integral equations takes form (12)-(13), but in expressions for generalized elliptic integrals (14) it is accepted that $l = 2$. After solving spectral problem (15), the liquid vibration frequencies and modes in the tank with vertical baffles are received. These modes are used as basic functions for solving system (9) to estimate the changing in filling level.

3.4 Fuel Tank with Horizontal Baffles

The multi-domain boundary element method [2, 23] is used to determine liquid vibrations in the tank with horizontal baffles. Here the artificial interface surface S_{int} is introduced [2], which divides the liquid domain into two parts Ω_1 and Ω_2, bounded by the surfaces $S_{\text{bot}}, S_1, S_{\text{baf}}, S_{\text{int}}$ and $S_2, S_{\text{baf}}, S_{\text{int}}, S_0$, respectively, Fig. 1c). The boundaries of Ω_1 and Ω_2 are $\sum_1 = S_{\text{baf}} \cup S_1 \cup S_{\text{bot}} \cup S_{\text{int}}$, $\sum_2 = S_{\text{baf}} \cup S_2 \cup S_{\text{bot}} \cup S_0$.

Denote the potential values at nodes in S_1, S_2, and S_0 as φ_1, φ_2, and φ_0, respectively. Fluxes q_1, q_2 are known at the rigid parts $S_1 \cup S_{\text{bot}}$ and $S_2 \cup S_{\text{bot}}$ from the non-penetration boundary conditions; on the free surface the unknown flux is denoted as q_0. The values of the flux and potential on the interface surface S_{int} are the unknown functions $q_1 = \frac{\partial\varphi}{\partial\mathbf{n}}\Big|_{S_{\text{int}}}$, $q_2 = \frac{\partial\varphi}{\partial\mathbf{n}}\Big|_{S_{\text{int}}}$, $S_{\text{int}} \in \Sigma_j, j = 1, 2$. It should be noted that the following compatibility conditions are valid on the interface surface [2]:

$$\varphi_1 = \varphi_2, \mathrm{q}_1 = \mathrm{q}_2. \tag{16}$$

Denote as $\tilde{S}_1 = S_{\text{baf}} \cup S_1 \cup S_{\text{bot}}$, $\tilde{S}_2 = S_{\text{int}}$, $\tilde{S}_3 = S_{\text{baf}} \cup S_2$, $\tilde{S}_4 = S_0$ and introduce operators

$$\mathrm{A}(\mathrm{S}, \sigma)\psi = \iint_{\mathrm{S}} \psi \frac{\partial}{\partial \mathrm{n}} \frac{1}{|\mathrm{P} - \mathrm{P}_0|} \mathrm{dS}, \; \mathrm{B}(\mathrm{S}, \sigma)\psi = \iint_{\mathrm{S}} \psi \frac{1}{|\mathrm{P} - \mathrm{P}_0|} \mathrm{dS}, \; \mathrm{P}_0 \in \sigma. \tag{17}$$

In formulas (17), the surfaces S and σ can be different or coincide. If the surface S coincides with σ, then the integrals in (17) are singular ones, and at their numerical implementation, the presence of these singularities has to be taken into account. The kernels here are significantly non-homogeneous, and standard quadrature lose its accuracy. So, the special algorithms for calculating such integrals [17, 22] are involved. Using (17), the matrices $A_{ij} = A(\tilde{S}_i, \tilde{S}_j)$ and $B_{ij} = B(\tilde{S}_i, \tilde{S}_j)$ are introduced.

Applying the multi-domain approach [23], system (12) is received as follows:

$$A_{11}\varphi_1 + A_{12}\varphi_{1i} = B_{12}q_1, P_0 \in \tilde{S}_1, A_{21}\varphi_1 + A_{22}\varphi_{1i} = B_{22}q_1, P_0 \in \tilde{S}_2, \tag{18}$$

$$A_{32}\varphi_{1i} + A_{33}\varphi_2 + A_{34}\varphi_0 - \omega^2 B_{34}\varphi_0 = -B_{32}q_1, P_0 \in \tilde{S}_3,$$

$$A_{22}\varphi_{1i} + A_{23}\varphi_2 + A_{24}\varphi_0 - \omega^2 B_{24}\varphi_0 = -B_{22}q_1; \quad P_0 \in \tilde{S}_2$$

$$A_{42}\varphi_{1i} + A_{43}\varphi_2 + A_{44}\varphi_0 - \omega^2 B_{44}\varphi_0 = -B_{42}q_1; \quad P_0 \in S_0, \omega^2 = \chi^2/g.$$

After excluding unknowns φ_1, φ_{1i}, φ_2, and q_1, system (18) is transformed to the eigenvalue problem $\mathbf{A}\varphi_0 - \omega^2\mathbf{B}\varphi_0 = 0$, where expressions for matrixes $\mathbf{A}$ and $\mathbf{B}$ are presented in [2]. Solutions of this SBVP are the basic functions for estimating the free surface level and position.

3.5 Liquid-Filled Reservoir with Floating Cover

The coupled problem of the liquid vibration in the rigid cylindrical shell with floating membrane cover on the free surface is considered, Fig. 1d). The next system of differential equations is used for describing the liquid motion in the tank in presence of the floating membrane cover:

$$\mu\frac{\partial^2 w}{\partial t^2} + T\Delta^2 w = -\rho_l\frac{\partial \Phi}{\partial t} - (g + a_z(t))w - a_x(t)x, \nabla^2\Phi = 0 \tag{19}$$

The boundary conditions at the boundary of the liquid domain and at the membrane contour are following:

$$\left.\frac{\partial \Phi}{\partial \mathbf{n}}\right|_{S_1} = 0, \left.\frac{\partial \Phi}{\partial \mathbf{n}}\right|_{S_0} = \frac{\partial w}{\partial t}, \left.\frac{\partial \mathrm{w}}{\partial r}\right|_{r=R} = 0, z = 0 \tag{20}$$

In (19)–(20) the function w is the membrane's deflection, μ and T are the membrane's mass per unit area and tension per unit length, respectively. Equations (19) describe the membrane vibrations at the free liquid surface, and the velocity potential behavior in presence of the membrane. The mode superposition method is used, so [24]

$$w = \sum\nolimits_{k=1}^{M} c_k w_k, \Phi = \sum\nolimits_{k=1}^{M} \dot{c}_k \varphi_k, \tag{21}$$

where w_k are the own membrane modes, and functions φ_k are solutions of the SBVP

$$\nabla^2\varphi_k = 0, \left.\frac{\partial \varphi_k}{\partial \mathbf{n}}\right|_{S_0} = \frac{\partial w_k}{\partial t}, \left.\frac{\partial \varphi_k}{\partial \mathbf{n}}\right|_{S_1} = 0. \tag{22}$$

The final step is substituting series (21) into system (12) for receiving time history of the free surface level.

4 Results and Discussion

The SBVPs for all tanks under consideration (Fig. 1) have been solved, and the lowest sloshing frequencies are received. The results are shown in Table 1. Here the cylindrical tank of radius $R = 1$m is examined, with filling level $H = 1$ m. The horizontal circle baffles of radius $R_1 = 0.7$ m are installed at levels $H_1 = 0.5$ m or $H_1 = 0.9$ m. The results for these tanks were compared with ones from [1]. It was found that the lowest frequencies correspond to first harmonic. For the shell with floating cover, the lowest frequencies of the membrane and liquid are equals, but the sloshing frequency became lower comparing with the shell without baffles. The results for coupled system "membrane-liquid" are obtained for $\mu = 1$ kg/m^2 and $T = 10$ N/m for comparison with data [25].

Table 1. Natural sloshing frequencies for different tanks

The tank type	χ_{11}	χ_{21}	χ_{31}	χ_{41}	χ_{51}
Without baffles	4.1424	7.2286	9.1472	10.7123	11.9624
[1]	4.1424	7.2284	9.1472	10.7112	11.9616
Vertical baffles	5.4582	8.1067	9.8791	11.2574	12.657
Horizontal baffle	2.6350	6.6446	8.9661	10.6468	11.9876
$H_1 = 0.9$m, [1]	2.6350	6.6444	8.9661	10.6467	11.9874
Membrane	3.2879	7.0231	10.0071	10.8872	12.0271
[25]	3.2899	7.0265	10.0134	10.8967	12.0567

Convergence of numerical results is achieved when the numbers of boundary elements along the walls, bottom, and radius of the free surface are equal to 150. The obtained results demonstrate good agreement with data received by the analytically oriented method [1] and finite element method [25]. Having defined the basic functions φ_k for each tank, substitute them into system (9) for estimating the liquid level changing under given harmonic loads. Suppose the tanks were at state of rest at the initial time. So, initial data are following:

$$d_{0k}(t) = 0,\ \dot{d}_{0k}(t) = 0,\ d_{1k}(t) = 0,\ \dot{d}_{1l}(t) = 0. \tag{23}$$

From (9) and (23) it follows that $d_{0k}(t) = 0$. Consider the harmonic loads as $a_x(t) = a_0 \cos f_0 t, a_z(t) = a_1 \cos f_1 t$. Let's focus on the most extreme case of parametric resonance, when the load frequency is twice the first fundamental one of unbaffled shell. So, let $f_0 = f_0 = 8.28$ Hz, and the amplitude' acceleration are $a_0 = a_1 = 0.1$ m/sec^2.

Figure 2 below shows time-histories of the liquid filling level in the tanks.

In case of the parametric resonance one can observe an unlimited increase in the amplitude of fluid vibrations, which can lead to loss of stability (Fig. 2a)). The installation of partitions leads to amplitudes decreasing (Fig. 2b),c)). In the quarter tank (Fig. 1b)), the load frequency is close to the second fundamental one, which led to the beating mode. The installation of the floating cover significantly reduced the amplitude of vibrations (Fig. 2d)), but such covers are difficult to install in fuel tanks.

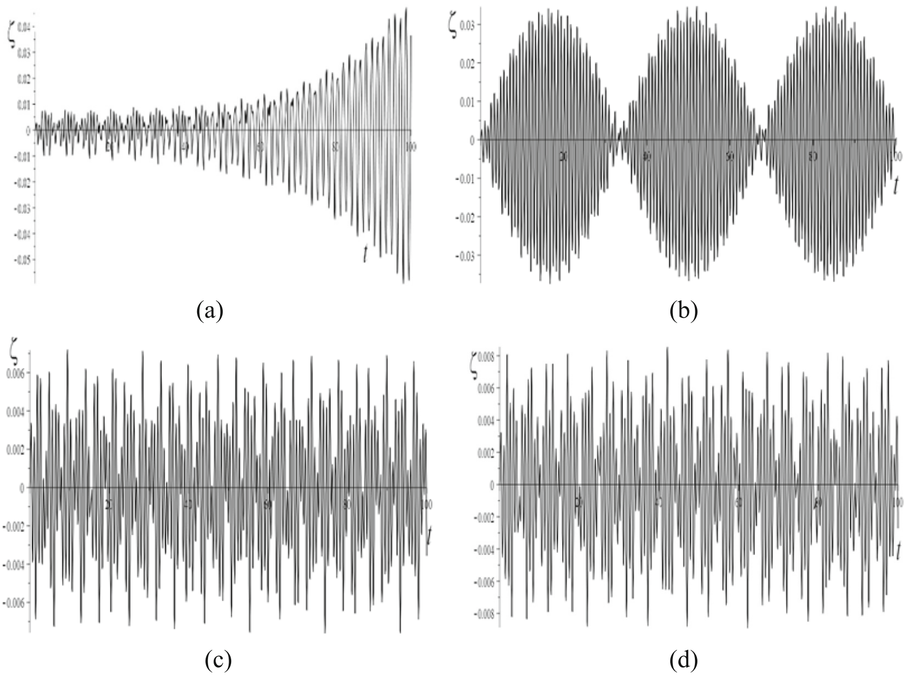

Fig. 2. Time-histories of the free surface level in the tanks

5 Conclusion and Future Research

Dampers in the form of baffles and floating covers have been studied to mitigate the sloshing amplitudes in reservoirs and fuel tanks. In storage facilities for flammable substances, installing the floating covers will reduce sloshing and prevent hazardous contents from spilling out. In the fuel tanks of launch vehicles, it is possible to tune out unwanted resonant frequencies by installing baffles. In the future, a study of nonlinear fluid vibrations in tanks under impulse and seismic loads will be carried out.

Acknowledgments. The authors are very grateful to professor Stavros Syngellakis, Wessex Institute of Technology, UK, for his constant support.

References

1. Raynovskyy, I.A., Timokha, A.N.: Sloshing in Upright Circular Containers: Theory, Analytical Solutions, and Applications. CRC Press/Taylor and Francis Group (2020)
2. Gnitko, V., Degtyariov, K., Naumenko, V., Strelnikova, E.: BEM and FEM analysis of the fluid-structure interaction in tanks with baffles. Int. J. Comput. Methods Exp. Measur. Southampton **5**(3), 317–328 (2017). https://doi.org/10.2495/CMEM-V5-N3-317-328
3. Zang, Q., Liu, J., Lu, L., Lin, G.: A NURBS-based isogeometric boundary element method for analysis of liquid sloshing in axisymmetric tanks with various porous baffles. Europ. J. Mech.-B/Fluids **81**, 129–150 (2020)

4. Misura, S., Smetankina, N., Misiura, I.: Optimal design of the cyclically symmetrical structure under static load. In: Nechyporuk, M., Pavlikov, V., Kritskiy, D. (eds) ICTM 2020. LNCS, vol. 188, pp. 256–266. Springer, Cham (2021). https://doi.org/10.1007/978-3-030-66717-7_21
5. Zulfiqar, Y., et al.: Numerical investigation of an optimum ring baffle design to optimize the structural strength of a tank subjected to resonant seismic sloshing. Struct. Eng. Int. **33**(2), 350–360 (2023)
6. Gontarovskyi, P., Smetankina, N., Garmash, N., Melezhyk, I.: Numerical analysis of stress-strain state of fuel tanks of launch vehicles in 3D formulation. In: Nechyporuk, M., Pavlikov, V., Kritskiy, D. (eds.) Integrated Computer Technologies in Mechanical Engineering - 2020. ICTM 2020. Lecture Notes in Networks and Systems, vol. 188. Springer, Cham. 609–619 (2021). https://doi.org/10.1007/978-3-030-66717-7_52
7. Rusanov, A., Khorev, O., Agibalov, Y., Bykov, Y., Korotaiev, P.: Numerical and experimental research of radial-axial pump-turbine models with spliters in Turbine mode. In: ICTM 2020, Lecture Notes in Networks and Systems, 188 (2021). https://doi.org/10.1007/978-3-030-66717-7_36
8. Strelnikova, E., Kriutchenko, D., Gnitko, V., Tonkonozhenko, A.: Liquid Vibrations in cylindrical tanks with and without baffles under lateral and longitudinal excitations. Int. J. Appl. Mech. Eng. **25**(3), 117–132 (2020). https://doi.org/10.2478/ijame-2020-0038
9. Zheng, Jh., Xue, M.A., Dou, P., et al.: A review on liquid sloshing hydrodynamics. J. Hydrodyn. **33**, 1089–1104 (2021). https://doi.org/10.1007/s42241-022-0111-7
10. Gao, H., Yin, Z., Liu, J., Zang, Q., Lin, G.: Finite element method for analyzing effects of porous baffle on liquid sloshing in the two-dimensional tanks. Eng. Comput. **38**(5), 2105–2136 (2021). https://doi.org/10.1108/ec-12-2019-0567
11. Farahmandpey, S., Broumand, P., Amiri, S.M., Shekari, M.R.: On the nonlinear dynamic analysis of annular baffled steel containers isolated by bearings. In Structures, Elsevier. 56, p. 105012 (2023). https://doi.org/10.1016/j.istruc.2023.105012
12. Kumar, N., Choudhary, N.: Sloshing reduction in three-dimensional rectangular container using rigid baffles. Vibroengineering PROCEDIA **42**, 39–44 (2022). https://doi.org/10.21595/vp.2022.22550
13. Choudhary, N., Kumar, N., Strelnikova, E., Gnitko, V., Kriutchenko, D., Degtyariov, K.: Liquid vibrations in cylindrical tanks with flexible membranes. J. King Saud Univ. – Sci. **33**(8), 101589 (2021). https://doi.org/10.1016/j.jksus.2021.101589
14. Zhang, Z.L., Khalid, M.S.U., Long, T., Chang, J.Z., Liu, M.B.: Investigations on sloshing mitigation using elastic baffles by coupling smoothed finite element method and decoupled finite particle method. J. Fluids Struct. **94**, 102942 (2020). https://doi.org/10.1016/j.jfluidstructs.2020.102942
15. Sierikova, O., Koloskov, V., Degtyarev, K., Strelnikova, O.: The deformable and strength characteristics of nanocomposites improving. materials science forum. Trans. Tech. Publications, Ltd, Switzerland **1038**, 144–153 (2021). https://doi.org/10.4028/www.scientific.net/MSF.1038.144
16. Liu, S., Yang, Z.: Virtual water wave simulation with multiple wavenumbers. Virtual Reality **27**(2), 1221–1231 (2023). https://doi.org/10.1007/s10055-022-00729-0
17. Gnitko, V., Karaiev, A., Degtyariov, K., Strelnikova, E.: Singular boundary method in a free vibration analysis of compound liquid-filled shells. WIT Trans. Eng. Sci. **126**, 189–200 (2019). https://doi.org/10.2495/BE420171
18. Zhang, T., Yang, J.: Nonlinear dynamics and robust control of sloshing in a tank. J. Vib. Control **25**(1), 132–140 (2019). https://doi.org/10.1177/1077546318772256
19. Narváez-Cruz, A.J., Useche-Vivero, J.F., Martínez-Trespalacios, J.A., Castro-Suarez, J.R.: A novel full boundary element formulation for transient analysis of elastic membranes coupled to acoustics fluids. In: IOP Conference Series: Materials Science and Engineering, IOP Publishing. 844(1), p. 012073 (2020). Doi:https://doi.org/10.1088/1757-899X/844/1/012073

20. Karthick, S, Satish, V.: Theoretical characterization of liquid sloshing in Containers. In: ASME International Mechanical Engineering Congress and Exposition, 85666, V010T10A010, American Society of Mechanical Engineers (2021). https://doi.org/10.1115/IMECE2021-70152
21. Al-Zughaibi, A., Hussein, E., Rashid, F.: Studying and analysis of nonlinear sloshing (vibrating) of interaction fluid structure in storage tanks. J. Mech. Eng. Res. Dev. **44**, 180–191 (2021)
22. Karaiev, A., Strelnikova, E.: Singular integrals in axisymmetric problems of elastostatics. Int. J. Model. Simul. Sci. Comput. **11**(1), 200003 (2020). https://doi.org/10.1142/S1793962320500038
23. Nguyen, H.P., Wang, C.M.: Finite element - Multi-domain boundary element method for hydroelastic analysis of large floating pontoons with perforated plates. Ocean Eng. **246**, 110659 (2022). https://doi.org/10.1016/j.oceaneng.2022.110659
24. Avramov, K., Cheshko, K., Polishchuk, O.: Chaotic oscillations of a kinematically excited flat shell during geometrically non-linear deformation. J. Mech. Eng. **22**(3), 26–36 (2019). https://doi.org/10.15407/pmach2019.03.026
25. Kolaei, A., Rakheja, S.: Free vibration analysis of coupled sloshing-flexible membrane system in a liquid container. J. Vib. Control **25**(1), 84–97 (2019). https://doi.org/10.1177/107754631877122

Development and Implementation of Energy-Saving Control Algorithms for Pumping Units of Power Plants to Increase Their Operational Quality

Gennadii Kaniuk, Andrii Mezeria, Tetiana Fursova(✉), Maksym Kaniuk, and Igor Babenko

Ukrainian Engineering Pedagogics Academy, Universytetska Str. 16, Kharkiv 61003, Ukraine
fursova.t.m@uipa.edu.ua

Abstract. The work is dedicated to increasing the operational quality of pump units for the thermal and nuclear power plants in Ukraine, which are characterized by physical and moral aging. The problem is addressed through the development and implementation of energy-saving control algorithms for pump units that were realized at the Zmiiv Thermal Power Plant. A centrifugal-type circulation pump which supplies cooling water to the condenser is considered as an example of the implementation of the algorithm. The article presents mathematical models of pump operation modes, conducts experimental research on their characteristics to identify the proposed mathematical models, and determines the numerical parameters of energy-efficient control algorithms. Universal laws and algorithms for energy-efficient control of pump operation modes have been developed to achieve maximum efficiency values in their main operating modes, associated with reducing energy and fuel consumption for internal needs of power plants that is relevant to the United Nations Development Goals.

Keywords: Algorithm · Energy-Efficient Control · Pump

1 Introduction

A significant part of auxiliary power for the internal energy needs of power plants (up to 80%) is attributed to the operation of pump and other superchargers (hydraulic, aerodynamic, and steam paths of boilers, turbines, condensers, heat exchange equipment, and heating systems). At the stage of designing and commissioning Ukrainian power plants, serious scientific research to ensure maximum efficiency of these systems was typically not carried out. The issue becomes particularly critical during the operation of power units under variable modes and due to various independent structural modernizations of pumps and networks. Therefore, it is precisely in this direction that significant reserves for energy saving and implementation of energy-efficient control should be conducted.

The design norms of energy consumption for the internal needs of power plants constitute 3–7%. However, over the last 10–20 years, due to moral and physical

M. Nechyporuk et al. (Eds.): ICTM 2023, LNNS 1008, pp. 431–440, 2024.
https://doi.org/10.1007/978-3-031-61415-6_37

aging of power equipment and deviations from the designed operating modes, energy consumption for internal needs has been increasing [1].

According to the United Nations' Sustainable Development Goals, energy-saving approaches can help reduce fuel costs and greenhouse gas emissions, thus impacting the environment and the profitability of power plants. The goals emphasize the importance of ensuring access to affordable, reliable, sustainable, and modern energy for all (Goal 7) while promoting actions to combat climate change and its impacts (Goal 13) [2, 3].

2 Literature Review

Literature review concerning control systems and operation of pumping units primarily address general technical issues such as structure, completeness, purpose, technical requirements, safety rules, transportation, etc. [4–10] However, they do not define scientific and methodological principles for ensuring optimal energy-saving modes of pump operation under variable loads. The current regulatory documents lack comprehensive and effective solutions capable of significantly reducing energy losses in pumping units to ensure the necessary performance indicators of the technological process, quality, reliability, and safety.

Problems of energy and resource saving in pumping units were considered in articles [11–15]. Scientific works [16–20] are devoted to issues of the qualimetry.

The purpose of this work is to improve the operational quality of power plant pumping units through the development and implementation of energy- and resource-saving control algorithms.

3 Mathematical Models and Experimental Studies of Pumps

The basic object of the research is a pump (Fig. 1) designed for supplying liquid in technological processes of power plants of the required volumes.

One of the most powerful pumps, crucial for determining the efficiency of the power unit's operation and ensuring the necessary operational modes of the low-pressure system (steam turbine condenser and its auxiliary equipment), is the circulating pump that supplies cooling water to the condenser.

The operation of pumps directly influences the efficiency of the main equipment at the power plant. For instance, the power of the circulating pump and the water flow through it determine the parameters of the vacuum in the condenser, subsequently affecting the energy efficiency of the turbine's operation. Analysis has shown that increasing the flow rate of the circulation water improves the vacuum and enables more electricity generation. However, this also leads to increased power consumption by the circulating pump.

The pump's power constitutes more than 0.5% of the power of the unit in general and nearly 10% of the internal power requirements of the 300 MW unit at Zmiiv Thermal Power Plant (TPP). The passport data of the circulating pump is provided in Table 1.

The energy efficiency of pumping systems is determined by the hydraulic characteristics of the network they operate within. In turn, the network's characteristic is defined

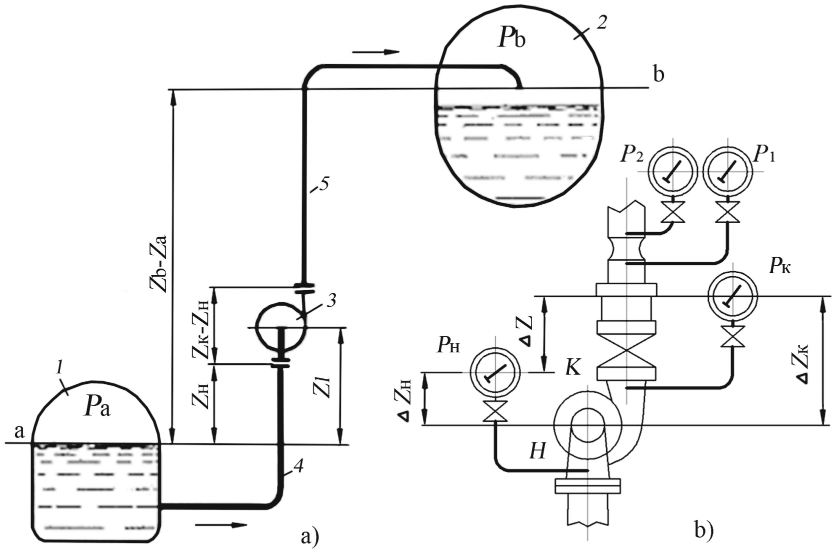

Fig. 1. Scheme of the pump unit: a) schematic diagram of the pump unit, b) installation diagram of measuring devices; 1 and 2 – receiving and pressure tanks; 3 – pump; 4 and 5 – suction and pressure pipelines; P is the pressure; Z is the level.

Table 1. Passport data for the circulating pump at Zmiiv TPP

Type	Nominal engine power N_{en}, kW	Flow rate Q, m^3/h (m^3/s)	Head, m	Rotation frequency *n*, s^{-1}	Type of electric motor
ОП-2–145	1700	30000 (8,333)	15	4,17 – 6,25	ВДД-213/54–16

by the required flow rate of the working fluid, as well as the geometric parameters of the network and coefficients of local and linear losses.

The solution to the optimization problem of hydraulic networks can be obtained graphically (Fig. 2). The criterion for optimality in creating an energy-efficient control system for pumps can be the minimum of the total energy losses while maintaining necessary parameters at a specified level, determined by the technological process, reliability indicators, and other factors.

Throughout the entire flow range, the position values of the gate valve and rotational frequency '*n*' are determined, at which the energy losses in the pump will be minimal. These dependencies can be utilized in microprocessor-based automatic pump control devices and periodically updated in real-time mode. This ensures obtaining minimal energy losses in the pump under current conditions, including the pump's technical state, working fluid parameters, necessary technological process parameters, and limitations.

Simplified mathematical models consist of a set of equations and can be identified based on experimental characteristics:

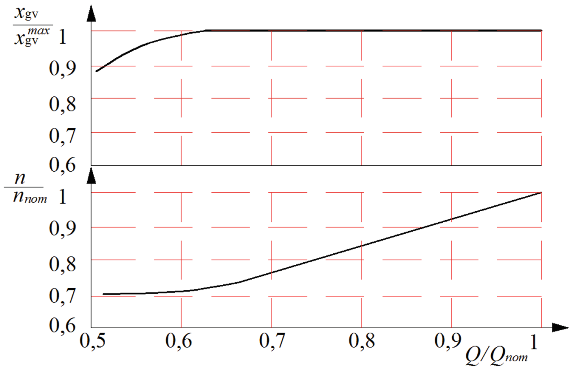

Fig. 2. The graphical representation of solving the problem of energy-saving control of pumping units through frequency-throttle regulation.

The pump flow rate (the flow rate at operating point):

$$Q_p = A_{Q_p}^{n} \cdot n + A_{Q_p}^{x_{gv}} \cdot x_{gv} + C_{Q_p}, \tag{1}$$

where n is the rotational speed, x_{gv} - the gate valve position, A and C – the linearization coefficients.

The pump head:

$$H_p = A_{H_p} \cdot Q_p^2 + B_{H_p} \cdot Q_p + C_{H_p}, \tag{2}$$

where A, B, C – the corresponding linearization coefficients.

The pump efficiency:

$$\eta = A_\eta \cdot Q_p^2 + B_\eta \cdot Q_p + C_\eta. \tag{3}$$

The pump power consumption:

$$N_{com} = \frac{N_e}{\eta_e} = C_N^x x_{gv} + C_N^n n. \tag{4}$$

where N_e and η_e are the electric power and efficiency.

Experimental studies of the circulating pump OП-2–145 at the 300 MW Zmiiv TPP unit, whose characteristics are presented in Fig. 3, demonstrated the reliability of simplified mathematical models (1 - 4) and revealed potential energy-saving effects with various control methods.

Based on experimental research, the relationship between the relative efficiency $\eta^* = \eta/\eta_{\max}$ and the flow rate Q for various rotational frequencies has been established (Fig. 4).

At the power plants, control of the circulation pump is achieved at a single frequency by altering the local resistance of the gate valve.

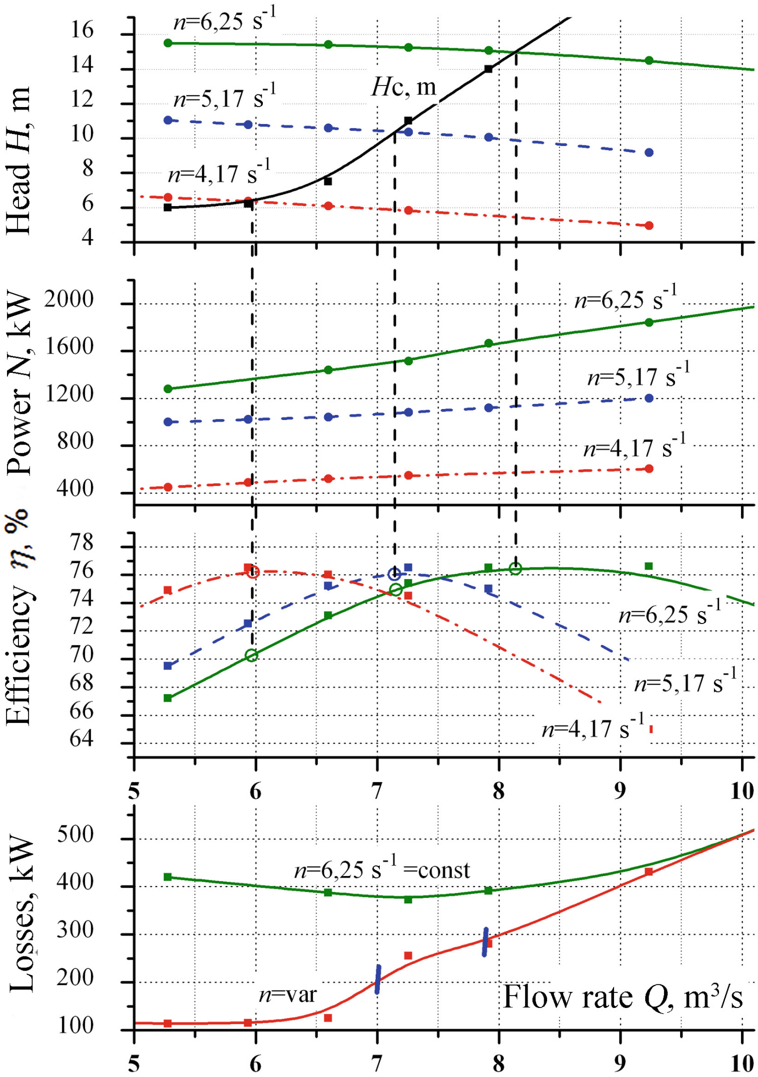

Fig. 3. Experimental studies of the ОП-2–145 circulation pump at the Zmiiv TPP.

The authors have defined a control law for the circulation pump, under which the efficiency will be maximum:

$$n(Q) = 0,001045 \cdot Q^2 + 0,95495 \cdot Q - 1,8794. \tag{5}$$

or in the linear approximation:

$$n(Q) = 0,9703 \cdot Q - 1,9353.$$

Based on mathematical modeling and approximating experimental data, in accordance with the proposed methodologies for determining energy-efficient operating

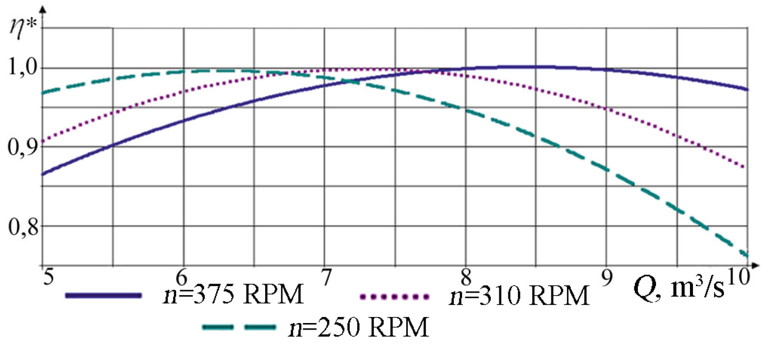

Fig. 4. Dependence of the relative efficiency $\eta^* = \eta/\eta_{max}$ on the flow rate Q for various rotation frequencies.

modes of pumps, universal dimensionless dependencies of the pump's rotational frequency corresponding to the maximum efficiency values have been constructed as a function of flow rate (Fig. 5).

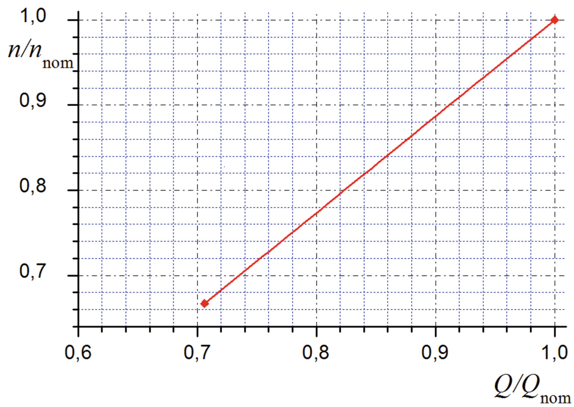

Fig. 5. Dimensionless dependencies of the rotational frequency corresponding to maximum efficiency for the ОП-2–145 pump.

These dependencies can be utilized for developing regulatory methods and technical conditions for creating energy-saving systems of automated control for various types of pumps in power plants.

4 Algorithm for Energy-Saving Control of Pumping Units

The automatic control system of the pump is a complex of technical devices that ensures, without operator involvement, the specified rotation frequency of the pump rotor and the position of the gate valve in accordance with the operating mode of the main technological object.

Energy-saving control of pumping units involves determining the necessary rotational frequency of the working wheel and the position of the gate valve at which losses will be minimal within specified constraints. The solution to this problem depends on the parameters of the pump and the network it operates on. For preliminary adjustment of the working wheel's rotational frequency, a separate regulator can be used, which operates to implement similarity equations. The algorithm of its operation is shown in Fig. 6. The coefficient of hydraulic friction, λ, is a function of the flow regime of the liquid, determined by the Reynolds number criterion *Re*.

The application of a regulated electric drive ensures energy conservation and enables the attainment of new qualities within systems and objects. Significant energy savings are achieved through the adjustment of technological parameters. For instance, in the case of a pump, it's possible to maintain pressure or regulate productivity.

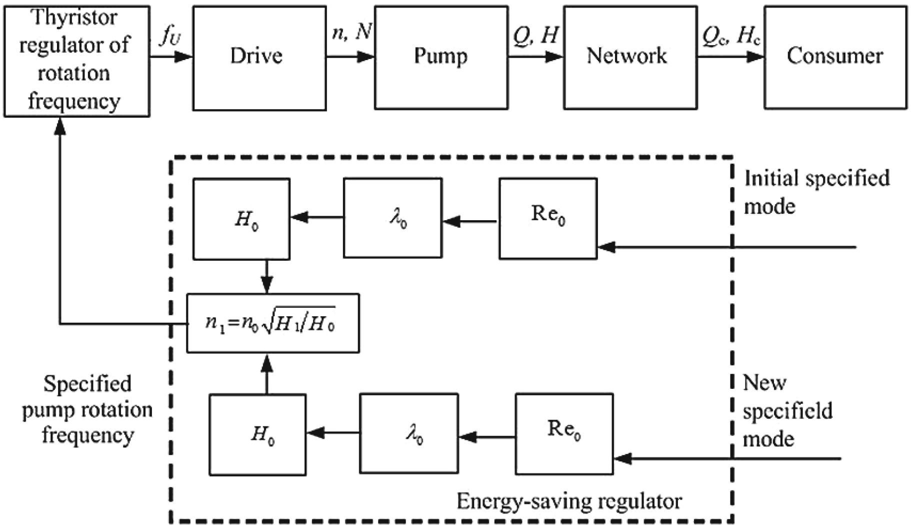

Fig. 6. The regulator for energy-saving control of pumping units.

The complete algorithm for energy-saving control of pumping units is depicted in Fig. 7.

A graphical representation of energy-saving control solutions depending on the parameters of the pump and the network is shown in Fig. 8.

The developed algorithm is unified and multifunctional. It allows for frequency-throttle regulation, changing the blade angle, and adjusting the pump's wheel diameter.

The algorithm enables the determination of both the base characteristics of the pump and the network, as well as their current values. This allows for a comprehensive assessment of the pump and network's technical condition (the diagnostic effect), building a database of pumping unit operation parameters, and identifying optimal operation modes for the pump over a wide range of flow rates in terms of minimizing energy losses.

Adjusting the gate valve characteristics can be implemented in cases where the pump operates in a higher-level automated control system, for instance, a condenser. Maintaining optimal characteristics for the higher-level structure may prove more efficient than compromising the pump's efficiency through additional gate valve regulation.

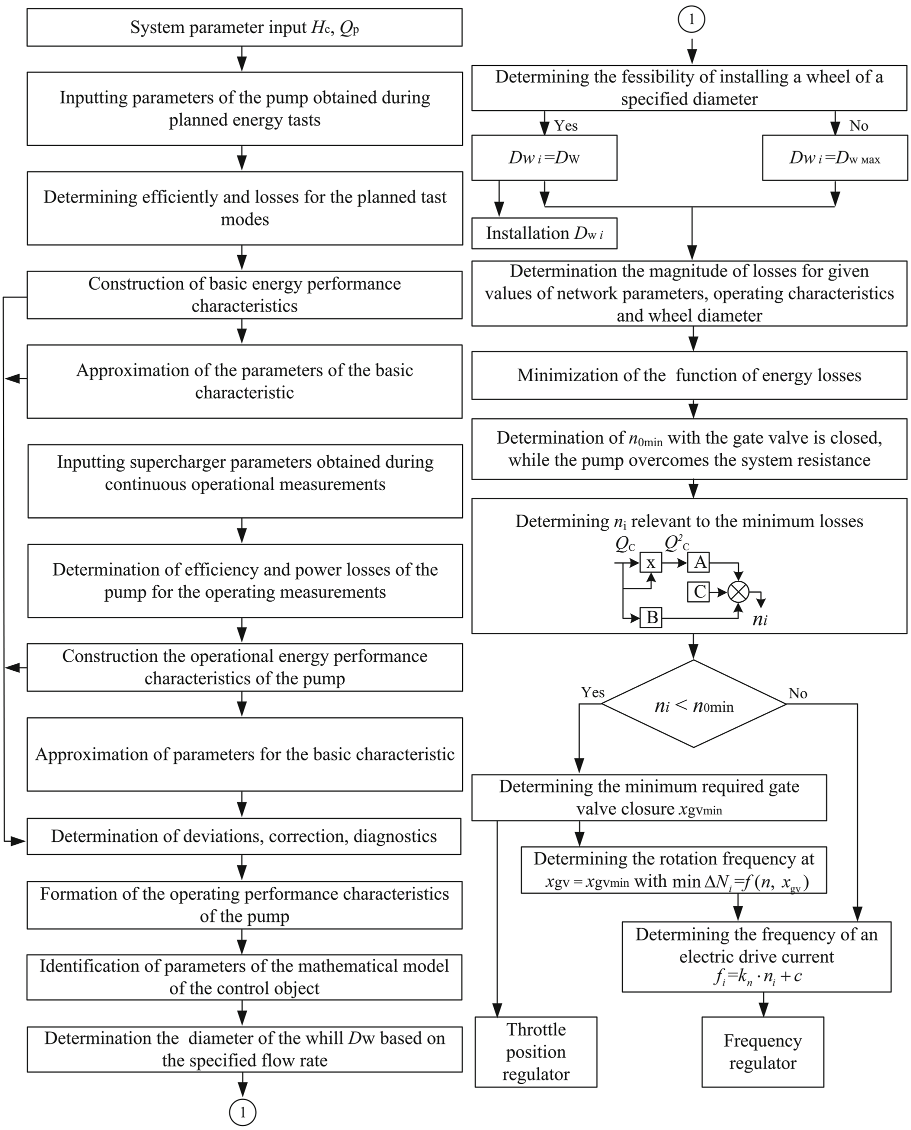

Fig. 7. Algorithm for energy-saving control of pumping units.

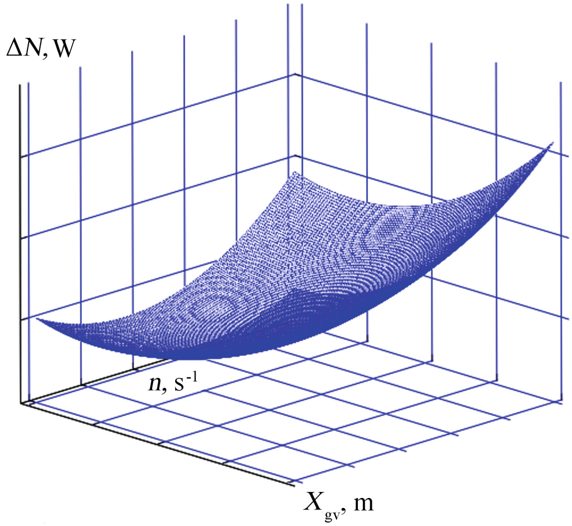

Fig. 8. Graphical representation of the energy-saving control solution depending on the parameters of the pump and the network.

5 Conclusions

Based on a series of theoretical and experimental studies conducted by the authors of the article, along with a synthesis of scientific experience, algorithms for energy-saving control of power station pump units have been developed.

The obtained analytical dependencies and calculation methods for optimal operation modes of power plant pump units significantly reduce energy consumption for driving these units while maintaining process parameters.

The research findings have been practically implemented in the automated control systems of circulation pumps in the Zmiiv Thermal Power Plant, PJSC ‘Centrenergo,’ and can be beneficial for power stations both in Ukraine and abroad.

References

1. Project of the Recovery Plan of Ukraine. Materials of the “Energy Security” working group [in Ukrainian]. https://www.kmu.gov.ua/storage/app/sites/1/recoveryrada/ua/energy-security.pdf
2. The Sustainable Development Goals: https://www.un.org/sustainabledevelopment/sdgs-framework-for-covid-19-recovery/
3. Contributing to the UN Sustainable Development Goals with ISO standards: https://www.iso.org/publication/PUB100429.html
4. Bachus, L., Custodio, A.: Know and understand centrifugal pumps. Oxford, Elsevier Advanced Technology (2003). https://www.sciencedirect.com/book/9781856174091/know-and-understand-centrifugal-pumps
5. Geoff Brown. Understand pump fundamentals for best efficiency. https://assets.markallengroup.com//article-images/27341/Basics%20of%20pumps.pdf

6. Nesbitt, B.: Handbook of Pumps and Pumping, 1th ed. Elsevier Science, p. 424 (2006). http://www.iqytechnicalcollege.com/Handbook%20of%20Pumps%20and%20Pumping.pdf
7. Chaurette, J.: Centrifugal pump specific speed primer and the affinity laws. https://www.pumpfundamentals.com/download/spec_speed_primer.pdf
8. Pozos-Estrada, O., Sánchez-Huerta, A., Breña-Naranjo, J.A., Pedrozo-Acuña, A.: Failure analysis of a water supply pumping pipeline system. Water **8**(9), 395 (2016). https://doi.org/10.3390/w8090395
9. Ma, G., Zhang, S., Meng, F.: Failure analysis and research of key auxiliaries in thermal power plant. E3S Web Conf. **118**, 02064 (2019). https://doi.org/10.1051/e3sconf/201911802064
10. Chaurette, J.: Pump performance measurements. https://www.pumpfundamentals.com/download/pump_performance.pdf
11. Xia, L., Liu, D., Wang, F., Jiao, S., Luo, C.: Optimal operation of circulating water pump in thermal power plant under different weather conditions. J. Drainage Irrigation Mach. Eng. **31**(6), 490–495 (2013). https://doi.org/10.3969/j.issn.1674-8530.2013.06.007
12. Marchis, D., et al.: Energy recovery in water distribution networks. Implementation of pumps as turbine in a dynamic numerical model. Procedia Eng. **70** (2014). https://doi.org/10.1016/j.proeng.2014.02.049
13. Kaniuk, G., Mezeria, A., Kniazeva, V., Khoroshun, D., Fursova, T., Blyznychenko, O.: Energy efficient control by the group of oil pumping stations operation. Probl. Regional Energetics **4**(52) (2021). https://doi.org/10.52254/1857-0070.2021.4-52.02
14. Torregrossa, D., Capitanescu, F.: Optimization models to save energy and enlarge the operational life of water pumping systems. J. Clean. Prod. **213**, 10 (2019). https://doi.org/10.1016/j.jclepro.2018.12.124
15. Narendhiran, S., Velan, M.: Energy efficient coatings for improved wear and tear performance of a circulating water pump employed in thermal power plant—a case study. In: Resent Trends in Thermal and Fluid Sciences, pp. 319–329 (2023). https://doi.org/10.1007/978-981-19-3498-8_27
16. Trishch, R., Maletska, O., Hrinchenko, H., Artiukh, S., Burdeina, V., Antonenko, N.: Development and validation of measurement techniques according to ISO/IEC 17025:2017. In: Proceedings of the 8th International Conference on Advanced Optoelectronics and Lasers, Sozopol, pp. 715–720 (2019). https://ieeexplore.ieee.org/document/9019539
17. Kupriyanov, O., Trishch, R., Dichev, D., Bondarenko, T.: Mathematic model of the general approach to tolerance control in quality assessment. In: InterPartner 2021. Lecture Notes in Mechanical Engineering, pp. 415–423. Springer, Cham (2021). https://doi.org/10.1007/978-3-030-91327-4_41
18. Trishch, R., Nechuiviter, O., Hrinchenko, H., Bubela, T., Riabchykov, M., Pandova, I.: Assessment of safety risks using qualimetric methods. MM Sci. J., 6668–6674 (2023). https://doi.org/10.17973/MMSJ.2023_10_2023021
19. Trishch, R., Cherniak, O., Kupriyanov, O., Luniachek, V., Tsykhanovska, I.: Methodology for multi-criteria assessment of working conditions as an object of qualimetry. Eng. Manage. Prod. Serv. **13**(2), 107–114 (2021). https://doi.org/10.2478/emj-2021-0016
20. Trishch, R., Sichinava, A., Bartoš, V., Stasiukynas, A., Schieg, M.: Comparative assessment of economic development in the countries of the European union. J. Bus. Econ. Manage. **24**(1), 20–36 (2023). https://doi.org/10.3846/jbem.2023.18320

Analyzing Thermophysical Phenomena in a Thermopressor for Air Intercooling Systems

Halina Kobalava[1](✉), Dmytro Konovalov[1,2], Oleksandr Voinov[1], and Viktor Samokhvalov[1]

[1] Admiral Makarov National University of Shipbuilding, 44, Ushakov Avenue, Kherson 73003, Ukraine
halyna.kobalava@nuos.edu.ua

[2] Norwegian University of Science and Technology, 1, Høgskoleringen, 7034 Trondheim, Norway

Abstract. Employing interstage contact cooling techniques can enhance the efficiency of multistage air compression, which is critical for gas turbine performance. Traditionally, intercooling has relied on ambient cooling methods. The proposed solution utilizes a thermopressor in the intercooling system. To examine the complex thermophysical phenomena occurring within the thermopressor, a computational model based on the finite volume technique was developed. The discrete phase models enabled simulating the water evaporation. The simulation quantified key output parameters representing the primary two-phase flow (air-water) characteristics at the thermopressor outlet. The results showcase the thermopressor's effectiveness in realizing finely-dispersed water atomization, consequently enabling near-isothermal compression. Hence, applying the thermopressor could substitute traditional air cooling, decreasing compressor work and power by about 10%, while simultaneously increasing working fluid mass flowrate, ultimately translating to improved gas turbine performance. The consistent results validate the feasibility of substituting conventional inter-cooling via the designed thermopressor leading to improved gas turbine efficiency and operational economy.

Keywords: Evaporative Cooling Techniques · Efficiency · Compressor · Specific Power

1 Introduction

Conserving energy resources is a critical challenge in the global economy, especially in the operation of power plants employing gas turbine technology. The compressor is a key component, utilized to produce pressurized air. To achieve higher pressures, multi-stage configurations are employed, with sequential compression across discrete stages. Implementing interstage cooling (returning air to initial temperature) between compression stages can substantially reduce energy consumption, bringing the process closer to isothermal compression. This directly enhances cycle efficiency and compressor performance, increasing by 1% for every 3 degrees reduction in inlet temperature [1]. Studies

M. Nechyporuk et al. (Eds.): ICTM 2023, LNNS 1008, pp. 441–450, 2024.
https://doi.org/10.1007/978-3-031-61415-6_38

by Azizifar et al. confirm intercooling meaningfully reduces cycle energy consumption, particularly in summer, with up to 9.6% possible savings. Several technologies seek improving multistage compression efficiency [2].

Significant research targets injecting water/steam to humidify the working fluid, consequently lowering temperature. Hence, advanced theoretical, numerical, and experimental investigations into enhancing multistage compressor performance are presently demanded within gas turbine power plants. In summary, interstage cooling methods are important for thermal efficiency and compressor effectiveness in gas turbine power systems. More research focused on cooling approaches and their feasibility is still required.

2 Literature Review

Research into evaporative cooling techniques at compressor inlets and interstages within gas turbine engines emerged in the 1950s, with early contributions by Brown Boveri [3], Jones et al. [4], and Wilcox et al. [5]. The primary aim was reducing air compression work via water injection (Fig. 1).

General Electric's (GE's) SPRINT intercooling technology effectively employs water injection for contact cooling in two-stage compressors, decreasing compressor drive power by up to 15% [6]. Similarly, in 1990s Japan, The Tokyo Electric Power Co.'s 122 MW gas turbine prototype with 220 kg/s air flow realized a relative humidity increase to 90% using interstage water injection [7].

The TopHAT concept by Alpha Power Systems recovers waste heat by heating compressed air with exhaust gases while simultaneously enabling wet compression through uniform SwirlFlash water injection [8].

Recent computational studies by Lin et al. analyzed the impact of 5–100 microns diameter water droplets injection on compressor inlet airflow dynamics. Varying liquid injection speeds (10–80 m/s), water flow rates (1–10 kg/s) and spray angles (15–75 degrees) resulted in approximately 130 K temperature decrease and 2% lower friction losses compared to dry air [9]. In summary, water injection techniques for direct evaporative cooling and interstage humidification have been researched since the mid-1900s for boosting gas turbine efficiency.

While these studies showcase the immense potential of compressor "wet compression", some considerable efficiency limitations persist in its implementation. A key impediment is inappropriate liquid phase flow behavior, particularly blade and casing deposition, which results in substantial energy losses. Reasons for declining compressor power include inadequate water evaporation, extra losses from droplet acceleration/deceleration through deposition and stripping, and liquid films-induced frictional losses. These effects counter the benefits of injection and deteriorate compression work [10].

One straightforward approach to mitigate blade surface deposition is to realize highly dispersed spraying, where droplets follow the airflow due to insufficient inertia. Preliminary inferences suggest restricting droplet diameter within 10–20 microns is important for this purpose [11, 12].

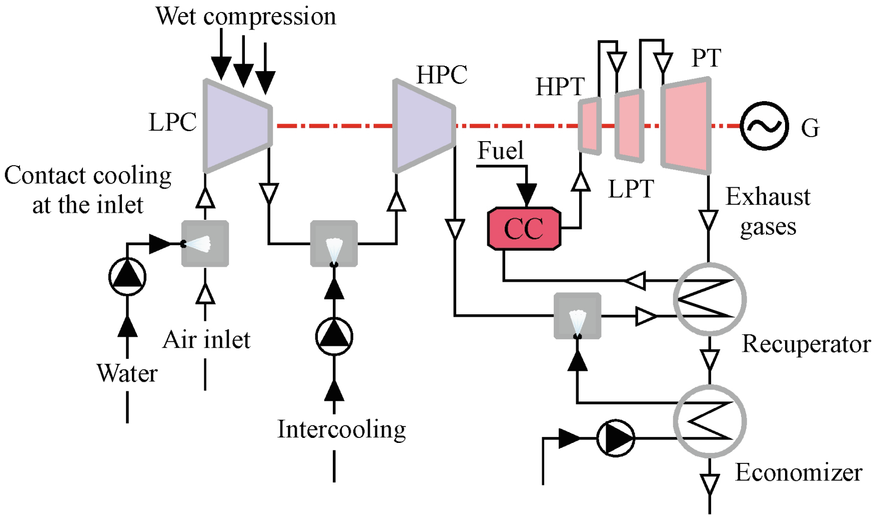

Fig. 1. Water injection approaches for gas turbine compressor cooling.

An innovative technique for cooling and humidifying the compressed working fluid employs a two-phase thermopressor apparatus [13]. It achieves ultra-efficient finely-dispersed atomization and supplemental thermo-gas-dynamic compression for contact air cooling [14].

Additional experimental and numerical studies investigating the working phenomena within the thermopressor are required to quantify its influence on enhancing compressor performance and efficiency through interstage contact cooling.

3 Research Methodology

A computational approach based on the proven finite volume methodology was undertaken to examine the intricate heat and mass transfer phenomena occurring within the thermopressor. The numerical framework was implemented in ANSYS Fluent to develop a CFD model for simulating the interstage contact cooling process [15].

Established theoretical formulations representing the discretized conservation laws of mass, momentum and energy were utilized to construct the model equations [16, 17]. The airflow was modeled as a steady, compressible, turbulence-prone, continuous medium, employing Reynolds-Averaged Navier Stokes (RANS) equations coupled with a two-equation turbulence hypothesis for closure [18]. By employing the standard k-ε turbulence model as a closure model, we achieved coupling between turbulent viscosity and stresses, heat flux, and mass.

A sequential approach was utilized to model the complex two-phase flow. Firstly, the airflow was independently simulated excluding water droplet interactions. Subsequently, the discrete phase calculations used a Lagrangian framework to determine trajectories, sizes, velocities, positions and temperature changes of individual droplets, based on the computed airflow field [19].

The next stage involved coupling the discrete and continuous phases. During this step, inter-phase exchanges of mass, momentum and energy were numerically evaluated. Resulting data was incorporated back into the airflow computations, enabling two-way coupling. Simulations proceeded through iterations until attaining a converged solution.

Simultaneous interaction between the two phases leads to heat, mass, and momentum transfer, which alters the main flow parameters such as droplet size, heat transfer coefficient, mass transfer coefficient, relative velocity, and resistance coefficient. Accordingly, with the constant fluctuation of the main flow parameters, a mathematical approach is necessary for analyzing the contact cooling process based on the following assumptions:

- No heat exchange occurs between the flow part elements of the thermopressor (inlet chamber, convergent nozzle, evaporation chamber, diffuser) and the environment.
- The air parameters correspond to the air parameters between the compressor stages of a gas turbine engine.
- The air flow is assumed to be compressible (changes in air density significantly influence flow velocity, temperature, and pressure).
- For modeling the two-phase flow, the airflow is assumed to be a continuous, bulk phase (the flow is described by the Euler's model), while the injected water droplets are regarded as a discrete phase (the flow of separate particles is described by the Lagrangian's model) [20].
- Droplet evaporation occurs until complete air saturation, i.e. the partial pressure of water vapor in the droplet boundary layer equals the saturated vapor pressure at that temperature, while evaporation in the whole apparatus may be incomplete.
- In the thermopressor, water droplets are injected into the moving air flow at a velocity equal to $M = 0.4$–0.8.
- The cross-sectional area of the evaporation chamber is constant (the chamber shape is cylindrical).
- The droplet shape is spherical and does not change its shape when moving in the thermopressor's flow part.
- The state of the vapor layer near the droplet surface is saturated.
- The injected water is a polydisperse flow (droplet range $\delta = 0$–$30\ \mu$m).
- At the inlet of the evaporation chamber, the velocity vectors of the droplets are directed parallel to the axis of the thermopressor's evaporation chamber.
- Droplet trajectory modeling is performed separately for each droplet.

The analysis utilized an experimental thermopressor model (Fig. 2) having the following dimensions: length $L_{tp} = 387$ mm; evaporation chamber diameter $D_{ch} = 25$ mm. Optimized confuser convergent and diffuser divergent angles were selected as $\alpha_c = 35°$ and $\beta_d = 5°$ respectively to minimize frictional and localized pressure drop losses.

Key inlet parameters for the post-compression airflow and injected water are: inlet air pressure $P_1 = 301325$ Pa; inlet temperature $T_{air1} = 473$ K; inlet velocity $w_{air1} = 55$ m/s; air mass flow rate $G_{air} = 0.29$ kg/s; relative water injection velocity $(w_w/w_{air1}) = 0.33$; water-to-air mass flow ratio $g_w = 10\%$; inlet Mach number $M = 0.67$.

The simulation enabled quantification of key output parameters that characterize the essential two-phase flow (air-water mixture) properties at the thermopressor outlet:

On the simulation results, the following output parameters that represent the primary characteristics of the two-phase flow (air-water) at the exit of the thermopressor were

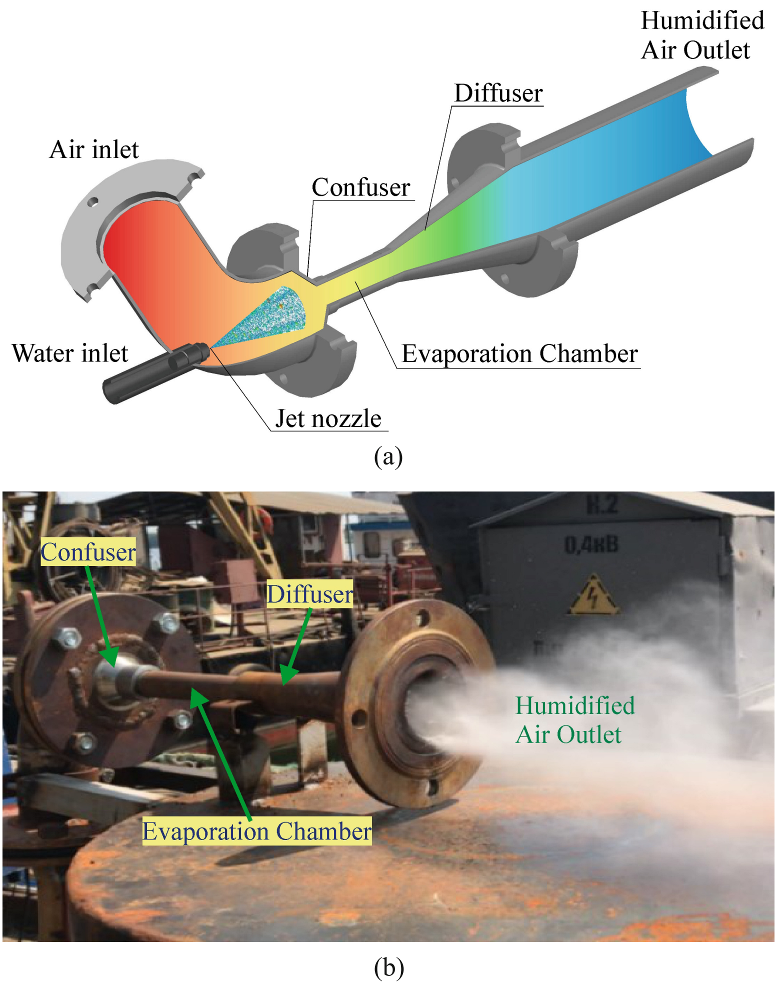

Fig. 2. 3D model (a) and experimental model (b) of the thermopressor.

obtained. These parameters include total air pressure (P_{tp}), air velocity (w_{tp}), temperature (T_{tp}), water droplet diameter in the air flow (δ_d), and mass concentration of water (m_{H2O}).

4 Results and Discussion

A sequential modeling approach was adopted comprising two discrete steps: simulating the “dry” thermopressor (excluding water injection) aimed to determine the inherent pressure deficit from aerodynamic drag without interstage cooling influences, and incorporating liquid injection at the entrance enabled examining the comprehensive heat and mass transfer phenomena within the thermopressor.

Notably, the airflow velocity entering the evaporation chamber is quite high, at $w_{tp} = 326$ m/s (Mach 0.67) (Fig. 3a). However, substantial thermal energy extraction for evaporation causes considerable velocity reduction to 230–250 m/s downstream, owed to the sharp air density rise from intense cooling. Fortunately, flow visualizations confirmed absence of recirculation zones throughout the diffuser (Fig. 3b), mitigating additional pressure losses.

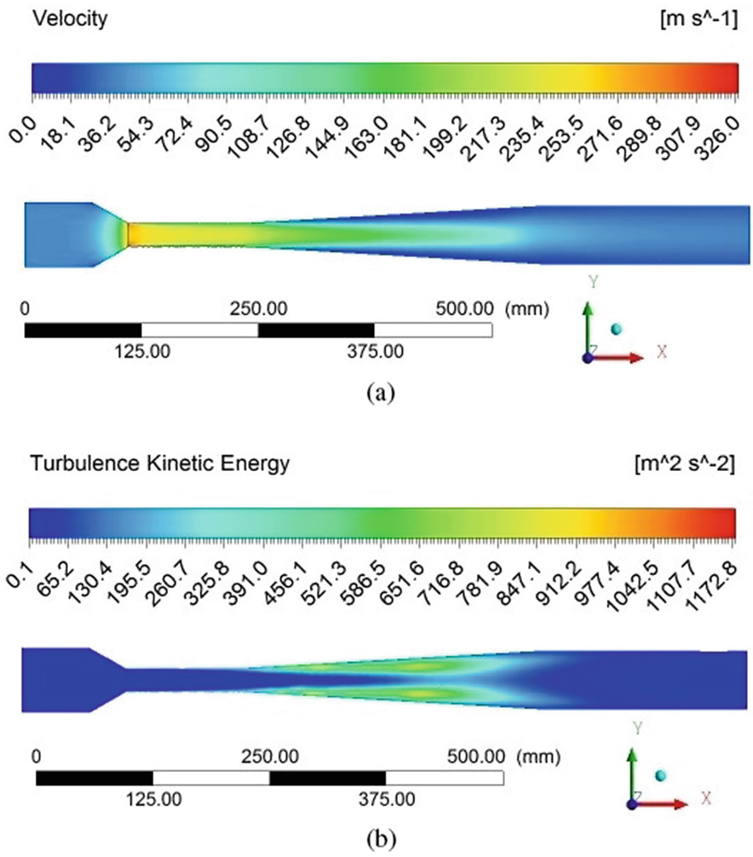

Fig. 3. The distribution of flow velocity w_{tp}, and turbulent kinetic energy k fields along the length of the thermopressor L_{tp} during incomplete evaporation.

The analysis determined the degree of compressed air cooling achievable within the thermopressor under different conditions (Fig. 4a):

- Complete droplet evaporation: $\Delta T_{tp} = 106$ K.
- Partial evaporation in diffuser: $\Delta T_{tp} = 118$ K.
- Incomplete evaporation: $\Delta T_{tp} = 133$ K.

For the inlet temperature of 473 K (200 °C), cooling levels of 133–140 K were attained, yielding exit temperatures between 340–367 K (67–94 °C).

The dispersed two-phase flow encounters velocity reduction to 40–45 m/s within the diffuser, improving pressure recovery. The “dry” apparatus exhibited a pressure increase of $\Delta P_{tp.dry}$ = 65 kPa (21.5%). However, water injection boosted this growth to ΔP_{tp} = 54.5 kPa (18.1%) owed to favorable thermogasic effects from vaporization. This corresponds to 24.5 kPa (8.1%) enhancement over the baseline configuration. Overall, the achieved outlet absolute pressure was 302.7 kPa (Fig. 4b).

Optimized injection realization facilitated substantial isothermal compression by reducing temperatures to 94 °C from 200 °C. This directly boosted pressure rise available for the next compressor stage.

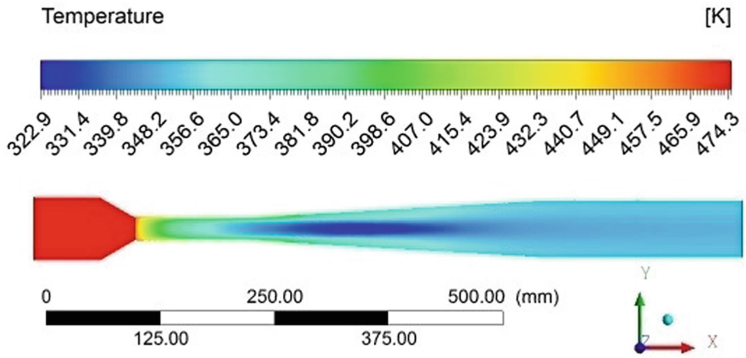

(a)

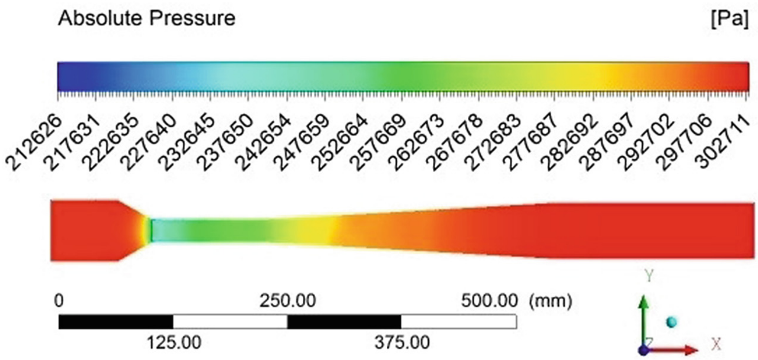

(b)

Fig. 4. The distribution of flow temperature T_{tp}, and absolute pressure P_{tp} fields along the length of the thermopressor L_{tp} during incomplete evaporation.

To quantify droplet fragmentation levels and diameter reduction from partial evaporation, measurements were made at the diffuser exit under intentionally incomplete vaporization conditions. The initial spray comprised between 0–30 μm droplets entering the evaporation chamber. Under these non-fully evaporated circumstances, further breakup was achieved, with the thermopressor outlet exhibiting a finely dispersed spray with mean diameter lowered to approximately 18 μm (Fig. 5). Moreover, a uniform spatial distribution of the two-phase mixture was attained across the exit cross-section.

Comparison of different relative injection ratios highlights optimum performance for 10% liquid content. This corresponded with only 1% total pressure rise over single-phase flow, yet demonstrated substantial 130 K cooling. Such observations reinforce that supplying excess water beyond evaporation requirements helps mitigate frictional losses. Hence, pressure drop can be recovered to almost initial values through appropriate injection schemes.

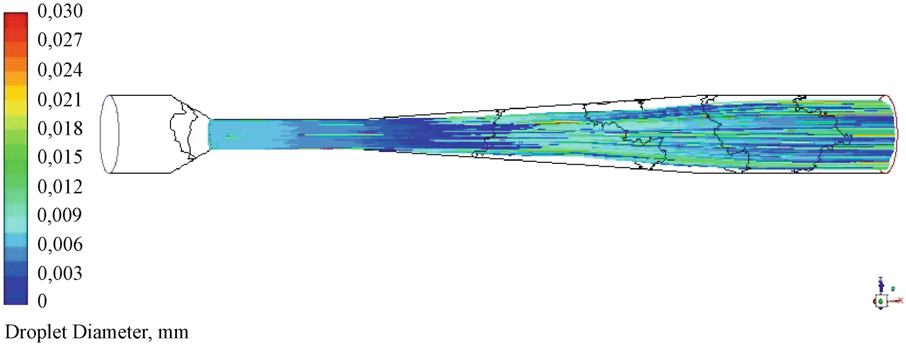

Fig. 5. Droplet dispersion of sprayed water in the thermopressor flow part.

In summary, the two-phase flow field analysis and optimization study enabled designing a thermopressor capable of realizing finely-atomized sprays for efficient isothermal

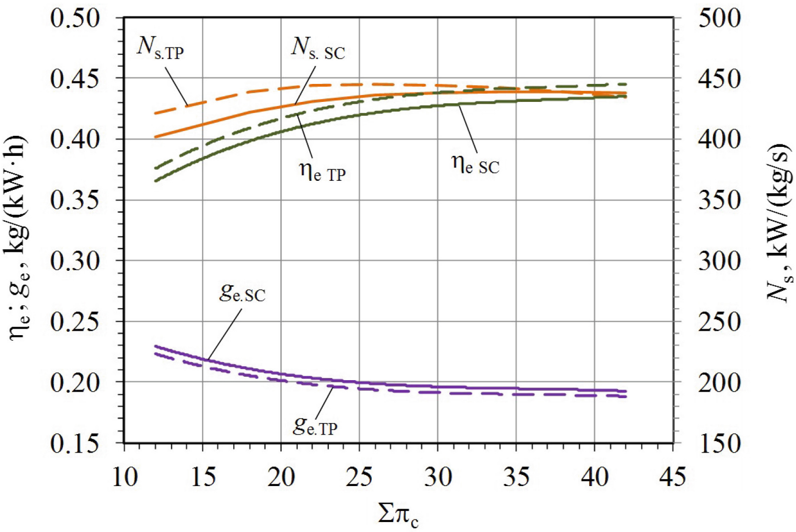

Fig. 6. Dependences of efficiency (η_e), specific fuel consumption (g_e), and specific power output (N_s) concerning the total compression ratio ($\Sigma\pi_c$) in compressors for the system with a surface air cooler (SC) and system with a thermopressor (TP).

compression along with marginal losses or even pressure enhancement to boost next stage compressor performance.

The use of the thermopressor in air intercooling facilitates the evaporation of water droplets during compression in a high-pressure compressor, thereby bringing the process closer to isothermal conditions (Fig. 6).

Consequently, both compression work and compressor power experience a reduction of up to 1–4 MW. Simulation of the gas turbine plant's operation illustrated that employing the thermopressor for cyclic air intercooling has the potential to enhance efficiency. The injected water, post-evaporation, served as an additional working fluid, contributing to an increase in the gas turbine's specific power. This reduction in compressor operation, coupled with the simultaneous increase in the working fluid within the cycle, resulted in an efficiency improvement of $\Delta\eta_e = 0.01–0.02$ (1–2%) for the gas turbine plant. Therefore, it is possible to achieve a reduction in specific fuel consumption by $\Delta g_e =$ 8 g/(kW·h). Additionally, there was an increase in the specific power of the gas turbine by $\Delta N_S = 25$ kW/(kg/s), equivalent to 10%.

5 Conclusions

Implementing a thermopressor within interstage cooling schemes has been proposed for boosting gas turbine efficiency. A CFD-based mathematical framework determined the device's thermodynamic performance. Integrated analysis of obtained droplet distribution metrics validated the effectiveness of extreme fine atomization and intensive evaporation induced by turbulence and thermal mixing.

Observed droplet mean diameters reached 18 μm at the exit. Additionally, uniform dispersion was accomplished across the section. Hence, the model enables reliable characterization of two-phase flows within the apparatus to attain optimized humidification, cooling and pressure recovery.

The use of the thermopressor in the air intercooling system enables the evaporation of water droplets during compression in a high-pressure compressor, consequently approaching the process to isothermal conditions with minimal compression work. Therefore, the application of the thermopressor can be an alternative to traditional air-cooling methods, and leads to a reduction in work, and consequently, the power of the compressor by approximately 10%, while simultaneously increasing the amount of working fluid in the cycle. This enhancement contributes to improved gas turbine efficiency.

References

1. Ritchey, I., Fisher, E.H., Agnew, G.D.: Water spray cooling of gas turbine cycles. Proc. Instit. Mech. Eng. Part A: J. Power Energy **214**(3), 203–211 (2000). https://doi.org/10.1243/0957650001538308
2. Azizifar, S., Banooni, S.: Modeling and optimization of industrial multi-stage compressed air system using actual variable effectiveness in hot regions. J. Modern Process. Manuf. Prod. **4**(2), 29–46 (2015). https://doi.org/10.1177/1687814016647231
3. The Brown Boveri Review, XXIX. The House Journal of Brown, Boveri & Company 9/10, 220–315 (1942)

4. Jones, J.B., Hawkins, G.A.: Engineering Thermodynamics. John Wiley & Sons Inc, USA (1960)
5. Wilcox, E.C., Trout, A.M.: Analysis of thrust augmentation of turbojet engines by water injection at compressor inlet including charts for calculation compression processes with water injection. NASA Report No: 1006 (1951)
6. Biasi, V.: LM6000 Sprint design enhanced to increase power and efficiency. Gas Turbine World **30**, 16–19 (2000)
7. Takeya, K., Oteki, Y., Yasui, H.: AGTJ-100A. Part-1: Experemental results of shop tests. Tokyo, Japan (1984)
8. The TopHat turbine cycle. http://www.modernpowersystems.com/features/featurethe-tophat-turbine-cycle/. Accessed 21 Nov 2022
9. Lin, A., Zhou, J., Fawzy, H., Zhang, H., Zheng, Q.: Evaluation of mass injection cooling on flow and heat transfer characteristics for high-temperature inlet air in a MIPCC engine. Int. J. Heat Mass Transf. **135**, 620–630 (2019). https://doi.org/10.1016/j.ijheatmasstransfer.2019.02.025
10. Liu, C., Zheng, Q., Wang, Q., Lin, A., Jiang, Y., Luo, M.: Sensitivity analysis of multistage compressor characteristics under the spray atomization effect using a CFD model. Energies **12**, 1–30 (2019). https://doi.org/10.3390/en12020301
11. Dayyabu, G.K., Qun, Z., Hai, Z., Lanxin, S.: Effects of water droplets on the numerical simulation of a complete gas turbine. Int. J. Thermodyn. **21**(1), 7–14 (2018). https://doi.org/10.5541/ijot.308766
12. López-Paniagua, I., Rodríguez-Martín, J., Sánchez-Orgaz, S., Roncal-Casano, J.J.: Step by step derivation of the optimum multistage compression ratio and an application case. Entropy **22**, 678 (2020). https://doi.org/10.3390/e22060678
13. Yu, Z., et al.: Investigation of thermopressor with incomplete evaporation for gas turbine intercooling systems. Energies **16**(1), 20 (2023). https://doi.org/10.3390/en16010020
14. Kobalava, H., Konovalov, D., Radchenko, R., Forduy, S., Maksymov, V.: Numerical simulation of a thermopressor with incomplete evaporation for intercooling of the gas turbine engine. In: Nechyporuk, M., Pavlikov, V., Kritskiy, D. (eds.) Integrated Computer Technologies in Mechanical Engineering 2020. LNNS, vol. 188, pp. 519–530. Springer, Cham (2021). https://doi.org/10.1007/978-3-030-66717-7_44
15. ANSYS Fluent Tutorial Theory Guide Release 17.0.: ANSYS, Inc. Canonsburg (2016)
16. Narayanan, D., Anand, S., Anish, S.: Numerical investigation on the effect of dry and wet compression on a linear low speed compressor cascade. J. Appl. Fluid Mech. **13**(1), 67–77 (2020). https://doi.org/10.29252/JAFM.13.01.30026
17. Wang, Y., et al.: Numerical study of indoor oil mist particle concentration distribution in an industrial factory using the Eulerian-Eulerian and Eulerian-Lagrangian methods. Fluids **8**(10), 264 (2023). https://doi.org/10.3390/fluids8100264
18. Sirignano, W.A.: Fluid Dynamics and Transport of Droplets and Sprays, 2nd edn. Cambridge University Press, New York (2010)
19. Deng, S.Y.: Comparing simulation for turbulent dispersion and coalescence of droplets within a spray with two models. Appl. Mech. Mater., 2473–2476 (2013). https://doi.org/10.4028/www.scientific.net/amm.353-356.2473
20. Xu, Z., Han, Z., Qu, H.: Comparison between Lagrangian and Eulerian approaches for prediction of particle deposition in turbulent flows. Powder Technol.der Technol. **360**, 141–150 (2020). https://doi.org/10.1016/j.powtec.2019.09.084

Methods of Parametric Modeling and Simulation Numerical Analysis of Rotor Dynamics in Active Magnetic Bearings on Example of the Turbocompressor

Mykhailo Kuchma(✉) and Gennadii Martynenko

National Technical University "Kharkiv Polytechnic Institute", 2, Kyrpychova Street, Kharkiv 61002, Ukraine

ku4ma.m@gmail.com, gmartynenko@ukr.net

Abstract. The article includes the comparison of two methods of modeling and evaluating the dynamics of rotors in active magnetic bearings (AMBs). An analysis of the dynamics of the rotor of the turbocompressor of the gas-pumping unit is considered, taking into account AMBs which are used as systems for control of motion stability. Two different methods of modeling were used to simulate the rotor dynamics of the rotor-AMBs system: the first is solid modeling which takes into account the deformability of the hinged elements of the rotor and its effect on its natural frequencies and critical speeds and the second is mass modeling where all hinged elements are replaced by mass-inertial elements. Both approaches are based on the application of finite element methods. The work aims to identify the advantages and disadvantages of using different methods for modeling and calculating rotordynamics characteristics of rotors supported by AMBs. The identification is based on various static and dynamic analyses. The results of numerical experiments are presented in the form of calculations of critical speeds and modes of oscillation (precession). This makes it possible to judge the possibility of the resonance regimes of the system and prevent dangerous situations. Obtained results indicate the accuracy and adequacy of results generated using different methods. The results could be used to determine the applicability of certain approaches depending on the specific needs of an engineer or researcher.

Keywords: Turbocompressor · Rotor Dynamics Analysis · Active Magnetic Bearing · Package for General Technical Engineering Analysis

1 Introduction

Currently, natural gas is transported over long distances primarily through trunk pipelines, which rely on gas compressor units (GCUs) to maintain the required pressure. These GCUs utilize single- or multi-circuit centrifugal compressors for gas compression [1, 2]. These compressors, integral to the functioning of the units and stations, operate continuously and require careful attention during both the design and operation phases [3, 4].

M. Nechyporuk et al. (Eds.): ICTM 2023, LNNS 1008, pp. 451–463, 2024.
https://doi.org/10.1007/978-3-031-61415-6_39

Centrifugal compressors, belonging to dynamic compressors, achieve gas compression and pressure increase through the interaction of gas flow with rotating blade apparatus. The compressor shaft rotation is powered by a turbine through a coupling, and the compression occurs as the gas passes through inter-blade spaces due to centrifugal forces. The compressor rotor, which consists of movable blade apparatus called impellers, is mounted on bearings, mainly plain bearings with oil systems and active magnetic bearings (AMBs) with control systems [5–7].

The use of high-pressure oil systems in plain bearings can be a drawback due to the substantial rotor mass and dynamic loads during operation. Consequently, AMBs, based on controlled electromagnetic suspension principles, are promising alternatives [8–10]. AMB systems comprise electromagnets to create attractive forces, power amplifiers for required electromagnet currents, a microprocessor controller, and rotor position sensors for feedback on rotor position changes [11, 12]. AMBs offer non-contact operation, eliminating friction. However, their complex structure requires sophisticated control systems to ensure stability [13].

Given the intricate nature of rotor-AMBs systems, their rotation, and dynamic loads, studying rotor dynamics in AMBs is crucial [14, 15]. Accurate determination of rotor dynamic characteristics, such as natural frequencies, critical rotation speeds, and forms of natural or precessional vibrations, is vital during the design and modernization stages [16, 17]. Implementing AMBs to support rotors presents an algorithmic approach to reduce vibrations and excitations, necessitating the development of mathematical models for the precise determination of critical speeds and corresponding forms of rotor oscillations [18]. These parameters significantly influence rotor forced oscillation amplitudes within the AMB air gap.

2 Literature Review

Various methods and approaches have been developed to understand the distinctive features of rotors. One approach involves employing mathematical techniques such as Lagrange or Lagrange-Maxwell, particularly in the case of electromechanical systems like rotors in active magnetic bearings [19]. This method formulates a mathematical model as a system of differential motion constraints involving generalized coordinates. The problem can be expressed in linear or non-linear forms, accounting for potential hazards or unrelated equations of motion [14, 15]. While this method offers advantages such as creating specific rotor system models with few unknowns, incorporating accurate descriptions of bearings considering their physical and design properties [20, 21], and providing analytical-computed formulas for precise analysis, it falls short in representing the rotor shaft and its attached elements comprehensively. This limitation can significantly impact results when determining velocity frequencies, oscillation modes, precessional motion, and other resonant mode characteristics, particularly in the presence of geometric or physical nonlinearities.

Another approach involves numerical methods such as the finite element method (FEM) or finite difference method (FDM). In this technique, the continuum system is discretized into an equivalent discrete system with a high degree of freedom [22]. The accuracy of mathematical modeling and result calculation depends on the number of degrees of freedom. When using finite elements, equations of motion are formulated in a matrix form, considering the inertial, stiffness, and damping properties of the system [23]. Linear or non-linear problem formulations are applied based on the material properties and elements [24]. This approach is commonly utilized in specialized engineering analysis software with modules designed for rotor dynamics analysis, including software like ANSYS Mechanical APDL (Rotordynamic Analysis) [25], NX CAE/NX Nastran (MSC Nastran Rotor Dynamics) [26], COMSOL (Rotordynamics Module) [27], PTC Creo (Pro/Engineer) [28], and Abaqus/Standard. These programs primarily employ finite element approaches to provide solutions, offering analyses of natural frequencies, critical speeds, trajectories of elastic axis movement, Campbell diagrams, three-dimensional spectra in excitation (rotation) frequency coordinates, response frequency, and oscillation amplitude. While these tools enable both linear and nonlinear analyses of various structural aspects, selecting appropriate finite elements to accurately represent unique rotor system elements poses a challenge [29–31].

For specific rotor dynamics analysis with a detailed consideration of traditional rotor system components such as bearings (rolling and sliding bearings, hydrostatic and hydrodynamic bearings, gas seals, and elastic couplings), specialized programs like Rotordynamic Software MADYN 2000 [32, 33] and AxSTREAM RotorDynamicsTM [34, 35] are utilized. Unlike general-purpose software, these programs allow in-depth analyses of rotor dynamics characteristics, including Campbell diagrams, critical speed maps, unbalance response, harmonic and transient analyses, three-dimensional spectra, and balancing maps. They integrate the advantages of general-purpose software systems and analytical approaches by comprehensively accounting for rotor systems and their components.

These specialized programs offer diverse modeling options for rotor dynamics, considering various features and structural elements. Factors such as the temperature state of mechanical seals or a hydrostatic oil film in plain bearings can be taken into account. The inclusion of active magnetic bearings with control systems introduces unique characteristics to the system. When employing engineering analysis software, the calculation of rotor dynamics characteristics in AMB can vary based on the level of consideration given to specific elements or phenomena. For instance, volumetric or beam-mass finite element models of the rotor may be used, and active magnetic bearings can be substituted with elastic-damping elements with linear or nonlinear characteristics, which may vary based on parameters like the rotor's rotational speed [16].

3 Initial Data to the Study

This work aims to determine the advantages and disadvantages of using different methods for modeling and calculating rotordynamics characteristics of turbomachine rotors in active magnetic bearings using the general technical tool. This problem is solved based on a series of computational experiments with static and dynamic analyzes on the example of an industrial turbomachine with active magnetic bearings. The rotor of a double-circuit turbocompressor of a gas-pumping unit is considered. Its scheme is shown in Fig. 1.

The total length of the rotor is ~ 3 m, the mass of the shaft with attachments is ~ 1600 kg, the diameter of the impellers is ~ 1.7 m. Two impellers (2) are located in the middle of the shaft (1). Near the right wheel is a dummy (3). Its purpose is to unload the axial load on the rotor from the action of the gas. Two radial and one axial AMB were used for support. The journals of the radial bearings (4) are located on both sides of the shaft, and the disk of the axial AMB (5) is on the right. A half-coupling (6) is located on the left end of the shaft and is used for connection with the rotor of the gas turbine engine. This engine is the drive and ensures the rotation of the turbocompressor shaft at the required speed to create a certain level of pressure at the outlet. The rotor speed in the operating mode is 5000 rpm.

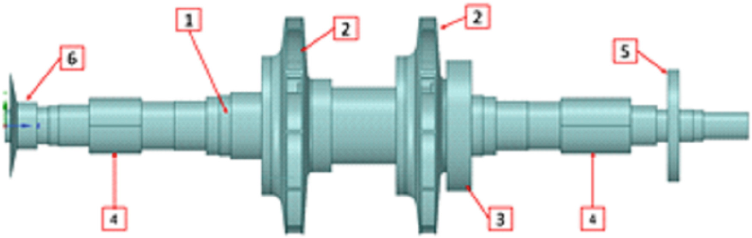

Fig. 1. The rotor of a gas compressor unit with active magnetic bearings.

It is supposed to apply rotor dynamics analysis tools from the general technical software package. This package is a comprehensive toolset that empowers engineers to simulate and evaluate the behavior of structures under diverse conditions. It plays a crucial role in the design and validation process, helping ensure that structures are not only safe and durable but also optimized for performance. However, the functionality related to the control system is out of the scope of this study.

4 Creating Calculation Models Using Different Approaches

4.1 Solid Modeling of the Compressor Rotor

The construction of geometric and computational models of the rotor of a centrifugal compressor in the software package for general technical analysis was carried out in a full volume setting (3D model). These models are shown in Fig. 2. To create a finite element model of the rotor as a shaft with hinged elements, three-dimensional ten-node tetrahedral finite elements and a free meshing method were used, is shown in Fig. 3. The properties of the material correspond to steel 1020. To simulate active magnetic bearings, special elastic-damping finite elements are used, for each of the supports. Their total rigidity was chosen corresponding to the rigidity of the magnetic support in the operating mode ($3.75 \cdot 10^6$ N/m). The dependence of this rigidity on the speed of rotation of the rotor was taken into account differentially when conducting separate analyses. The use of a three-dimensional model pursued an additional goal. This is obtaining the inertial characteristics of all elements of the rotor of a gas-pumping unit for subsequent use in beam-mass FE models.

To carry out verification calculations using the same software package, a beam-mass model of the compressor rotor was created. In it, the shaft was modeled as full solid and the hinged elements were represented by mass FEs with mass moments of inertia. These parameters depend on the properties of the material and the geometry of the attachments. They were determined using a three-dimensional model.

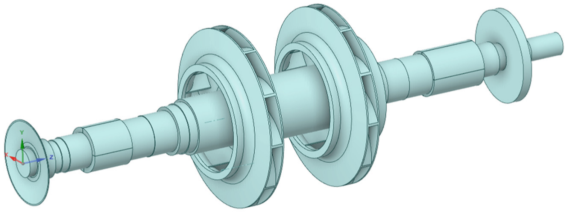

Fig. 2. Geometric of solid modeled rotor

Fig. 3. Finite element models of solid modeled rotor

For the model verification the 3 additional static calculations with gravity only load were made. The first calculation is made with mesh element size of 20 mm, the second with 25 mm and the third one with 15 mm. The comparison is shown in Table 1.

Table 1. Model verification results

Comparison results	
Mesh size	Maximum Deflection, m
25 mm	$5.3351 \cdot 10^{-6}$
20 mm	$5.5308 \cdot 10^{-6}$
15 mm	$5.7165e \cdot 10^{-6}$

The comparison showed that the error of calculations is approximately 3 percent. This means that the mesh with element size equal to 20 mm can be used for further calculations.

4.2 Beam-Mass Rotor Model

A feature of the approach is the use of beam-mass FE model for creating equivalent simulation models. Thus, there is no possibility of geometric modeling of the hinged elements of the rotor, and hence the vibration modes associated with their deformation. Such hinged elements are replaced by mass-inertial elements, as with the use of such models in the software package for general technical analysis.

Determination of the inertial parameters of hinged elements (masses and moments of inertia) was carried out when performing static calculations. The found mass-inertial parameters are shown in Table 2, and the beam-mass model of the rotor itself, is shown in Fig. 4. Active magnetic bearings, as in the previous case, are modeled by elastic-damping elements with the above stiffness values.

Table 2. Mass-inertial parameters of hinged elements

Mass-inertial elements				
Name	Mass, kg	Ix, kg·m^2	Iy, kg·m^2	Iz, kg·m^2
Coupling	10	0.069	0.069	0.119
Disk 1	157.9	7.069	7.069	12.724
Disk 2	157.2	6.983	6.983	12.64
Dymis	53.9	1.491	1.491	2.909
Support Bearing	51	0.7	0.7	1.394

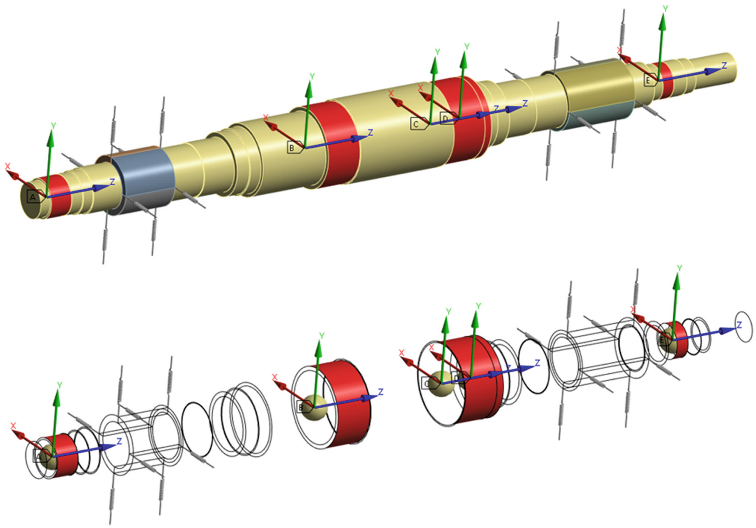

Fig. 4. Beam-mass model of the rotor

4.3 Boundary Conditions

The two models used the same boundary conditions. They are presented by 16 springs with the formulation Body to Ground, is shown in Fig. 5.

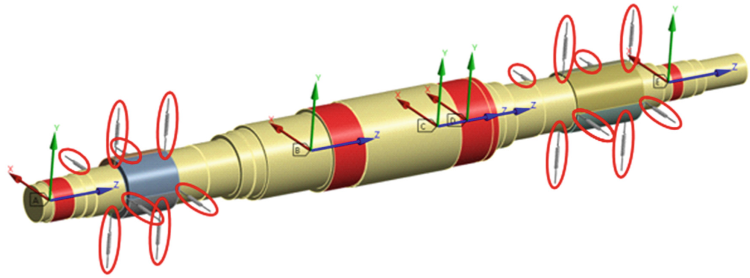

Fig. 5. Body-Ground boundary conditions (longitudinal stiffness $3.75 \cdot 10^9$ N/m)

5 Research Results

5.1 Static Analysis of Turbocompressor Rotor

In the first stage, a static strength analysis was carried out to determine the parameters of the stress-strain state under the action of only the own weight of the structure with infinite stiffness of the support. This analysis aims to check the identity of the rotor models built with different methods. The results of this calculation are presented in Table 3. And in Fig. 6.

Table 3. Static analysis results

Comparison results	
Approach	Maximum Deflection, m
Solid model	$5.5308 \cdot 10^{-6}$
Beam-mass model	$5.9465e \cdot 10^{-6}$

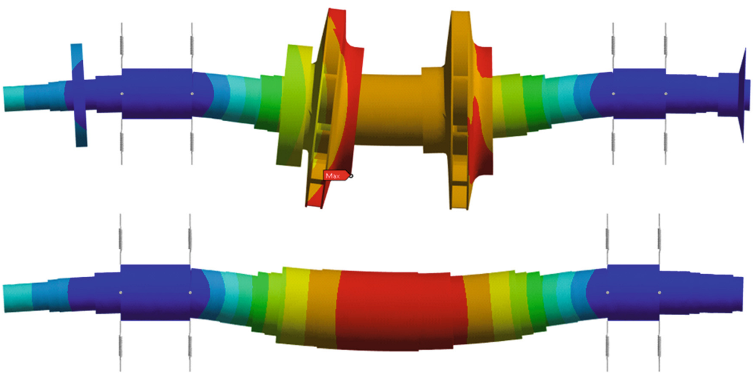

Fig. 6. Result of static comparison

5.2 Determination of Natural Frequencies, Shape Modes and Critical Speeds

The critical speeds of the rotor can be determined by considering or neglecting the gyroscopic moment, factoring in the natural oscillation frequencies and accounting for the angular speed dependence of the rotor's rotation. Modal analysis conducted for two approaches provides the frequencies and patterns of natural vibrations for a stationary rotor. The resulting critical rotation speeds are outlined in Table 4. A comparative analysis reveals a significant agreement in the translational mode shapes. Discrepancies in critical speed values for deformation patterns are attributed to the influence of flexible hinge elements, as evident in the shapes. Critical velocity values obtained through both methods differ by no more than 1%, indicating high result accuracy and confirming the validity of the calculation models. Furthermore, the accuracy of the finite element discretization was validated by comparing nodal and elemental results from preliminary static analyses.

Table 4. The modal analysis results

Critical speeds, rpm		
Mode (precession) shape	Solid model	Beam-mass model
Bending nodeless	8341	8144
Bending nodeless	8377	8178
Bending with one node	21060	21143
Bending with one node	21120	21204
Bending with two nodes	24420	24480

Figures 7, 8, 9 shows the eigenmodes obtained using the general technical analysis software packages.

Figures 10, 11, 12 display the eigenforms acquired through a beam-mass model for rotor dynamics analysis. A comparative examination of the initial three modes medates the accuracy of the numerical simulation.

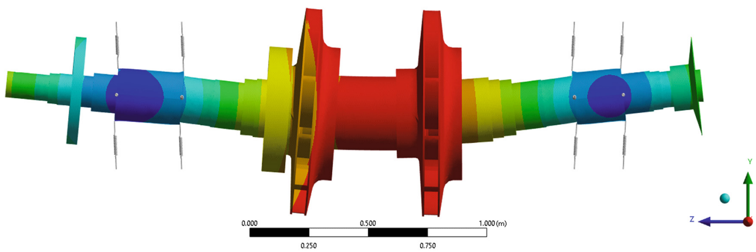

Fig. 7. The first – bending mode of vibrations

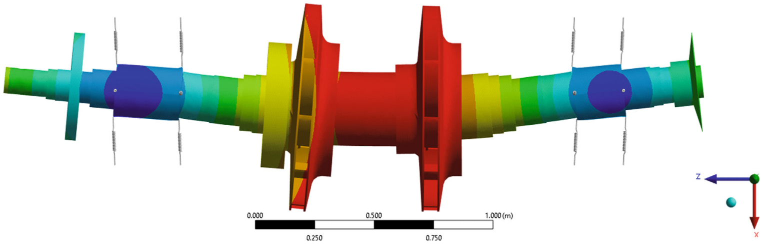

Fig. 8. The second – bending mode of vibrations (on another plane)

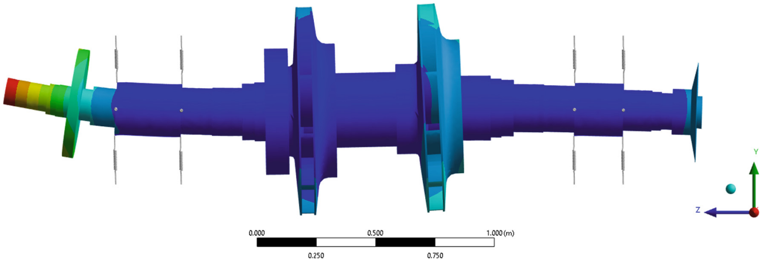

Fig. 9. The third – bending with one node.

The software package offers analyses to determine critical speeds and the patterns of processional motion of the shaft's elastic axis. Moreover, this package allows obtaining critical speed values while considering the gyroscopic moment. Alternatively, critical speeds can be derived from damped response analysis and graphically depicted against varying rotor speeds on the Campbell diagram. Similar analyses were conducted, revealing a difference of less than 2% when comparing the results between the approaches.

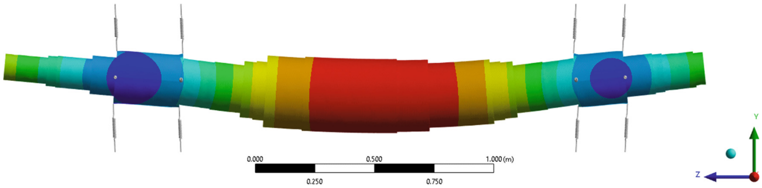

Fig. 10. The first – bending mode of vibrations (beam-mass model).

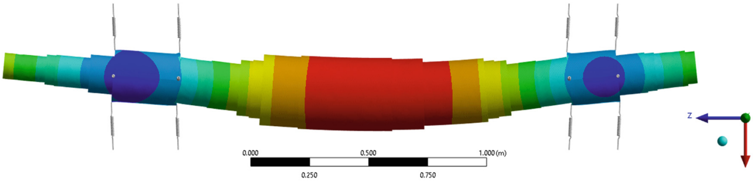

Fig. 11. The second – bending mode of vibrations on another plane (beam-mass model)

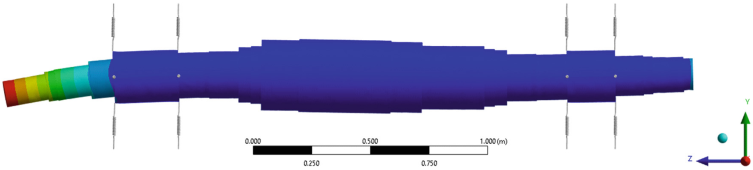

Fig. 12. The third – bending with one node (beam-mass model).

6 Conclusion

This article investigates a detailed static analysis of the GCU turbocompressor rotor. The main focus is on using solid modeling and mass modeling methodologies for rotor dynamics analysis, with a special attention on their applicability in the context of taking into account modeling features of active magnetic bearings.

The solid modeling method is used to provide a detailed understanding of individual components, including flexible hinge elements into the model. This allows more accurate take into account the impact of these elements on natural frequencies and critical speeds within the rotor system. The findings from this approach contribute to a more detail view of the dynamic behavior of the system.

On the other hand, the mass modeling model is researched for its ability to speed up calculations. This model makes easier the generation of frequency responses resulting from unbalancing, offering understanding of the dynamic characteristics of the systems with a focus on speed and responsiveness.

The comparative analysis of these two approaches shows that both methods give highly accurate results in characterizing dynamic processes within rotor systems with AMBs. A comparative analysis of the results obtained using mass and volumetric three-dimensional models revealed that the assumptions adopted in the first of them, as well as the failure to take into account the deformability of wheels, overestimate the values of natural frequencies and critical rotation speeds by 3% or more for some deformation modes of vibrations. For translational modes of vibrations the situation is opposite.

In conclusion, the choice between solid modeling and mass modeling depends on specific project requirements and needs. Each method presents distinct advantages, and the decision should be based on a careful consideration of factors such as computational speed, the level of detail required, and the specific objectives of the rotor system project. This comprehensive evaluation contributes to a more informed decision-making process when ensuring that the chosen method aligns with the goals of the project at hand.

References

1. Patrascioiu, C., Popescu, M.: Modelling and simulation of natural gas compression plant. In: The 13th International Conference on Electronics, Computers and Artificial Intelligence, pp. 1–6 (2021). https://doi.org/10.1109/ECAI52376.2021.9515118
2. Rozova, L., Martynenko, G.: Information technology in the modeling of dry gas seal for centrifugal compressors. CEUR Workshop Proc. **2608**, 536–546 (2020). https://doi.org/10.32782/cmis/2608-41
3. Stewart, M.: Dynamic Compressors. In: Surface Production Operations–Pump and Compressor Systems: Mechanical Design and Specification, vol. 4, pp. 527–653. Elsevier (2019). https://doi.org/10.1016/b978-0-12-809895-0.00008-9
4. Kim, K., Hong, G., Jang, G.: Dynamic analysis of a flexible shaft in a scroll compressor considering solid contact and oil film pressure in journal bearings. Int. J. Refrig. **127**, 165–173 (2021). https://doi.org/10.1016/j.ijrefrig.2021.01.032
5. Siva Srinivas, R., Tiwari, R., Kannababu, C.: Application of active magnetic bearings in flexible rotordynamic systems – a state-of-the-art review. Mech. Syst. Signal Process. **106**, 537–572 (2018). https://doi.org/10.1016/j.ymssp.2018.01.010
6. Wan, Z.: A review of active magnetic bearings supported systems optimization design. Int. J. Magn. Electromagn. **6**(1), 1–10 (2020). https://doi.org/10.35840/2631-5068/6527
7. Martynenko G.: Analytical method of the analysis of electromagnetic circuits of active magnetic bearings for searching energy and forces taking into account control law. In: 2020 IEEE KhPI Week on Advanced Technology (KhPIWeek 2020), pp. 86–91, 9250138. Kharkiv, Ukraine (2020). https://doi.org/10.1109/KhPIWeek51551.2020.9250138
8. Kandil, A., Sayed, M., Saeed, N.A.: On the nonlinear dynamics of constant stiffness coefficients 16-pole rotor active magnetic bearings system. Eur. J. Mech. A. Solids **84**, 104051 (2020). https://doi.org/10.1016/j.euromechsol.2020.104051
9. Martynenko, G., Martynenko, V.: Numerical determination of active magnetic bearings force characteristics taking into account control laws based on parametric modeling. In: 2019 IEEE International Conference on Modern Electrical and Energy Systems (MEES 2019), pp. 358–361. Kremenchuk, Ukraine (2019). https://doi.org/10.1109/MEES.2019.8896501
10. Kuznetsov, B.I., Nikitina, T.B., Bovdui, I.V.: Multiobjective synthesis of two degree of freedom nonlinear robust control by discrete continuous plant. Tech. Electrodynamics **2020**(5), 10–14 (2020). https://doi.org/10.15407/techned2020.05.010
11. Martynenko, G., Ulianov, Y.: Combined rotor suspension in passive and active magnetic bearings as a prototype of bearing systems of energy rotary turbomachines. In: 2019 IEEE International Conference on Modern Electrical and Energy Systems (MEES 2019), pp. 90–93. Kremenchuk, Ukraine (2019). https://doi.org/10.1109/MEES.2019.8896571
12. Kuznetsov, B., Voloshko, A., Bovdui, I., Vinichenko, E., Kobilyanskiy, B., Nikitina, T.: High voltage power line magnetic field reduction by active shielding means with single compensating coil. In: International Conference on Modern Electrical and Energy Systems, pp. 196–199. IEEE, Kremenchuk, Ukraine (2017). https://doi.org/10.1109/MEES.2017.8248887
13. Martynenko, G., Martynenko, V., Pidkurkova, I.: Parametric numerical analysis of restoring magnetic forces dependences in radial active magnetic bearings with a given control law. In: 2022 IEEE 4th International Conference on Modern Electrical and Energy System (MEES 2022), pp. 1–6, 186060. Kremenchuk, Ukraine (2022). https://doi.org/10.1109/MEES58014.2022.10005766
14. Matsushita, O., Tanaka, M., Kanki, H., Kobayashi, M., Keogh, P.: Vibrations of rotating machinery. In: Basic Rotordynamics: Introduction to Practical Vibration Analysis, vol. 1. Springer Japan, Tokyo (2017)

15. Matsushita, O., Tanaka, M., Kanki, H., Kobayashi, M., Keogh, P.: Vibrations of rotating machinery. In: Advanced Rotordynamics: Applications of Analysis, Troubleshooting and Diagnosis, vol. 2. Springer Japan, Tokyo (2019). https://doi.org/10.1007/978-4-431-55453-0
16. Martynenko, G., Martynenko, V. Rotor dynamics modeling for compressor and generator of the energy gas turbine unit with active magnetic bearings in operating modes. In: 2020 IEEE Problems of Automated Electrodrive. Theory and Practice (PAEP), pp. 1–4, 9240781. IEEE, Kremenchuk, Ukraine (2020). https://doi.org/10.1109/PAEP49887.2020.9240781
17. Srinivas, R.S., Tiwari, R., Babu, C.K.: Modeling, analysis, and identification of parallel and angular misalignments in a coupled rotor-bearing-active magnetic bearing system. J. Dyn. Syst. Meas. Control Trans. ASME 143(1), 011007, 115 (2021). https://doi.org/10.1115/1.4048352
18. Ran, S., Hu, Y., Wu, H.: Design, modeling, and robust control of the flexible rotor to pass the first bending critical speed with active magnetic bearing. Adv. Mech. Eng. **10**(2), 1–13 (2018). https://doi.org/10.1177/1687814018757536
19. Ri, K., Han, P., Kim, I., Kim, W., Cha, H.: Stability analysis of composite shafts considering internal damping and coupling effect. Int. J. Struct. Stab. Dyn. **20**(11), 2050118 (2020). https://doi.org/10.1142/S0219455420501187
20. Jiang, H., Su, Z., Wang, D.: Dynamic modeling of magnetic bearing-rotor system on moving platform. Diangong Jishu Xuebao/Trans. China Electrotech. Soc. **34**, 4880–4889 (2019). https://doi.org/10.19595/j.cnki.1000-6753.tces.181510
21. Saeed, N.A.F., Mahrous, E., Nasr, E.A., Awrejcewicz, J.: Nonlinear dynamics and motion bifurcations of the rotor active magnetic bearings system with a new control scheme and rub-impact force. Symmetry **13**(8), 1502 (2021). https://doi.org/10.3390/sym13081502
22. Shen, Z., Chouvion, B., Thouverez, F., Beley, A.: Enhanced 3D solid finite element formulation for rotor dynamics simulation. Finite Elem. Anal. Des. **195**, 103584 (2021). https://doi.org/10.1016/j.finel.2021.103584
23. Ahmed, S., Abdelhamid, H., Ismail, B., Ahmed, F.: Differential quadrature finite element and the differential quadrature hierarchical finite element methods for the dynamics analysis of on board shaft. Eur. J. Comput. Mech. **29**, 303 (2020). https://doi.org/10.13052/ejcm1779-7179.29461
24. Huang, F., Wang, X., Fu, H., Sima, L., Cui, Y.: Nonlinear vibration characteristics of gear-rotor-bearing system. J. Phys. Conf. Ser. **2229**(1), 1–7 (2022). https://doi.org/10.1088/1742-6596/2229/1/012002
25. Torabi Asr, M., Masoumi, M.M., Mustapha, F.: Modal behaviour of vertical axis wind turbine comprising prestressed rotor blades: a finite element analysis. Pertanika J. Sci. Technol. **25**(3), 977–982 (2017)
26. Chen, M., Ma, Y., Liu, S., Hong, J.: Rotordynamic analysis of whole aero-engine models based on finite element method. Beijing Hangkong Hangtian Daxue Xuebao/J. Beijing Univ. Aeronaut. Astronaut. **33**, 1013–1016 (2007)
27. Uddin, M., et al.: Design a cooling pillow to support a high-speed supercritical CO2 turbine shaft. Appl. Therm. Eng. **196**, 117345 (2021). https://doi.org/10.1016/j.applthermaleng.2021.117345
28. Miya, S., Sandhya, K.: Design and analytical investigations of crack propagation on rotor shaft. Int. J. Innov. Technol. Res. **6**(6) (2018)
29. Martynenko, V.G.: An original technique for modeling of anisotropic viscoelasticity of orthotropic materials in finite element codes applied to the mechanics of plates and shells. Mech. Mech. Eng. **21**, 389–413 (2017)
30. Martynenko, V.: Analysis of strength and bearing capacity of the auxiliary mine ventilation fan connected to the rotor of its electrical drive. In: 2020 IEEE KhPI Week on Advanced Technology (KhPIWeek), pp. 19–23, 9250078. Kharkiv, Ukraine (2020). https://doi.org/10.1109/KhPIWeek51551.2020.9250078

31. Merculov, V., Kostin, M., Martynenko, G., Smetankina, N., Martynenko, V.: Force simulation of bird strike issues of aircraft turbojet engine fan blades. In: International Conference on Reliable Systems Engineering (ICoRSE 2021), Lecture Notes in Networks and Systems, vol. 305, pp. 129–141. Springer, Cham (2022). https://doi.org/10.1007/978-3-030-83368-8_13
32. Rouwenhorst, D., Jäger, D., Schmieder, M., Hermann, J.: Root cause analysis of torsional and lateral vibrations on a compressor test rig. In: ASME Turbo Expo, 10B-2020, GT2020–15564 (2020). https://doi.org/10.1115/GT2020-15564
33. Ghalea, A., Varshitha, H., Kumar, M.V., Mathd, M.M.: Design validation of high inertia generator rotor. AIP Conf. Proc. 2316 (2021). https://doi.org/10.1063/5.0038271
34. Moroz, L., Romanenko, L., Kochurov, R., Kashtanov, E.: Hydrodynamic journal bearings optimization considering rotor dynamics restrictions. In: ASME Turbo Expo 2018: Turbomachinery Technical Conference and Expositio, vol. 7B-2018, GT2018–75790, pp. 1–11. Oslo, Norway (2018). https://doi.org/10.1115/GT2018-75790
35. Patel, A., Biradar, V., Kumar, P.: Harmonic analysis of the high speed direct coupled SCO2 turbo-generator. In: ASME 2021 Gas Turbine India Conference, GTINDIA2021–76448, V001T10A010, pp. 1–6 (2021). https://doi.org/10.1115/GTINDIA2021-76448

Adaptation of the Rotor Design of Expander-Compressor Unit for the Installation of Magnetic Bearings Based on Dynamic Analysis Using Integrated Computer Systems

Gennadii Martynenko(✉) and Lyudmyla Rozova

Kharkiv Polytechnic Institute, National Technical University, 2, Kyrpychova Street, Kharkiv 61002, Ukraine
gmartynenko@ukr.net

Abstract. The article discusses the issues of studying the possibilities of modernizing components and elements of rotary machines by static and dynamic analyzes of structures using integrated computer systems. Such machines include gas turbine and turbojet engines, turbocompressors, and turboexpanders. The main goal of the work is to select a modified rotor design for installing a different type of support. In this case, the search of rational design of expander-compressor rotor unit is considered to use a combination of passive and active bearings instead of plain bearings. Since these types of supports have different levels of support rigidity, topological rationalization of the structure is carried out using static structural analysis (for the estimation of rotor static equilibrium position) and dynamic analysis (for the estimation of the critical rotation speeds). The last one makes it possible to detune critical speeds from the range of operating rotation speeds. For the rotor of an expander-compressor unit with the impellers of the expander and compressor cantilevered on a single shaft, multivariate calculation studies made it possible to find a rational rotor design for the installation of magnetic bearings. The following parameters varied within certain limits, when changing the design: locations of support sections, diameters and lengths of shaft sections. Analyzes were carried out using a numerical finite element method. The results are presented for the final design in the form of displacement distributions, corresponding to the static equilibrium position, as well as the values of natural frequencies and critical rotation speeds and the shapes corresponding to them. The accuracy of the numerical simulation results was assessed using traditional finite element methods and was confirmed by comparison with the results of model numerical experiments. The presented approach to searching for a rational design made it possible to prove the possibility of using a combination of passive and active magnetic bearings as rotor supports for small and medium-sized rotors. That reduces friction losses in the system and provides all the other advantages of this combination of this type of support.

Keywords: Turbomachines · Sliding Bearings · Magnetic Bearings · Design Modification · Computer Analysis Systems · Parametric Modeling · Rotor Dynamics · Numerical Simulation · Resonance Detuning

M. Nechyporuk et al. (Eds.): ICTM 2023, LNNS 1008, pp. 464–475, 2024.
https://doi.org/10.1007/978-3-031-61415-6_40

1 Introduction and Literature Review

The development of modern gas turbine and compressor technology requires constant modernization of both machines as a whole and their separate components, based on operating experience [1, 2]. High-tech rotary turbomachines include gas turbine engines [3], including turbojet engines [4], turbocompressors [5], turboexpanders [6], various electrical energy generators [7, 8], industrial fans [9]. One of the main structural elements of such complex machines is the rotor. It consists of a rotating shaft with attachments attached to it. Such elements are impellers, parts of support units (bearings) and mechanical gas seals, couplings or half-couplings and other auxiliary parts. Impellers are the main working elements, which, due to the special structure of the blade apparatus, can either increase the gas pressure in the system (for example, compressors) [10] or reduce it, converting the internal energy of the gas into mechanical energy (expanders) [11]. Often, if such a possibility exists, the impellers of several technological processes in the operating cycle are placed on one shaft. The gas turbine engines (GTE) can be as example [12]. They are classified according to technological operating features and are divided into turbojet, turbofan, turboprop and turboshaft.

The common is that they are air engines. Compressed air from the compressor part enters the combustion chamber, where fuel is supplied. Then, in a gas turbine, part of the energy of the combustion products is converted into turbine rotation, which is spent on compressing the air in the compressor. The rest of the energy is useful and can be transferred to the driven unit (ground-based GTE) or used to create jet thrust (aviation GTE). Among them there are also designs with cantilever impellers on one shaft. The operating cycle of a gas turbine engine with a single-stage radial compressor, turbine, recuperator and air bearings is schematically shown on Fig. 1.

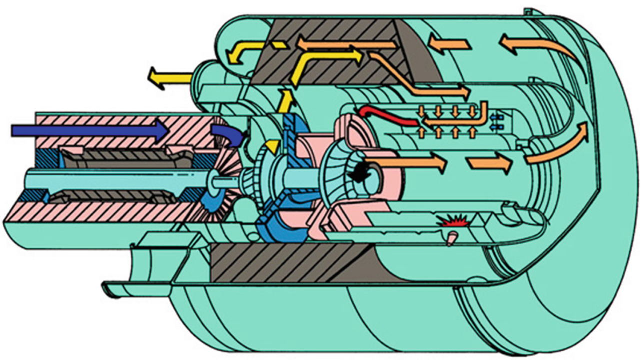

Fig. 1. Gas turbine engine with single-stage radial compressor, turbine, recuperator and air bearings [13]

Another important element of the rotor system is the rotor support units (bearings), since they secure the rotating shaft to a stationary body. The mentioned above rotary machines can use various types of bearings. These are sliding and rolling bearings [14]. Rolling bearings are used much less frequently. Classic sliding bearings use oil lubrication under pressure. It requires oil systems, that is a disadvantage.

Sliding bearings also include [15]: hydrostatic bearings, hydrodynamic bearings, gas-static bearings, gas-dynamic bearings and magnetic bearings. Each of these types has its own advantages and disadvantages. For example, one of the main characteristics is the load-bearing capacity (load capacity), which is related to the rigidity of the support. For oil-lubricated sliding bearings, the stiffness is about 10^7 N/m, while for hydraulic bearings it is an order of magnitude less ~ 10^6 N/m.

The correct choice of bearing units for a specific machine is an important and complex task. Its solution requires a thorough study of the dynamic characteristics of the rotor system, in order to tune out possible resonances in the range of operating rotor speeds.

Mechanical engineering software packages and integrated computer systems of such class make it possible to simulate and analyze processes of various physical natures in various structures and machines to determine the strength and dynamic characteristics of their elements, for example, rotors [16], impeller blades [17], bodies [18]. The task of improving existing turbomachines is relevant and can be based on numerical simulation of static and dynamic processes in them when making design changes [19].

The capabilities of numerical simulation of physical processes, including rotor dynamics, are implemented in many engineering analysis software packages. Among them are general technical software systems (with special modules for rotor dynamics analyze) ANSYS Mechanical APDL (Rotordynamic Analysis) [20], NX CAE/NX Nastran (MSC Nastran Rotor Dynamics) [21], COMSOL (Rotordynamics Module) [22], PTC Creo (Pro/Engineer) [23], Abaqus/Standard and specialized programs for rotor dynamics analyze, e.g. Rotordynamic Software MADYN 2000 [24] and AxSTREAM RotorDynamics [25]. Besides, such analysis can be performed using specialized integrated computer systems [26].

This work is devoted to the consideration of one of the approaches to the parametric and structural modification of the "rotor-support" system based on comparative numerical modeling with the aim of modernizing the turbomachine as a whole.

2 The Aim and Rationale of the Research

The object of these study is the rotor dynamics of the expander-compressor unit (ECU). This unit is part of a full-size natural gas liquefaction plant. It is based on a stand for the recondensation of methane vapor during the transportation of liquefied gas on tanker ships. The original geometric model of the rotor of ECU is presented on Fig. 2. On a single shaft there are two impellers (expander and compressor), radial journals and a disk of axial sliding bearings (journal and thrust oil film bearings). This rotor with a length of ~ 1 m and a total mass of ~ 55 kg is installed in segmented sliding bearings. The rigidity of these supports is $1.5 \cdot 10^7$ N/m. The support scheme contains two radial bearings and one axial thrust bearing. The operating speed range of the rotor of ECU is from 13,500 to 15,000 rpm.

One of the most modern types of bearings are magnetic bearings of passive and active types [27–29]. Passive magnetic bearings (PMBs) are mainly made of annular permanent magnets and perform self-centering due to repulsive or attractive forces [30]. Their main advantage is the relative ease of manufacture, lack of energy consumption and relatively large frequency of technological servicing. Passive magnetic bearings are highly wear-resistant and can operate for a long time without the need for replacement.

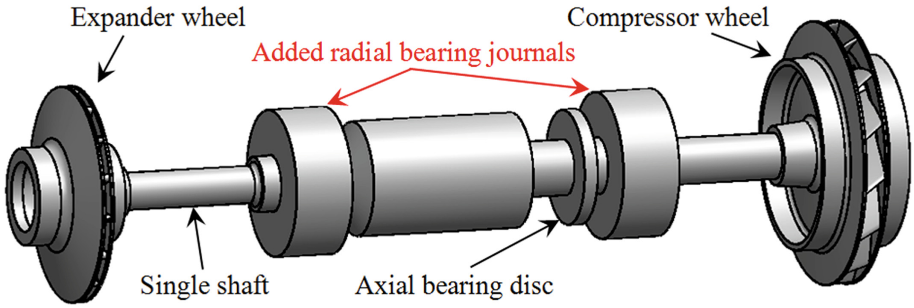

Fig. 2. Geometric model of the rotor of ECU of the original design

However, the main disadvantage of the PMBs is the fact, that stable levitation under normal conditions cannot be achieved using a static passive magnetic bearing system (proven in Earnshaw's Theorem) [31]. The operating principle of active magnetic bearings is based on the control of electromagnetic fields [32, 33]. Centering of the rotor is achieved only due to the forces of attraction. To create the necessary restoring forces and stabilize the position of the rotating rotor in the presence of its own imbalance and disturbing influences, control systems are used [34, 35].

The maximum stiffness of passive and active magnetic bearings depends on their design, dimensions and materials. The stiffness of permanent magnet bearings can reach 10^7 N/m. They are used in electric motors, fans, pumps and other devices. Active magnetic bearings have higher rigidity than passive magnetic bearings. This is due to the fact that in AMBs the restoring force is electronically controlled. The highest rigidity of active magnetic bearings is 10^8 N/m. They are used in turbocompressor, turboexpanders, electric motors, fans, pumps and other devices that require high precision and rigidity.

Based on these data, the work sets the task of modernizing of ECU by replacing the sliding bearings with a combination of passive and active magnetic bearings with the obligatory detuning of the critical rotor speeds from the operating range. The support scheme assumes the presence of two passive radial bearings and one axial active magnetic bearing. This scheme was tested experimentally for a model rotor [36]. In parametric calculation studies, the lengths and diameters of the cantilever sections of the shaft on both sides and the location of the bearings are selected as varied parameters. The constraints for the varied parameters are selected based on technological limitations. The bearing stiffness is set to be the same and equal to $1.3 \cdot 10^7$ N/m, based on the maximum possible values for PMB and AMB.

Thus, the problem of topological optimization or rationalization of the design of a turbomachine using the example of an expander-compressor unit in order to change the configuration of the rotor support and the rotor itself for the installation of bearings of a different type is solved in this work.

3 Modification of the ECU Rotor Design for Installation of Magnetic Bearings

Since the rotor of a real operating expander-compressor unit is considered, it is a priori assumed that for it the critical rotation speeds have been detuned from the operating range. But when installing the rotor parts of the PMB at the locations of the sliding bearings, the rotor mass characteristics significantly change. Such a direct replacement leads to the increasing of rotor total mass by 15% with the same rigidity characteristics of the shaft (see “Added radial bearing journals” on Fig. 2). It changes the critical speeds and leads to possible resonances in the operating range of rotation speeds, which will be shown below. Therefore, to avoid it, additional design changes are necessary.

To replace sliding bearings (journal and thrust oil film bearings) with a combination of passive and active magnetic bearings, a search for a structural arrangement was carried out based on multivariate analyzes of rotor dynamics using integrated computer modeling and the implementation of software for engineering modeling and simulation of physical processes [26]. In this case, complete three-dimensional models of the rotor with attached elements on a single shaft (wheels and disks) were considered, and the supports were modeled with elastic elements with given rigidity values. A finite element approach was used for static and dynamic structural analyses.

The scheme of complete magnetic suspension with two radial PMBs and one centrally located axial double-sided acting AMB is proposed in the work for ECU rotor, tested on a laboratory stand of a complete combined magnetic suspension of a model rotor [36]. The main distinctive advantage of such a scheme is its relative simplicity while ensuring high reliability and relatively low cost in relation to suspension in which AMBs are used for the stabilization in five degrees of freedom.

The series of multivariate parametric calculation studies made it possible to arrive to the rotor design, shown on Fig. 3.

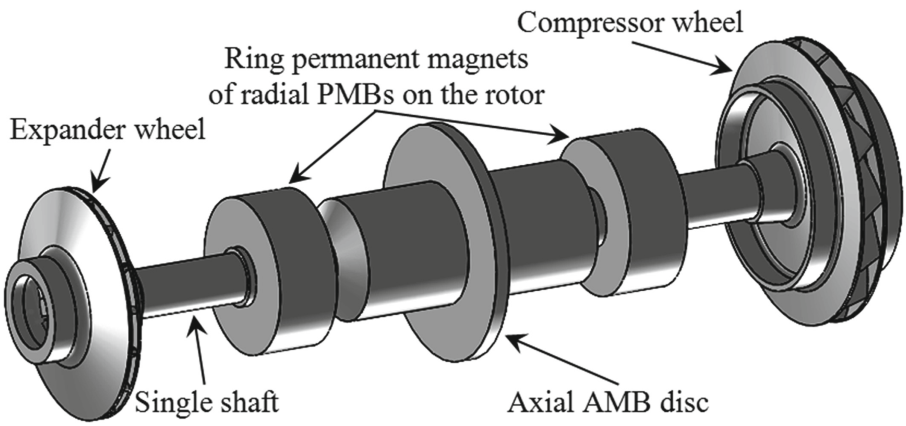

Fig. 3. Rotor design adapted for installation of magnetic bearings

The total mass of the modified rotor, considering the rotor parts of the PMBs (sets of permanent ring magnets), is also close to 55° kg with the lengths and diameters of the shaft sections changed within technological ranges. With the changes made, the total length of the rotor decreased to ~ 0.9° m.

4 Justification of the Possibility of Using PMBs as Radial Supports of the ECU Rotor

To calculate the natural frequencies and shapes of the rotor in order to determine the critical speeds, the finite element method was used in a three-dimensional formulation. Finite element solution models of rotors and bearings are presented on Fig. 4. Geometric modeling of all attached elements is carried out with mandatory compliance with mass values, and the bearings are modeled by linking elements with the specified values of radial and axial stiffness $1{,}3 \cdot 10^7$ N/m. The convergence and accuracy of the numerical solution was checked by performing calculations of the static stress–strain state from the action of gravity.

Thus, the models were found for which the calculated error due to grid discretization does not exceed 1%. The results of analyzes performed using these models are presented on Fig. 5. It was determined that the static displacement does not exceed 40 µm (Fig. 5a), and the geometry change made it possible to shift the center of mass of the rotor to the middle between the radial supports and ensure equality of the displacements of the centers of the support sections in the static equilibrium position (Fig. 5b).

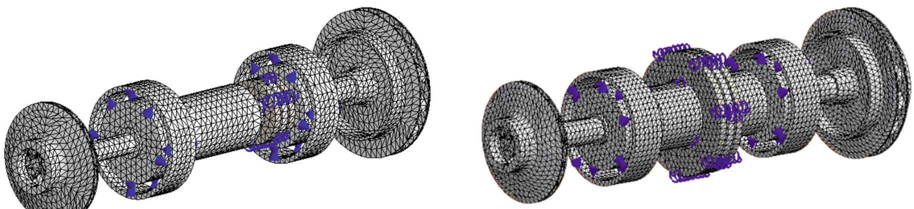

a) b)

Fig. 4. Finite element models of the ECU rotor with elastic links: a) original; b) modified design (195,051 and 325,815 degrees of freedom, respectively)

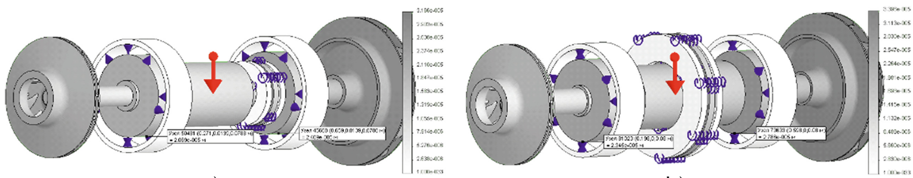

a) b)

Fig. 5. Static displacement of the ECU rotor due to the action of gravity: a) original; b) modified design

The results of calculations of natural frequencies are summarized in Table 1, and the corresponding translational and deformation modes of the rotor's natural vibrations are shown on Fig. 6. They are obtained as a result of performing modal analyses.

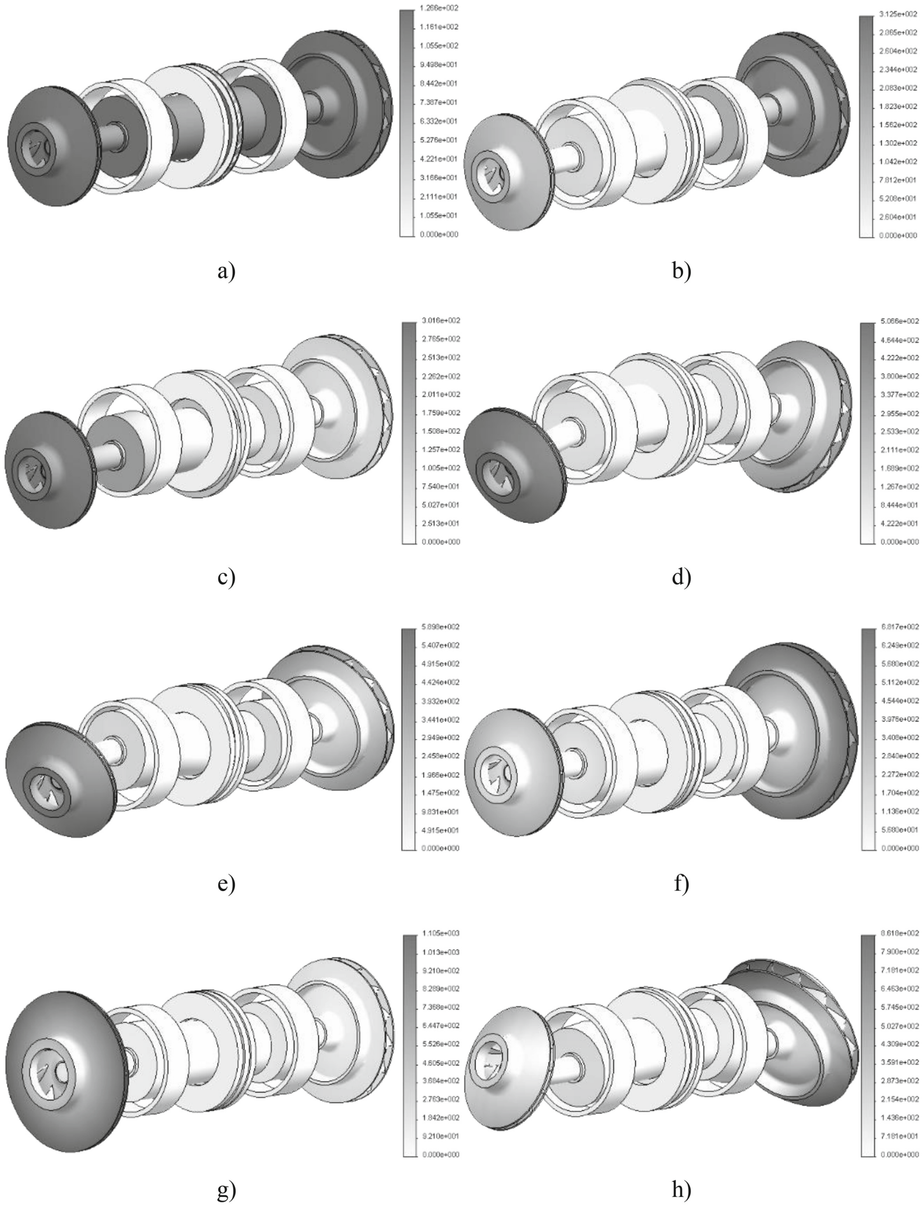

Fig. 6. Natural mode shapes of the modified design: a) 1st; b) 2nd; c) 3rd; d) 4th; e) 5th; f) 6th; g) 7th; h) 8th

Table 1. Natural frequencies and critical speeds of rotation of the ECU rotor in magnetic bearings with the given rigidity

#	Movement type / Direct synchronous precession	Original design		Modified design	
		Natural frequency, Hz	Critical rotation speed, rpm	Natural frequency, Hz	Critical rotation speed, rpm
1	Axial oscillations / -	77.8	-	72.2	-
2	Angular oscillations / Conical	93.1	5277	92.9	5571
3	Translational oscillations / Cylindrical	111.3	6278	101.1	6064
4	Bending oscillations / Curved axle	227.0	*13,622*	347.2	20,834
5	Bending oscillations / Curved axle	378.3	22,607	537.8	32,269
6	Torsional oscillations / -	444.8	-	570.7	-
7	Torsional oscillations / -	576.9	-	809.9	-
8	Bending oscillations / Curved axle	1044.9	48,619	1031.4	61,884

The calculated critical speeds corresponding to translational and deformation precessional movements allow us to judge the possibility of resonances occurring in the operating range of 13,500–15,000°rpm. The calculation of critical speeds based on the frequencies of the rotor's natural oscillations is, of course, approximate and does not take into account the dependence on the rotation speed. Refinement, taking into account such dependence, can be made when constructing Campbell diagrams. However, even such estimated values of critical speeds are very informative, if we take into account that direct precession increases critical speeds, and reverse precession reduces them [37, 38]. The estimation of results of the natural vibrations analysis for the initial rotor design, obtained on the base of a refined calculation using a volumetric model, shows the possibility of resonance occurring at operating rotation speeds (Table 1, #4). In its turn, modification of the rotor makes it possible to detune from resonant modes, increasing the value of the first critical speed at which the rotor makes precessional movement with the bended shaft axis (Table 1, #4), in 1.5 times. At the same time, the values of the critical velocities corresponding to the conical and cylindrical precession remain practically unchanged (Table 1, #2 and #3 respectively).

5 Discussion and Conclusion

So, parametric multivariate numerical simulations made it possible to find a rational design of the rotor of an expander-compressor unit suitable for replacing sliding bearings (journal and thrust oil film bearings) with a combination of passive and active magnetic bearings. This was achieved by changing the location of the thrust sections, and for the axial thrust AMB this location was changed radically. In this case, the maximum possible stiffnesses of known radial PMBs were used.

The results of dynamic analyze in a linear formulation showed the possibility of detuning the critical rotation speeds of the ECU rotor modified and adapted to the set-point of the magnetic bearings (Table 1). In this case, the critical speeds of translational vibration modes, at which the rotor makes precessional conical and cylindrical movements, are below the lower limit of the operating range. The first deformation mode of vibration, in which the rotor makes the precession of the bended axis, has a critical speed 38% higher than the upper limit of the operating range. This combination guarantees self-centering of the rotating rotor at speeds within the operating range.

Thus, the results of the work prove the possibility of re-equipment of the considered expander-compressor unit by replacing the sliding bearings with a more progressive and economical type of bearings. Of course, the final examination of the dynamic characteristics of the rotor system must be carried out for the actual stiffness of a particular version of the passive permanent magnetic bearing selected for technical use in a particular machine. In this case, an in-depth analysis of rotor dynamics in a nonlinear formulation is necessary [39], since magnetic bearings are nonlinear elastic supports. To a greater extent this concerns to the PMB, since in the AMB the control laws allow us to vary the force characteristics, setting them closer to linear. Nonlinear analysis is also required in the presence of other structural elements made of nonlinear materials [40]. But this is a subject for future research. It is important to note that the maximum stiffness of a passive magnetic bearing is not always the optimal choice. In some cases, it may be necessary to use a bearing with less rigidity to ensure the necessary smoothness of rotation or resistance to dynamic loads.

This approach can be used to modify the rotors of various turbomachines (gas turbine engines, turbocompressors, turboexpanders, generators, industrial fans, etc.) in order to switch to magnetic bearings, the use of which in new technology is very common.

References

1. McMillan, R.B.: Rotating Machineries, Aspects of Operation and Maintenance. River Publishers (2020)
2. Getu Hailu, (ed.): Rotating Machinery. IntechOpen (2020). https://doi.org/10.5772/intechopen.77579

3. Schobeiri, M.T.: Gas Turbine Design, Components and System Design Integration: Second Revised and Enhanced Edition. Springer International Publishing, Cham (2019). https://doi.org/10.1007/978-3-030-23973-2
4. Merculov, V., Kostin, M., Martynenko, G., Smetankina, N., Martynenko, V.: Force simulation of bird strike issues of aircraft turbojet engine fan blades. In: Daniela Doina Cioboată, (ed.) International Conference on Reliable Systems Engineering (ICoRSE) - 2021, pp. 129–141. Springer International Publishing, Cham (2022). https://doi.org/10.1007/978-3-030-83368-8_13
5. Casey, M., Robinson, C.: Radial Flow Turbocompressors: Design, Analysis, and Applications. Cambridge University Press, Cambridge (2021). https://doi.org/10.1017/9781108241663
6. Jadhav, M.M., Chakravarty, A., Atrey, M.D.: Experimental investigations on high pressure ratio cryogenic turboexpanders for helium liquefier. Cryogenics **117**, 103304 (2021)
7. Jichao, H., Yufei, L., Jiechen, D., Yutian, S., Baojun, G., Weili, L.: Thermal modeling and experimental validation in the rotor region of hydrogenerator with different rotor structures. IEEE Access **9**, 120001–120009 (2021). https://doi.org/10.1109/ACCESS.2021.3098319
8. Patel, M.R., Beik, O.: Wind and Solar Power Systems. CRC Press, Boca Raton (2021)
9. Martynenko, V.: Analysis of strength and bearing capacity of the auxiliary mine ventilation fan connected to the rotor of its electrical drive. In: 2020 IEEE KhPI Week on Advanced Technology (KhPI Week), pp. 19–23, 9250078. IEEE, Kharkiv, Ukraine (2020). https://doi.org/10.1109/KhPIWeek51551.2020.9250078
10. Rozova, L., Martynenko, G.: Information technology in the modeling of dry gas seal for centrifugal compressors. CEUR Workshop Proc. **2608**, 536–546 (2020). https://doi.org/10.32782/cmis/2608-41
11. Meng, Y., et al.: Spontaneous desublimation of carbon dioxide in turbo-expander applied for cryogenic carbon capture. Int. Commun. Heat Mass Transf. **140**, 106528 (2023). https://doi.org/10.1016/j.icheatmasstransfer.2022.106528
12. Ghojel, J.: Fundamentals of heat engines: reciprocating and gas turbine internal combustion engines. Wiley (2020). https://doi.org/10.1002/9781119548829
13. Weaver H.F.: Cross-section cutaway illustration of generator and engine. 25 (2003). Source: http://www.grc.nasa.gov/www/rt2002/5000/5960weaver.html (PD).
14. Doll, G.L.: Rolling bearing tribology: tribology and failure modes of rolling element bearings. Elsevier (2022). https://doi.org/10.1016/B978-0-12-822141-9.09993-3
15. Breńkacz, Ł: Bearing Dynamic Coefficients in Rotordynamics: Computation Methods and Practical Applications. Wiley (2021). https://doi.org/10.1002/9781119759287
16. Martynenko, G.Y., Marusenko, O.M., Ulyanov, Y.M., Rozova, L.V.: The use of information technology for the design of a prototype engine with rotor in magnetic bearings. In: International Scientific and Technical Conference on Integrated Computer Technologies in Mechanical Engineering (ICTM 2019). Kharkiv, Ukraine (2019). Advances in Intelligent Systems and Computing, vol. 1113, pp. 301–309. Springer International Publishing, Cham (2020). https://doi.org/10.1007/978-3-030-37618-5_26
17. Martynenko, V.: An original technique for modeling of anisotropic viscoelasticity of orthotropic materials in finite element codes applied to the mechanics of plates and shells. Mech. Mech. Eng. **21**(2), 389–413 (2017)
18. Chen, S., et al.: Experimental and numerical investigation of the thermomechanical load on a turbine housing in a radial turbocharger. Proc. Inst. Mech. Eng. Part D J. Automobile Eng. **236**(10–11), 2489–2502 (2022). https://doi.org/10.1177/09544070211052198
19. Bednarz, A., Kabalyk, K., Jakubowski, R., Bartłomowicz, R.: Numerical study on sensitivity of turbofan engine performance to blade count of centrifugal compressor impeller. Energies **16**(14), 5251 (2023). https://doi.org/10.3390/en16145251

20. Torabi Asr, M., Masoumi, M.M., Mustapha, F.: Modal behaviour of vertical axis wind turbine comprising prestressed rotor blades: a finite element analysis. Pertanika J. Sci. Technol. **25**(3), 977–982 (2017)
21. Chen, M., Ma, Y., Liu, S., Hong, J.: Rotordynamic analysis of whole aero-engine models based on finite element method. Beijing Hangkong Hangtian Daxue Xuebao J. Beijing Univ. Aeronaut. Astronaut. **33**, 1013–1016 (2007)
22. Uddin, M., et al.: Design a cooling pillow to support a high-speed supercritical CO2 turbine shaft. Appl. Therm. Eng. **196**, 117345 (2021). https://doi.org/10.1016/j.applthermaleng.2021.117345
23. Lei, X.: Optimal design of one-rotor orchard inter-row rake based on tines trajectory analysis. Int. Agric. Eng. J. **28**(4), 11–19 (2019)
24. Ghalea, A., Varshitha, H., Kumar, M.V., Mathd, M.M.: Design validation of high inertia generator rotor. AIP Conf. Proc. 2316 (2021). https://doi.org/10.1063/5.0038271
25. Patel, A., Biradar, V., Kumar, P.: Harmonic analysis of the high speed direct coupled SCO2 turbo-generator. In: ASME 2021 Gas Turbine India Conference (GTINDIA), V001T10A010, pp. 1–6 (2021). https://doi.org/10.1115/GTINDIA2021-76448
26. Martynenko, G., Rozova, L.: Integrated computer modeling of dynamic processes in rotor machines and systems with elastic-damper and magnetic bearings. In: International Scientific and Technical Conference on Integrated Computer Technologies in Mechanical En-gineering (ICTM 2022). Kharkiv, Ukraine (2022). Lecture Notes in Networks and Systems, vol. 657 LNNS, pp. 371-383. Springer, Cham (2023). https://doi.org/10.1007/978-3-031-36201-9_32
27. Samanta, P., Hirani, H.: On the evolution of passive magnetic bearings. J. Tribol. **144**(4), 040801 (2022). https://doi.org/10.1115/1.4051815
28. Das, U., Debnath, S., Gupta, S., Biswas, P.K., Sudhakar Babu, T., Nwulu, N.I.: Active magnetic bearing system using I-Type and U-Type actuator. IEEE Access **11**, 62780–62798 (2023). https://doi.org/10.1109/ACCESS.2023.3276324
29. Jastrzebski, R.P., Liukkonen, O.: Analysis of a segmented axial active magnetic bearing for multi-MW compressor applications. IEEE/ASME Trans. Mechatron. **28**(5), 2799–2809 (2023). https://doi.org/10.1109/TMECH.2023.3254812
30. Martynenko, G., Martynenko, V.: Permanent magnets with magnetizing winding for varying mechanical stiffness. In: 20th IEEE International Conference on Modern Electrical and Energy Systems (MEES 2021), pp. 1–6, 9598716. IEEE, Kremenchuk, Ukraine (2021). https://doi.org/10.1109/MEES52427.2021.9598716
31. Slininger, T.S., Chan, W.Y., Severson, E.L., Jawdat, B.: An overview on passive magnetic bearings. In: 2021 IEEE International Electric Machines and Drives Conference (IEMDC 2021), pp. 1–8. IEEE, Hartford, CT, USA (2021)
32. Kuznetsov, B.I., Nikitina, T.B., Bovdui, I.V.: Multiobjective synthesis of two degree of freedom nonlinear robust control by discrete continuous plant. Tech. Electrodynamics **2020**(5), 10–14 (2020). https://doi.org/10.15407/techned2020.05.010
33. Kuznetsov, B., Voloshko, A., Bovdui, I., Vinichenko, E., Kobilyanskiy, B., Nikitina, T.: High voltage power line magnetic field reduction by active shielding means with single compensating coil. In: International Conference on Modern Electrical and Energy Systems (MEES 2017), pp. 196–199. IEEE, Kremenchuk, Ukraine (2017)
34. Martynenko G.: Analytical method of the analysis of electromagnetic circuits of active magnetic bearings for searching energy and forces taking into account control law. In: 2020 IEEE KhPI Week on Advanced Technology (KhPIWeek 2020), pp. 86–91, 9250138. Kharkiv, Ukraine (2020). https://doi.org/10.1109/KhPIWeek51551.2020.9250138

35. Martynenko, G., Martynenko, V., Pidkurkova, I.: Integrated software for numerical calculation of active magnetic bearings force characteristics with data accumulation for various parameters. In: 2022 IEEE 3rd KhPI Week on Advanced Technology, (KhPI Week 2022), pp. 108–113. Kharkiv, Ukraine (2022). https://doi.org/10.1109/KhPIWeek57572.2022.9916476
36. Martynenko, G., Ulianov, Yu.: Combined rotor suspension in passive and active magnetic bearings as a prototype of bearing systems of energy rotary turbomachines. In: 2019 IEEE International Conference on Modern Electrical and Energy Systems (MEES 2019), pp. 90–93. Kremenchuk, Ukraine (2019). https://doi.org/10.1109/MEES.2019.8896571
37. Matsushita, O., Tanaka, M., Kanki, H., Kobayashi, M., Keogh, P.: Vibrations of Rotating Machinery, vol. 1. Basic Rotordynamics: Introduction to Practical Vibration Analysis. Springer Japan, Tokyo (2017). https://doi.org/10.1007/978-4-431-55456-1
38. Matsushita, O., Tanaka, M., Kanki, H., Kobayashi, M., Keogh, P.: Vibrations of Rotating Machinery, vol. 2. Advanced Rotordynamics: Applications of Analysis, Troubleshooting and Diagnosis. Springer Japan, Tokyo (2019). https://doi.org/10.1007/978-4-431-55453-0
39. Sun, H., Zhang, H., Zhou, Q.: Nonlinear dynamics analysis of rotor system. J. Phys.: Conf. Ser. **2528**(1) (2023). https://doi.org/10.1088/1742-6596/2528/1/012069
40. Martynenko, V.G., Lvov, G.I., Ulianov, Y.N.: Experimental investigation of anisotropic viscoelastic properties of glass fiber-reinforced polymeric composite material. Polym. Polym. Compos. **27**(6), 323–336 (2019). https://doi.org/10.1177/0967391119846362

Analyzing Exergy Losses When Utilizing the Heat of Exhaust Gases in Boiler

Victoria Kornienko[1](✉), Roman Radchenko[1], Volodymyr Korobko[1], Oleksii Ostapenko[1], and Serhii Shevchenko[2]

[1] Admiral Makarov National University of Shipbuilding, 9 Heroes of Ukraine Avenue, Mykolaiv 54025, Ukraine
kornienkovika1987@gmail.com

[2] Pukhov Institute for Modelling in Energy Engineering, General Naumov Street 15, Kyiv 03164, Ukraine

Abstract. The operating efficiency of the ship power plant (SPP) largely depends not only on the perfection of the processes occurring in its elements, but also on the degree of utilization of heat lost with exhaust gases and coolants. The aim of research is to analyze the effect of exergy losses, when using the available heat of exhaust gases in the exhaust gas boiler (EGB). A methodology was presented for analyzing the influence of ambient and exhaust gas temperatures on the values of exergy losses when using the available heat of exhaust gases in EGB. The mathematical dependencies were obtained that make it possible to determine the relationship between the operating conditions of the SPP and the parameters of each coolant. The exergy losses, when using the available heat of exhaust gases in the EGB was analyzed. Analysis of calculation results showed increasing a specific steam production and entropy of gases with decreasing the temperature in the outlet of EGB from 160°C to 90°C. It is possible to obtain comprehensive characteristics of the available boiler performance basing on the results of measuring the operating parameters of the boiler only in one mode.

Keywords: Ship Power Plant · Exhaust Gases · Entropy · Steam Productivity · Feed Water · Exergy Losses

1 Introduction

The operating efficiency of the ship power plant (SPP) largely depends not only on the perfection of the processes occurring in its elements, but also on the degree of heat utilization lost with exhaust gases and coolants [1, 2]. For most modern internal combustion engines (ICE) used as main engines on ships, the total heat loss to the environment amounts to up to 50% of the heat released in the cylinders during fuel oil combustion [3, 4]. In this case, the operating conditions of the ICE have a certain influence on the magnitude of these losses [5]. Their utilization does not change the efficiency of the diesel engine, but it allows reducing the overall fuel consumption of the SPP and increasing the efficiency of its operation [6]. Currently, most ships are equipped with installations for using the heat of exhaust gases of ICEs - to produce steam in the

M. Nechyporuk et al. (Eds.): ICTM 2023, LNNS 1008, pp. 476–486, 2024.
https://doi.org/10.1007/978-3-031-61415-6_41

exhaust gas boiler (EGB), and the heat of their cooling water - to obtain fresh water from sea water in vacuum evaporation plants [7].

A rational, justified choice of the types and characteristics of these auxiliary installations at the stages of design or modernization of the SPP, made on the basis of an analysis of the technical characteristics of the installations, taking into account the joint influence of operational loads and environmental parameters on them, can indicate a significant impact on increasing the operating efficiency of the SPP [8]. In addition, increasing the level of technically competent operation of the installation will also help to increase the efficiency of the SPP by providing the ability to select optimal operating modes of the SPP [9, 10]. This can reduce not only heat losses fuel thermal energy, but also reduce the level of thermal pollution of the environment.

The task of managing the efficiency of a power plant comes down to finding an indicator that reflects the relationship between the complete use of fuel thermal energy and the noted operational parameters. That is an indicator that provides the ability to conduct an operational ongoing analysis of thermal efficiency. Since the main final objectives of any method of thermal efficiency of SPP elements is to determine the degree of thermodynamic perfection of heat use and transfer. Its results can be used to develop measures to reduce fuel consumption and heat loss [11, 12].

A particular difficulty in developing an indicator for modern power plants is that most of them are complex systems of combined simultaneous production of propulsive, electrical and thermal energy. On certain types of ships, propulsion energy can be transmitted to the shaft line simultaneously from the main engine, recovery turbomachine, or diesel generator. Electrical energy can be generated by diesel generators, shaft generators, recovery turbogenerators, thermal energy - by an auxiliary boiler, EGB, more complete use of high-temperature coolants by heat pumps, absorption refrigeration units. In such complex installations, the perfection of each element of the control system is assessed by its generally accepted indicator [13, 14].

2 Literature Review

All this confirms the advisability of using simplified and unified indicators to assess the thermal efficiency of processes in the elements of the power plant with the developed use of waste heat from ICEs so that the indicators themselves represent the simplest connection of homogeneous coefficients. That is using the exergy method.

The exergy method has two varieties: the exergy flow method and the exergy loss method [15]. The first method is based on the recording of all exergy flows, both an increase and a decrease in exergy in the work processes of the elements and installations of the SPP. It turns out that in installations with combined energy production, some of these flows close on themselves or return to the main input flow, bypassing contact with the energy received at the output. This circumstance does not allow the exergy at the entrance to the next element of the installation to always be equal to the exergy at the exit from the previous element of the installation. The method of subtracting exergy losses (entropy) is based on the fact that there is no need to analyze all exergy flows, since, knowing the primary introduced exergy. It is sufficient to further take into account only exergy losses. The useful energy of any complex combined power plant can be calculated as the difference between the primary exergy and the sum of exergy losses [15]. Experience in the practical use of the entropy method shows that exergy loss coefficients quantitatively describe the influence of irreversibility on the excessive consumption of fuel energy introduced into the installation [16].

The nature of the change in the specific exergy of gases from the transfer of heat from the exhaust gases of the ICE to the environment significantly depends on the temperature of the gases at the outlet into the environment. As the specified temperature decreases, the loss value decreases. For medium-speed engines they can reach 300 kJ/kg, with their values decreasing to 200 kJ/kg for low-speed engines (at an ambient temperature of 40 °C). It is also important to note that for medium-speed engines these losses increase with increasing ambient temperature, while for low-speed engines their increase is less significant or even absent [17, 18].

Data on the type of main engine, its power, temperature and amount of exhaust gases allow, after a theoretical analysis of the ship's energy balance, to consider the possibility of using a turbogenerator to produce the appropriate amount of steam. Such data allows the boiler manufacturer to design, manufacture and supply the EGB of the required parameters. The heat balance data of the selected ICE allows the manufacturer to design and manufacture a charge air cooler and determine the maximum possible heating temperature of the boiler water. The same data is necessary for the manufacture of desalination plants to select and supply an evaporator with maximum fresh water productivity [19, 20].

Low-temperature economizers [21, 22] or low-pressure economizers [23, 24] are used to increase the efficiency of exhaust gas heat recovery. These installations use the heat of condensation of sulfuric acid vapor and water in the exhaust gases. Condensed acid vapors glue the ash in the exhaust gases and stick to the heating surface [25, 26], which increases the hydraulic and thermal resistance, affecting the reliability and efficiency of operation. The experience of using water-fuel emulsions (WFE) in boilers and ICEs indicates the undeniable advantages of this type of fuel: the effective specific fuel consumption is reduced by approximately 8%, the concentration of nitrogen oxides in the exhaust gases is reduced by 1.4–3.1 times, CO concentration – 1.3–1.5 times, smoke – 1.3–2.4 times [27, 28]. The influence of the parameters of the combustion process of WFE in a low-power boiler on the level of formation of nitrogen oxides, carbon monoxide and soot were studied. The results of experimental research of low-temperature condensation economizer approved the appropriate corrosion rate when water-fuel emulsion combustion and good perspective for their application in ship waste heat recovery [29, 30].

The aim of research is to analyze the effect of exergy losses, when using the available heat of exhaust gases in the exhaust gas boiler (EGB).

3 Research Methodology

When analyzing the effect on the values of exergy losses when using the available heat of exhaust gases in the EGB, ambient and exhaust gas temperatures, the following assumptions were made:

– there are no significant heat losses in the EGB;

– there are no pressure losses in the elements of the systems (EGB and pipelines);
– unused heat is released into the environment (into the atmosphere).

These assumptions significantly reduce the cumbersomeness of calculations and subsequent analysis.

When using the available heat of the exhaust gases to obtain saturated steam in the EGB, the total exergy losses will decrease and amount to [18]

$$\Delta ex_{\text{guk}} = ex_{\text{g}} - ex_{\text{s}}, \text{ kJ/kg gas} \quad (1)$$

where ex_{g} – exergy of combustion products; ex_{s} – exergy of steam, determined using the equation

$$ex_{\text{p}} = q_{\text{s}} - m_{\text{s}} \cdot \Delta s_{\text{s}} \cdot T_{\text{os}}, \text{ kJ/kg gas} \quad (2)$$

where q_{s} – amount of heat transferred from 1 kg of gases to water and equal to that received by water in the process of steam formation, kJ/kg gas

$$q_{\text{s}} = i_{\text{in}} - i_{\text{out}} = \Delta i_{\text{g}} \quad (3)$$

where m_{s} – amount of steam obtained from 1 kg of exhaust gases;

$$m_{\text{s}} = q_{\text{s}}/(i_{\text{s}} - i_{\text{w}}) = q_{\text{s}}/\Delta i_{\text{ps}}, \text{ kg steam/kg gas} \quad (4)$$

where i_{s}, i_{w} – heat content of steam and water, kJ/kg;

$$\Delta s_{\text{s}} = s_{\text{s}} - s_{\text{w}} \quad (5)$$

where s_{s}, s_{w} – entropy of steam and water, kJ/(kg · K). Taking into account the conservation of heat transferred from the exhaust gas to the water in EGB, the equation for calculating the entropy losses of 1 kg of gases takes the following form:

$$\Delta ex_{\text{guk}} = ex_{\text{g}} - ex_{\text{p}} = \Delta s_{\text{g}} - m_{\text{s}} \cdot \Delta s_{\text{s}} = T_{\text{os}} \cdot [(s_{\text{in}} - s_{\text{out}}) - m_{\text{s}} \cdot (s_{\text{s}} - s_{\text{w}})], \text{ kJ/kg gas} \quad (6)$$

4 Results

According to [18], the equation can be used to determine the entropy of the exhaust gases on the gas temperature at the inlet t_{in} and outlet t_{out} of EGB:

$$\Delta s_{\text{g}} = 0.0037 \cdot (t_{\text{in}} - t_{\text{out}}) - 5.0117 \cdot 10^{-6} \cdot \left(t_{\text{in}}^2 - t_{\text{out}}^2\right) + 3.931 \cdot 10^{-9} \cdot \left(t_{\text{in}}^3 - t_{\text{out}}^3\right) \quad (7)$$

In Fig. 1 is presented a dependence showing the relationship Eq. 7.

Data processing by the methods described above made it possible for the two-factor dependence shown in Fig. 2.

The correlation equation reflecting the surface shown in Fig. 2 has the form:

$$\Delta s_{\text{g}} = 0.0942 - 2.6451 \cdot 10^{-3} t_{\text{in}} - 3.4763 \cdot 10^{-3} t_{\text{out}} - 1.4714 \cdot 10^{-6} t_{\text{in}}^2 + 3.3622 \cdot 10^{-6} t_{\text{out}}^2 \quad (8)$$

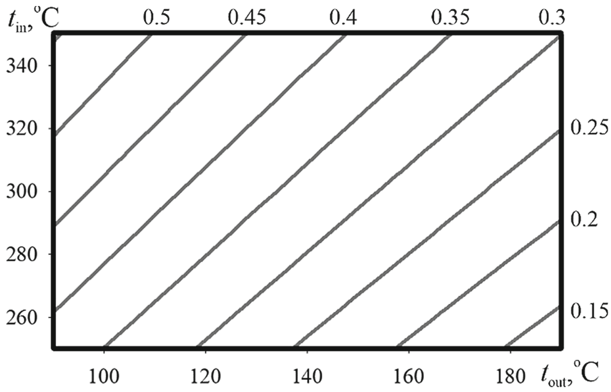

Fig. 1. Dependence of the entropy of gases of EGB on the exhaust gas temperature at the inlet and outlet of EGB.

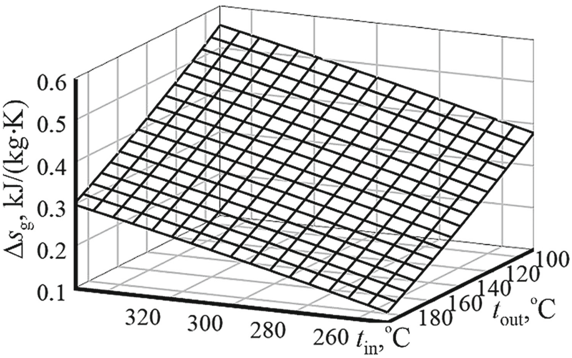

Fig. 2. Two-factor dependence of the entropy of gases of EGB on the exhaust gas temperature at the inlet and outlet of EGB.

Analysis of the data presented in Fig. 2 shows that in the case of a decrease the temperature in outlet of EGB t_{out} from 160°C to 90°C the entropy of gases Δs_g increases: at $t_{in} = 250$°C – by 1.73 times, at $t_{in} = 350$°C – by 1.4 times, at $t_{in} = 300$°C – by 1.53 times.

An equation was used to analyze the effect of ambient temperature on exergy losses associated with the release of gases from the EGB [18]:

$$\Delta s_g = 0.0037 \cdot (t_{out} - t_{os}) - 5.0117 \cdot 10^{-6} \cdot \left(t_{out}^2 - t_{os}^2\right) + 3.931 \cdot 10^{-9} \cdot \left(t_{out}^3 - t_{os}^3\right) \quad (9)$$

Figure 3 shows graphs of changes in the entropy of gases leaving the EGB, depending on their temperature and the ambient temperature, calculated using Eq. 9.

Data processing by the methods described above made it possible for the two-factor dependence shown in Fig. 4.

The correlation equation reflecting the surface shown in Fig. 4 has the form:

$$\Delta s_g = 9.8389 \cdot 10^{-3} + 3.4759 \cdot 10^{-3} t_{out} - 3.7038 \cdot 10^{-3} t_{os} - 3.3607 \cdot 10^{-6} t_{out}^2 + 4.9233 \cdot 10^{-6} t_{os}^2 \quad (10)$$

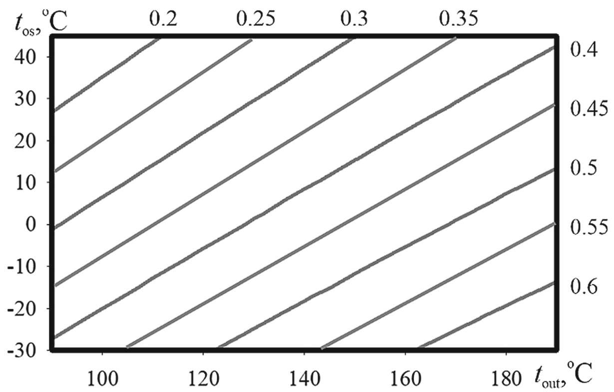

Fig. 3. Dependence of the entropy of gases of EGB on the temperature of air and gases at the outlet of EGB.

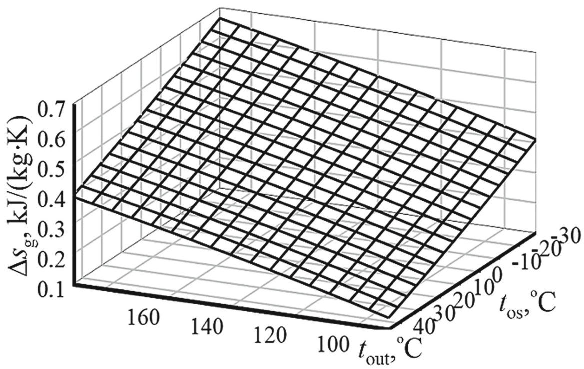

Fig. 4. Two-factor dependence of the entropy of gases of EGB on the temperature of air and gases at the outlet of EGB.

As can be seen from the presented dependencies (Figs. 3 and 4), the greatest influence on the decrease in entropy has a decrease in ambient temperature. The nature of the change in entropy does not depend on the gas temperature at the outlet of the EGB.

According to [18], the required amount of heat given off by 1 kg of exhaust gas to the EGB water during the vaporization process to determine the value of the specific steam production Δi_g, can be calculated using the equation:

$$\Delta i_g = 1.0032 \cdot (t_{in} - t_{out}) + 8 \cdot 10^{-6} \cdot \left(t_{in}^2 - t_{out}^2\right) + 2 \cdot 10^{-7} \cdot \left(t_{in}^3 - t_{out}^3\right) - 1 \cdot 10^{-10} \cdot \left(t_{in}^4 - t_{out}^4\right) \quad (11)$$

In Fig. 5 shows the curves reflecting the dependence of the specific heat transfer by combustion products to water in the EGB on their inlet and outlet temperatures.

The processing of the presented dependences (Fig. 6) by the methods described earlier and the analysis performed showed that to calculate the specific amount of heat transferred to the EGB by exhaust gases to water, a dependence similar to that obtained earlier can be used.

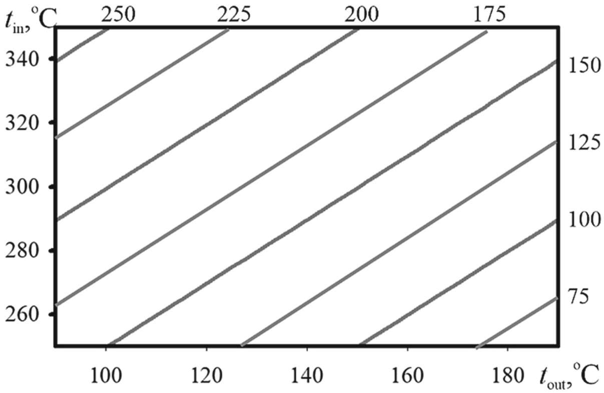

Fig. 5. Dependence of the specific heat transfer by combustion products to water in the EGB on their inlet and outlet temperatures.

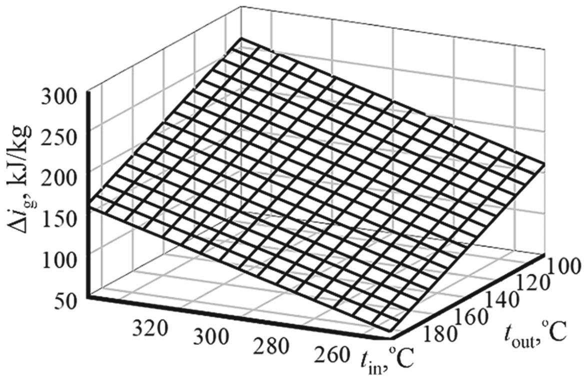

Fig. 6. Two-factor dependence of the specific heat transfer by combustion products to water in the EGB on their inlet and outlet temperatures.

The correlation equation reflecting the surface shown in Fig. 6 has the form:

$$\Delta i_g = 9.5278 \cdot 10^{-13} + 1.0032 \cdot t_{in} - 1.0032 \cdot t_{out} \tag{12}$$

Analysis of the data presented in Fig. 6 shows that in the case of a decrease the temperature in outlet of EGB t_{out} from 160°C to 90°C the specific steam production Δi_g increases: at t_{in} = 250°C – by 1.78 times, at t_{in} = 300°C – by 1.64 times, at t_{in} = 350°C – by 1.38 times.

Exhaust gas temperature at the inlet of EGB, exhaust gas temperature at the outlet of EGB and steam pressure values were taken constant to study the degree of influence of parameters on the amount of exergy losses of ICE (specific steam productivity).

In Fig. 7 shows the dependence of the values of specific steam productivity m_s in the EGB on the temperatures of the feed water t_w and exhaust gases at the inlet of EGB t_{in} (t_{out} = 200 °C, steam pressure 0.7 MPa).

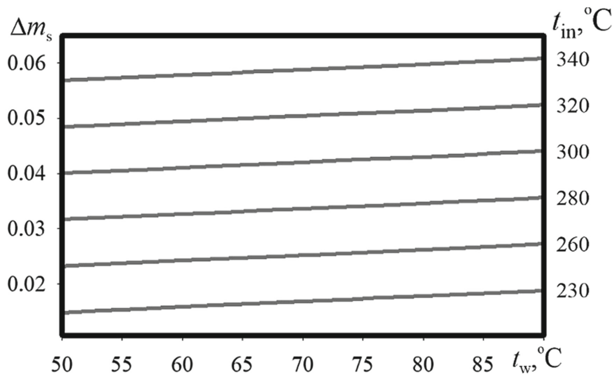

Fig. 7. Dependence of specific steam productivity in the EGB on the temperatures of the feed water and exhaust gases at the inlet of EGB.

The specific steam productivity m_s, can be calculated using the equation:

$$m_s = -0.091 + 4.2 \cdot 10^{-4} t_{in} + 1.0 \cdot 10^{-4} t_w \tag{13}$$

In Fig. 8 the dependences of the specific steam productivity in the EGB on the temperatures of the feed water and exhaust gases at the outlet of EGB are presented. A constant temperature of the exhaust gases at the inlet of EGB is assumed when these dependencies are obtained.

The specific steam productivity m_s, can be calculated using the equation:

$$m_s = 0.13–3.75 \cdot 10^{-4} t_{out} + 1.25 \cdot 10^{-4} t_w \tag{14}$$

As can be seen from the presented dependencies (Figs. 7–8), the increase in specific steam productivity for each degree of change in gas temperature depends on the gas temperature at the inlet and outlet of EGB to a greater extent than on the feed water temperature.

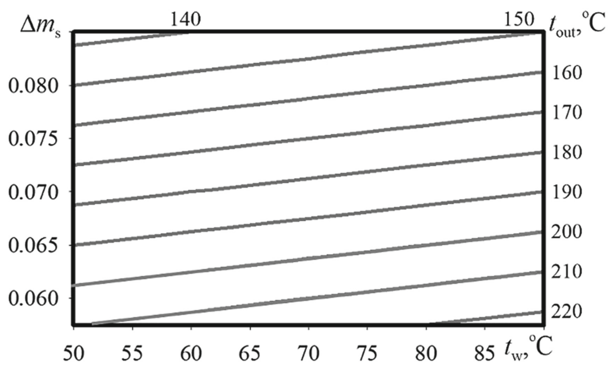

Fig. 8. Dependence of specific steam productivity in the EGB on the temperatures of the feed water and exhaust gases at the EGB outlet.

This means that using the presented data, having the results of measuring the operating parameters of the EGB in only one mode, it is possible to obtain comprehensive characteristics of the available boiler performance. In comparison with published data from other authors [18], curves and equations were presented for calculating a specific steam production and entropy of gases with decreasing the temperature in the outlet of EGB from 160 °C to 90 °C.

5 Conclusions

The use of the exergy method (entropy method) for the analysis of power plants with the production of thermal energy due to deep heat recovery is justified.

Analysis of the literature data on the influence of various factors on the values of exergy losses made it possible to make assumptions that significantly reduce the cumbersomeness of calculations and subsequent analysis.

In accordance with the task mathematical dependencies were obtained. That make it possible to determine the relationship between the operating conditions of the SPP and the parameters of each coolant.

The effect of exergy losses, when using the available heat of exhaust gases in the EGB was analyzed. Analysis of calculation results showed increasing a specific steam production and entropy of gases with decreasing the temperature in the outlet of EGB from 160 °C to 90 °C.

It is possible to obtain comprehensive characteristics of the available boiler performance basing on the results of measuring the operating parameters of the boiler only in one mode.

References

1. Behrendt, C, Motorny, A.: The influence of ambient temperature on the efficiency factor of main engine operation. Sci. J. Maritime Univ. Szczecin, Zeszyty Naukowe Akademia Morska w Szczecinie **1**(73), 21–29 (2004)
2. Radchenko, A., Tsoy, A., Portnoi, B., Kantor, S.: Increasing the efficiency of gas turbine inlet air cooling in actual climatic conditions of Kazakhstan and Ukraine. AIP Conf. Proc. **2285**, 030071 (2020)
3. Agrebi, S., Dreßler, L., Nishad, K.: The exergy losses analysis in adiabatic combustion systems including the exhaust gas exergy. Entropy (Basel) **24**(4), 564 (2022)
4. Forduy, Radchenko, S.: Enhancing the gas engines fuel efficiency in integrated energy system by chilling cyclic air. In: Tonkonogyi, V. (ed.) InterPartner 2019. LNME, pp. 500–509. Springer, Cham (2020). https://doi.org/10.1007/978-3-030-40724-7_51
5. Behrendt, C.: Energy efficiency operational indicator of the selected type of polish fleet fishing cutter in dependence of the main engine type. J. Phys. Conf. Ser. **1172**(1), 012073 (2019)
6. Radchenko, N., Trushliakov, E., Radchenko, A., Tsoy, A., Shchesiuk, O.: Methods to determine a design cooling capacity of ambient air conditioning systems in climatic conditions of Ukraine and Kazakhstan. In: AIP Conference Proceedings, vol. 2285, no. 030074 (2020)
7. Kornienko, V., Radchenko, R., Bohdal, T., Radchenko, M., Andreev, A.: Thermal characteristics of the wet pollution layer on condensing heating surfaces of exhaust gas boilers. In: Ivanov, Pavlenko, V. (ed.) DSMIE 2021. LNME, pp. 339–348. Springer, Cham (2021). https://doi.org/10.1007/978-3-030-77823-1_34

8. Radchenko, N.: A concept of the design and operation of heat exchangers with change of phase. Arch. Thermodyn. **4**(25), 3–19 (2004)
9. Nishida, K., Takagi, T., Kinoshita, S.: Analysis of entropy generation and exergy loss during combustion. Proc. Comb. Inst. **29**, 869–874 (2002)
10. Radchenko, M., Mikielewicz, D., Andreev, A., Vanyeyev, S., Savenkov, O.: Efficient ship engine cyclic air cooling by turboexpander chiller for tropical climatic conditions. In: Nechyporuk, Pavlikov, M. (ed.) ICTM 2020. LNNS, vol. 188, pp. 498–507. Springer, Cham (2020). https://doi.org/10.1007/978-3-030-66717-7_42
11. Radchenko, N., Radchenko, A., Tsoy, A., Mikielewicz, D., Kantor, S., Tkachenko, V.: Improving the efficiency of railway conditioners in actual climatic conditions of operation. In: AIP Conference Proceedings, vol. 2285, no. 030072 (2020)
12. Radchenko, A., Mikielewicz, D., Forduy, S., Radchenko, M., Zubarev, A.: Monitoring the fuel efficiency of gas engine in integrated energy system. In: Nechyporuk, M., Pavlikov, V., Kritskiy, D. (eds.) Integrated Computer Technologies in Mechanical Engineering (ICTM 2019). Advances in Intelligent Systems and Computing, vol. 1113, pp. 361–370. Springer, Cham (2020)
13. Radchenko, A., Radchenko, M., Mikielewicz, D., Radchenko, R., Andreev, A.: A novel degree-hour method for rational design loading. Proc. Inst. Mech. Eng. Part A: J. Power Energy **237**(3), 570–579 (2022)
14. Yang, Z., et al.: Analysis of efficiency of thermopressor application for internal combustion engine. Energies **15**(4), 2250 (2022)
15. Punov, P., Evtimov, T., Chiriac, R., Clenci, A., Danel, Q., Descombes, G.: Progress in high performance, low emissions, and exergy recovery in internal combustion engines. Int. J. Energy Res. **41**, 1229–1241 (2017)
16. Trushliakov, E., Radchenko, M., Radchenko, A., Kantor, S., Zongming, Y.: Statistical approach to improve the efficiency of air conditioning system performance in changeable climatic conditions. In: 5th International Conference on Systems and Informatics, ICSAI 2018, Jiangsu, Nanjing, China, pp. 256–260 (2019)
17. Liu, P., Shu, G., Tian, H., Wang, X.: Engine load effects on the energy and exergy performance of a medium cycle/organic Rankine cycle for exhaust waste heat recovery. Entropy **20**, 137 (2018)
18. Behrendt, C. Mathematical model of the functioning of a ship power complex with deep heat recovery. Dissertation (2004)
19. Radchenko, N.I.: On reducing the size of liquid separators for injector circulation plate freezers. Int. J. Refrig. **5**(8), 267–269 (1985)
20. Radchenko, A., Radchenko, M., Trushliakov, E., Kantor, S., Tkachenko, V.: Statistical method to define rational heat loads on railway air conditioning system for changeable climatic conditions. In: 5th International Conference on Systems and Informatics, ICSAI 2018, pp. 1294–1298, 8599355 (2019)
21. Huang, S., Li, C., Tan, T., Fu, P., Xu, G., Yang, Y.: An improved system for utilizing low-temperature waste heat of flue gas from coal-fired power plants. Entropy **19**(423), 1–17 (2017)
22. Konovalov, D., Trushliakov, E., Radchenko, M., Kobalava, G., Maksymov, V.: Research of the aerothermopresor cooling system of charge air of a marine internal combustion engine under variable climatic conditions of operation. In: Tonkonogyi, V., et al. (eds.) Grabchenko's International Conference on Advanced Manufacturing Processes. InterPartner-2019. Lecture Notes in Mechanical Engineering, pp. 520–529. Springer, Cham (2020) https://doi.org/10.1007/978-3-030-40724-7_53
23. Li, F., Duanm, L., Fu, L., Zhao, X.: Research and application of flue gas waste heat recovery in cogeneration based on absorption heat–exchange. Procedia Eng. **146**, 594–603 (2016)

24. Konovalov, D.: Research of characteristics of the flow part of an aerothermopressor for gas turbine intercooling air. Proc. Institut. Mech. Eng., Part A: J. Power Energy **236**(4), 634–646 (2022). https://doi.org/10.1177/09576509211057952
25. Liang, R., Liu, L., Han, Y.: Sulfur deposition on corrosion of N80 carbon steel in high acid environment. Corros. Sci. Prot. Technol. **25**(3), 184–188 (2013)
26. Yang, Z., Kornienko, V., Radchenko, M., Radchenko, A., Radchenko, R.: Research of exhaust gas boiler heat exchange surfaces with reduced corrosion when water-fuel emulsion combustion. Sustainability **14**(19), 11927 (2022)
27. Woo, S., Lee, K.: Effect of injection strategy and water content on water emulsion fuel engine for low pollutant compression ignition engines. Fuel **3431**, 127809 (2023)
28. Yang, Z., Kornienko, V., Radchenko, M., Radchenko, A., Radchenko, R., Pavlenko, A.: Capture of pollutants from exhaust gases by low-temperature heating surfaces. Energies **15**(1), 120 (2022)
29. Lee, T.-H., Lee, S.-H., Lee, J.-K.: Exhaust gas emission improvements of water/bunker C oil-emulsified fuel applied to marine boiler. J. Mar. Sci. Eng. **9**, 477 (2021)
30. Kornienko, V., Radchenko, R., Radchenko, M., Radchenko, A., Pavlenko, A., Konovalov, D.: Cooling cyclic air of marine engine with water-fuel emulsion combustion by exhaust heat recovery chiller. Energies **15**(1), 248 (2022)

Signal and Image Processing

Methodology of Detection and Recognition of Faults in the Unit Components

Tran Manh Hung(✉)

National Aerospace University "Kharkiv Aviation Institute", Street Chkalov 17, Kharkiv 61070, Ukraine
tranmanhhung1202@gmail.com

Abstract. Detection and diagnosis of faults that may arise in the work process of the unit are carried out to increase the resource, reliability, and stability of its exploitation. In the article, the object of research is the detection and recognition of faults that occur in the main components of the steering unit AR20N – in the electrohydraulic amplifier (EHA) and the power cylinder (PC). The main purpose of the research is to develop a methodology for detecting and recognizing faults in the EHA and PC of the AR20N unit based on the results of measurements of the current values of the parameters of these units when various faults appear and develop. To achieve the set purpose, the following tasks were solved: using simulation modeling, the parameters of the unit model were determined, the numerical values of which contain information (diagnostic signs of the technical condition of the EHA and PC) about the appearance of various faults in the units; Shewhart diagnostic charts and the methodology of identification of current values of these parameters are developed. For this purpose, the following methods are used in the article: analytical, numerical, and statistical. The following results have been obtained: a methodology of detection, development, and recognition of faults of EHA and PC has been developed, in which hypothesis testing and determination of the probability of committing errors of the first and second type in decision-making are provided. The scientific and practical novelty of the obtained results consists in the development of a methodology for determining the diagnostic signs of the technical condition of the EHA and PC.

Keywords: Detection · Recognition · Fault · Diagnostic Chart · Hypothesis Testing

1 Introduction

Detection and recognition of faults that may arise in the work process of the unit are carried out to increase the resource, reliability, and stability of its exploitation. Units have different designs and operate in different operating environments, so it is desirable to have individual methods of fault detection and recognition for each unit [1–4].

In the article, the object of research is detection and recognition of faults in the main units of the AR20N steering unit – in the electrohydraulic amplifier (EHA) and in the power cylinder (PC). The AR20N steering unit is a device installed in the tail section

M. Nechyporuk et al. (Eds.): ICTM 2023, LNNS 1008, pp. 489–500, 2024.
https://doi.org/10.1007/978-3-031-61415-6_42

of the aircraft, has a complex design of the hydraulic system, and uses a reciprocating piston mechanism to deflect the rudder direction by an electrical control signal generated by the steering control system [1, 2].

The article uses: a simulation model of the AR20N unit with a PID controller in Matlab/Simulink environment, diagnostic signs of the technical condition of the EHA and PC, and the results of identification of parameters of mathematical models of these units obtained in articles [1, 2]. The methodology of detection and recognition of faults of the unit is based on the use of Shewhart diagnostic charts and the results of identification of the current values parameters of mathematical models of the EHA and PC, performed by the least squares method (LSM) after each aircraft flight.

In the article the following main tasks are solved: parameters (diagnostic coefficients) whose numerical values contain information about the influence of various factors on the technical condition of the unit are determined; Shewhart diagnostic charts for these parameters are developed; diagnostic signs of appearance of various faults are determined; hypotheses testing is performed and probabilities of making errors of the first (I) and second (II) types when making decisions are determined.

2 Objectives of the Research

The main purpose of the research of this article is: to develop a methodology of the detection and recognition of faults in the EHA and PC of the AR20N unit based on the results of measurements of the current values of the parameters of these units at the occurrence and development of various faults; hypotheses testing and determining the probabilities of committing errors of the I and II types when making decisions about the technical condition of the unit.

3 Problem Statement

In the control mode, the output link (OL) (or rod) of the AR20N unit PC performs a full stroke of movement ±53 mm, and the developed force on the OL, proportional to the movement, reaches the required maximum value of 60 kN in two extreme positions. Faults in the unit may arise when the external load acting on the OL changes or as a result of changes in internal factors, such as the friction force of moving parts, the elasticity force of the "flat mechanical feedback spring", fluid leaks, etc. [1, 2]. When faults appear and develop, the unit's work process, the current values of state variables available for measurement, and the trajectories of state variables transition from the initial state to the final state change.

Processes occurring in units are described using mathematical models. External and internal influencing factors determine the parameter values of the unit mathematical model. Therefore, by changing the values of the mathematical model parameters, it is possible to determine the technical condition of the unit and recognize occurring faults [3–5].

To achieve the set purpose it is necessary to solve the following tasks: to identify the current values of the parameters of the mathematical model of the unit after each flight of the aircraft; to determine the diagnostic signs that have the most probable influence on the change of the parameters of the mathematical model of the unit; to develop a methodology of detection and recognition of faults of the unit; to develop Shewhart diagnostic charts; to perform hypothesis testing and determine the probabilities of occurrence of errors of the first and second type when making decisions.

4 Mathematical Model of the EHA and PC of the Unit

The mathematical model of the EHA and PC of the AR20N unit, which was obtained in articles [1, 2], was developed based on the balance of forces acting on the distributor spool (DS) of the EHA and on the output link (OL) of the PC when they move. In this article, the models were transformed and presented as follows:

– Mathematical model of the EHA:

$$\ddot{x}_{ds}(t) = a_1 \cdot i(t) + a_2 \cdot \dot{x}_{ds}(t) + a_3 \cdot x_{ds}(t), \tag{1}$$

– Mathematical model of the PC:

$$\ddot{x}_{ol}(t) = b_1 \cdot \Delta p(t) + b_2 \cdot \dot{x}_{ol}(t) + b_3 \cdot x_{ol}(t), \tag{2}$$

where $a_1 = \frac{S_{ds} \cdot k_{pd.ds}}{m_{ds}}$; $a_2 = -\frac{k_{vf.ds} \cdot \eta \cdot l \cdot \pi \cdot d_{ds}}{\delta \cdot m_{ds}}$; $a_3 = -\frac{k_{df.ds} + k_{sp}}{m_{ds}}$; $b_1 = \frac{S_p \cdot k_{pd.pc}}{m_s}$; $b_2 = -\frac{k_{v.d.}}{m_s}$; $b_3 = -\frac{k_{d.e.s.}}{m_s}$; $\ddot{x}_{ds}(t)$, $\ddot{x}_{ol}(t)$ – acceleration of the DS and OL; $\dot{x}_{ds}(t)$, $\dot{x}_{ol}(t)$ – speed of the DS and OL; $x_{ds}(t)$, $x_{ol}(t)$ – displacement of the DS and OL; S_{ds}, S_p – working area of the end face of the DS and piston working area of the OL; $i(t)$ – electrical current control signal; $\Delta p(t)$ – differential pressure of the fluid in the PC; m_{ds}, d_{ds} – mass and diameter of the end face of the DS; δ, l –gap and gap length between the surface of the DS and the surface of the sleeve; η – dynamic viscosity of the fluid; $k_{pd.ds}$ – coefficient of gain of proportionality between the pressure difference in both ends of the DS $\Delta p_{pd.ds}(t)$ and signal $i(t)$; $k_{vf.ds}$, $k_{df.ds}$ – coefficient of viscous friction and dry (contact) friction of the DS; k_{sp} – coefficient of stiffness of the "flat mechanical feedback spring"; $m_s = m_{ol} + m_l$ – total mass of the OL and load; $k_{pd.pc}$ – proportionality gain coefficient between differential fluid pressure in PC cavities in the presence of factors causing change of fluid pressure, and in the absence of such factors; $k_{v.d.} = k_{vf.ol} + k_{dh.si}$ – sum of viscous friction coefficient of the OL $k_{vf.ol}$ and damping coefficient of the hydraulic cylinder (constant load simulator); $k_{d.e.s.} = k_{df.ol} + k_{el.si} + k_{sl}$ – sum of the dry friction coefficient of the OL $k_{df.ol}$, elasticity coefficient of the proportional load simulator $k_{el.si}$ and load stiffness coefficient k_{sl}.

5 Identification of Parameters of the Mathematical Model of the EHA and PC

Identification of the current values of the parameters of the mathematical model of the EHA and PC was carried out using LSM based on measurements of the output signals of the EHA and PC sensors after each aircraft flight [2]. The algorithm of the identification of parameter vectors $\hat{a}_{LSM}$ and $\hat{b}_{LSM}$ are represented in the following form:

$$\hat{a}_{LSM} = \left[a_1\ a_2\ a_3\right]^T = \left(H_{ds}^T \cdot H_{ds}\right)^{-1} \cdot H_{ds}^T \cdot X_{ds} \tag{3}$$

$$\hat{b}_{LSM} = \left[b_1\ b_2\ b_3\right]^T = \left(H_{ol}^T \cdot H_{ol}\right)^{-1} \cdot H_{ol}^T \cdot X_{ol} \tag{4}$$

where

$$H_{ds} = \begin{bmatrix} i(t_1) & \dot{x}_{ds}(t_1) & x_{ds}(t_1) \\ \ldots & \ldots & \ldots \\ i(t_N) & \dot{x}_{ds}(t_N) & x_{ds}(t_N) \end{bmatrix}; X_{ds} = \begin{bmatrix} \ddot{x}_{ds}(t_1) \\ \ldots \\ \ddot{x}_{ds}(t_N) \end{bmatrix};$$

$$H_{ol} = \begin{bmatrix} \Delta p(t_1) & \dot{x}_{ol}(t_1) & x_{ol}(t_1) \\ \ldots & \ldots & \ldots \\ \Delta p(t_N) & \dot{x}_{ol}(t_N) & x_{ol}(t_N) \end{bmatrix}; X_{ol} = \begin{bmatrix} \ddot{x}_{ol}(t_1) \\ \ldots \\ \ddot{x}_{ol}(t_N) \end{bmatrix}.$$

6 Determination of Diagnostic Signs of Faults of the EHA and PC

In articles [1, 2], estimates of parameters of vectors a and b of the mathematical model of the EHA and PC were obtained depending on the change of each coefficient of the influencing factors, upper and lower acceptable limits of parameters, as well as the change of average values of these parameters are obtained.

The obtained results show that:

- to change parameters a_1, a_2 and a_3 are most likely to be influenced by changes in coefficients $k_{pd.ds}$, $k_{vf.ds}$, k_{sp} and dynamic viscosity η;
- to change parameters b_1, b_2 and b_3 are most likely to be influenced by changes in coefficients k_{sp}, $k_{dh.si}$, $k_{el.si}$, indicates the presence of internal leakage of fluid k_{il} and bulk modulus of elasticity of liquid E.

7 Methodology of Detection of Faults in the EHA and PC

Detection of faults in the EHA and PC consists of analyzing the parameters of their mathematical models, the numerical value of which can be found in Eqs. (5)–(10). For the EHA, the diagnostic signs are the coefficients $k_{pd.ds}$, $k_{vf.ds}$, and k_{sp}, and for the PC are the coefficients $k_{pd.pc}$, $k_{dh.si}$, and $k_{el.si}$. Each diagnostic coefficient contains a certain physical property characterizing this or that fault. Diagnostic signs of faults and their relationship with diagnostic coefficients for the EHA and PC are presented in Table 1.

Table 1. Diagnostic signs of the EHA and PC.

	Diagnostic sign
EHA	$k_{pd.ds} = \frac{a_1 \cdot m_{ds}}{S_{ds}}$; (5) – Proportionality gain coefficient between the pressure difference in both ends of the DS in the EHA $\Delta p_{pd.ds}(t)$ and the control electric current signal $i(t)$: – indicates a problem with the electromagnetic converter of the EHA, which changes the speed of the armature movement, leads to changes in the fluid pressure in the spool cavities and the speed of the spool movement (e.g., due to the presence of air or water in the hydraulic fluid).
	$k_{vf.ds} = -\frac{a_2 \cdot \delta \cdot m_{ds}}{\eta \cdot l \cdot \pi \cdot d_{ds}}$; (6) – Coefficient of viscous friction of the DS: – indicates the presence of sticking or misalignment of the DS (there is a sharp but short-term increase in the coefficient), as well as the formation of scoring, sticking of metal crumbs on the edges of the spool pairs, or the presence of impurities in the hydraulic fluid, or the presence of changes in dynamic viscosity η due to temperature.
	$k_{sp} = -a_3 \cdot m_{ds} - k_{df.ds}$; (7) – The stiffness coefficient of the “flat mechanical feedback spring” in the EHA: – indicates a fault in the flat mechanical feedback spring (e.g., leakage in the spool due to mechanical wear of the seals or spool pair, or deviation of the spool from the neutral position, or change in spring elasticity).
PC	$k_{pd.pc} = \frac{b_1 \cdot m_s}{S_p}$; (8) – Coefficient of increasing proportionality between the differential pressure of the fluid in the cavities of the PC in the presence of factors that cause a change in fluid pressure, and in the absence of such factors: – indicates the presence of internal leakage of fluid k_{il} in the PC, or the change in fluid pressure due to leakage in the EHA, or the change in the bulk modulus of elasticity of the fluid E (e.g., due to temperature change), or the change in the external force.
	$k_{dh.si} = -b_2 \cdot m_s - k_{vf.ol}$; (9) – The damping coefficient of the hydraulic cylinder (constant load simulator): – indicates the presence of a change in the external force acting from the hydraulic cylinder.
	$k_{el.si} = -b_3 \cdot m_s - k_{df.ol} - k_{sl}$; (10) – Elasticity coefficient of the proportional load simulator: – indicates the presence of a change in the external force acting from the proportional load simulator (torsion bar).

8 Methodology of Recognition of Faults in the EHA and PC

To recognize faults in the EHA and PC, Shewhart diagnostic charts are used, constructed for individual diagnostic coefficients obtained from Eqs. (5)–(10).

Diagnostic charts are made by calculating the average values by subgroups of diagnostic coefficients. It is assumed that each subgroup of measurements has a sample volume $n_{samples} = 13$, which corresponds to 13 different simulated results of unit fault given a measurement condition of $n_{measurement} = 200$. Control value limits are calculated on the measure of variation [5] obtained from moving ranges. Preliminarily calculates the average range $\overline{R}$, on the basis of which the moving range chart is constructed. Also, for all data, calculate the average $\overline{\overline{k}}$ for each coefficient. Table 2 shows the formulas for calculating the control limits for the average and moving ranges of the diagnostic coefficients. The results of the diagnostic charts are shown in Figs. 1, 2, 3, 4, 5, 6, 7, 8, 9, 10, 11 and 12.

Table 2. Formulas for calculating control limits.

Statistics	Average value (CL)	Control limit	
		Upper (UCL)	Lower (LCL)
Individual value of diagnostic coefficients	$\overline{\overline{k}}$	$\overline{\overline{k}} + A_2 \cdot \overline{R}$	$\overline{\overline{k}} - A_2 \cdot \overline{R}$
Moving range R	$\overline{R}$	$D_4 \cdot \overline{R}$	$D_3 \cdot \overline{R}$

According to the sample size $n_{samples} = 13$, value $A_2 = 0,249$, $D_4 = 1,692$, $D_3 = 0,308$.

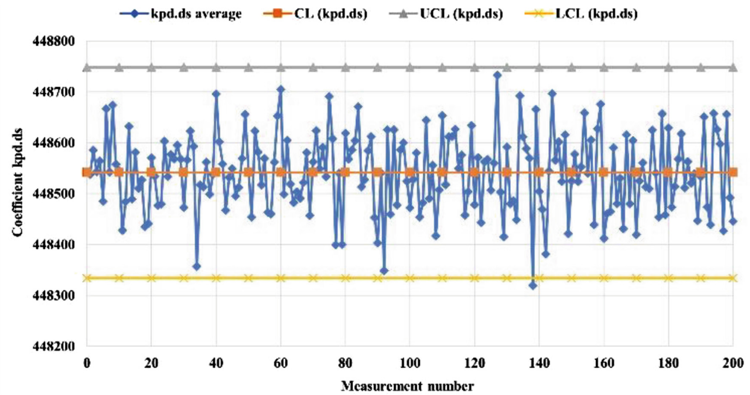

Fig. 1. Change of average value $k_{pd.ds}$

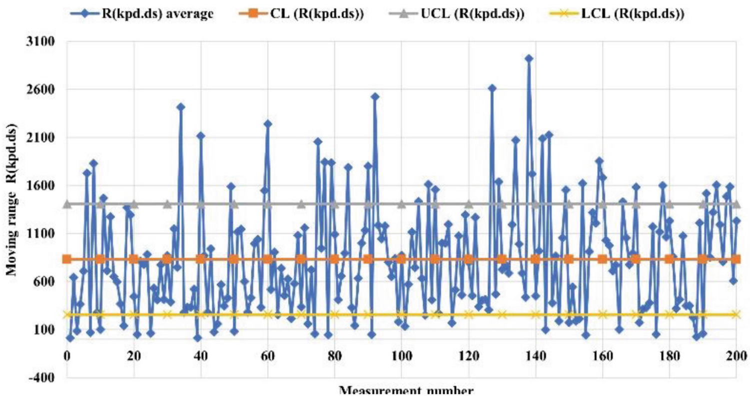

Fig. 2. Change of the range of the coefficient $k_{pd.ds}$

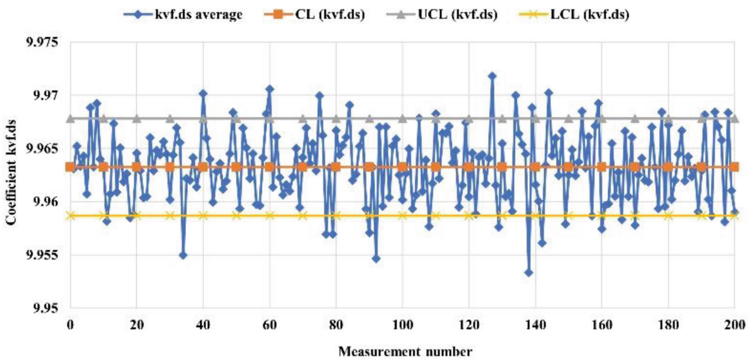

Fig. 3. Change of average value $k_{vf.ds}$

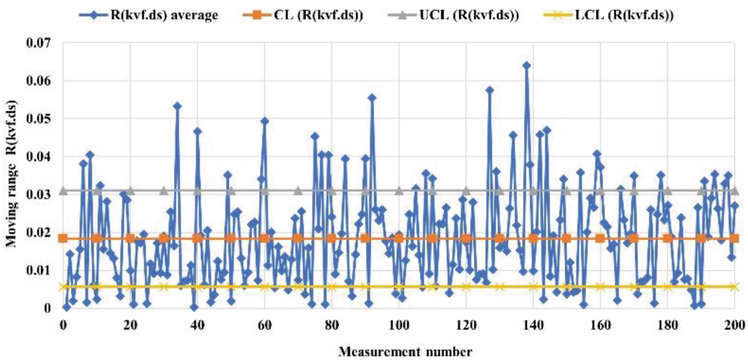

Fig. 4. Change of the range of the coefficient $k_{vf.ds}$

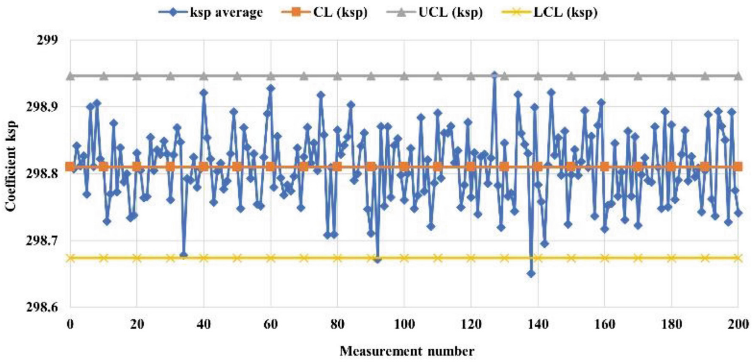

Fig. 5. Change of average value k_{sp}

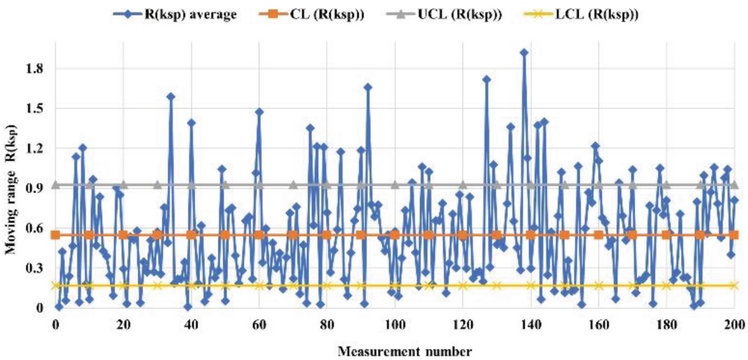

Fig. 6. Change of the range of the coefficient k_{sp}

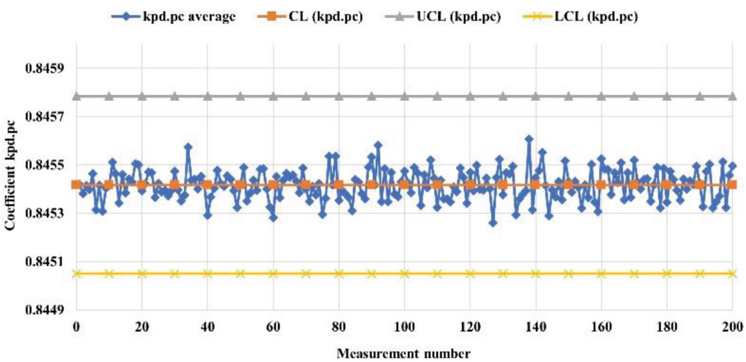

Fig. 7. Change of average value $k_{pd.pc}$

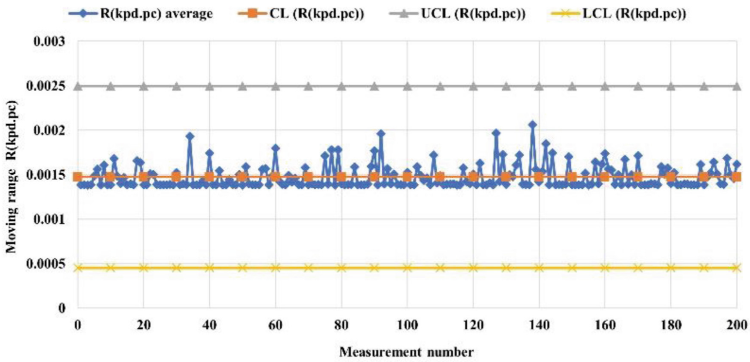

Fig. 8. Change of the range of the coefficient $k_{pd.pc}$

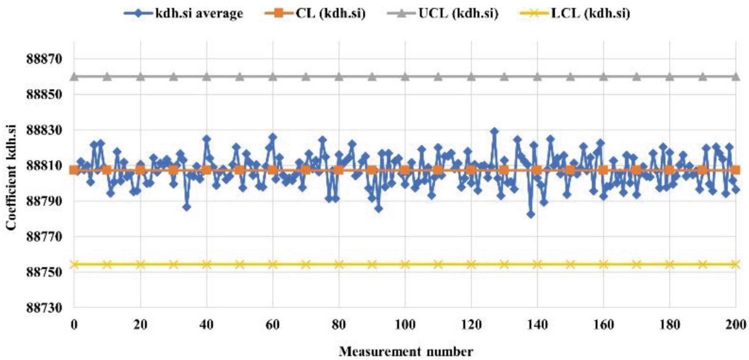

Fig. 9. Change of average value $k_{dh.si}$

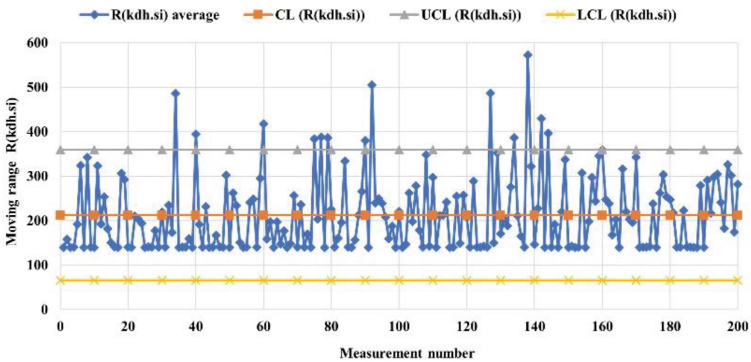

Fig. 10. Change of the range of the coefficient $k_{dh.si}$

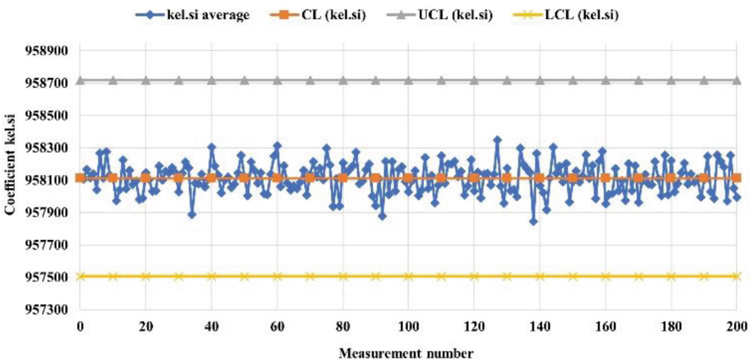

Fig. 11. Change of average value $k_{el.si}$

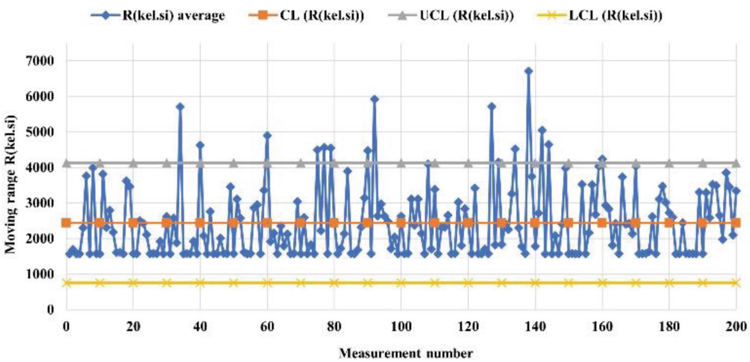

Fig. 12. Change of the range of the coefficient $k_{el.si}$

9 Hypothesis Testing and Determination of the Probability of Error Occurrence

When making decisions about the technical condition of the unit, the article performs hypothesis testing and determines the probabilities of occurrence of errors of the I and II types for the average values of diagnostic coefficients. An error of the first type occurs when the hypothesis is true but is rejected. An error of the second type occurs when the hypothesis is not true but is accepted (not rejected).

To determine the probability of occurrence of errors of the I type, it is assumed that the average permissible values of diagnostic coefficients are equal to μ_0. μ_0 – corresponds to the value for a serviceable unit (obtained when performed on the test bench).

The diagnostic charts used were sample size $n_{samples} = 200$ (corresponding to the number of measurements performed $n_{measurement} = 200$), average values μ_k, and variance σ_k^2 (standard deviations σ_k) for each coefficient.

The null hypothesis H_0 was tested, which is that the average value of diagnostic coefficients $\mu_k = \mu_0$. The alternative hypothesis H_1 is that $\mu_k \neq \mu_0$. If the significance level is $\alpha = 0,05$ (probability of a type first error), the hypothesis H_0 is accepted for the symmetric two-sided Student's t-criterion if $t_k = |\mu_k - \mu_0| \cdot \frac{\sqrt{n_{samples}}}{\sigma_k} < t_{1-\frac{\alpha}{2}}$. Otherwise, H_0 is rejected and H_1 is accepted.

To determine the probability of occurrence of the type II errors, it is assumed that hypothesis H_0 ($\mu_k = \mu_0$) is true. Then, if in reality $\mu_k \neq \mu_0$, we can calculate the power of the t-criterion, used in determining the probability of occurrence of type I errors, above (probability of the type II error is β). The power of this criterion is equal to $1 - \beta = P\left\{\left|\frac{\mu_\kappa - \mu_0}{\sigma_\kappa/\sqrt{n_{samples}}}\right| > t_{1-\frac{\alpha}{2}};\ \mu_\kappa = \mu_1\right\}$.

If the average value of the diagnostic coefficients is μ_0 and by assumption σ_k, $\alpha = 0,05$ and $\nu = n - 1 = 199$, the power of the two-sided criterion with respect to the mean μ_1, is calculated as follows:

$$1 - \beta \approx P\{U_1 \leq u_1\} + P\{U_2 \leq u_2\} \tag{11}$$

where

$$u_{1,2} = \frac{t_{\alpha/2} \mp \lambda}{\sqrt{1 + \frac{t_{\alpha/2}^2}{2 \cdot \nu}}};\ \lambda = \frac{\mu_1 - \mu_0}{\sigma_\kappa/\sqrt{n}}.$$

The results of hypothesis testing are summarized in Table 3 and Table 4.

Table 3. Results of hypothesis testing and determination of the occurrence of the type I error

Coefficients	Value from diagnostic charts		Average permissible value μ_0	t_k	$t_{1-\frac{\alpha}{2}}$	Range of coefficient values
	Average value μ_k	Standard deviation σ_k				
$k_{pd.ds}$	448541,369	76,218	448537,743	0,67	1,96	448527,1798 < … < 448548,3062
$k_{vf.ds}$	9,96325	0,003	9,96309	0,67	1,96	9,96262 < … < 9,96356
k_{sp}	298,810	0,055	298,807	0,67	1,96	298,7998 < … < 298,8150
$k_{pd.pc}$	0,845417	6,321E−05	0,845420	0,57	1,96	0,8454112 < … < 0,8454287
$k_{dh.si}$	88807,266	8,631	88806,807	0,75	1,96	88805,6103 < … < 88808,0027
$k_{el.si}$	958111,521	93,888	958106,554	0,75	1,96	958093,5414 < … < 958119,5658

Table 4. Results of hypothesis testing and determination of the occurrence of the type II error

Coefficients	Value from diagnostic charts		Average permissible value μ_0	u_1	u_2	β	1 − β
	Average value μ_1	Standard deviation σ_k					
$k_{pd.ds}$	448548	76,218	448537,743	−3,845	−0,057	0,5239	0,4761
$k_{vf.ds}$	9,9635	0,003	9,96309	−3,646	−0,255	0,6026	0,3974
k_{sp}	298,8	0,055	298,807	−3,849	−0,052	0,5199	0,4801
$k_{pd.pc}$	0,845428	6,321E-05	0,845420	−3,747	−0,154	0,5569	0,4431
$k_{dh.si}$	88807,95	8,631	88806,807	−3,815	−0,086	0,5359	0,4641
$k_{el.si}$	958119	93,888	958106,554	−3,816	−0,085	0,5359	0,4641

10 Conclusion

The article identified the current values of the parameters of the mathematical model of the EHA and PC of the AR20N unit and determined the diagnostic signs that have the most probable influence on the change of parameters. Shewhart diagnostic charts for diagnostic coefficients and methods of detection and recognition of faults of the unit are developed. Hypothesis testing was performed and probabilities of occurrence of the I and II types errors were determined when making decisions on the technical condition of the unit.

References

1. Tran, M.H.: Simulation model of the steering unit AR20N with PID controller. In: Proceedings of 27th International Scientific Conference. Transport Means 2023 (Part I), pp. 207–213 (2023)
2. Tran, M.H.: Identification of parameters of mathematical models and determination of diagnostic features. Aerosp. Tech. Technol. **4**(Sup1. (189)), 75–84 (2023)
3. Himmelblau, D.M.: Fault Detection and Diagnosis in Chemical and Petrochemical Processes. Elsevier Publishing Company, New York (1978)
4. Iserman, R.: Fault–Diagnosis Applications. Model–Based Condition Monitoring: Actuators, Drives, Machinery, Plants, Sensors and Fault–Tolerant Systems. Springer, New York (2011). https://doi.org/10.1007/978-3-642-12767-0
5. Himmelblau, D.M.: Process Analysis by Statistical Methods. Wiley, New York (1970)
6. Montgomery, D.C: Introduction to Statistical Quality Control, 7th edn. Wiley, New York (2013)
7. Scheaffer, R.L., Mulekar, M.S., McClave, J.T.: Probability and Statistics for Engineers, 5th edn. Cengage Learning, Boston (2011)

Methods for Time Series Analysis Using Segmented Regression with Heteroskedasticity

Valeriyi Kuzmin[1], Olga Ivanets[1], Maksym Zaliskyi[1](✉), Olga Shcherbyna[1], Oleksii Holubnychyi[1], and Oksana Sevriukova[2]

[1] National Aviation University, Liubomyra Huzara Avenue 1, Kyiv 03058, Ukraine
maximus2812@ukr.net

[2] National Technical University "Kharkiv Polytechnic Institute", Kyrpychova Street 2, Kharkiv 61002, Ukraine

Abstract. The paper considers the problem of building and choosing the best mathematical model for describing the time series of the dependence of the airline's profit on the received revenue, taking into account the costs of aviation safety. The development of adequate forecasting models will make it possible to use available resources to achieve production goals of airlines while simultaneously solving aviation safety challenges. Several variants of approximation algorithms are considered. The first algorithm is based on the use of cluster analysis technologies. At the same time, visual analysis of the time series became a prerequisite for choosing three clusters for grouping data. A separate group linear approximation for each of the clusters made it possible to calculate the preliminary values of the abscissas of the breakpoint. The second approximation algorithm is based on the use of a three-segmented linear approximation. To find the optimal abscissa of the breakpoint, a three-dimensional optimization paraboloid was used. For the final approximation of the researched time series, the heteroskedasticity index was taken into account. The resulting final version of the approximation was used to solve forecasting problems.

Keywords: Data Processing · Time Series · Approximation · Segmented Linear Regression · Optimization of Abscissas of Breakpoint · Optimization Paraboloid

1 Introduction

1.1 Introduction to the Problem

Time series are widely used in signal processing, pattern recognition tasks, automatic control, and in many other areas of applied engineering. The time series analysis allows to determine the quantitative characteristics of the process that gave rise to this time series (frequency-time characteristics of the signal, its energy, etc.); to decompose the time series into elementary components in order to further analyze their quantitative characteristics and quantitatively compare time series to determine similarities and differences between the processes that generated them. The classic approach to time series signal processing is to use spatio-temporal, frequency, and time-frequency signal processing methods [1].

M. Nechyporuk et al. (Eds.): ICTM 2023, LNNS 1008, pp. 501–512, 2024.
https://doi.org/10.1007/978-3-031-61415-6_43

Separately, it is necessary to highlight the tasks of analysis and forecasting based on time series, which in turn make up four categories: statistical, machine learning, pattern recognition and sentiment analysis. A common approach to forecasting time series is a combination of several methods from the groups mentioned above [2]. Therefore, in the proposed paper, mathematical modeling is used to describe time series in order to build a forecasting model of airline revenues for planning safety management system measures.

The use of statistical methods of time series analysis allows providing the ability to connect the components of objects and phenomena using mathematical dependencies and formulas [3]. The mathematical models building allows:

– to understand the objects or phenomena;
– to analyze the phenomena with mathematical tools;
– to perform studies with the model based on statistical simulation [4].

The basis for mathematical models building is experimental study of objects. In this research, the dependence of the revenue received by the airline on its profit was used as the initial data for building a mathematical model. Obtained data provide the ability to formulate mathematical relationships. Usually, to build the best mathematical model, it is necessary to consider the alternative variants. The main criteria to choose the best model are:

a) mathematical formulas simplicity with required accuracy,
b) minimal quantity of different parameters in mathematical formulas,
c) minimal standard deviation between results of measurement and predicted values and others [4, 5].

1.2 Motivation

In the econometrics problems, it is very often necessary to analyze time series in order to build optimal mathematical models. There are time series, which are considered as non-stationary random processes with a rapidly changing structure. To describe time series of this type, elements of regression analysis, splines, moving averages, harmonic analysis, and others are used [6, 7]. However, for a more correct solution of forecasting problems, it is necessary to use new approaches and algorithms [8, 9]. One of such algorithms can be the use of segmented regression.

In order to increase approximation accuracy while using segmented models, it is also necessary to take into account heteroskedasticity. An analysis of the literature shows that enough attention is paid to the issues of mathematical models building based on regression analysis with taking into account heteroskedasticity [10, 11]. At the same time, heteroskedasticity has become a generally recognized fact and it must be taken into account in the problems of regression analysis. If heteroskedasticity is not taken into account (if it actually takes place), estimates of unknown coefficients of the approximating function become less effective.

To solve approximation problems, the ordinary least squares (OLS) method and the weighted least squares (WLS) method are used [11]. However, in econometric problems, the variances of each observations are usually unknown, and therefore there is a problem of finding weight coefficients to take into account heteroskedasticity. There are different approaches to the calculation of weight coefficients, and these approaches are not methodically formalized.

Therefore, this paper solves the actual scientific and technical problem of choosing the best mathematical model for describing econometric data of airlines with taking into account heteroskedasticity.

1.3 Contribution

The goal of this paper is to show the example of data processing while model building for given empirical data. The step-by-step procedure for building and choosing the best mathematical model is shown in the methods and materials section and new approach of determining heteroskedasticity are presented for numerical example of calculation.

1.4 The Organization of the Paper

The paper is organized as follows: Sect. 1 discusses background information. Section 2 highlights related works. Section 3 discusses the method of segmented regression building with optimization of breakpoint abscissas. Section 4 introduces the approach for heteroskedasticity calculation and its taking into account while models building. Sections 5 and 6 present the conclusions and future scope.

2 Literature Review

At the recent stage of science development, regression analysis is a research tool while models building [5, 7]. The techniques of regression analysis help to determine mathematical formula for one or more random variables realization in time [12]. During time series study, regression analysis provides the ability to forecast random variable values using information on its previous behavior.

The advantages of regression analysis allowed using corresponding techniques in many industrial and scientific applications:

- in biology: to describe different biological processes [13];
- in econometrics: to build mathematical model of economics parameters for various countries or cities dependent on different factors [14];
- in cybersecurity: to describe the network traffic behavior [15];
- in radio engineering: to build mathematical model of radio signals [16];
- for navigation systems: to solve the problem of configuration analysis of Ukrainian flight routes network [17, 18];
- in maintenance theory: to describe the basic parameters of maintenance and repair [19, 20];
- during equipment operation: for model building of equipment diagnostic variables in case of technical condition deterioration [21];
- for control systems: to find the dependence between statistical data observed during unmanned aerial vehicles control [22, 23];
- for aircraft systems: to analyze the efficiency of operation of onboard equipment using different information processing techniques [24];

– for evaluation of complex objects with stochastic parameters in biomedicine [25].

To build mathematical models, researchers usually use linear and nonlinear regressions [7, 26]. There are polynomial (usually quadratic or cubic), logistic, exponential and segmented regressions among nonlinear type [8]. Literature review gives the possibility to conclude that not enough attention is paid to increasing the accuracy of mathematical model based on determining the optimal breakpoints for segmented regression. Some attempts were made using applied programs to solve this problem, but concrete mathematical formulas at the same case are not discussed.

A review of relevant literature shows a gap in research devoted to the increasing the accuracy of segmented regression usage based on abscissas of breakpoint calculation and taking into account heteroskedasticity.

3 Materials and Methods

To increase the level of safety in the conditions of modern challenges, a systematic and comprehensive approach to risk management for flight safety is necessary. Systemic flight safety management is based on risk and predictability, which combines elements of quality management and risk management into an integrated system, and helps aviation operators: identify threats and associated risks that affect the entire organization; monitor, report and review such risks; ensure the quality of products and services, adhering to standards; constantly improve products and services. Establishing the causes of aviation events helps to understand the mechanism of interaction of organizational and management factors that lead to the event. In the aviation system, various means of protection are built in against improper actions or erroneous decisions at all levels of this system (i.e., at the workplaces of direct performers and only at the level of administrators). This model shows that although organizational factors, including management decisions, may create hidden conditions capable of leading to an event, they simultaneously strengthen the system's defenses [27]. Even in the most effectively managed organizations, most hidden unsafe conditions are created by decision makers. Subjectivity and limitations are characteristics of these individuals, and they are also affected by the very real constraints imposed by time, budget, politics, etc. Since some number of such dangerous decisions cannot be prevented, it is necessary to make steps to identify and mitigate their adverse consequences [25].

Flight safety is the state in which the risk of harm or damage is reduced to an acceptable level. Sources of threats, which constitute a risk, become obvious after cases of obvious failure in ensuring security.

An analysis of the management process for flight safety risk consists of the following stages:

1. Identification of sources of danger. The service provider shall develop and implement a process to identify the sources of hazards associated with its aviation products or services. Identification of sources of danger should be based on a combination of reactive and proactive methods.
2. Risk assessment and mitigation. The service provider must develop and maintain a process to ensure the analysis, assessment of the flight safety risks associated with

identified hazards. To ensure this procedure, this stage in turn, is divided into the following components: the process of identifying sources of danger, their analysis and identification; the reporting process in the field of flight safety and storage of mandatory and voluntary notifications in the database [25].

The effectiveness of the listed stages lies in the identification of dangers associated with human and organizational factors. Since they are included in the general list of hazards necessary for consideration, namely: possible scenarios for the development of aviation events, human and organizational factors, corporate solutions and business processes, by third-party organizations.

Although organizational factors, including management decisions, can create hidden conditions that can lead to an accident. Managing a profitable and at the same time safe airline or service organization requires a constant balance between the need to achieve production goals and the simultaneous solution of flight safety issues. The production environment in aviation is saturated with potentially unsafe conditions that cannot be completely eliminated; however, flights must continue.

Consider an example of a time series regarding of the dependence of the airline's profit on the received revenue, taking into account the costs of aviation security. This time series was described by linear regression using OLS during analysis in [10]:

$$y(x) = -1.082 + 0.118x. \tag{1}$$

The choice of linear regression (1) was justified by the fact that the correlation coefficient is 0.958. However, a more detailed statistical analysis based on the use of the linearity test showed that the observed data are non-linear with a probability of 0.95.

As an alternative option, a parabola of the second degree can be taken as mathematical model [10]

$$y(x) = 0.202 - 0.0525x + 0.00511x^2. \tag{2}$$

The graphical representation of single linear (1) and quadratic (2) OLS mathematical models are shown in Fig. 1. The standard deviations for the linear and quadratic mathematical models are 0.189 and 0.15, respectively.

Although a straight line can be chosen as approximation function due to the fact that the correlation coefficient is quite large, however, even visual analysis shows that the initial data can be divided into three segments: 1) a monotonous decrease, 2) stabilization (in in our case is four to five years), 3) a monotonous increase. The paper [10] also considers a two-segmented linear regression, which was chosen as the best one:

$$y(x) = 1.168 - 0.098x + 0.236(x - 11.2)h(x - 11.2), \tag{3}$$

where $h(x)$ is the Heaviside step function.

As an alternative, consider a more accurate approximation method based on three-segmented linear regression. A visual analysis of observed data shows that three segments can be distinguished in their structure: decrease, stabilization, and increase. In this case, the stabilization period includes 4–5 years. Such a model can become typical for describing the dependence of financial profit on total revenue for enterprises in the countries with after crisis economies. For approximation using segmented regressions, it

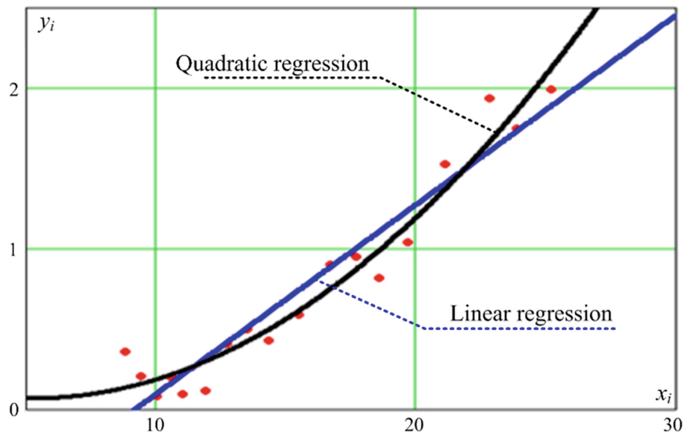

Fig. 1. Linear and quadratic functions as mathematical models.

is necessary to solve the optimization problem of finding the optimal abscissas of breakpoint. Optimizing the abscissa of the breakpoint will especially improve the predictive properties of the approximating function [28]. In the first approximation, the abscissas of the breakpoint can be found using following technique. As a result of visual analysis, the following clusters of data points can be distinguished: 1) from the first to the fifth; 2) from the second to the sixth; 3) from the fifth to the eighteenth.

The points of each cluster are approximated using straight lines and OLS method:

$$y_1(x) = 1.138 - 0.095x, y_2(x) = 0.402 - 0.025x, y_3(x) = 1.480 + 0.138x. \quad (4)$$

Determine the intersection points of the first and second equations, as well as the second and third equations. As a result, we get abscissas of breakpoint $x_{br1} = 10.424$, $x_{br2} = 11.585$. These values can be taken as preliminary values of the abscissas of breakpoint. Let the ranges of change of breakpoint abscissas are $x_{br1} = \{9.92;\ 10.17;\ 10.42;\ 10.67;\ 10.92\}$ and $x_{br2} = \{11.08;\ 11.33;\ 11.58;\ 11.83;\ 12.08\}$. The width of the change range is only five points.

The three-segmented regression equation with two breakpoints in general form is:

$$y(x) = a_0 + a_1x + a_2(x - x_{br1})_+ + a_3(x - x_{br2})_+, (x - x_{br1})_+ = (x - x_{br1})h(x - x_{br1}), \quad (5)$$

where a_0, a_1, a_2, a_3 are constant coefficients.

In this case, for 25 possible values of the abscissa of breakpoint, the sum of squared deviations was calculated, which made it possible to construct a three-dimensional optimization paraboloid of the following form [28]

$$S(x_{br1}, x_{br2}) = b_0 + b_1x_{br1} + b_2x_{br1}^2 + b_3x_{br2} + b_4x_{br2}^2 + b_5x_{br1}x_{br2}, \quad (6)$$

where b_0, …, b_5 are the constant coefficients of the paraboloid need to be calculated. The optimization paraboloid equation has the form

$$S(x_{br1}, x_{br2}) = 1.28 + 0.16x_{br1} - 0.011x_{br1}^2 - 0.324x_{br2} + 0.01x_{br2}^2 + 0.00772x_{br1}x_{br2}, \quad (7)$$

Find the values of the optimal abscissas of breakpoint. To do this, we determine the partial derivatives for Eq. (7) and equate them to zero. After solving the system of linear equations, we obtain.

$$x_{br1} = \frac{-b_1 - b_5 x_{br2}}{2b_2} = 10.901, x_{br2} = \frac{2b_2 b_3 - b_5 b_1}{b_5^2 - 4b_2 b_4} = 11.543. \quad (8)$$

The optimal three-segmented regression equation without heteroskedasticity, i.e. using only the OLS method has the following form:

$$y(x) = 1.180 - 0.100x + 0.128(x - 10.901)_+ + 0.110(x - 11.543)_+. \quad (9)$$

The Eq. (9) will be called the base equation. Such an equation is obtained for the zero heteroskedasticity index and all weight coefficients equaled to one. The result of model building is shown in Fig. 2. The calculation of the critical value for the linearity test (which in this case is 8.6496) confirmed the non-linearity of the initial data with even greater probability. At the same time, the standard deviations for the optimal three-segmented regression is 0.139.

The use of segmented regression (9) is explained by the fact that three intervals of the development of time series can be distinguished, which correspond to decrease, stabilization and increase.

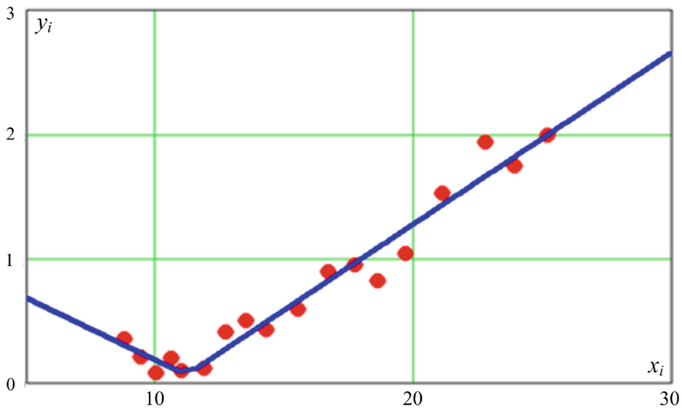

Fig. 2. Approximation of initial data using three-segmented linear regression.

4 Heteroskedasticity Analysis

The literature review shows that taking into account heteroskedasticity improves the approximation accuracy, especially in the case of solving forecasting problems [7, 11]. Therefore, we calculate the heteroskedasticity parameter.

In this paper, we discuss two methods for heteroskedasticity accounting. The first method is based on the use of cluster analysis and the corresponding average values of clusters. The second method is based on a new approach of determining heteroskedasticity parameter.

1. Consider the first method in more detail. Visual analysis and classical clustering rules make it possible to identify five clusters, which are shown in Fig. 3. Two clusters have the same points. For each of the clusters, cluster means and standard deviations were calculated.

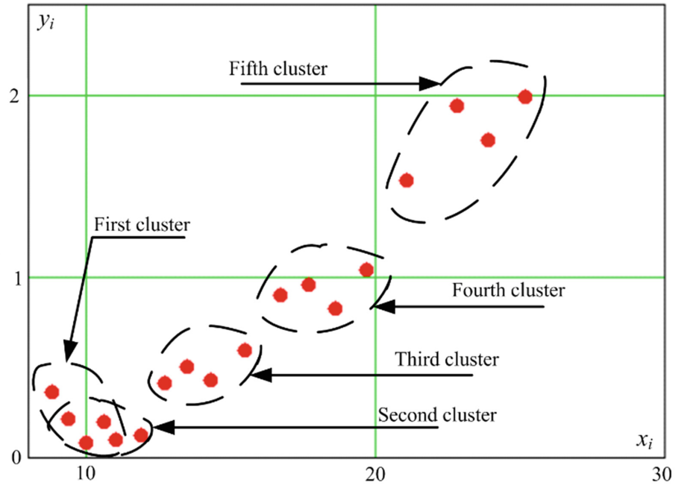

Fig. 3. Clusters formation.

These data are approximated using the linear function and OLS method. The result is heteroskedasticity equation of the following form

$$\sigma(m) = 0.05404 + 0.06135\,\text{m}. \tag{10}$$

The weight coefficients will be calculated by the formula

$$W_i = \left(\frac{\overline{\sigma}}{\sigma(x_i)}\right)^2, \tag{11}$$

where $\overline{\sigma}$ is the average standard deviation for all clusters, $\sigma(x_i)$ is the current standard deviation for the empirical point x_i calculated using the heteroskedasticity equation.

Then the mathematical model with taking into account the heteroskedasticity for the first method will take the form

$$y(x) = 1.135 - 0.092x + 0.113(x - 10.901)_+ + 0.112(x - 11.543)_+. \tag{12}$$

2. For the second method for taking into account heteroskedasticity, we use the three-segmented linear regression equation as a base equation.

The weight coefficients will be calculated according to the formula:

$$W_i = \left(\frac{\overline{y}}{y(x_i)}\right)^h, \tag{13}$$

where $\overline{y}$ is the arithmetic mean for all initial values, $y(x_i)$ is the current value determined according to the base equation, h is the heteroskedasticity parameter. The weighted sums of squared deviations were calculated for the different values of the heteroskedasticity parameter. We approximate calculated data with a parabola of the second degree using the OLS method:

$$S(h) = 0.271 - 0.070\,\mathrm{h} + 0.107\,\mathrm{h}^2. \tag{14}$$

The minimum of this parabola corresponds to the optimal value of the heteroskedasticity parameter. The result is $h_{\mathrm{opt}} = 0.326$.

Then the optimal mathematical model with taking into account the heteroskedasticity for the second method will take the form

$$y(x) = 1.137 - 0.095x + 0.134(x - 10.901)_+ + 0.098(x - 11.543)_+. \tag{15}$$

Figure 4 shows the results of the approximation using two methods for taking into account the heteroskedasticity.

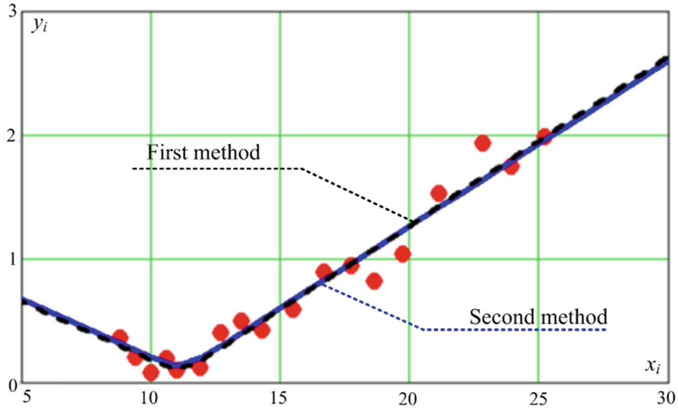

Fig. 4. Approximation of initial data using three-segmented linear regression with taking into account the heteroskedasticity.

5 Results and Discussions

In the analyzed example, taking into account the heteroskedasticity parameter for the two methods slightly changed the coefficients of the mathematical model. The standard deviations for the first and second method are approximately equal to 0.139. The resulting equations for the first and second methods of taking into account the heteroskedasticity almost coincide. This is because the heteroskedasticity indicator was not significant enough. However, there are some econometric tasks in which it achieves $h = 2$ and this significantly affects the final mathematical model, especially for forecasting purposes.

Taking heteroskedasticity into account can be considered as one of the options for constructing a robust regression. At the same time, each sample value of the primary dataset is assigned a certain weight coefficient. Naturally, for small values of the sample population, this coefficient equals to large values, and for large values of the sample population, the coefficient is usually less than one. This situation corresponds to the case of a nonstationary time series with a linearly increasing variance.

The analysis of the existing methods of accounting for heteroskedasticity showed that there is still no single standardized approach to the calculation of weight coefficients. In certain cases, these coefficients are determined even on the basis of subjective analysis of the available dataset. Therefore, the proposed procedure can be used as a basis for a methodical approach to determining these coefficients and estimating the degree of heteroskedasticity in the trend of statistical data.

The proposed procedure for building a mathematical model of time series taking into account heteroskedasticity can also be used for various real-world examples, in particular for the analysis of determining parameters and reliability indicators during the operation of technical complexes in cases of deterioration of their condition, analysis of trends in stock and currency quotations, analysis of medical data to detect diseases and others.

6 Conclusions

The paper analyzes the peculiarities of the formation of the safety management system in combination with taking into account the profit and income of the airline industry. The proposed intelligent analysis of retrospective data made it possible to determine an adequate mathematical model for forecasting the level of profit from the revenues of the airline company for the possibility of choosing the optimal strategy of the flight safety management system. The paper considers the problem of constructing and choosing the best mathematical model to describe the statistical dependence of the airline's profit on the received revenue, taking into account the costs of aviation security. Analytical expressions are obtained for mathematical models for various approximating functions without and with taking into account the heteroskedasticity parameter. The three-segmented linear regression has minimum value of standard deviation and better represents the geometrical structure of initial data, so it has been chosen as the basic function for heteroskedasticity analysis.

To take into account the heteroscedasticity, two methods have been proposed. The first method is based on clustering technique and weight coefficients calculation using each clusters standard deviation value. The second method is based on heteroskedasticity parameter determining using heuristic approach. The both methods have given the possibility to minimize the weighted sum of squared deviations and therefore to increases the accuracy of model.

The research results can be used to build more correct mathematical models under heteroskedasticity conditions.

7 Future Scope

Future scope of this research are as follows:

- statistical simulation for efficiency estimation of heteroskedasticity calculation;
- comparative analysis of proposed method for taking into account the heteroskedasticity with existing ones;
- comparative analysis of forecasting properties of mathematical model without and with taking into account the heteroskedasticity;
- formulation of methodology for calculating breakpoint abscissas for segmented regression.

References

1. Brockwell, P. J., Davis, R. A.: Time Series: Theory and Methods. Springer, New York (1991). https://doi.org/10.1007/978-1-4419-0320-4
2. Banwatth-Kuhn, M., Sindi, S.: How and why to build a mathematical model: a case study using prion aggregation. J. Biol. Chem. **295**(15), 5022–5034 (2020)
3. Davis, P.J.: Interpolation and Approximation. Dover Publications, New York (1975)
4. Himmelblau, D.M.: Process Analysis by Statistical Methods. Wiley, New York (1970)
5. Ryan, T.: Modern Regression Methods, 2nd edn. Wiley, New York (1997)
6. Kuzmenko, N.S., Ostroumov, I.V., Marais, K.: An accuracy and availability estimation of aircraft positioning by navigational aids. In: 5th International Conference on Methods and Systems of Navigation and Motion Control, Kyiv, Ukraine, pp. 36–40. IEEE (2018)
7. Weisberg, S.: Applied Linear Regression. Wiley, New York (2005)
8. Seber, G.A.F., Wild, C.J.: Nonlinear Regression. Wiley, New York (2003)
9. Solomentsev, O.V., Zaliskyi, M.Yu., Zuiev, O.V., Asanov, M.M.: Data processing in exploitation system of unmanned aerial vehicles radioelectronic equipment. In: IEEE 2nd International Conference Actual Problems of Unmanned Air Vehicles Developments, Kyiv, Ukraine, pp. 77–80. IEEE (2013). https://doi.org/10.1109/APUAVD.2013.6705288
10. Kuzmin, V.M., Lapach, S.M.: Use of polygonal regression in economic research. Econ. Manag. **3**, 79–84 (2004). (in Ukrainian)
11. Kaufman, R.L.: Heteroskedasticity in Regression. SAGE Publications, Thousand Oaks (2013)
12. Atkinson, A., Riani, M.: Robust Diagnostic Regression Analysis. Springer, New York (2000). https://doi.org/10.1007/978-1-4612-1160-0
13. Radonja, P., Stankovic, S., Matovic, B., Drazic, D.: Regional models for biological processes based on linear regression and neural networks. In: 8th Seminar on Neural Network Applications in Electrical Engineering, Belgrade, Serbia, pp. 189–193. IEEE (2006)
14. Wang, Y.: Linkages between metropolitan economy and modem logistics based on linear regression analysis. In: International Conference on Economic Management and Model Engineering, Chongqing, China, pp. 64–67. IEEE (2020). https://doi.org/10.1109/ICEMME51517.2020.00019
15. Zaliskyi, M., Odarchenko, R., Gnatyuk, S., Petrova, Y., Chaplits, A.: Method of traffic monitoring for DDoS attacks detection in e-health systems and networks. In: CEUR Workshop Proceedings, vol. 2255, pp. 193–204 (2018)
16. Zuiev, O., Petrova, J.: Efficiency analysis of control and regulation processes in modern surveillance systems. In: 9th International Conference on Advanced Computer Information Technologies, Ceske Budejovice, Czech Republic, pp. 9–12. IEEE (2019). https://doi.org/10.1109/ACITT.2019.8780091

17. Ostroumov, I.V., Kuzmenko, N.S.: Accuracy assessment of aircraft positioning by multiple radio navigational aids. Telecommun. Radio Eng. **77**(8), 705–715 (2018)
18. Ivashchuk, O., et al.: A configuration analysis of Ukrainian flight routes network. In: International Conference on The Experience of Designing and Application of CAD Systems, Lviv, Ukraine, pp. 6–10. IEEE (2021). https://doi.org/10.1109/CADSM52681.2021.9385263
19. Okoro, O.C., et al.: Optimization of maintenance task interval of aircraft systems. Int. J. Comput. Netw. Inf. Secur. **14**(2), 77–89 (2022). https://doi.org/10.5815/ijcnis.2022.02.07
20. Solomentsev, O., et al.: Method of optimal threshold calculation in case of radio equipment maintenance. In: Shukla, S., Gao, X.Z., Kureethara, J.V., Mishra, D. (eds.) Data Science and Security. LNNS, vol. 462, pp. 69–79. Springer, Singapore (2022). https://doi.org/10.1007/978-981-19-2211-4_6
21. Solomentsev, O., Zaliskyi, M., Zuiev, O.: Estimation of quality parameters in the radio flight support operational system. Aviation **20**(3), 123–128 (2016). https://doi.org/10.3846/16487788.2016.1227541
22. Sushchenko, O., et al.: Algorithms for design of robust stabilization systems. In: Gervasi, O., Murgante, B., Hendrix, E.M.T., Taniar, D., Apduhan, B.O. (eds.) ICCSA 2022. LNCS, vol. 13375, pp. 198–213. Springer, Cham (2022). https://doi.org/10.1007/978-3-031-10522-7_15
23. Dergachov, K., et al.: GPS usage analysis for angular orientation practical tasks solving. In: International Conference on Problems of Infocommunications. Science and Technology, Kharkiv, Ukraine, pp. 187–192. IEEE (2022). https://doi.org/10.1109/PICST57299.2022.10238629
24. Solomentsev, O., Zaliskyi, M., Kozhokhina O., Herasymenko, T.: Efficiency of data processing for UAV operation system. In: IEEE 4th International Conference Actual Problems of Unmanned Aerial Vehicles Developments, Kyiv, Ukraine, pp. 27–31. IEEE (2017). https://doi.org/10.1109/APUAVD.2017.8308769
25. Ivanets, O., Morozova, I., Burichenko M., Kvach, Y.: Actual aspects of flight safety on the basis of measuring electrical indicators. In: International Scientific Symposium on Metrology and Metrology Assurance, Sozopol, Bulgaria, pp. 1–4. IEEE (2021). https://doi.org/10.1109/MMA52675.2021.9610872
26. Kharchenko, V.P., Kuzmenko, N.S., Ostroumov, I.V.: Identification of unmanned aerial vehicle flight situation. In: IEEE 4th International Conference on Actual Problems of Unmanned Aerial Vehicles Developments, Kyiv, Ukraine, pp. 116–120. IEEE (2017). https://doi.org/10.1109/APUAVD.2017.8308789
27. Ostroumov, I.V., Kuzmenko, N.S., Marais, K.: Optimal pair of navigational aids selection. In: IEEE 5th International Conference on Methods and Systems of Navigation and Motion Control, Kyiv, Ukraine, pp. 32–35. IEEE (2018). https://doi.org/10.1109/MSNMC.2018.8576293
28. Al-Azzeh, J., et al.: A method of accuracy increment using segmented regression. Algorithms **15**(10), 1–24 (2022). https://doi.org/10.3390/a15100378

Two Factor Dispersion Analysis of the Capacitive Grain Moisture Meters' Transfer Function

O. V. Zabolotnyi(✉), V. A. Zabolotnyi, and N. D. Koshevoy

National Aerospace University "Kharkiv Aviation Institute", Kharkiv 61070, Ukraine
o.zabolotnyi@khai.edu

Abstract. Moisture content in many cases determines the consumer properties of different food products. The main task of the study was to analyze robustness for the two types of the transfer function for the capacitive grain moisture meter when working with different types of grain. To check the robustness of the transfer function, we applied dispersion analysis. For both transfer functions we can choose two factors: influence of moisture content, and influence of grain type, which is of a special interest. Besides, the values of repeatability and adequacy dispersions for both of the transfer functions were calculated. The values of the repeatability and adequacy dispersions for the new transfer function were approximately three times smaller, and F-test values were seven times smaller, proving its' better workability.

Keywords: moisture measurement · capacitive sensor · direct comparison · robust transfer function · two factor dispersion analysis

1 Introduction

The grain industry in Ukraine has always been and remains a leader in the agricultural sector. Grain production is one of the budget-forming branches of the agrarian sector with strong export potential and dynamically developing. The level of grain production development is one of the most important indicators of the country's economy. It directly affects the material well-being of the population, is an object of foreign trade, and is a determining factor in the country's food security. And grain moisture is one of the main factors affecting the duration of storage without possible damage and loss [1–6]. It is reasonable that grain producers always try to use its food potential most fully, especially peripheral components and fetuses, as a source of valuable nutrients. However, the grain processing industry implements a list of technologies for that purpose [7–9].

Most European countries have already changed their local standards for moisture meters following international recommendation OIML R59 "Moisture Meters for Cereal Grain and Oilseeds" [10], which restricts the maximal permissible value of moisture content uncertainty to not more than 3% of relative full-scale error. From the other hand, even the most popular laboratory moisture meters like Kett, AgraTronix, Isoelectric, and Next Instruments series have a significant accuracy decrease when determining moisture in different kinds of grains of the same type, for example, in different kinds of wheat.

M. Nechyporuk et al. (Eds.): ICTM 2023, LNNS 1008, pp. 513–524, 2024.
https://doi.org/10.1007/978-3-031-61415-6_44

An extensive list of factors influences the accuracy of capacitive moisture meters in different bulk substances [11, 12]. Besides, grain products' physical and chemical composition depends not only on the grains' type but the origin and ways of cultivation, storage, and processing – factors that can hardly be predicted [13].

That's why the development of the new methods of moisture measurement, which can be less sensitive to the change of 'grain matrix' properties and more versatile, is an important task in agriculture.

2 Problem Statement

The idea to measure grain moisture content with a help of four capacitive sensors (two in a reference and another two in measuring channel) was introduced by the authors previously [14]. As a result, two variants of the transfer function for the capacitive moisture metering were suggested [15]. The first variant is described with formula (1):

$$W = K \cdot \frac{C_3 - C_4}{C_2 - C_1}, \tag{1}$$

where C_1, C_2, C_3 and C_4 are measured values of electric capacitances; $C_2 - C_1$ and $C_3 - C_4$ are the differences between corresponding pairs of electric capacitances in reference and measuring channels; K is a normalizing coefficient. If we take the values of electric capacitances, equal to 15 pF for C_1, C_4 and 50 pF for C_2, C_3 (when capacitive sensors are empty) normalizing coefficient would be equal to $K = 28.599$.

Another variant was obtained after the process of linearization, applied to function (1) [15]:

$$W_m = -1.019 + 1.269 \cdot \frac{\left(\frac{C_3 - C_4}{C_2 - C_1} - a\right)}{b} - 0.00527 \cdot \frac{\left(\frac{C_3 - C_4}{C_2 - C_1} - a\right)^2}{b^2} - 0.000112 \cdot \frac{\left(\frac{C_3 - C_4}{C_2 - C_1} - a\right)^3}{b^3}. \tag{2}$$

The task of the research is to investigate the ability of the both transfer functions (1 and 2) to retain stability (grain type invariance) when applied for moisture measurement in grain with different 'grain matrix' composition and different values of moisture content.

3 Materials and Methods

To carry out experimental researches with the purpose to check the workability of a transfer functions (1) and (2) we took five different grain types with significantly different values of dielectric permittivity in dehydrated state. Among them we had wheat cereals ($\varepsilon = 2.55$), pea ($\varepsilon = 2.97$), millet ($\varepsilon = 3.17$), poppy ($\varepsilon = 3.56$), and pearl barley ($\varepsilon = 3.68$). Reference samples were prepared by grain dehydration in the drying oven [16, 17], and subsequent addition of water into dry grain samples with a special pipette [18].

Following air-oven reference method standards, 20 g weights with grain samples were placed in a drying oven with 130 °C temperature during 120 min (Fig. 1).

Fig. 1. Preparation of 30 aluminum containers with 20 g weights of pea, further drying and cooling in desiccators

The next step of reference samples preparation was careful mixing with the necessary proportion of water and holding in desiccators for an hour [16].

Electrical functional circuit, involved into the process of grain moisture measurement, is given on Fig. 2.

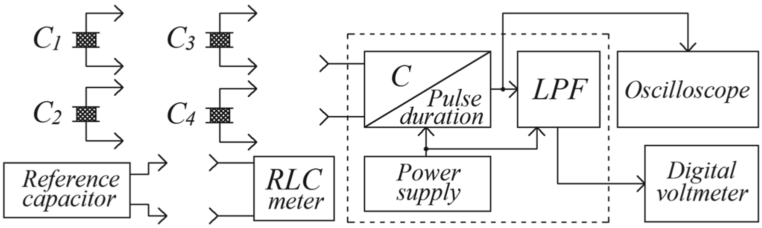

Fig. 2. Electrical functional circuit of the grain moisture measurement laboratory setup

It consists of mentioned above capacitive sensors C_1, C_2, C_3 and C_4, one channeled capacitance into dc-voltage transducer which performs a sequence of transformations ‘capacitance – pulse duration – dc voltage’, variable air capacitor (reference capacitor), oscilloscope, digital voltmeter and RLC meter. The process of measurement was performed following the substitution method, which is of extensive use when measuring electrical quantities, such as resistance, capacitance and inductance.

Schematic of the capacitive instrument measuring transducer is described below (Fig. 3). Both of its’ sensors consist of a system of flat plates 1, where two pairs of flat plates belong to capacitors C_1 and C_4, and rest of flat plates create another pair of capacitors C_2 and C_3. All flat plates with equal length l are fixed inside two fluoroplastic rings 2 at an equal gap Z [19].

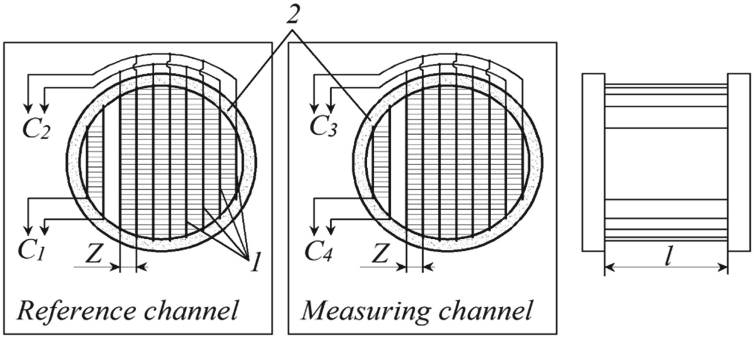

Fig. 3. Schematic of the capacitive instrument measuring transducer

One pair of capacitive sensors has bigger (48 pF) and another one – smaller (15 pF) capacitance. Each pair with two corresponding sensors was placed in personal container which, in its turn, was assembled on the front panel of the aluminum case (Fig. 4).

Fig. 4. Hardware design of the capacitive instrument measuring transducer

Besides instrument measuring transducer, laboratory setup for moisture measurement included a list of instruments, demonstrated on Fig. 5. At first, two capacitive sensors C_1 and C_2 from the reference channel were filled with a dehydrated grain sample and connected one-by-one to the input of the capacitance into the dc-voltage transducer. Corresponding values of dc voltage, taken from the screen of a digital multimeter, were fixed by the operator (Fig. 6).

After that, capacitive sensors were substituted by variable reference capacitor. Its capacitance had been slowly increased till dc voltage value on the voltmeter's screen has become equal to the corresponding voltage for C_1, detected before. To measure capacitance value of the reference capacitor, it was disconnected from the input of the secondary transducer and connected to the input of accurate RLC-meter. Similar operations took place for the rest of capacitive sensors, and ten random measurements of electric capacitance were received for each of them [20].

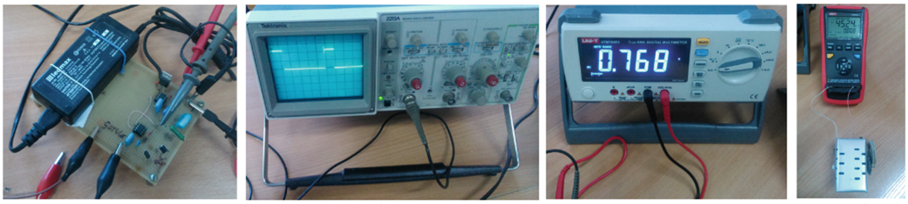

(a) (b) (c) (d)

Fig. 5. Instruments, which entered the laboratory setup: a) capacitance – pulse duration – dc voltage secondary transducer with power supply; b) oscilloscope Tektronix 2213A; c) digital multimeter UTM 18803; d) RLC-meter UTM-1612 with reference capacitor, connected to its' input

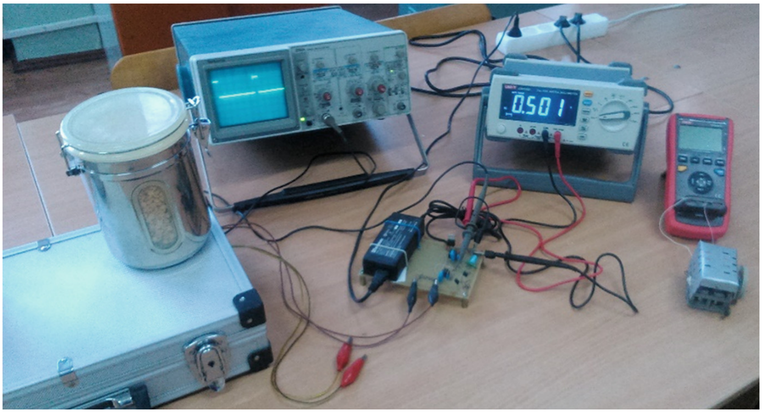

Fig. 6. One of capacitive sensors in a reference channel is connected to secondary transducer

4 Theory/Calculation

Arithmetic mean values, calculated for ten multiple measurements of capacitive sensors C_1, C_2, C_3 and C_4, measured in different grain samples, are given in Table 1. To build a system of conditional Eqs. (4) we took average values for $(C_3 - C_4)/(C_2 - C_1)$ relation.

Calculated values of moisture content with mean values of sensors' capacitances for the transfer function (1) can be found in Table 2. And calculated values of moisture content for the same mean values for the transfer function (2) can be found in Table 3.

And, when examining the possibility for both transfer functions to retain invariance to grain type (physicochemical composition of grain) and defining which transfer function will be more stable to grain type variability, dispersion analysis application seemed to be rational.

Both in table II and table III we have two factors: influence of moisture content (let it be factor A), and influence of grain type (factor B), which is going to be of a special interest.

Firstly, the corresponding arithmetic mean values should be calculated for data in table II: common mean value for all values of moisture content $\overline{\overline{X}}$ (3), mean values for

Table 1. Arithmetic mean values of sensors' capacitance

$W = 0\%$		$W = 10\%$		$W = 20\%$		$W = 30\%$	
$\overline{C}_1$	$\overline{C}_2$	$\overline{C}_3$	$\overline{C}_4$	$\overline{C}_3$	$\overline{C}_4$	$\overline{C}_3$	$\overline{C}_4$
Pearl barley							
56.73	189.58	251.34	76.87	322.70	103.99	419.16	135.95
Poppy							
53.42	178.40	230.20	69.32	293.69	88.35	370.47	112.74
Millet							
47.46	158.90	210.34	64.95	266.48	79.93	335.26	103.12
Pea							
44.51	150.05	195.19	58.54	249.81	75.49	316.96	96.61
Wheat cereals							
38.10	127.85	166.47	48.26	217.29	67.13	274.44	84.51

Table 2. Calculated values of a transfer function (1) using mean values

$W_{nominal}$, %	$W_{calculated}$, %				
	Pearl barley	Poppy	Millet	Pea	Wheat cereals
0	0.268	0.268	0.268	0.268	0. 268
10	8.960	8.215	8.708	8.43	9.069
20	18.483	18.389	19.276	18.638	19.25
30	32.368	30.377	30.975	31.111	32.878

Table 3. Calculated values of a transfer function (2) using mean values

$W_{nominal}$, %	$W_{calculated}$, %				
	Pearl barley	Poppy	Millet	Pea	Wheat cereals
0	0.268	0.268	0.268	0.268	0.268
10	10.423	9.575	10.157	9.852	10,54
20	19.886	19.678	20.597	20.026	20.574
30	30.240	29.013	29.422	29.504	29.984

the all grades of factor A (lines of table II) $\overline{X}_i$ (4), and mean values for the all grades of factor B (columns of table II) $\overline{X}_j$ (5).

$$\overline{\overline{X}}_{II} = \frac{1}{n}\sum_{i=1}^{a}\sum_{j=1}^{b} X_{ij} = \frac{0.268 + ... + 29.984}{20} = 14.8234, \tag{3}$$

$$\overline{X}_{IIi} = \frac{1}{b}\sum_{j=1}^{b} X_{ij}, \overline{X}_{II1} = \frac{0.268 \cdot 5}{5} = 0.268, \tag{4}$$

$$\overline{X}_{II2} = \frac{8.960 + 8.215 + 8.708 + 8.430 + 9.069}{5} = 8.6764,$$

$$\overline{X}_{II3} = \frac{18.483 + 18.389 + 19.276 + 18.638 + 19.250}{5} = 18.8072,$$

$$\overline{X}_{II4} = \frac{32.368 + 30.377 + 30.975 + 31.111 + 32.878}{5} = 31.5418,$$

$$\overline{X}_{IIj} = \frac{1}{a}\sum_{i=1}^{a} X_{ij}, \tag{5}$$

$$\overline{X}_{II1} = \frac{0.268 + 8.960 + 18.483 + 32.368}{4} = 15.01975,$$

$$\overline{X}_{II2} = \frac{0.268 + 8.215 + 18.389 + 30.377}{4} = 14.31225,$$

$$\overline{X}_{II3} = \frac{0.268 + 8.708 + 19.276 + 30.975}{4} = 14.80675,$$

$$\overline{X}_{II4} = \frac{0.268 + 8.430 + 18.638 + 31.111}{4} = 14.61175,$$

$$\overline{X}_{II5} = \frac{0.268 + 9.069 + 19.250 + 32.878}{4} = 15.36625.$$

Then it would be possible to calculate corresponding sums: the sum of squared discrepancies SS_a (6), explained with the influence of factor A, the sum of squared discrepancies SS_b (7), explained with the influence of factor B, and the sum of squared deviations of the error SS_e (8), and the common sum of squared discrepancies SS (9).

$$SS_{aII} = b\sum_{i=1}^{a}\left(\overline{X}_{IIi} - \overline{\overline{X}}_{II}\right)^2 = 2725.104, \tag{6}$$

$$SS_{bII} = a\sum_{j=1}^{b}\left(\overline{X}_{IIj} - \overline{\overline{X}}_{II}\right)^2 = 2.558347, \tag{7}$$

$$SS_{eII} = \sum_{i=1}^{a}\sum_{j=1}^{b}\left(X_{IIij} - \overline{X}_{IIi} - \overline{X}_{IIj} + \overline{\overline{X}}_{II}\right)^2 = 3.006936, \tag{8}$$

$$SS_{II} = \sum_{i=1}^{a}\sum_{j=1}^{b}\left(X_{IIij} - \overline{\overline{X}}_{II}\right)^2 = SS_{aII} + SS_{bII} + SS_{eII} = 2730.669. \tag{9}$$

Formulas to calculate the dispersions: MS_a, explained with the influence of factor A; MS_b, explained with the influence of factor B; and MS_e (dispersion of the error), – are given below.

$$MS_{aII} = \frac{SS_{aII}}{a-1} = 908.3681, \tag{10}$$

$$MS_{bII} = \frac{SS_{bII}}{b-1} = 0.63959, \tag{11}$$

$$MS_{eII} = \frac{SS_{eII}}{(a-1)(b-1)} = 0.25058. \tag{12}$$

To estimate the influence of factor A on the results in table II, we have to calculate the experimental value of F-test and compare it with the critical F value (13):

$$F_{aII} = \frac{MS_{aII}}{MS_{eII}} = 3625.091. \tag{13}$$

For the influence of factor B, we have to calculate the corresponding value of F-test and again compare it with the critical F value (14):

$$F_{bII} = \frac{MS_{bII}}{MS_{eII}} = 2.5524. \tag{14}$$

After that, we can repeat the same calculations for data in Table 3.

$$\begin{gathered}
\overline{\overline{X}}_{III} = \tfrac{1}{n}\sum_{i=1}^{a}\sum_{j=1}^{b} X_{ij} = \tfrac{0.268+\ldots+29.964}{20} = 15.0406, \\
\overline{X}_{III1} = \tfrac{0.268\cdot 5}{5} = 0.268, \overline{X}_{III2} = 10.1094, \overline{X}_{III3} = 20.1522, \overline{X}_{III4} = 29.6326, \\
\overline{X}_{IIIj} = \tfrac{1}{a}\sum_{i=1}^{a} X_{ij}, \overline{X}_{III1} = 15.20425, \overline{X}_{III2} = 14.6335, \overline{X}_{III3} = 15.111, \overline{X}_{III4} = 14.9125, \\
\overline{X}_{III5} = 15.3415, \\
SS_{aIII} = b\sum_{i=1}^{a}\left(\overline{X}_{IIIi} - \overline{\overline{X}}_{III}\right)^2 = 2408.007, SS_{bIII} = a\sum_{j=1}^{b}\left(\overline{X}_{IIIj} - \overline{\overline{X}}_{III}\right)^2 = 1.217673, \\
SS_{eIII} = \sum_{i=1}^{a}\sum_{j=1}^{b}\left(X_{IIIij} - \overline{X}_{IIIi} - \overline{X}_{IIIj} + \overline{\overline{X}}_{III}\right)^2 = 1.04482, \\
SS_{III} = \sum_{i=1}^{a}\sum_{j=1}^{b}\left(X_{IIIij} - \overline{\overline{X}}_{III}\right)^2 = SS_{aIII} + SS_{bIII} + SS_{eIII} = 2410.269, \\
MS_{aIII} = \tfrac{SS_{aIII}}{a-1} = 802.6689, MS_{bIII} = \tfrac{SS_{bIII}}{b-1} = 0.304418, . \\
MS_{eIII} = \tfrac{SS_{eIII}}{(a-1)(b-1)} = 0.087068 \\
F_{aIII} = \tfrac{MS_{aIII}}{MS_{eIII}} = 9218.839, F_{bIII} = \tfrac{MS_{bIII}}{MS_{eIII}} = 3.4963.
\end{gathered}$$

5 Results/Discussion

The calculated values of the sensors' capacitances and moisture content for the transfer function (2) were received with the help of the universal Wiener equation as one of the most popular dielectric mixture models:

$$\varepsilon_{mix} = \varepsilon_n\left(1 + \frac{3W}{(\varepsilon_W + 2\varepsilon_n)/(\varepsilon_W - \varepsilon_n) - W}\right),$$

where ε_{mix} is the dielectric permittivity of a binary material-water mixture; ε_n is the dielectric permittivity of dry material; $\varepsilon_W = 80$, and is the dielectric permittivity of water; and W is the volumetric moisture content, taken in absolute values.

Suppose we apply the universal Wiener equation to the dielectric permittivity values, taken for different values of moisture content, and use it as the moisture meter's transfer function. In that case, we obtain a family of curves (Fig. 7).

Figure 7 illustrates the situation when the grain matrix composition changes and the water content (grain type uncertainty). If no type-uncertainty compensation happens, we have a family of transfer functions for the moisture meter instead of one, taken as nominal [21–23]. The transfer function (1) helps to solve this problem and provides the possibility of measurements in grains, where the dielectric permittivity of a dry grain ε_n varies in a wide range from 2 to 3.5 without any preliminary calibration [24].

Firstly, lets' compare F-test values F_{aII} and F_{bII} with corresponding critical values: $F_{aIIcritical} = 3.49$, $F_{bIIcritical} = 3.259$. Following the dispersion analysis methodology it is possible to conclude, that factor A (moisture content) is of a strong influence on the result of moisture measurement, what is evident. The greater interest should be present for the factor B (grain type).

We can see that $F_{bII} = 2.5524$, and $F_{bIIcritical} = 3.259$. It means that the influence of factor B (grain type) is insignificant to the result of moisture measurement. Now lets' move to the linearized transfer function (2). We have the same critical F-test values: $F_{aIIIcritical} = 3.49$, $F_{bIIIcritical} = 3.259$. But we have $F_{aIII} = 9218.839$ versus $F_{aII} = 3625.091$, what means that formula (2) provides approximately three times greater sensitivity to moisture content then formula (1).

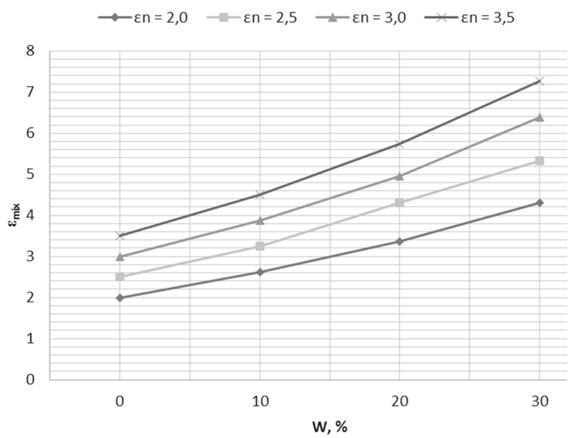

Fig. 7. Influence of the changes in the composition of a dry substance ε_n on the value of the dielectric permittivity of a binary mixtire ε_{mix}

From the other hand, if we compare F_{bIII} with $F_{bIIIcritical}$, we can see that $F_{bIII} = 3.4963$ while $F_{bIIIcritical} = 3.259$. So, it may seem that for the transfer function (2) the influence of factor B (grain type) became more significant. But, if we dig deeper into the problem and compare the values of MS_b and MS_e, we can find that $MS_{bII} = 0.63959$,

$MS_{bIII} = 0.304418$ (two times smaller). From the other hand, $MS_{eII} = 0.25058$, and $MS_{eIII} = 0.087068$ (approximately three times smaller), what is the reason for F_{bIII} to increase. For our case, it would be more adequate to compare the values of two MS_b dispersions and conclude that transfer function (2) is less sensitive to the change of a grain type.

To strengthen the conclusion we used another type of dispersion analysis. At first, two dispersions of repeatability were calculated (15):

$$S_{rep}^2 = \sum_{j=1}^{m} \sum_{i=1}^{n} \left(W_{i,j} - \overline{W}_j\right)/(n \cdot m - 1). \tag{15}$$

Then two dispersions of adequacy were defined (16):

$$S_{ad}^2 = \sum_{j=1}^{m} \left(\overline{W}_j - \overline{W}_{jnominal}\right)/(N - (m + 1)), \tag{16}$$

where: N is total number of moisture content values $W_{calculated}$; m – number of nominal points of moisture content $W_{nominal}$.

To compare dispersions of adequacy with corresponding dispersions of repeatability we again used F-test (Table 4). In Table 4 the smaller is the F-test value, the smaller is the grain type influence on the result of moisture measurement. For data in Table 3, we have smaller values of both adequacy and repeatability dispersions, so as the smaller value of F-test.

Table 4. Calculated values of a transfer function (2) using mean values

Data source	S_{rep}^2	S_{ad}^2	F
Table 2	0.29244	0.3750	1.282
Table 3	0.09344	0.0161	0.172

6 Conclusions

To check the workability of the two moisture content transfer functions in practice, we took five different grains: wheat cereals, pea, millet, poppy, and pearl barley. Following air-oven reference method standards, grain samples were preliminarily dehydrated in a drying oven (130 °C temperature during 120 min) and mixed with appropriate proportions of water. We developed a prototype product of the moisture measurement experimental setup. It helped to fulfill multiple measurements for capacitive sensors C_1, C_2, C_3, C_4 and check the robustness of the modified static function of a moisture meter. Values of moisture content for two transfer functions, calculated for the arithmetic mean values of C_1, C_2, C_3, and C_4 capacitance, had been compared through dispersion analysis.

For both transfer functions two factors were examined: the influence of moisture content (factor A) and the influence of grain type (factor B). The decision was to compare the values of MS_b dispersions, explained with the influence of factor B. The transfer function (2) is less sensitive to the change of a grain type because it has approximately two times smaller value of MS_b (0.304418 versus 0.63959). Later the dispersions of repeatability and adequacy had been calculated and compared. It was possible to conclude that modified transfer function (2) provides minimal dispersions of repeatability and adequacy and a minimal value of the F-test. Values of both dispersions for the transfer function (2) are approximately three times smaller, and F-test values are seven times smaller in comparison with the initial transfer function (1) what proves its' better robust properties.

References

1. Pathaveerat, S., Pruengam, P.: Low cost measurement of moisture content in long grain paddy. J. Stored Prod. Res. **89**, 101728 (2020)
2. Befikadu, D.: Factors affecting quality of grain stored in Ethiopian traditional storage structures and opportunities for improvement. Int. J. Sci. Basic Appl. Res. (IJSBAR) **18**(1), 235–257 (2014)
3. Tahir, A.R., Neethirajan, S., Jayas, D.S., Shahin, M.A., Symons, S.J., White, N.D.G.: Evaluation of the effect of moisture content on cereal grains by digital image analysis. Food Res. Int. **40**(9), 1140–1145 (2007)
4. Starchenko, G., Hrytsyk, A. Raal, A., Koshovyi, O.: Phytochemical profile and pharmacological activities of water and hydroethanolic dry extracts of Calluna vulgaris (L.). Hull. Herb. Plants **9**(6), 751 (2020)
5. Zabolotnyj, A.V., Koshevoj, N.D.: Development, examination and optimization of the device for quality control of dielectric materials. Pribory i Sistemy Upravleniya **1**, 39–43 (2004)
6. Mhiko, T.A.: Determination of the causes and the effects of storage conditions on the quality of silo stored wheat (Triticum aestivum) in Zimbabwe. Nat. Prod. Bioprospect. **2**, 21–28 (2012)
7. Jung, H., Lee, Y.J., Yoon, W.B.: Effect of moisture content on the grinding process and powder properties in food: a review. Processes **6**, 69 (2018)
8. Probst, K.V., Kingsly Ambrose, R.P., Pinto, R.L., Bali, R., Krishnakumar, P., Ileleji, K.E.: The effect of moisture content on the grinding performance of corn and corncobs by hammer milling. Trans. ASABE **56**(3), 1025–1033 (2013)
9. Dabbour, M., Bahnasawy, A., Ali, S., El-Haddad, Z.: Grinding parameters and their effects on the quality of corn for feed processing. J. Food Process. Technol. **6**(9), 482 (2015)
10. Moisture Meters for Cereal Grain and Oilseeds. OIML R59, Paris, France (2006). 40 p.
11. Wanga, W.C., Wang, L.: Design of moisture content detection system. Phys. Procedia **33**, 1408–1411 (2012)
12. Wu, S., Zhang, B., Tian, Y., Zhou, S., Ma, H.: A grain moisture model based on capacitive sensor. J. Phys. Conf. Ser. **1074**, 012120 (2018)
13. Thakur, R., Chatterji, S., Kumar, A., Bansod, B.S.: Development of multi-grain capacitive sensor for determination of moisture content in grains. Qual. Assur. Saf. Crops Foods **7**(2), 201–206 (2015)
14. Zabolotnyi, O.: Moisture content control in heavy fuel during the process of emulsification with a help of capacitive sensors. In: Proceedings of the 25th International Scientific Conference "Transport Means 2021", Part 1, Kaunas, Lithuania, pp. 215–222 (2021)

15. Zabolotnyi, O., Zabolotnyi, V., Koshevoy, N.: Capacitive water-cut meter with robust near-linear transfer function. Computation **10**, 115 (2022)
16. Diane Lee, G., Harris, G.: Examination of grain moisture meters using air-oven reference method transfer standards. Natl. Inst. Stand. Technol. (2016). 80 p.
17. Cereals and Cereal products – Determination of moisture content – Reference method. ISO 712:2009, Switzerland (2009). 20 p.
18. Laboratory glassware – Graduated pipettes. ISO 835:2007, Switzerland (2007). 12 p.
19. Zabolotnyi, O., Zabolotnyi, V., Koshevoy, N.: Adequacy and robustness analysis of the capacitive moisture meters' static function. In: 2022 IEEE 41st International Conference on Electronics and Nanotechnology (ELNANO), Kyiv, Ukraine, pp. 506–512 (2022)
20. Zabolotnyi, O.V., Zabolotnyi, V.A., Koshevoy, N.D.: Method of grain moisture measurement with application of testing influences on a substance under research. In: Nechyporuk, M., Pavlikov, V., Kritskiy, D. (eds.) ICTM 2021. LNNS, vol. 367, pp. 229–245. Springer, Cham (2022). https://doi.org/10.1007/978-3-030-94259-5_21
21. Nelson, S.O., Trabelsi, S.: A century of grain and seed moisture measurement by sensing electrical properties. Trans. ASABE **55**(2), 629–636 (2014)
22. Nandi, N., Bhattacharyya, K., Bagchi, B.: Dielectric relaxation and solvation dynamics of water in complex chemical and biological systems. Chem. Rev. **100**(6), 2013–2046 (2000)
23. Wobschall, D.: A theory of the complex dielectric permittivity of soil containing water: the semidisperse model. IEEE Trans. Geosci. Electron. **Ge-15**(1), 129–143 (1977)
24. Zabolotnyi, O., Koshevoi, M.: An effective method of bulk materials moisture measurement using capacitive sensors. J. Stored Prod. Res. **89**, 101733 (2020)

Simulation of Onboard Helicopter Radar Signals for Surface Elevation Measurements

Anatoliy Popov[1], Semen Zhyla[1], Olha Inkarbaieva[1](✉), and Mariya Bortsova[2]

[1] National Aerospace University "Kharkiv Aviation Institute", Kharkiv, Ukraine
o.inkarbayeva@khai.edu

[2] Ivan Kozhedub Kharkiv National Air Force University, Kharkiv, Ukraine

Abstract. The stage of landing a helicopter on unequipped fields in low visibility or adverse weather conditions is particularly dangerous for pilots and passengers. One of the possible ways to reduce risks is to use additional safe landing systems. Among the variety of such systems the terrain radars that use space-time signal processing and operate effectively in various environmental conditions deserve special attention. An important and relevant task in developing and analyzing these radars is a preliminary assessment of their general performance and accuracy. To solve this problem, simulation models of the surface and reflected signals that are detected by a two-antenna onboard radar are developed. The surface is represented as a two-dimensional random process with a given correlation function of elevation variation. The models of space-time fields after their sum and difference processing in the receiver channels are shown and analyzed in detail. The modeling results are the input data for the approbation of heuristic and optimal algorithms for measuring elevation of the surface selected for a safe landing. The performance and accuracy of the developed model are researched on the example of a three-dimensional surface with a spatially extended obstacle.

Keywords: Helicopter Radar · Amplitude Direction Finding · Surface Elevation Measurements · Surface Simulation

1 Introduction

Nowadays, helicopters play an important role in a variety of civilian and military tasks, ranging from tourist flights to air mobility of troops in operations zone. One of the most difficult and dangerous operations in helicopter piloting is landing on unprepared surfaces, which is associated with an increased risk for the crew and passengers [1]. Statistics of aerospace accidents in the world show that the largest share of accidents and disasters occurs during landing [2, 3]. Landing in rain, snowfall, dense fog, smoke, or volcanic activity is even more dangerous. Onboard devices such as Global Positioning System (GPS), Inertial navigation system (INS), accelerometer and gyroscope [4, 5], Doppler navigation system (DNS) [6], radar altimeter (RA), Distance Measuring Equipment (DME) [7] help to reduce risks for the pilot and crew. The combined operation of

M. Nechyporuk et al. (Eds.): ICTM 2023, LNNS 1008, pp. 525–540, 2024.
https://doi.org/10.1007/978-3-031-61415-6_45

these systems and the pilot's experience prevent a dangerous landing when helicopters approach the ground. At the same time, a preliminary analysis of the ground surface near the helicopter, measuring its altitude and determining a safe landing zone, are more relevant. Modern systems for terrain mapping from UAVs are known, but such systems use ultrasonic signals, which is unacceptable for helicopters due to the short remote sensing range [8].

Safe landing systems are promising and are being developed all over the world. Thus in [9], the research is based on photometric and altimetric data, but this method cannot be implemented at night and requires altitude measurement, which does not allow to determine the terrain area for landing in advance. The results of work [10] are highly accurate due to the use of the terahertz waveband, but the use of such a terrain estimation system in cloudy weather and dust storms is almost impossible due to significant attenuation in a heterogeneous atmosphere. The article [11] presents the results of the practical application of helicopter terrain systems based on the use of millimeter-wave radars. However, most of the presented developments rely on heuristic methods, which involve using ready-made technological solutions, and subsequent processing is performed based on the generalization of engineering experience. In addition, their effectiveness decreases when landing in low visibility conditions. In this context, the development of a new method and device for measuring surface relief for safe helicopter landing is relevant. The most optimal for the operation of such systems is the radio range, as it is all-weather and has penetrating properties through snow, dust clouds, smoke screens, etc. An example of a terrain measurement system is a direction finder. Modern radio direction finders are based on various schemes, which generally can be divided into single-channel and multi-channel. Single-antenna direction finder is relatively easy to implement, but the measurement accuracy is low. Therefore it is necessary to use larger antennas to improve accuracy [12], which is not appropriate for the task in question. A two-antenna direction finder with special signal processing lets avoid these disadvantages. These direction finders allow to performing measurements with increased accuracy due to the high direction-finding characteristic curvature and determining the direction of signal arrival by measuring the difference in signal power at the output of the channels.

To improve the quality of terrain reconstruction and achieve the potential accuracy, the authors of paper [13] proposed an optimal algorithm for an onboard helicopter radar system that should estimate the terrain elevation. In that work, the problem of end-to-end signal processing was solved, starting with generation of sensing signals, reception of electromagnetic fields by antennas, the algorithm for analyzing parameters by the maximum likelihood method, and the estimation of terrain elevation. The proposed method implies operation in the radio range, so it can be used in all weather conditions, day and night. However, the research [13] shows only the ideology of radar construction, which needs to be specified, tested for performance, and evaluated for accuracy by conducting simulations using different surface models.

This paper proposes a model that can be used to simulate radar signals of a two-antenna helicopter radar for elevation measurement. These radar signals are necessary for further analysis of the method of their space-time processing proposed by the authors or will be useful for any other research of new algorithms for extracting information about surface characteristics. In the simulation model coded in the FORTRAN programming language, the sensing signals are formed considering the construction theory of radio engineering radar systems, and the structure of the scattered signals takes into account the electromagnetic wave propagation theory and electrodynamic characteristics of the surface.

2 Problem Geometry and Signals Detected in the Radar

Let us consider in Fig. 1 the geometry of measuring terrain elevation from a helicopter, which is based on the following equation:

$$h(x) = H - R_h(x)\cos(\theta_h(x)), \tag{1}$$

where H is barometric altitude, $R_h(x)$ is slant range from the helicopter to each point of the surface, $\theta_h(x)$ is the elevation angle of each point on the surface, measured from the z axis

Out of (1) it follows that it is necessary to estimate the distance and elevation angle of each surface point to measure $h(x)$. The practice of radar measurements shows that the distance can be estimated by the pulse method and the elevation angle by sum-and-difference monopulse systems. There are other algorithms for estimating these parameters, but the proposed ones are the simplest and do not pose any special requirements for radio equipment, such as a phased array antenna, coherent processing, and phase unwrapping.

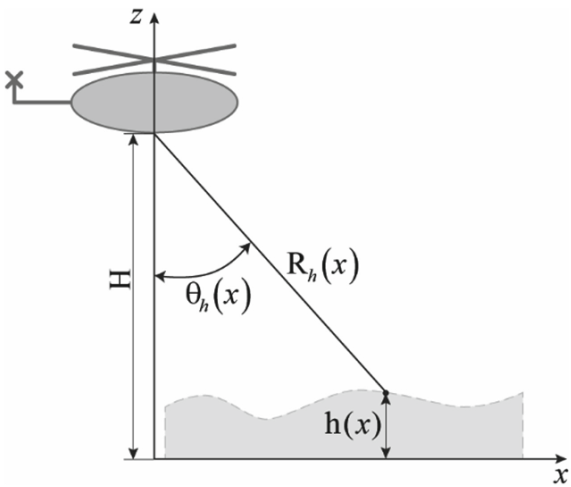

Fig. 1. Geometry of elevation measurement.

In this case, Fig. 2 proposed a basis altitude measurement geometry using a two-antenna amplitude sum-and-difference direction finder and radio-range finder operating in a complex.

The following symbols are used in the figure: θ_0 is angle that defines the equisignal direction, θ_δ is angle by which the maximums of the radiation patterns are shifted relative to the equisignal direction.

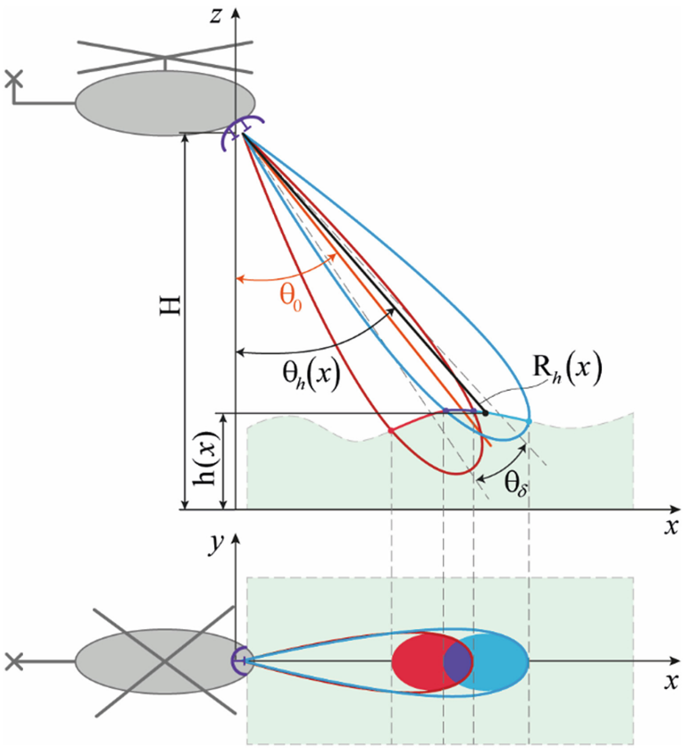

Fig. 2. Geometry of radar elevation measurements.

It is assumed that the antennas emit a pulse in the direction of the surface, which, considering the antenna patterns $\dot{\Psi}_{1(2)}\left(\theta - \theta_{0\,1(2)}\right)$, has the following form:

$$s_{pr\,1(2)}\left(t, \theta, \theta_{0\,1(2)}\right) = \mathrm{Re}\left\{\dot{\Psi}_{1(2)}\left(\theta - \theta_{0\,1(2)}\right)\dot{A}(t)e^{j2\pi f_0 t}\right\}, \quad (2)$$

where indexes 1 and 2 correspond to the first and second antennas, $\dot{\Psi}(\theta)$ is radiation pattern, $\dot{A}(t) = A(t)e^{j\phi}$ is the complex envelope of the sensing signal, f_0 is the resonance frequency, ϕ is the initial phase, $A(t)$ is the signal amplitude, $\theta_{0\,1(2)}$ is maximum directions of the radiation patterns.

For the convenience of further processing, let us convert the angles θ to the surface coordinates x, considering that the altitude of the antenna does not change.

$$s_{pr\,1(2)}\left(t, x, X_{0\,1(2)}\right) = Re\left\{\dot{\Psi}_{1(2)}\left(x - X_{0\,1(2)}\right)\dot{A}(t)e^{j2\pi f_0 t}\right\}, \quad (3)$$

where $X_{0\,1(2)}$ is maximum amplitude points of radiation patterns on the surface.

The emitted signal reaches some defined area on the surface x, then it is reflected from it, and arrives with some time delay $t_{del}(t)$. Then the received signal, according to the phenomenological description [14], will be observed in the antennas as follows:

$$\dot{s}_{bs\,1(2)}\left(t, \mathrm{X}_{0\,1(2)}\right) = \int_{\mathrm{X}} \dot{\Psi}^2_{1(2)}\left(x - \mathrm{X}_{0\,1(2)}\right) \dot{F}(x)\dot{s}_0(t, x)\, dx, \tag{4}$$

where $\dot{F}(x)$ is the complex backscattering coefficient at every point of the observation area, x is surface coordinate, $\dot{s}_0(t,x) = \dot{A}\left(t - t_з(x)\right)\exp\left(-j2\pi f_0\left(t - t_з(x)\right)\right)$is unit signal.

For sum-and-difference systems, the signals (4) take the form:

$$\begin{aligned}\dot{s}_{bs\,\Sigma}(t, \mathrm{X}_0) &= \int_{\mathrm{X}} \left[\dot{G}_1(x - \mathrm{X}_{0\,1}) + \dot{G}_2(x - \mathrm{X}_{0\,2})\right] \dot{F}(x)\dot{s}_0(t, x)\, dx \\ &= \int_{\mathrm{X}} \left[\dot{G}_1\left(x - \mathrm{X}_0 + \frac{\mathrm{X}_\delta}{2}\right) + \dot{G}_2\left(x - X_0 - \frac{\mathrm{X}_\delta}{2}\right)\right] \dot{F}(x)\dot{s}_0(t, x)\, dx,\end{aligned} \tag{5}$$

$$\begin{aligned}\dot{s}_{bs\,\Delta}(t, X_0) &= \int_{\mathrm{X}} \left[\dot{G}_1(x - \mathrm{X}_{0\,1}) - \dot{G}_2(x - \mathrm{X}_{0\,2})\right] \dot{F}(x)\dot{s}_0(t, x)\, dx \\ &= \int_{\mathrm{X}} \left[\dot{G}_1\left(x - \mathrm{X}_0 + \frac{\mathrm{X}_\delta}{2}\right) - \dot{G}_2\left(x - \mathrm{X}_0 - \frac{\mathrm{X}_\delta}{2}\right)\right] \dot{F}(x)\dot{s}_0(t, x)\, dx,\end{aligned} \tag{6}$$

where $\dot{s}_{bs\,\Sigma}(t, \mathrm{X}_0)$ is received signals in the sum channel, $\dot{s}_{bs\,\Delta}(t, \mathrm{X}_0)$ is difference channel signals, $\dot{G}(x) = \dot{\Psi}^2(x)$, X_0 is a point of equisignal direction on the surface, $\mathrm{X}_\delta/2$ is some deviation from the equisignal direction.

To simplify the analysis, let us consider the antenna patterns as Gaussian curves without side lobes, as they are in Fig. 3, which, as an example, shows the first and second antenna radiation patterns relative to the equisignal direction in the Cartesian coordinate system, as well as the radiation patterns resulting from processing in the sum and difference channels.

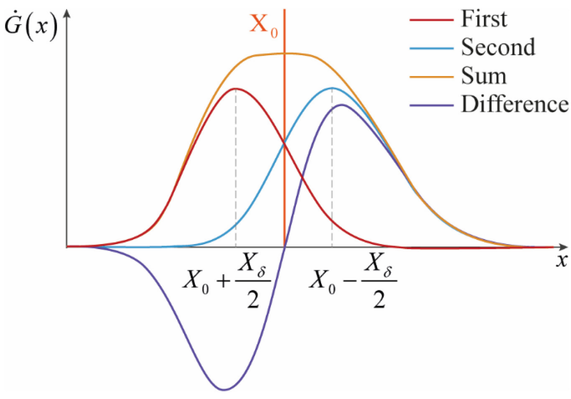

Fig. 3. Directional patterns in surface coordinates.

After sum-and-difference processing, the signals are transmitted to the receiver, where internal noise is added. The observation equation to be processed by new heuristic or optimal algorithms is as follows:

$$u_{\Sigma(\Delta)}(t, \mathrm{X}_0) = \mathrm{Re}\left\{\dot{s}_{bs\,\Sigma(\Delta)}\left(t, \mathrm{X}_0, \vec{\lambda}(x)\right)\right\} + n_{\Sigma(\Delta)}(t), \tag{7}$$

where $n_{\Sigma(\Delta)}(t)$ is delta-correlated and mutually independent internal noise of the sum and difference channels, $\vec{\lambda}(x) = \|R_h(x),\ \theta(x)\|$ a vector of parameters that should to be estimated for measurement of $h(x)$. Spectral density of noise $N_0/2$ is the same in each channel.

The authors in [13] proposed an optimal processing algorithm (7) and other approaches to measuring elevation from a helicopter were reported in the literature. The performance and accuracy of the main algorithmic operations require simulation research. For this purpose, in the following sections, the model of real surfaces with obstacles and the signals reflected by them is developed (7).

3 Methodology for Modelling Reflected Signals in Helicopter Elevation Measurement Radar

For the simulation of the signals (7), firstly, let us present (4) in discrete form:

$$s_{bs\,1(2)}(t) = \sum_{i=1}^{\infty} \dot{\Psi}^2_{1(2)}(x_i) \cdot \dot{S}_i \cdot A(t) \cdot \exp\left\{j\left(2\pi f_0 t + 2\pi f_0 \frac{\Delta R_{h\,i}}{c}\right)\right\}, \tag{8}$$

where $\dot{S}_i$ is averaged within the elementary area backscattering coefficient of each single reflector or radar cross section of an elementary discrete reflector, $\Delta R_{h\,i}$ is differences of distances to elementary reflectors on the surface, $A(t)$ is envelope of the sensing signal pulses without intra-pulse phase modulation.

Radar cross section, according to research [15–17], can be presented in general terms:

$$\dot{S} = \left(\sqrt{4\pi}\right)^3 \left(\frac{f_0}{c}\right)^2 \cdot C \cdot \iint\limits_A h(x, y) \cdot \cos(\vartheta_x) \cdot \cos\left(\vartheta_y\right) \cdot \exp\left(-j\frac{f_0}{c} 4\pi\,\Delta R_h(x, y)\right) dxdy, \tag{9}$$

where C is a normalization factor depending on the polarization of emission and reception, environment electrophysical characteristics, and the angle of incoming electromagnetic waves, A is surface area ‘covered’ by radar, $h(x, y)$ is surface elevation distribution function, ϑ_x, ϑ_y are angles of wave incidence on the surface in the radar resolution element.

According to expression (9), the radar cross section depends on the angle of observation of the illuminated surface, its electrophysical properties, geometric shape, and polarization characteristics of the emitted and received signals, so to obtain reliable results, this should be taken into account in the modelling of radar signals.

There are three main models of the underlying surface that characterize its profile [18]: a mirror surface; a small-scale roughness surface with irregularities smaller than a wavelength; and a flat surface with large irregularities. Real surfaces with complex roughness can be represented as a combination of the above models.

Any uniform rough surface can be represented as a two-dimensional random process $h(x_i, y_j)$ with a certain two-dimensional correlation function of elevations $R\left(\tau_x, \tau_y\right)$:

$$R(\tau_x, \tau_y) = \int_{-\infty}^{+\infty}\int_{-\infty}^{+\infty} h(x, y) \cdot h(x + \tau_x, y + \tau_y)\, dxdy. \tag{10}$$

In the discrete representation of a stochastic surface, neighboring points form quadrangular-shaped platforms – facets, for which reflected signals can by calculated using hybrid geometric optics (GO) and physical optics (PO) methods.

The general view of the proposed model of the underlying surface is shown in Fig. 4.

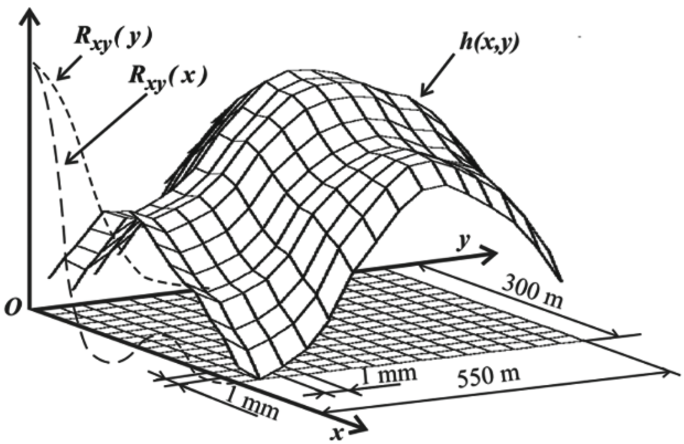

Fig. 4. General view of the surface model.

Most researchers use the method of two-dimensional linear convolution or the spectral method to model two-dimensional processes with a given correlation function [19]. However, both methods require significant computational resources. To save computer memory without storing large datasets, fractal geometry methods are often used, as in [20]. In paper [21], an alternative two-dimensional recursive filtering method was proposed, which significantly speeds up calculations and does not require a large storage space.

The two-dimensional digital recursive filter for modeling surface elevations has the form:

$$h_{i,j} = \sum\nolimits_{k=0}^{K_1}\sum\nolimits_{l=0}^{K_2} a_{k,l} \cdot x_{i-k,j-l} - \sum\nolimits_{k=0}^{M_1}\sum_{l=0}^{M_2} b_{k,l} \cdot h_{i-k,j-l}\big|_{k=l\neq 0}, \tag{11}$$

where $h_{i,j}$ is an output process samples – elevations of surface points, $x_{i,j}$ is samples of the input two-dimensional uncorrelated Gaussian process, K and M are filter order, $a_{k,l}$,

$b_{k,l}$ are constant coefficients, which are determined by the iterative method proposed in [21].

The autocorrelation functions of elevations (see Fig. 4) for the main types of surfaces can be approximated by the expression

$$R(x, y) = \exp\left(-\frac{1}{R_x}x - \frac{1}{R_y}y\right)\cos\left(2\pi \cdot f_x \cdot x\right) \cdot \cos\left(2\pi \cdot f_y \cdot y\right), \tag{12}$$

where R_x, R_y are the surface correlation radiuses along the x and y axes, f_x, f_y are the spatial frequencies along the x and y axes.

Changing the parameters (R_x, R_y, f_x, f_y) in (12), it is possible to get small-scale or large- scale rough, periodic, or non-periodic surfaces. In this case, the order of the filter (11) $K = M = 2$ and impulse response of the filter (11) will correspond to the autocorrelation function $r(x, y)$ (12), and the filter transfer function $W\left(f_x, f_y\right)$ will correspond to the spectral density of the random process that describes variation of the elevations of the surface points [21].

Modeling of rough surfaces with a complex frequency structure is performed by superposition of different simple surfaces, as shown in Fig. 5.

Thus, the surface modeling methodology is as follows:

- The wide-band spatial spectrum density of the required rough surface is divided into n narrow-band spectra series;
- For each of the narrow-band spectra, the sampling steps are calculated at the frequencies Δf_x, Δf_y, and at the coordinates Δx, Δy, so that the Kotelnikov theorem is observed;
- The surface is modeled with a narrow-band spatial spectrum with appropriate steps of sampling by coordinates using the vector recursive filtering method [21];
- The spatial linear interpolation of the obtained surfaces to the required (smallest) sampling step is performed;
- The resulting interpolation surfaces are centered and normalized;
- The n surfaces are added with the required coefficients which correspond to the elevations.

The proposed methodology is used to model the earth's surface, a fragment of which is shown in Fig. 6.

For modeling the work of the elevation measurement system with the elevation dataset $h_{i,j}$ shown in Fig. 6, it is necessary to calculate the radar cross section for each facet $S_{i,j}$ (9). For this purpose, the incident angles ϑ_x, ϑ_y of the radar signal on the facet with coordinates i, j should be derived. The facets shown in Fig. 4 are described by four points, while the surface is defined by three points. Therefore, each facet is divided into 2 triangles. For each triangle the orientation angles $\vartheta_{x,1}$, $\vartheta_{y,1}$, $\vartheta_{x,2}$, $\vartheta_{y,2}$ relative to the surface (x, y) and the triangle centroid coordinates (points of median intersection) (x, y, h) are calculated according to the rules of geometry.

Out of the centroid elevation h and its coordinates $\left(x_i, y_j\right)$, the slant ranges $\Delta R_{h\ i,j,1}$,, $\Delta R_{h\ i,j,2}$, and the complex reflectance of the facet are determined as

$$\dot{S}_{i,j} = \sum\nolimits_{k=1}^{2} C \cdot \cos(\vartheta_{x,k}) \cdot \cos(\vartheta_{y,k}) \cdot \exp\left\{j\left(2\pi f_0 \Delta R_{h\ i,j,k}/c\right)\right\}. \tag{13}$$

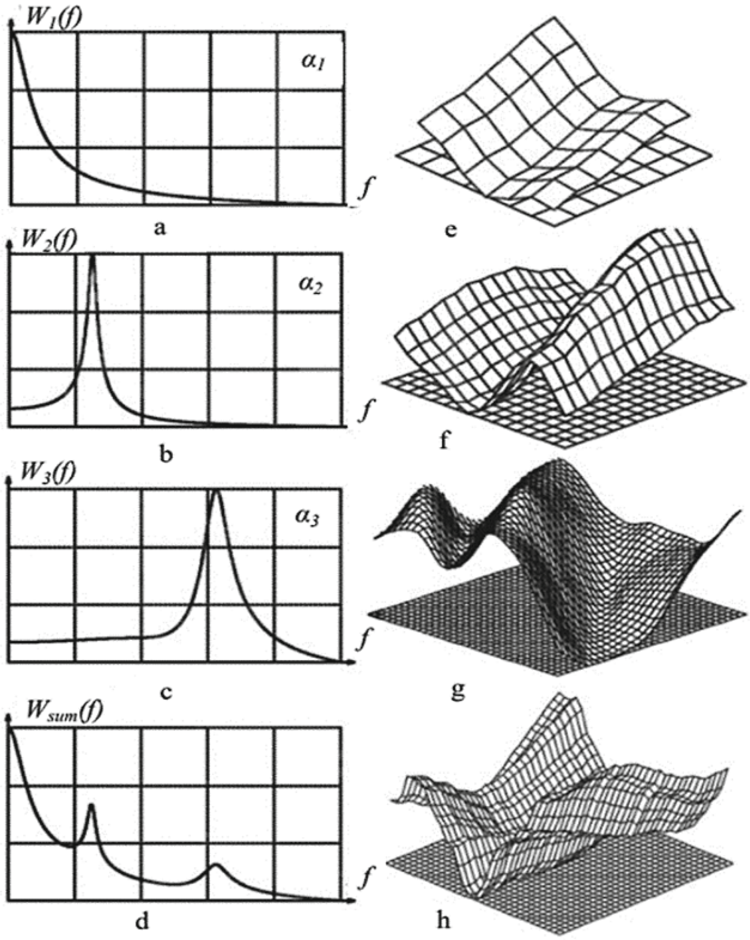

Fig. 5. Construction of a multilayer model (here $W_i(f)$ is a section of the two-dimensional spectral density of the i^{th} layer; α_i is the angle of the i^{th} layer; $W_{sum}(f)$ is a section of the result spectral density of the whole surface).

The radar cross section of each facet calculated as the modulus of the complex reflection coefficient for the surface (Fig. 6) is shown in Fig. 7.

The viewing angles θ_x, θ_y of each facet by radar are calculated similarly (using the coordinates of the centroids), which makes it possible to consider the radiation pattern of radar (Fig. 8)

$$\dot{S}_{i,j}\left(\theta_x, \theta_y\right) = \Psi\left(\theta_{x(i)}\right) \cdot \Psi\left(\theta_{y(j)}\right) \cdot \dot{S}_{i,j}. \tag{14}$$

Fig. 6. Fragment of a three-scale model of the earth's surface.

The reflected radar signal is formed by a set of elementary reflectors located at different distances from the antenna, so the received signal is a superposition of signals from elementary reflectors considering the difference of distances ΔR_h to them [22]:

$$\dot{S}(t) = \sum_{i=1}^{Nx} \sum_{j=1}^{Ny} \dot{S}_{i,j} \cdot \exp\{j(2\pi f_0 t + 2\pi f_0 \Delta R_{h\,i}/c)\}, \qquad (15)$$

where $\dot{S}_{i,j}$ is backscattering coefficient of each single facet (14) considering the radar radiation pattern.

Fig. 7. Fragment of the radar cross section (13) of the Earth's surface image (Fig. 6).

Fig. 8. Fragment of the radar cross section (13) of the Earth's surface image (Fig. 6) observed by the radar.

For modeling the signal (15) it is necessary to specify the shape and parameters of the sensing pulse, since the signal received by the radar is a convolution of the signal

$\dot{S}(t)$ with the pulse $A(t)$. To calculate the convolution over time, it is necessary to set the signal sampling interval Δt and calculate the time moments $t_k = \Delta t \cdot k$, $k = 0...K$, where K is the number of signal samples in time, depending on the given maximum radar coverage range.

The signal reflected from the surface (Fig. 8) and received by the radar (Fig. 9) is simulated as

$$\dot{S}_R(t_k) = \sum\nolimits_{m=k}^{K} A(t_m + t_k) \cdot \sum\nolimits_{i=1}^{Nx} \sum\nolimits_{j=1}^{Ny} \dot{S}_{i,j} \cdot \exp\left\{ j\left(2\pi f_0 t_k + 2\pi f_0 \frac{\Delta R_i}{c}\right)\right\}. \quad (16)$$

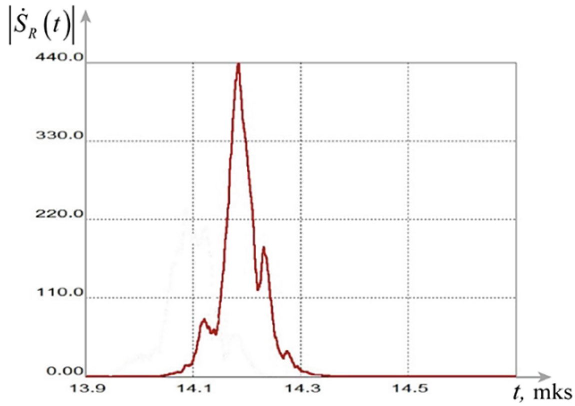

Fig. 9. Signal received by the radar.

4 Program Implementation and Testing of Signal Modeling Algorithm in Two-Channel Elevation Measurement System

The methodology for modeling surface topography and reflected signals discussed in Sect. 3 is implemented in Fortran 2023 [23]. The functions of this programming language for processing large datasets, multiplying them, and the possibilities of parallel computing are used to implement fast processing.

The developed program allows to set the surface parameters (surface and facet sizes, quantity of layers, parameters of autocorrelation functions and elevation dispersion of each layer), helicopter flight altitude, quantity of radar beams, width of the radiation pattern and slope angle of each antenna beams, duration and shape of the radar pulse, signal sampling, etc. In addition, random surfaces can contain deterministic objects of a given elevation and shape to test radar signal processing algorithms.

As an example, a two-antenna radar for elevation measurement is simulated with the following parameters: helicopter flight altitude of 1.5 km, quantity of radar beams is 2, pulse duration is 60 ns, pulse shape is Gaussian, width of the radiation pattern is 0.5°, surface viewing angles are 44.5 and 45.5°. For these radar parameters, a surface of 75 × 150 m was generated with a distance step of 7.5 mm with a complex three-layer roughness and the mean-square deviation of elevations is 0.5 m. A long-distance obstacle with a length of 5 m, a width of 10 m, and a height of 5 m with a Gaussian shape is placed on the surface along the direction of the helicopter's motion. The view of the surface with the obstacle obtained as a result of modeling is shown in Fig. 10. The surface cross-section in the direction of flight is shown in Fig. 11.

Fig. 10. Model of a two-dimensional surface with an obstacle.

Taking into account the orientation of the elementary surface units to the antenna patterns, the spatial distribution of the radar cross section is obtained, as shown in Fig. 12.

A dark-colored area in the resulting image is located behind the long-distance obstacle, which forms a shadow zone for the selected geometry. The result of the radar cross section calculation is introduced to the block for calculating reflected signals. The signal model also includes radiation patterns in the form of two-dimensional Gaussian functions that isolate illuminated area from the given radar cross section, as shown in Fig. 13.

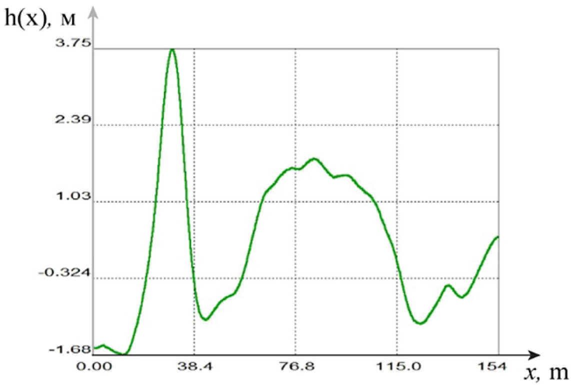

Fig. 11. Surface cross-section along the flight track.

The modulus of signals scattered by the surface and received by antennas with Gaussian radiation patterns in the coordinates of the slanted range are shown in Fig. 14 (a).

Fig. 12. Radar cross section of a surface with an obstacle.

(a)

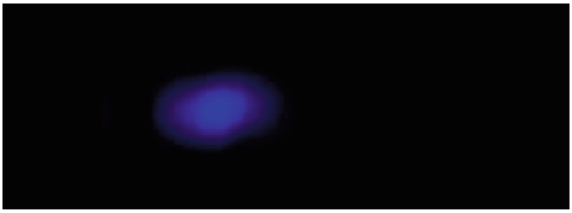

(b)

Fig. 13. Surface irradiation areas with radar cross section within first (a) and second (b) radiation patterns.

It follows from this figure that the second radiation pattern (located to the right of the equisignal direction) covers a homogeneous area and the signals practically (almost) repeat its shape. The signals in the first radiation pattern have a maximum in the area of the obstacle, followed by a fragment of shadowing, and then a signal reflected by the unshaded surface area.

To confirm the modeling reliability, signals from the same surface without an obstacle are obtained; they are in Fig. 14 (b).

As was mentioned in the problem statement, to detect the elevation, it is necessary to determine the signal delay time by the sum radiation pattern and the angular position of the pulse in the equisignal direction by the difference radiation pattern. The simulation model can generate signals of the sum and difference channels, which are shown in Fig. 15.

This program allows gradual change of the helicopter position (flight simulation) and cyclic recording of signals from the sum and difference channels. The obtained data can be used to analyze the performance and accuracy of various algorithms for measuring

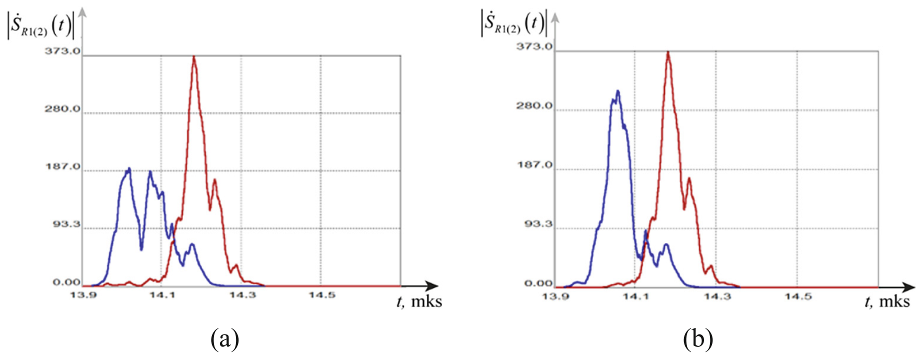

Fig. 14. Signals in the first and second radiation patterns scattered by a surface with obstacle (a) and a homogeneous surface (b).

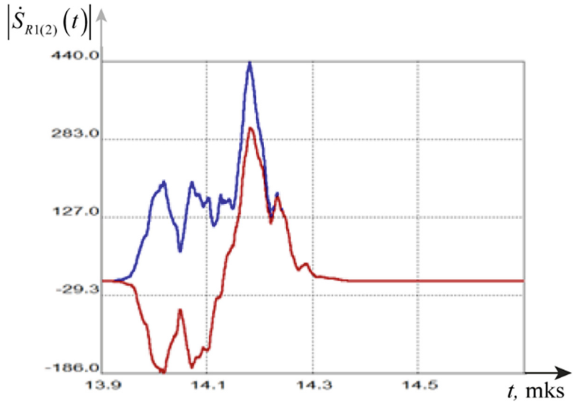

Fig. 15. Signals of sum and difference channels of helicopter radar

surface relief. The results of these algorithms should be compared with the values of the surface elevation averaged within the radiation pattern along the flight track.

5 Conclusion

The use of helicopters for various purposes is growing worldwide. When performing rescue operations in low visibility conditions, the pilot cannot always navigate and make the right decisions, which can lead to helicopter crash. The use of weather-resistant systems can save lives. Radars with optimal signal processing can operate in adverse conditions and detect obstacles, thus warning the pilot of danger.

The paper presents a simulation model of radar signal formation that carries information about the elevation of the underlying surface. It is expedient to use the generated signals for testing various heuristic, numerical, and optimal algorithms for estimating the surface elevation before helicopter landing. The feasibility of the developed model is achieved by taking into account the diffraction theory, the Huygens-Fresnel method, and using hybrid geometric optics and physical optics methods.

References

1. Lacerda, M., De Carvalho Paulino, A., Shiguemori, E., Damiao, A., Guimaraes, L., dos Anjos, C.: Identification and classification of drop zones and helicopter landing zones in images obtained by small size remotely piloted aircraft systems. In: 2018 IEEE International Geoscience and Remote Sensing Symposium (IGARSS), Valencia, Spain, pp. 7906–7909. IEEE (2018)
2. International Civil Aviation Organization: Accident Statistics. https://www.icao.int/safety/iStars/Pages/Accident-Statistics.aspx. Accessed 15 Aug 2023
3. Konieczka, R.: Defines causes and the circumstance of air accidents in preparatory conducts connected with their appearing. Transp. Overv. Przeglad Komunikacyjny **1**, 10–16 (2018)
4. Rodriguez, R., Jenkins, D., Leary, J., Nolan, K., Mahnken, B.: Performance analysis of GNSS units in manned helicopter operations. IEEE Aerosp. Electron. Syst. Mag. **33**(10), 14–20 (2018)
5. Zhang, L., Zhai, Z., He, L., Niu, W.: Infrared-based autonomous navigation for civil aircraft precision approach and landing. IEEE Access **7**, 28684–28695 (2019)
6. Prasad, C., Mishra, S.: Doppler navigation on helicopter: error analysis. In: 2022 IEEE Microwaves, Antennas, and Propagation Conference (MAPCON), Bangalore, India, pp. 384–387. IEEE (2022)
7. Ostroumov, I., Kuzmenko, N., Sushchenko, O.: Modelling and simulation of DME navigation global service volume. Adv. Space Res. **68**(8), 3495–3507 (2021)
8. Mardiyanto, R., Hidayat, R., Aprilian, E., Suryoatmojo, H.: Development of autopilot system of unmanned aerial vehicle for aerial mapping application. In: 2018 International Seminar on Intelligent Technology and Its Applications (ISITIA), Bali, Indonesia, pp. 357–361. IEEE (2018)
9. Kornienko, Y., Dulova, I.: Optimal surface relief reconstruction from both the photometric and the altimetric data. Radiofizika i elektronika **24**, 46–52 (2019)
10. Prophète, C., Pierrat, R., Sik, H., Kling, E., Carminati, R., de Rosny, J.: Modeling of an active terahertz imaging system in brownout conditions. Appl. Opt. **57**(21), 6017–6026 (2018)
11. Planting a Helicopter Blindly: A Synthetic Vision Technology Review. https://sudonull.com/post/55036-Planting-a-Helicopter-Blindly-A-Synthetic-Vision-Technology-Review. Accessed 09 Sept 2016
12. Ren, K.: Direction finding using a single antenna with blade modulation. IEEE Antennas Wirel. Propag. Lett. **21**(5), 873–877 (2022)
13. Volosyuk, V., Zhyla, S., Inkarbaieva, O., Kolesnikov, D.: Optimization of the surface formation algorithm by the airborne helicopter radar. In: 2022 IEEE 16th International Conference on Advanced Trends in Radioelectronics, Telecommunications and Computer Engineering (TCSET), Lviv-Slavske, Ukraine, pp. 398-403. IEEE (2022)
14. Volosyuk, V., Zhila, S., Kolesnikov, D.: Phenomenological description of coherent radar images based on the concepts of the measure of set and stochastic integral. Telecommun. Radio Eng. **78**(1), 19–30 (2019)
15. Zhang, X., Xu, F.: Multi-dimensional scattering distribution function for rough surface in SAR images. In: 2021 International Applied Computational Electromagnetics Society (ACES-China) Symposium, Chengdu, China, pp. 1–2. IEEE (2021)
16. Yang, J., Li, Y., Shi, J., Du, Y.: Modification of the extended advanced IEM for scattering from randomly rough surfaces. IEEE Geosci. Remote Sens. Lett. **18**(2), 236–240 (2021)

17. Zhang, Y., He, S., Zhu, G., Li, X., Li, Y.: Electromagnetic scattering study of complex targets on rough surfaces. In: 2019 International Applied Computational Electromagnetics Society Symposium, Nanjing, China, pp. 1–2. IEEE (2019)
18. Park, S., Oh, Y.: Accuracies of theoretical models for estimating reflection coefficients of rough sea surfaces. In: 2016 IEEE International Geoscience and Remote Sensing Symposium (IGARSS), Beijing, China, pp. 3699–3701. IEEE (2016)
19. Zhang, C., Cai Q., Cao, X., Zhu, M., Zhu, Y., Zhao, Y.: Research on radar scattering modeling and characteristics of moving unmanned air vehicle above a randomly rough surface. In: 2020 9th Asia-Pacific Conference on Antennas and Propagation (APCAP), Xiamen, China, pp. 1–2. IEEE (2020)
20. Yang, X., Tong, L., Li, M.: An improved two-scale method for simulating the backscattering of random rough surfaces. In: 2021 IEEE International Geoscience and Remote Sensing Symposium (IGARSS), Brussels, Belgium, pp. 3530–3533. IEEE (2021)
21. Popov, A., Bortsova, M., Sobkolov, A.: A fast algorithm for modeling rough surfaces in the remote sensing tasks. In: 2019 IEEE 15th International Conference on the Experience of Designing and Application of CAD Systems (CADSM), Polyana, Ukraine, pp. 1–4. IEEE (2019)
22. Jing, W., Wei, Y., Liu, X., Yang, C., Jiang, G.: Mean return waveform computations of rough surface for low-altitude radar altimeter. In: 2021 International Conference on Microwave and Millimeter Wave Technology (ICMMT), Nanjing, China, pp. 1–3. IEEE (2021)
23. Kedward, L., et al.: The State of Fortran. Comput. Sci. Eng. **24**(2), 63–72 (2022)

Current Trends in Bulk Solids Quantity Monitoring Inside the Large Capacity Industrial Tanks and Reservoirs

Oleksandr V. Zabolotnyi(✉) and Dmitriy O. Tsyban

National Aerospace University "Kharkiv Aviation Institute", Kharkiv 61070, Ukraine
o.zabolotnyi@khai.edu

Abstract. The surface of a bulk substance is usually very irregular and can include very high peaks and deep tunnels, what make single point level measurements rather tricky. The main task of the study was to investigate the possibility of bulk solids quantity or volume monitoring by surface 3D scanning with a help of the only one single point high frequency radar combined with a hexapod movable platform. Desirable position and orientation of a hexapod platform can be provided by solving the inversed kinematics task, when we can estimate the length of each kinematic rod knowing the displacement of the movable platform in relation to the stationary base . The possible algorithm for the grain volume calculation was suggested, similar to what is used together with acoustic or laser systems for surface 3D scanning, which provides the possibility of accurate bulk solids quantity monitoring.

Keywords: level measurement · high frequency radar · hexapod platform · density point cloud · 3D visualization

1 Introduction

Level (quantity) measurement of solids is typically implemented to reservoirs, which can store a variety of materials, such as cement, plastic pellets, coal, lime, flour, grain, aggregates, wood dust etc. [1]. Depending on the dedication, such reservoirs have different design, shapes and sizes [2]. Silo in the most cases is a cylindrical storage vessel for bulk substances in either steel or concrete. It typically has two to thirty meters in diameter and ten to sixty meters in height. Hoppers or bins are traditionally smaller than silos. These reservoirs are used as intermediate buffers between inventory and daily production [3]. Hoppers are temporary storage containers for dry solids, holding product for later use.

Many level measurement methods have been developed to measure the amount of solids in silos, starting from the very basic techniques and up to the high tech [1, 4]. In the present market of level measurements for solids we can detect: rope measurement; plumb bob; load cell/strain gauge; capacitance; ultrasonic; laser; guided wave radar and radar.

M. Nechyporuk et al. (Eds.): ICTM 2023, LNNS 1008, pp. 541–552, 2024.
https://doi.org/10.1007/978-3-031-61415-6_46

Among the direct, we can mention rope measurement and plumb bob methods [5]. These methods are reasonably accurate and suitable for materials with very low bulk density. Among the main disadvantages we can detect the impossibility to operate during the filling process, damage of cables and weights in turbulent applications, possible failures when the cable collects dust and debris.

The oldest continuous level measurement technology for solids is the static weight system. The silo or hopper sits directly on multiple load cells that put out a signal level directly proportional to the weight of the silo [6]. Strain gauges operate similarly by reporting a varying voltage output with load. The method provides accurate measurements of the mass of the silo with its content. From the other hand, the installation of load cells can be difficult and expensive if the silo must be completely lifted onto the cells. The process of the static weight system calibration with the necessity to define zero and mass span points can be tricky [7].

Capacitance technology of level detection had been used for over fifty years. A capacitive measuring instrument uses an electronics transmitter with a non-insulated probe and a ground reference. The ground reference can be a metallic silo wall, connected to electrical earth [8, 9]. Capacitance technology can be used in wide range of applications, including high temperature and high pressure. It has installation flexibility and can be assembled on the top, on the side or at the bottom of a silo, if necessary [10]. Among disadvantages, we can name the increased sensitivity to moisture and dielectric properties of a bulk substance [11–13].

Ultrasonic technology uses the time-of-flight principle, directing high frequency sound waves to the material by a transducer and measuring the time lapse of the return [14]. Frequencies around 5 kHz are commonly used for solids while frequencies at 44 kHz or above are used for primarily liquid targets. Ultrasonic meters are non-contact, low cost and reliable devices and can be used in completely opened silos or hoppers. In the other hand dust can prevent the return of the ultrasonic signal, high temperature leads to measurement uncertainty and sloped surfaces may cause indirect reflection [15].

Laser technology is a second example of the time-of-flight principle, operating at laser wavelength. Laser technology is effective for scanning the surface and accurate volume measurements in mediums with minimal dust. When applied for solids it requires an air purge option [16]. Laser technology provides narrow beam and accurate point measurements with very fast update rates. Negatives are high maintenance associated with cleaning and poor performance in dusty applications. Extremely dusty environments absorb the laser signal and there is no reflection from the surface [17].

Guided wave radar (TDR) technology sends an electromagnetic pulse trough a guided conductor until it hits the tank contents and then returns [18]. This technology is generally limited to 20 m or less range of measurement and materials that are not extremely heavy or abrasive. Like ultrasonic, it is easy to set up and has relatively low cost. Besides, it is not sensitive to atmospheric conditions (dust, temperature and pressure). Big list of restrictions for the guided conductor (cable system) installation can be a significant disadvantage of the TDR technology [19].

Radar technology had been used successfully for liquid level measurement since the middle of 1970s on large storage vessels. After 2000, when 24 GHz radar systems appeared, they quickly became the preferred measurement technology for all leading manufacturers [20]. Present radar measuring instruments are cost effective, work well in dusty mediums, are effective up to 100 m range and provide high accuracy. Among the disadvantages, we can mention the possible influence of a filling stream, causing false measurements, and tricky measurements of very top and very bottom levels [21].

For the most tasks of bulk substances quantity monitoring inside the large capacity industrial tanks radar technology prevails the others.

2 Problem Statement

One of the important factors in silo level measurement is the structure of a grain surface inside the silo. These complex structures occur after the grain is unloaded from the silo or after its filling (Fig. 1).

Fig. 1. Example of a complex surface structure inside the silo

Single-point level measuring systems like ultrasonic, laser or traditional radar provide a perfect solution for level measurement of liquids. Measurement of the silo level with single-point measuring instruments cannot be a good solution because of low accuracy and possibility to operate only with estimated volume values. The surface of a bulk substance is usually very irregular and can include very high peaks and deep tunnels. The error can be reduced by increasing the number of sensors or acoustic 3D scanners application, what is a traditional solution.

The task of a present research is to investigate the possibility of surface 3D scanning with a help of the only one single point high frequency (80…120 GHz) radar combined with an automated rotary device, based on Stuart hexapod movable platform [22]. It seems to be an effective solution to solve the current problems of point radar level or volume measurements in silos.

3 Materials and Methods

However, when it comes to measuring the level in silos, tanks containing bulk solids with high material stacking, using single-point measurement methods may not accurately reflect the level of material inside the silo, nor accurately estimate the remaining volume of the material.

At a present moment acoustic 3D scanners with multi-point measurement function is the only solution, capable to solve this problem [23]. 3D level scanners provide holistic imaging of the level of the bulk substance inside the silo. The 3D level scanner is based on a non-contact continuous level transmitter technique, which is appropriate for not just measuring irregular surfaces but also provides imaging inside the silos. The technology implements the acoustic pulse system, which helps in mapping a representation of the interiors of closed and/or open silos, bins, and bunkers. It also helps in detecting sidewall buildup [24].

Traditional 3D level scanner consists of 3 antennas. These antennas work as trans-receivers that transmit low-frequency pulses and receive them back to create an image of that point. The 3D level transmitter receives echoes of the pulses and measures the distance based on the time of flight principle and the beam angle. Usually it has a digital signal processor unit, which analyses each echo to measure all levels such as maximum, minimum, average along with the volume and mass of the goods stored in the silos. To measure the volume and mass, the 3D level transmitter assigns each echo received with a weight instead of averaging it out. This weight is later being used to digitally map the points of level and measure the mass and volume accurately irrespective of the type and size of the material that is being stored.

When investigating the possibility of surface 3D scanning with a help of a single radar measuring instrument, it seemed possible to use one high frequency radar with a 80 GHz frequency and more. It has a very small beam angle (not more than 3.5°), measuring range up to 120 m and high accuracy (nearly ±5 mm for 80 GHz frequency and ±1 mm for 120 GHz frequency). The result of level measurement is invariant to changing process conditions such as temperature, pressure or strong generation of dust.

The next task is to combine the high frequency radar with an automated rotary device, to make it possible the automated complex radar movement with high precision. Here Stuart hexapod movable platforms seems to become a perfect solution (Fig. 2). Mechanisms of a parallel kinematic structure, based on a Stuart platform, consist of a stationary base, movable platform and six kinematic rods, which length can be adjusted with a help of six servo drives. Desirable position and orientation of a hexapod platform can be provided by changing the length of six kinematic rods and converting six transitional levels of freedom into three positional (vector of movement) and three orientation levels of freedom (steering angles of a solid body). Complexity of the hexapod dynamics makes it impossible to implement decentralized control without taking into account the mutual influence between different levels of freedom in kinematic rods' motion, because the movement of a separate kinematic rod is dependent [25]. Common instructions for hexapod control systems are absent, and it makes evident the necessity to synthesize an accurate hexapod dynamics equation.

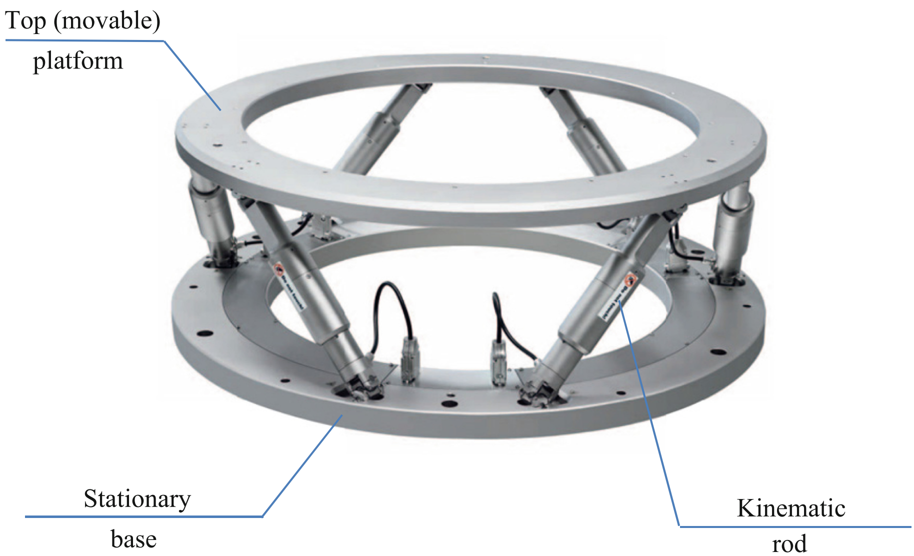

Fig. 2. Stuart hexapod movable platform

Modern Stuart platforms can provide motion ranges to ±200 mm and to ±20° with up to 1 µm and 0.5 µrad resolution respectively, what is quite enough to build an effective 3D scanning system for the bulk solids volume measurement inside the silo.

4 Theory/Calculation

Firstly, it is necessary to analyze the geometry and kinematic scheme of a hexapod platform (Fig. 3).

Let's introduce two systems of coordinates: inertial $O_0X_0Y_0Z_0$, connected with a center of a stationary base, and movable, $O_1X_1Y_1Z_1$, connected with a center of mass of the movable platform [26]. Movable platform coordinates can be described with a vector

$$r = (x, y, z, \alpha, \beta, \gamma)^{/}. \tag{1}$$

It contains linear displacements x, y, and z of the movable platform center of rotation O_1 in relation to the inertial system of coordinates $O_0X_0Y_0Z_0$, so as angular displacements: α – yaw angle, β – pitch angle, γ – roll angle. They describe the movable platform rotation in relation to the $O_1X_1Y_1Z_1$ system of coordinates. Kinematic rods length is usually described with another vector

$$q = (L_1, L_2, L_3, L_4, L_5, L_6)^{/}, \tag{2}$$

connected with an inertial system of coordinates $O_0X_0Y_0Z_0$.

Because of the specific design of a Stuart platform, we have a nonlinear dependence between the kinematic rods length and movable platform displacement [27]. This fact

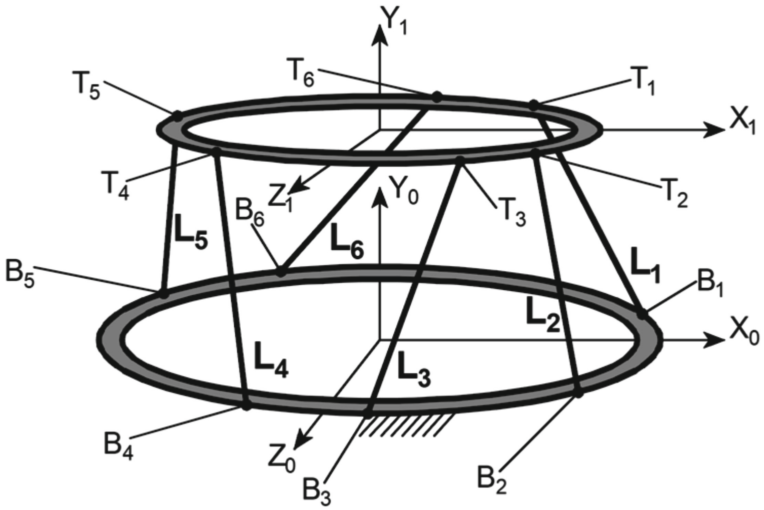

Fig. 3. Kinematic scheme of a hexapod platform

creates a task to define the movable platform coordinates when we know the length of each kinematic rod (task of forward kinematics), or a task to define the length of each kinematic rod when we know the movable platform displacement (task of inversed kinematics). The task of forward kinematics can be expressed with the Eq. (3):

$$\Delta X = J\Delta q, \tag{3}$$

where Δq is a vector of kinematic rods length increment, ΔX is a vector of x, y, z, and α, β, γ coordinates increment. A Jacobian J can be described with formula (4):

$$J = \lfloor J_1, J_2, J_3, J_4, J_5, J_6 \rfloor. \tag{4}$$

As for the task of inversed kinematics, we can describe it with the Eq. (5):

$$\Delta q = J^{-1}\Delta X. \tag{5}$$

The inversed kinematics task is when we can estimate the length of each kinematic rod knowing the displacement of the movable platform in relation to the stationary base. This is mathematically straightforward task to solve [28]. Consider the geometry of a hexapod shown in Fig. 3, we can write the next formulas:

$$L_1 = \sqrt{(T_{1x} - B_{1x})^2 + \left(T_{1y} - B_{1y}\right)^2 + (T_{1z} - B_{1z})^2},$$

$$L_2 = \sqrt{(T_{2x} - B_{2x})^2 + \left(T_{2y} - B_{2y}\right)^2 + (T_{2z} - B_{2z})^2},$$

$$L_3 = \sqrt{(T_{3x} - B_{3x})^2 + \left(T_{3y} - B_{3y}\right)^2 + (T_{3z} - B_{3z})^2},$$

$$L_4 = \sqrt{(T_{4x} - B_{4x})^2 + \left(T_{4y} - B_{4y}\right)^2 + (T_{5z} - B_{5z})^2},$$

$$L_5 = \sqrt{(T_{5x} - B_{5x})^2 + \left(T_{5y} - B_{5y}\right)^2 + (T_{5z} - B_{5z})^2},$$
$$L_6 = \sqrt{(T_{6x} - B_{6x})^2 + \left(T_{6y} - B_{6y}\right)^2 + (T_{6z} - B_{6z})^2}.$$

Necessary displacements and rotations of the movable platform can be directly implemented to the points $T_1 \ldots T_6$. The post-movement length of six kinematic rods $L_1 \ldots L_6$ can be recalculated for the new joint coordinates of the movable platform. Then it should be compared with the pre-movement leg length, to determine the necessary change in the length of each individual kinematic rod.

It makes possible to suggest the next structural control scheme for the hexapod platform movement (Fig. 4).

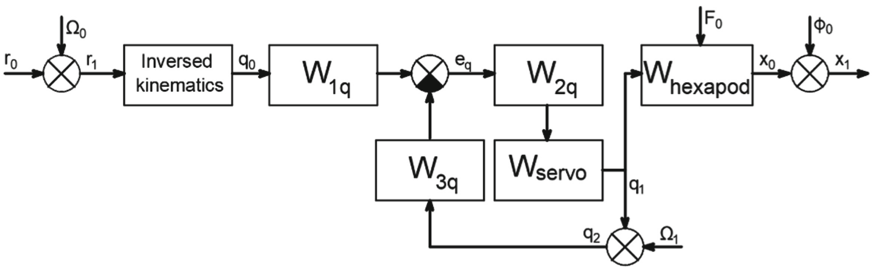

Fig. 4. Structural control scheme of a hexapod platform for the inversed kinematics task

Designations, present on Fig. 4, are described below:

- r_0 – vector, which describes the necessary displacement of the movable platform (six degrees of freedom) $r_0 = [x_0\ y_0\ z_0\ \alpha_0\ \beta_0\ \gamma_0]'$;
- Ω_0 – vector of errors (errors of interpolation and other factors, which influence the implementation of vector r_0) $\Omega_0 = [\Omega_x{}^0\ \Omega_y{}^0\ \Omega_z{}^0\ \Omega_\alpha{}^0\ \Omega_\beta{}^0\ \Omega_\gamma{}^0]'$;
- r_1 – real programmable vector of the movable platform displacement, which takes into account the errors $r_1 = r_0 + \Omega_0$;
- q_0 – vector of the six kinematic rods length set values $q_0 = [L_1{}^0\ L_2{}^0\ L_3{}^0\ L_4{}^0\ L_5{}^0\ L_6{}^0]'$;
- q_2 – vector of the six kinematic rods length measured values $q_2 = q_1 + \Omega_1 = [L_1{}^2\ L_2{}^2\ L_3{}^2\ L_4{}^2\ L_5{}^2\ L_6{}^2]'$, where q_1 is a vector of kinematic rods real length and Ω_1 is a vector of kinematic rods length measurement errors;
- x_0 – vector of the hexapod platform coordinates without disturbance in relation to the $O_0X_0Y_0Z_0$ system of coordinates, when the resistance to the platform movement is absent $x_0 = [x_0{}^0\ y_0{}^0\ z_0{}^0\ \alpha\ {}_0{}^0\ \beta_0{}^0\ \gamma_0{}^0]'$;
- Φ_0 – vector of disturbances, which influence the displacement coordinates of a movable platform $\Phi_0 = [\Phi_x{}^0\ \Phi_y{}^0\ \Phi_z{}^0\ \Phi_\alpha{}^0\ \Phi_\beta{}^0\ I_\gamma{}^0]'$.

Master regulator in the structural control scheme is divided into three parts: W_{1q}, W_{2q} and W_{3q}, to increase the control quality and take into account the cross-links inside the hexapod platform.

5 Results/Discussion

The next important step is to model the grain surface inside the silo and to determine grain quantity or grain volume. Firstly, it would be necessary to define the required number of control points for the radar 3D scanner displacement (Fig. 5).

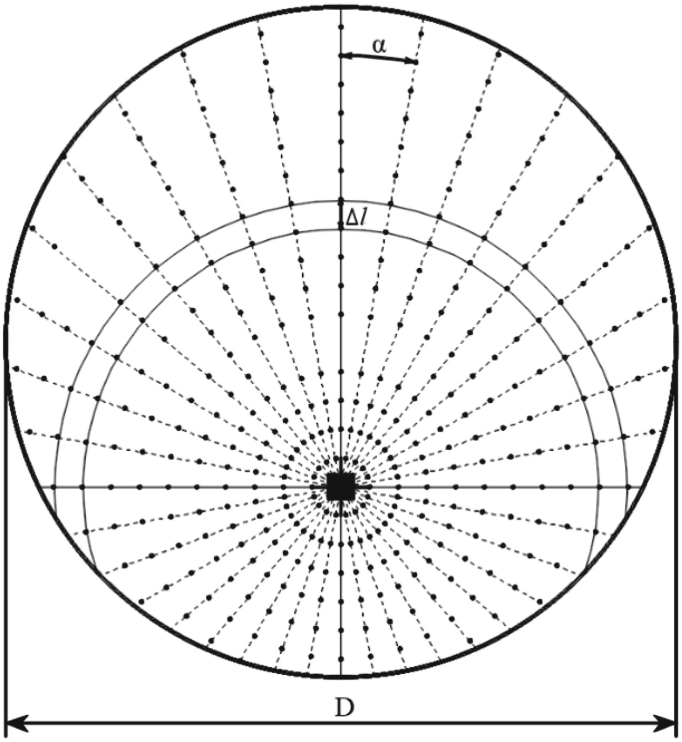

Fig. 5. Representation of a silo cross section with diameter D and distribution of the control points

At the initial processing step, the grain surface position at each control point can be estimated by transforming distances and angles, collected from the 3D scanner [29]. It is required to recalculate the point cloud data from spherical to Cartesian coordinates.

The X and Y coordinates form the horizontal plane are not adjusted because the 3D scanner was used as the XY origin. It is necessary to determine Z coordinate, which directly gives the displacement of a grain surface points in relation to the silo bottom. The final elevation of the grain surface can be calculated with a help of equation:

$$Z = H + \sin(\Theta)r - h, \tag{6}$$

where Z is a final elevation of the grain surface in relation to the silo bottom, m;

H is a height from the silo bottom to the eave, m;
Θ is a polar angle between origin and eave, °;

r is a distance from the origin to the eave, m;
h is an original elevation from the measurement system to the grain surface, m.

Further data processing can be performed with a help of dedicated software tools like MATLAB, ModelBuilder, ArcScene etc. [30]. The possible algorithm of the grain volume calculation is given on Fig. 6.

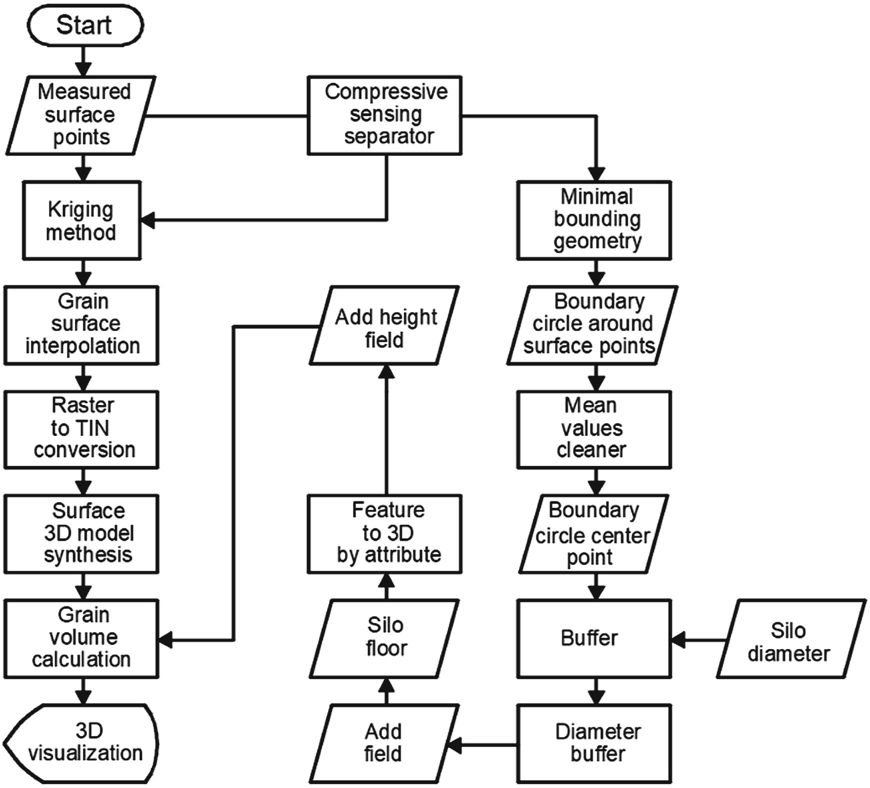

Fig. 6. Algorithm for the ModelBuilder procedure of the grain volume calculation

All of the measured points along the grain surface represent the only input feature. This density point cloud should pass compressive sensing tool, which performs effective separation of bulk grain reflections from wall reflections [20]. Silo diameter and height of the silo floor have to be defined within the model. Then a circular bounding geometry, which encompass the data set in the *XY* plane should be created, and the center of a bounded circle feature can be established with the mean center tool. A buffer that represented the silo diameter was created about the center point. An additional field contains the silo floor height, and the 3D attributes were created for the buffered polygon. For the measured surface points, it was possible to apply the Kriging method to interpolate the surface of the grain [31]. The resulting raster was converted to a Triangular Irregular Network (TINs are commonly used in engineering applications to calculate areas and volumes) [32]. The TINs allowed the surface model displacement and storage in a 3D format. Finally, the polygon volume tool is necessary to calculate the volume between the grain surface (a TIN feature) and silo bottom (a polygon feature). The 3D visualization of the silo floor and grain surface as a both a points and TIN feature can be conducted with ArcScene software.

6 Conclusions

Single-point level measuring systems like ultrasonic, laser or traditional radar provide a perfect solution for level measurement of liquids. Measurement of the silo level with single-point measuring instruments cannot be a good solution because of low accuracy and possibility to operate only with estimated volume values. The surface of a bulk substance is usually very irregular and can include very high peaks and deep tunnels, what makes single-point measurements rather tricky.

The possibility of surface 3D scanning with a help of a single radar was investigated. It seems quite possible to use one high frequency radar with 80 GHz frequency and more as a combination with an automated Stuart hexapod movable platform. Desirable position and orientation of a radar can be provided by changing the length of six kinematic rods. A hexapod implementation is perhaps the most efficient method of achieving six degrees of freedom in terms of space, economics, and possibly design. A traditional method might consist of three linear stages, a tip/tilt stage, and a rotary stage, stacked on top of each other. Each axis will require an actuator and the mechanism to define the desired degree of freedom. By comparison, a hexapod likely has six identical linear actuators with identical drive parameters to accomplish the same six degrees of freedom.

The structural control scheme for the hexapod platform movement is suggested, following the inversed kinematics task, when we can estimate the length of each kinematic rod knowing the displacement of the radar, assembled on the top of the movable platform, in relation to the stationary base.

Besides, the possible algorithm for the grain volume calculation was suggested, similar to what is used together with acoustic or laser systems for surface 3D scanning. We expect our high frequency radar surface 3D scanner to be more effective in comparison with laser or acoustic 3D scanners, because they have enough small beam angle, measuring range up to 120 m and high accuracy. What is very important, the results of radar level measurement are invariant to changing process conditions such as temperature, pressure or strong generation of dust unlike laser and acoustic systems.

References

1. Heywood, N., Tily, P.J.: Survey and selection of techniques for bulk solids level measurement in storage vessels. In: 12th Transport and Sedimentation Conference, Prague, Czech Republic, pp. 1–15 (2004)
2. Saleem, M., Khurshid, H., Qureshi, H., Siddiqi, Z.: A Simplified approach for analysis and design of reinforced concrete circular silos and bunkers. Open Constr. Build. Technol. J. **12**, 234–250 (2018)
3. McGlinchey, D.: Bulk Solids Handling: Equipment Selection and Operation. Blackwell Publishing Ltd., USA (2008)

4. Yigit, E.: A novel compressed sensing based quantity measurement method for grain silos. Comput. Electron. Agric. **145**, 179–186 (2018)
5. Joseph, D.L.: Level Measurement of Bulk Solids in Bins, Silos and Hoppers. Technology Review. Monitor Technologies LLC, USA (2004)
6. Stergioulas, L., Cebon, D., Macleod, M.: Static weight estimation and system design for multiple-sensor weigh-in-motion. Proc. Inst. Mech. Eng. Part C J. Mech. Eng. Sci. **214**, 1019–1035 (2000)
7. Muhammad, M.M., Syed, W.H.: Effect of static weight errors on Weigh-in-Motion (WIM) system accuracy. Measurement **206**, 112301 (2023)
8. Kumar, B., Rajita, G., Mandal, N.: A review on capacitive-type sensor for measurement of height of liquid level. Meas. Control **47**(7), 219–224 (2014)
9. Bento, R.T., Silva, R.W.O., Dias, L.A., et al.: Design, development and application of a real-time capacitive sensor for automatically measuring liquid level. SN Appl. Sci. **1**, 734 (2019)
10. Pal, A., Kalyan, U., Harika, C., Balasubramanian, V.: Capacitive sensor for level measurement in hopper/silos - experimental evaluation. In: 2nd International Conference on Intelligent Computing, Instrumentation and Control Technologies (ICICICT), Kannur, India, pp. 202–205 (2019)
11. Zabolotnyi, O., Zabolotnyi, V., Koshevoy, N.: Capacitive water-cut meter with robust near-linear transfer function. Computation **10**, 115 (2022)
12. Zabolotnyi, O., Zabolotnyi, V., Koshevoy, N.: Adequacy and robustness analysis of the capacitive moisture meters' static function. In: 2022 IEEE 41st International Conference on Electronics and Nanotechnology (ELNANO), Kyiv, Ukraine, pp. 506–512 (2022)
13. Zabolotnyi, O., Zabolotnyi, V., Koshevoy, N.: Grain moisture measurement system with robust transfer function, invariant to the change of a grain matrix composition. INMATEH Agric. Eng. **69**(1), 389–398 (2023)
14. Gao, W., Liu, W., Li, F., Hu, Y.: Analysis and validation of ultrasonic probes in liquid level monitoring systems. Sensors **21**(4), 1320 (2021)
15. Milligan, S., Vandelinde, H., Cavanagh, M.: Understanding Ultrasonic Level Measurement, 3rd edn. Siemens Milltronics Process Instruments, Canada (2012)
16. Sun, J.P., Jiang, J.: Laser monitoring of the coal level of coal silo by depth pre-calibration. Meitan Xuebao J. China Coal Soc. **37,** 172–176 (2012)
17. Rhee, J.H., Kim, S.I., Lee, K.M., Kim, M.K., Lim, Y.M.: Optimization of position and number of hotspot detectors using artificial neural network and genetic algorithm to estimate material levels inside a silo. Sensors **21**, 4427 (2021)
18. Sahare, A.: Guided wave radar for precise level measurement using time domain reflectrometry (TDR) principle. Int. J. Innov. Res. Comput. Commun. Eng. **03**, 4987–4995 (2015)
19. Wegner, T.E., Gebhardt, S., Del Galdo, G.: Fill level measurements using an M-sequence UWB radar. Int. J. Microw. Wirel. Technol. **15**, 74–81 (2023)
20. Yigit, E., Işiker, H., Toktas, A., Tjuatja, S.: CS-based radar measurement of silos level. In: IEEE International Geoscience and Remote Sensing Symposium (IGARSS), Milan, Italy, pp. 3746–3749 (2015)
21. Zini, M., et al.: Radar sensor system for unobtrusive level monitoring of granular solids stored in silos. In Book: Sensors and Microsystems, pp. 147–152 (2023)
22. Dragne, C., Chiroiu, V.: Hexapod workspaces – positions, speeds, forces. In: The 9th International Conference on Computational Mechanics and Virtual Engineering, Romania, pp. 1–9. Transilvania University of Brasov (2021)

23. Feed&Grain Homepage. https://www.feedandgrain.com/grain-handling-processing/article/15394475/3d-level-sensors-can-address-grain-storage-challenges?__cf_chl_tk=kZHmgznI2HHmp3HIBY2gcJKbJwMpsz.PXsPGcLJI6mo-1700926946-0-gaNycGzNDyU. Accessed 20 Nov 2023
24. Sodsri, C.: Measurement of material volumes in a cylindrical silo using acoustic wave and resonance frequency analysis. Bull. Electr. Eng. Inform. **9**(4), 1585–1594 (2020)
25. Blaise, J., Bonev, I., Montsarrat, B., Briot, S., Lambert, M.: Kinematic characterisation of hexapods for industry. Ind. Robot Int. J. **37**(1), 79–88 (2010)
26. DeWitt IV, F.A.: An inverse kinematics approach to hexapod design and control. In: Proceedings of SPIE, Advances in Optomechanics, 74240O, vol. 7424 (2009)
27. Bülthoff, H.: Towards simulating a mid-size stewart platform on a large hexapod simulator. In: AIAA Modeling and Simulation Technologies Conference, Chicago, Illinois, USA, pp. 1–10 (2009)
28. Conti, J.P., Clinton C.M., Zhang, G.: Workspace Variation of a Hexapod Machine Tool, 2nd edn. U.S. Department of Commerce, USA (1998)
29. Turner, A.P., et al.: Stored grain volume measurement using a low density point cloud. Appl. Eng. Agric. **33**(1), 105–112 (2017)
30. Steer, P., Guerit, L., Lague, D., Crave, A., Gourdon A.: Size, shape and orientation matter: fast and automatic measurement of grain geometries from 3D point clouds. EGUsphere 75 preprint, 1–31 (2022)
31. Erdogan, S.: A comparison of interpolation methods for producing digital elevation models at the field scale. Earth Surf. Process. Landf. **34**(3), 366–376 (2009)
32. Bhargava, N., Bhargava, R., Tanwar, P.S.: Triangulated irregular network model from mass points. Int. J. Adv. Comput. Res. **3**(2), 172–176 (2013)

Complexity Reduction in DAT-Based Image Processing

Viktor Makarichev(✉), Vladimir Lukin, and Iryna Brysina

National Aerospace University "KhAI", Chkalov Street 17, Kharkiv 61070, Ukraine
victor.makarichev@gmail.com

Abstract. The atomic functions-based image processing system (AFIPS) is based on discrete atomic transform (DAT). It provides a combination of image encryption and compression features with a machine learning-oriented data format. Taking into account the current data processing and analysis trends, applying AFIPS is promising. In this paper, a problem of its complexity reduction is considered. The new coding scheme, which ensures a significant decrease in the number of arithmetic operations, is proposed, and its efficiency exploration is given in terms of different indicators. In particular, it is shown that the proposed modification of AFIPS provides a higher compression ratio and, hence, greater memory savings when applying this algorithm with three modes of the DAT procedure: classic, block-splitting, and chroma-subsampling. Also, the suggested improvement reduces the time complexity that is illustrated by processing a satellite image dataset. In addition, the practical aspects of the further applications, including UAV image processing and analysis, are discussed.

Keywords: Discrete Atomic Transform · Lossy Image Compression · Data Coding · Image Encryption

1 Introduction

Data processing is a rapidly developing branch of information technology. Due to different reasons, in particular the significant increase in computational capabilities and reduction in hardware price, it has become an integral part of all kinds of production [1, 2], economic and financial processes [3, 4], social communication [5, 6], etc. Data manipulation is a key component. Its proper management ensures solving the required tasks, a decrease in resource expenses, and sustainable development. Taking into account a set of current challenges, including cybercriminal activity [7], deepfake threats [8], and huge amounts of information [9], it requires new approaches and principles. Their design and development can be based on non-classic mathematical tools that combine fundamental validation with the simplicity of practical implementation. In this paper, we consider the data processing method that is constructed using such objects. Image processing is a focus of the current research. Criminal activity [7], deepfake threats [8], and huge amounts of information [9], it requires new approaches and principles. Their design and development can be based on non-classic mathematical tools that combine fundamental

M. Nechyporuk et al. (Eds.): ICTM 2023, LNNS 1008, pp. 553–565, 2024.
https://doi.org/10.1007/978-3-031-61415-6_47

validation with the simplicity of practical implementation. In this paper, we consider the data processing method that is constructed using such objects. Image processing is a focus of the current research.

Digital images are a particular part of data [10]. They have numerous applications, for instance, in security [11, 12] and ecology monitoring [13, 14], agriculture development [15, 16], medicine [17, 18], remote sensing [19, 20], etc. There are many classes of images, and their common feature is the high resource expenses needed for storing, processing, transferring via networks, and analyzing [21, 22]. Compared to other data types, for instance, texts and audio recordings, they require much greater memory costs. Moreover, in most cases, digital images belong to the unstructured data category, which complicates their application in artificial intelligence (AI) and machine learning (ML) [23]. In addition, some of their classes, in particular medical, security camera, aerial, and satellite data, must be protected from hackers and terrorists [24, 25].

Hence, the following features of image processing methods are required: encryption, compression, and structured content representation.

There are many algorithms that ensure either data encryption [26, 27] or compression features [28]. Also, methods that are focused on images only have been developed [29, 30]. Nevertheless, none of them can be considered the perfect one. Indeed, in most cases, just protection or memory expense reduction is ensured. In some applications, a combination of compression and encryption is obtained by combining several approaches that lead to additional computational expenses, especially when processing large datasets. Moreover, most existing image formats do not provide AI/ML-oriented representation, i.e., data from such files cannot be used directly without preprocessing. In particular, decompression and decryption are required.

So, the problem of creating methods that ensure a combination of image compression and protection with AI/ML-oriented data formats is opened. Considering the explosive increase in computer vision (CV) applications, it is of particular interest. The necessity to satisfy current data manipulation regulations [31, 32] and AI technology development declarations [33] makes this problem of particular importance.

In [34], an atomic functions-based image processing system (AFIPS) is proposed. It can be considered an attempt to solve the problem stated. AFIPS provides image encryption as well as lossy and lossless compression [35, 36]. Besides, the proposed data format is supposed to be useful in ML and CV [34].

Discrete atomic transform (DAT) is a core of the AFIPS system [34]. It is based on applying the special class of atomic functions [37, 38]. The DAT procedure has low time [39] and spatial complexity [40] that makes AFIPS use promising especially in autonomous and edge computing systems [41, 42].

In this paper, we improve the performance of coding the DAT coefficients, which is an essential part of AFIPS [34]. We propose a computation reduction approach that forms a novelty of the current research. Our contribution is a comprehensive investigation of the proposed method of applying the AFIPS system in various image processing modes. The paper is organized as follows. First, the research task is formulated. Then, the proposed solution is given and its performance is investigated by processing test image dataset. After that, the results obtained are discussed. Finally, the conclusions follow.

2 Task Formulation

The AFIPS system is shown in Fig. 1. It works as follows [34].

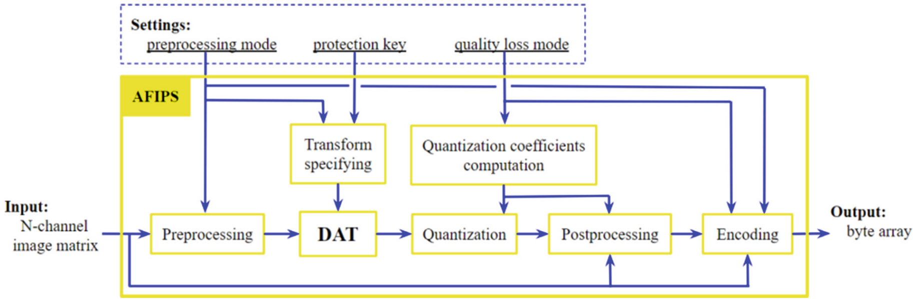

Fig. 1. Atomic function-based image processing system.

An input is a matrix of multi-channel digital image. When processing a grayscale 8-bit data, the number of channels is equal to 1. When processing 24-bit full color images, it is given by a matrix of RGB-components: red (R), green (G) and blue (B) AFIPS operation is specified by a group of the following settings: preprocessing mode, protection key and quality loss mode.

Preprocessing settings define a set of procedures that have to be applied to the input matrix:

- RGB-to-YCrCb transform that computes three matrices of luma (Y) and chroma (Cr, Cb) components;
- chroma-subsampling procedure, which may follow the RGB-to-YCrCb transform;
- block-splitting, i.e. a source matrix is splitted into fixed size blocks.
- Then, the transform can be applied to both grayscale color and full images as well as to multi-channel ones.

The image preprocessing step can be skipped. Otherwise, its parameters are encoded in order to provide correct reconstruction.

A protection key, given as a bit set, specifies a structure of the DAT transform. The protection feature of AFIPS is ensured by storing it separately from the output data which is a byte array. Further, this data can be stored in a binary file or transferred via networks.

Quality loss mode defines the type of compression: lossless or lossy. When applying lossy image compression, the parameter denoted by *UBMAD* is provided. It defines quantization coefficients and, hence, distortions level (see [35] for more details).

The main computations are performed in the following order:

Preprocessing. The image matrix A is preprocessed. This stage provides the set of matrices $\{B_1, \ldots, B_m\}$.

Discrete Atomic Transform. The DAT is applied to each matrix B_k. A structure of DAT is specified by the protection key and preprocessing mode. The set $\{W_1, \ldots, W_m\}$ of matrices of DAT-coefficients is an output of this stage.

Quantization. The elements of $\{W_1, \ldots, W_m\}$ are quantized. Wherein, the coefficients of quantization are defined by *UBMAD*. An output of this stage is the set $\{T_1, \ldots, T_m\}$ of matrices of quantized DAT-coefficients.

Postprocessing. When applying the lossy compression mode, this stage is skipped. Otherwise, the following steps are performed:

1) dequantize matrices $\{T_1, \ldots, T_m\}$;
2) apply inverse DAT to each matrix computed at the previous step;
3) applying inverse preprocessing and compute the matrix R, which is a reconstruction of the source matrix A;
4) compute the difference matrix $D = A – R$.

Coding. Matrices $\{T_1, \ldots, T_m\}$ and the difference matrix D are encoded using a combination of Golomb codes with context adaptive binary arithmetic coding (CABAC).

Consider this procedure more in detail. Since the Golomb coding works with positive numbers, the AFIPS system uses its minor modification. Each positive integer k is assigned to a bit sequence as follows:

$$k \leftrightarrow \underbrace{11 \ldots 1}_{2k-1} 0, \tag{1}$$

and each negative integer ($–k$) is encoded as follows:

$$-k \leftrightarrow \underbrace{11 \ldots 1}_{2k} 0. \tag{2}$$

Then, the binary stream obtained is compressed using CABAC that requires a lot of arithmetic operations [28]. This is a bottleneck of AFIPS for the following reasons.

Currently, digital images have a great number of pixels. Therefore, matrices $\{T_1, \ldots, T_m\}$ and D contain a lot of elements, which are encoded using (1), (2). This implies that the corresponding binary stream consists of a huge number of bits, each of which requires applying a lot of arithmetic operations. So, the coding stage is computationally expensive and, hence, its improvement is a must. The task of this research is to reduce a number of arithmetic operations at the coding stage of AFIPS.

3 Task Solution

3.1 Coding Improvement

In order to reduce the number of arithmetic operations when coding data in AFIPS we propose the following binary stream assignment:

$$0 \leftrightarrow 0, \tag{3}$$

$$k \leftrightarrow \underbrace{11 \ldots 1}_{k} 01, \tag{4}$$

$$-k \leftrightarrow \underbrace{11 \ldots 1}_{k} 00, \tag{5}$$

where k is a positive integer.

The main features of the proposed approach are:

– the first bit indicates if an encoded number is equal to zero or not;
– the last bit of each non-zero value representation defines its sign.

Next, we suggest to perform the following bypass:

1) scan the first bit of each encoded value;
2) scan the last bit of each non-zero value;
3) for each non-zero value, scan the rest of bits, except the first and the last ones.

Further, we call the proposed binary stream assignment *progressive*.

Finally, the obtained data are compressed using CABAC. In Fig. 2, an illustration of the suggested approach is given.

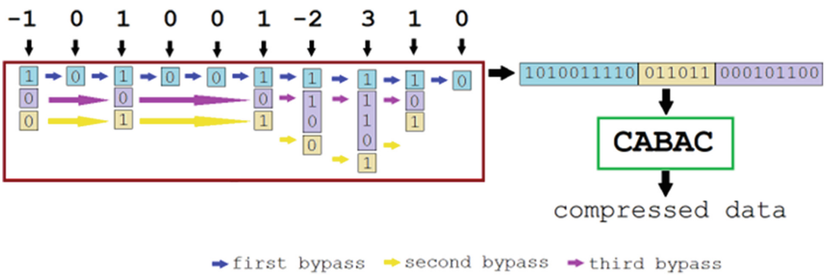

Fig. 2. Progressive encoding scheme: example.

Now, we investigate the efficiency of the progressive scheme. First, it follows that its applying in the AFIPS system can only affect the compression ratio (CR), which is defined as follows:

$$CR = \frac{size\ of\ \ the\ source\ image}{size\ of\ \ the\ compressed\ image}.$$

Wherein, the loss of quality, which is introduced at the quantization stage, remains unchanged. Hence, values of distortions indicators, in particular, root mean square error (RMSE) and peak signal-to-noise ratio (PSNR), are the same.

Second, Table 1 allows the comparison of the Golomb coding (1), (2) with the progressive scheme given in (3)–(5).

It follows that

1) both the Golomb and progressive approaches encode zero values in the same way;
2) the Golomb coding requires one less bit than progressive, when coding 1;
3) when encoding (-1) and 2, both methods provide the same number of bits;
4) when coding integers that are greater than 1 in absolute value, the progressive scheme needs less bits.

It is clear that the length of the bit sequence, which is further compressed by CABAC, significantly depends on the encoded value distribution that is specified by image content as well as its processing settings. In order to investigate the performance of the proposed coding approach, we process the test images dataset with various AFIPS settings and explore the efficiency measured by CR, total memory expenses and processing time.

Table 1. Bit sequence lengths comparison.

Value	Golomb		Progressive	
	bit sequence	length	bit sequence	length
0	0	1	0	1
1	10	2	101	3
–1	110	3	100	3
2	1110	4	1101	4
–2	11110	5	1100	4
3	111110	6	11101	5
–3	1111110	7	11100	5
...	...	...	...	...
k	$\underbrace{11\ldots1}_{2k-1}0$	$2k$	$\underbrace{11\ldots1}_{k}01$	$k+2$
$-k$	$\underbrace{11\ldots1}_{2k}0$	$2k+1$	$\underbrace{11\ldots1}_{k}00$	$k+2$
...	...	...	...	...

3.2 Test Data Processing

Now, we study the efficiency of the proposed method. For this purpose, a set of 93 three-channel large-scale satellite images of European Space Agency () is processed. The total size is 7.22 GB. Each sample has a lot of small-sized objects and sharp changes of color. In other words, the test dataset has the complex content. Raw images can be found at the following link: https://drive.google.com/drive/folders/1ndK4VkaQBO2hWU_mYE8xG9CHL_2TYNco?usp=sharing.

The test images are processed by the AFIPS system with the following preprocessing modes:

– *classic* – the RGB-to-YCrCb color space transform is applied to source matrix;
– *block-splitting* – a combination of RGB-to-YCrCb transform with splitting image into 512 × 512 blocks is applied;
– *chroma-subsampling* – the RGB-to-YCrCb conversion and chroma subsampling are performed.

The *UBMAD* parameter, which defines coefficients of quantization of DAT-coefficients, is varied. Lossy compression is evaluated in terms of *CR* and total memory expenses. In addition, *PSNR* is computed. Besides, time of compression/decompression is determined.

Tables 2, 3, 4, 5, 6 and 7 presents the obtained results. Due to page limitations, the averaged values are presented. One can find all data processing results at the following link: https://drive.google.com/drive/folders/1B--jCaN6VIXxVqQEkwjxJlZAM1T-UVs8?usp=drive_link. Test data processing is carried out on the AMD Ryzen 5 5600H CPU, 16 GB RAM.

In the next subsection, a comprehensive analysis is provided.

Table 2. Lossy compression performance: the classic mode.

UBMAD	*PSNR, dB*	*CR*		Total size, MB	
		Golomb	Progressive	Golomb	Progressive
36	46.04	2.34	2.46	3193.12	3057.14
63	41.00	3.84	4.17	1990.63	1855.24
95	38.25	5.00	5.49	1554.42	1434.05
155	35.24	7.44	8.31	1081.48	981.08

Table 3. Time performance: the classic mode.

UBMAD	Average time: compression/decompression		Total time: compression/decompression	
	Golomb, sec	Progressive, sec	Golomb, sec	Progressive, sec
36	10.17/8.65	6.45/5.19	946/804	600/483
63	6.89/5.12	4.25/3.24	641/476	396/302
95	5.84/4.15	3.62/2.68	543/386	337/249
155	4.83/3.17	3.01/2.08	449/295	280/194

Table 4. Lossy compression performance: the block-splitting mode.

UBMAD	*PSNR, dB*	*CR*		Total size, MB	
		Golomb	Progressive	Golomb	Progressive
36	45.99	2.32	2.43	3220.32	3094.95
63	40.96	3.87	4.14	1991.99	1875.90
95	38.21	5.06	5.46	1549.63	1447.78
155	35.20	7.60	8.32	1071.92	986.99

Table 5. Time performance: the block-splitting mode.

UBMAD	Average time: compression/decompression		Total time: compression/decompression	
	Golomb, sec	Progressive, sec	Golomb, sec	Progressive, sec
36	10.47/8.44	7.52/5.42	974/785	700/505
63	6.97/4.90	5.48/3.50	648/456	510/326
95	5.98/3.89	4.65/2.82	556/362	433/263
155	4.92/2.90	3.98/2.17	458/270	371/202

Table 6. Lossy compression performance: the chroma-subsampling mode.

UBMAD	*PSNR, dB*	*CR*		Total size, MB	
		Golomb	Progressive	Golomb	Progressive
36	36.91	3.97	4.16	1863.00	1784.43
63	35.78	6.04	6.53	1242.00	1158.35
95	34.70	7.51	8.22	1008.32	931.15
155	33.08	10.32	11.50	751.57	682.48

Table 7. Time performance: the chroma-subsampling mode.

UBMAD	Mean: compression/decompression		Total: compression/decompression	
	Golomb, sec	Progressive, sec	Golomb, sec	Progressive, sec
36	6.23/5.63	3.69/3.08	579/524	344/287
63	4.12/3.38	2.63/2.08	383/243	245/194
95	3.54/2.61	2.25/1.73	329/243	210/161
155	2.88/2.05	1.90/1.40	268/191	177/130

3.3 Analysis

From results, presented in Tables 3, 5 and 7, this implies that progressive coding provides lower time costs than Golomb encoding for each mode and any *UBMAD*. It is indicated by both average compression/decompression time and total time expenses.

Also, progressive coding ensures better compression in terms of CR and total memory expenses (see Tables 2, 4 and 6).

Hence, the suggested coding approach outperforms the Golomb one with respect to the applied efficiency metrics.

Next, it follows that decompression is faster than compression. So, the method considered is non-symmetric. Although, the difference is insignificant.

Now, let us focus on a performance of the AFIPS system with the progressive coding of quantized DAT-coefficients.

We see that both classic and block-splitting modes ensure near the same compression efficiency, measured by *CR* (see Tables 2, 4). Nevertheless, the first one provides lower total memory costs. Although comparing the difference with the size of the source data, one can see that it is minor.

Moreover, Tables 3 and 5 show that the classic mode is faster than the block-splitting one. However, there is no significant difference between them.

Finally, Tables 2, 3, 4, 5, 6 and 7 indicate that the chroma-subsampling mode ensures the best compression and time complexity performance for each value of *UBMAD*. However this comparison is not completely correct due to the difference in the distortions introduced when processing images.

Indeed, from Tables 2 and 4, this implies that the classic and block-splitting modes provide nearly the same loss of quality, measured by *PSNR*. At the same time, Table 6 shows that the chroma-subsampling mode produces greater distortions for any *UBMAD*. The reason is an introduction of information loss when subsampling matrices of chroma components.

The chroma-subsampling mode of the AFIPS system might be useful for processing images that were previously compressed by methods applying subsampling of chroma matrices, and the JPEG algorithm is the most famous of them. We illustrate this in the next subsection.

3.4 JPEG-Images Processing

Consider the Semantic Drone Dataset (http://dronedataset.icg.tugraz.at). It contains 400 full color 6000×4000 pixel images in the JPEG format. The total size is 3.8 GB (JPEG). The size of the raw data is 26.89 GB (BMP).

This data are processed by AFIPS with $UBMAD = 155$ and the chroma-subsampling mode. As it can be seen from the previous subsection, this setting of the AFIPS system produces the highest distortions when processing satellite images.

The following results are obtained: the average *PSNR* is 36.67 dB; the average *CR* is 21.23 (comparing to the raw data); the total size of compressed data is 1.408 GB; the average time of compression and decompression are respectively 1.144 and 0.793 s.; the total time of compression and decompression are 459 and 318 s., respectively.

Moreover, comparing decompressed images with the source ones, practically no visual distortions have been observed. This feature is also indicated by the mean value of *PSNR* that is greater than 35 dB.

So, using AFIPS, it is possible to get significant memory costs reduction, when compressing JPEG images.

3.5 Discussion

This implies that the suggested coding scheme, called progressive, provides improvement of the AFIPS system in terms of compression ratio and time performance. Nevertheless, when implementing it, one can find out that an additional memory buffer is required for storing binary stream, which is further compressed by CABAC. The Golomb coding scheme does not possess this feature. However, when applying the block-splitting mode of AFIPS, the size of this buffer is small.

Next, bitstream encoding by CABAC is not modified, and there is room for improvement [28]. However, in many cases, the optimization of this step leads to the significant complexity of software implementations and maintenance, which can be a huge blocker for further usage and development.

Further, the efficiency of the proposed coding approach is proved by both theoretic reasons and test data processing results. Images of the complex content are used in this research. The results obtained show that complexity is reduced.

If we compare block-splitting and classic modes of the AFIPS system, we see that the first one is preferable in terms of spatial complexity [40]. Indeed, it operates blocks of a small size, and, hence, can be an optimal choice for edge devices. Nevertheless, when rapid computations are a must or a higher compression ratio is a requirement, the classic mode should be used. Moreover, if the image matrix is split into blocks, then DAT-coefficients present features of the corresponding block, not the whole image. For this reason, the classic mode of AFIPS might be preferable, when applied in combination with ML/CV methods.

The AFIPS system provides an image format. Currently, there are a great number of digital image formats, and the usage of another one can be debated. Especially, the application in machine learning and neural networks is questionable. Nevertheless, the existing deep learning frameworks have image tools that can be easily modified to support the AFIPS format. *ImageDataGenerator* of the TensorFlow framework (https://www.tensorflow.org) is an example. It provides operating images stored in different formats, and creating an AFIPS add-on is not a complicated task. Moreover, the data encryption feature of AFIPS can ensure the protected AI/ML.

Finally, the results obtained show that the AFIPS system decreases resource expenses required for storing JPEG images. The chroma-subsampling mode provides significant memory saving in combination with visually lossless compression. However, just one value of the *UBMAD* parameter is used. Search for the value, that provides the best performance in terms of different metrics, should be carried out.

In addition, DAT-based image compression outperforms the JPEG algorithm. Indeed, this statement has been proved in the paper [43] by compressing six types images: classic test and classic aerial images, screenshots, Canon and Nikon test photos, as well as images from the TID2013 database. Also, lossless DAT-based compression provides better performance than TIFF, PNG and ZIP [36].

So, applying the AFIPS system is promising. This requires an appropriate approach. Especially, hardware features should be considered. We suggest C/C++ software implementation that is a core of the A-Methods lab activity (https://www.amethods.net). It ensures near native performance of computations and wide variety of target platforms, including web (here, C/C++ -to-WebAssembly export by the Emscripten tool and the further use in JavaScript/TypeScript packages can be applied).

4 Conclusions

So, the AFIPS system performance has been improved and its coding stage complexity has been reduced. The proposed progressive encoding approach provides better compression in combination with faster processing. Three modes of AFIPS have been explored and their efficiency has been compared:

– the classic mode should be recommended if the highest compression ratio and the fastest computations are required;
– the block-splitting mode should be preferred when the lowest spatial complexity is a requirement;
– the chroma-subsampling mode should be considered as a tool for visually lossless compression of images that have been already processed by JPEG.

Also, an application of AFIPS to ML/CV algorithms is promising. It can be useful, especially, in tiny ML technologies. This will be studied in the future research.

References

1. Karnik, N., Bora, U., Bhadri, K., Kadambi, P., Dhatrak, P.: A comprehensive study on current and future trends towards the characteristics and enablers of industry 4.0. J. Ind. Inf. Integr. **27**, 100294 (2022)
2. Mourtzis, D., Angelopoulos, J., Panopoulos, N.: A literature review of the challenges and opportunities of the transition from industry 4.0 to society 5.0. Energies **15**, 6276 (2022)
3. Cao, L.: AI in finance: challenges, techniques, and opportunities. ACM Comput. Surv. **55**(3), 64, 1–38 (2022)
4. Limna, P., Kraiwanit, T., Siripipatthanakul, S.: The growing trend of digital economy: a review article. Int. J. Comput. Sci. Res. **6**, 1–11 (2022)
5. Kreijns, K., Xu, K., Weidlich, J.: Social presence: conceptualization and measurement. Educ. Psychol. Rev. **34**, 139–170 (2022)
6. Bataeva, E.V.: An ethno-methodological analysis of on-line communications. A crisis experiment in chats. Sotsiologicheskie Issledovaniya **12**, 88–97 (2011)
7. Global Losses from Cybercrime Skyrocketed to Nearly $1 Trillion in 2020, New Report Finds. https://www.washingtonpost.com/politics/2020/12/07/cybersecurity-202-global-losses-cybercrime-skyrocketed-nearly-1-trillion-2020. Accessed 25 Nov 2023
8. Sharma, M., Kaur, M.: A review of deepfake technology: an emerging AI threat. In: Ranganathan, G., Fernando, X., Shi, F., El Allioui, Y. (eds.) Soft Computing for Security Applications. AISC, vol. 1397, pp. 605–619. Springer, Singapore (2022). https://doi.org/10.1007/978-981-16-5301-8_44
9. Creating a world of potential. Cisco 2023 Annual Report. https://www.cisco.com/c/dam/en_us/about/annual-report/cisco-annual-report-2023.pdf . Accessed 25 Nov 2023
10. Gonzalez, R., Woods, R.: Digital Image Processing, 4th edn. Pearson, London (2018)
11. Kulkarni, D., Soni, R.: Smart AIOT based woman security system. In: 2021 International Conference of Modern Trends in Information and Communication Technology Industry (MTICTI), pp. 1–6 (2021)
12. Motwani, Y., Seth, S., Dixit, D., Bagubali, A., Rajesh, R.: Multifactor door locking systems: a review. Mater. Today Proc. **46**, 7973–7979 (2021)
13. Himeur, Y., Rimal, B., Tiwary, A., Amira, A.: Using artificial intelligence and data fusion for environmental monitoring: a review and future perspectives. Inf. Fus. **86–87**, 44–75 (2022)

14. Van Klink, R., et. al.: Emerging technologies revolutionise insect ecology and monitoring. Trends Ecol. Evol. **37**(10), 872–885 (2022)
15. Sishodia, R.P., Ray, R.L., Singh, S.K.: Applications of remote sensing in precision agriculture: a review. Remote Sens. **12**(19), 3136 (2020)
16. Kussul, N., Lavreniuk, M., Skakun, S., Shelestov, A.: Deep learning classification of land cover and crop types using remote sensing data. IEEE Geosci. Remote Sens. Lett. **14**(5), 778–782 (2017)
17. Castiglioni, I., et. al: AI applications to medical images: from machine learning to deep learning. Physica Medica **83**, 9–24 (2021)
18. Xie, Y., Li, Q.: A review of deep learning methods for compressed sensing image reconstruction and its medical applications. Electronics **11**, 586 (2022)
19. Lechner, A.M., Foody, G.M., Boyd, D.S.: Applications in remote sensing to forest ecology and management. One Earth **2**(5), 405–412 (2020)
20. Lian, R., Wang, W., Mustafa, N., Huang, L.: Road extraction methods in high-resolution remote sensing images: a comprehensive review. IEEE J. Sel. Topics Appl. Earth Observ. Remote Sens. **13**, 5489–5507 (2020)
21. Salomon, D.: Data Compression: The Complete Reference. Springer, London (2007). https://doi.org/10.1007/978-1-84628-603-2
22. Chui, C.K., Jiang, Q.: Applied Mathematics: Data Compression, Spectral Methods, Fourier Analysis, Wavelets, and Applications. Atlantis Press, Paris (2013)
23. Aggarwal, C.: Neural Networks and Deep Learning, 1st ed., Springer, Cham (2018). https://doi.org/10.1007/978-3-319-94463-0
24. European Parliament declares Russia to be a state sponsor of terrorism. https://www.europarl.europa.eu/news/en/press-room/20221118IPR55707/european-parliament-declares-russia-to-be-a-state-sponsor-of-terrorism. Accessed 25 Nov 2023
25. Hockstader, L.: Murder, torture, rape: Russia's crimes are a long-running horror show. The Washington Post. https://www.washingtonpost.com/opinions/2023/10/31/russian-war-crimes-ukraine. Accessed 25 Nov 2023
26. Rai, S., Choubey, V., Suryansh, Garg, P.: A systematic review of encryption and keylogging for computer system security. In: 2022 Fifth International Conference on Computational Intelligence and Communication Technologies (CCICT), India, pp. 157–163 (2022)
27. Ahmed, S.T., Hammood, D.A., Chisab, R.F., Al-Naji, A., Chahl, J.: Medical image encryption: a comprehensive review. Computers **12**, 160 (2023)
28. Sayood, K.: Introduction to Data Compression, 5th edn. Morgan Kaufman, Cambridge (2017)
29. Zolfaghari, B., Koshiba, T.: Chaotic image encryption: state-of-the-art, ecosystem, and future roadmap. Appl. Syst. Innov. **5**, 57 (2022)
30. Shi, Y.-Q., Sun, H.: Image and Video Compression for Multimedia Engineering, 3rd edn. CRC Press, Boca Raton (2019)
31. General Data Protection Regulation GDPR. https://gdpr-info.eu. Accessed 25 Nov 2023
32. California Consumer Privacy Act. https://theccpa.org. Accessed 25 Nov 2023
33. The Bletchley Declaration by Countries Attending the AI Safety Summit, 1–2 November 2023. https://www.gov.uk/government/publications/ai-safety-summit-2023-the-bletchley-declaration/the-bletchley-declaration-by-countries-attending-the-ai-safety-summit-1-2-november-2023. Accessed 25 Nov 2023
34. Makarichev, V., Lukin, V., Kharchenko, V.: Image compression and protection systems based on atomic functions. Int. J. Comput. **22**(3), 283–291 (2023)
35. Makarichev, V., Vasilyeva, I., Lukin, V., Vozel, B., Shelestov, A., Kussul, N.: Discrete atomic transform-based lossy compression of three-channel remote sensing images with quality control. Remote Sens. **14**, 125 (2022)

36. Makarichev, V., Lukin, V., Illiashenko, O., Kharchenko, V.: Digital image representation by atomic functions: the compression and protection of data for edge computing in IoT systems. Sensors **22**, 3751 (2022)
37. Rvachev, V.: Compactly supported solutions of functional-differential equations and their applications. Russ. Math. Surv. **45**, 87–120 (1990)
38. Makarichev, V.A.: Approximation of periodic functions using $\mathrm{mup}_s(x)$. Math. Notes **93**, 858–880 (2013)
39. Makarichev, V., Lukin, V., Brysina, I.: On the applications of the special class of atomic functions: practical aspects and perspectives. In: Nechyporuk, M., Pavlikov, V., Kritskiy, D. (eds.) ICTM 2020. LNNS, vol. 188, pp. 42–54. Springer, Cham (2021). https://doi.org/10.1007/978-3-030-66717-7_4
40. Makarichev, V., Lukin, V., Brysina, I., Vozel, B.: Spatial complexity reduction in remote sensing image compression by atomic functions. IEEE Geosci. Remote Sens. Lett. **19**(6517305), 1–5 (2022)
41. Sachenko, A., Kochan, V., Kharchenko, V., Yastrebenetsky, V., Fesenko, H., Yanovsky, M.: NPP post-accident monitoring system based on unmanned aircraft vehicle: concept, design principle. Nucl. Radiat. Saf. **73**, 24–29 (2017)
42. Chang, Z., Liu, S., Xiong, X., Cai, Z., Tu, G.: A survey of recent advances in edge-computing-powered artificial intelligence of things. IEEE Internet Things J. **8**, 13849–13875 (2021)
43. Lukin, V., Brysina, I., Makarichev, V.: Discrete atomic compression of digital images: a way to reduce memory expenses. In: Nechyporuk, M., Pavlikov, V., Kritskiy, D. (eds.) Integrated Computer Technologies in Mechanical Engineering. AISC, vol. 1113, pp. 492–502. Springer, Cham (2020). https://doi.org/10.1007/978-3-030-37618-5_42

Features of Biomedical Signal Processing Using Data Mining Elements

Mikle Burichenko, Olga Ivanets, Maryna Arkhyrei(✉), and Oleg Melnykov

National Aviation University, Lubomyr Huzar Avenue 1, Kyiv 03058, Ukraine
marina_arkhyrei@ukr.net

Abstract. The paper considers the problem of intellectual analysis of biomedical data to obtain an additional information component about the stability of the functioning of the human body. The use of biomedical data in the form of time series allows obtaining an information component about changes in the state of a biological object over time. The development of adequate approaches for obtaining an additional informational component of available biomedical data will allow to evaluate the quantitative and qualitative characteristics of a biological object in order to make a decision regarding the stability of its functioning. The considered approach to the study of dynamic processes in the cardiovascular system suggests the use of recurrence plots and quantitative analysis of recurrence, which can be used to determine the features of changes in phase trajectories and to determine the moments of transition of different states at different moments of time. When processing biomedical signals, this approach can be especially useful, since the human body is a multicomponent and multidimensional dynamic system, and its behavior is determined by the interaction between components. Analysis of signals in physiological dynamic systems using recurrence plots complements the statistical methods of studying such systems and can provide additional information about their properties. The results of research into the functioning of the human cardiovascular system as a multidimensional dynamic system using the methods of recurrence quantitative analysis (RQA) in the MATLAB software environment are presented, you can also use other software packages Python, Excel. In addition, this method can be used to analyze other biological signals such as heart rate variability, electroencephalogram, phonocardiogram, etc. [1].

Keywords: Data Mining · Time Series · Recurrence Plots · Recurrence Quantitative Analysis · Data Processing · Electrocardiography · Time Series Analysis · Dynamic System

1 Introduction

1.1 Introduction to the Problem

Recently, more and more attention has been paid to the intelligent analysis of biomedical data with the aim of finding new, non-trivial and practically useful methods of interpreting empirical data. Physiological (biological) systems are non-linear dynamic

M. Nechyporuk et al. (Eds.): ICTM 2023, LNNS 1008, pp. 566–577, 2024.
https://doi.org/10.1007/978-3-031-61415-6_48

systems that constantly change under the influence of external noises (disturbances) and changes in the physiological state. The output signals of such systems are formed as a result of complex dynamic interactions between its components, and most of the signals from such components are not available for experimental evaluation. Also, it should be noted that it is impossible to take into account all the factors causing the uncertainty of measuring biomedical signals. Therefore, even taking into account all instrument errors, corrections, influences of external factors and subjective influences of operators, biomedical signals still contain inaccuracies, inhomogeneities, are often incomplete, can also be contradictory, heterogeneous, indirect, and at the same time have large amounts of data [4]. Therefore, the use of data mining [2] especially for the analysis of biomedical signals [3, 4] and their forecasting and diagnosis requires certain creative and intellectual efforts. The use of mathematical approaches in intellectual analysis allows us to describe patterns and trends that may exist in the data, but such trends are impossible with traditional (classical) analysis, since biomedical signals are too complex and have a large number of biological feedback relationships [1]. Therefore, the use of intelligent analysis of biomedical signals is part of a complex information processing process with a method of obtaining additional useful information and identifying patterns and trends in them, which is the basis of clinical decision support systems, CDSS. Assist in decision-making, including excessive amounts of data. As a result, the use of intellectual analysis of biomedical data makes it possible to find previously unknown regularities in their dynamics, practically useful and accessible interpretations of knowledge [1]. Clustering [5], statistical methods, search for associative rules, time series analysis, classification methods, fractal analysis and others are used as data mining.

1.2 Motivation

Due to the fact that when making a decision regarding the stability of the organism's functioning, it is necessary to assess the state of a dynamic object according to certain indicators, in order to reduce information uncertainty, it is necessary to investigate various methods that implement the transformation of information parameters of such an object. Recently, more and more studies prove the need to study the variability of the course of biological processes in order to obtain additional information about their transformation and ensure the balance of functioning due to reverse biological connections, as well as to analyze the chaotic nature of these processes. When studying the complex dynamics of parameters of the cardiovascular system, the approach based on solving systems of differential equations describing the system is not convenient due to the complexity of the system model; there is a need to study the functional stability of the organism on the basis of invariant transformations of the information parameters of the cardiovascular system and the analysis of the geometric structure of the trajectories of time series formed from the electrocardiographic signal. Although this approach does not make it possible to present the solution in an explicit form, it allows qualitatively describing many important features of the studied dynamic system.

1.3 Contribution

The goal of this paper is to the purpose of the study is to evaluate the possibilities and expediency of using recurrent diagrams and quantitative analysis of the recurrence of the output signals of the cardiovascular system (electrocardiographic signals) to obtain numerical characteristics that can be additional criteria when assessing the state of stability of the functioning of the human body. Given the nonlinearity of such a dynamic system, the use of nonlinear dynamics methods allows to investigate the chaotic nature of processes in it [4].

1.4 The Organization of the Paper

The paper is organized as follows. Section 1 discusses background information. Section 2 highlights related works. Section 3 considers the method of constructing recurrent plot. Section 4 presents an approach to visual and quantitative assessment of biomedical signals. Sections 5 and 6 present the conclusions and future scope.

2 Literature Review

In the last decade, more and more publications related to the analysis of biomedical signals consider the human body as a dynamic system. The approach based on the use of dynamic chaos theory and fractal analysis to evaluate the behavior of such a complex system was used in subsequent publications [6–8]. Most of these studies are aimed at discovering regularities that estimate the dynamic transformation of biological systems, the human organism, in particular [9, 10]. Many nonlinear methods based on the concepts of chaos, fractality, and complexity were used to assess heart rate variability [4, 10–12]. Literary sources [4, 13] are used summarization of the visualization of the dynamics of heart rate variability with a quantitative assessment, obtained on the basis of nonlinear and fractal dynamics (fractal, entropy, symbolic dynamics, attractors, representation of the Poincaré plot), which allow understanding the dynamics of the cardiovascular system in both healthy and pathological conditions.

The main contributions authors of [14, 15] are as follows a detailed description of the nonlinear methods most used to assess heart-rate dynamics presenting their relationship and stating the limitations of methods; and they found that the Poincaré plot has been one of the most used methods in the last years. It is a method easy to compute, it gives a visual display, and its interpretation is understandable by many clinicians. However, when trying to quantify the visual information, it presents some limitations such as it assumes an elliptical shape of the data distribution.

In accordance with the proposed work, an intellectual analysis of time series using recurrent diagrams was carried out. With this approach, the system state variables in time form a trajectory in the n-dimensional phase space, and each system state corresponds to a certain point in the phase space. The methodology of recurrent diagrams allows you to project the results of measuring one signal (time series) into a multidimensional space using delay and embedding procedures. Recurrence plots are a basic tool for visualizing the recurrence of dynamic systems, and the quantitative analysis of recurrence

(Recurrence Quantification Analysis, RQA) provides the evaluation of several quantitative measures [16, 17]. Examples of the use of recurrent plots and quantitative analysis of the recurrence of physiological systems are described in [18–24].

Due to the fact that when making a decision regarding the stability of the organism's functioning, there is a need to assess the state of a dynamic object according to certain indicators, to reduce information uncertainty, it is necessary to research various methods that implement the transformation of information parameters of such an object. Recently, more and more studies prove the need to study the variability of the course of biological processes in order to obtain additional information about their transformation and ensure the balance of functioning due to reverse biological connections, as well as to analyze the chaotic nature of these processes. When studying the complex dynamics of the parameters of the cardiovascular system, the approach based on solving systems of differential equations describing the system is not convenient due to the complexity of the system model; there is a need to study the functional stability of the organism on the basis of invariant transformations of the information parameters of the cardiovascular system and the analysis of the geometric structure of the trajectories of time series formed from the electrocardiographic signal. Although such an approach does not make it possible to present the solution in an explicit form, it allows qualitatively describing many important features of the studied dynamic system.

3 Materials and Methods

The technique for analyzing the recurrence of electrocardiographic signals has several stages: 1) experimental acquisition of electrocardiographic signals (time series); 2) assessment of input parameters for calculating the distance matrix and recurrence matrix; 3) construction of a recurrence diagram; 4) calculation of quantitative measures of the recurrence plot.

The data under study (electrocardiographic signal from one lead) is a one-dimensional time series containing the results of measuring one of the available parameters of a multidimensional dynamic system. Using the mutual dependence of all multidimensional data of a physiological system, data from other dimensions can be modeled by the method of delaying available data and constructing multidimensional data from delayed copies (embedding) [12].

The state of a dynamic system can be described by a vector of state variables $\mathbf{x}(t) = [x_1(t),\ x_2(t), ...,\ x_d(t)]$. The state vector changes over time, and the direction of movement is determined by the velocity vector $d\mathbf{x}_i/dt = \dot{\mathbf{x}}_i$. The sequence of state vectors forms a trajectory in phase space, and the evolution of the trajectory characterizes the dynamics of the system and its attractor. Integrating the last equation provides information about the state of the system at time t. Graphic representation of the phase trajectory Allows one to judge the nature of the process; in this case, chaotic or periodic processes have characteristic phase portraits.

In many applications, observation of a natural process does not allow obtaining information about most of the system's state variables because they are either unknown or their values cannot be measured. In complex systems, it is possible to judge the dynamics of the entire system based on the evolution of even one state variable $x(t_i)$

by constructing an attractor that is similar to the initial one in terms of properties. By observing (measuring) one state variable in the form of a time series, it is possible to restore the trajectory of the phase space due to the information communication between the system components.

An equivalent phase trajectory that preserves the structure of the original phase trajectory can be reconstructed from one time series using the method of time delays according to the Takens theorem [6], and the two-dimensional space will be described as $x_i(t) \rightarrow [x(t_i),\ x(t_i+\tau)]^T$, three-dimensional space – $x_i(t) \rightarrow [x(t_i),\ x(t_i+\tau),\ x(t_i+2\tau)]^T$, *m*-dimensional space –$x_i(t) \rightarrow [x(t_i),\ x(t_i+\tau),\ \ldots, x(t_i+(m-1)\tau)]^T$, where τ – is the delay (lag). The lag and dimension of the space can be chosen such that the obtained set of points will reproduce the attractor of the system. The reconstructed phase space is not exactly the same as the original phase space, but its topological properties are preserved provided that the embedding dimension is large enough. In this way, the recovered trajectory is sufficiently accurate for further data analysis.

The theory of recurrent plots [16] makes it possible to study multidimensional dynamic systems and establish regularities in their behavior by observing (measuring) one state variable (in the form of a time series). Let the point $x(i)$ correspond to the *i-th* point of the phase trajectory, which describes the dynamic system in the m-dimensional space. The values of the elements of the recurrence matrix show that the point $x(j)$ will be located close enough to the point $x(i)$. Through the coordinates of the points in the m-dimensional phase space, the elements of the recurrence matrix are calculated as

$$R_{ij} = \begin{cases} 1 \ : \ \left\| \mathbf{x}_i - \mathbf{x}_j \right\| \le \varepsilon \\ 0 \ : \ \left\| \mathbf{x}_i - \mathbf{x}_j \right\| > \varepsilon; \quad i, j = 1, 2, \ldots n. \end{cases} \tag{1}$$

where $\|\cdot\|$ – distance norm in *m*-dimensional phase space; ε – threshold (radius); are used to determine whether points are close enough in phase space to be considered recurrent.

A recurrence diagram is a graphical representation of a recurrence matrix on a plane as a two-dimensional array of points, in which an element with coordinates (i, j) means that the point $x(j)$ will be located close enough to the point $x(i)$. . The recurrent plots display the values of the recurrent matrix elements on the graph with black and white dots: black dots (1) mean the presence of recurrence, white (0) - its absence. The time is postponed according to the schedule.

In addition to the recurrent plot, a global recurrent plot is also used; the elements of the corresponding matrix are calculated without taking into account the threshold.

$$R_{ij} = \left\| \mathbf{x}_i - \mathbf{x}_j \right\|; \quad i, j = 1, 2, \ldots n \tag{2}$$

Using recurrence, it is possible to obtain from the data of any one-dimensional time series **X** a recurrence plots, which is a two-dimensional portrait of the dynamics of the time series expressed through its recurrent characteristics.

Each recurrence plots have structural features. The main structural features include points and diagonal lines, as well as areas of their accumulation. Diagonal lines correspond to the situation when some part of the phase trajectory runs parallel to another phase trajectory. The length of these lines shows the evolution of the process taking place in this area. Cluster areas correspond to time intervals during which the state of the system does not change or changes slightly. In this work, several quantitative measures of recurrence diagrams are used for the quantitative assessment of the dynamics of the cardiovascular system, namely: 1) Recurrence Rate (RR), that is, the density of recurrent points; 2) Determinism (DET), or a measure of system predictability; 3) the ratio of determinism to recurrence rate (RATIO = DET/RR); 4) the maximum length of the diagonal lines (Lmax) indicates the moments when the trajectory of the phase process passes close to another section; 5) divergence is the inversion of the measure Lmax; 6) the average length of the diagonal lines (<L>) is the average time during which two sections of the phase trajectory pass close to each other (it can be considered as the average time of predictability); 7) Entropy (ENT) is the Shannon entropy of the frequency distribution of the length of the diagonal lines and characterizes the deterministic component in the system; 8) Laminarity (LAM) – characterizes the presence of states of freezing of the system, when the movement of the system along the phase trajectory stops or is very slow; 9) Trapping Time, (TT) characterizes the average time that the system can spend in a certain state; 10) the maximum length of vertical structures (Vmax) does not have a clearly defined dynamic interpretation, but may be related to singular states of the system.

Calculation formulas of these quantitative measures are given, for example, in [27].

4 Results

The data obtained as a result of the experiment are recorded in text format files. Processing of experimental data was performed using the functions of the software package Cross Recurrence Plot Toolbox for MATLAB [28] and MATLAB functions developed by the authors specifically for the study of biological signals.

In the work, the signals from the physionet.org website database were investigated [25]. The database contains fragments of ambulatory recordings of electrocardiographic signals, the signal sampling frequency is 360 Hz. Using the PhysioBank ATM program [30], the database signal files were converted to *.mat format of the MATLAB system.

Time delay, embedding dimension, and threshold value (radius) are important parameters for quantitative recurrence analysis. The delay time (lag) for the reproduction of the phase space is calculated by the method of Average Mutual Information (AMI) [29].

$$S(\tau) = \sum_{i,j} p_{i,j}(\tau) \ln \frac{p_{ij}(\tau)}{p_i p_j} \tag{3}$$

where p_i - is the probability of finding the value of the time series in the *i-th* interval of the distribution, $p_{ij}(\tau)$ is the joint probability of finding the value of the time series in the *i-th* interval and the value of the time series in the *j-th* interval after time τ (probability of transition from the *i-th* to the jth time interval τ). The calculation was performed by the *mi*() function of the package [23]. Graphs of the dependence of the average mutual information were constructed for the studied signals (Fig. 1).

The embedding dimension is chosen using the False-Nearest Neighbors (FNN) method. The calculation was performed by the fnn() function of the package [28], graphs of the dependence of the relative number of nearest neighboring points on the nesting dimension for the given Lag value were plotted for the studied signals (Fig. 2).

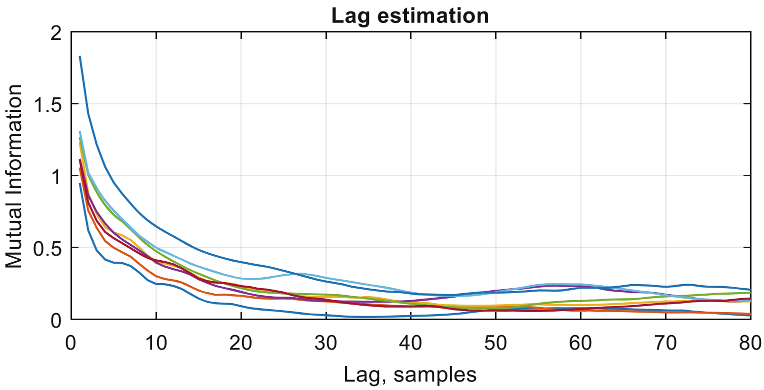

Fig. 1. Clusters formation lag estemation.

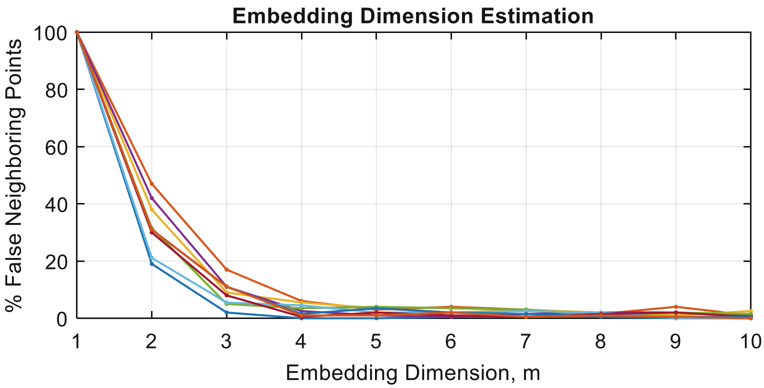

Fig. 2. Clusters formation embedding dimension estemation.

The graphs show that the time delay (lag) $\tau = 40$ (counts) and the embedding dimension $m = 4$ can be selected for all investigated signals. The threshold value (radius) $\varepsilon = 5\%$ of the mean square distance of the state space [26] is also selected.

Visual analysis of the constructed diagrams allows to determine the phase spaces in different time intervals, and according to the direction of the sequence of states of parts of the time series, the internal transformations occurring in these sub-processes are characterized.

Distance matrices and regular recurrence diagrams are constructed for ECG signals. Examples of the obtained recurrent plots are shown in Figs. 3, 4 and 5.

The paper also calculated the calculated quantitative measures of recurrent diagrams. This approach allows, in addition to qualitative characteristics, to obtain quantitative values of the stability of the functioning of the cardiovascular system, as the main indicator of the stability of the body. The results of the calculations of the quantitative measures of the processed electrocardiogram files presented in Fig. 3 are given in the Table 1.

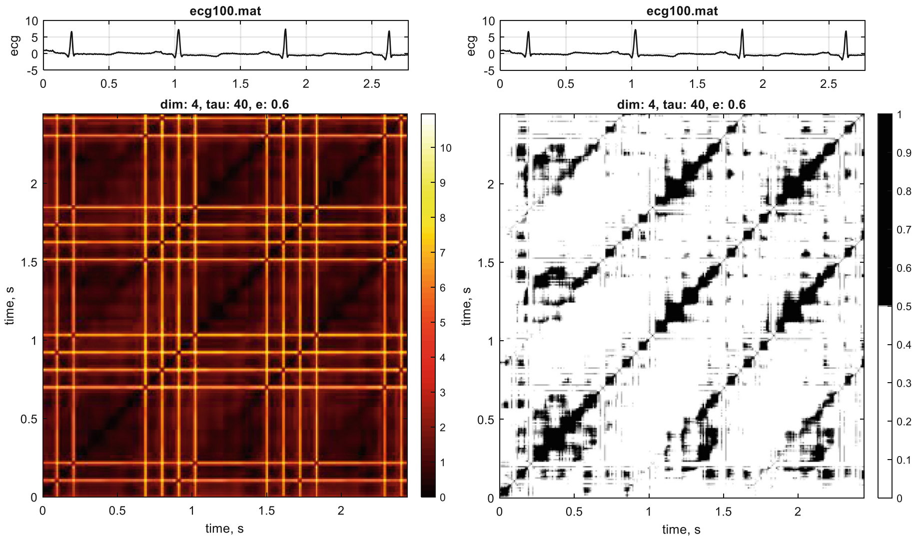

Fig. 3. An example for a signal ecg100.

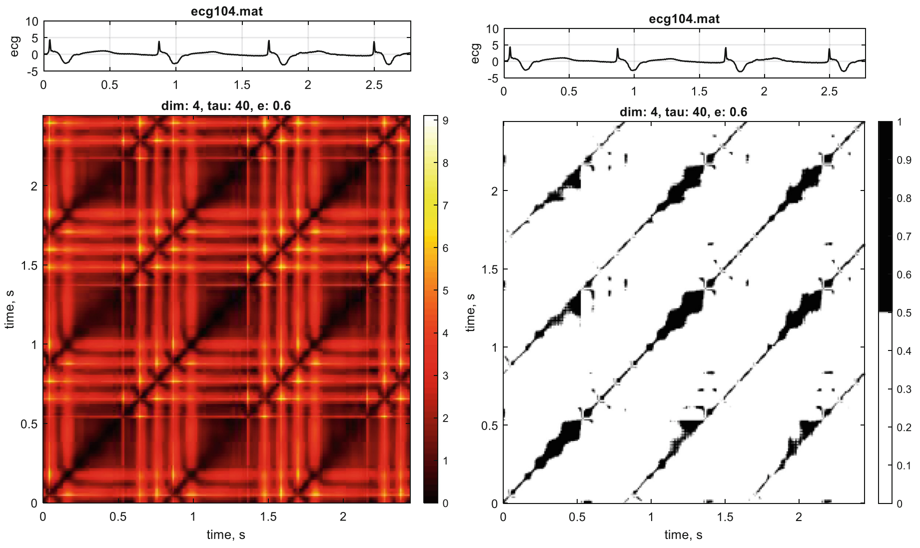

Fig. 4. An example for a signal ecg104.

As can be seen from Fig. 3 and confirmed by the data in the Table 1. The electrocardiogram of the ecg100 file has a certain constancy of the functioning of the cardiovascular system, as evidenced by the green ellipses in Fig. 2. While the recurrent plots of the ecg104 and ecg109 signals show the absence of repetition of the diagram zones, which may indicate a violation of the functional stability of the cardiovascular system (green color in Fig. 6b, c). The peculiarity of this study is that the visual analysis of recurrent

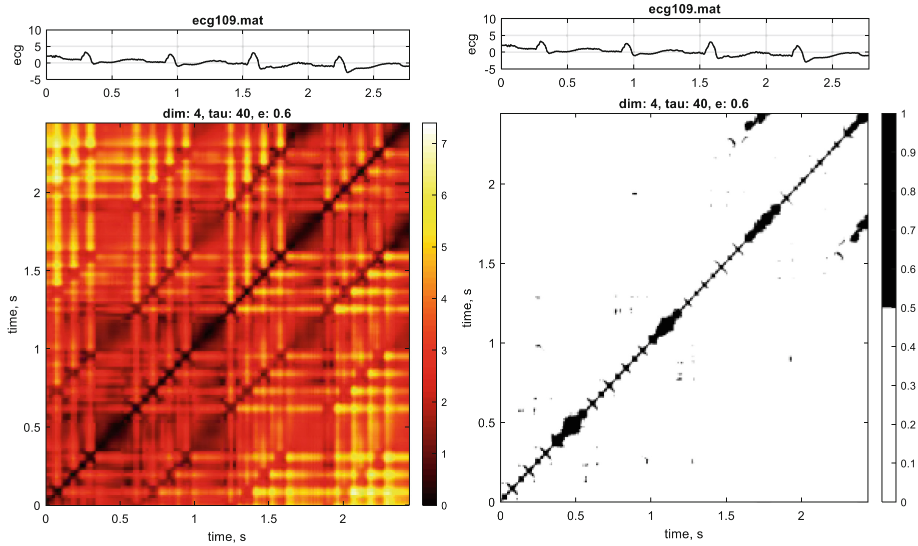

Fig. 5. An example for a signal ecg109.

Table 1. Quantitative measures of recurrent plot of electrocardiographic data.

Signal	%RR	DET	RATIO (DET/RR)	DIV	< L >	ENT	LAM	TT	Vmax
ecg100	27.4	0.926	3.37	0.00625	7.68	2.52	0.957	10.7	143
ecg104	9.31	0.975	10.5	0.00575	13.2	2.99	0.986	13.4	90
ecg109	8.37	0.941	11.2	0.00123	6.67	2.25	0.964	7.68	81

plots is confirmed by quantitative calculations. Thus, the RR value of the first signal is equal to 27.4%, compared to the data in Fig. 2b, which is 9.4%. Accordingly, in turn, the DET/RR ratio is 3, 37 and 10.5, respectively. Also, the Vmax values differ by quantitative indicators of 143, 90, and 81, respectively. Thus, the visual assessment of recurrent plots is confirmed by the quantitative values of their measures, which can be used in further research and determination of individual normal limits for each separate biological system and used as predictors of cardiovascular system dysfunction.

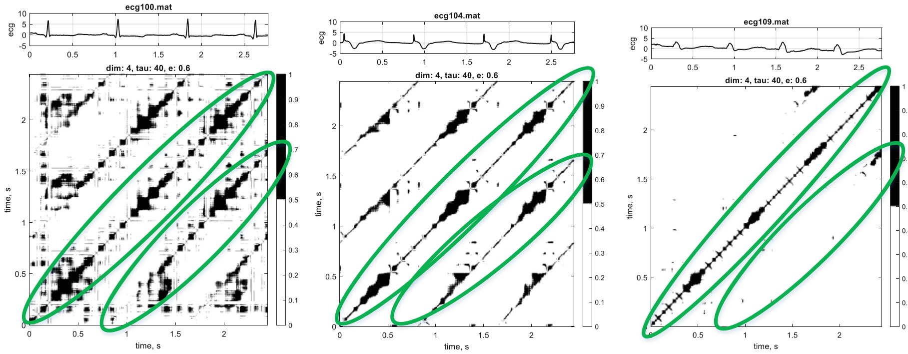

Fig. 6. Visual assessment of recurrent plots.

5 Conclusions

A comparative analysis of recurrent plots of the cardiovascular system (ECG signals) was carried out from the point of view of ensuring the objectivity of diagnostic conclusions about the state of stability of its functioning based on empirical data.

It was established that when analyzing the recurrence of ECG signals, it is effective to use the input parameters of the embedding dimension m = 4 and the lag time $\tau = 40$ (counts).

Phase portraits of ECG signals were obtained and a comparative analysis of various signals was carried out in order to study the stability of the functioning of the cardiovascular system, which characterizes the stability of the functioning of the entire organism.

Quantitative measures of recurrent diagrams were obtained for the specified signals, it was determined that the value of Vmax measures is more sensitive for determining the stability of the functioning of the cardiovascular system. An increase in the value of TT means an increase in non-stationarity of the process and characterizes the average time that the system can spend in a certain state. The value of DET decreases with the stability of the system functioning, although the range of changes is quite small. The LAM complexity measure quantifies small-scale structures of recurrent diagrams that describe the number and duration of recurrent processes in a dynamic system, i.e., an increase in its value may indicate the exit of the system from the equilibrium state.

The values of quantitative measures of recurrence significantly depend on the specified threshold (radius) during calculation, therefore, additional research is needed for the ECG data of each individual biological system. The interpretation of changes in recurrence measures requires additional research.

Quantitative analysis of recurrent diagrams can be used to assess the stability of the functioning of the cardiovascular system and, as a consequence, the body as a whole.

6 Future Scope

Subsequent studies will carry out a comprehensive analysis of this approach with other methods of nonlinear dynamics such as Poincaré maps, strange attractors, and others to confirm the derivation of data. Plans to conduct intellectual analysis of various biomedical data to obtain an additional information component using recurrent diagrams, strange attractor and quantitative characteristics to reduce information uncertainty.

Also, in the future, it is planned to conduct a comparative analysis of the results of repeated plots with their quantitative values, which aims to reduce errors of the first and second kind when making decisions about the state of the biological system.

References

1. Ivanets, O.B., Khrashchevskyi, R.V., Kulik, M.S., Burichenko, Yu, M.: Intelligence Analysis Of Empirical Data Based On Time Series No. 2. Radio Electronics, Computer Science, Control (2023)
2. Subbotin, S.A.: Sample formation and reduction for data mining. Radio Electron. Comp. Sci. Control (1) (2013). https://doi.org/10.15588/1607-3274-2013-1-18
3. Bakumenko, N.S., et al.: Computational intelligence methods to patients stratification in the medical monitoring systems. Radio Electron. Comp. Sci. Control (1), 24 (2023). https://doi.org/10.15588/1607-3274-2023-1-3
4. Amigó, J.M., Small, M.: Mathematical methods in medicine: Neuroscience, cardiology and pathology. Philos. Trans. R. Soc. A Math. Phys. Eng. Sci. **375**(2096), 20170016 (2017). https://doi.org/10.1098/rsta.2017.0016
5. Subbotin, S.A.: Data clustering based on inductive learning of neuro-fuzzy network with distance hashing. Radio Electron. Comp. Sci. Control **4**, 71 (2022). https://doi.org/10.15588/1607-3274-2022-4-6
6. Ott, E.: Chaos in Dynamical Systems. Cambridge University Press, Cambridge (2002)
7. Hastings, H.: Fractal geometry in biological systems: An analytical approach edited by Phillip M. Iannacone and Mustafa Khokha. Bull. Math. Biol. **59**(4), 791–794 (1997). https://doi.org/10.1016/S0092-8240(97)00016-5
8. Voss, A., Schulz, S., Schroeder, R., Baumert, M., Caminal, P.: Methods derived from nonlinear dynamics for analysing heart rate variability. Philos. Trans. R. Soc. A Math. Phys. Eng. Sci. **367**(1887), 277–296 (2008). https://doi.org/10.1098/rsta.2008.0232
9. Xiong, W., Faes, L., Ivanov, P.C.: Entropy measures, entropy estimators, and their performance in quantifying complex dynamics: effects of artifacts, nonstationarity, and long-range correlations. Phys. Rev. E **95**, 062114 (2017)
10. De Godoy, M.F.: Nonlinear analysis of heart rate variability: a comprehensive review. J. Cardiol. Ther. **3**, 528–533 (2016)
11. Mansier, P., et al.: Linear and non-linear analyses of heart rate variability: a minireview. Cardiovasc. Res. **31**, 371–379 (1996)
12. Norris, P.R., Anderson, S.M., Jenkins, J.M., Williams, A.E., Morris, J.A.: Heart rate multiscale entropy at three hours predicts hospital mortality in 3,154 trauma patients. Shock **30**(1), 17–22 (2008). https://doi.org/10.1097/SHK.0b013e318164e4d0
13. Nayak, S.K., Bit, A., Dey, A., Mohapatra, B., Pal, K.: A review on the nonlinear dynamical system analysis of electrocardiogram signal. J. Healthc. Eng. **2018**, 1–19 (2018). https://doi.org/10.1155/2018/6920420

14. Henriques, T., Ribeiro, M., Teixeira, A., Castro, L., Antunes, L., Costa-Santos, C.: Nonlinear methods most applied to heart-rate time series: a review. Entropy **22**(3), 309 (2020). https://doi.org/10.3390/e22030309
15. Ivanets, O.B., Burichenko, M.Yu., Arkhyrei, M.V., Bratko, V.Yu.: Peculiarities of using non-linear dynamics methods for biomedical data processing. Scientific technologies **N4**(56), 317–334 ISSN 2075-078 (2022). https://doi.org/10.18372/2310-5461.56.17131
16. Eckmann, J.-P., Kamphorst, S.O., Ruelle, D.: Recurrence plots of dynamical systems. Europhys. Lett. **4**(9), 973–977 (1987)
17. Marwan, N., Carmenromano, M., Thiel, M., Kurths, J.: Recurrence plots for the analysis of complex systems. Phys. Rep. **438**(5–6), 237–329 (2007). https://doi.org/10.1016/j.physrep.2006.11.001
18. Webber, C.L., Zbilut, J.P.: Dynamical assessment of physiological systems and states using recurrence plot strategies. J. Appl. Physiol. **76**(2), 965–973 (1994). https://doi.org/10.1152/jappl.1994.76.2.965
19. Schlenker, J., Schlenker, T., Nedělka, T., et al.: Recurrence quantification analysis: a promising method for data evaluation in medicine (2014). https://doi.org/10.24105/ejbi.2014.10.1.7
20. Burichenko, M.Yu., Onykiienko, Y.Y., Arkhyrei, M.V.: Quantitative analysis of recurrence of kephalographic data. In: Proceedings of the II International Scientific and Technical Conference. "Modern technologies of biomedical engineering", May 17−19, 2023, Odesa, Ukraine, pp. 23–27 (2023)
21. Lyby, M.S., Mehlsen, M., Jensen, A.B., et al.: Intervention and reductions in distress symptoms in women with breast cancer. Front. Appl. Math. Stat. Sec. Dyn. Syst. 5 (2019). https://doi.org/10.3389/fams.2019.00037
22. Takakura, I.T., Hoshi, R.A., Santos, M.A., Pivatelli, F.C., et al.: Recurrence plots: a new tool for quantification of cardiac autonomic nervous system recovery after transplant https://doi.org/10.21470/1678-9741-2016-0035
23. Zimatore, G., Falcioni, L., Gallotta, M.C., Bonavolontà, V., Campanella, M., De Spirito, M., et al.: Recurrence quantification analysis of heart rate variability to detect both ventilatory thresholds. PLoS ONE **16**(10), e0249504 (2021). https://doi.org/10.1371/journal.pone.0249504
24. Kirichenko, L., Radivilova, T., Stepanenko, J.: Applying recurrence plots to classify time series. In: COLINS-2021: 5th International Conference on Computational Linguistics and Intelligent Systems, April 22–23, 2021, Kharkiv, Ukraine). https://ceur-ws.org/Vol-2870/paper128.pdf
25. https://physionet.org/about/database. (application data 20.09.2023)
26. Schinkel, S., Dimigen, O., Marwan, N.: Selection of recurrence threshold for signal detection. Eur. Phys. J. Spec. Topics **164**(1), 45–53 (2008). https://doi.org/10.1140/epjst/e2008-00833-5
27. http://www.recurrence-plot.tk/. (application data 18.10.2020)
28. Cross Recurrence Plot Toolbox for Matlab. Reference Manual. Version 5.17, Release 28.17. http://tocsy.pik-potsdam.de. (application data 15.01.2019)
29. Wallot, S., Mønster, D.: Calculation of average mutual information (AMI) and false-nearest neighbors (FNN) for the estimation of embedding parameters of multidimensional time series in Matlab. https://www.ncbi.nlm.nih.gov/pmc/articles/PMC6139437/. (application data 19.02.2021)
30. https://archive.physionet.org/cgi-bin/atm/ATM. (application data 20.09.2023)

Statistical Optimisation of the Static Aperture Synthesis Method

Denys Kolesnikov(✉), Volodymyr Pavlikov, Semen Zhyla, Dmytro Vlasenko, Danyil Kovalchuk, and Kseniia Shcherbina

National Aerospace University "Kharkiv Aviation Institute", Kharkiv, Ukraine
d.kolesnikov@khai.edu

Abstract. Using the statistical theory of optimisation of radio systems for remote sensing and radiolocation, a method of static synthesis of the antenna aperture for a radiovision system of static surface area is synthesized. The models of signals, noise and their correlation characteristics are determined. The likelihood functional is developed and its maximum is found. The optimal algorithm is analyzed and a block diagram for radio images formation of surfaces using the method of static synthesis of aperture is developed.

Keywords: Algorithms Optimisation · Stochastic Signals · Aperture Synthesis · Block Diagrams

1 Introduction

The ability to analyze the electrophysical parameters and statistical characteristics of surfaces using radio waves is relevant in many fields of science, technology and the economy. The interest of scientists in the application and development of radio engineering systems of the measuring type is due to the all-weather radio range, its independence from surface illumination and high information content of radio waves [1, 2]. The disadvantage of this range compared to the optical range familiar to the human eye is the low resolution of radio images. To increase the resolution, a method of synthesizing the aperture of radar antennas mounted on aircraft was proposed in the 50s of the last century. Today, this method has been significantly developed both theoretically and practically [3–5]. In particular, modern synthetic aperture radars (SAR) achieve decimeter resolution from low-orbit satellites, have examples of implementation on a digital element base with phased array antennas, and much more [6]. At the same time, all existing methods are limited by the type of carrier, its motion characteristics and measurement conditions [7].

In addition to the tasks of global radiovision from aerospace carriers, there are also tasks of static study in laboratories or at specially equipped testing grounds, in anechoic chambers [8]. Today, the formation of test images of surfaces, ground structures, aircraft and various vehicles is relevant [9, 10]. Technologies for creating components, devices, and assemblies with the possibility of non-destructive testing through radiotransparent windows in the cases are also constantly evolving [11]. Such measurements open up new

M. Nechyporuk et al. (Eds.): ICTM 2023, LNNS 1008, pp. 578–586, 2024.
https://doi.org/10.1007/978-3-031-61415-6_49

possibilities for choosing measurement conditions, movement trajectories, and variations in measuring equipment (different wave bands, antennas, and operating modes).

In connection with the new measurement capabilities, the paper [12] proposed a new method of static synthesis of aperture, which involves the formation of radar images of a static area on the surface not from a constantly moving carrier, but with the help of a software-defined scanning device. All studies in that article are performed heuristically based on many years of experience in synthesizing signal processing algorithms and engineering intuition. The task of statistical optimization of such a method, study of its basic algorithmic operations, and development of a block diagram of the measuring device is relevant. It is assumed that the optimization performed using statistical theory and functional analysis will lead to the creation of a method for forming radio images of a static scene with the highest resolution and low errors rate in parameter estimation according to the results obtained in [13–15].

2 Problem Geometry, Signal and Noise Models, Observation Equations

2.1 Problem Geometry and Desired Signal Model

Consider that the antenna with coordinates $\vec{r}'$, moving along an arbitrary trajectory, emits in the direction of the surface with coordinates $\vec{r}$ in a wide sector of angles the following signal:

$$s_t(t) = A(t)\cos(2\pi f_0 t + \phi) = \mathrm{Re}\left\{\dot{A}(t)e^{j\omega_0 t}\right\}, \tag{1}$$

where $\dot{A}(t) = A(t)e^{j\phi}$ is the complex envelope of the desired signal, $A(t)$ is the amplitude of the desired signal, ϕ is the initial phase, $\omega_0 = 2\pi f_0$ is the angular frequency, f_0 – frequency. The complex envelope is a general representation of all possible forms of modulation of the radiated signal.

The surface sensing geometry is shown in Fig. 1. The following notations are used in the figure: $\vec{r} = (x, y, z)$ – surface coordinates, $\vec{r}' = (x', y', z')$ – coordinates of the signal registration area, $\vec{r}_t = (x_t, y_t, z_t)$ – coordinates of movement of the signal registration area, D' – the area of all possible coordinate $\vec{r}'$ values, D – the area of all possible coordinate $\vec{r}$ values, $d\vec{r}$ – elementary surface plane, considered as a point source of backscattering, $R(\vec{r})$ – inclined range from the center of the registration area to each point of the surface, $R(\vec{r}, \vec{r}')$ – slant range from each point of the registration area to each point of the surface.

In accordance with the phenomenological description of signals backscattered by a statistically homogeneous surface [16, 17], the received oscillations are represented as follows:

$$s_r(t, \vec{r}', \vec{r}_t) = \mathrm{Re}\left\{\int\limits_D \dot{F}(\vec{r})\, \dot{s}_0(t, \vec{r}, \vec{r}', \vec{r}_t)d\vec{r}\right\}, \tag{2}$$

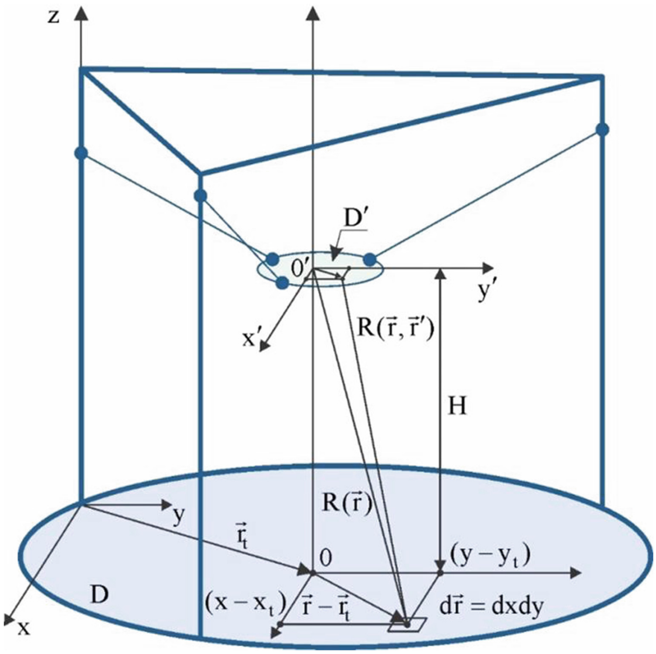

Fig. 1. Surface sensing geometry for static synthesis of antenna aperture

where $\dot{F}(\vec{r})$ is the complex coefficient of backscattering electromagnetic wave by a statistically inhomogeneous surface,

$$\begin{aligned}&\dot{s}_0(t, \vec{r}, \vec{r}', \vec{r}_t)\\&= \dot{I}(\vec{r}')\dot{A}\big(t - t_{del}(\vec{r}, \vec{r}', \vec{r}_t)\big)e^{j2\pi f_0(t - t_{del}(\vec{r}, \vec{r}', \vec{r}_t))}\end{aligned} \tag{3}$$

is a unit signal that will be received by each element of the antenna array from an elementary surface area $d\vec{r}$ in the case of, when $\dot{F}(\vec{r}) = 1$,

$$t_{del}(\vec{r}, \vec{r}', \vec{r}_t) = \frac{2R\big(\vec{r}, \vec{r}', \vec{r}_t\big)}{c} \tag{4}$$

is a delay time of signal propagation from each point of the surface to each point of the registration area moving along the coordinate $\vec{r}_t$,

$$\begin{aligned}&R\big(\vec{r}, \vec{r}', \vec{r}_t\big) = R\big(x, y, x', y', y_t, x_t\big)\\&= R_0(\vec{r} - \vec{r}_t) - \frac{(x - x_t)x'}{R_0(\vec{r} - \vec{r}_t)} - \frac{(y - y_t)y'}{R_0(\vec{r} - \vec{r}_t)}\end{aligned} \tag{5}$$

is the range from each point of the moving registration area to each point of the surface, assuming that the measurements are made in the Fresnel zone.

2.2 Noise Model, Observation Equation and Their Correlation Characteristics

Received signals are observed on the background of internal noise of the receiver $n(t, \vec{r}')$. The observation equation to be further processed has the following form:

$$u(t, \vec{r}', \vec{r}_t) = s_r(t, \vec{r}', \vec{r}_t) + n(t, \vec{r}'). \tag{6}$$

Internal noise is assumed to be uncorrelated between channels. The type of noise is additive Gaussian noise with the following correlation function

$$\begin{aligned} R_n(t_1, t_2, \vec{r}'_1, \vec{r}'_2) &= \langle n(t_1, \vec{r}'_1) n(t_2, \vec{r}'_2) \rangle \\ &= 0,5 N_{0n}\, \delta(t_1 - t_2) \delta(\vec{r}'_1 - \vec{r}'_2). \end{aligned} \tag{7}$$

Power spectral density of noise in each channel with coordinates $\vec{r}'$ is considered the same.

Coefficient $\dot{F}(\vec{r})$ will be considered random with the following correlation characteristics

$$\dot{R}_F(\vec{r}_1, \vec{r}_2) =< \dot{F}(\vec{r}_1) \dot{F}(\vec{r}_2) >= \sigma^0(\vec{r}_1) \delta(\vec{r}_1 - \vec{r}_2), \tag{8}$$

where $\sigma^0(\vec{r}_1)$ is the normalized radar cross-section.

The correlation function of the received signals, taking into account the stochasticity of the complex backscattering coefficient, will take the following form:

$$\begin{aligned} &R_s(t_1, t_2, \vec{r}'_1, \vec{r}'_2, \vec{r}_{t1}, \vec{r}_{t2}) \\ &= \frac{1}{2} \mathrm{Re} \int_D \sigma^0(r) \dot{s}_0\big(t_1, \vec{r}, \vec{r}'_1, \vec{r}_{t1}\big) \dot{s}^*_0\big(t_2, \vec{r}, \vec{r}'_2, \vec{r}_{t2}\big) d\vec{r}. \end{aligned} \tag{9}$$

Taking into account the correlation characteristics of signals and noise, the correlation function of the observation equation is equal to

$$\begin{aligned} R_u(t_1, t_2, \vec{r}'_1, \vec{r}'_2, \vec{r}_{t1}, \vec{r}_{t2}) &= \langle u(t_1, \vec{r}'_1, \vec{r}_{t1}) u(t_2, \vec{r}'_2, \vec{r}_{t2}) \rangle \\ &= R_s(t_1, t_2, \vec{r}'_1, \vec{r}'_2, \vec{r}_{t1}, \vec{r}_{t2}) + R_n(t_1, t_2, \vec{r}'_1, \vec{r}'_2) \\ &= 0,5 \mathrm{Re} \int_D \sigma^0(r) \dot{s}_0(t_1, \vec{r}, \vec{r}'_1, \vec{r}_{t1}) \dot{s}^*_0\big(t_2, \vec{r}, \vec{r}'_2, \vec{r}_{t2}\big) d\vec{r} \\ &\quad + 0,5 N_{0n}\, \delta(t_1 - t_2) \delta(\vec{r}'_1 - \vec{r}'_2). \end{aligned} \tag{10}$$

Normalized radar cross-section $\sigma^0(r)$ is the power spectral density of the statistically heterogeneous random complex backscattering coefficient $\dot{F}(\vec{r})$ of radio waves by the surface. In this task $\sigma^0(r)$ is the main parameter that should be high-precision recovered and will be further determined as the radar image.

3 Problem Statement

The stochastic signals received by the scanning system, which are backscattered by a static area, in combination with the receiver's internal noise, must be optimally restored to the radar image of this area in the form of a spatial distribution of the normalized radar cross-section.

4 Solving the Optimization Problem

For optimal estimation of $\sigma^0(r)$ method of maximum likelihood functional will be used. For the task of estimating energy parameters, Prof. Volosyuk V. K. in [18] developed a likelihood functional for the case of receiving stochastic signals

$$\begin{gathered} P\left[u(t,\vec{r}',\vec{r}_t)|\sigma^0(\vec{r})\right] = \kappa[\sigma^0(\vec{r})] \\ \times \exp\left\{-\frac{1}{2}\int\limits_T\int\limits_T\int\limits_{D'}\int\limits_{D'}\int\limits_{D_t}\int\limits_{D_t} u(t_1,\vec{r}_1',\vec{r}_{t1}) \right. \\ \times W(t_1,t_2,\vec{r}_1',\vec{r}_2',\vec{r}_{t1},\vec{r}_{t2},\sigma^0(\vec{r})) \\ \left. \times u(t_2,\vec{r}_2',\vec{r}_{t2})\ dt_1 dt_2 d\vec{r}_1' d\vec{r}_2' d\vec{r}_{t1} d\vec{r}_{t2} \right\}, \end{gathered} \tag{11}$$

where the multiplier $\kappa[\sigma^0(\vec{r})]$ has a complex functional definition, but depends on the radio image, T – observation time, D' – the area of all possible coordinate values of the registration area, D_t – the area of all possible positions of the radio system over the study area, $W(t_1,t_2,\vec{r}_1',\vec{r}_2',\vec{r}_{t1},\vec{r}_{t2},\sigma^0(\vec{r}))$ – inverse correlation function. The inverse correlation function can be found from the integral equation

$$\begin{gathered} \int\limits_T\int\limits_{D'}\int\limits_{D_t} R_u\Big(t_1,t_2,\vec{r}_1',\vec{r}_2',\vec{r}_{t1},\vec{r}_{t2},\sigma^0(\vec{r})\Big) \\ \times W\Big(t_2,t_3,\vec{r}_2',\vec{r}_3',\vec{r}_{t2},\vec{r}_{t3},\sigma^0(\vec{r})\Big) d\vec{r}_{t2} d\vec{r}_2' dt_2 \\ = \delta(t_1-t_3)\delta(\vec{r}_1'-\vec{r}_3')\delta(d\vec{r}_{t1}-d\vec{r}_{t3}). \end{gathered} \tag{12}$$

The maximum of likelihood function (11) is found by applying the derivative and equating the result to zero. The radar image to be evaluated is a function of spatial coordinates. In this case, it is necessary to apply not the usual, but the variational derivative.

The likelihood functional contains an exponential function that has a monotonic relation with its argument. In this case, taking the derivative of the logarithm of the likelihood functional instead of the derivative of the functional itself will not change its maximum. Considering the above, write down

$$\begin{gathered} \left.\frac{\delta \ln P\left[u(t,\vec{r}',\vec{r}_t)|\sigma^0(\vec{r})\right]}{\delta\sigma^0(\vec{r})}\right|_{\sigma^0(\vec{r})=\sigma^0_{opt}(\vec{r})} \\ = \left.\frac{d \ln P\left[u(t,\vec{r}',\vec{r}_t)|\sigma^0_{opt}(\vec{r})+\alpha\gamma(\vec{r})\right]}{d\alpha}\right|_{\alpha=0} = 0, \end{gathered} \tag{13}$$

where δ and d – notation for the variational and ordinary derivative.

The whole expression (13) will be equal to zero in the following form

$$\left|\dot{Y}(\vec{r})\right|^2 = \frac{1}{2}\int\limits_D \sigma^0(\vec{r}_1)\left|\dot{\Psi}_w(\vec{r},\vec{r}_1)\right|^2 d\vec{r}_1 + N_{0n}\mathrm{Э}_W(\vec{r}). \tag{14}$$

The following notations are used in Eq. (14):

$$\dot{Y}(\vec{r}) = \int\limits_T \int\limits_{D'} \int\limits_{D_t} u(t_1, \vec{r}_1', \vec{r}_{t1})\ \dot{s}_{0W}\Big[t_1, \vec{r}_1', \vec{r}_{t1}, \sigma^0(\vec{r})\Big] d\vec{r}_{t1} d\vec{r}_1' dt_1 \tag{15}$$

is an optimal algorithm for processing received oscillations $u(t_1, \vec{r}_1', \vec{r}_{t1})$ by each element of the antenna array, in different spatial positions $\vec{r}_{t1}$. The processing corresponds to the classic matched processing of the observation equation with the reference signal

$$\begin{aligned} \dot{s}_{0W}\Big[t_1, \vec{r}_1', \vec{r}_{t1}, \sigma^0(\vec{r})\Big] = \int\limits_T \int\limits_{D'} \int\limits_{D_t} W\Big(t_1, t_3, \vec{r}_1', \vec{r}_3', \vec{r}_{t1}, \vec{r}_{t3}, \sigma^0(\vec{r})\Big) \\ \times \dot{s}_0(t_3, \vec{r}, \vec{r}_3', \vec{r}_{t3}) d\vec{r}_{t3} d\vec{r}_3'\, dt_3, \end{aligned} \tag{16}$$

which is previously formed in accordance to the geometry of the problem. The novelty of the resulting algorithm lies in a new operation of decorrelation of the received oscillations in a filter with an impulse response $W(t_2, t_3, \vec{r}_2', \vec{r}_3', \vec{r}_{t2}, \vec{r}_{t3}, \sigma^0_{opt}(\vec{r}))$ and in the matched filtering of the received signals by the coordinate of the sensor movement $\vec{r}_{t1}$. New trajectories of two-dimensional movement of the radio sensor over a stationary circuit require an additional analysis and simulation modeling.

In (14), the function

$$\begin{aligned} \dot{\Psi}_W(\vec{r}, \vec{r}_1) = \int\limits_T \int\limits_{D'} \int\limits_{D_t} \dot{s}_0\big[t_1, \vec{r}_1, \vec{r}_1', \vec{r}_{t1},\big] \\ \times \dot{s}^*_{0W}\Big[t_1, \vec{r}_1', \vec{r}_{t1}, \sigma^0(\vec{r}_1)\Big] d\vec{r}_{t1} d\vec{r}_1'\, dt_1 \end{aligned} \tag{17}$$

is a spread function of the radar imaging system $\sigma^0(\vec{r})$, the spatial distribution of the normalized radar cross-section, which is the system's response to a point source of emission. The spread function (17) determines the resolution in angular coordinates of the radar system with the technology of static synthesis of aperture.

The following is also introduced in (14):

$$Э_W(\vec{r}) = \frac{1}{2} \int\limits_T \int\limits_{D'} \int\limits_{D_t} \left| \dot{s}_{0W}(t_3, \vec{r}_3', \vec{r}_{t3}, \sigma^0(\vec{r})) \right|^2 d\vec{r}_{t3} d\vec{r}_3'\, dt_3 \tag{18}$$

is an energy of the matched signal $\dot{s}_{0W}(t_3, \vec{r}_3', \vec{r}_{t3}, \sigma^0(\vec{r}))$ taking into account its decorrelation.

The obtained Eq. (15) forms the basis of the method of static synthesis of aperture in radio systems for radiovision of a static surface area. In contrast to the classical synthetic aperture algorithm, which integrates the product of the received signal and the reference signal, the obtained modified algorithm additionally performs decorrelation of signals backscattered from the surface. As a result, the distinctive intervals of the speckles in the radar image will be much smaller than in the classic synthesis of aperture. Therefore, their subsequent smoothing can be performed with the same efficiency by windows of smaller width, which allows to increase the resolution of the radar scanner. The decorrelation procedure provides a certain ultra-resolution and can be performed using an inverse filter with impulse response, which is usually used in solving incorrect inverse problems of restoring various functions and, in particular, images.

5 Block Diagram of the Radar with Static Synthesis of Aperture

Consider the main signal processing operations according to expression (15). Received oscillations $u(t, \vec{r}', \vec{r}_t)$ by each antenna element with coordinates $\vec{r}'$ over a period of time T when the sensor moves at the selected coordinate $\vec{r}_t$ are first processed in the antenna in the form of weighted averaging with amplitude-phase distribution $\dot{I}(\vec{r}')$. After processing in the antenna, the signals are transferred to an intermediate frequency and processed in the receivers in the form of matched filtering with complex amplitude $\dot{A}(t)$. To increase the information content of the received signals, the envelopes are fed to a decorrelation filter after matched processing. The degree of decorrelation is proportional to the a priori determined normalized radar cross-section. The main operation of static synthesis of aperture consists in the matched filtering of the envelopes of the received signals with the trajectory signal accumulated during the movement of the radiosensor along the coordinate $\vec{r}_t$. All matched filtering processes can be performed in the form of convolution of the received oscillations with the reference signals. As a result of matched filtering along the trajectory, a high-resolution radar image is formed, which is determined by the cross section of the ambiguity function $\dot{\Psi}_W(\vec{r}, \vec{r}_1)$. All these operations are presented in the form of a block diagram in Fig. 2.

Further research will focus on modeling and experimental studies of the system depicted on Fig. 2. In real implementation, stabilization systems for building highly stable platforms and precise coordinate determination will be appropriate [19, 20]. Given the current trends, the use of machine learning algorithms (both with and without a decision support system [21, 22]) for searching and recognizing different objects on radio images is of particular interest.

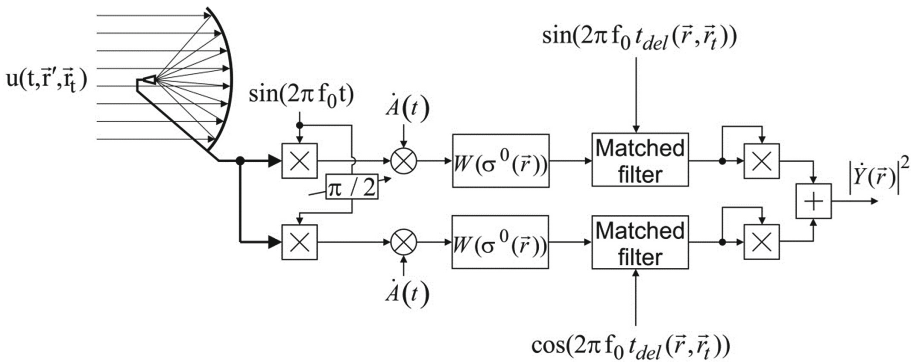

Fig. 2. Block diagram of forming radio images of surfaces using static synthesis of aperture

6 Conclusions

A new method of forming radar images of a static observation area using a radar system moving along arbitrary trajectories by a software-controlled scanner is suggested. The observation geometry, desired signals, receiver internal noise model, and correlation characteristics of all components of the observation equation are determined. The optimal algorithm for restoring radar images of a static scene is synthesized by the method of maximum likelihood functional. A distinctive feature of the obtained algorithm is the operation of decorrelation of the received signals. From the analysis of the likelihood equation, an ambiguity function that defines the potential resolution of the radar system was also obtained. The analysis of this function shows that decorrelation leads to a decrease of the distinctive intervals of the speckles in the radar image and increases its resolution. All basic signal processing operations are represented in the form of a radar block diagram.

References

1. Meng, Z., Gao, W., Li, X.: Ground stationary target detection method for airborne wide-band radar based on statistical characteristics. In: 2021 CIE International Conference on Radar (Radar), pp. 1842–1845. IEEE, Haikou, Hainan, China (2021)
2. Dergachov, K., Zaliskyi, M., Nikitina, T., Averyanova, Y., Ostroumov, I.: Invariant polarization signatures for recognition of hydrometeors by airborne weather radars. In: Gervasi, O., et al. (eds.) Computational Science and Its Applications – ICCSA 2023. Lecture Notes in Computer Science, vol. 13956, pp. 201–217. Springer, Cham (2023). https://doi.org/10.1007/978-3-031-36805-9_14
3. Kraus, T., Krieger, G., Bachmann, M., Moreira, A.: Spaceborne demonstration of distributed SAR imaging with TerraSAR-X and TanDEM-X. IEEE Geosci. Remote Sens. Lett. **16**(11), 1731–1735 (2019)
4. Tserne, E., et al.: Practical imaging algorithms in ultra-wideband radar systems using active aperture synthesis and stochastic probing signals. Radioelectronic Comput. Syst. **105**(1), 55–73 (2023)
5. Schreiber, E., Heinzel, A., Peichl, M., Engel, M., Wiesbeck, W.: Advanced buried object detection by multichannel, UAV/drone carried synthetic aperture radar. In: 13th European Conference on Antennas and Propagation (EuCAP), pp. 1–5. IEEE, Krakow, Poland (2019)
6. Kim, H., Song, J., Natsuaki, R., Hirose, A.: Dependence of polarimetric characteristics on sar resolutions: experimental analysis. In: IGARSS 2019 - 2019 IEEE International Geoscience and Remote Sensing Symposium, p. 3289. IEEE, Yokohama, Japan (2019)
7. Solomentsev, O., Zaliskyi, M., Averyanova, Y., Ostroumov, I., Nikitina, T.: Method of optimal threshold calculation in case of radio equipment maintenance. In: Shukla, S., Gao, X.Z., Kureethara, J.V., Mishra, D. (eds.) Data Science and Security 2022. Lecture Notes in Networks and Systems, vol. 462, pp. 69–79. Springer, Singapore (2022). https://doi.org/10.1007/978-981-19-2211-4_6
8. Reniers, A.C.F., Hubrechsen, A., Federico, G., Bronckers, L.A., Smolders, A.B.: Spherical mm-wave anechoic chamber for accurate far-field radiation pattern measurements. In: 52nd European Microwave Conference (EuMC), pp. 318–321. IEEE, Milan, Italy (2022)
9. Ezuma, M., Anjinappa, C.K., Funderburk, M., Guvenc, I.: Radar cross section based statistical recognition of UAVs at microwave frequencies. IEEE Trans. Aerosp. Electron. Syst. **58**(1), 27–46 (2022). https://doi.org/10.1109/TAES.2021.3096875
10. Ruzhentsev, N., Kuznetsov, B., Kuzmenko, N., Volosyuk, V., Tserne, E., Popov, A.: Radio-heat contrasts of UAVs and their weather variability at 12 GHz, 20 GHz, 34 GHz, and 94 GHz frequencies. ECTI Trans. Electr. Eng. Electron. Commun. **20**(2), 163–173 (2022)
11. Chizh, M., Zhuravlev, A., Razevig, V., Ivashov, S.: Non-destructive testing of the rails rolling surface and joints with synthetic aperture radar. In: 21st International Radar Symposium (IRS), pp. 112–116. IEEE, Warsaw, Poland (2020)

12. Volosyuk, V., Zhyla, S., Pavlikov, V., Kolesnikov, D., Inkarbaieva, O., Tserne, E.: Method of static synthesis of aperture in tasks of remote sensing and non-destructive testing. In: IEEE 3rd International Conference on System Analysis & Intelligent Computing (SAIC), pp. 1–5. IEEE, Kyiv, Ukraine (2022)
13. Shmatko, O., Volosyuk, V., Ostroumov, I., Ruzhentsev, N., Tserne, E., Popov, A.: Statistical synthesis of aerospace radars structure with optimal spatio-temporal signal processing, extended observation area and high spatial resolution. Radioelectronic Comput. Syst. **101**(1), 178–194 (2022)
14. Volosyuk, V., Shmatko, O., Zhyla, S., Pavlikov, V., Ruzhentsev, N., Tserne, E.: Synthesis of the optimal algorithm and structure of contactless optical device for estimating the parameters of statistically uneven surfaces. Radioelectronic Comput. Syst. **4**, 199–213 (2021)
15. Volosyuk, V., Shmatko, O., Pavlikov, V., Ruzhentsev, N., Tserne, E., Popov, A.: Optimal method for polarization selection of stationary objects against the background of the earth's surface. Int. J. Electron. Telecommun. **68**(1), 83–89 (2022)
16. Volosyuk, V., Zhyla, S., Vlasenko, D., Inkarbaieva, O., Kolesnikov, D., Cherepnin, G.: Concepts of primary and secondary coherent images in radar and optical systems. In: IEEE 3rd International Conference on System Analysis & Intelligent Computing (SAIC), pp. 1–6. IEEE, Kyiv, Ukraine (2022)
17. Volosyuk, V.K., Zhila, S.S., Kolesnikov, D.V.: Phenomenological description of coherent radar images based on the concepts of the measure of set and stochastic integral. Telecommun. Radio Eng. **78**(1), 19–30 (2019)
18. Volosyuk, V.K., Kravchenko, V.F.: Statisticheskaja teorija radiotehnicheskih sistem distancionnogo zondirovanija i radiolokacii [Statistical Theory of Radio-Engineering Systems of Remote Sensing and Radar]. Fizmatlit, Moscow (2008)
19. Sushchenko, O., Averyanova, Y., Ostroumov, I., Kuzmenko, N., Zaliskyi, M., Solomentsev, O.: Algorithms for design of robust stabilization systems. In: Gervasi, O., Murgante, B., Hendrix, E.M.T., Taniar, D., Apduhan, B.O. (eds.) Computational Science and Its Applications – ICCSA 2022. Lecture Notes in Computer Science, vol. 13375, pp. 198–213. Springer, Cham (2022)
20. Dergachov, K., Havrylenko, O., Nikitina, T., Zaliskyi, M., Solomentsev, O.: GPS usage analysis for angular orientation practical tasks solving. In: IEEE 9th International Conference on Problems of Infocommunications. Science and Technology (PIC S&T), pp. 187–192. IEEE, Kharkiv, Ukraine (2022)
21. Passah, A., Sur, S.N., Abraham, A., Kandar, D.: Synthetic aperture radar image analysis based on deep learning: a review of a decade of research. Eng. Appl. Artif. Intell. **123**, 106305 (2023). https://doi.org/10.1016/j.engappai.2023.106305
22. Havrylenko, O., Dergachov, K., Zaliskyi, M., Ostroumov, I., Averyanova, Y.: Decision support system based on the ELECTRE method. In: Shukla, S., Gao, X.Z., Kureethara, J.V., Mishra, D. (eds.) Data Science and Security. Lecture Notes in Networks and Systems 2022, Lecture Notes in Networks and Systems, vol. 462, pp. 295–304. Springer, Singapore (2022). https://doi.org/10.1007/978-981-19-2211-4_26

ECG Signal Denoising by Cross-Bispectrum Data Processing

Oleh Viunytskyi(✉) and Alexander Totsky

National Aerospace University "KhAI", Chkalov Street 17, Kharkiv 61070, Ukraine
o.viunytskyi@khai.edu

Abstract. The paper is devoted to the issues of digital data processing in ECG signal application. The benefits and disadvantages of common methods dedicated to extraction useful signal component in interference environment have been compared and analyzed. A novel technique for filtering the ECG signal and extraction useful signal component based on cross-bispectrum signal processing strategy is proposed and studied. New algorithm for ECG signal processing has been developed and studied. The proposed algorithms have shown their efficiency and high quality of ECG extraction in the interference environment.

Keywords: ECG signal processing · bispectrum · noise suppression

1 Introduction

Due to the presence of a large number of interfering components in the ECG signal, it is common to use advanced algorithms for extracting a useful signal component in the interference environment, such as independent component analysis methods [1–3], filtering methods [4], their combinations [5] to achieve the best result [6], wavelet transforms [7], methods of decomposition of signals into empirical modes [8], correlation methods [9], non-adaptive methods [10]. In turn, they can be divided into single-channel methods for ECG extraction [11] and multi-channel methods [12, 13].

The main concept of the methods based on the analysis of independent sources is based on the feature that the source is statistically independent, while the ECG signal is a mixture of output signals [14]. These methods belong to the class of second-order estimates which have the name of Independent Component Analysis (ICA) [3, 15]. There is also another group of these methods named as periodic component analysis (PiCA) [16, 17]. The main problem with the use of ICA methods is that after obtaining estimates of individual sources of the ECG signal, it is impossible to reliably determine the order of the sources, as well as the scaling of the sources and their sign. However, a large number of modifications based on these algorithms were introduced recently.

The FastICA method [18], a modification of the ICA algorithm, additionally uses the value of the maximum number of iteration cycles for calculation, as well as the convergence criterion. At the very beginning data processing, the algorithm creates random initial weights for the mixing matrix and in the next processing step a new

M. Nechyporuk et al. (Eds.): ICTM 2023, LNNS 1008, pp. 587–598, 2024.
https://doi.org/10.1007/978-3-031-61415-6_50

vector is computed using the kurtosis calculation. After that, normalization is performed and the weight of the product of the new vector and the previous one is checked taking into account the convergence criterion. These procedures are repeated until the weight is found at the largest value corresponding to the convergence criterion or when the number of iterations is exceeded [19].

The JADE algorithm provides computation the accumulation matrix, which is further used to divide the abdominal signal into separate sources [20]. The source estimates are calculated in such a way as to achieve the maximum kurtosis value for individual components. First, the maximum set of accumulation matrices is evaluated, and after which they are optimized by finding the rotation matrix that has the largest degree of diagonality [21].

The SOBI algorithm uses second-order statistics to estimate the correlation of changes in the signal to estimate the output signals. First, the delay matrices are calculated, and then the sample covariance is diagonalized using the input data. In order to calculate the distribution matrix, an estimate of the obtained matrix is used, after which the obtained matrix is used to separate the sources of the abdominal signal [22].

There are also other modifications such as multivariate ICA [23], non-parametric ICA [24], and others. The authors of the paper [1] considered most of these algorithms, calculating the efficiency using the following parameters: the accuracy of searching for QRS complexes after selecting the ECG component; sensitivity to interference; positive predictive value; average value between sensitivity and value. According to the authors' results, the FastICA algorithm turned out to be the most effective, and the best results were achieved with a combination of this algorithm and an adaptive filter.

The first problem of these methods is related to the number of input channels when evaluating individual sources, since the channels themselves are used directly for their evaluation [23]. These methods assume that the sources are informationally independent of each other, and therefore require as many channels of ECG signals as there are components contained in it. The results of the authors [24] demonstrate this dependence. They try to solve this problem by using combined methods, which consist of either using several algorithms at once [25], or by introducing additional methods in the preprocessing of ECG signals, for example, using filtering of low-energy components [26], or by using adaptive filters [1].

The second problem is the output components. The main problem is related to the fact that when using PiCA methods, the first and main component or signal source has the largest variance, and therefore it contains the ECG component [27]. Whereas when using ICA methods, the decomposition of signals into sources takes place without taking into account the values of the signal variance, and therefore during the decomposition it is impossible to say exactly in which order the estimates of the sources are located. Therefore, it is necessary to use additional estimates of sources to detect ECG channels after applying these methods. However, the advantage of ICA methods is that the estimation of sources takes place without known previously determined information, so the separation of the ECG signal into ECG components and interference does not require additional determinations while PiCA methods require prior determination of the location of QRS complexes in the ECG signal. In addition, ICA methods are more effective in isolating the ECG component [1, 3, 28].

The main task of the proposed paper is the development of a new adaptive method of extracting useful information in the interference environment in multichannel ECG signal recording system.

2 Description of Proposed Approach

A set of open-source electrophysiological tools (Open-Source Electrophysiological Toolbox, OSET) [29] was used to perform the study. This set includes such tools as ECG signal and interference generators which are developed on the basis of real-life signal models. There are also tools for filtering ECG signals such as Kalman filters, linear filters, baseline filters, and tools for using blind source separation techniques and others. OSET is an open-source collection of biological signal generation, modeling, processing, and filtering, released in June 2006. The toolkit is distributed under the license (Berkeley Software Distribution, BSD) and can be freely used. The system also allows the generation of signals with variations in the positions of QRS complexes. Figure 1 shows an example of generating single-channel ECG signal.

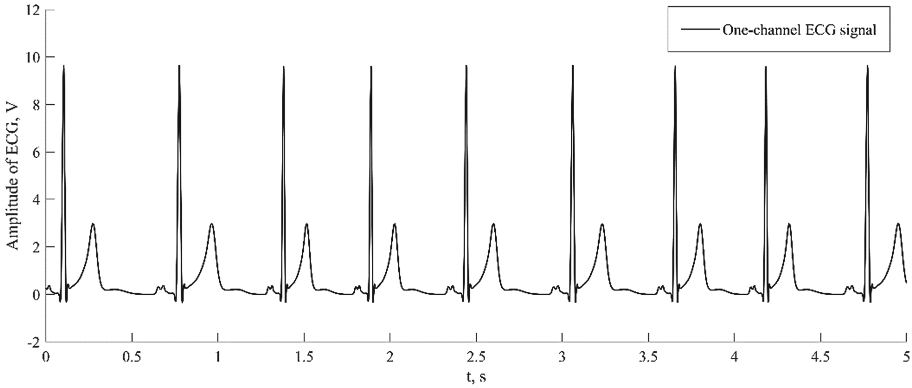

Fig. 1. ECG signal generated in separate single-channel

The OSET system allows us to create a number of disturbances namely white noise, colored noise, to simulate disturbances caused by muscle contractions, electrode movement, and baseline wandering. There is also the possibility of generating combined noise, which contained the previous ones. For example, it is possible to simulate the simultaneous noise superimposition caused by electrode movements, muscle contractions, and baseline wandering. This combined noise can be used to examine the immunity of the developed methods, or to test adaptive filters to suppress exactly these classes of interference that occur when recording real data.

Figure 2 shows an example of a generated single-channel ECG signal with an over-lay of combined noise with a value of signal-to-noise ratio (SNR) = 30 dBW.

In order to examine the effectiveness of filtering, a combined analysis is performed. It consists of determining the following parameters: the study of Pearson correlation

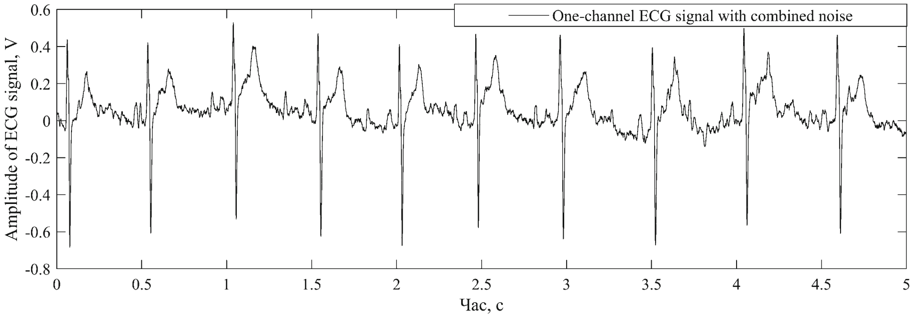

Fig. 2. Generated ECG signal contaminated by combined noise

values; root mean square error (RMSE); variation values of ECG components before and after filtering to determine the degree of distortion of the shape of this component; SNR values after using filtering to study the degree of interference suppression. Pearson correlation values R are calculated using:

$$R = \frac{1}{n}\sum_{j=1}^{n}\frac{\sum_{i=1}^{n}(x_{j,i}-\overline{x}_j)(y_{j,i}-\overline{y}_j)}{\sqrt{\sum_{i=1}^{n}(x_{j,i}-\overline{x}_j)^2\sum_{i=1}^{n}(y_{j,i}-\overline{y}_j)^2}}, \tag{1}$$

where *n* is the element number under study; $\overline{x}_j$, $\overline{y}_j$ are the signal mean values before and after filtering, respectively; $x_{j,i}$, $y_{j,i}$ are the signals before and after filtering, respectively.

RMSE values are calculated in the following form:

$$RMSE = \sqrt{\frac{\left(\sum_{i=1}^{n}(x_i - y_i)\right)^2}{n}} \tag{2}$$

where x_i, y_i are the signals before and after filtering; *n* is the number of signal samples.

Variance D is calculated as follows:

$$D = \frac{1}{n}\sum_{i=1}^{n}|X_i - \mu|^2 \tag{3}$$

where $X_i = x_i - y_i$ is the difference of noiseless initial signal and signal contained the noise after filtering; $\mu = \frac{1}{n}\sum_{i=1}^{n} X_i$ is the mean value of the signal difference before and after filtering.

SNR is defined as follows:

$$SNR_{dB} = 10\log_{10}\left(\frac{D_s}{D}\right) \tag{4}$$

where D_s is the variance of the noiseless initial signal.

Taking into account the above-mentioned expressions for calculating the efficiency of filtering, it is necessary to implement an algorithm for maximum interference suppression using multi-channel signal processing. At the same time, the greater (1) is for the ECG component without noise and after filtering, the more efficient the filtering algorithm is. The smaller (2) is for the ECG component without noise and after filtering, the better the filtering efficiency. The smaller (3) is for the ECG component without noise and after filtering, the more effective the filtering. The greater (4), the more effective the filtering. By using this filtering evaluation approach, it is possible to determine the degree of interference suppression and the influence of the filtering on the shape of the initial signal.

To solve this problem, we propose to use cross-bispectral signal processing. The assessment of bispectral density (spectral density of the third order or cumulant spectrum) allows to correctly describe the statistical characteristics of the observed process and determine the presence of correlations of spectral components. The main difference between the bispectrum and the energy spectrum is the preservation of phase information and the possibility of its recovery. By definition, the bispectrum is the Fourier transform of the triple correlation function (TCF). The bispectrum is described by a complex function of two frequency variables and has a number of the following advantages over the classical Fourier spectrum estimation [30]: for a stationary Gaussian process with a zero average value, the TCF and the bispectrum tend to zero; bispectrum of a process with an asymmetric distribution law is not equal to zero; bispectrum is invariant to the time shifts of the initial process.

Bispectrum $\dot{B}_x(p, q)$ can be written as:

$$\dot{B}_x(p, q) = \left\langle \dot{X}^{(m)}(p)\dot{X}^{(m)}(q)\dot{X}^{*(m)}(p + q) \right\rangle_{\infty} \tag{5}$$

where $p = -I + 1,\ldots,I-1$, $q = -I + 1,\ldots,I-1$ are the frequency indexes in the Fourier transforms $\dot{X}(\ldots)$; * denotes complex conjugation.

Cross-bispectral signal processing differs from the common bispectral processing by using two signal channels for calculations. Expression for calculating the cross-bispectrum can be represented in the following form:

$$\dot{B}c_x(p, q) = \left\langle \dot{X}_1^{(m)}(p)\dot{X}_1^{(m)}(q)\dot{X}_2^{*(m)}(p + q) \right\rangle_{\infty} \tag{6}$$

where $\dot{X}_1^{(m)}$ is the Fourier transform corresponding to the first channel; $\dot{X}_2^{*(m)}$ is the complex conjugated Fourier transform corresponding to the second channel.

The calculations are performed in such a way that the cross-bispectrum contains only those spectral components of the Fourier transform that have spectral-phase relationships in two channels at the same time. Since the common components for the ECG signals are the ECG component, the noise must be suppressed in this estimation.

The algorithm of the proposed ECG signal processing based on the proposed cross-bispectral technique consists the following steps.

1. The length of the signal window L in which the cross-bispectrum calculation will be performed (L = 512 samples) is determined;
2. The shift of the window is determined (N = 1 sample);

3. L/2 number of zero-valued samples are added to the initial signals on the left and right signal array ends;
4. The number of signal segments M is formed by L samples (M = signal length/ L);
5. Fragments of ECG signals in two channels falling into the window are selected;
6. The cross-bispectrum is calculated according to (6);
7. Signal of the length of 512 samples is recovered from cross-bispectrum estimate;
8. Recovered signals are averaged;
9. The averaged data is stored as one new sample of the filtered ECG signal;
10. The window is shifted by one sample and all steps are repeated until the end of the recording of ECG signals is reached;
11. At the end of the processing, the initially added zero elements are removed, after which one channel of the filtered record is obtained;
12. The calculation according to (1)–(4) is performed to compare the received filtered signal with the initial noiseless signal in the first channel.
13. The results are compared with the methods of analysis of independent sources, by calculating the results of these methods (1)–(4) when using only two channels.

3 Results of Computer Simulations

Figure 3 demonstrates the results of processing performed for two channels of ECG signals and the calculation of two cross-channels i.e., channels obtained as a result of cross-bispectral processing of two initial channels of abdominal signals.

As can be seen from Fig. 3, it is possible to use the algorithm by changing the order of the signals in the calculation performed by (6). The resulting cross-channels are not the average between the original two channels, and the resulting cross-channels are not identical to each other.

Accordingly, this is new information that was obtained using cross-bispectral approach, and it can be applied, for example, to solve two following problems: the first is suppression of interference between channels, where the original channel will be replaced by the calculated cross-channel; the second is the use of cross-channels when using methods of blind source separation, where additional channels should improve the quality of source separation.

You can additionally perform a cross-channel calculation between two already received cross-channels. Figure 4 shows the calculation of two additional cross-channels, using for calculation the cross-channels data computed earlier and presented in Fig. 3 (C, D).

Figure 5 demonstrates the result of using the JADE algorithm to decompose the signal into independent sources, using the initial ECG signals as input arguments (see Fig. 3A and B). Table 1 presents the performance of the proposed algorithm in comparison with three methods of analysis of independent components by using only two channels. Figure 6 shows the result of extracting the ECG signal component from a two-channel recording using all the studied algorithms at SNR = 10 dBW.

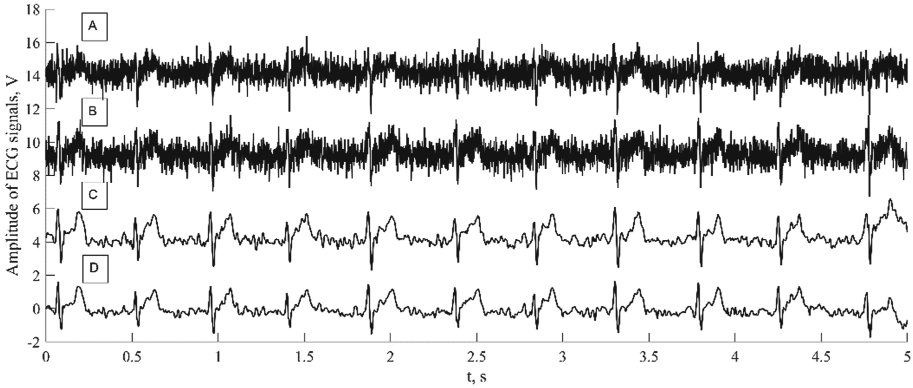

Fig. 3. The results obtained by proposed algorithm of cross-bispectral processing of abdominal signals for L = 16 samples: A – the initial ECG signal in the first channel, SNR = 10 dBW; B – initial ECG signal in the second channel, SNR = 10 dBW; C is the result of calculation by using (6), when X_1 is the Fourier transform for the first channel, and X_2 is the Fourier transform for the second channel; D is the result of calculation by using (6), when X_1 is the Fourier transform for the second channel, and X_2 is the Fourier transform for the first channel

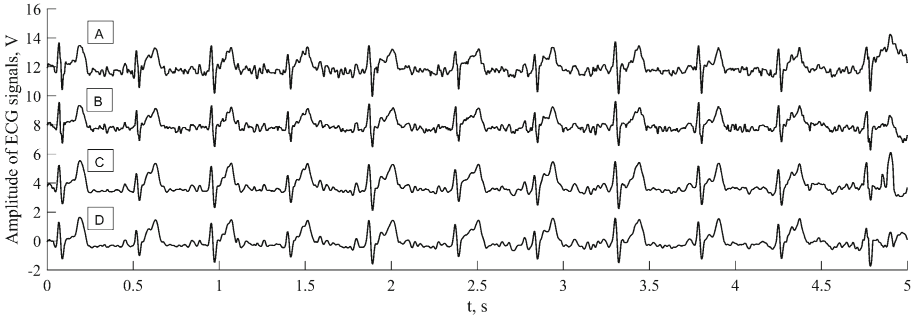

Fig. 4. The result of applying proposed algorithm of cross-bispectral processing of abdominal signals for L = 16 samples: A – cross-channel C (Fig. 3); B – cross-channel C (Fig. 3); B is the result of calculation by (6), when X_1 is the Fourier transform for the first cross-channel, and X_2 is the Fourier transform for the second cross-channel; D is the result of calculation (6), when X_1 is the Fourier transform for the second cross-channel, and X_2 is the Fourier transform for the first cross-channel

From the results of Table 1, it can be seen that the proposed algorithm with an initial SNR of −20 dBW provides the best result and increases the SNR by an average of 22 dBW. However, the output signal has considerable distortions demonstrated by the value of R = 0.32. In the SNR range from −10 to 10 dBW, the proposed algorithm provides best interference suppression increasing the SNR by an average of 8.47 dBW. At the value of SNR = 20 and 30 dBW, the best result was obtained for the PiCA method, however, the developed algorithm has smaller values of RMSE and variance, which indicates a better preservation of the shape of the initial ECG signal, and the difference in the initial value of SNR = 1.23 dBW. Within SNR = 40 dBW of the initial SNR, the

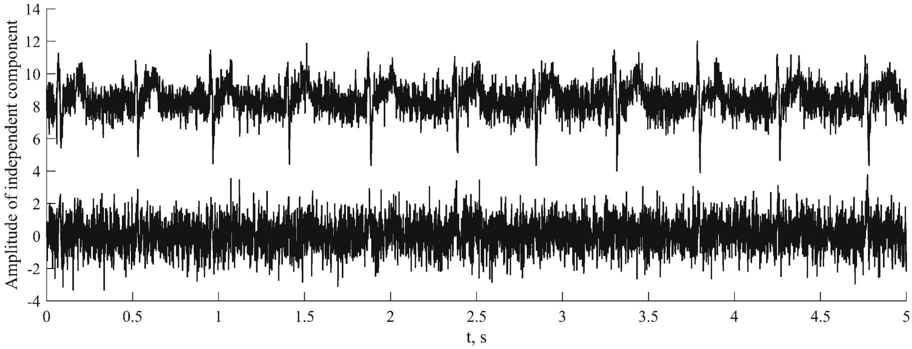

Fig. 5. The result of applying the JADE algorithm for the analysis of independent sources of the initial ECG signal

Table 1. Results demonstrating performance of noise suppression

Method	Numbers of channel	SNR raw, dBW	R	RMSE	D	SNR result, dBW
JADE	2	−20	0,11	$2{\cdot}10^{-3}$	$4{,}09{\cdot}10^{-6}$	−22,68
		−10	0,14	$6{,}4{\cdot}10^{-4}$	$4{\cdot}10^{-6}$	−12,88
		0	0,81	$2{,}5{\cdot}10^{-4}$	$5{,}99{\cdot}10^{-8}$	−4,46
		10	0,93	$1{,}5{\cdot}10^{-4}$	$2{,}35{\cdot}10^{-8}$	−0,42
		20	0,90	$1{,}3{\cdot}10^{-4}$	$1{,}60{\cdot}10^{-8}$	1,19
		30	0,79	$1{,}4{\cdot}10^{-4}$	$1{,}86{\cdot}10^{-8}$	0,92
		40	0,75	$1{,}4{\cdot}10^{-4}$	$2{,}07{\cdot}10^{-8}$	0,56
		50	0,67	$1{,}5{\cdot}10^{-4}$	$2{,}38{\cdot}10^{-8}$	−0,06
PiCA	2	−20	0,10	$2{,}1{\cdot}10^{-1}$	0,44	−29,58
		−10	0,12	$4{\cdot}10^{-4}$	$1{,}81{\cdot}10^{-7}$	−7,97
		0	0,62	$1{,}95{\cdot}10^{-4}$	$5{,}13{\cdot}10^{-8}$	−1,25
		10	0,95	$1{,}24{\cdot}10^{-4}$	$1{,}81{\cdot}10^{-9}$	2,39
		20	0,97	$5{,}14{\cdot}10^{-5}$	$2{,}99{\cdot}10^{-9}$	9,56
		30	0,86	$7{,}15{\cdot}10^{-5}$	$9{,}04{\cdot}10^{-9}$	11,39
		40	0,64	$1{,}16{\cdot}10^{-4}$	$1{,}62{\cdot}10^{-9}$	3,23
		50	0,33	$2{,}46{\cdot}10^{-4}$	$6{,}77{\cdot}10^{-9}$	−4,11
FastICA	2	−20	0,07	$2{\cdot}10^{-1}$	0,2	−29,09
		−10	0,11	$5{,}4{\cdot}10^{-4}$	$3{,}08{\cdot}10^{-7}$	−11,16
		0	0,81	$1{,}94{\cdot}10^{-4}$	$4{,}14{\cdot}10^{-8}$	−1,94

(*continued*)

Table 1. (*continued*)

Method	Numbers of channel	SNR raw, dBW	R	RMSE	D	SNR result, dBW
		10	0,93	$1{\cdot}10^{-4}$	$1{,}24{\cdot}10^{-8}$	4,27
		20	0,90	$1{,}1{\cdot}10^{-4}$	$1{,}25{\cdot}10^{-8}$	2,95
		30	0,96	$1{,}1{\cdot}10^{-4}$	$1{,}52{\cdot}10^{-8}$	4,27
		40	0,94	$1{,}2{\cdot}10^{-4}$	$1{,}72{\cdot}10^{-8}$	4,35
		50	0,98	$6{,}04{\cdot}10^{-5}$	$6{,}85{\cdot}10^{-9}$	10,65
Cross-B	2	−20	0,32	$2{,}6{\cdot}10^{-4}$	$6{,}93{\cdot}10^{-8}$	−4,81
		−10	0,68	$1{,}5{\cdot}10^{-4}$	$2{,}24{\cdot}10^{-8}$	−0,11
		0	0,91	$7{,}55{\cdot}10^{-5}$	$5{,}74{\cdot}10^{-9}$	5,83
		10	0,95	$5{,}60{\cdot}10^{-5}$	$3{,}30{\cdot}10^{-9}$	8,56
		20	0,96	$5{,}18{\cdot}10^{-5}$	$2{,}84{\cdot}10^{-9}$	9,19
		30	0,97	$4{,}70{\cdot}10^{-5}$	$2{,}37{\cdot}10^{-9}$	10,16
		40	0,95	$6{,}13{\cdot}10^{-5}$	$4{,}11{\cdot}10^{-9}$	8,09
		50	0,94	$6{,}69{\cdot}10^{-5}$	$4{,}66{\cdot}10^{-9}$	6,99

best result was achieved for the proposed algorithm. It provides an average of 4 dBW better SNR after filtering. For SNR = 50 dBW, the best results were achieved for the FastICA algorithm. On average, it provides a better SNR value after filtering by 3.66 dBW. This result can be explained by the fact that the proposed algorithm introduces more distortions into the initial signal than removes the interference.

4 Conclusion

Performance of novel cross-bispectral technique has been studied for the extraction of an ECG signal in two-channel recordings in combined interference environment. The results were compared with common methods of analysis of independent sources, such as JADE, PiCA, FastICA. The results indicate that the proposed algorithm with an initial SNR of −20 dBW provides the best result and increases the SNR by an average of 22 dBW, although the output signal has considerable distortion, as demonstrated by the Pearson correlation value of R = 0.32. In the SNR range from −10 to 10 dBW, the proposed algorithm provides best noise suppression, increasing the SNR by an average of 8.47 dBW. At SNR = 20 and 30 dBW, the best result was obtained for the PiCA method, however, the proposed algorithm has smaller values of RMSE and variance, which indicates a better preservation of the shape of the initial ECG signal, and the difference in the initial value of SNR = 1.23 dBW. Within SNR = 40 dBW of the initial SNR, the best result was achieved for the proposed algorithm. It provides an average of 4 dBW better SNR after filtering. For SNR = 50 dBW, the best results were achieved for the FastICA algorithm. On average, it provides a better SNR after filtering by 3.66

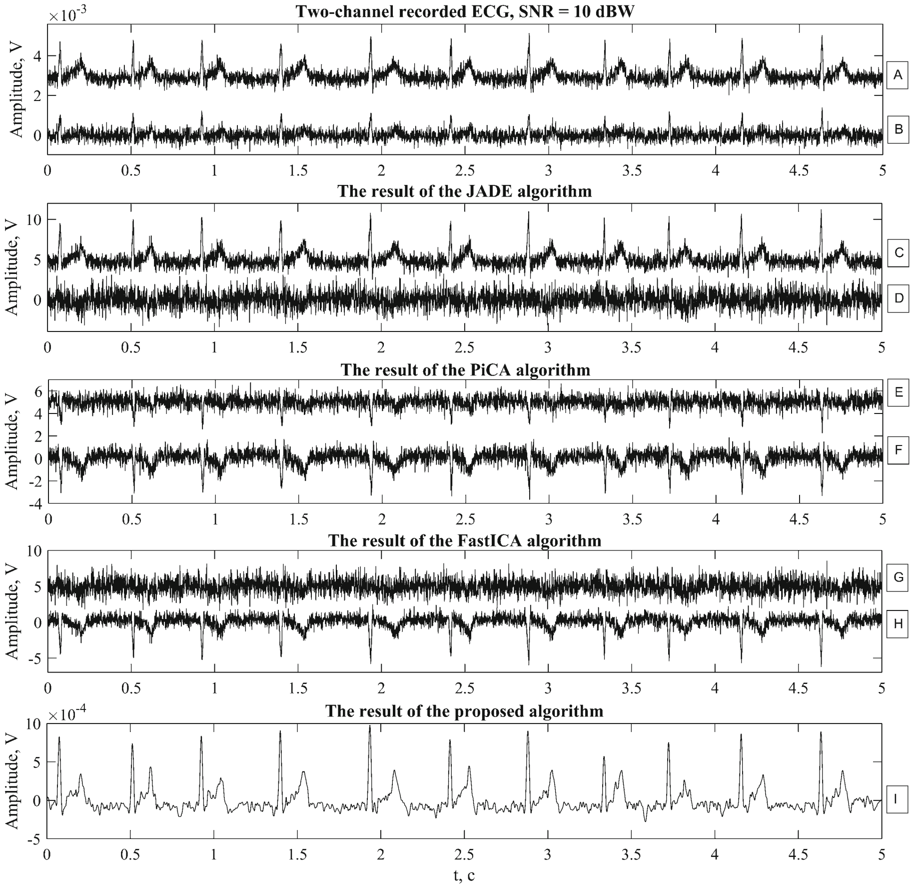

Fig. 6. ECG signal processing: A and B – the initial ECG signals in the first and second channel, respectively; C, D – the result of the selection of independent sources by the JADE algorithm; E, F – the results of selection of independent sources by the PiCA algorithm; G, H – the results of the selection of independent sources by the FastICA algorithm; I – the results of ECG signal selection using the proposed algorithm

dBW. This result can be explained by the fact that the proposed algorithm introduces more distortions into the initial signal than removes the interference.

In the future, it is necessary to carry out additional studies on the performance of the proposed method, as well as a comparison with other non-linear filtering methods, in addition to independent component analysis methods.

References

1. Viunytskyi, O., Shulgin, V., Totsky, A., Egiazarian, K., Polotska, O.: Recognition of premature births by bispectrum-based abdominal electromyography signal processing. Telecommun. Radio Eng. USA **78**(1), 59–69 (2019). https://doi.org/10.1615/TelecomRadEng.v78.i1.70

2. Jaroš, R., Barnova, K., Kahánková, R., Pelisek, J., Litschmannová, M., Martínek, R.: Independent component analysis algorithms for non-invasive fetal electrocardiography. PLoS ONE **18**(6), e0286858 (2023). https://doi.org/10.1371/journal.pone.0286858
3. Viunytskyi, O.G., Shulgin, V.I., Roienko, A.A., Totsky, A.V., Eguiazarian, K.O.: Fetal ECG extraction from the abdominal signal using wavelet bispectrum technique. Telecommun. Radio Eng. USA **82**(9), 29–46 (2023). https://doi.org/10.1615/TelecomRadEng.2023047588
4. Sarafan, S., Le, T., Lau, M.P.H., Hameed, A., Ghirmai, T., Cao, H.: Fetal electrocardiogram extraction from the mother's abdominal signal using the ensemble Kalman filter. Sensors **22**(7), 2788 (2022). https://doi.org/10.3390/s22072788
5. Jaros, R., Martinek, R., Kahankova, R., Koziorek, J.: Novel hybrid extraction systems for fetal heart rate variability monitoring based on non-invasive fetal electrocardiogram. IEEE Access **7**, 131758–131784 (2019). https://doi.org/10.1109/access.2019.2933717
6. Barnova, K., et al.: A novel algorithm based on ensemble empirical mode decomposition for non-invasive fetal ECG extraction. PLoS ONE **16**(8), e0256154 (2021). https://doi.org/10.1371/journal.pone.0256154
7. Cardenas-Lattus, J., Kaschel, H.: Fetal ECG multi-level analysis using Daubechies wavelet transform for non-invasive maternal abdominal ECG recordings (2017).https://doi.org/10.1109/chilecon.2017.8229511
8. Gupta, P., Sharma, K.K., Joshi, S.D.: Fetal heart rate extraction from abdominal electrocardiograms through multivariate empirical mode decomposition. Comput. Biol. Med. **68**, 121–136 (2016). https://doi.org/10.1016/j.compbiomed.2015.11.007
9. Yu, S., Chou, K.: Integration of independent component analysis and neural networks for ECG beat classification. Expert Syst. Appl. **34**(4), 2841–2846 (2008). https://doi.org/10.1016/j.eswa.2007.05.006
10. Viunytskyi, O., Shulgin, V.: Spatio-temporal signal processing for fetus and mother state monitoring during pregnancy, In: IEEE 9th International Conference on Dependable Systems, Services and Technologies, Kyiv, Ukraine, pp. 677–680 (2018). https://doi.org/10.1109/DESSERT.2018.8409210
11. Bandi, S., Dutt, I.: Single-channel fetal ECG extraction method based on extended Kalman filtering with singular value decomposition algorithm. Soft. Comput. **27**(13), 9119–9129 (2023). https://doi.org/10.1007/s00500-023-08421-4
12. Shokouhmand, A., Tavassolian, N.: Fetal electrocardiogram extraction using dual-path source separation of single-channel non-invasive abdominal recordings. IEEE Trans. Biomed. Eng. **70**(1), 283–295 (2023). https://doi.org/10.1109/TBME.2022.3189617
13. Viunytskyi, O., Shulgin, V.: Fetal ECG and heart rhythm analyzing using BabyCard. In: IEEE Signal Processing Symposium, Poland, Jachranka, pp. 21–24 (2017). https://doi.org/10.1109/SPS.2017.8053640
14. Ravindrakumar, S., Raja, K.B.: Fetal ECG extraction and enhancement in prenatal monitoring—review and implementation issues. IEEE Xplore. https://doi.org/10.1109/TISC.2010.5714599
15. Zarzoso, V., Nandi, A.K.: Noninvasive fetal electrocardiogram extraction: blind separation versus adaptive noise cancellation. IEEE Trans. Biomed. Eng. **48**(1), 12–18 (2001). https://doi.org/10.1109/10.900244
16. Sameni, R., Jutten, C., Shamsollahi, M.B.: A deflation procedure for subspace decomposition. IEEE Trans. Signal Process. **58**(4), 2363–2374 (2010). https://doi.org/10.1109/tsp.2009.2037353
17. Kharabian, S., Shamsollahi, M.B., Sameni, R.: Fetal R-Wave detection from multichannel abdominal ECG recordings in low SNR. PubMed 2009 https://doi.org/10.1109/iembs.2009.5333578

18. Martín-Clemente, R., Camargo-Olivares, J.L., Hornillo-Mellado, S., Elena, M., Román, I.: Fast technique for noninvasive fetal ECG extraction. IEEE Trans. Biomed. Eng. **58**(2), 227–230 (2011). https://doi.org/10.1109/tbme.2010.2059703
19. Hyvärinen, A., Oja, E.: Independent component analysis: algorithms and applications. Neural Netw. **13**(4–5), 411–430 (2000). https://doi.org/10.1016/s0893-6080(00)00026-5
20. Sameni, R., Jutten, C., Shamsollahi, M.B.: Multichannel electrocardiogram decomposition using periodic component analysis. IEEE Trans. Biomed. Eng. **55**(8), 1935–1940 (2008). https://doi.org/10.1109/TBME.2008.919714
21. Ramli, D.A., Shiong, Y.H., Hassan, N.: Blind source separation (BSS) of mixed maternal and fetal electrocardiogram (ECG) signal: a comparative study. Procedia Comput. Sci. **176**, 582–591 (2020). https://doi.org/10.1016/j.procs.2020.08.060
22. Turnip, A.: Comparison of ICA-based JADE and SOBI methods EOG artifacts removal. J. Med. Bioeng. **4**(6), 436–440 (2015). https://doi.org/10.12720/jomb.4.6.436-440
23. Viunytskyi, O., Sharonov, V., Totsky, A.: Extraction of averaged fetal and maternal QRS complexes from abdominal signal by using bispectrum-based signal processing. In: IEEE 16th International Conference on Advanced Trends in Radioelectronics, Telecommunications and Computer Engineering (TCSET), Lviv-Slavske, Ukraine, pp. 202–205 (2022). https://doi.org/10.1109/TCSET55632.2022.9766910
24. Sevim, Y., Atasoy, A.: Performance evaluation of nonparametric ICA algorithm for fetal ECG extraction. Turk. J. Electr. Eng. Comp. Sci. (2011) https://doi.org/10.3906/elk-0912-311
25. Agostinelli, A., et al.: Noninvasive fetal electrocardiography: an overview of the signal electrophysiological meaning, recording procedures, and processing techniques. Ann. Noninvasive Electrocardiol. **20**(4), 303–313 (2015). https://doi.org/10.1111/anec.12259
26. Andreotti, F., Behar, J., Zaunseder, S., Oster, J., Clifford, G.D.: An open-source framework for stress-testing non-invasive foetal ECG extraction algorithms. Physiol. Meas. **37**(5), 627–648 (2016). https://doi.org/10.1088/0967-3334/37/5/627
27. de Lathauwer, L., de Moor, B., Vandewalle, J.: Fetal electrocardiogram extraction by blind source subspace separation. IEEE Trans. Biomed. Eng. **47**(5), 567–572 (2000). https://doi.org/10.1109/10.841326
28. Jaros, R., Martinek, R., Kahankova, R.: Non-adaptive methods for fetal ECG signal processing: a review and appraisal. Sensors **18**(11), 3648 (2018). https://doi.org/10.3390/s18113648
29. OSET. http://www.oset.ir. Accessed 29 Nov 2023
30. Totsky, A., Zelensky, A., Kravchenko, V.: Bispectral Methods of Signal Processing, Walter de Gruyter GmbH, Berlin/Munich/Boston, 199p

Methodological Approach to the Design of Radio Equipment Operation System

Oleksandr Solomentsev, Maksym Zaliskyi(✉), Bohdan Chumachenko, and Vasyl Yehunko

National Aviation University, Liubomyra Huzara Avenue 1, Kyiv 03058, Ukraine
maximus2812@ukr.net

Abstract. Radio equipment is widely used in many spheres of industry and society, including civil aviation. The main requirement for this equipment is stable and reliable operation during intended use. Reliable properties can be achieved due to the correct technical decisions during the design and use of modern and reliable elemental base. The stage of operation is the longest in terms of time. At this stage, the reliability is supported by the operation system. Issues of development and modernization of operation systems are relevant, because it is necessary to constantly take into account new achievements of science and new positive advanced experience of operation system functioning. The issue of improving the content, methods and technologies of methodological support for operation systems is modern trend. Therefore, this paper considers the topical issues of building a structural scheme for methodological support of operation, a structural scheme of information exchange during the management of the efficiency during radio equipment operation, and the interconnection of data processing algorithms during the management of efficiency. In general, methodological issues are the basis for solving specific problems and guaranteeing rational costs, material and intellectual resources during the design and modernization of radio equipment operation systems.

Keywords: Operation System · Design · Process Model · Data Processing Algorithms · Decision-making

1 Introduction

1.1 Introduction to the Problem

It is known that methodological aspects are the basis for solving specific design problems of creating a new product or modernizing an existing one [1, 2]. The tasks of methodological support are especially relevant now in Ukraine in the conditions of post-war development, when something has been destroyed and something has stopped and is not functioning. At the same time, it is possible to develop new technologies, tools, and organizational solutions that were difficult to implement in the conditions of the pre-war period. The content of the methodological support is very large in structure [3, 4]. It

M. Nechyporuk et al. (Eds.): ICTM 2023, LNNS 1008, pp. 599–610, 2024.
https://doi.org/10.1007/978-3-031-61415-6_51

includes principles, approaches, theorems, axioms, methods and procedures for data processing, decision-making, optimization, including taking into account new achievements of science and technology in the field of artificial intelligence [5, 6]. Technologies for managing operational processes are often associated with the use of a system approach [7, 8]. According to the system approach, it is necessary to justify the structure, content, main elements, their relationships and description for the subject area under study [9, 10]. In this case, the structure of the subject area includes government regulatory authorities, research organizations, and production design enterprises [11]. They have structure, resources, documentation, personnel, data processing and decision-making technologies [12, 13].

It is very important to correctly formulate the goals of the structural elements and determine ways to measure their achievement. Measuring the achievement of goals is associated with efficiency indicator [14, 15]. Often, several alternative solutions to a specific problem are created and the most effective is selected [16]. The tasks of developing methodological support are multi-alternative and multi-criteria [17].

1.2 Motivation

Issues of ensuring the safety and regularity of flights of civil aviation aircraft are constantly at the center of the attention of civil aviation workers, who are solving important problems for the development of the state and society [18]. The reliability and efficiency of using radio equipment have a direct impact on the solution of this problem [19]. Currently, with significant material costs for the operation of radio equipment, the value of which significantly exceeds the initial cost of the equipment, there are cases of disruption of flight activities due to unreliable operation of the systems [20]. Therefore, the problem of increasing the efficiency of using radio equipment while simultaneously reducing the costs of their maintenance is relevant.

One of the main ways to solve this problem at the design and operation stage is the use of advanced technological processes for servicing radio equipment using automated systems for monitoring and managing the technical condition and operational processes of the equipment [21]. The introduction of operation management systems will allow realizing the main advantages of modern technologies for predictive and prescriptive maintenance, thereby reducing operating costs, promptly detecting failures and carrying out corrective actions [22]. The use of operation management system is a comprehensive solution towards the implementation of the doctrine of data-based decision-making and the use of intelligent technologies of Industry 4.0 [23].

Taking into account the above, it should be noted the need to develop a generalized methodological approach to the design of operation systems to achieve effective management of the technical condition of radio equipment.

1.3 Contribution

The goal of this paper is to demonstrate the design features of radio equipment operation system. The developed diagram of the interconnection of methodological support subsystems for operation can be used as a basis for creating new operation systems and is an effective tool for synthesizing data processing algorithms to manage the efficiency of using equipment for its intended purpose in the theory of reliability and operation of radio systems.

1.4 The Organization of the Paper

The paper consists of six sections. The Sect. 1 deals with background information. The Sect. 2 considers the state-of-the-art. The Sect. 3 discusses the approaches to operation system methodological support design. The Sect. 4 presents the data processing structure to increase the operational efficiency. The last two sections discuss the conclusions and future scope.

2 Literature Review

The main element of the operation system is the equipment that is used for its intended purpose [24]. In civil aviation, to ensure regularity and safety of flights, such equipment is radio equipment [25, 26]. This equipment includes communication systems, telecommunications, surveillance, navigation, inspection equipment, access control, video surveillance, security and fire alarms [27].

Radio equipment is complex in structure and requires highly qualified personnel to operate it. This equipment is influenced by various random and organized factors, including power supply stability, electromagnetic environment, human factor, degradation processes of equipment circuit elements, and others [28, 29].

To ensure the efficient operation of radio equipment, a set of measures, algorithms, decisions, and control actions are used, which are implemented in the operation system. One of the ways to solve this problem is to have a checklist for inspecting the constituent elements of methodological support and the compliance or non-compliance of their provisions with specific technological operational processes [30].

The concept of methodological support includes:

– various kinds of decision-making schemes;
– algorithms for analyzing generalized technical and economic efficiency, which are carried out by state regulatory authorities in the field of radio equipment operation, design organizations and civil aviation operational enterprises;
– regulatory and administrative documents on the operation of radio equipment;
– various kinds of technological processes and specific technologies [9, 30].

In general, we can talk about methodological support system that has a specific organizational structure and content for each element of this structure.

An analysis of the literature [5, 14] in the field of theory and practice of operating complex systems shows that the issues of developing methodological support have not yet obtained enough attention, although they are quite important in ensuring the efficiency of operation systems of radio equipment for civil aviation. Therefore, this paper is devoted to the issues of describing the structure of methodological support, including data processing algorithms at the control level of radio equipment operational processes.

3 Structure of Methodological Support for the Operation of Radio Equipment

Let's consider a variant of the structure of methodological support for the operation of radio equipment.

A block diagram of the relationship between subsystems of methodological support for the operation of radio equipment is shown in Fig. 1. There are several elements of this subject area:

– state authority for regulating operation;
– a design organization that carries out developments for the operation of radio equipment;
– technological system of operation for radio equipment;
– unit for collecting and processing technical and economic information;
– unit for management of the operational efficiency of radio equipment.

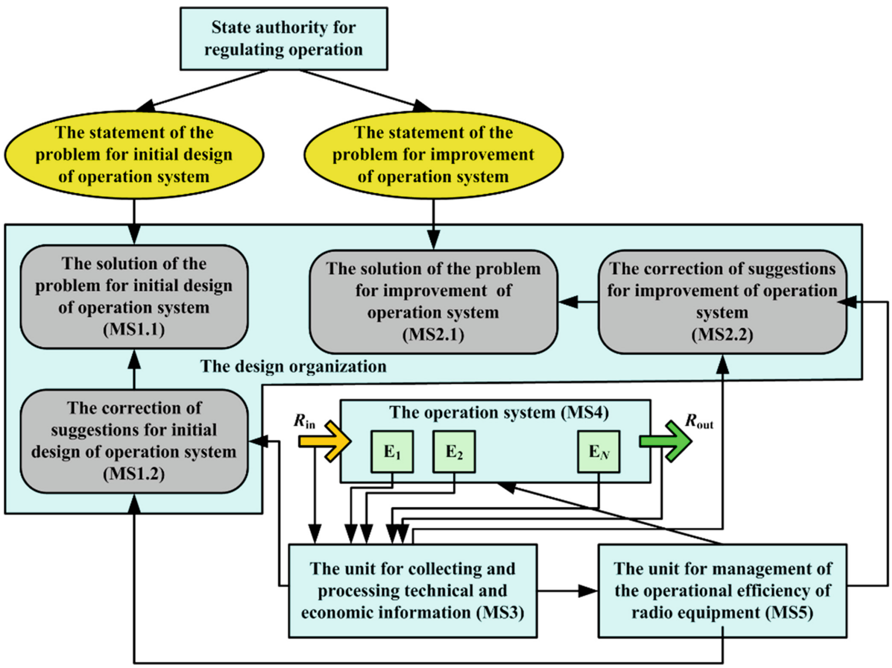

Fig. 1. The diagram of the relationship between subsystems of methodological support for the operation of radio equipment.

We believe that methodological support solves several main problems. The first problem is related to the initial design of the operation system for airports under construction or restoration. The second problem is related to improving operation systems for equipment that has already been in operation for a certain time. In the first case, it is proposed to have MS1.1 to perform the task of searching for a primary design solution and MS1.2 to correct this solution if the theoretical result does not correspond to operational practice. In the second case, it is advisable to have MS2.1 to develop recommendations for improving the operation system of radio equipment already in use and MS2.2 to correct recommendations if they do not correspond to operational practice. In both cases, the specified methodological support subsystems receive data from the unit in which, using MS3, the collection and processing of technical and economic information from the elements of the operation system is carried out.

To ensure current production activities, MS4 is used. This support includes technologies for using radio equipment for their intended purpose, technologies for maintenance, repair, diagnostics, monitoring, control, commissioning, and others.

The radio equipment operation system control unit using MS5 and based on data from MS3 generates commands for elements of the operation system to ensure the required efficiency. If management does not give the desired result, then the tasks of improving a separate component of the operation system are solved.

In general, the methodological support system is quite complex, therefore we will consider in detail only one of the subsystems associated with managing the operation of radio equipment.

The efficiency management unit, as well as other elements of the organizational structure of methodological support, must be specified by a description vector $\vec{A}$. Such a vector at the design stage will make it possible to determine a functionally complete set of elements that should be objects of synthesis of the technological system. At the improvement stage, this vector will help solve the problem of selecting the most suitable modernization objects to ensure efficient operation of the equipment.

An analysis of the literature has shown that one of the key elements of the efficiency management unit is its methodological support MS5, which includes the technology of the unit's functioning or a set of algorithms for processing information and making decisions on the choice of certain control actions.

Taking into account the generalized structure of methodological support, a scheme of information exchange between efficiency management unit and elements of the subject area can be constructed, which is shown in Fig. 2.

Figure 2 contains N organizational elements $\vec{E}$ that are part of the radio equipment operation system and perform the functions of the i-th subsystem TS_i. The system TS_i services the flow of input requests $\overrightarrow{R_{in}}$, so at the output we have a flow of serviced requests $\overrightarrow{R_{out}}$. Vectors $\overrightarrow{I_1}$ and $\overrightarrow{I_2}$ carry information about the flow of requests $\overrightarrow{R_{in}}$ and $\overrightarrow{R_{out}}$. These vectors include data on the number of requests, requirements for input requests $\overrightarrow{R_{in}}$ and the actual quality of served requests $\overrightarrow{R_{out}}$. The vector $\overrightarrow{I_3}$ carries information about the results of the functioning of the elements $\vec{E}$. Control actions and commands $\overrightarrow{CA}$ are communicated to the elements $\vec{E}$ to ensure the efficiency of the technological system TS_i.

The information collection and processing unit receives signals $\overrightarrow{I_1}$, $\overrightarrow{I_2}$, $\overrightarrow{I_3}$ and, after analyzing input data, provides information $\overrightarrow{I_4}$ to the efficiency management unit where a decision is made about the need for commands $\overrightarrow{CA}$ to the elements $\vec{E}$.

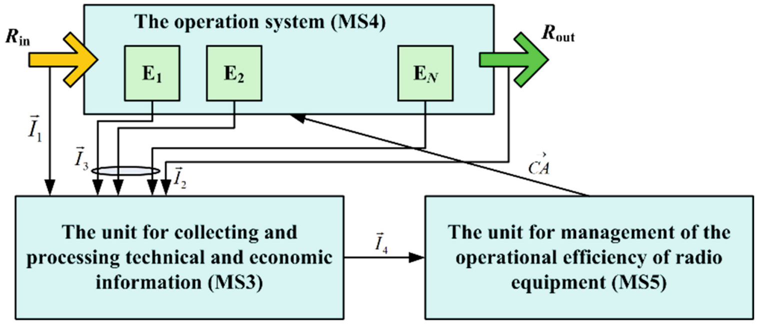

Fig. 2. The scheme of information exchange between efficiency management unit and elements of the subject area.

An analysis of the literature allows to conclude that the issues of managing the efficiency of the radio equipment operation system at the level of a particular state have not been resolved. Most of the questions are devoted to assessing the efficiency of certain components of the operation of radio equipment. In this case, as a rule, integrated technical and economic efficiency indicators $\vec{\Lambda}$ are developed for maintenance systems, repair systems, technical condition diagnostic systems, and others.

The parameters $\vec{\Lambda}$ include the frequency of inspections to monitor the technical condition of equipment, the amount of maintenance procedures, the probability of errors of the first and second types, the veracity of control operations, and others. As a rule, single-parameter models of radio equipment are used. Knowing the analytical expression for $\vec{\Lambda}$, we can solve the problem of managing the operational efficiency of radio equipment.

Experience in solving similar problems for other application areas allows to conclude that when developing the efficiency management unit, it is necessary to know:

– the purpose of the TS_i functioning;
– efficiency criteria $\overrightarrow{EC}$;
– models of vector $\overrightarrow{I_4}$;
– list of control actions or commands $\overrightarrow{CA}$;
– a set of rules (algorithms) for selecting control actions or commands $\overrightarrow{A_{alg}}$.

The theory of automatic control states that the control system, like efficiency management unit, must have stability in control, have a certain speed when processing control actions, have noise immunity and have a number of other performance indicators.

Analysis of information flow $\overrightarrow{I_4}$ in Fig. 2 indicates that the data are generally stochastic, for example due to the randomness of radio equipment failures, the randomness of the flow of requests for radio technical support for flights, the randomness of weather conditions, and others.

Thus, the above algorithms $\overrightarrow{A_{alg}}$ must process random data. Therefore, to solve the problem of synthesis of algorithms it is necessary to use methods of probability theory and mathematical statistics described in [31, 32]. The practice of solving synthesis problems in related applied areas shows that, along with classical approaches, heuristic methods are often used, which are based on common engineering sense, operating experience and intuition.

When justifying the list of algorithms and the set of control commands, we will first of all proceed from the goals $\vec{G}$ of the functioning of the technological system of operation and the restrictions that must be met to achieve the goals. We will assume that the restrictions are included in the set $\vec{G}$. According to ICAO regulatory documents and documents relating to service of the radio equipment operation in Ukraine, we can conclude that the main goal G_1 of the operation system is to most fully satisfy the needs of airspace users and civil aviation departments in radio-electronic flight support. We will assume that the main goal is divided into two subgoals. The subgoal $G_{1,1}$ is related to the most complete satisfaction of the needs of airspace users in terms of radio-electronic support for flights in the upper and lower airspace. The subgoal $G_{1,2}$ is related to the provision of communication services to support the steam production activities of civil aviation enterprises. The goal G_2 will be to ensure a level of flight safety in terms of the influence of radio equipment that is no worse than required. The goal G_3 will be to ensure regularity of flights in terms of the influence of radio equipment no worse than required. The goal G_4 will be to comply with ICAO requirements and recommendations. The goal G_5 will be to ensure that operating costs are either minimal or do not exceed a given threshold level. Goals G_2, G_3, G_4 and G_5 have a hierarchical subordination. The goal G_2 has the highest priority.

We assume that the strategy for managing the efficiency of the radio equipment operation system is based on the following statements and assumptions:

1. The set of goals $\vec{G}$ can be associated with corresponding parameters that make it possible to quantify the degree of achievement of these goals: $x_{1,1}(t)$, $x_{1,2}(t)$, $x_2(t)$, $x_3(t)$, $x_4(t)$ and $x_5(t)$.
2. To assess the efficiency of TS_i from the point of view of achieving each goal, a two-alternative classification of each signal is performed according to the principle: "the j-th goal of the TS_i has been achieved" or "the j-th goal of the TS_i has not been achieved".
3. For an integral assessment of efficiency, three alternative classifications are used: normal, satisfactory and unsatisfactory efficiency.
4. The integral assessment is performed at a given calendar observation interval.
5. The integral efficiency criterion is not exceeding the thresholds for the number of decisions on satisfactory and unsatisfactory efficiency assessment.
6. Efficiency evaluation is carried out continuously.
7. If several control strategies satisfy the efficiency criterion, then the one with the minimum operating costs is selected.
8. For assessment of TS_i efficiency, a regulatory framework $\overrightarrow{H_n^{(0)}}$ is used, where n is the quantity of goals.
9. In case of a decision about normal efficiency, the control system generates a command to continue operation of the radio equipment.
10. In case of a decision about satisfactory efficiency, the control system forms a command to search for the reasons for such assessment and develop corrective actions to eliminate these reasons.

11. In case of a decision about unsatisfactory efficiency, similar procedures are performed, but much faster.
12. If the possibilities in terms of controllability are exhausted, then the system is improved using MS2.1.

4 Analysis of Data Processing Structure to Increase the Operational Efficiency

Taking into account the accepted assumptions about the strategy for managing the efficiency of the radio equipment operation system and Fig. 2, we will draw up a structural diagram of information processing at the efficiency management unit. This diagram is shown in Fig. 3 and includes generalized data processing operators (algorithms). We believe that from the output of the unit for collecting and processing technical and economic information, signals $x_{1,1}(t)$, $x_{1,2}(t)$, $x_2(t)$, $x_3(t)$, $x_4(t)$ and $x_5(t)$ are received that quantitatively characterize the set of goals $\vec{G}$.

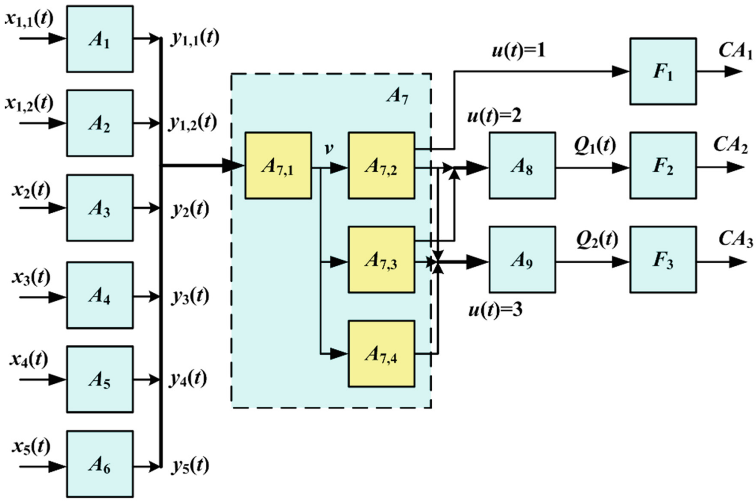

Fig. 3. The structural diagram of information processing at the efficiency management unit.

In Fig. 3 algorithms A_1, A_2, A_3, A_4, A_5, A_6 evaluate the efficiency of TS_i operation. The algorithm A_1 is implemented as follows

$$y_{1,1}(t) = A_1\big(x_{1,1}(t)\big) = \begin{cases} 1, if x_{1,1}(t) \geq H_1^{(0)}, \\ 0, if x_{1,1}(t) < H_1^{(0)}, \end{cases}$$

where $H_1^{(0)}$ is threshold level for parameter $x_{1,1}(t)$.

For definiteness, we assume that if $y_{1,1}(t) = 1$, then the goal $G_{1,1}$ is achieved, otherwise the goal $G_{1,1}$ is not achieved. We assume that the algorithms A_2, A_3, A_4, A_5, A_6 work in a similar way.

Algorithm A_7 performs processing the signals $y_{1,1}(t)$, $y_{1,2}(t)$, $y_2(t)$, $y_3(t)$, $y_4(t)$ and $y_5(t)$ to estimate integral efficiency. Signal $u(t) = 1$ corresponds to the decision about normal efficiency. Signal $u(t)$ can be equal to $u(t) = 2$ and $u(t) = 3$. Algorithm A_7 is complex. The processing consists of two steps. The first step is associated with the analysis of signals $y_2(t)$, $y_3(t)$, $y_4(t)$ and $y_5(t)$. Therefore, the initial assessment of integral efficiency is implemented. This classification is three-alternative and forms signal of three types $v(t) = 1$, $v(t) = 2$, and $v(t) = 3$. The algorithm A_7 at the first step is described by sub-algorithm $A_{7,1}$. At the second step, signals $y_{1,1}(t)$ and $y_{1,2}(t)$ are analyzed. The possible decisions for different signals values are shown in Table 1.

Table 1. The possible decisions for different signals values.

#	$y_{1,1}(t)$	$y_{1,2}(t)$	$y_2(t)$	$y_3(t)$	$y_4(t)$	$y_5(t)$	$u(t)$	Case
1	1	1	1	1	1	1	1	Normal
2	1	0	1	1	1	1	2	Satisfactory
3	1	1	1	1	1	0	2	Satisfactory
4	1	1	1	1	0	1	2	Satisfactory
5–32	All other possible combinations						3	Unsatisfactory

Algorithms A_8 and A_9 perform search for reasons of decision-making on signals $u(t) = 2$ and $u(t) = 3$ formation.

Output signals of operators A_8 and A_9 are $Q_1(t)$ and $Q_2(t)$. These signals are vector quantities, since TS_i is the complex system, so there may be many reasons for the deterioration of the technical condition of TS_i. Techniques of technical diagnostics can be applied during the synthesis of algorithms A_8 and A_9. Note that when searching for reasons, it is advisable to use the method of decomposition of the subject area, for example, based on the selection of the organizational structure of TS_i, technological processes, personnel, and others. However, it is necessary to have TS_i model that would allow tracking the relationship of parameters $x_{1,1}(t)$, $x_{1,2}(t)$, $x_2(t)$, $x_3(t)$, $x_4(t)$ and $x_5(t)$ with the internal parameters of the system for the selected hierarchical level. That is, this model should connect the goals of TS_i operation with the reasons that ensure their achievement. The relationship scheme of parameters with the internal parameters of the system can also have the hierarchical structure.

The degree of detailing of the possible reasons for the insufficient efficiency of TS_i operation will depend on the available analytical and other types of correlations between the parameters, the amount of statistical information, its veracity, and others.

It should be noted that the task of synthesis and analysis of certain subsystems TS_i and the entire efficiency management unit is quite complex. For example, the insufficient level of air navigation fees, a decrease in the number of serviced aircraft, an increase in the level of operational costs may be the possible reasons for the insufficient efficiency of TS_i with respect to goal G_5.

Algorithms F_1, F_2 and F_3 are intended for the formation of control actions. These algorithms are also composite. The algorithm F_1 forms commands CA_1 to continue TS_i

operation and performs the pre-planned scope of procedures. Control actions CA_2 are commands aimed at improving the TS_i efficiency. Control actions CA_3 include commands aimed at eliminating the causes that led to a significant loss of the TS_i efficiency. During control actions CA_2, CA_3 formation, it is necessary to apply the principle of priority, i.e., to implement such control influences that would ensure the efficiency of TS_i operation, taking into account the significance of the goals $\vec{G}$. If for the same element of TS_i can be defined several variants of influences, then the choice of the most rational variant should be carried out taking into account some criterion of efficiency, which should for example depend on time and cost factors.

5 Conclusions

The paper deals with topical issues regarding the improvement of methodological support for the operation of radio equipment. It is emphasized that methodological issues are the basis for the effective solution of the problems of the subject area from the point of view of rational expenditure of resources in the system covering three main hierarchical levels: state authority, operational enterprises, design and construction institutions and organizations. This paper considers the problem of building the structural scheme for methodological support of operation, the structural scheme of information exchange during the operation efficiency management, and the interconnection of data processing algorithms during the management of radio equipment efficiency. The obtained results will allow further development of methodological support for operation and are aimed at providing the reliability of radio equipment operation under the conditions of rational consumption of resources.

6 Future Scope

The further development and implementation of management decision support systems will be realized using artificial intelligence methods, tools, and technologies. In order to adopt and implement timely corrective and preventive actions, it is advisable to create modern databases of statistical data (hubs), in which a variety of information is accumulated for characterizing the conditions and main events for three defined levels (state regulation, operational enterprises, research and design organizations).

Future research in terms of improving the methodical support for radio equipment operation may also be related to the development of new technologies for statistical data processing for the detecting events of changes in the trends of technical and economic parameters, predicting the future trends, evaluating statistical parameters of trends, diagnosing possible causes of insufficient efficiency for the use of methodical support for radio equipment operation system.

References

1. Anand, A., Ram, M.: System Reliability Management: Solutions and Techniques. CRC Press, Boca Raton (2021)
2. Tachinina, O.M., Lysenko, O.I., Ponomarenko, S.O., Alekseeva, I.V.: Conceptual proposals for the creation of a fully reusable light-class aerospace system in Ukraine. In: IEEE 6th International Conference on Methods and Systems of Navigation and Motion Control, pp. 85–88. IEEE, Kyiv, Ukraine (2020). https://doi.org/10.1109/MSNMC50359.2020.9255504
3. Solomentsev, O., Zaliskyi, M., Kozhokhina O., Herasymenko, T.: Efficiency of data processing for UAV operation system. In: IEEE 4th International Conference Actual Problems of Unmanned Aerial Vehicles Developments, pp. 27–31. IEEE, Kyiv, Ukraine (2017). https://doi.org/10.1109/APUAVD.2017.8308769
4. Sushchenko, O.A., Bezkorovainyi, Y.M., Golitsyn, V.O.: Fault-tolerant inertial measuring instrument with neural network. In: International Conference on Electronics and Nanotechnology, pp. 797–801. IEEE, Kyiv, Ukraine (2020). https://doi.org/10.1109/ELNANO50318.2020.9088779
5. Dhillon, B.S.: Reliability, Quality, and Safety for Engineers. CRC Press, Boca Raton (2005)
6. Zhukov, I., Synelnikov, O., Chaikovska, O., Dorozhynskyi, S.: Modern approaches to software optimization methods. CEUR Workshop Proc. **3188**, 1–10 (2021)
7. Solomentsev, O., et al.: Data processing through the lifecycle of aviation radio equipment. In: IEEE 17th International Conference on Computer Sciences and Information Technologies (CSIT), pp. 146–151. IEEE, Lviv, Ukraine (2022). https://doi.org/10.1109/CSIT56902.2022.10000844
8. Tachinina, O., Ponomarenko, S., Shevchenko, V., Lysenko, O., Romanchenko, I.: Synthesis of a launch trajectory of aircraft optimal in the minimum fuel consumption based on sufficient conditions of optimal control. In: Nechyporuk, M., Pavlikov, V., Kritskiy, D. (eds.) Integrated Computer Technologies in Mechanical Engineering - 2021. ICTM 2021. Lecture Notes in Networks and Systems, vol. 367, pp. 67–77. Springer, Cham (2022). https://doi.org/10.1007/978-3-030-94259-5_7
9. Smith, D.J.: Reliability, Maintainability and Risk. Practical Methods for Engineers, 10th edn. Elsevier, London (2021)
10. Sushchenko, O.A., Tunik, A.A.: Robust optimization of the inertially stabilized platforms. In: 2nd International Conference on Methods and Systems of Navigation and Motion Control, pp. 101–105. IEEE, Kyiv, Ukraine (2012). https://doi.org/10.1109/MSNMC.2012.6475102
11. Okoro, O.C., Zaliskyi, M., Dmytriiev, S., Solomentsev, O., Sribna, O.: Optimization of maintenance task interval of aircraft systems. Int. J. Comput. Network Inf. Secur. **14**(2), 77–89 (2022). https://doi.org/10.5815/ijcnis.2022.02.07
12. Al-Azzeh, J., Mesleh, A., Zaliskyi, M., Odarchenko, R., Kuzmin, V.: A method of accuracy increment using segmented regression. Algorithms **15**(10), 378 (2022). https://doi.org/10.3390/a15100378
13. Zhukov, I., Okhrimenko, T., Balakin, S., Chaikovska, O., Sulkowski, K.: Risk assessment in critical infrastructure computer networks. CEUR Workshop Proc. **3421**, 272–277 (2023)
14. Jardine, A.K.S., Tsang, A.H.C.: Maintenance, Replacement, and Reliability: Theory and Applications, 2nd edn. CRC Press, Boca Raton (2017)
15. Kuzmenko, N.S., Ostroumov, I.V., Marais, K.: An accuracy and availability estimation of aircraft positioning by navigational aids. In: 5th International Conference on Methods and Systems of Navigation and Motion Control, pp. 36–40. IEEE, Kyiv, Ukraine (2018). https://doi.org/10.1109/MSNMC.2018.8576276
16. Gertsbakh, I.: Reliability Theory: With Applications to Preventive Maintenance. Springer, New York (2005). https://doi.org/10.1007/978-3-662-04236-6

17. Ivashchuk, O., et al.: A configuration analysis of Ukrainian flight routes network. In: International Conference on the Experience of Designing and Application of CAD Systems, pp. 6–10. IEEE, Lviv, Ukraine (2021). https://doi.org/10.1109/CADSM52681.2021.9385263
18. Ostroumov, I.V., Kuzmenko, N.S.: Accuracy assessment of aircraft positioning by multiple radio navigational aids. Telecommun. Radio Eng. **77**(8), 705–715 (2018). https://doi.org/10.1615/TelecomRadEng.v77.i8.40
19. Zaliskyi, M., et al.: Model building for diagnostic variables during aviation equipment maintenance. In: IEEE 17th International Conference on Computer Sciences and Information Technologies (CSIT), pp. 160–164. IEEE, Lviv, Ukraine (2022). https://doi.org/10.1109/CSIT56902.2022.10000556
20. Solomentsev, O., Zaliskyi, M., Zuiev, O.: Estimation of quality parameters in the radio flight support operational system. Aviation **20**(3), 123–128 (2016). https://doi.org/10.3846/16487788.2016.1227541
21. Sushchenko, O.A., Bezkorovainyi, Y.M., Golytsin, V.O.: Modelling of microelectromechanical inertial sensors. In: IEEE 15th International Conference on the Experience of Designing and Application of CAD Systems (CADSM), pp. 1–5. IEEE, Polyana, Ukraine (2019). https://doi.org/10.1109/CADSM.2019.8779286
22. Kuzmenko, N., et al.: Airplane flight phase identification using maximum posterior probability method. In: 3rd International Conference on System Analysis & Intelligent Computing, pp. 1–5. IEEE, Kyiv, Ukraine (2022). https://doi.org/10.1109/SAIC57818.2022.9922913
23. Sushchenko, O., et al.: Airborne sensor for measuring components of terrestrial magnetic field. In: 41st International Conference on Electronics and Nanotechnology (ELNANO), pp. 687–691. IEEE, Kyiv, Ukraine (2022). https://doi.org/10.1109/ELNANO54667.2022.9926760
24. Solomentsev, O., Zaliskyi, M., Nemyrovets, Y., Asanov, M.: Signal processing in case of radio equipment technical state deterioration. In: Signal Processing Symposium 2015 (SPS 2015), pp. 1–5, IEEE, Debe, Poland (2015). https://doi.org/10.1109/SPS.2015.7168312
25. Ostroumov, I., et al.: Relative navigation for vehicle formation movement. In: 3rd KhPI Week on Advanced Technology, pp. 1–4. IEEE, Kharkiv, Ukraine (2022). https://doi.org/10.1109/KhPIWeek57572.2022.9916414
26. Larin, V., et al.: Prediction of the final discharge of the UAV battery based on fuzzy logic estimation of information and influencing parameters. In: 3rd KhPI Week on Advanced Technology, pp. 1–6. IEEE, Kharkiv, Ukraine (2022). https://doi.org/10.1109/KhPIWeek57572.2022.9916490
27. Zuiev, O., Petrova, J.: Efficiency analysis of control and regulation processes in modern surveillance systems. In: 9th International Conference on Advanced Computer Information Technologies, pp. 9–12. IEEE, Ceske Budejovice, Czech Republic (2019). https://doi.org/10.1109/ACITT.2019.8780091
28. Galar, D., Sandborn, P., Kumar, U.: Maintenance Costs and Life Cycle Cost Analysis. CRC Press, Boca Raton (2017)
29. Sushchenko, O., et al.: Integration of MEMS inertial and magnetic field sensors for tracking power lines. In: XVIII International Conference on the Perspective Technologies and Methods in MEMS Design (MEMSTECH), pp. 33–36. IEEE, Polyana (Zakarpattya), Ukraine (2022). https://doi.org/10.1109/MEMSTECH55132.2022.10002907
30. Modarres, M., Groth, K.: Reliability and Risk Analysis. CRC Press, Boca Raton (2023)
31. McClave, J.T., Sincich, T.: Statistics, 13th edn. Pearson, London (2020)
32. Deisenroth, M.P., Faisal, A.A., Ong, C.S.: Mathematics for Machine Learning. Cambridge University Press (2020)

Relationships of Colorimetric Parameters of Digital Images of Animals' Color Under Different Ecological Situations

T. O. Klochko[1](✉), V. I. Kalashnikova[1], I. M. Bereshko[1], K. V. Nosov[2], and Yu. G. Bespalov[2]

[1] NationalAerospace University, Kharkiv Aviation Institute, 17 Chkalova Street, Kharkiv 61070, Ukraine
t.klochko@khai.edu

[2] V.N Karazin Kharkiv National University, 4 Svobody Sq., Kharkiv 61022, Ukraine

Abstract. The paper aims to is the influence of environmental situations on the systemic parameters of the protective coloration of animals. In this regard, ideally, the diversity of disruptive protective coloration of animals should coincide in space and time with the diversity of the values of colorimetric parameters of Magalef's model of succession. In the case of disruptive protective coloration of an animal, the shortage of diversity can be compensated by the evenness of values of colorimetric parameters. For Australian camels, the population and area of which are increasing very quickly, it is shown that in this case the role of diversity of disruptive protective coloration is more expressed. For kangaroos, whose population and area are more stable, the role of the even-ness of coloration is more expressed. Based on the comparative analysis of these two cases, an approach to a remote determination of the state of stability of animal populations is proposed. The proposed approach is new due to the use of correlations of captured colorimetric parameters for deter-mining the role of the diversity and evenness of disruptive protective coloration of animals. According to the results of such analysis, the subsequent diagnosis of a stable or unstable population can be performed. In connection with the meaning of obtained results, it can be about aspects related to fundamental biology problems. At the same time, practical applications of results are also possible for the development of distance (aerospace) methods for registering the state of stability of animal populations.

Keywords: adaptive strategies · protective coloration of animals · Margalef's model of succession · remote methods in ecology

1 Introduction

Global climatic changes are accompanied by deep changes in the environmental situation in many regions of our planet. These changes occur very quickly in significant spaces. it is often about spaces of a hard-to-reach terrain. This creates problems for their registration by traditional means. At the same time, these changes in the environmental situation

M. Nechyporuk et al. (Eds.): ICTM 2023, LNNS 1008, pp. 611–620, 2024.
https://doi.org/10.1007/978-3-031-61415-6_52

can give rise to various threats of biosecurity. A significant part of these threats can be associated with the violation of the animal population's stability. We are talking primarily about the violation of the stability of animal populations, which are real or potential carriers of dangerous infections or natural reservoirs of their pathogens. It should also be about animals—agricultural pests. Threats of biosecurity can appear in connection with outbreaks of numbers and bulk migrations of such animals. Outbreaks and migrations of animals are due to the change in factors stabilizing the populations of these animals. Such a factor may be, in particular, the weakening of external influence that regulates the number of animal populations. For example, a weakening of the influence of predators and competitors by reducing the number of their populations. This can also be a consequence of the violation of stability of the population, which will be the result of the change in the environmental situation. The threats of biosecurity associated with the risk of epidemics and pandemics are often due to the violation of the stability of populations of rodents and insects. Representatives of these groups of animals are often also pests of agriculture. However serious threats of biosecurity can also arise in connection with the violation of the stability of populations of other animals. A vivid example is the outbreak of numbers and mass migration of camels in Australia. These animals were delivered in Australia less than two centuries ago. During this short period, the number of their population increased very significantly with the corresponding extension of the area of distribution. During their mass migrations, Australian camels destroy, searching the water, water supply, and sewage systems of small cities in deserted areas. As a result, a serious threat of biosecurity of people arose in these cities.

The above is the relevance of the problem of expanding the arsenal of high-tech methods for registering signs of violation of animal population stability. The speed of global climatic changes and related changes in the environmental situation create some extreme aspects of this problem. It is about the following. In this situation, there may not be enough time for long-term observations of the state of populations of certain species of animals. It is about observations, the analysis of the results of which allows you to register the condition of animal populations with known traditional methods. In connection with the time shortage, there is a need for other approaches. It is about approaches to use the results of simultaneous observations of the state of the animal population for a rough assessment of the state of their population and estimation of its stability. In works [1, 2], the role of diversity and evenness of colorimetric parameters (CPs) in the strategies of performing protective coloration of animals (PCA) is described. The assumption that these strategies is affected by the environmental situation is reasonable affecting the stability of the animal population's state.

This work aims to study the influence of the environmental situation on the populations' PCA, the stability of which is significantly different. It is about the population of Australian camels, which in less than two centuries expanded their habitat to a significant part of the Australian continent accompanied by a corresponding increase in the population and Australian kangaroos, whose number of populations and area of distribution is much more stable than that of camels. An extreme factor of the current situation is not only a shortage of time to collect information about the state of animal populations. Such a factor may be the vastness of areas on which such information will need to be collected. Quite often these areas may be hard-to-reach. This causes the need to use remote (aerospace) methods. In particular, drones may be involved. In this regard, now those CPs are used, the values of which can be obtained by computer analysis of the RGB color model of digital images of animals. It is about digital images that, in principle, can be taken from a board of drones. This equipment is included in the standard supply of relatively inexpensive and widespread drone models.

2 Review of Literary Sources and Problem Statement

This work is devoted to the problem of the influence of differences in the environmental situation on PCA. It is about the differences of systemic nature observed in PCA, in which the stability of populations is significantly different. In particular due to the difference in the evolutionary history of forming these populations under certain conditions. Particularly, it is about the conditions that determine the stability of areas of distribution of the population. This stability can be relatively high like Australian kangaroos. Or the environmental situation determines the constant expansion of the area similar to the population of Australian camels.

Various aspects of animal coloration are currently an important subject of biological and environmental research [3]. For the subject of this work, the interest of research is represented by the influence on CPs of animals by changing their habitats [4, 5]. It can be about the impact of changes in natural habitats in connection with climate change [4]. Also, it can be about the artificial factors of such impact, e.g., in conditions of aquaculture [5]. The formation in the phylogenesis and ontogenesis of PCA and the adaptive strategies for its performance have quite complex systemic character. Mathematical modeling has been developed and used in this area of biological and environmental research. On the first side, we keep in mind works [6, 7] associated with direction developed by the pioneering work of A. Turing [8]. In our paper, the method of correlation pleiades was used [9, 10]. It is relatively simple and available for use by researchers who do not have special training in mathematics and computer science. The results of the application of approaches associated with this method enable in many cases to give an interpretation of the systemic nature of many aspects of the behavior of biological objects [11, 12]. In this connection, this method was applied in works [13, 14], devoted to a very wide range of zoological problems.

The aim of this work is the study of the adaptation of disruptive PCA described in [15]. Its implementation requires a color blending of part of PCA stains into the background. The effect implementation disrupts a holistic visual perception of the contour and silhouette of an animal. In this regard, PCA should have a certain degree of color diversity, which should correspond to the color diversity of the background on which the silhouette of an animal is observed. This diversity has to ensure the color blending of part of the stains into the background. In a significant number of cases, the animal silhouette will be seen on the plant background against the background of a plant community of animal habitats. The dynamics in time of CPs values of many plant communities are more or less satisfactorily described by the well-known [16] Margalef's model of succession. In [17], the results of the mathematical modeling of dynamics of Margalef's model were obtained. In the model, we used CPs obtained by computer processing of RGB color model of digital images of relatively simple phytocenosis. In present work, the following CPs were used:

- The parameter of Margalef's model corresponding to the photo-synthetic productiveness of a plant community; this parameter corresponds to the value of G/(R + G + B); the parameter of Margalef's model ("yellow-green index") reflecting stability and pigment diversity of a relatively simple plant community; this parameter corresponds to the value of R/G;
- The parameter, reflecting the summary significance of the live and dead biomass of the plant community (R + G)/(R + G + B);
- The parameter reflecting the meaning of the dead biomass of the plant community, R(R + G + B).

For a long time, for the measurement of the spectral parameters of the earth's surface, researchers used methods of the remote assessment of the state of various plant communities [18, 19]. The aforementioned CPs used in this work are rather colorimetric than spectral parameters. Remote measurements carried out with their use will be quite rough. The possibility of measuring such CPs using equipment that is included in a standard supply kit of relatively inexpensive and widespread modifications of drones is practically important.

In the paper, the aforementioned CPs are also considered as aspects of PCA performance. In particular, in connection with the adaptation role of diversity and evenness of PCA. Ideally, the colorful diversity of PCA has to be equal to the colorful diversity of CPs observed in Margalef's model. It is about diversity in time by the dynamics of Margalef's model. At the same time, it can be about the diversity of CPs of various sections of a plant community of animal habitats. In this regard, it is necessary to mention the "rechronization" method described in [17]. It is based on a premise, according to which different sections of the plant community in their dynamics are sequentially at the same phases of Margalef's model. But at the time of registration of CPs values of the plant background, these sections can be at different phases. The use of rechronization enables us to consider the diversity of values of a plant community both in time and in space. We are talking about the plant community of animal habitats, which serves as a background on which adaptive strategies for PCA are implemented. In particular, these adaptive strategies are related to the diversity of CPs values. It has already been said that the ideal strategy for the performance of PCA assumes its color diversity equal to the color diversity of the plant background. It is about the diversity of plant background in time and space, determined by the dynamics of Margalef's model of its plant community in time and the distribution in space of different values of CPs taking into account the effect described by rechronization method. But in real conditions, such a high value of PCA color diversity often cannot be achieved. This is due to the case of the concept of optimal diversity [20, 21], by which the level of diversity of biological systems can be limited by a shortage of a resource. In our case, the role of such a resource plays an angular size of the animal's silhouette. This size is limited by an optimal number of multi-colored spots in PCA. In [1, 2] was shown that the shortage of PCA diversity can be compensated by its evenness. With some probability, such compensation will have a different effect in the following two cases. It will have the best effect on animals, whose population and area of distribution are relatively stable. For PCA of such animals, we can expect more evenness in comparison with diversity. A less pronounced positive effect of this compensation can be expected in animals whose population and area of distribution increase all the time with high speed. In PCA of such animals, it can be expected more expressiveness of diversity in comparison with evenness. A very convenient indicator of the evenness and diversity of PCA in this case is the correlation of the values of certain CPs and a shift of its values in a positive or negative direction. The values of the standard deviation of these CPs are also a convenient indicator of the diversity of PCA.

This work aims to find parameters that allow, based on the results of simultaneous registration, to diagnose the state of stability of the animal population; it is about remote registration: specifically with use of computer analysis of the RGB color model of digital images.

To achieve this aim, it is supposed to solve the following problems:

- to find CPs, which correlations are different for PCA of animals with different stability of ecological conditions of performance of their populations;
- to determine systemic parameters in the structure of indicated correlations that enable to determine the stability of the population of life it is about systemic parameters related to the diversity and evenness of PCA.

3 Material and Methods

In the paper, we used the data of computer processing of free digital images of Australian camels (Camelus Dromedarius) and kangaroos (Macropus Rufus). The values of CPs mentioned in the previous section were obtained. Later, the Pearson correlation coefficient and standard deviation of specified CPs were calculated. A comparative analysis of correlation pleiads was performed.

4 Results

During the implementation of this work, the obtained results enable us to solve the research problem stated above. Specifically, to find the parameters of systemic character, which are significantly different for animals PCA, the state of the population of which is relatively stable, and for PCA, the state of the population was changed by the standards of the evolutionary process.

In connection with the solution to the above problem, we investigated the system parameters of PCA of Australian kangaroos (Macropus rufus), the formation of which population took place in relatively stable conditions of the Australian continent. Through a long evolutionary process, this animal species has evolved over a relatively stable and limited area of distribution. Due to its stability and relative limitation in size for a long period of the evolutionary history of Macropus Rufus, this area has a relatively small diversity of natural conditions. This, in particular, also determines the relatively small diversity of CPs values of the KP present in PCA occupying this area of animal species. Following the above, PCA of Australian kangaroos (Macropus rufus) is considered in present work as a working standard of protective coloration of animals whose population is in relatively stable conditions. This premise corresponds to a certain aspect of the working hypothesis used in this paper. Following the specified aspect of PCA, a relatively small diversity of CPs values should be observed in kangaroos. This relatively small diversity can, with some degree of confidence, correspond to the shift in a certain direction of the values of correlations between the values of some CPs. Specifically, the expressed tendency to a positive direction is observed. This consideration allows one to add another aspect to the above working hypothesis. Following this, there is a tendency to shift of correlations between the values of certain CPs in a positive direction for kangaroos.

Along with this, in connection with the solution to this problem, the system parameters of the PCA of Australian one-humped camel-dromedarus (*Camelus dromedarius*) were investigated. The process of the formation of a population of these animals took an extremely short term of biological evolution. Unlike the case of kangaroos, camel-dromedary existed in precarious spacial conditions. These conditions are sufficiently different from the habitat conditions in which the processes of the evolutionary history of this biological species took place. (As the existence, in which there was a domestication of camel-dromedaries the process of formation by humans in East and North Africa. It should be noted that the Australian population of camels was formed and is not being formed in the process of domestication as a result of the reverse process of becoming wild.) During the processes of introduction into the Australian desert wilderness, populations of these animals have developed on an extremely unstable in size, ever-increasing area of distribution. Due to its instability during the very short period of Camelus dromedaries introduction to vast Australian deserts, this area has a significant diversity of natural conditions. This, in particular, determines a significant diversity of CPs values in PCA of animal species occupying this area. Following the above, PCA of Australian camels (Camelus dromedarius) is considered in this work as a working standard of protective coloration of animals whose population is in unstable conditions. This premise corresponds to a certain aspect of the working hypothesis used in this paper. Following the above aspect, there should be a relatively high diversity of CPs values for Australian camels' PCA. With a certain degree of probability, this significant diversity can correspond to the shift in a certain direction of correlations between the values of some CPs. Specifically, the expressed tendency to a negative direction is observed. This consideration allows you to add another aspect to the above working hypothesis. According to this consideration, Australian camels' PCA should tend to shift the correlations between certain CPs in a negative direction.

By summing the foregoing, a working hypothesis can be put forward, according to which Australian camels' PCA has greater diversity than kangaroos' ones by certain CPs. This greater diversity can be assessed directly. For example, by the values of standard deviation of the values of specified CPs. Or indirectly, by a shift in a negative direction of the correlation values between the CPs values. We note that, following the results of [1, 2], the shortage of PCA diversity can be compensated by the evenness of CPs values. The value of the correlation coefficient between CPs can also be used as a measure of this evenness. Greater evenness corresponds to a higher value of this coefficient. It is about the above-mentioned CPs, reflecting, according to the results of [17], the parameters whose values can be obtained by computer processing digital images. It is about parameters, which change is observed in the dynamics of Margalef's model. These dynamics form the diversity of CPs in time and space of plant communities of areas of distribution of animals. PCA should be adapted to this diversity using the value of its diversity and/or evenness.

In present work, results confirming the provisions of the above working hypothesis have been obtained. They are represented in Tables 1 and 2.

Table 1. Standard deviationd of CPs of PCA of Australian kangaroos (*Macropus rufus*).

Colorimetric parameter	Standard deviation
G/(R + G + B)	0.006
R/(R + G + B)	0.03
(R + G)/(R + G + B)	0.03
R/G	0.08

Table 2. Standard deviations of CPs of PCA of Australian camels (*Camelus dromedarius*).

Colorimetric parameter	Standard deviation
G/(R + G + B)	0.037
R/(R + G + B)	0.074
(R + G)/(R + G + B)	0.06
R/G	0.86

In present work, we have found values for certain measures of diversity and evenness of PCA in Australian camels and kangaroos. The sign of correlation coefficient between the values of certain CPs was used as a measure indirectly characterizing the diversity of PCA. It is about the sign of statistically significant value ($p < 0.05$) of correlations of these CPs.

Statistically significant ($p < 0.05$) negative values of correlation between R/G and G/(R + G + B) are present in correlation pleiads for digital photos of Australian camels. This is consistent with the fact that PCA of these animals is characterized by a greater diversity of combinations of R/G and G/(R + G + B) values and possibly a greater diversity of R/G. This corresponds to a lower stability of their area and their population whose number over less than two centuries has increased significantly. At the same time, the expansion of the area of distribution should inevitably be accompanied by an increase in the diversity of habitat conditions of Australian camels. The diversity of CPs values of plant communities also increases. Note that it is about CPs of the background, at which adaptive strategies for PCA camels are implemented.

Correlation pleiads built on digital images of kangaroos' PCA, the other systemic effects are observed. Specifically, statistically significant ($p < 0.05$) positive correlations between values R/G and G/(R + G + B) are observed. There are certain grounds to assume that this may correspond to a lesser diversity of combinations of R/G and G/(R + G + B) values, in particular, due to a lesser diversity of R/G value. The further comparison of the values of standard deviation of the R/G value obtained for populations of Australian camels and kangaroos, confirms this assumption. It should also be noted that the value of correlations between R/G and G/(R + G + B) observed in PCA of camels is closer than that of kangaroos observed in Margalef's model. This can be considered as an adaptation to the relatively high diversity of CPs values Margalef's model. This is not so important for kangaroos, whose area and population are more stable than that of camels. The correlation between R/G and (G + R)/(R + G + B) values is not so noticeably different in pleiads built for Australian camels and kangaroos. In both of these cases, correlations are statistically significant ($p < 0.05$) and positive.

The Pearson correlation coefficient between G/(R + G + B) and R/(R + G + B) was used as a measure of the evenness of PCA. A comparative analysis of such a PCA indicator of Australian camels and kangaroos results in the following. It is negative and statistically significant ($p < 0.05$) for P of Australian camels. Such values of specified correlation correspond to a relatively poorly expressed degree of evenness of red and green components of PCA. For kangaroos' PCA, this correlation is positive and statistically significant ($p < 0.05$). This can be interpreted as an indicator of a higher degree of evenness of PCA red and green components.

From the point of view of our study, the following should also be noted. PCA's digital photos of camels are bored with relevant high values of standard deviation of R/G of PCA. For correlation pleiads, values of standard deviation are about ten times smaller for correlations of digital images of kangaroos' PCA.

Thus, approaches based on the analysis using the correlation, evenness, and diversity of red and green components of PCA enable possibilities to distinguish systemic colorimetric parameters, which makes it possible to diagnose the stable and unstable state of animal populations. Thus, the aim of this work has been achieved. To achieve this aim, in order to solve the problems of this work, correlations are indicated between the values of certain CPs and the values of these correlations, which can be considered as markers of the stable and unstable state of the animals' population. These approaches have some significance from the point of view of theoretical biology. At the same time, they create prerequisites for the development of remote methods for such diagnostics. That can help to solve the practical problems of elimination of some threats of biosecurity.

5 Discussion

The results obtained during the implementation of this work make it possible to give a certain interest in interpreting the role of diversity and evenness in the performance of PCA, the populations of which are in relatively stable or unstable conditions. At the same time, the evenness of PCA is interpreted as a parameter that compensates for the shortage of its diversity. The first, PCA of kangaroos, whose population is in relatively stable conditions, enables the adaptation value of such compensation. It is proposed to use the values of correlations of some CPs as markers of the diversity and evenness of PCA. It is about CPs having analogies with the dynamics of Margalef's model. These markers can be used to diagnose the state of stability of animal populations. It is about markers registered remotely and with the use of computer processing digital images. Such markers were found as a result of the comparative analysis performed. CPs, the nature of correlations between which may play the role of indicated markers, were found. The system parameters are determined in the structure of these correlations, the values of which allow one to distinguish stable states of animal populations from unstable ones.

Thus, the aim of this study has been achieved.

6 Conclusions

The results of this work, according to the authors, are purely preliminary. They were obtained based on the analysis of systemic parameters of digital images of animals, the stability of the populations of which differs significantly (Australian camels and kangaroos). The results obtained create certain prerequisites for the development of approaches to studying the influence of change in the environmental situation on PCA on wider zoological data. In particular, influences associated with global climatic changes may be studied. From the point of view of fundamental biology, the results obtained are of some interest. This interest is determined by the creation of prerequisites for expanding the arsenal of modern methods of studying adaptive strategies for PCA with use of mathematical models and computer science. At the same time, it can be about the applied importance of these results. Specifically, we can talk about finding specific systemic colorimetric parameters of PCA. Due to the increase in availability of relatively cheap drones, they can be used in automatic and automated remote registration systems of animal populations' stability. In particular, these systems can be used for the elimination of threats of biosecurity arising in connection with violation of this stability. This should include, in particular, the threats, risks of which have increased significantly in the context of global climate change.

Taking into account the aforementioned issues, the conclusion about a certain theoretical and applied interest of these is fairly reasonable.

References

1. Bespalov, Y., Nosov, K., Levchenko, O., Grigoriev, O., Hnoievyi, I., Kabalyants, P.: Mathematical modeling of the protective coloration of animals with usage of parameters of diversity and evenness. BioRxiv (2020). https://doi.org/10.1101/822999
2. Bespalov, Y., Kabalyants, P., Zuev, S.:. Relationships of diversity and evenness in adaptation strategies of the effect of protective coloration of animals. bioRxiv, 05.06.441914 (2021). https://doi.org/10.1101/2021.05.06.441914
3. Endler, J.A., Mappes, J.: The current and future state of animal coloration research. Philos. Trans. R. Soc. Lond. B Biol. Sci. **372**, 1724 (2017)
4. Panayotova, I.N., Horth, L.: Modeling the impact of climate change on a rare color morph in fish. Ecol. Model. **387**, 10–16 (2018)
5. Vissio, P.G., Darias, M.J., Di Yorio, M.P., Pérez Sirkin, D.I., Delgadin, T.H.: Fish skin pigmentation in aquaculture: the influence of rearing conditions and its neuroendocrine regulation. Gen. Comp. Endocrinol. **301**, 113662 (2021). https://doi.org/10.1016/j.ygcen.2020.113662
6. Iber, Bagnar. "Turing Pattern" (PDF). Computational Biology (CoBI). Switzerland: ETH Zurich. (2018)
7. Jeremy, B.A.: Green, computational biology: turing's lessons in simplicity. Biophys. J. **120**(19), 4139–4141 (2021)
8. Turing, A.M.: The chemical basis of morphogenesis. Philos. Trans. R. Soc. Lond. B Biol. Sci. **237**(641), 37–72 (1952). https://doi.org/10.1098/rstb.1952.0012
9. Terentev, P.V.: Metod korrelyacionnyh pleyad. Vestn Leningrad. un-ta **9**, 137–141 (1959)

10. Rostova, N.S.: Korrelyacii: struktura i izmenchivost. SPb.: 1–308 (2002)
11. Herrera, J.: The variability of organs differentially involved in pollination, and correlations of traits in genisteae (Leguminosae: Papilionoideae). Ann. Bot. **88**(6), 1027–1037 (2001)
12. Esteve-Altava, B.: In search of morphological modules: a systematic review. Biol. Rev. **92**(3), 1332–1347 (2017)
13. Klingenberg, C.P.: Cranial integration and modularity: insights into evolution and development from morphometric data. Hystrix **24**(1), 43–58 (2013)
14. Haber, A., Dworkin, I.: Disintegrating the fly: a mutational perspective on phenotypic integration and covariation. Evolution **71**(1), 66–80 (2017)
15. Duarte, R.C., Flores, A.A.V., Stevens, M.: Camouflage through colour change: mechanisms, adaptive value and ecological significance. Phil. Trans. Royal Soc. B: Biol. Sci. **372**(1724), 20160342 (2017). https://doi.org/10.1098/rstb.2016.0342
16. Margalef, R.: Some concepts relative to the organization of plankton. Oceanogr. Mar. Biol. Annu. Rev. **5**, 257–289 (1967)
17. Bespalov, Y., Nosov, K., Kabalyants, P.: Discrete dynamical model of mechanisms determining the relations of biodiversity and stability at different levels of organization of living matter. bioRxiv 161687 (2017). https://doi.org/10.1101/161687
18. Löptien, U., Dietze, H.: Retracing cyanobacteria blooms in the Baltic Sea. Sci. Rep. **12**, 10873 (2022)
19. Sirin, A.A., Medvedeva, M.A., Makarov, D.A., Maslov, A.A., Joosten, H.: Multispectral satellite based monitoring of land cover change and associated fire reduction after large-scale peatland rewetting following the 2010 peat fires in Moscow region (Russia). Ecol. Eng. **158**, 106044 (2020). https://doi.org/10.1016/j.ecoleng.2020.106044
20. Bukvareva, E.N. The principle of optimal biodiversity and ecosystem functioning / E. N. Bukvareva, G. M. Aleshchenko. Int. J. Ecosyst. **2**(4), 78–87 (2012)
21. Bukvareva, E.N. Optimization, niche and neutral mechanisms in the formation of biodiversity / E. N. Bukvareva, G. M. Aleshchenko. Am. J. Life Sci. **1**(4), 174–183 (2013)

Frequency Sub-band Reduction of Spatially Correlated Noise in Images

Oleksandr Miroshnichenko[1], Mykola Ponomarenko[2](✉), Sergey Abramov[1], and Vladimir Lukin[1]

[1] Kharkiv Aviation Institute, National Aerospace University, Kharkiv, Ukraine
[2] Tampere University, Tampere, Finland
mykola.ponomarenko@tuni.fi

Abstract. This study addresses the challenge of mitigating additive spatially correlated noise in images. Our proposed solution involves breaking down the image into frequency sub-bands and individually reducing noise in each segment. By doing so, the noise spectrum within each sub-band becomes more uniform compared to the entire image, enabling the effective use of a neural network originally designed for reducing additive white Gaussian noise. This segmented approach enhances the method's flexibility and adaptability, particularly in handling noise with varying levels of horizontal and vertical correlation. We also investigated the enhancement of noise suppression efficiency through preliminary equalization of noise levels across different frequency sub-bands. Comparative analyses reveal that our method achieves state-of-the-art peak signal-to-noise ratios in processed images, effectively handling both white and spatially correlated Gaussian noise.

Keywords: image denoising · spatially correlated noise · convolutional neural networks

1 Introduction

Noise suppression remains a longstanding challenge in digital image processing [1]. As digital camera technology continues to evolve, with heightened demands for high-quality low-light photography, coupled with increased sensor resolutions achieved through reduced pixel sizes, the imperative for effective noise suppression has become increasingly critical [2–5].

In the present study, we address the challenge of restoring an original, noise-free image $\boldsymbol{x}$ from its noisy representation $\boldsymbol{y} = \boldsymbol{x}+\boldsymbol{n}\otimes\boldsymbol{k}$, where the image degradation involves an additive white Gaussian noise (AWGN) denoted by $\boldsymbol{n}$, with a standard deviation σ. The operation $\otimes\boldsymbol{k}$ signifies a two-dimensional convolution with a blur kernel $\boldsymbol{k}$. Consequently, the image $\boldsymbol{x}$ is degraded by additive spatially correlated Gaussian noise (ASCGN), which is a result of the convolution $\boldsymbol{n} \otimes \boldsymbol{k}$.

The occurrence of ASCGN can be observed in various stages of image handling, including acquisition and processing phases. Common examples include digital zooming, image super-resolution, residual noise following incomplete noise elimination,

M. Nechyporuk et al. (Eds.): ICTM 2023, LNNS 1008, pp. 621–631, 2024.
https://doi.org/10.1007/978-3-031-61415-6_53

applying geometrical transforms to noisy images, rendering of 3D scenes, demosaicing, and the compression of noisy images in a lossy format. In the context of this research, for ease of noise modeling, we assume $\boldsymbol{k}$ to be a rotationally symmetric Gaussian low-pass filter, characterized by a standard deviation σ_k. Within this framework, the noise intensity is indicated by the σ value, while σ_k value depicts the extent of correlation among the noise values in adjacent pixels of the image.

While the removal of AWGN and the estimation of its variance [6–9] have been extensively explored, the challenges presented by ASCGN are inherently more complex [2, 10–12]. The presence of correlation between noise in neighboring image pixels greatly complicates the separation of the image into information and noise components.

To effectively suppress correlated noise, it's essential to accurately estimate its spectrum and develop robust algorithms for its reduction. However, this task is challenging due to the diverse range of spatially correlated noise parameters and the additional distortions that are often present in practical scenarios [11, 12].

While there are numerous effective denoising neural networks intended for AWGN removing, such as DRUNet [3] and Restormer [4], adapting these methods for suppressing ASCGN is a crucial task.

Additionally, there are blind denoising methods, such as VDNet [4, 13], which could potentially be used for ASCGN removal. However, these methods require training with a specific noise spectrum, which is not known in advance. This limitation significantly restricts their effectiveness in dealing with ASCGN.

In this paper, we introduce a novel and adaptable approach for ASCGN removal. Our method involves splitting an image into frequency sub-bands, followed by sequential noise reduction within these components. We explore various strategies for denoising these frequency sub-bands and methods for initially whitening the noise in the image before processing.

Section 2 details our rationale for selecting DRUNet as the primary noise suppression tool in our method. In Sect. 3, we describe our proposed denoising scheme and examine its quasi-optimal parameters. Section 4 presents a numerical analysis, comparing the effectiveness of our proposed scheme against current state-of-the-art methods.

2 Choosing an Effective Method for AWGN Suppression

In our proposed technique, we require a method for suppressing AWGN that remains effective even when the noise characteristics, especially its spectrum, slightly deviate from AWGN. Deep learning networks, like Restormer [4], are currently leading in AWGN suppression effectiveness. However, many of these networks are trained for very specific scenarios. Restormer, for instance, achieves optimal noise reduction when trained for a particular standard deviation of AWGN. This specificity makes it less effective when faced with noise characteristics that slightly differ from AWGN.

In contrast, the DRUNet [3] network is designed for flexibility. It can process images with a map indicating varying standard deviations of noise for each pixel. This feature makes DRUNet more adaptable to variations in noise characteristics.

To evaluate these networks in practical scenarios, we conducted a comparative analysis using DRUNet and Restormer. We considered two situations: AWGN with a standard deviation $\sigma = 15$, and ASCGN with $\sigma = 15$ and a correlation factor $\sigma_k = 0.5$.

Here, $\sigma_k = 0.5$ represents a relatively low level of spatial noise correlation, where an AWGN-oriented method might still perform well.

The comparison, based on the performance of both methods across 300 images from the Tampere17 dataset [6] for both noise types, is presented in Table 1.

Table 1. Effectiveness of noise reduction by DRUNet and Restormer, PSNR, dB

Noise type	Noisy	DRUNet	Restormer, pre-trained for $\sigma = 15$	Restormer, pre-trained for blind denoising
AWGN, $\sigma = 15$	24.7	31.4	31.4	30.6
ASCGN, $\sigma = 15$, $\sigma_k = 0.5$	24.7	29.6	27.4	25.8

From our analysis, it's evident that for AWGN, both DRUNet and Restormer (when pre-trained for $\sigma = 15$) exhibit roughly equivalent noise suppression efficiency. However, the scenario changes with ASCGN. In this case, the performance of Restormer, whether pre-trained for $\sigma = 15$ or for blind denoising, significantly decreases, whereas DRUNet maintains a markedly better, on 2 dB, performance level.

This difference is clearly demonstrated in Fig. 1, where we processed an image from the Tampere17 set distorted by ASCGN. The figure shows that after processing with DRUNet, some residual noise remains visible in uniform areas like the sky, but its overall level is substantially reduced. On the other hand, the image processed with Restormer exhibits almost no reduction in visible noise, providing PSNR by 5 dB smaller than DRUNet.

Given the focus of this paper on robustness against ASCGN, we have decided to utilize the DRUNet network as the foundation for our proposed method.

3 Proposed Denoising Scheme

Our proposed method involves dividing the image into frequency sub-bands, where the noise characteristics more closely resemble AWGN, as illustrated in Fig. 2.

To streamline our analysis, we employ a 2x2 Haar transform, splitting the image into four distinct frequency sub-bands: low frequencies *LL*, high frequencies in the vertical and low frequencies in the horizontal direction *HL*, low frequencies in the vertical and high frequencies in the horizontal direction *LH*, and high frequencies *HH*.

One key benefit of using this transformation is that it does not introduce nonlinear distortions into the image, thereby preserving the original noise distribution parameters. However, a limitation is the relatively coarse segmentation of the image's frequency components.

In cases of correlated noise with high σ_k values, the *LL* sub-band, which essentially represents a downscaled version of the original image, can be further subdivided into four additional subranges. For the sake of simplicity in our study, we will operate under

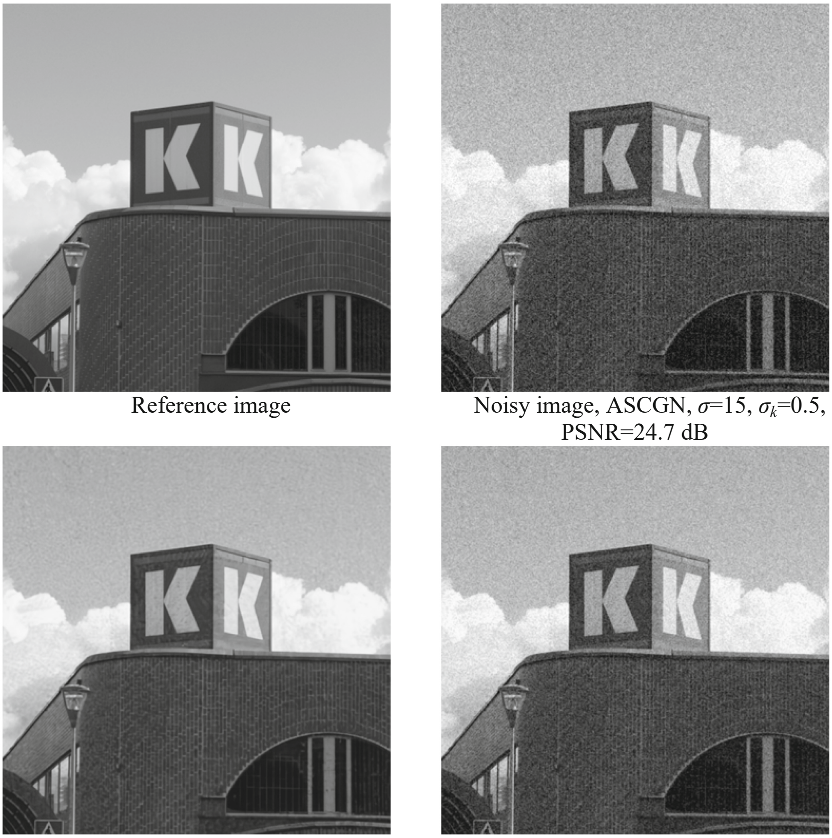

Reference image

Noisy image, ASCGN, σ=15, σ_k=0.5, PSNR=24.7 dB

DRUNet, PSNR=33.6 dB

Restormer, PSNR=28.2 dB

Fig. 1. Example of image t062 of Tampere17 set, distorted by ASCGN, and its denoising by DRUNet and Restormer, pre-trained for suppression of AWGN

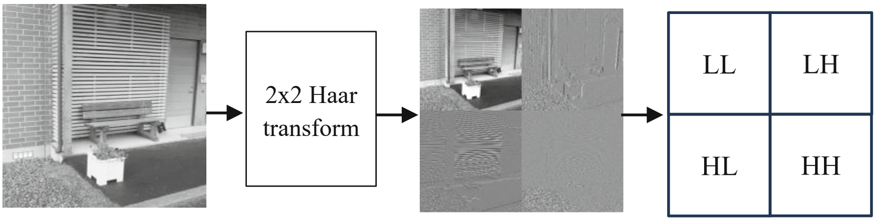

Fig. 2. Illustration for dividing an image on sub-bands, which is used in the paper

the assumption that the standard deviations of noise in each frequency sub-band (σ_{LL}, σ_{HL}, σ_{LH}, and σ_{HH}) are either known a priori or estimated using one of the existing methods for blind noise level assessment in images [6–9].

We then apply the DRUNet network [3] to individually suppress noise in each of these frequency sub-bands.

The process begins by targeting the lowest frequency components and progresses towards the highest frequencies. In the noise suppression stage for high-frequency components, we construct an image comprising the high frequencies (still affected by noise) and the low frequencies that have already been processed. This approach aids DRUNet in more effectively analyzing and processing the high-frequency components.

DRUNet is versatile across a range of noise parameters, but it achieves optimal performance with AWGN. Therefore, while processing each frequency sub-band, we aim to temporarily equalize the noise level in the lower frequency sub-bands to match the noise level in the sub-band currently being addressed. This step ensures more consistent noise characteristics across the frequency spectrum, enhancing DRUNet's efficiency.

Upon completing the noise reduction in each individual frequency sub-band, we reconstruct the final image by aggregating the processed frequency sub-bands. This reconstruction is achieved using an inverse Haar transform, resulting in a composite image where noise has been effectively reduced across all frequencies.

3.1 Processing of Low Frequency Sub-band

Let us explore four different approaches for noise suppression in the low-frequency sub-band LL of a given image, denoted as I.

Scheme SLL1. Given that the LL sub-band essentially represents a downscaled version of the original image I, we can treat and process it independently. In this scheme, the LL sub-band is processed using the DRUNet network, with σ_{LL} (the standard deviation of noise in the LL sub-band) as the input parameter of DRUNet:

$$LL^n = \text{DRUNET}(LL, \sigma_{LL}), \tag{1}$$

where DRUNET(X,Y) is output of DRUNet network with input image X and input noise level Y.

Scheme SLL2. In this approach, instead of focusing solely on the low-frequency sub-band, the entire image I is processed through the DRUNet network. Here, the input parameter for noise level is σ_I, which represents the overall noise level of the entire image:

$$LL^n = \text{Haar}^{\text{LL}}(\text{DRUNET}(I, \sigma_I)), \tag{2}$$

where $\text{Haar}^{\text{LL}}(\text{X})$ is frequency sub-band LL of the 2D array X.

Scheme SLL3. In cases of spatially correlated noise, the standard deviation of noise in the LL sub-band σ_{LL} is typically higher than in the LH, HL, and HH sub-bands. To address this, we can artificially increase the noise levels in the LH, HL, and HH sub-bands, making their noise standard deviations (σ_{LH}, σ_{HL}, and σ_{HH}) equal to that of σ_{LL}. After this adjustment, we process the modified image, which we'll call I^{an}, using the DRUNet network with the noise level set to σ_{LL}. This method aims to create a uniform noise level across all sub-bands, potentially enhancing the effectiveness of the noise reduction process:

$$LL^n = \text{Haar}^{\text{LL}}(\text{DRUNET}(I^{an}, \sigma_{LL})). \tag{3}$$

Scheme SLL4. Entire image I is processed by the DRUNet network. Here, the input parameter for noise level is σ_{LL}, which represents the noise level in the LL sub-band:

$$LL^n = \mathrm{Haar}^{\mathrm{LL}}(\mathrm{DRUNET}(I, \sigma_{LL})) \tag{4}$$

Table 2 presents the results from a comparative analysis of the aforementioned noise suppression schemes. This analysis was conducted on 300 images from the Tampere17 dataset, each distorted by ASCGN with parameters $\sigma = 15$ and $\sigma_k = 0.5$.

Table 2. Effectiveness of different schemes of LL sub-band denoising, PSNR, dB

Noise type	Noisy	SLL1	SLL2	SLL3	SLL4
ASCGN, $\sigma = 15$, $\sigma_k = 0.5$	22.7	27.1	26.4	27.1	27.2

From these results, it's evident that Scheme SLL2, which uses the overall noise level of the image (σ_I, noted to be lower than σ_{LL}) as the input parameter for the DRUNet network, yields significantly poorer noise suppression compared to the other methods. Meanwhile, Scheme SLL4 demonstrates a marginal improvement, outperforming both SLL1 and SLL3 by approximately 0.1 dB in terms of PSNR.

3.2 Processing of Medium Frequency Sub-band

Let's examine four potential approaches for reducing noise in the mid-frequency sub-band LH of a given image I. The same methods will also be applied to the HL sub-band.

Scheme SLH1. This strategy involves processing the entire image I using the DRUNet network. Here, the noise level parameter set for the network is σ_I, representing the overall noise level across the entire image:

$$LH^n = \mathrm{Haar}^{\mathrm{LH}}(\mathrm{DRUNET}(I, \sigma_I)), \tag{5}$$

where $\mathrm{Haar}^{\mathrm{LH}}(\mathrm{X})$ is frequency sub-band LH of the 2D array X.

Scheme SLH2. Entire image I is processed by the DRUNet network with the input parameter for noise level equal *to* σ_{LH}:

$$LH^n = \mathrm{Haar}^{\mathrm{LH}}(\mathrm{DRUNET}(I, \sigma_{LH})). \tag{6}$$

Scheme SLH3. In this method, we substitute the low-frequency LL component of the image I with its processed counterpart, denoted as LL^n. Then, we process the resulting image, which we'll refer to as I^L, through the DRUNet network. The noise level parameter for this processing is set to σ_{LH}, specifically targeting the noise characteristics of the LH sub-band. This approach focuses on refining the image by integrating the already processed low-frequency component with the mid-frequency components for more effective noise reduction.

$$LH^n = \mathrm{Haar}^{\mathrm{LH}}(\mathrm{DRUNET}(I^L, \sigma_{LH})). \tag{7}$$

Scheme SLH4. This approach involves a more complex manipulation of the low-frequency LL component. First, we estimate the residual noise level, σ_{LLR}, in the processed low-frequency component LL^n. We then reintroduce a portion of the suppressed noise back into LL^n to match its noise level with that of the LH sub-band:

$$LL^m = LL^n + (LL - LL^n)\left(\sigma_{LH}^2 - \sigma_{LLR}^2\right)^{0.5} / \left(\sigma_{LL}^2 - \sigma_{LLR}^2\right)^{0.5}. \tag{8}$$

In this formula, LL^m represents the modified low-frequency component. Next, we replace the original low-frequency LL component in image I with this adjusted component LL^m. The resulting image, now denoted as I^M, is processed using the DRUNet network with the noise level set to σ_{LH}. This method aims to harmonize the noise levels between the low and mid-frequency components, potentially enhancing the overall effectiveness of noise reduction:

$$LH^n = \text{Haar}^{\text{LH}}\left(\text{DRUNET}\left(I^M, \sigma_{LH}\right)\right). \tag{9}$$

Table 3 presents a comparison of the results for the different noise suppression schemes applied to 300 images from the Tampere17 set, each distorted by ASCGN with parameters $\sigma = 15$ and $\sigma_k = 0.5$.

Table 3. Effectiveness of different schemes of LH and HL sub-bands denoising, PSNR, dB

Noise type	Noisy	SLH1	SLH2	SLH3	SLH4
ASCGN, $\sigma = 15, \sigma_k = 0.5$	25.0	30.7	30.7	31.0	31.1

From this comparison, it's observed that the noise equalization technique used in Scheme SLH4 results in a slightly improved PSNR. Specifically, SLH4 achieves a PSNR that is 0.1 dB higher than that of SLH3, indicating a marginal yet measurable enhancement in noise suppression effectiveness.

3.3 Processing of High Frequency Sub-band

Let's explore four potential strategies for mitigating noise in the high-frequency HH sub-band of a specific image I.

Scheme SHH1. This approach entails processing the entire image I through the DRUNet network. The noise level parameter set for the network in this case is σ_I, which represents the overall noise level of the image:

$$HH^n = \text{Haar}^{\text{HH}}(\text{DRUNET}(I, \sigma_I)), \tag{10}$$

where $\text{Haar}^{\text{HH}}(\text{X})$ is frequency sub-band HH of the 2D array X.

Scheme SHH2. Entire image I is processed by the DRUNet network with the input parameter for noise level equal to σ_{HH}:

$$HH^n = \text{Haar}^{\text{HH}}(\text{DRUNet}(I, \sigma_{HH})). \tag{11}$$

Scheme SHH3. In this method, we replace both the low-frequency and mid-frequency components of the image I with their processed versions, LL^n, HL^n, and LH^n. Once these components are substituted, the resulting composite image, which we'll call I^L, is processed through the DRUNet network. For this processing, the noise level is set to σ_{HH}, aligning with the noise characteristics of the HH (high-frequency) sub-band. This approach aims to integrate the refined low and mid-frequency components with the high-frequency component for a more effective overall noise reduction:

$$HH^n = \text{Haar}^{\text{HH}}(\text{DRUNet}(I^L, \sigma_{HH})). \tag{12}$$

Scheme SHH4. In this approach, we use Eq. (8) to equalize the residual noise levels in the processed components LL^n, LH^n, and HL^n to match σ_{HH}, the noise level of the high-frequency HH sub-band. After adjusting these components, we combine them with the unprocessed HH component to create a new image, which we will refer to as I^T. Once formed, this I^T image is processed through the DRUNet network, with the noise level parameter set to σ_{HH}. This method is designed to harmonize the noise characteristics across all frequency components before the final noise reduction step, potentially improving the effectiveness of the overall noise suppression:

$$HH^n = \text{Haar}^{\text{HH}}\left(\text{DRUNet}\left(I^T, \sigma_{HH}\right)\right). \tag{13}$$

Table 4 presents the outcomes from comparing the different noise suppression schemes applied to 300 images from the Tampere17 set. These images were distorted by ASCGN with parameters $\sigma = 15$ and $\sigma_k = 0.5$.

Table 4. Effectiveness of different schemes of HH sub-band denoising, PSNR, dB

Noise type	Noisy	SHH1	SHH2	SHH3	SHH4
ASCGN, $\sigma = 15$, $\sigma_k = 0.5$	27.3	33.3	33.2	32.9	33.5

The data reveals that within this specific high-frequency range, the Scheme SHH4, which involves equalizing the noise level across the different frequency components, demonstrates the best performance. This indicates that the noise level equalization strategy used in SHH4 is particularly effective for this set of images and noise conditions.

4 Numerical Analysis

The previous section demonstrated that the most effective way to use the DRUNet network for suppressing ASCGN is through sequential noise reduction in the frequency sub-bands LL, HL, LH, and HH. This is achieved by employing the denoising schemes SLL4, SLH4, and SHH4, respectively. Notably, SLH4 and SHH4 incorporate noise level equalization across the image's frequency sub-ranges. For convenience, we will refer to this combined approach as DRUNet + Haar.

Next, we will compare the effectiveness of our DRUNet + Haar method against several other techniques: the standard application of the DRUNet network using an average image noise level [11], the Restormer network [4], and state-of-the-art methods for ASCGN suppression, namely DRUNET + NLNET + M2 [11] and NSPNet + GDNet [12].

The results of this comparative analysis, conducted on 300 images from the Tampere17 set, are summarized in Table 5.

Table 5. Effectiveness of noise reduction by compared methods, PSNR, dB

Noise type	Noisy	DRUNet	Restormer	NSPNet + GDNet	DRUNet + NLNet + M2	Proposed scheme DRUNet + Haar
AWGN, $\sigma = 15$	24.7	**31.4**	**31.4**	30.8	30.5	**31.4**
ASCGN, $\sigma = 15$, $\sigma_k = 0.5$	24.7	29.6	27.4	29.9	29.8	**30.1**

The data clearly indicates that our DRUNet + Haar denoising approach not only outperforms the standard use of DRUNet by 0.5 dB in suppressing ASCGN but also surpasses the two state-of-the-art methods evaluated, DRUNet + NLNet + M2 and NSPNet + GDNet.

Additionally, the DRUNet + Haar method demonstrates a performance in suppressing AWGN that is on par with both DRUNet and Restormer. This underscores the versatility of DRUNet + Haar, positioning it as a universal solution effective for both ASCGN and AWGN suppression.

The effectiveness of ASCGN reduction using these methods is visually represented in Fig. 3. This figure features a comparison based on the denoising of an image from the Tampere17 set, illustrating the practical impact of these techniques.

It is clear that for DRUNet and especially for Restormer there is visible residual noise on the denoised image.

One can see also, that NSPNet + GDNet and DRUNet + NLNet + M2 produce oversmoothed images with removed of most low contrast high frequency details.

At the same time, the proposed DRUNet + Haar not only provides the best PSNR value of denoised image, but better preserves fine details and low contrast textures, providing best visual quality among compared methods.

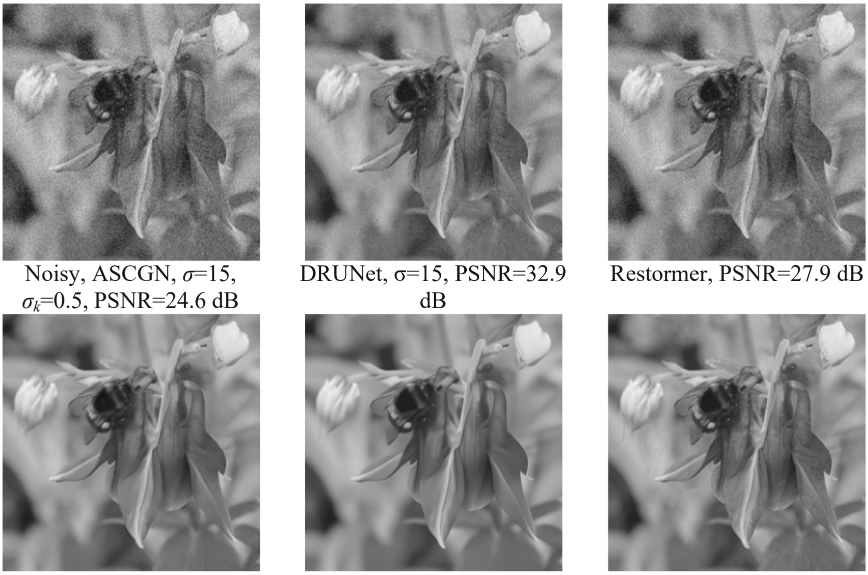

Noisy, ASCGN, σ=15, σ_k=0.5, PSNR=24.6 dB

DRUNet, σ=15, PSNR=32.9 dB

Restormer, PSNR=27.9 dB

NSPNet + GDNet, PSNR=35.1 dB

DRUNet + NLNet + M2, PSNR=35.0 dB

Proposed scheme DRUNet+Haar, PSNR=35.3 dB

Fig. 3. Example of image t095 of Tampere17 set, denoised by compared methods

5 Conclusions

This paper introduces a novel and straightforward DRUNet-Haar scheme for suppressing ASCGN, utilizing sequential noise reduction across the frequency sub-bands of an image. The scheme offers a versatile solution for noise suppression across various spectral types, including noise with differing horizontal and vertical correlations. This versatility eliminates the need for numerous specialized denoising neural networks, as one efficient DRUNet network trained for AWGN suffices.

Our findings demonstrate that the combination of DRUNet with the proposed noise level equalization technique, dubbed DRUNet + Haar, achieves superior ASCGN suppression compared to other examined methods. Importantly, DRUNet + Haar maintains the original AWGN suppression efficiency characteristic of the DRUNet network.

Additionally, DRUNet + Haar has shown a better capability in preserving fine details and textures in images than other state-of-the-art ASCGN suppression methods. However, it's important to note that the effectiveness of this scheme depends on either a priori knowledge or accurate estimation of noise levels in the image's frequency subbands. This underscores the importance of developing reliable methods for such blind estimation of noise spectra.

The efficacy of DRUNet + Haar largely relies on the robustness of the DRUNet network against deviations between the noise characteristics and standard AWGN parameters. Thus, employing even more robust networks in place of DRUNet or optimizing DRUNet specifically for this task could further enhance ASCGN suppression.

Moreover, exploring different transformations beyond the Haar transform for dividing the image into frequency sub-bands may potentially lead to even greater efficiency in noise suppression.

References

1. Astola, J., Kuosmanen, P.: Fundamentals of Nonlinear Digital Filtering. CRC Press (1997)
2. Mäkinen, Y., Azzari, L., Foi, A.: Collaborative filtering of correlated noise: exact transform-domain variance for improved shrinkage and patch matching. IEEE Trans. Image Process. **29**, 8339–8354 (2020)
3. Zhang, K., Li, Y., Zuo, W., Zhang, L., Van Gool, L., Timofte, R.: Plug-and-play image restoration with deep denoiser prior. arXiv preprint arXiv:2008.13751 (2020)
4. Zamir, S.W., Arora, A., Khan, S., Hayat, M., Khan, F.S., Yang, M.H.: Restormer: efficient transformer for high-resolution image restoration. In: Proceedings of the IEEE/CVF Conference on Computer Vision and Pattern Recognition, pp. 5728–5739 (2022)
5. Zhang, K., Zuo, W., Zhang, L.: FFDNet: toward a fast and flexible solution for CNN-based image denoising. IEEE Trans. Image Process. **27**(9), 4608–4622 (2018)
6. Ponomarenko, M., Gapon, N., Voronin, V., Egiazarian, K.: Blind estimation of white Gaussian noise variance in highly textured images. In: Proceedings of International Conference Image Processing: Algorithms and Systems, p. 5 (2018)
7. Pyatykh, S., Hesser, J., Zheng, L.: Image noise level estimation by principal component analysis. IEEE Trans. Image Process. **22**(2), 687–699 (2013). https://doi.org/10.1109/TIP.2012.2221728
8. Liu, X., Tanaka, M., Okutomi, M.: Noise level estimation using weak textured patches of a single noisy image. In: IEEE International Conference on Image Processing, pp. 665–668 (2012)
9. Bahnemiri, S.G., Ponomarenko, M., Egiazarian, K.: Learning-based noise component map estimation for image denoising. IEEE Signal Process. Lett. **29**, 1407–1411 (2022)
10. Ponomarenko, M., Bahnemiri, S.G., Egiazarian, K.: Deep convolutional network for spatially correlated Rayleigh noise suppression on TerraSAR-X images. In: IEEE 6th International Symposium on Microwaves, Radar and Remote Sensing, pp. 458–463 (2020)
11. Ponomarenko, M., Miroshnichenko, O., Lukin, V., Egiazarian, K.: Blind estimation and suppression of additive spatially correlated Gaussian noise in images. In: European Workshop on Visual Information Processing, p. 6 (2021)
12. Ponomarenko, M., Miroshnichenko, O., Lukin, V., Krivenko, S., Egiazarian, K.: Blind denoising of dental X-Ray images. Electron. Imaging **35**, 1–6 (2023)
13. Yue, Z., Yong, H., Zhao, Q., Zhang, L., Meng, D.: Variational denoising network: toward blind noise modeling and removal. arXiv preprint arXiv:1908.11314 (2019)

Author Index

M. Nechyporuk et al. (Eds.): ICTM 2023, LNNS 1008, pp. 633–635, 2024.
https://doi.org/10.1007/978-3-031-61415-6